CD-ROM Included



2014

Magnesium Technology

EDITED BY

Martyn Alderman

Michele V. Manuel

Norbert Hort

Neale R. Neelameggham

TMS

WILEY

Magnesium Technology 2014

TMS2014

143rd Annual Meeting & Exhibition



New proceedings volumes from the TMS2014 Annual Meeting, available from publisher John Wiley & Sons:

- 5th International Symposium on High-Temperature Metallurgical Processing
- Advanced Composites for Aerospace, Marine, and Land Applications
- Celebrating the Megascale: Proceedings of the Extraction and Processing Division Symposium on Pyrometallurgy in Honor of David G.C. Robertson
- Characterization of Minerals, Metals, and Materials 2014
- Energy Technology 2014: Carbon Dioxide Management and Other Technologies
- EPD Congress 2014
- Light Metals 2014
- Magnesium Technology 2014
- Rare Metal Technology 2014
- Shape Casting: 5th International Symposium 2014
- TMS 2014 Supplemental Proceedings

To purchase any of these books, visit www.wiley.com.

TMS members: Log in to the Members Only area of www.tms.org and learn how to get your discount on these and other books offered by Wiley.



Magnesium Technology 2014

Proceedings of a symposium sponsored by the
Magnesium Committee of the Light Metals Division of
The Minerals, Metals & Materials Society (TMS)
held during

TMS2014
143rd Annual Meeting & Exhibition

February 16-20, 2014
San Diego Convention Center
San Diego, California, USA

Edited by:

Martyn Alderman

Michele V. Manuel

Norbert Hort

Neale R. Neelameggham

WILEY | TMS

Copyright © 2014 by The Minerals, Metals & Materials Society.
All rights reserved.

Published by John Wiley & Sons, Inc., Hoboken, New Jersey.
Published simultaneously in Canada.

No part of this publication may be reproduced, stored in a retrieval system, or transmitted in any form or by any means, electronic, mechanical, photocopying, recording, scanning, or otherwise, except as permitted under Section 107 or 108 of the 1976 United States Copyright Act, without either the prior written permission of The Minerals, Metals, & Materials Society, or authorization through payment of the appropriate per-copy fee to the Copyright Clearance Center, Inc., 222 Rosewood Drive, Danvers, MA 01923, (978) 750-8400, fax (978) 750-4470, or on the web at www.copyright.com. Requests to the Publisher for permission should be addressed to the Permissions Department, John Wiley & Sons, Inc., 111 River Street, Hoboken, NJ 07030, (201) 748-6011, fax (201) 748-6008, or online at http://www.wiley.com/go/permission.

Limit of Liability/Disclaimer of Warranty: While the publisher and author have used their best efforts in preparing this book, they make no representations or warranties with respect to the accuracy or completeness of the contents of this book and specifically disclaim any implied warranties of merchantability or fitness for a particular purpose. No warranty may be created or extended by sales representatives or written sales materials. The advice and strategies contained herein may not be suitable for your situation. You should consult with a professional where appropriate. Neither the publisher nor author shall be liable for any loss of profit or any other commercial damages, including but not limited to special, incidental, consequential, or other damages.

Wiley also publishes books in a variety of electronic formats. Some content that appears in print may not be available in electronic formats. For more information about Wiley products, visit the web site at www.wiley.com. For general information on other Wiley products and services or for technical support, please contact the Wiley Customer Care Department within the United States at (800) 762-2974, outside the United States at (317) 572-3993 or fax (317) 572-4002.

Library of Congress Cataloging-in-Publication Data is available.

ISBN 978-1-118-88816-2

Printed in the United States of America.

10 9 8 7 6 5 4 3 2 1

WILEY | TMS

TABLE OF CONTENTS
Magnesium Technology 2014

Preface xiii
About the Editors xv
Session Chairs xix
Reviewer Pool xxi

Keynote Session

Automotive Magnesium: Impacts and Opportunities 3
W. Joost

Alloy Development, Manufacturing and Design for Magnesium Applications 5
A. Luo

Life Cycle Assessment of Eco-Magnesium® Alloy Produced by Green Metallurgy EU Project Process Route 7
F. D'Errico, G. Plaza, F. Giger, and S. Kim

The IMA Study on the Life Cycle Assessment (LCA) of Magnesium 13
H. Friedrich, and S. Ehrenberger

Dynamic Behaviour of a Rare Earth Containing Mg Alloy, WE43B-T5, Plate with Comparison to Conventional Alloy, AM30-F 15
S. Agnew, W. Wittington, A. Oppedal, H. El Kadiri, M. Shaeffer, K. Ramesh, J. Bhattacharyya, R. DeLorme, and B. Davis

Thermodynamic and Kinetic Calculations for TRC (Twin Roll Casting) Mg Alloy Design 17
I. Jung and M. Paliwal

Powders, Recycling, Hydrometallurgy, Primary Production, and Creep

Emerging Applications Using Magnesium Alloy Powders: A Feasibility Study 21
R. Tandon and D. Madan

Isothermal Hydrogenation Kinetics Study of Magnesium Hydride with TiH_2 Additive 27
J. Li, P. Fan, C. Zhou, and Z. Fang

Magnesium Electrorefining in Non-Aqueous Electrolyte at Room Temperature 31
K. Kwon, J. Park, P. Kusumah, B. Dilasari, H. Kim, and C. Lee

Recovery of Rare Earth Metals in Used Magnets by Molten Magnesium 35
T. Akahori, Y. Miyamoto, T. Saeki, M. Okamoto, and T. Okabe

Recovery of Magnesium and Recycling of Spent Solution in Chloride-Based Atmospheric Acid Leaching of Nickel Laterite 39
Y. Ge, W. Ding, D. Tan, and S. Guo

Effect of Physical Properties of Dolomite on Carbothermic Reduction 43
S. Wang, Y. Wang, G. Bin, and J. Diao

Time Dependent Springback of a Magnesium Alloy....49
B. Li, Z. McClelland, S. Horstemeyer, I. Aslam, P. Wang, and M. Horstemeyer

Precipitate Formation in Uniaxially Stressed High Pressure Die Cast Binary Mg-Nd Alloy during Creep Testing...55
D. Choudhuri, S. Nag, N. Dendge, M. Gibson, and R. Banerjee

A Review of the Influence of Production Methods and Intermetallic Phases on the Creep Properties of AZ91.....59
P. Roodposhti, A. Sarkar, and K. Murty

Indentation Creep Behavior of Mg-10Gd-3Y-0.5Zr (wt.%) Alloy at Elevated Temperatures 65
H. Wang, Q. Wang, and J. Yuan

Deformation I

The Athermal Component of the Strength of Binary Mg Solid Solutions.....73
S. Abaspour and C. Cáceres

Crack Propagation under Bending in Cast Mg10GdxNd-T4 Alloys 77
P. Maier, C. Mendis, M. Wolff, and N. Hort

High Shear Deformation to Produce High Strength and Energy Absorption in Mg Alloys 83
V. Joshi, S. Jana, D. Li, H. Garmestani, E. Nyberg, and C. Lavender

As-Cast Microstructure and Texture of Twin-Roll Cast AZ31 89
M. Masoumi, F. Zarandi, and M. Pekguleryuz

Post Deformation Annealing Behaviour of Mg-Al-Sn Alloys.....95
A. Kabir, J. Su, M. Sanjari, I. Jung, and S. Yue

Acoustic Emission Analysis of Plane Strain-Compressed Mg Single Crystals 101
D. Drozdenko, P. Dobroň, M. Knapek, D. Letzig, J. Bohlen, and F. Chmelík

Precipitation Strengthening of a Mg-Zn Alloy in Tension and Compression.....105
J. Rosalie, H. Somekawa, and A. Singh

Characterization of Damage in Magnesium Using Digital Image Correlation and Electron Backscattered Diffraction Patterning 111
M. Nemcko, P. Mas, M. Bruhis, and D. Wilkinson

Low Cycle Fatigue Properties of Extruded Mg10GdxNd Alloys.....115
G. Tober, P. Maier, S. Müller, and N. Hort

Quantification of Microstructure-Properties-Behavior Relations in Magnesium Alloys Using a Hybrid Approach 121
K. Hazeli, J. Cuadra, P. Vanniamparambil, R. Carmi, and A. Kontsos

Deformation II

Dislocation Activity in AZ31B Magnesium Deformed at Moderately Elevated Temperatures via EBSD 127
T. Ruggles, A. Khosravani, D. Fullwood, and M. Miles

Deformation, Recrystallization and Grain Growth Behavior of Large-Strain Hot Rolled Binary Mg-1Dy Alloy....133
I. Basu and T. Al-Samman

Strain Recrystallization and Grain Growth in AZ31B-H24 Magnesium Alloy Sheet.....139
A. Antoniswamy, J. Carter, L. Hector Jr., and E. Taleff

Deformation Behavior and Dynamic Recrystallization of Micro-Alloyed Mg-Al-Ca Alloys during High Temperature Deformation 143
J. Su, A. Kabir, I. Jung, and S. Yue

Physically-Based Model for Static Recrystallization in AZ31 149
P. Okrutny, S. Liang, L. Meng, and H. Zurob

The Role of Deformation Modes on Ductility and Dynamic Recrystallization Behavior of AZ31 Mg Alloy at Low Temperatures 155
E. Dogan, M. Vaughan, C. Hayrettin, I. Karaman, and G. Ayoub

Effect of Microstructure on Deformation and Fracture of Thixomolded and Thermomechanically Processed AZ61 161
T. Berman, W. Donlon, R. Decker, T. Pollock, and J. Jones

Microstructure Evolution and Mechanical Properties of Mg-14%Li-1%Al Alloy during the High-Pressure Torsion 167
C. Tian, H. Lu, and L. Zhao

Melting, Modeling, and Solidification

Finite-Element Analysis of Melt Flow in Horizontal Twin-Roll Casting of Magnesium Alloy AZ31 173
J. Park

Nucleation and Growth of Metastable Phases in Mg-Nd, Mg-Gd and Mg-Gd-Nd Based Alloys 179
S. El Majid, G. Atiya, M. Bamberger, and A. Katsman

A Numerical and Experimental Study of Flow Behavior in High Pressure Die Casting 185
M. Saeedipour, S. Schneiderbauer, S. Pirker, and S. Bozorgi

In Situ Synchrotron Radiation Diffraction during Melting and Solidification of Mg-Al Alloys Containing CaO 191
B. Wiese, C. Mendis, D. Tolnai, G. Szakács, A. Stark, N. Schell, H. Reichel, R. Brückner, K. Kainer, and N. Hort

Solidification Characteristics of Wrought Magnesium Alloys Containing Rare Earth Metals 197
A. Javaid, F. Czerwinski, R. Zavadil, M. Aniolek, and A. Hadadzadeh

Strengthening due to the Percolating Eutectic Microstructure in Squeeze Cast MRI230D 203
B. Zhang, A. Nagasekhar, and C. Cáceres

Effect of Al Addition on Microstructure of AZ91D 209
U. Joshi and N. Babu

In Situ Synchrotron Radiation Diffraction during Solidification of Mg4Y and Mg4YxGd Alloys (x = 1, 4 wt.%) . 213
G. Szakács, B. Wiese, C. Mendis, D. Tolnai, A. Stark, N. Schell, M. Nair, K. Kainer, and N. Hort

A New Method for Melting Mg-Li Alloys 219
L. Gong, J. Zhang, T. Yin, J. Wei, and G. Wu

Texture and Wrought Processing I

Deformation Behavior of ZE10 Magnesium Alloy Sheet 227
P. Dobroň, J. Balík, F. Chmelík, K. Illková, D. Drozdenko, J. Bohlen, D. Letzig, and P. Lukáč

Texture Evolution during Grain Growth of Magnesium Alloy AZ31B 233
J. Bhattacharyya, B. Radhakrishnan, G. Muralidharan, and S. Agnew

Effect of Annealing on Microstructure, Texture and Tensile Properties of Twin-Roll Cast AZ31B 239
M. Masoumi, F. Zarandi, and M. Pekguleryuz

Influence of Rolling Direction and Temperature on the Texture Formation in Rolled AZ31B Magnesium Alloy ... 245
L. Catorceno and N. de Lima

Texture Evolution during Wire Drawing of Mg-RE Alloy 251
M. Chatterton, J. Robson, and D. Henry

Extrusion of Hollow Magnesium Profiles and Investigation of Extrusion Seams 257
F. Gensch, R. Nitschke, S. Gall, and S. Müller

Microstructural Evolution and Its Relationship to the Mechanical Properties of Mg AZ31B Friction Stir Back Extruded Tubes 263
J. Milner and F. Abu-Farha

Effect of Yttrium Addition on Texture Development in a Cast Mg-Al-Y Magnesium Alloy during Compression 269
N. Tahreen, D. Chen, M. Nouri, and D. Li

Wrought Processing II and Joining

Spike-Forging of As-Cast TX32 Magnesium Alloy 275
K. Rao, K. Suresh, N. Hort, and K. Kainer

An Introduction to the Forging of Elektron®43 - A High Performance Wrought Magnesium Alloy 281
D. Henry, M. Turski, P. Lyon, and T. Wilks

Structure and Properties of Interlayer Formed between Magnesium Alloy Core and Aluminium Alloy Coating during Deformation 285
S. Boczkal, P. Korczak, B. Płonka, W. Szymański, and M. Nowak

A Novel Process for Producing Large Scale Mg-Sheets 289
G. Norbert, E. Marcus, N. André, K. Christian, H. Sven, B. Bernd-Arno, and H. Maier

Effect of Volume Fraction of Icosahedral Phase in CaO Added Mg-Zn-Y Alloys 293
H. Lim, D. Kim, T. Kwak, W. Yang, H. Kim, Y. Yoon, and S. Kim

Effect of CaO on Hot Workability and Microstructure of Mg-9.5Zn-2Y Alloy 297
T. Kwak, D. Kim, J. Yang, Y. Yoon, S. Kim, H. Lim, and W. Kim

Welding of Dissimilar Light Metals by Disk Laser 301
M. Sahul, M. Turňa, and M. Sahul

Design of Binary Zinc-Based Solder for Joining Mg Alloy Type AZ 31 B 307
M. Jáňa, M. Turňa, and M. Ožvold

Friction Stir Welding of Magnesium Alloy Type AZ 31 311
T. Kupec, M. Behúlová, M. Turňa, and M. Sahul

Corrosion and Coatings

Enhancing Corrosion Resistance by a Hydrophobic Surface Feature for Magnesium Alloy AZ91D 319
X. Chen, C. Ke, and N. Birbilis

Oxidation and Corrosion Behavior of Non-Flammable Magnesium Alloys Containing Ca and Y 325
B. You, Y. Kim, C. Yim, and H. Kim

Corrosion Behavior of Magnesium Alloys Containing Sn and Zn 331
C. Yim, S. Woo, J. Yang, and B. You

Effect of Surface Condition on the Localized Corrosion Behavior of Magnesium Alloy AZ31B 335
Z. Cano, J. Kish, and J. McDermid

Formation of Self-Assembled Monolayer on Cerium Conversion Coated AZ31 Mg Alloy 341
S. Salman, N. Akira, K. Kuroda, and M. Okido

Effects of Current Density on Microstructure and Corrosion Property of Coating on AZ31 Mg Alloy Processed via Plasma Electrolytic Oxidation 345
K. Lee, F. Einkhah, M. Sani, Y. Ko, and D. Shin

Corrosion-Stress Relaxation Effects on Tensile Properties of an AZ61 Magnesium Alloy 351
H. Martin, C. Walton, K. Bruce, A. Hicks, M. Horstemeyer, W. Whittington, and P. Wang

Corrosion Behavior of Friction Stir Welded AZ31 Joints for Automotive Applications 357
X. Zhang, Z. Cano, B. Wilson, J. Kish, and J. McDermid

Biomedical Applications

Development of a Generalised Understanding of Environmentally-Assisted Degradation of Magnesium-Aluminium Alloys 365
N. Winzer, H. Höpfel, and P. Casajus

Coating Systems for Biodegradable Magnesium Applications 371
J. Seitz, R. Eifler, M. Vaughan, C. Seal, M. Hyland, and H. Maier

Improvement of Cytocompatibility of Magnesium Alloy ZM21 by Surface Modification 375
A. Witecka, A. Yamamoto, and W. Swieszkowski

Cytocompatibility of Mg Alloys and the Effect of Cells on Their Degradation in Biological Environment 381
A. Yamamoto and Y. Kohyamda

Alloy Design

In-Situ Neutron Diffraction Study of Aging in Alloy ZK60A 389
S. Agnew, C. Calhoun, and B. Clausen

Development of a High Strength Ductile Wrought Mg-Zn Based Alloy 395
L. Ma, T. Sasaki, T. Nakata, T. Ohkubo, K. Hono, and S. Kamado

Significant Precipitation Strengthening in Extruded Mg-Sn-Zn Alloys 401
T. Sasaki, F. Elsayed, T. Nakata, S. Kamado, T. Ohkubo, and K. Hono

Al and Zn Impurity Diffusion in Binary and Ternary Magnesium Solid-Solutions 407
C. Kammerer, N. Kulkarni, R. Warmack, and Y. Sohn

Formation and Evolution of Intermetallic Phases in the Mg-Nd-Zn-Zr System 413
K. Peng, J. Zhang, Z. Zhang, and Q. Li

Light-Metal Matrix (Nano)-Composites

Microstructure-Property Relationships I

An Insight into Processing and Characteristics of Magnesium Based Composites 423
M. Gupta and W. Wong

Hot Extruded Carbon Nanotube Reinforced Magnesium Matrix Composites and Its Microstructure, Mechanical and Corrosion Properties 429
H. Mindivan, A. Efe, and E. Kayali

Hardening and Softening Processes in AJ51 Magnesium Alloy Reinforced with Short Saffil Fibres 435
Z. Trojanová, G. Farkas, K. Máthis, and P. Lukáč

Microstructure-Property Relationships II: Modeling and Advanced Characterization

Fabrication and Tensile Properties of Al_2O_3 Particle and Fibre Hybrid Magnesium (AM60)-Based Composites 443
X. Zhang, Q. Zhang, H. Hu, and X. Nie

Enhancing Tensile and Compressive Strength of AZ41 Magnesium Alloy by Adding Nano-Sized Al_2O_3 449
M. Alam and A. Hamouda

Phase-Field Modeling of Solidification in Light-Metal Matrix Nanocomposites 455
T. Pusztai, L. Rátkai, A. Szállás, and L. Gránásy

Advanced Characterization of Metal Matrix Nano-Composites 461
M. Maher and L. Williams

Emerging Processes

Achieving Uniform Distribution and Dispersion of a High Percentage Nanoparticles in Mg18Sn Matrix by Solidification Processing 467
L. Chen, J. Peng, J. Xu, H. Choi, and X. Li

Effect of Nano-Reinforcement on Properties of Cast Mg-Al Alloy AZ91 471
M. Mahmoud, I. El-Mahallawi, and R. Rashad

In-Situ Synthesis and Novel Additions

Ceramic Dispersions in Metal Castings Created by Direct Injection of a Liquid Organic Precursor into the Melt 479
R. Sudarshan

Magnesium Technology 2013

Addendum

Corrosion and Adhesion Properties of Cerium-Based Conversion Coatings on Magnesium Alloys 487
S. Maddela and M. O'Keefe

Corrosion of Ultrasonic Spot Weldbonds of Magnesium to Steel 491
T. Pan, Z. Feng, M. Santella, and J. Chen

Friction Stir Back Extrusion of Mg AZ31B-F: A Preliminary Investigation 497
J. Milner and F. Abu-Farha

Impurity Diffusion Coefficients of Al and Zn in Mg Determined from Solid-to-Solid Diffusion Couples 505
C. Kammerer, N. Kulkarni, R. Warmack, K. Perry, I. Belova, G. Murch, and Y. Sohn

Microstructure Evolution and Mechanical Behavior of Mg-10Gd-3Y-0.4Zr Alloy Processed by ECAP at High Temperature 511
Y. Zhou, D. Li, X. Zeng, Y. Wu, and W. Ding

The USAMP Magnesium Front End Research and Development Project – Results of the Magnesium "Demonstration" Structure 517
J. Forsmark, M. Li, X. Su, D. Wagner, J. Zindel, A. Luo, J. Quinn, R. Verma, Y. Wang, S. Logan, S. Bilkhu, and R. McCune

Author Index 525

Subject Index 529

PREFACE

The most significant structural field of application of magnesium alloys remains in the field of automotive die castings, where the mass saving and consequent fuel efficiency provide a life cycle benefit in terms of reduced carbon dioxide emissions, although this life cycle benefit is very dependent upon the source of primary energy. For this reason, the U.S. government has channelled new funding into alternative processes for the generation of primary magnesium outside of China, but it remains to be seen whether these will be commercialized in the timescale required to have a significant impact on the future of low-carbon vehicles. In Magnesium Technology 2014, we look forward to hearing more on this subject from Will Joost at the U.S. Department of Energy.

Although the lightweighting benefits of magnesium in large castings continues to be exploited in the rotorcraft industry to enhance performance, payload, and time on station, the use of magnesium in commercial fixed-wing structures declined in the 1970s. This decline was due to increased engine power and concern about corrosion and flammability. Seven years of work to change the opinion of the Federal Aviation Authority about the acceptability of magnesium inside the aircraft cabin is very close to bearing fruit, and the life cycle analysis of increased magnesium use in the cabin suggests that in aviation fuel saving alone a payback will be achieved in less than a month in the air. The industry however needs to continue to address the challenges of alternative materials such as carbon fibre composites and aluminium lithium alloys if it is to make headway into the structure of the aircraft. In 2014 the Magnesium Committee and Aluminum Committee of the TMS Light Metals Division have joined forces under the leadership of Wim Sillekens and Dmitry Eskin to offer our own view of potential strengthening mechanisms in nanocomposite materials based on both magnesium and aluminium.

There are, however, other applications for magnesium alloys beyond aerospace and automotive, and in 2013 we saw a significant number of papers at TMS in the field of magnesium biotechnology which is also represented in this year's program. The technical and economic press talks incessantly about the game changing nature of 3D printing or additive layer manufacturing in our world, and with the emerging availability of magnesium alloys powders the potential for lightweight innovative structures incorporating magnesium alloys is beginning to be explored.

The magnesium industry continues to need innovation in alloy design to remain competitive with alternative materials, and understanding deformation mechanisms in alloy systems with limited room temperature ductility and methods of reducing anisotropy and asymmetry remain important in widening structural applications whether it be automotive or aerospace. Ultimately if the technology presented in the volume is to be useful it must be affordable in its target market.

This year is the 15th of Magnesium Technology as a symposium within the TMS Annual Meeting. It will be held in San Diego from February 16 to 20, 2014, and there will again be a keynote session, a poster session, and a number of technical sessions in which the content of Magnesium Technology 2014 will be available to all to discuss these and other related issues.

This volume represents the proceedings of these sessions and contains content from over 16 countries. In addition there is a small addendum that includes papers that were submitted for Magnesium Technology 2013 that could not be published at that time. All contributions to Magnesium Technology are peer reviewed by volunteers acting on behalf of the Magnesium Committee. Our reviewers are critical to the success of the volume and are listed in the following pages, and we thank them and the volunteer chairs of our sessions for their contribution.

We continue to insist that our presenters provide a paper to this proceedings volume or other TMS approved journal as we believe our readers and participants wish to take the ideas away and explore them in more detail, and build upon them. Maintaining notes over four days of a diverse conference like the TMS Annual Meeting is difficult and this volume acts as a valuable source of reference throughout the following year, and in many cases for years to come. We thank all those who have contributed high quality written manuscripts to this volume.

2014 Magnesium Technology Symposium Organizers

Martyn Alderman - Chair
Michele V. Manuel - Co-Chair
Norbert Hort - Past Chair
Neale R. Neelameggham – Advisor

ABOUT THE LEAD EDITOR



MARTYN ALDERMAN
MAGNESIUM TECHNOLOGY 2014 LEAD EDITOR

Martyn Alderman is Divisional Director of Technology for the Magnesium Elektron Group Worldwide. He obtained a Master's Degree in Material Science from the University of Cambridge (United Kingdom) in 1979, and for the next 20 years he worked in aluminium rolling mills producing and developing Al-Cu-Zr, Al-Mn, Al Mg-Mn, Al-Zn-Mg, and Al-Li-Cu alloys for superplastic forming. He also has significant operational experience of direct chill casting and in the extrusion of high strength aluminium alloys.

In 2003 he joined Magnesium Elektron during the acquisition of their large Madison, Illinois rolling operation in the United States. For the next few years he was travelling between the United States and Europe encouraging the wider use of magnesium sheet in transport applications, in particular by use of superplastic forming, and later in managing the post-acquisition integration of the Revere North American Graphic Arts business. He chaired the 2010 International Magnesium Association Conference in Hong Kong, and in 2011-2012 was involved in editing and producing a 270-page *Handbook on Designing with Magnesium Alloys*.

More recently he has been involved in a UK Technology Strategy Board Project aimed at the design of a magnesium-intensive vehicle in conjunction with the Morgan Motor Company and as an advisor to the International Magnesium Association Life Cycle Study on automotive and aerospace applications.

As a member of TMS, SAE, and ASM, he is a regular attendee at worldwide magnesium conferences keeping abreast of global technology development with the aim of maintaining Magnesium Elektron's position as a world leader in magnesium alloys and their end use applications.

MAGNESIUM TECHNOLOGY 2014 EDITORS



Michele V. Manuel is an Assistant Professor in the Department of Materials Science and Engineering at the University of Florida. She received her Ph.D. in Materials Science and Engineering at Northwestern University in 2007 and her B.S. in Materials Science and Engineering at the University of Florida. Her postdoctoral work was in alloy design at the General Motors Technical Center in Warren, Michigan. She is the recipient of the National Science Foundation (NSF) CAREER and National Aeronautics and Space Administration (NASA) Early Career awards, ASM Bradley Stoughton Award for Young Teachers, AVS Recognition for Excellence in Leadership, TMS Young Leaders Professional Development, and University of Florida Excellence Award for Assistant Professors. Her research lies in the basic understanding of the relationship between processing, structure, properties, and performance. She uses a systems-based materials design approach that couples experimental research with theory and mechanistic modeling for the accelerated development of materials. Her current research is focused on the use of systems-level design methods to advance the development of new materials through microstructure optimization. Of specific interest are biodegradable, formable, and high temperature magnesium alloys; self-healing metals; shape memory alloys; nuclear fuels; and computational thermodynamics and kinetics.



Norbert Hort is the head of the Magnesium Processing Department at the Magnesium Innovation Centre (MagIC) within the Helmholtz-Zentrum Geesthacht Zentrum für Material- und Küstenforschung, Geesthacht, Germany (formerly the GKSS Research Centre). Concurrently he is lecturer at the Leuphana University, Lüneburg, Germany. He studied Materials Sciences at the Clausthal University of Technology (CUT), Germany, where he already got involved in magnesium research since the early 1990s. His diploma thesis (1994) dealt with gas-atomized, hot-extruded magnesium alloys. During 1994-1995 he worked as a researcher at the Institute of Materials Sciences (CUT) and he joined the HZG in 2000. He got his Ph.D. degree in Materials Sciences in 2002 from the Clausthal University of Technology. In the MagIC he is responsible for the development of new creep resistant magnesium alloys, grain refinement and the castability of magnesium alloys (viscosity and density of melts, fluidity, and mold filling). Additionally, a major focus of his research is the development of new magnesium alloys for biodegradable implants in a close collaboration with biologists and clinicians. He is co-author of more than 150 peer-reviewed journal papers and contributions to conference proceedings. In recent years he was involved in the organizing committees of the conference series Magnesium Alloys and Their Applications and of the conference Light Metal Technologies 2011 and acted as the organizer of the TMS 2013 Annual Meeting symposium, Magnesium Technology. Since 2009, he has also served as the chairman of the Magnesium Technical Committee of the German Society of Materials (DGM).



Neale R. Neelameggham is "The Guru" at IND LLC, involved in technology marketing and international consulting in the field of light metals and associated chemicals [boron, magnesium, titanium, lithium, and alkali metals], rare earth elements, battery and energy technologies, etc. Neale has been an advisor in various environmental extractive processes for metal production and energy process firms.

He has over 38 years of expertise in magnesium production technology from the Great Salt Lake brine in Utah, involved in Process Development of its startup company NL Magnesium through the present US Magnesium LLC from where he retired. Dr. Neelameggham was involved in most of the process and equipment development of all areas of the plant from the raw material source – the Great Salt Lake Brine, which is concentrated by solar evaporation into a plant feed, which was further purified of impurities, followed by spray drying and preparation of anhydrous magnesium chloride cell feed to electrolytic cells and then into magnesium metal product and chlorine.

In addition, Dr. Neelameggham's expertise includes an in-depth and detailed knowledge of all competing technologies worldwide of magnesium production, both electrolytic and thermal processes (Pidgeon Process, Murex Process, Zuliani Process, etc.) , as well as alloy development. This expertise is used in engineering a tailor made magnesium process to fit any resources, and has developed a near zero-waste sustainable magnesium production process and equipment. He was a visiting expert at Beihang University of Aeronautics and Astronautics, Beijing, China.

Dr. Neelameggham holds 13 patents and a patent application on boron production, and has several technical papers to his credit. As a member of TMS, AIChE, and a former member of American Ceramic Society, he is well versed in energy engineering, bio-fuels, rare-earth minerals and metal processing and related processes. Dr. Neelameggham served in the TMS Light Metals Division's Magnesium Committee since its inception in 2000 and chaired it in 2005; in 2007, he was made a permanent co-organizer for the Magnesium Technology symposium at the TMS Annual Meeting. He has been a member of the Reactive Metals Committee, Recycling Committee, Titanium Committee, Program Committee, and the Light Metals Division council.

In 2008, LMD and the TMS Extraction & Processing Division created the Energy Committee following the symposium on CO_2 Reduction Metallurgy Symposium, which he initiated. Dr. Neelameggham was the inaugural chair for the Energy Committee. He has been a co-editor of the Energy Technology symposium since 2008. He received the LMD Distinguished Service Award in 2010. Dr. Neelameggham holds a doctorate in extractive metallurgy from the University of Utah. He has been selected as the Chairman of Hydrometallurgy and Electrometallurgy Committee of EPD for the 2013-2015 term.

LIGHT-METAL MATRIX (NANO)-COMPOSITES EDITORS



Wim H. Sillekens is a project manager in the New Materials & Energy Unit at the research and technology center of the European Space Agency (ESA–ESTEC), where he is currently acting as the coordinator of the European Community research project ExoMet. He obtained his Ph.D. from Eindhoven University of Technology, Netherlands, on a subject relating to metal-forming technology. Since then he has been engaged in aluminum and magnesium research, among others on (hydro-mechanical) forming, recycling /refining, (hydrostatic) extrusion, forging, magnesium-based biodegradable implants, and as of late on light-metal matrix nanocomposites. His professional career includes positions as a post-doc researcher at his alma mater and as a research scientist / project leader at the Netherlands Organization for Applied Scientific Research (TNO). International working experience covers a placement as a research fellow at MEL (now AIST) in Tsukuba, Japan, and – more recently – shorter stays as a visiting scientist at GKSS (now HZG) in Geesthacht, Germany, and at PNNL in Richland Washington, USA. He has authored or co-authored book chapters, journal papers, patents, conference papers, (keynote/invited/contributed) oral presentations, and so on (about 135 entries to date). Other professional activities include an involvement in association activities (among others, as the lead organizer of TMS 2011 Annual Meeting Magnesium Technology symposium), international conference committees, and as a peer reviewer of manuscripts for scientific journals and conference proceedings as well as of research proposals. Research interests are in physical and mechanical metallurgy in general and in light-metals technology in particular.



Dmitry G. Eskin received his Engineering and Ph.D. degrees from Moscow Institute of Steel and Alloys (Technical University, Russia) in 1985 and 1988, respectively. After that he worked as a Senior Scientist in the Baikov Institute of Metallurgy (Russian Academy of Sciences) with a main research focus of alloy development, heat treatment and metal processing of aluminum alloys. From 1999 to 2011 he was a Fellow in Materials innovation institute and since 2008 also held a position of associate professor in Delft University of Technology (The Netherlands), where he conducted fundamental and applied research on solidification processing of metallic materials. In 2011, he joined Brunel University (UK) as professor in solidification research. His current research concerns application of ultrasonic cavitation to melt processing. He is a well-known specialist in physical metallurgy and solidification processing of light alloys, author and co-author of more than 180 scientific papers, 5 monographs, and a number of patents. Among his books are M*ulticomponent Phase Diagrams: Applications for Commercial Aluminum Alloys* (2005), *Physical Metallurgy of Direct-Chill Casting of Aluminum Alloys* (2008), and *Direct-Chill Casting of Light Alloys: Science and Technology* (2013). Dr. Eskin has been a member of TMS since 2000 and is a regular speaker at TMS Annual Meetings.

MAGNESIUM TECHNOLOGY 2014
Session Chairs

Keynote Session
Martyn Alderman

Powders, Recycling, Hydrometallurgy, Primary Production, and Creep
Neale R. Neelameggham
Petra Maier

Deformation I
Fabrizio D'Errico
Alok Singh

Deformation II
Kiran Solanki
Warren Poole

Melting, Modelling, and Solidification
Dallas Trinkle
James Saal

Texture and Wrought Processing I
Julian Rosalie
Eric Nyberg

Wrought Processing II and Joining
Amit Pandey
Suveen Mathaudhu

Corrosion and Coatings
Adam Powell
Soobhankar Pati

Biomedical Applications
Michele V. Manuel
Wim Sillekens

Alloy Design
Alan Luo
Sean Agnew

SYMPOSIUM: LIGHT-METAL MATRIX (NANO)-COMPOSITES

Session Chairs

Microstructure-Property Relationships I
Wim Sillekens

Microstructure-Property Relationships II; Modeling and Advanced Characterization
Xiaochun Li

Emerging Processes
Manoj Gupta

In-Situ Synthesis and Novel Additions
Dmitry Eskin

MAGNESIUM TECHNOLOGY 2014
Reviewer Pool

The completion of this volume would not have been possible without the volunteer assistance of these individuals from 13 different countries. Their commitment to the advancement of magnesium research and scientific knowledge is to be commended. They are listed here in alphabetical order of their last names:

ALDERMAN, Martyn	Magnesium Elektron
AGNEW, Sean	University of Virginia
BARNETT, Matthew	Deakin University
BLAWERT, Carsten	Helmholtz Zentrum Geesthacht
BOHLEN, Jan	Helmholtz Zentrum Geesthacht
CACERES, Carlos	University of Queensland
CARTER, Jon	General Motors
DAS, Subodh	Phinix LLC
DAVIS, Bruce	Magnesium Elektron
DECKER, Ray	Thixomat
DEMIRCI, Gokhan	Aselsan Inc
D'ERRICO, Fabrizio	Polytecnico di Milano
DIERINGA, Hajo	Helmholtz Zentrum Geesthacht
DIETZEL, Wolfgang	Helmholtz Zentrum Geesthacht
DOHERTY, Kevin	U.S. Army Research Lab
EASTON, Mark	Monash University
ESSADIQI, Elhachmi	Université Internationale de Rabat
FOLEY, David	Texas A&M University
FORSMARK, Joy	Ford Motor Company
GIBSON, Mark	CSIRO
HECTOR, Louis Jr.	General Motors
HENRY, Dominic	Magnesium Elektron
HOECHE, Daniel	Helmholtz Zentrum Geesthacht
HORT, Norbert	Helmholtz Zentrum Geesthacht
HUANG, Yuanding	Helmholtz Zentrum Geesthacht
JAIN, Vipin	National Physical Laboratory
JOOST, William	Department of Energy VTP
JORDON, Brian	University of Alabama
KABIRIAN, Farhoud	University of Maryland
KAINER, Karl	Helmholtz Zentrum Geesthacht
KARAKAYA, Ishak	Middle East Technical University

KIM, Shae	KITECH
KRAJEWSKI, Paul	General Motors
LI, Bin	Mississippi State University
LIU, Zi-Kui	Penn State University
LUO, Alan	The Ohio State University
MA, Quancang	University of Kentucky
MACKENZIE, Luke	Novelis
MADAN, Deepak	Magnesium Elektron
MAIER, Petra	University of Applied Sciences Stralsund
MANSOOR, Bilal	Masdar Institute of Technology
MANUEL, Michele V.	University of Florida
MATHAUDHU, Suveen	
MCCUNE, Robert	Robert C. McCune and Associates LLC
MENDIS, Chamini	Helmholtz Zentrum Geesthacht
MISHRA, Rajiv	University of North Texas
MISIOLEK, Wojtek	Lehigh University
NAGASEKHAR, Anumalasetty	Carpenter Technology Corporation
NEELAMEGGHAM, Neale R.	IND LLC
NIE, Jian-Feng	Monash University
NYBERG, Eric	Pacific Northwest National Laboratory
PANDEY, Amit	Rolls Royce LG Fuel Cell Systems Inc.
PATI, Soobhankar	IIT Bhubaneswar
PAXTON, Dean	Pacific Northwest National Lab
PEKGULERYUZ, Mihriban	McGill University
PENG, Liming	Shanghai Jiaotong University
POOLE, Warren	University of British Columbia
POWELL, Adam	Infinium Metals
PRENTICE, Leon	CSIRO
ROBSON, Joe	University of Manchester
ROSALIE, Julian	National Institute for Materials Science
SAAL, James	Northwestern University
SADAYAPPAN, Kumar	CANMET
SINGH, Alok	National Institute for Materials Science
SLADE, Susan	US Magnesium LLC
SOLANKI, Kiran	Arizona State University
SONG, Guangling	Oak Ridge National Laboratory
SRINIVASAN, A. Srini	Helmholtz Zentrum Geesthacht

STJOHN, David	University of Queensland
TALEFF, Eric	University of Texas
TANDON, Rajiv	Magnesium Elektron
TARTAGLIA, John	Stork Climax Research Services
TOLNAI, Domonkos	Helmholtz Zentrum Geesthacht
TURSKI, Mark	Magnesium Elektron
VENKATESAN, Kishore	CSIRO
VERMA, Ravi	General Motors
WILKS, Tim	Magnesium Elektron
YI, Sangbong	Helmholtz Zentrum Geesthacht

Magnesium Technology 2014

Keynote Session

Magnesium Technology 2014
Edited by: Martyn Alderman, Michele V. Manuel, Norbert Hort, and Neale R. Neelameggham
TMS (The Minerals, Metals & Materials Society), 2014

AUTOMOTIVE MAGNESIUM: IMPACTS AND OPPORTUNITIES

William J. Joost
Vehicle Technologies Office
U.S. Department of Energy

Extended Abstract

Structural magnesium alloys are simultaneously among the most promising and most challenging options as materials for next-generation, lightweight vehicles. Compared to conventional automotive materials, magnesium alloys can reduce the weight of structural components and systems by more than 50%. Vehicle fuel economy improves by 6-8% for every 10% reduction in weight [1], thus the significant potential for weight savings makes magnesium alloys an attractive technology to support improved efficiency in our cars and trucks. However, magnesium alloys for use in commercial and passenger vehicles face a variety of technical challenges [2] [3]. The maturity of magnesium alloys will be discussed in three main categories: (1) properties and manufacturability of alloys that meet automotive performance and cost requirements on a part-by-part basis, (2) joining and multi-material enabling technologies that support integration of magnesium components into structural systems, and (3) modeling and simulation of magnesium alloys and processes that allow rapid development and compatibility with existing, computationally-intensive vehicle design techniques.

Exceeding the properties and manufacturability requirements for automotive components is critical for implementation of magnesium alloys. Broadly speaking, the high cost of producing magnesium components with adequate properties limits applications of Mg to less than 0.5% of the weight of an average vehicle [4]; however, the scientific and manufacturing drivers for high cost vary by alloy and manufacturing process. In general, cast magnesium components are the most mature among automotive systems though significant improvement in strength and heat treatability, ductility and uniformity, and material cost would enable wider use. Magnesium sheet products have seen wide consideration in the automotive industry owing to general compatibility with the sheet-based architecture of most vehicles; while some successful automotive sheet demonstrations exist, broad application of magnesium sheet is limited by high material cost, infrastructure limitations for high temperature forming, and mechanical properties of the final product. Magnesium extrusions present excellent weight savings opportunities for rail-type geometries in the vehicle structure as well as window/sun-roof frames and similar components. Low extrusion speed, and thus high cost, contributes along with challenges in anisotropy of mechanical properties to preventing the use of magnesium extrusions in vehicles. Properties and manufacturability of magnesium alloys represents an enormous technical space, thus the highest priority needs and promising technology pathways will be addressed.

Perhaps the steepest barriers to the increased use of magnesium in vehicles lie in the areas of joining and multi-material enabling technologies. Resistance spot welds of Mg-Mg joints are possible but prone to severe heat affected zones, cracking, and void formation; resistance spot welds of Mg-Al and Mg-steel joints are similarly difficult with the compounding effects of intermetallic formation, thermal mismatch, and formation of galvanic couples. A variety of other techniques such as friction stir welding and ultrasonic welding of magnesium have been demonstrated with varying degrees of success in quickly producing strong, durable joints. Magnesium and its alloys are highly anodic to essentially all other automotive structural materials; the resulting galvanic couples between magnesium and aluminum or steel make design of strong, stable multi-material systems quite difficult. A wide array of alloying, joining, and coating strategies exist – particular needs and the most encouraging opportunities will be discussed.

Finally, design of vehicles (and, increasingly, design of materials) is a computationally intensive process where accurate simulation results are critical to enabling rapid testing, analysis, and iteration. Simulating the mechanical behavior of magnesium alloys is complicated by severe anisotropy in the deformation mechanisms. Further, while a vast scientific knowledge base has developed around steel and aluminum alloys owing to their broad range of applications, structural magnesium has historically lacked sustained demand by the automotive, aerospace, or defense industries and the basic science input required for accurate modeling and integrated computational materials engineering (ICME) often does not exist. Computational materials science and ICME for magnesium alloys will be described, with a particular emphasis on integrated development of new alloys and processes with development of new automotive structures.

Bibliography

[1] W. Joost, "Reducing Vehicle Weight and Improving U.S. Energy Efficiency Using Integrated Computational Materials Engineering," *JOM,* vol. 64, no. 9, pp. 1032-1038, 2012.
[2] U.S. Department of Energy, Energy Efficiency and Renewable Energy, "Workshop Report: Light-Duty Vehicles Technical Requirements and Gaps for Lightweight and Propulsion Materials," 2013.

[Online]. Available: http://www1.eere.energy.gov/vehiclesandfuels/pdfs/wr_ldvehicles.pdf.

[3] U.S. Department of Energy, Energy Efficiency and Renewable Energy, "Workshop Report: Truck and Heavy-Duty Vehicles Technical Requirements and Gaps for Lightweight and Propulsion Materials," 2013. [Online]. Available: http://www1.eere.energy.gov/vehiclesandfuels/pdfs/wr_trucks_hdvehicles.pdf.

[4] Oak Ridge National Laboratory, "Transportation Energy Data Book," 2013. [Online]. Available: http://cta.ornl.gov/data/index.shtml.

Magnesium Technology 2014
Edited by: Martyn Alderman, Michele V. Manuel, Norbert Hort, and Neale R. Neelameggham
TMS (The Minerals, Metals & Materials Society), 2014

Alloy Development, Manufacturing and Design for Magnesium Applications

Alan A. Luo
Department of Materials Science & Engineering
Department of Integrated Systems Engineering
The Ohio State University, Columbus, OH 43210, USA

Keywords: Magnesium alloys, alloy development, manufacturing, design, applications

Extended Abstract

Materials, manufacturing and design are critical pillars in lightweight structures. As the lightest structural metal, magnesium has emerged as a promising structural material for lightweight applications in automotive and other transportation industries. This talk presents examples of magnesium alloy development using phase equilibria calculations and experimental validation. This talk will also summarize the latest process innovations in magnesium manufacturing (casting, forming and joining) for structural applications. Process simulation and multi-scale microstructure modeling techniques are used to develop and optimize these manufacturing processes for automotive lightweighting. Engineering design is a system optimization and iteration process that combines material properties and manufacturing processes to meet product requirements at the lowest mass and/or cost. Future trends in multi-material applications and the integrated computational materials engineering (ICME) are also discussed.

Mg-Al-Sn alloy system offers good combination of strength, ductility, castability and corrosion resistance for potential structural applications. The solidification microstructure and mechanical properties of as-cast Mg-Al-Sn alloys have been investigated using computational thermodynamics and experiments. The as-cast microstructure of Mg-Al-Sn alloys consists of α-Mg, $Mg_{17}Al_{12}$ and Mg_2Sn phases. The amount of $Mg_{17}Al_{12}$ and Mg_2Sn phases formed increases with increasing Al and/or Sn content, and show good agreement between the experimental results and the Scheil solidification calculations. Generally, the yield strength of as-cast alloys increases with Al and/or Sn content, while the ductility decreases. Two experimental alloys, AT72 (Mg-7Al-2Sn) and AT96 (Mg-9Al-6Sn), were designed and prepared using high pressure die casting process. The microstructure of as-cast Mg-Al-Sn alloys was investigated using computational thermodynamics modeling and experimental techniques. Both alloys show improved mechanical properties and excellent die castability compared with the conventional AZ91 (Mg-9Al-1Zn) and AM50 (Mg-5Al-0.3Mn) alloys.

This talk summarizes the melting and casting processes for magnesium alloys. It also reviews the historical development of magnesium castings and their structural uses in the western world since 1921 when Dow began producing magnesium pistons. Magnesium casting technology was well developed during and after World War II, both in gravity sand and permanent mold casting as well as high-pressure die casting, for aerospace, defense and automotive applications. In the last 20 years, most of the development has been focused on thin-wall die casting applications in the automotive industry, taking advantages of the excellent castability of modern magnesium alloys. Recently, the continued expansion of magnesium casting applications into automotive, defense, aerospace, electronics and power tools has led to the diversification of casting processes into vacuum die casting, low-pressure die casting, squeeze casting, lost foam casting, ablation casting as well as semi-solid casting. This talk will also review the historical, current and potential structural use of magnesium with a focus on automotive applications.

As magnesium is expanding into more critical structural applications, there is a great need for developing wrought magnesium products to provide improved mechanical and physical properties, crash performance and corrosion resistance. Most critical is to improve the plasticity of wrought magnesium, which becomes dramatically reduced as the various working methods used to create the primary fabrications, like sheet and extrusions, rotate the grains to less favorable orientations for isotropic plasticity. As a result, secondary forming processes like stamping and tube hydroforming need to be executed at warm temperatures to promote non-basal slip to occur so that the larger strains targeted can be accommodated. This need increases manufacturing costs and puts magnesium at a disadvantage compared with traditional metals. Further, since final performance occurs at ambient temperatures, the plasticity of magnesium at these temperatures remains paramount to their in structural applications. Finally, the high electrochemical activity of magnesium has limited its application due to concerns for galvanic corrosion. Mitigating solutions are either still not robust enough or too expensive for high volume manufacturing. Similar to magnesium plasticity, the use of magnesium for exterior exposed panels, requiring a high degree of finish for their appearance, remains an equally challenging situation.

Integrating magnesium into today's steel-dominated structures is challenging, and requires intelligent selection of materials and manufacturing processes for critical lightweight applications. The Mg-intensive front end body structures were selected by USAMP (United States Automotive Materials Partnership) to demonstrate the lightweight benefits of magnesium applications and the enabling technologies. The Mg-intensive front end design achieved 44.57 kg (45%) mass saving compared with the steel baseline (unibody architecture), with equivalent stiffness, durability (fatigue) and crashworthiness predicted by simulations.

Integrated Computational Materials Engineering (ICME) is the integration of materials information, captured in computational tools, with engineering product performance analysis and manufacturing-process simulation. The development and application of ICME tools will accelerate the use of magnesium in lightweight structural applications.

Magnesium Technology 2014
Edited by: Martyn Alderman, Michele V. Manuel, Norbert Hort, and Neale R. Neelameggham
TMS (The Minerals, Metals & Materials Society), 2014

LIFE CYCLE ASSESSMENT OF ECO-MAGNESIUM® ALLOY PRODUCED BY GREEN METALLURGY EU PROJECT PROCESS ROUTE

Fabrizio D'Errico[1], Gerardo Garces Plaza[2], Franz Giger[3], Shae K. Kim[4]
[1]Politecnico di Milano, Department of Mechanical Engineering, Via La Masa 34, 20156 Milan, Italy
[2]Centro Nacional de Investigaciones Metalúrgicas, Department of Physical Metallurgy, Avda. Gregorio del Amo, 8, Madrid 28040
[3]Buhler AG, New Technologies AMT Advanced Materials Division, Gupfenstrasse 5, Uzwil 9240, Switzerland
[4]Casting Research Center, Korea Institute of Industrial Technology, 7-47 Songdo-dong, Yeonsu-gu, Incheon 406-840, Korea

Keywords: Magnesium alloys, Life Cycle Assessment, Eco-Magnesium, sustainability, CO_2 reduction

Abstract

Employing AZ31B Eco-Magnesium® (Eco-Mg) alloy in the European project Green Metallurgy (Green Metallurgy Project) process route provides the lowest carbon footprint since precursor materials. Chips produced from the machining phase can be used directly in the cold compaction step, and followed by direct extrusion to produce fully densified semifinished bars. These materials are of great interest in certain manufacturing sectors as they can impact future market scenarios based on the high rate of recycled material. Specifically, there are two key-points which can be considered sources of improvement: a) Eco-Mg alloys contribute to drastically reduce of the Global Warming Potential (GWP) of the entire process route as recycled chips have been used as feedstock material; b) Eco-Mg are less expensive materials, and therefore of interest to the automobile sectors for cost-driven lightweight components. Using 30% in-situ recycled chips material allows manufacturers to keep the total GWP of semifinished bar produced by the tested process route to about 76.2 kgCO2eq per kg of bar.

Introduction

The magnesium industry is experiencing a significant growth due in part to the automotive industry's demand for improved fuel economy, and subsequently reduced greenhouse gases (GHG) emissions. Substituting magnesium for conventional metals in vehicles can potentially reduce GHG emissions by up to 15% over the vehicle life time. As all magnesium processes are energy intensive and expensive in comparison with steel-making, to properly evaluate the impact of magnesium usage on medium-size passenger cars in terms of final net reduction of kgCO2eq over the vehicle's travel-life distance, it is necessary to calculate the negative impact on the environment starting from the GWP of the cradle-to-exit gate path. In this scenario, the European Project "Green Metallurgy", a 2 ML€ project co-financed by the European Community, aimed to demonstrate that it is possible to manufacture Mg-alloy products based on a single process route that allows either new high performance nanostructured magnesium alloys, or a highly environmentally friendly process route specifically optimized for the Eco-Magnesium alloys that have been recently introduced to the marketplace. As these lighter structural materials can be used in the transport sector, excellent weight saving possibilities are achievable. However, to effectively use lighter materials a general reduction of total specific energy consumed and the overall carbon-footprint produced in the cradle-to-exit gate phase must be targeted. The Green Metallurgy Project has investigated the possibility to develop a fully integrated process lay-out with a substantially reduced carbon footprint. The Green Metallurgy Project is led by three partners, two public scientific research institutes, the Politecnico di Milano (ITA) and the Centro Nacional de Investigaciones Metalurgica (SPA), and one company, Buhler AG (GER).

Past results of Green Metallurgy Project

One of the main purposes of the Green Metallurgy Project was to establish and assess a pre-industrial process capable of utilizing both nanostructured based high performance Mg-Zn(Y) magnesium alloys (also called, Basic Alloy System, BAS) and a fully-recyclable Eco-Magnesium alloys (also called, Alternative Alloy System, AAS) applying the same process route (Fig.1) which addresses environmental and competitiveness issues.

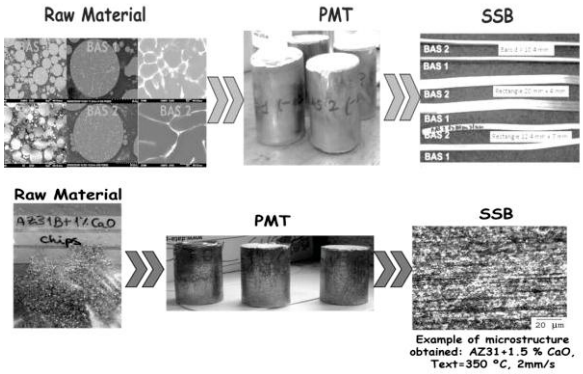


Figure 1 – Scheme of three main Green Metallurgy Project process route stages: from left to right, the primary materials fabricated the cold-compacted billets (precursor billets) and the final extruded materials for: a) BAS alloy fabricated by powder atomized materials to produce nanostructured Mg-alloys; b) AAS alloy fully recycled process route using commercial Eco-Mg alloys in the form of chips.

Specifically, the two different Mg-alloys systems consist of:

- The Basic Alloy System (BAS) is a Mg alloy systems based on chemical compositions developed at CEN; these material are Mg-Y-Zn base systems, capable of reaching the highest mechanical properties experimented with to date for Mg-based alloys;
- the Alternative Alloy System (AAS) is a commercial Eco-Magnesium AZ31 base alloy, namely a commercial Mg alloy system modified by the addition of a specific amount of CaO. The Eco-Mg series was recently developed by the Korean Institute of Industrial Technology (KITECH). It is spreading rapidly as it does not require the protective use of highly-environmental

impacting gases as the presence of CaO provides a protective cover during the melting phase.

The mechanical properties of BAS and AAS alloys addressed by project are shown respectively in Fig.2 and Fig.3.

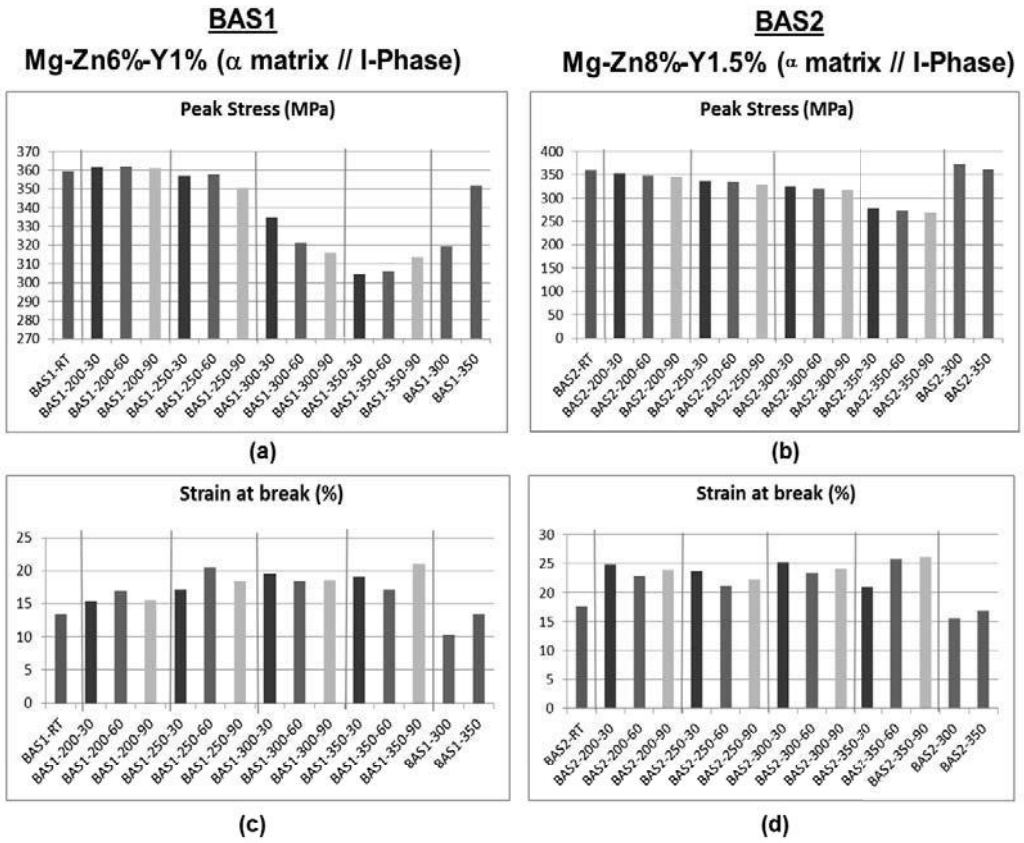


Figure 2 – Summary of main mechanical properties addressing resistance and ductility from the tensile tests conducted on BAS1 and BAS2 samples cut from semi-finished round section extruded bars. The sample code, for example "BAS1-200-30" means that the tensile tests have been conducted on an extruded bar BAS1 material BAS1-300, BAS1-350, BAS2-300 and BAS2-350 means bars of BAS1 and BAS2 materials have been directly extruded at 300°C and 350°C and not heat treated [1].

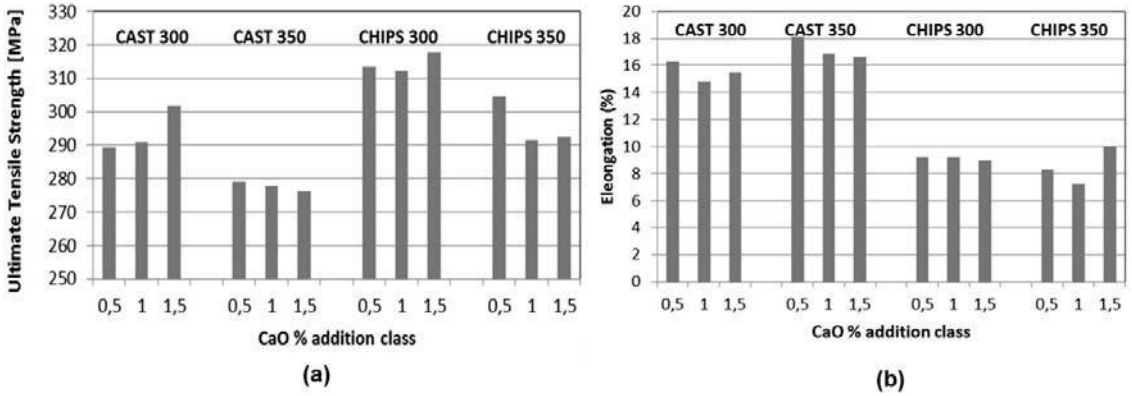


Figure 3 - Summary of main mechanical properties addressing resistance and ductility from the tensile tests conducted on Eco-Mg alloys (various CaO addition) samples cut from semi-finished round section extruded bars. The sample code "CAST-300" means that the tensile tests have been conducted on an extruded bar of Eco-Mg directly extruded from cast billet (reference material), meanwhile the code "CHIPS-350" means the test sample has been cut from a semi-finished bar extruded at 350°C from precursor billets compacted from raw materials in the form of chips.

During pilot plant layout design and optimization performed according to the industrial partner's requirements, both BAS and AAS materials were judged excellent for their adaptability to a very simplified process. The industrial partner Buhler's requests mainly focused on obtaining a final process lay-out that was easily scalable with cost-effective implementation. Compared to original lay-out proposals, the final optimized process allows both machinery and final product costs savings, which are key-factors in the marketability of the Green Metallurgy process for the automotive sector.
Several expensive steps have been eliminated in the final optimized lay-out, such as the intermediate ball-milling treatment which is both expensive and potentially hazardous, and has an extended process time, as well as the asymmetric rolling step, which is not necessary for preparing flat parts which can be directly produced by extrusion.
Fig.3 shows the final version of the optimized process lay-out after the completion of project activities.

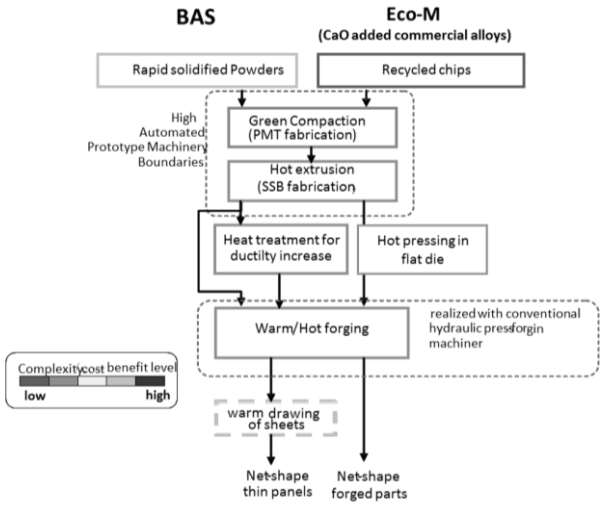
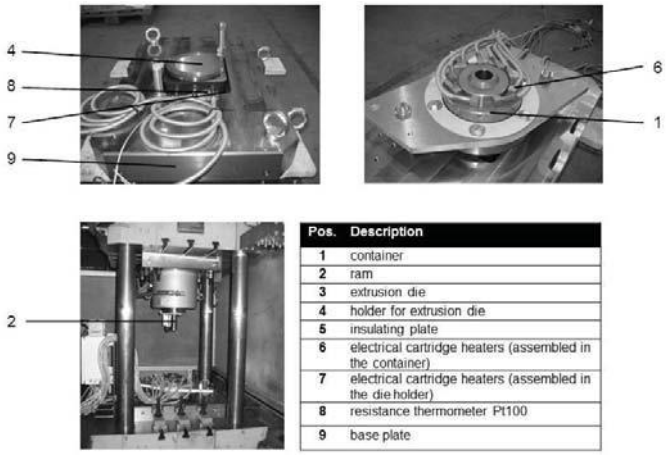


Figure 4 - The optimized process lay-out after the completion of project action [1].

The pilot plant was designed and built by Buhler AG and installed at the Buhler site in Viernheim, GER (Fig.5). It includes a compact, integrated line capable of processing the BAS and AAS systems in a single step even though BAS is in powder form and AAS is in chips. The pilot plant was evaluated as highly efficient in terms of low technological energy consumption as the integrated machinery works in fully solid state. Specifically, any stage conducted below 350°C realizes an energy reduction of 20% to 60%, respectively, if the BAS or the AAS routes are compared to conventional melting process routes. The pilot plant does not need high impacting protective gases to prevent magnesium oxidation and burning, which usually occurs at the melt stage.
In 2013 the pilot was set-up and definitively fine-tuned by running trials that produced SSB bars. The pilot is compliant with DIRECTIVE 2006/42/CE.



Pos.	Description
1	container
2	ram
3	extrusion die
4	holder for extrusion die
5	insulating plate
6	electrical cartridge heaters (assembled in the container)
7	electrical cartridge heaters (assembled in the die holder)
8	resistance thermometer Pt100
9	base plate

Figure 5 – Details of the special unit for the hot-extrusion unit equipping prototype machinery.

As previously commented and deeply explained in the following, Eco-Mg alloys in the Green Metallurgy process provides the lowest carbon footprint since chips produced from the machining phase can be used following the warm compaction step. The choice of Eco-Magnesium alloys is based on the possibility to exploit beneficial aspects derived from the particular chemical composition that can pursue and improve a project's objectives which have been originally set for the AAS system.
Specifically, two key-points are considered to be sources of improvements:

- Eco-Mg alloys are capable of providing a further reduction of the GWP in the process as they can be fully recycled as feedstock material and are suitable for manufacturing processes;
- Eco-Mg are more economical and could be more easily accepted for low-performance components in automotive sectors, primarily for cost-driven components.

Concerning the first point, it has been demonstrated in the Green Metallurgy Project that Mg type alloys added with CaO can be successfully re-used since they can be directly recycled in form of chips as feedstock material to produce semifinished extruded bars, avoiding re-melting processes [1]. Confirming previous literature [2-7], Mg alloys with added CaO showed excellent mechanical properties [1]. This is also attributable to the capability of CaO to prevent the coarsening of the refined grains produced in the preliminary machining operation step.
The use of Eco-Mg in the Green Metallurgy project has been chosen in order to successfully combine some benefits of both Eco-Magnesium alloys, that are characterized by lower oxidation sensitivity with specific Green Metallurgy process lay-out of direct extrusion pathway.

Life Cycle Assessment of ECO-Mg type used in Green Metallurgy path

This study has been carried out with results provided through the courtesy of KITECH, which was part of the Green Metallurgy project. The objectives of the study have been:

- to estimate the GWP as measure of product-process carbon footprint of the Green Metallurgy manufacturing process that would employ Eco-Magnesium AZ31D type, a novel manufacturing process for Eco-Magnesium alloy-based parts produced by low-impacting process route that starts from recycled chips;
- to compare the results with the conventional production routes as reported in the literature.

Life Cycle Assessment has been used as a tool to estimate the GWP of the life cycle of AAS to produce 1 kg of semi-finished product in the form of extruded bars.

Basic framework of Life Cycle Assessment tool applied to metallurgy processes

The Life Cycle Assessment is the process of quantifying material and energy and potential environmental impact of technological systems. It involves the evaluation of various environmental aspects of a product in order to assess the impact of a product throughout its life. Generally it starts with the compilation of relevant environmental exchanges during the life cycle of a product, with the evaluation of the potential environmental impact expressed by GWP and measured in kgCO2eq, that can be estimated and calculated for all the exchanges. A full product life cycle is usually divided into two stages:

- the production phase that goes from raw material extraction and refining, to final product;
- usage phase that covers the estimated carbon footprint emissions from product use, recycling and disposal.

As the production of metals generally results in the overall supply of material, mineral resource extraction and intermediate phases for processing raw materials, and following secondary manufacturing processes that are particularly critical for the potential release of pollutant emissions and the consumption of a significant number of various sources for non-renewable energy (i.e. zero-emission energy), it is suggested that the life cycle products be divided into three steps to include an intermediate phase:

- cradle-to-entry gate (raw material extraction and refining);
- entry gate-to-exit gate (product manufacture);
- exit gate-to-grave (product use, recycling and disposal).

The Life Cycle Assessment applied to Green Metallurgy processes

For the project, and the purpose of this work, the system boundaries have been identified as the "cradle-to-exit gate" material pathway. The "exit gate" is considered the boundary of the projects demonstrative activities, thus limited to the output of the machinery prototype, namely the semi-finished extruded bars of AAS. This overt carbon footprint was estimated by considering the functional unit of 1kg of semi-finished product produced by the Green Metallurgy process that employs Eco-Mg chips as feedstock material. More specifically, for the final calculation of total GWP for the "cradle-to-exit gate" Green Metallurgy path with Eco-Mg, the material flow was split into the two subsequent stages described below.

The upstream path: Life Cycle Assessment results for the "cradle-to-entry gate" route

Upstream process route steps necessary for the production of raw materials used in the prototype machinery have been considered as reference material flow in the unit process as it is shown in Fig.6. Therefore results obtained in this case actually accounts for the carbon footprint expressed in kgCO2eq for the output product, the functional unit 1kg of Eco-Mg type alloy AM30 that is actually equivalent to the AZ31B used in the project demonstrations for Life Cycle Assessment purposes.

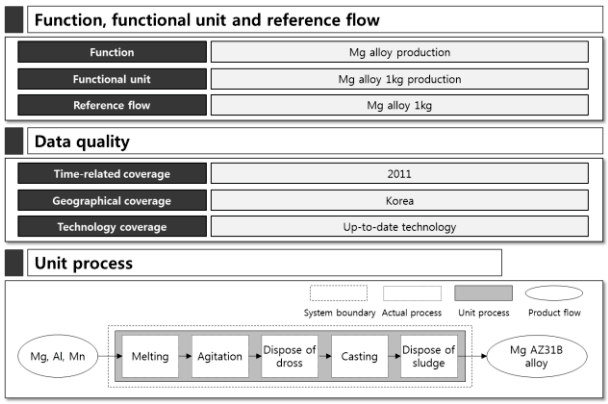


Figure 6 – Reference flow and main input data for Global Warming Potential calculation over the "cradle-to-entry gate" (courtesy of KITECH).

At the first step, the system boundaries for the material flow have been defined. They take into account the following stages:

- extraction of raw materials (Mg, Al and Mn mining in China);
- marine transportation of raw materials from China to Korea;
- production of Mg alloy in Korea;
- scrap recycling/disposal in Korea.

Shown in Table I is the second step of the inventory analysis that is based on data collected for the input and output of materials and energy sources associated with the production of the functional unit, 1kg of Eco-AM30 type alloy.

Sorting		Name	Amount	Unit
Input	Raw materials	Mg	1.02E+00	kg
		Al	3.19E-02	kg
		Mn	4.57E-03	kg
		CaO	5.32E-03	kg
	Energy	Electricity	1.51E+00	kWh
Output	Product	Eco-Mg AM30 alloy	1.00E+00	kg
	Wastes	Dross & Sludge	6.38E-02	kg

Table I – Inventory analysis results for production of 1kg of Eco-AM30 type alloy, 0.5% CaO added (courtesy of KITECH).

At the third step, a Life Cycle Impact Assessment (LCIA), part of a Life Cycle Assessment process route analysis, was performed. As a first element, LCIA requires the definition of such impact categories (e.g. abiotic resources, biotic resources, land use,

global warming, stratospheric ozone depletion, etc. [7]) which refer to the resulting quantifying environmental impact of inventory data (refer to Table I). Due to the nature of sources considered in the inventory category, it was decided to take into account the greenhouse effects of the production of 1kg of Eco-AM30 type alloy, accounting for the greenhouse effect on the environment resulting from the sources consumed in the process flow. The greenhouse impact of sources is expressed as CO2-equivalents, i.e. the effect of the input and output sources are expressed in relationship to the effect of CO2 either locally (e.g. usage of SF6 gases during melting steps, usage of methane for furnace heating, etc.) or remotely (usage of non-renewable energy sources) produced in the process flow steps. The results of the LCIA performed on functional unit product are shown in Figure 7.

Sorting	Name	Effects [kg CO_2 eq./kg]	Contribution ratio
Input	Mg lumps	9.96E+01	98.61%
Input	Electricity	7.47E-01	0.71%
Input	Al lumps	9.68E-02	0.10%
Input	Mn powder	3.11E-02	0.03%
Input	Transportation	1.21E-02	0.02%
Input	CaO powder	4.56E-03	0.01%
Output	Dross & Sludge	1.55E-04	0.01%
Total		1,0049E+02	

Table II – LCIA results for production of 1kg of Eco-AM30 type alloy, 0.5% CaO added (courtesy of KITECH).

The production of a raw Eco-Mg AM30 type system, equivalent to an AZ31B system in terms of total GWP accounts for 100.49 kgCO2eq/ kg of raw material produced.

The downstream path: LCA results for the "entry gate-to-exit gate" route

The downstream process route spans from the cold compaction of input material feedstock, Eco-Mg type alloy in the form of chips, to the hot-extrusion stage to produce semi-finished bars . All those steps are realized by the prototype machinery in Germany.
The total GWP of the downstream process accounts for 6.2 kgCO2eq per kg of semi-finished bars produced, respectively from 3.4 kgCO2eq for the hot extrusion step and 2.8 kgCO2eq for the cold compaction [1]. The majority of the GWP in the cold compaction and hot extrusion process is due to the consumption of electricity, which adds around 15% to the total [1].

The Life Cycle Analysis results for Green Metallurgy "cradle-to exit gate" stage

First of all it was necessary to define the functional product unit for the overall process. Since the scraps left at the end of the extrusion step are fully recycled, the amount of raw fresh materials, the ECO-Mg type alloy, used to produce 1kg of semi-finished extruded bars must be accounted for taking into consideration the average recycling ratio obtained by mixing fresh Eco-Mg type alloy with the parent material obtained by in-situ recycling of scraps resulting from the hot extrusion process. The conservative assumption we adopted in the present LCA calculation is 30% of in-situ recycled materials.

Two scenarios are therefore considered: a) feedstock materials is composed of fresh Eco-Mg type alloy produced in Korea with process flow discussed in the previous section; b) lowest environmental impact scenario that considers feedstock Eco-Mg type alloy ideally procured from a mature market that will supply fully recycled Eco-Mg type alloy in the form of eco-chips.
For both scenarios we calculated the GWP of the Green Metallurgy path using Eco-Mg type alloys.

Scenario a): 30% in-situ recycled chips and 70% of fresh material

Per kg of semi-finished bars produced, GWP of feedstock material is counted as:

- 70% of Eco-Mg type alloy in form of chips accounts for around 70.34 $kgCO_2eq$ (= 0.7 kg x 100.49 $kgCO_2eq./kg$);
- 30% of in-situ recycled material, accounts for 0 $kgCO_2eq$,

for a total 70.34 $kgCO_2$ per kg of feedstock materials. It represents the "cradle-to-entry gate" carbon footprint in terms of GWP.
The total GWP for this base scenario accounts for 76.54 $kgCO_2eq/kg$ of SSB produced, which results from adding an upstream and downstream process path.

Scenario b): 30% in-situ recycled chips and fresh feedstock materials consisting in 100% of recycled material

Per kg of semi-finished bar produced, the GWP of feedstock material is counted as 0 $kgCO_2eq.$ per kg of feedstock materials. It represents the zero-emission "cradle-to-entry gate" carbon footprint in terms of GWP.
Therefore the total GWP results for this base scenario accounts for 6.2 $kgCO_2eq/kg$ of SSB produced as it results from the addition of two contributes of upstream and downstream process paths.

Conclusions

This work has estimated for the first time the carbon footprint and primary energy demand for the Alternative Alloy System (AAS) being developed within the "Green Metallurgy" European Project, which concluded in August 2013. The carbon footprint of manufacturing process steps realized by novel prototype machinery developed by Buhler AG is estimated at 6.2 $kgCO_2eq./kg$ semi-finished extruded bars (SSB) produced. Such a low value has to be added to the Global Warming Potential (GWP) resulting from usage of feedstock material used in the manufacturing process. Results obtained by splitting the life cycle process (namely the material feedstock and the transforming steps carbon footprint contributions) into two-stages demonstrates the main carbon footprint 'hotspots' are in the upstream feedstock material generation. On one hand, Green Metallurgy manufacturing process carbon footprint is quite aligned with a conventional low-impacting extrusion process; on the other hand it allows us to employ novel low-impact Mg alloys, as Eco-Mg are indisputably considered today, at best: the pre-industrialized process have demonstrated suitability of employing recycling chips of Eco-Mg type as feedstock material.
This successful combination of environmentally friendly material and a low-impact technology process allows us to achieve the lowest carbon footprint if Eco-Mg type alloy in the form of recycled chips (most produced by extensive secondary machining operations) can actually be supplied in future market scenarios.

Acknowledgements

This work makes use of results produced by the Green Metallurgy project (http://www.green-metallurgy.eu), co-funded by the European Commission within the 2009 LIFE+ Programme. Authors thank support provided by European Commission for supporting project dissemination activities. This work reflects only the authors' views. The Community is not liable for any use that may be made of the information contained therein.

References

1. F.D'Errico, G.Garces Plaza, F. Giger and Shae K. Kim, *"Final Assessment of Preindustrial Solid-State Route for High-Performance Mg-System Alloys Production: Concluding the EU Green Metallurgy Project"*, *JOM*, October 2013, Volume 65, Issue 10, 1293-1302.

2. J. K. Lee et al., "Effect of CaO addition on ignition behavior in molten AZ31 and AZ91D Magnesium alloys." Rare Matals, 25 (2006) 155-159.

3. S. H. Ha et al., "The behavior of CaO and Ca in pure Mg", Rare Metals, 25 (2006) 150-154.

4. S. H. Ha et al., "Effect of CaO on oxidation resistance and microstructure of pure Mg", Materials Transactions, JIM, 49, (2008), 1081-1083.

5. D. I. Jang et al., "Effect of CaO on AZ31 Mg Strip Castings", Materials Transactions, JIM, 49 (2008), 976-979.

6. J. K. Lee et al., "Development of Novel Environment-friendly magnesium alloys", Advanced Materials Research, 47-50 (2008) 940-943.

7. ISO 14040 (1997) Environmental Management – Life Cycle Assessment – Principles and Framework. ISO/FDIS.

Magnesium Technology 2014
Edited by: Martyn Alderman, Michele V. Manuel, Norbert Hort, and Neale R. Neelameggham
TMS (The Minerals, Metals & Materials Society), 2014

The IMA Study on the Life Cycle Assessment (LCA) of Magnesium

Horst E. Friedrich, Simone Ehrenberger
Institute of Vehicle Concepts, German Aerospace Centre (DLR), Pfaffenwaldring 38-40, 70563 Stuttgart, Germany
horst.friedrich@dlr.de

Extended abstract:

Goal and Scope
Magnesium shows considerable potentials as lightweight material for weight sensitive applications. To assess the potential environmental benefits of magnesium in transport applications, the International Magnesium Association (IMA) initiated a study on the life cycle assessment (LCA) of magnesium.
The goal of this study was to assess the environmental potential of magnesium as lightweight material for the use in road vehicles and aircrafts. For magnesium production and processing, up-to-date technologies are evaluated. Two application examples represent the use of magnesium in transport: a steering wheel for road vehicles and magnesium parts for an aircraft door. The evaluation of the end-of-life of magnesium parts aims to assess a representative recycling path for magnesium.
The overall life cycle of both magnesium parts is compared to aluminium as an alternative material. We focus on the impact assessment results for greenhouse gas (GHG) emissions (CO_{2eq}).

Life Cycle Steps
Primary magnesium can be produced via thermal reduction or electrolysis. This study assesses the state of the art Pidgeon process of the year 2011 in China. The weighted result for GHG of the Pidgeon process according to the production figures in 2011 is 25.8 kg CO_{2eq} per kg primary magnesium. The use of production wastes from fuel production can be credited to the primary magnesium production. When applying this approach, the weighted average GHG emissions of the Pidgeon process is 19.9 kg CO_{2eq} / kg Mg.
Furthermore, we evaluated a representative, state-of-the art electrolysis process. The GHG emissions amount to 17.8 kg CO_{2eq} per kg primary magnesium. When crediting the by-products of the process, the net emissions of the electrolysis for primary magnesium amount to 14.0 CO_{2eq}.
The study focuses on two exemplary applications for magnesium which also represent two different production routes for components. The steering wheel for cars is manufactured by die-casting. The door parts for aircrafts are manufactured via sand casting for which a separate energy and material flow model has been developed. Magnesium needs less energy and material for manufacturing compared to aluminium in both processes. Thus, GHG are lower as well.
Concerning the end-of-life of the products, we focus on the evaluation of road vehicles. The end-of-life scenario influences the overall balance for automotive applications, whereas in case of aircraft components the emissions during the use stage are too dominant. After the end-of-life treatment, magnesium usually ends up in the light metal fraction together with aluminium.

Overall Life Cycle Balance for Magnesium Use in Transport
A major goal of using lightweight materials in transport is to save weight and fuel. We calculated the overall fuel reduction over a life mileage of 200,000 km. All magnesium scenarios have lower greenhouse gas emissions over the whole life cycle of the steering wheel. The CO_{2eq} emissions are calculated as net differences to the aluminium reference. Magnesium made by electrolysis has lower emissions already during its production stage due to the fact that less material has to be produced. The average Pidgeon process with credits for the use of waste gases shows a break-even point of about 46,000 km. The average Pidgeon magnesium without credits shows an advantage in the overall balance when end-of-life is included.
For the application of magnesium in aircrafts, the use as door parts in a middle haul aircraft has been analyzed. The higher emissions from production of the door parts are amortized after less than ten flights for all Pidgeon process based magnesium scenarios. The high energy consumption of aircrafts justifies the use of magnesium as lightweight material after a short time of operation.

Conclusions
The assessment of the current primary magnesium production shows that the processes have been subject to considerable technological improvements during the past years. The results show the positive effects of lightweight design in transport applications and the potentials of magnesium for such applications. Nevertheless, further improvements in the efficiency of the production process and the effective recycling of magnesium post-consumer scrap are necessary to enhance the environmental performance of magnesium. Recent developments of the existing magnesium production routes and plans for new production sites point in the right direction.

Magnesium Technology 2014
Edited by: Martyn Alderman, Michele V. Manuel, Norbert Hort, and Neale R. Neelameggham
TMS (The Minerals, Metals & Materials Society), 2014

DYNAMIC BEHAVIOR OF A RARE EARTH CONTAINING Mg ALLOY, WE43B-T5, PLATE WITH COMPARISON TO CONVENTIONAL ALLOY, AM30-F

Sean Agnew[1], Wilburn Wittington[2], Andrew Oppedal[2], Haitham El Kadiri[2], Matthew Shaeffer[3], K.T. Ramesh[3], Jishnu Bhattacharyya[1], Rick DeLorme[4] and Bruce Davis[4]

[1] Materials Science and Engineering, University of Virginia, Charlottesville, Virginia, 22904-4745, USA
[3] Mechanical Engineering, Mississippi State University, Starkville, Mississippi, 39762, USA
[2] Mechanical Engineering, Johns Hopkins University, Baltimore, Maryland, 21218-2682, USA
[4] Magnesium Elektron North America, Madison, Illinois 62060, USA

Keywords: texture, dynamic, high strain rate, strain rate sensitivity, twinning

Extended Abstract

The dynamic behavior of Mg alloys is an area of interest for applications, such as crash-sensitive automotive components and armor. The Mg alloy designated WE43 (which contains additions of 3.7-4.3 wt% yttrium (W), 2.4-4.4 wt% neodymium-rich mischmetal (E), and at least 0.4 wt% zirconium) was originally introduced as a casting alloy with similar high temperature strength and improved ductility, relative to sister alloy, WE54 [1,2]. More recently, the alloy has been developed into a commercially produced direct-chill cast and hot rolled plate product [e.g. 3]. This material has demonstrated potential as an armor material, given its good ballistic performance, relative to competing lightweight metallic materials, such as Al-Mg alloy 5083 [4].

The goal of the present study was to examine the high strain rate deformation behavior of commercially produced thick (38 mm) plate of Mg alloy WE43B-T5. Tests were also performed on a more conventional extruded Mg alloy, AM30-F, which was recently proposed as a replacement for some potential applications of AZ31B, since it can be extruded at higher rates [5]. One feature that has been emphasized in prior studies is the dominant role of crystallographic texture. Thus, a complete description of the texture in the material prior to testing is pursued using x-ray and neutron diffraction. Figure 1 shows that this rare earth element containing alloy develops a texture of moderate strength (peak pole figure intensity of 4.6 multiples of a random distribution, after averaging data collected through the thickness.) **Note:** The complete experimental details, results, analysis and list of references are given in a full paper with the same title submitted for publication in a special issue of the journal JOM.

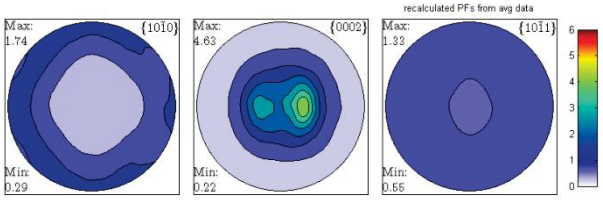


Figure 1. X-ray pole figures obtained by averaging data collected at 1/6th, 1/3rd, and 1/2 thickness planes.

The quasistatic (10^{-3} 1/s) and dynamic (~600 - 5100 1/s) mechanical behaviors of two Mg alloys, rolled WE43B-T5 and extruded AM30-F were investigated using servohydraulic and Kolsky bar testing in uniaxial tension and compression. WE43B-T5 plate is shown to exhibit a relatively isotropic yield strength at quasi-static (0.001 1/s) and dynamic (~1000 – 5000 1/s) strain rates. This is despite the fact that the plate is revealed to have a crystallographic texture of moderate strength (Fig. 1). See Figure 2 for sample compression data obtained in the study.

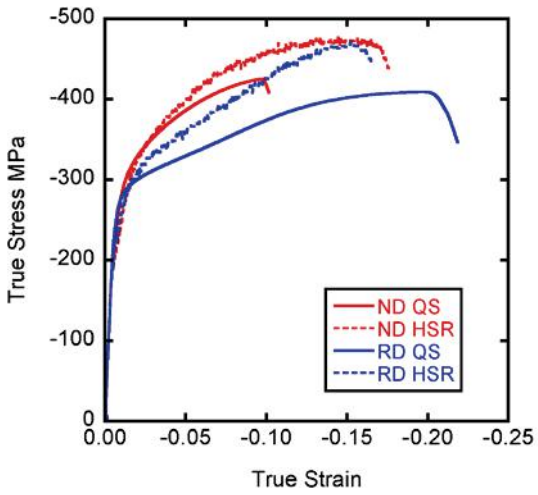


Figure 2. High strain rate (HSR~1000/s) and quasi-static (QS=0.001/s) compression test results for alloy WE43-T5 tested parallel to the rolling (RD) and normal (ND) directions.

In comparison, extruded AM30-F exhibits stronger anisotropy in strain hardening behavior (Fig. 3), which is related to the strong <10.0> fiber texture and the significant level of {10.2} twinning which occurs during compression along the extrusion direction. The strain rate sensitivity of the yield strength is observed to vary with testing direction. This is related to the fact that different deformation mechanisms control yielding along the different directions [6] and these different mechanisms have different rate controlling processes. For example, {10.2} extension twinning is known to be relatively rate insensitive [7], so the yield strength is observed to be rate insensitive when that mechanism is dominant.

At larger strain levels, the rate sensitivities along different directions converge, similar to recent observations of Ulacia et al. [8]. The average values of m = 0.013 and 0.008 obtained for AM30-F and WE43B-T5, respectively, are comparable to those observed for a variety of conventional Mg alloys, processed in a variety of ways, suggesting that there is not a strong alloy, microstructure, or texture dependence.

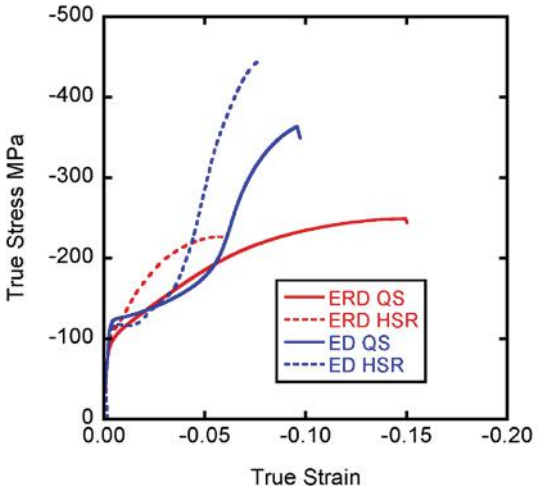


Figure 3. High strain rate (HSR~1000/s) and quasi-static (QS=0.001/s) compression test results for extruded alloy AM30 tested parallel to the extrusion (ED) and radial (ERD) directions.

The ductility of the two alloys is similar, though the average value (over all the directions tested) is higher for the new plate alloy WE43B-T5. This cannot be associated with a higher resistance to strain localization due to higher rate sensitivity, since the WE43B-T5 actually has a lower strain rate sensitivity than the AM30-F. Instead, it must be due to details of the failure mechanism. The details are presently under investigation. As highlighted in an early study of the material [9], the energy absorption capacity of WE43B-T5 is good, due to the combination of high strength (~300 MPa), moderate ductility (0.07 – 0.20) and low density.

Acknowledgements:

SRA would like to thank McMaster University for sponsoring a visiting faculty appointment during which this paper was written. The research at UVA and MSU was sponsored by the United States Army Research Office under contract number W911NF-12-1-0455 monitored by Dr. Suveen Mathaudhu. The research at MENA and JHU was sponsored by the Army Research Laboratory and was accomplished under Cooperative Agreement No. W911NF-07-2-0073 with technical monitor, Kyu Cho. The views and conclusions contained in this document are those of the authors and should not be interpreted as representing the official policies, either expressed or implied, of the Army Research Laboratory or the U.S. Government. The U.S. Government is authorized to reproduce and distribute reprints for Government purposes notwithstanding any copyright notation hereon.

References:

1. W. Unsworth et al., US Patent #4,401,621, 1983.
2. Magnesium Elektron, Elektron WE43, Datasheet: 467
3. M. Turski et al., "Validation of Predicted Residual Stresses within Direct Chill Cast Magnesium Alloy Slab," *Metall. Mater. Trans. A*, 43A (5) (2012), 1547-57.
4. K. Cho et al. , "Magnesium Technology and Manufacturing for Ultra Lightweight Armored Ground Vehicles," Army Research Laboratory Report, ARL-RP-326, (DTIC Online, 2009) Accession Number: ADA499411.
5. A.A. Luo and A.K. Sachdev, "Development of a New Wrought Magnesium-Aluminum-Manganese Alloy AM30," *Metall. Mater. Trans. A*, 38A (6) (2007), 1184-1192.
6. A. Oppedal et al., "Anisotropy in hexagonal close-packed structures: improvements to crystal plasticity approaches applied to magnesium alloy," *Phil. Mag.* (2013) doi:10.1080/14786435.2013.827802.
7. M.T. Tucker et al., "Anisotropic effects on the strain rate dependence of a wrought magnesium alloy," *Scripta Mater.*, 60 (2009) 182-185.
8. I. Ulacia et al., "Mechanical behavior and microstructural evolution of a Mg AZ31sheet at dynamic strain rates" *Acta Mater.*, 58 (2010) 2988–2998.
9. T. Mukai et al., "Experimental study of a structural magnesium alloy with high absorption energy under dynamic loading," *Scripta Mater.*, 39 (9) (1998), 1251-1253.

Magnesium Technology 2014
Edited by: Martyn Alderman, Michele V. Manuel, Norbert Hort, and Neale R. Neelameggham
TMS (The Minerals, Metals & Materials Society), 2014

THERMODYNAMIC AND KINETIC CALCULATIONS FOR TRC (TWIN ROLL CASTING) Mg ALLOY DESIGN

In-Ho Jung[1] and Manas Paliwal[1]

[1]Department of Mining and Materials Engineering, McGill University; 3610 University, Montreal, Quebec, H3A2B2, Canada

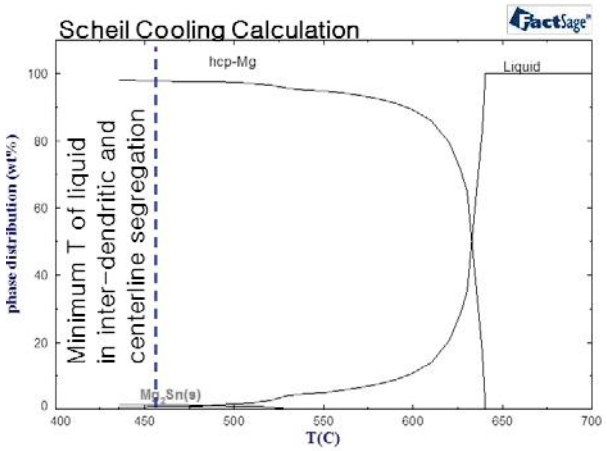
Keywords: Twin Roll Casting, Mg alloy, Inverse segregation, Thermodynamic calculations

Abstract

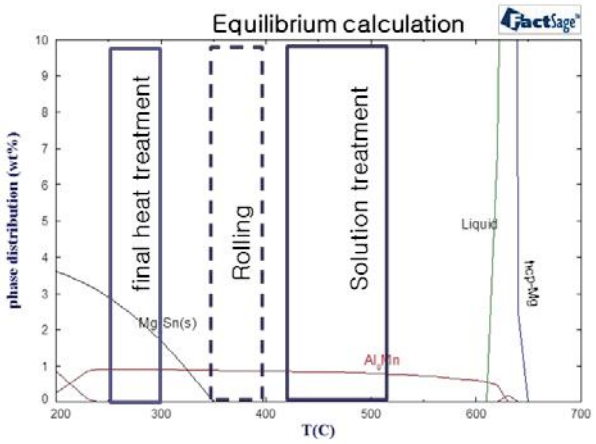
Twin roll casting (TRC) process is most cost competitive casting process to produce wrought Mg alloys. At the moment, this process is successfully applied to the production of AZ series Mg alloys with low Al content. From microstructure viewpoint, one of the most concerns in the process is the control of inverse segregation which is inherent problem in TRC process. The inverse segregation is known to be formed when the remaining highly solute enriched liquid between solidified columnar zone is squeezed out through the weak columnar layer due to the compressed force during the solidification in TRC process. The alloys with a large amount of remaining liquid at low temperature and a long solidification range can be more prone to produce severer inverse segregation in TRC process. The other constraint of TRC alloys is the secondary phase amount during rolling process. Too much secondary phase can increase the roll force and induce defects during warm rolling. However, the precipitation of secondary phase at low temperature during the final heat treatment will be beneficial for increasing strength. In the design of new TRC Mg alloys, all these aspects should be considered.

In the present study, the simple calculation scheme to predict as-cast microstructure of Mg alloy in twin roll casting was developed based on non-equilibrium Scheil cooling calculations. This calculation can give the evaluation of the tendency for the formation of inverse segregation. In addition, the equilibrium calculations were performed to evaluate the heat treatment condition for homogenization (300°C ~ 450°C) and final annealing process (150°C ~ 200°C) for secondary phase precipitation. FactSage thermodynamic software with FTlite database was used for the thermodynamic calculation. The newly developed kinetic solidification model was also used to calculate the solidification behavior at the cooling rate of TRC process. All the possible conventional alloying elements for Mg alloys were classified into primary alloying elements and secondary alloying elements based on the solubility limit of alloying element in hcp Mg. Then, the combinations of primary and secondary alloying elements were tested to find the optimum TRC alloys which can have similar or less inverse segregation tendency as AZ31 alloy, have similar or low roll force, but have a large precipitation hardening during final heat treatment. Several modifications of Mg-Al based alloys and Mg-Sn based alloys were designed for the possible candidates of TRC process.

For example, Fig. 1 shows the thermodynamic and Scheil cooling calculation for the Mg-3%Sn-1%Al-0.3%Mn alloy. According to the Scheil cooling calculations in Fig. 1(a), the amount of remaining liquid during the solidification (that is, the liquid amount concentrated between growing columnar dendrites from the water-cooled rolls) in this alloy is smaller than that of AZ31 alloy. Therefore the tendency of inverse segregation becomes lower. The amount of Al_6Mn phase for this new alloy is almost the same as the AZ31 at the temperature between 350°C to 500°C. Thus, if the work hardening by Al and Sn in the hcp Mg is similar, the rolling behavior of new alloy would be similar to that of AZ31 alloy. After the rolling process, the alloy can be heat treated below 300°C and can produce a large amount of Mg_2Sn phase. As the precipitation can occur at solid state, the fine Mg_2Sn precipitates can be formed homogeneously in the matrix Mg phase which can increase the strength significantly.



(a)



(b)

Fig. 1. TRC alloy design calculations. (a) Scheil cooling calculation and (b) equilibrium calculation for Mg-3%Sn-1%Al-0.3%Mn alloy.

Magnesium Technology 2014

Powders, Recycling, Hydrometallurgy, Primary Production, and Creep

Magnesium Technology 2014
Edited by: Martyn Alderman, Michele V. Manuel, Norbert Hort, and Neale R. Neelameggham
TMS (The Minerals, Metals & Materials Society), 2014

EMERGING APPLICATIONS USING MAGNESIUM ALLOY POWDERS: A FEASIBILITY STUDY

Rajiv Tandon and Deepak Madan
Magnesium Elektron Powders, 2590 Ridgeway Blvd, Manchester NJ 08759, USA

Keywords: magnesium powders, lightweight, powder metallurgy

Abstract

The use of powder metallurgy offers a potential processing route based on tailored compositions and unique microstructures to achieve high performance in magnesium alloys. This paper highlights recent advances in the production, qualification, and characterization of gas atomized AZ91E, WE43 and Elektron21 alloy powders. Transmission electron microscopy (TEM) was used to understand the bulk and surface structure of the atomized powder. The potential for using these magnesium alloy powders for emerging applications involves establishing compatibility with viable consolidation processes such as cold spray, laser assisted deposition, forging and extrusion. This study summarizes the preliminary results for various ongoing investigations using WE43 powder as an example. Results show that powder metallurgy processed WE43 results in comparable properties to those obtained from cast and wrought and offers potential for improvement.

Introduction

Background

There is an emerging interest in the use of magnesium alloys in various engineering applications which are driven largely by the need for lightweighting to achieve higher levels of fuel efficiency [1-6]. Several powder metallurgy routes are being investigated with the goal of targeting novel compositions and unique microstructures leading to high performance lightweight magnesium applications. Rapidly solidified powder and the use of nanostructured powder have been studied and reported in the literature with promising results [7-10]. For example, tensile yield strengths of 610 MPa (87 ksi) with an elongation of 5% have been reported for a Mg-0.8Zn-2.1Y alloy [7], and yield strength of 425 MPa (60 ksi) with an elongation of 9.6% have been reported for a Mg-6Al-0.5Mn-2Ca alloy [8] using a powder metallurgy approach.

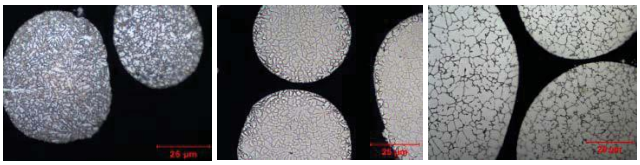
Other magnesium powder based manufacturing processes in the early stages of investigation include additive manufacturing [11], metal injection molding [12,13], and cold spray. Additive manufacturing and metal injection molding offer a unique path for fabricating intricate components, such as Mg alloy based bio-absorbable implants. Cold spray technology using Mg alloy powders offers a potentially novel approach to repair and refurbish expensive Mg castings and structures that have to be taken out of service due to wear and corrosion, in addition to fabricating near net shaped structures such as casings and liners.

Most of the published work in the literature has relied on laboratory scale powder manufacturing and consolidation methods. To some extent, these approaches have been based on alleviating concerns about magnesium powder production and handling. To develop a commercial scale process it is important to establish at the onset the compatibility of Mg alloy powders with the processing hardware and equipment, while taking into account the specific characteristics of that particular magnesium alloy.

Recently, a scalable technology for the production of atomized magnesium alloy powders was established based on collaboration between the US Army Research Laboratory (ARL), US Army RDECOM and Magnesium Elektron Powders. Gas atomized AZ91E, WE43, and Elektron21 powders have been developed and characterized. In a parallel effort, prealloyed powders having the same composition as the above mentioned alloys were also produced on a commercial scale by grinding. Selected consolidation routes including forging, extrusion, cold spray deposition, and laser additive deposition were investigated using the WE43 prealloyed powder and early stage results are discussed in this paper.

Procedure

Magnesium Alloy Powders: Magnesium alloy powders AZ91E, WE43, and Elektron21 were produced using an inert gas atomization process. Figure 1 shows the cross section optical micrographs of the lightly etched -100/+325 mesh fractions for the three atomized powders. All three powders showed a fine dendritic microstructure resulting from the rapid solidification during the atomization process. The interdendritic spacing for all three alloys were measured between 1 to 3 microns for the -100/+325 mesh distribution.



(a) (b) (c)

Figure 1. Optical micrographs of (a) gas atomized AZ91E -100/+325 mesh, (b) gas atomized WE43 -100/+325 mesh and (c) gas atomized Elektron21 -100/+325 mesh, alloy powders.

The powder characteristics of the three atomized magnesium alloy powders are shown in Table I. The -325 mesh fraction was non free flowing. All three powders had similar tap density and flow rate behavior for similar size fractions.

The atomized WE43 alloy powder was prepared via FIB-INLO technique for TEM analysis. Figure 2 shows two adjacent powder particles mounted in epoxy. The surface and bulk region of one of the particles (shown by inset photo of Powder 2) was analyzed using X-ray Energy Dispersive Spectrometry (XEDS). The surface region of the powder in area 1 shows the presence of oxygen and rare earth elements such as Nd and Y, as compared to the bulk region in area 2. Enrichment of Y, Nd, Gd, and Sm was also observed in the interdendritic regions of the solidified powder. The presence of surface oxygen can be attributed to a passive film that is created during the atomization process.

Table I. Apparent density, tap density, flow rate, and particle size distribution for atomized magnesium alloy powders.

Powder Designation	Apparent Density g/cm^3	Tap Density g/cm^3	Flow Rate s/50g	D_{10}, D_{50}, D_{90} µm
AZ91E -325 mesh	0.75	0.93	No flow	7, 21, 41
AZ91E -100/+325 mesh	0.97	1.09	73	55, 94, 153
WE-43 -325 mesh	0.78	0.94	No flow	7, 21, 40
WE-43 -100/+325 mesh	0.99	1.09	67	50, 83, 133
E-21 -325 mesh	0.75	0.89	No flow	7, 21, 42
E-21 -100/+325 mesh	1.0	1.11	79	50, 95, 163

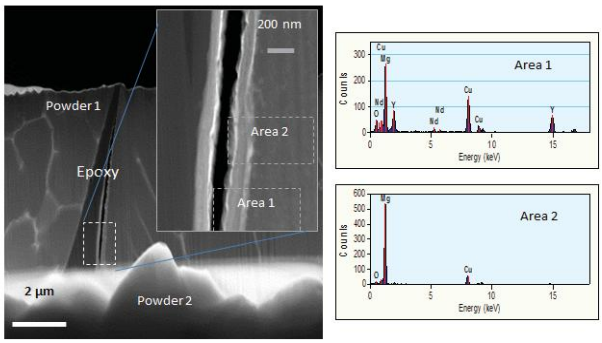


Figure 2. TEM image of the cross section of atomized WE43 powder showing the surface and interior regions of powder and the elemental segregation.

Forging: Atomized WE43 powder (80/325 mesh) with a d_{50} of 90µm was used for powder forging. The powder was first consolidated into a preform using cold isostatic pressing and subsequently forged by heating and placing in a granular pressure transmitting media. One billet was subsequently forged a second time (double forged). The single forged billet was approximately 10 cm in diameter and 13 cm in height, wand weighed 2.5kg. The double forged billet was approximately 12 cm in diameter and 11.4 cm in diameter. The billet was machined into tensile specimens of 0.64 cm gauge diameter and 2.54 cm gauge length and tested according to ASTM E8-09 as shown in Figure 3.

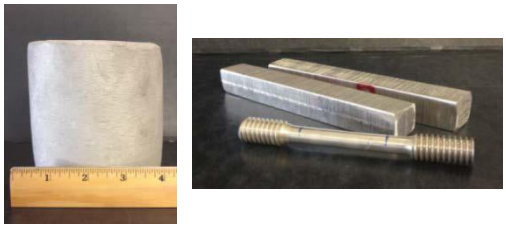


Figure 3. Tensile specimens machined from the forged billet.

Rolling: A feasibility study into rolling was also performed on the consolidated WE43 billet. For the rolling trials a forged cylinder was machined into flat plates by water-jet cutting into 0.64 cm thick sections. The plates were preheated between 340-470°C and rolled at 10, 15 and 20% reduction per pass for total reduction ranging from 50 to 72%, as shown in Figure 4.



(a) (b)

Figure 4. Photographs showing (a) a 0.64cm thick plate used for rolling trials, and (b) a rolled plate and the tensile specimens machined from a rolled plate.

The forged WE43 generally exhibited good formability under the rolling conditions used. However, it was noted that a 20% reduction per pass resulted in cracks and tears along the edges and in transverse direction. Some of these defects resulted from pre-existing surface flaws. Mechanical properties were measured on two rolled plates that were rolled at 10% reduction per pass for a total of 72% reduction in thickness.

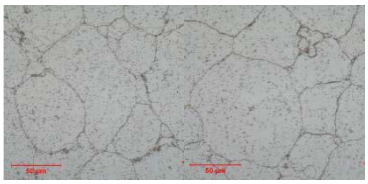
Laser Deposition: Laser deposition trials using atomized WE43 were conducted using a customized setup which involved fabrication of an inert gas purged glove box with an oxygen sensor. This was done to address potential flammability concerns. The laser head and the powder feed nozzle were placed inside the glove box and a preplaced powder bed of varying thickness was used to initially conduct trials by changing laser power (from 500 to 1000W), travel speed (12.7 to 50.8 cm/min), and powder depth (from 0.254 to 0.508 mm). A total of 48 trials were run and samples were examined macroscopically for voids, quality of deposit and cross sectioned to examine internal microstructure. Further trials were performed to study multipass builds. After narrowing the process window, multi pass builds were conducted using a coaxial powder feed nozzle on a WE43 wrought substrate (that had been heat treated to a T5 condition [15]). For these deposits, the Vickers microhardness was measured to determine hardness profile across the interface.

Cold Spray Deposition: Feasibility studies were performed using a CGT Kinetics 400 High Pressure Cold Spray System. Both the -400 mesh ground powder (AZ31B) and gas atomized powder (WE43) were evaluated. Process parameters that were investigated included the gas pressure, gas temperature, gas flow, powder flow and stand-off distance. A polymer DeLaval spray nozzle was used and helium was used as a process gas. The coatings were examined optically for microstructure. Hardness and density (using image analysis) were also measured.

Results and Discussions

The optical micrographs of the gas atomized WE43 (single and double forged) powder billet are shown in Figure 5. The gas atomized WE43 powder resulted in a homogeneous microstructure with well dispersed precipitates in the matrix, along with the presence of prior particle grain boundaries. There

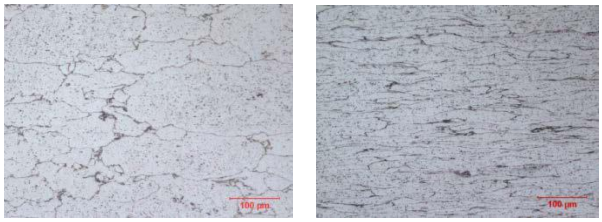
were no significant differences between the microstructures of the single and double forged atomized WE43.



(a) (b)

Figure 5. Optical micrographs of (a) single forged gas atomized WE43 and (c) double forged atomized WE43.

The microstructure of the rolled WE43 plate along the rolling direction and the short transverse direction is shown in Figures 6a and 6b, respectively. This plate was rolled at 10% reduction per pass to a 72% total reduction. The grain elongation is evident in the micrographs. The resulting anisotropy was not studied in this investigation.



(a) (b)

Figure 6. Optical micrographs of WE43 along (a) longitudinal rolling direction, and (b) short transverse direction, showing grain elongation.

The mechanical properties of the ground and gas atomized WE43 powders consolidated using forging and rolling are compared in Figure 7. Also shown are typical values of WE43B alloy produced via extrusion, forging and casting (each in a heat treated T6 condition). The prefix SF and DF refer to single forged and double forged condition, while Long. and Trans. refer to longitudinal and transverse direction, respectively.

The graph highlights several important results. For example, the main difference between the ground WE43 and gas atomized WE43 powder was manifested mainly in terms of an enhanced ductility for the atomized powder as seen in the results of single-forged specimen in the longitudinal direction. The yield strength and UTS for the ground WE43 and atomized WE43 were quite similar (at approximately 200 and 245 MPa, respectively), while there was a significant improvement in overall ductility from 3.5 to 6.5%. This is attributed to a more homogenous microstructure and a significantly thinner surface passive film on the surface of the atomized powder as compared to the ground powder.

A similar trend was observed on comparing the single-forged and double-forged atomized WE43. The yield strength and UTS were similar except for a gain in ductility of almost 50%. The reasons for the differences in ductility are under investigation.

On comparing the atomized single and double-forged WE43 to the rolled WE43 in both the longitudinal and transverse directions, it can be seen that there was a significant increase to the yield strength (from approximately 200MPa to 280MPa) and UTS (from approximately 250MPa to 300MPa) by rolling. The rolled WE43 exhibited a ductility of about 6% even after significant work hardening.

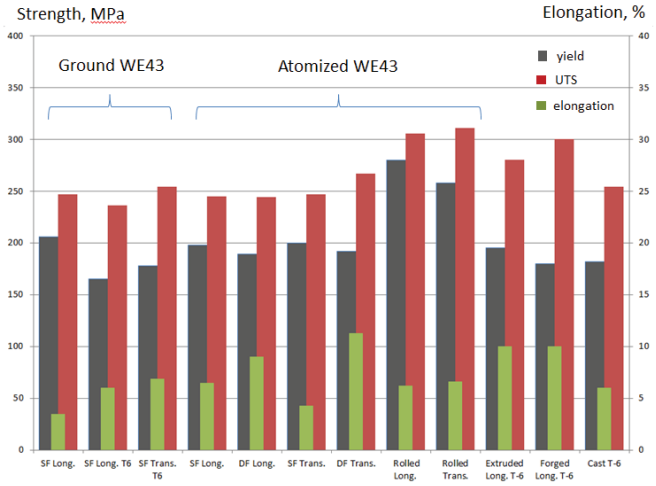


Figure 7. Typical mechanical properties of the P/M consolidated ground and atomized WE43 alloy comparison against commercial extruded, forged, and cast WE43B [14,15].

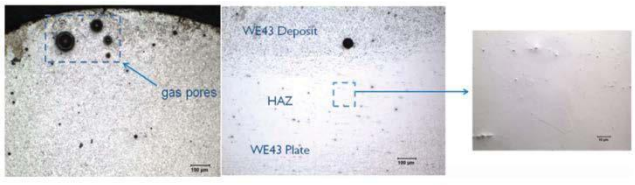
Laser deposition studies showed that an increase in laser power had a positive impact on the overall quality of the deposits as shown in Figure 8. The samples shown were tested with a bed height of 0.5mm and using a speed of 50cm/min. The top surfaces of multi-pass and multi-layer builds appeared acceptable, with no obvious macroscopic defects.



870 W 1000W

Figure 8. Top surface and cross sections of samples deposited at 870W and 1000W.

However, cross sections of the pre-placed powder bed deposits showed the presence of pores on the top portion of the weld bead. The circular shape of the pores was indicative of gaseous desorption which can be observed in the WE43 alloy. An example cross section of gas pores is shown in Figure 9(a) which was deposited at 870W and 38mm/min. These pores can be mitigated with improvements to the processing parameters. Figure 9(b) shows the grain coarsening associated with the heat affected zone.



a b

Figure 9. Cross section showing (a) gas pores on top surface of the deposit, and (b) grain coarsening in the HAZ of sample deposited at 870W at 38mm/min.

By comparison, using a commercial co-axial powder feeder for multipass and multilayer deposits resulted in improved results and showed significantly lower levels of porosity as compared to the preplaced powder approach.

The microhardness plot of the sample deposited at 1750W is shown in Figure 10. The graph shows a hardness drop across the heat affected zone (HAZ) into the deposited layer. The hardness of the base metal was measured to be about 104 HVN using a 300g load. There was no statistical difference in the hardness values between the HAZ and the deposited layer (both had mean values of 74VHN). Further metallurgical investigations and heat treatment studies are being performed to fully characterize the HAZ and the deposited layer.

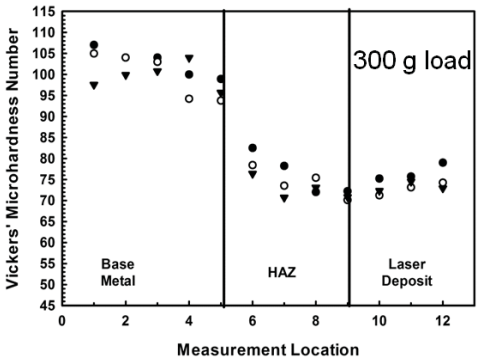
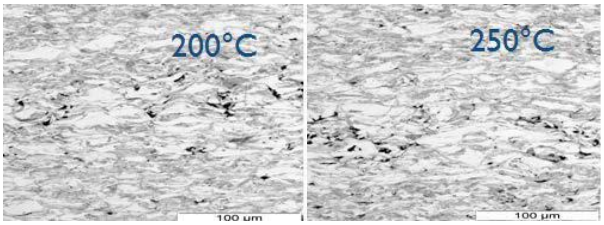
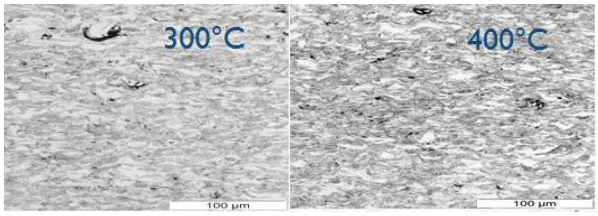


Figure 10. Hardness profile across the three layer buildup, five pass wide sample made using co-axial powder feeder at 1750W (speed: 63.5 cm/min).

The results of cold spray tests showed that it was possible to use both ground powder and atomized powder and obtain high density coatings. The result using ground AZ31B powder is shown in Figure 11. The optical micrographs show that by increasing the gas temperature, there was an increase in the coating density. The peak hardness was obtained at about 300°C, above which the hardness decreased.



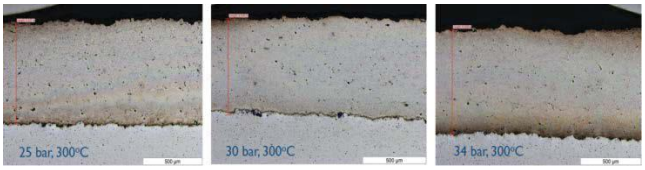
5.4% porosity, 146 HVN 3.7% porosity, 159 HVN



2.7% porosity, 161 HVN 2.5% porosity, 135 HVN

Figure 11. Effect of gas temperature on the porosity and hardness of -400 mesh AZ31B ground powder.

Improved results were obtained using gas atomized WE43 powder. Figure 12 shows effects of increasing gas pressure at 300°C on the cold sprayed coating microstructure. The deposited hardness and density increased by increasing the gas pressure from 25 bar to 34 bar.



1% porosity 122 HVN | 1.2% porosity 148 HVN | 0.6% porosity 157 HVN

Figure 12. Effect of gas pressure on the cold spray microstructure of a gas atomized WE43 powder.

The deposition efficiency using cold spray was about 40%, which was below what experimental model had predicted. However, initial results are encouraging enough and warrant further optimization and characterization of resulting mechanical properties to determine suitability in their intended end applications.

Summary and Conclusions

The results of this study have shown that it is possible to obtain properties using commercially developed gas atomized WE43 alloy that match and, in some cases, exceed typical properties of extruded, forged and cast WE43B. Gas atomized Mg alloy powders with homogeneous fine scale microstructure and lower surface oxygen content lead to enhanced ductility as compared to mechanically ground powder. Further optimization work is planned to develop a more comprehensive understanding of structure-property relationship to justify the economics of a powder based approach. Investigating optimal heat treatment parameters, studying the effects of thermal processing history, and the influence of high shear rate deformation processes, such as extrusion, are ongoing.

It has also been demonstrated that Magnesium alloy powders can be cold sprayed using existing commercial powder coating system. The achievement of high density and high hardness is the first step towards optimization and conducting tests that are necessary to demonstrate their use in repair applications.

Investigations into laser deposition process using Mg based prealloyed powder such as WE43 have shown that under the right combination of laser powder and travel speed it is possible to obtain deposits that are visually acceptable using qualitative visual standards based on other alloy systems. However, the source of gas pores and its effect on deposited mechanical properties of the coating needs to be studied in the next step.

Acknowledgement

The authors would like to thank Dr. Yongho Sohn at the University of Central Florida for TEM analyses and Todd Palmer at Applied Research Lab, Penn State University for laser deposition investigation. Powder development was sponsored by the U.S. Army Research Laboratory and the U.S. Army Research, Development, and Engineering Center and was accomplished under Cooperative Agreement W911NF-10-2-002 and Army Contract W15QKN-09-C-2008.

References

1. R. Tandon *et.al*., "Magnesium Powder technology for Ultra Lightweight Applications," *Proceedings of The 2011 International Conference on Powder Metallurgy and Particulate Materials*, II (2011), Metal Powder Industries Federation, 07-157-07-163.

2. S. Mathaudhu, "Magnesium Alloys in U.S. Military Applications: Past, Current and Future Solutions", *Magnesium Technology 2010,* The Minerals, Metals and Materials Society, (2010) 27-32.

3. B. Gywnne, "Magnesium Alloys in Aerospace Applications-Flammability Testing and Results", *Magnesium Technology 2010*, The Minerals, Metals and Materials Society, (2010), 13.

4. K.Cho *et.al*, "Magnesium Technology and Manufacturing for Ultra Lightweight Armored Ground Vehicles", *Proceedings of the 2008 Army Science Conference,* Orlando, FL 2008.

5. Rick Delrome *et.al*., "Ultra Light Metallic Armor (ULMA)-Magnesium Hard Alloys as the Defense Against Modern Warfare Threats", *presented at Magnesium Technology 2010*, TMS 2010.

6. T. Jones, K. Kondoh, "Ballistic Analysis of New Military Grade Magnesium Alloys for Armor Applications", *Magnesium Technology 2011*, The Minerals, Metals and Materials Society, (2011) 425-430.

7. Y. Kawamura and A. Inoue, "Rapidly Solidified Powder Metallurgy Mg97Zn1Y2 Alloys with Tensile Yield Strength of 610 MPa and Elongation of *5%", Magnesium Technology 2002*, TMS (The Minerals, Metals and Materials Society), 2002.

8. A. Elsayed, J. Umeda, and K. Kondoh, "The Production of Powder Metallurgy Hot Extruded Mg-Al-Mn-Ca Alloy With High Strength and Limited Anisotropy", *Magnesium Technology 2011*, The Minerals, Metals and Materials Society, (2011) 475-480.

9. C.J. Bettles, M.H. Moss, and R. Lapovok, "A Mg-Al-Nd Alloy Produced via a Powder Metallurgical Route", *Materials Science and Engineering* A 515, (2009) 26-32.

10. V.M. Segal, "Engineering and Commercialization of Equal Channel Angular Extrusion (ECAE)", Materials Science and Engineering A 386, 2004, pp 269-276.

11. C.C. Ng *et. al*.,"Layer Manufacturing of Magnesium and its Alloy Structures for Future Applications," *Virtual and Physical Prototyping*, Vol 5, No.1, (2010), 13-19.

12. M. Wolff *et.al*.,"Properties of Sintered Mg Alloys for Biomedical Applications," *Materials Science Forum,* Vol.690, (2011) 491-494.

13. M. Wolff *et.al*.,"Advances in the Metal Injection Molding of Mg-Ca Alloys for Biomedical Applications," *PIM International,* Vol.6, No.4, (2012).

14. Magnesium Elektron 21 Datasheet 455, www.magnesium-elektron.com

15. Magnesium Elektron WE43B Datasheet 467A & Datasheet 478, www.magnesium-elektron.com.

Magnesium Technology 2014
Edited by: Martyn Alderman, Michele V. Manuel, Norbert Hort, and Neale R. Neelameggham
TMS (The Minerals, Metals & Materials Society), 2014

Isothermal Hydrogenation Kinetics Study of Magnesium Hydride with TiH_2 Additive

Jingzhu Li†, Peng Fan†, Chengshang Zhou† and Z. Zak Fang*
Department of Metallurgical Engineering, The University of Utah, 135 South 1460 East, Room 412, Salt Lake City, Utah 84112-0114

Keywords: Hydrogenation, thermal effect, magnesium hydride

Abstract
Detailed absorption kinetics studies of magnesium hydride with Ti-based additive are still unavailable, even though such material has been demonstrated to have a much faster hydrogenation/dehydrogenation rate. Moreover, thermal effect during hydrogenation process of magnesium-based materials is usually neglected in previous studies, which could render the analysis inaccurate. In this work, both copper and graphite have been used as thermal ballast to minimize the thermal effect. Absorption kinetics of ball-milled magnesium hydride with TiH_2 additive at low temperatures are examined via a Sieverts type apparatus. Results show that graphite could effectively minimize the thermal effect.

I. Introduction

Due to the high theoretical H_2 storage capacity (7.6 wt.%), high desorption enthalpy (-74.5 kJ/mol) and low cost[1,2], magnesium is proposed as a promising material for hydrogen storage, as well as thermal devices such as heat pumps, cooling and heating machines, and solar thermal storage systems. However, these applications of MgH_2 are limited due to the relative high thermodynamic stability and slow kinetics in both hydrogenation and dehydrogenation.

Usually, the kinetics of MgH_2 can be improved by several methods: 1) use mechanical ball milling to produce nano-scaled particles; 2)add transition metal alloy[3] and intermetallic compounds as catalytic additives. Ti-based additives such as TiH_2 and $TiMn_2$ have been demonstrated as effective catalysts to allow MgH_2 to absorb hydrogen even at room temperature,. However, detailed kinetics studies of MgH_2 with Ti-based additives are still unavailable.

Another important issue, thermal effect or self-heating phenomenon, is often neglected in hydrogenation kinetics studies among literature reports, which could render the kinetics studies inaccurate. Usually, kinetics analysis of metal hydride is based on fitting kinetics data to various theoretical or empirical models. Most of these kinetics models for metal hydrides, such as Jander diffusion model and volume contracting model, are based on isothermal conditions, i.e., reaction should be conducted at a constant temperature. It is not appropriate to analyse non-isothermal kinetics data using isothermal kinetics model to obtain reliable mechanistic conclusions.

Unfortunately during hydrogenation, isothermal condition is usually difficult to sustain due to thermal effect or self-heating [5,6]. Thermal effect or self-heating phenomenon refers to the rise of temperature during the initial stage of H_2 absorption [5,6]caused by the large exothermic hydrogenation reaction heat and poor heat conductivity of the hydrogen storage materials. Moretto *et al*. reported that during hydrogen absorption of Mg based materials, sample temperature could rise by as much as 80°C[6].

Usually three ways were used to minimize the self-heating effect: using less sample[6], changing reaction vessel design, or/and adding thermal ballast[7]. Thermal ballast serves as a heat buffer to accelerate heat conduction as well as absorb excessive heat itself, thus minimizing the temperature fluctuation. Thermal ballast materials are required to have high thermal conductivity and high heat capacity, and should be inert to H_2 as well as the reaction metal.

In this work, we aim to find a method to minimize the thermal effect. Thermal effect was characterized and carefully avoided by using graphite as the thermal ballast material to obtain isothermal conditions. Hydrogenation was conducted under different temperatures and pressures within a low temperature range from room temperature to 200 ^{o}C.

II. Experimental details

The raw materials for this work, magnesium hydride (MgH_2,98%) and titanium hydride (TiH_2, 99%), were purchased from Sigma-Aldrich (Milwaukee, WI) and Alfa-Aesar (Ward Hill, MA)respectively, and used as received without any further purification. It should be pointed out that, the reason why MgH_2 and TiH_2 are used instead of Mg and Ti metal is that hydride is more brittle, less ductile than metal, allowing a more efficient mill. Copper powder (-625 mesh, 99%) is purchased from Alfa-Aesar (Ward Hill, MA).Expandable graphite was purchased from Asbury Carbons (Asbury, NJ). Before being used, graphite has been degassed at 300 ^{o}C for 3 hours and stored in vacuum condition to avoid surface contamination[5]. It should be noted that the impurities content in the as received MgH_2 is significant, which would result in lower than theoretical content of hydrogen in the raw material. All the material handling was carried out in a glove box filled with purified argon (99.999%), which contains less than 1 ppm water vapor and 1 ppm oxygen.

Three grams of the mixtures of MgH_2 and TiH_2 with a molar ratio of 10:1 were mixed and milled via a custom-made ultrahigh-energy-high-pressure (UHEHP) ball milling device under 15 MPa hydrogen pressure. The milling was carried out at room temperature for 6 hours with a ball to powder ratio of 110:1 by weight.

Hydrogen absorption kinetics measurements were performed by using a commercial Sieverts type apparatus (PCTPro-2000). Hydrogen pressures were measured by a Teledyne Taber model 206 piezoelectric transducer, 0-20 MPa, with a resolution of 10^{-4} MPa. Temperature is

detected by a K-type thermal couple connected to PCT. The amount of hydrogen release-uptake was calculated by the pressure changes in calibrated volumes, of which the details are described elsewhere[8]. About 0.5 gram mixture of MgH_2-0.1 TiH_2 and thermal ballast was loaded into a stainless steel container as loosely packed powder and then sealed inside the PCT autoclave in the glove box. Absorption kinetics under 5 different temperatures (25, 60, 100, 150and 200 ^oC) had been characterized. Fresh sample would first undergo 3 cycles at 300 ^oC, with an absorption pressure of 10 bar and desorption pressure of 0.01bar to eliminate the residual stress produced during mechanical milling. Before each hydrogenation test, sample was vacuumed at 300 ^oC for 1 hour to fully dehydrogenate then cooled down to the required temperature.

III. Results and Discussion

1. Thermal Ballast Selection

Ni, Al, Mn, and Cu had been reported as effective thermal ballasts for Mg_2Ni and $LaNi_5$ alloys [7,9,10]. However, Mg powder differs from Mg2Ni alloy both physically and chemically, thus these thermal ballasts listed above could be improper for Mg. Song et al. confirmed that Ni would act on the dissociation of H_2 during the hydrogenation process and affect the hydrogenation/dehydrogenation kinetics of Mg powder [10,11]. However, graphite and copper are potential candidate because they are relatively stable to Mg and have excellent heat conductivity, graphite is also inert to Mg, Ti[12] and H_2 [13] under a temperature range from room temperature to 400 ^oC. The effect of copper and expandable graphite on minimizing thermal effect is compared in this section, as well as the thermal effect reducing performance of two different expandable graphite content to get an appropriate mix ratio.

Figure 1 is a real non-isothermal absorption kinetics data of MgH_2-0.1TiH_2. Due to the thermal effect, sample reached the peak temperature 114.8 ^oC and absorbed 1.91 wt.% hydrogen in as soon as 9.3 s. Assume sample was well insulated without any heat conduction, take expandable graphite as the thermal ballast, the maximum temperature change could be as much as 554 ^oC based on hydrogenation enthalpy, heat capacity of both materials. However, due to heat conduction, the actual temperature rise is 11 ^oC, much smaller than the calculated temperature change under thermal isolation condition. Even though the calculation is conducted under thermal isolation condition, it could serve as a reference in determining the desirable amount of thermal ballast. Furthermore, the calculated temperature deviation relationship with respect to the graphite amount is shown in Figure 2. The effect of graphite on reducing temperature change becomes negligible if more than 10 times of graphite is added. Therefore adding more graphite is meaningless considering the limited sample vial volume and the machine resolution. Similar phenomenon could be observed if copper is used as thermal ballast.

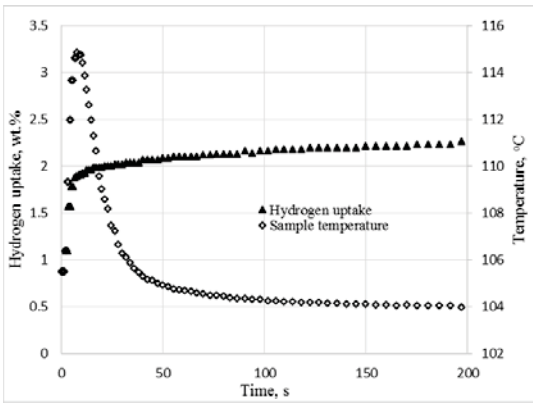


Figure 1.Temperature and H_2 uptake profile of non-isothermal hydrogenation at 100 ^oC and 10 bar for MgH_2-0.1TiH_2 milled for 6hr

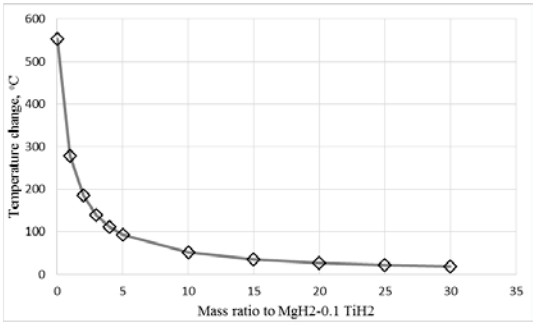


Figure 2.Calculated temperature change when MgH_2-0.1TiH_2 is mixed with different amount of graphite, with the assumption that sample is thermally isolated

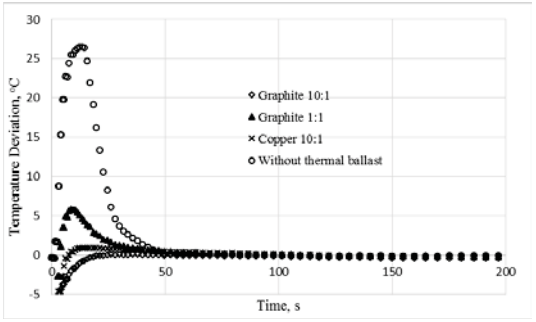


Figure 3.Temperature Deviation during hydrogenation at 200 ^oC

Therefore, 3 thermal ballasts were mixed with MgH_2-0.1TiH_2, and the temperature deviation during hydrogenation at 200 ^oC is compared in Figure 3 along with MgH_2-0.1TiH_2 without thermal ballast.

Table 1 shows the ballasts used in each set and the peak temperature deviation caused by thermal effect. It is shown that when mass ratio of MgH_2-0.1TiH_2 and graphite is 1:1, thermal effect is apparently reduced but not enough yet. However, when 10 times thermal ballast by weight was added, both graphite and copper were able to minimize the temperature fluctuation within 1 ^oC. In this way, we could

regard such hydrogenation kinetics as isothermal or at least quasi-isothermal.

Table 1 The peak temperature deviations at different thermal ballast addition

Thermal ballast	Copper	Expandable Graphite	Expandable Graphite
Mass ratio to MgH_2-0.1 TiH_2	10:1	10:1	1:1
Peak Temperature Deviation (^oC)	0.9	0.1	5.9

Based on their effects on minimizing temperature deviation, copper and graphite are both good thermal ballast candidates. However, further examination on the hydrogenation kinetics behavior is necessary in order to verify the thermal ballast. In Figure 4, the hydrogenation kinetics at 200 ^oC and 10 bar is plotted for comparison. Within 500 seconds, MgH_2-0.1TiH_2 without thermal ballast absorbs 6.0 wt.% hydrogen, while samples with 1:1 graphite addition, 10:1 graphite addition and 10:1 copper addition absorb 4.8, 2.4 and 0 wt.% hydrogen, respectively. The larger the thermal effect is, the more hydrogen is absorbed at same period of time, indicating the reaction rate of the non-isothermal hydrogenation is much higher than that of isothermal hydrogenation. Particularly, the different hydrogenation rate is developed within the first few seconds, a time interval coinciding with that of the temperature spike caused by self-heating. This is because the instant hydrogen absorption produces considerable heat, which couldn't be conducted outward immediately therefore heat up the whole sample by more than 10 ^oC, which in return increase hydrogenation rate considerably. As hydrogenation proceeds, the hydrogenation rate gradually slows down. As a result, reaction heat is able to dissipate outward to allow the sample temperature to fall back to the set value.

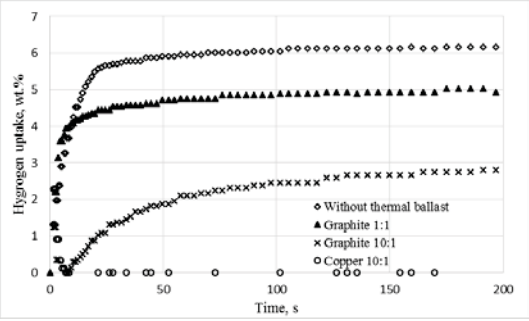


Figure 4.Hydrogenation behavior at 200 ^oC of MgH_2-0.1TiH_2 with different thermal ballast

However, MgH_2-0.1$TiH_2$with copper as thermal ballast cannot absorb any hydrogen as shown in Figure 4. In fact, after the test, the sample with copper as thermal ballast was found to sinter together and even unable to be taken out from the sample vial. The eutectic point of Cu and Mg is 486 ^oC[14]. It could be highly possible that during or after dehydrogenation while magnesium hydride gradually transfers to magnesium metal, copper alloys with magnesium via eutectic reaction. Therefore, even though copper is effective in reduce the thermal effect, it cannot serve as a valid thermal ballast for MgH_2-0.1TiH_2 because the two material will somehow alloy with each other.

2. Temperature difference

Based on the above-mentioned the temperature and hydrogenation behavior, 10:1 graphite addition was chosen for thermal ballast. Figure 6 presents temperature deviations during hydrogenation at 25, 60, 100, 150 and 200 ^oC. The maximum temperature deviations during hydrogenation at these temperatures are 0.04, 0.10, 1.08, 1.27 and 0.6^oC, respectively, which is negligible regarding to the corresponding experimental temperature. To this point, we could claim that the hydrogenation of MgH_2-0.1TiH_2 with 10 times graphite addition is isothermal or at least quasi-isothermal within a temperature range from 25-200 ^oC.

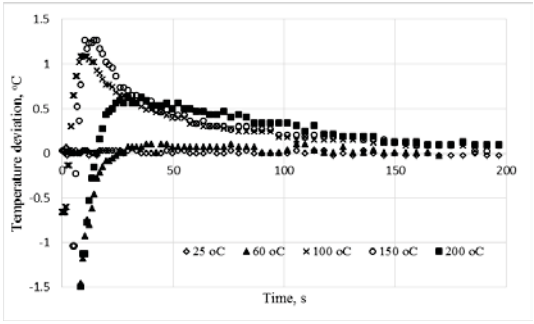


Figure 6.Temperature change profiles of MgH_2-0.1TiH_2milled for 6 hours under various temperatures

3. Isothermal hydrogenation kinetics

Hydrogenation behavior under isothermal condition at various temperatures (25, 60, 100, 150 and 200 ^oC) is shown in Figure 7. Obviously, more hydrogen was absorbed at higher temperature. Each absorption profile appears to be a two-stage process. Take hydrogenation at 100 ^oC as an example. During the first stage (within first 500 seconds), 2.13 wt.% is absorbed while in the second stage H_2 amount slowly increases to 2.75 wt.%. The difference in H_2 uptake amount at various temperatures mainly forms in the first stage, which is 1.38, 1.80, 2.13, 2.38 and 2.81 wt.% at room temperature, 60, 100, 150 and 200 ^oC, respectively. If absorption is allowed for infinite period of time, the final H_2 amount would reach the capacity of selected sample. However, absorption under lower temperature takes more time to complete.

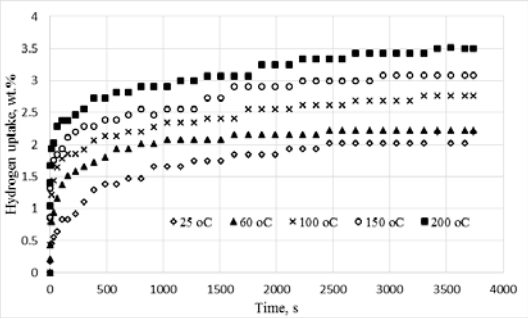


Figure 7. Hydrogenation kinetics at room temperature, 60, 100, 150 and 200 ^{o}C for MgH_2-0.1TiH_2 milled for 6 hours

IV. Summary

There is a significant temperature spike during the initial stage of the hydrogenation process. The method of adding graphite as thermal ballast has been proved to be effective in minimizing temperature spike. Non-isothermal hydrogenation rate is much faster than isothermal one, since sample temperature in non-isothermal experiment is higher than that in isothermal experiment, suggesting that isothermal kinetics data should be used for kinetics study while non-isothermal kinetics data is not appropriate.

ACKNOWLEDGEMENT

This research was supported by the U.S. Department of Energy (DOE) under contract number DE-AR0000173.

References

(1) Muthukumar, P.; Satheesh, A.; Linder, M.; Mertz, R.; Groll, M. Int. J. Hydrogen Energy2009, 34, 7253.
(2)Lu, J.; Choi, Y. J.; Fang, Z. Z.; Sohn, H. Y.; Ronnebro, E. J. Am. Chem. Soc.2010, 132, 6616.
(3)Jain, I. P.; Lal, C.; Jain, A. Int. J. Hydrogen Energy2010, 35, 5133.
(4)Zhou, C.; Fang, Z. Z.; Ren, C.; Li, J.; Lu, J. J. Phys. Chem. C2013, 117, 12973.
(5)Broom, D. Int. J. Hydrogen Energy2007, 32, 4871.
(6)Moretto, P.; Zlotea, C.; Dolci, F.; Amieiro, A.; Bobet, J. L.; Borgschulte, A.; Chandra, D.; Enoki, H.; De Rango, P.; Fruchart, D.; Jepsen, J.; Latroche, M.; Jansa, I. L.; Moser, D.; Sartori, S.; Wang, S. M.; Zan, J. A. Int. J. Hydrogen Energy2013, 38, 6704.
(7)Han, J.; Lee, J. Int. J. Hydrogen Energy1987, 12, 417.
(8)Gross, K. J.; Carrington, K. R. Recommended Best Practices for the Characterization of Storage Properties of Hydrogen Storage Materials, U.S. Department of Energy Office of Energy Efficiency and Renewable Energy Hydrogen Storage Program, 2012.
(9)Akiyama, T.; Tazaki, T. A.; Takahashi, R.; Yagi, J. Intermetallics1996, 4, 659.
(10)Wang, X. L.; Suda, S. J. Alloys Compd.1995, 231, 660.
(11)Song, M. Y.; Ivanov, E.; Darriet, B.; Pezat, M.; Hagenmuller, P. J. Less Common Met.1987, 131, 71.
(12)Kessler;, H. D.; Rostoker;, W.; Thyne, R. J. V. Titanium Phase Diagrams, Wright Air Development Center, 1953.
(13)Gulbransen, E. A.; Andrew, K. F.; Brassart, F. A. J. Electrochem. Soc.1965, 112, 49.
(14)Hugh Baker, ed., ASM handbook-volume 3, Alloy Phase Diagram, 2006, 747.

Magnesium Technology 2014
Edited by: Martyn Alderman, Michele V. Manuel, Norbert Hort, and Neale R. Neelameggham
TMS (The Minerals, Metals & Materials Society), 2014

MAGNESIUM ELECTROREFINING IN NON-AQUEOUS ELECTROLYTE AT ROOM TEMPERATURE

Kyungjung Kwon[1], Jesik Park[2], Priyandi Kusumah[1], Bonita Dilasari[1], Hansu Kim[3], and Churl Kyoung Lee [2,*]

1 Department of Energy & Mineral Resources Engineering, Sejong University, Seoul 143-747, Republic of Korea

2 School of Advanced Materials & Systems Engineering, Kumoh National Institute of Technology, Gumi, Gyungsangbuk-do 730-701, Republic of Korea

3 Department of Energy Engineering, Hanyang University, Seoul 133-791, Republic of Korea

Keywords : magnesium, electrorefining, recycling, non-aqueous electrolyte

Abstract

Magnesium, of which application is often limited by its poor corrosion resistance, is more vulnerable to corrosion with existence of metal impurities such as Fe. Therefore, for the refining and recycling of magnesium, high temperature electrolysis using molten salts has been frequently adopted. In this report, the purification of magnesium scrap by electrolysis at room temperature is investigated with non-aqueous electrolytes. An aprotic solvent of tetrahydrofuran (THF) was used as a solvent of the electrolyte. Magnesium scrap was used as anode materials and ethyl magnesium bromide (EtMgBr) was dissolved in THF for magnesium source. The purified magnesium can be uniformly electrodeposited on copper electrode under potentiostatic conditions. The deposits were confirmed by scanning electron microscopy (SEM) and energy-dispersive X-ray spectroscopy (EDS) analysis.

Introduction

Utilization of magnesium metal is increasing due to its high strength compared to other light metals mainly in the automotive and aircraft industries[1]. Considering the fact that 32% of magnesium had been produced in United States by 2007 by die-casting process where only half of the material input ends up as finished products and the remaining is accumulated as scrap, the approach of recycling magnesium from die-casting scrap has many advantages and is expected to increase for global demand[2,3]. By far the dominant extraction technology is molten salt electrolysis by using magnesium chloride to produce liquid magnesium at temperatures over 650℃ and therefore high energy consumption and costs are required. In addition, this process incurs a byproduct of chlorine gas which causes environmental issues[4,5].

Electrodeposition of metals from non-aqueous solutions has attracted much attention in the last few years. As magnesium is oxidized by water and other protic solvents, only aprotic media are feasible as solvents for cases where electrodeposition of magnesium is required such as secondary magnesium batteries[6,7]. Thus, only a few organic electrolyte solutions containing Grignard reagents have been shown to be suitable for electrochemical magnesium deposition from organic solvents[8-14]. For example, C. Liebenow[14] has reported the utilization of ethyl magnesium bromide (EtMgBr) prepared by Grignard reagents in THF for the application of magnesium as secondary batteries. In this report, the purification of magnesium scrap by electrolysis at room temperature is investigated with non-aqueous electrolytes. An aprotic solvent of tetrahydrofuran (THF) was used as a solvent of the electrolyte.

Experimental

The cathodic deposition and anodic dissolution processes of magnesium were carried out at room temperature in the mixed electrolyte containing THF + 1 M EtMgBr in a three-electrode electrolysis cell. Magnesium scrap was used as anode and copper plate as cathode. Platinum wires were used as working electrode and counter electrode with magnesium wire as reference electrode. The electrode potential in this paper is represented versus the potential of magnesium metal in the non-aqueous electrolyte. Alloying elements in magnesium scrap were analyzed to illustrate their behavior toward magnesium electrorefining process. In order to investigate the morphology of electrodeposited magnesium, the surface of cathode was examined with scanning electron microscopy (SEM) and energy-dispersive X-ray spectroscopy (EDS).

Result and Discussion

Behavior of alloying elements

Magnesium alloy used as anode was AZ31B (3 ~ 6 % of aluminum, less than 1 % of copper, zinc and manganese), a representative commercial magnesium alloy scrap. Fig.1 shows the anodic polarization behaviors of the magnesium alloy and each alloying element. The anodic polarization curves were assumed to represent the oxidation behaviors of magnesium alloy and each alloying element. The dissolution potential for magnesium alloy, magnesium and alloying elements in THF + 1 M EtMgBr obtained from anodic polarization test is summarized in Table 1. In the the anodic polarization curve, zinc and manganese show a sharp increase in anodic current once anodic current starts to flow, which might indicate that they have higher exchange current densities for metal dissolution compared to the other samples.

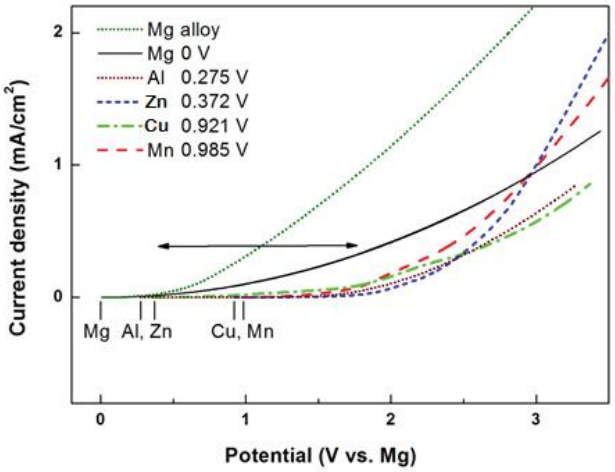


Fig. 1. Anodic polarization of magnesium alloy and alloying elements in THF + 1 M EtMgBr electrolyte

Table. 1. Onset potential for metal dissolution in THF + 1 M EtMgBr system

	Standard reduction potential		Potential (V vs. Mg) in THF + 1 M EtMgBr system		
	(V vs. SHE)	(V vs. Mg)	OCV	at 0.01 mA/cm^2	at 0.1 mA/cm^2
Mg	-2.37	0	0	0.322	1.038
Mg alloy			0.011	0.265	0.654
Al	-1.66	0.71	0.275	1.523	1.986
Zn	0.763	3.133	0.372	0.797	1.822
Cu	0.337	2.707	0.921	1.652	2.093
Mn	-1.185	1.185	0.985	1.295	1.831

To determine onset potentials for metal dissolution, we arbitrarily chose two current density values (0.01 and 0.1 mA/cm^2) and compared the behaviors of each metal. At the current density of 0.01 mA/cm^2, we observed the onset potentials in the nearest order to OCV are magnesium alloy > magnesium > zinc > manganese > aluminum > copper with their respective onset potentials at 0.265 V, 0.322 V, 0.797 V, 1.295 V, 1.523 V and 1.652 V. At the current density of 0.1 mA/cm^2, we obtained the same order of onset dissolution potentials. Therefore, we could conclude that the occurrence of dissolution would be first observed for magnesium and lastly observed for copper considering the fact that the magnesium alloy is supposed to dissolve first once one of its components starts to dissolve. Although zinc is the next to magnesium in the onset potential order, it is unlikely that the dissolution of zinc is substantial in a low potential range around 1 V because the dissolution current of zinc is very low in this range. For the selective dissolution of magnesium for the separation from the other alloying elements, the potential should be controlled in between 1 V and 2 V depending on the required impurity level of Mg electrorefining. For the same reason, a potentiostatic electrolysis at a very low potential could be conducted to obtain high purity magnesium[15].

Surface analysis

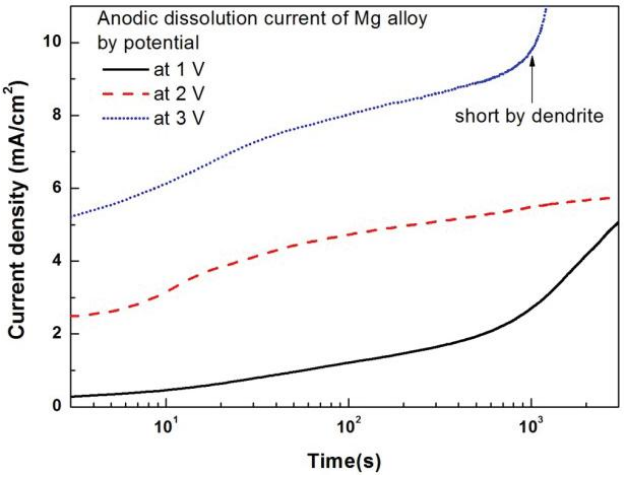


Fig. 2. Effect of applied potential on the oxidation behavior of magnesium alloy

Fig. 2 shows the measured value of anodic dissolution current density of magnesium alloy. It can be seen that an increase in potential is followed by a significant increase in current density. However, if the applied potential was increased as high as 3 V, an abrupt loss of magnesium alloy observed around 1000 s, which would lead electrodeposited magnesium to form dendritic morphology on the surface of cathode, occurred. The dendritic deposition on cathode surface could act as a trap for impurities and electrolyte[16]. Excessive growth of dendrites may cause an electrical short. Potentiostatic condition at a potential between 1 V and 2 V is considered to be a preferable condition for electrorefining process of magnesium.

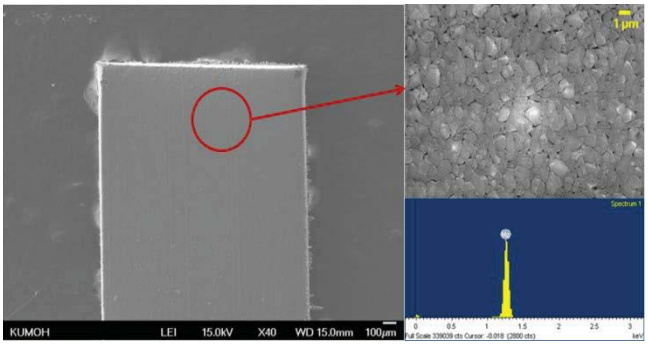


Fig. 3. SEM images and EDS analysis of cathode surface after a potentiostatic electrolysis at 2 V after 1 h

As can be seen from Fig. 3, a relatively smooth and dense deposit of magnesium can be obtained at the potential of 2 V after 1 h of deposition. Primary magnesium particles had a fine spherical morphology with no apparent dendrite formation. In order to know whether the electrodeposit contains crystalline of impurities from the alloying elements or not, EDS analysis was performed. The EDS detected only a very strong peak of magnesium with no significant peak of impurities from the alloying elements.

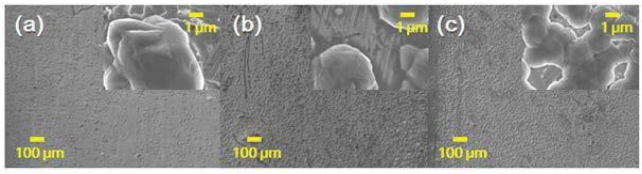


Fig. 4. SEM images of cathode surface after a potentiostatic electrolysis at (a) 1 V, (b) 2 V, and (c) 3 V

The surface of electrorefined magnesium at cathode is compared depending on the applied potential in Fig. 4. The surface morphology appears to be uniform in each condition and the deposited magnesium layers are composed of crystallites of which size ranges from 1 to 10 μm. If the applied potential becomes higher, the corresponding current density is also increased and the resulting crystallite size tends to decrease as can be seen more clearly in the insets of Fig. 4. The effect of applied potential on the crystallite size can be interpreted by the comparison between the mass transfer of magnesium ion in the electrolyte and the reduction kinetics to magnesium metal at the cathode. A separate experiment revealed that the diffusion coefficient of magnesium ion in THF is on the order of 10^{-8} cm^2/s. Although this level of diffusion coefficient is lower than that in aqueous system, the mass transfer of magnesium ion in the THF-based electrolyte seems fast enough for magnesium reduction to be controlled mainly by electrochemical reduction kinetics. The rate-determining reduction kinetics is enhanced by the increase in applied potential and makes the nucleus formation dominant over the crystal growth. Therefore, a potentiostatic electrolysis at higher potentials induces smaller crystallites.

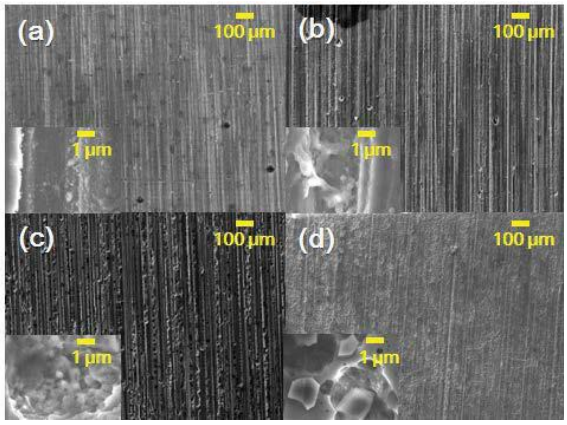


Fig. 5. SEM images of the magnesium alloy surface (a) before and after potentiostatic electrolysis at (b) 1 V, (c) 2 V, and (d) 3 V

Fig. 5 shows the surface of magnesium alloy anode after potentiostatic electrolysis for 30 min. The alloy dissolution is developed not by general dissolution but by local dissolution as exemplified in the insets where pores are enlarged as the applied potential is increased. A higher potential accompanies an increase in anodic dissolution current density as confirmed in Fig. 1. This enhanced alloy dissolution could be further accelerated by the increase of anode surface area triggered by the pore formation.

4. Conclusions

Electrochemical dissolution behaviors of magnesium alloy and its alloying elements were investigated in the electrolyte consisting of 1 M EtMgBr + THF. The dissolution onset potentials for the alloying elements are in ascending order as follows: magnesium > zinc > manganese > aluminum > copper. Based on their anodic polarization curves, it was confirmed that the selective dissolution of magnesium from the magnesium alloy is possible by applying an adequate potential to obtain high purity magnesium. The dissolution behavior of the magnesium alloy in potentiostatic electrolysis depends on applied potential. If the applied potential is as high as 3 V, a rapid dissolution of the magnesium occurrs, which can eventually lead to the dendrite formation of magnesium on cathodic side. However, the potentiostatic electrolysis at 1 V and 2 V generates a uniform magnesium deposit with no dendritic growth as confirmed by SEM. In addition, EDS analysis shows a very strong peak of magnesium with no impurities detected. Therefore, the electrorefining of low purity magnesium or magnesium alloy scraps in non-aqueous electrolyte can be a feasible recycling process for high purity magnesium production.

Acknowledgement

This study was supported by the R&D Center for Valuable Recycling (Global-Top Environmental Technology Development Program) funded by the Ministry of Environment. (Project No.: GT-11-C-01-140-0)

References

1. S. Kamado and Y. Kojima, *Magnesium Alloy-the Ultra-Light Metallic Materials in the 21 Century: General Properties and Trend of Magnesium Alloys for Diecasting*, Mat. Japan, 38 (4) (1999), 285-290.
2. Tzamtzis S et al., *Recycling of High Grade Die Casting AM Series Magnesium Scrap with the Melt Conditioned High Pressure Die Casting (MC-HPDC) Process*, Mat. Sci. Eng. A., 528 (2011), 2664-2669.
3. H. Antrekowitsch, G. Hanko, and P. Ebner, *Recycling of Different Types of Magnesium Scrap*, in: H.I. Kaplan (Ed.), Magnesium Technology 2002, TMS, Washington, (2002), 43-48.
4. Javaid A et al., *Literature Review on Magnesium Recycling*, in: A.A. Luo, N.R. Neelameggham, and R.S. Beals (Eds.), Magnesium Technology 2006, TMS, Texas, (2006), 7-12.
5. C. Scharf, and Ditze *Magnesium Alloys and Their Applications*, ed. B.L.A.. Mordike, and K.U. Kainer (Wolfsburg, WB: Werkstoff-Informations Gesellschaft GmbH, 1998), 685-690.
6. J. H. Conner, W.E. Reid, and G.B. Wood, *Electrodeposition of Metals from Organic Solutions V: Electrodeposition of Magnesium and Magnesium Alloys*, J. Electrochem. Soc., 104 (1957), 38-41.
7. Y. NuLi, J. Yang, and L. Wu, *Reversible Deposition and Dissolution of Magnesium from $BMIMBF_4$ Ionic Liquid*, J. Electrochem. Commun., 7 (2005), 1105 - 1110.
8. Zhao et al., *Reversibility of Electrochemical Magnesium Deposition from Tetrahydrofuran Solutions Containing Pyrrolidinyl Magnesium Halide*, Electrochimica Acta, 56 (18) (2011), 6530-6535.
9. Y. NuLi, J. Yang, and P. Wang, *Electrodeposition of Magnesium Film from $BMIMBF_4$ Ionic Liquid*, Appl Surf Sci, 252 (23) (2006), 8086-8090.
10. J. Fuller, R. T. Carlin, and R. A. Osteryoung, *The Room Temperature Ionic Liquid 1-ethyl-3-methylimidazolium tetrafluoro Borate: Electrochemical Couples and Physical Properties*, J. Electrochem. Soc., 144 (11) (1997), 3881-3886.
11. I. Haas, and A. Gedanken, *Synthesis of Metallic Magnesium Nanoparticles by Electrochemistry*, Chem. Commun., 15 (2008),

1795-1797.
12. O. Shimamura et al., *Electrochemical Co-deposition of Magnesium with Lithium from Quaternary Ammonium Based Ionic Liquid*, J. Power Sources, 196 (2005), 1586-1588.
13. M. Egashira et al., *Functionalized Imidazolium Ionic Liquids as Electrolyte Components of Lithium Batteries*, J. Power Sources, 147 (2007), 560-564.
14. C. Liebenow, *Reversibility of Electrochemical Magnesium Deposition from Grignard Solutions*, J. Appl. Electrochem., 27 (1997), 221-225.
15. T. Takenaka et al., *Electrorefining of Magnesium in Molten Salt and Its Application for Recycling*, Mat. Trans., 44 (4) (2003), 546-551.
16. R. Selim and P. Bro, *Some Observations on Rechargeable Lithium Electrodes in a Propylene Carbonate Electrolyte,* J. Electrochem. Soc., 121 (11) (1974), 1457-1459.

Magnesium Technology 2014
Edited by: Martyn Alderman, Michele V. Manuel, Norbert Hort, and Neale R. Neelameggham
TMS (The Minerals, Metals & Materials Society), 2014

Recovery of Rare Earth Metals in Used Magnets by Molten Magnesium

Tomohiko Akahori[1], Yu Miyamoto[1], Tomonori Saeki[1], Masahide Okamoto[1], Toru H Okabe[2],
[1]Yokohama Research Laboratory, Hitachi, Ltd.; 292 Yoshida-cho, Totsuka-ku; Yokohama, 244-0817 Japan
[2]Institute of Industrial Science, Tokyo University; 4-6-1 Komaba, Meguro-ku; Tokyo, 153-8505, Japan

Keywords: Rare earth, Neodymium, Dysprosium, recycling, magnesium

Abstract

We report here Hitachi's approach to recycle rare earth (RE) metals in used magnets by using molten magnesium (Mg). The process consists of 3 steps; (1) extraction of RE metals from magnets into molten Mg, to form Mg-RE melt, (2) mechanical separation of magnets from the Mg-RE melt, (3) collection of RE metals by evaporation of Mg in the Mg-RE melt. In the step 1, extraction of RE metals proceeds rapidly and completes in about 3 h. The efficiency strongly depends on the temperature (T) and Mg/magnet ratio (η). One of the optimal conditions is T=1273 (K) and η is 10, where the efficiencies for Nd and Dy extraction are almost 100 % and 60 %, respectively. Further increase of Dy extraction efficiency is possible by addition of Ca to suppress the oxidation of Dy.

Introduction

Rare earth metals are indispensable in the manufacture of electronic products. For example, because of their strong magnetic flux density, neodymium (Nd) and dysprosium (Dy) are used as materials for magnets. Rare earth magnets are used in the motors of compressors in air conditioners and the hard disk drives (HDDs) of personal computers, where compactness and high performance are required. Currently, the rare earths are produced in extremely limited countries and a risk of supply shortage is rising due to export restrictions. To sustain the manufacturing of those products, countermeasures to this procurement risk must be instituted. One countermeasure gathering interest is recycling. In fact, the amount of minor metals accumulated in Japan is said to be comparable to the one produced in a major, resource-rich country in the world [1]. As a new procurement route for metal resources, recycling of rare earth metals contained in end-of-life products is considered to be valid. Thus, Hitachi Ltd. has stared to develop the rare-earth recycling technology for high-performance magnetic motors since 2009 with a contracted subsidy from the Ministry of Economy, Trade and Industry, and the New Energy and Industrial Technology Development Organization in Japan. The outline of the project is shown in Fig. 1.

The project entailed; (1) the development of an automatic disassembly apparatus to remove rare-earth magnets from compressors in air conditioners and from 3.5-inch HDDs in personal computers, (2) the study of the technology to extract rare-earth alloys (Nd, Dy) from removed magnets;, and (3) an economical and environmental evaluation of these recycling processes. Among the project topics, the research in this report concerns item (2). Fig.2 shows the Process flow diagram of neodymium magnet manufacturing and recycling. Magnet alloy producers operate recycling of scrap from magnet production by solvent extraction method [2]. In the hydrometallurgical process, solutions such as acid, alkali and organic solvent are needed and

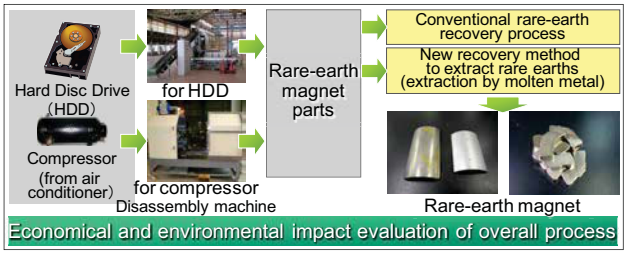


Fig. 1 Outline of the rare earth recycling project in Hitachi, Ltd.

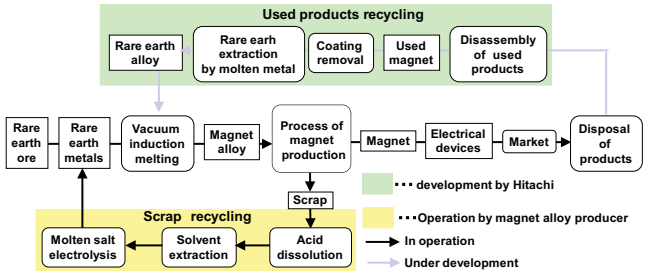


Fig. 2 Process flow diagram of neodymium magnet manufacturing and recycling

waste liquid treatment is a proposition in the conduct of the operation. In contrast, we have developed rare earth extraction method by using molten magnesium (Mg) to extract rare earths from the used magnets. The method is pyometallurgical process and it is not necessary to take care of water treatment. Until now, we have studied the optimized condition that rare earth metals were extracted to Mg. We have succeeded to extract almost 100 % of Nd could be extracted, while extraction efficiency is below 100 % for Dy. We report here our approach to improve the extraction efficiency for Dy by changing the extraction conditions as well as by addition of chemicals to remove obstacles of dy extraction into Mg.

Experimental

Rare earth recycling by molten magnesium

The recycling process involves 3 steps; (1) rare earth metals are extracted to molten magnesium and Mg-RE (rare earth) melt is formed, (2) Mg-RE melt is separated from Fe-B alloy block, which is formed after the extraction of rare earth, and (3) Mg was evaporated from the melt to recover both Mg and rare earth separately. Fig. 3 shows the schematic diagram of the process for recovering rare earths from rare earth magnets by using molten magnesium. In the furnace, a container to recover rare earth metals and the basket including rare earth magnet and Mg are

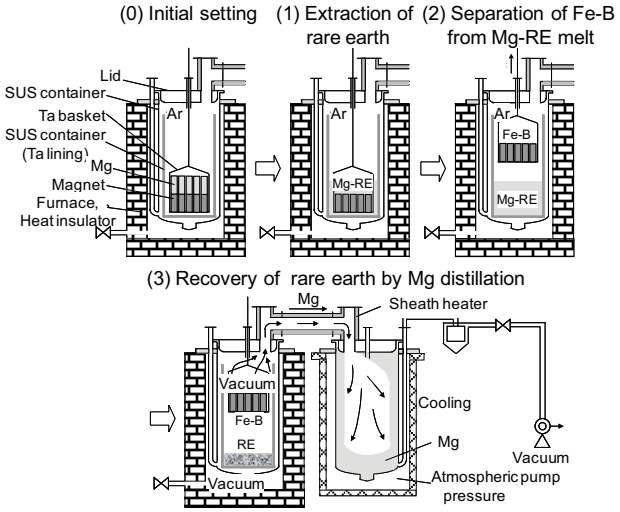


Fig. 3 Schematic diagram of process for recovering rare earths from rare earth magnets by using molten magnesium

placed. In the step (1), Mg is melted by heating and rare earth metals in the magnet are extracted to molten magnesium. In the step (2), Fe-B alloy block is separated from Mg-RE melt at the bottom of the container by pulling out the basket. Finally in the step (3), Mg is evaporated by heating under vacuum and recovered at the right-side container, and rare earth alloy remains and is recovered at the bottom of the left-side container. In this paper, step (2) is the target.

Study on the condition of Dy extraction

From the past experiments, it was found that rare earth extraction efficiency depended on the ratio of Mg to magnet. Fig. 4 shows the extraction efficiency for rare earth at the each ratio. The extraction efficiency is defined as the proportion of the mass of extracted rare earth to that of the whole rare earth in the magnets. The extraction temperature and period were 1000 ^{o}C and 6 hours, respectively. The extraction efficiency for Nd was almost 100% at any condition, but that for Dy was 60 % at maximum, where Mg / magnet ratio was 10. Then factors and the provisions were studied.

(1) Oxidation of Dy in the magnet

As a one of the reason that a part of Dy was not extracted to Mg, it seemed that Dy was partly oxidized and the oxidized Dy was not extracted. The source of oxygen would be the oxygen in the magnet or Mg. Therefore, we tried to remove these oxygen by

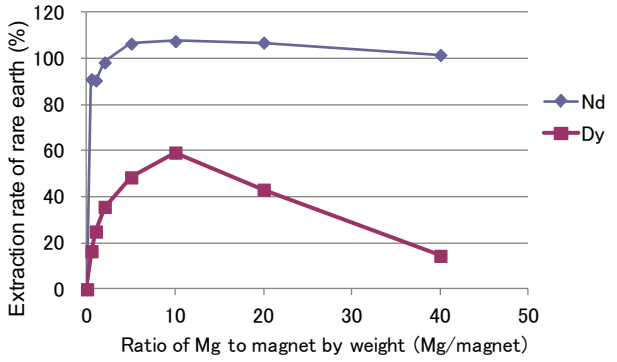


Fig. 4 Extraction rate of rare earth (1000°C 6h)

reductant agent. We used calcium (Ca) as the reductant, since Ca was oxidized easier than Nd or Dy. The amount of Ca was decided by the chemical composition analysis result of oxygen in the magnet and Mg.

(2) Incomplete of Dy extraction

It was suspected that Dy extraction was not completed in 6 hours. In general, the speed of the extractive reaction becomes faster in accordance with temperature. Further extraction experiments were therefore conducted at various temperatures and processing time, and the relationship between rare earth extraction efficiency and temperature or time was evaluated.

(3) Influence of material used for the container

In the past experiments, crucible made from iron containing 2000-ppm carbon (S20C) was used. Since the reaction of rare earth and carbon or other impurity in iron was suspected to suppress the extraction of rare earth, experiments were operated with the crucible made from pure iron and boron nitride (BN).

Procedure of rare earth extraction experiments

Mg used for experiments was flaky reagent. Rare earth magnets were unused and made for the motor of compressors in air conditioners. Table 1 shows the chemical composition of the magnet. For the crucibles, those made from S20C, pure iron, and boron nitride (BN) were adopted. The reason of adoption of BN was that the BN contained little impurity and had high heat resistivity. These reagents and crucible were handled in argon atmosphere to avoid the oxidation of them by air. Then the crucibles were heated at a certain temperature and kept for a certain time in the furnace. After the extraction, the crucible was cooled and the composition of Mg-RE alloy in the crucible was analyzed by ICP-AES. Table 2 summarizes the conditions of rare earth extraction experiments. The experiments No.1 to No. 5 were the examination of Ca addition for the improvement of the Dy extraction efficiency due to Dy reduction. The ratio of Ca to Mg was set 5% by weight, because it seemed to be enough to

Table 1 Chemical composition of specimen

	Concentration(wt%)								
	Fe	B	Co	Nd	Pr	Dy	Al	O	Mg
magnet	65.6	0.97	0.89	20.8	5.89	4.06	0.2	0.5	-
Mg	-	-	-	-	-	-	-	0.002	97.5

Table 2 Conditions of rare earth extraction experiments

No.	Material of crusible	Temperature (°C)	Time (h)	Mg / magnet	Mg / Ca	Purpose
1	S20C	1000	6	2	20	(1) Reduction of Dy
2	S20C	1000	6	10	20	
3	S20C	1000	6	15	20	
4	S20C	1000	6	20	20	
5	S20C	1000	6	40	20	
6	S20C	700	6	10	-	(2) Evaluation of relation between Dy extraction rate and temperature, hour
7	S20C	800	6	10	-	
8	S20C	900	6	10	-	
9	S20C	1060	6	10	-	
10	S20C	1000	0.5	10	-	
11	S20C	1000	1	10	-	
12	S20C	1000	2	10	-	
13	S20C	1000	3	10	-	
14	S20C	1000	12	10	-	
15	Pure Iron	1000	6	10	-	(3) Evaluation of material of crusible
16	BN	1000	6	10	-	
17	Pure Iron	1000	6	10	20	(4) Mix of (1) ~ (3)
18	Pure Iron	1000	12	10	20	

reduce the oxygen in the magnet and Mg magnet and Mg if the reaction was arisen as follows.

$$Ca + O \rightarrow CaO$$

The experiments No.6 to No.9 were conducted as a validation were conducted to evaluate the relationship between Dy extraction efficiency and the temperature. Mg / magnet ratio was set as 10 and the rare earth extraction processing time was set as 6 hours.
The maximum temperature was set as 1060 °C, just below its boiling temperature, 1090 °C. The experiments No.10 to No.14 were conducted to confirm the completion of Dy extraction. As similar to the experiments No. 6 to No. 9, Mg / magnet ratio, the extraction temperature were 10 and 1000 °C, respectively. The extraction processing time was varied from 0.5 hours to 12 hours. No.15 and No.16 were the experiments to evaluate the influence of the material of the crucible; pure iron and BN crucible were used, respectively. Other conditions, such as Mg / magnet ratio, the extraction temperature, and the extraction time, were set at the standard values of 10, 1000 °C and 6 hours, respectively. The experiments No. 17 and No. 18 were conducted to examine the highest efficiency by applying best values of all influencing factors.

Result and discussion

Reduction effect by Ca addition

In Fig. 4, the Dy extraction efficiency decreased with increasing Mg / magnet ratio when the Mg/magnet ratio was larger than 10. Since the proportion of the oxygen from Mg to Dy increased with an increase in the Mg/magnet ratio, it seemed that the decrease of Dy extraction efficiency at high Mg/magnet ratio was caused by the oxygen in Mg.
Fig. 5 shows the effect of Ca addition on the rare-earth extraction leaded by the results of experiments No.1 to No.5. The extraction efficiency of Dy was improved by Ca addition, especially at higher Mg/magnet ratio. We therefore concluded that, Ca addition enhanced the Dy extraction by reduction of the oxygen derived from Mg.

Effect of the temperature during rare earth extraction

Fig 6 shows the relativity of the extraction efficiency to the process temperature obtained by experiments No. 6 to No. 9. The extraction efficiency of Nd was almost 100% at each temperature. On the other hand, the Dy extraction efficiency, 30% at 700 °C, increased with increasing temperature. It seems that the diffusion

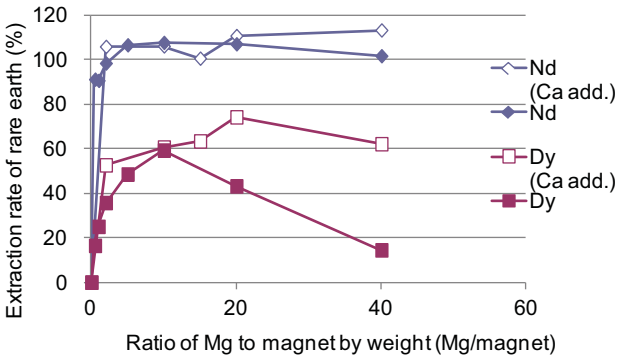


Fig. 5 Effect of Ca addition on the rare-earth extraction (1000 °C 6h)

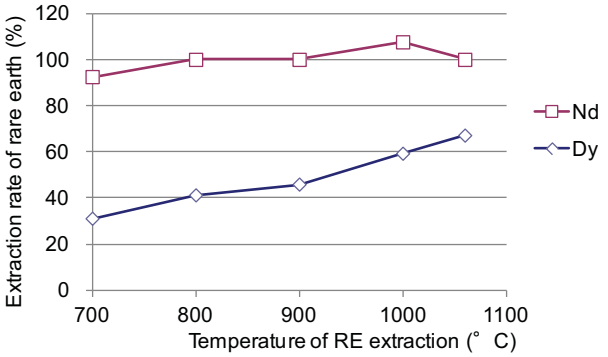


Fig.6 Effect of temperature on the rare-earth extraction (Mg/magnet = 10, 6h)

rate of Dy became faster at higher temperature and the extraction into Mg was accelerated. However, the maximum efficiency was 66%, obtained at 1060 °C, and further increase was not expected due to the limitation of the boiling point of Mg, 1090 °C.

Effect of the processing time

Fig. 7 shows the variation of the rare earth extraction efficiency towards extraction processing time. The extraction efficiency of Nd increased with increasing processing time and reached 100 % at 3 hours. On the other hand, the extraction efficiency of Dy also increased with the time to 60% at 3 hours but didn't increase further.
As a reason for the limitation of extraction efficiency for Dy, it could happen that Dy was completely extracted from magnet but moved to the vicinity of the crucible wall and reacted with it. Therefore, the contact surfaces of the crucible used for experiments were analyzed to confirm whether rare earth metals existed.
Table 3 shows the results of the analysis. Both Nd and Dy were detected on the surface. The corresponding extraction efficiency for Dy was bigger than that for Nd, indicationg Dy was more reactive with iron. The amount of rare earth metals on the cruicible surface increased slightly with the extraction time but the value of corresponding extraction efficiency was about 6% at most.
From these results, we concluded that the rare earth extraction proceeds but terminated at about 3 hours. The extraction efficiency of Dy remained 60% even if the time was more than 3

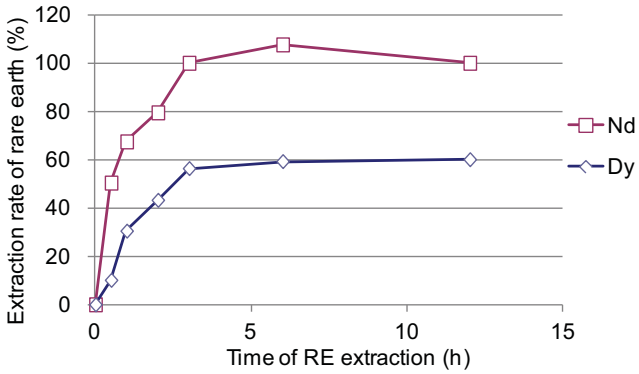


Fig.7 Effect of time on the rare-earth extraction (Mg/magnet = 10, 1000 °C)

Table 3 Amount of rare earth in a S20C crucible

Extraction time (h)	Ratio of absorbed RE to the total RE (%)	
	Nd	Dy
6	0.50	5.73
12	0.58	6.72

hours. Though some rare earth metals absorbed to the crucible, the amount was about 6% to the total.

The effect of the material of the crucible

Fig. 8 shows the effect of material of the crucible on the rare earth extraction. The Nd extraction efficiency became was 100% regardless of the material of the crucible. In contrast, the extraction efficiency for Dy was about 60 % in the case of S20C or pure iron crucible but it was about 30 % when BN crucible was used. It would be because there was a chemical reaction between Dy and BN and Dy was captured in the crucible wall from Mg.

The combined effect of multiple measures

Fig. 9 shows the result of the experiments No. 17 and 18 conducted applying the above-mentioned measures. The extraction efficiency of Dy became 77% and it was the highest extraction efficiency among the all experiments. In the case that processing time was 12 hours, the extraction efficiency became 66% and the enhancement became diminished in comparison with the case of 6 hours. The causation of decrease of Dy extraction efficiency with increase of time was considered as a reaction between crucible and Dy. Selection of the material of the crucible and the optimization of their pretreatment such as cleaning should be important to improve the extraction efficiency.

Conclusions

Hitachi, Ltd. have developed the pyometallurgical process of rare earth metals recycling used molten Mg and tried to improve the extraction rate of Dy. It is considered the causes for the low efficiency of Dy extraction as follows; oxidation of Dy, non-completion of Dy extraction and Material of crucible or contamination. As countermeasures for these caused, experiments under various conditions were conducted and the following results

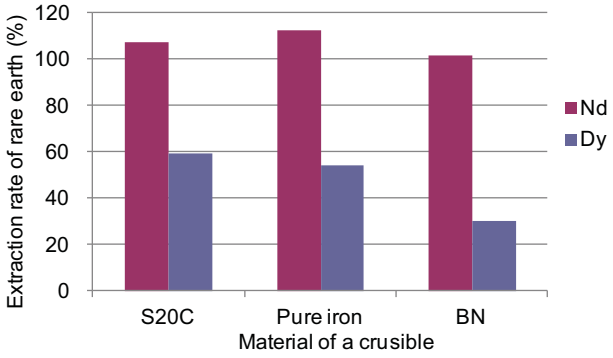


Fig. 8 Effect of material of crucible on the rare-earth extraction
(Mg/magnet = 10, 1000°C 6h)

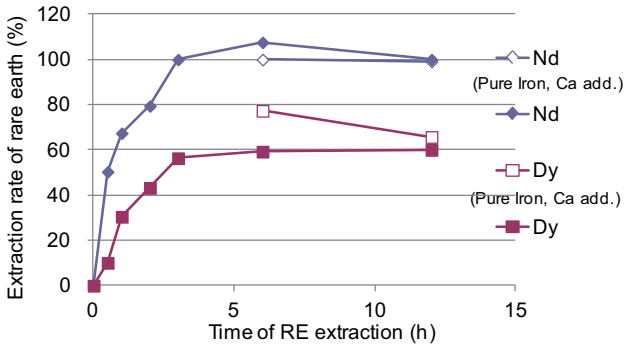


Fig. 9Effect of material of crucible, Ca addition and time on the rare-earth extraction
(Mg/magnet = 10, 1000°C)

were obtained. By Ca addition, the extraction rate of Dy increased especially when the proportion of Mg to magnet is large.

The increase in temperature did not show significant effect for higher efficiency. Our standard condition of time was almost sufficient to complete the Dy extraction. In the case of BN crucible, we obtained 30% of Dy from the rare-earth magnet and the extraction rate became low compared to the case of S20C crucible. As a combination of these countermeasures, the extraction of rare earth with Ca addition and in a pure iron crucible showed the highest efficiency of Dy extraction

Acknowledgement

This work was partly supported by New Energy and Industrial Technology Development Organization (NEDO), Japan National Project in FY 2012, "Development of Technology for Recycling High-performance Rare Earth Magnets from Used Motors". As for the development of the rare earth extraction prototype equipments, we received the cooperation from Toho Titanium Co., Ltd..

Reference

[1] Kohmei H (2009), “Demand and Supply of Rare Metals” in *Material cycles and waste management research* 20(2), 2009-03-31 p-49,

[2] Kohmei H, Nakamura T (2008), Technology of Alternatives and recycling to rare metals: CMC publishing

Magnesium Technology 2014
Edited by: Martyn Alderman, Michele V. Manuel, Norbert Hort, and Neale R. Neelameggham
TMS (The Minerals, Metals & Materials Society), 2014

Recovery of Magnesium and Recycling of Spent Solution in Chloride-Based Atmospheric Acid Leaching of Nickel Laterite

Yong Ge, Weizhong Ding, Dingsheng Tan, Shuqiang Guo
Shanghai Key Laboratory of Modern Metallurgy&Materials Processing, Shanghai University, Shanghai China, 200072

Key Words: Nickel laterite, Chloride-based Leaching, Recycling, Regeneration

Abstract

In this work, the equilibrium relationship of $MgCl_2$-$MgSO_4$-HCl-H_2SO_4-H_2O system at 75℃ was studied. This system is of interest because of its relevance to the process designed for recovery of magnesium and recycling of spent solution in chloride-based atmospheric acid leaching of nickel laterite. Experimental results showed that the concentration of Mg^{2+} ion decreases with the increase of H^+ ion concentration when $m_{SO_4^{2-}}/(0.5m_{Cl^-} + m_{SO_4^{2-}})$ is the same. With the same H^+ concentration, the concentration of Mg^{2+} ion decreases sharply at first and then increases slightly when $m_{SO_4^{2-}}/(0.5m_{Cl^-} + m_{SO_4^{2-}})$ changes from 0.1 to 1. And in all experiments, $MgSO_4 \cdot H_2O$ was the only crystallization phase.

Introduction

Due to the increasing demand for nickel production and declining global reserves of nickel sulphides, more laterite ores need to be processed[1~2].

Recent years, chloride-based aqueous leaching processes get more and more attention because of their faster leaching kinetics and more complete leaching rate. All of these processes consist of an atmosphere leaching in hydrochloride acid solution containing a high background of chloride salts [3~8]. It is noted that the activity of the proton is dramatically increased with the increasing concentration of chlorides in the lixiviant[9]. In addition, a background of $MgCl_2$ in solution may decrease the dissolution of Mg in ores during leaching due to the common-ion effect and further decrease the consumption of hydrochloride acid [8]. In fact, the consumption of hydrochloride acid is a key factor which makes these processes economically sensitive. Thus, the regeneration of hydrochloride acid is a critical operation of all these processes.

To regenerate hydrochloride acid in a cheap way from a spent leaching solution only containing high concentration of $MgCl_2$, Smit[8] suggested adding sulfuric acid, much cheaper than hydrochloride acid, into $MgCl_2$ solution to fulfill the regeneration with the crystallization of $MgSO_4 \cdot H_2O$. The reaction of $MgCl_2$ solution with H_2SO_4 is as below:

$$MgCl_{2(aq)} + H_2SO_{4(aq)} + nH_2O \rightarrow MgSO_4 \cdot nH_2O_{(s)} + 2HCl(aq) \qquad (1)$$

This reaction occurs because of the low solubility of $MgSO_4$ in $MgCl_2$ solution. However, as $MgSO_4$ is not completely insoluble in $MgCl_2$ solution, after reaction the treated solution becomes a quinary system of $MgCl_2$-$MgSO_4$-HCl-H_2SO_4-H_2O. In order to define the equilibrium relationship of the quinary system, the solubility of this system has been investigated at 75℃.

Experimental

Chemicals All solution samples were prepared by dissolving following reagents in deionized water: $MgSO_4$ with a purity of 99%, $MgCl_2 \cdot 6H_2O$ at a purity level of 99.5%, HCl (mass fraction 36.5~38%) and H_2SO_4 (mass fraction 96~98%).

Apparatus A capped beaker equipped with magnetic stirrer was used as a container of the solution. Equilibrium measurements were carried out in a temperature controlled water bath (±0.2K to the desired temperature).

Procedure A solution with desired composition and exceeded Mg salts were introduced to the beaker. Then the beaker was immersed in the water bath and allowed the solution to be stirred continuously about 10 hours. After that the solution was in a stationary state at least 50 hours for settlement of Mg salts. A supernatant sample was quickly taken using a sampler and then weighted. The remaining liquid and solid in the beaker were separated by rapid filtration. The compositions of ions in supernatant samples were determined by chemical methods. Solid samples were taken from the filter and washed immediately with acetone. Dried solid samples were analyzed by XRD.

Chemical analysis Four types of ion concentration in liquid sample were required to determine. The Mg^{2+} ion concentration was determined by complexometric titration against ethyl diamine tetraacetic acid (EDTA) using Eriochrome black T as indicator. The concentration of H^+ ion was determined by neutralization titration with phenolphthalein as indicator. The concentration of Cl^- ion was determined by precipitation titration against $AgNO_3$ solution using K_2CrO_4 solution as indicator. And the concentration of SO_4^{2-} was figured out according to the rule of electric neutrality.

Results and Discussion

Presentation of solubility data According to the reaction (1), hydrochloride acid will be regenerated and magnesium sulfate with different crystal water will simultaneously be precipitated when adding sulfuric acid to a spent leaching solution. The problem is that we don't know the solubility of magnesium ion in the solution in the existence of different acid radicals and an excess of H^+. No data can be used to predict the equilibrium compositions from the literature.

In the quinary system of $MgCl_2$-$MgSO_4$-HCl-H_2SO_4-H_2O, for simplicity, anions include sulfate ion and chloride ion. Magnesium and hydrogen are present as cations. The Mg^{2+} solubility depends on the concentrations of different anions (or their ratio) and hydrogen ion. A divalent magnesium ion may combine with one sulfate ion or two chloride ions. From the point of stoichiometric view, the Mg^{2+} solubility should be as a function of the anion ratio, described as $m_{SO_4^{2-}}/(m_{SO_4^{2-}} + 0.5m_{Cl^-})$. In the paper, all ions in the solution are expressed in the unit of molality, *ie* mol/kg solution. In addition to the anion ratio, the Mg^{2+} solubility is also related with H^+ concentration. So the presentation of the relationship between Mg^{2+} and other ions applies two arguments, the anion ratio and the concentration of hydrogen ion.

***$MgCl_2$-$MgSO_4$-H_2O* system** The Mg^{2+} solubility in the system of $MgCl_2$-$MgSO_4$-H_2O at 75℃ is tabulated in Table Ⅰ and

plotted in Fig.1.

The solubility of magnesium ion in the system $MgCl_2$-$MgSO_4$-H_2O at 75℃ has been investigated by Balarew *et al.*[10]. As they mentioned, the stable precipitate is kieserite, $MgSO_4 \cdot H_2O$, at this temperature. Their result is also presented in Fig. 1. There is a fairly good agreement with each other.

As expected, the increment of sulfate ion concentration will reduce the Mg^{2+} solubility at the beginning of sulfuric acid adding to spent leaching solution, specifically in a field of the anion ratio below 0.25. That is considered to lower Mg^{2+} solubility in the system $MgSO_4$-H_2O compared with in the system $MgCl_2$-H_2O. As shown in fig.1, further increasing sulfate ion content makes a slight raise of the solubility. Lower Mg^{2+} solubility means more $MgSO_4 \cdot H_2O$ precipitation taken out when a spent leaching solution is treated.

Table Ⅰ. The Mg^{2+} solubility in $MgCl_2$-$MgSO_4$-H_2O system at 75℃

$m_{Mg^{2+}}$	3.324	2.979	2.935	3.016	3.113
$\frac{m_{SO_4^{2-}}}{m_{SO_4^{2-}} + 0.5m_{Cl^-}}$	0.113	0.205	0.373	0.789	1.000

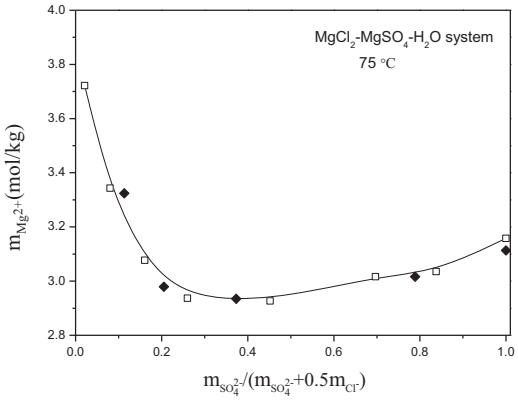


Fig.1 The Mg^{2+} solubility in $MgCl_2$-$MgSO_4$-H_2O system at 75℃.(◆) this wok, (□) Balarew *et al*[10].

***H_2SO_4-$MgSO_4$-H_2O* system** In order to survey the common ion effect on the Mg^{2+} solubility, the system H_2SO_4-$MgSO_4$-H_2O was investigated using the same method. The result obtained is listed in Table Ⅱ and represented in Fig.2. The Mg^{2+} solubility is expressed as a function of H_2SO_4 concentration. There is, of course, an excess of hydrogen ion in the system due to the addition of sulfuric acid. The Mg^{2+} solubility exhibits a sharp decline with sulfuric acid increasing.

The common ion effect can be applied to industry processes to reduce leaching of magnesium from nickel ores. Thus less acid consumption for leaching process is expected.

Table Ⅱ. The Mg^{2+} solubility in H_2SO_4-$MgSO_4$-H_2O system at 75℃

$m_{Mg^{2+}}$	3.113	2.476	1.831	1.269	0.858
$m_{H_2SO_4}$	0	1.059	2.097	3.184	4.236

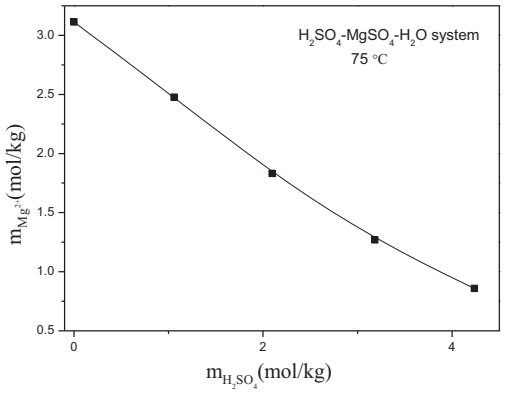


Fig.2 The Mg^{2+} solubility in H_2SO_4-$MgSO_4$-H_2O system at 75℃

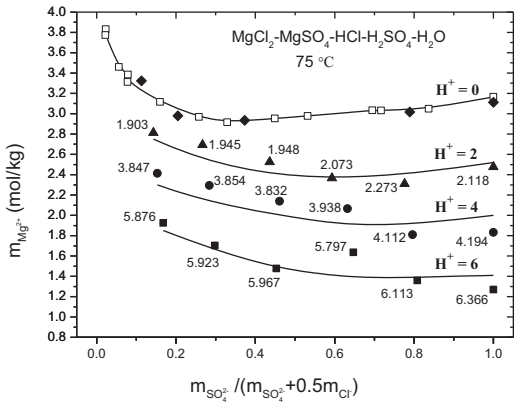


Fig.3 The Mg^{2+} solubility in $MgCl_2$-$MgSO_4$-HCl-H_2SO_4-H_2O system at 75℃. Lines are contour of the H^+ concentration. Figure close to symbol points the H^+ concentration. Solid symbols are from this work and open symbols from Balarew *et al* [10].

$MgCl_2$-$MgSO_4$-HCl-H_2SO_4-H_2O System For the quinary system of $MgCl_2$-$MgSO_4$-HCl-H_2SO_4-H_2O, as mentioned above,

Table Ⅲ. Solubility in $MgCl_2$-$MgSO_4$-HCl-H_2SO_4-H_2O System at 75℃

m_{H^+} (mol/kg)	$m_{Mg^{2+}}$	$\frac{m_{SO_4^{2-}}}{0.5m_{Cl^-} + m_{SO_4^{2-}}}$	m_{H^+} (mol/kg)	$m_{Mg^{2+}}$	$\frac{m_{SO_4^{2-}}}{0.5m_{Cl^-} + m_{SO_4^{2-}}}$	m_{H^+} (mol/kg)	$m_{Mg^{2+}}$	$\frac{m_{SO_4^{2-}}}{0.5m_{Cl^-} + m_{SO_4^{2-}}}$
2.118	2.476	1.000	4.194	1.831	1.000	6.366	1.269	1.000
2.273	2.310	0.776	4.112	1.809	0.796	6.113	1.358	0.808
2.073	2.367	0.593	3.938	2.066	0.632	5.797	1.636	0.647
1.948	2.525	0.436	3.832	2.139	0.461	5.967	1.477	0.453
1.945	2.693	0.267	3.854	2.293	0.284	5.923	1.702	0.298
1.903	2.813	0.143	3.874	2.413	0.153	5.876	1.925	0.168

both the anion ratio and the concentration of hydrogen ion will affect the Mg^{2+} solubility. The solubility data measured are given in TableⅢ and Fig.3. Lines in Fig. 3 represent the contour of the H^+ concentration. The figure gives us an oveall image to know the influence of the anion ratio and the concentration of hydrogen ion on the Mg^{2+} solubility. Higher hydrogen ion concentration in the solution causes the Mg^{2+} solubility to dramatically decrease.

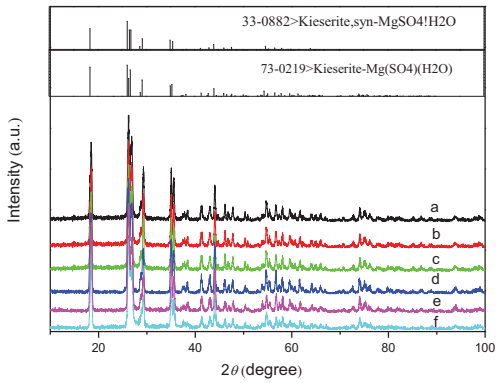


Fig.4 XRD patterns of solid phase precipitated from the measurements of $MgCl_2$-$MgSO_4$-HCl-H_2SO_4-H_2O system at 75℃. $m_{H^+} \approx 4$ mol/kg, $m_{SO_4^{2-}}/(m_{SO_4^{2-}} + 0.5m_{Cl^-})$: (a) 1.000, (b) 0.776, (c) 0.593, (d) 0.436, (e) 0.267, (f) 0.143.

Identification of Hydrates The hydrates of magnesium sulfate precipitated from the solubility measurements have been identified by XRD. Figure 4 shows a part of the XRD patterns which are a perfect match to the standard kieserite in XRD database. Robson[11] and Balarew *et al* [10] also found that the stable hydrate phase at 75℃ is kieserite, $MgSO_4 \cdot H_2O$. When the precipitate is subjected to calcinations for Mg recovery, monohydrate requires lower energy input.

Conclusion

The Mg^{2+} solubility in $MgCl_2$-$MgSO_4$-HCl-H_2SO_4-H_2O system at 75 ℃ has been investigated. Experimental results indicate that the solubility dramatically decreases with the increase of the H^+ ion concentration. The solubility also drops within a range of the anion ratio from 0 to 0.25. Further increasing in the anion ratio does not seem to effect on the solubility. Solid precipitate has been identified as monohydrate of magnesium sulfate. The detailed research in equilibrium relationship of the quinary system would give process developers indications to facilitate process design and development.

Acknowledgment

This research was supported by the National Basic Research Program of China (973 Program, 2012CB722805).

Reference

1. McDonald R G, Whittington B, “Atmospheric acid leaching of nickel laterites review. Part I. Sulphuric acid technologies,” *Hydrometallurgy*, 91(2008), 35–55.

2. McDonald R G, Whittington B, “Atmospheric acid leaching of nickel laterites review. Part II. Chloride and bio-technologies,” *Hydrometallurgy*, 91(2008), 56–69.

3. Harris, B., Magee, J., “Atmospheric chloride leaching: The way forward for nickel laterites” (Paper presented at the Hydrometallurgy—2003, TMS Annual Meeting & Exhibition, Warrendale, PA), 501–515.

4. Harris, G.B., Lakshmanan, V.I., Sridhar, R., “Process for the recovery of value metals from material containing base metal oxides” (US Patent 2004/0228783 A1).

5. Harris, G.B., Magee, T.J., Lakshmanan,V.I., Sridhar, R., “The Jaguar Nickel Inc. Sechol laterite project atmospheric chloride leach process” (Paper presented at the International Laterite Nickel Symposium —2004, The Minerals, Metals and Materials Society, Warrendale, PA), 219–241.

6. Moyes, J., Houllis, F., Tong, A., “Recovery of metals from oxidised metalliferous materials” (World Patent WO 2005 /093107 A1).

7. Moyes, J., Houllis, F., Tong, A., “The Intec nickel laterite process” (Paper presented at the ALTA 2005 Nickel/Cobalt10, ALTA Metallurgical Services, Melbourne).

8. Smit, J.T., Steyl, J.D.T., “Leaching process in the presence of hydrochloric acid for the recovery of a value metal from an ore” (World Patent 2006/043158 A1).

9. Demopoulos G. P.， Li Z., “New Technologies for HCl Regeneration in Chloride Hydrometallurgy,” *World of Metallurgy – ERZMETALL*， 61(2)(2008), 89-98.

10. Balarew Chr.，Tepavitcharova S.，Rabadjieva D.，Voigt W., “Solubility and Crystallization in the System $MgCl_2$ -$MgSO_4$ - H_2O at 50 and 75℃,” *Journal of Solution Chemistry*, 30(9) (2001), 815-823.

11. Robson H. L., “The system $MgSO_4$-H_2O from 68 to 240°,”*Journal of the American Chemical Society*, 49(1927), 2772-2783.

Magnesium Technology 2014
Edited by: Martyn Alderman, Michele V. Manuel, Norbert Hort, and Neale R. Neelameggham
TMS (The Minerals, Metals & Materials Society), 2014

EFFECT OF PHYSICAL PROPERTIES OF DOLOMITE ON CARBOTHERMIC REDUCTION

Siya Wang, Yu Wang, Guangyong Bin, Jiang Diao

College of Materials Science and Engineering, Chongqing University, Chongqing, China

Keywords: Carbothermic Reduction, Dolomite, Graphite, Magnesium

Abstract

Magnesium is widely utilized in machine building industry. Compared to other industry routes, carbothermic reduction method has many advantages in producing magnesium, particular saving energy and reducing cost. The mixture of calcined dolomite and graphite was agglomerated to cylinder, which was carried out under the condition with 1773K, 60min and 5000Pa. The effect of particle size, the mole ratio of C:MgO and pressure of agglomeration are studied and discussed. Furthermore, the decomposition of dolomite contains two stages. The optimal conditions (reduction ratio of MgO reaches to 69.64%) were: mole ratio of C:MgO is 3:1, pressure of agglomeration is 8MPa, particle size of calcined dolomite is 120-160 mesh.

Introduction

Magnesium is the lightest metal of all the commonly utilized metal and applied in car industry, medical industry and other industries [1-3]. The global production of magnesium is based on Pidgeon process [4] and electrolytic process. However the both process cause high cost and environment problem, such as emission HCl and Cl_2. The carbothermic reduction [5, 6] provides the potential process, which can produce magnesium with a lower-energy and higher-productivity than existing industrial routes [7].

The conditions of sample are the important factors in the process. Several investigations have been carried out to exam the magnesium recovery from the magnesia. Mohammad NUSGEH et al. [8] presented the results of an investigation on the effect of mechanical milling sample in carbothermic reduction route on magnesia. They carried out the experiments by milling the magnesia and graphite with keeping different times. And the characters of the mixture were analysis by SEM, SSA and XRD and had changed significantly. The reaction of milled mixture occurred at lower temperature than that of unmilled sample. Tian Yang et al. [9] investigated the other factors of carbothermic reduction on magnesia and coking coal. It clearly showed that the conditions of pellets and content of CaF_2 affected the losing ratio obviously. In our work, the effect of mole ratio of C:MgO, pressure of agglomeration and the particle size of calcined dolomite on the reduction ratio were researched.

Experiments

The chemical composition of the dolomite was investigated by XRF and given in Table Ⅰ. The main compounds of the dolomite were CaO and MgO.

Table Ⅰ. Chemical composition of dolomite, wt-%

CaO	SiO_2	Fe_2O_3	MgO	Al_2O_3
53.04	2.67	0.48	42.31	0.65

The calcined dolomite was obtained after calcined at 1223K for 15min and separated to several size conditions by sieving process. The reduction experiments were carried out in the electronic furnace and the schematic of experimental system shown as Figure 1. The temperature was controlled with B type thermocouple, which could detective temperature precision 1K. The mixture (calcined dolomite and graphite) was forming to the shape with height-18mm and diameter-19mm. And the samples and mold are shown as

Figure 2. The mixture was put into the Al_2O_3 Crucible in the furnace. The argon was charged into the furnace at a rate of 66cm^3/min. The furnace was filled with argon air for 5min, and then the gas was drained out by vacuum pump. Then the protect air would been charged into the furnace again. These processes were recycling for five times. The samples was heated from room temperature to 573K at rate of 3K/min and held for 15min aim to remove the absorbed gas and water. Then the temperature was heated to 1773K at rate of 5K/min. The experiments were carried out under the condition with 1773K, 60min and 5000Pa. X-ray fluorescence (XRF), X-ray diffraction (XRD) and chemical analysis method were utilized in the experiments.

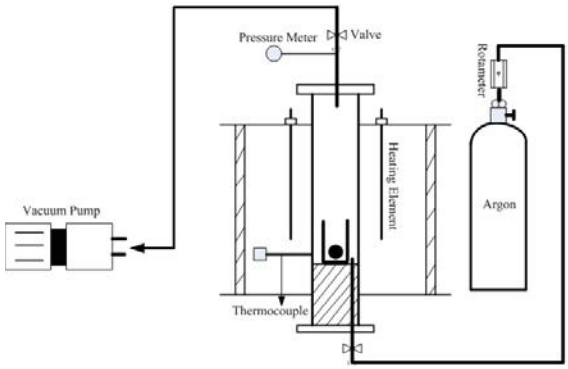


Figure 1.The schematic of experimental system



Figure 2.The photographs of samples (1) and mold (2)

Results and Discussions

Materials Prepared

The XRD patterns in Figure 3 indicated that $Mg(Ca)(CO_3)_2$ is the only Mg containing phase in dolomite. And the phases of calcined dolomite which only contained CaO and MgO were studied by XRD patterns. Figure 4 showed the DSC and TG curves of dolomite. It could be seen from Figure 4 that the mass of mixture decreased with increasing temperature from 373K to 1500K. The main mass losing of dolomite was absorbed water and gas at the temperature range of 373K to 573K. The decomposition of dolomite occurred as above 880K, which was proved by the TG curves. However, the TG curve changed to smooth when the temperature was above 1110K. It could be seen that the dolomite had decomposed completely. The decomposition of dolomite can be described as equation (1) and equation (2).

$$Mg(Ca)(CO_3)_2 = MgO + CaCO_3 + CO_2 \quad (1)$$

$$CaCO_3 = CaO + CO_2 \quad (2)$$

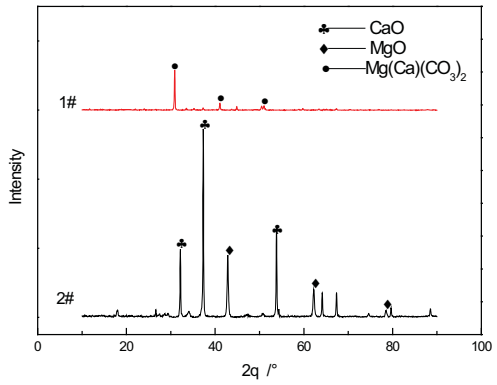


Figure 3.The XRD patterns of dolomite (1#) and calcined dolomite (2#)

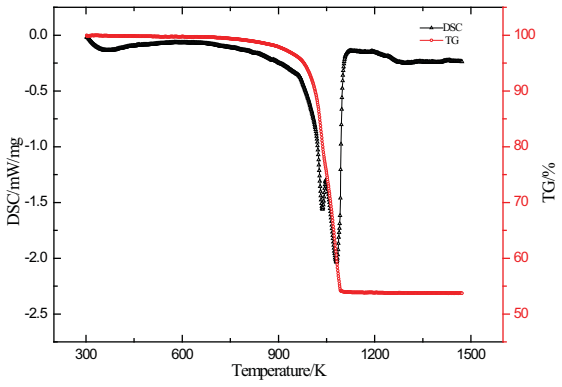


Figure 4.The DSC and TG curves of dolomite

Reduction Reaction

The main reaction was described as equation (4). And the thermodynamic feasibility of the reduction reaction had been considered and the Gibbs free energy ΔG_T was calculated with the results of ΔG_T<0. Furthermore, the XRD patterns of mixture were shown in Figure 5 which indicated that only Mg existed in sample 2# and proved that the reduction reaction between graphite and calcined dolomite occurred in the experiments. Then the reduction ratio used for evaluated the degree of reduction reaction could be calculated according to formula (5).

$$\mathrm{MgO(s)+C(s)=Mg}(g)+\mathrm{CO}(g)$$
$$\Delta G^0=618300-291.76T \quad (4)$$

$$R=\frac{m_1\times\beta-m_2\times\alpha}{m_1\times\beta}\times100\% \quad (5)$$

R: reduction ratio of calcined dolomite, %

m_1,β: the weight and mass percent of initial sample, g, %

m_2,α: the weight mass percent of final sample after reaction, g, %

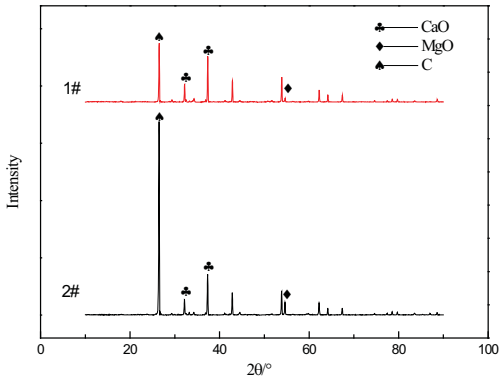


Figure 5.The XRD patterns of mixture

(1#: the final sample of C and calcined dolomite after reaction, 2#: the initial sample of C and calcined dolomite)

The effect of mole ratio of C:MgO on reduction ratio was shown in Figure 6. The samples were prepared with the conditions: the agglomeration pressure was 5MPa and the particle size of calcined dolomite was 160-200 mesh. The reduction ratio was 12.52% with the mole ratio 1:1 of C:MgO. And the reduction ratio increased quickly in the earlier stage with the mole ratio from 1:1 to 2:1 and reached to 55.48% with mole ratio of 2:1. It increased slower in the second stage with the mole ratio from 2.5:1 to 3:1 than first stage and reached to 62.31% with mole ratio 3:1. The reduction reaction between C and MgO could be described as a solid-solid reaction as equation (6), which was greatly affected by the contacting area of mixture powder. And the contacting area was increased significantly with the increasing of mole ratio, which was benefit for the reduction ratio. However when the mole ratio of C:MgO was higher than 2.5:1, the effect of mole ratio was not as greatly as the earlier stage. It could be explained by that the contacting area did not always keep increasing with the increasing of mole ratio.

$$\mathrm{A}(s)+\mathrm{B}(s)=\mathrm{C}(g)+\mathrm{D}(g) \quad (6)$$

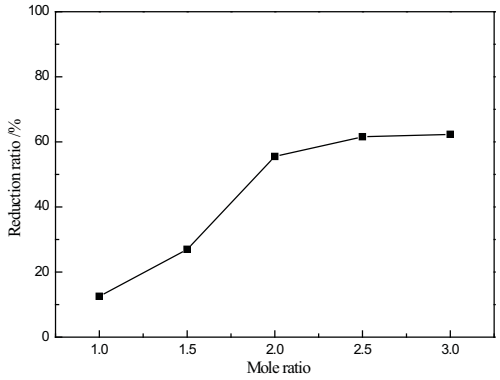


Figure 6.Effect of mole ratio of C:MgO on reduction ratio

Figure 7 shows the effect of agglomeration pressure on reduction ratio. The samples were prepared with the conditions: the mole ratio was 2:1 of C:MgO and the particle size was 160-200 mesh. The reduction ratio was 36.45% with agglomeration pressure of 2MPa and kept increasing until the agglomeration pressure reached 8MPa with reduction ratio of 68.51%. However it began to decrease when the agglomeration pressure was beyond 8MPa. It was probably because the path of compact mixture was blocked by

increasing agglomeration pressure. The products of Mg (g) and CO (g) could not be released as soon as possible. The degree of reaction was limited with the increasing agglomeration pressure.

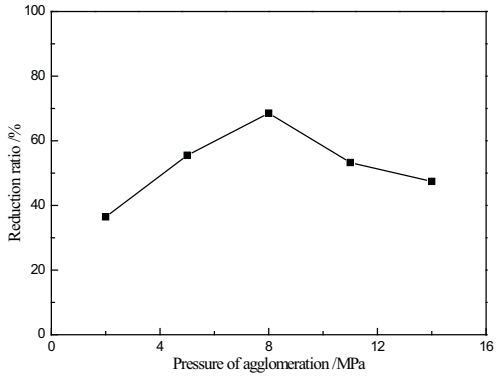


Figure 7.Effect of agglomeration pressure on reduction ratio

Figure 8 shows the effect of powder size on reduction ratio. The samples were prepared with the conditions: the mole ratio was 2:1 (C:MgO) and the agglomeration pressure was 5MPa. The reduction ratio reached to 62.56% with the size of 120-160 mesh. The phenomenon could be explained by relationship between contacting area of powder and the gas releasing path. When samples were prepared with 80-120 mesh, the contacting area of graphite and dolomite increased and the path has not been blocked completely. Therefore the reduction ratio increased. However when the size of samples decreased to 160-200 mesh, blocked path do much more effect than the increasing contact area to the reduction reaction. That was the reason the reduction ratio began to decrease.

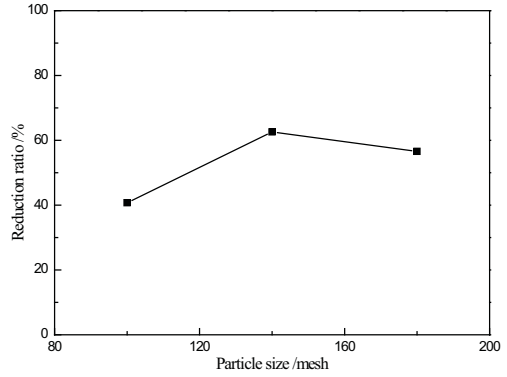


Figure 8.Effect of size of calcined dolomite on reduction ratio

According to our previous researches, other experiments were carried out under 1773K, 60min and 5000Pa with the physical properties: mole ratio of C:MgO was 3:1, pressure of agglomeration was 8Mpa, size of calcined particle was 120-160 mesh. And the reduction ratio reached to 69.64%.

Conclusions

The present work did not carry out the separation of reaction [4] products Mg and CO. we just focused on requirements for the forward reaction. We will carry out the separation of products Mg and CO to prevent back reaction in another study. According to present investigation, the following conclusions can be obtained:

(1) The decomposition of dolomite occurs as two steps. The dolomite decomposes to MgO and $CaCO_3$ at 880K firstly, and then $CaCO_3$ begins to decompose to CaO at 1050K.

(2) The reduction reaction between calcined dolomite and graphite occurs under the conditions with 1773K, 60min and 5000Pa.

(3) The reduction ratio of calcined dolomite is greatly affected by physical properties of the materials.

(4) The optimum conditions are: the mole ratio of C:MgO is 3:1, the pressure of agglomeration is 8MPa and the particle size of calcined dolomite is 120-160 mesh.

References

1. F.H.Froes, et al., “The science, Technology, and Applications of Magnesium,” The Journal of the Minerals, Metals & Materials Society, Vol.50 (1998), 30-34.
2. D.Eliezer, et al., “Magnesium Science, Technology and Applications,” Advanced Performance Materials, Vol. 5(1998), 201-212.
3. L.Schlapbach, et al., “Hydrogen-Storage Materials for Mobile Applications,” Nature, Vol. 414 (2001), 353-358.
4. M.Halmann, et al., “Magnesium Production by Pidgeon Process Involving Dolomite Calcinations and MgO Silicothermic Reduction: Thermodynamic and Environmental Analyses,” Industrial & Engineering

Chemistry Research, Vol. 47(2008), 2146-2154.

5. M.S.Mohamed, et al., “Laser-induced Magnesium Production from Magnesium Oxide Using Reducing Agents,” Journal of Applied Physics, Vol. 104(2008).
6. Li Rongti, et al., “Kinetics and Mechanism of Carbothermic Reduction of Magnesia,” Metallurgical and Materials Transactions B, Vol.34B (2003), 433-437.
7. Geoffrey Brooks, et al., “The Carbothermic Rout to Magnesium,” The Journal of the Minerals, Metals & Materials Society, Vol.58 (2006), 51-55.
8. Mohammad NUSGEH, et al., “Effect of Mechanical Milling on Carbothermic Reduction of Magnesia,” ISIJ International, Vol.50 (2010), No.5, 668-672.
9. Tian Yang, et al., “Magnesium Extraction from Magnesia by Carbothermic Reduction in Vacuum,” Journal of Vacuum Science and Technology, Vol.32 (2012), No. 4, 306-311

Magnesium Technology 2014
Edited by: Martyn Alderman, Michele V. Manuel, Norbert Hort, and Neale R. Neelameggham
TMS (The Minerals, Metals & Materials Society), 2014

TIME DEPENDENT SPRINGBACK OF A MAGNESIUM ALLOY

B. Li, Z. McClelland, S.J. Horstemeyer, I. Aslam, P.T. Wang, M.F. Horstemeyer
Center for Advanced Vehicular Systems, Mississippi State University, Starkville, MS 39759

Keywords: Magnesium; Bending; Springback; Creep

Abstract

A time dependent springback was observed in a Mg-Al-Zn (AZ31) rolled sheet after three-point bending at room temperature (RT). The springback increased nonlinearly with time at RT. After bending, specimens were held in the bent state for up to five months, and the springback dramatically decreased after being held for one month compared with specimens that were not held. The decline in springback increased as the holding time increased. These results indicate that creep and creep recovery occurred at RT. Microstructure examinations revealed that high density $\{10\bar{1}2\}<10\bar{1}\bar{1}>$ twins in the form of localized twin bands were present in the compression zone of the bent specimens. After the specimens were unloaded, detwinning occurred and continued spontaneously over the five month time period at RT, contributing to the observed time dependent springback.

Introduction

In recent years magnesium (Mg) alloys have drawn significant attention because their low densities are attractive for structural applications where energy efficiency is a priority. However, extensive application of Mg alloys is bottlenecked by their relatively low ductility and poor formability at room temperature (RT). In contrast to metals with cubic crystal structures where deformation is dominated by dislocation slip at RT, the mechanical behavior of Mg alloys vastly differs in that twinning plays a crucial role during plastic deformation. Twin-twin interaction and twin-slip interaction lead to unique hardening behavior, tension-compression asymmetry, and anisotropy in plastic deformation [1-4].

Sheet forming of magnesium (Mg) alloys is an important manufacturing process in which bending is significantly involved. Mg sheet metals are usually highly textured. During bending $\{10\bar{1}2\}<10\bar{1}\bar{1}>$ twinning is activated in grains in which the stress favors twinning. The combination of anisotropy, twinning and dislocation slip makes the springback behavior of Mg alloys sharply different from metals where slip dominates plastic deformation [5]. Springback has been considered the immediate recovery of elastic strain after unloading. However, we recently observed a significant decrease in springback in an Mg alloy after the specimen was held in the bent state for an extended amount of time at RT, indicating that time dependent inelasticity plays a role. This observation motivates the current work, in which we designed and conducted experiments to investigate such time dependent springback behavior at RT. Interesting results were obtained.

Experimental Method

A twin-roll cast AZ31 magnesium sheet with a 1.0 mm thickness was used in our experiments [6]. Strong basal texture was developed during rolling. More details of microstructure and texture of the experimental material can be found in [7]. Strips with a dimension 76 (l)×9 (w)×1 (t) mm^3 were sheared for three-point bending tests. Two groups of specimens were prepared with the length either parallel to the rolling direction (RD) or the transverse direction (TD). Figure 1 shows the experimental setup in this work. Three-point bending was performed on an Instron 5882 at a displacement rate 10.0 mm/min. Figure 1a shows the geometry of the bottom half of the in-house bending fixture. The span distance is 28.8 mm. A sheet specimen (indicated by the block arrow) was bent and entirely slid into the opening of the fixture. A steel block with a trough (Figure 1b) was machined to hold the bent specimens for different lengths of time. The trough has a width 28.8 mm which is the same as the span distance of the bending fixture. After a specimen was bent and entirely slid into the opening, the fixture and the bent specimen inside was removed from the Instron 5882, and the specimen was carefully slid out of the fixture and transferred to the trough such that no relaxation occurred and the specimen remained bent by the trough. Figure 1c and d show the designation of the specimens in this work: the bend parallel to the RD was designated as the "RD specimen" and the bend parallel to the TD was designated as the "TD specimen". Five RD specimens and five TD specimens were prepared, bent and transferred to the trough. Every month, an RD and a TD specimen were taken out of the trough and the springback was measured as the distance between the two legs of the bent specimen. In addition, an RD and a TD specimen were bent and immediately taken out of the fixture, and the springback was measured as the baseline. The springback of the baseline specimens was then measured every month. For those specimens that were held in the trough for different lengths of time, their springback was also measured every month after retrieval from the trough. All the tests were performed at RT.

In order to examine the microstructural evolution while the specimens remained unloaded, another RD specimen was sheared, bent, immediately released and mounted for metallography examinations. The microstructure of the freshly bent RD specimen was compared to that of the baseline RD specimen which was bent five months earlier. The mounted specimens were mechanically polished with a series of sand papers down to 2400 grit number. The final polish was performed with a suspension composed of alumina powder (50 nm in particle size) and ethylene glycol. An etchant comprising picric acid, deionized water, acetic acid and ethanol was used to reveal the microstructure.

Results

Figure 2 shows the evolution of the springback of the baseline RD and TD specimens. In general, the springback distance increases as time increases. The rate of increase in the first month is most significant. However, for the RD specimens, a conspicuous increase in springback is observed at the third month. Afterwards, the springback falls and decreases to levels before the third month. The burst in springback of the RD specimen at the third month was measured with different calipers and the results were the same. For both the RD and the TD baseline specimens, the

springback reaches a maximum at the third month, and then unexpectedly decreases.

The springback, however, dramatically declined after the specimens were held in the trough for extended lengths of time. Figure 3 shows the evolution of the springback of the specimens that were held in the trough for up to five months. We can observe a sharp decrease in springback after the specimen was held for one month, and then the rate of decrease slows down gradually. Note that, for the TD specimens, a data point is missing at the first month because the TD specimen accidentally popped out of the trough for unknown reasons. Despite the accident, the missing data point does not affect the general trend of the evolution of the springback of the constrained specimens. The difference in springback between the baseline and the five-month specimen is 7.0 mm for the RD and 6.52 mm for the TD, which is fairly significant.

After retrieval from the trough, the springback of those specimens that were held for different times was also measured every month. Figure 4 shows such evolutions in the RD specimens that were held for up to three months, so that at least three data points can be acquired for each specimen. It can be observed that generally the springback of each specimen monotonically increases as time increases, and no decrease in springback was observed in the available data points, in contrast to the baseline specimen (Figure 2). The rate of increase in springback is most significant in the first month, and higher than that of the baseline specimens. The evolution trend is similar for the TD specimens (Figure 4b).

Figure 5 shows the microstructure of the baseline RD specimen that remained in the free state for five months at RT. We can observe that high density $\{10\bar{1}2\}<10\bar{1}\bar{1}>$ twins were present in the compression zone. The twins appear in the form of localized twin bands. As the bending angle increased, the twin bands merged. In the tension zone, deformation twins can hardly be observed at the low magnification. The microstructure of the freshly bent RD specimen looks similar at the same magnification (not shown).

Analysis and discussion

The anomalous springback behavior observed in this work is a manifestation of creep of Mg alloys, which have been investigated extensively at relatively high temperatures [8-9]. Mg alloys are known for their poor creep resistance at elevated temperatures [8]. RT creep of Mg alloys, however, has received much less attention and discussions in the literature are very limited. Gjestland et al. [10] investigated stress relaxation and creep behavior of AZ91 Mg alloys at 423 K (150°C) and at RT. Tensile samples were loaded to two-thirds of the yield stress for 100 hours. It was found that the remaining stress slightly decreased with time at RT. RT creep and creep recovery of Ti alloys were investigated by Mills et al. [11-12], and formation of dislocation pileups where significant stress concentrations were created was proposed as the responsible mechanism.

In three-point bending, a stress gradient with two stress states (compression and tension) is created in the specimen. For HCP metals, the neutral axis does not coincide with the geometrical center line of the specimen through the thickness, and shifts toward the tension zone [13-14]. In highly textured Mg sheets, during bending $\{10\bar{1}2\}<10\bar{1}\bar{1}>$ extension twinning is favored in the compression zone, but disfavored in the tension zone. Recently, Baird et al. observed localized twin bands in the compression zone in bending of an AZ31 sheet [7]. Conceivably, the presence of the $\{10\bar{1}2\}<10\bar{1}\bar{1}>$ extension twins should affect the time dependent springback observed in this work.

The effect of twinning on creep at RT in α-Ti was studied by Ankem et al. [15-16]. It was found that at low strain levels (≤2%) dislocation slip was the rate-controlling mechanism, whereas at strain levels above 2%, both slip and twinning were significant deformation mechanisms. Hence, a transition from slip to twinning occurred in the RT creep of α-Ti. Ankem et al. [17] further observed that the $\{10\bar{1}2\}<10\bar{1}\bar{1}>$ twinning was time dependent or rate-limited. The growth rate of the twins was measured as slow as 1.0 nm s^{-1}, many orders of magnitude slower than the speed of sound which is the maximum growth speed of shear controlled twinning in metals. The time dependent twinning was interpreted as a result of the diffusion of oxygen atoms away from the octahedral interstitial lattice sites during twin boundary (TB) migration as the parent lattice was converted to the twin lattice. At RT, the slow diffusion of the oxygen atoms was considered rate limiting mechanism during RT creep of α-Ti alloys.

Recently, Li and Ma proposed that $\{10\bar{1}2\}<10\bar{1}\bar{1}>$ twinning is accomplished by atomic shuffling [18]. In this model, atomic shuffling converts the parent basal planes to the twin prismatic planes, and the parent prismatic planes to the twin basal planes, without involving twinning dislocations. This indicates that the twinning shear of $\{10\bar{1}2\}<10\bar{1}\bar{1}>$ twinning mode equals zero, and a misfit strain is created along the *c*-axis as a result of reorientation of the lattice. This shuffling dominated twining mechanism has been confirmed by the most recent in-situ transmission electron microscopy observations of twinning in single crystal Mg [19-20]. It was observed that during $\{10\bar{1}2\}$ twinning and detwinning no shear strain was produced on the specimen. The shuffling model explains well the mechanisms for reversible twinning or pseudo-elasticity [21-22], the non-Schmid effect [23], extremely incoherent TBs [24], penetration of a twin variant through a grain boundary [25], and the low critical stress for twin growth (~2.4 MPa [26]).

The reversibility and low critical stress of $\{10\bar{1}2\}<10\bar{1}\bar{1}>$ twinning sheds some light on the time dependent springback observed in this work. Since the twin growth kinetics is not controlled by fast shear deformation, atomic shuffling is the rate-limiting factor, and the kinetics of twinning or detwinning can vary over a wide range depending upon the local stress and microstructure near the TBs [18]. For the baseline specimens that were unloaded immediately after bending, relaxation continued with time due to the local stress in the substructures, and twin-slip interaction. The interfacial energy of the TBs is another important driving force for detwinning. Excess interfacial energy from the TBs tends to be reduced by detwinning. Since high density $\{10\bar{1}2\}$ twins were generated in the compression zone, when the external load was removed, the bent specimens immediately sprang back and detwinning occurred. Detwinning continued occurring with time by atomic shuffling driven by the local stress and the interfacial energy. Consequently, as detwinning continued, the springback increased with time. This conclusion was confirmed by the examinations on the microstructural evolution in the baseline RD specimen that was bent, immediately released and maintained in the free state for five months at RT, as shown in Figure 6a. For comparison, the microstructure of the freshly bent RD specimen is shown in Figure 6b. The images were taken in the tension zone away from the localized twin bands. Because the

density of the twins in the compression zone is high, it is hard to tell the difference in the twin density in the compression zone of the two specimens. However, in the tension zone, a significant difference can be observed. In the baseline RD specimen that was bent five months earlier, twins can be occasionally observed in the grains (Figure 6a), but in the freshly bent RD specimen, the density of the twins is considerably higher. These observations indicate that detwinning continued over the five month time period while the specimens remained in the free state at RT, and the spontaneous detwinning is a major contribution to the observed time dependent springback of the AZ31 sheet. It should be noted that dislocation slip may also play a role in the time dependent springback, as suggested by Mills et al. [11-12]. However, the mechanism for the burst in springback in the RD specimen at the third month remains unclear. Also, why the springback decreases following the third month in both the RD and the TD specimens is not understood either.

The significant drop in springback of the specimens held for extended times indicates that RT creep recovery occurred during holding. There are two possible contributing sources. First, slip dominated recovery in the tension zone. Geometrically necessary dislocations (GNDs) have to be generated to compensate the strain gradient through the thickness during bending, and the GNDs are mostly basal slip because the basal plane of the crystals is nearly parallel to the rolling direction. Prismatic and pyramidal slip may also be activated during bending but the critical stresses for these non-basal slip systems are much higher than that of the basal slip. During holding, the dislocations may evolve into lower energy configurations such as pileups or subgrain boundaries. Second, twinning involved recovery in the compression zone. As stated above, detwinning may occur. Additionally, dislocations may interact with the TBs when intersecting with the TBs. More systematic investigations are needed to further understand the mechanism of the interesting time dependent springback in Mg alloys at RT.

Conclusions

The springback behavior of an AZ31 Mg rolled sheet at RT was investigated and very interesting, time dependent springback was uncovered. The following conclusions can be reached:

The springback after three-point bending increased with time nonlinearly. A burst in the springback in the RD specimen at the third month was revealed. For the specimens that were held in a trough for different lengths of times, the springback dramatically decreased compared with the samples without being held. These results clearly indicate that creep and creep recovery occurred at RT. From the perspective of structural design, such behavior should be taken into consideration in engineering applications and constitutive modeling.

Microstructure examinations show that during bending, high density $\{10\bar{1}2\}<10\bar{1}\bar{1}>$ twins were generated in the compression zone in the form of localized twin bands, but the density of the twins is much lower in the tension zone. After unloading, detwinning occurred and continued over the five month time period in our experiments in the free state at RT, contributing to the time dependent springback.

Acknowledgements

B.L., Z.M., S.J.H., I.A., P.T.Wang, M.F.H. gratefully thank the support form Center for Advanced Vehicular Systems, Mississippi State University.

References

[1] R.E. Reed-Hill, W.D. Robertson, Acta Met 5 (1957) 728.
[2] B.C. Wonsiewicz, W.A. Backofen, Trans AIME 239 (1967) 1422.
[3] E.W. Kelley, W.F. Hosford, Jr, Trans AIME 242 (1968) 5.
[4] S.L. Couling, J.F. Pashak, L. Sturkey, Trans ASM 51 (1959) 94-107.
[5] R.H. Wagoner, H. Lim, M.-G. Lee, Int J Plasticity 45 (2013) 3.
[6] C. Dreyer, F. Polesak, T. Shultz and S. Agnew, 2009, "Blind Study of the Effect of Processing History on the Constitutive Behavior of Alloy AZ31B", Magnesium Technology 2009, edited by E.A. Nyberg, S.R. Agnew, N.R. Neelameggham, M.O. Pekguleryuz, Proceedings of the 2009 TMS Annual Meeting and Exhibition, San Francisco, CA, February 15th - 19th 2009, pp. 491-496.
[7] J.C. Baird, B. Li, S. Yazdan Parast, S.J. Horstemeyer, L.G. Hector Jr., P.T. Wang, M.F. Horstemeyer, Scripta Mater 67 (2012) 471-474.
[8] B.L. Mordike, Mater Sci Eng A 324 (2002) 103-112.
[9] F.R.N. Nabarro, Acta Mater 54 (2006) 263.
[10] H. Gjestland, G. Nussbaum, G. Regazzoni, O. Lohne, Ø. Bauger, Mater Sci Eng A 134 (1991) 1197-1200.
[11] T. Neeraj, D.-H. Hou, G.S. Daehn, M.J. Mills, Acta Mater 48 (2000) 1225-1238.
[12] M.F. Savage, T. Neeraj, M.J. Mills, Metall Mater Trans A 33A (2002) 891.
[13] A. Ben-Artzy, L.G. Hector, Jr., P.E. Krajewski, "Strain Field Measurement during Bending of Extruded Magnesium Alloys," in Magnesium Technology 2010, edited by S.R. Agnew, N.R. Neelameggham, E.A. Nyberg, W.H. Sillekens, TMS, Warrendale, PA. pp. 69-75.
[14] M.M. Avedesian, H. Baker, Magnesium and magnesium alloys. Materials Park, OH: ASM International; 1999.
[15] S. Ankem, C.A. Greene, S. Singh, Scripta Met et Mater 30 (1994) 803-808.
[16] P.G. Oberson, S. Ankem, Int J Plasticty 25 (2009) 881-900.
[17] Z.W. Wyatt, W.J. Joost, D. Zhu, S. Ankem, Int J Plasticity 39 (2012) 119-131.
[18] B. Li, E. Ma, Phys Rev Lett 103 (2009) 035503.
[19] B.Y. Liu, Z.W. Shan, X.Y. Zhang, J. Sun, E. Ma, "In Situ Quantitative Tension and Compression Study on Twinning and Detwinning in Submicron-sized Mg Crystals inside a Transmission Electron Microscopy", TMS 2012, Orlando, USA.
[20] B.Y. Liu, B. Li, Z.W. Shan, "Twin boundary migration creating zero shear strain – in-situ transmission electron microscopy observations and atomistic simulations", TMS 2013, San Antonio, USA.
[21] L .Wu, A. Jain, D. W. Brown, G. M. Stoica, S. R. Agnew, B. Clausen, D. E. Fielden, P. K. Liaw, Acta Mater 56 (2008) 688.
[22] C. H. Caceres, T. Sumitomo, M. Veidt, Acta Mater 51 (2003) 6211.
[23] M.R. Barnett, Z. Keshavarz, A.G. Beer, X. Ma, Acta Mater 56 (2008) 5.
[24] X.Y. Zhang, B. Li, X.L. Wu, Y.T. Zhu, Q. Ma, Q. Liu, P.T. Wang and M.F. Horstemeyer, Scripta Mater 67 (2012) 862-865.
[25] B. Li, E. Ma, K. T. Ramesh, Metall Mater Trans A 39 (2008) 2607.
[26] Q. Yu, J. Zhang, Y. Jiang, Phil Mag Lett 91 (2011) 757.

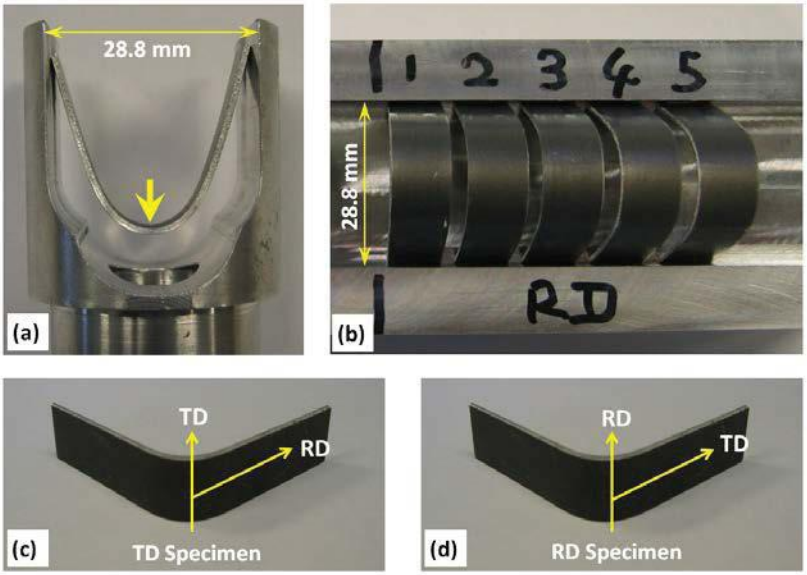


Figure 1. Experimental setup: (a) The bottom half of the three-point bending fixture in which an AZ31 sheet specimen (indicated by the block arrow) was bent into the opening. (b) The bent specimens were carefully transferred and remained in the bent state in the trough in a steel block. Every month, a specimen was taken out and the springback was measured. (c) The bend parallel to the transverse direction (TD) is designated as TD specimen. (d) The bend parallel to the rolling direction (RD) is designated as RD specimen.

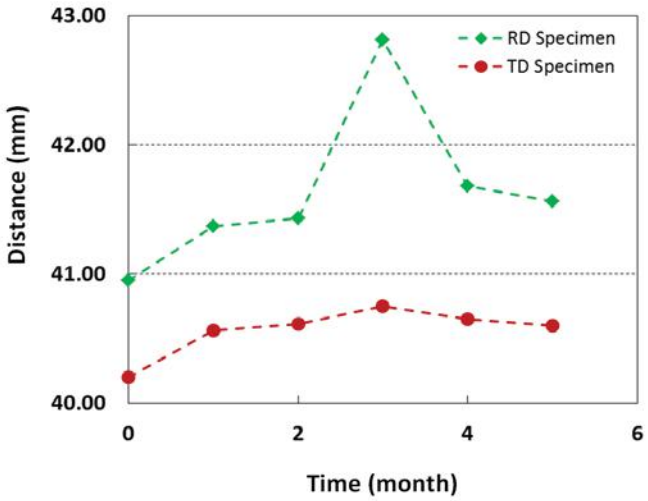


Figure 2. Time dependent springback of the baseline specimens which were retrieved immediately after bending. The distance between the two legs of the bent specimens (RD and TD) was measured in a time interval of one month. It can be seen that the springback increases with time. For the RD specimen, a conspicuous increase in springback can be observed at the third month. For both the RD and the TD specimens, the springback reaches a maximum at the third month, and then decreases.

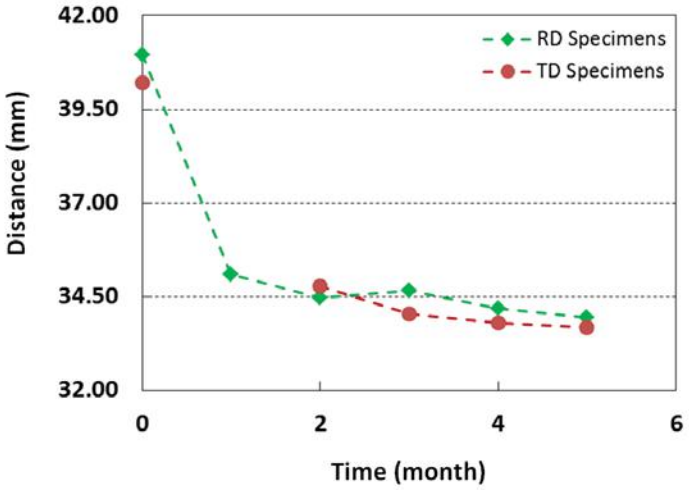


Figure 3. Time dependent springback of the specimens that were bent and held for one to five months in the trough. After held for one month, the springback decreases dramatically compared to the baseline specimens (zero holding time). The longer the specimens were held in the trough, the larger decrease in the springback. The data point for the TD specimen at the first month was not recorded due to the accidental pop-out of the specimen.

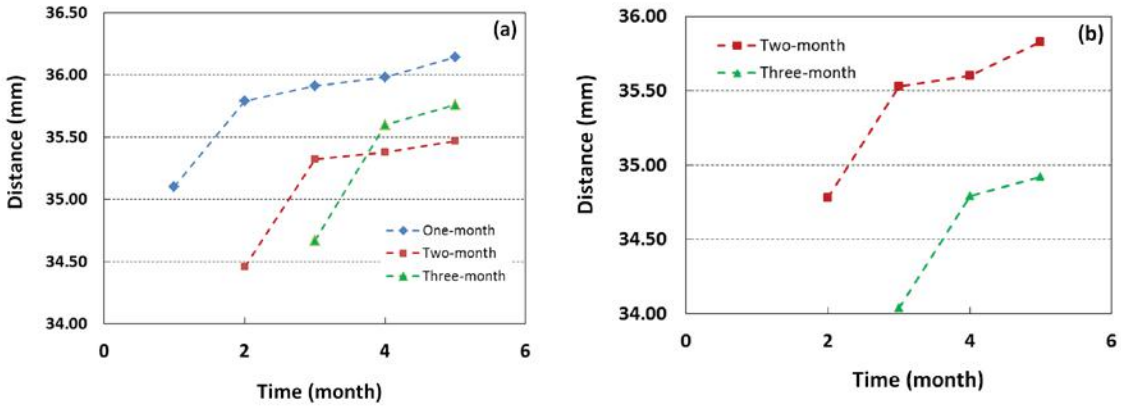


Figure 4. Time dependent springback of the RD (a) and the TD (b) specimens that were bent and held for one to three months, then the springback of individual specimens was measured every month after retrieval from the trough. For all the specimens, a sharp increase in the springback can be observed at the first month.

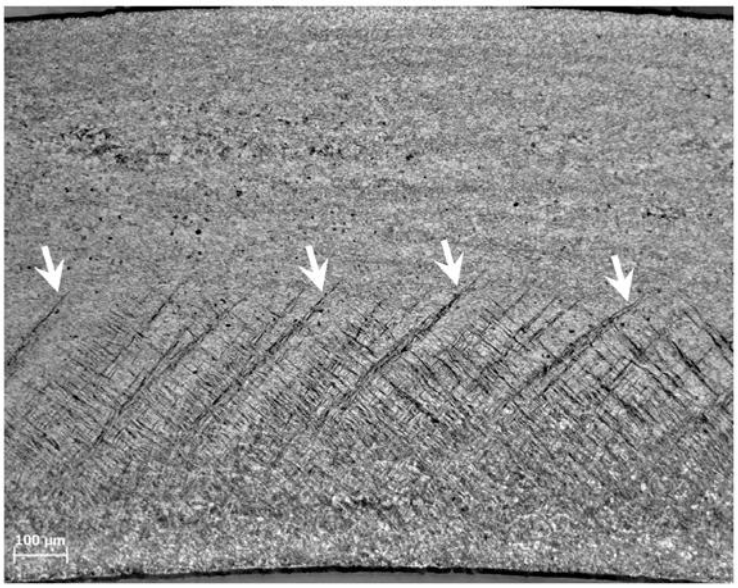


Figure 5. Optical microscopy with differential interference contrast (DIC) illumination of the RD baseline specimen that was bent, immediately released and maintained in the free state for five months. High density deformation twins in the form of localized twin bands (indicated by the arrows) were observed in the compression zone. In sharp contrast, twins can hardly be observed in the tension zone at this magnification.

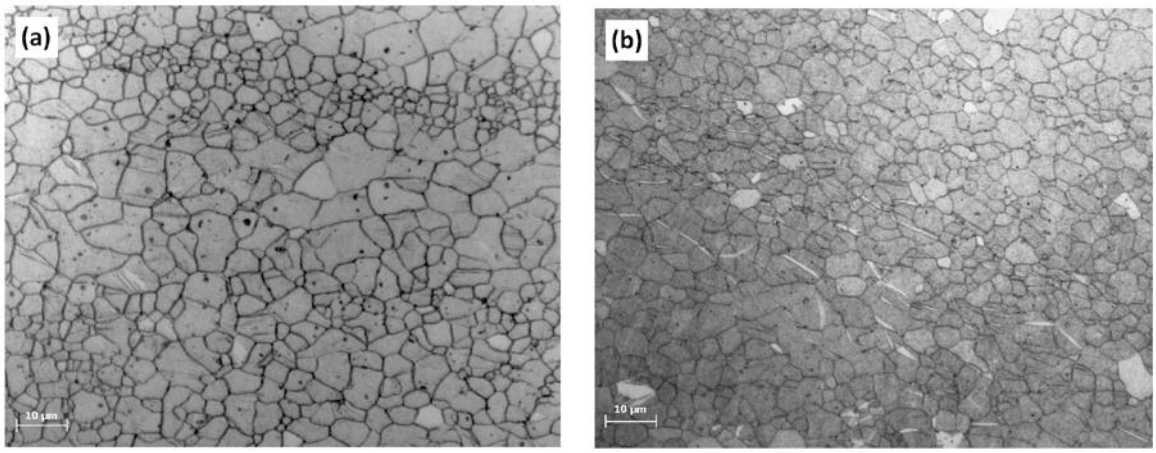


Figure 6. In the tension zone away from the localized twin bands in Figure 5, deformation twins were also observed at a high magnification. (a) The baseline RD specimen that was bent, immediately released and maintained in the free state for five months. Twins were occasionally observed in the grains; (b) An RD specimen that was bent, immediately released and mounted for optical microscopy examinations. Compared to (a), a higher density of twins can be observed, indicating that detwinning continued occurring in the baseline RD specimen while remaining in the free state.

Magnesium Technology 2014
Edited by: Martyn Alderman, Michele V. Manuel, Norbert Hort, and Neale R. Neelameggham
TMS (The Minerals, Metals & Materials Society), 2014

Precipitate Formation in Uniaxially Stressed High Pressure Die Cast Binary Mg-Nd Alloy during Creep Testing

Deep Choudhuri [1], Soumya Nag [1], Nilesh Dendge [1], Mark A Gibson [2] and Rajarshi Banerjee [1]

[1] Center for Advanced Research and Technology, Department of Materials Science and Engineering, University of North Texas, Denton, TX-76207, USA
[2] CAST CRC and CSIRO Process Science & Engineering, Private Bag 33, Clayton South MDC, Clayton, 3169 Vic., Australia

Keywords: Mg-Nd, dynamic precipitation, creep

Abstract

Role of applied stress on intragranular precipitation in Mg-Nd alloys was investigated by subjecting Mg-0.5at%Nd tensile bars to creep deformation at a nominal stress of 90 MPa and 177ºC. Prior work on creep–tested Mg-Nd studied precipitation after 100 Hrs of creep deformation [Choudhuri et.al. Metal Trans A Comm.2013, **44**, 2905]. Developing on this published work, the present investigation systematically examined precipitate formation during early (5 Hrs) to middle (100 Hrs) stages of creep. Very early stages of creep resulted in a homogeneous distribution of fine-scale β' precipitates within α-Mg matrix. Contrastingly, within similar time frame a relatively localized distribution of β_1 precipitates was noted - presumably decorating dislocation lines. Interesting, throughout the creep deformation, β_1 plates exhibited preferential alignment tendencies on a specific set of $\{10\bar{1}0\}_{Mg}$ planes / $<11\bar{2}0>_{Mg}$ directions. Such preferential alignment along favorable slip directions within the α-Mg matrix may influence the creep response of the Mg-Nd alloy.

Introduction

Due to the technological importance of Mg-RE (rare earth) based alloys [1,2], it is of interest to know the precipitation behavior during creep deformation of such alloy systems. Recent studies on binary high pressure die cast (HPDC) Mg-Nd have shown that dynamic precipitation within stressed α-Mg matrix resulted in favorable creep response [2]. Furthermore, Mg-Nd alloys serve as a good model system for well-know commercial Mg-Nd-Y systems, e.g. WE43, WE54, since they share comparable precipitation phases [3-7].

Past studies have shown that precipitation in isothermally annealed Mg-Nd occurred in the following sequence [3]: GP zones, β'' (*DO_{19}*, Mg_3Nd), β' (*orthorhombic*, Mg_7Nd), β_1 (*fcc* , Mg_3Nd), β (*tetragonal*, $Mg_{12}Nd$) and β_e (*tetragonal*, $Mg_{41}Nd_5$, equilibrium phase). In most cases the metastable phases (GP zones, β'', β' and β_1) are observed [3], while β and the more stable β_e were observed after prolonged heat treatment or aging at very high temperatures e.g. 500ºC [8]. It may be noted that the majority of the precipitation studies were performed on a solutionized microstructure – containing primarily α-Mg matrix. On the other hand, HPDC Mg-Nd microstructure contains prior of interdendritic Mg_3Nd precipitates, which surrounds α-Mg dendrites in the HPDC microstructure. [1,2,8].

Thus, the primary goal of this work is to examine the influence of applied stress on intragranular precipitate phases in HPDC Mg-0.5at%Nd alloy subjected to creep deformation. For this purpose, precipitation in crept specimens was systematically probed after 0 (initial), 5 and 100 Hrs of creep deformation.

Experimental details

Mg-0.5wt%Nd tensile dog-bone specimens, prepared using high-pressure die cast (HPDC) process, were subjected to creep at 90MPa / 177ºC (450K) till 100 Hrs Description of the HPDC process and experimental conditions for creep testing are provided elsewhere [9]. Transmission electron microscopy (TEM) was performed in conventional, high angle annular dark field scanning TEM (HAADF-STEM) and high-resolution TEM (HRTEM) modes. Atomic mass sensitive (Z - contrast) HAADF-STEM mode reveals phases with heavier element in brighter contrast [5]. TEM foils were prepared by conventional techniques [7,9], or extracting FIB (focused ion beam) lift-outs [9].

Results and discussion

Initial microstructure and Creep response

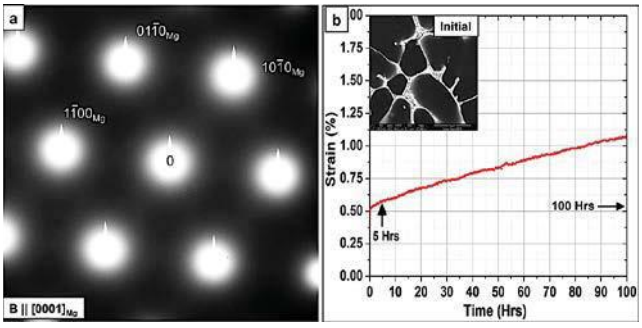


Figure 1. (a) SAD pattern recorded along $[0001]_{Mg}$ zone axis, and (b) strain vs. time plot – creep response curve. Inset in (b) shows backscattered SEM image showing interdendritic precipitates and α-Mg matrix in brighter and darker contrast respectively.

Precipitation in the initial HPDC microstructure was examined with $[0001]_{Mg}$ selected area diffraction (SAD) pattern (Figure 1(a)), which was recorded from the α-Mg matrix near the larger interdendritic precipitates (inset Figure 1(b), in brighter contrast). In the SAD, the absence extra precipitate reflections between the primary Mg reflections (e.g. from $\{1\bar{1}00\}_{Mg}$ planes) indicated that the α-Mg matrix is free of precipitation. Figure 1(b) shows strain vs. time plot obtained from uniaxially loading Mg-Nd specimen a 90MPa at 177ºC (or 90MPa / 177ºC). A parallel analysis of the plot suggested that that majority of the creep response curve (Figure 1(b)) suggest steady state creep

deformation. The next few section will present results, depicting β' and β_1 precipitation after 5 and 100 Hrs of creep deformation.

β' (*orthorhombic*) precipitation

Precipitation of β' phase after 5 Hrs of creep is presented in Figure 2. $[0001]_{Mg}$ SAD pattern show reciprocal lattice streaks passing through $½\{1100\}_{Mg}$ and $½\{1120\}_{Mg}$ locations in Figure 2(a) are consistent with the presence of β' [9]. Since, dark-field imaging using these reciprocal lattice streaks did not reveal any prominent diffraction contrast features, the atomic mass contrast (commonly referred to as Z-contrast) revealed by high angle annular dark field – scanning TEM (or HAADF-STEM) imaging, with the beam approximately parallel to $[0001]_{Mg}$, was employed to clearly reveal the precipitates in Figures 2(b). The HAADF-STEM image show the β' precipitates as thread-like fragments dispersed homogeneously throughout the matrix. Background corrected HRTEM image (along $[0001]_{Mg}$ zone axis) from one β' precipitate is shown in Figure 2(c). The corresponding Fourier transform diffraction pattern, indexed with β' and Mg reflections, is depicted in Figure 2(d). Together, Figure 2(a) and 2(d) confirm the presence of β' precipitate phase: orthorhombic structure, a = 0.64nm, b = 1.11nm and c = 0.54nm, and previously established orientation relationship (OR) between α-Mg and β' [3]: $[100]\beta' \parallel [11\bar{2}0]_{Mg}$, $[010]\beta' \parallel [\bar{1}100]_{Mg}$, and $(001)\beta' \parallel (0001)_{Mg}$. A (001)β' motif is also indicated in the HRTEM image in Figure 2(c). Thus, compared to the initial α-Mg microstructure (Figure 1(a)), creep deformation (at 90MPa / 177ºC) results in the formation of β' phase just after 5 Hrs.

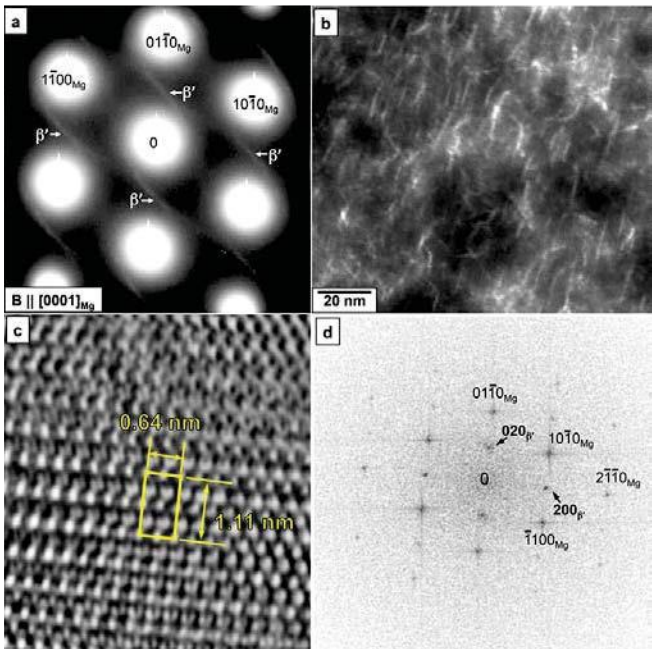


Figure 2. β' precipitation after 5Hrs of creep :(a) $[0001]_{Mg}$ SAD showing reciprocal lattice streaking, (b) HAADF-STEM image showing β' precipitates, (c) HRTEM image from a region containing β' precipitate, and (d) corresponding FFT showing diffraction pattern from the HRTEM image

After 100 Hrs, β' precipitates had coarsened (Figure 3(a)) into prominent lenticular morphology. Evidence of β' is presented via $[0001]_{Mg}$ SAD pattern, which shows β' precipitate reflections at $½\{1100\}_{Mg}$ and $½\{1120\}_{Mg}$ locations (Figure 3(b)). A careful examination of the SAD pattern indicated that intensity from one particular variant of β' (V1) is relatively more than the others. An intensity line profile measurement (Figure 3(c)) from the three $½\{1100\}_{Mg}$ locations corresponding to all β' reflections (from all the detected variants) further indicate that V1 has a higher intensity than V2 and V3. A higher intensity is typically associated with a greater volume fraction of a phase. Thus the intensity profile measurements (Figure 3(c)) suggest that application of stress favors the nucleation of limited number of β' variants resulting in a higher volume fraction of the favored β' variants. Further evidence of preferential β' variant formation, under applied stress, is revealed by the 5 Hrs results presented in Figure 2(a), where the SAD pattern (Figure 2(a)) shows reflections corresponding to only one variant. Further investigation regarding this issue is under progress.

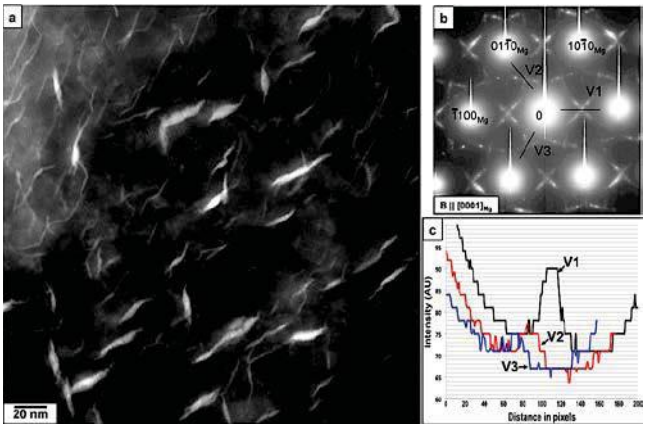


Figure 3. β' precipitation after 100Hrs of creep : (a) HAADF-STEM image showing lenticular β' precipitates, (b) $[0001]_{Mg}$ SAD pattern showing reflections from reflections from different variants of β' precipitates in (a), (c) intensity v.s. pixel plots obtained from three $½\ 1\bar{1}00\}_{Mg}$ locations on the $[0001]_{Mg}$ SAD show that intensity from one variant is greater than others.

β_1 (*fcc*, $Fm\bar{3}m$) precipitation

Observation of β_1 phase (*fcc*, a = 0.73nm) precipitates during creep deformation is summarized in Figure 4. HAADF-STEM image presented in Figure 4(a) shows β_1 precipitation (white arrow main figure) after 5 Hrs of creep. Note that the α-Mg matrix also contains a homogeneous distribution of finer β' precipitates (black arrow, Figure 4(a)). A notable difference with β' is that β_1 precipitates have a relatively more localized distribution with a-Mg matrix than β'.

A closer inspection of the β_1 precipitates (inset in Figure 4(a)) indicated that the β_1 plates were preferentially oriented along a particular crystallographic α-Mg direction. Figure 4(a) show that although the β_1 plates exhibit preferential alignment, but such plates are organized along curved trajectories – presumably prior dislocations lines resulting from the HPDC process. Discussion regarding the formation of β_1 in crept microstructure will be delayed till a latter section. Nonetheless, β_1 precipitates shown in Figure 4(a) point towards the early stage of precipitate formation on dislocation lines.

After 100 Hrs of creep the β_1 plates had coarsened (bright field (BF) image, Figure 4(b)), which permitted

identification though electron diffraction (Figure 4(c)). A $[0001]_{Mg}$ SAD pattern from the same region (as the BF image in Figure 4(b)) showed precipitate β_1 (*fcc*, a = 0.73nm) and β' reflections. For clarity, the precipitate reflections, along with primary Mg reflections, are shown in Figure 4(d). The SAD pattern further confirms the published OR between α-Mg and β_1 [3,4] : (110)β1 ‖ $(0001)_{Mg}$ and $[\bar{1}1\bar{1}]\,\beta1$ ‖ $[2\bar{1}\bar{1}0]_{Mg}$. The BF image obtained close to $[0001]_{Mg}$ zone axis (Figure 4(b)) indicated that the β_1 plates appears to largely lie preferentially on a specific set of $\{10\bar{1}0\}_{Mg}$ planes / $<11\bar{2}0>_{Mg}$ directions. Inset in Figure 4(b) further highlights preferential orientation/alignment of β_1 plates. Such preferential alignment tendencies, especially at the middle stages of creep deformation, were previously observed in creep-tested HPDC Mg-Nd alloy [9]. Moreover, the β_1 plates after 100Hrs lie lay on curved trajectories (Figure 4(b)), while , simultaneously, exhibiting preferential alignment; a consistent trend observed from 5 Hrs creep results.

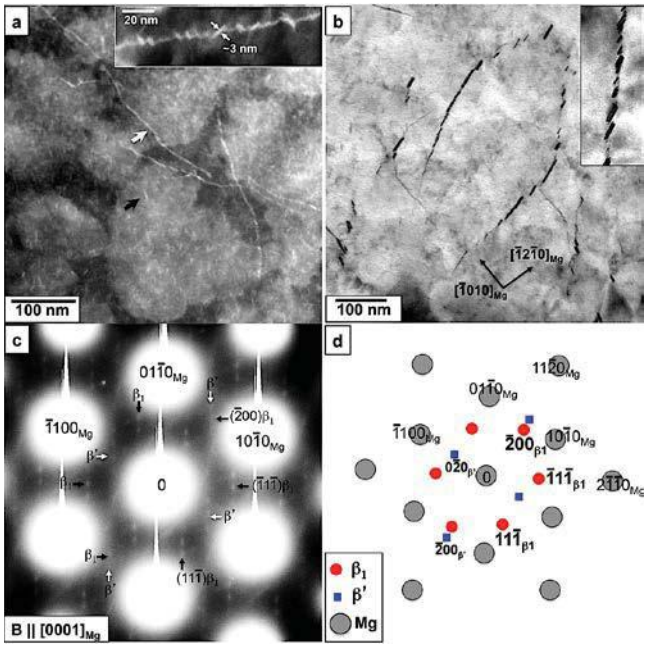


Figure 4. (a) HAADF-STEM image showing β_1 precipitation after 5 Hrs of creep ay 90MPa / 177ºC, while the inset shows a high magnification image of preferentially aligned β_1 plates. White arrow indicates β1, while black shows finer scale β'. After 100 Hrs of creep (b) bright field TEM image shows coarsened β_1 plates, and the inset depict the preferentially aligned β_1 plates, (c) $[0001]_{Mg}$ SAD pattern indexed with β_1 and β' precipitate reflections and primary Mg reflections, and (d) schematically showing the same SAD in (c).

Creep deformation of Mg-alloys results from dislocation movement, specifically dislocation climb [2, 10]. Recently Zhu etl.al. suggested that dislocation climb governs the deformation behavior of HPDC Mg-0.5at%Nd alloy at 90MPa / 177ºC [2]. Therefore, it appears that dislocation generated during creep may have intersected the prior dislocation that had formed due to the HPDC process. During creep deformation, β_1 precipitates could have dynamically nucleated at such intersection points which may have results in the β_1 arrangement distinctly observed after 100 Hrs of creep. It should also be pointed out that, $(0001)<11\bar{2}0>_{Mg}$ is the primary slip system in Mg [10], therefore alignment of β_1 along $<11\bar{2}0>_{Mg}$ may affect dislocation motion along that direction, thus influencing the mechanical response (e.g. creep) of these Mg-Nd alloys.

Summary

Effect of externally applied stress on precipitation in Md-Nd alloys was investigated by subjecting Mg-0.5at%Nd tensile bars to creep deformation at 90MPa / 177ºC. Applied stress appeared to promote an initial (after 5 Hrs) homogeneous distribution of β' (*orthorhombic*, a = 0.64nm, b = 1.11nm and c = 0.54nm) precipitates within α-Mg matrix. On the other hand, β_1 (*fcc*, a = 0.73nm) have a more localized distribution, and, throughout creep deformation, β_1 plates exhibited preferential alignment tendencies on a specific set of $\{10\bar{1}0\}_{Mg}$ planes / $<11\bar{2}0>_{Mg}$ directions.

Acknowledgements

The authors gratefully acknowledge the Center for Advanced Research and Technology (CART) at the University of North Texas. CAST Cooperative Research Centre (CAST CRC) was established under, and is supported in part by, the Australian Government's Cooperative Research Centres scheme. MAG would like to acknowledge the technical assistance of Mrs. M. Gershenzon and Mr. A. Yob in the HPDC of the samples used in this work.

References

1. T.L. Chia, M.A. Easton, S.M.Zhu M.A. Gibson, N. Birbilis and J.F. Nie : Intermetallics, 2009, vol 17, pp. 481-490
2. S. M. Zhu, M.A. Gibson , M.A. Easton and J.F. Nie : Scripta Mater, 2010, vol. 63, pp.698-703
3. K. Saito and K. Hiraga: Mater trans, 2011, vol. 52, pp. 1860-1867
4. J.F. Nie and B.C. Muddle : Acta. Mater. , 2000, vol. 48, pp. 1691-1703
5. J.F. Nie : Metal Mater Trans A. 2012, vol. 43 pp. 3891
6. Mengucci P, Barucca G, Riontiono G, Lussana D, Nassazza M, Ferragut R, Aly EH. Mater Sci Eng A 2008; 479: 37
7. Choudhuri D, Meher S, Nag S, Dendge N, Hwang JY, Banerjee R. Philos Mag Lett 2013; 93: 395
8. Easton MA, Gibson MA, Qiu D, Zhu SM, Grobner J, Schmid-Fetzer R, Nie JF , Zhang MX. Acta Mater 2012;60: 4420
9. D. Choudhuri, N. Dendge, S. Nag, M.A. Gibson and R. Banerjee: Metal Mater Trans A Comm. 2013, vol. 44, pp. 2905
10. M. Celiki and M. Pekguleryuz: Mater Sci Engg A, 2012, vol. 556, pp.911-920

Magnesium Technology 2014
Edited by: Martyn Alderman, Michele V. Manuel, Norbert Hort, and Neale R. Neelameggham
TMS (The Minerals, Metals & Materials Society), 2014

A REVIEW OF THE INFLUENCE OF PRODUCTION METHODS AND INTERMETALLIC PHASES ON THE CREEP PROPERTIES OF AZ91

Peiman Shahbeigi Roodposhti[1], Apu Sarkar[2], Korukonda Linga Murty[2]
[1]Mater. Sci. Eng. Department; 911 Partner Way, 3035 EB1, Raleigh, NC 27606-7907 USA
[2]Nuclear Engineering Department; 2500 Stinson Drive, 3143 Burlington Engineering Labs, Raleigh, NC 27606-7909 USA

Keywords: Creep, Magnesium, AZ91, Die cast, Mild steel cast, Thixoform, intermetallic phases

Abstract

A review on the creep properties of AZ91 magnesium alloys is presented with a major emphasis on the influence of production methods that include steel mold casting, die casting and Thixoforming. Various creep characteristics such as the stress exponent and activation energy along with their resistance to creep for the alloys produced via different methods are compared. Role of intermetallic phases resulting from various alloying additions such as Si, Sb, Bi, Ca and rare earth elements on different creep mechanisms (grain boundary sliding and dislocation glide/climb) are also evaluated.

Introduction

Magnesium (Mg) and magnesium alloys are used in a wide variety of structural applications including automotive, aerospace, materials-handling, telecommunication and portable microelectronics industries due to their light weight, high specific strength, acceptable corrosion resistance, good ductility and cast-ability [1-4]. Over the years many Mg alloys have been developed to achieve better performance. Al, Zn and Mn are the primary alloying elements in commercial Mg alloys with AZ and AM series (containing Al, Zn and Al, Mn respectively) being commonly used in automobile industries. AZ91, AM60, AM50 and AM20 are the most popular Mg alloys containing 9%, 6%, 5% and 2% of Al respectively. These alloys exhibit relatively good performance in die cast-ability. Depending upon their concentration and temperature, the alloying elements are present in solid solution or form different intermetallic phases in Mg alloys. Intermetallic phases present in these alloys play important role in determining their physical and mechanical properties. $Mg_{17}Al_{12}$ is the most commonly observed equilibrium intermetallic phase (β phase) in these alloys while other phases such as $Mg_{17}Al_{12}Zn_{0.5}$ have been reported to form in Zn-containing Mg-Al alloys [5] and these intermetallic phases improve room temperature mechanical properties due to their higher strength. However, temperature stability of these phases is poor. They have low melting point and soften beyond 150°C [6, 7]. This leads to a serious limitation on high temperature applications of Mg alloys.

AZ91 is one of the most successfully used commercial Magnesium alloys in automobile industries [8, 9] and contains 9Al–1Zn with a small quantity of Mn. Since this alloy and its predominant intermetallic phase ($Mg_{17}Al_{12}$) have relatively low melting point (~ 600°C and ~ 450°C respectively) creep is one of the main degradation mechanisms at engineering applications. Creep behavior of AZ91 has been extensively studied over the years that revealed significant effect of the manufacturing process. Addition of different elements including some rare earths modifies the microstructure of AZ91 alloy and improves high temperature mechanical properties [3, 4, 9-11].

The aim of this study is to review results from the literature and analyze them in the light of existing creep theories to develop a unified comprehensive understanding of creep behavior of AZ91 alloy. A brief outline of general microstructural features is presented before describing the effects of manufacturing and alloying elements on creep characteristics.

Microstructure of AZ91

Microstructure of AZ91 contains eutectic hcp α phase of Mg [12] with discontinuous intermetallic $Mg_{17}Al_{12}$ precipitates (β phase). β precipitates are distributed either (i) along the grain boundaries mainly transformed from the supersaturated liquid phase at final solidification state or (ii) inside the grains formed by secondary and higher order branching [13]. Although β phase can increase the hardness, yield stress and UTS of AZ91 alloys, a continuous network along the grain boundaries can cause inter-granular fracture [6] and decrease the ductility [3]. Moreover, it is thermally unstable and dissolves in the matrix at high temperatures thereby becoming relatively soft.

Effect of Production Method on the Creep Resistance of AZ91

Various production methods have been developed to manufacture Mg alloys for industrial applications. High pressure die casting, mild steel casting and Thixoforming are most popular production methods used to produce AZ91. These production routes have extensive influence on the final microstructure of the alloy. Grain size of primary α phase, amount of Al in solid solution and volume fraction and distribution of β phase [14] which govern the creep properties of Mg alloys are influenced by the production method. Owing to the importance of creep resistance of Mg alloys in engineering applications, creep experiments have been conducted on various AZ91 alloys produced via different processing routes.

Steady-state Creep of Die Cast AZ91

Figure 1 depicts the minimum creep-rate results [3, 15, 16] on die cast AZ91 alloy in the temperature range of 70 °C to 180 °C. These results when plotted in terms of normalized strain-rate $(\dot{\varepsilon}/D)$ versus normalized stress (σ/G) as in Figure **2** reveal power-law dependence at lower stresses with exponential variation at higher ($>10^{-2}$G) stresses.

Here, the temperature variation of shear modulus (G) and diffusivity D are given by,

$$G\ (\text{MPa}) = 18{,}460 - 8.2T \text{ with T in K [17]} \quad (1)$$

$$D\ (m^2/s) = D_o e^{-Q/RT}, \text{ with } D_o = 1\times10^{-4}\ m^2/s \text{ and } Q = 135\ \text{kJ/mole [15]} \quad (2)$$

where R is gas constant and Q is lattice diffusion activation energy.

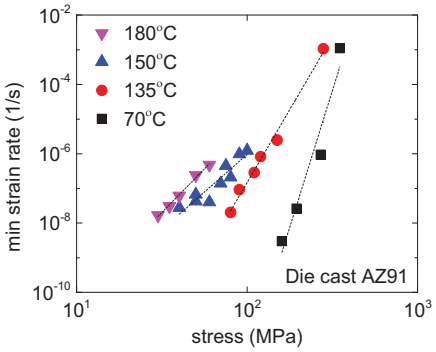


Figure 1. Log-log plot of minimum strain rate vs. stress obtained from creep tests on die cast AZ91 alloy at different temperature and stress ranges [3, 15, 16]

A stress exponent of 5.5 with power-law breakdown at higher stresses along with the activation energy equivalent to that for self-diffusion clearly indicate the underlying creep mechanism to be dislocation-based similar to those observed in pure metals and class-M alloys.

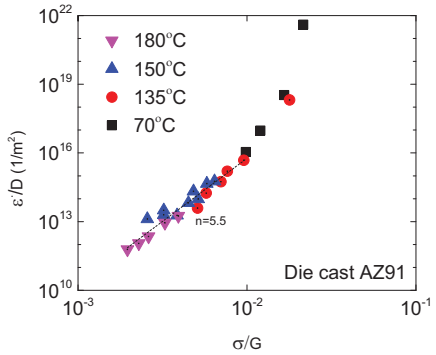


Figure 2. Creep data for die cast AZ91 [3, 15, 16]

Steady-state Creep of Mild Steel Casting AZ91

Using a permanent mold of mild steel is a conventional route for casting AZ91 alloy. In Mild casting method, the primary ingot is melted in a mild steel crucible under protection of CO_2 and/or SF_6 environment. Melted ingot is poured to a preheated permanent mold after reaching the temperature above 700 ℃. Most of the creep studies carried out on mild steel casted AZ91 alloys used materials produced via similar method. Samples were given T4 and T6 heat treatments prior to the creep tests.T4 heat treatment dissolves the β phase into the matrix and T6 heat treatment forms discontinuous stable β precipitates in lamellar form at grain boundaries and continuous plates like precipitates within the grains [10, 18]. Figure 3 shows the $(\dot{\varepsilon}/D)$ vs. (σ/G) plot for mild steel casted AZ91 alloy obtained from the creep tests conducted at temperature range of 150-200 °C [8, 10, 18-20].
Data plotted in Figure 3 are fitted with straight line to find the value of *n*. It can be seen that there is a transition in the value of *n* from 1.6 at low stress regime to 8.5 at high stress regime. This typically is indicative of change in creep mechanism in the alloy with increasing temperature or decreasing stress. *n* = 1.6 usually corresponds to diffusion controlled creep mechanism like grain boundary sliding. This mechanism plays significant role in creep mechanism at elevated temperature. Whereas n = 8.5 at higher stress regime is suggestive of dislocation based mechanism as underlying creep mechanism.

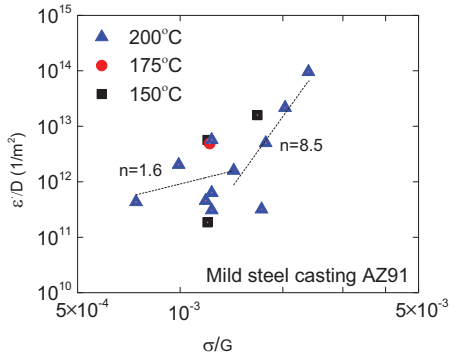
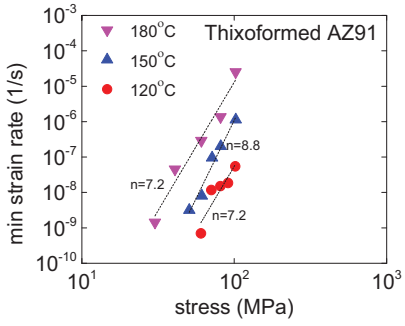


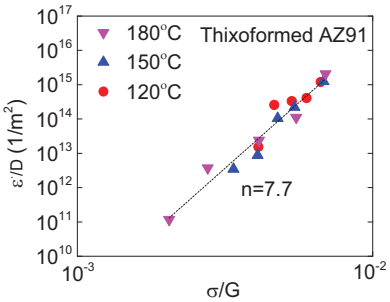
Figure 3. Creep results for mild steel cast AZ91 [8, 10, 18-20]

Steady-state Creep of Thixoform Casting AZ91

Thixoforming is a relatively new method of producing Mg alloys for automobile industry [21]. It is categorized as a semi-solid method of producing metals which contain characteristics of both casting and forging. In this process a preheated semi-solid metal (slug) is squeezed into the die cavity from a narrow hole in the upper or lower die [22, 23]. Figure 4a summarizes stress dependence of minimum creep-rate at different temperatures and depict power-law dependence with a stress exponent of around 8. These data at varied temperatures coalesce into a single line when plotted in terms of normalized parameters (Figure 4b) with an activation energy of 138 kJ/mole indicative of dislocation dominant creep mechanism. Spigarelli et al. [1] analyzed the similar data using Sinh function with stress exponent of 5.



(a)



(b)

Figure 4. (a) Creep data for Thixoformed AZ91 alloy
(b) Normalized Creep results for Thixoformed AZ91 alloy [1]

Effect of Intermetallic Phases on Creep Behavior of AZ91

As mentioned earlier most of the magnesium alloys contain some intermetallic phases which are harder than the matrix and play an important role in determining their creep behavior. Due to low thermal stability of the $Mg_{17}Al_{12}$ phase, several researches have been carried out to form new thermally stable intermetallic phases in Mg alloys by adding different alloying elements. These stable precipitates can act as obstacles against grain boundary movement and enhance creep resistance of Mg alloys at relatively higher temperatures. However, at high enough temperatures, close to melting point these phases dissolve in the matrix and facilitate grain boundary movement leading to grain boundary sliding to be the dominant creep mechanism at lower stresses [24]. Effect of various intermetallic phases on creep resistance of AZ91 alloys is summarized in this section following a brief description of the microstructures.

Silicon (Si), Antimony (Sb) and Bismuth (Bi) additions

Additions of Si, Sb and Bi in AZ91 are found to form fine Mg_2Si, Mg_3Sb_2 and Mg_3Bi_2 intermetallic phases respectively [18, 25]. These phases have comparatively better thermal stability and can act as barriers to grain boundary sliding at elevated temperatures. Addition of Bi combined with Sb has also been found to improve the creep resistance in AZ91. This combination produces thermally stable rod shaped Mg_3Bi_2 precipitates and also refines the β phase in the matrix [20]. Figure 5 shows various intermetallic phases present in AZ91 with different alloying elements. Microstructure of as cast AZ91 alloy (Figure 5a) contains α-Mg matrix, eutectic lamellar of α+β and massive β intermetallic phases. Addition of 0.5%Sb to the primary AZ91 alloy produces needle shaped Mg_3Sb_2 inter-metallic phase at grain boundaries (Figure 5b). Microstructure of an AZ91 alloy with 0.5% Si as shown in Figure 5c reveals a so called "Chinese script" phase of Mg_2Si at the grain boundaries. Addition of 0.2% Sb changes the shape of the intermetallic phase as depicted in Figure 5d for an AZ91 alloy with 0.5%Si+0.2%Sb containing polygonal shaped Mg_2Si precipitates [3, 6, 25, 26]. Si does not form any compound with Al and also has low solubility in Mg. Thus increasing amounts of Si only increase the size and amount of Mg_2Si precipitates with no influence on the content of the β phase [9]. On the contrary, some other alloying elements simultaneously change the amount of β phase in the microstructure [9, 27]. Addition of 2%Bi not only makes the β phase finer but also produces some rod shaped Mg_3Bi_2 precipitates (Figure 5e). Figure 5f shows microstructure of AZ91 alloy with 0.4%Sb which is similar to that of the previous one with 0.2% Bi with rod shaped Mg_3Sb_2 precipitates [19, 20, 25] while the effect of 0.1%Bi and 0.4%Sb addition on the microstructure of AZ91 alloy is seen in Figure 5g.

Figure **6** depicts the influence of various amounts of Si, Sb and Bi on the steady-state creep-rate of AZ91 alloys at 200°C and 50 MPa. It is clearly evident that the addition of these elements improves the creep resistance due essentially to the presence of different intermetallic phases. Meshinchi Asl et al. [9] reported the effect of Si on the creep resistance of the alloy as summarized in Figure 6b and the creep rate decreases with increasing Si content. Thus it can be concluded from Figure **5**c that, although increase of Si content has no effect on the amount of β phase, it increases the content of the "Chinese Script" leading to a brittle microstructure with increased creep resistance [9, 25]. Figure **6**d shows the effect of Sb on the creep behavior of AZ91 alloy and we note that Sb like other elements increases the creep resistance of AZ91 alloy. It is interesting to note that Gyangyin et al. [20] obtained a Q value of ~130kJ/mole close to that for self-diffusion in Mg[28] with a stress exponent varying from 4.2 to 5 indicating that creep in these alloys is controlled by the climb of edge dislocations as shown in Figure 7 which clearly reveals the beneficial effects of alloying.

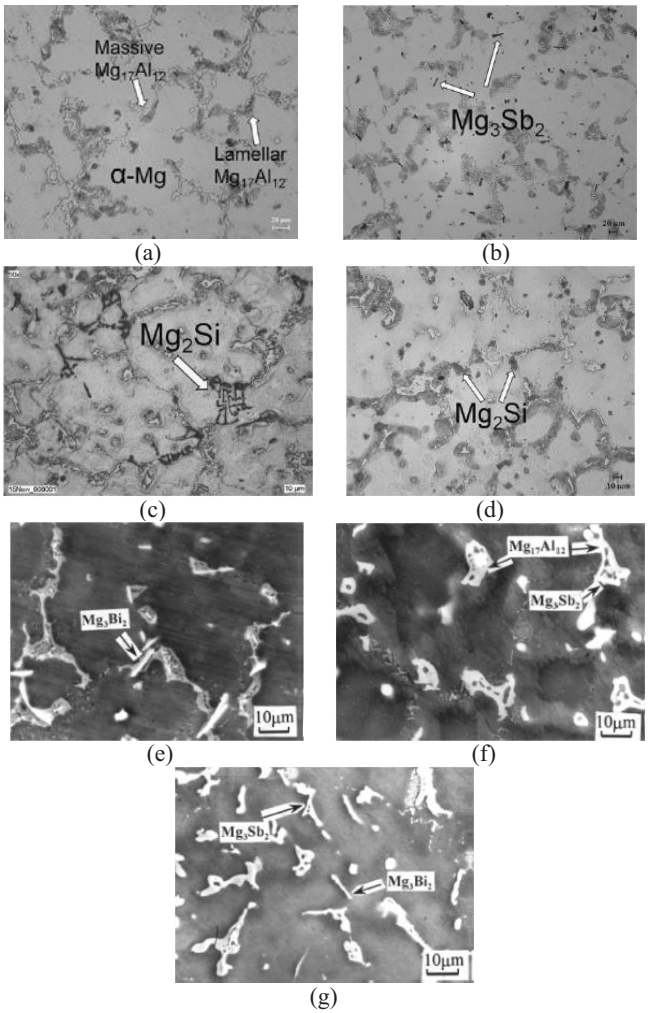


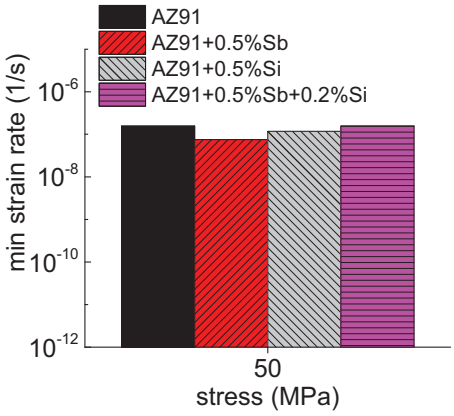
Figure 5. Micrographs of as cast AZ91 depicting different intermetallic phases produced by addition of Si and Sb. (a) AZ91, (b) AZ91+0.5%Sb, (c) AZ91+0.5%Si, (d) AZ91+0.5%Si+0.2%Sb (e) AZ91+2%Bi (f) AZ91+0.4%Sb and (g) AZ91+1%Bi+0.4%Sb. a-d from Srinivasan et al. [25] and e-g from Guangyn et al. [20]

Effect of addition of Rare Earth Elements

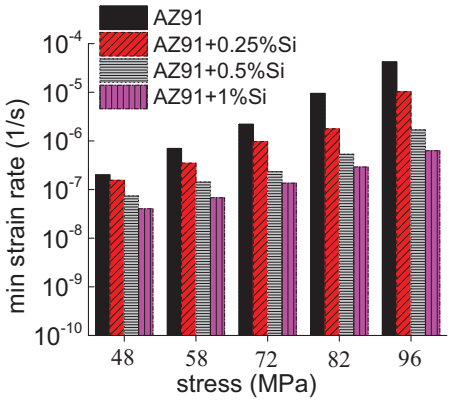
Creep property of Mg alloys has been found to be significantly improved by addition of different rare earth (RE) elements [9, 10]. Addition of different amount of REs forms thermally stable needle shaped $Al_{11}RE_3$ precipitates (Figure 8a). These intermetallic phases remain in the microstructure even after solution treatment at 400 °C for 24 hours, whereas the β phase dissolves in the matrix due to its lower melting point as revealed in Figure 8b [10]. Improvement in creep resistance at 200 °C due to RE additions is noted in Figure 9[10].

Addition of REs +Ca

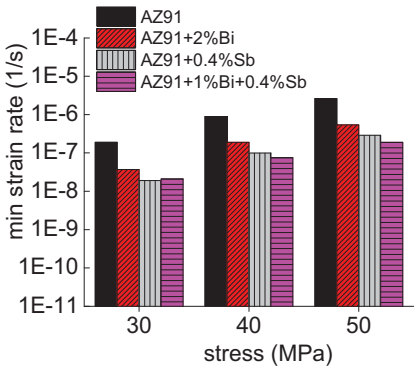
Addition of Ca has also been found to have significant effect on the creep behavior of Mg alloys. Unlike most of the other alloying elements, addition of Ca to AZ91 alloys does not produce any new precipitates. It enhances the thermal stability of β phase and makes them finer and consequently increases the creep resistance [8, 29]. Wenwen et al. [8] investigated the effect of addition of different amount of Ca and REs (Lanthanum-rich misch metal) on AZ91 alloys. Figure 10 shows the microstructure of these samples after T6 heat-treatment and needle shaped $Al_{11}La_3$ phase is noted which enhances creep resistance. The creep resistance of these alloys with/without T6 treatment is shown in Figure 11. AZ91+0.3%Ca+3.0%RE alloy shows best creep resistance property with a minimum creep rate of one order of magnitude less than other AZ91 alloys.



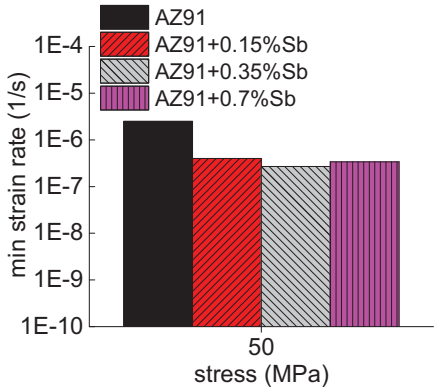
(a)



(b)



(c)



(d)

Figure 6. Effect of (a) Sb and Si [25] (b) Si [9](c) Sb and Bi [20] (d) Sb [19]on creep of AZ91 alloy

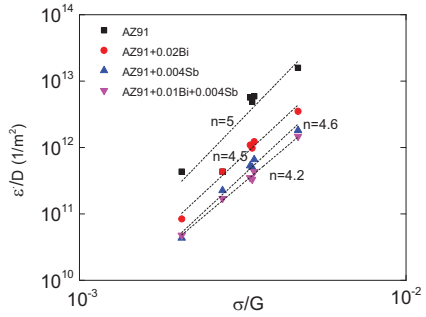


Figure 7. Normalized creep rate versus stress for AZ91 alloy depicting the effect of alloying elements [20]

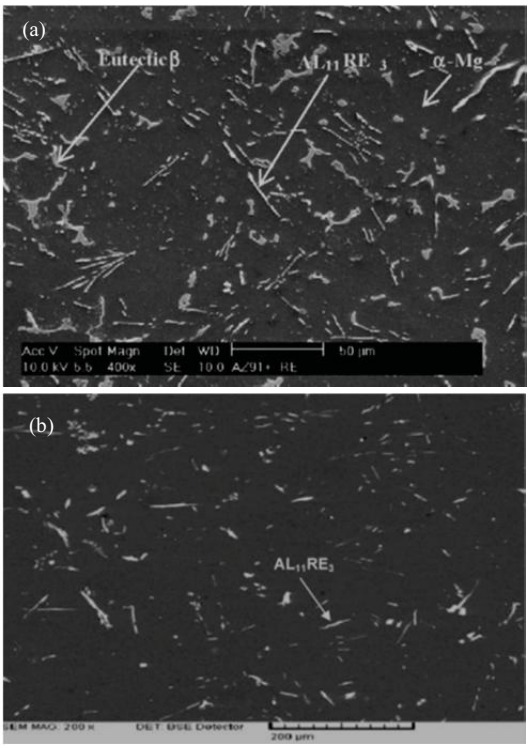


Figure 8. Microstructure of AZ91+2% RE alloy (a) before solution treatment [9] and (b) after solution treatment [10]

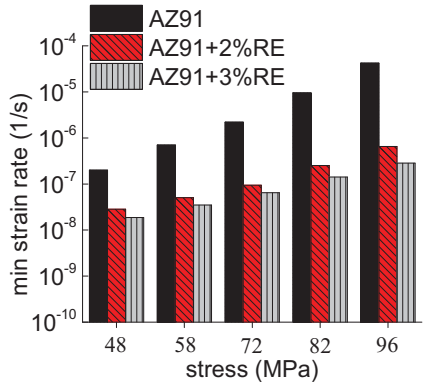


Figure 9. Comparison of creep properties of AZ91 alloy with different amounts of RE elements[10]

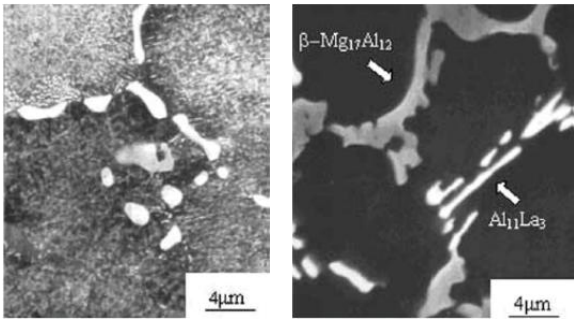


Figure 10. Microstructures of different alloys after T6 treatment - AZ91+0.3%Ca (left) and AZ91+0.3%Ca+0.3%RE (right) [8]

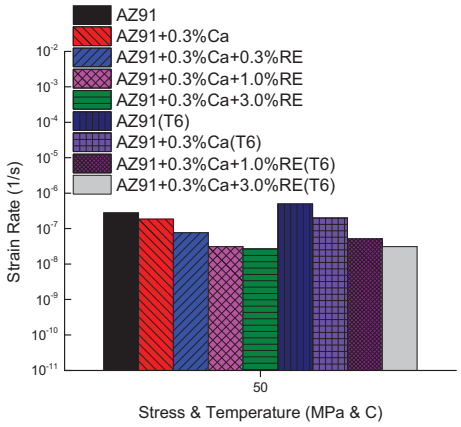


Figure 11. A comparison of the creep resistance properties of different AZ91 alloy with different amounts of Ca and RE [8]

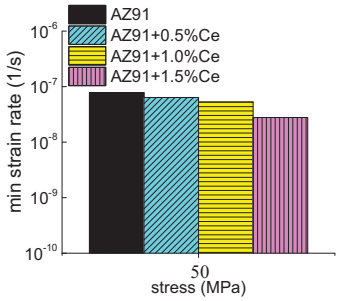


Figure 12. Minimum creep rates of AZ91 with different amount of Ce[30].

Ineffective REs

Although there are many reports on the obvious effect of addition of some REs on the improvement of creep resistance of AZ91 alloy [8-10], some RE elements, like Ce, have small or no influence on creep properties [30]. Figure 12 shows a comparison between the creep resistances of AZ91 alloy with different amounts of Ce. Steady state creep rates of these alloys indicate that addition of Ce in the AZ91 alloy has insignificant effect on the creep properties of the AZ91 alloy. This is attributed to the facts that (i) the $Al_{11}Ce_3$ precipitates decrease the grain size enhancing grain boundary sliding and (ii) although $Al_{11}Ce_3$ is a thermally stable precipitate, it will change during creep tests from a needle shape to granular shape, leading to poor creep resistance [30].

Conclusions

Creep behavior of AZ91 alloy produced via three different methods of Die casting, Mild steel casting and Thixoforming is reviewed. Analyses revealed that high temperature creep mechanism of the alloys produced using different methods is essentially similar. Grain boundary sliding at low stresses and dislocation climb at higher stresses are the underlying creep mechanism for this alloy. Various alloying elements improve creep property of AZ91 alloy by introducing new thermally stable precipitates and correlations between microstructures and creep resistance are summarized. While most of the rare earth elements improve creep resistance of AZ91 alloy, Ce has been noted to be detrimental.

Acknowledgements

This work is supported by financial support by National Science Foundation through Grant DMR-0968825.

References

1. Spigarelli, S., et al., *Analysis of the creep behaviour of a thixoformed AZ91 magnesium alloy.* Materials Science and Engineering: A, 2000. 289(1–2): p. 172-181.

2. Mordike, B.L. and T. Ebert, *Magnesium: Properties — applications — potential.* Materials Science and Engineering: A, 2001. 302(1): p. 37-45.

3. Kang, D.H., S.S. Park, and N.J. Kim, *Development of creep resistant die cast Mg–Sn–Al–Si alloy.* Materials Science and Engineering: A, 2005. 413–414(0): p. 555-560.

4. Blum, W., et al., *Comparative study of creep of the die-cast Mg-alloys AZ91, AS21, AS41, AM60 and AE42.* Materials Science and Engineering: A, 2001. 319–321(0): p. 735-740.

5. *Magnesium Alloys- Design, Processing and Properties*. 2011: Intech.

6. Kim, B.H., et al., *The microstructure, tensile properties, and creep behavior of AZ91, AS52 and TAS652 alloy.* Journal of Alloys and Compounds, 2010. 493(1–2): p. 502-506.

7. Zhang, P., *Creep behavior of the die-cast Mg–Al alloy AS21.* Scripta Materialia, 2005. 52(4): p. 277-282.

8. Wenwen, D., et al., *Microstructure and mechanical properties of Mg–Al based alloy with calcium and rare earth additions.* Materials Science and Engineering: A, 2003. 356(1–2): p. 1-7.

9. Meshinchi Asl, K., A. Tari, and F. Khomamizadeh, *The effect of different content of Al, RE and Si element on the microstructure, mechanical and creep properties of Mg–Al alloys.* Materials Science and Engineering: A, 2009. 523(1–2): p. 1-6.

10. Meshinchi Asl, K., A. Masoudi, and F. Khomamizadeh, *The effect of different rare earth elements content on microstructure, mechanical and wear behavior of Mg–Al–Zn alloy.* Materials Science and Engineering: A, 2010. 527(7–8): p. 2027-2035.

11. Amir Esgandari, B., et al., *The effect of Ca and RE elements on the precipitation kinetics of Mg17Al12 phase during artificial aging of magnesium alloy AZ91.* Materials Science and Engineering: A, 2011. 528(15): p. 5018-5024.

12. Dahle, A.K., et al., *Development of the as-cast microstructure in magnesium–aluminium alloys.* Journal of Light Metals, 2001. 1(1): p. 61-72.

13. Choong Do Lee, K.S.S., *Effect of precipitate and dendrite arm spacing on tensile properties and fracture behavior of as cast magnesium aluminium alloys.* Metal and Materials International 2003. 9(1): p. 7.

14. S.M Zhu, B.L.M., J.F Nie, *Creep and rupture properties of squeeze-cast Mg-Al-Ca alloy* metallurgical and materials transactions, 2006. 37A: p. 9.

15. s. spigarelli, M.R., E. Evangelista and A. Rosen, *review of creep behaviour of AZ91 magnesium alloy produced by different technologies.* Material Science Technology, 2001. 17: p. 12.

16. Regev, M., E. Aghion, and A. Rosen, *Creep studies of AZ91D pressure die casting.* Materials Science and Engineering: A, 1997. 234–236(0): p. 123-126.

17. Ishikawa, K., H. Watanabe, and T. Mukai, *High strain rate deformation behavior of an AZ91 magnesium alloy at elevated temperatures.* Materials Letters, 2005. 59(12): p. 1511-1515.

18. Srinivasan, A., et al., *Effect of combined addition of Si and Sb on the microstructure and creep properties of AZ91 magnesium alloy.* Materials Science and Engineering: A, 2008. 485(1–2): p. 86-91.

19. Guangyin, Y., S. Yangshan, and D. Wenjiang, *Effects of Sb addition on the microstructure and mechanical properties of az91 magnesium alloy.* Scripta Materialia, 2000. 43(11): p. 1009-1013.

20. Guangyin, Y., S. Yangshan, and D. Wenjiang, *Effects of bismuth and antimony additions on the microstructure and mechanical properties of AZ91 magnesium alloy.* Materials Science and Engineering: A, 2001. 308(1–2): p. 38-44.

21. Spigarelli, S., *Creep of a thixoformed and heat treated AZ91 Mg-Al-Zn alloy.* Scripta Materialia, 2000. 42(4): p. 397-402.

22. Lee, S.-Y. and S.-I. Oh, *Thixoforming characteristics of thermo-mechanically treated AA 6061 alloy for suspension parts of electric vehicles.* Journal of Materials Processing Technology, 2002. 130–131(0): p. 587-593.

23. Sheng, J.Z., et al., *Numerical and experimental investigations of semi-solid AZ91D magnesium alloy in thixoforming process.* Journal of Materials Processing Technology, 2008. 202(1–3): p. 412-418.

24. Linga Murty, K., *Grain boundary sliding and viscous glide mechanisms of high-temperature creep in Pb-6% Sn.* Scripta Metallurgica, 1973. 7(10): p. 1083-1088.

25. Srinivasan, A., et al., *Effect of intermetallic phases on the creep behavior of AZ91 magnesium alloy.* Materials Science and Engineering: A, 2010. 527(6): p. 1395-1403.

26. Guangyin, Y., et al., *Microstructure and mechanical properties of Mg–Zn–Si-based alloys.* Materials Science and Engineering: A, 2003. 357(1–2): p. 314-320.

27. Lü, Y., et al., *Effects of rare earths on the microstructure, properties and fracture behavior of Mg–Al alloys.* Materials Science and Engineering: A, 2000. 278(1–2): p. 66-76.

28. Vagarali, S.S. and T.G. Langdon, *Deformation mechanisms in h.c.p. metals at elevated temperatures—I. Creep behavior of magnesium.* Acta Metallurgica, 1981. 29(12): p. 1969-1982.

29. Amberger, D., P. Eisenlohr, and M. Göken, *Microstructural evolution during creep of Ca-containing AZ91.* Materials Science and Engineering: A, 2009. 510–511(0): p. 398-402.

30. Tong, G.-d., H.-f. Liu, and Y.-h. Liu, *Effect of rare earth additions on microstructure and mechanical properties of AZ91 magnesium alloys.* Transactions of Nonferrous Metals Society of China, 2010. 20, Supplement 2(0): p. s336-s340.

Magnesium Technology 2014
Edited by: Martyn Alderman, Michele V. Manuel, Norbert Hort, and Neale R. Neelameggham
TMS (The Minerals, Metals & Materials Society), 2014

Indentation Creep Behavior of Mg-10Gd-3Y-0.5Zr (wt.%) Alloy at Elevated Temperatures

Huan Wang [a, b], Qudong Wang [a, b, *], Jie Yuan[a]
[a] National Engineering Research Center of Light Alloy Net Forming, Shanghai Jiao Tong University, 800 Dongchuan Road, Shanghai 200240, P.R. China
[b] The State Key Laboratory of Metal Matrix Composites, Shanghai Jiao Tong University, 800 Dongchuan Road, Shanghai 200240, P.R. China

Keywords: Mg-10Gd-3Y-0.5Zr alloy; Indentation creep; Creep mechanism; Microstructure characterization

Abstract

The indentation creep behavior of a cast Mg-10Gd-3Y-0.5Zr (GW103) alloy was investigated by flat cylindrical indenter at temperatures ranging from 250 to 325 ^{o}C and stresses ranging from 80 to 505 MPa. The indentation creep stress exponents varied from 1.36 to 5.10, which were lower at lower temperatures and stresses. The creep activation energies increased from 106.11 kJ/mol to 190.65 kJ/mol with increasing stress. Dislocation-controlled creep was suggested in high temperature and stress regime, while grain boundary sliding could contribute more at lower temperatures and stresses. The zone just beneath the indenter almost maintained the same during indentation creep, while the zone inside cycle segments under the indenter deformed severely. The zone at the edge of the indenter underwent largest stress and strain, resulting in broken of grain boundaries and bending of most intragranular precipitates.

Introduction

Magnesium alloys with rare earth elements additions (Mg-RE alloys) are being widely used in applications where the components need to work at elevated temperatures, due to their high specific strength and good creep resistance [1-4]. Various research has focused on the development of heat-resistant Mg-RE alloys in last decade. Among those, magnesium alloys with Gd and Y additions exhibit high strength at both ambient and elevated temperatures, and greater creep resistance than commercially-available WE alloys [5-12]. The high performance was attributed to the significant precipitation strengthening provided by the fine β′ phase in a convex lens morphology, which was involved in the four-stage precipitation sequence: S.S.S.S. (hcp)→β″ (DO_{19})→β′ (cbco)→β_1 (fcc)→β (fcc) as reported previously [7]. The Mg-Gd-Y-Zr alloy especially optimized Mg-10Gd-3Y-0.5Zr (GW103) is promising to be widely used in aerospace and automotive industries, such as engine pistons, gearbox housings etc. In these components, good creep resistance at elevated temperatures is crucial for evaluating its applications.

It is well known that conventional creep investigation always used uniaxial creep tests, especially tensile creep tests. An alternative can be provided by an indentation creep testing, which uses a flat-ended cylindrical punch to push into a small zone of the specimen by a constant load. The method was first developed in some model alloys [13-16]. Compared to conventional creep testing, indentation creep testing exhibited several attractive features. Firstly, small amounts of materials are needed to obtain sufficient creep data and sample preparation is simple. Also, as a localized creep technique, it is meaningful for the characterization of the local deformation and damage behavior in materials. Moreover, the flat-ended cylindrical indenter was chosen since a constant load was maintained under the indenter, and a steady state could be achieved after a transient primary stage, while with other spherical or pyramid indenters the load varied with creep time. Thus, the another advantage of this technique shows us that it enables the specimen under a steady loaded condition and the specimen dimensions do not change significantly during test, which can eliminate the effect of geometry factor in conventional tensile creep tests. To validate the application of indentation creep testing in more materials, various research related it with conventional tensile creep in many materials by both simulation and experimental investigation [17-24]. Although analytical solutions to creep problem do not exist, theoretical elastic-plastic analysis by finite element simulation could be obtained for indentation creep. And the results showed a similar steady-state stage was achieved during indentation creep as in conventional tensile creep. It was attributed to a steady-state elastic-plastic zone formed beneath the indenter under a constant load. Besides previous model materials, many engineering materials are good candidates to be investigated using indentation creep testing. Yue et al. [22,23] proposed a reference stress method to correlate indentation and tensile creep data by simulation, and determined creep parameters of a single-phase and two-phase material. The rationality was verified in subsequent experimental investigation in an Al alloy. Dorner et al. [19] also successfully compared two kinds of creep behavior in a Ti alloy, indicating that indentation creep testing was quite practicable to evaluate its creep behavior. Kabirian et al. did the very first work on magnesium alloys using indentation creep and characterized the localized deformation [25-27]. Now the method is being used extensively to characterize the creep properties of various engineering alloys.

Although there are many reports on creep properties of GW103 alloy, almost all of them have used conventional tensile creep tests for the evaluation of its creep properties [9-12]. Indentation creep investigation in this Mg-RE engineering alloy could provide a new way to characterize its creep performance. Moreover, for high performance Mg-Gd-Y-Zr alloys, in its promising applications, such as engine pistons, the component are always under localized load in service, meaning that indentation creep behavior is of great significance. So the aim of this study is to investigate the indentation creep behavior and deformation mechanism of Mg-10Gd-3Y-0.5Zr alloy. And microstructure before and after indentation creep was also characterized to investigate the localized deformation and damage behavior.

* Corresponding author at: National Engineering Research Center of Light Alloy Net Forming, School of Materials Science and Engineering, Shanghai Jiao Tong University, 800 Dongchuan Road, Shanghai 200240, P.R. China.
E-mail address: wangqudong@sjtu.edu.cn (Q.D. Wang).

Experimental procedure

The studied Mg-10Gd-3Y-0.5Zr (wt.%) alloy was prepared by melting high purity Mg (99.95%, wt.%) and master alloys of Mg-25Gd (wt.%), Mg-25Y (wt.%) and Mg-30Zr (wt.%) in a mild steel crucible at approximately 750 ^{o}C. The melting was under a mixed flowing protective atmosphere of CO_2 and SF_6 with a volume ratio of 100:1. The melt was poured into a steel mold which was pre-heated to 200 ^{o}C. The diameter of ingot was 110 mm. The actual chemical composition of the cast ingot in wt.% was Mg-9.67Gd-2.9Y-0.39Zr. The subsequent heat treatment involves solution treatment at 500 ^{o}C for 6 hours and ageing at 225 ^{o}C for 16 hours [7].

Cylindrical specimens for indentation creep tests, 25 mm in diameter and 16 mm in height, were cut from the ingot by an electric discharge machine (EDM). The self-designed indenter was made by stainless steel, which was thermodynamically stable in the stress and temperature range of the present study, and it was 5 mm in diameter and 4 mm in height. The indentation creep tests were performed at temperatures ranging from 250 to 325 ^{o}C and stresses ranging from 80 to 505 MPa by the ATS-3620 creep testing machine in air. The clamping fixture in the furnace used in present study enabled the load on the cylindrical specimens compressive. The indenter was positioned on the top surface of the cylindrical specimen, thus making the indentation creep testing performed when a constant load was applied. The temperature of the furnace was controlled within $\pm$1 ^{o}C. The displacement data was measured by two high-temperature extensometers which were attached with linear variable differential transformers (LVDT).

Metallographic characterization before and after indentation creep testing was performed. The specimens were polished and then etched with an alcohol solution containing 4% of nitric acid (volume fraction) [7] for optical microscopy (OM, Olympus XJL-30) observation.

Results and Discussion

Initial peak-aged microstructure

Fig. 1 shows the optical micrograph of the peak-aged cast GW103 alloy. It can be seen that the microstructure consists of equiaxed α-Mg matrix and some particles distributed both at the boundaries and inside the grains. These particles, which are rich in Gd and Y as identified by He et al. [7], are thermal-stable and contribute to its strength at elevated temperatures [9]. Also, some precipitates form during peak-ageing treatment, which are mostly suggested to be metastable β′ phase according to previous study [7,9]. The average size of the equiaxed α-Mg was approximately 140 μm, determined by the linear intercept method.

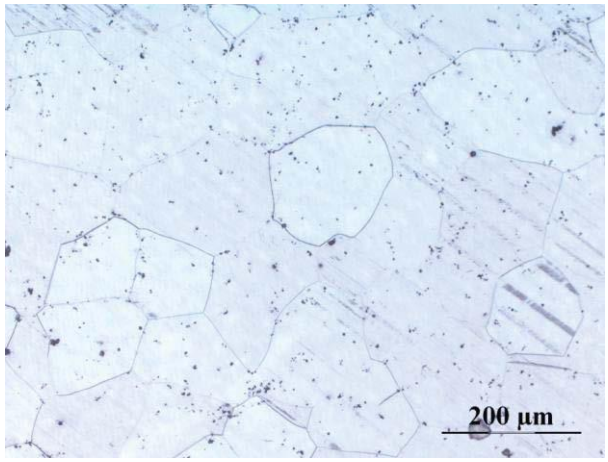


Fig. 1 Optical micrograph of the peak-aged cast GW103 alloy.

Indentation creep behavior

The indentation creep curves at 250 ^{o}C and 300 ^{o}C are illustrated in Fig. 2, which shows the indentation depth as a function of creep time. It is seen that the creep curves clearly approach a steady-state stage after a primary stage where the indentation rates decrease rapidly. The indentation depth was typically dependent on applied stress at the same temperature, and the value was quite bigger under higher stress (>270 MPa). Fig. 3 illustrates the indentation depth-time curves under 270 MPa at various temperatures, showing a dependence of the indentation depth on the temperature. At 325 ^{o}C, the indentation depth was significantly higher than at temperatures of 250 ^{o}C, 275 ^{o}C and 300 ^{o}C for the same creep time. It reveals a poor indentation creep resistance at temperature higher than 300 ^{o}C. Similar to conventional creep curves, the information of steady-state stage is significant for investigating the deformation behavior.

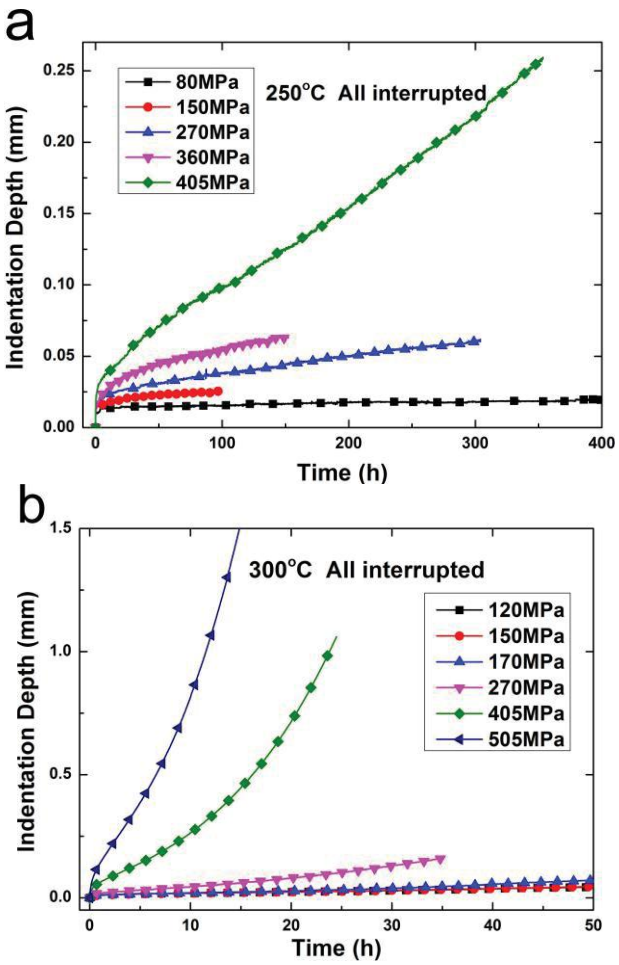


Fig. 2 Representative curves of indentation depth versus creep time at (a) 250 ^{o}C and (b) 300 ^{o}C.

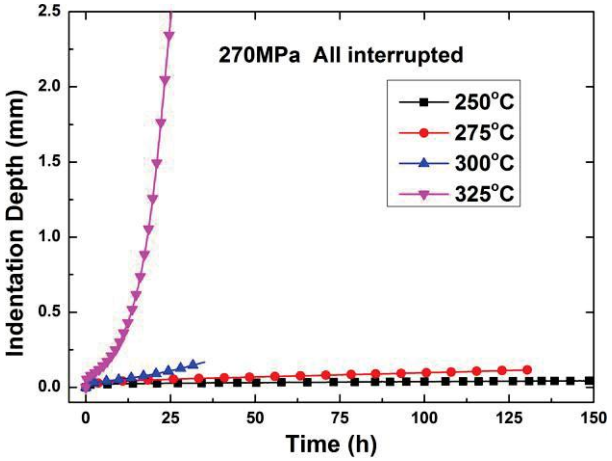


Fig. 3 Representative curves of indentation depth versus creep time under 270 MPa at various temperatures.

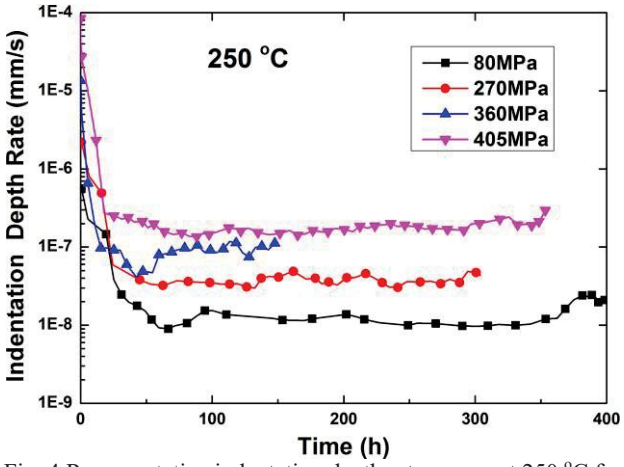


Fig. 4 Representative indentation depth rate curves at 250 °C for various applied stresses.

Representative indentation depth rate curves at 250 °C for various applied stresses are shown in Fig. 4. It is seen that the indentation rate was high when the creep began, then it eventually decreased to a steady value, suggesting that a steady-state stage followed the primary stage in indentation creep. And the steady-state indentation rate also depended on applied stresses, which increased from 5.40×10^{-9} mm/s to 1.30×10^{-7} mm/s, when applied stress increased from 80 to 405 MPa respectively.

Using conversion factors, we can correlate the indentation creep data with conventional uniaxial creep. As a result, a similar power-law constitution equation was reported to be valid to characterize the deformation behavior [17,19,23]. In this study for engineering Mg-RE alloy, a linear relationship is also obtained in the double logarithm plots of the steady-state indentation rate versus applied stress, as shown in Fig. 5. It demonstrates that the dependence of indentation depth rate on stress can be expressed by Eq. (1).

$$\dot{d}_I \sim \sigma_I^n \tag{1}$$

The results show that the stress exponents in this study varied in different temperature and stress regimes. At temperature of 250 °C, the exponent was 1.36 in the stress regime of 80~270 MPa, and 3.82 from 270 to 450 MPa. While at temperature of 300 °C, the values of n was 2.24 from 80 to 270 MPa, and 5.10 from 270 to 505 MPa. The Arrhenius plots of indentation rate versus reciprocal of the absolute temperature on a semi-logarithmic scale are also illustrated in Fig. 5(b), indicating that the relation in Eq. (2) is valid for indentation creep in this study.

$$\dot{d}_I \sim \exp(-Q/RT) \tag{2}$$

The results show that the activation energy varied between 105.11 kJ/mol and 190.65 kJ/mol for all tested stresses. It is known that the self-diffusion activation energy (Q_s) of pure magnesium is 135 kJ/mol [4,11]. So as shown in Fig. 5(b), the activation energies of indentation creep tests were lower than its self-diffusion activation energy for stresses from 80 MPa to 150 MPa, while the values were higher than Q_s from 270 MPa to 405 MPa. Since the stress exponent and activation energy are inherently related to creep mechanism, the differences in n and Q values probably reveal that various mechanisms donated the creep process at various conditions. It is generally believed that in magnesium alloys there exist four types of creep mechanism associated with the values of n and Q [4,28-30]. According to the results of indentation creep tests, at 250 °C, in stress regime of 80~270 MPa, the n value of 1.36 with activation energies lower than Q_s, suggests that grain boundary sliding acted as a predominant role during creep, while in stress regime of 270~405 MPa, higher n and Q values reveal it was dislocation-controlled. At 300 °C, in stress regime of 80~270 MPa, n value of 2.24 means that dislocation sliding also contributed a lot, while in stress regime of 270 to 505 MPa, a typical n value of 5.10 for dislocation climb controlled creep was obtained, and the corresponding Q values (> Q_s) also agreed well.

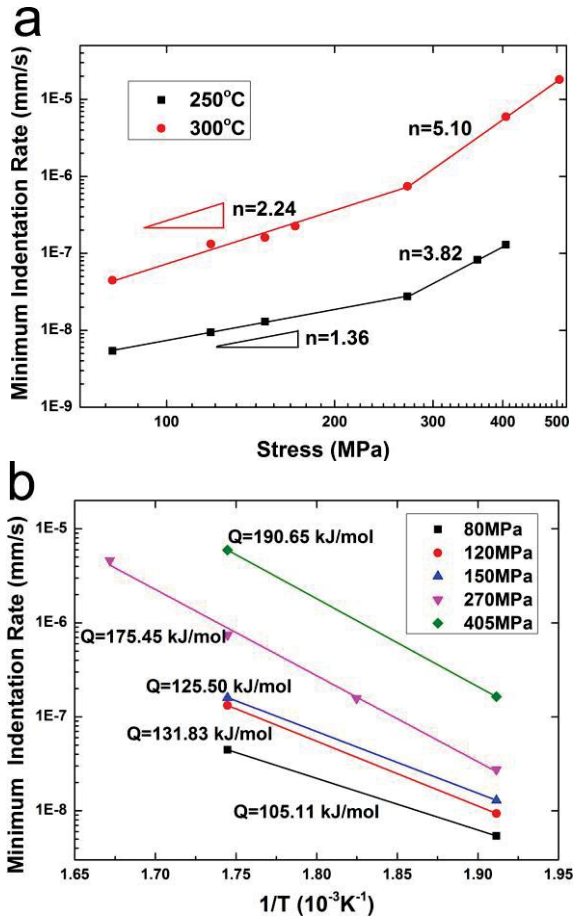


Fig. 5 Illustration of the indentation creep (a) stress exponent and (b) activation energy.

In previous reports, dislocation creep mechanism was always

regarded as the main mechanism of indentation creep in both simulation and practical experiments [17,19]. Now the different mechanisms was suggested from the obtained values of n and Q. The tensile creep result of the studied alloy reported by Janic et al. [9] showed that a stress exponent approximately 5 was obtained at 250 ^{o}C and 300 ^{o}C in the stress regime of 30~120 MPa. It is noted that classical approach directly correlate the stress and creep rate between two kinds of creep testing by using conversion factors[17,19-23]. And the conversion factor relates the indentation stress σ_I to a uniaxial reference creep stress as 0.26~0.36, meaning that the stress range in present work corresponds to a range of 20~180 MPa for uniaxial creep. It is consistent with the stress distribution analysis under indenter by finite element simulation [14,17,20]. It is noted that the compressive yield strength of the studied alloy at 200 ^{o}C and 300 ^{o}C is 347 MPa and 185 MPa, respectively [9]. So the stress regime can be regarded under the yield strength. Now the present indentation data shows that various stress exponents for different stress regimes. The n value of high stress regime is approximately 5.1 at both temperatures, while in low stress regime it results in 1.36 and 2.24 as above mentioned. This means indentation and tensile creep data are in good agreement for high stress regime. Although some researchers claimed that there were dependence of indentation rate on dimension of indenter, but from experimental results the constant value of n and Q were measured for various indenter diameters in the same material [13,17,21]. Thus, it is believed that the indentation creep data in this work revealed different mechanisms at various temperature and stress regimes. However, more research is needed to systematically compare the indentation creep with tensile or compressive creep of the studied material.

Microstructure after indentation creep

Fig. 6 shows representative optical micrographs of the zone far away from the indenter under 270 MPa at different creep temperatures. Compared with the microstructure before creep, the grain size did not change a lot after indentation creep, even for 304 h at 250 ^{o}C and 270 MPa. It can be seen more precipitates formed inside the grain, and the phenomenon appears more evident at 325 ^{o}C. The large amount of coarse plate-shaped precipitates, seen in Fig. 6(b), must be β phase according to the four-stage precipitation sequence [7].

Fig. 7 shows the optical micrographs in the longitudinal section along the axis after indentation creep test for 30 h at 325 ^{o}C and 270 MPa. The full view shows the indentation depth and the deformation condition around the indenter, as seen in Fig. 7(a). Obvious plastic flow can be observed beneath the indenter, and it seems that the flow lines are converged at the edge of the indenter. It is interesting to find that the zone in which flow lines appear could be contoured by two circle segments, as marked in Fig. 7(a). And the dimension of this circle segments is comparable to the diameter of the indenter. The flow lines are supposed to be associated with material deformation during indentation creep [19, 26,27]. The micrographs of different zones adjacent to the indenter are provided to comprehensively understand the characteristics of microstructure evolution and deformation process, as shown in Fig. 7(b-f), which refer to the zones 1-5 as marked in Fig. 7(a), respectively. Fig. 7(b) shows the side zone of the indenter. It can be seen this zone also deformed and the grains changed more significantly where it was closer to the indenter.

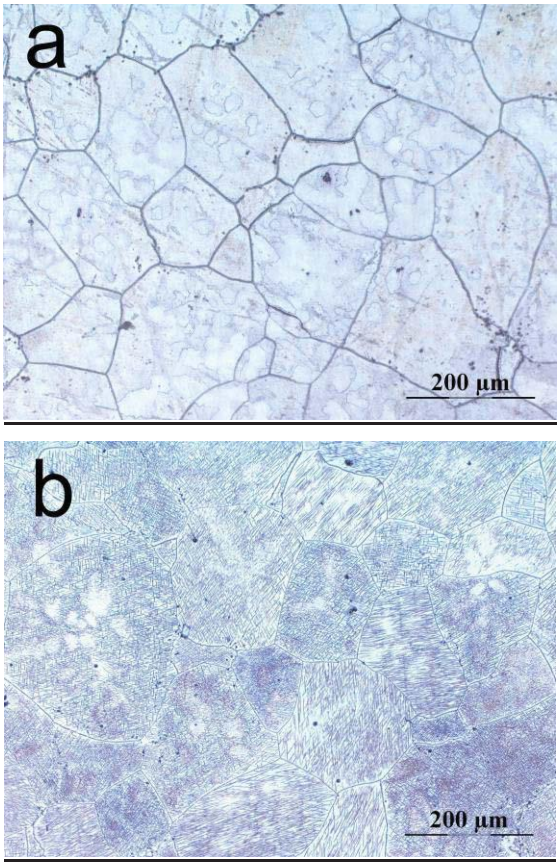


Fig. 6 Optical micrographs of the zone far away from the indenter: (a) 250°C/270MPa crept for 304h; (b) 325°C/270MPa crept for 30h.

The edge of the indenter, where flow lines concentrated, underwent severe plastic deformation, as seen in Fig. 7(c) and (d).The equaxied grains became elongated morphology during the deformation process.The grains boundaries in this zone changed a lot, even were broken to be discontinuous revealed by the observation of broken of initial continuous strip precipitates at grain boundaries. Also the coarse plate-shaped precipitates inside the grain turned to be bent and disorderly distributed. Fig. 7 (e) shows the micrograph in the zone between above mentioned circle segments. Similar to the zone at the edge of the indenter, the grains in this zone also deformed, but less severely than the former one. Fig. 7(f) shows the micrograph just beneath the indenter, revealing that the grains almost retained the same in the zone. In previous research [14,17,20], the finite element simulation of the Von-Misses stress and strain filed distribution in the specimen revealed that after primary stage, the stress/strain filed became steady especially for the zone just beneath the indenter. It is generally believed that the steady-state of stress distribution within the elastic-plastic zone brings out the steady-state creep behavior in indentation creep, although it is spatially non-uniform [19,20]. Thus, considering it in three-dimension, the zone just beneath the indenter and upper than the severely deformed zone formed a semi-spherical zone, then this elastic-plastic zone pushed into the material under punch stress. So the apparent indentation rate is believed to depend upon the velocity of the elastic-plastic boundary proceeding into the material. The stress level of the zones away from the indenter for a dimension of indenter diameter would be less than on tenth of the applied one,

and it decreases rapidly with distance increasing. All the results of microstructure characterization are quite consistent with the strain/stress filed analysis.

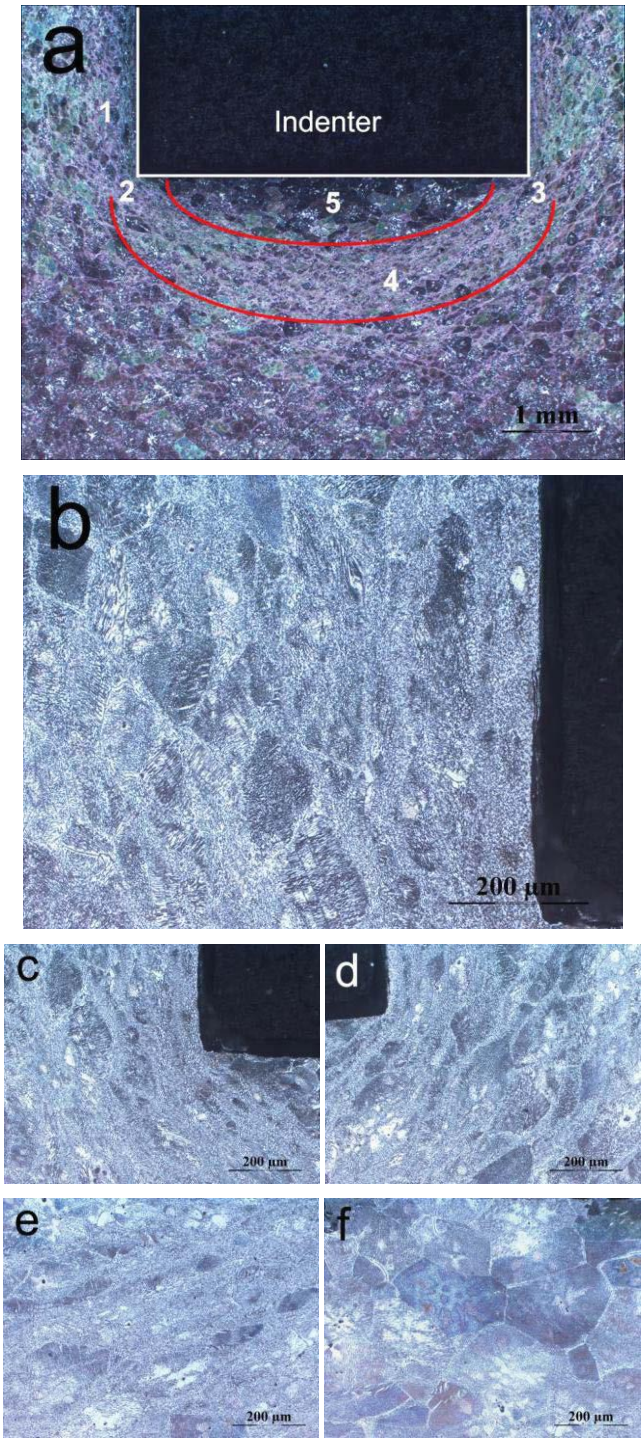


Fig. 7 Optical micrograph of different zones adjacent to the indenter after indentation creep for 30 h at 325°C/270MPa.

Conclusion

The indentation creep behavior of a cast Mg-10Gd-3Y-0.5Zr (GW103) alloy was investigated by flat cylindrical indenter at temperatures ranging from 250 to 325 °C and stresses ranging from 80 to 505 MPa. Then the microstructure before and after indentation creep was also characterized. Following conclusions are drawn from this work:

1. The indentation creep stress exponents varied from 1.36 to 5.10, which was lower at lower temperatures and stresses. The creep activation energies increased from 106.11 kJ/mol to 190.65 kJ/mol with increasing stress.
2. Dislocation-controlled creep was suggested in high temperature and stress regime, while grain boundary sliding could contribute more at lower temperatures and stresses.
3. The zone just beneath the indenter almost maintained the same during indentation creep, while the zone under the indenter inside cycle segments deformer significantly.
4. The zone at the edge of the indenter underwent the largest stress and strain, resulting in broken of grain boundaries and bending of intragranular precipitates.

Acknowledgement

This work was supported by the National Natural Science Foundation of China N0. 51074106, Key Hi-Tech Research and Development Program of China 2009AA033501, National Key Technology R & D Program of China 2011BAE22B01-5, International Cooperation Fund of Shanghai Science and Technology Committee and Shanghai/Rhone-Alpes Science and Technology cooperation fund No.06SR07104.

References

[1] N. Zeumer, B. Mordike and K.U. Kainer (Eds.), Proceedings of the Magnesium Alloys and their Applications, Werkstoff-Information-Sgesellschaft,Wolfsburg, Germany, 1998, pp. 125-132.
[2] L.L. Rokhlin, Magnesium Alloys Containing Rare Earth Metals, Taylor and Francis, London, UK, 2003, p. 1.
[3] L. Mordike, J. Mater. Process. Tech. 117 (2001) 391-394.
[4] B.L. Mordike, Mater. Sci. Eng. A 324 (2002) 103-112.
[5] I. Anthony, S. Kamado, and Y. Kojima, Mater. Trans. 42 (2001) 1206-1211.
[6] I. Anthony, S. Kamado, and Y. Kojima, Mater. Trans. 42 (2001) 1212-1218.
[7] S.M. He, X.Q. Zeng, L.M. Peng, X. Gao, and J.F. Nie, J. Alloy Compd. 421 (2006) 309-313.
[8] S.M. He, X.Q. Zeng, L.M. Peng, X. Gao, J.F. Nie, and W.J. Ding, J. Alloy Compd. 427 (2007) 316-323.
[9] V. Janik, D.D. Yin, Q.D. Wang, S.M. He, C.J. Chen, Z. Chen, and C.J. Boehlert. Mater. Sci. Eng. A 528 (2011) 3105-3112.
[10] V. Janik, Q.D. Wang, D.D. Yin, and W.J. Ding, Mater. Sci. Forum 675-677 (2011) 487-490.
[11] H. Wang, Q.D. Wang, D.D. Yin, J. Yuan, and B. Ye, Mater. Sci. Eng. A 578 (2013) 150-159.
[12] H. Wang, Q.D. Wang, B. Ye, D.D. Yin, and J. Yuan, Mater. Sci. Forum 765 (2013) 568-573.
[13] S.N.G. Chu and J.C.M. Li, J. Mater. Sci. 12 (1977) 2200-2208.
[14] S.N.G. Chu and J.C.M. Li, J. Mater. Sci. 12 (1977) 2214-2222.
[15] E.C. Yu and J.C.M. Li, Phil. Mag. 36 (1977) 811-825.
[16] S.N.G. Chu and J.C.M. Li, Mater. Sci. Eng. A 39 (1979) 1-10.
[17] T.H. Hyde, K.A. Yehia, and A.A. Becker, Int. J. Mech. Sci. 35 (1993) 451-462.

[18] J.C.M. Li, Mater. Sci. Eng. A 322 (2002) 23-42.
[19] D. Dorner, K. Röller, B. Skrotzki, B. Stöckhert, and G. Eggeler, Mater. Sci. Eng. A 357 (2003) 346-354.
[20] D. Pan and I. Dutta, Mater. Sci. Eng. A 379 (2004) 154-163.
[21] D.H. Sastry, Mater. Sci. Eng. A 409 (2005) 67-75.
[22] Z.F. Yue, Acta Metall. Sin. 41 (2005) 15-18.
[23] Y.J. Liu, B. Zhao, and Z.F. Yue, J. Mech. Strength 30 (2008) 854-859.
[24] Sh. Ansary, R. Mahmudi, and M.J. Esfandyarpour, Mater. Sci. Eng. A 556 (2012) 9-14.
[25] H. Liu, Y. Chen, Y. Tang, S. Wei, and G. Niu, Mater. Sci. Eng. A 464A (2007) 124–128.
[26] F. Kabirian and R. Mahmudi, Metall. Mater. Trans. A 40A (2009) 116-27.
[27] A.K. Mondal and S. Kumar, Compos. Sci. Technol. 68 (2008) 3251-3258.
[28] S.S. Vagarali and T.G. Langdon, Acta Metall. 29 (1981) 1969-1982.
[29] S.S. Vagarali and T.G. Langdon, Acta Metall. 30 (1982) 1157-1170.
[30] O.A. Ruano, J. Wadsworth, and O.D. Sherby, Acta Metal. 36 (1988) 1117-1128.

Magnesium Technology 2014

Deformation I

Magnesium Technology 2014
Edited by: Martyn Alderman, Michele V. Manuel, Norbert Hort, and Neale R. Neelameggham
TMS (The Minerals, Metals & Materials Society), 2014

The Athermal Component of the Strength of Binary Mg Solid Solutions

Saeideh Abaspour, C.H. Cáceres*
ARC-Centre of Excellence for Design in Light Metals
Materials Engineering, School of Engineering
The University of Queensland, QLD 4072, Australia

Keywords: Solid solution strengthening, Stress relaxation, Athermal behaviour, Short range order, Mg alloys

Abstract

Stress relaxation tests at predetermined strain/stress were used to assess the athermal stress, σ_a, component of the flow stress between room temperature and 180°C for Mg-0.8at% Gd, Mg-0.87at% Nd, Mg-1.3at% Y and Mg-2.5at %Al solid solutions. σ_a decreased monotonically with increasing temperature for the Mg-2.5at%Al whereas it remained constant for Mg-Gd or increased for Mg-Y and Mg-Nd. The limited athermal behaviour of Mg-2.5at% Al alloy can be attributed to the random solid solution introduced by the Al. The remarkably athermal behaviour of the Mg-RE alloys is consistent with an increasingly strong tendency to develop short range order in conjunction with strain induced precipitation hardening.

Introduction

The strength of an alloy is normally split into two components [1-3]:

$$\sigma = \sigma^* + \sigma_a .$$

σ^*identifies the thermally activated component and σ_a the athermal component of the strength. The thermal nature of the stress arises from the interaction of dislocations with short range obstacles which can be overcome with help from the available thermal energy. In binary solid solutions of Mg the thermally activated component is closely connected to the solid solution softening of the prismatic and pyramidal slip systems [4,5]. The athermal component results from the interaction between dislocations and long range obstacles, such as short range order (SRO) when present. Short range interactions involving atomic size and shear modulus misfit, as expected for random solid solution effects are dominant in Mg-Al alloys [6] and in general in dilute (<0.4at.%) solid solutions. In concentrated alloys, the phase diagram of most Mg binary solid solutions suggests that SRO should be the dominant strengthening mechanism [7,8]. SRO is a textbook example of an athermal strengthening mechanism that increases the creep strength of the alloy by preventing climb and cross slip and lowering the stacking fault energy [9].

The extent of the athermal regime determines the alloy creep strength [1-3,8-10] and thus, extending the athermal regime to as high a temperature as possible, for instance by introducing or maximizing SRO, can be considered as a basic criterion for designing a creep resistant alloy.

The tendency for developing SRO is evident from the phase diagram [7,11] through either two deep eutectics separated by a high melting point intermetallic, as in Mg-Zn alloys, or through the formation of multiple compounds as in Mg-RE alloys. Order in the solid solution, as opposed to the tendency to phase separation leading to precipitation hardening, stems from a negative enthalpy of mixing between solute and the host [7].

The sign and magnitude of the enthalpy of mixing can be predicted using the so called Miedema's scheme[7]. Mg-Al alloys with a low enthalpy of mixing show the weakest tendency to form, and hence the lowest strengthening from, SRO [7]. The larger (negative) enthalpy of mixing in Mg-Zn and Mg-Gd binary solid solutions should lead to stronger SRO effects and are thus expected to exhibit extended athermal behaviour, well beyond that of Mg-Al solid solutions. The behavior of other rare earth (RE) elements which are widely used to enhance the creep performance of Mg alloys, such as Nd and Y, with similar phase diagrams and enthalpy of mixing to that of Mg-Gd is expected to be similar to that of Mg-Gd.

In the current work stress relaxation tests were used to determine the athermal component of the strength of several Mg-RE binary solid solutions. The results are then discussed in terms of the expected strength of SRO.

2. Experimental Details

Mg binary alloys with nominal compositions (at.%) 2.5 Al, 1.0 Gd, 1.0 Nd and 1.6 Y were prepared by melting commercially pure Mg, Al, Gd, Nd and Y in steel crucibles coated with boron nitride in an electric furnace. The actual compositions are given in Table 1. The molten alloys were protected with SF6+CO_2 atmosphere. A mechanical stirrer was used to mix the melt for 20 minutes to ensure the dissolution of the solutes. Castings were made in steel moulds of size 80 x 80 x 10 mm^3, preheated to 300°C under an argon atmosphere. Solution treatments were performed on the cast plates under Ar atmosphere as per the times and temperatures given in Table 1, and quenched into water. Compression tests were carried out on cylindrical specimens, 18 mm in height and 9 mm in diameter, on a screw driven machine at 25°C, 100°C and 180°C in a temperature controlled chamber. The crosshead speed was 0.016 mm/min for all the tests (initial strain rate = $1.5x10^{-5}s^{-1}$). Stress relaxation tests were carried out at 180°C during the compression test at 0.2mm/min. In sequential stress relaxation tests the alloys were deformed to a certain predetermined strain/stress, the test stopped and the stress monitored for 30 minutes in Mg-Al, and for 60 minutes in Mg-Gd, Mg-Y and Mg-Nd. The specimens were then reloaded to a higher stress/strain and the test was repeated.

3. Results

Figure 1 shows the deformation flow curves of Mg-2.5Al, Mg-0.8Gd, Mg-1.3Y and Mg-0.87Nd at 25 and180°C. An Extended

linear hardening regime was observed in all the alloys at room temperature. Mg-Al exhibited an extensive loss of strength at 180°C, whereas it was limited in Mg-Gd alloy. Mg-Y and Mg-Nd alloys showed no loss of strength. Figure 2 compares the flow stress at 0.005 and 0.05 strains, showing that the behavior of the Mg-1.3Y and Mg-0.87Nd is athermal, and Mg-0.8Gd is nearly athermal, followed by Mg-2.5Al. There was a limited increase in the strength of Mg-2.5Al at lower strain at 100°C. The strength of the Mg-0.87Nd and Mg-1.3Y alloys remained constant between room temperature and 100°C and increased at 180°C. Figure 3 reveals the relaxation behavior of the alloys. The slope of the curves at a given time determines the stress relaxation rate. There was a dramatic decrease in the strength of the Mg-2.5Al alloy while, Mg-0.8Gd, Mg-1.3Y and Mg-0.87Nd hardly showed any stress relaxation.

Table 1. Chemical composition of the alloys studied determined by inductively coupled plasma atomic emission spectroscopy (ICP-AES), and the respective grain sizes and solution heat treatment schedule.

Alloy	Solute (at.%)	Grain size (μm)	Time (h)	Temperature (°C)
Mg-2.5%Al	-	129	10	413
Mg-1%Gd	0.8	119	4	535
Mg-1.6%Y	1.3	108.4	2	540
Mg-1%Nd	0.87	120	6	540

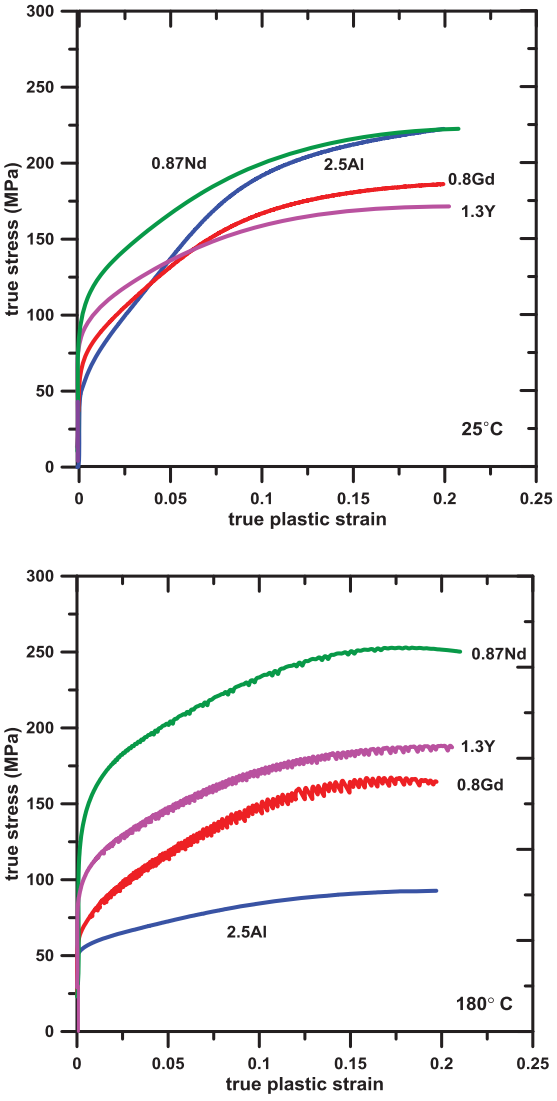


Figure1. Compressive flow curves of the alloys studied, at 25°C and 180°C.

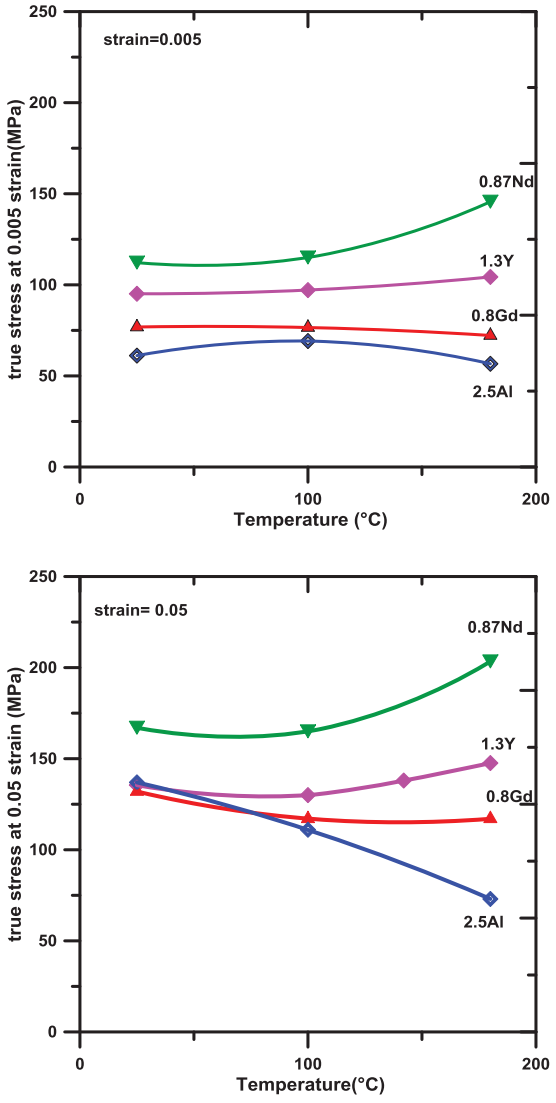


Figure 2. The strength as a function of temperature, determined at a strain of 0.5% and 5% .

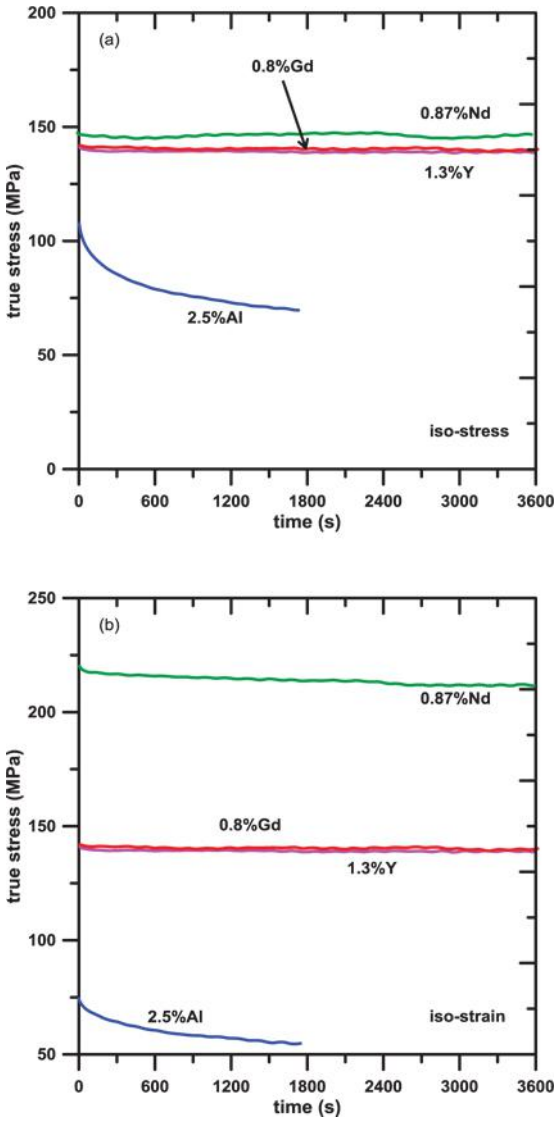


Figure 3. Stress relaxation tests a)iso-stress(all tests started at 150 MPa), b)at 5% strain.

4. Discussion

In the Mg-2.5Al alloy the substantial drop in strength at high temperature (Fig.2) and the high stress relaxation rate (Fig.3) both are consistent with the absence of SRO. Stress relaxation near to zero (Fig.3) corresponds well with the athermal behaviour of the Mg-0.8Gd alloy and constitutes further evidence of the presence of SRO already confirmed by diffuse X-ray scattering [12]. The extended linear hardening regime (Fig.1), the remarkably athermal behaviour of Mg-1.3Y and Mg-0.87Nd (Fig.2) and a nil stress relaxation (Fig. 3) are also consistent with a strong tendency to develop short range.

4. Conclusions

The Mg-2.5Al alloy showed no athermal regime in the temperature range studied. The strength dropped substantially during stress relaxation as expected for a random solid solution.
The remarkably athermal behaviour of Mg-0.8Gd Mg-1.3Y and Mg-0.87Nd alloys, despite their low solute content, appears consistent with a strong tendency to develop SRO.

References

[1] Hull D., Bacon, D. J., *Introduction to dislocations*. 3rd ed.; (Pergamon Press: Oxford, 1984).

[2] Kuhlmann-Wilsdorf D., Wilsdorf, H. G. F., Wert, J. A., "LEDS theory of workhardening stages and "planar" versus "distributed" glide," *Scripta Metallurgica et Materialia*, 31 (1994), 729-734.

[3] Seeger A. "The mechanism of glide and work hardening in face-centered cubic and hexagonal close-packed metals," In: Fisher, J.C., Johnston W.G., Thomson R., Vreeland T., eds.; "*The mechanism of glide and work hardening in face-centered cubic and hexagonal close-packed metals*," (London,Chapman and Hall: 1957) 243-329.

[4] Akhtar A., Teghtsoonian, E., "Solid solution strengthening of magnesium single crystals - II. The effect of solute on the ease of prismatic slip," *Acta Metallurgica*, 17 (1969), 1351-1356.

[5] Ando S. , Tonda, H., "Pyramidal slip in magnesium alloy single crystals," *Materials Science Forum*, 419-422 (2003), 87-92.

[6] Cáceres C. H., Rovera, D. M., "Solid solution strengthening in concentrated Mg-Al alloys," *Journal of Light Metals*, 1/3 (2001), 151-156.

[7] Cáceres CH, Abaspour, Saeideh, "Bounds to Hardening by Solid Solution, Precipitation and Short Range Order in Mg Binary Alloys," *Magnesium Technology 2013*, (2013), 225-230.

[8] Abaspour Saeideh, Cáceres, CH, "Creep Behaviour of Mg Binary Solid Solutions," *Magnesium Technology 2013*, (2013), 17-20.

[9] Nabarro F. R. N., de Villiers, H. L., *The physics of creep*. (Taylor and Francis London, 1995).

[10] Chino Y., Kado, M., Ueda, T., Mabuchi, M., "Solid solution strengthneing for Mg-3.0 mass pct. (2.71 at.pct) Al and Mg-0.06 mass pct (0.036 at. pct) Ca alloys," *Metall and Mat Trans A*, 42 (2011), 1965-1973.

[11] Haasen P., *Physical Metallurgy*. (Cambridge University Press: Cambridge, 1996).

[12] Gencheva D. S., Katsnel'son, A. A., Rokhlin, L. L., Silonov, V. M., Khavadzha, F. A., "Investigation of short-range order in magnesium alloys with erbium and gadolinium," *Fiz metal metalloved*, 51 (1981), 788-793.

Magnesium Technology 2014
Edited by: Martyn Alderman, Michele V. Manuel, Norbert Hort, and Neale R. Neelameggham
TMS (The Minerals, Metals & Materials Society), 2014

CRACK PROPAGATION UNDER BENDING IN CAST Mg10GdxNd-T4 ALLOYS

Petra Maier[1], Chamini Mendis[2], Martin Wolff[2] and Norbert Hort[2]
[1]University of Applied Sciences Stralsund, Zur Schwedenschanze 15, D-18435 Stralsund, Germany
[2]Helmholtz-Zentrum Geesthacht, Magnesium Innovation Center, Max-Planck-Straße 1, D-21502 Geesthacht, Germany

Keywords: Mg-RE, bending, crack growth, twinning, corrosion

Abstract

Mg-alloys containing RE additions are promising candidates for structural applications, as they combine low density with high strength, which is important for lightweight construction. Medical applications, like bone screws and nails, benefit from their moderate corrosion rate. All these components are exposed to bending, more or less influenced by corrosion. In this study the Mg-10Gd-xNd (x=0,1,2 wt.%) were subjected to solution heat treatment to increase ductility and to reduce the dendritic microstructure. Plates of 110x20x6 mm³ in size were tested by three-point bending with a deformation speed of 1 mm/min. Crack growth is discussed using light microscopy and correlated to bending stress - outer strain curves. Crack propagation is mostly found transgranular and interacts with twinning. Double and secondary twinning occurs near the crack path in appropriately oriented grains. Corroded samples after pre-bending show an increase in yield strength but reduced toughness. Cracked samples show a strong reduction in flexural strength after corrosion.

Introduction

Mg-10Gd shows the lowest corrosion rate within the binary Mg-Gd alloying system, increased strength at moderate ductility for as-cast Mg alloys with a coarse grained microstructure.[1] Mg alloys twin strongly during plastic deformation, which will influence further deformation by assisting crack initiation. When mechanical loading up to material failure and exposure to a corrosive environment happen simultaneously or after each other, mechanisms are not fully understand yet. Medical implants, such as stents undergo crimping and expanding, bone plates are often pre-bent to fix curved bone contour[2], pre-bending in nails is applied to increase stability of fixation[3]. Permanent implants are corrosion resistant, but Mg alloys, which are designed as biodegradable implant material undergo loading during corrosion. Pitting corrosion is very common in Mg alloys and often in focus of research. Localized corrosion in form of pits initiate cracks, also known as stress corrosion cracking. Work was done on commercially AZ91 alloys, but also on new developed RE containing Mg alloys, such as EV31A[4]. So, twins do not only assist crack initiation, they also assisted corrosion. The influence of microstructure and corrosion behavior is also not fully understood. The corrosion is mainly influenced by second phases, but also by generated dislocations and twins[5].

To eliminate the role of second phases on the corrosion behavior as well on the crack propagation (here they could leave stress fields) the alloys investigated are solution heat treated. Recent work[6] has shown that Mg10GdxNd alloys after T4 treatment presents highest elongation at fracture in tension and reduced dendritic microstructure. T4 treatment also aims to reduce porosity, which has been found to influence the fracture process in three point bending tests on die-cast alloys AM50 and AM60[7].

Experimental

Alloys investigated were prepared using the permanent mold direct chill casting technique[8,9] at Helmholtz-Zentrum Geesthacht under a protective gas mixture of Ar and 2 % SF_6. The casting temperature was 730 ^oC and the mild steel mold (inner surface has a thin BN coating) was preheated to 500 ^oC. Gd and Nd were added as pure elements to the Mg melt before casting. The ternary alloys under investigation had nominal compositions of 10 wt.% Gd in addition to 1 and 2 wt.% Nd. The binary alloy Mg10Gd consists of 9.2 wt.% Gd. In the alloy Mg10Gd1Nd, Gd and Nd were present in the amounts of 8.13 and 0.74 wt.%. The actual composition of Mg10Gd2Nd is 9.17 wt.% Gd and 1.75 wt.% Nd. For the analysis of the overall chemical composition, inductively coupled plasma–optical emission spectroscopy (ICPOES) was applied. The specimens were dissolved in concentrated nitric acid and diluted by a factor of 32,000. The alloys were solution treated (T4) at 525 ^oC for 24 h and quenched into water at room temperature. The mechanical properties were measured at room temperature with a Zwick 050 testing machine with an initial strain rate of $1x10^{-3}$ mms^{-1}, a number of 10 samples were tested at each alloy. Since tensile tests are not a reliable methods for determining the Young's modulus of magnesium, resonance frequency damping analysis method has been applied to determine the dynamic modulus of elasticity. Brinell hardness was tested with a HPO250 machine (sample surface was grinded after cutting to reduce residual stresses).

Three-point bending tests were conducted on a TIRA28100 universal testing machine. A span of 90 mm, a diameter of the support brackets and plunger of 10 mm and a deformation speed of 1 mm/min was used for testing of all plates. Mg10Gd samples had a geometry of 110x20x4 mm³. The plates were tested in the upright position to guarantee a crack propagation up to 20 mm in length. Due to the higher flexural strength by alloying Nd Mg10GdxNd plates had a size of 110x20x6 mm³ to avoid tilting during the test. Samples were cut by a hack sawing machine, the surface were then milled and grinded to reduce residual stresses. The deflection during bending was monitored and converted into outer strain (strain at the outer surface of the sample) in dependence of bending stress. To evaluate the influence of corrosion on fracture strength and crack growth, samples were exposed to Ringer-Acetate solution, where 1 l consists of 6 g sodium chloride, 3.7 g sodium acetate, 0.134 g calcium chloride, 0.203 g magnesium chloride and 0.4 g potassium chloride, with an initial pH-value of 6.5. Since these alloys could be candidates for biodegradable implant materials[1] this solution is used due to its similarity to human blood. Plates were corroded for 1 day in 500 ml electrolyte each. To fit the body temperature a test temperature of 37°C was applied. The pH-level increased to 8.5. The white $Mg(OH)_2$ layer was not removed before the bending test, however, some parts fall off during testing. Samples, which were corroded after pre-bending or cracking were exposed to Ringer solution seconds after the bending.

Materials

Microstructure

During solution heat treatment (T4) the dendritic microstructure resulting from the as-cast process almost disappears and second phases are dissolved, see figure 1 a-c. The average grain size decreases with increasing Nd: Mg10Gd shows 1200 µm large grains (mean value), Mg10Gd1Nd 925 µm and Mg10Gd2Nd 775 µm, respectively. Figure 1 a-c show clearly that the grain size is not homogeneously distributed; the range in grain size is rather high as a result of the solidification process. Mg10Gd1Nd, for example, shows in figure 1b in some areas grains of a size of 100 µm, other grains are 1 mm in size.

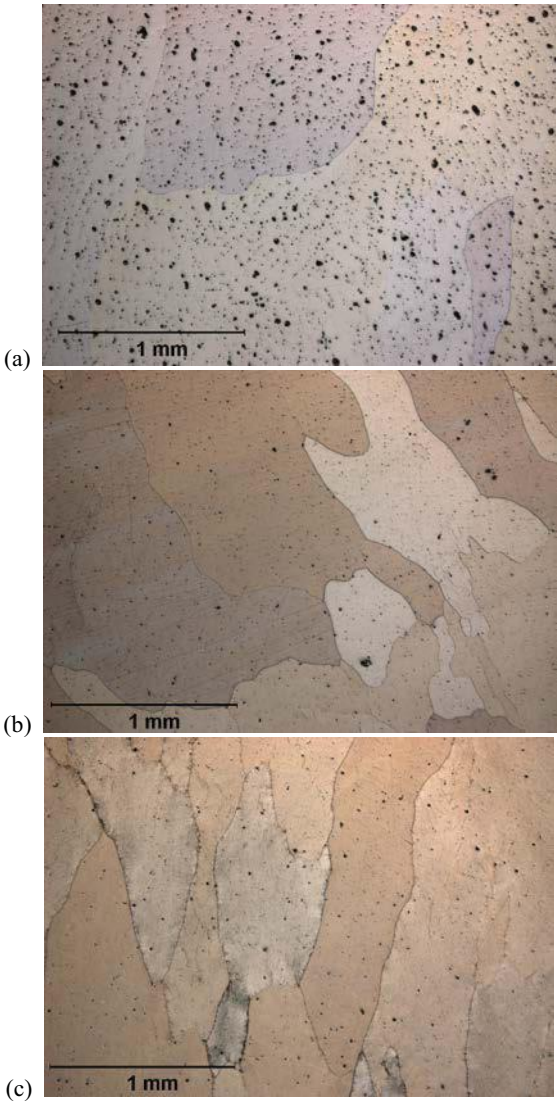


Figure 1. Microstructure (a) Mg10Gd, (b) Mg10Gd1Nd, (c) Mg10Gd2Nd

Transmission electron microscopy on these alloys in T4 condition (not shown here) underline the fact, that all second phases are dissolved during solution heat treatment, no particles have been found[6]. The black spots seen in figure 1a-c are small casting defects, like very small pores, originally formed in dendrite arms.

Mechanical Properties

Table 1 presents the mechanical properties of the alloys. It can be seen that adding Nd to the binary alloy Mg-10Gd increases strength, hardness and dynamic Modulus (DME). Comparing the ternary alloys with each other results in trends in opposite directions: tensile yield strength (TYS) and ultimate tensile strength (UTS) decreases slightly as a result of increased solid solution strengthening. Compression yield strength CYS shows the lowest value for Mg10Gd1Nd, caused by preferred twinning under compression when alloying Nd (see also the ratio of CYS/TYS being smaller than 1). Elongation in tension shows the highest value for Mg10Gd1Nd, in compression elongation (CS) increases with increasing Nd, same applies to Brinell hardness.

Table I. Mechanical properties of Mg10GdxNd_T4

	Mg10Gd	Mg10Gd1Nd	Mg10Gd2Nd
TYS(MPa)	68.7 ± 2.4	108.3 ± 3.4	106.4 ± 5.8
UTS (MPa)	111.7 ± 9.3	174.4 ± 0.8	162.1 ± 5.8
El. (%)	3.2 ± 0.5	7.0 ± 1.2	2.9 ± 0.4
CYS (MPa)	81.0 ± 3.5	59.8 ± 8.6	68.1 ± 16.3
UCS (MPa)	222.8 ± 10.5	278.2 ± 7.4	276.1 ± 11.1
CS (%)	17.4 ± 2.1	18.2 ± 1.3	22.3 ± 3.8
ratio CYS/TYS	1.18	0.55	0.64
DME (GPa)	43.71 ± 0. 38	44.22 ± 0.15	44.45 ± 0.15
HBW2.5/31.25	59	70	73

Results and Discussion

Influence of Nd on bending properties and stress-strain curve

To get an overview of the bending behavior of the three investigated alloys bending tests were done up to a stress reduction down to 10% of maximum stress or the complete failure of the sample. Figure 2 shows an increase in fracture (maximum) strength under bending and flexural modulus with increasing Nd. This increase agrees with increasing UTS, UCS, CS, Dynamic Modulus and hardness with adding Nd to the binary alloy Mg-10Gd. Crack initiation and growth starts when bending stress starts to decrease (at the fractural strength). Mg10Gd2Nd shows very high stress drops after some crack propagation. This indicates low fracture toughness, which will be a result of the lowest elongation at fracture (2.9 %).

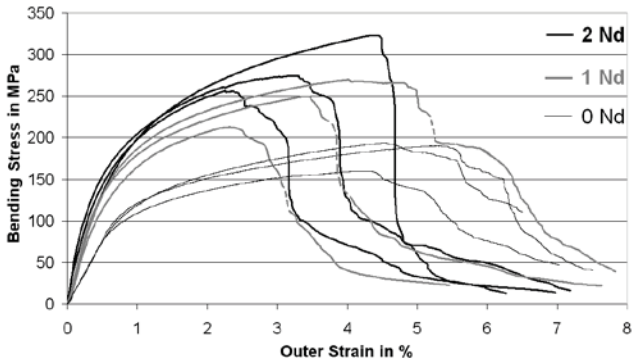


Figure 2. Bending stress - outer strain curves of Mg10GdxNd: increase in yield and fracture strength and flexural modulus with increasing Nd, causing a reduction in strain to crack initiation

The stress drops mentioned above are influenced by the local microstructure in the neutral axis of the bending sample. If the

grains in the neutral axis are large and do not tend to twin during bending the crack growth is not hindered, the crack can propagate without redirection by twin interfaces leading to a very high, almost vertical stress slope and the fracture toughness around this area of crack growth is very low. Figure 3 presents an overview of crack propagation, here in Mg10Gd. Cracking started on the left side of the image propagating to the right. The area slightly left of the initial neutral axis (circled) is free of grain boundaries and twins, so the crack propagation happens rather fast. Crack branching (see arrows) as a result of delayed crack growth (caused by grain boundaries, twins) improves fracture toughness. The stress-strain curve indicates this behavior by less stress loss with increasing strain, mostly after high stress drop.

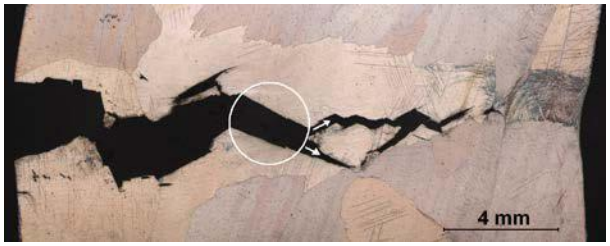


Figure 3. Micrograph of crack path in Mg10Gd: overview

If slip systems in grains are orientated that twinning occurs crack propagation is delayed[10]. Figure 4a shows a section of a crack path passing through a twinned grain, revealing a zigzag growth. The crack path is redirected by following a twin interface, might change over to another twin interface by twin interfaces of double or secondary twins. Figure 4a indicates clearly that the grain was heavily twinned before the crack worked its way through, both crack sides fit into each other quite well. The increase in fracture toughness after the crack passed the neutral axis can also be explained by entering the compression side of the sample, which has been strain hardened, indicated by twinned grains (figure 4b).

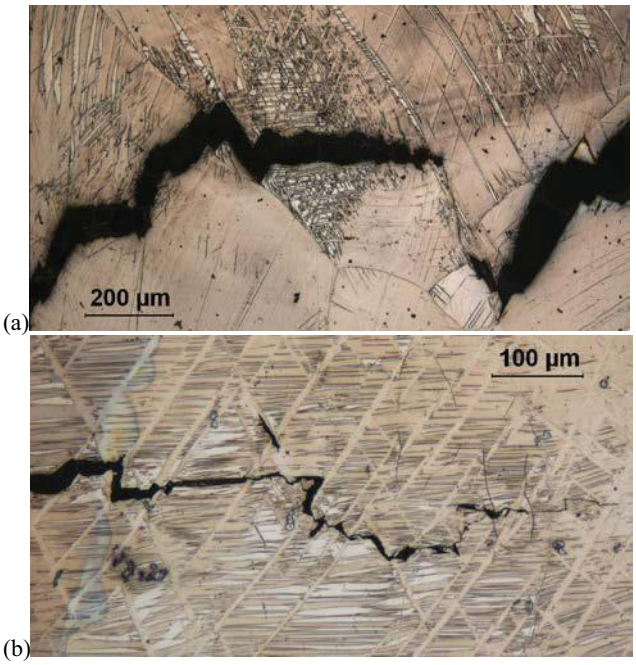


Figure 4. Micrograph of zigzag crack path in Mg10Gd2Nd, delay by strongly twinned grains: (a) crack path middle (b) crack tip entered the initial compression side of the sample

Influence of pre-corrosion

Since it is known that these Mg-RE alloys suffer from pitting corrosion, it was investigated how much fracture strength is reduced by pre-corrosion. Focus of this investigation was Mg10Gd. The grey curves in figure 5 show bending stress – outer strain behavior of non-corroded material as a reference. Pre-corrosion (1day, 37°C) reduces fracture strength by 50 MPa (black lines without symbols). It is noticeable that one pre-corroded samples shows high fracture toughness (area below the stress-strain curve is large), the micrograph of this sample (not shown here) reveals many twinned grains along the crack path, like in figure 4a, where twin interfaces redirect crack propagation.

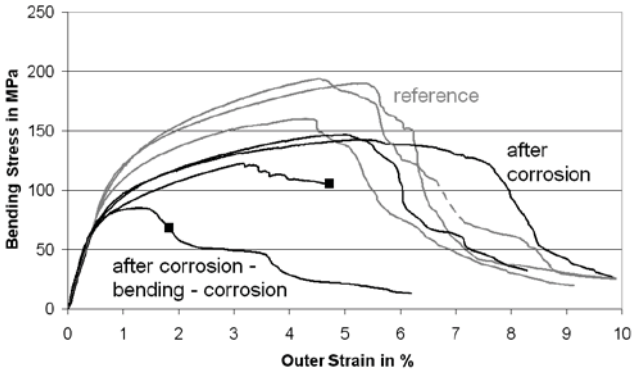


Figure 5. Bending stress - outer strain diagram of Mg10Gd: corrosion reduces fracture (maximum) strength

Figure 6 a and b show that pits act as crack initiation. The stress intensity due to the notch effect caused by pits is increased and the critical energy needed for cracking is given. The white arrow in the micrographs indicates the crack starting point, in figure 6 a also supported by selective corrosion attack.

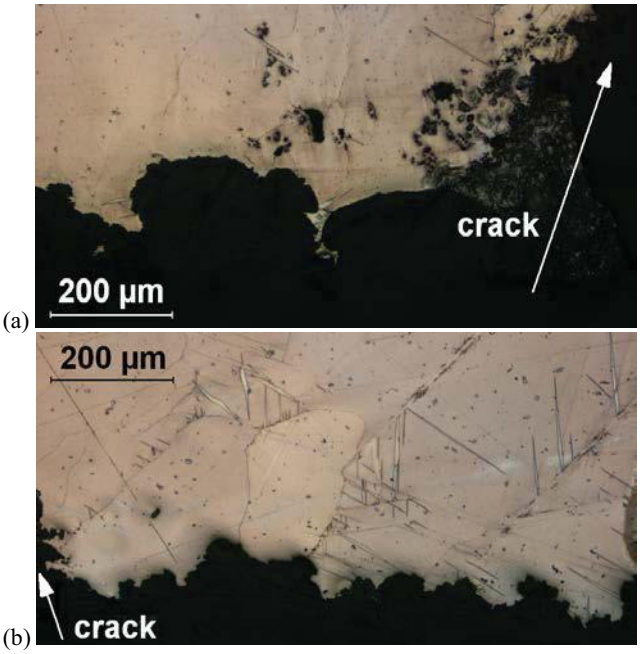


Figure 6. Micrograph of crack path in Mg10Gd after corrosion (pre-corroded) - pits act as crack initiation (a) near crack origin (b) pitted surface very close to fracture initiation

The black curve with the symbol ■ in figure 5 presents following procedure: pre-corrosion, cracked to 5 % outer strain (approx. 6 mm crack length, up to the tip of the white arrow in Figure 7a), second corrosion exposure and final cracked. Figure 5 shows a reduction in maximum stress (20 MPa) of bending of the cracked and corroded sample. Known from stress corrosion cracking mechanisms corrosion is accelerated by the strain hardened material of the plastic zone mostly in front of the crack tip and around the crack path. The material near the crack tip after the first bending/cracking test (white arrow) shows crack branching, which will be initiated by pitting corrosion in twinned grains. However, the main crack follows the favoured stress direction.

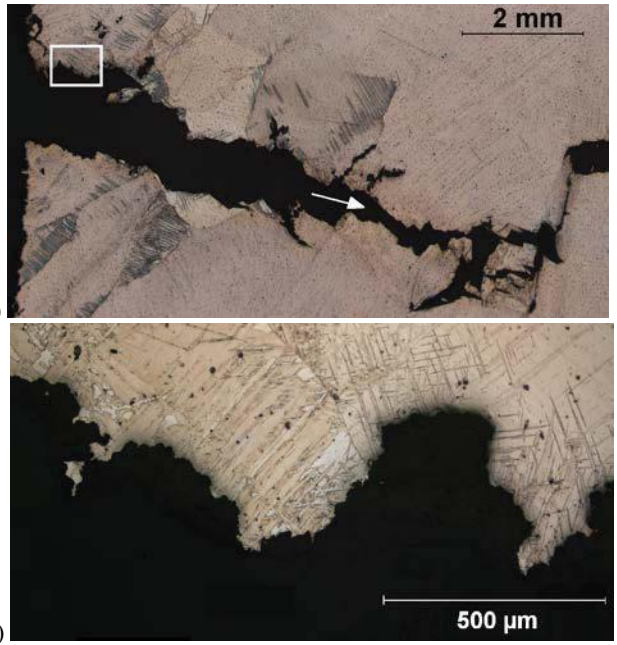


Figure 7. Micrograph of crack path in Mg10Gd after combined corrosion – bending – corrosion: (a) an overview presenting that pits act as crack initiation for secondary cracking (b) pits forming at cracked surface during corrosion mostly at twinned grains

Figure 7b shows a higher magnified micrograph out of figure 7a and indicates clearly that grains which are twinned corrode preferentially. This will be disused in more detail in paragraph "Influence of corrosion of cracked samples", where pre-corrosion will be eliminated.

Strain hardening: effect of pre-strain

After a few samples showed an increase in flexural yield strength after cracking and corrosion during second (final) bending test, this strain hardening appearance was investigated in more detail. The amount of yield strength increase depends of the crack length: the higher the crack length, the less the strain hardening effect, see Figure 10. Is a certain crack length reached, no increase in yield strength has been seen, also influenced by the microstructure.

Figure 8 a and b present bending stress - outer strain curves of Mg10Gd1Nd and Mg10Gd2Nd samples which were strain hardened up to 2% outer strain, corroded and the tested under bending load to stress reduction down to 10 % . It is noticeable that Mg10Gd2Nd still strain hardens (the fracture strength during second mechanical testing is higher than the stress at 2 % strain of the first test). The higher amount of Nd leads to higher strain hardening ability under bending. This agrees with the mechanical properties given in table 1: similar increase in stress from TYS to UTS between Mg10Gd1Nd (66 MPa) and Mg10Gd2Nd (56 MPa), but within less elongation (less than half the elongation for Mg10Gd2Nd). This indicates a higher strain hardening coefficient by increasing Nd content. On the other hand this increase in alloying element leads causes a reduction in fracture toughness (see stress drops of reference curves in figure 8b).

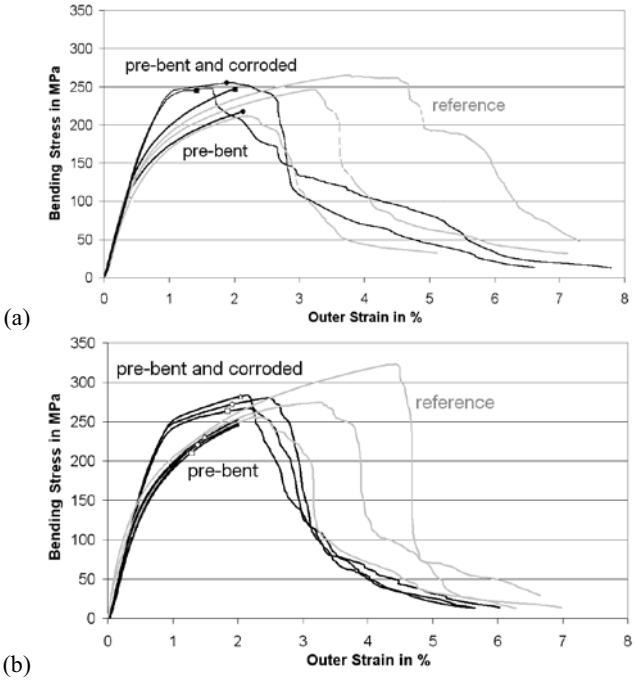


Figure 8. Bending stress - outer strain diagram of (a) Mg10Gd1Nd and (b) Mg10Gd2Nd: pre-bending before corrosion leads to strain hardening

Even the compression strain is increasing with increasing Nd content (see table 1), the elongation to fracture under tension is the lowest of Mg10Gd2Nd with 2.9 %. Therefore this material shows even on the initial compression side of the sample cracks, which are mostly in or near grains which are twinned, nowadays often called twinning assisted crack initiation and also found in extruded Mg alloys during fatigue exposure (twin assisted fatigue cracking)[11]. Here it is described that the twinning process plays a main role in crack initiation at high strain amplitudes.

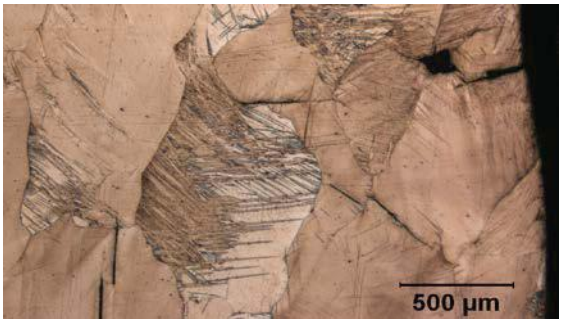


Figure 9. Micrograph presenting cracks induced by twinning on the compression side in Mg10Gd2Nd

Influence of corrosion of cracked samples

Twins do not only assist crack initiation, they also accelerate corrosion (already seen in Figure 7b). To eliminate pre-corrosion samples were cracked up to different length (see curves with filled symbol ■), corroded and tested again under bending (see curves with open symbol □). Also the strain hardening effect in dependence of crack length is seen by looking at the black line.

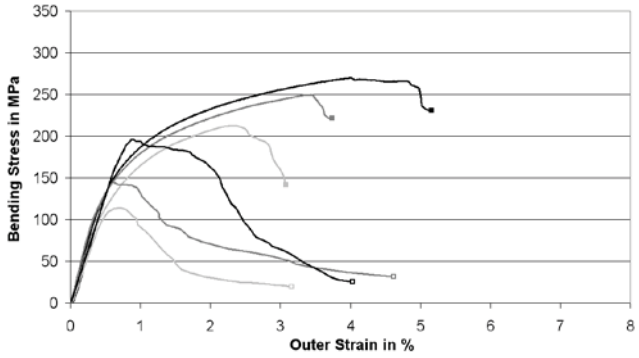


Figure 10. Bending stress - outer strain diagram of Mg10Gd1Nd crack propagation influenced by corrosion: bending before corrosion: ■, bending after corrosion: □

Figure 11a (Mg10Gd1Nd) and 7b (Mg10Gd) show representative examples for deformed material with increased density of dislocation and twin interfaces accelerating corrosion. Especially twinned grains show undercutting pitting corrosion. Aung[12] also found this in AZ31B-H24 sheet in 3.5% NaCl solution, the corrosion rate was higher in the twinned microstructure compared with the untwinned one. Hamu[13] points out that a higher density of dislocation and twins probably lead to high hardness values and high anodic dissolution. Recent study by Maier[6] has shown that corrosion of Mg10Gd1Nd in T4 condition in a 3-electrode-cell, even up to high anodic potential, only causes shallow pits. Here, due to increased density of lattice defects, undercutting pits form.

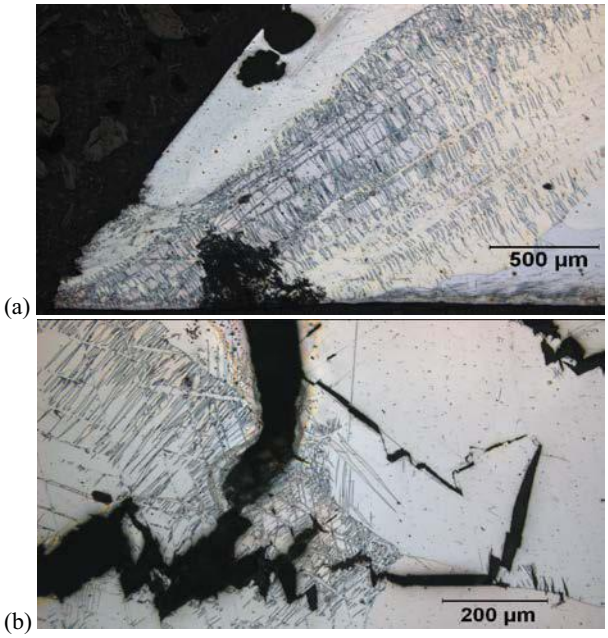


Figure 11. Micrograph of crack in Mg10Gd1Nd (a) twinned grain at crack initiation, (b) crack branching in twinned grains

Figure 11b shows the remaining crack tip area, where crack branching is seen, caused by twinned grains on the initial compression side of the sample. Crack branching and redirection of the crack path along twin interfaces increases the fracture toughness for the moment (stress curve rises with increasing outer strain). However, the ongoing crack growth is assisted by twin interfaces in adjusted grains after local stress built around them.

Crack propagation

To investigate the crack path in more detail concerning the stress drops, crack propagation was stopped at significant points of the bending stress – outer strain curve (see Figure 12): just after stress drop, see sample 7 and 5 and after stress rising, see sample 9, 8 and 6 at different degrees.

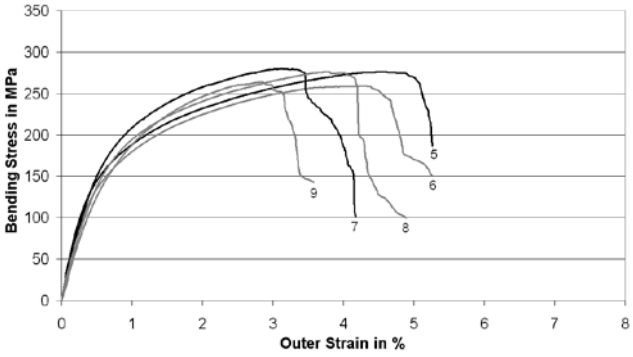


Figure 12. Outer strain – bending stress diagram of Mg10Gd2Nd: stopped crack propagation

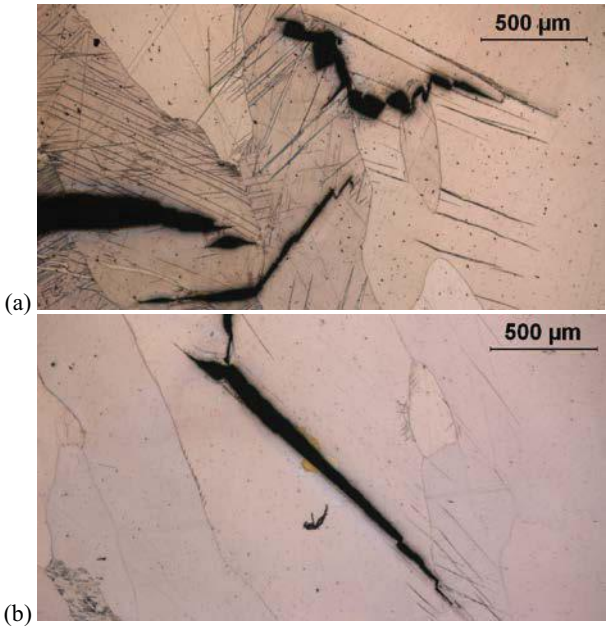


Figure 13. Micrograph of crack tip in Mg10Gd2Nd (a) high fracture toughness (b) low fracture toughness

To work out the correlation between stress - strain curve turned out to be rather difficult, because the samples have a thickness of some mm. There are samples, where both plate sides show a different crack path, obviously depending on the microstructure. However, figure 13 a shows a crack tip of a sample, where bending was stopped after stress curve rising, indicating increased

fracture toughness. The crack is branched and redirected by the twin interfaces. It was already seen in Figure 4b that double and secondary twinning is the reason for the zigzag propagation of the crack. When twin interfaces are orientated perpendicular to crack propagation they act as a blockage. Here stresses will be locally enhanced by the formation of dislocation pile-ups blocked by the interfaces, which act as effective barriers to dislocation motion. A further explanation for rising bending stress with ongoing outer strain is that propagating twins (double or secondary) are also stopped by the interfaces. However, the defects and imperfections of the interface structure will help to nucleate new dislocation loops, which after all assist crack propagation or even crack initiation of secondary cracks (figure 13 a).

Figure 13 b on the other hand shows a crack tip, where the stress-strain curve just passed the stress drop. The crack followed a twin interface which is orientated parallel to the main crack growth direction, indication low fracture toughness. The crack growth rate in such a microstructure is rather high. In case the crack propagation of more than a 1 mm in length correlates exactly with the stress drop of approximately 50 MPa, then the crack propagated that length in less than 1 second.

Conclusion

An extensive study of the influence of the microstructure on the bending behavior and crack propagation of Mg10GdxNd-T4 alloys has been presented. Various combinations of deformation and corrosion have been investigated. To meet the requirements of future applications, corrosion tests were done in Ringer-Acetate solution at 37 °C.

To improve ductility (accompanied with reducing dendritic microstructure) all three alloys studied (Mg10Gd, Mg10Gd1Nd and Mg10Gd2Nd) were solution heat treated. Alloying Nd to the binary Mg-10Gd alloy mainly improves tensile strength, dynamic modulus, hardness, flexural modulus and fracture strength under bending. Mg10Gd1Nd shows the lowest value in compression yield strength, but ultimate compression strength and compression strain in increasing with alloying Nd. The highest elongation at fracture under tension is also found in Mg10Gd1Nd. This gives the explanations for the highest fracture toughness for this alloy. Mg10Gd2Nd shows the highest fracture strength, but when the crack is propagating through the sample, mainly when passing the initial neutral axis, very high stress drops can be found. The slope and amount of stress dropping is dependent on the microstructure. When grains tend to twin crack propagation is hindered and often bound to branch off, which increases fracture toughness.

Pre-corrosion strongly reduces fracture bending strength explained by the notch effect of corrosion pits. Pre-bending accelerates corrosion due to the increase in dislocations and twins by plastic deformation (twinning assisted corrosion). Cracked samples show after corrosion exposure even undercutting pits, which reduces maximum bending stress after second bending. A correlation of crack path and twins has been found. Grains, which are strongly twinned (double and secondary twinning), hinder crack propagation. The crack follows twin boundaries and gets redirected by double and secondary twins.

After all, the complete picture would be given by combining corrosion and stress in Stress Corrosion Cracking. This study is under current investigation, on pin shaped samples as well on screws to have notch effects and to meet further applications. To use material with smaller grain sizes to improve mechanical properties, alloys have been extruded. However, by using the coarse grained alloys in this study the mechanisms of corrosion and crack initiation by twinning could be worked out better. Fine grained microstructure might reduce the deformation of twins.

Acknowledgement

The authors appreciate the support of J. Briesemeister (UAS Stralsund) in carrying out tree-point-bending tests. The assistance of H. Habeck (UAS Stralsund) during corrosion tests is greatly appreciated. G. Wiese (HZG) is thanked for sample preparation.

References

1. N. Hort, Y. Huang, D. Fechner, M. Störmer, C. Blawert, F. Witte, C. Vogt, H. Drücker, R. Willumeit, K. U. Kainer, F. Feyerabend, “Magnesium alloys as implant materials - Principles of property design for Mg-RE alloys,” *Acta Biomaterialia* 6 (2010), 1714-1725.
2. A.J. Thakur: The elements of fracture fixation, Elsevier 2007
3. M.M. Kaiser, G. Zachert, R. Wendlandt, R. Eggert, C. Stratmann, N. Gros, M. Schulze-Hessing, M. Rapp, “Increasing stability by pre-bending the nails in elastic stable intramedullary nailing,“ *Journal of Bone and Joint Surgery Series B* 94B (2012), 713-718.
4. B. S. Padekar, R.K. Singh Raman, V.S. Raja, L. Paul, “Stress corrosion cracking of a recent rare-earth containing magnesium alloy, EV31A, and a common Al-containing alloy, AZ91E,“ *Corrosion Science* 71 (2013), 1-9.
5. T. Zhang, Y. Shao, G. Meng, Z. Cui, F. Wang, “Corrosion of hot extrusion AZ91 magnesium alloy: I-relation between the microstructure and corrosion behavior,“ *Corrosion Science* 53 (2011), 1960–1968.
6. P. Maier, C. Mendis, G. Tober, N. Hort, “Tailoring properties of cast Mg10Gd by alloying Nd and heat treatment,” *Emerging Materials Research* 2 (2013), 1-10.
7. G. Chadha, J. Allison, J.W. Jones, “The role of microstructure on ductility of die-cast AM50 and AM60 magnesium alloys,” *Metallurgical and Materials Transactions A* 38 (2007), 286-297.
8. F.R. Elsayed, N. Hort, M.A. Salgado-Ordorica, K.U. Kainer, “Magnesium Permanent Mold Casting Optimization,” *Materials Science Forum* 690 (2011), 65-68.
9. M.A. Salgado-Ordorica, W. Punessen, S. Yi, J. Bohlen, K.U. Kainer, N. Hort, “Macrostructure evolution in directionally solidified Mg-RE alloys,” *Magnesium Technology 2011*, Editors: W. Sillekens, S.R. Agnew, N. Neelameggham, S.N. Mathaudhu, ISBN 978-1-11829-121-4 (2011), 113-118.
10. P. Maier, C. Mendis, G. Tober, J. Briesemeister, E. Minciel, N. Hort, “Bending strength and crack propagation in cast Mg10Gd influenced by corrosion,” *European Cells and Materials* 26 (2013), 23.
11. Q. Yu, J. Zhang Y. Jiang, Q. Li, “An experimental study on cyclic deformation and fatigue of extruded ZK60 magnesium alloy,“ *International Journal of Fatigue* 36 (2012), 47-58.
12. N.N. Aung, W. Zhou, “Effect of grain size and twins on corrosion behaviour of AZ31B magnesium alloy,“ *Corrosion Science* 52 (2010), 589–594.
13. G. Ben Hamu, D. Eliezer, L. Wagner, “The relation between severe plastic deformation microstructure and corrosion behaviour of AZ31 magnesium alloy,” *Journal of Alloys Compound* 468 (2009), 222–229.

Magnesium Technology 2014
Edited by: Martyn Alderman, Michele V. Manuel, Norbert Hort, and Neale R. Neelameggham
TMS (The Minerals, Metals & Materials Society), 2014

High Shear Deformation to Produce High Strength and Energy Absorption in Mg Alloys

Vineet V. Joshi[1], Saumyadeep Jana[1], Dongsheng Li[1], Hamid Garmestani[2], Eric Nyberg[1], Curt Lavender[1]
[1]Pacific Northwest National Laboratory, Richland WA 99354
[2]Georgia Tech, Atlanta, GA, 30332

Keywords: ICME, Materials Modeling, High Shear Deformation, Extrusion, Mg-Si alloys, ZK60.

Abstract

Magnesium alloys have the potential to reduce the mass of transportation systems however to fully realize the benefits it must be usable in more applications including those that require higher strength and ductility. It has been known that fine grain size in Mg alloys leads to high strength and ductility. However, the challenge is how to achieve this optimal microstructure in a cost effective way. This work has shown that by using optimized high shear deformation and second phase particles of Mg_2Si and Mg_xZnZr_y the energy absorption of the extrusions can exceed that of AA6061. The extrusion process under development described in this presentation appears to be scalable and cost effective. In addition to process development a novel modeling approach to understand the roles of strain and state-of-strain on particle fracture and grain size control has been developed.

Introduction

In recent times, magnesium and its alloys are being widely investigated for their high strength to weight ratio and have related potential applications in automotive, consumer electronics and in biodegradable stents[1-3]. In order to compete with the traditional and popular materials such as steel and aluminum alloys, the strength of the magnesium alloys needs to be enhanced, corrosion resistance and formability need to be improved while maintaining low-cost in the final part [4]. A more rational approach to address this challenge is to use integrated computational materials engineering (ICME); wherein specific microstructure and desired properties are provided by the modeling and is later achieved by carefully selecting/ developing a process that will yield the desired microstructure and properties[4, 5]. For the current work the development of low cost magnesium alloys for automotive applications were sought and the applications included bumper beams, crush tips, intrusion beams, etc. whose primary requirement for these structures is high strength under both compression and tension. It is well known that the magnesium alloys are low symmetry materials with hexagonal closed pack structure (HCP) that leads to tension-compression yield strength asymmetry, thus preventing its application where high compressive forces are needed or where simultaneous tension-compression loads are applied[6-9]. In order to address all these challenges a computational method was used to predict the microstructure, texture and the mechanical properties and a novel extrusion technique was used to develop the desired microstructure and properties.
The first part of the paper discusses the use of ICME that was used to define the criterion for mechanical properties, grain size and precipitate size. Only significant results will be discussed here whereas the details of which can be found elsewhere[6, 10]. The second part describes the development of a novel extrusion process that was used to accomplish the properties defined by the computational techniques.

Defining the Grain Size and Mechanical Properties using ICME

Strengthening of the magnesium alloys is usually performed by grain refinement or by alloying additions. The current authors[6] and others[8, 11] have also demonstrated that the yield asymmetry i.e the ratio of compressive yield stress and tensile yield stress (CYS/TYS) is drastically improved as the grain size decreases (Figure 1). It was demonstrated that as the grain size is decreased, the twinning in Mg is suppressed and compressive yield strengths are increased. Conventionally processed Mg alloys have a compressive strength normally 70 percent that of the tensile strength, resulting in buckling during bending and compression. In addition, a significant increase in ductility can be expected when the grain size decreases. Therefore the fine-grained alloy should be expected to absorb more energy, which is critical to the current applications under consideration.

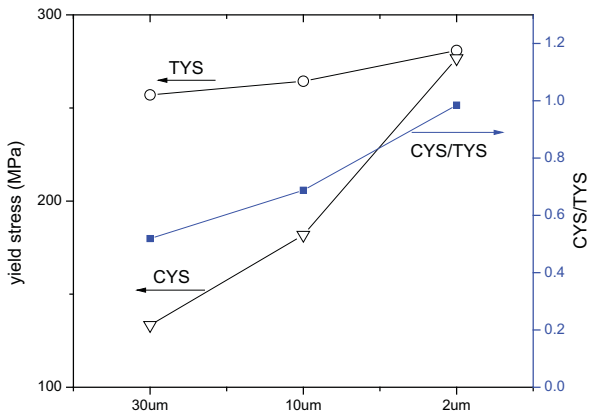


Figure 1. Tension and compression yield stress and CYS/TYS along rolling direction for rolled AZ31 sheets with different grain sizes of 30 μm, 10 μm and 2 μm, respectively[6].

Grain refinement is usually achieved by thermomechanical processing, alloying-element additions or by use of second phase precipitates [9, 12, 13]. Thermomechanical processing techniques apart from grain refinement can also be used engineer the dislocation density, grain boundary and texture to further improve the strength of the material and for removing the yield asymmetry. Despite the advantages offered by plastic deformation to refine the grains and eliminate yield anisotropy the techniques being used are usually time consuming and costly or are used in conjunction with the other conventional techniques. As compared to these strengthening mechanisms, second phase particle strengthening is a popular method in improving mechanical performance, such as hardness, yield strength, and asymmetry,

due to its affordability and efficiency. There are two types of second particles strengthening: 1) dispersion strengthening, where insoluble particles are incoherent and 2) precipitation strengthening (also called "aging"), where precipitates are produced in a solid-state reaction during thermal treatment from a metastable solution. Generally, second phase particles are the most potent strengthening agent in practical high-strength engineering materials[5, 6, 10]. From the physics perspective, second phase particle strengthening comes from two areas: one contributed by the high strength of the particles and the other from the impediment of dislocation motion with the same effect on grain refinement. The refinement of the grain can either be performed with alloying addition or processing the alloy to break these structures and finely disperse them in the alloy matrix. The advantage with latter will be the combination of plastic deformation along with grain size refinement and locking the precipitates along the grain boundaries by Zener pinning, thus avoid grain growth during any recrystallization mechanism during processing.

In order to understand the effect of precipitate size on the grain size and the mechanical properties was simulated quantitatively by coupling a stochastic second phase grain refinement model and a modified polycrystalline crystal viscoplasticity φ-model. The models were developed assuming dispersion of hard intermetallics having aspect ratio 1:2 in an unalloyed magnesium matrix. The details of which can be found elsewhere[10], however significant results will be discussed here. Using the stochastic second phase grain refinement model, grain size was quantitatively determined from the precipitate size and volume fraction as shown in Figure 2. It was determined that if the precipitate shape and size are kept constant, grain size decreases with increasing precipitate volume fraction. If the precipitate volume fraction was kept constant, grain size decreases with decreasing precipitate size during precipitate refinement. The stochastic effect with length scale was also studied. The grain size variance was large when the precipitate volume fraction was low and the precipitate size was large. Yield strength in different directions (yield asymmetry), and deformation behavior are calculated from the modified φ-model and the results are shown in Figures 3a and b. The mechanical behavior of magnesium alloys was also improved by precipitate refinement. Yield strengths and asymmetry increase with decreasing grain size and contributions from increasing precipitate volume fraction or decreasing precipitate size. The evolution of yield strengths and asymmetry with precipitate volume fraction and size has been quantitatively simulated by coupling the stochastic grain refinement model and modified φ-model. This provides guidance for second phase strengthening via precipitate engineering, both for precipitate content control and precipitate refinement.

With these tools in hand selection of alloys was primarily decided based on the secondary precipitate form, shape and highest plausible strength attainable. Strengthening using second phase particle currently is being employed using rare earth elements. Despite the advantages the cost of these alloys is disruptive and thus alternatives are being sought[14]. Aluminum Zinc (AZ), Zinc-zirconium (ZK) based magnesium alloys and magnesium silicon (Mg-Si) alloys do provide alternatives to the current alloy system. These alloys used in extruded or cast conditions usually have large grain sizes or in the case of Mg-Si alloys have large brittle Chinese script or blocky Mg_2Si precipitates. These large grains and phases are usually associated with lowering of the strength and causing anisotropy in the material. In order to combat this fine dispersion of precipitates would eliminate the anisotropy and refine the grain size.

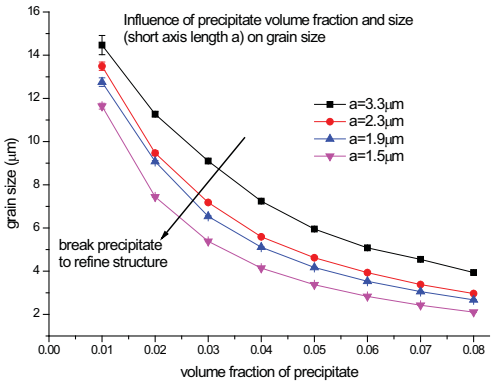
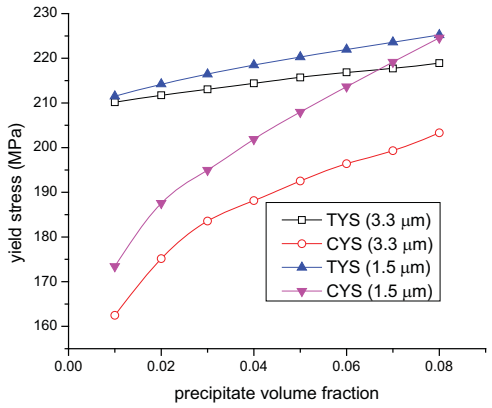
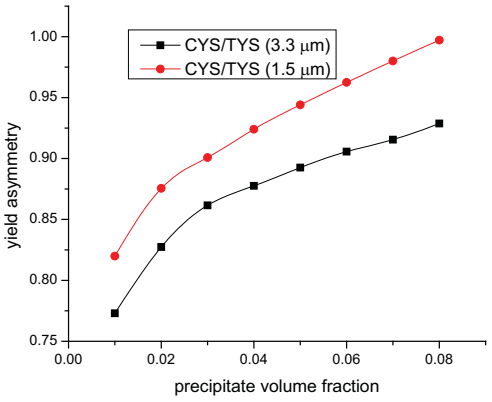


Figure 2. Evolution of grain size with precipitate volume fraction and size, from [10]



(a)



(b)

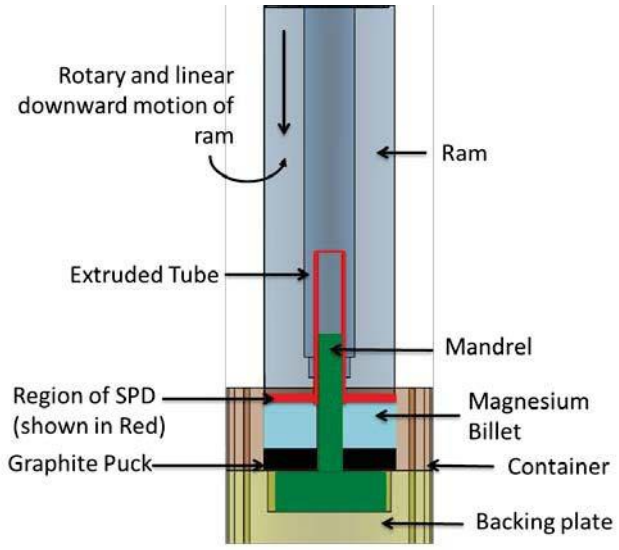
Figure 3. Evolution of (a) yield strengths and (b) yield asymmetry with precipitate volume fraction when the precipitate size is kept constant, from [10]

Process Selection & Development

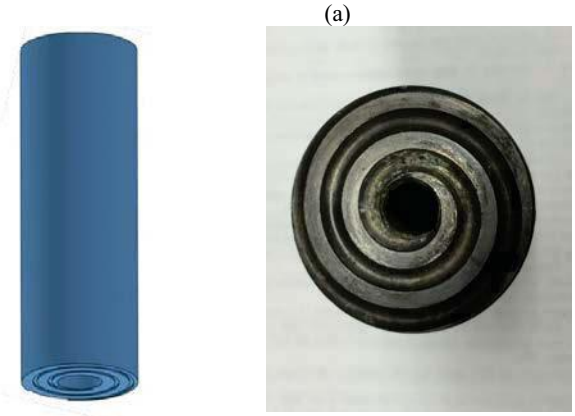
It has been demonstrated that the application of magnesium alloys in bumper beams, crush tips and intrusion beams would result in significant vehicle weight savings. However, to increase the structural use of Mg alloys, development of cost-effective bulk metal forming methods are necessary. In this regard, extrusion technique, which is typically used to produce cylindrical bars or hollow tubes or even with complex cross-sections at a fairly rapid speed, is an important metal-forming method to investigate. Several researchers have studied the role of different process variables during extrusion of Mg alloys[9, 15-17]. It is to be noted that in all the above mentioned studies, extrusion experiments were conducted at elevated temperatures, since Mg alloys suffer from limited room temperature ductility due to limited slip systems. In order to control the grain size of the extruded material the feed rates are kept to a low value or need to be followed by severe plastic deformation processes to refine the grain size. These techniques have shown significant promise over the past several years but are usually associated with high costs.[12, 18]

Lately, there have been a few reports on the development of novel extrusion techniques that rely on the rotational motion of the ram face to generate heat through friction/deformation at the ram/billet interface.[19-21] Reynolds et. al.[19, 21] demonstrated the consolidation of aluminum alloy chips to produce wires via a technique called friction extrusion. The technique was similar to indirect extrusion but used a rotating ram. The face of the ram was grooved with a helical pattern to assist flow of the material into the ram exit. It was observed that the grain size increased with increase in the rotation rate of the ram, and attained a maximum grain size of 14 μm or less. At rotation rates above 250 rev/min, the temperature at the ram/billet interface increased and resulted in dynamic recrystallization, causing grain coarsening. At a low extrusion power, formation of equiaxed grains of size less than 5 μm was observed. In a similar approach, Fadi Abu-Farha[20] reported production of fine-grained tubes via the concept of friction stir back extrusion (FSBE). In this work, a rotating ram was plunged into a solid aluminum round billet contained inside the ram chamber. Application of the forging load forced processed material to flow radially outwards and move up through the gap between the ram chamber and the rotating ram, forming a hollow tube, with significant grain refinement and no volumetric defect. These techniques not only demonstrated grain refinement but in case of the systems/ alloys being considered would significantly help in breaking the second phase precipitates to a fine structure and help further in grain refinement and locking the grain size to a minimum.

The current technique being demonstrated in this paper is similar to one developed by Reynolds et. al.[19, 21] However, instead of a solid cross-section, we have been able to extrude a hollow tube by the use of a mandrel. The current technique of torsional shear assisted indirect extrusion process (SAIE) uses a rotating ram as opposed to the axially fed ram used in the conventional indirect extrusion process. The ram face contains scroll features in a spiral manner. When the rotating ram face comes in contact with the solid billet underneath and a forging load is applied, significant heating occurs due to friction, thus softening the underlying billet material. The combined action of the forging load together with the rotating action of the ram face, force the underlying material to flow plastically. The scroll features on the ram face are believed to help in the material flow[21]. The ram is turned in such a way that scroll features rotate towards the center of the ram, and, thus material is fed continuously to the central hollow inside the ram. The deformation process adds additional heat to the process. Significantly low ram load has been noted in this process compared to conventional extrusion process, which is possibly related to the rotational motion of the ram. The mandrel in the center of the ram helps in forming of the tubes.



(a)



(b)

Figure 4: (a) Diagram of the shear assisted indirect extrusion (SAIE) process and (b) shows the scrolls on the face of the ram which assists in heating and flow of material.

Experimental Procedure

The SAIE has been carried out in an existing Transformation Technology Inc. LS2-2.5 friction stir welding (FSW) machine present at the Pacific Northwest National Laboratory. The tests were performed in a position-controlled mode. The FSW machine is equipped with a load cell transducers that has the ability to log the force data along the x, y and z direction. The motor in the FSW machine is an 80104M Baldor Inc. 30 kW Vector driven AC induction motor, which can provide speeds from 25 to 1500 RPM. For the current set of experiments the ram, ram chamber and the mandrel were fabricated using a H13 tool steel and heat treated and tempered to achieve a hardness of HRC 50 combined with significant toughness. The ram had an outer diameter (OD) of

31.75 mm, and an inner diameter (ID) of 7.5 mm. A slight taper was given to the ID to allow relief, if any, in the material upon forming. The mandrel was 6 mm in diameter, and, thus forms a 0.75 mm thick tube. The scrolls on the ram face were 0.5 mm in depth and had a pitch of 4 mm with a total of 2.25 turns.

For the present work, the starting material was in the form of an extruded ZK60-T5 (henceforth referred as ZK60) rod, 76.2 mm (3") in diameter and 3.5 m in length, obtained from MetalMart International Inc., California, USA and a Mg-2 wt% Si (Mg-2Si) alloy was book cast to 30 mm in thickness. These materials were further machined down to form a puck 31.75 mm in diameter and 18 mm in height with a center-hole approximately 6 mm in diameter to accommodate the mandrel. A graphite puck with similar inner and outer diameter, and~ 2 mm in height was placed between the machined billet and the base plate, to eliminate any type of bonding between and the base plate during the actual extrusion process. The assembly containing the ram chamber, backing plate, mandrel, billet and the graphite puck was rigidly clamped down on the FSW machine bed. The ram was clamped to the overhead rotating spindle. The ram was then carefully positioned atop the assembly such that the centerline of the mandrel and the ram aligned with each other. After the final alignment, the ram was lowered to bring the ram face in contact with the billet located inside the chamber/ container. A schematic of the process is presented in Fig. 1. The area on the billet that undergoes severe plastic deformation (SPD) and thus forms the tube has been marked as well. The current indirection extrusion trial used a spindle RPM of 500, and an axial feed rate of 0.06 mm/s for the ZK60 alloy and 0.6 mm/s feed rate for the Mg-2Si alloy. This resulted in an extrusion ratio of 47:1 and an extrusion rate of 3 mm/s and 30 mm/s respectively.

Results and Discussion

Figures 5 shows the plots of ram plunge depth as a function of load and spindle torque respectively. It was observed that as the ram plunges into the puck, a breakthrough pressure and torque is required to achieve steady state conditions similar to direct extrusion. The response in vertical load build-up as a function of plunge depth during this process is similar to that observed during plunging stage of the FSW process. The initially cold billet material offers resistance to flow, and hence high load is noted. As the material heats up due to friction/deformation at the ram/billet interface, it starts flowing, thus lowering the process load considerably. It is interesting to note the presence of two peaks in the load-depth plot. It is likely that the first peak corresponds to initial resistance of the cold billet, while the second one corresponds to frictional resistance at the ram throat as the extrudate tries to move up through the gap between mandrel and the inner ram wall. However, it should be noted that the process load required for current technique is considerably lower than the conventional indirect extrusion technique. The peak pressure in this case was approximately 90% less whereas the operating pressure was approximately 95% less than the one required in indirect extrusion of the similar material.

The formed tubes and a cross-sectional image (only half section) of the billet and the extruded tube is shown in Fig. 6. We were able to extrude 5" tall tube at the end of this process. The tube was homogenous with no porosity and had a uniform cross section with an OD of 7.45 ± 0.02 mm and an ID of 5.84 ± 0.03 mm. The flow behavior in the underlying billet is shown in Fig. 6b. Formation of a basin shaped region near the top surface of the billet can be clearly noted in this micrograph. A closer observation reveals that the original column-like grain structure of the as-received material has ceased to exist in this basin shaped region. Further examination of the micrograph showed the presence of a flow pattern, as indicated by the white and the red arrows. It is likely that the material present on the top layer softened as the billet heated up. Under the combined action of ram rotation and the extrusion pressure, this softened layer of material tried to flow downwards and towards the center of the ram. As it reaches the central region, it is forced to move upwards since the material at bottom layer of the billet is relatively cooler, and hence stronger. Finally, the softened material extrudes through the gap between the inner ram wall and the mandrel. Presence of scroll features on the ram face facilitated in this material movement.

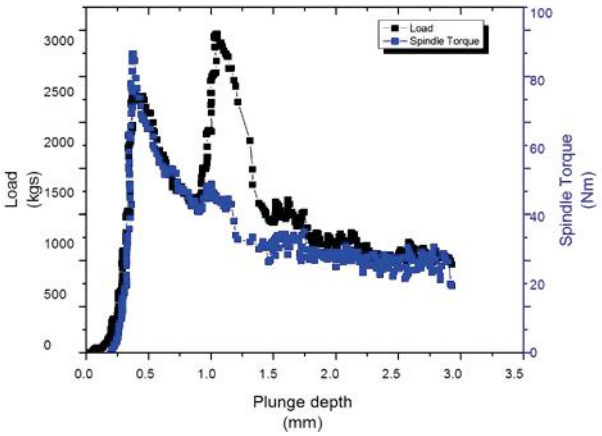
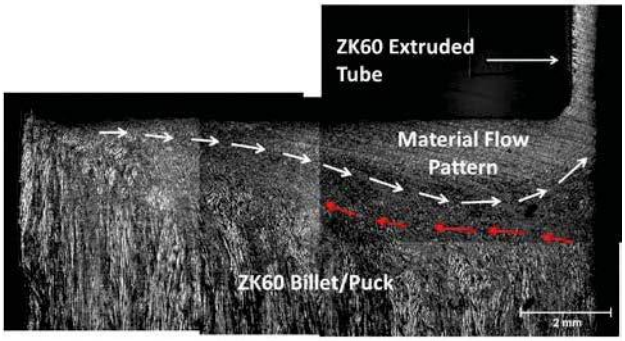


Figure 5. Extrusion load and torque on the ram during the extrusion of ZK60 as a function of ram plunge depth.



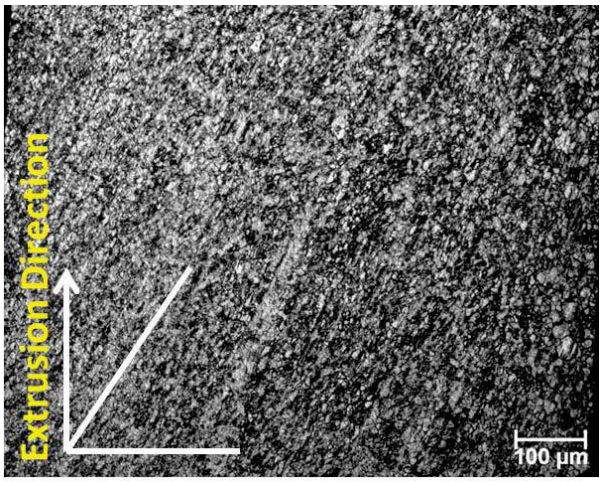
(a)



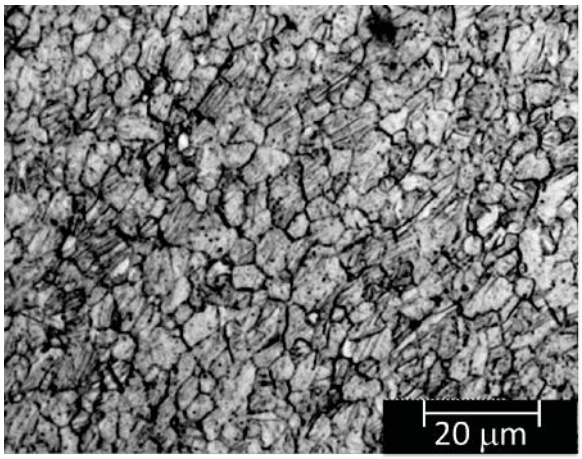
(b)

Figure 6. (a) Formed tube, showing the uniform cross-section and defect free surface and (b) montage showing the possible material flow pattern in the puck/billet during the formation of the tube.

The cross sectional analysis of the extruded tube revealed the grains to be oriented ~ 30° to the extrusion axis, indicating a spiral flow pattern. Figures 4 a, b and c are the microstructures of the extruded ZK-60 sample, near the billet, approximately 2" from the billet and approximately 4.5" from the billet respectively. The grain size was the finest near the ram-face/billet interface and had a grain size of ~ 2-5 μm and was severely twinned. The twins were observed in almost 60% of the grains. The grain structure was uniform from the outer diameter to the inner diameter. The formation of the twinned structure is beneficial in Mg alloys and helps in improving the strength and ductility of these alloys. The grain size is noted have increased by almost 50% along the length of the extrudate (Fig. 7a, b). However, the twinned structure was retained. The grain size at the outer edge was slightly smaller than the inner edge indicating recrystallization and differential cooling rates.



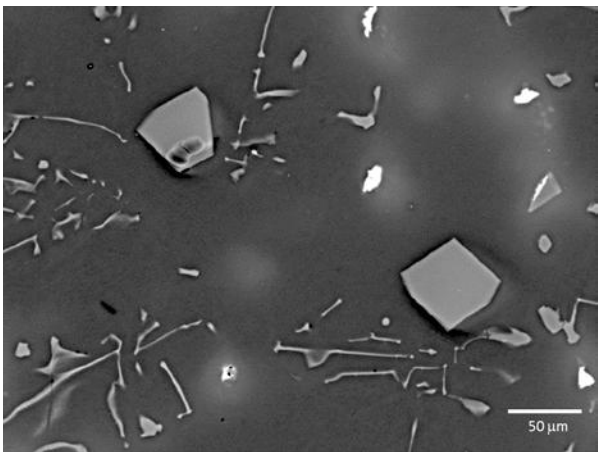
(a)



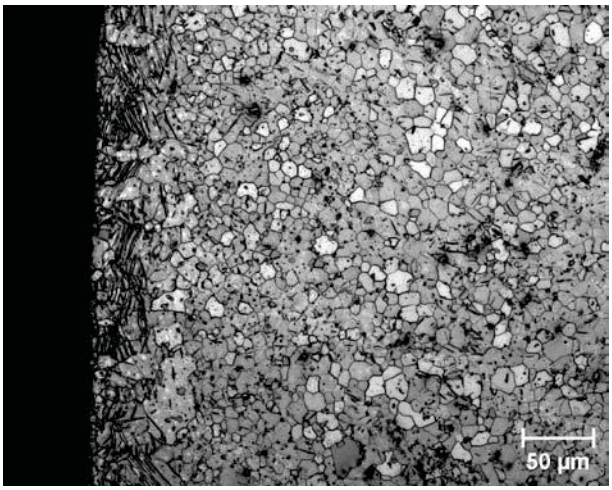
(b)

Figure 7. Optical image showing the ZK60 tube longitudinal cross-section at the central region of formed tube, image magnifications at (a) 50X and (b) 500X

Similar to the ZK60 alloy the Mg-2Si alloy, which was extruded at higher rate, displayed processing trends similar to the ZK60 alloy. Mg-2wt Si alloy contains Chinese script eutectic Mg_2Si along with blocky intermetallic Mg_2Si in a magnesium matrix (Figure 8a). In this case the grain size of the as-cast sample was between 150-200 μm. Upon processing these Mg_2Si precipitates were finely dispersed in the metal matrix and the grain size decreased significantly to less than 10 μm (Figure 8b). The rotary motion of the ram might have helped in breaking the intermetallics similar to the friction stir welding process. The scrolls may have further helped in this deformation of the intermetallics, however more studies need to be conducted to study the same phenomenon. Slight twining was observed on the outer edge of the sample, whereas the interior grains were fairly equiaxed with no twinning. Similar to ZK60 it was observed that the grain size increases from the ram-billet interface to the top of the tube. However this can be controlled very easily by using a coolant.



(a)



(b)

Figure 8. (a) Backscattered electron image of as-cast Mg-2wt% Si showing blocky and Chinese script Mg_2Si particles and (b) is the optical image of the longitudinal cross-section after processing cast structure using SAIE shows dispersion of and breakage of the blocky and Chinese script intermetallic in the magnesium matrix along with significant grain refinement.

The current process demonstrated pressures significantly lower than the ones used currently to process magnesium alloys. Preheating of the billets may not be needed. The scroll pattern is responsible to directly change the orientation of the grain alignment and hence the texture (not shown here). All this provides significant opportunities towards cost reduction of the

end product without compromising the properties and at the same time tailoring the microstructure to the desired properties.

Conclusions

The current paper discusses the critical factors necessary to refine grain size and remove the yield anisotropy in the material. Based on this computational materials modeling knowledge a targeted grain size and precipitate size was sought and achieved via a novel shear assisted extrusion process. The current SAIE technique demonstrated shows significant promise with regards to tailoring the microstructure and is readily scalable to produce large parts relevant to automotive applications.

Acknowledgements

The authors would like to thank the U. S. Department of Energy, Office of Fuel Cell and Vehicle Technologies (DOE/OFCVT) Program for the financial support provided for this project. Pacific Northwest National Laboratory is operated by Battelle Memorial Institute for the United States Department of Energy under Contract DE-AC06-76RLO1830.

References

[1] G. Fang, W.-j. Ai, S. Leeflang, J. Duszczyk, J. Zhou, Materials Science and Engineering: C, 33 (2013) 3481-3488.
[2] Q. Ge, D. Dellasega, A.G. Demir, M. Vedani, Acta Biomaterialia.
[3] P. Minárik, R. Král, M. Janeček, Applied Surface Science.
[4] W. Joost, JOM, 64 (2012) 1032-1038.
[5] D.S. Li, H. Garmestani, S. Ahzi, Acta Materialia, 55 (2007) 647-654.
[6] D. Li, V. Joshi, C. Lavender, M. Khaleel, S. Ahzi, Computational Materials Science, 79 (2013) 448-455.
[7] J. Hirsch, T. Al-Samman, Acta Materialia, 61 (2013) 818-843.
[8] S. Graff, W. Brocks, D. Steglich, International Journal of Plasticity, 23 (2007) 1957-1978.
[9] E.F. Emley, Principles of Magneisum Technology, Pergamon Press Ltd., Oxford, 1966.
[10] C. Lavender, D. Li, J. P. Choi, V. V. Joshi, A. Rohatgi, and E Nyberg, DOE Annual Merit review, May, 2013, Availble online at http://www4.eere.energy.gov/vehiclesandfuels/resources/merit-review/sites/default/files/lm056_lavender_2013_o.pdf.
[11] S.M. Yin, C.H. Wang, Y.D. Diao, S.D. Wu, S.X. Li, Journal of Materials Science & Technology, 27 (2011) 29-34.
[12] Y. Estrin, A. Vinogradov, Acta Materialia, 61 (2013) 782-817.
[13] H. Somekawa, C.A. Schuh, Acta Materialia, 59 (2011) 7554-7563.
[14] J.-F. Nie, Metall and Mat Trans A, 43 (2012) 3891-3939.
[15] G. Liu, J. Zhou, J. Duszczyk, Journal of Materials Processing Technology, 186 (2007) 191-199.
[16] F.A. Slooff, J. Zhou, J. Duszczyk, L. Katgerman, Journal of Materials Processing Technology, 211 (2011) 1241-1246.
[17] L. Li, J. Zhou, J. Duszczyk, Journal of Materials Processing Technology, 172 (2006) 372-380.
[18] D. Orlov, G. Raab, T.T. Lamark, M. Popov, Y. Estrin, Acta Materialia, 59 (2011) 375-385.
[19] W. Tang, A.P. Reynolds, Journal of Materials Processing Technology, 210 (2010) 2231-2237.
[20] F. Abu-Farha, Scripta Materialia, 66 (2012) 615-618.
[21] X. Li, W. Tang, A.P. Reynolds, Material Flow and Texture in Friction Extruded Wire, Friction Stir Welding and Processing VII, John Wiley & Sons, Inc., 2013, pp. 339-347.

Magnesium Technology 2014
Edited by: Martyn Alderman, Michele V. Manuel, Norbert Hort, and Neale R. Neelameggham
TMS (The Minerals, Metals & Materials Society), 2014

AS-CAST MICROSTRUCTURE AND TEXTURE OF TWIN-ROLL CAST AZ31

Mohsen Masoumi, Faramarz Zarandi, Mihriban O. Pekguleryuz

McGill University, Mining and Materials Engineering,
3610 University, Montreal, QC, Canada H3A 2B2

Keywords: Twin-roll casting, Magnesium, Microstructure, Texture

Abstract

In this study, the microstructure and texture of twin roll cast (TRC) AZ31 (Mg-3wt.%Al-1wt.%Zn) alloy has been investigated. The structure of the as-cast TRC AZ31 was dendritic containing both columnar and equiaxed grains. Second phase particles, Al-Mn and Mg-Al-Zn, were distributed evenly in matrix. The macro-texture analysis shows that as-received TRC AZ31 had a basal texture. The micro-texture analysis by electron-back-scattered diffraction (EBSD) revealed that the large grains were mostly basal, however the smaller grains tended to have varying orientations.

Introduction

Magnesium is the lightest structural metal with a density of 1.74g/cm^3; 35% and over 400% lighter than Al and iron respectively [1]. To date, the use of Mg in cars has been limited to die cast parts, in application, such as steering column upper brackets, steering wheel cores, engine head cover, disk wheels, brake pedal brackets, meter panel housings, seat frames, air bag plates, oil pans, instrument panel reinforcement, transmission cases and engine block [2, 3]. Application of Mg in automotive body panel, and closure, has a great potential for further weight reduction [4]. In general, the automotive body largely consists of sheet metal parts and comprises almost 25% vehicle weight. Due to several heating and rolling processes, Mg sheet production by conventional process is relatively costly [4], which is an impediment to its wider use [5]. Twin-roll casting process produces a sheet with thickness less than 6mm, directly from molten metal [6]. In comparison to conventional sheet production, twin roll casting has lower processing costs (1/3 to 1/2), lower operating /investment costs (1/4 to 1/3), and reduced space and labour requirements [7].

Despite the interest in TRC AZ31, which is available on a limited scale globally, little information exists on its microstructure and the texture. TRC which combines casting and in-situ warm rolling produces a unique combination of cast and deformed structure. This paper studies the as-cast microstructure and texture of the TRC AZ31 sheet produced on an industrial scale. This is part of a larger investigation which aims at optimizing the thermomechanical processing of TRC AZ31 for use in automotive applications and at developing alternative Mg alloys for the TRC process [8-11].

Experimental procedure

A TRC AZ31B sheet with a thickness of 6mm and chemical composition of Mg-2.96wt%Al-0.87wt%Zn-0.36wt%Mn was investigated. The metallographic specimens were taken from rolling direction (RD) and normal direction (ND) plane, prepared by grinding on SiC abrasive papers to 1200 grit followed by polishing successively with 6μm, 3μm, and 1μm diamond paste. The specimens were chemically etched with acetic-picral (10ml acetic acid, 4.2 g picric acid, 10 ml H2o, 70 ml ethanol (95%)) for optical microscopy examination. Secondary dendrite arm spacing (SDAS) was measured using the mean-intercept method. The detailed features of the microstructure were characterized With SEM. X-ray elemental distribution was obtained in a JEOL 8900 electron probe micro-analysis (EPMA) SEM with a resolution of 70 nm.

For texture analysis, the specimen surface was ground until 10% of the sheet thickness was removed. The ground surface was polished with 1 μm diamond paste, and then etched for 120 s in 10% nital in order to remove surface strain. X-ray texture analysis was performed using a Siemens D-500 X-ray diffractometer. Incomplete pole figures of (0 0 0 2), {10-10} and {10-11} were recorded, and the orientation distribution function (ODF) was constructed using TexTools, a texture analysis software. Recalculated pole figures were derived from the ODFs.

The grain orientation was also studied using the electron back scattered diffraction (EBSD) method in a SEM at 20 kV

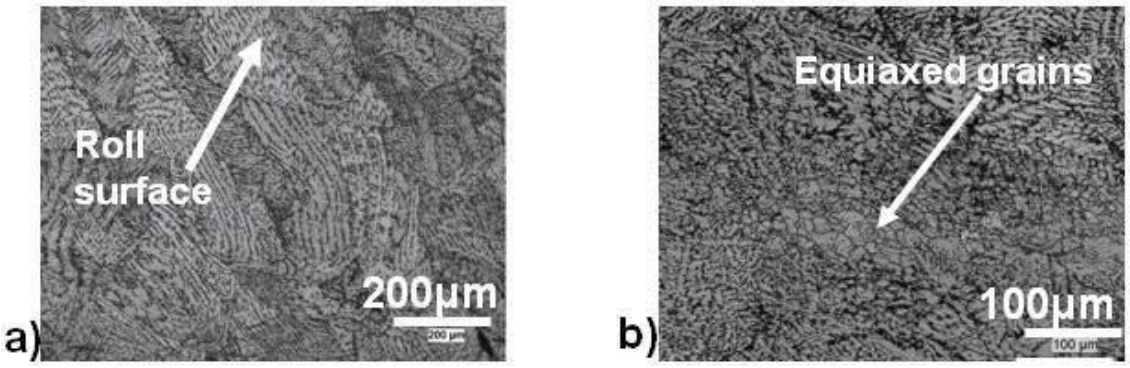


Fig. 1 As-cast microstructure of twin-roll cast AZ31 (a) edge (b) mid-thickness.

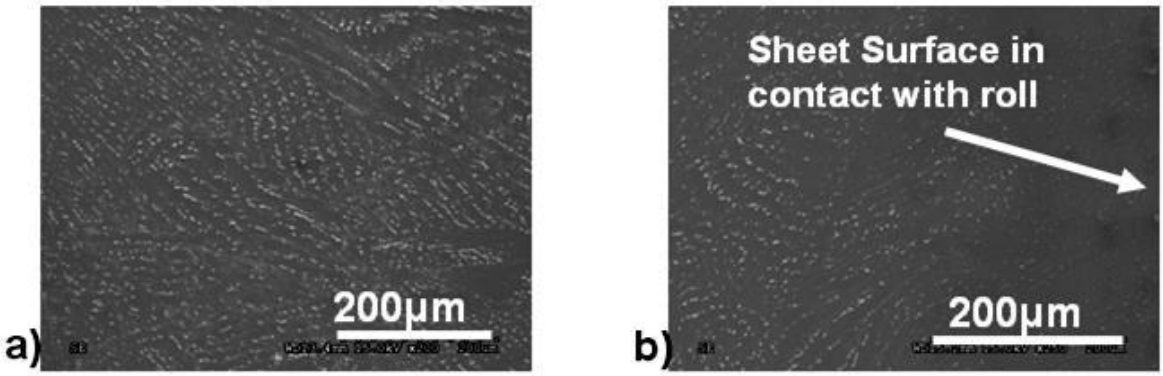


Fig. 2 Distribution of second phases in the as-received TRC AZ31 sheet; (a) away from the sheet surface and (b) close to the sheet surface.

accelerating voltage and 70° tilt angle. EBSD specimens, after polishing with 1 µm diamond slurry, were further polished using 0.05µm colloidal-silica, and etched in a solution of 10 ml HNO_3, 30 ml acetic acid, 40 ml H_2O and 120 ml ethanol for about 10 seconds.

Results and discussions

I. Microstructure of As-cast TRC

The thickness microstructure of as-received twin-roll cast sheet, shown in Fig. 1, reveals a dendritic structure with coarse grains. Due to high cooling rate and directional heat-transfer, columnar grains are seen which have grown against the heat extraction direction (where the solidifying material was in contact with the cold casting rolls) under a reduced temperature gradient. In addition to the large columnar grains, equiaxed grains (Fig. 1b) with average grain size of 16µm were also observed in the mid-thickness of the sheet, which formed as a result of compositional segregation (constitutional undercooling).

The secondary-dendrite arm spacing (SDAS) was measured as 7.5 µm and 10.3 µm at the edge and mid-thickness of sheet, respectively. Accordingly, the cooling rates (CR) of 325 °C/s and 150 °C/s were estimated for the edge and mid-thickness using the relationship between SDAS and CR [12];

$$SDAS\ (\mu m) = 85.15(CR)^{-0.42} \quad (1)$$

These cooling rates are significantly higher than those commonly observed for DC ingot (about ~10 K/s)[13] . Therefore, the second phase particles are finer and distributed more evenly, Fig. 2. It was also noticed that at the edge area, a thickness of about 150-200 µm underneath the surface is poor of the second phase, Fig. 2b. It is well known that at very fast cooling rates, the rejection of solute atoms from the solid into the interface between the solid and liquid phases is restricted and the eutectic transformation is restrained so that a supersaturated single-phase solid solution forms and the amount of eutectic phase is reduced.

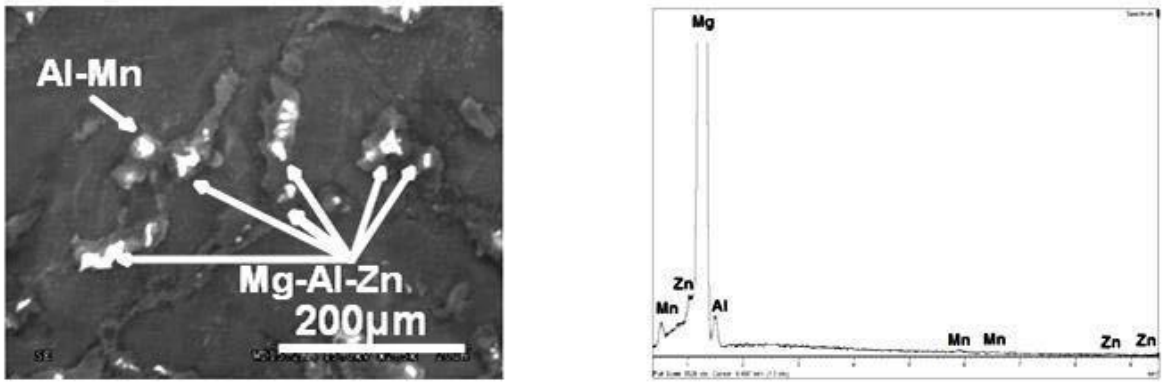


Fig. 3 SEM micrograph showing the second phase particles and EDS spectrum of the matrix in the as-received TRC AZ31 sheet.

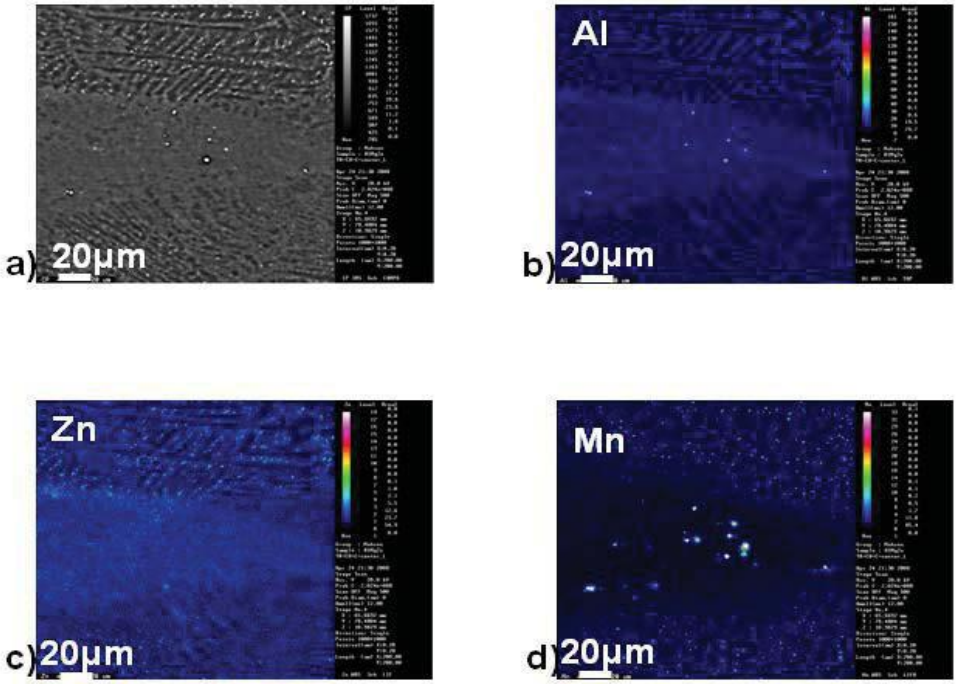


Fig. 4 (a) Centerline segregation in as-cast sheet and EPMA (b) Al (c) Zn and (d) Mn.

EDS analysis, Fig 3, indicates that the matrix is α-Mg (Mg-Al-Zn-Mn solid solution) and there are two types of particles; some are composed of Mg, Al, and Zn (presumably $(Al,Zn)_{49}Mg_{32}$ phase [14]) and the rest contain Al and Mn, which could be a mixture of $Al_{11}Mn_4$, Al_8Mn_5, Al_9Mn_{11} and β-Mn(Al) intermetallics [15].

The EPMA results revealed some centerline segregation, which is rich in Al and Zn with a distribution of rather coarse Al-Mn intermetallics (the region with higher element percent, is seen brighter in Fig. 4). However, no segregation was observed in the area close to the sheet surface. This type of macrosegregation is due to non-equilibrium solidification, and also attributed to squeezing backwards of solute rich liquid towards the sump, caused by the rolling action.

In order to compare the twin-roll cast microstructure with that of DC casting, a cylinder with a diameter and height of 30mm and 60mm was cast in a graphite die at a cooling rate close to that of direct-chill (DC) ingot casting, i.e. 9.5 ^{o}C/s (the DC ingot is used in the conventional process of Mg sheet production) [13]. For DC cast the metallographic sample, were taken from a location close to the thermocouple tip. Figure 5 shows the

microstructure of slow cooled AZ31.

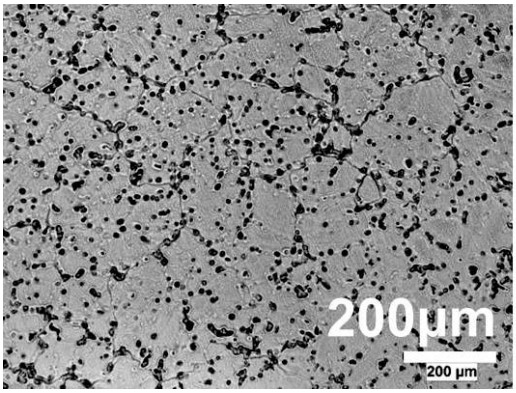


Fig. 5 as-cast microstructure of simulated DC AZ31

The area fraction of the second phases, f_{sp}, is 0.12 in the TRC AZ31 sheet, compared to 0.06 usually observed in a DC casting. The average size of second-phase particles in the as-received TRC AZ31 sheet is 1 µm, compared to 2.7 µm in the DC casting. The phenomenon of an increase in f_{sp} with an increase in CR is attributed to Scheil non-equilibrium freezing which lowers the solute in the solid-solution phase and increases the amount of the secondary phases. At low CR (close to equilibrium) the back diffusion in the solid occurs and, as a result, the eutectic-phase fraction decreases. At much higher CR, the rejection of solute atoms from solid into the interface between the solid and liquid phases reduces and the eutectic transformation is restrained so that a supersaturated single-phase solid solution forms. Between these two conditions, the Scheil non-equilibrium freezing mode prevails, where back-diffusion of the solute into the solid is limited (formation of an "undersaturated" solid-solution) while high solute rejection into the liquid occurs. This leads to higher-than-equilibrium amount of second phases [12, 16].

II. Texture of as-cast TRC

Figure 6 show (0001) pole figures taken from the surface of the as-cast twin roll sheet. It can be seen that most of the crystals are orientated with their basal planes parallel to the casting direction. However, there are some crystals with their basal planes tilted by about 60° across the casting direction. This texture is similar to the texture of hot roll AZ31 sheet where a strong basal texture prevails on the sheet surface [17, 18].

The presence of a basal texture in the as-received TRC AZ31 sheet can be either a deformation texture (due to the rolling

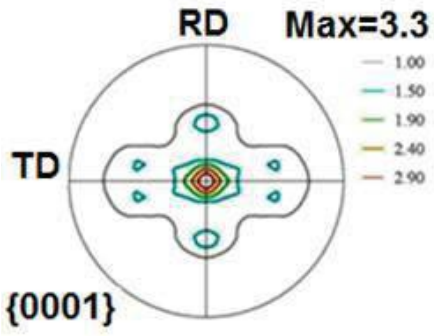


Fig. 6 texture pole figure of twin roll magnesium sheet in as cast condition (a) surface, (b) mid-thickness**.**

associated in the TRC process) or a casting texture (due to the directional growth of columnar grains). In order to verify this, A 4mm thick plate was cast in a vertical copper die at a cooling rate close to that experienced during the TRC process, i.e.~185 °C/s. This casting is referred to as 'quasi-TRC plate'. The microstructure and texture of the quasi-TRC plate was studied. The thickness microstructure of the plate-cast AZ31 comprises columnar grains grown against the die surface (Fig. 7a) and, in this respect; it is similar to the microstructure observed in the as-received TRC AZ31 sheet (Fig. 1). The SDAS is ~9.5 µm which corresponds to the range of the cooling rates experienced in the TRC process. However, in contrast to the as-received TRC AZ31 sheet, the prismatic planes $\{1\bar{1}00\}$, and not the basal planes $\{0001\}$, are inclined toward the plate surface in the quasi-TRC plate, as illustrated by the pole figures in Fig. 7b. Since no rolling deformation was associated with the production of the quasi-TRC plate, it is inferred that the development of basal texture in the as-received TRC AZ31 sheet is a result of the in-situ rolling deformation applied by the casting rolls.

EBSD texture analysis was also carried out on the surface of the as-received samples (RD-TD plane; As shown in Fig. 8., the large grains are mostly basal, however, the smaller grains tend to have random orientation.

4. Conclusions

1. As-cast TRC AZ31 sheet is characterized mainly by dendritic large columnar grains; however, small grains are also seen near the sheet edge and in the mid-thickness area. Centerline segregation of Al, Zn and Mn is also observed.

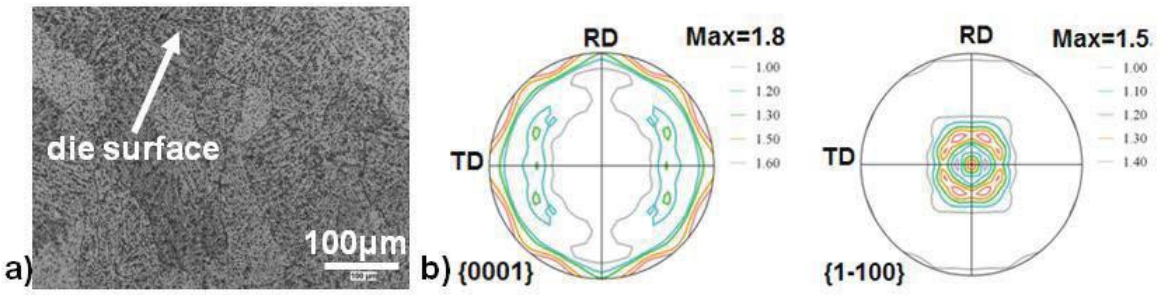


Fig. 7 The Quasi-TRC plate; a) thickness microstructure, b) surface texture (heat transfer axis is parallel to ND in this figure and RD-TD plane is the plate surface).

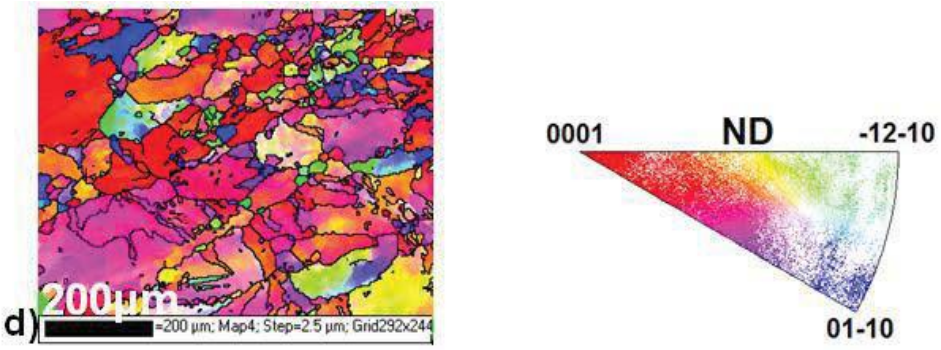


Fig. 8 EBSD map from the RD-TD plane of the as-received TRC AZ31 sheet.

2. The cooling rate near the sheet edge (surface) is at rapid solidification rates (325 ^{o}C/s), while the mid-thickness has solidified in Scheil solidification mode (150 ^{o}C/s). As a result, the surface is depleted of the second phases due to the solute supersaturation while the amount of second phases in the mid-thickness is higher than the equilibrium amount.
3. The basal texture prevails in the as-received TRC sheet due to the rolling deformation applied during the TRC process. It seems the large grains which are predominant in the structure are the main contributor to the overall basal texture in the sheet even though the small grains have a random texture.

Acknowledgement

This research was supported by funding from the NSERC Magnesium Strategic Research Network. More information on the Network can be found at www.MagNET.ubc.ca. Authors are grateful to Pierre Vermette for assistance in experimental work.

References

1. M.M. Avedesian, H. Baker, Magnesium and Magnesium Alloys 1999: ASM International, Materials Park, OH 44073-0002, USA.
2. T. Kaneko and M. Suzuki. Mater. Sci. Forum., 419–422 (2003), pp. 67–72.
3. B. Engl. Light Metal Age**,** 63 5 (2005), pp. 14–19.
4. I.-H. Jung, W. Bang, I.J. Kim, H.I. Sung, W.J. Park, D. Choo and S. Ahn, R.S. Beals, Editor, Magnesium Technology, TMS, Orlando, FL, USA (2007), pp. 85–88.
5. Y. Nakaura, A. Watanabe and K. Ohori. Mater. Trans**.,** 47 7 (2006), pp. 1743–1749.
6. C. Yang, P. Ding, D. Zhang and F. Pan. Mater. Sci. Forum., (2005), pp. 427–430.
7. D.R. Herling, J.A. Carpenter and P.S. Sklad, FY2005 Progress Report for Automotive Lightweighting Materials, US department of Energy (2005).
8. L.W.F. Mackenzie and M.O. Pekguleryuz. Scripta Mater., 59 6 (2008), pp. 665–668.
9. L.W.F. Mackenzie and M. Pekguleryuz. Mater. Sci. Eng. A, 480 1–2 (2008), pp. 189–197.
10. M. Masoumi, and M. Pekguleryuz. Mater. Sci. Eng. A, 529 (2011), pp. 207-214.
11. M. Masoumi, M. Hoseini and M. Pekguleryuz. Mater. Sci. Eng. A, 528 7–8 (2011), pp. 122–3129.
12. M. Masoumi and M. Pekguleryuz. Trans. Am. Foundry Soc., 117 (2009), pp. 617–626
13. Y. Nakaura and K. Ohori. Mater. Sci. Forum., (2005), pp. 419–426.

14. G.F. Vander Voort, Editor, Metallography and Microstructures, vol. 9 ASM International, Materials Park, OH (2004).
15. P. Cao, D.H. StJohn and M. Qian. Mater. Sci. Forum., 488–489 (2005), pp. 139–142.
16. J.A. Sarreal and G.J. Abbaschian. Metall. Trans. A, 17A 11 (November) (1986), pp. 2063–2073.
17. F. Kaiser, J. Bohlen, D. Letzig, K.-U. Kainer, A. Sfyczynski and C. Hartig. Adv. Eng. Mater., **5** 12 (2003), pp. 891–896.
18. M.R. Barnett, M.D. Navea and C.J. Bettlesb. Mater. Sci. Eng. A**,** 386 (2004), pp. 205–211.

Magnesium Technology 2014
Edited by: Martyn Alderman, Michele V. Manuel, Norbert Hort, and Neale R. Neelameggham
TMS (The Minerals, Metals & Materials Society), 2014

POST DEFORMATION ANNEALING BEHAVIOUR OF Mg-Al-Sn ALLOYS

Abu Syed Humaun Kabir, Jing Su, Mehdi Sanjari, In-Ho Jung and Stephen Yue
Department of Mining and Materials Engineering, McGill University,
3610 University Street, Montreal, Quebec, Canada H3A 0C5

Keywords: Mg-Al-Sn, Dynamic recrystallization, Annealing, Texture randomization.

Abstract

In this study, effects of dynamically formed precipitates on the microstructure and texture evolutions were investigated after the post deformation annealing for various times. Two ternary alloys of Mg, Al and Sn were designed, produced and deformed at 300°C at a strain rate of $0.01s^{-1}$ to form different amounts of strain induced precipitates during deformation. Subsequent annealing at deformation temperature was performed for up to 4 hours. Microstructures and precipitation were investigated by optical and scanning electron microscopes and macro and micro-texture were measured by X-ray diffraction (XRD) and Electron Back-Scattered Diffraction (EBSD) techniques, respectively. It was found that certain amount of strain induced precipitates was necessary to prevent grain growth for a certain time during annealing by grain boundary pinning effect. Also, texture randomization was possible with the presence of precipitates after certain time of annealing.

Introduction

Magnesium alloys are attractive materials for weight reduction applications in automotive industries due to their high specific strength [1]. However, one of the most severe disadvantages of magnesium wrought products is the poor formability at lower temperatures. Grain refinement is one of the most important techniques to improve the strength as well as ductility of wrought magnesium products because of the strong influence of grain size on the mechanical properties [2]. Barnett *et al*. [3] reported the increase in compression yield strength twice by reducing the grain size from 23μm to 3μm for extruded AZ31. In general, grain refinement is achieved through the operation of dynamic recrystallization (DRX) during hot deformation for magnesium alloys. However, annealing after the deformation may increase the DRX grain size that may decline the mechanical properties of the final products. Yamamoto *et al.* [4] reported more than ten times increase in final grain size of hot-rolled AZ31 after annealing at 400°C for 1 h. Low formability of magnesium alloys are also associated with the severe basal texture formation tendency of magnesium alloys during the deformation which brings severe tension compression yield asymmetry [5].

The basal texture is considered to be almost inevitable for the typical industrial wrought magnesium alloys and processing techniques due to the lowest critical resolved shear stress (CRSS) of basal slip system [1]. The potential to improve the formability of magnesium alloys by modifying its texture has been reported number of times. Specimen with more random texture showed higher formability than stronger basal texture [6]. Huang *et al*. [7] reported the improvement of formability of AZ31 alloy by rolling at high temperature followed by annealing. They reported the improvement in stretch formability due to the texture weakening after the annealing process. It has been observed that the addition of yttrium (Y) and rare earth (RE) randomize the texture during hot deformation [5, 8]. In these cases, particle stimulated nucleation (PSN) process has been reported as the texture randomization mechanism. Now a days, PSN became an attractive explanation for the texture randomization where the size of the indestructible second phase particle is important and considered to be more than 1 μm [9]. Recently, Farzadfar *et al.* [10] reported that Y in the solid solution randomizes the texture during the annealing process.

In this study, effort has been taken to prevent grain growth during the post deformation annealing with the presence of fine strain induced second phase particles and possible texture modification after annealing.

Experimental Procedures

Thermodynamic software FactSage [11] was used to design the potential Mg alloys with Al and Sn as alloying elements. Two alloys were designed; AT32 (Mg-3wt% Al- 2wt% Sn) and AT33 (Mg-3wt% Al- 3wt% Sn). The alloys were produced with commercially pure Mg, Al and Sn melted using an induction furnace (20 kW, 5 kHz) in a graphite crucible and cast in a copper mold preheated to 250°C. The cast ingots were homogenized for 24 hours at 440°C to fully dissolve the precipitates. Compression samples of 11.4 mm in height and 7.6 mm in diameter (h/d ratio of 1.5) were machined from the homogenized bar. The uniaxial compression tests were performed using a computer controlled servo-hydraulic materials testing system (MTS) with 100 kN capacity, coupled with a radiant furnace. Isothermal compression testing was performed 300°C with a strain rate of $0.01s^{-1}$. The specimens were held at the deformation temperatures for up to 4 hour after the deformation and water quenched immediately after to preserve the microstructure. Specimens for metallurgical examination were cut along the compression axis. Polished specimens were etched in a fresh solution of 10 ml acetic acid, 4.2 gm picric acid, 10 ml water and 70 ml alcohol for 3-8 seconds. Microstructural examination was carried out using Nikon Epiphot 200 optical microscope and Philips XL30 FEG

scanning electron microscope. Volume fraction of dynamic recrystallized grains and precipitates were determined using the point counting method according to the ASTM E 562 standard [12] from optical images and back scattered electron images, respectively. The bulk texture was assessed by XRD using a Bruker D8 diffractometer (Co Kα source). The incomplete pole figures of $\{10\bar{1}0\}$, $\{0002\}$ and $\{10\bar{1}1\}$ were analysed to calculate the orientation distribution functions (ODF) using the arbitrary defined cell (ADC) method by TexTools software. Then, the ODFs were used to recalculate the pole figures. Electron back-scattered diffraction (EBSD) analysis was done by using the Phillips XL30 FEG SEM and the samples were electro-polished at 20V in a 10% Nital solution at -15°C.

Results and Discussions

The microstructural evolutions of both alloys, deformed at a strain of 0.9, and subsequently annealed at deformation temperature for increasing times, are presented in Figure 1. Zero minute in the figure corresponds to the "as-deformed" condition. It can be seen that larger grains are developed after certain increase in annealing times, with the degree of grain coarsening being higher for the alloy AT32. For alloy AT32, grain coarsening is visible after one minute of annealing and significant after 10 minutes. However, for alloy AT33, even after 30 minutes of annealing, the grain size remains almost unchanged. To quantify the effects of deformation and annealing conditions on the microstructure, the evolution of the average recrystallized grain size is plotted against annealing time in Figure 2. For alloy AT32, where the amount of precipitation after deformation has been measured as 0.24 vol. % at 300°C for a strain of 0.9, grain growth is visible at an early stage of annealing. Whereas, for alloy AT33, where 0.75 vol. % precipitates are present after deformation, can pin the grain boundaries up to 30 minutes or more during annealing. Grain growth is observed at 120 minutes of annealing.

Figure 3 shows the distribution of dynamic precipitates after the deformation and annealing for both alloys. It is clear from the figure that the amount of precipitation is higher for alloy AT33 than AT32. Also, the precipitates are distributed mostly within the recrystallized grain boundary areas and along or close to the recrystallized grain boundaries. The precipitates are identified as Mg_2Sn intermetallics by XRD analysis. Mg_2Sn forms a non-coherent interface with the matrix, and it is well-known that dislocations cannot shear the non-coherent precipitates [13]. So, it is expected that the precipitates will pin the recrystallized grain boundary effectively and prevent the grain growth resulting in, refined grain structure.

Here in this study, 70-200 nm in size dynamic precipitates form during the deformation process that is smaller to be considered as particles suitable for PSN. The effect of such a small dynamic particles on texture evolution has not been reported for magnesium alloys before. Macro-texture study by XRD analysis indicates that during annealing at deformation temperature the alloys showed randomized texture. {00.2} pole figures are shown in Figure 4 for the as-deformed and annealing for 10 and 30 minutes for alloy AT32 and AT33, respectively and 240 minutes for both alloys.

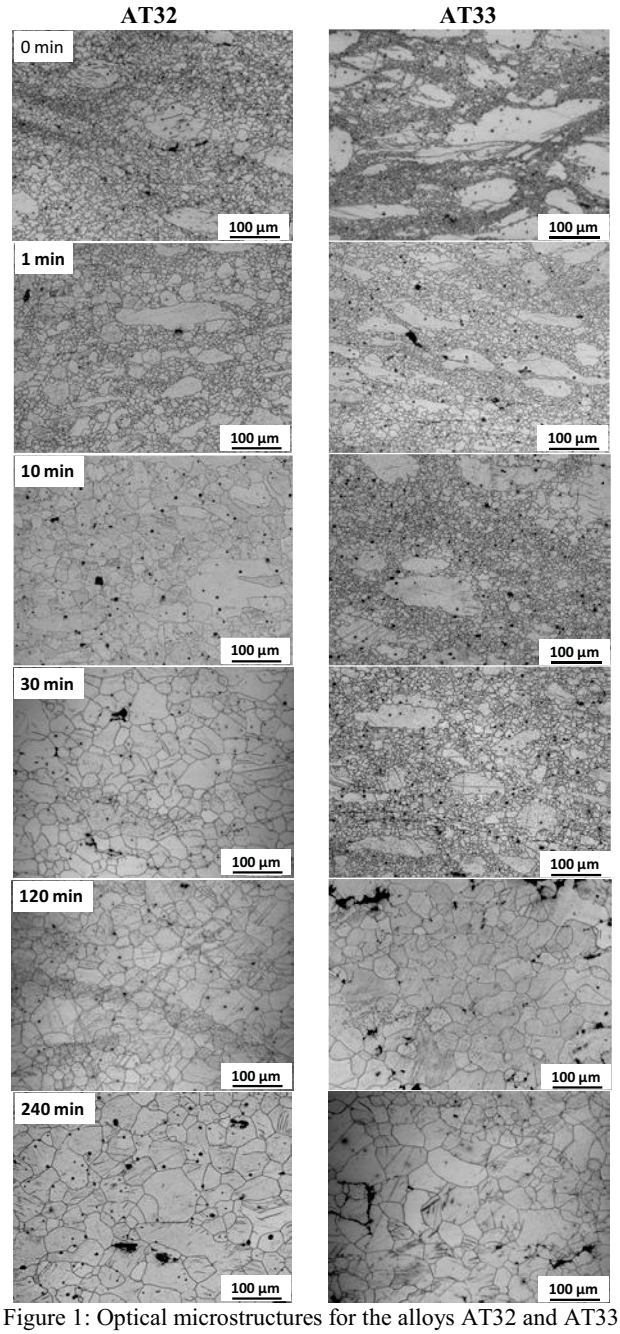


Figure 1: Optical microstructures for the alloys AT32 and AT33 after deformation and subsequent annealing at deformation temperature.

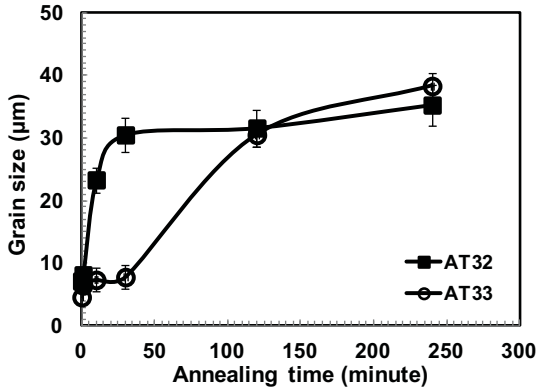


Figure 2: Grain size after deformation and annealing for two alloys.

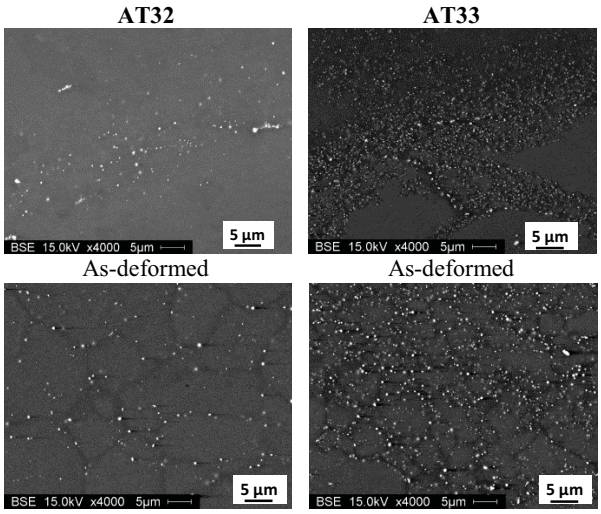


Figure 3: Back scattered electron micrographs of the two alloys at as-deformed and after 30 minutes of annealing.

At the beginning, both alloys show strong basal textures, showing the contours mostly concentrated at the CD direction. AT33 shows an extra component in the CD/TD direction and also the intensity of the pole figure is little less than AT32, indicating slight weaker texture for AT33. Intensity of the basal pole figure drops sharply right after one minute of annealing for both alloys and the minimum intensities were observed after 10 minutes and 30 minutes of annealing for alloy AT32 and AT33, respectively. Non-basal texture components in the CD directions were observed in the figure for both alloys at the lowest intensity value. Then the intensity starts to increase again with further annealing. The non-basal components in the CD direction start to disappear and the textures restore as strong basal again. This kind of texture weakening was reported before during annealing of Mg alloys by Farzadfar *et al.* [10]. In their study, they reported the yttrium in the solid solution randomizes the texture by solute drag effect without the presence of any precipitates. In the current study, aluminum remains in the solid solution both during the deformation as well as after annealing. Solute drag control mechanism has been reported for magnesium alloys when aluminium is in the solid solution but this mechanism occurs only at very low strain rates ($\leq 10^{-4}$ s^{-1}) [14]. At higher strain rates the consequent stresses are higher and probably the solutes are not able to control the dislocation activities. Therefore, the precipitates may be responsible for the texture weakening during the annealing process. There is no mechanism exists to explain this texture randomization with the presence of fine precipitates but may be related to the precipitation pinning at the recrystallized grain boundary.

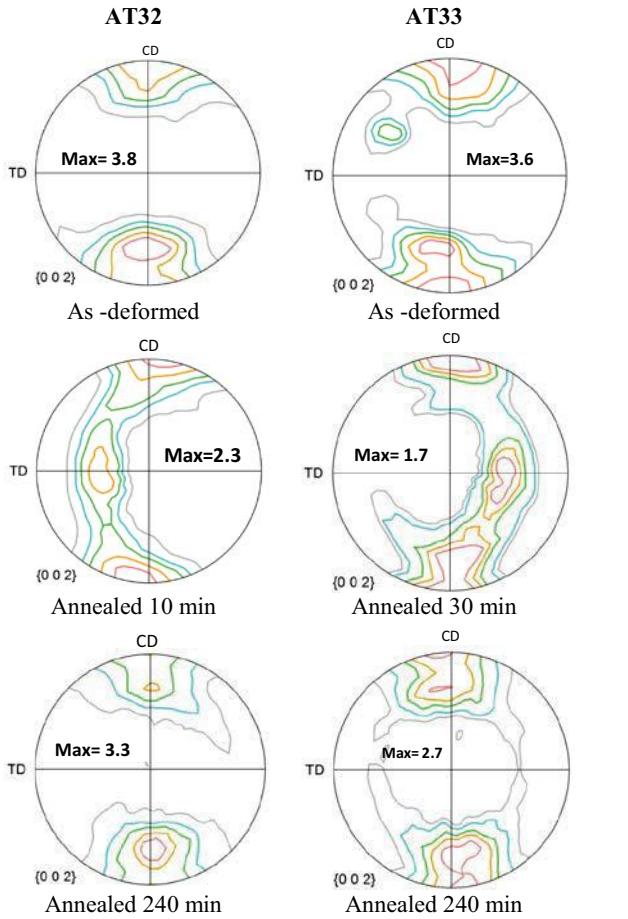


Figure 4: {00.2} pole figures of the two alloys in the as-deformed condition and 10 minutes of annealing for AT32, and 30 minutes for AT33.

Variation in intensity in basal pole figure can be explained by plotting the distribution of basal planes with the tilt angle. Figure 5 shows the vol. % of basal plane in different angles from the normal direction (ND) for the alloy AT33. For the as-deformed (0 min in the figure) condition, the basal planes are mostly concentrated within the angular range of 30-40° from the ND. Whereas, specimen annealed at 1, 10 and 30 minutes show less significant peaks for the concentration of the basal planes meaning randomized texture. Specimens annealed at 120 and 240 minutes have the tendency to develop the same intensity of

the as-deformed condition. So, texture is weakened after certain time of annealing and start to be strong again after increasing annealing time.

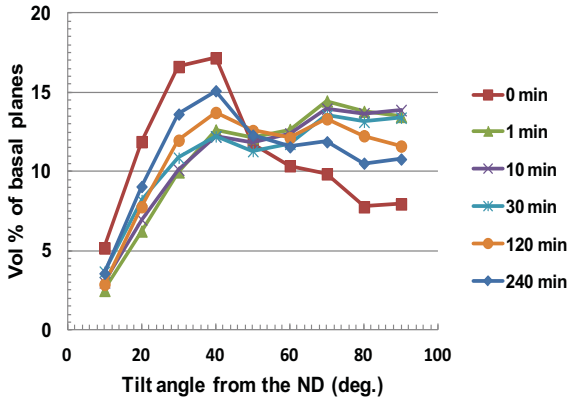
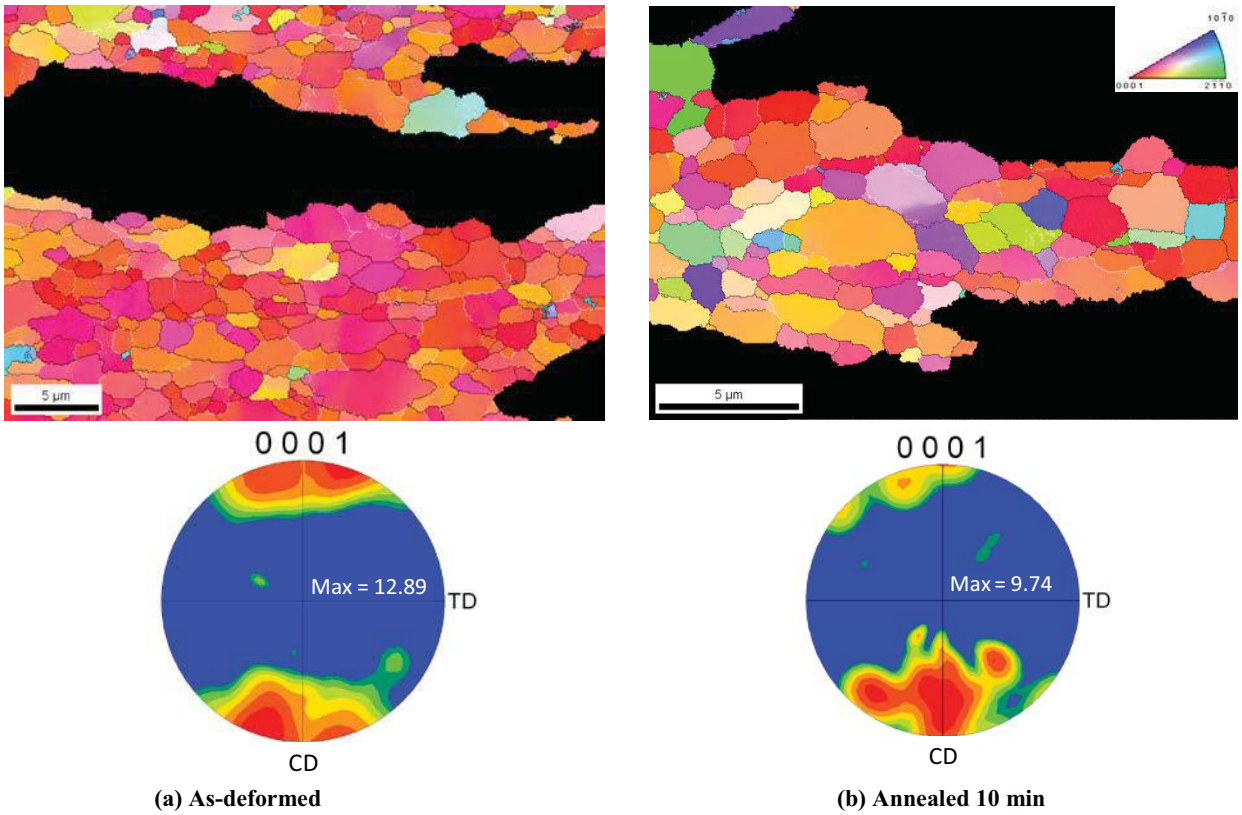


Figure 6: Distribution of basal planes in different angle from ND direction for the alloy AT33.

To confirm the macro-texture results obtained by XRD analysis, micro-texture study was done by EBSD analysis. Figure 7 shows the inverse pole figure maps for alloy AT32 in the as-deformed condition and annealed for 10 minutes, where XRD analysis showed the weakest texture. Only the recrystallized grains are compared for two alloys to show the effect of precipitates as there are no precipitates in the un-recrystallized regions. Low-angle grain boundaries (LAGB) are (mis-orientation angle 3-15°) are marked out by thin white lines, while high-angle boundaries (HAGB) with mis-orientation angle more than 15° are by black lines. It is clear from the figure that most of the grains developed have a strong texture near (0001) corresponds to basal texture for the as-deformed condition. It is now well known that during deformation, the basal plane of the Mg-HCP lattice lies perpendicular to the deformation direction. It is remarkable to note that after 10 minutes of annealing more grains are rotated from basal to non-basal directions indicated by variations in colors. The corresponding pole figures obtained only from the recrystallized grains are also shown in the figure. The intensity of the pole figure for the annealed condition is much lower than the as-deformed condition indicating the texture weakening. The result is a good agreement with the XRD analysis results showed before.



(a) As-deformed **(b) Annealed 10 min**

Figure 7: Inverse pole figure maps of only the recrystallized grains and the corresponding pole figures for alloy AT32 (a) As-deformed (b) Annealed 10 minutes.

Summary

Two alloys have been designed in the target that the alloys will form different amount of precipitate during the deformation. The effect of this strain induced precipitates after annealing has been discussed based on microstructures and texture analysis. The main results from this study can be summarized as follows:

1. The effective grain boundary pinning during the annealing depends on the vol. % precipitates. In this case, at least 0.75 vol% Mg_2Sn precipitates was necessary to maintain refined grain structure up to 30 minutes of annealing at 300°C.
2. Texture randomization was observed both by macro and micro- texture analysis with the presence of precipitate during annealing for a certain time.

Acknowledgements

Financial supports from General Motors and NSERC, Canada are highly acknowledged.

References

1. X. Huang et al., "Influence of rolling temperature on static recrystallization behavior of AZ31 magnesium alloy," *Journal of Materials Science*, 47(11) (2012), 4561-4567.
2. A.G. Beer, and M.R. Barnett, "Microstructure evolution in hot worked and annealed magnesium alloy AZ31," *Materials Science and Engineering A*, 485(1-2) (2008), 318-324.
3. M.R. Barnett et al., "Influence of grain size on the compressive deformation of wrought Mg-3Al-1Zn," *Acta Materialia*, 52(17) (2004), 5093-5103.
4. A. Yamamoto et al., "Grain Refinement on AZ31 Magnesium Alloy by Highly Strained and Annealed Method," *Materials Science Forum*, 449-452 **(**2004), 669-672.
5. J. Bohlenet et al., "The texture and anisotropy of magnesium-zinc-rare earth alloy sheets," *Acta Materialia*, 55(6) (2007), 2101-2112.
6. E. Yukutake, J. Kaneko, and M. Sugamata, "Anisotropy and Non-Uniformity in Plastic Behavior of AZ31 Magnesium Alloy Plates," *Matrerials Transactions,* 44(4) (2003), 452-457.
7. X. Huang et al., "Improvement of stretch formability of Mg–3Al–1Zn alloy sheet by high temperature rolling at finishing pass," *Journal of Alloys and Compounds*, 509(28) (2011), 7579-7584.
8. E.A. Ball, and P.B. Prangnell, "Tensile-compressive yield asymmetries in high strength wrought magnesium alloys*," Scripta Metallurgica et Materialia*, 31(2) (1994), 111-116.
9. F.J. Humphreys, and M. Hatherly, *Recrystallization and related annealing phenomena*, *vol. 2*, Elsevier, 2004.
10. S.A. Farzadfar et al., "Texture weakening and static recrystallization in rolled Mg–2.9Y and Mg–2.9Zn solid solution alloys," *Journal of Materials Science*, 47(14) (2012), 5488-5500.
11. C.W. Bale et al., "FactSage thermochemical software and databases," *Calphad*, 26(2) (2002), 189-228.
12. *ASTM Book of Standards*, Volume 03.01, Metals Test Methods and Analytical Procedures in Metals-Mechanical Testing; Elevated and Low-Temperature Tests, Metallography, 2009.
13. M. Masoumi, and M. Pekguleryuz, "The influence of Sr on the microstructure and texture evolution of rolled Mg–1%Zn alloy," *Materials Science and Engineering A*, 529(0) (2011), 207-214.
14. N.V. Ravi Kumar et al., "Grain refinement in AZ91 magnesium alloy during thermomechanical processing," *Materials Science and Engineering A*, 359(1-2) (2003), 150-157.

Magnesium Technology 2014
Edited by: Martyn Alderman, Michele V. Manuel, Norbert Hort, and Neale R. Neelameggham
TMS (The Minerals, Metals & Materials Society), 2014

ACOUSTIC EMISSION ANALYSIS OF PLANE STRAIN-COMPRESSED Mg SINGLE CRYSTALS

Daria Drozdenko[1], Patrik Dobroň[1], Michal Knapek[1], Dietmar Letzig[2], Jan Bohlen[2], František Chmelík[1]

[1]Charles University in Prague, Faculty of Mathematics and Physics, Department of Physics of Materials, Ke Karlovu 5, 12116, Prague 2, Czech Republic
[2]Helmholtz-Zentrum Geesthacht, Zentrum für Material- und Küstenforschung GmbH, Max-Planck-Straße 1, D21502 Geesthacht, Germany

Keywords: Acoustic emission, Twinning, Dislocation, Mg single crystal.

Abstract

Mg single crystals with three different crystallographic orientations have been channel die (plane strain) compressed at applied rate of $10^{-3}s^{-1}$ and at room temperature. The concurrent acoustic emission (AE) measurement was used as a method to analyze the dislocation dynamic during plastic deformation of Mg single crystals. The AE count rate and the maximum amplitudes of the AE event were correlated with stress-strain curves to determine the activity of various deformation mechanisms. The presence of large AE signals in the first stage of plastic deformation in single crystals with favorable orientation for (10.2)-twinning indicates twin nucleation and subsequent decrease of the AE activity, which can be connected with twin growth and collective dislocation processes. Compression along the c-axis (hard deformation mode) produces almost no AE activity.

Introduction

Magnesium alloys are used in many technical applications, such as air and automotive industry due to their low density and high damping capacity. They belong to the lightest construction metals and to HIDAMETS (High Damping Metals and alloys) group. A limiting factor for their wider use is a lack of initially active deformation modes based on distinctive differences in the critical resolved shear stresses (CRSS) for different slip and twinning systems [1,2]. According to [1-5], CRSS for dislocation slip in the basal plane is much lower then that in the other systems.

Nowadays, the utilization of magnesium sheets is the one of main industrial applications of Mg alloys. Information regarding the activation of various deformation processes (modes) with respect to deformation conditions is very important. It can be obtained by the simulation of rolling process (especially plane strain compression test), which was performed on Mg single crystals loaded along various crystallographic axes.

The influence of orientation and temperature on the flow stress was discussed in early works of Wonsiewicz and Backofen [6], Bakarian and Mathewson [7], Kelley and Hosford [8]. Later progress of such explorations can be seen in the work of Chapuis and Driver. For the identification of operating slip and twinning systems in plain strain compressed Mg single crystals electron backscatter diffraction (EBSD) measurements have been used [9].

Acoustic emission can be used for obtaining further information, especially about the dislocation dynamics and twin nucleation. The AE is based on transient elastic waves, which are generated during deformation due to sudden localized structure changes. Overview of results of *in-situ* AE measurements during mechanical tests on single crystals of various metals (such as Al, Zn, Fe, Cd, Ti) can be found in [4,10]. Twinning and dislocation processes were also characterized in polycrystalline Mg alloys by AE with respect to their chemical composition, initial preparation, and deformation conditions [11,12].

Collective dislocation dynamics in single crystals could be explained by the general concept of self-organized criticality (SOC) [13]. According to the previous experiments, the occurrence of SOC in a system does not depend on microscopic details (type of material, nature of atomic bonds), which are related to the individual behavior of the interacting entities. The behavior could have a universal character [14]. Richeton et al. [13] observed scale-free patterns in plastic deformation of Zn and Cd and it may appear in other materials, as well.

Therefore, SOC turns out to be a suitable and powerful tool for an investigation of deformation processes. The self-organization of the dislocations in scale-free patterns of dislocation avalanches is reflected in a power-law distribution of AE event energies E. It is assumed that $P(E) \sim E^{-\tau}$, where P(E) is the probability density function of AE event energies [13]. The square of maximum amplitude of the AE event (A^2) reflects the statistics of the energy dissipated by plastic deformation during an event [15] and therefore the approach $P(E) \sim (A^2)^{-\tau}$ can be used.

The lack of AE investigations on Mg single crystals, which can be used as reference measurements for further experiments on polycrystalline Mg alloys in order to improve their mechanical properties, is a motivation of the present work. The main aim of this paper is to characterize plastic deformation mechanisms of plain strain compressed Mg single crystal with various loading direction by AE parameters (AE count rates and maximum amplitudes of the AE events).

Experimental procedure

The channel die compression tests (plane strain) were performed on Mg single crystals of commercial purity at a strain rate of 10^{-3} s^{-1} at room temperature. Specimens (5 x 6 x 10 mm^3) were compressed along three different crystallographic orientations (see Figure 1.): perpendicular to the prismatic (11.0) and (10.0) planes (with flow axis perpendicular to the basal (00.1) plane) (hereafter called orientations O1 and O2) and perpendicular to basal (00.1) plane (with flow axis perpendicular to prismatic (11.0) plane) (hereafter called orientation O3).

Pole figures on polished samples (specimens) in reflection geometry up to a sample tilt of 70° were measured by a Panalytical X-ray diffractometer setup using CuKα radiation.

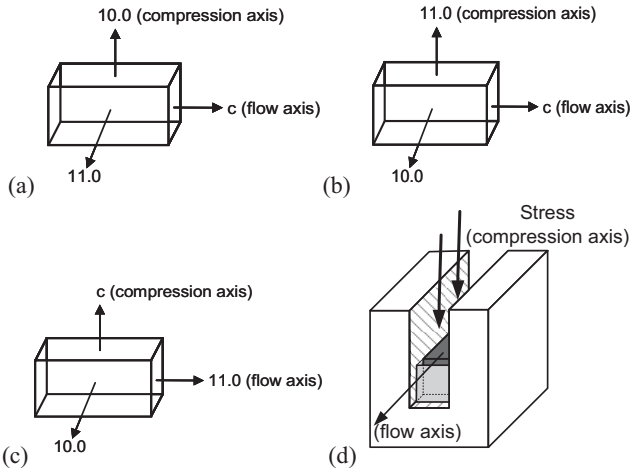


Figure 1. Orientations of Mg single crystals (a) O1, (b) O2, (c) O3 and schematic plot of channel die compression experiment (d).

A computer controlled DAKEL-IPL AE system was used to monitor the AE activity, which is based on continuous storage of AE signals with 2 MHz sampling frequency. The full scale of the A/D converter was ± 2.4 V. A preamplifier with a gain of 35 dB was used for amplifying very weak signals. A miniaturized MST8S piezoelectric transducer was used with diameter of 3 mm and a flat response in a frequency band from 100 to 600 kHz, sensitivity 55 dB ref. 1 Veff. The sensor was attached to the specimen surface using silicon grease and a spring. The AE system has a threshold level detection, which can yield a comprehensive set of AE parameters. The count rate $\Delta NC/\Delta t$ is the count number per unit time [10] at specified threshold voltage level, which was chosen as 15 % of the maximum voltage. The deadtime for the separation of individual AE events was set as 50 μs. Maximum amplitudes of the AE events can be then used as a parameter for calculation of the SOC method.

Results and discussion

Pole figures of channel die compressed Mg single crystals are seen in Figure 2. They are represented by the distributions of basal (00.1) and prismatic (10.0) poles. As mentioned above, three different orientations were used for plane strain compression experiments and denoted as O1, O2, and O3. The prismatic (10.0), (11.0) planes (in O1 and O2, respectively) and basal (00.1) planes (in O3) are perpendicular to the compression axis.

Figure 3. represents dependencies of engineering stress, AE count rate, and the maximum amplitude of the AE events on time for Mg single crystals with different crystallographic orientation (as mentioned above). Orientations of the crystals are schematically depicted with respect to the deformation axis (see Figure 1). The dependencies can be used to describe the development of the dislocation structure. As we can see from Figure 3 for orientations O1 and O2, plastic deformation starts with the easiest dislocation slip in the basal plane due to the lowest CRSS from all slip systems in *hcp* and relatively low density of dislocations.

The plateau on the deformation curves ("the plateau regime") can be explained by the dislocation glide and the activation of twins, what was also observed using EBSD in channel-die compressed Mg single crystals with a similar orientation [9]. Reorientation of basal planes due to twinning (rotation of basal planes by 86.3 degrees to their original orientation [6]) enables to proceed plastic deformation.

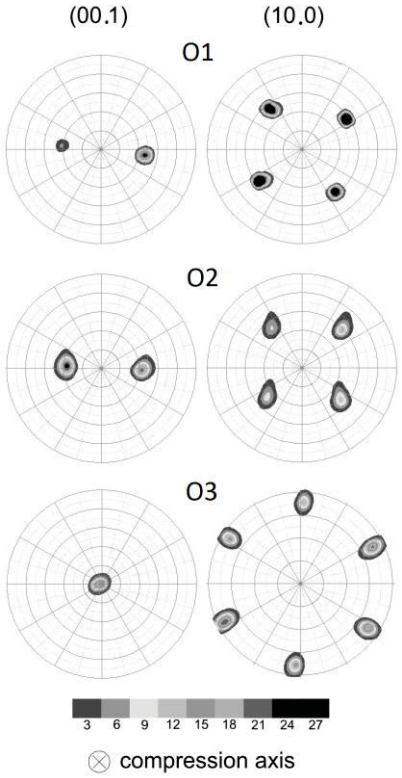


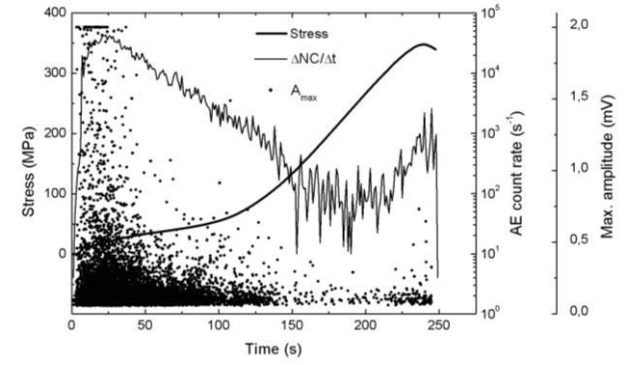
Figure 2. Pole figures of channel die compressed Mg single crystals with different orientations to compression axis (perpendicular to prismatic (11.0) and (10.0) planes (O1 and O2) and perpendicular to basal (00.1) plane (O3)), denoted as O1, O2 and O3. (Horizontal axis is flow direction).

In the next deformation stage, the activation of non-basal slip system with higher CRSS is clearly manifested as a stronger increase in the engineering stress. However, it should be noted that the work hardening is slightly higher in the orientation O1 in comparison to O2. This can indicate a bit higher twinning activity during deformation process for the orientation O1 (the prismatic (10.0) plane is perpendicular to the compression axis).

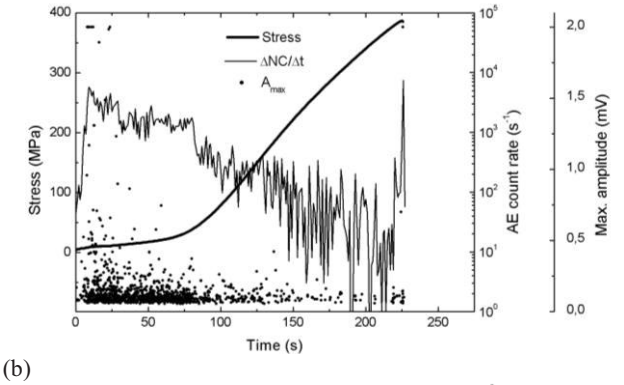
Channel-die compression along the axis, which is perpendicular to the basal plane (O3), does not favour slip in the basal (00.1) planes and the plastic deformation is consequently accommodated by "hard activated" non-basal slip systems (with higher CRSS). This scenario results in very strong work hardening immediately at the beginning of deformation test.

The AE analysis can be correlated to stress *vs.* time deformation curves (see Figure 3). We found a very strong correspondence for the single crystals with the orientations O1 and O2. AE count rates for the orientations O1 and O2 exhibit a maximum at the beginning of plastic deformation and the AE activity slowly decreases in the next stage. This effect can be explained by collective motion of dislocations, whose total length and flight distance reaches maximum at the beginning of plastic deformation. Then their density increases due to immobilization of many dislocations, which leads to a decrease in the free path of the moving dislocations and therefore to a reduction of the AE

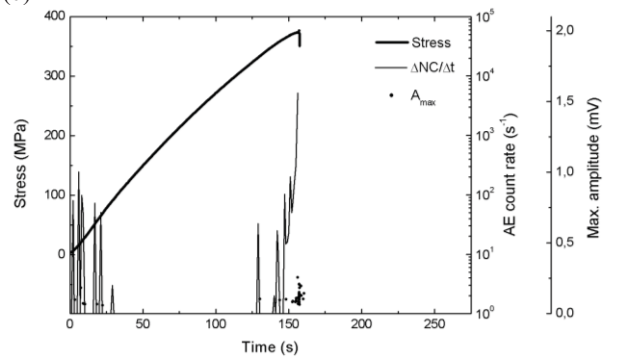
activity. The AE count rate maximum and the maximum amplitudes of the AE event for O1 are higher then those for O2. Slight difference in amount of (10.2)-twins can be a reason for the higher AE activity (they produce strong AE signals) for O1. The activation of non-basal slip (decrease in the free path of the moving dislocations) in "the plateau regime" does not lead to the reduction of the AE count rate. Such behaviour indicates the presence of deformation twinning, which is an excellent source of AE [16].



(a)



(b)



(c)

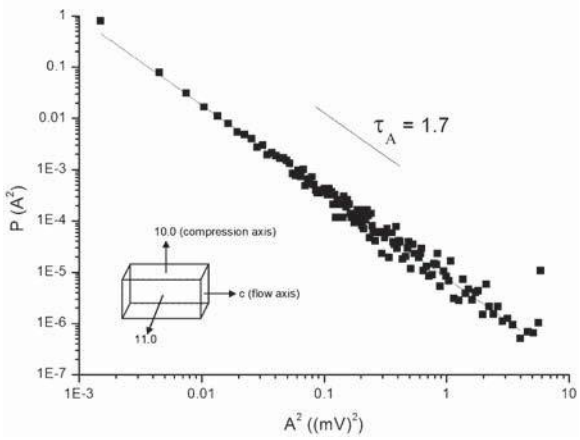
Figure 3. Engineering stress, AE count rate, and the maximum amplitude of the AE event vs. time curves for different orientations of Mg single crystals with respect to loading direction (O1, O2, O3).

The situation for the orientation O3 is different. At the beginning of deformation test, the activation of non-basal slip systems and twins lead to low AE activity. Then almost no AE signals were observed because of strain hardening, at which newly created twin boundaries and increasing number of dislocations reduce the free path of the moving dislocations.

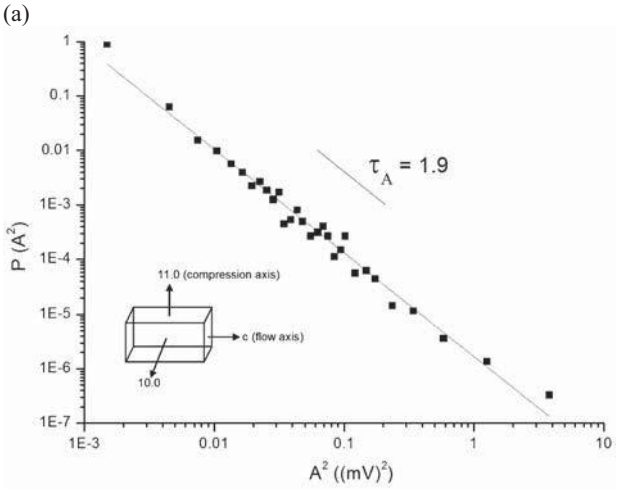
Finally, cracks propagation emits an AE signal short before the fracture.

AE count rate cannot offer information about the magnitude of amplitude. Therefore, to better discriminate the AE signals produced by the nucleation of twins from collective dislocation movement, the AE events and their maximum amplitudes were determined. Keeping in mind that twinning in comparison to continuous dislocation glide mainly generates AE of a burst type character [10]. Thus twinning plays an important role in generating of burst AE signals. The magnitudes of AE amplitudes for orientation O1 are higher than that for O2, while the deformation curves are comparable, what indicates that AE is very sensitive method for a study of plastic deformation (see Figure 3.). Based on higher values of maximum AE amplitudes for orientation O1, in comparison to O2, and EBSD measurements [9], it can be pointed out that O1 is more favorable for activation of twins. Consecutive glide in reoriented grains contributes to strain hardening and results in lower amount of high amplitude AE signals. For orientation O3, almost no AE events with relative high value of maximum amplitudes are observed.

Analyzing the probability density function of AE energies (related to square of maximum amplitudes) according to concept of SOC is a useful method for investigation dislocation dynamics in various crystalline materials (Figure 4).



(a)



(b)

Figure 4. Probability density functions of energies (related to square of AE maximum amplitudes*)* for orientations O1 (a) and O2 (b).

As mentioned above, the probability density function of the AE event energies comply with a power law distribution, $P(E) \sim E^{-\tau}$. So far as for orientation O3 almost no AE activities were noticed, our attention should be focused on more favorable orientation for twinning O1 and O2 (Figure 4 (a) and (b), respectively).

Values of the exponent τ_A were determined as 1.7-1.9, which is in very good agreement with those found for dislocation avalanche size distributions in single crystals of ice, Cd and Zn ($\tau_A = 1.5 \pm 0.1$) [13,15]. This fact strongly suggests that the general features of the observed intermittent flow regime are of generic nature in plastic deformation of crystalline materials.

According to [13], the probability density functions of AE energies (square of maximum amplitudes) are the same for dislocation glide and twinning. Therefore, we cannot distinguish twinning from dislocation slip by probability density function of maximum AE amplitudes (although twinning can exhibit higher amplitudes and shorter events).

Conclusions

Channel-die compression tests of Mg single crystals using various crystallographic orientations at room temperature were performed with in-situ recording of acoustic emission (AE) signals. The AE count rate and maximum amplitudes of AE events indicate changes in dislocation dynamics and the presence of twins.

Analysis of maximum AE amplitudes shows that orientation (10.0) is more favourable for activation of twins in comparison to orientation (11.0). Channel-die compression along c-axes (00.1) is hard deformation mode, resulting in almost no AE signals.

The self-organized criticality model for maximum amplitudes of AE events (which related to energies) was applied on the experimental data in order to study an influence of twinning on dislocation dynamic. The values of the criticality exponent τ_A of 1.7-1.9 are very close to those found for other materials (ice, Cd, Zn) and, therefore, dislocation dynamics seem to have a general features.

Acknowledgements

This work received support from the Czech Science Foundation under grant 13 - 19812S. The work of P.D. is a part of activities of the Charles University Research Center "Physics of Condensed Matter and Functional Materials". D.D. is grateful for financial support from the grant SVV-2013- 267303. F.C. is grateful to the Alexander von Humboldt Stiftung for financial support during his stay in Germany and to the Czech Science Foundation for financial support of the AE analysis under research grant No. P108-11/1267. M.K. is grateful to the Grant Agency of Charles University No. 946213.

References

1. S. Ando, H. Tonda, "Non-basal Slip in Magnesium and Magnesium-Lithium Alloy Single Crystals," *Materials Science Forum*, 350-351 (2000), 43-48.
2. A. Staroselsky, L. Anand, "A constitutive model for hcp materials deforming by slip and twinning: application to magnesium alloy AZ31B," *International Journal of Plasticity*, 19 (10) (2003), 1843-1864.
3. S Kleiner, P.J Uggowitzer, "Mechanical anisotropy of extruded Mg–6% Al–1% Zn alloy," *Materials Science and Engineering: A,* 379 (1–2) (2004), 258-263.
4. P. Dobroň, J. Bohlen, F. Chmelík, P. Lukáč, D. Letzig, K.U. Kainer, "Mechanical anisotropy of AZ31 magnesium alloy sheet investigated by the acoustic emission technique," *Kovove Mater*., 45 (3) (2007), 129-133.
5. M.R. Barnett, M.D. Nave, C.J. Bettles, "Deformation microstructures and textures of some cold rolled Mg alloys," *Materials Science and Engineering: A*, 386 (1–2) (2004), 205-211.
6. B.C. Wonsiewicz and W.A. Backofen, "Plasticity of Magnesium Crystals," *Trans. TMS-AIME*, 239 (1967), 1422–1431.
7. P.W. Bakarian, C.H. Mathewson, "Slip and twinning of magnesium single crystals at elevated temperatures," *Trans. AIME*, 152 (1943), 226.
8. E.W. Kelley, W.F. Hosford, "Plane-strain compression of Magnesium and Magnesium Alloy Crystals," *Trans. Metall. Soc. AIME*, 242 (1968), 5–13.
9. A. Chapuis, J.H. Driver, "Temperature dependency of slip and twinning in plane strain compressed magnesium single crystals," *Acta Materialia*, 59 (5) (2011), 1986-1994.
10. Standard Practice for Acoustic Emission Examination of Fiberglass Reinforced Plastic Resin, *ASTM E 1067-85. Tank/Vessels*, (1985).
11. C.R. Heiple and S.H. Carpenter, "Acoustic Emission Produced by Deformation of Metals and Alloys - A Review: Part I," *J. Acoustic Emission*, 6 (1987), 177-204.
12. E. Meza-García, P. Dobroň, J. Bohlen, D. Letzig, F. Chmelík, P. Lukáč, K.U. Kainer, "Deformation mechanisms in an AZ31 cast magnesium alloy as investigated by the acoustic emission technique," *Materials Science and Engineering: A*, 462 (1–2) (2007), 297-301
13. T. Richeton, P. Dobron, F. Chmelik, J. Weiss, F. Louchet, "On the critical character of plasticity in metallic single crystals," *Materials Science and Engineering: A*, 424 (1–2) (2006), 190-195.
14. H.E. Stanley, "Scaling, universality, and renormalization: Three pillars of modern critical phenomena," *Reviews of Modern Physics*, 71 (SUPPL. 2) (1999), S358-S366.
15. T. Richeton, J. Weiss, F. Louchet, "Dislocation avalanches: Role of temperature, grain size and strain hardening," *Acta Materialia*, 53 (16) (2005), 4463–4471.
16. C.R. Heiple, S.H. Carpenter, "Acoustic emission produced by deformation of metals and alloys – A review: Part II.," *J. Acoustic Emission* 6 (1987) 215-237.

Magnesium Technology 2014
Edited by: Martyn Alderman, Michele V. Manuel, Norbert Hort, and Neale R. Neelameggham
TMS (The Minerals, Metals & Materials Society), 2014

Precipitation Strengthening of a Mg-Zn Alloy in Tension and Compression

Julian M Rosalie, Hidetoshi Somekawa, Alok Singh

Structural Materials Unit, National Institute for Materials Science, Tsukuba, 305-0047, Japan.

Keywords: Magnesium-zinc; Precipitation; Tensile-compressive asymmetry; Transmission electron microscopy

Abstract

The effectiveness of precipitation strengthening against slip and twinning was quantified for a Mg-Zn containing different distributions of rod-shaped β_1' precipitates. Tensile and compressive testing was carried out on identically heat-treated samples to determine the effect of a well-characterised particle distribution on each deformation mode. Precipitation strengthening was more effective at resisting deformation via slip (in tension) than via twinning (in compression), with increases in the yield strength of 95-110% and 77-86%, respectively, increasing the tensile-compressive asymmetry. Refining the precipitate size distribution via pre-ageing deformation increased the yield strength in tension to a greater extent than compression, but had little influence on the tensile-compressive asymmetry.

Introduction

One of the outstanding difficulties with magnesium alloys is their anisotropic behaviour during deformation, which can result in poor room temperature formability [1]. As with other hexagonal metals, magnesium alloys deform via basal slip, with this deformation mode having the lowest critical resolved shear stress at room temperature. This deformation mode alone does not allow for strain compatibility and deformation inevitably involves other deformation modes, including prismatic slip and twinning. Of particular concern in magnesium is "tensile" $\{10\bar{1}2\}$ twinning which occurs at low-strains, in suitably aligned grains. In textured alloys this results in substantial tensile-compressive asymmetry, with the compressive yield strength frequently reaching only 60-70% of the tensile yield strength.

Several classes of wrought Mg alloys, including the widely-used ZK (Mg-Zn-Zr) and AZ31 (Mg-Al-Zn) series show age-hardening behaviour and there is considerable interest in improving the precipitation strengthening behaviour in such alloys. The effectiveness of precipitation strengthening against slip depends on the intersection cross-section between dislocations and the precipitates and is heavily dependent on precipitate morphology and aspect ratio [3].

The effect of precipitation strengthening on twinning is less well understood but has also been shown to depend on the precipitate geometry [4]. Basal slip occurs rapidly in the newly-twinned material and the precipitates are thought to contribute to strengthening the alloy by resisting this process. The reorientation of the crystal planes in the twin means that the intersection cross-section differs from that in the matrix, giving different strengthening behaviour. This "selective" strengthening of different deformation modes has been shown to affect the asymmetry ratio in AZ91[4] and Mg-5Zn [5] alloys. Rod-like precipitates with [0001] habit are highly effective against basal slip in the matrix, but poor in the twin and in a Mg-5wt%Zn alloys, precipitation changed the asymmetry ratio from 0.61 to 0.53 [5].

Pre-ageing deformation has been shown accelerate and enhance the precipitation strengthening response in extruded Mg-Zn [7] and Mg-Zn-Y alloys [8] deformed in tension, by resisting slip. In addition to increasing the precipitate number density of rod-like β_1' particles, pre-ageing deformation reduced the aspect ratio of the precipitates. This should reduce the selectively of the precipitation strengthening in the matrix and twin, and potentially reduce the tensile-compressive asymmetry. The present work set out to determine how precipitation strengthening affected both tensile and compressive mechanical properties of an isothermally aged alloy and to relate this to the aspect ratio and number density of the precipitates.

Experimental details

This study was conducted using a billet with a nominal composition of Mg-3.4at.%Zn prepared by direct chill casting. The starting materials were high-purity elemental Mg (99.99%) and Zn (99.999%) and the final composition was verified using inductively-coupled plasma mass spectroscopy (ICP-MS). The billet was homogenised at a temperature of 300°C

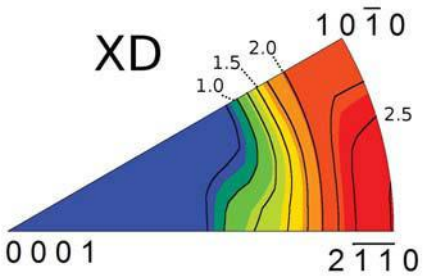
for 15 hours, and extruded at 300°C to form a 12 mm diameter rod.

Tensile testing samples were prepared by machining cylindrical dog-bone samples (gauge length 15 mm, diameter 3 mm) from the extruded rod. Samples for compressive testing (height 6 mm, diameter 3 mm) were also prepared. Both kinds of sample were solution treated at 300°C for 0.5 h. in glass ampules filled with a protective argon atmosphere. The tensile samples were subjected to pre-ageing strain (0, 2% or 4% plastic strain) at strain rate of of $1{\times}10^{-3}\,\mathrm{s}^{-1}$ using an Instron mechanical tester. Samples were aged in an oil-bath at 150°C, and the ageing response measured by Vickers microindentation hardness testing (300g load) to establish the time required to reach maximum hardness.

Peak-aged tensile samples were tested to failure in compression and tension at a strain rate of $1 \times 10^{-3}\,\mathrm{s}^{-1}$. Compressive samples were prepared by cutting peak aged tensile sample using a slow-speed diamond saw to produce cylindrical compression samples (nominal size 6 mm height, 3 mm diameter). These samples were tested to failure in compression at an identical strain rate.

Samples were examined using reflected light microscopy following solution treatment, after pre-ageing deformation and after testing to fracture in the peak-aged condition. Preparation was by standard mechanical grinding and polishing methods using an acetic picral reagent to highlight the grain boundaries. Solution-treated samples were examined using electron back-scattered diffraction (EBSD) on a field emission scanning electron microscope.

Samples for TEM analysis were prepared by grinding to $\sim 70\,\mu$m and thinning to perforation using a Gatan precision ion polishing system. Stereological measurements of the β_1' precipitate size and number density in peak-aged T6 and T8 samples were made using a JEOL 2100 transmission electron microscope, operating at 200 kV. Precipitate diameter was determined using images obtained along the [0001] zone while precipitate lengths where measured using images obtained perpendicular to this zone. Data was collected from a total of 300–500 precipitates along each axis for each heat-treatment condition. Volume fractions were determined from the projected area fraction along the [0001], using thickness values determined using CBED and corrected for particle overlap. Number density values were determined from the volume fraction and mean particle volume.



(a) IPF

Figure 1: EBSD inverse pole figure of extruded, solution-treated Mg-Zn, showing a high intensity of 2.76 for $[2\bar{1}\bar{1}0]$ poles in the extrusion direction.

Results

Light microscopy

The microstructure in the solution-treated conditions consists of equiaxed grains with a grain size of approximately $20\,\mu$m. The twin volume fraction is $< 1\%$ in the solution-treated condition, $\sim 2 \pm 1\%$ after 2% strain and $\sim 4 \pm 1\%$ after 4% strain. Extension to failure in tension results in twin volume fractions of between 4% and 6%, consistent with slip being the predominant deformation mode for extruded Mg-Zn deformed in tension. Samples deformed to failure in compression showed extensive twinning, most notably in the solution-treated condition where $30 \pm 3\%$ of the material had undergone twinning. Heat-treatment reduced the extent of twinning, particularly in the T6 condition, where the volume fraction of twins was $10 \pm 2\%$.

Texture analysis

Inverse pole figures (Figure 1(a)) show that alloy has a $[2\bar{1}\bar{1}0]$ texture, as expected for extruded Mg-Zn, with an intensity in the extrusion direction of 2.76, compared to ∼2.3 for $[10\bar{1}0]$ and <0.8 for [0001] poles.

Ageing response

The Vickers hardness curves (provided in Figure 2) show a reduction in the time required to reach maximum hardness ("peak-aged" condition) from 250 h for T6 treatment to 48 h and 32 h hours for T8 treatment after 2% and 4% strain, respectively. There was a slight increase in the maximum hardness form $77{\pm}2\mathrm{H}_v$ (T6 treatment) to $79{\pm}2\mathrm{H}_v$ (T8 treatment with 4% pre-strain).

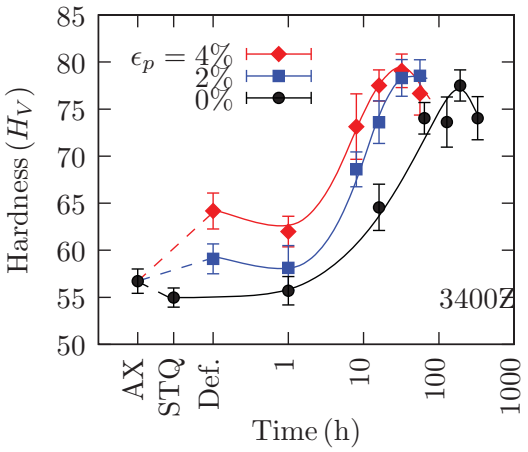
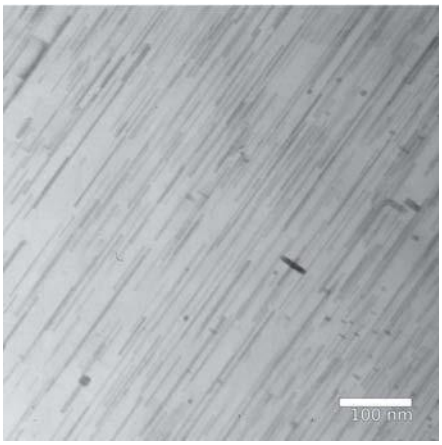


Figure 2: Isothermal ageing curves at 150°C as a function of pre-ageing strain (ϵ_p)



(a) T6 treatment



(b) T8 treatment (4% pre-strain)

Figure 3: Electron micrographs demonstrating precipitate refinement with pre-ageing deformation. Micrographs were recorded with $\boldsymbol{B} \perp [0001]$, showing the change in length of β_1' precipitates as a function of pre-ageing deformation.

Precipitate size and number density

Typical micrographs of samples in the T6 and T8 condition are provided in Figures 3 and 4 and show that pre-ageing deformation resulted in refinement of the precipitates and and increase in the number of particles. T6 treatment resulted in a coarse distribution of high aspect-ratio β_1' precipitates, with an average length of 280 nm and an average diameter of 19.8 nm (Figure 3(a)). Pre-ageing deformation reduced the precipitate length to an average of 68 nm for 2% strain and 60 nm for 4% strain (Figure 3(b). The reduction in the precipitate diameter is less significant with an average value of 10.3 nm measured in the T8 condition with 4% pre-strain (Figure 4). The precipitate volume fractions were in the range 0.03 ± 0.0013 and the number density of precipitates increased from 1.25×10^{21} m^{-3} to 5.53×10^{21} m^{-3}.

Mechanical properties

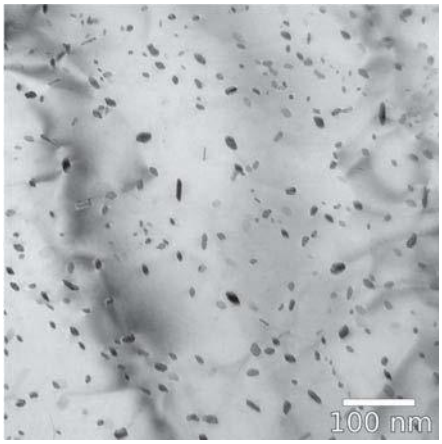
Engineering stress-strain curves for samples deformed in tension are provided in Figure 5(a). The average tensile yield strength of 142 ± 2 MPa in the solution treated condition increased to 278 ± 5 MPa after T6 treatment. T8 treatment or pre-ageing deformation enhanced the effectiveness of precipitation strengthening, increasing the yield strength by 5% to 293 ± 1 MPa after 2% pre-strain and by 7% to 298 ± 4 MPa and after 4% pre-strain. Four samples were tested in the solution-treated condition and two in each aged condition.

The increase in compressive yield stress after heat treatment was less pronounced as can be seen in Figure 5(b). The compressive yield strength of 105 ± 2 MPa in the STQ condition increased to 183 ± 4 MPa after T6 treatment. T8 treatments slightly enhanced the effectiveness of the precipitation strengthening, increasing the yield strength by 2% to 186 ± 4 MPa after 2% pre-strain and by 6% to 195 ± 2 MPa and after 4% pre-strain. Three samples were tested in the solution-treated condition, four in the T6 condition and and two in each T8 condition.

The yield strengths in tension and compression are plotted against the pre-ageing strain in Figure 6. This highlights that T6 treatment is responsible for the majority of the increase in the yield strength. The tensile yield strength increases at a rate 5 ± 2 MPa per % plastic strain. The rate of increase in



(a) T6 treatment



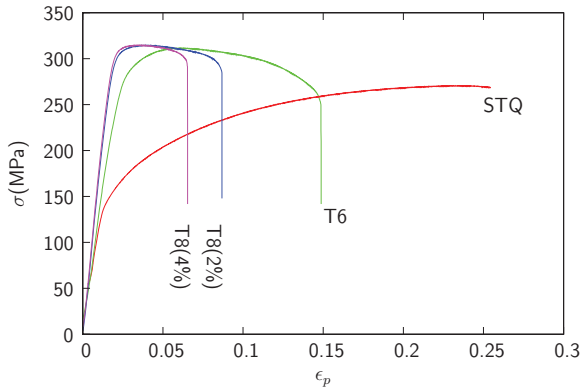
(b) T8 treatment (4% pre-strain)

Figure 4: Electron micrographs demonstrating precipitate refinement with pre-ageing deformation. Micrographs were recorded with $\boldsymbol{B} \parallel [0001]$ and showing the change in diameter of β_1' precipitates

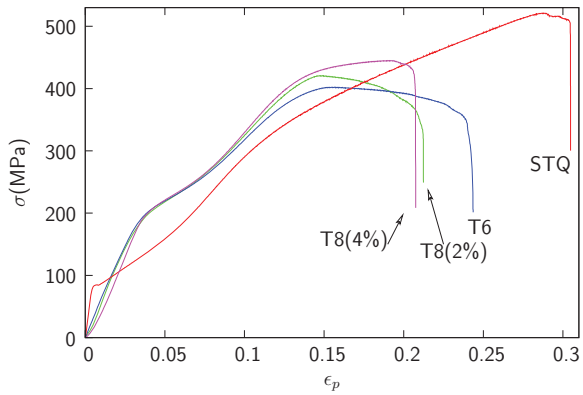
compressive yield stress is 3.5 ± 0.7 MPa per % plastic strain, approximately 30% less than the rate of increase in tension.

Discussion

The presence of precipitates in Mg-Zn alloy has been shown to increase the number density of twins while reducing the total twin volume fraction, indicating that precipitation assists in the nucleation of twins [5]. Despite this, precipitation increased the resistance to compressive deformation, suggesting that twinning is essentially growth-limited. Accordingly it is necessary to examine the effect of precipitates on the growth of the twin.



(a) Tension



(b) Compression

Figure 5: Tensile and compressive stress-strain curves for Mg-Zn for different heat treatment conditions.

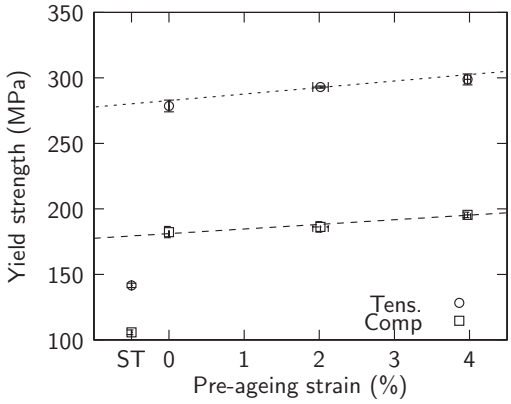


Figure 6: Yield strength in tension and compression as a function of pre-ageing strain.

The increase in asymmetry ratio for rod-shaped particles [5] and a similar decrease in the asymmetry ratio for plate-shaped precipitates [4] have been ascribed primarily to the effect of selective strengthening of different deformation modes, depending on the slip system and particle geometry [9]. This is based on comparison of the Orowan strengthening for rod and plate-shaped particle in the matrix and twin, with high aspect-ratio rods being particularly effectively against basal slip in the matrix [3]. In the present study, rod-like β_1' precipitates increase the tensile-compressive asymmetry in Mg-Zn alloys to a similar degree as in previous reports. The asymmetry ratio of 0.75 ± 0.02 in the ST conduction decreases to 0.65 ± 0.02 for T6 samples, which is similar to the change from 0.61 to 0.53 in Mg-5wt.%Zn [5] given isothermal treatment without pre-strain.

Pre-ageing deformation reduces the aspect ratio of the particles, which should in turn affect the relative resistance to slip in the matrix and twin. Previous studies have modelled strengthening of the alloy using Orowan looping calculations [7] where the increase in critical resolved shear stress is given by: $\delta\tau = \frac{2G}{2(1-\nu)\lambda} ln(d/b)$, where G is the shear modulus, ν is Poisson's ratio, d is the precipitate diameter in the slip plane and b is the Burgers vector of the dislocation and λ is the interparticle spacing on the slip plane. Tensile twinning reorients the matrix planes by 86° degrees, meaning that the basal planes of the matrix are near-parallel to the prismatic planes of the twin and vice versa. Therefore a reasonable approximation for the precipitate spacing in the twin can be obtained by using the Orowan strengthening equations for prismatic slip in the matrix. The equations for precipitate spacing in the matrix and twin are set out in Table 1.

Figure 7 plots the ratio of the Orowan strengthening expected in the matrix and twin. Data points co-responding to the strengthening ratios applicable to the T6 and T8 conditions are indicated on the plot. Strengthening against basal slip is greater under all conditions and the difference becomes more pronounced as the aspect ratio and precipitate length increases. The high aspect ratio particles in the T6 condition are expected to give about 40% greater strengthening in the matrix, compared to the twin. For the lower aspect ratios in the T8 condition, strengthening in the matrix is expected to be approximately 20% greater than in the twin, which should manifest as a a reduction in the tensile-compressive asymmetry.

Contrary to the expected behaviour, the change in aspect-ratio due to pre-ageing strain did not result in significant changes in the asymmetry ratio. Figure 8 plots the asymmetry ratio as a function of the precipitate number density. The heat treatment condition is indicated for each data point and the aspect ratio for the aged samples is included in the parentheses. Despite the change in number density and precipitate aspect ratio, the aged samples had no significant differences in asymmetry.

The present work, and previous reports which show that rod-like precipitates increase the asymmetry [5],

Table 1: Precipitate spacing equations for Orowan looping. The equations are for basal slip around [0001] rods in the matrix and twin.

Slip system	Spacing (λ)	Ref
Matrix	$\left(\frac{0.953}{\sqrt{f}} - 1\right) d$	[3]
Twin	$\frac{1}{\sqrt{N_A}}\sqrt{\left((k^2 + 1 - k\sqrt{3}\right)}$ where $k = l/L_p$	[7]

λ: interparticle spacing (nm)
L_p: centre-centre distance (nm)
d: precipitate diameter (nm)
l: precipitate length (nm)

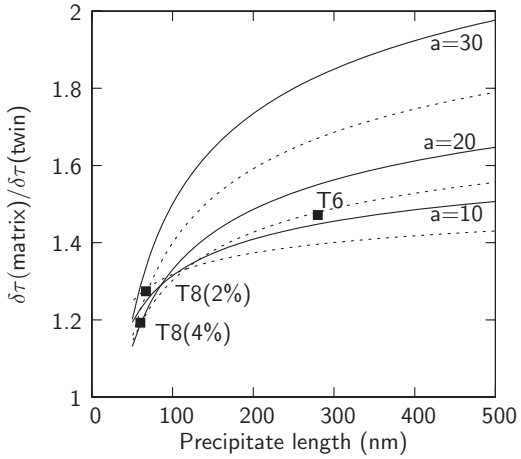


Figure 7: Orowan strengthening in the matrix and twin. The y-axis indicates the ratio of the Orowan strengthening for basal slip in the matrix relative to basal slip in the twin. The curves show change in the the strengthening ratio as a function of precipitate length for a series of precipitate aspect ratios (a). The strengthening ratios for precipitates in the Mg-Zn alloys are indicated.

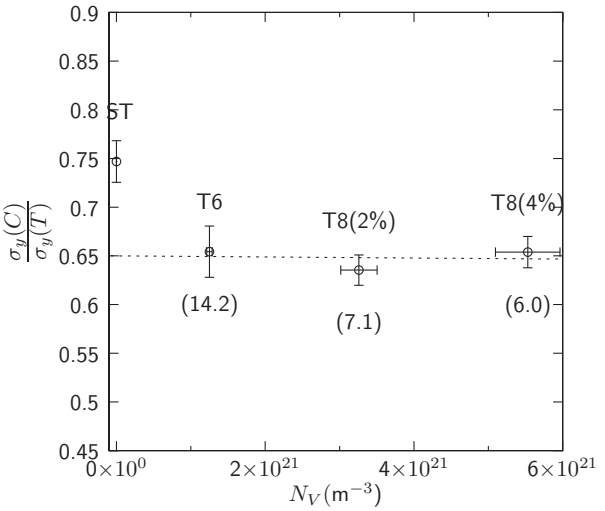


Figure 8: Tensile-compressive asymmetry as function of precipitate number density. The heat treatment condition is indicated for each data point and the aspect ratio for the aged samples is included in the parentheses.

whereas plate-like precipitates with (0001) habit reduce it [4] demonstrate that the precipitate morphology clearly influences tensile-compressive asymmetry. However, the insensitivity of the tensile-compressive asymmetry to the aspect ratio of the β_1' precipitates suggests that factors aside from "selective" strengthening are also important. Further analysis is underway to clarify this behaviour.

Conclusions

- Precipitation strengthening by rod-shaped β_1' particles with [0001] habit increased the tensile yield strength relative to the solution treated condition by 95-110% depending on the amount of pre-ageing deformation applied. Pre-ageing deformation increased the yield strength by 5 ± 2MPa per % plastic strain applied.

- Increases in the compressive yield stress were more modest at 77-86% greater than the solution treated condition, depending on the amount of deformation applied. Pre-ageing strain increased the yield strength by 3.5 ± 0.7MPa per % plastic strain applied.

- Precipitation heat treatment lead to a worsening of the asymmetry ratio from 0.75 to 0.65, due to the greater strengthening effect of the precipitates against basal slip in the matrix, compared to the twin.

- Pre-ageing deformation increased the number density and reduced the aspect ratio of the rod-shaped β_1' precipitates. It was expected that the reduction in aspect ratio would reduce the selective strengthening effect of the rod-shaped particles, however, the asymmetry ratio was found not to vary as a function of aspect ratio of precipitate number density.

References

[1] D.-G. Kim, H.-T. Son, *et al.* "The effect of texture and strain conditions on formability of cross-roll rolled AZ31 alloy." *Journal of Alloys and Compounds*, 509 (2011), 9413–9418.

[2] T. Kobayashi, J. Koike, *et al.* "Anomalous activity of nonbasal dislocations in AZ31 Mg alloys at room temperature." *Materials Science Forum*, 419-4, (2003), 231–236.

[3] J. F. Nie. "Effects of precipitate shape and orientation on dispersion strengthening in magnesium alloys." *Scripta Materialia*, 48 (2003), 1009-1015.

[4] N. Stanford, J. Geng, *et al.* "Effect of plate-shaped particle distributions on the deformation behaviour of magnesium alloy AZ91 in tension and compression." *Acta Materialia*, 60 (2012), 218–228.

[5] N. Stanford, M. R. Barnett. "Effect of particles on the formation of deformation twins in a magnesium-based alloy." *Materials Science and Engineering A*, 516 (2009), 226–234.

[6] J. B. Clark. "Transmission electon microscopy study of age hardening in a Mg-5wt.%Zn alloy." *Acta Metallurgica*, 13 (1965), 1281–1289.

[7] J. M. Rosalie, H. Somekawa, *et al.* "The effect of size and distribution of rod-shaped precipitates on the strength and ductility of a Mg-Zn alloy." *Materials Science and Engineering A*, 539 (2012), 230–237.

[8] J. M. Rosalie, H. Somekawa, *et al.* "The effect of precipitation on strength and ductility on Mg-Zn-Y alloys." *Journal of Alloys and Compounds*, 550 (2013), 114–123.

[9] J. D. Robson, N. Stanford, *et al.* "Effect of precipitate shape on slip and twinning in magnesium alloys." *Acta Materialia*, 59 (2011), 1945–1956.

Magnesium Technology 2014
Edited by: Martyn Alderman, Michele V. Manuel, Norbert Hort, and Neale R. Neelameggham
TMS (The Minerals, Metals & Materials Society), 2014

CHARACTERIZATION OF DAMAGE IN MAGNESIUM USING DIGITAL IMAGE CORRELATION AND ELECTRON BACKSCATTERED DIFFRACTION PATTERNING

Michael J. Nemcko[1], Pauline Mas[1], Moisei Bruhis[1], David S. Wilkinson[1]
[1]McMaster University (Department of Materials Science and Engineering); 1280 Main Street West; Hamilton, ON, L8S 4L8, Canada

Keywords: Digital image correlation, magnesium, microstructure, damage

Abstract

The microscopic strain distribution of commercially pure magnesium has been investigated during room temperature deformation. Digital image correlation (DIC) coupled with electron backscattered diffraction (EBSD) patterning has been used to relate strain measurements with the microstructure. Sheet magnesium tensile samples were etched and a random pattern of points were machined onto the sample surface using a focused ion beam (FIB). The samples were pulled in tension under an optical microscope. Images were obtained in increments and the DIC method was used to calculate the strain distribution. The strain distribution was compared to the EBSD pattern and the results show that strain localization is associated with twin and grain boundaries.

Introduction

Magnesium and its alloys have great potential for the design of lightweight components. However, magnesium has a hexagonal-close packed crystal structure which exhibits limited ductility prior to fracture at room temperature [1]. The dominating deformation mode at room temperature is basal dislocation slip. This mode of deformation only provides two independent slip systems which is inadequate to satisfy the von Mises criterion for an arbitrary shape change [2]. In addition, basal slip does not accommodate strain along the c-axis of the crystal. As a result, pyramidal slip and twinning are required to accommodate strain incompatibilities [3]. When strain incompatibilities cannot be accommodated by deformation mechanisms, micro-cracks form. It has been established that these micro-cracks initiate in the vicinity of grain boundaries and twin boundaries in magnesium materials [4,5]. Strain mapping using the DIC method during tension tests has been reported in the literature [6,7]. However, no effort has been made in the past to combine DIC method with high magnification optical micrograph images to study the deformation mechanisms and crack formation of pure magnesium sheet material during the tension tests.

Experiments

The material studied was hot rolled commercially pure magnesium sheet with a thickness of approximately 125 μm. Tensile samples were machined with a reduced gage section 0.7 mm in width and 0.5 mm in length. This specimen design was used in order to accommodate the limiting load capacity of the in-situ tensile stage. Samples were annealed at 400°C for 1 hour in an argon atmosphere. The average grain size was approximately 55 μm with a standard deviation of 30 μm. Mechanical polishing with 0.05 μm colloidal silica was carried out to obtain a smooth surface. The finer scratches were removed by chemical etching with a 10% nital solution. EBSD patterns were obtained on the undeformed samples using a JEOL-7000F field emission scanning electron microscope. A surface pattern was created on the sample surface using focused ion beam machining. Room temperature tensile tests were carried out using a special mini tensile stage that was designed at McMaster University and shown in Figure 1.

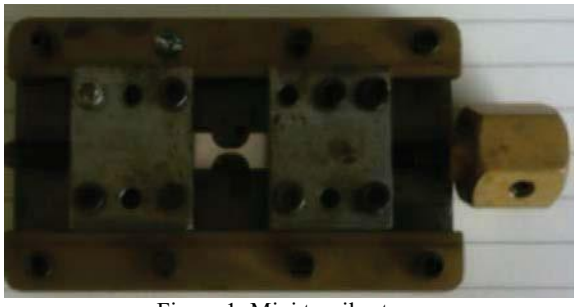


Figure 1: Mini tensile stage

The test was stopped at several increments of deformation to obtain optical micrographs of the samples using a Nikon AZ 100M stereoscope. The gray level images were imported into the ARAMIS system produced by GOM, to calculate the strain distribution using the DIC method [8]. Examination of the strain distribution at the microstructural level was carried out and the results were compared with the EBSD pattern.

Results

Optical Micrographs

The contrast in the micrographs resulted from the etched grain boundaries and machined points on the sample surface. The development of deformation in the gage section is shown in Figure 2. The macroscopic true strain was defined as:

$$\varepsilon = \ln\left(\frac{l}{l_0}\right)$$

where l is the current length of the gage section and l_0 is the initial gage length. Twin boundaries were visible in the microstructure at a macroscopic true strain of 0.042. The boundaries significantly changed the local greyscale pattern in the microstructure and strain calculations became more difficult to obtain in these areas. As a result, interpolation was required to obtain local strain measurements when these features were observed in the microstructure.

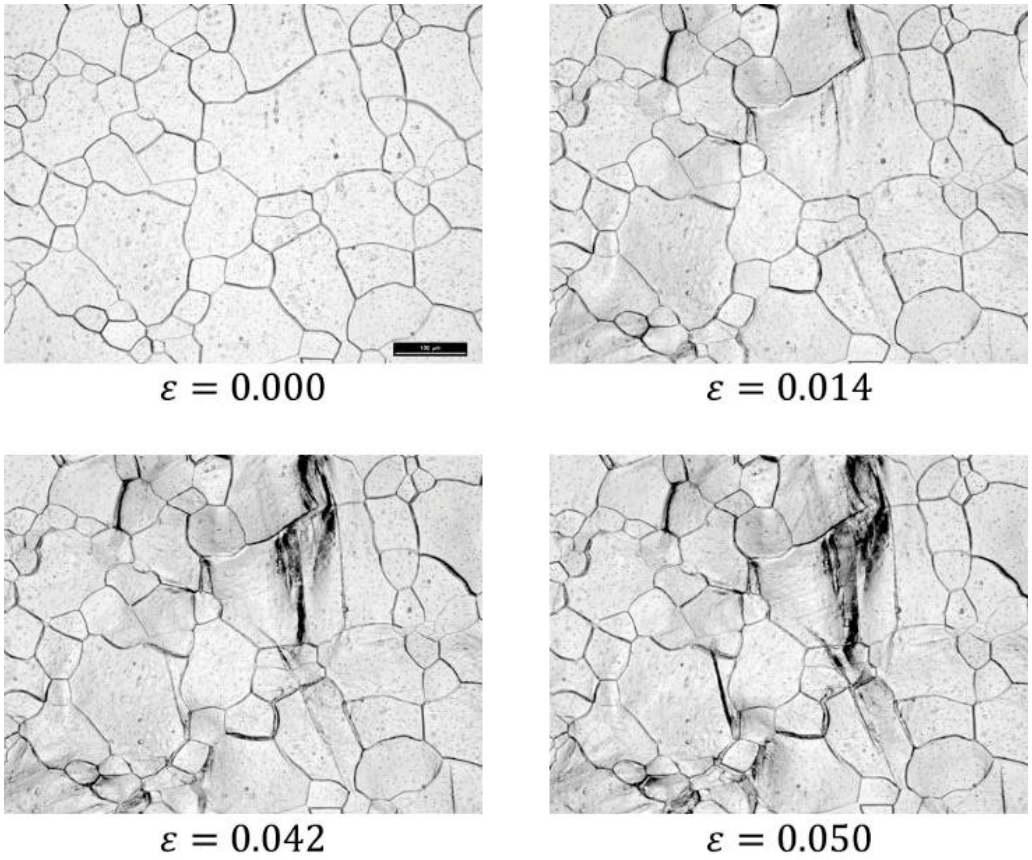


Figure 2: Optical micrographs of the gage section at various stages of macroscopic true strain. The tensile direction is horizontal.

Calculation Validation

In order to assess the validity of the DIC calculations the results were compared to measurements obtained using Image J software. Two indentations were made in the center of the gage section. The distance between the two points were measured at each increment of deformation to compare with the calculations. The strain calculated by ARAMIS showed an excellent agreement with the measurements obtained using Image J as shown in Figure 3.

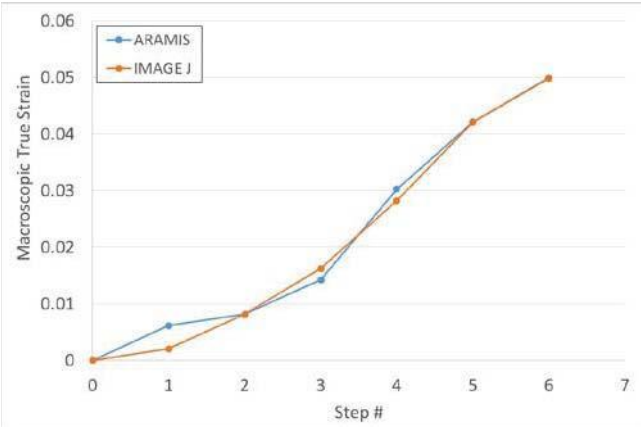


Figure 3: Macroscopic true strain as a function of deformation stage calculated using ARAMIS and Image J measurements.

Initial Texture

The crystallographic orientation of the undeformed specimen was determined using EBSD patterning and is shown in Figure 4. The majority of the grains were in the typical rolling orientation with the c-axis aligned through the sample thickness. These orientations do not favor basal dislocation slip and are known as hard orientations. Analysis of the EBSD data revealed that the majority of the grains were in orientations where the Schmid factor for basal dislocation slip was less than 0.2.

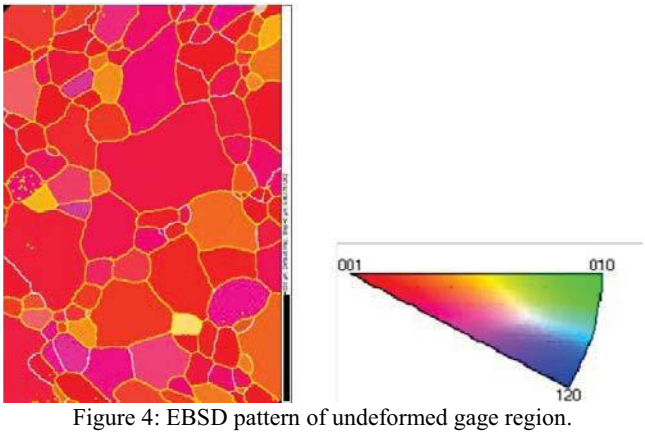


Figure 4: EBSD pattern of undeformed gage region.

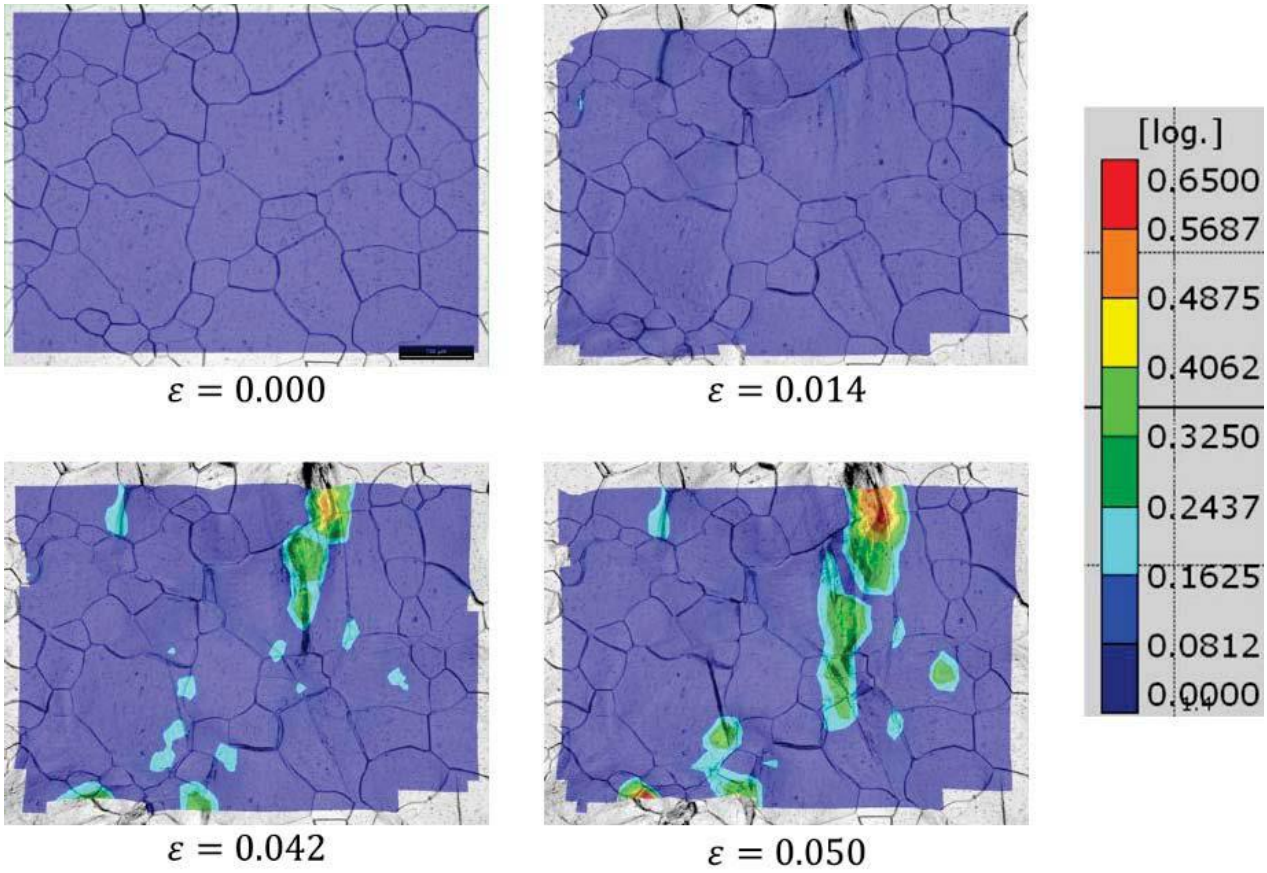


Figure 5: Microscopic strain distribution in the tensile direction at various stages of macroscopic true strain. The tensile direction is horizontal.

Microscopic Strain Distribution

The microscopic strain distribution was calculated from the gray level images at each step of deformation using ARAMIS software. The facet size used for the calculation was 45 x 45 pixels, which corresponds to an actual size of approximately 23 μm. The maximum error Δ in the strain calculation based on a facet size of 45 x 45 pixels is given by [9]:

$$\Delta = \frac{0.01}{45} = 0.00022 = 0.022\%$$

The distribution of strain in the tensile direction is shown in Figure 5 at various increments of deformation. At a macroscopic true strain of 0.014, localized strain had developed at several boundaries within the microstructure. These regions were associated with twin and grain boundaries. Upon further deformation the strain continued to localize in the vicinity of twin and grain boundaries until the final failure of the boundaries. In addition, it was observed that the grains did not experience a significant amount of deformation prior to the final fracture. This can be attributed to the hard orientations of the grains.

Conclusions

Several characterization techniques have been employed to understand the evolution of strain in magnesium samples deformed in tension. Strain maps were obtained using grain boundaries and machined markers as calculation points. The validity of the calculations were assessed by comparing the ARAMIS results to measurements obtained using Image J. The undeformed crystallographic texture of the material studied was observed using EBSD and showed the typical rolling orientation. This is known to be a hard orientation since the basal plane is oriented parallel to the tensile direction. The strain map revealed that the grains experienced very little deformation prior to fracture. Five independent slip systems are required within a single grain of a polycrystalline material for grain boundary continuity to occur. The lack of active deformation mechanisms in the grains examined resulted in strain concentrations at the grain boundaries. When the grain boundaries are strong enough, additional stresses occur to maintain compatibility between grains. This compatibility stress results in stress concentrations at the grain boundaries, which are sufficient to activate other deformation mechanisms such as non basal slip and twins. When the boundaries are weak, grain boundary separation occurs. Furthermore, it has been observed that twins contribute both a positive and negative effect on the mechanical integrity of the material. In the early stages of deformation, twins nucleate to accommodate strain incompatibilities. Upon further deformation, dislocations pile up on the twin boundaries and produce strain localizations. The strong strain localizations associated with twin and grain boundaries resulted in the final failure of the material. The results are different from what has been observed in tension tests performed on aluminum alloys which exhibit a higher degree of mechanical isotropy [10]. The aluminum alloys studied as well as other face centered cubic materials have sufficient deformation mechanisms to maintain compatibility between grains.

Consequently, the main mechanism responsible for the final failure of isotropic materials is shear localization associated with dislocation slip. The results from the experiments can be used to validate crystal plasticity models and provide insights into the development of stronger magnesium alloys.

References

[1] Emley, E.F., *Principles of Magnesium Technology*1966, Oxford: Pergamen Press.

[2] von Mises, R., *Mechanik der plastischen formänderung von Kristallen.* Zeitschrift für Angewandte Mathematik und Mechanik, 1928. **8**: p. 161-185.

[3] Yoo, M.H., *Slip, twinning, and fracture in hexagonal close-packed metals.* Source: Metallurgical Transactions A, 1981. **12A**(3): p. 409-418.

[4] M.J. Nemcko, and D.S. Wilkinson, "Investigation of Void Linkage in Magnesium Using SEM and Micro Computed X-ray Tomography" (Proceedings paper for ICF13, June 2013, Beijing)

[5] Barnett, M.R., *Twinning and the ductility of magnesium alloys: Part II. "Contraction" twins.* Materials Science and Engineering: A, 2007. **464**(1–2): p. 8-16.

[6] Kang, J., et al., *Microscopic strain mapping using scanning electron microscopy topography image correlation at large strain.* Journal of Strain Analysis for Engineering Design, 2005. **40**(6): p. 559-70.

[7] Kang, J., et al., *Digital image correlation studies for microscopic strain distribution and damage in dual phase steels.* Scripta Materialia, 2007. **56**(11): p. 999-1002.

[8] GOM mbH. Aramis-deformation measurement using the grating method, User's Manual, V5.3.08, 2004 (Braunschweig).

[9] Smith, B.W., M. Li, and W. Tong, *ERROR ASSESSMENT FOR STRAIN MAPPING BY DIGITAL IMAGE CORRELATION.* Experimental Techniques, 1998. **22**(4): p. 19-21.

[10] Herdawandi, H., et al., *The Portevin–Le Chatelier (PLC) effect and shear band formation in an AA5754 alloy.* Acta Materialia, 2007. **55**: p. 4151–4160.

Magnesium Technology 2014
Edited by: Martyn Alderman, Michele V. Manuel, Norbert Hort, and Neale R. Neelameggham
TMS (The Minerals, Metals & Materials Society), 2014

Low Cycle Fatigue Properties of Extruded Mg10GdxNd Alloys

Gerhard Tober[1], Petra Maier[1], Sören Müller[2], Norbert Hort[3]
[1]University of Applied Sciences Stralsund, Mechanical Engineering, Zur Schwedenschanze 15, Stralsund 18435, Germany
[2]Extrusion Research and Development Center TU Berlin, Gustav-Meyer-Allee 25, Berlin 13355, Germany
[3]Helmholtz-Zentrum Geesthacht, Magnesium Innovation Center, Max-Planck-Straße 1, Geesthacht 21502, Germany

Keywords: Rare Earth, magnesium alloy, low cycle fatigue, extruded

Abstract

The Rare Earth (RE) containing magnesium alloys Mg10Gd and Mg10Gd1Nd show after extrusion very good low cycle fatigue (LCF) properties. Considering extruded AZ31 as a possible benchmark alloy, life times as a function of LCF stress values are similar to the alloys investigated in this study. Mechanical properties determined in tension and compression show smaller values for both RE containing alloys. Therefore the LCF behavior is analyzed by the stress-strain hysteresis evaluation resulting in cyclic creep and plastic hardening or softening. LCF tests were strain controlled with amplitude of 0.5 % and 0.8 % at a frequency of 5Hz. The fracture surfaces are examined by SEM, where the area of crack propagation and overload were of main interest. Micrographs of longitudinal cross sections reveal twinning along the region of crack propagation. The correlation between the amount of twins and the number of cycles is discussed.

Introduction

Extruded magnesium alloys promise better strength and ductility than cast alloys but the main disadvantage is their anisotropic properties. Kleiner et al. [1] and Bohlen et al. [2] investigate extruded rods of AZ61 and AZ31, which can be taken exemplarily for Mg-Al-Zn alloys, according to its mechanical anisotropy. A texture with the majority of the basal planes lying parallel to the extrusion direction was observed. The two preferred deformation modes basal slip and pyramidal twinning and this texture are responsible for the anisotropy. Yang et al. [3] shows in their work that the magnesium alloy containing RE has refined grains and dispersed small precipitates. The RE content induces randomization of texture. These effects support the activation of basal slip and twinning is restrained. From that follows the absence of the tension–compression yield asymmetry observed for AZ31. RE elements are also useful substitutes for aluminum in Mg alloys when creep resistance is required [4]. Since creep resistance is influenced by the grain size, it increases due to the fine-grained structure as a result of recrystallization during extrusion. Hort et al. [5] show that Mg10Gd has a good corrosion resistance and Maier et al. [6] examined the fatigue behavior (in HCF) of the extruded alloys Mg10Gd and Mg10Gd1Nd, showing an improvement in fatigue strength and life by adding Neodymium (Nd). It was shown that even for 150 MPa stress amplitude a number of cycles to failure of more than 4000 are reached even the tensile yield strengths are only 132 MPa for Mg10Gd and 137 MPa for Mg10d1Nd.

Mirza et al. [7] investigated LCF properties of Mg10Gd3Y0.5Zr (GW103K). They reported symmetrical hysteresis loops caused by weaker crystallographic texture and the absence of twinning-detwinning activities due to the fine-grained structure and the RE precipitates.

It is necessary to investigate the LCF properties of both alloys to find out how they can be compared with the well understood extruded alloy AZ31. Huppmann et al. [8] investigate the influence of the indirect extrusion process with and without counterpressure on the LCF properties of AZ31 in stress and strain controlled tests. The conventional extruded AZ31 will be the benchmark material for this work. One has to take into account that there are some differences: the extrusion ratio for AZ31 is 25 and the ram speed is 0.5 mm s^{-1} and furthermore the frequency of the fatigue tests was 10 Hz.

Materials and experiments

Mg10Gd1Nd contains 9.8 wt.% Gd, 0.88 wt.% Nd and balance magnesium and Mg10Gd has an amount of 9.7 wt.% Gd. The extruded bars of both alloys were produced at the Extrusion Research and Development Center TU Berlin. They were directly extruded at 420°C with a product speed of 22 m/min and an extrusion ratio of 37.

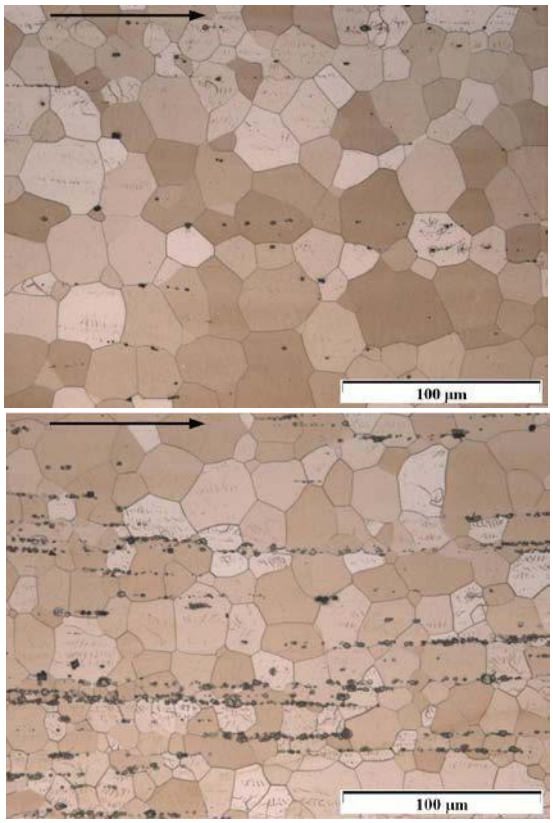


Figure 1: Microstructure of Mg10Gd (a) and Mg10Gd1Nd (b), black arrow indicates the extrusion direction

The fine grained microstructure, prepared according to Kree [9], as a result of the extrusion process, of both materials is shown in figure 1. Mg10Gd (Figure 1a) has an average grain size of 18 µm and Mg10Gd1Nd (Figure 1b) of 18 µm. The added 1 wt.% Nd increases the amount of second phases, acting as nuclei for the recrystallization in the extrusion process.

The mechanical properties of the investigated alloys and AZ31 are listed in Table 1. The ratio compressive yield strength divided by tensile yield strength is for Mg10Gd and Mg10Gd1Nd close to one, so it is expected that the compressive and tensile values of the absolute maxima are almost equal at the beginning of the tests. For AZ31 that ratio is only 0.59 so a more asymmetrical progression of the hysteresis loops is expected.

Table 1: Tensile properties (TYS: tensile yield strength, UTS: ultimate tensile strength, El.: elongation at fracture) and the compression properties (CYS: compressive yield strength, CS: compressive strain at fracture) of extruded Mg10Gd1Nd, Mg10Gd and AZ31 [6]

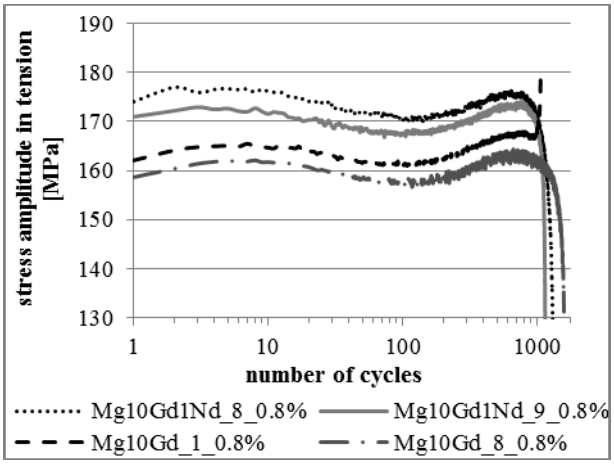
	TYS [MPa]	UTS [MPa]	El. [%]	CYS [MPa]	CS [%]	CYS / TYS
Mg10Gd	132	250	23	134	26	1.01
Mg10Gd1Nd	137	256	17	152	16	1.11
AZ31[6]	191	259	23	112	10.9	0.59

LCF tests were performed on a closed-loop servo hydraulic testing machine system MTS820. The test execution was done using the template "ASTM LCF Strain" which is according to ASTM standard E606-04. Specimens of circular cross-section with a diameter of 6 mm for the cylindrical gauge length were machined with a surface roughness of 6.3 µm. The tests were undertaken in strain controlled mode, with a strain ratio of S = -1 and sine shaped with a frequency of 5 Hz (loading direction was extrusion direction). Fracture surfaces were characterized using a Scanning Electron Microscope EVO 40 by Carl Zeiss.

Results and discussion

The amplitudes in tension and compression are shown in the figures 2 and 3. For the strain amplitude of ε_A = 0.8 % the curves for both amplitudes have a similar start, until 100 cycles a decrease is followed by an increase of the amplitude up to around 750 cycles. The specimen Mg10Gd_8_0.8% is an exception because for it the amplitude in tension is significantly higher than in compression, which was not expected by taken the CYS/TYS – ratio into account, and the curve decrease in tension from cycle number 650. The amount of decrease in tension is bigger than in compression. The resulting stresses from the strain amplitude of 0.8 % are higher for Mg10Gd1Nd than for Mg10Gd.

a)



b)

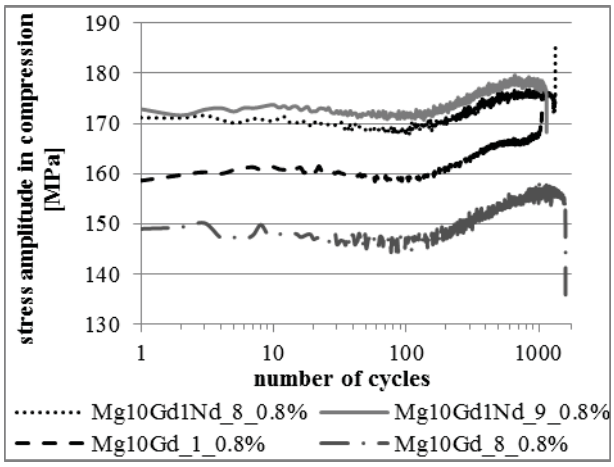
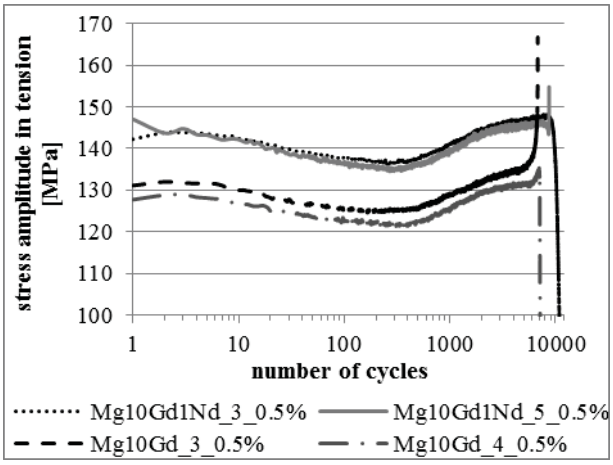


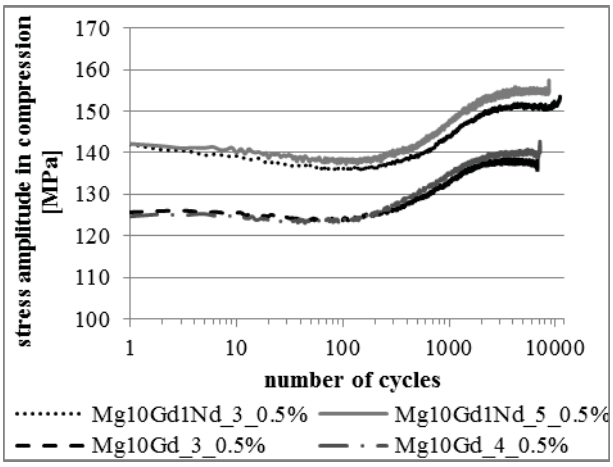
Figure 2: Stress over number of cycles for ε_A = 0.8 %: absolute minimum stress (a) and absolute maximum stress (b)

Figures 3 shows the amplitudes for ε_A = 0.5 %. Here it can be seen, that the maximal stresses in tension and compression are higher for Mg10Gd1Nd compared to Mg10Gd. Further it can be observed that the amplitude values in compression are higher than in tension at cycles higher than 40; that counts for both alloys.

The decrease in stress observed for ε_A = 0.8 % within the first cycles is also present. In compression the increasing amplitude starts almost at cycle number 100. In tension there is a decrease observable until around 250 cycles. Between 2000 and 3000 cycles all curves reach an almost constant value in compression and in tension the increasing slope declines. Only specimen Mg10Gd_3_0.5% shows a small decrease of the stress amplitude in compression from cycle 4000 and an increase in tension until damage.



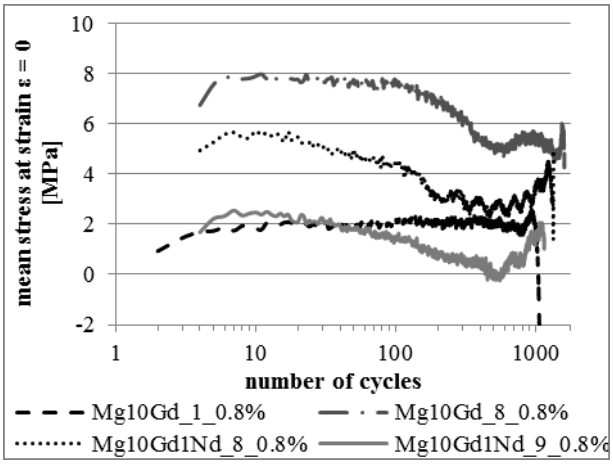
a)



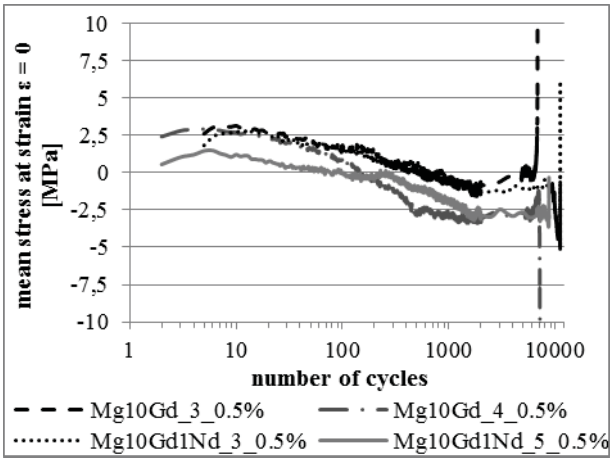
b)

Figure 3: Stress over number of cycles for ε_A = 0.5 %: absolute minimum stress (a) and absolute maximum stress (b)

The mean stresses at strain ε = 0 are shown in figure 4a) for ε_A = 0.8 % and in b) for ε_A = 0.5 %. For both alloys cyclic softening at the beginning of the tests in tension is higher than in compression. After that the mean stresses shift to smaller values. For ε_A = 0.8 % cyclic hardening in tension is also higher than in compression. Cyclic hardening for ε_A = 0.5 % in both directions is similar, so mean stress stays at an almost constant value.



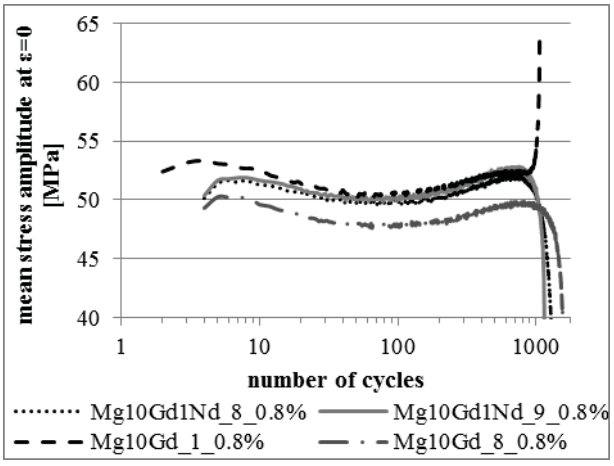
a)



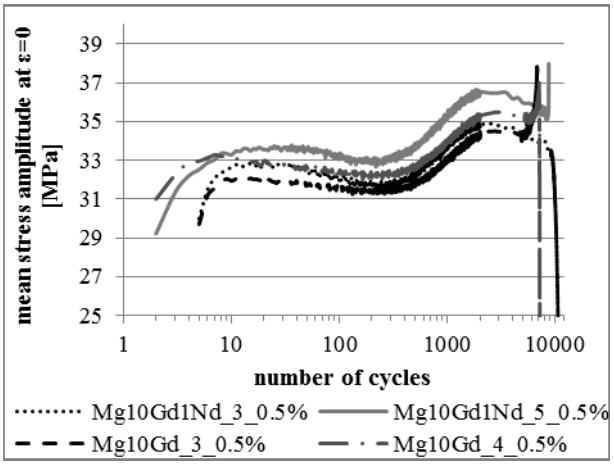
b)

Figure 4: Mean stress at ε = 0 over the number of cycles: ε_A = 0.8 % (a) and ε_A = 0.5 % (b)

Hardening and softening behavior is shown in figure 5. The stress amplitude at ε = 0 is an indicator for the residual stresses due to the strain hardening in the cyclic loading: the higher that residual stress the more strain hardening. For ε_A = 0.8 % both materials start with softening. Hardening is present from cycle 70 to 600. Only Mg10Gd_8_0.8% has hardening up to cycle number 700.



a)



b)

Figure 5: Mean stress amplitude at ε=0 over the number of cycles: ε_A = 0.8 % (a) and ε_A = 0.5 % (b)

For ε_A = 0.5 % (Figure 5b) both materials show softening up to cycle number 200 and hardening up to 3000 cycles, followed by softening up to cycles to fracture. Mg10Gd shows hardening before fracture whereas Mg10Gd1Nd shows softening up to fracture. The formation and growth of secondary cracks (Figure 8b) could be the reason for that cyclic softening. Further analyses of the microstructure near the fracture surface (cross-sections) are required to investigate how the crack propagates.

In figure 6 exemplary hysteresis loops (1, 3 and half-time) of the two alloys and strain amplitudes are presented. Both alloys show symmetric hysteresis loops at the given cycles. The symmetry of the hysteresis has no recognizable influences from twinning and detwinning. The fine-grained structure of both magnesium alloys inhibits twinning as the main deformation mechanism.

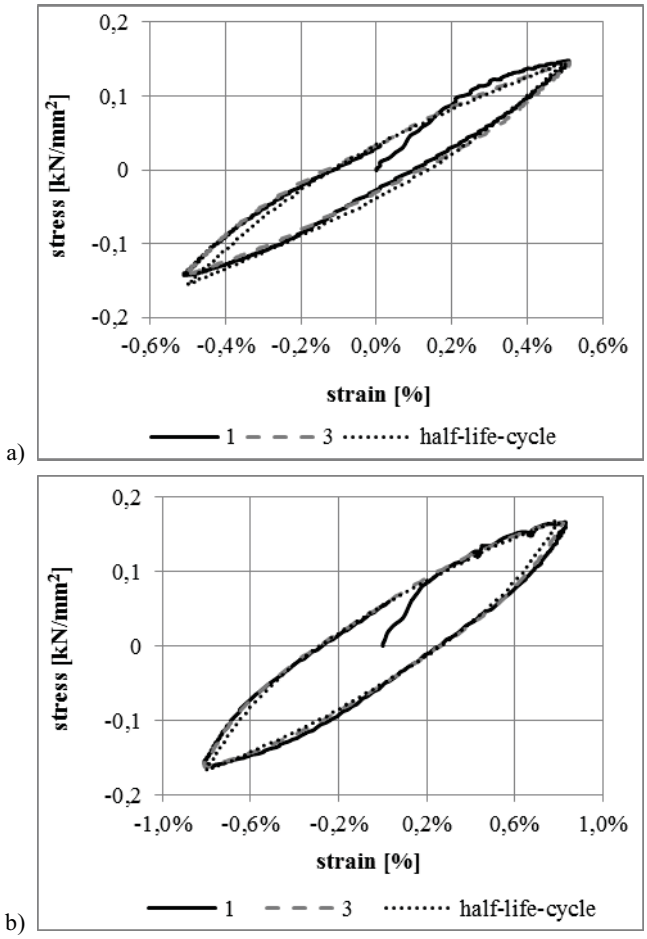


Figure 6: Hysteresis loops: Mg10Gd1Nd_5_0.5% (a) and Mg10Gd_1_0.8% (b)

In figure 7 examples of fracture surfaces for both strain amplitudes and materials, respectively, are shown in a) to d). Mg10Gd1Nd_5_0.5% and Mg10Gd_1_0.8% are discussed in more detail by higher magnification; the white rectangles indicate where images of higher magnification were taken (see figure 8). Specimen Mg10Gd1Nd_5_0.5% (figure 7a) has seen the longest test duration out of the four presented fractured samples (8689 cycles). A typical fatigue fracture surface can be seen, the crack is initiated at only one side (bottom) and the crack is propagated up to the residual fracture surface (top).

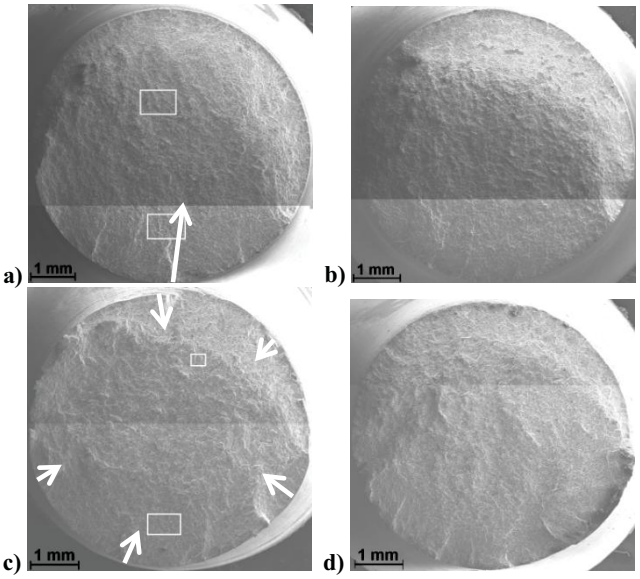
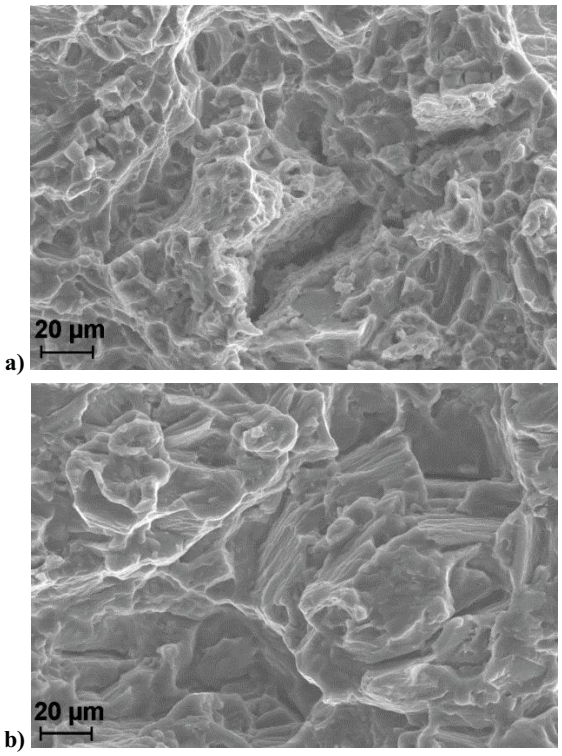


Figure 7: SEM: Fracture Surfaces of a) Mg10Gd1Nd_5_0.5%; b) Mg10Gd1Nd_9_0.8%; c) Mg10Gd_1_0.8%; d) Mg10Gd_3_0.5%

Specimen Mg10Gd_1_0.8% has seen the shortest test duration (1059 cycles) because of the lower strength due to the missing Nd content and the higher load of 0.8 % strain amplitude. This fractured samples presents crack initiations at different points on the contour (see white arrows in figure 7c). That could be an indication for a notch effect due to surface defects, which act stronger at high strain amplitudes. Therefore fatigue striations are spread over the entire surface. The residual fracture surface is in the central upper right-hand region.



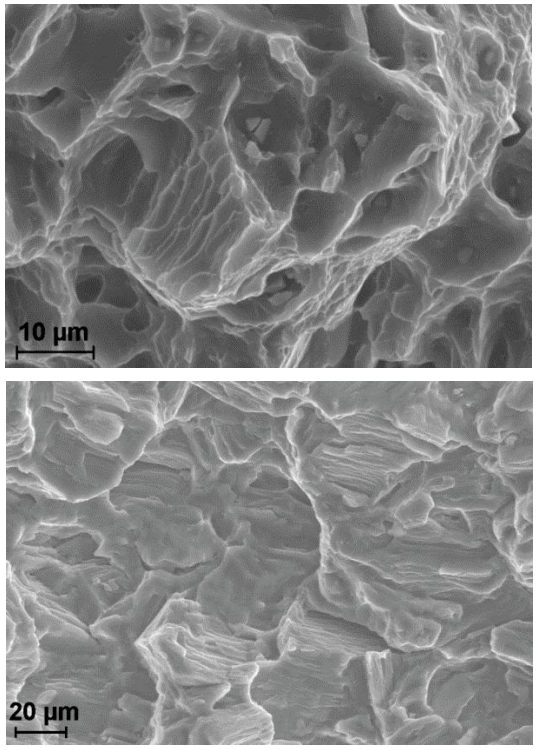


Figure 8: SEM fractured surfaces: Mg10Gd1Nd_5_0.5% overload area (a) Mg10Gd1Nd_5_0.5% area of crack propagation (b) Mg10Gd_1_0.8% overload area (c) Mg10Gd_1_0.8% area of crack propagation (d)

At higher magnification of the fracture surface of Mg10Gd1Nd in Figure 8a second phases are recognizable. The formation and chemical compositions are not established yet. The residual fracture surface is characterized by a ductile fracture. The detail of the bottom section in Figure 8b shows micro cracks and fatigue striations as signs of the ongoing crack propagation. The fracture surface of the sample for Mg10Gd is not like expected due to the large number of crack initiations. In Figure 8c the residual fracture area is shown presenting ductile fracture. Also Figure 8d shows ductile morphology by fatigue striations indicating the direction of crack propagation.

For comparison with the results of Huppmann et al. [8] the number of cycles to failure are listed in Table 2. For the strain amplitude of 0.5 % Mg10Gd1Nd achieves a number of cycles to failure of 9883 and Mg10Gd a number of 6985 cycles. For the AZ31 alloy in Figure 9 that value is around 10000 cycles and for a slightly smaller strain amplitude of 0.75 % between 1500 and 2000 cycles. That strain amplitude 0f 0.75 % is slightly smaller compared to this study, but both investigated alloys reaches around 1300 cycles at a strain amplitude of 0.8 %. From that point of view Mg10Gd1Nd is closer to AZ31 than Mg10Gd, but for a final statement more tests are necessary, which is also the reason for the missing standard deviation.

A further benchmark for the comparison is the stress value in tension. AZ31 can resist higher loads at the selected strain amplitudes than the RE alloys. In the 0.5 % strain amplitude test it starts at 180 MPa for AZ31. In comparison for Mg10d1Nd it starts circa at 145 MPa and for Mg10Gd at 129 MPa. This large difference in the stress level is also seen for the higher amplitudes.

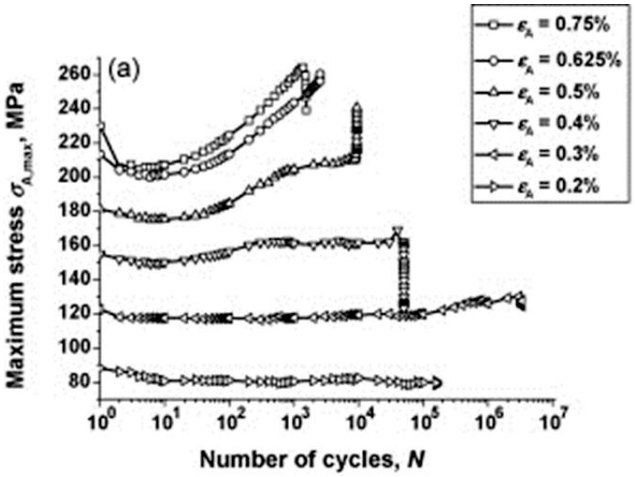


Figure 9: Maximum tensile stress for conventional extruded AZ31 according to Huppmann et al. [8]

If the ratio CYS/TYS is taken into account it is obviously that the behavior during a cycle is very different between the RE alloys and AZ31. The RE alloys have a ratio higher than 1, so at the beginning the larger plastic strain will occur in tension. For AZ31 the plastic strain in compression is higher because the CYS is much smaller than the TYS. The ultimate tensile strength varies for the three alloys only in an amount of 9 MPa. Mg10Gd1Nd and Mg10Gd have the benefit that they behave in tension and compression very similar. That explains why they can resist the both strain amplitudes with almost the same number of cycles to failure as AZ31.

Table 2: Number of cycles to failure of Mg10Gd and Mg10Gd1Nd for the strain amplitudes of 0.5 % and 0.8 %

specimen	Load in % strain amplitude	Number of cycles to failure	Mean value of number of cycles to failure
Mg10Gd_3_0.5%	0,5	6791	6985
Mg10Gd_4_0.5%	0,5	7179	
Mg10Gd_1_0.8%	0,8	1059	1326
Mg10Gd_8_0.8%	0,8	1594	
Mg10Gd1Nd_3_0.5%	0,5	11077	9883
Mg10Gd1Nd_5_0.5%	0,5	8689	
Mg10Gd1Nd_8_0.8%	0,8	1334	1240
Mg10Gd1Nd_9_0.8%	0,8	1146	

The addition of RE elements in magnesium alloys refines the grains in the extrusion process from what results a better ductility. [10,11] Stanford and Barnett [10] show that Lanthanum (La) and Gadolinium (Gd) relieve the extrusion texture. According to Yang et al. [3] both, finer grains and weaker extrusion texture enforce the basal slip deformation mechanism and a more symmetrical compression – tension behavior of the RE containing magnesium alloys. Both the microstructures in Figure 1 show second phase precipitates and the Nd content increases its amount significantly, resulting in a finer grained microstructure due to recrystallization. That improves the strength of Mg10Gd1Nd but the precipitates reduce the ductility.

The SEM pictures in Figure 7 demonstrate that the surface of the specimen is the preferred region where the crack is initiated. Its roughness or defects close to the surface enforce the crack forming.

Conclusion

Both alloys reach the durability of AZ31 if loaded with strain amplitudes of 0.5 % and 0.8 %. The resulting stresses are much smaller than of AZ31 due to its higher yield strength in tension. Mg10Gd1Nd reaches higher stress levels than Mg10Gd which is expected because of the better strength values. Mg10Gd1Nd reaches for $\varepsilon_A = 0.5$ higher cycles to failure than Mg10Gd and is closer to the values of AZ31. This work shows that Mg10Gd1Nd and Mg10Gd deliver comparable results to AZ31.

For both strain amplitudes Mg10Gd and Mg10Gd1Nd retain their symmetrical hysteresis loops during the LCF tests. It can be concluded that the plastic deformation behavior of both alloys in cyclic tension and compression loading is similar for the resulting stresses. The strain ratio S = -1 and that symmetrical hysteresis causes mean stress values close to zero.

In further work texture measurements will be helpful for better comparison of starting material to after cycling. Even the hysteresis does not show evidence of twinning, hardening and softening indicate that re-orientation takes place. Micrographs of fractured samples (cross-sectional) are needed to evaluate twinning.

Acknowledgements

The authors appreciate the support of Chamini Mendis (HZG) and Gert Wiese (HZG) for sample preparation and light microscopy.

References

1. S Kleiner, P.J Uggowitzer, “Mechanical anisotropy of extruded Mg–6% Al–1% Zn alloy,” *Materials Science and Engineering*: A, Volume 379, Issues 1–2, (2004), 258-263.

2. J. Bohlen et al., “Microstructure and texture development during hydrostatic extrusion of magnesium alloy AZ31,” *Scripta Materialia*, Volume 53, Issue 2, (2005), 259-264.

3. F. Yang, et al., “Enhanced very high cycle fatigue performance of extruded Mg–12Gd–3Y–0.5Zr magnesium alloy”, *Materials Science and Engineering*: A, Volume 528, Issue 6, (2011), 2231-2238.

4. L.L. Rokhlin, *Magnesium alloys containing rare earth elements – structure and properties*, (Taylor & Francis, London, UK 2003).

5. N. Hort et al., “Magnesium alloys as implant materials – Principles of property design for Mg–RE alloys”, *ActaBiomaterialia*, Volume 6, Issue 5, (2010), 1714-1725.

6. P. Maier et al., “Influence of Nd in extruded Mg10Gd base alloys on fatigue strength” *Materials Science Forum,* 8th THERMEC2013, Las Vegas, Nevada (2013) in press.

7. F.A. Mirza et al., “Low cycle fatigue of a rare-earth containing extruded magnesium alloy”, *Materials Science and Engineering*: A, Volume 575, (2013), 65-73.

8. M. Huppmann et al., “Fatigue properties of the hot extruded magnesium alloy AZ31”, *Materials Science and Engineering*: A, Volume 527, Issues 21–22, (2010), 5514-5521.

9. V. Kree et al., Metallographische Gefügeuntersuchungen von Magnesiumlegierungen / The Metallographical Examination of Magnesium Alloys,*Practical Metallography*, 41 (2004), 233-246.

10. N. Stanford, M.R. Barnett, “The origin of “rare earth” texture development in extruded Mg-based alloys and its effect on tensile ductility”, *Materials Science and Engineering: A*, Volume 496, Issues 1–2, (2008), 399-408.

11. J. Bohlen et al., “Effect of rare earth elements on the microstructure and texture development in magnesium–manganese alloys during extrusion”, *Materials Science and Engineering: A*, Volume 527, Issue 26, (2010), 7092-7098.

12. F. Wang et al., Cyclic deformation and fatigue of extruded Mg–Gd–Y magnesium alloy, *Materials Science and Engineering: A, Volume 561*, (2013), 403-410.

Magnesium Technology 2014
Edited by: Martyn Alderman, Michele V. Manuel, Norbert Hort, and Neale R. Neelameggham
TMS (The Minerals, Metals & Materials Society), 2014

QUANTIFICATION OF MICROSTRUCTURE-PROPERTIES-BEHAVIOR RELATIONS IN MAGNESIUM ALLOYS USING A HYBRID APPROACH

K. Hazeli[1], J. Cuadra, P.A. Vanniamparambil[1], R. Carmi[1] and A. Kontsos[1]
[1]Department of Mechanical Engineering & Mechanics, Drexel University, Philadelphia, PA, USA

Keywords: Magnesium Alloys, Fatigue, Twinning-detwinning, Digital image correlation, Acoustic emission

Abstract

This study presents a hybrid experimental mechanics approach combining multi-scale mechanical testing, in situ nondestructive evaluation and targeted microscopic quantification to identify and quantify critical microstructural parameters that affect properties and overall plasticity of Mg alloys. Room temperature monotonic and cyclic experiments monitored by Digital Image Correlation (DIC) coupled with Acoustic Emission (AE) of Mg Alloys of the AZ series were used for this investigation. Data obtained using the optico-acoustic nondestructive system revealed for the first time the direct connection between surface strain localization effects similar to Luder's bands and pronounced twin activity. Electron Back Scatter Diffraction (EBSD) measurements showed the profuse and spatially inhomogeneous nature of twinning at early stages of plasticity which is related with the onset of yielding and the macroscopic plateau region in the stress-strain curve. Furthermore, twinning/detwinning activity was identified in several grains of tested specimens and during characteristic points of fatigue cycles.

Introduction

Deformation of polycrystalline materials is greatly associated to the local response of the material to the grain scale operating deformation mechanisms [1, 2]. This topic has been promoted by advancement of experimental methods for *in situ* and *ex situ* measurement of microstructure evolution at various length scales. This is particularly important when a deeper understanding of local deformation response, and subsequently, driving force for crack initiation are of interest. In this framework, many studies have been conducted to investigate the influence of microstructure attributes to fatigue crack formation. For instance, Mughrabi [3] demonstrated that localized plastic deformation, which is precursor to Persistent Slip Bands (PSB) supports fatigue crack initiation. Additionally, Miao et al [4] combined EBSD measurement with quantitative fractography analysis, to link microstructural features associated with internal crystallographic fatigue crack initiation in nickel based super alloy. They further reported a large crystallographic facets development at crack initiation sites due to cyclic strain localization on slip planes. In this regard, Carroll et al. [1] presented a quantitative sub-grain full-field measurement of strain plastic strain accumulation near a growing fatigue crack. In this study, they also utilized high resolution DIC measurements to show strain field inhomogeneities within a grain. Similarly, the authors [5] provided a quantitative analysis of grain scale heterogeneities due to twinning in Mg alloys. In addition to the strain heterogeneities and its association with crack initiation[6], the significant effect of local texture on plastic anisotropy [7], grain incompatibilities[1] has been also explored.

Here we confine our attention on the major parameters that effect on fatigue behavior of Mg alloys by a hybrid experimental mechanics approach combining multi-scale mechanical testing, in situ nondestructive evaluation and targeted microscopic quantification. It is important to notice that due to the limited number of active deformation system in room temperature, twinning plays a crucial role to accommodate strain[8]. The twinning operation is widely sensitive to the material texture[9, 10], grain size[11, 12], alloying elements[7, 13], testing temperature[14] and strain rate[15]. Twinning results in a sudden reorientation of the volume fraction of the crystal. Thus, twinned region creates a new grain boundaries [16] and markedly influences on strain hardening rate[17] and indeed accentuated the characteristic Bauschinger effect in Mg alloys [18, 19]. This is also important to develop a more accurate fatigue life model as dislocation interaction with grain boundaries can leads to a stress concentration sites for crack formation. Currently, none of the fatigue life estimation models explicitly address the damage accumulation, strain localization and crack initiation as a function of local texture changing due to the twinning[9]. As specified, these parameters can potentially introduce new possibilities to consider the role of microstructure in the formation and growth of cracks during cyclic loading.

Experimental Procedure

In order to eliminate grain size disparity effect, thermo-mechanical processing on the as received previously warm-rolled AZ31 plate (25 mm thickness) was conducted. The Mg rolled plate was received in the H24 temper, shown in Figure 1(a), with a bimodal grain size distribution and an average grain size of ~7 μm. After annealing to put the material in the O temper, Figure 1(b), the bimodal grain size distribution was still intact with an average grain size of ~10 μm. With an intention of producing a larger grain size material, a small amount of strain (3%) was applied in compression parallel to the c-axis at room temperature using a screw-driven INSTRON, followed by annealing. Anealing was conducted for 50hours at 450°C. As a consequence of the noted thermo-mechanical processing fairly uniform microstructure with average grain size of ~28 μm was obtained (see Figure 1(c)).

The mechanical test procedure consisted of comression, tension and fatigue. Refering to figure 1(d), compresion tests were performed in different orientations. Due to the plate size limitation in normal to the surface direction (ND), tensile and fatigue test were examined only along the Transverse Direction (TD). Compression, tension and fatigue specimens were cut using Electron Discharged Maching (EDM) according to ASTM E9, ASTM E8 and ASTM E466 respectivley. Prior to the mechanical testing, material texture were measured by collecting Electron Back-Scattered Difraction (EBSD) using TSL channel installed on scanning electron microscopy (Philipes FEI XL30). Figure 1(c)

illustrates the final microstructure and texture of the tested samples which shows a sharp texture along the ND direction. As it was expected texture concentration were deviated from the ND direction in the samples in which were cut from 60° and 45° respect to the ND directions (Figure 1(e)). Monotonic compression and tension tests were caried out using MTS hydraulic loading unit at a constant strain rate of $4.5\times10^{-4}s^{-1}$ in room temperature. The same hydraulic loading frame was utilized to apply strain control cyclic compression-tension loading profile. Fatigue tests were performed with strain amplitude of 1% with the strain ratio of -1 and frequency of 0.5Hz. In addition to the macroscopic strain which was measured by a 10 mm gage length extensometer, full field strain were computed *in situ* using the GOM ARAMIS Digital Image Correlation (DIC). A stochastic speckle pattern was applied on the front surface to create a vivid surface light contrast and to track the deformation process. DIC images were captured at a rate of 7Hz. Furthurmore, in situ Acoustic Emission (AE) measurments during cyclic loading were used to determine the activation of possible twinning mechanisms during fatigue cycles. Hence, AE signals were recorded using a piezoelectric transducer (Pico) with an operating frequency range of 200-750kHz and a peak frequency at 500kHz.

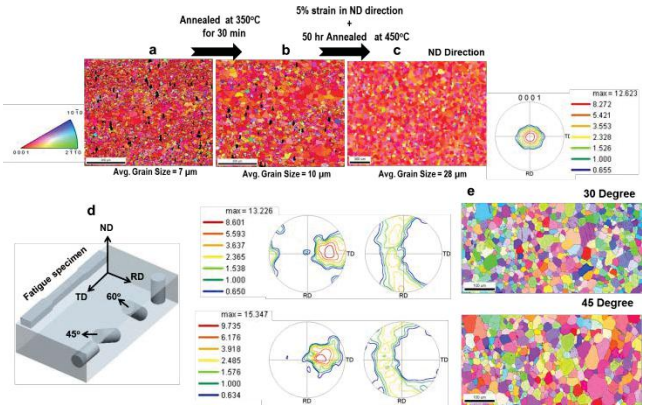


Figure 1. Inverse Pole Figure (IPF) for (a) as recived matrial (b) Anealing (c) final microstructure after thermo-mechanical process. (d) Compression, tension and fatigue speimen respect in the magnesium plate. (e) IPF obtaine for the sample cuts from 60 and 45 respect to the rolling direction

Results and Discussion

to understand the length-scale effect of plastic deformation mechanisms, in situ surface imaging of the strain field and continuous AE recording was utilized and correlated to the microstructure. Carroll et al.[20] proposed an experimental methodology for high resolution full-field strain map in polycrystalline material. Here, Carroll et al.[20] successfully overlaid the microscopic information calculated by EBSD on optical images which were taken before and during deformation to meet DIC needs. Accordingly, qualitative analysis of *cumulative* plastic strain in relation to microstructure was obtained. It must be recognized that this methodology (*ex situ*) relies on test interruption. Thus, it was not convincible to utilize this method in our investigation as the objective was to identify the effect of twinning and twinning occurs at a fraction of second, and therefore, impossible to interrupt the test at the right strain level.

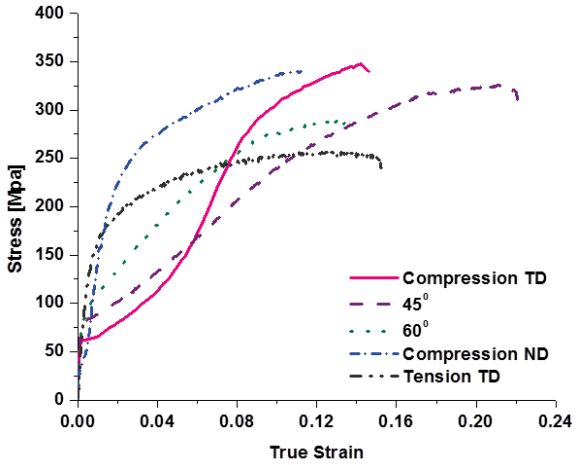


Figure 2. Stress-strain curve for compression and tension sample cutting from different orientation as shown in figure 1

Compression and tension stress-strain curve for four different compression orientation and tension along TD direction is given in figure 2. Evidently the highest flow stress is observed for compression along the ND direction. Figure 2 also displays that the remarkable elongation is obtained for the specimen which cut with 45 angle degree. Notice that the flow stress decreases remarkably when the specimen orientation inclines toward TD direction. Since the grain size of the specimens were very similar this observation can be attributed to significant effect of texture on mechanical property.

In fact, the high twinning Schmid factor (SF) for the compression TD is high[21] and twinning-dominated results to characteristic s-type stress-strain curve[22, 23]. In addition, the mechanical results along the TD direction show a notable flow stress and strain rate difference between tension and compression (mechanical asymmetry). As noted, the mechanical asymmetry in a magnesium alloy extrusion with strong basal texture is expected to be largely determined by the relative ease with which tension twinning occurs (controlling yield in axial compression) compared to prismatic slip (controlling yield in axial tension)[24].
Figure 3 demonstrates fatigue hysteresis loop for the first four cycles along with the full-filled in situ measured strain map. Strain maps are corresponded to the $10\times6.25mm^2$ area restricted between extensometer knives. It is important to notice that the initial loading was compressive along the TD direction, which results in significant twinning during the first quarter cycle [9, 22, 25]. Figure 3 presents the evolution of the stress-strain hysteresis behavior associated with strain localizations. The strain fields were extracted at 6 different locations of the hysteresis loop, where the quadrant location and average strain level are provided (e.g. +,+ refers to the first quadrant). Figure 3 (a) exhibits the initiation (0.25% total strain) and stabilization (0.8% total strain) of strain localization at very early stage of plasticity. Close attention to the presented cycles reveals that the local strain accumulation relaxes gradually after first cycle.

The effect of texture on AE produced by slip and twinning during monotonic mechanical loading for Mg alloys have been subjected to several studies [9, 26, 27]. These studies show AE events occur prior to yielding and the event peak takes place at the onset of plasticity (macroscopic yield point). Such explaination has been

verified by neutron difraction coupled with AE [28] and direct EBSD measurment integrated with DIC [9]. Infact, these independent investigation explained that the onset of plasticity in Mg alloys taking place by twin nucleation and growth[28]. Importantly Hazeli et al. [9] experimentaly demonstrated that the twin nucleation is a very localized phenomena and is controlled

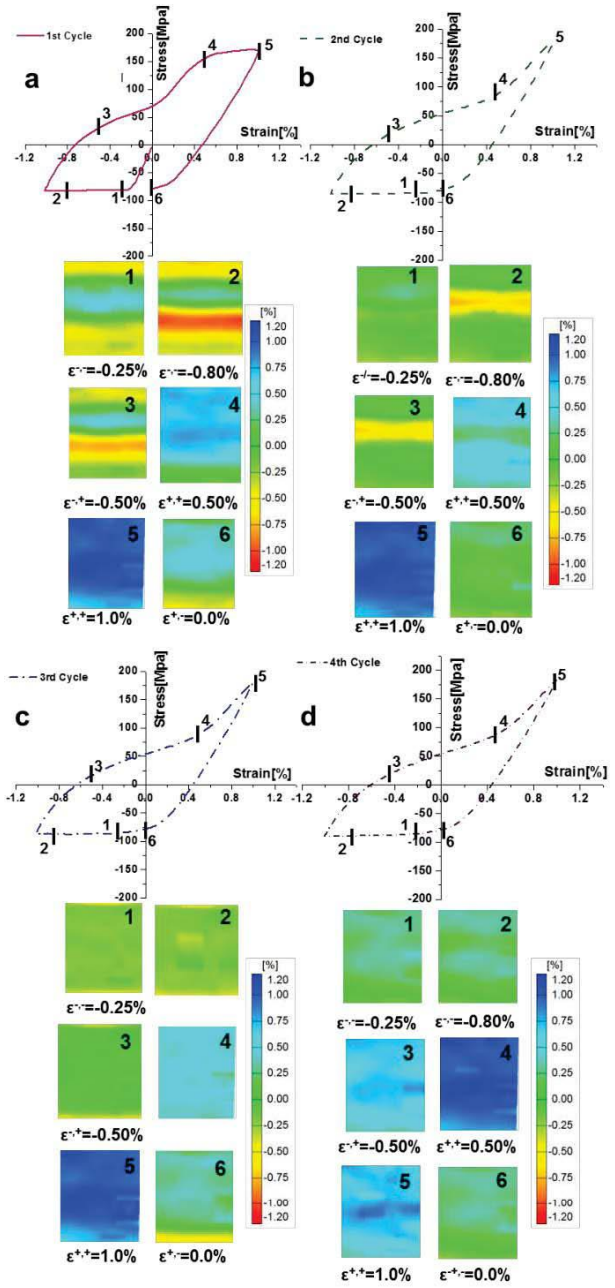


Figure 3. Stress-strain hysteresis loop and full field strain localization at different strain levels for the (a) first, (b) second, (c) third, and (d) fourth cycle

by collectivley effect of local grain misorientation respect to the basal plan [7].

In figure 4, the evolution of AE amplitude and Root Mean Square (RMS), which represents the measure of the energy of the signals, can be oberved as a function of time and correlated with the strain. As expected, during the initial compressive loading cycle, where twinning is favaroble, high amplitude (figure 4 (a)) was recorded. According to the current observation lower AE event generate during uloading, which can be justifid with remarkably lowe number of twinning . Additionaly, the current experimental data shows the remarkably higher AE peak for the first compressive leg than the subensquent compression legs, which importantly underlines the significant effect of twinng in first cycle AE counts subsequent loading. Similarly, in figure 4(b), the RMS follows a similar behavior as the amplitude. The RMS is observed to be dominant at the initial load cycle indicating.

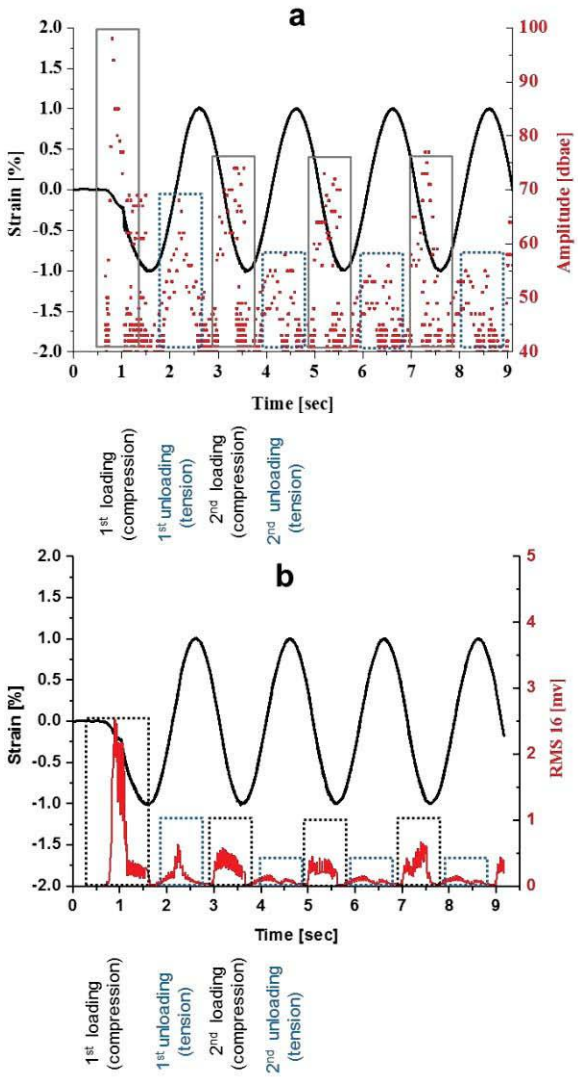


Figure 4: AE features correlated with the applied strain and time (a) Amplitude (b) RMS

Conclusion

The current results exhibit a good agreement upon twinning and detwinng with pertinent literature [29, 30] and beyond shows the saturation of twinning after first few cycle of fatigue life.

References

[1] Carroll, Jay D, et al. "High Resolution Digital Image Correlation Measurements of Strain Accumulation in Fatigue Crack Growth." *International Journal of Fatigue* (2012). Print.

[2] McDowell, David L. "Simulation-Based Strategies for Microstructure-Sensitive Fatigue Modeling." *Materials Science and Engineering: A* 468 (2007): 4-14. Print.

[3] Mughrabi, Hael. "Cyclic Slip Irreversibilities and the Evolution of Fatigue Damage." *Metallurgical and Materials Transactions B* 40.4 (2009): 431-53. Print.

[4] Miao, Jiashi, Tresa M. Pollock, and J. Wayne Jones. "Crystallographic Fatigue Crack Initiation in Nickel-Based Superalloy René 88dt at Elevated Temperature." *Acta Materialia* 57.20 (2009): 5964-74. Print.

[5] Hazeli, Kavan, et al. "Surface Effects of Twinning in Magnesium Alloys." *Acta Materialia* Submitted (2013). Print.

[6] Gall, Ken, Huseyin Sehitoglu, and Yavuz Kadioglu. "A Methodology for Predicting Variability in Microstructurally Short Fatigue Crack Growth Rates." *Journal of Engineering Materials and Technology* (1997): 171-79. Print.

[7] Hazeli, K., et al. "The Effect of Strontium in Plasticity of Magnesium Alloys." *Materials Science and Engineering: A* 578.0 (2013): 383-93. Print.

[8] Yoo, MH, and JK Lee. "Deformation Twinning in Hcp Metals and Alloys." *Philosophical Magazine A* 63.5 (1991): 987-1000. Print.

[9] Hazeli, K., et al. "In Situ Identification of Twin-Related Bands near Yielding in a Magnesium Alloy." *Scripta Materialia* 68.1 (2013): 83-86. Print.

[10] Barnett, M. R., M. D. Nave, and C. J. Bettles. "Deformation Microstructures and Textures of Some Cold Rolled Mg Alloys." *Materials Science and Engineering: A* 386.1–2 (2004): 205-11. Print.

[11] Watanabe, H, et al. "Effect of Temperature and Grain Size on the Dominant Diffusion Process for Superplastic Flow in an Az61 Magnesium Alloy." *Acta materialia* 47.14 (1999): 3753-58. Print.

[12] Jain, A, et al. "Grain Size Effects on the Tensile Properties and Deformation Mechanisms of a Magnesium Alloy, Az31b, Sheet." *Materials Science and Engineering: A* 486.1 (2008): 545-55. Print.

[13] Agnew, SR, JA Horton, and MH Yoo. "Transmission Electron Microscopy Investigation of< C+ a> Dislocations in Mg and A-Solid Solution Mg-Li Alloys." *Metallurgical and Materials Transactions A* 33.3 (2002): 851-58. Print.

[14] Jain, A., and S. R. Agnew. "Modeling the Temperature Dependent Effect of Twinning on the Behavior of Magnesium Alloy Az31b Sheet." *Materials Science and Engineering: A* 462.1–2 (2007): 29-36. Print.

[15] Ishikawa, Koichi, Hiroyuki Watanabe, and Toshiji Mukai. "High Strain Rate Deformation Behavior of an Az91 Magnesium Alloy at Elevated Temperatures." *Materials Letters* 59.12 (2005): 1511-15. Print.

[16] Myshlyaev, M. M., et al. "Twinning, Dynamic Recovery and Recrystallization in Hot Worked Mg–Al–Zn Alloy." *Materials Science and Engineering: A* 337.1–2 (2002): 121-33. Print.

[17] Knezevic, Marko, et al. "Deformation Twinning in Az31: Influence on Strain Hardening and Texture Evolution." *Acta Materialia* 58.19 (2010): 6230-42. Print.

[18] Hasegawa, S., et al. "Evaluation of Low Cycle Fatigue Life in Az31 Magnesium Alloy." *International Journal of Fatigue* 29.9-11 (2007): 1839-45. Print.

[19] Hyuk Park, Sung, et al. "Low-Cycle Fatigue Characteristics of Rolled Mg–3al–1zn Alloy." *International Journal of Fatigue* 32.11 (2010): 1835-42. Print.

[20] Carroll, J, et al. "An Experimental Methodology to Relate Local Strain to Microstructural Texture." *Review of Scientific Instruments* 81.8 (2010): 083703-03-9. Print.

[21] Wang, YN, and JC Huang. "The Role of Twinning and Untwinning in Yielding Behavior in Hot-Extruded Mg–Al–Zn Alloy." *Acta Materialia* 55.3 (2007): 897-905. Print.

[22] Barnett, MR. "Twinning and the Ductility of Magnesium Alloys: Part I: “Tension” Twins." *Materials Science and Engineering: A* 464.1 (2007): 1-7. Print.

[23] Kleiner, S, and PJ Uggowitzer. "Mechanical Anisotropy of Extruded Mg–6% Al–1% Zn Alloy." *Materials Science and Engineering: A* 379.1 (2004): 258-63. Print.

[24] Robson, JD, N Stanford, and MR Barnett. "Effect of Precipitate Shape on Slip and Twinning in Magnesium Alloys." *Acta materialia* 59.5 (2011): 1945-56. Print.

[25] Wu, L, et al. "Twinning–Detwinning Behavior During the Strain-Controlled Low-Cycle Fatigue Testing of a Wrought Magnesium Alloy, Zk60a." *Acta materialia* 56.4 (2008): 688-95. Print.

[26] Lu, You, Michael Gharghouri, and Farid Taheri. "Effect of Texture on Acoustic Emission Produced by Slip and Twinning in Az31b Magnesium Alloy—Part Ii: Clustering and Neural Network Analysis." *Nondestructive Testing and Evaluation* 23.3 (2008): 211-28. Print.

[27] Máthis, K, et al. "Investigating Deformation Processes in Am60 Magnesium Alloy Using the Acoustic Emission Technique." *Acta materialia* 54.20 (2006): 5361-66. Print.

[28] Muránsky, O., et al. "Investigation of Deformation Twinning in a Fine-Grained and Coarse-Grained Zm20 Mg Alloy: Combined in Situ Neutron Diffraction and Acoustic Emission." *Acta materialia* 58.5 (2010): 1503-17. Print.

[29] Lou, XY, et al. "Hardening Evolution of Az31b Mg Sheet." *International Journal of Plasticity* 23.1 (2007): 44-86. Print.

[30] Yin, S. M., et al. "The Role of Twinning–Detwinning on Fatigue Fracture Morphology of Mg–3%Al–1%Zn Alloy." *Materials Science and Engineering: A* 494.1-2 (2008): 397-400. Print.

Magnesium Technology 2014

Deformation II

Magnesium Technology 2014
Edited by: Martyn Alderman, Michele V. Manuel, Norbert Hort, and Neale R. Neelameggham
TMS (The Minerals, Metals & Materials Society), 2014

Dislocation Activity in AZ31B Magnesium Deformed at Moderately Elevated Temperatures via EBSD

[1]T. Ruggles, [2]A. Khosravani, [1]D. Fullwood, [3]M.P. Miles
[1]Brigham Young University, Mechanical Engineering, 435 CTB, Provo, UT 84602
[2]Georgia Tech, Materials Science and Engineering, Atlanta, GA 30332
[3]Brigham Young University, Manufacturing Engineering Technology, 265 CTB, Provo, UT 84602

Keywords: Magnesium alloy, microstructure, formability

Abstract

Activation of <c+a> type slip in wrought magnesium has typically been associated with forming temperatures of 200°C or higher, while contraction twinning has been observed to be more prevalent at lower temperatures. A recent investigation showed that when AZ31B sheets with strong basal texture were formed in biaxial or plane strain tension at room temperature, contraction twins were observed in banded structures. These banded structures disappeared at moderate forming temperatures of 75°C and 125°C. The hypothesis is that <c+a> type slip was sufficiently activated at the moderate forming temperatures that thinning of the sheet was accommodated less by twinning and more by slip. This paper uses mesoscale electron backscatter diffraction continuum dislocation microscopy in an SEM to determine <c+a> type geometrically necessary dislocation density. Preliminary results suggest that the relative amount of <c+a> geometrically necessary dislocations is unrelated to the onset of twinning.

Introduction

Wrought magnesium alloys are suitable for many components, such as body panels in auto frames; however, these materials present difficulties of fabrication. Room (or near-room) temperature forming of magnesium alloys is desirable to reduce energy and lubricant costs; but, formability of magnesium alloys at ambient temperature is poor since the HCP lattice doesn't provide a sufficient number of active slip systems for deformation [1-6]. According to the von Mises' criterion, five independent slip systems are required for plastic deformation of polycrystalline materials, but most magnesium alloys only have two easily activatable (basal), and two semi-active (prismatic) systems. Deformation twinning plays an important role in plastic deformation of magnesium alloys by adding additional active systems [2, 7-10] but it can affect the hardening and fracture properties adversely.

Commercial grade AZ31B magnesium alloy sheet has a strong basal texture, aligning the c-axis of the HCP crystals with the sheet normal. This texture can be as high as 20x random [11]. Slip in the basal plane is the easiest slip system to activate. For example, the critical resolved shear stress (CRSS) for basal slip in a pure Mg crystal is about 1 MPa at room temperature [12]. Models predict that the CRSS for basal slip in polycrystalline AZ31B is about 10 MPa. The basal plane contains two independent slip systems, both of which accommodate slip only in the <a> direction. Any thinning of the sheet requires slip with a <c> component. The pyramidal <c+a> slip systems and twins have a <c> component, but the CRSS for the former is reported to be of the order of 100 MPa or higher [13] while estimates for compression twin CRSS vary greatly, ranging from 25 MPa to well over 100 MPa [14-17]. At the same time, there is disagreement about the precise values of CRSS of non-basal slip systems, and the current work would suggest easier non-basal slip than has previously been reported, especially for mildly elevated forming temperatures. According to Ono [18], the primary mechanism for through-thickness deformation is <c+a> slip which can account for 40% of the total dislocations at room temperature. However, many researchers have observed significant compression twinning whenever c-axis contraction is imposed by the deformation process [19, 20].

The usual approach to overcoming the low formability of AZ31B is to form the material at an elevated temperature, typically 250 C or higher [21-23]. When the temperature increases there is a greater availability of slip planes as the CRSS of different slip systems decrease unevenly with temperature, effectively increasing the formability of the material. However, forming at high temperatures is expensive and difficult to implement in a high-volume production environment. It is therefore of interest to study the formability of wrought magnesium at room temperature and at moderately elevated temperatures, in order to understand the failure initiation mechanisms that precede fracture to develop cost effective solutions for manufacturing with Mg alloys. Furthermore, since the majority of part failures during forming or stamping occur in plane-strain tension [24], accurate understanding of the material behavior under complex strain path deformation, including plane strain conditions, can aid in finding a solution to manufacturing challenges involving wrought Mg alloys. If an understanding of failure mechanisms can be gained, then it is possible that the starting microstructure or the forming path can be manipulated in order to increase formability using modest increases in forming temperature.

Experimental Methods

2.05 mm thick sheets of cold rolled magnesium alloy AZ31B, with composition 3% Al and 1% Zn (wt %), were annealed at 350 °C for a minimum of 15 minutes and then air-cooled outside the oven. Specimens were rough cut using a water-jet before annealing from these sheets for all experiments. Average grain size for this alloy was 12 µm.

Plane strain specimens were stretched using limiting dome height (LDH) tooling, with a standard 100 mm diameter punch and punch speed of 38 mm/min. Plane strain was achieved by using the LDH tooling with an 88 mm wide specimen, which was determined by experimenting with specimens of various widths until plane strain tension was achieved in the area between the top of the punch and the clamped region of the sheet. Samples were lubricated by placing a thin layer of boron nitride paste on the portion of the specimen in contact with the punch. Strain measurements were taken from the area of the sheet that had been determined experimentally to be in plane strain. Specimens were strained to 4% and 8%. The specimens were heated by conduction with belt heaters attached to the forming die. At 125 °C there was a variation of 5 °C within the forming area.

The samples were polished and automatic EBSD scans were performed using an SEM equipped with OIM™ data acquisition software and a high-speed camera. In order to generate dislocation maps, the EBSPs (electron backscattered patterns) were later were

post-processed. Using cross correlation techniques, the lattice perturbation between the neighboring scan points can be measured from their corresponding EBSPs from which relative elastic distortion, $\boldsymbol{\beta}_{,m}$, can be measured, and hence the geometrically necessary dislocation (GND) density can be deduced [25-28]. The Nye tensor [29]aggregates dislocation activity from individual slip systems as follows:

$$\boldsymbol{\alpha}_{ij} = \sum_{m} \boldsymbol{\rho}^{(m)} \boldsymbol{b}_i^{(m)} \boldsymbol{v}_j^{(m)} \quad (1)$$

where $\rho^{(m)}$ is the dislocation density for GNDs of the mth dislocation system (defined here as a unique combination of Burgers vector and line vector for a pure edge or screw dislocation); b is the Burgers vector and V is the associated line vector. The measured distortion is related to the Nye tensor via [30]:

$$\boldsymbol{\alpha} = \nabla \times \boldsymbol{\beta} \quad (2)$$

Because this study uses 2D EBSD, derivative normal to the sample surface are unavailable, meaning that only the right-most column of α is fully known. If strain is assumed to be negligible compared to lattice rotations, then an additional three degrees of freedom (two terms and one difference of terms) are available [31].

Because magnesium has 36 possible slip systems and 27 unique dislocation systems, the problem of determining GND density is underconstrained. To find the most physical solution, typically the total line length of dislocations is minimized [32, 33]. In this case, the dislocation densities were weighted by their CRSS factor:

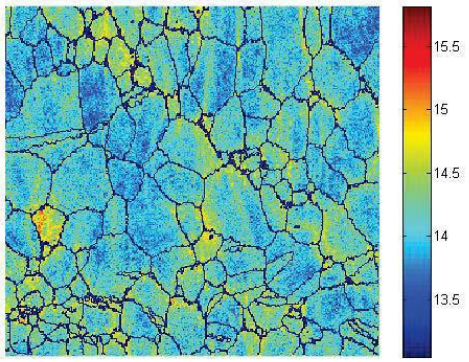
Minimize

$$f = \sum_{t=1}^{N} \left| w^t \rho^t \right| \text{ , s.t. } \alpha_{ij} = \sum_{t=1}^{N} \rho^m b_i^m v_j^m \quad (3)$$

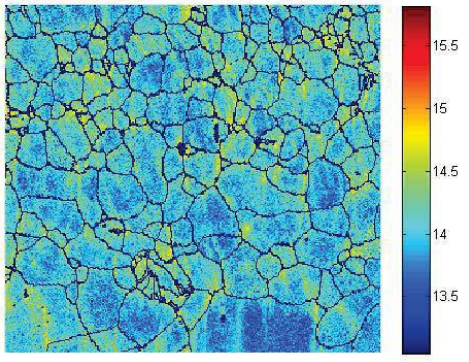
The <c+a> to total slip ratio and the total dislocation density is then calculated from the individual dislocation system densities [34, 35]. The samples for this study were cut such that the microscope sample surface was parallel with rolling direction. This was done because the plastic effects of sheet thinning were being observed, and EBSD dislocation microscopy techniques work best on the plane of deformation [36, 37].

Results

The total GND density maps calculated as described for samples deformed in plane strain to 4% effective strain at room temperature and 125 C are shown in Figure 1. Note that twinning has begun at room temperature.



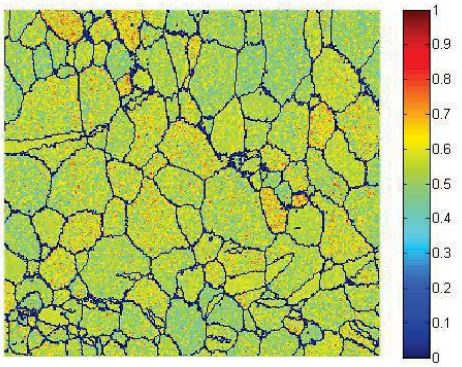
(a)



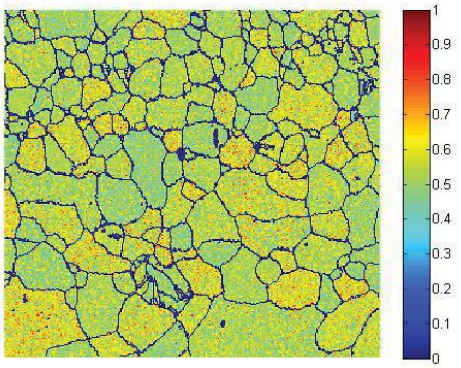
(b)

Figure 1. GND density maps for AZ31 samples deformed to 4% effective strain in plane strain at (a) room temperature and (b) 125 C plotted in log units of m/m^3. The average GND density for the room temperature sample (a) is 1.68×10^{14} and 1.40×10^{14} for the 125 C sample (b). The sample is 90 microns x 90 microns.

The <c+a> to total slip ratio for these samples is shown in Figure 2.



(a)

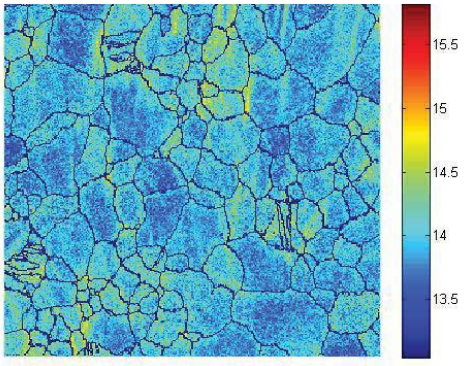


(b)

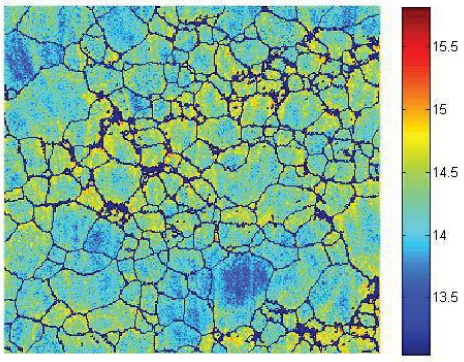
Figure 2. These maps show the <c+a> slip to total slip ratio in AZ31 samples deformed to 4% effective strain in plane strain at (a) room temperature and (b) 125 C. The average <c+a> ratio for both samples is .55. The sample is 90 microns x 90 microns.

Several things may be noted from these samples. First of all, the relative amount of <c+a> slip is quite high. Despite the fact that <c+a> slip is so energetically unfavorable, it is the only way to accommodate strong thinning through the thickness of the sheet because of the highly textured nature of this magnesium. The <c+a> slip ratio remains constant at the moderately elevated temperature, suggesting that the reduced twin content of the sample deformed at a moderately elevated temperature are not due to the increased availability of dislocation types, as was previously assumed.

The biggest difference between the samples is the magnitude of the dislocation content. The elevated temperature sample has 20 % less GND density than the room temperature sample, 1.40×10^{14} m/m^2 versus $1.68 \times 10^{14} m/m^2$. This suggests that even at only 125 C, dislocations are able to order themselves to have lower distortion gradients. At the higher strain, 8%, twinning still occurs at room temperature, but has not appreciably begun at 125 C. The dislocation density maps, however, now show the opposite of the 4% strain data, namely the sample deformed at 125 C has higher GND density. Also striking is the fact that GND density has actually dropped slightly in the room temperature sample, supporting similar findings from Khosravani, et al [38]. See Figure 3.



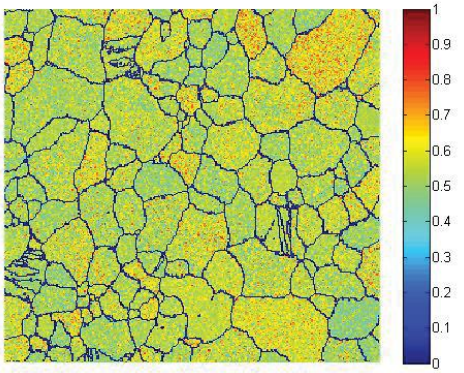
(a)



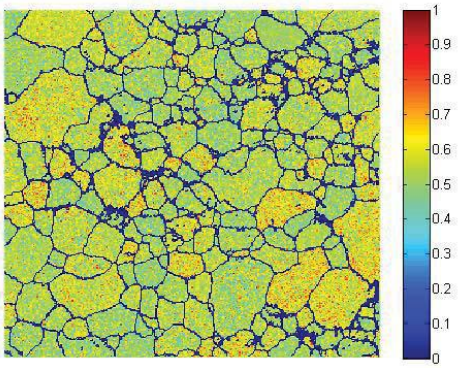
(b)

Figure 3. GND density maps for AZ31 samples deformed to 8% effective strain in plane strain at (a) room temperature and (b) 125 C plotted in log units of m/m^3. The average GND density for the room temperature sample (a) is 8.90×10^{13} and 1.71×10^{14} for the 125 C sample (b). The sample is 90 microns x 90 microns.

However, the <c+a> ratio has remained relatively constant for both temperatures. See Figure 4.



(a)



(b)

Figure 4. These maps show the <c+a> slip to total slip ratio in AZ31 samples deformed to 8% effective strain in plane strain at (a) room temperature and (b) 125 C. The average <c+a> ratio for both samples is .56. The sample is 90 microns x 90 microns.

Discussion

Current results confirm work done in a previous study [38], namely that compression twinning is significantly reduced at moderate forming temperatures of 75C and 125C compared to room temperature. The reduction of compression twinning at the moderately elevated temperatures is accompanied by an increase in ductility, where thinning strains (causing c-axis compression) are now postulated to be accommodated by some <c+a> slip. Current results also confirm that GND density actually decreases as strain increases during room temperature forming, where increased twin density consumes material, which previously had higher GND content.

However, this study did not demonstrate a change in relative <c+a> activity at moderately elevated forming temperatures. This result does not support the assumption that twinning partially replaces <c+a> slip as a thinning mechanism at these temperatures. Further work on reducing the noise in the GND density calculation is needed before conclusions can be drawn about the relative <c+a> activity magnitudes and trends from room to mildly elevated forming temperatures.

References

1. Agnew, S.R., M.H. Yoo, and C.N. Tomé, *Application of texture simulation to understanding mechanical behavior of Mg and solid solution alloys containing Li or Y.* Acta Materialia, 2001. **49**(20): p. 4277-4289.
2. Agnew, S.R., J.A. Horton, and M.H. Yoo, *Transmission Electron Microscopy of <c + a> Dislocations in Mg and Alpha-Solid Solutions of Mg-Li Alloys.* Metallurgical and Materials Transactions A, 2002. **33A**: p. 851-858.
3. Koike, J., et al., *The activity of non-basal slip systems and dynamic recovery at room temperature in fine-grained AZ31b magnesium alloys.* Acta Mater, 2003. **51**: p. 2055-65.
4. Koike, J., *Enhanced deformation mechanisms by anisotropic plasticity in polycrystalline magnesium alloys at room temperature.* Metall. Mater. Trans.A, 2005. **36**: p. 1689-96.
5. Wu, L., *Twinning-detwinning behavior during the strain-controlled low-cycle fatigue testing of a wrought magnesium alloy, ZK60A.* Acta Materialia, 2008. **56**(4): p. 688-695.
6. Sandlöbes, S., *On the role of non-basal deformation mechanisms for the ductility of Mg and Mg-Y alloys.* Acta Materialia, 2011. **59**(2): p. 429-439.
7. Jiang L, J.J., Mishra RK, Luo AA, Sachdev AK, Godet S., *Twinning and texture development in two Mg alloys subjected to loading along three different strain paths.* Acta Mater. , 2007(55): p. 3899-3910.
8. Martin, É., *Variant selection during secondary twinning in Mg-3%Al.* Acta Materialia, 2010. **58**(11): p. 3970-3983.
9. Park, S.H., S.-G. Hong, and C.S. Lee, *Activation mode dependent {10–12} twinning characteristics in a polycrystalline magnesium alloy.* Scripta Materialia, 2010. **62**(4): p. 202-205.
10. Hong, S.-G., S.H. Park, and C.S. Lee, *Role of {10-12} twinning characteristics in the deformation behavior of a polycrystalline magnesium alloy.* Acta Materialia, 2010. **58**(18): p. 5873-5885.
11. Chino, Y., K. Kimura, and M. Mabuchi, *Deformation characteristics at room temperature under biaxial tensile stress in textured AZ31 Mg alloy sheets.* Acta Materialia, 2009. **57**(5): p. 1476-1485.
12. Hutchinson, W.B. and M.R. Barnett, *Effective values of critical resolved shear stress for slip in polycrystalline magnesium and other hcp metals.* Scripta Materialia, 2010. **63**(7): p. 737-740.
13. Agnew, S.R., et al., *Study of slip mechanisms in a magnesium alloy by neutron diffraction and modeling.* Scripta Materialia, 2003. **48**: p. 1003-1008.
14. Brown, D., et al., *Internal strain and texture evolution during deformation twinning in magnesium.* Materials Science and Engineering: A, 2005. **399**(1-2): p. 1-12.
15. Barnett, M., *Twinning and the ductility of magnesium alloys Part II Contraction twins.* Mater. Sci. Eng A, 2007. **464**: p. 8-16.
16. Chapuis, A. and J.H. Driver, *Temperature dependency of slip and twinning in plane strain compressed magnesium single crystals.* Acta Materialia, 2011. **59**(5): p. 1986-1994.
17. Chapuis, A. and J. Driver, *A fundamental study of the high temperature deformation mechanisms of magnesium.* Journal of Physics A: Mathematical and General, 2012: p. 420.
18. Ono, N., R. Nowak, and S. Miura, *Effect of deformation temperature on Hall-Petch relationship registered for polycrystalline magnesium.* Materials Letters, 2003. **58**(1-2): p. 39-43.
19. Barnett, M.R., *Twinning and the ductility of magnesium alloys: Part I: 'Tension' twins.* Materials Science and Engineering: A, 2007. **464**(1-2): p. 1-7.
20. Li, H., et al., *Determination of Active Slip/Twinning Modes in AZ31 Mg Alloy Near Room Temperature.* JMEPEG, 2007. **16**(321-326).
21. Chen, F.-K. and T.-B. Huang, *Formability of stamping magnesium-alloy AZ31 sheets.* Journal of Materials Processing Technology, 2003. **142**(3): p. 643-647.
22. Jager, A., *Tensile properties of hot rolled AZ31 Mg alloy sheets at elevated temperatures.* Journal of Alloys and Compounds, 2004. **378**(1-2): p. 184-187.
23. Lee, Y., et al., *Experimental and analytical studies for forming limit of AZ31 alloy on warm sheet metal forming.* Journal of Materials Processing Technology, 2007. **187-188**: p. 103-107.
24. Miles, M.P., et al., Metall. Trans. A, 1993. **24A**: p. 1143-1151.
25. Gardner, C.J., et al., *EBSD-based continuum dislocation microscopy.* International Journal of Plasticity, 2010. **26**: p. 1234-1247.
26. Ruggles, T.J. and D.T. Fullwood, *Estimations of bulk geometrically necessary dislocation density using high resolution EBSD.* Ultramicroscopy, 2013. **133**: p. 8-15.
27. Wilkinson, A.J., G. Meaden, and D.J. Dingley, *High resolution mapping of strains and rotations using electron back scatter diffraction.* Materials Science and Technology, 2006. **22**(11): p. 1-11.
28. Wilkinson, A.J., G. Meaden, and D.J. Dingley, *High-resolution elastic strain measurement from electron*

backscatter diffraction patterns: New levels of sensitivity. Ultramicroscopy, 2006. **106**: p. 307-313.
29. Nye, J.F., *Some geometrical relations in dislocated crystals.* Acta Metallurgica, 1953. **1**: p. 153-162.
30. Kroner, E., *Continuum theory of dislocations and self-stresses.* Ergebnisse der Angewandten Mathematik, 1958. **5**: p. 1327-1347.
31. Pantleon, W., *Resolving the goemetrically necessary dislocation content by conventional electron backscattering diffraction.* Scripta Materialia, 2008. **58**: p. 994-997.
32. Sun, S., B.L. Adams, and W.E. King, *Observations of lattice curvature near the interface of a deformed aluminium bicrystal.* Philosophical Magazine A: Physics of Condensed Matter, Structure, Defects and Mechanical Properties, 2000. **80**(1): p. 9-25.
33. Field, D.P., *Improving the spatial resolution of EBSD.* Microsc Microanal, 2005. **11**: p. 52-53.
34. El-Dasher, B.S., B.L. Adams, and A.D. Rollett, *Viewpoint: Experimental recovery of geometrically necessary dislocation density in polycrystals.* Scripta Materialia, 2003. **48**(2): p. 141-145.
35. Littlewood, P.D., T.B. Britton, and A.J. Wilkinson, *Geometrically necessary dislocation density distribution in Ti-6Al-4V deformed in tension.* Acta Materialia, 2011. **59**: p. 6489-6500.
36. Kysar, J.W., et al., *Experimental lower bounds on geometrically necessary dislocation density.* International Journal of Plasticity, 2010. **26**: p. 1097-1123.
37. Kysar, J.W., et al., *High strain gradient plasticity associated with wedge indentation into face-centered cubic single crystals: Geometrically necessary dislocation densities.* Journal of the Mechanics and Physics of Solids, 2007. **55**: p. 1554-1573.
38. Khosravani, A., et al., *Twinning in magnesium alloy AZ31B under different strain paths at moderately elevated temperatures.* International Journal of Plasticity, 2013. **45**: p. 160-173.

Magnesium Technology 2014
Edited by: Martyn Alderman, Michele V. Manuel, Norbert Hort, and Neale R. Neelameggham
TMS (The Minerals, Metals & Materials Society), 2014

Deformation, Recrystallization and Grain Growth Behavior of Large-Strain Hot Rolled Binary Mg-1Dy Alloy

I. Basu[1], T. Al-Samman[1]
[1]*Institut für Metallkunde und Metallphysik, RWTH Aachen, 52056 Aachen, Germany*

Keywords: Rare-earth elements, Texture, Shear-band nucleation, Oriented nucleation, Favorable growth

Abstract

Binary alloy, Mg-1Dy (wt. %), was subjected to large strain hot rolling treatment (LSHR), followed by annealing at different temperatures. Subsequent texture and microstructural characterization revealed that nucleation of recrystallization took place inside shear bands, at 300°C. The deformation texture was split basal in nature, which on recrystallization was replaced by an off-basal fiber about ND, connecting the RD and TD. The observed texture evolution was attributed to oriented nucleation and selective growth phenomena.

Introduction

Modifying the alloying chemistry in wrought magnesium alloys with special emphases on RE elements have shown numerous indications of improved properties, such as grain refinement, better room temperature formability and enhanced strength and creep resistance [1]. In recent years, texture control in magnesium alloys via rare earth addition has gained considerable interest. The advantage of dilute addition of rare earths to obtain weaker and deformable textures in wrought magnesium alloys have been reported by many researchers [1-6]. Moreover, such transition has been primarily attributed to annealing related phenomenon, wherein evolution of new softer orientations has been observed [2, 3]. Such characteristics of Mg-REs are quite unique, since previous studies on conventional alloys have established that the recrystallization renders primarily weakening and randomization of the deformation texture with no qualitative changes [7-9]. What still remains subject to controversy and further investigation is the fact that how these rare-earths influence the recrystallization and grain growth behavior in magnesium alloys, which brings about such significant texture modification. Though the findings in these areas are still in their preliminary stages, there have been quite a few arguable theories explaining the RE-effect on texture modification.

Initial attempts made by Ball and Prangnell [10], who investigated the effect of REs, came to the conclusion that the observed texture randomization arises from particle stimulated nucleation (PSN). However, the relatively low contribution of PSN texture to the overall texture [11] has often been regarded as a negating factor. Though, a recent study [12] revealed that PSN related texture modification is possible during growth of these nuclei.

In light of the already established recrystallization theories of nucleation and growth, Stanford and co-workers [6] were the first to propose that RE-related texture modification is facilitated by oriented nucleation events. They reported nucleation of a new orientation, with <11-21>|| ED in extruded Mg-REs. Furthermore, they proposed that such oriented nucleation events occur due to shear band formation, which subsequently act as the primary nucleation sites. However, the nucleation of such orientations is still unclear and is possibly arising as a result of solute partitioning of REs to dislocations [13]. Stanford et.al., also reported that the texture modification in their case was entirely an oriented nucleation event and was independent of growth phenomenon [14] .

Interestingly, in a recent study [3], the authors investigated the recrystallization and grain growth behavior in binary Mg-RE alloys and obtained quite contrasting results. It was found that the addition of RE elements is not always sufficient to impart texture changes during deformation and recrystallization, and the level of recrystallization texture modification depends strongly on the choice of the rare earth element and the annealing temperature. A significant texture change was displayed by Mg-1wt. %Gd. Shear band recrystallization was found to play a critical role in generating a wide spectrum of recrystallization nuclei, which was aided by selective growth behavior giving rise to the formation of new annealing textures. Such favorable growth related texture modification was also reported by Mackenzie and co-workers [4] during recrystallization of Mg-Zn-Ce alloys.

In purview of the afore-mentioned theories, the present work is an attempt to further extend our understanding of the RE-related recrystallization and grain growth, especially with respect to Mg-1wt.%Gd. Dysprosium (~179 pm) being a solute based RE reveals similar characteristics as that of Gd (~180 pm), but is relatively heavier (164 u vis-à-vis 157 u). The findings in this study have thus been outlined on the basis of the preliminary investigations that were conducted on Mg-1Dy alloys, so as to throw further light on the inherent complexities of magnesium-rare earth alloys.

Experimental Procedure

Mg-1Dy (wt.%) alloys were produced by induction melting under a protective gas atmosphere of Ar/CO_2, followed by casting and homogenization at 450° C for 20 hours. Rolling blocks of dimensions, 60mm x 40mm x 4mm were hot rolled at 450°C (nominal furnace temperature) to 80% thickness reduction in a single-rolling pass and rapidly water quenched. With a true strain of 1.6 ($\varphi_h=\ln(h_1/h_0)$; h_1 and h_0 final and initial thicknesses), the single-pass approach enforced somewhat a severe plastic deformation condition that gave rise to significant shear banding. Post rolling, the rolled specimens were subjected to annealing treatments at 5 different temperatures viz. 300° C, 350° C, 400° C and 450° C, for 60 minutes followed by water quenching. Optical microscopy, X-ray diffraction and EBSD measurements were carried out on the rolled and annealed specimens. Specimens for optical microscopy were prepared by conventional grinding and diamond polishing (down to 0.25 microns), followed by electropolishing in a 5:3 solution of ethanol and H_3PO4 for 30 minutes at 1.93 V. Acetic picral and 5%-Nital were used as etchants to reveal the microstructure. The macro-texture was determined by measuring incomplete pole figures between $\alpha = 5°$ and 75° in the back reflection mode using Co-Kα radiation at 35 kV and 28 mA. A set of six measured pole figures, [$\{10\bar{1}0\}$, $\{0002\}$, $\{10\bar{1}1\}$,$\{10\bar{1}2\}$,$\{11\bar{2}0\}$,and $\{10\bar{1}3\}$] was used to calculate the orientation distribution function (ODF) using MTEX

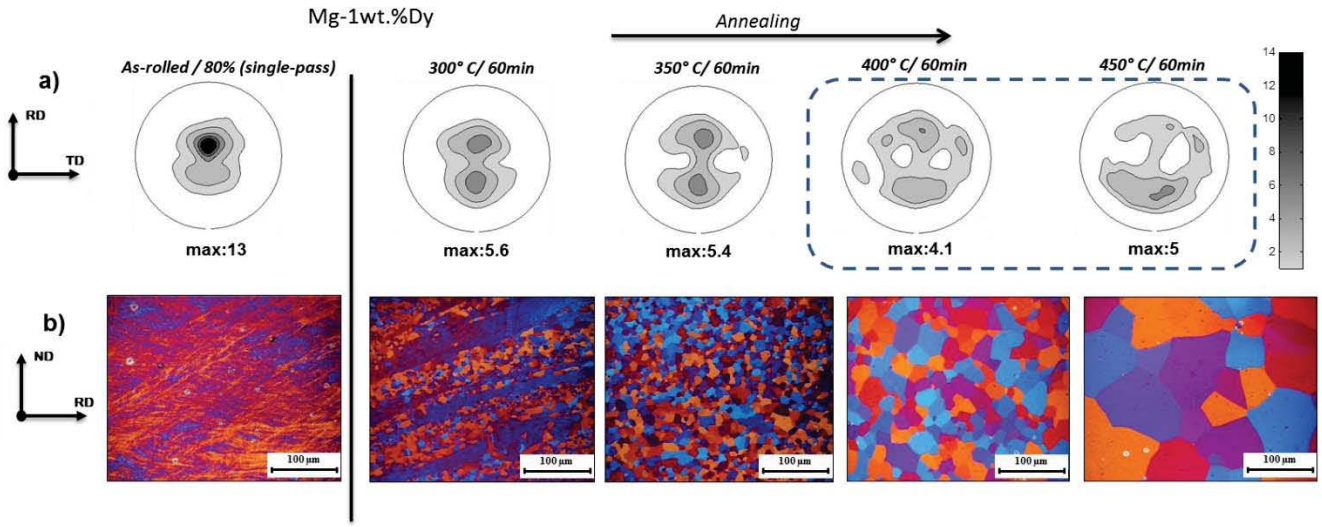


Figure 1 XRD (0001) pole figures and corresponding optical microstructures of Mg-1Dy at rolled and annealed conditions

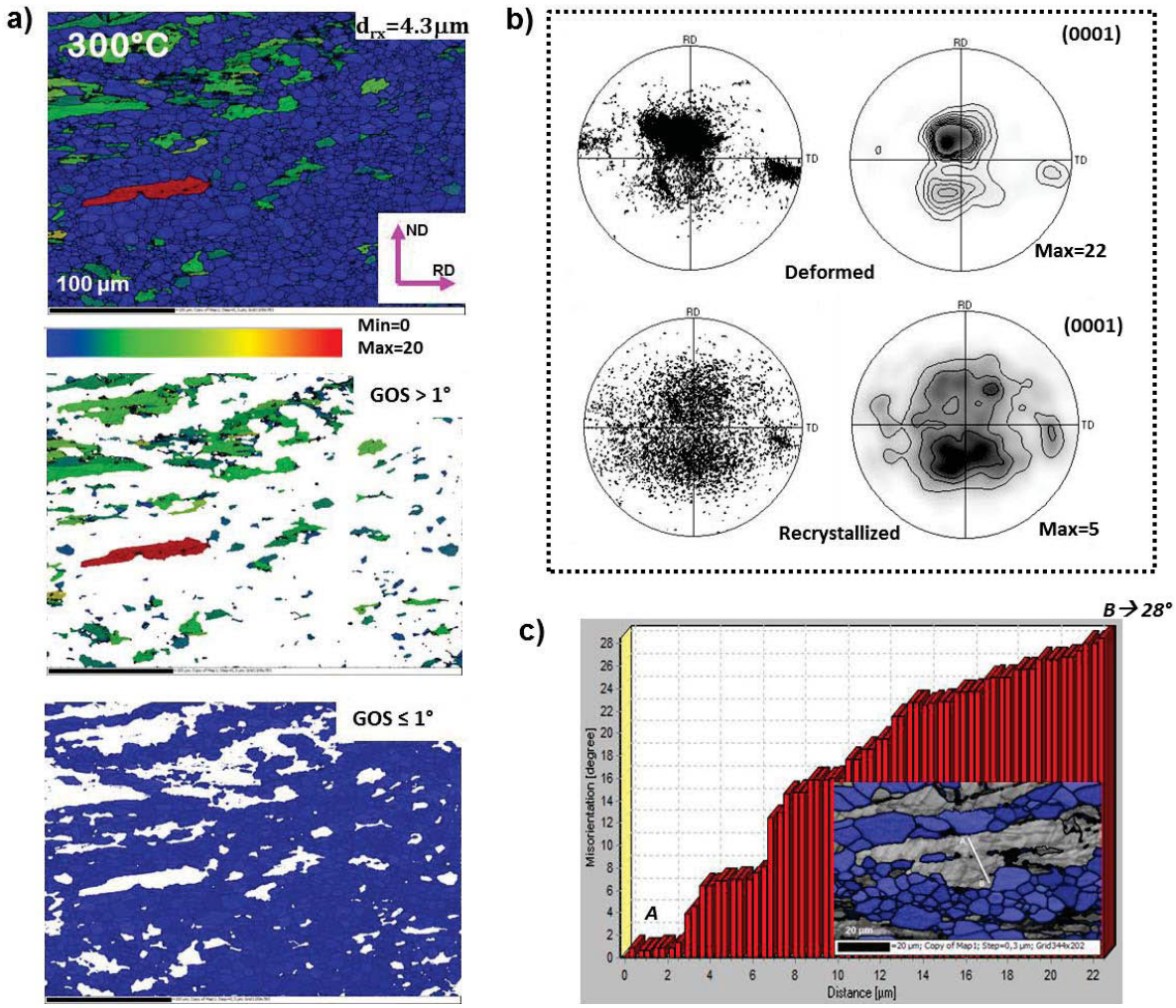


Figure 2 a) EBSD-GOS map at 300°C for Mg-1Dy (with average grain size), classifying deformed and recrystallized subsets; b) deformed and recrystallization texture data c) misorientation analysis inside shear bands (inset image showing selected line profile in the shear bands)

toolbox. EBSD measurements were performed with a LEO-1530 scanning electron microscope equipped with a field emission gun and an HKL-Nordlys II EBSD detector. Specimens for EBSD were subjected to electropolishing in Struers AC-2 reagent using Lectro-Pol 5. All specimen preparation techniques were conducted under ambient conditions.

Results

Texture and Microstructural Analysis

Figure 1a shows the macrotexture development with increasing annealing temperature. The rolling treatment produced sharp split basal textures with peaks along the rolling direction (RD). The basal poles were tilted by approximately ±20°, away from the sheet normal direction (ND). The peak intensity showed slight asymmetry about the ND and in terms of texture strength showed a maximum of 13 MRD (multiples of random distribution). The as rolled material exhibited a dense network of shear bands and deformation bands, distributed homogeneously throughout the microstructure (see Figure 1b). No evidence of dynamic recrystallization was observed. The bands exhibited a wavy nature and formed symmetric pairs that were inclined at angle ±β from the rolling direction, where β ranged from 28° to 36°.

At 300°C, appearance of fine grains was observed all along the shear bands in both the alloys. Further heat treatments carried out at 350° C, 400° C and 450° C displayed complete recrystallization accompanied with significant grain coarsening observed at 450°C (Fig 1b). With respect to texture evolution Mg-1Dy retained its split basal character until 350°C (c.f. Fig. 1a), which on further increase in annealing temperature to 400°C, resulted in development of a significant texture spread along the transverse direction (TD) and strong weakening of the peaks along RD. Annealing at 'high enough' temperatures (450° C) facilitated emergence of new softer orientations, wherein the basal poles were tilted away from the ND, producing an angular spread connecting the RD and TD (c.f. Fig. 1a). Apart from overall weakening of the texture strength, the basal component of the texture showed significant weakening with higher annealing temperatures.

Electron back-scatter diffraction characterization

Fig 2a-c presents the EBSD analysis results for Mg-1Dy at 300°C. The original indexing rate was 78%, which on further noise reduction up to a minimum of five-indexed neighbours, produced a final indexing of 98%. Fig. 2a shows the grain orientation spread (GOS) map of Mg-1Dy at 300°C, along with the corresponding deformed and recrystallized subsets, represented as inverse pole figure maps. The GOS can be typically defined as the standard deviation of all the orientations inside a grain [15]. The recrystallized grains were distinguished from the deformed ones on the basis of a maximum GOS value of 1° [3, 16]. The white regions represent the anti-subset of a chosen subset. The black regions correspond to Zero solutions. Fig. 2b represents the local texture contribution from the deformed and recrystallized subsets in terms of single orientation scatter and corresponding recalculated basal pole figure. The deformation texture seems to comprise of a dominant basal fiber and an additional but relatively weaker TD-oriented fiber. The recrystallized subset on the other hand gives rises to a variety of orientations, comprising both basal and off-basal components. To achieve statistically validity regarding the obtained EBSD textures, multiple mappings at similar magnifications were acquired at different locations and the resultant texture shown in Fig. 2b is a superposition of these individual mappings, covering ~ 15000 grains. An example of large orientation gradients in the shear bands is given in Fig. 2c wherein a cumulative misorientation of ~28° is observed inside the bands. The inset image shows one of the selected regions inside the shear band, where such misorientation profile was measured. The average recrystallized grain size was reported as ~4.3 μm (Standard Error (SE) = 0.73).

Fig. 3 presents the EBSD analysis results for Mg-1Dy at 350°C and 450°C. The original indexing values were 86% at 350°C and 91% at 450°C. The map color coding is on the basis of degree of tilt of the c-axes from the sheet normal, such that the blue and blue-green grains represent near basal orientations, whereas the green, yellow/red orientations indicate non-basal grains. Fig. 3a displays the c-axes tilt map at 350°C with corresponding local texture data and tilt histogram. The measured average grain size was ~9.1 μm (SE = 0.53). The tilt maxima can be observed between 25° and 30°. The recalculated pole figure correlates well with the X-Ray texture, depicting the still existent split-basal feature. Similar analysis conducted at 450°C revealed a transition of the c-axis tilt maxima to 40°-45°. Due to considerable grain coarsening, multiple EBSD maps were used for subsequent analysis. Texture and grain size measurements were thus made over ~800 grains. The recalculated pole figure displayed a continuous spread of off-basal orientation about ND, producing a texture peak located between RD and TD. The EBSD data suggested considerable grain growth at 450°C, with the measured average grain size value reaching ~75 μm (SE = 0.61). A reasonable agreement between the XRD textures (c.f. Fig. 1) and EBSD data (c.f. Figs 2 and 3) indicates that the observed texture evolution is as a result of recrystallization.

Discussion

Correlation of the annealing texture evolution with respective microstructural changes suggests that the observed texture evolution is as a result of shear band recrystallization and grain growth phenomenon. The shear banded microstructure gives rise to primarily two orientations viz. a near basal fiber and relatively weaker TD-oriented component (c.f. Fig. 2b). The former orientation, which is the dominant component, primarily contributes to the basal deformation texture and has been previously observed to give rise to the split basal feature. The latter orientation is quite an uncommon observation in case of magnesium sheet texture, wherein rolling generally produces a basal or near basal fiber. Thus the presence of an additional off-basal component in the deformation texture, with the basal poles inclined towards TD, seems to be a novel finding. Hereafter, for the sake of simplicity, this TD-oriented component observed in our case will be referred to as the 'RE-orientation'.

Conventional magnesium alloys exhibit recrystallization at temperatures in the range of ~0.4-0.5T_m. However, in the present study, recrystallization was delayed to 300°C (~0.6T_m). Such a delay might be attributed to solute pinning effects, retarding both recovery and recrystallization kinetics [11]. At the onset of recrystallization, the shear bands nucleate a large spread of orientations (c.f. Fig. 2b). Such nucleation events inside shear bands have been previously reported [3, 5] and is attributed to the inherent heterogeneities inside these bands. In the current case, the recrystallized orientations could thus be broadly classified into the following categories,

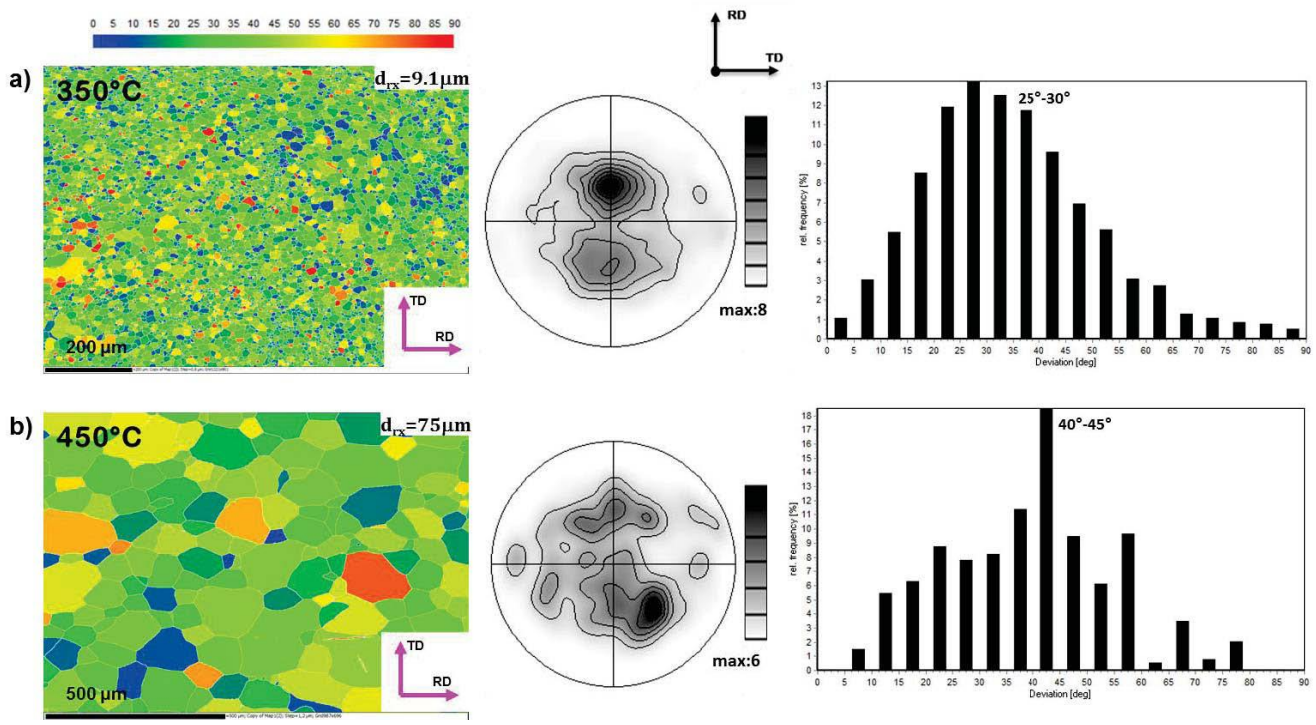


Figure 3 EBSD c-axis tilt maps at a) 350°C and b) 450°C along with corresponding grain sizes, recalculated pole figures and c-axis tilt histograms

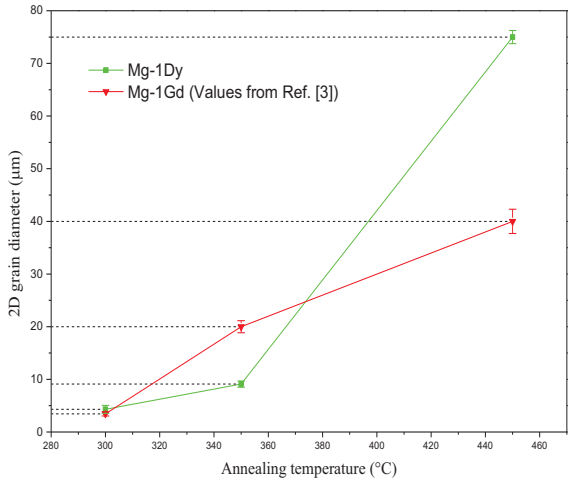


Figure 4 Relative grain coarsening rates for Mg-1Dy and Mg-1Gd [3] with increasing annealing temperature.

i) Basal nuclei,
ii) RE-oriented nuclei, and
iii) Off-basal nuclei

Both basal and off-basal nuclei originate from the basal oriented shear bands, such that off-basal ones nucleate at regions inside bands with larger shear strains or greater inherent distortions. The RE-oriented ones, on the other hand, arise from the TD- oriented component in the deformation texture. With respect to nuclei growth, the rate of growth will be classically governed by three main parameters, viz. a) stored dislocation energy, b) neighboring grain boundary misorientation and, c) solute drag on the boundaries. While the former two accelerate the recrystallization kinetics, the latter one is responsible for the observed recrystallization retardation effects [11]. Before moving further it is imperative to understand the probable recrystallization accelerating and retarding mechanisms active in the alloy under investigation,

Mechanisms 'accelerating' recrystallization and growth: On comparing the off-basal and RE-oriented nuclei with the basal ones, it can be hypothesized that the off-basal and RE-orientations will possess both higher stored energies (associated with greater distortions) and greater neighboring misorientations (since the deformed matrix has a basal texture) as compared to the basal ones. Therefore, the relative growth rates for nuclei of types-(ii) and (iii) should be greater than type-(i). Such favorable growth conditions could also continue into the grain growth stage, wherein the shear difference between the off-basal/RE and basal grain sizes will propel this growth advantage.

Mechanisms 'retarding' recrystallization and growth: Dysprosium, existing as a substitutional solute, is both larger and heavier than Mg atom (~150 pm, 24 u). With respect to size and weight effects, Dy should thus demonstrate relatively lower diffusivity rates than Mg [17] and hence is expected to exert large solute-grain boundary drag at lower annealing temperatures.

Table 1 High angle grain boundary fraction for Mg-1Gd and Mg-1Dy at 300°C

Alloy	*Number of measured grains*	*H.A.G.B fraction at 300°C (%)*
Mg-1Gd	**4947**	**63**
Mg-1Dy	**5091**	**29**

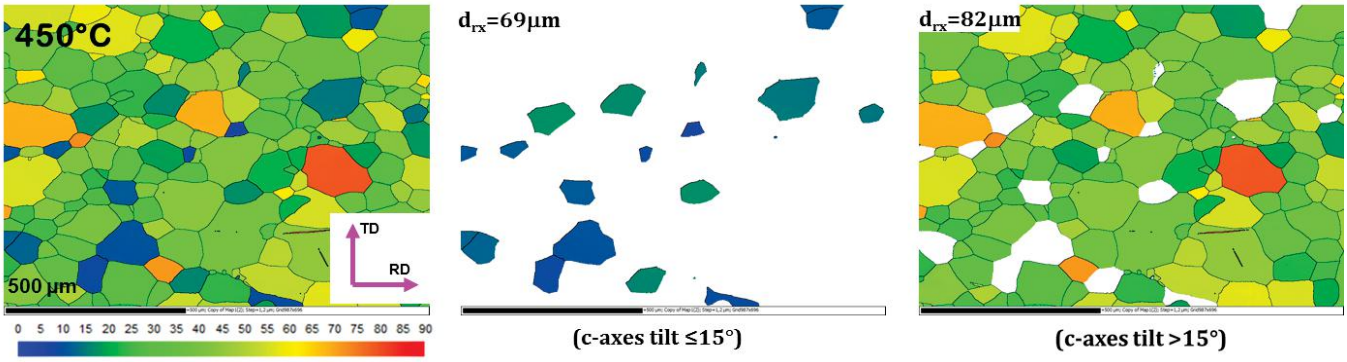


Figure 5 EBSD c-axis tilt map at 450°C classified into basal and non-basal subsets with respective average grain sizes.

Indeed such seems to be the case, when the average grain size value at 300°C (~4.3 µm) is juxtaposed to that at 350°C (~9.1 µm). Fig. 4 shows the grain coarsening rates in Mg-1Dy, with respect to Mg-1Gd [3]. On comparing, the observed grain sizes with those reported for Mg-1Gd, subjected to identical treatment (c.f. Ref. [3]); it is quite evident that the solute drag is quite pronounced in Mg-1Dy alloy up to 350°C. Table 1 shows the high angle grain boundary fraction values for Mg-1Dy vis-à-vis Mg-1Gd (c.f. Ref [3]) at 300°C. The lower percentage noted for Mg-1Dy is most likely as a result of greater solute drag. Furthermore, such drag effects seem to become ineffective at 'higher' annealing temperatures resulting in strong grain coarsening [17]. The sudden increase in average grain size on moving from 350°C to 450°C (c.f. Fig. 3) can thus be attributed to the higher grain boundary migration rates against solute drag, due to additional thermal activation. Interestingly, comparing the grain sizes of Mg-1Dy and Mg-1Gd [3] at 450°C, it can be seen that the former alloy exhibited much stronger grain coarsening (c.f. Fig. 4). Such behavior might again be attributed to greater solute drag pressures at lower temperatures, resulting in slower recrystallization kinetics and subsequent lower grain density in Mg-1Dy, as compared to Mg-1Gd (c.f. Table 1). A lower grain density in turn implies that the average local driving force available for each recrystallized grain will be larger, resulting in greater grain coarsening rates. Such retardation in nucleation kinetics due to increasing solute drag has also been previously reported by Barnett et.al. [18]

EBSD grain size analysis was further extended to classification based on orientations, wherein the blue/blue-green (basal) grains where separated from the non-basal ones. The average grain sizes obtained for the basal and off-basal orientations at 350°C were ~ 8.7 µm (S.E = 0.51) and ~9.1 µm (S.E = 0.53), respectively. However, a similar classification at 450°C yielded grain sizes of ~69 µm (S.E = 0.48) for basal vis-à-vis ~82 µm (S.E = 0.6) for the off-basal grains (c.f. Fig. 5).

Correlating the grain size classification with the aforementioned mechanisms, it is proposed that the negligible grain coarsening observed on moving from 300°C to 350°C is as a result of impending solute-boundary pinning that suppresses any growth related texture modification. On increasing the annealing temperature, grain boundary diffusivity is expected to be significantly accelerated due to increase in the overall driving pressure. In contrast, a large and heavy solute such as Dysprosium would still exhibit relatively lower diffusivities, whereby it will be unable to maintain high solute concentrations at the grain boundaries [17]. In such conditions, the off-basal and RE-orientations: nucleating at regions with higher distortion and greater neighboring misorientations, will display relatively faster growth rates. The position of the maximum texture intensity at 450°C, observed between RD and TD (Fig. 3b), seems to originate from the superposition of RE- and off-basal orientations, both of which would display advanced growth kinetics. It is possible that at 'higher' annealing temperatures competitive growth sets in between the RE-oriented and off-basal grains, whereby the relative difference in stored energies becomes the primary factor dictating the fate of further texture evolution.

Here it is proposed that the observed annealing texture evolution in Mg-1Dy alloy seems to arise from an interesting interplay between oriented nucleation and favorable growth phenomenon. Even though shear band recrystallization (along with oriented nucleation events) produces a wide range of orientations, the texture transition events seems to be primarily facilitated by favorable growth kinetics.

The above proposed mechanisms are suggested to be one of the responsible factors behind such RE-texture modification. However, the possibility of a number of other contributing factors such as, preferential RE-solute segregation altering the grain boundary mobility-orientation relationships and resulting in new special boundaries with high mobility, electronic and chemical interactions between RE and matrix atoms cannot be negated and may be instrumental in further amplifying such RE-effects. In this regard, further investigations are underway.

Summary and Conclusions

To summarize, the deformation, recrystallization and grain growth behavior of Mg-1Dy alloy could be highlighted by the following characteristics –

1) Mg-1Dy displayed severe shear banding post rolling.
2) Deformed shear bands produced two orientations viz. Basal fiber and RE-oriented component (wherein basal poles were inclined towards TD).
3) Nucleation of recrystallization was delayed to 300°C. Recrystallization initiated inside shear bands, giving rise to a wide range of orientations with varying stored energies.
4) Nuclei and grain growth events were delayed due to solute drag effects, suppressing any growth related texture modification until 350°C.
5) At 450°C, additional thermal activation resulted in the grain boundaries to break free of solute pinning and the off-basal and RE-oriented nuclei displayed favorable growth rates.

Acknowledgements

The financial support of the Deutsche Forschungsgemeinschaft (DFG), Grant no. AL 1343/1 is gratefully acknowledged.

References

[1] Hirsch J, Al-Samman T. Acta Materialia 2013;61:818.
[2] Al-Samman T, Li X. Materials Science and Engineering: A 2011;528:3809.
[3] Basu I, Al-Samman T, Gottstein G. Materials Science and Engineering A 2013;579:50.
[4] Mackenzie LWF, Pekguleryuz MO. Scripta Materialia 2008;59:665.
[5] Senn J, Agnew S. Ref 2006;4:115.
[6] Stanford N, Barnett M. Materials Science and Engineering: A 2008;496:399.
[7] Gottstein G, Al-Samman T. Materials Science Forum 2005;495-497:623.
[8] Ion S, Humphreys F, White S. Acta Metallurgica 1982;30:1909.
[9] Cottam R, Robson J, Lorimer G, Davis B. Materials Science and Engineering: A 2008;485:375.
[10] Ball E, Prangnell P. Scripta Metallurgica et Materialia;(United States) 1994;31.
[11] Humphreys FJ, Hatherly M. Recrystallization and related annealing phenomena: Pergamon press, 2004.
[12] Al-Samman T. Materials Science and Engineering: A 2013;560:561.
[13] Stanford N. Materials Science and Engineering: A 2010;527:2669.
[14] Stanford N. Recrystallisation of Magnesium Alloys Containing Rare-Earth Elements. Materials Science Forum, vol. 753: Trans Tech Publ, 2013. p.297.
[15] Wouters O, Vellinga W, Van Tijum R, De Hosson JTM. Acta Materialia 2006;54:2813.
[16] Cho J-H, Rollett A, Oh K. Metallurgical and Materials Transactions A 2005;36:3427.
[17] Cahn JW. Acta Metallurgica 1962;10:789.
[18] Stanford N, Atwell D, Barnett MR. Acta Materialia 2010;58:6773.

Magnesium Technology 2014
Edited by: Martyn Alderman, Michele V. Manuel, Norbert Hort, and Neale R. Neelameggham
TMS (The Minerals, Metals & Materials Society), 2014

STATIC RECRYSTALLIZATION AND GRAIN GROWTH IN AZ31B-H24 MAGNESIUM ALLOY SHEET

Aravindha R. Antoniswamy[1], Jon T. Carter[2], Louis G. Hector, Jr.[2], and Eric M. Taleff[1, 3]
[1]The University of Texas at Austin; Materials Science and Engineering; 1 University Station C2200; Austin, TX 78712-0292, USA
[2]General Motors Research and Development Center; 30500 Mound Rd.; Warren, MI 48090-9055, USA
[3]The University of Texas at Austin; Mechanical Engineering; 1 University Station C2200; Austin, TX 78712-0292, USA

Keywords: AZ31B, recrystallization, grain growth, hardness, Hall-Petch effect

Abstract

The effects of static annealing on recovery, recrystallization and grain growth in a magnesium alloy sheet are investigated at 50°C to 450°C. Full recrystallization is observed after annealing at 250°C or higher temperatures. Recrystallized grain size increases with temperature through normal grain growth. Room-temperature hardness drops abruptly following recrystallization and then decreases with increasing grain size. Predictive relationships are proposed for recrystallized grain size as a function of temperature and time and for hardness as a function of recrystallized grain size.

Introduction

Wrought magnesium (Mg) alloy sheets have an enticing potential to reduce vehicle mass by replacing denser non-ferrous and ferrous alloy sheet materials in vehicle body closure panels. Among the several barriers that must be overcome to realize this potential, low room-temperature formability is one. Forming at elevated temperatures, where Mg alloy ductilities can be quite high, is a possible solution for manufacturing Mg closure panels with complex geometries [1], and the manufacturing implementation of such a technology was recently announced [2]. Forming at elevated temperatures inevitably produces various annealing phenomena, such as recovery, recrystallization and grain growth. The implementation of hot- and warm-forming processes requires understanding these because they not only affect forming, but they also control the final service properties of the formed component, including strength, hardness, ductility and plastic anisotropy.

This investigation addresses annealing phenomena in a wrought Mg alloy AZ31B-H24 sheet material. Recovery, recrystallization and static grain growth are characterized in AZ31B-H24 sheet material across temperatures from 50°C to 450°C for the relatively slow heating rates that may occur in the application hot- and warm-forming technologies. Of particular interest are the minimum temperature for recrystallization and the effects of static annealing on hardness and microstructure evolution. A predictive relationship for static grain growth, based on annealing conditions, is sought. This relationship is expected to be necessary to the future development of microstructure-based constitutive models for finite-element-method simulations of hot- and warm-forming.

Experimental Procedure

The material studied is a 2-mm-thick sheet of wrought Mg alloy AZ31B received in H24 temper (strain hardened and partially annealed) with a nominal composition of 3.1% Al, 1% Zn, 0.4% Mn, and bal. Mg, by weight. This material has a strong basal texture, as previously reported by Min *et al.* [3]. Annealing studies were carried out by using the undeformed grip regions of tension specimens tested at elevated temperatures. The furnace used for all tests was first preheated to the desired test temperature, which ranged from 50 to 450°C in increments of 50°C. A specimen was then inserted into the furnace, and its temperature was monitored with two type-K thermocouples in direct contact with the specimen. The time to reach the desired temperature was approximately 1500 s, which translates into heating rates in the range of 2 to 18°C/min., with slower rates at lower temperatures. Upon reaching the desired temperature, each specimen was held at that temperature for either a "short" time of 2 to 8 s or a "long" time of 300 to 1000 s. The short time is intended to mimic a rapid forming operation after reaching temperature, such as stamping, and the long time is intended to mimic a slow forming operation after reaching temperature, such as gas-pressure forming. Specimens were immediately quenched in water upon the completion of annealing. The annealing temperatures and "exposure times" are provided in Tables 1 and 2 for the long and short annealing times, respectively. The exposure time (t) was calculated by adding time held at temperature to the portion of the heating time for which the temperature of the specimen was at least 90% of the absolute test temperature, in K.

Specimens were prepared for observation in an optical microscope using standard metallographic specimen preparation procedures. These included epoxy cold mounting, rather than hot compression mounting, to prevent the formation of twin artifacts in the microstructure during mounting. Two pieces of material were excised from each specimen. These were mounted to enable observations along both the short-transverse direction (i.e., to examine the plane containing the rolling and long-transverse directions) and along the long-transverse direction (i.e., to examine the plane containing the rolling and short-transverse directions). Specimens mounted for observation along the short-transverse direction were ground sufficiently to observe approximately the mid-plane of the sheet. All specimens were ground, polished and then etched using an acetic-picric etchant (4.2 g picric acid, 10 ml water, 10 ml acetic acid and 70 ml ethanol).

Optical metallography was performed on the etched specimens using an optical microscope equipped with a digital camera. The average grain size, $\bar{d}$, was calculated by taking the geometric mean of lineal intercept grain size measurements along the sheet rolling (d_{RD}), sheet long-transverse (d_{LTD}) and short-transverse (d_{STD}) directions, as recommended by ASTM E 112 [4]. The uncertainty of the grain size along each direction, Δd, was

determined by calculating the 95% confidence limit from the standard error of the mean, *SE*, using the relationship

$$\Delta d = 2 \times SE = 2\ \frac{s}{\sqrt{n}} \qquad (1)$$

where s is the standard deviation of the sample grain size measurements and n is the number of measurements acquired [5]. The uncertainty of $\bar{d}$ was calculated from the uncertainties of d_{RD}, d_{LTD}, and d_{STD} using a standard formula for the propagation of uncertainty,

$$\Delta y = \sqrt{\sum \left(\frac{\partial y}{\partial x_i} \Delta x_i\right)^2} \qquad (2)$$

where x_i are the variables used to calculate the parameter of interest, y, and Δx and Δy are the uncertainties of x and y, respectively [5]. Specimens annealed at 200°C were partially recrystallized and the percentage of recrystallized grains was calculated using the point counting technique suggested by ASTM E1181 [6]. An array of points was overlaid on top of the photomicrograph using ImageJ [7]. The ratio of the number of points that that fall on the recrystallized grains to the total number of points in the array was used to calculate the percentage of recrystallized grains.

Hardness was measured using a Rockwell hardness tester with the F scale [8] and a tungsten carbide indenter, which provided hardness in HRF units. Five different hardness measurements were made in each specimen, and an average HRF value was calculated from these.

Results and Discussion

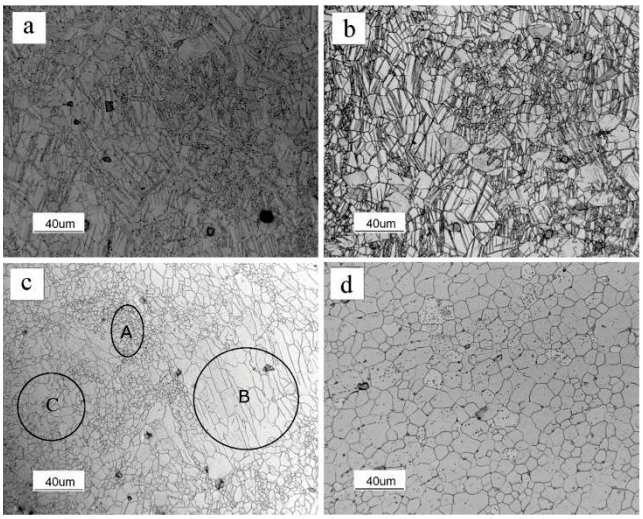


Figure 1: Photomicrographs are shown of the AZ31-H24 material (a) as-received, (b) annealed at 150°C for 1621 s, (c) annealed 200°C for 967 s and (d) annealed at 450°C for 965 s. Region A in (c) consists of grains that only recovered or newly recrystallized grains that did not grow. Region B shows elongated, deformed grains that have only undergone recovery. Region C shows recrystallized grains. The sheet rolling direction (RD) is vertical, and the long-transverse direction (LTD) is horizontal.

The as-received microstructure viewed along the short-transverse direction is shown in Figure 1(a). A heavily deformed microstructure with twins is evident. Microstructures of specimens annealed at 150, 200 and 450°C are shown in Figures 1(b), (c) and (d) as views along the short-transverse direction. These show deformed, partially recrystallized and fully recrystallized microstructures, respectively. The specimen annealed at 200°C for 967 s was partially recrystallized and exhibits three distinct regions (A, B and C in Figure 1(c)). Region A contains very small grains of size 1 to 2 μm, region B contains elongated grains with some twins, and region C contains grains of average size 5.5 ± 0.3 μm. The small grains in region A are thought to be remnants of the deformed microstructure that recovered without recrystallizing or newly recrystallized grains that did not grow. The elongated grains in region B are most likely to be unrecrystallized, deformed grains that have undergone only recovery. This is because these elongated grains resemble the original deformed grains in Figures 1(a) and (b) but show only a few twins. The grains in region C are fully recrystallized. The percentage of recrystallized grains at 200°C increases from 78 % at a short exposure time of 967 s to 95 % at a long exposure time of 1562 s. Temperatures of 250 to 450°C produced complete recrystallization. The recrystallized grains are generally equiaxed; see Figure 1(d).

Table 1. Recrystallized grain sizes after long exposure times. RX stands for recrystallization.

Temperature (°C)	Exposure time, t (seconds)	Grain Size, $\bar{d}$ (μm)
450	1985	11.3 ± 0.5
400	1744	9.0 ± 0.5
350	1801	7.9 ± 0.4
300	1623	7.1 ± 0.4
250	1623	5.8 ± 0.3
200	1562	4.5 ± 0.2
150	1621	No RX
100	1507	No RX
50	1628	No RX

Table 2. Recrystallized grain sizes after short exposure times. RX stands for recrystallization.

Temperature (°C)	Exposure Time, t (seconds)	Grain Size, $\bar{d}$ (μm)
450	965	9.2 ± 0.5
400	973	8.5 ± 0.5
350	969	7.8 ± 0.3
300	965	6.5 ± 0.4
250	966	5.3 ± 0.3
200	967	Partial RX
150	1022	No RX
100	1203	No RX
50	1082	No RX

Grain sizes measured after annealing are reported in Tables 1 and 2. Grain size steadily increases with annealing temperature from 4.5 ± 0.2 μm at 200°C to 11.3 ± 0.5 μm at 450°C for the long exposure times, and from 5.3 ± 0.3 μm at 250°C to 9.2 ± 0.5 μm at 450°C for the short exposure times. Figure 2 presents the logarithm of grain size *versus* the logarithm of temperature-adjusted time, $t \times \exp(-Q/RT)$, where t is the total exposure time in seconds, Q is the activation energy in kJ/mol, R is the universal gas constant (8.314 kJ/mol) and T is the temperature in Kelvin. The activation energy, Q, is assumed to be 80.8 kJ/mol; this is the

activation energy reported for grain growth in a hot rolled Mg AZ31 alloy by Miao *et al.* [9]. Figure 2 illustrates a fit of the form shown in Equation 3 to experimental data, where $\bar{d}$ is the average grain size in µm, A is a constant, $t\times\exp(-Q/RT)$ is temperature-adjusted time in seconds, and $1/n$ is the inverse grain-growth exponent.

$$\bar{d}=A\times(t\times\exp(-\frac{Q}{RT}))^{\frac{1}{n}} \qquad (3)$$

Fitting Equation 3 to the data produces A = 21.6 µm $s^{-1/n}$ and $1/n$ = 0.12. Figure 2 demonstrates that Equation 3 reasonably represents the data. However, the $1/n$ value of 0.12 is different from that of 0.25 determined by Miao *et al.* for Mg AZ31 [9]. A possible reason for this difference is that the starting microstructure is not recrystallized, unlike that of Miao *et al*. Because recrystallization must occur before static grain growth, there is less time for static grain growth in the present study. The heating rates of this study, approximately 2 to 18°C/min., are significantly slower than those of Miao *et al.*, a natural result of the different intents of these two studies. Even though theory predicts an inverse grain-size exponent of $1/n$ = 0.5 [10], experimentally measured values of $1/n$ for static grain growth are usually less than 0.5 [11]. For example, the value of $1/n$ measured in high-purity Al is 0.25 [12]. The reason for lower $1/n$ values can be attributed to a variety of causes [11]. Those applicable to the sheet material of this study include alloy additions, impurities, particle pinning of grain boundaries and texture effects. The strong basal texture [3] of this material may reduce the rate of grain growth, leading to a low $1/n$ value.

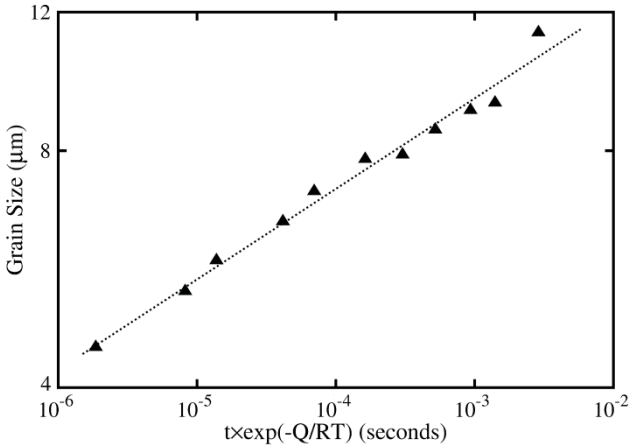


Figure 2: Recrystallized grain size is shown as a function of temperature-adjusted time, $t\times\exp(-Q/RT)$ with Q=80.8 KJ/mol [9], on dual logarithmic scales.

Hardness and grain size are shown as functions of test temperature in Figure 3. These data show little difference between short and long exposure times except at 450°C, the highest annealing temperature, which is consistent with the grain sizes reported in Tables 1 and 2. Hardness remains constant at approximately 70 to 72 HRF in specimens annealed at temperatures up to 150°C. Hardness drops abruptly for the specimens annealed 200°C, the temperature at which recrystallization begins. Hardness continues to decrease as the annealing temperature increases, reaching a low value of 48 HRF for the longest annealing time at the highest temperature, 450°C. A Hall-Petch type relationship [13, 14] was fit to the hardness *versus* recrystallized grain size data as follows:

$$HRF=18.7+\frac{97.9}{\sqrt{\bar{d}}} \qquad (4)$$

Here, HRF is the hardness on the Rockwell F scale and $\bar{d}$ is the average recrystallized grain size in µm. The data and resulting fit are shown in Figure 4. The fit parameters of Equation 4, 18.7 and 97.9, have associated standard errors of 7% and 3%, respectively.

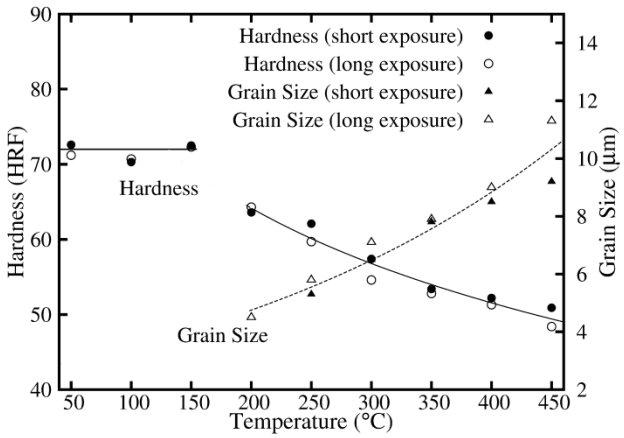


Figure 3: Hardness and average recrystallized grain size are shown as functions of temperature. For values of long and short exposure times at each temperature, please see Tables 1 and 2.

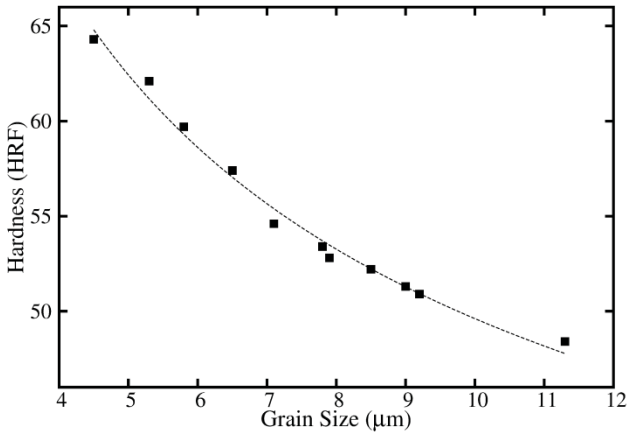


Figure 4: Hardness is shown as a function of average recrystallized grain size.

Conclusions

Data from annealing of 2-mm-thick wrought Mg alloy AZ31B-H24 sheet produced the following new insights.

1. For the annealing times investigated, recrystallization begins at approximately 200°C, but only specimens annealed at 250°C and higher fully recrystallized.
2. Static grain growth occurs following recrystallization at temperatures from 250 to 450°C.
3. The inverse grain growth exponent is calculated to be 0.12, which is about half of the value reported elsewhere for hot rolled Mg AZ31.
4. A Hall-Petch type relationship exists between the hardness and the recrystallized grain size.

Acknowledgements

The authors express thanks to Junying Min of Tongji University, China; Joshua Lasceski, Willie Dixon, Josh Campbell and Mark Verbrugge of General Motors; and Alexander Carpenter of Southwest Research Institute for assistance with the experimental work. Aravindha Antoniswamy thanks GM for a summer internship supporting this research.

References

1. R.Verma et al., "The finite element simulation of high-temperature magnesium AZ31 sheet forming," *JOM*, 61 (2009), 29.

2. General Motors Co., GM Pioneers Use of Lightweight Magnesium Sheet Metal, Published on 10/23/2012, Retrieved from http://media.gm.com/media/us/en/gm/news.detail.html/content/pages/news/us/en/2012/Oct/1023_GM_Magnesium.html

3. J. Min et al., "Comparison of Tensile Properties and Crystallographic Textures of Three Magnesium Alloy Sheets," S.M. Mathaudhu, W.H. Sillekens, N.R. Neelamaeggham, N. Hort (Eds.), *Magnesium Technology 2012*, John Wiley & Sons Inc., New Jersey, 2012, 355-360

4. ASTM E 112-96, "Standard Test Methods for Determining Average Grain Size", ASTM: West Conshohocken, PA. (1996).

5. R.S. Figliola, D.E. Beasley, *Theory and Design for Mechanical Measurements*, 2nd ed., John Wiley & Sons Inc., New York, 1995, 177-182.

6. ASTM E 1181-02, "Standard Test Methods for Characterizing Duplex Grain Sizes", ASTM: West Conshohocken, PA (2008).

7. T.J. Collins, "ImageJ for microscopy." *Biotechniques* 43 (2007), 25-30.

8. ASTM E18-08b, "Standard Test Methods for Rockwell Hardness of Metallic Materials", ASTM: West Conshohocken, PA. (2008).

9. Q. Mia et al., "Grain Growth Kinetics of a Fine-grained AZ31 Magnesium Alloy Produced by Hot Rolling," *J. Alloys Compd.,* 493 (2010), 87.

10. J.E. Burke and D.Turnbull, "Recrystallization and Grain Growth, Progress in Metal Physics," *Prog. Met. Phys.*, 3 (1952), 220.

11. F.J. Humphreys, M. Hatherly, *Recrystallization and Related Annealing Phenomena*, Second ed., (2004), Elsevier, Oxford, pp. 333-378.

12. P. Gordon, T.A. El-Bassyouni, "Effect of Purity on Grain Growth in Aluminum," *Trans. AIME*, 233 (1965), 391.

13. H.O. Hall, "The Deformation and Ageing of Mild Steel: III Discussion of Results," *Proc. Phys. Soc., London*, Sect. B, 64 (1951), 747.

14. N.J. Petch, "The Cleavage Strength of Polycrystals," *J. Iron Steel Inst.*, 174 (1953), 25.

Magnesium Technology 2014
Edited by: Martyn Alderman, Michele V. Manuel, Norbert Hort, and Neale R. Neelameggham
TMS (The Minerals, Metals & Materials Society), 2014

DEFORMATION BEHAVIOR AND DYNAMIC RECRYSTALLIZATION OF MICRO-ALLOYED Mg-Al-Ca ALLOYS DURING HIGH TEMPERATURE DEFORMATION

Jing Su, Abu Syed Humaun Kabir, In-Ho Jung and Steve Yue
Department of Mining and Materials Engineering, McGill University, Montreal, Canada

Keywords: Dynamic recrystallization, Dynamic Precipitation and Twinning

Abstract

Two micro-alloyed magnesium alloys, Mg-0.3Al-0.2Ca (AX0302) and Mg-0.1Al-0.5Ca (AX0105), were designed based on the thermodynamics calculation in terms of precipitation temperature. Hot compression tests were conducted at temperatures of 300°C, 350°C and 400°C with strain rates of $0.1s^{-1}$, $0.01s^{-1}$ and $0.001s^{-1}$. Dynamic precipitation of Al_2Ca could be found below 400°C in AX0302, while Mg_2Ca dynamically formed in AX0105 during deformation at all three temperatures. At high temperature and low strain rate (400°C at $0.01s^{-1}$ and $0.001s^{-1}$ and 350°C at $0.001s^{-1}$), DRX mainly developed at the grain boundaries and formed necklace type microstructure in both alloys. However, at lower temperature and higher strain rate, DRX grains formed at both grain boundaries and twinning boundaries. The combination effect of twinning and dynamic precipitation on dynamic recrystallization was studied by comparing with two alloys.

Introduction

Mg-Al-Ca alloy system is regarded as possible a light structural materials having high strength at elevated temperature without expensive and scarce rare-earth elements. Calcium has a low density (1.55 g/cm^3) [1], low cost and has been shown to improve properties of magnesium for practical applications [1-4]. Addition Ca into Mg showed increases in strength, creep resistance [1, 2, 5, 6], castability [5], corrosion resistance [1, 2] and cost. It is also well known that addition of Ca to magnesium is effective in preventing high-temperature oxidation and increasing ignition temperature [1, 5].

It was reported in the literatures that the precipitates or particles can alter the textures developed during thermo-mechanical processing and manipulate grain size by influencing recrystallization. Particles can either promote or suppress recrystallization depending on their size, spacing and volume fraction [4, 7]. Mg-Al-Ca alloys can form second phases: $(Mg,Al)_2Ca$, Al_2Ca and/or Mg_2Ca phases [8], due to the low solubility of Ca in Mg-Al alloys [8]. According to the isothermal cross sections of the Mg-Al-Ca phase diagrams, the equilibrium intermetallic phases ($Mg_{17}Al_{12}$, Mg_2Ca and/or Al_2Ca) can be seen at the Mg-rich end of the phase diagram [3, 4].

In this study, two micro-alloyed Mg-Al-Ca alloys, Mg-0.3Al-0.2Ca (AX0302) and Mg-0.1Al-0.5Ca (AX0105), were selected based on the thermodynamic calculation in order to form precipitates at typical hot rolling temperatures. In high strength low alloy (HSLA) steels, dynamic precipitation has proven to be beneficial in grain refinement by stopping recrystallization of austenite, thus leading to a much refined ferrite created by strain induced transformation. Although Mg does not undergo a phase transformation, retarding dynamic recrystallization to higher strains may result in a finer, more homogenous grain size once dynamic recrystallization is triggered. The objective of this study is to investigate the effect of dynamic precipitation on flow behaviour and dynamic recrystallization in Mg-Al-Ca alloys.

Experimental Procedure

Casting and Heat treatment

The raw materials used for casting were 99.9% pure magnesium, 99.9% pure aluminium and magnesium with 30 wt.% calcium master alloy. The alloys were cast in a copper mold, and then the ingots were solution treated at 500°C for 8 h to dissolve the eutectic precipitates and homogenize the distribution of the alloying elements.

Compression Test

Hot compression tests were conducted using a 100kN MTS servo-hydraulic testing machine at temperatures of 300°C, 350°C and 400°C with strain rates of $0.1s^{-1}$, $0.01s^{-1}$ and $0.001s^{-1}$and at a strain of 90%. The compression specimens were heated to the deformation temperature and held for 10min prior to compression in order to ensure a uniform temperature along the specimen. The specimens were quenched as soon as possible after compression to freeze the deformed microstructure. Compression specimens were machined from the solution heat-treated bars into cylinders with a length of 11.4mm and a diameter of 7.6mm (a ratio of 1.5).

Microstructure Characterization

The compressed samples were cut into halves along the compression axis. The microstructure of middle part of the sample was characterized and compared, since it is the uniform deformation zone.

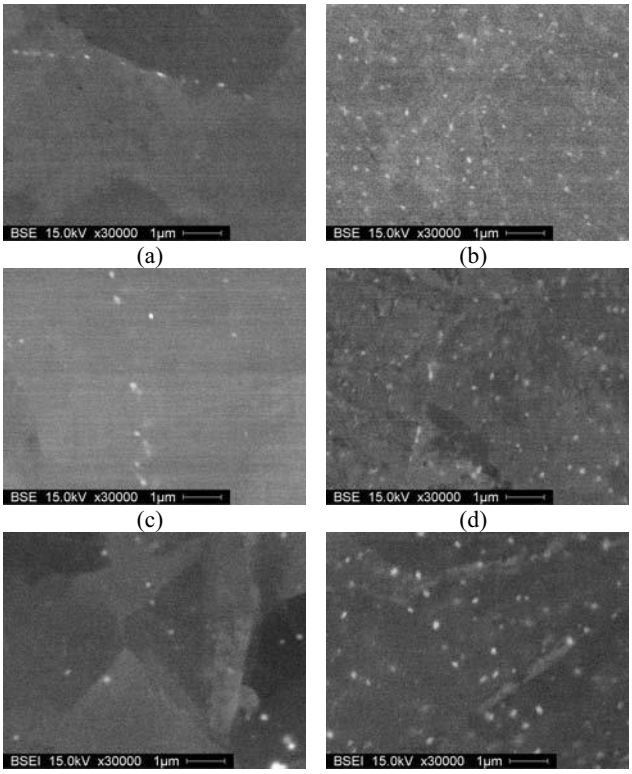
Samples used for microstructure analysis ground with SiC papers and then polished with 3μm and 1μm diamond suspension, and 0.05μm alumina powder or colloidal silica. To reveal the grain boundaries by optical microscopy, a picric–acetic solution (6g picric acid, 15ml acetic acid, 10ml H_2O and 100ml ethanol) was used to etch the samples. A Philips XL30 FEG SEM with BSE (back scatter electron) and energy dispersive (EDS) were utilized to characterize precipitation, including their distribution, morphology and size.

Results and Discussion

Precipitation

The SEM images of precipitates of both alloys deformed at 350°C with strain rates of $0.1s^{-1}$, $0.01s^{-1}$ and $0.001s^{-1}$ at 90% strain are shown in Fig. 1. In AX0302, most of the precipitates form along grain boundaries at strain rates of $0.1s^{-1}$ and $0.01s^{-1}$ and there is no significant difference in the amount of precipitates with increasing strain rate from $0.01s^{-1}$ to $0.1s^{-1}$ (Fig. 1 (a) and (c)). However, at the lowest strain rate ($0.001s^{-1}$) (Fig. 1 (e)), there appears to be a slightly higher number of precipitates and these can be found not only along grain boundaries, but also inside grains. It can be observed that the size of precipitates does not increase with decreasing strain rate in AX0302. In AX0105, precipitates are formed at grain boundaries and within grains at all three strain rates (Fig. 1 (b), (d) and (f)). There is no significant change in precipitate behaviour with strain rate, except a slight coarsening at the lowest strain rate of $0.001s^{-1}$.

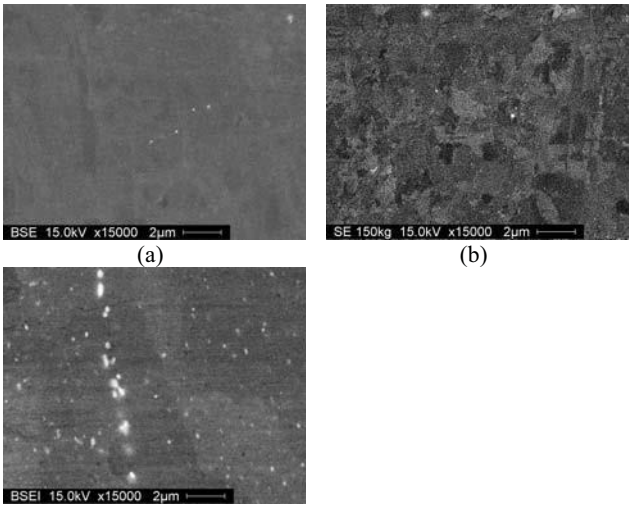
The amount of precipitates formed in AX0105 alloy is larger than that in AX0302 alloy. The precipitate is Al_2Ca and Mg_2Ca for AX0302 and AX0105, respectively. The formation of Al_2Ca precipitates requires for the diffusion of both aluminum and calcium elements. However, the formation of precipitate of Mg_2Ca only requires the diffusion of calcium since magnesium is the matrix. The diffusivity of aluminum is an order larger than that of calcium. Therefore, the rate controlling factor for precipitation of both alloys is calcium, regardless of different type of precipitates. The larger addition of Ca in AX0105 alloy results in the higher chemical potential of AX0105 than that of AX0302, therefore larger amount of precipitates formed in AX0105.



(a) (b) (c) (d) (e) (f)

Fig. 1 BSE images of AX0302 and AX0105 compressed at 350°C with strain rates of $0.1s^{-1}$ ((a) and (b)), $0.01s^{-1}$ ((c) and (d)) and $0.001s^{-1}$ ((e) and (f)) and a strain of 90%

The SEM images of AX0302 deformed at temperature of 300°C and AX0105 deformed at 300°C and 400°C at the strain rate of $0.01s^{-1}$ and a strain of 90% are shown in Fig. 2. Using SEM, it was rare to find precipitates at 400°C in AX0302. In AX0302, most precipitates form along grain boundaries at 300°C (Fig. 2 (a)), which is similar as what was found at 350°C. However, in AX0105, precipitates were formed at all three temperatures. (Figs. 2 (b) and (c)). In AX0105, the size of precipitates, which formed both along grain boundaries and inside grains, increased with increasing temperature.

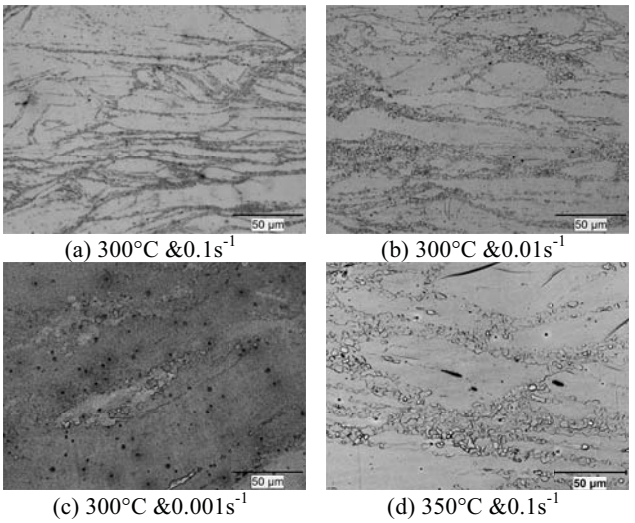


(a) (b) (c)

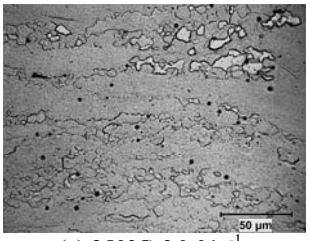
Fig. 2 The SEM images of AX0302 deformed at temperature of 300°C (a) and AX0105 at 300°C (b), 400°C (c) at the strain rate of $0.01s^{-1}$ and a strain of 90%

Dynamic Recrystallization

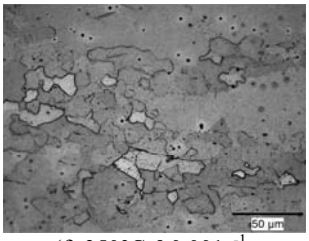
The optical microstructures of AX0302 deformed at the temperatures from 300°C to 400°C at strain rates of $0.1s^{-1}$, $0.01s^{-1}$ and $0.001s^{-1}$ to a strain of 90% are shown in Fig. 3. The DRX grain size increased with increasing temperature and decreasing strain rate. Partial recrystallization occurred in both alloys at all deformation conditions, even at the highest temperature of 400°C and the lowest strain rate of $0.001s^{-1}$ with the strain of 90%. The microstructure evolution of AX0105 with temperature and strain rates is similar as that of AX0302.



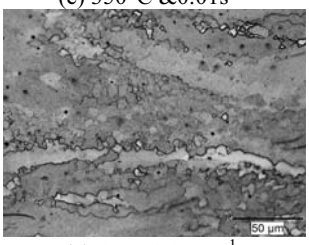
(a) 300°C &$0.1s^{-1}$ (b) 300°C &$0.01s^{-1}$ (c) 300°C &$0.001s^{-1}$ (d) 350°C &$0.1s^{-1}$



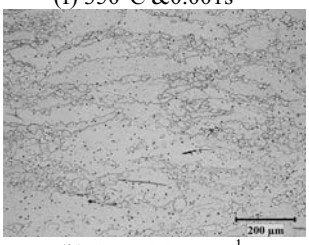
(e) 350°C &0.01s^{-1}



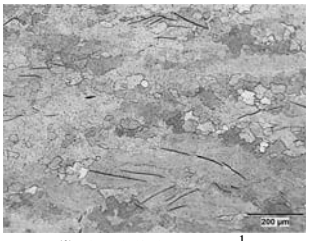
(f) 350°C &0.001s^{-1}



(g) 400°C &0.1s^{-1}



(h) 400°C &0.01s^{-1}
(Low magnification)



(i) 400°C &0.001s^{-1}
(Low magnification)

Fig. 3 The optical microstructures of AX0302 deformed at 300°C to 400°C with strain rates of 0.1s^{-1}, 0.01s^{-1} and 0.001 s^{-1} to a strain of 90% (Note that the magnifications are not same)

At high temperature and low strain rate (400°C at 0.01s^{-1} and 0.001s^{-1} and 350°C at 0.001s^{-1}), DRX mainly developed at the grain boundaries and formed necklace type microstructure in both alloys. However, at lower temperature and higher strain rate, DRX grains formed at both grain boundaries and twinning boundaries. For example, at 350°C with strain rate of 0.01s^{-1} DRX grains can be found on the original grain boundaries and the intersections of grain boundaries and grain boundary and twinning boundary (Fig. 4).

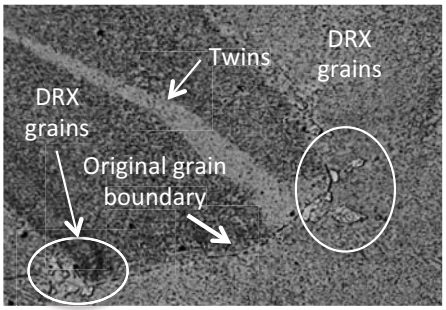


Fig. 4 Optical microstructures of AX0105 during hot compression at 350°C with a strain rate of 0.01s^{-1} and strains of 30%

The relationship of the size of DRX-ed grains with temperature at strain rates of 0.1s^{-1}, 0.01s^{-1} and 0.001s^{-1} to a strain of 90% of AX0302 and AX0105 is compared in Fig. 5. The values of DRX-ed grain sizes at 300°C are relatively close, but diverge at higher temperatures, in particular at 400 °C. It can also be seen that the difference of grain size between AX0302 and AX0105 at the strain rate of 0.001s^{-1} was larger than that at higher strain rates of 0.01s^{-1} and 0.1s^{-1}.

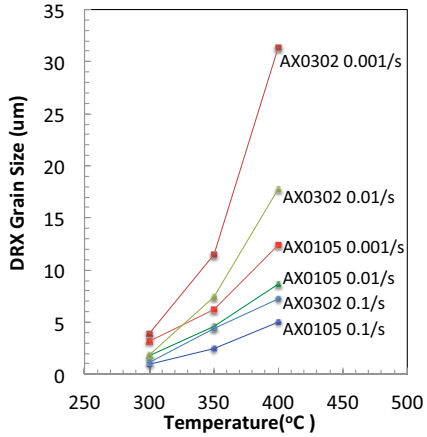


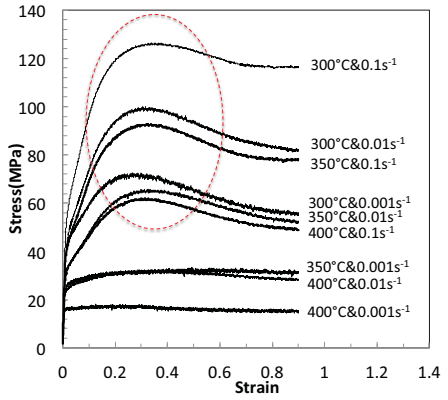
Fig. 5 Variation of DRX grain size with temperature and strain rate of AX0302 and AX0105

As the temperature increased from 300°C to 400°C, the DRX grain size increases in both alloys. This is due to higher migration rates of DRX grains boundaries, which is temperature driven [9], but can also be due to decreased precipitation lowering any precipitation pinning effects [10]. With increasing strain rate from 0.001s^{-1} to 0.1s^{-1}, the DRX grain size became smaller. The dislocation density is higher at higher strain rates, providing more nucleation sites for DRX grains, which then forms finer DRX grains [9].

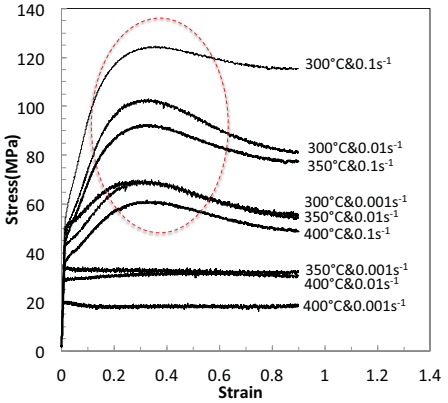
In addition, the increase of the DRX grain size with increasing temperature from 350°C to 400°C of AX0302 was larger than that in AX0105. Because more precipitates occurred in AX0105 than that in AX0302, formation of precipitates during hot compression in AX0105 could drag movement of grain boundaries or pin them and suppress dynamic recrystallization.

Flow Behaviour

Typical true stain–true stress compression flow curves of AX0302 and AX0105, which were deformed at 300°C, 350°C and 400°C with different strain rates of 0.1s^{-1}, 0.01s^{-1} and 0.001s^{-1} to a strain of 90% are shown in Fig. 6. As expected, at a given strain rate and temperature, by increasing the strain it can be seen that the flow stress firstly increases up to a peak and then decreases to a steady state. The flow softening beyond the peak stress is mainly attributed to DRX. The flow stress increases with increasing strain rate and decreasing temperature. Obvious peaks can be seen in the flow curves with all strain rates at 300°C and strain rates of 0.1s^{-1} and 0.01s^{-1} at 350°C, strain rate of 0.1s^{-1} at 400°C; these curves are designated as 'group 1' (circled in Figs. 6 (a) and (b)). Group1 curves also reveal "s" - shape work hardening behavior, which indicates that twinning [11]. In AX0302, for the other deformation conditions, the curves exhibit broad peaks (categorized as group 2), whereas in AX0105 the curves at the strain rate of 0.001s^{-1} at 350°C and 400°C exhibit what appears to be a yield point, followed by a plateau, and at the strain rate of 0.01s^{-1} at 400°C shows a broad peak.



(a) AX0302



(b) AX0105

Fig. 6 Flow curves of AX0302 (a) and AX0105 (b) deformed at temperature from 300°C to 400°C at strain rate of $0.1s^{-1}$, $0.01s^{-1}$ and $0.001s^{-1}$ to a strain of 90%

The deformation peak is caused by a superposition of hardening by dislocation storage and softening by dynamic recrystallization (DRX). Therefore, it is a measure for the onset of DRX, although the true start of DRX occurs somewhat before the peak. [12]

Usually, in pure magnesium and its alloys (AZ31, AZ61 and ZK60), the peak strain (εp) decreases as the temperature increases and strain rate decreases [12-14]. Increasing temperature leads to higher diffusivity, which in general allows grain boundaries to be more mobile, thus allowing DRX to occur at smaller strains. With increasing strain rate, there is an increase in work hardening, but this is insufficient to increase the DRX rate to match the increase in strain rate. Therefore DRX takes place at higher strains. [9]

However, the variation of peak strain with temperature and strain rate for both alloys in this study were not consistent with that observed in other magnesium alloys. These observations can be attributed to the combination effect of twinning and dynamic precipitation. The values of peak strain at different temperature and different strain rate with information of twinning and precipitation in these two alloys are shown in Tables 1 and 2.

Table 1. Peak strain of AX0302 with temperature and strain rate

Peak strain / Strain rate	Temperature		
	300°C	350°C	400°C
$0.1s^{-1}$	34%	33%	33%
	Twinning &Precipitation	Twinning &Precipitation	Twinning
$0.01s^{-1}$	32%	33%	35%
	Twinning &Precipitation	Twinning &Precipitation	
$0.001s^{-1}$	30%	50%	15%
	Twinning &Precipitation	Precipitation	

Table 2. Peak strain of AX0105 with temperature and strain rate

Peak strain / Strain rate	Temperature		
	300°C	350°C	400°C
$0.1s^{-1}$	34%	34%	33%
	Twinning &Precipitation	Twinning &Precipitation	Twinning &Precipitation
$0.01s^{-1}$	33%	34%	61%
	Twinning &Precipitation	Twinning &Precipitation	
$0.001s^{-1}$	32% Twinning &Precipitation	(No obvious peak) Precipitation	(No obvious peak) Precipitation

At 300°C and all three strain rates, twinning and dynamic precipitation both occurred in the two alloys, it can be seen that peak strains did not vary significantly with strain rate. At 350°C, dynamic precipitates could be found at all three strain rates in AX0302, but the peak strains at the strain rates of $0.1s^{-1}$ and $0.01s^{-1}$ where twinning occurred, were smaller than that at higher strain rate ($0.001s^{-1}$). This means that even if there were precipitates forming dynamically, twinning played a strong role on the peak strain and had effect on the flow curves. It has been found that twins possess much higher stored deformation energy compared to untwinned areas and are therefore favorable nucleation sites for DRX [15].

The variations of peak strain with temperature can be explained in a similar fashion. The peak strain decreased with increasing temperature at the region where no twining occurred, which was as same as most previous results in the literature. This is consistent with the study of Ion et. al. (Fig. 7), where it can be seen that the peak strain increases with increasing temperature when there is extensive twinning (A and H in Fig. 7) at low temperature (423 K and 533 K) [16]. The same phenomenon was also be found in the investigation of Sakai et.al on as-annealed AZ31, in which the curves showed twinning features, and therefore the peak strain did not vary with increasing temperature from 473K to 523K [17]. The amount of precipitates increased with decreasing temperature, suggesting that there will be a stronger effect on retarding DRX at lower temperatures. In another words, the peak strain will be even larger at lower temperature with occurrence of dynamic precipitation.

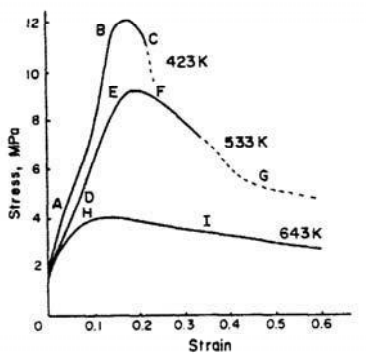


Fig. 7 Flow curves of AZ31 deformed at temperatures from 423 K (150 °C) to 643 K (370 °C) [16] The onset of the main microstructural features is indicated by the letters: A= extensive twinning, D= extensive twinning, H=extensive grain boundary bulging and migration of leading to recrystallization; I= maintenance of a steady state microstructure by repeated dynamic recrystallization. [16]

When there was twinning, the peak strain of both alloys in this study was almost the same, whether precipitation occurred or not. However the peak strain of AX0105 was larger than that of AX0302 when there was no twinning in both alloys, but precipitates in AX0105 and no precipitates in AX0302. This also proves that dynamic precipitates retarded dynamic recrystallization.

Conclusion

(1) The larger size of DRX-ed grains of AX0105 than that of AX0302 may be due to larger amount of precipitates in AX0105 more strongly inhibiting nucleation and growth of DRX grains.

(2)Dynamic precipitation retards dynamic recrystallization, which can be due to the pinning effect of precipitates on grain boundary migration.

(3)At high temperature and low strain rate (400°C at $0.01s^{-1}$ and $0.001s^{-1}$ and 350°C at $0.001s^{-1}$), DRX mainly developed at the grain boundaries and formed necklace type microstructure in both alloys. However, at lower temperature and higher strain rate, DRX grains formed at both grain boundaries and twinning boundaries.

Reference

1. S. Wang, et al., *Precipitates effect on microstructure of as-deformed and as-annealed AZ41 magnesium alloys by adding Mn and Ca.* J Mater Sci, 2011. **46**: p. 3060- 3065.
2. M. Bamberger, G. Levi and J. B. V. Sande, *Precipitation Hardening in Mg-Ca-Zn Alloys.* METALLURGICAL AND MATERIALS TRANSACTIONS A 2006. **37A**: p. 481-487.
3. L. L. Rokhlin, N. I. Nikitina, and V. A. Volchenkova, *Magnesium-Rich Mg–Al_2Ca Alloys.* Russian Metallurgy (Metally), 2006. **2**: p. 185-188.
4. J. D. Robson, D. T. Henry and B. Davis, *Particle effects on recrystallization in magnesium–manganese alloys: Particle-stimulated nucleation.* Acta Materialia, 2009. **57**: p. 2739-2747.
5. W.J. Kim, et al., *Microstructure and superplasticity of Mg–Al–Ca electromagnetic casting alloys after hot extrusion.* Materials Science and Engineering A 2008. **494**: p. 391-396.
6. Kinji Hirai, et al., *Effects of Ca and Sr Addition on Mechanical Properties of a Cast Az91 Magnesium Alloy at Room and Elevated Temperature.* Materials Science and Engineering A, 2005 **403**: p. 276－280.
7. A. Sadeghi and M. Pekguleryuz, *Recrystallization and texture evolution of Mg-3%Al-1%Zn-(0.4-0.8)%Sr alloys during extrusion.* materials Science and Engineering A, 2011. **528**: p. 1678-1685.
8. H. Watanabe, et al., *Mechanical properties of Mg–Al–Ca alloy processed by hot extrusion.* Materials Science and Engineering A, 2007. **454-455**: p. 384-388.
9. Y. Zhang, et al., *Deformation behavior and dynamic recrystallization of a Mg–Zn–Y–Zr alloy.* Mater. Sci. Eng. A, 2006. **428**: p. 91-97.
10. G. R. Ebrahimi, et al., *Effect of thermomechanical parameters on dynamically recrystallized grain size of AZ91 magnesium alloy.* J. Alloy. Compd., 2011. **509**: p. 2703-2708.
11. B. Wang, et al., *Effect of crystal orientation on the mechanical properties and strain hardening behavior of magnesium alloy AZ31 during uniaxial compression.* Mater. Sci. Eng. A, 2012. **534**: p. 588–593.
12. A. Galiyev, R. Kaibyshev, and G. Gottstein, *Correlation of Plastic Deformation and Dynamic Recrystallization in Magnesium Alloy ZK60.* Acta Mater., 2001. **49**: p. 1199-1207.
13. S. M. Fatemi-Varzaneh, A. Zarei-Hanzaki, and H. Beladi, *Dynamic recrystallization in AZ31 magnesium alloy.* Mater. Sci. Eng. A, 2007. **456** p. 52–57.
14. L. Liu, et al., *Dynamic Recrystallization Behavior of AZ61 Magnesium Alloy*, in *J. Mater. Online*2006.
15. T. Al-Samman and G. Gottstein, *Dynamic recrystallization during high temperature deformation of magnesium.* Mater. Sci. Eng. A, 2008. **490**: p. 411-420.
16. S. E. Ion, F. J. Humphreys, and S. H. White, *Dynamic Recrystallisation and the Development of Microstructure during the High Temperature Deformation of Magnesium* Acta Metall. Mater., 1982. **30**: p. 1909-1919.
17. T. Sakai and H. Miura, *Mechanical Properties of Fine-Grained Magnesium Alloys Processed by Severe Plastic Forging*, in *MAGNESIUM ALLOYS* F. Czerwinsk, Editor 2011, InTech. p. 219-244.

Magnesium Technology 2014
Edited by: Martyn Alderman, Michele V. Manuel, Norbert Hort, and Neale R. Neelameggham
TMS (The Minerals, Metals & Materials Society), 2014

PHYSICALLY-BASED MODEL FOR STATIC RECRYSTALLIZATION IN AZ31

Paul Okrutny[1], Shenglong Liang[1], Lingyao Meng[1] and Hatem Zurob[1]
[1]Department of Materials Engineering, McMaster University, Hamilton, ON, L8S4L7, Canada

Keywords: Recrystallization, Modeling, Grain Growth, Recovery

Abstract

A physically-based model for static recrystallization in alloy AZ31 is presented. The model predicts the kinetics of recrystallization as a function of the applied strain and the annealing temperature. A key feature of the model is the incorporation of the effects of recovery and solute drag on the recrystallization kinetics. In addition, the model attempts to take into account the effect of heterogeneity of the deformed state on recrystallization kinetics. Preliminary experimental studies were carried out in order to estimate the parameters that enter into the model. Grain-growth experiments were carried out on pure Mg, Mg-Al and Mg-Zn alloys in order to estimate the boundary mobility. Recovery kinetics was measured at low temperatures in order to quantify the contribution of recovery to the depletion of the stored energy.

Introduction

Wrought magnesium alloys are attracting increasing attention for automotive applications. In order for these alloys to be viable in the automotive industry it is necessary to develop reliable thermomechanical processing schedules for controlling grain size and texture. These schedules could be developed and optimized with the aid of physically-based models for microstructure evolution during hot-deformation, cold-deformation and annealing. Such models are already in wide use in the steel and aluminum industries. Similar developments for Mg alloys have traditionally been hampered by the lack of fundamental thermodynamic and kinetic data for Mg alloys, as well as, the complexity of deformation in HCP materials, like Mg. The situation has significantly changed in recent years, as reliable estimates of phase equilibria and diffusion coefficients have become available. In addition, the community has achieved a better understanding of the key events taking place during deformation and annealing of Mg alloys. The purpose of this contribution is to present a "minimum-ingredients" model for the static recrystallization of cold-rolled alloy AZ31. We hope to demonstrate that in spite of the complexity of the microstructure, it is possible to obtain reasonable predictions of the recrystallization kinetics and recrystallized grain size. The model could be applied to other AZ series alloys provided that annealing is carried out in the single phase region.

The proposed model is based on a generic approach that has been applied successfully to pure Al [1], pure Cu[1], Zr-alloys [2] and microalloyed steels[3]. We start by reviewing the key features of this approach. We then describe the modifications that need to be incorporated into the model in order to apply it to alloy AZ31. A series of simple experiments is then carried out in order to determine (within an order of magnitude) the values of the physical parameters that enter into the model. The model is validated against measured recrystallization kinetics and the key features and limitations of the model are discussed.

Modeling Framework

This contribution builds on the recrystallization model of Rehman and Zurob [3]. The model considers only the mechanism of strain induced boundary migration [4]. The subgrains within the deformed material grow at the rate: $dR/dt \sim D\sinh(\sigma V_a/kT)$, where D is the bulk self-diffusion coefficient, σ is the stress due to dislocations, V_a is the activation volume for recovery and T is temperature. The boundary can overcome the curvature barrier and bulging takes place as per the Bailey-Hirsch criterion [5] when the subgrain size, *R,* reaches a critical value of $2\gamma/F$, where γ is the grain boundary energy and F is the energy difference across the bulging boundary. The nucleation rate is derived by considering a size-distribution of subgrains and tracking when different subgrains within the distribution reach the critical condition [1]. The nucleation model is coupled to a growth model which considers that the nuclei are all formed at the grain boundaries and grow to consume the non-recrystallized grain interiors. The model is capable of predicting the nucleation rate of recrystallization, the recrystallized fraction and the final grain-size.

Implementation of the model requires knowledge of the recovery kinetics and the grain-boundary mobility. Recovery is described in terms of an activation energy and an activation volume as per the model of Verdier et al [6]. Both quantities are not available for present alloy. For this reason, the yield stress evolution during low temperature annealing of deformed AZ31 was measured in order to estimate of the recovery kinetics by fitting the model of Verdier et al [6]. Similarly, experimental estimates of the intrinsic grain boundary mobility of Mg and of the effects of Al and Zn on the grain boundary mobility were not available. A first order estimate was obtained by measuring grain growth kinetics in pure Mg, Mg-3%Al and Mg-1%Zn at high temperatures within the one phase region. The details are described in the Experimental section.

Experimental

Three types of experiments were carried out; grain growth experiments to estimate the grain boundary mobility, low temperature annealing experiments to quantify the recovery kinetics and high temperature annealing experiments to measure the recrystallization kinetics.

Grain Growth:

Three materials were used, the first is pure Mg (>99.99%), Mg-1wt%Zn and Mg-3%Al. The pure material was donated by Magnesium-Elecktron. The binary alloys were induction melted at McMaster University using high purity additions of Al and Zn. The binary alloys were then hot-rolled above 450°C in order to break down the as cast structure. They were then annealed to ensure complete recrystallization. The resulting grain sizes were

50 and 80 μm for the Mg-Al and Mg-Zn alloys, respectively. The initial grain size of as-received pure Mg was too large; as a result, a cold-rolling and recrystallization treatment was employed to reduce the grain size to less than 20 μm. In order to study grain-growth kinetics the materials were annealed at 400°C for 0.5 to 16 hrs. The average grain area was measured by optical metallography and the equivalent diameter was calculated for each annealing time. These diameters were then multiplied by 1.7 in order to convert the present 2-D observations to the actual diameter. In the case of the pure material, grain growth was also followed at 500°C. An example of the grain-growth kinetics is shown in Fig.1. The grain boundary mobility was extracted by fitting the experimental data to Hillert's grain-growth model [7] and assuming the grain boundary energy is 0.5 J/m^2. In this way, the mobility values for Mg, Mg-1%Zn and Mg-3%Al at 400°C were estimated to be 2.2 x 10^{-12}, 8.6 x 10^{-13} and 3.7 x 10^{-13} m^4/J.sec, respectively. The mobility of pure Mg at 500°C was estimated to be 1.1 x 10^{-11} m^4/J.sec. These values are believed to be accurate to within a factor of 2 with the uncertainty originating from the experimental data as well as the model used to fit it.

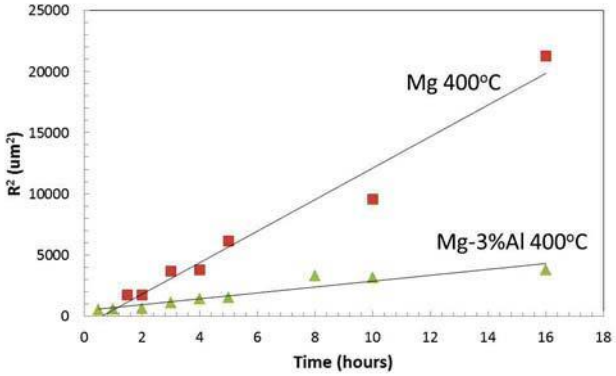


Fig. 1: An example of the grain growth data which was used to estimate the grain boundary mobility. The square of the grain radius is plotted against time.

Recovery:

Alloy AZ31 (Mg-3%Al-1%Zn-0.4%Mn) was received in the form of 2.01 mm sheets. The as-received material was subjected to a homogenization treatment at 400°C for 24 hrs, followed by a grain-growth treatment which consisted of a 5% cold-reduction and annealing at 470°C for 2 hr. The resulting grain size was in the range of 50 to 60 μm. The material was then cross-rolled at room-temperature to equivalent von Mises strains of 0.10 and 0.30. The rolling procedure consisted of a 0.03 mm reduction per pass and the rolling direction was rotated by 90° after each pass. Flat ASTM sub-size tensile specimens were then machined out of the rolled sheet and annealed in an oil bath for various times at 120 and 150°C. The evolution of the 0.2% offset yield strength is shown in Fig. 2. The tensile specimens were examined by optical metallography in order to ensure that recrystallization did not take place during annealing. The data was then fitted to the model of Verdier [6] in order to estimate the activation energy and activation volume. The solid lines in Fig. 2 represent the predictions of the model using an activation energy of 180 kJ/mole and an activation volume of 21 b^3 for the specimens pre-deformed to a strain of 0.3 and 26 b^3 for those pre-deformed to a strain of 0.1, where b is the burger's vector. Other combinations of activation energy and activation volume could have been used to fit the data. The present values should therefore be considered preliminary estimates until additional data is obtained.

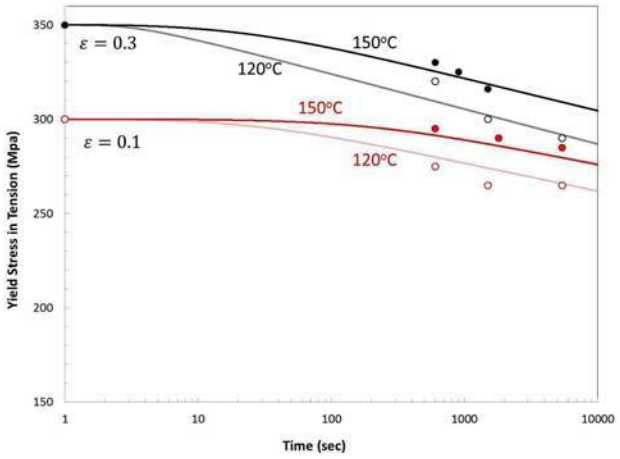


Fig. 2: Evolution of the 0.2% off-set yield strength as a function of time and temperature for two different strain levels. The points represent experimental measurements. The solid lines are obtained by fitting the data to Verdier's model [6].

Recrystallization:

The AZ31 sheet was rolled to equivalent strains of 0.1 and 0.3 using the procedure described in the recovery section. Annealing at 200, 250, 275 and 300°C for times ranging from 3 to 10,000 sec was carried out in a salt bath. The recrystallized fraction was measured by optical metallography. Selected specimens were prepared for Electron Back Scatter Diffraction (EBSD) and the recrystallized fraction was estimated based on measurements of the misorientations present within grains. The results are shown in Fig. 3. Comparison of the EBSD and optical metallography results suggest that the later provides an accurate estimate of the recrystallized fraction, X, when X is less than 40%. The optical metallography tends to overestimate the recrystallized fraction during the later stages of the transformation because the new recrystallized grains become comparable in size and shape to the deformed ones and because detwinning takes place within some of the deformed grains. This tendency is reflected in the error bars on the optical metallography data.

Particular Features of Recrystallization of Mg Alloys

Before applying the above recrystallization model to Mg alloys, it is necessary to review the key features of the deformed state and sequence of events that lead to recrystallization in these alloys. This would ensure that the model is adjusted to reflect these events. Based on the literature, as well as, work carried out within our group [8, 9] it is found that:

- The cold-deformed state of AZ31 is heterogeneous at many levels. At the level of an individual grain, it is found that deformation is localized in the vicinity of grain boundaries. The grain interiors experience very little deformation at low strains. With increasing strain, localization occurs at the scale of microshear bands which involve multiple grains.
- Twins play an important role in the deformation process. The initial AZ31 sheets employed for this investigation had a strong basal texture. During rolling, contraction twins and double (contraction-extension) twins are formed.

- As the strain increases (ε=0.3) bundles of twins appear within the grain interior.
- Recrystallization takes place, primarily, at the intersections of twins and grain boundaries as well as twin-twin intersections. Recrystallization also takes place within individual twins and twin bundles and within microshear bands.
- The new recrystallized grains do not appear to grow readily into the deformed material. Deformed/recovered grains persist for very long times within the microstructure.

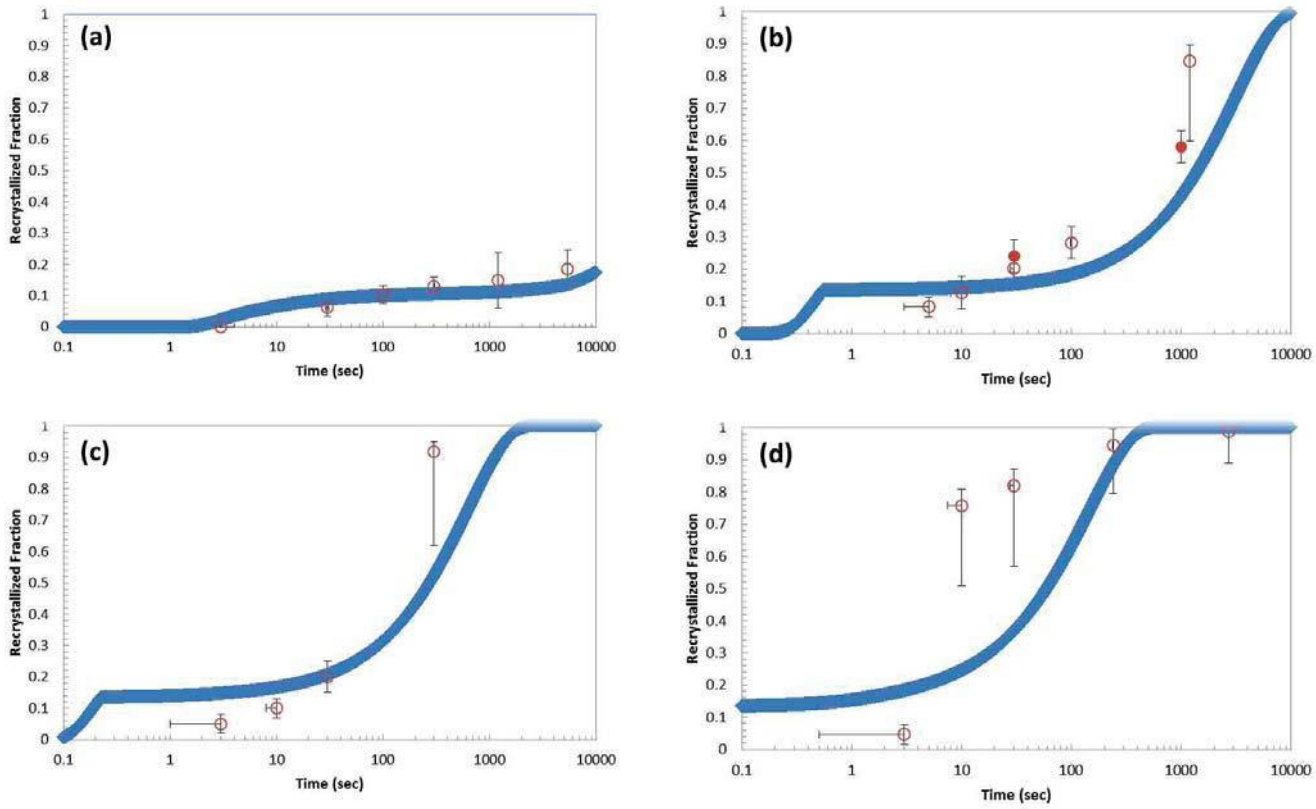


Fig. 3: Recrystallization kinetics of alloy AZ31 after cold-rolling to an equivalent von Mises strain of 0.3 and annealing at (a) 200°C, (b) 250°C, (c) 275°C and (d) 300°C. Optical metallography data is shown by the open symbols while EBSD results are shown by solid circles. The lines represent the model predictions.

Recrystallization Model

The challenge is to develop the simplest possible model that could capture the recrystallization of cold-deformed AZ series alloys. The model of [3] has several attractive features. In particular, it includes the effect of concurrent recovery on recrystallization. Recovery may contribute to the slow growth of the recrystallizing grains and the persistence of some deformed grains. The above model, however, is based on the mechanism of strain induced boundary migration and does not take into account the possibility of nucleation within twins or shearbands. To address this point, we have introduced an effective grain size which represents the diameter of a region that does not contain any potent nucleation sites but is surrounded by such sites. This is illustrated in Fig. 4. As an initial approximation, the competition between nucleation sites has not been considered; nucleation is thus assumed to take place at the same rate along all the boundaries surrounding an effective grain of the type shown in Fig. 4. We have also assumed that the stored energy is constant throughout the material. Admittedly, the experimental evidence does not support this simplification. The consequences of this simplification will be discussed in detail in the discussion section. In what follows, the model is described in detail with special emphasis on the various physical quantities employed.

Nucleation:

In the present material nucleation takes place by a variety of mechanisms and at a wide range of nucleation sites. For the sake of simplicity, a description based on strain induced boundary migration will be employed. Grain boundary bulging takes place when the stored energy, *F*, is enough to overcome that curvature term, 2γ/R:

$$F(t)>2\gamma/R(t)$$

Initially, the subgrains are small and the driving force is insufficient for bulging. It should be noted, however, that both sides of Eq. 1 will evolve with time. The stored energy will decrease as a result of recovery and the subgrain size will increase due to subgrain growth. The evolution of the dislocation density, ρ, was described in terms of a recovery model [6] and using the activation volume and activation energy that were determine experimentally in this work. The subgrain growth was assumed to be controlled by the climb of extrinsic dislocations [10] and modeled in terms of the equation [3]:

$$v = 2\frac{D}{L}\sinh\left(\frac{K_{ad}\sigma_D L\Omega}{KTb}\right)$$

where L is the spacing of extrinsic dislocations (V_a/b^2) and K_{ad} is an adjustable parameter which is used to fit the experimental data. The value of this parameter was set to 2.3 for all simulations. The first nucleation event takes place when the largest subgrain in the material reaches the critical size defined by Eq. (1). The nucleation rate is derived by considering a size-distribution of subgrains and tracking when different subgrains within the distribution reach the critical condition. In this work a Rayleigh distribution was assumed.

Growth:

The rate of growth of the recrystallizing grains is the product of the driving force (stored energy) and the grain boundary mobility. The driving force was defined as ½ $\rho(t)\mu b^2$, where $\rho(t)$ is the dislocation density. The evolution of the dislocation density as a function of time is described in terms of the recovery model describe earlier. As for the grain boundary mobility, it is necessary to extrapolate the values measured at 400°C down to the temperature range of interest (200-300°C). This was done by employing Cahn's solute drag model [11]. The model contains three key parameters; the intrinsic mobility, the binding energy of solute to grain boundaries and the cross-boundary diffusion coefficient of the solute. A rough estimate of the intrinsic mobility was obtained by fitting the mobility of pure Mg at 400 and 500°C to an Arrhenius relationship:

$$M = 5.3 \times 10\text{-}7 \exp(-69000/RT)$$

It is reassuring that the resulting activation energy is comparable to that of grain-boundary diffusion. As for the binding energy, it was estimated based on the lattice misfit of Al and Zn atoms in Mg [12]. A value of 15 kJ/mole was used for both solutes. This value should be interpreted as an educated guess in the absence of more reliable data. Finally, the cross boundary diffusion coefficients were estimated to be ten times the bulk self-diffusion coefficients of Mg [13]. Given the above approximations, the extrapolated mobility should be treated as an order of magnitude estimate. The best fit of the experimental data was obtained using a mobility which is 5 times larger than the values calculated using the above approach.

Model Predictions:

The predicted recrystallization kinetics is shown by the solid lines in Fig. 3. It was assumed that each of the initial grains (60μm) was subdivided into four subgrains corresponding to an effective grain size of 15 μm. The model predictions are generally in good agreement with the experimental data over the above temperature range. The disagreement at the shortest times (3 sec) is probably due to the fact that this represents the total time in the bath and does not take into account the time needed for the specimen to reach the target temperature. It is also possible to predict the grain size of the recrystallized material. The predicted values were of the order of 9 μm for the material deformed to a strain of 0.3. This value is somewhat smaller than experimental values which are typically in the range of (~15 -25 μm).

Discussion

A preliminary model for the static recrystallization of cold-deformed alloy AZ31 has been developed. The model predictions are in good general agreement with measured recrystallization kinetics. Further development of the model, however, would require better quantification of the recovery kinetics and the grain boundary mobility. The use of the yield stress evolution to follow recovery has several drawbacks in the case of Mg alloys. In particular, twinning is expected to contribute to the increase in yield stress during deformation. Therefore, the increase in the flow stress of the cold-rolled material compared to that of the annealed material should not be completely attributed to the increase in dislocations density. Similarly, there is a large uncertainly associated with the extrapolation of the grain boundary mobility. Grain-growth kinetics over a wider range of temperatures is needed in order to obtain better estimates.

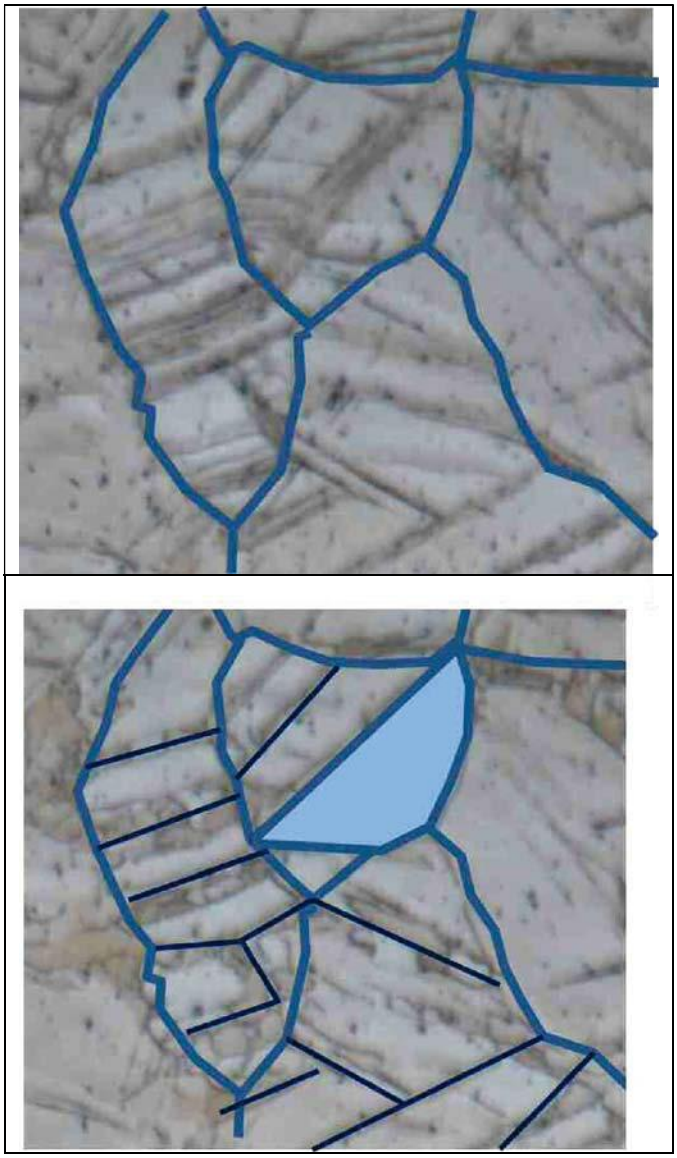


Fig. 4: (a) Actual microstructure of a deformed (ε=0.3) AZ31 specimen. The grain boundaries are highlighted for clarity. (b) In order to model this microstructure the material is subdivided into new volumes which are surrounded by potent nucleation sites. The shaded region is then treated as an effective grain.

In spite of the above limitations, valuable insights are gained from the present modeling exercise. In particular, the non-sigmoidal

recrystallization kinetics, which are often observed in Mg alloys (e.g. Fig. 3(b)), can now be interpreted in terms of the low mobility of the grain boundaries. The model suggests that nucleation takes place quickly at a wide range of nucleation sites. The recrystallized fraction rises rapidly during the nucleation stage. Once the nucleation sites are consumed, the recrystallization kinetics slows down due to the unusually low boundary migration rate. In order to confirm this point, the calculations were repeated at constant driving force (no recovery). The shape of the recrystallization curve was unchanged, confirming that the slow growth kinetics is mainly due to the low mobility of grain boundaries and not the result of the depletion of stored energy a result of rapid recovery.

One of the key approximations made in the model concerns the assumption that the stored energy is uniform throughout the microstructure. This approximation is questionable as the experimental data clearly points to a very heterogeneous microstructure. In order to explore the effect of the heterogeneity, a two-site model was developed, in which, a fraction of the material was assumed to be highly deformed with high stored energy and small effective grain size. The rest of the material was assigned lower stored energy and a larger grain size. This is inspired by the actual microstructure shown in Fig. 5. In this EBSD band contrast map (ε=0.3) the dark areas experienced greater deformation than the lighter regions. The calculations were performed assuming that ratio of the stored energy in the two regions is 7.8. The effective grain sizes were 10 μm in the highly deformed areas and 40 μm in the less deformed regions.

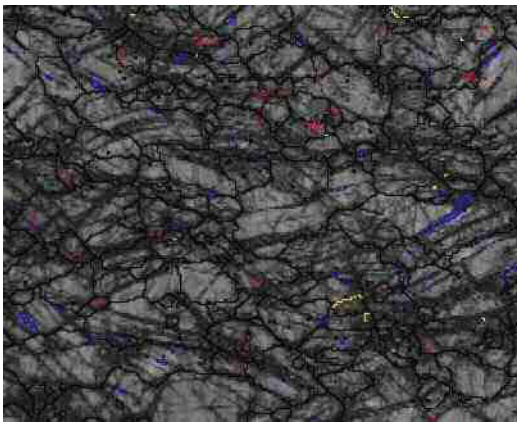


Fig. 5: EBSD band contrast map of a specimen which has been cold-rolled to an equivalent strain of 0.3. The microstructure could be subdivided into high and low deformation regions.

The best fit of the experimental data using the two-site model was obtained using K_{ad} =1.6. When the strain is 0.3, the agreement between the model predictions and the experimental recrystallized fraction data was comparable to that obtained using the much simpler model with a uniform stored energy. This is attributed to the rapid recovery kinetics which quickly reduced amount of stored energy in the highly deformed regions of the heterogeneous material. The key advantage of the two-site model is the prediction of the recrystallized grain size. The (volume) averaged recrystallized grain size was 15 μm which is in better agreement with the experimental data. The difference between the two models is more apparent in the case of low deformation strains (ε=0.1). In this case, the two-site model can predict incomplete recrystallization due to the low driving force available within the lightly deformed regions.

Summary

A physically-based model for static recrystallization of alloy AZ31 has been developed. The model includes the effects of solute drag and concurrent recovery on recrystallization kinetics. A number of simplifications have been made. In particular, the competition between recrystallization nucleation sites was not considered. The stored energy of deformation was also assumed to be uniformly distributed. In spite of these simplifications, the model predictions were in good agreement with experimental data. The model offers valuable insights into the recrystallization of alloy AZ31. From the fundamental point of view it appears that the sluggish kinetics of recrystallization are largely due to the low grain boundary mobility due to solute drag. Practical applications of the model could include the development of recrystallization-time-transformation diagrams for the present alloy and other AZ series alloys in which precipitation does not take place.

Acknowledgement

This work was funded by the Natural Science and Engineering Research Council of Canada through the Magnesium Strategic Research Network (MagNET).

References

[1] H. S. Zurob et al., Acta Mater., 50 (2002) 3075-3092.
[2] J. W. C. Dunlop et al., J. Nuc. Mater. 336 (2007) 178-186.
[3] K. Rehman and H. S. Zurob, Met. Mater. Tras., 44A (2013) 1862-1871.
[4] F. J. Humphreys, Acta Mater., 45 (1997) 4231-4240.
[5] J. E. Bailey and P.B. Hirsch., Proc. Roy. Soc. London. Series A, 267 (1962) 11-30.
[6] M. Verdier, Y. Brechet and P. Guyot, Acta Mater., 47 (1998) 127-134.
[7] M. Hillert, Acta Metall., 13 (1965) 227-238.
[8] S. Liang et al, 9th Int. Conf. Mg Alloys & Their App (2012) 663-668.
[9] S. Liang, X. Wang and H. S. Zurob, 9th Int. Conf. Mg Alloys & Their App (2012) 1049-1054.
[10] M. Winning et al, Phil. Mag., 90 (2010), 3107–3128.
[11] J. W. Cahn, Acta Metall. Mater., 10 (1962) 789-798.
[12] K. Lucke and K. Detert, Acta Metall., 5, (1957) 628.
[13] Das et al, Mater. Sci. Forum, 765 (2013) 516-520.

Magnesium Technology 2014
Edited by: Martyn Alderman, Michele V. Manuel, Norbert Hort, and Neale R. Neelameggham
TMS (The Minerals, Metals & Materials Society), 2014

THE ROLE OF DEFORMATION MODES ON DUCTILITY AND DYNAMIC RECRYSTALLIZATION BEHAVIOR OF AZ31 Mg ALLOY AT LOW TEMPERATURES

E. Dogan[a], M. W. Vaughan[b], C.Hayrettin[b], I. Karaman[a,b], G.Ayoub[c]
[a]Department of Mechanical Engineering, Texas A&M University, College Station, TX, USA
[b]Department of Materials Science and Engineering, Texas A&M University, College Station, TX, USA
[c]Department of Mechanical Engineering, Texas A&M University at Qatar, Doha, Qatar

Keywords: AZ31, Magnesium, Texture, Twinning, Dynamic recrystallization, Failure

Abstract

Tensile ductility and dynamic recrystallization of AZ31 (Mg–3Al–1Zn) alloy samples were investigated at the temperature range of 25°C-200°C. Samples were cut from a strongly textured, hot rolled AZ31 plate from three different orientations in order to activate alternate deformation mechanisms during uniaxial tensile loading. Dynamic recrystallization (DRX) behavior was found to be highly dependent on the active deformation modes at temperatures between 100°C and 200°C, where non-basal slip mechanisms (prismatic and pyramidal <c+a>) retards DRX whereas basal slip promotes DRX. The final microstructure and elongation to failure vary with active deformation modes at moderately elevated temperatures (>50°C), while at room temperature elongation to failure seems to be insensitive to the deformation modes. There is a significant indication that twinning initiated shear localization and induced an earlier fracture at elevated temperatures. More homogenous deformation until necking was observed when prismatic slip was the main active deformation mode.

1. Introduction

Mg alloys show poor formability at low temperatures due to limited available slip systems, activation of twinning, and strong final texture in wrought products. In addition to basal and prismatic slips, $\{10\bar{1}2\}$ tensile twinning is a common deformation mode, providing c axis extension at low temperatures in Mg alloys. However, low temperature anisotropy is mainly due to tensile twinning activity, which causes an earlier yield, rapid texture change, and hardening.
Pyramidal<c+a> slip is difficult to activate at low temperatures due to its high critical resolved shear stress (CRSS)[1]. Therefore, especially at high strains, compression twinning was widely observed when the c-axis of the Mg alloy experiences compression [2]. However, $\{10\bar{1}1\}$ compressive twins and double twins (tensile twins inside compressive twins) act as a source of fracture at low temperatures due to localization and cracking in these regions [2].
It is well reported that wrought AZ31 (Mg–3Al–1Zn) alloys can be processed at temperatures higher than 200°C, as dynamic recrystallization (DRX) and thermally activated additional slip systems (prismatic and <c+a> pyramidal) can significantly improve the ductility[3, 4]. Therefore, a large number of studies focused on high temperature (>200°C) deformation and DRX behavior of AZ31 [4-7]. However, a detailed investigation of low temperature ductility, DRX, and failure mechanisms of AZ31 is scarce in the literature.
In this study, the uniaxial tensile ductility of AZ31 samples having different orientations with respect to the loading axis was investigated at various temperatures between 25 and 200°C. In addition, the microstructures at failure of tensile samples were analyzed, and the effect of deformation modes on ductility and failure was also investigated.

2.Experimental Procedures

A commercial, 25mm-thick AZ31 hot-rolled plate was annealed at 350°C for 12hrs in order to have a fully recrystallized initial microstructure. After annealing, the average grain size was around 25µm. Flat, "dog-bone" tension specimens were cut via electro-discharge machining (EDM) along the following three different directions: the normal and transverse directions (ND and TD), as well as 45° to ND (45toND) from the T-Plane, as illustrated in Fig.1. The gauge sections of the tensile specimens were 8 × 3 × 1.5 mm^3. An extensometer with an 8 mm gauge length was directly attached to the samples for strain measurement of tension tests. Tension tests were performed using a strain rate of 5×10^{-4}/s for all temperatures, using an MTS test frame.
The microstructure of the samples was examined using a digital Keyence VH-Z100 optical microscope (OM) and FEI Quanta-600 scanning electron microscope (SEM). The OM and SEM samples were etched using acetic-picral. Texture of the hot-rolled plate was measured via a Bruker-AXS D8 X-ray diffractometer (XRD).

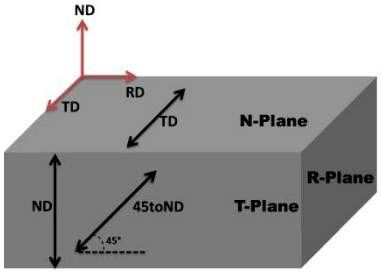


Figure 1. Schematic of orientation of the different tensile samples cut from the hot-rolled AZ31 alloy.

3.Results

Fig. 2a displays $(10\bar{1}0)$ and (0002) pole figures for the hot-rolled AZ31 material. Here, a typical hot-rolled AZ31 texture is evident; basal poles are parallel to the normal direction, and the spread in the basal pole is towards the rolling direction (RD).
Figure 2b displays an SEM image of the initial microstructure (from the normal plane), which consists of equiaxed grains. Al-Mn($\sim Al_8Mn_5$) secondary particles in different sizes(1-30µm) are present and mostly align themselves along the rolling direction (Fig. 2a) both in N- and T- planes.

3.1 Tensile Properties:

Figures 3a-c presents true stress-strain curves of TD, 45toND, and ND samples at different temperatures, respectively. Room

temperature (RT) samples for each direction show a similar elongation to failure (EF) strain of around ~15%. Increased temperature significantly improves the ductility of TD and 45toND samples, as shown in Figs 3a and b. The EF levels for each case, TD and 45toND, are close but the former has slightly higher EF strain at elevated temperatures. On the other hand, EF strain of ND specimens only slightly increased with temperature, and much lower ductility was obvious, as compared to other directions.

Significant hardening, a prominent feature of the 45toND and ND samples tested up to 200°C, is an indication of tensile twinning activity. The yield stress of TD samples dramatically decreased with increasing temperature. The decrease in yield stress of 45toND samples is less pronounced than in the TD case. However, the yield stress does not change with temperature in ND specimens, suggesting an athermal twin-dominated yielding [8].

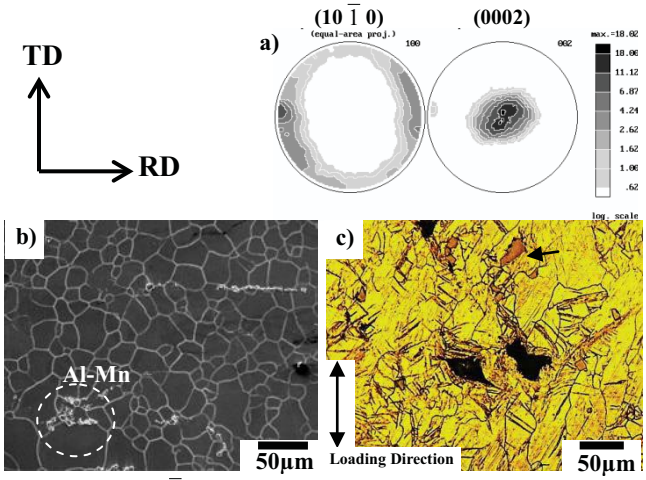


Figure2. (a) (10 $\bar{1}$ 0) and (0002) pole figures of hot-rolled AZ31 material. (b) SEM image of AZ31 alloy before uniaxial tensile tests. (c) OM image of TD specimen tested at room temperature showing a crack formed in the twinned area.

3.2 Microstructure at failure:

The final microstructures of all samples tested at room temperature consisted of significant twin concentrations. The twin volume fractions can be compared as ND>45toND and ND>TD. The twins are more prevalent in areas close to the fracture surface. Cracks that formed in twinned regions are prominent features of all samples, and one example image is given in Fig. 2c. Al-Mn particles are also visible in Fig.2c (indicated by arrow), showing no crack associated with them.

The microstructures of specimens become remarkably different at 100°C, as shown in Fig. 4. Grains are mostly elongated, and twins are only present very near to the fracture surface in the TD specimen tested at 100°C (TD@100°C) (Fig.4a). Significant necking was observed in TD@100°C in contrast to alternative cases at 100°C. This suggests that twins formed after necking caused deformation localization. The twins are passing across the grain boundaries of elongated grains, further confirming that they formed after elongation/deformation of the grains by slip. It is worth noting that, for the TD@100°C case, the volume fraction of twins and the number of cracks significantly decreased as compared to RT specimens for the TD case. In the TD@100°C case, no DRXed grains were observed in the microstructure, which was also free of shear bands/zones except necking region.

Figures 4b and c show the microstructure of the 45toND sample after tensile testing at 100°C (45toND@100°C). The sample failed due to a shear band formation which consisted of twins, as shown in Fig.4b. Small shear bands (with twinning inside) were prevalent throughout the specimen. Some grains are free of twins and elongated. Cracks are still present near the fracture surface, as shown via the arrow in Fig. 4b. More uniform elongation up to fracture was observed compared to the TD@100°C case due to a more pronounced tensile twinning activity [9]. DRX within the twin were observed in the 45toND@100°C specimen, and a micro-crack initiation can be seen inside the twin (Fig. 4c).

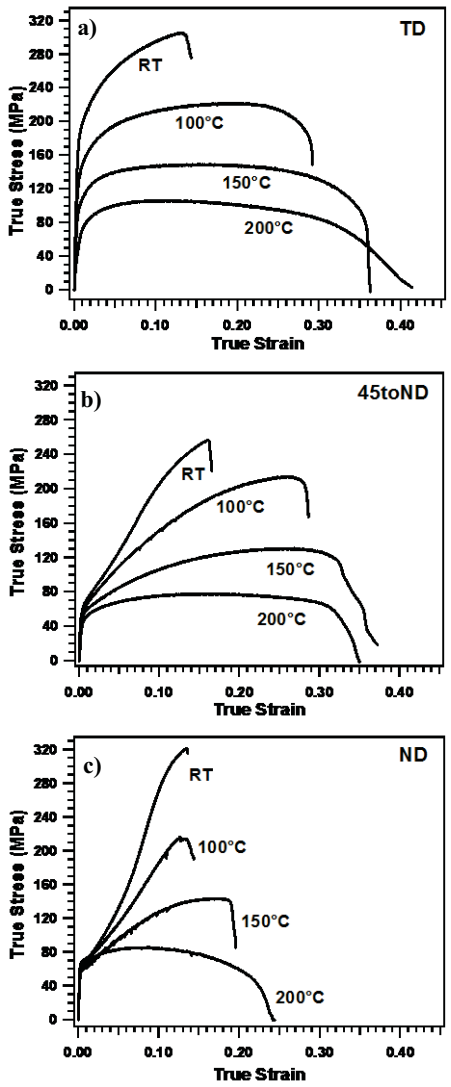


Figure 3. True stress vs. strain response of AZ31 specimens from tensile tests at a temperature range of 25°C to 200°C. (a) TD, (b)45toND and (c) ND. TD: Transverse direction, ND: normal direction.

OM and SEM images of the ND specimen tested at 100°C (ND@100°C) are given in Figures 4d and e. Numerous twins are observed throughout the specimen, and most of the twin boundaries are not straight and mostly serrated (Fig.4e). Grain boundaries are unclear, and most of the grains are segmented. Voids are abundantly prevalent just near the fracture surface, as seen in Figs. 4d. Large sample–scale shear bands (indicated by the oval in Fig.4d) are obvious in ND@100°C, as compared to 45toND@100°C. In addition, no trace of DRX was apparent here, even inside the shear bands and twins (Fig.4e).

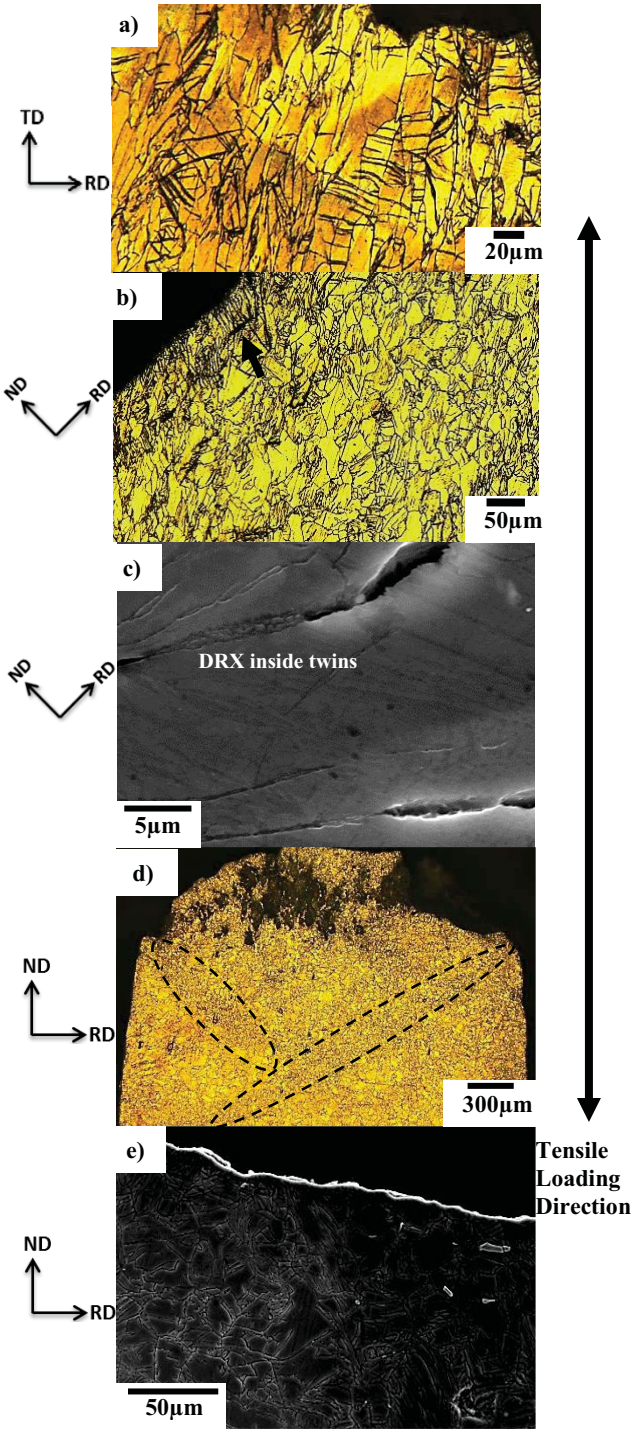


Figure 4. OM and SEM micrographs of uniaxial tension tested samples at 100°C (a) TD, (b and c) 45toND and (d and e) ND. Loading direction is vertical.

Figures 5a and b display the microstructure of TD sample which failed at 150°C (TD@150°C). As opposed to TD@100°C, twinning was not observed near the fracture surface of TD@150°C (Fig. 5a). Here, grains were elongated, and necklace type DRX was evident around them (Fig.5b). Similar to TD@100°C, a remarkable necking was detected in TD@150°C. Interestingly, the sample is free of shear bands/zones, except in the necking region.

Micrographs of the 45toND specimen after failure at 150°C (45toND@150°C) are given in Figs. 5c and d. 45toND@150°C failed due to the prevalent shear band which consisted of twins similar to 45toND@100°C, but with a larger shear band width in the former one (Figs. 4b and 5c). 45toND@150°C specimen displayed successive, extensive shear bands throughout the specimen. A micrograph taken from a shear band is given in Fig. 5d. Grains are segmented, and very fine DRX grains are also present. In addition, twinning is evident in Fig.5d.

Fig. 5e shows an OM image near the fracture surface of the ND sample tested at 150°C (ND@150°C). Shear localization near the fracture surface is obvious in Fig. 5e. Grains are serrated by twins similar to ND@100°C; however, the twin volume fraction is less than in ND@100°C (Figs. 4e and 5f). DRX were not observed in ND@150°C, as shown in a micrograph taken from a shear band (Fig 5f).

Micrographs of the TD sample which failed at 200°C (TD@200°C) are given in Figs.6a and b. The TD@200°C microstructure approximately resembles that of TD@150°C; however, a higher volume fraction of DRX is observed in the former (Figs 6b and 5b). Crack initiation started from the DRXed region, as shown by arrow in Fig.6a.

The 45toND sample tested at 200°C (45toND@200°C) displayed pronounced DRX, and these DRX grains formed large shear bands (Fig.6c). Here, the microstructure is mostly free of twins, and more pronounced DRX is a distinctive characteristic of 45toND@200°C (Figs.6c and 5c) in contrast to the alternate 45toND specimens. In addition, a significant necking was observed in the 45toND@200°C specimen, unlike the 45toND specimens tested at lower temperatures. Crack formation inside the DRX shear bands can be seen in Figs.6c and d.

Figs.6e and f display the micrographs of ND sample tested at 200°C (ND@200°C). Similar to other samples tested at 200°C, failure occurred from the DRXed region (Fig.6e). However, large DRX-free grains are evident just near the fracture surface. Twin volume fraction seems to be significantly decreased at this temperature, although scattered twin boundaries (Fig.6f) and twins away from the shear bands are visible. Deformation is highly localized in contrast to other samples tested at 200°C. Limited and localized DRX is the unique feature of ND@200°C (Figs. 6e and f).

4.Discussion

Microstructures of AZ31 specimens cut from different directions of the strongly textured hot-rolled plate were examined after tension tests at different temperatures (25-200°C). Tensile ductility and the final microstructure remarkably varied with sample orientation and temperature.

4.1 Active deformation modes

When the basal planes are perpendicular to the tensile loading axis, the schmid factor of basal slip is close to zero. Therefore, prismatic slip is the most favorable deformation mode in TD samples [10, 11]. A large decrease in yield stress of TD specimens with temperature further confirms that thermally activated prismatic slip is the main deformation mode [1].

On the other hand, when basal planes are oriented 45° to the tensile loading axis (45toND) basal slip should be the most favorable deformation mode since it has the lowest CRSS and highest schmid factor. Since CRSS of basal slip is less temperature-sensitive than the prismatic slip[1], the yield stress of

45toND samples showed less dependence on temperature (Fig 3b).
Tensile loading of the c-axis (ND case) promotes tensile twinning at low temperatures. Therefore, in the TD, 45toND, and ND samples prismatic and basal slips along with tensile twinning are the most favorable deformation modes at low temperatures, respectively. It is worth mentioning that thermally activated pyramidal <c+a> slip which provides c axis deformation should initiate activation at elevated temperatures in the ND case.
The stress-strain curve of ND@200°C indicates a slip-dominated yielding and, most importantly, the yield stress at this temperature is slightly higher than the others (Fig.3c). This indicates that a significant contribution of pyramidal <c+a> systems is evident. In addition, the microstructure of ND@200°C has fewer twins as compared to other ND specimens at lower temperatures (Fig.6f).
Grains are reoriented by ~86° after tensile twinning. However, reorientation direction depends on the loading condition. For example, basal planes reorient towards the loading axis under compression loading, whereas they reorient away from the loading axis in tension loading[12]. Therefore, in current loading conditions after tensile twinning activity (45toND and ND cases) grains are reoriented such that basal planes are almost perpendicular to the loading axis, which afterwards promotes prismatic slip. This is also evident from the stress-strain curves given in Fig.2; the final stage of the curves has similar hardening behavior and stress levels for a given temperature until 200°C.
Compressive twins were observed with prismatic slip activity after in-plane tensile loading of AZ31 sheets[10]. Tensile loading of TD sample (which promotes prismatic slip) cause a c-axis contraction which promotes compressive twinning at low temperatures. Thin twins most likely compressive type [2] are clear in RT specimens (Fig.2c) and in TD@100°C (Fig.4a), especially near the fracture surface. However, an orientation map is required to identify the twinning type.

4.2 Shear localization and failure mechanisms

Microstructures at failure of all samples tested at RT are similar, and EF strain levels are also identical. Cracks are prevalent in all samples; however, they are more pronounced in the TD sample (Fig.2c). Therefore, failure at room temperature seems to occur due to compressive twinning [2] in all cases.
The microstructure of TD@100°C (Fig.4a) indicates that twinning most likely compressive type is responsible for failure. However, Figs.5a and b indicate that the fracture surface of TD@150°C is free of twins. Therefore, the failure mechanisms should be different in these temperatures. Fig.5a indicates that cracks/voids initiate in soft DRXed region around grain boundaries at 150°C (Fig.5b). A crack is indicated by an arrow in Fig.5a where DRXed grains are accumulated in the junction of grains. The micrographs demonstrate that compressive twinning is less active at temperatures higher than 100°C in TD cases, which promotes prismatic slip and most likely compressive twinning afterwards at the late stage of the deformation.
On the other hand, shear localization due to twinning was observed in 45toND and ND specimens and is more pronounced in the latter case (Figs.4 and 5). The localization occurs much more rapidly and severely in the ND case; thus, EF stain is much lower than 45toND specimens at all temperatures. The results indicated that tensile twinning promotes shear localization. As discussed earlier, tensile twinning reorients the grains in such a way that prismatic slip is favorable afterwards. It is not yet clear if compressive twinning (expected after prismatic slip) causes crack/void initiation at 100°C and 150°C for 45toND and ND cases. A detailed orientation map is required. However, a micro-crack inside a twin that has DRX inside is evident in Figure 4c. Here, the DRXed region seems to act as a soft region, and appears crack initiated. DRX inside the tensile twinning was reported before [4]. However, the type of twinning in Fig. 4c needs to be identified.
A large number of voids are observed in ND@100°C only near the fracture surface; however, the sample failure is caused via localized regions consisting of twins and free of Al-Mn particles (Fig.4e). Figures 7a and b show micro-cracks at the interface of an Al-Mn particle surrounded by twins. No significant crack initiation was captured in the other samples tested at 100°C. It is believed that cracks are formed at the interface of Al-Mn particles due to stress concentration by twins. Cracks seem to be more opened near the fracture surface (Fig 7).
Failure occurred at a shear band consisting of twins in 45toND@150°C and ND@150°C samples (Figs.5c and e), where the former possesses DRX inside (Figs 5d and f). DRX seem to provide extra ductility in the 45toND@150°C specimen since higher EF was recorded as compared to ND@150°C (Figs 2b and c).
Microstructures at failure of TD@200°C and 45toND@200°C specimens look similar (Figs, 6a and c, respectively). Accumulation of small DRXed soft grains formed easy shear paths as described by Ion et al.[1] , and failure occurred in these regions. However, these shear bands are more pronounced in 45toND@200°C (Figs.6c and d). DRX is only evident near the fracture surface of ND@200°C (Fig.6e), which indicates that failure occurred due to localized soft DRX regions as a result of deformation localization.
The micrographs of TD specimens indicated that compressive twinning is the main factor for crack initiation and failure up to 100°C (Figs 2c and 4a). However, at higher temperatures (150°C and 200°C) crack initiation started from soft DRXed regions/bands (Figs. 5a and 6a).
Failure in 45toND specimens initiated from the shear bands which consist of twins up to 200°C (Figs 4b and 5c). DRXed grains were observed even at 100°C. Figs 6d and c clearly showed that soft shear zones which consist of DRXed grains caused the failure at 200°C.
Microstructure at failure of ND specimens indicated that failure is due to shear bands which consist of twins but free of DRXed grains up to 200°C (Figs 4e and 5e). At 200°C, twins are replaced by DRXed grains in highly localized shear zones (Fig 6e).

4.3 The role Al-Mn particles

The Al-Mn particles are mostly aligned along the rolling direction (Fig. 2b) and are present in all specimens. They are aligned perpendicular to the tensile loading axis in the TD and ND cases, at which the stress state promotes the crack initiation. However, the ductility levels of the TD and ND specimens are remarkably different at elevated temperatures, indicating that failure is not associated with the Al-Mn particles. At 100°C, the numerous voids near the fracture surface and the crack initiation around the particles are shown in Fig.4c and Fig.7, respectively. However, the ND@100°C specimen failed at a shear band that is free of particles (Fig.4e), although many voids are present near the fracture surface.

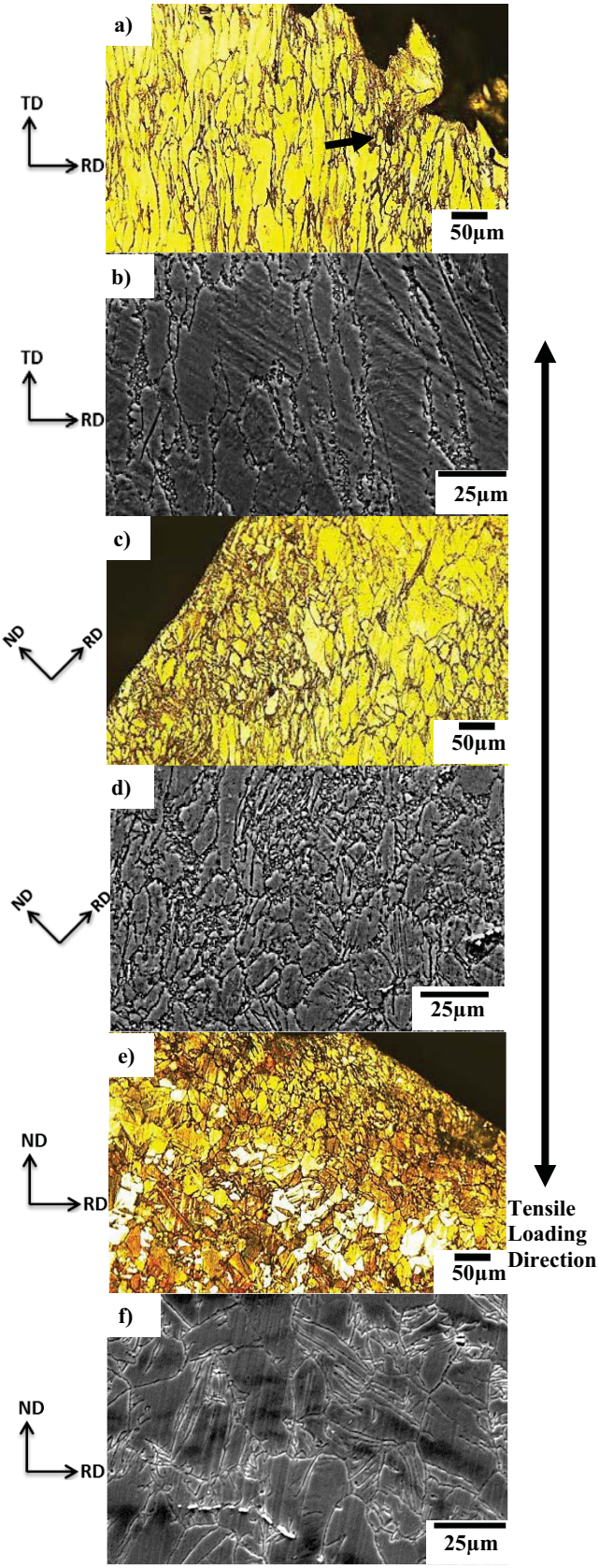


Figure 5. OM and SEM micrographs of uniaxial tension tested samples at 150°C (a and b) TD, (c and d) 45toND, and (e and f) ND. Loading direction is vertical.

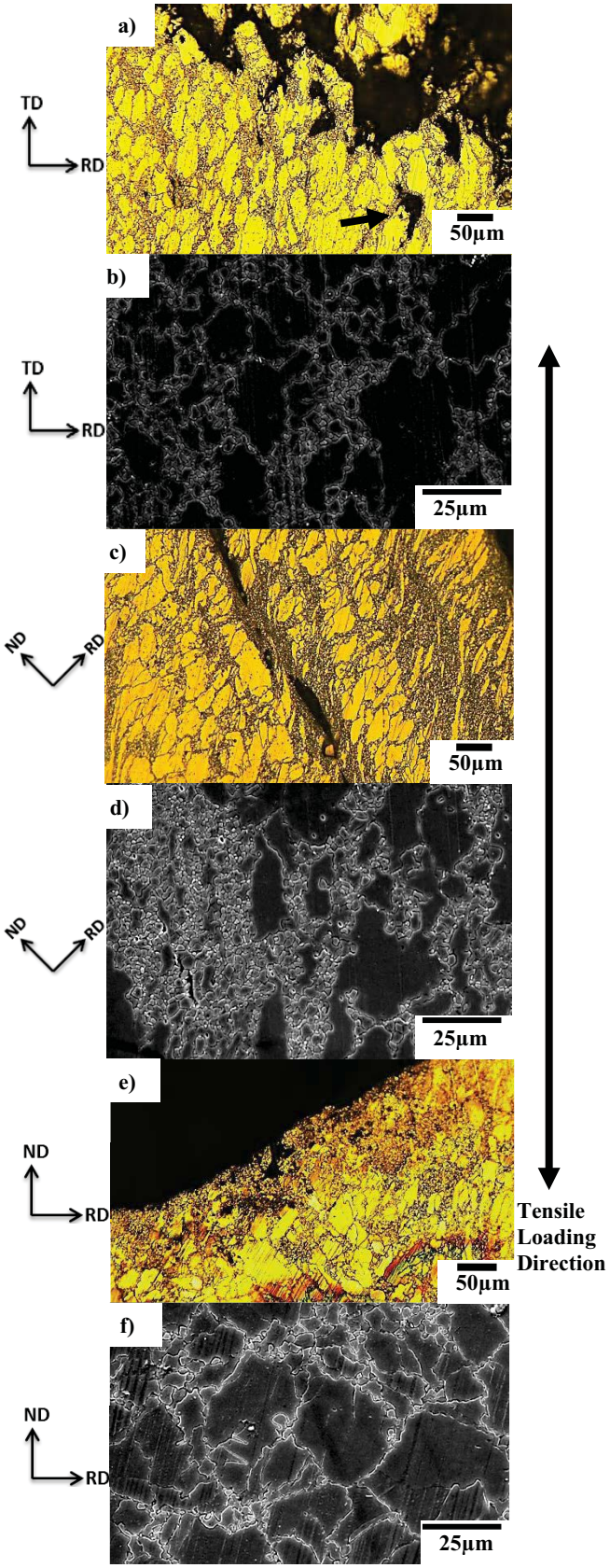


Figure 6. OM and SEM micrographs of uniaxial tension tested samples at 200°C (a and b) TD, (c and d) 45toND and (e and f) ND. Loading direction is vertical.

4.4 Effect of deformation modes on DRX and ductility

It was reported that the stacking fault energy for non-basal slip systems is much higher than that for the basal slip [13]. Less pronounced DRX was observed in TD specimens where prismatic slip is readily active as compared to 45toND specimens (mostly basal slip) at all temperatures. In addition, DRX seems to be reluctant in the ND case. Basal slip is the least favorable slip system in the ND case since initially the basal planes are parallel to the loading direction and thus are perpendicular to the loading axis after reorientation due to tensile twinning. However, prismatic slip after tensile twinning and pyramidal<c+a> slip at elevated temperatures are favorable in the ND case. Therefore, ready activation of non-basal slips remarkably retards the DRX in ND case, even at 200°C (Figs. 6b, d and f).

It is worth mentioning that the yield stress of the ND sample slightly increased at 200°C, which suggest a pronounced pyramidal<c+a> slip (higher CRSS than that of tensile twinning[8]) as compared to lower temperatures. The large EF strain difference between the ND@200°C specimen and other directions at 200°C (Fig.2) appears due to low volume fraction of DRX.

Readily activated prismatic slip in the TD case promotes uniform deformation until necking when compared to the tensile twinning cases (45toND and ND). Therefore, a higher EF strain is a distinctive characteristic of TD samples at all temperatures (Fig.2). On the other hand, uniform elongation up to failure and no significant post-necking was observed in the 45toND and ND specimens, up to 200°C, as a result of pronounced tensile twinning activity. Tensile twinning seems to cause non-uniform DRX due to deformation localization in the ND and 45toND cases. Results indicated that twining deteriorate ductility at moderately elevated temperatures due to deformation localization, whereas it is an extra source of ductility at room temperature[8] (Fig 2).

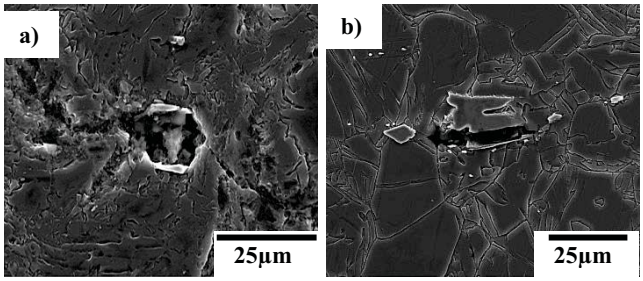


Figure 7. SEM images of ND specimen tested at 100°C showing crack/void near Al-Mn particles (a) near fracture surface (b) away from the fracture surface. Loading direction is vertical.

5. Conclusion

Final microstructures of AZ31 specimens cut from different directions of a strongly textured, hot-rolled plate were examined after uniaxial tension tests at different temperatures (25-200°C). The active deformation modes showed a great influence on dynamic recrystallization (DRX) behavior and the ductility of the AZ31 Mg alloy at low temperatures (≤200°C). The main findings of this study can be summarized in the following:

1. Basal slip promotes the DRX, whereas non-basal slips retard the DRX at low temperatures (≤200°C).
2. When tensile twinning is activated, uniform elongation is more pronounced due to the hardening associated with tensile twining. Conversely, twinning caused shear localization and thus non-uniform DRX, thereby inducing earlier fractures at moderately elevated temperatures (≤200°C).
3. Soft DRXed regions act as a source of fracture at 200°C for all differently oriented specimens.
4. Higher ductility, homogeneous deformation, and widespread DRX were observed when prismatic slip is the primary deformation mode at temperatures above room temperature.

Acknowledgment

This research was supported by NPRP grant No 4-1411-2-555 from the Qatar National Research Fund (a member of Qatar Foundation). The statements made herein are solely the responsibility of the authors.

References

1. S.E. Ion, F.J. Humphreys, and S.H. White," Dynamic recrystallisation and the development of microstructure during the high temperature deformation of magnesium," Acta Metallurgica, 30(10) (1982), 1909-1919.
2. M.R. Barnett," Twinning and the ductility of magnesium alloys Part II. "Contraction" twins," Materials Science and Engineering a-Structural Materials Properties Microstructure and Processing, 464(1-2) (2007), 8-16.
3. S.R. Agnew and Ö. Duygulu," Plastic anisotropy and the role of non-basal slip in magnesium alloy AZ31B," International Journal of Plasticity, 21(6) (2005), 1161-1193.
4. T. Al-Samman and G. Gottstein," Dynamic recrystallization during high temperature deformation of magnesium," Materials Science and Engineering: A, 490(1–2) (2008), 411-420.
5. M.M. Myshlyaev, et al.," Twinning, dynamic recovery and recrystallization in hot worked Mg–Al–Zn alloy," Materials Science and Engineering: A, 337(1–2) (2002), 121-133.
6. A.G. Beer and M. R. Barnett," Microstructural development during hot working of Mg-3Al-1Zn," Metallurgical and Materials Transactions A: Physical Metallurgy and Materials Science, 38(8) (2007), 1856-1867.
7. M. Al-Maharbi, et al.," Microstructure, crystallographic texture, and plastic anisotropy evolution in an Mg alloy during equal channel angular extrusion processing," Materials Science and Engineering: A, 528(25–26) (2011), 7616-7627.
8. A. Jain and S.R. Agnew," Modeling the temperature dependent effect of twinning on the behavior of magnesium alloy AZ31B sheet," Materials Science and Engineering: A, 462(1–2) (2007), 29-36.
9. M.R. Barnett," Twinning and the ductility of magnesium alloys: Part I: "Tension" twins," Materials Science and Engineering: A, 464(1–2) (2007), 1-7.
10. Z. Keshavarz and M. R. Barnett," EBSD analysis of deformation modes in Mg-3Al-1Zn," Scripta Materialia, 55(10) (2006), 915-918.
11. S.M. Razavi, et al.," Effect of grain size on prismatic slip in Mg–3Al–1Zn alloy," Scripta Materialia, 67(5) (2012), 439-442.
12. A. Jérusalem, A. Fernández, and M. T. Pérez-Prado," Continuum modeling of {10$\bar{1}$2} twinning in a Mg-3%Al-1%Zn rolled sheet," Revista de Metalurgia, 46(Extra) (2010), 133-137.
13. M. Igarashi, M. Khantha, and V. Vitek," N-Body Interatomic Potentials For Hexagonal Close-Packed Metals," Philosophical Magazine B-Physics of Condensed Matter Statistical Mechanics Electronic Optical and Magnetic Properties, 63(3) (1991), 603-627.

Magnesium Technology 2014
Edited by: Martyn Alderman, Michele V. Manuel, Norbert Hort, and Neale R. Neelameggham
TMS (The Minerals, Metals & Materials Society), 2014

Effect of Microstructure on Deformation and Fracture of Thixomolded and Thermomechanically Processed AZ61

T.D. Berman[1], W. Donlon[1], R. Decker[2], T.M. Pollock[3], J.W. Jones[1]

[1]Materials Science and Engineering, University of Michigan, 2300 Hayward St; Ann Arbor, MI, 48109, USA
[2]nanoMAG, LLC., 13753 Otterson Court; Livonia, MI, 48150, USA
[3]Materials Department, University of California, Santa Barbara; Santa Barbara, CA, 93106-5050, USA

Keywords: AZ61, Microstructures, Texture, Mechanical Properties, Fractography, Thermomechanical Processing

Abstract

This paper investigates the deformation, damage accumulation and fracture behavior of fine-grained AZ61 sheet produced by combined Thixomolding and Thermomechanical (TTMP) processing. In the TTMP process, warm rolling of a fine-grained, untextured Thixomolded plate with subsequent recrystallizion produces a sheet with an α-Mg grain size of 3 to 5 μm and β-particles with an average diameter of 0.5 μm. The fine grain size and weak texture in the sheet results in nearly isotropic mechanical properties. Damage during tensile straining occurs in the form of cracking in the β-particles in both the as-Thixomolded plate precursor and in the recrystallized sheet. However, the material fails due to strain localization in shear bands and microvoid coalescence.

Introduction

Mg alloys are of considerable interest in automotive, personal electronic, and medical applications because of their low specific density. Widespread use of Mg-alloys requires the production of high strength sheet; however, the process of sheet-forming of Mg alloys results in poor formability. The dominant basal slip activity during rolling of Mg alloys results in the c-axis of the majority of the grains becoming aligned with the sheet normal [1].

Reducing texture leads to improved ductility [2–4]. Effective strategies to reduce or eliminate this deleterious basal texture in Mg alloy sheet include solute additions to increase activity of non-basal slip [4–6] and alternative processing, such as asymmetric rolling [7, 8], cross rolling [9], twin-roll casting (TRC) [10, 11], and multiple-pass-rolling with annealing and/or a high temperature final pass [12–14]. Recrystallization, both dynamic and static, may also result in a weak texture if the new grains nucleate on secondary phase particles via particle stimulated nucleation (PSN) [15].

In an attempt to produce a high strength sheet with good tensile ductility and formability, we have used AZ61 Thixomolded plate as our sheet precursor. Although AZ31 is the most commonly used wrought Mg alloy sheet, for this investigation AZ61 was chosen as it Thixomolds well [16] and the higher Al content allows for the possibility of increased precipitation and solid solution strengthening. The rapidly solidified Thixomolded plate is composed of fine, randomly oriented grains and fine secondary phase particles [17]. Another attribute of Thixomolding is low porosity [18] and minimal inclusions which prevent premature failure [19]. In earlier publications [20–22] we reported preliminary results of the microstructure, texture evolution, and static recrystallization process in TTMP AZ61; here we present a study of the damage and failure resulting from tensile deformation.

Experimental

The TTMP process begins with 200 mm x 200 mm x 3 mm Thixomolded® plates of AZ61 (nominally 6 wt% Al, 1 wt% Zn; balance Mg). The plates are preheated for 5 minutes at 315 °C and then warm-rolled in a single-pass with a roll temperature near 200 °C. Rolled sheets are cooled to room temperature in ambient air. In this work, the final sheet thickness is 1.8 mm, a thickness reduction of approximately 40%.

Dogbone tensile specimens with a gauge length of 25.4 mm and cross section of 6.35 mm x 3 mm or 1.8 mm were machined from the as-molded plates and as-rolled sheets, respectively. The sheet specimens were machined both with the tensile axis oriented 0 ° or 90 ° from the rolling direction. The tensile specimens from the sheet were annealed at 285 °C for 10 minutes to promote recrystallization [21] followed by a water quench.

Metallographic specimens were prepared using standard techniques with a final polish using 1 μm diamond paste. As-Thixomolded specimens were etched for 10 seconds at room temperature in a 1:9 solution of o-phosphoric acid in ethanol. Sheet material was etched for 5 s at room temperature in an solution of 10

ml water, 10 ml acetic acid, 4.3 grams of picric acid, and 70 ml of ethanol. SEM examination was conducted with a Philips XL30 FEG.

A Rigaku rotating anode XRD system was used for XRD pole figure measurements. MTEX [23] was used to generate complete basal pole figures from the experimental $\{10\bar{1}0\}$,$\{0002\}$, $\{10\bar{1}1\}$ and $\{10\bar{1}2\}$ pole figures.

Room temperature tensile tests were performed with an Instron 5505B load frame with an initial strain rate of $4x10^{-4}s^{-1}$. An extensonometer with a 25.4 mm gage length was attached to the gage section to measure tensile elongation. At least 6 specimens for each condition were pulled monotonically to failure. The fracture surfaces of selected specimens were examined by SEM before one piece of the specimen gage section was polished to mid-thickness for additional SEM analysis.

Results and Discussion

Microstructure

The microstructure of the as-Thixomolded plate is composed of fine α-Mg grains surrounded by a divorced β-$Mg_{17}Al_{12}$ eutectic (Fig. 1(a)). The average grain diameter of the as-Thixomolded material is 4 μm. Fine β-particles are evenly distributed primarily along the α-Mg grain boundaries. The dark regions in the as-Thixomolded microstructure are depressions caused by the enchant preferentially attacking grains with a low Al content. The β-particles have an average diameter of 0.31 mum with over 95% of the particles being less than 1 μm. As expected, the cast material has no texture (Fig. 1(c)).

The microstructure of TTMP AZ61 sheet after the recrystallization anneal at 285 °C for 10 minutes (Fig. 1(b)) consists of equiaxed α-Mg grains with an average grain diameter of 4 μm. The grain size distributions in the as-Thixomolded plate and recrystallized sheet are similar. As a result of the 40% reduction by rolling, strands of large β-particles become aligned parallel to the sheet rolling direction (RD) and are no longer surrounding the α-Mg grains. The rolling process introduces a weak near-basal texture to the material that is significantly reduced by the subsequent recrystallization anneal (Figure 1(c)) [21]. More importantly the TTMP process increases the volume fraction of β-$Mg_{17}Al_{12}$ compared to the as-molded condition. The β-particles in the recrystallized sheet can be classified into 2 groups, (1) coarser irregularly shaped particles and (2) fine platelet-like particles that precipitated during rolling process. The coarse particles tend to be elon-

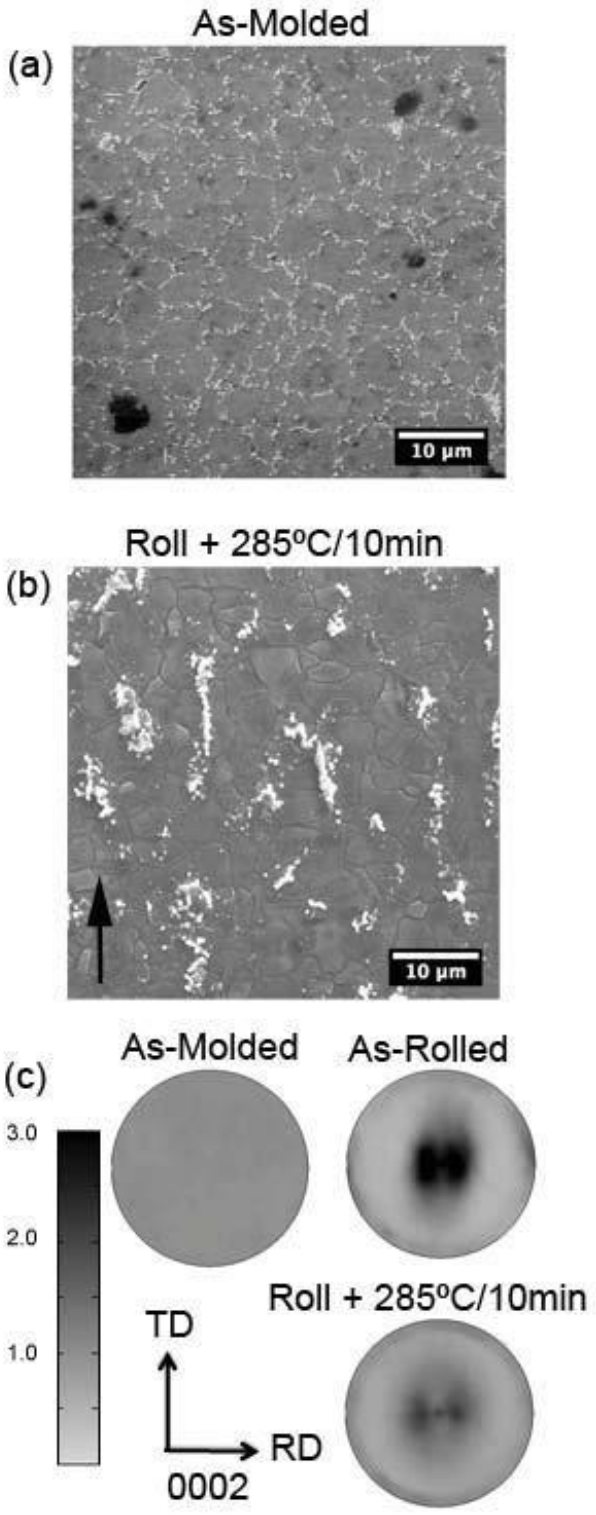


Figure 1: Secondary electron image of the microstructures of (a) the as-Thixomolded plate and (b) sheet annealed at 285 °C for 10 minutes to promote recystallization. (c) Recalculated basal (0002) pole figures of as-molded plate, as-rolled sheet, and rolled sheet annealed for 285 °C for 10 minutes.

Table I: Tensile properties of thermally treated TTMP AZ61 sheet. Average represent at least 4 individual specimens.

Thermal Treatment	Orientation	YS (MPa)	UTS (MPa)	Ave. Elong. (%)	n - value
As-molded		160 ± 9	293 ± 8	18.7 ± 3.1	0.317
Roll + 285 °C/10min	RD	219 ± 4	310 ± 7	22.2 ± 3.7	0.188
Roll + 285 °C/10min	TD	210 ± 10	310 ± 11	20.0± 3.0	0.245

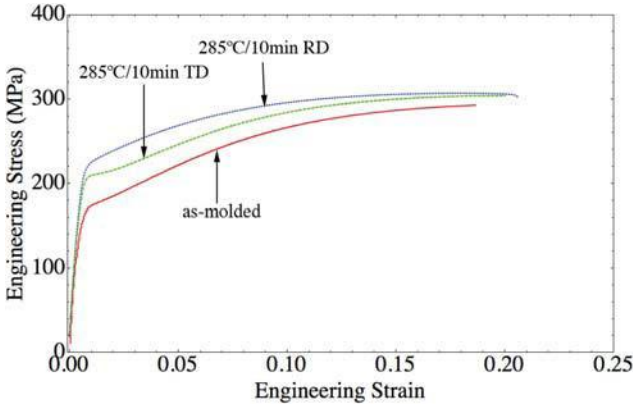


Figure 2: Representative monotonic tensile curves for the as-Thixomolded plate and recrystallized sheet tested along the RD and TD.

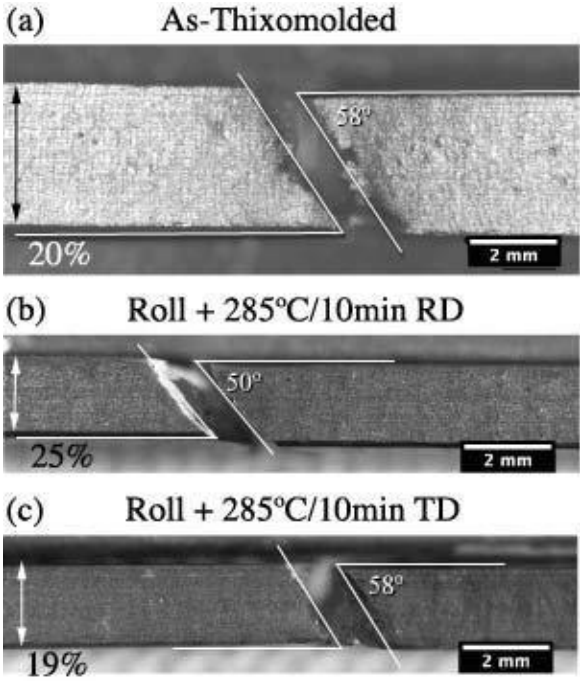


Figure 3: Optical images of (a) Thixomolded plate at 20% strain (failure) and recrystallized sheet at 25% and 19% (failure) strain for specimens deformed parallel to the (b) RD and (c) TD respectively. The arrows indicate the thickness of the specimens; the tensile axis is horizontal.

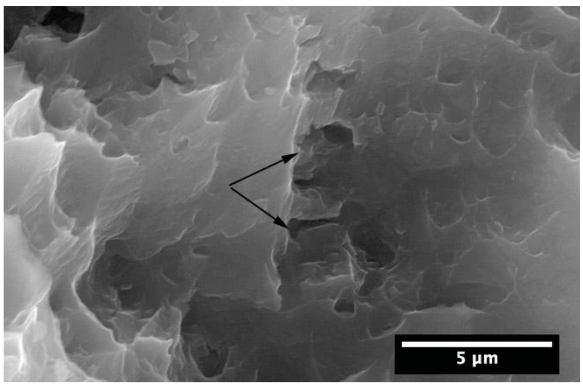


Figure 4: Secondary electron image of the fracture surface of an as-molded specimen at 20% strain (failure) taken with the electron beam at 45 ° from the tensile axis. The black arrows point out cracks in the β-particle network.

gated along the RD (Fig. 1(b)).

Tensile Properties

Representative monotonic tensile curves of the as-Thixomolded plate and recrystallized sheet tested along both the RD and TD, are shown in Fig. 2. Table I summarizes the tensile properties for each condition. The as-molded plate has a yield strength of 160 MPa and an average ductility of 18.7%. The yield strength of the recrystallized sheet is 219 MPa, representing an increase of 37%. The YS and UTS along the RD and TD in the recrystallized sheet are similar as a result of the lack of texture in the material. The strain hardening exponent (n-value) between 3% and 15% strain for all three conditions ranges from 0.188 along the RD of the sheet to 0.317 in the as-Thixomolded plate.

Damage and Failure

Material from both the plate and recrystallized sheet exhibit ductile shear. The average shear angle is approximately 60 ° for the as-molded plate and 50 ° for the recrystallized sheet (Fig. 3). Fractography indicates failure caused predominately by microvoid coalescence (Fig. 5(b), (d), and (f)). The dimple size is on the order of a few microns, similar to the grain size. Larger coalesced dimples of ∼20 μm in diameter are present in the fracture surface as well. Cracks

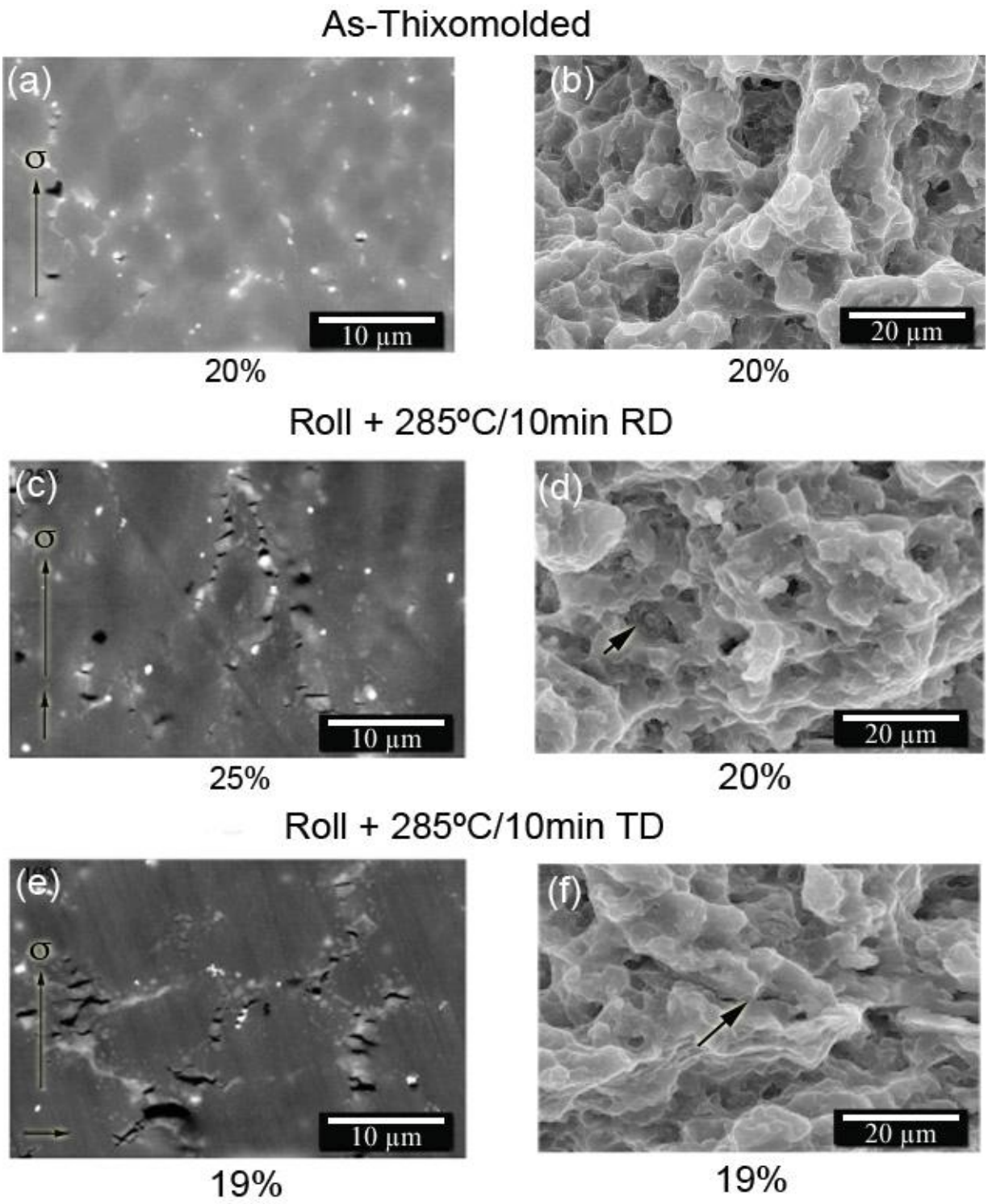


Figure 5: Backscattered electron images of (a) Thixomolded plate and recrystallized sheet tested parallel to the RD and TD respectively (c and e). In the left column the stress axis is vertical and the smaller arrows indicate the rolling direction. Images are taken mid-thickness approximately 150 μm from the fracture surface. The small, bright particles in these micrographs are Al-Mn intermetallics. Secondary electron images of the fracture surface in (b) Thixomolded plate and recrystallized sheet tested parallel to the RD and TD respectively (d and f). Black arrows in the right hand column indicate cracks at the bottom of dimples.

and secondary particles are found in the bottom of several of the larger voids. Fig. 4 shows a larger void which nucleated on the cracks in a cluster of β-particles.

Damage in the form of visible cracks or voids in both the as-Thixomolded plate and the recrystallized sheet is confined to the β-particle network as illustrated by the micrographs at mid-thickness near the fracture (Fig. 5(a),(c), and (e)). The damage in the as-Thixomolded plate, which has finer β-particles is less extensive than in the sheet material. In all conditions, only a few instances were observed in which the cracks propagate from the β-particle network into the matrix. By viewing a specimen at mid-width, such as in Fig. 6, it is clear that the cracks in and between β-particles serve as easy nucleation sites for voids, however there is little evidence of coalescence of the voids associated with the β-particles. Thus, it appears that the damage in the β-particles only plays a small roll in the failure, perhaps by promoting the formation of shear bands in the matrix. Coalescence of microvoids that nucleate in these bands lead to ductile shear failure of the specimens in all conditions.

The effects of the β-phase volume and distribution on ductility in Mg are therefore not completely resolved. Failure via secondary particle cracking in Mg alloys has been reported, in materials with larger particles [24] or in AZ91 with a higher β-phase volume fraction [19, 25]. Luo demonstrated cracked β-$Mg_{17}Al_{12}$ particles in the bottoms of dimples on the fracture surface of an AZ91 specimen [24]. While investigating the dependence of tensile strength on variations in microporosity in AZ91 and AM60, Lee found that additional void area was created by damage in the $Mg_{17}Al_{12}$ phase, and concluded that further research on the contribution of the distribution and volume fraction of $Mg_{17}Al_{12}$ to tensile deformation is needed [19]. Chung et al also observed that damage was confined mainly to the β-phase (in this case in AZ91); they observed an increase in ductility after 2 ECAP passes which fragmented the large, blocky β-particles [26]. Marya et al observed that elongation to failure in an AZ31 specimen aged to have fine $Mg_{17}Al_{12}$ particles on the order of 1 μm increased compared to single-phase AZ31 with the same grain size. They concluded that recovery during the aging process or more uniform deformation arising from the presence of the β-particles was responsible for the increase ductility [27].

As the fracture of the β-phase particles is a distinct damage mechanism, it is interesting that there is little difference in average ductility between the sample conditions. Neither the increase in the β-phase volume fraction and particles size between the as-molded and recrystallized conditions nor the difference in the β-network orientation the RD and TD samples seem to effect the ductility. Fractography indicates that the specimens fail as a result of microvoid coalescence, thus the matrix controls the ductility. In-situ SEM tensile testing, potentially combined with digital image correlation, as well as investigation of damage and failure in TTMP AZ61 annealed to have little, or no macroscopic β-particles is planned to further explore the failure of TTMP AZ61. Future work will also include modeling the deformation process.

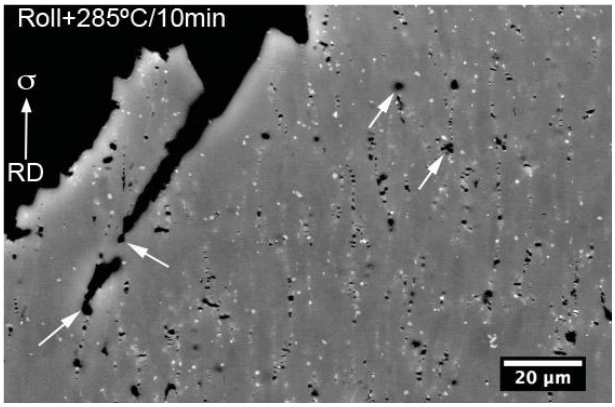


Figure 6: Backscatter electron image of recrystallized sheet at 20% (failure) strain for a recrystallized sheet specimen deformed parallel to the RD. Image is taken at mid-width in the specimen. The white arrows highlight voids that have nucleated in the β-particle network.

Summary

We have established that by combining Thixomolding and Thermomechanical processing one can produce a nearly isotropic AZ61 sheet with moderate strength and an average room temperature ductility greater than 20%. The sheet recrystallized at 285 °C for 10 minutes has a comparable grain size to the as-Thixomolded precursor; however, the β-phase morphology and distribution is altered by the rolling process. Despite the differences in the β-phase distribution, the as-Thixomolded plate and recrystallized sheet exhibit the same damage and failure mechanisms. Early in the deformation process cracking occurs in the β-phase network, the crack growth is arrested at the α-Mg grain boundaries. Failure occurs via coalescence of voids in the α-Mg matrix.

Acknowledgements

This material is based upon work supported by the National Science Foundation under Grant No. 0847198.

References

1. S. Agnew and O. Duygulu: *International Journal of Plasticity*, 2005, vol. 21, pp. 1161–1193.
2. T. Mukai, H. Watanabe, K. Ishikawa, and K. Higashi: *Materials Science Forum*, 2003, vol. 419-422, pp. 171–176.
3. N. Stanford and M. Barnett: *Journal of Alloys and Compounds*, 2008, vol. 466, pp. 182–188.
4. N. Stanford, D. Atwell, and M. Barnett: *Acta Materialia*, 2010, vol. 58, pp. 6773–6783.
5. S. Agnew, M. Yoo, and C. Tome: *Acta Materialia*, 2001, vol. 49, pp. 4277–4289.
6. J. Bohlen, M. R. Nurnberg, J. W. Senn, D. Letzig, and S. Agnew: *Acta Materialia*, 2007, vol. 55, pp. 2101–2112.
7. B. Radhakrishnan, S. B. Gorti, G. M. Stoica, and G. Muralidharan: *Metallurgical and Materials Transactions A*, 2012, vol. 43, pp. 1509–1516.
8. W. Kim, J. Park, and W. Kim: *Journal of Alloys and Compounds*, 2008, vol. 460, pp. 289–293.
9. Y. Chino, K. Sassa, and M. Mabuchi: *Journal of Materials Science*, 2009, vol. 44, pp. 1821–1827.
10. M. Masoumi, F. Zarandi, and M. Pekguleryuz: *Materials Science and Engineering: A*, 2011, vol. 528, pp. 1268–1279.
11. I. Bayandorian, I. Stone, Y. Huang, and Z. Fan: in *Magnesium Technology*, 2012 pp. 135–140.
12. X. Huang, K. Suzuki, Y. Chino, and M. Mabuchi: *Journal of Alloys and Compounds*, 2011, vol. 509, pp. 7579–7584.
13. Q. Miao, L. Hu, G. Wang, and E. Wang: *Materials Science and Engineering: A*, 2011, vol. 528, pp. 6694–6701.
14. Y. Chino and M. Mabuchi: *Scripta Materialia*, 2009, vol. 60, pp. 447–450.
15. F. Humphreys and M. Hatherly: *Recrystallization and Related Annealing Phenomena*, Elsevier, Netherlands, 2 edn., 2004.
16. R. F. Decker: *Solid State Phenomena*, 2012, vol. 192-193, pp. 47–57.
17. R. F. Decker, S. Kulkarni, and J. Huang: *Technology*, 2009, pp. 1–5.
18. T. K. Nandy, R. M. Messing, J. W. Jones, T. M. Pollock, D. M. Walukas, and R. F. Decker: *Metallurgical and Materials Transactions A*, 2006, vol. 37, pp. 3725–3736.
19. C. D. Lee: *Metals and Materials International*, 2010, vol. 16, pp. 543–551.
20. T. D. Berman, W. Donlon, R. F. Decker, J. Huang, T. M. Pollock, and J. W. Jones: in W. Sillekens, S. Agnew, N. Neelameggham, and S. Mathaudhu, editors, *Magnesium Technology*, Wiley, pp. 599 – 603, 2011.
21. T. D. Berman, W. Donlon, V. M. Miller, R. F. Decker, J. Huang, T. M. Pollock, and J. W. Jones: in S. Mathaudhu, W. Sillekens, N. Hort, and N. Neelameggham, editors, *Magnesium Technology*, Wiley, pp. 339–344, 2012.
22. T. D. Berman, W. Donlon, R. F. Decker, J. Huang, T. M. Pollock, and J. W. Jones: in W. J. Poole and K. Kainer, editors, *Magnesium: Proceedings of the 9th International Conference Magnesium Alloys and Their Applications*, ICMAA2012, Vancouver, Canada, 2012 pp. 571–578.
23. F. Bachmann, R. Hielscher, and H. Schaeben: *Solid State Phenomena*, 2010, vol. 160, pp. 63–68.
24. A. Luo: *Metallurgical and Materials Transactions A*, 1995, vol. 26, pp. 2445–2455.
25. Z. Li, J. Dong, X. Q. Zeng, C. Lu, and W. J. Ding: *Materials Science and Engineering: A*, 2007, vol. 466, pp. 134–139.
26. C. W. Chung, R. G. Ding, Y. Chino, M. A. Hodgson, and W. Gao: *IOP Conference Series: Materials Science and Engineering*, 2009, vol. 4, p. 012012.
27. M. Marya, L. G. Hector, R. Verma, and W. Tong: *Materials Science and Engineering: A*, 2006, vol. 418, pp. 341–356.

Magnesium Technology 2014
Edited by: Martyn Alderman, Michele V. Manuel, Norbert Hort, and Neale R. Neelameggham
TMS (The Minerals, Metals & Materials Society), 2014

MICROSTRUCTURE EVOLUTION AND MECHANICAL PROPERTIES OF Mg–14%Li–1%Al ALLOY DURING THE HIGH-PRESSURE TORSION

Chenguang Tian[1], Huimin Lu[1*], Liyuan Zhao[1]
[1]Beihang Univ., School of Materials Sci. & Eng.; 37 Xueyuan Road; Beijing 100191, China
[*]Corresponding Author: lhm0862002@aliyun.com

Keywords: High-pressure torsion, Magnesium–lithium alloy, Grain refining, Microstructure.

Abstract

The super-light LA141 (Mg–14%Li–1%Al) alloy was produced and processed by high-pressure torsion (HPT) under the imposed pressure of 3 GPa and different shear strains γ through 3, 6, 9 and 12 turns at room temperature (RT). The microstructure evolution of the alloy during the HPT treatment was investigated by transmission electron microscope (TEM) and optical microscope (OM). It turned out that the grains were substantially refined, and the optical microscope revealed that the grains of HPT processed samples at the edge of the disc were finer by comparison with the ones near the center of the disc. Later, Vickers indentation analysis was used to evaluate the micro-hardness of deformed samples, and tension test was employed to obtain the strength and elongation at room temperature. The results indicated that the micro-hardness and tensile strength had increased to a certain extent, and the elongation had been significantly improved.

Introduction

As the lightest alloy, Mg–Li alloy has attracted increasing interests in aerospace, missile, and armor application as these sectors seek increasing fuel efficiency through weight reduction [1-4]. Mg-14Li-1Al (LA141) alloy has the density of 1.35 − 1.40 g/cm^3 and has superior plasticity and ductility because its full BCC structure and full β-Li phase at room temperature. However, LA141 possess relatively low strength which limits its wider applications, especially for the alloys with high lithium contents [5]. We can get higher strength alloy through composite reinforcement [6] and multi-elements alloying [7], but we have to sacrifice the lightness and plasticity of the alloys. Besides, higher strength alloys can be achieved by grain refinement induced by severe plastic deformation (SPD) [8], such as Equal channel angular pressing (ECAP), High-pressure torsion (HPT), Accumulative Roll Bonding (ARB) and Reciprocal Extrusion and Compression (CEC) without reducing its lightness and plasticity. High-pressure torsion (HPT) which is considered to be the strongest plastic deformation and refine the grain size in alloys down to nanometer level were developed and applied to refine the microstructures of sundry metals and alloys. Professor Bridgman first proposed HPT in 1943 and the technology has made great progress in recent years. It has been suggested that HPT process can refine grains to process polycrystalline metals for the production of ultrafine-grained microstructures. With the increase of pressure and torsion turns, the grain sizes produced using HPT are in the submicrometer or nanometer range.

In this work, HPT was used to refine grains of LA141. The evolution of microscopic structure and mechanical properties during deformation in LA141 alloy were studied.

Experimental

The used alloy is commercial LA141 alloy and its main composition (mass fraction) is 13.56% Li, 0.94% Al and balance Mg. Disc-shaped samples of about 2.5 mm thickness and 10 mm diameter were cut out by spark erosion from the ingot and polished with sand paper in order to achieve smooth surfaces. HPT was performed on these samples at room temperature in a constrained set-up with a groove depth of 1.0 mm and a diameter of 10 mm. The disc-shaped sample was inserted into the groove between two anvils, twisted approximately 1 revolution per minute under the pressure of 3 GPa, and, subsequently, sheared under pressure with 3, 6, 9 and 12 anvil turns.

The microstructures of the HPT-processed materials were observed by optical microscopy (OM) and transmission electron microscopy (TEM). Mechanical properties were examined by tensile test. The sample preparation for OM consisted of the standard grinding and polishing steps, followed by etching with a 4 vol. % nital solution. For TEM, samples were grinded by abrasive paper until the thickness was about 50μm and 3 mm diameter specimens were cut from the edge of the disc. The 3 mm specimens were further thinned in a solution of 10vol. % perchloric acid and 90 vol. % ethanol at a temperature of 253 K with a voltage of 20 V using a twin-jet electro polishing apparatus. The specimens were observed by JEM 2100 LaB6 TEM, and the acceleration voltage was 200 KV. Tensile tests were examined using SANS 5504 universal testing machine with a tensile rate of 0.1 mm min^{-1} at room temperature. Then, the fracture surfaces of tensile tests specimens were analyzed by JSM-5800 scanning electron microscope (SEM), operating at an accelerating voltage 20 KV.

Results and Discussion

Microstructures of The LA141 alloy After HPT Process

Figure 1(b), (d) show microstructures near the center of the disc and after straining through 6 turns, and 12 turns, respectively. The grains became smaller and smaller after rotation and with the increasing of revolutions number, the homogeneities of material tend to be in-homogeneity. The microstructures near the edge of the disc can be seen in Fig. 1(c), (e). The grains were too small to be observed by OM. This suggests that the deformation of the

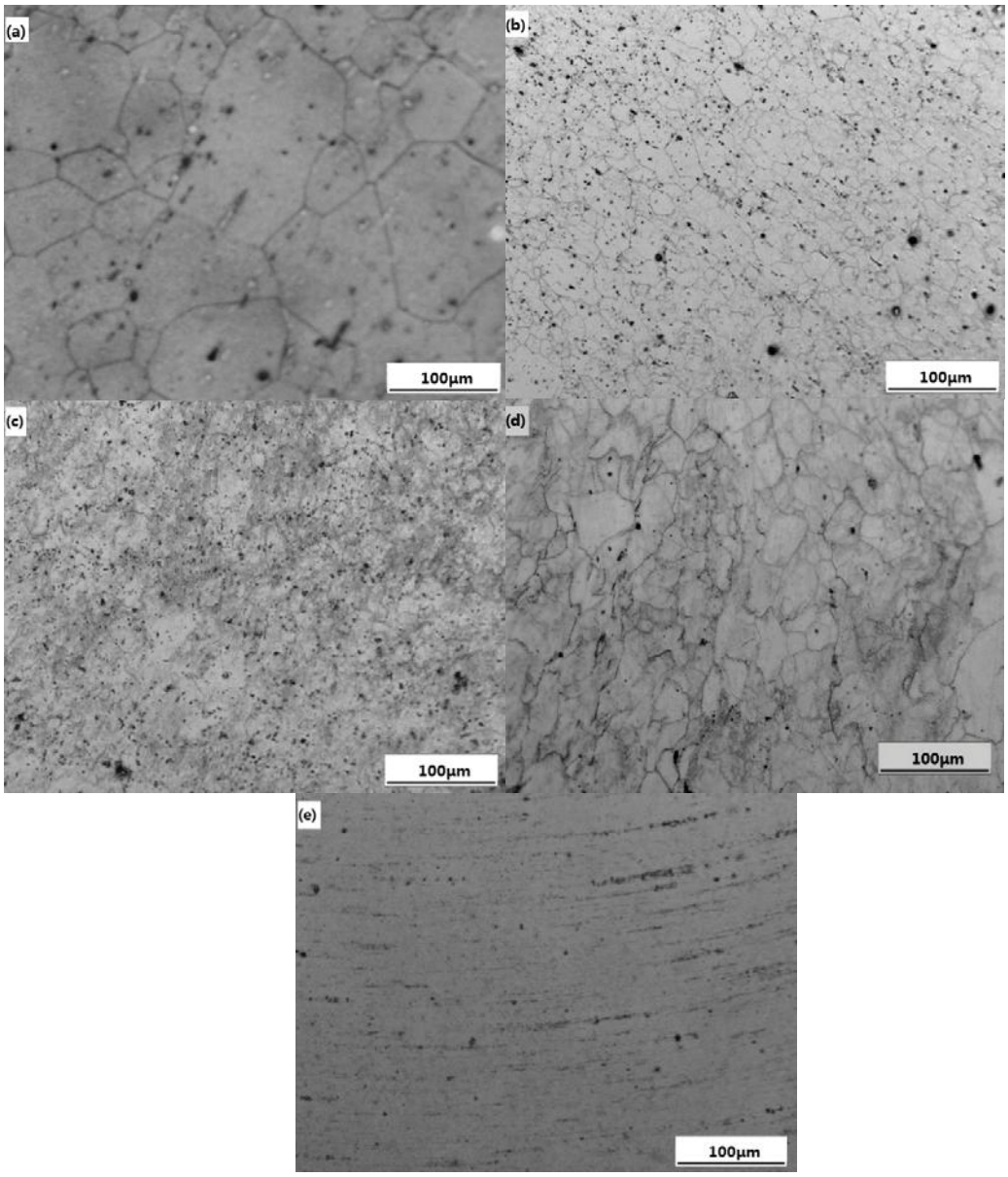


Figure 1. Microstructures of disc unprocessed (a) and processed by HPT through 6 turns (b) and (c), 12 turns (d) and (e) under pressure of 3GPa taken by OM

disc is not uniform through HPT. The microstructure of the disc without HPT processing can be seen in Figure 1(a). The original sample without HPT consist of large equiaxed grains, in all cases exceeding 50μm diameter, but the grains turned to be anisometric and small when the rotations number was increasing especially near the edge of the disc.

Figure 2 illustrates the microstructural evolution of the LA141 alloy after processing. Figure 2(a,) 2(b), 2(c), 2(d) are bright-field TEM micrograph of LA141 alloy processed by HPT through 3 turns, 6 turns, 9 turns and 12 turns under pressure of 3 GPa. It reveals the grains were refined to under 300nm and we could see the grains are almost 100μm in Figure 1(a) without HPT. The region of the diffraction patterns is the middle of the figures. The SAED patterns exhibit rings. Therefore, there are many ultra-fine grains with multiple orientations in the matrix and the grain boundaries are in high angles of misorientation. The grains are refined through HPT. The refined grains in Figure 2 can indicate the increase of tensile strength and ductility of the samples by HPT.

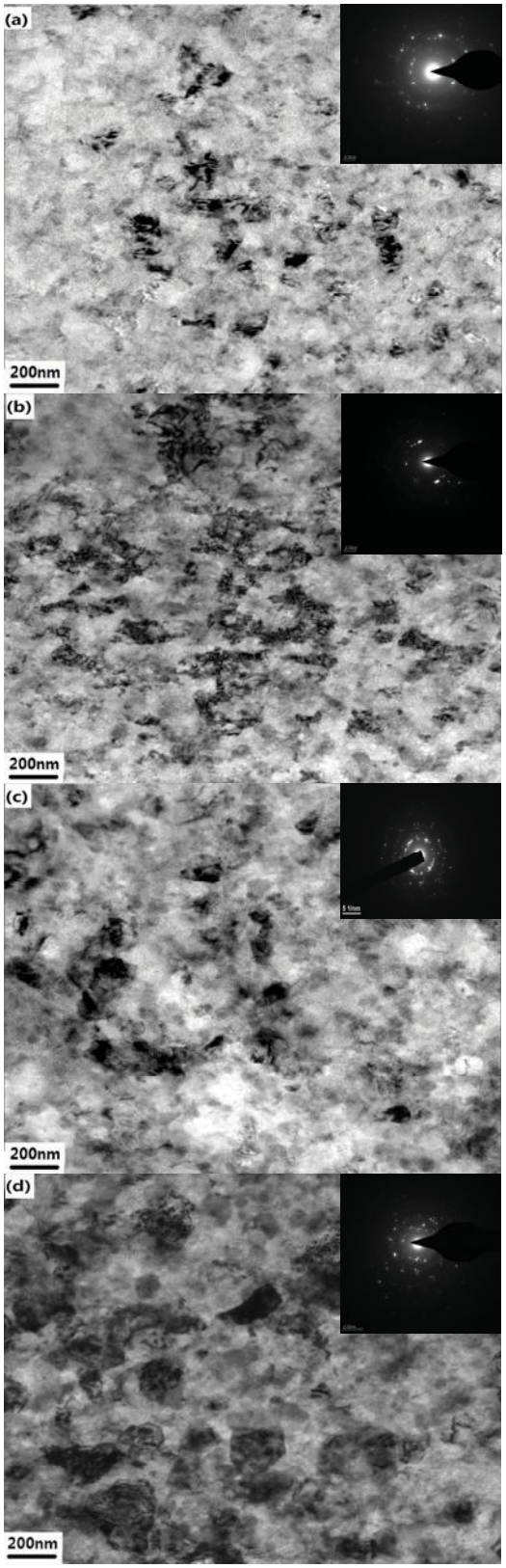


Figure 2. TEM micrograph of the HPT-processed LA141 alloy after (a) 3 turns, (b) 6 turns, (c) 9 turns and (d) 12 turns under pressure of 3GPa.

Mechanical Properties

Table I shows the values of tensile strength and elongation of tensile specimens cut from disc in different HPT process conditions. Because of the small size of disc, the tensile specimens are limited to be miniature correspondingly. The dimensions of the working segment were 3.75 mm, 0.85 mm, 0.80 mm in length, width and height respectively and they were cut from the disc with diameter of 10 mm at the position of 1.70mm away from the center. Compared with the initial state of 140MPa, the tensile strength is improved slightly following the processing by HPT. With the increase of torsion revolutions, the tensile strength is enhanced. Table 1 also presents the elongation of the specimens. Without HPT processed the elongation is only 20%, and it increases significantly to 85.33% when the torsion turns is 12. Generally speaking, the ductility promoted apparently after mechanical treatment. There are some reasons about the improvement of the performance of the mechanical properties. The original alloys contain defects and fracture from the defects. However, defects can be eliminated through HPT. Simultaneously, the mean grain size of the alloy is reduced with increasing the revolutions number especially near the edge of the disc. As a result, tensile strength and elongation are improved. As can be seen from the table, with the intensification of the deformation the tensile strength is gradually increased. The tensile strength did not significantly increase might be due to that deformation is not enough.

Table I Values of Tensile Strength and Elongation in Different HPT Process Conditions

Samples		Ultimate strength, MPa	Elongation, %
Initial state	0T	140	20.93
P=3GPa	3T	144.86	40.67
	6T	157.81	64.56
	9T	158.92	72.2
	12T	160.53	85.33

Fractography Analysis

Figure 3 depicts the fracture microstructure of tensile specimens in different process conditions. The fracture microstructure of LA141 alloy consists of evenly size dimples. Obviously, the tensile fracture surfaces are distinctly characterized by ductile rupture. This demonstrates the alloy has good deformation ability. As observed in Figure 3 (a), the dimples are big and non-homogeneous. So it can be informed that the specimen without HPT process in this experiment has low ductility. A lot of equiaxed dimples on the matrixes can be seen from figure 3 (b) and (c). As a result, the specimens processed by HPT after 3and 9 revolutions exhibit good toughness. The results are consistent with the tensile elongation above.

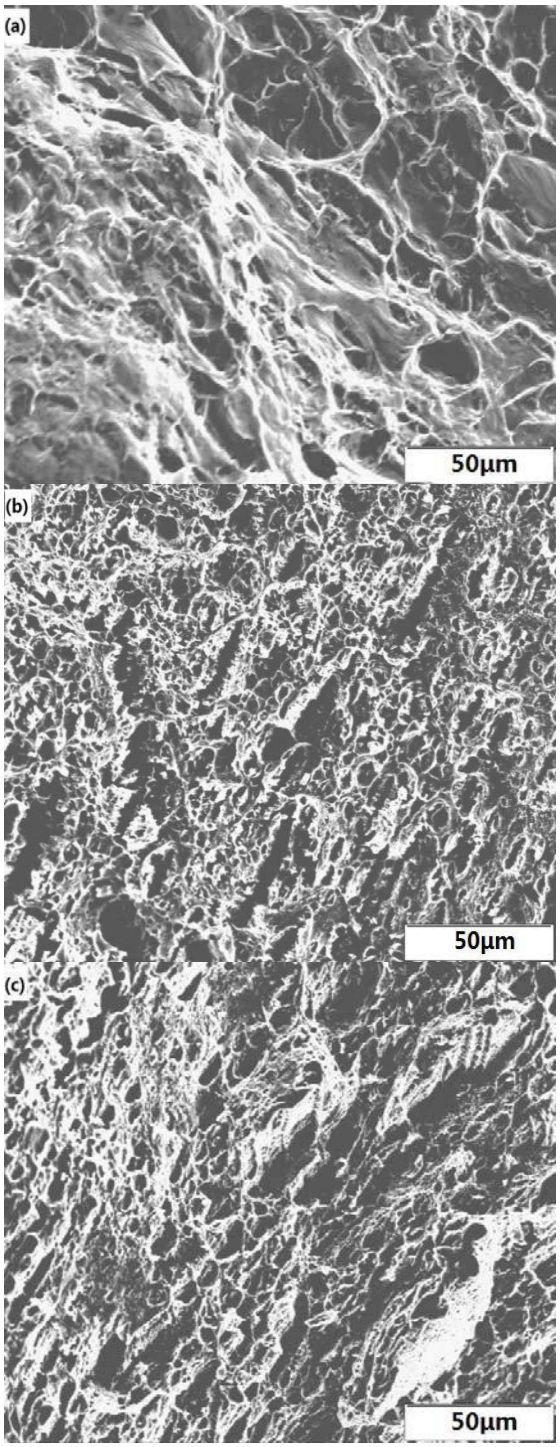


Figure 3**.** SEM fractographs after tensile test of disc in original state (a) and disc processed by HPT through 3 turns (b), and 9 turns (c) under pressure of 3 GPa.

Conclusions

High-pressure torsion method can remarkably refine the grains of LA141 alloy. The mean grain size of the LA141 alloy is reduced with increasing the revolutions number especially near the edge of the disc. Deformation of the specimen passes slowly from the peripheral regions to the center. The tensile fracture surfaces of the LA141 alloy with HPT processing and without HPT processing are distinctly characterized by ductile rupture. Simultaneously, because of the refined grains, the tensile strength and elongation of the alloy are improved.

Reference

[1] R.J.Jackson, P.D.Frost, "Properties and Current Applications of Magnesium-Lithium Alloys," Washington, D.C., NASA SP-5068, 1967.

[2] Haferkamp H et al., " Development, processing and applications range of magnesium lithium alloys," *Materials Science Forum,* 350/351(2000), 31 − 41.

[3] Wei X W, Zu X T, and Zhou W L, "Compressive creep behavior of Mg-Li-Al alloy," *Materials Science and Technology,* 22(2006),730-733.

[4] Cao F R et al., "Heat treatment behavior and microstructure evolution of superplastic Mg-8.5% Li alloy and effect of grain size and phase ratio on its elongation ," *Journal of Materials Science Technology*, 16(2000), 55-58.

[5] J.H.Jackson et al., "Magnesium-Lithium base Alloys Preparation, Fabrication, and General Characteristics," *Metallurgical Transactions,* 185 (1969), 149–168.

[6] Wolfenstine J, Gonzalez-Doncel G, Sherby O D, " Elevated temperature properties of Mg-14Li-B particulate composites," *Journal of Materials Research,* 5(1990), 1359-1362.

[7] Le Q C, Cui J Z, Liu H W, "Quenching and ageing behaviours of Mg-Li-Zn alloy," *Transactions of Nonferrous Metals Society of China,* 7(1997), 40-44.

[8] R .Z. Valiev, "The new trends in fabrication of bulk nanostructured materials by SPD processing," *J Mater Sci.*, 42 (2007), 1483-1490.

Magnesium Technology 2014

Melting, Modeling, and Solidification

Magnesium Technology 2014
Edited by: Martyn Alderman, Michele V. Manuel, Norbert Hort, and Neale R. Neelameggham
TMS (The Minerals, Metals & Materials Society), 2014

FINITE-ELEMENT ANALYSIS OF MELT FLOW IN HORIZONTAL TWIN-ROLL CASTING OF MAGNESIUM ALLOY AZ31

Jong-Jin Park

Department of Mechanical and System Design Engineering, Hongik University,
72-1, Sangsu-Dong, Mapo-Ku, Seoul 121-791, Korea

Keywords: Twin-roll casting, Vortex, Differential-speed casting

Abstract

Twin-roll casting has been useful in production of thin strips of metals. Especially, the process of horizontal twin-roll casting is often used for magnesium and aluminum alloys, which are lighter in weight and smaller in specific heat as well as latent heat in comparison to steel. In the present investigation, where magnesium alloy AZ31 was targeted, asymmetric behavior of the melt flow due to the gravity was examined in terms of contact length and pressure, and the nozzle for melt ejection was modified for its shape and location. Variations of the melt flow including vortexes were investigated in consideration of heterogeneous nucleation and uniform microstructure. The melt flow was further examined in the perspective of possible randomness of the grain orientation through thickness under differential speeds of rolls.

Introduction

Twin-roll casting (TRC) can produce metallic strips directly from the melt and therefore achieve energy saving as well as CO_2 gas reduction [1, 2]. As the productivity and the quality of the strip are the main issues of this process, several variations of the process with improvements have been proposed [3]. Recently, as Cu-Co-Be alloys with high thermal conductivities and tensile strengths were applied to the roll material, the productivity of the process has been enhanced [4].

A schematic of a horizontal twin-roll casting is shown in Fig. 1. The melt is ejected from the nozzle and flows through the gap between two identical rolls rotating opposite directions. During this process, a lot of heat is extracted from the melt to copper sleeves of the rolls and as a result the melt is cooled, solidified and rolled to a specific thickness. The heat is eventually removed by the cooling water flowing through internal cooling channels in the rolls. The setback length is the distance between the nozzle and the roll exit, where their thicknesses are designated by t_o and t_f, respectively. An increase in the setback length can extract more heat from the melt and helps to increase the roll speed. However, it also increases the nozzle thickness accordingly, resulting in leakage of the melt through gaps between the nozzle and the copper sleeves. As the depth of sump determined by process conditions gets larger, the deformation region becomes smaller and thus the reduction in thickness of a strip decreases. Consequently the roll separating force and the roll torque also decrease. Since the melt flow and cooling are asymmetric in this process, microstructures developed in the strip become asymmetric and so do the mechanical properties. In the present investigation, a commercial FEM code DEFORM was utilized to analyze this complicated phenomenon occurring in the process comprised of flow, cooling, solidification and plastic deformation.

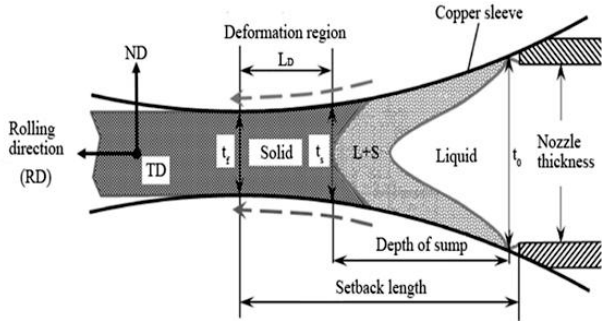


Figure 1. Schematic of the casting and deformation zone in a horizontal twin-roll casting

Asymmetric Flow

There were several studies to understand a steady-state flow in a horizontal twin-roll casting, without considering the effect of the gravity [5-7]. However, a recent study dealt with a nonsteady-state flow under the gravity where the symmetry was not enforced in the analysis [8]. The roll consisting of a steel core and a copper sleeve was 500 mm in diameter. The melt of Mg-AZ31 heated to 640°C was ejected from the nozzle into the gap between the rolls; the liquidus and solidus temperatures of the melt were 630°C and 565°C, respectively. Thermal properties of the alloy are provided in Table I. Magnitudes of t_o and t_f were set to 3 mm and 6 mm, respectively and the setback length was 40 mm. The melt flow was predicted for different values of the nozzle thickness, and the roll speed and the ejection speed were adjusted to take the melt into the sump accordingly.

Table I. Thermal properties of Mg-AZ31

solidus temp.	liquidus temp.	Density	specific heat	thermal conduct.	Latent heat
565℃	630℃	1780 kg/m^3	1040 J/kg·℃	55~110 W/m·℃	368 kJ/kg

Flows of the melt at an early and a later stage were predicted by the finite element analysis, as shown in Fig. 2. For smaller nozzles, the melt sagged due to the gravity and leaked through the gap between the nozzle and the lower sleeve. However, in the case of 6 mm, the gap was very small and the leakage was essentially prevented. The flow was observed to be asymmetric and to crumple along the surface of the lower sleeve. In order for the flow to be symmetric, the upper wall of the nozzle was shortened and the nozzle was shifted upward appropriately to minimize the gap between the nozzle and the copper sleeves.

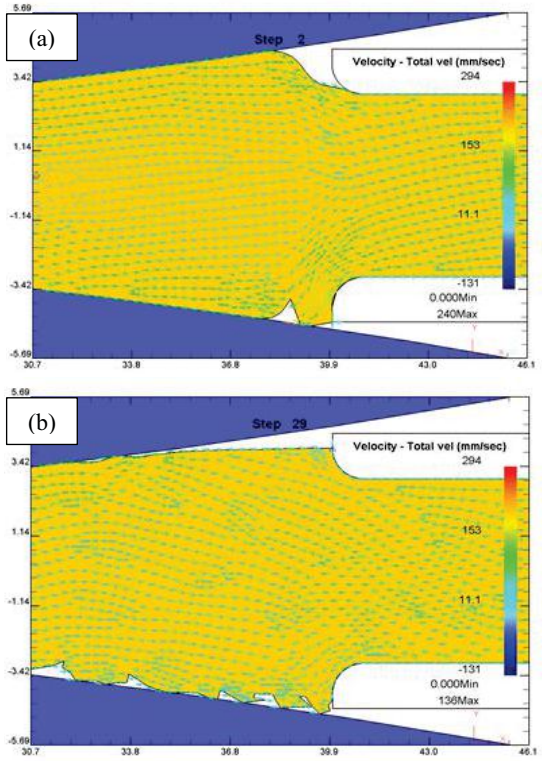


Figure 2. Flows under the nozzle thickness of 6 mm: (a) an early stage and (b) a later stage

The flow that would be developed by the nozzle with these modifications was examined and the result was good. The flow became symmetric with almost same lengths of contact with the upper and lower rolls. Although the upper surface of the melt in the sump sagged a little, the melt did not leak. However, the melt was found to be partially confined at the lower end of the nozzle. This confinement was suspected to develop to the crumpled flow on the surface of the lower sleeve. To resolve this problem, the end of the nozzle was further modified to be smoother in profile. Fig. 3 presents the predicted flow, which was developed by the shifted, asymmetric and smooth-end nozzle. The flow became finally smooth and symmetric without the confinement. Contour lines of liquidus and solidus temperatures were found also to be quite symmetric. The pressure distributions on the contact surfaces with the upper and lower sleeves were found to be identical. The pressure had a peak value at 1.5 degrees in contact angle measured from the roll exit, and was almost zero in the region above 4.5 degrees. The heat flux in the region under low pressure was insignificant, since the interface heat-transfer coefficient at the contact surface was given as a proportional function of the pressure.

Vortex Flow

Recently, melt conditioning by intensive shear was successfully used prior to twin-roll casting of AZ31 magnesium alloy strip to promote heterogeneous nucleation and to provide a refined and uniform microstructure without severe macro-segregation [9]. In this perspective, a vortex flow which would develop in the sump was expected to provide a similar effect to the strip although it is less in terms of magnitude. Therefore, an investigation was

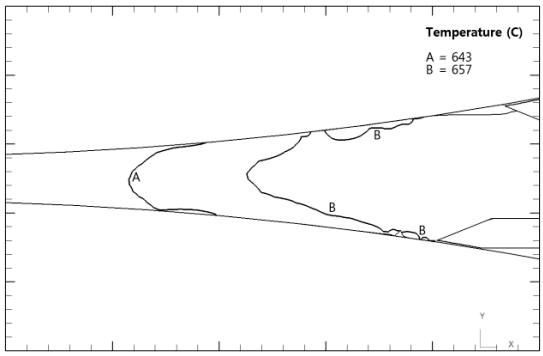


Figure 3. Temperature distribution developed by the nozzle with modifications

performed to find out under what conditions a vortex would be developed in the region of sump.

Under the condition that thicknesses of the nozzle and the roll exit were 13.4 mm and 3.2 mm, respectively, velocity distributions under two different roll speeds were obtained by the finite element analysis. In general, an increase in the roll speed increases the Reynold's number; the flow would be more unstable and more easily to form a vortex. On the contrary, as shown in Fig. 4, a vortex was found only in the case of low speed. The velocity profiles at the roll exit for the roll speeds are compared in Fig. 5; the profile of the case under the low speed is not varied at all while that under the high speed shows a higher velocity at the internal region. In the former, the whole region at the roll exit was cooled; the surface region at the roll exit was already below the solidus temperature. Thus, the viscosity of the whole region

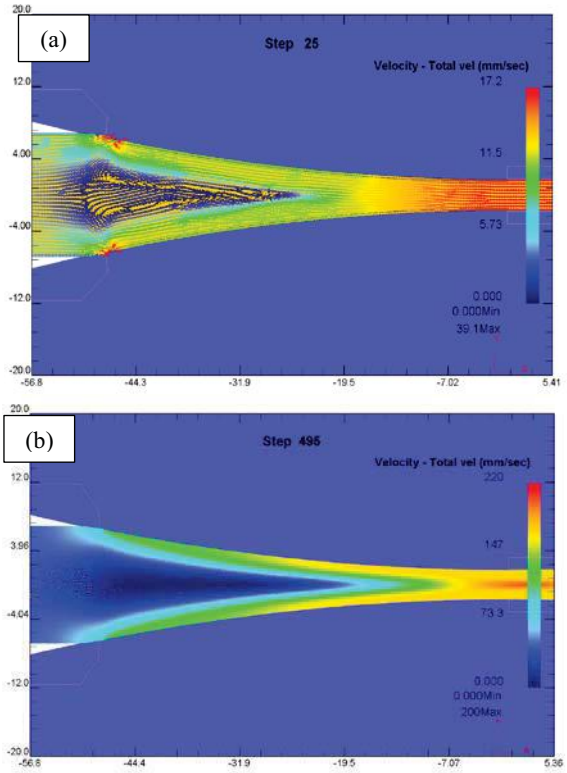


Figure 4. Velocity distributions under different roll speeds: (a) ω = 0.25 rad/s and (b) ω = 0.67 rad/s

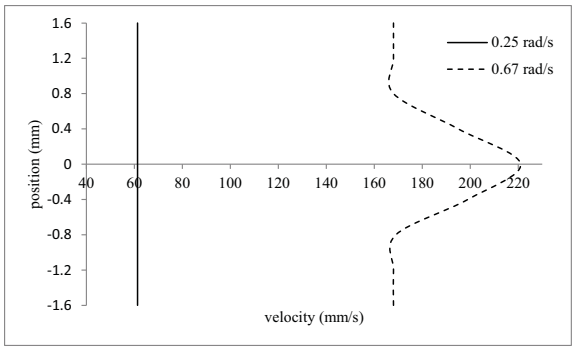


Figure 5. Velocity profiles at the roll exit under different roll speeds; ω= 0.25 rad/s and 0.67 rad/s

increased and the whole region flowed with the speed of the roll. Then the melt provided by the nozzle was unable to go out through the exit with such a speed profile, and as a result a portion of the melt formed a vortex by flowing backward. However, in the latter, the internal region was warm enough to maintain a low viscosity so that it was able to flow with a faster speed. Thus no vortex was formed.

As an indicator of the vortex development, a ratio was defined by dividing the nozzle thickness by the thickness of the roll exit. A series of the melt flow were examined for several values of the ratio, and a vortex was found to develop as the ratio is higher than a critical value that exists between 4.2 and 6.3. However, in reality, the surface of the melt should be at least solidified and thus a vortex is always expected to develop. A vortex is speculated to develop easier for a higher melt head, a faster roll speed, a larger roll gap, and a lower viscosity. The effect of gravity was not apparently shown in the present investigation because the roll gap was narrow. Trajectories of four points located in a vortex are presented in Fig. 6, revealing that the vortex was a forced one since outer points moved faster.

Differential-Speed Casting

The texture with a high density of basal planes is one of factors for the low formability of a magnesium alloy sheet. Many studies have been performed to reduce the density of the plane by imposing shear deformation to the strip through differential-speed rolling, where the upper and lower rolls rotate with different speeds [10-13]. The melt flow in a horizontal twin-roll casting is near symmetric, and so are the melt flow and deformation. As shown in Fig. 7, the elements originally squares in shape were severely compressed and deformed in shear in opposite direction during twin-roll casting. The density of a certain texture (or crystalline orientation) developed in a sheet was found to be dependent upon the reduction ratio, determined by the setback length and the depth of sump. Compared to the differential-speed rolling of a solid sheet, differential-speed casting was expected to impose shear flow or deformation more easily to the melt, which was in a state of liquid or semi-solid.

A case of a differential-speed casting was investigated under the following conditions: roll speeds of upper and lower rolls were 0.165 rad/s and 0.33 rad/s, respectively, thicknesses of the nozzle and the roll exit were 14.4 mm and 4.2 mm, respectively, initial temperature of the melt was 597.5℃ with 50% of solid fraction, and sticking condition at the interface between the melt and rolls. Several results obtained from finite-element analysis are as follows: the neutral point on the upper roll was located at a

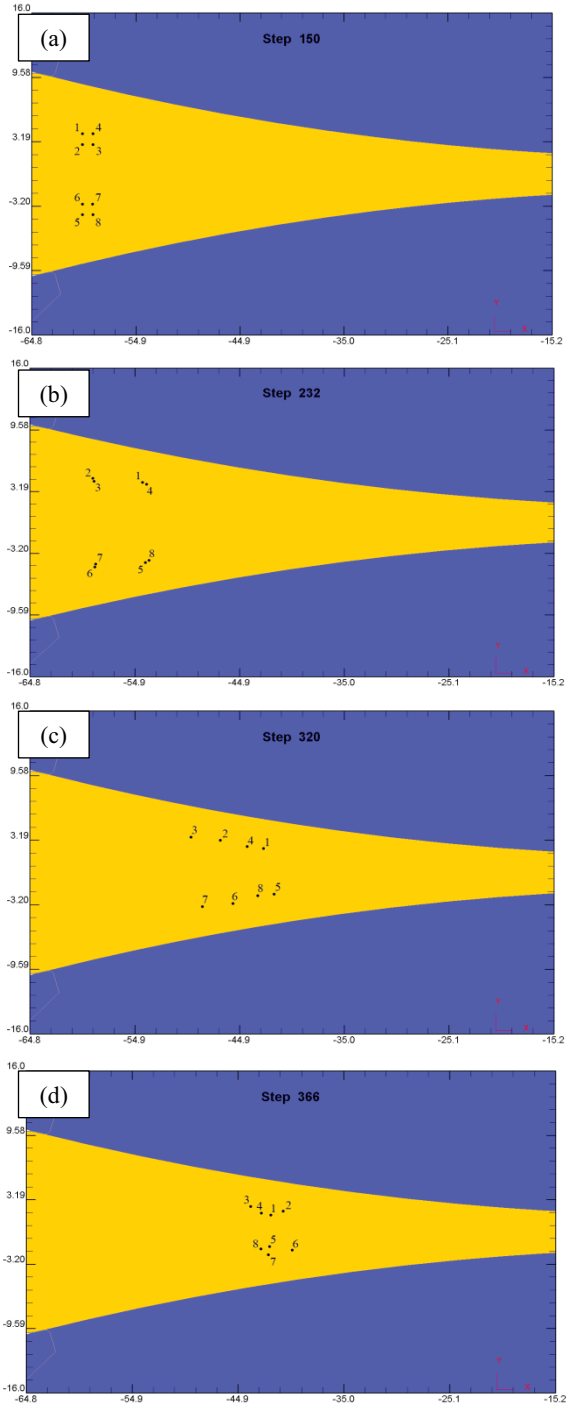


Figure 6. Changes of locations of four points in the vortex flow

distance of 18.5 mm from the roll exit while that on the lower roll was absent, roll separating forces of both rolls were in a range of 3.45~3.60 kN/mm, roll torques on the upper and lower rolls were 334 kN•mm/mm and 424 kN•mm/mm, respectively.

Distributions of velocity and temperature are presented in Fig. 8. The velocity field can be divided into two areas by a boundary, which connects the bottom of the nozzle and the top of the roll exit. The area above the boundary has a similar speed to the upper roll and the area below the boundary has a similar speed to the

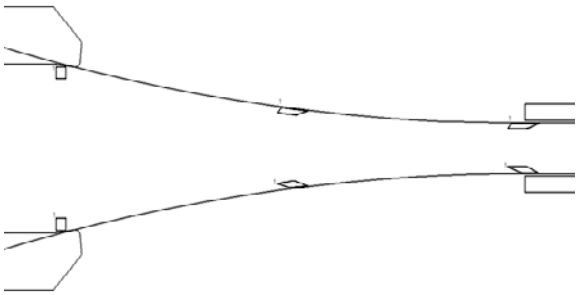


Figure 7. Symmetric flow and deformation by equal-speed casting

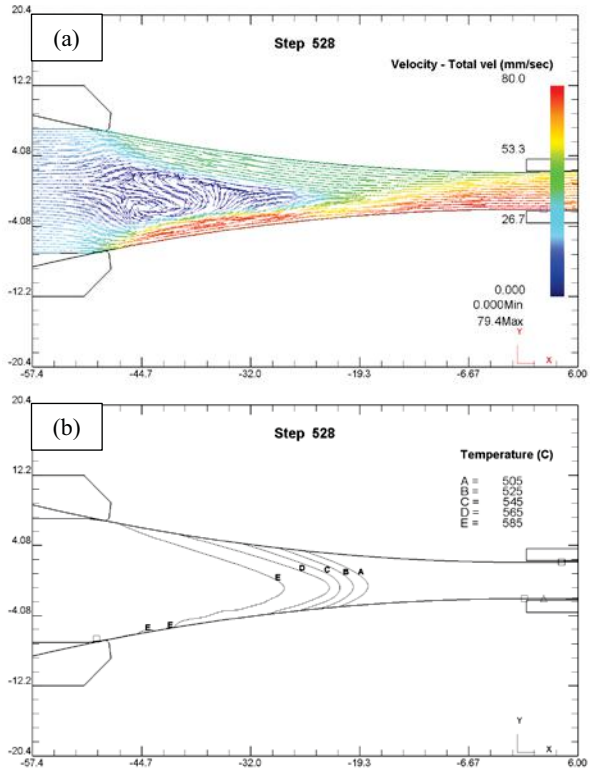


Figure 8. Results obtained for differential-speed casting: (a) velocity field and (b) temperature distribution

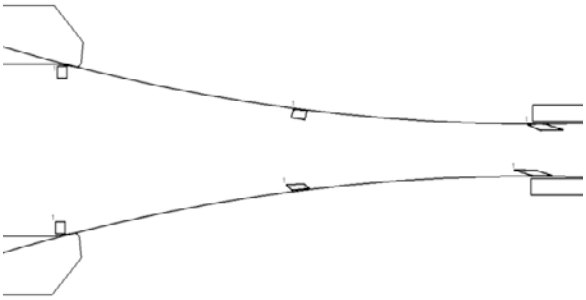


Figure 9. Asymmetric flow and deformation by differential-speed casting

lower roll. Temperature distribution is asymmetric; the upper area is cooler than the lower area due to the fact that the upper roll moves with a lower speed. Thus the amount of heat transferred from the melt to the upper roll was larger than that to the lower roll. In Fig. 9, through a differential-speed casting, two elements originally squares in shape were shown to be severely distorted, resulting in an asymmetric distribution. Both elements were rotated and deformed in shear counter-clockwise. Note that the lower one was distorted in the vicinity of the nozzle while the upper was in the vicinity of the roll exit.

Summary

In the present study, asymmetric behavior of the melt flow of magnesium alloy AZ31 in a horizontal twin-roll casting was investigated by finite-element analysis. Several results were obtained as follows: (1) the melt flow can be improved to be symmetric by modifying the melt-ejecting nozzle and adjusting its location, (2) a vortex was found to develop as the ratio, defined by dividing the nozzle thickness by the thickness of the roll exit, is greater than a critical value between 4.2 and 6.3, and (3) through differential-speed casting, proposed in the present study, the melt flow as well as the deformation were controlled to be asymmetric.

Acknowledgements

This research was supported by Basic Science Research Program through the National Research Foundation of Korea funded by the Ministry of Education, Science and Technology (2012-0007838). The author appreciates Mr. S. Baek and Mr. S. Yoo for their assistance.

References

1. M. Yun, S. Lokyer, and J.D. Hunt, “Twin Roll Casting of Aluminum Alloys,” Mater. Sci. Eng. A, 280 (2000) 116-123.
2. D. Liang and C.B. Cowley, “The Twin-Roll Strip Casting of Magnesium,” JOM (2004) 26-28.
3. H. Watari, R. Paisarn, T. Haga, K. Noda, K. Davey, and N. Koga, “Development of Manufacturing Process of Wrought Magnesium Alloy Sheets by Twin Roll Casting,” J. Achieve. Mater. Manuf. Eng., 20 (2007) 515-518.
4. G. Hugenschutt, D. Kolbeck, and H.-G. Wobker, “Copper Shells for Twin Roll Casting,” Proc. of Light Metals 2006, (2006) 859-863.
5. A. Saxena, and Y. Sahai, “Modeling of Fluid Flow and Heat Transfer in Twin-Roll Casting of Aluminum Alloys,” Mater. Trans, 43 (2002), 206-213.
6. M.A. Cruchaga, D.J. Celentano, and R.W. Lewis, “Modelling of Twin-Roll Strip Casting Processes,” *Communic. Num. Meth. Eng.*, 19 (2003) 623-635
7. A. Miehe, and U. Gross, “Modelling of Heat Transfer and Solidification Processes in Horizontal Twin-Roll Casting of Magnesium AZ31,” *Mater. Sci. Eng. A*, 33 (2012) 1-8.
8. J.J. Park, “Design of Melt-Ejection Nozzle in Horizontal Twin-Roll Casting of Al-1100 by Finite-Element Analysis,” *Adv. Mater. Res.*, 746 (2013) 543-547.
9. I. Bayandorian, Y. Huang, Z. Fan, S. Pawar, X. Zhou, and G.E. Thomson, “The Impact of Melt-Conditioned Twin-Roll Casting on the Downstream Processing of an AZ31 Magnesium Alloy,” *Metall. Mater. Trans. A*, 43A (2012) 1035-1047.
10. Y.H. Ji, J.J. Park, and W.J. Kim, “Finite Element Analysis of Severe Deformation in Mg-3Al-1Zn Sheets through Differential-Speed Rolling with a High Speed Ratio,” *Mater. Sci. Eng. A*, 454-455 (2007) 570-574.

11. H. Watanabe, T. Mukai, and K. Ishikawa, “Effect of Temperature of Differential Speed Rolling on Room Temperature Mechanical Properties and Texture in an AZ31 Magnesium Alloy,” *J. Mater. Process. Technol.*, 182 (2007) 644-647.
12. X. Huang, K. Suzuki, and Y. Chino, “Effects of Thickness Reduction per Pass on Microstructure and Texture of Mg-3Al-1Zn Alloy Sheet Processed by Differential Speed Rolling,” *Scripta Materialia*, 60 (2009) 964-967.
13. J.H. Cho, H.W. Kim, S.B. Kang, and T.S. Han, “Bending Behavior, and Evolution of Texture and Microstructure during Differential Speed Warm Rolling of AZ31B Magnesium Alloys,” *Acta Materialia*, 59 (2011) 5638-5651.

Magnesium Technology 2014
Edited by: Martyn Alderman, Michele V. Manuel, Norbert Hort, and Neale R. Neelameggham
TMS (The Minerals, Metals & Materials Society), 2014

Nucleation and Growth of Metastable Phases in Mg-Nd, Mg-Gd and Mg-Gd-Nd Based Alloys

S. Abd El Majid, , G. Atiya , M. Bamberger, A. Katsman*
Technion – Israel Institute of Technology, Haifa 3200, Israel
(*Corresponding author: akatsman@technion.ac.il)
KEYWORDS: Mg-Gd alloys, Mg-Gd-Nd alloys, Precipitation, Microstructure, Mechanical properties

ABSTRACT

High supersaturation of Mg matrix by rare earth (RE) elements after quenching of solution treated Mg-Nd, Mg-Gd and Mg-Gd-Nd alloys provides sequential precipitation of different metastable phases. Precipitation of β", β' and β_1 phases during aging was observed. Homogeneous nucleation of fully coherent metastable β" (Mg_3RE, DO_{19}) phase during aging is followed by its diffusional growth, coarsening and transformation to the coherent β' (Mg_7RE, BCO) phase or directly to the semicoherent β_1 (Mg_3RE, FCC) phase. The β"/ β' phase transformation involves additional Mg atoms from the adjacent Mg matrix resulting in nearly twice increase of precipitate volume. Heterogeneous nucleation of semicoherent β_1 (Mg_3RE, FCC) phase may occur on the β'-precipitates as in the Mg-Gd based alloys, or internal defects such as Zn_2Zr_3 rods and point defects at grain boundaries as in the Mg-Nd based alloy. The β'/ β_1 phase transformation is accompanied by reduction of precipitate volume for ~ 44.5% due to release of Mg atoms joined to Mg matrix. The β" and β_1 precipitates grow in $\{01\bar{1}0\}$ habit planes, while β' – in the $\{\bar{2}110\}$ plains. The combination of HRTEM, TEM with SAED and JEMS simulation was carried out to characterize the nanometer-scale precipitates. Microhardness measurements were performed to reveal the effect of precipitation on the mechanical properties of the alloys.

1. INTRODUCTION

Magnesium alloys containing heavy rare earth metals are very attractive candidates for the automotive industry including racing cars and aerospace applications [1-3], due to their high strength properties combined with low density. The high solubility of RE element in Mg matrix at high temperature and its rapid decrease with lowering temperature, show remarkable age-hardening response during isothermal aging.

Microstructural characterization of the Mg–RE alloys performed by many researchers [3-12] has confirmed a four staged precipitation sequence: [α-Mg supersaturated solid solution (S.S.S.S.) → β" (DO_{19})→ β' (BCO) → β_1 (FCC) → β (FCC) [4,5], where the later precipitate can coexist with the former. Among the four precipitated phases, the coherent β" and β' phases are considered to be the primary strengthening phases [4,5]. The yield strength or hardness usually reaches a maximum, as the materials form a microstructure with fine β' precipitates during aging [5-7]. The characterisitics of these precipitates (coherency, shape, size and density) play a significant role in the hardening effect. Among RE elements, Gd and Nd are considered as most promising for achievement of best Mg-RE alloys properties.

In the present work, nucleation and growth of metastable phases and their transformations during aging were investigated in the alloys Mg-3.1Nd, Mg-6Gd-3.7Nd and Mg-4.7Gd (wt. %) with additions of Zn, Y and Zr. They were investigated by a combination of transmission electron microscopy (TEM), high resolution transmission electron microscopy (HRTEM), energy dispersive X-ray spectrometry (EDS) and JEMS simulation. Microhardness measurements were performed to reveal the effect of precipitation on the mechanical properties of the alloy.

2. EXPERIMENTAL

High purity Mg (99.9 wt. %) was melted in a cemented graphite crucible under a protective atmosphere CO_2 and HFC-134a (CF_3CH_2F), high purity Gd (99.9 wt. %), Nd (99.9 wt. %) "for Mg-Gd-Nd-based alloy", Zn (99.9 wt.%), Mg–40Y (wt.%) and Mg–16Zr master alloys were added at a melt temperature of 760°C, then casting into steel mould. The chemical composition of the investigated alloys were Mg-3.1Nd-0.45Zr-0.25Zn, Mg-6Gd-3.7Nd-0.3Zn-0.18Y-0.15Zr and Mg-4.7Gd-0.37Zn-0.14Y-0.09Zr (wt. %).

Specimens were cut from the cast and encapsulated in quartz ampoules under Ar atmosphere. Solution treated (ST) at 540°C for 24hr, quenched into water, and then aged at 175°C in an oil bath for various periods of time up to 125 days, followed by water quenching.

The microhardness of aged specimens was measured by a Vickers hardness tester under a load of 50gr and holding time of 15sec. 20-40 indentations were conducted on each specimen.

The combination of HRTEM, TEM with SAED and JEMS simulation was carried out to characterize the nanometer-scale precipitates. The characterization includes crystal structure and composition of the precipitates, precipitation hardening sequence, orientation relationships between precipitates and the matrix and between precipitates themselves, if it exists. Thin foils for TEM characterization were prepared by ion beam thinning, and were examined at the acceleration voltage of 200 kV.

3. RESULTS

3.1. Aging Response

The combination of HRTEM, TEM with SAED and JEMS simulation was carried out to characterize the nanometer-scale precipitates. The characterization includes crystal structure and composition of the precipitates, precipitation hardening sequence, orientation relationships between precipitates and the matrix and between precipitates themselves, if it exists.

The age hardening curves of the three investigated alloys during aging at 175°C are presented in Fig. 1.

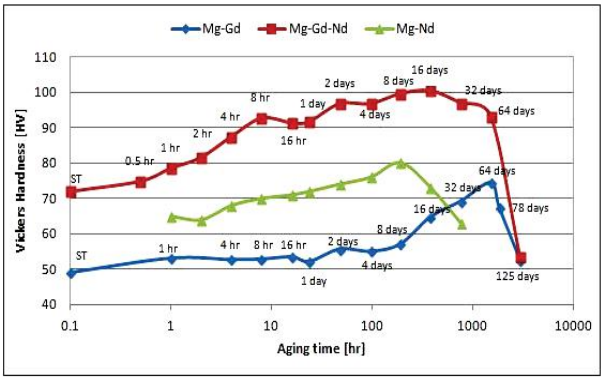


Fig. 1. Age hardening curve of the investigated alloys aged at 175°C.

The aging of ST samples was performed at 175°C up to 125 days. The microhardness of the Mg-3.1Nd based alloy increases and reaches the maximum value of about 80HV after 8 days and then decreases with the aging time. The Mg-Gd based alloy displays two-peaks, the first - after 2 days, and the second peak, with the maximum value of about 75 HV, after 64 days of aging. Mg-6Gd-3.7Nd based alloy displays three peaks: the first after 8 hours of aging, the second after 2 days and the third peak, with the maximum value of about 100HV, after 16 days of aging. Further aging led to decrease in the microhardness (over aging).

3.2. Microstructure of Aged Samples

Aging periods of 16 hours, 4 days, 8 days, 16 days, 32 days and 64 days were selected for microstructure investigation, which represent under-aged, peak-aged and over-aged conditions.

3.2.1. Under-aged samples

Electron microscopy examination of the under-aged samples of Mg-3.1Nd based alloy (4 days of aging) indicates the presence of Guinier Preston (G.P). Zones or very small β" precipitates as shown in Fig. 2.

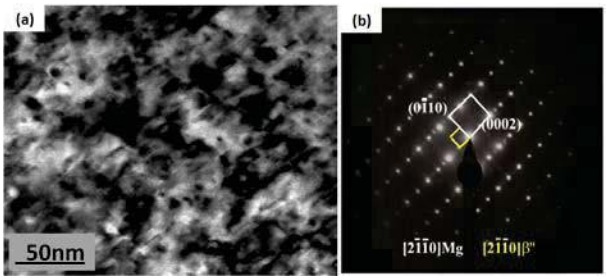


Fig. 1. (a) BF TEM micrograph and (b) corresponding SAED of the Mg-3.1Nd based alloy aged at 175°C for 4 days , show the presence of β" precipitates. Mg zone axis $[2\bar{1}\bar{1}0]_{\alpha-Mg} \parallel [2\bar{1}\bar{1}0]_{\beta''}$.

The microstructure of Mg-Gd-Nd alloy aged for 16 h (Fig. 3) contained very thin platelet-shape precipitates formed on $\{0\bar{1}10\}_{\alpha}$ planes and alongated along $[0001]_{\alpha}$ direction.

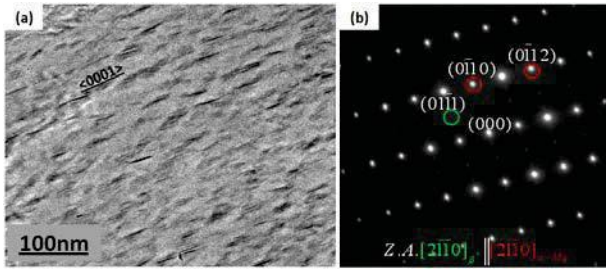


Fig. 3. (a) TEM image and (b) corresponding SAED pattern of Mg-Gd-Nd alloy aged for 16 h at 175°C with Z.A. $[2\bar{1}\bar{1}0]_{\alpha}$.

From TEM SAED and JEMS simulation, it was found that β" precipitate have DO_{19} structure with lattice parameters of $a=2a_{\alpha\text{-}Mg}$ and $c=c_{\alpha\text{-}Mg}$, while the composition of β" is Mg_3RE and are fully coherent with the Mg matrix.

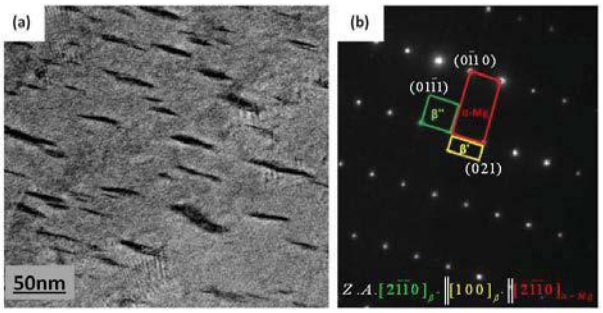


Fig. 4. (a) TEM image and (b) corresponding SAED pattern of Mg-Gd alloy aged for 16 days at 175°C; with Z.A. $[2\bar{1}\bar{1}0]_{\alpha}$.

In Mg-Gd based alloy, no precipitates appear in specimen aged for 16 h. Aging for 16 days resulted in precipitations of β" and β' phases.TEM image and SAED pattern of Mg-Gd specimen aged for 16 days are presented in Fig. 4. As seen from the SAED pattern, the precipitate reflections are from β" and β' precipitates.

It was found that β" precipitates have the same crystal structure and composition like that found in Mg-Gd-Nd alloy. The composition of β' is Mg_7RE and have BCO structure with lattice parameters *a=0.64nm, b=2.223nm, c=0.52nm*.

3.2.2. Peak-aged samples

BF TEM micrographs and associated diffraction patterns of the peak aged sample of the Mg-3.1Nd based alloy (175ºC for 8 days) are shown in Fig. 5. It can be seen that the precipitate reflections are midway between matrix reflections. The presence of maxima halfway across the intervals between the matrix spots in the diffraction pattern is an evidence for DO_{19} structure with lattice parameters of $a=2a_{Mg}$ and $c=c_{Mg}$.

It was found that Zn_2Zr_3 rod-shape particles are formed during solution treatment of the Mg-3.1Nd-0.45Zr-0.25Zn [8]. These particles were also observed in the peak aged sample and were investigated using TEM. STEM HAADF micrograph (Fig. 6a) shows different particle clusters built from Zn_2Zr_3 rods and adjacent Mg-Nd precipitates. Two morphology types were observed: T-shape and H-shape particles.

SAED patterns revealed that the particles Zn_2Zr_3 have a Base Centered Tetragonal structure, space group of p42mnm and lattice parameters a=0.768nm and c=0.699nm and are elongated along its [001] direction.

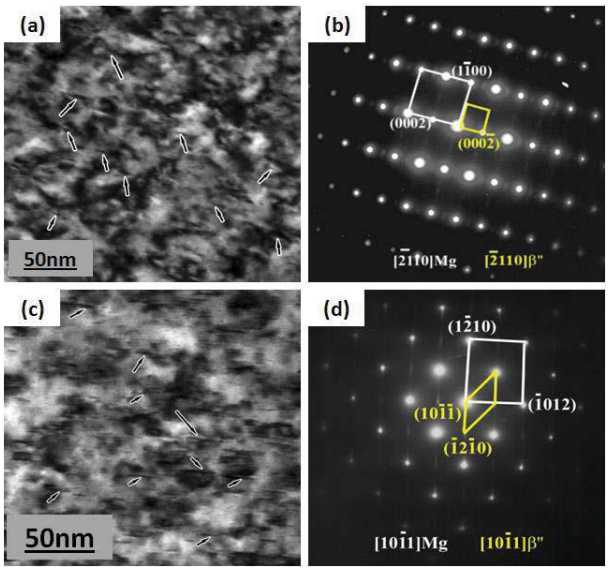


Fig. 5. (a,c) BF TEM micrograph and (b.d) corresponding SAED inside the grain of the Mg-3.1Nd based alloy aged at 175°C for 8 days , show the presence of β" precipitates. Z.A. $[2\bar{1}\bar{1}0]_{\alpha-Mg} \| [2\bar{1}\bar{1}0]_{\beta''}$ (a,b) and $[10\bar{1}1]_{\alpha-Mg} \| [10\bar{1}1]_{,\beta''}$ (c,d).

Bright Field TEM micrograph and corresponding SAED pattern (Fig. 6b,c) revealed that the plate-shape precipitates on the Zn_2Zr_3 particles are β_1 precipitates with FCC crystal structure and lattice parameter of a=0.739nm. In addition, the following orientation relationship between α-Mg and β_1 was found: $[0001]_{Mg} \| [101]_{\beta_1}$, $(1\bar{1}00)_{Mg} \| (\bar{2}02)_{\beta_1}$.

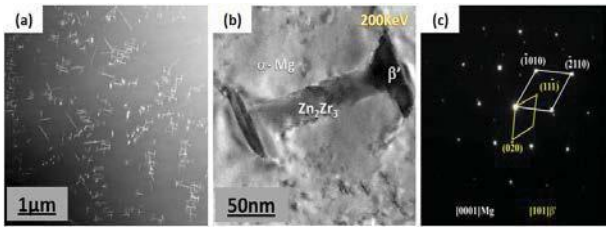


Fig. 6. (a) HAADF STEM micrograph of Zn_2Zr_3 rods and adjacent β_1 precipitates, Z.A. $[\bar{2}110]_{\alpha-Mg}$; (b) BF TEM micrograph of Zn_2Zr_3 rod particle with β_1 precipitates and (c) corresponding SAED of Mg matrix and β_1. Z.A $[0001]_{\alpha-Mg} \| [101]_{\beta_1}$.

The HAADF STEM image and SAED pattern typical of microstructure in Mg-Gd-Nd specimen aged for 16 days are presented in Fig. 7. As seen from the image, the microstructure contained three kinds of precipitates β', β_1 phases, and very thin precipitates with few tens of nanometer size that are probably β" precipitates.

The platelets β' are extending along $[0001]_\alpha$ direction and belong to the $(\bar{2}110)_\alpha$ habit plain, while β_1 precipitates are extending along directions of $<\bar{2}110>_\alpha$ and have $\{10\bar{1}0\}_\alpha$ habit planes.

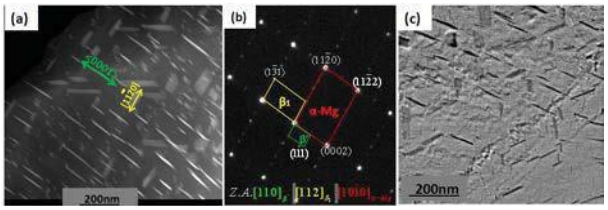


Fig. 7. (a) HAADF STEM image and (b) corresponding SAED pattern of Mg-Gd-Nd alloy aged at 175°C for 16 days with Z.A. $[\mathbf{10\bar{1}0}]_{\boldsymbol{\alpha}}$; (c) TEM image of the Mg-Gd alloy aged for 64 days at 175°C.

It was found that β' precipitates have the same crystal structure and composition like that found in Mg-Gd alloy. The β_1 precipitates have FCC crystal structure with the lattice parameter *a=0.74nm*, the composition of β_1 is Mg_3RE.

Typical TEM image of the Mg-Gd based alloy specimen aged for 64 days is shown in Fig. 7c. It was found that the microstructure contained β', β_1 precipitates and a small amount of β" precipitates. Crystal structure, composition and orientation relationships of the precipitates are similar to that found in Mg-Gd-Nd based alloy.

3.2.3. Over-aged samples

TEM micrographs and corresponding SAED patterns taken from the grain interior of the over-aged sample of the Mg-3.1Nd based alloy (32 days of aging) revealed β_1 precipitates (Fig. 8) elongated along three equivalent directions of $\langle\bar{2}110\rangle_{\alpha-Mg}$ with habit planes $\{\bar{1}010\}_{\alpha-Mg}$.

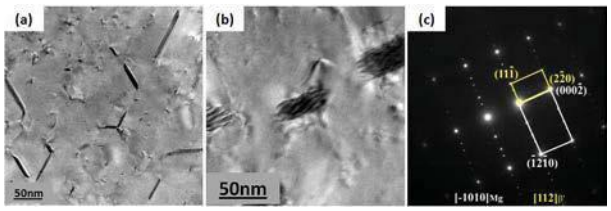


Fig. 8. (a) TEM micrograph of the over-aged sample of the Mg-3.1Nd based alloy, Z.A. $[0001]_{\alpha-Mg}$; (b) BF TEM micrograph of β_1 precipitates in Mg matrix and (c) corresponding SAED pattern, Z.A. $[\bar{1}010]_{\alpha-Mg} \parallel [112]_{\beta_1}$.

Typical HAADF STEM image and corresponding SAED pattern of the Mg-Gd-Nd based alloy specimen aged for 32 days are shown in Fig. 9. As can be seen, the microstructure contained β' and β_1 precipitates, while β_1 precipetates appear often to be associated with β' precipitate. β' precipitates are elongated along $[0001]_\alpha$ direction while β_1 precipitates are elongated along two directions of $\langle\bar{2}110\rangle_\alpha$.

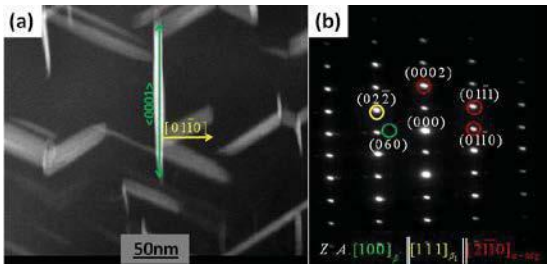


Fig. 9. (a) HAADF STEM image and (b) corresponding SAED pattern of Mg-Gd-Nd alloy aged for 32 days at 175°C; with Z.A. $[\mathbf{2\bar{1}\bar{1}0}]_\alpha$.

The OR $[100]_{\beta'} \| [111]_{\beta_1}$, $(00\bar{2})_{\beta'} \| (20\bar{2})_{\beta_1}$ between β' and β_1 precipitates was found (Fig. 9b). After aging for 64 days, the β' precipitates almost totally transformed to platalet β_1 precipitates. The typical TEM image and corresponding SAED pattern of Mg-Gd-Nd alloy specimen aged for 64 days (Fig. 10) show the platelet β_1 precipitates elongated along three equivalent directions $\langle\bar{2}110\rangle_\alpha$ with habit planes $\{10\bar{1}0\}_\alpha$.

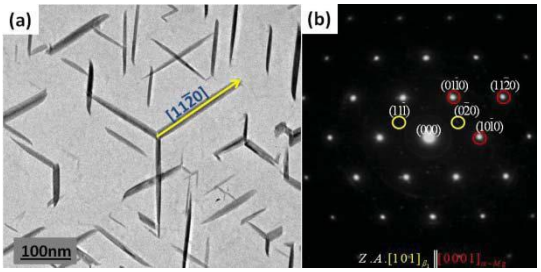


Fig. 10. (a) TEM image and (b) corresponding SAED pattern of Mg-Gd-Nd alloy aged for 64days at 175°C; with Z.A. $[0001]_\alpha$.

4. DISCUSSION

The precipitation sequence during isothermal aging in Mg-3.1Nd, Mg-6Gd-3.7Nd and Mg-4.7Gd based alloys is similar to that observed in binary Mg-Gd alloy (reported by Nishijima [9]). In the first stage the metastable phase β" (Mg_3RE) with HCP (DO_{19}) structure is precipitated from the α-Mg (S.S.S.S.). One can assume that high supersaturation of matrix by RE elements is resulted in homogeneous nucleation of fully coherent β" precipitates. The β" precipitates have a

platelet-like shape in habit planes $\{\bar{2}110\}_{\alpha-Mg}$ & $\{0\bar{1}10\}_{\alpha-Mg}$ with the OR: $[0001]_{\beta''}\|[0001]_{\alpha}$ and $(01\bar{1}0)_{\beta''}\|(01\bar{1}0)_{\alpha}$.

Nucleation and growth are controlled by diffusion of RE elements in the Mg matrix. Since the diffusion of Nd is faster than that of Gd, the first β" precipitates in the Mg-Gd-Nd based alloy have a composition of Mg_3Nd. After intensive β"(Mg_3Nd) nucleation, the Nd supersaturation of matrix decreases substantially, nucleation is terminated, but the growth of precipitates continues due to Nd diffusion and is accompanied by their coarsening (dissolution of some small Mg_3Nd precipitates in favor of larger precipitates). Apparently, these processes resulted in the first peak of microhardness observed in the Mg-Gd-Nd based alloy after ~ 8 hr aging. The following growth of β" occurs due to Gd diffusion and results in increase of microhardness during ~2 days of aging, whereupon the coarsening provides the second peak of the microhardness. In that time the supersaturation of the matrix by RE elements decreases substantially both in Nd and in Gd. It is noteworthy that only the second peak (after 2 days of aging) was observed in the Mg-Gd based alloy (Fig. 1).

During the second stage β" precipitates may transform to the metastable β' (Mg_7RE) precipitates with BCO structure as it was found in Mg-4.7Gd and Mg-6Gd-3.7Nd based alloys. The β' precipitates have a platelet-like shape in habit planes $\{\bar{2}110\}_{\alpha-Mg}$ and grew along $<0001>_{\alpha\text{-Mg}}$. The β' precipitates are coherent with the Mg matrix, with the following OR: $(001)_{\beta'}\|(0001)_{\alpha}$ and $[110]_{\beta'}\|[10\bar{1}0]_{\alpha-Mg}$. It is likely that nucleation of β' occurs heterogeneously at the β" /α-Mg interface. The phase transformation involves additional Mg atoms from the adjacent Mg matrix and transformation of the DO_{19} crystal structure of β" into the BCO crystal structure of β'. This transformation requires short range diffusion of Mg and RE atoms. It should be noted that the final volume of precipitated phase, β', is substantially larger than that of β" participating in reaction β" + α-Mg → β'. The volume of β" (Mg_3RE, DO_{19}) unit cell (consisting of 2 atoms of RE and of 6 atoms of Mg) is equal to ~ 0.18 nm^3, while the volume of β' (Mg_7RE, BCO) unit cell (consisting of 4 atoms of RE and of 28 atoms of Mg) is equal to ~ 0.73 nm^3 (*Table 1*). It means that the precipitated volume of β' is nearly twice of β" for the same amount of RE atoms. By these means, the transformation β" → β' is accompanied by substantial increase of precipitates' size. Additional growth of β' precipitates during aging occurs due to diffusion of RE elements from the Mg matrix. These processes are resulted in the microhardness increase up to 16 days of aging in the Mg-Gd-Nd based alloy and up to 64 days in the Mg-Gd based alloy (Fig. 1). It should be emphasized that the β' phase was not found in the Mg-3.1Nd based alloy where the next metastable phase, β_1, formed heterogeneously at the Zn_2Zr_3 particles immediately after β" precipitation.

Further aging of Mg-Gd and Mg-Gd-Nd based alloys resulted in transformation of all β' precipitates into the β_1(Mg_3RE) precipitates with FCC structure. The β_1 precipitates have a platelet-like shape in habit planes $\{0\bar{1}10\}_{\alpha-Mg}$, grew along three directions of $\langle 1\bar{2}\bar{1}0\rangle_{\alpha-Mg}$ (Figs. 8, 10) and are semi-coherent with the Mg matrix, with the following OR: $[110]_{\beta_1}\|[0001]_{\alpha}$ and $(1\bar{1}1)_{\beta_1}\|(11\bar{2}0)_{\alpha}$.

The nucleation of β_1 was associated with β' precipitates, apparently, due to very small lattice mismatch between β' and β_1 precipitates for their OR $[100]_{\beta'}\|[111]_{\beta_1}, (00\bar{2})_{\beta'}\|(20\bar{2})_{\beta_1}$. Such heterogeneous nucleation resulted in formation of K-like and V-like particle associations (Fig. 9a). Similar situation was realized in the Mg-3.1Nd based alloy, where very small lattice mismatch between Zn_2Zr_3 and β_1 precipitates for their OR $[\bar{2}110]_{Mg}\|[001]_{Zn_2Zr_3}$ and $(0001)_{Mg}\|(110)_{Zn_2Zr_3}$ allowed heterogeneous nucleation of β_1 on the Zn_2Zr_3 rods resulted in formation of T-like and H-like particle clusters.

Unit cell of the FCC β_1(Mg_3RE) phase consists of 4 RE atoms and 12 Mg atoms, with the total volume of 0.405 nm^3 (*Table 1*). It means that the transformation β' → β_1 is accompanied by reduction of precipitate volume by ~44.5% due to release of Mg atoms into the Mg matrix. Reduction of precipitates' size, together with a coarsening process resulted in a decrease of microhardness after 16 days of aging of the Mg-Gd-Nd based alloy (64 days aging of the Mg-Gd based alloy). The growth directions of β_1 - $\langle 1\bar{2}\bar{1}0\rangle_{\alpha-Mg}$ - differ from the growth directions of β' - $<0001>_{\alpha\text{-Mg}}$. It means that the β' → β_1 transformation should be accompanied by dissolution of the β' precipitate and diffusion of RE atoms from β' to adjacent β_1 precipitate.

In the fourth stage of aging, the β_1 precipitates transformed into a stable incoherent β (Mg_5RE) precipitates with FCC structure as observed in the over aging samples.

Table 1: Summary of composition, structure, lattice parameters, number of atoms per unit cell and volume of the unit cell for β" ,β' and β_1 precipitates in Mg-Gd and Mg-Gd-Nd alloys.

Phase	*composition*	*structure*	*Lattice parameters*	*Atoms*	*Volume of unit cell*
β''	*Mg_3RE*	*DO_{19}*	*a=0.64nm c=0.52nm*	*6 Mg 2 RE*	*0.1843 nm^3*
β'	*Mg_7RE*	*BCO*	*a=0.64nm b=2.223nm c=0.52nm*	*28 Mg 4 RE*	*0.7321 nm^3*
β_1	*Mg_3RE*	*FCC*	*a=0.74nm*	*12 Mg 4 RE*	*0.4052 nm^3*

5. CONCLUSIONS

- The α-Mg (S.S.S.S.) in Mg-6Gd-3.7Nd and Mg-4.7Gd based alloys decomposes during aging into the following four successive phases: β" (Mg_3RE, DO_{19})→ β' (Mg_7RE, BCO) → β_1 (Mg_3RE, FCC) → β (Mg_5RE, FCC); in the Mg-3.1Nd based alloy the β' was not recognized, possibly due to early heterogeneous nucleation of β_1 phase.
- β" phase nucleates homogeneously from the supersaturated Mg matrix, while β' nucleates heterogeneously on the β" phase and involves additional Mg atoms from the adjacent Mg matrix.
- β" and β' are coherent with the α-Mg matrix , β_1 is semi-coherent with the matrix.
- The nucleation of β_1 in Mg-Gd-Nd and Mg-Gd alloys was associated with β' precipitates, resulting in formation of K-like and V-like particle associations; in the Mg-3.1Nd based alloy heterogeneous nucleation of β_1 on the Zn_2Zr_3 rods resulted in formation of T-like and H-like particle clusters.
- Transformation β' → β_1 occurs with decrease of precipitated volume providing decrease of microhardness.
- The platelets β' have $\{\bar{2}110\}_{\alpha-Mg}$ and β_1 have $\{0\bar{1}10\}_{\alpha-Mg}$ habit planes; β_1 grows along three close packed directions of the matrix $\langle 1\bar{2}\bar{1}0\rangle_{\alpha-Mg}$, while β' grows along $<0001>_{\alpha\text{-Mg}}$.
- Hardening occurred with three-peaks in the Mg-6Gd-3.7Nd, two-peaks in Mg-4.7Gd and one peak in Mg-3.1Nd based alloys.

REFERENCES

1. B. L. Mordike and T. Ebert, "Magnesium: properties – applications – potential," Materials Science and Engineering A 302 (1), 37-45 (2001).
2. L. Huber, I. Elfimov, J. Rottler, M. Militzer, "Ab initio calculations of rare-earth diffusion in magnesium," Physical Review B 85, 144301 (2012).
3. K.Y. Zheng, J. Dong, X. Q. Zeng and W. J. Ding, "Effect of thermo-mechanical treatment on the microstructure and mechanical properties of a Mg–6Gd–2Nd–0.5Zr alloy," Materials Science and Engineering A 454-455 (2007), 314-321.
4. K.Y. Zheng, J. Dong, X. Q. Zeng and W. J. Ding, "Precipitation and its effect on the mechanical properties of a cast Mg-Gd-Nd-Zr alloy," Materials Science and Engineering A 489, 44-54 (2008).
5. K.Y. Zheng, X. Q. Zeng J. Dong, and W. J. Ding, "Effect of initial temper on the creep behavior of a Mg-Gd-Nd-Zr alloy," Materials Science and Engineering A 492, 185-190 (2008).
6. X. Gao, S.M. He, X.Q. Zeng et al., "Microstructure evolution in a Mg-15Gd-0.5Zr (wt. %) alloy during isothermal aging at 250 °C," Materials Science and Engineering A 431, 322-327 (2006).
7. L. Gao, R. S. Chen, E. H. Han, "Microstructure and strengthening mechanisms of a cast Mg–1.48Gd–1.13Y–0.16Zr (at.%) alloy," J Materials Science 44, 4443-4454 (2009).
8. G. Atiya, M. Bamberger, A. Katsman, Microstructure, Phase Evolution and Precipitation Strengthening of Mg-3.1Nd-0.45Zr-0.25Zn Alloy, Magnesium Technology 2011, Edited by: Wim H. Sillekens, Sean R. Agnew, Neale R. Neelameggham, and Suveen N. Mathaudhu, (TMS Proc. San Diego, CA, USA, February 27 – March 3, 2011) 249-253.
9. M. Nishijima, K. Hiraga, M. Yamasaki, Y. Kawamura, "Characterization of *β'* phase precipitates in an Mg-5 at% Gd alloy aged in a peak hardness condition," Materials Transactions 47(8), 2109-2112 (2006).

Magnesium Technology 2014
Edited by: Martyn Alderman, Michele V. Manuel, Norbert Hort, and Neale R. Neelameggham
TMS (The Minerals, Metals & Materials Society), 2014

A NUMERICAL AND EXPERIMENTAL STUDY OF FLOW BEHAVIOR IN HIGH PRESSURE DIE CASTING

Mahdi Saeedipour[1], Simon Schneiderbauer[1], Stefan Pirker[1], Salar Bozorgi[2]

[1]Department of Particulate Flow Modelling, Johannes Kepler University, Altenbergerstrasse 69, Linz, 4040, Austria
[2]LKR Leichtmetallkompetenzzentrum Ranshoden GmbH, Austrian Institute of Technology, Ranshofen, 5282, Austria

Keywords: High pressure Die casting (HPDC), Turbulent breakup, Eulerian-Lagrangian approach, Volume of fluid method (VOF), Water analogy experiment.

Abstract

High pressure die casting (HPDC) is one of the most important and yet little known manufacturing methods especially during liquid metal injection and filling phase. During its application different problems can arise: on the one hand, wavy disintegration of the jet might result in cold shut defect in the final product, on the other hand a high degree of atomization may strongly increase the porosity defect. A numerical simulation using volume of fluid approach (VOF), is carried out to model the global spreading of liquid metal jet. The formation of droplets, which are usually smaller than the grid spacing in computational domain, is determined by a surface energy-based criterion. An Eulerian-Lagrangian framework is introduced to track and model the droplets after formation. Since liquid metal is hardly to access, we performed experiments based on water analogy to capture the flow regime changes and drop formation. The comparison between numerical results and experiments shows a very good agreement.

Introduction

The high pressure die casting (HPDC) process is widely used for mass production of components based on aluminum, magnesium or zinc alloys. In high pressure die casting liquid metal is injected into the die at high speed (30-100 m/s) and under high pressure through complex gate and runner systems [1]. Due to the turbulent nature of the flow, it may undergo severe instability, breakup or even atomization which culminate to one or more typical casting defects including gas porosity, cold shut, inclusion and shrinkage [2]. These phenomena give rise to fragmented flows during mold filling, such as droplet-like flows, which are believed to yield inherent porosity defects and typical skin micro structures in HPDC [3]. Several studies have been carried out to understand the physics of HPDC during injection, filling and solidification and to find out how to model, control and reduce the defects. Analytical studies of HPDC must include the investigation of different simultaneous physical phenomena, such as flow instability, free surface behavior, turbulence, primary breakup, secondary breakup and solidification. Moreover, HPDC has its own characteristics: high temperature, high velocity, high turbulence effects, high density ratio, high viscosity ratio and so on, which complicate the problem. Although the influence of process parameters on the physics of HPDC is not fully understood so far [4], from an analytical point of view, the typical multiphase flow with a highly turbulent behavior is the main specification of its filling process. Common phenomena are turbulent breakup, jet disintegration and atomization.

The numerical simulation of injection and filling of liquid metal in HPDC has been a challenging area of research for decades.

Probably the earliest scientific effort to directly consider HPDC was conducted in early 1990s by Hu et al. [5] in which a computer model has been developed to simulate the flow, heat transfer and solidification during pressure die casting simultaneously. Later on two main approaches became common: (I) the implementation of conventional VOF-based methods [6] of other casting methods to HPDC and (II) the application of new branches of numerical models by meshless methods [7]. In recent years, a computer simulation software for High pressure die casting of magnesium was developed at the university of Kentucky. It is based on VOF method and LES turbulence modelling and shows a good agreement with their experiments [3]. In 2008 Homayonifar et al. [8] modified a VOF-based algorithm by using a concentration transport equation for calculating the air porosity distribution due to microbubbles entrapment and a coupled VOF-Lagrangian method for filling and splashing in HPDC. Recently Li et al. [9] have developed a numerical method to predict the air entrapment defects in high pressure die casting. They applied VOF to track

the micro bubbles entrapped in the liquid metal and validated this model by both water analogy and X-ray in the real model. In 2012, Schneiderbauer et al. [4] simulated the HPDC process with special focus on injection and primary breakup of the free jet. Although the drop formation at the interface could not be captured by the numerical model, the global spreading of the free jet in the casting mold was pictured well.
From experimental viewpoint, it is difficult to perform experiments with molten aluminum in the lab, therefore an analogy was used to conduct measurements. Several investigations in die casting have been done using water analogy and here some recent works are introduced:

In 2008, Zamora and his colleagues started a water analogue experiment on porosity formation in HPDC during pre-injection phase [10]. Later on, in 2012, Schneiderbauer et al. [4], studied the flow and filling characteristics during injection of liquid aluminum in HPDC using water analogy to capture the free jet regime changes and jet breakup for different nozzle types and inlet velocities. However, water analogy can only be used to capture the flow regime changes and visualizing filling path, droplet formation and porosity formation. Thus the effect of high tempreature, heat transfer and solidification cannot be observed by water analogy.
In accordance with this brief introduction, most of works done on HPDC can be divided into three categories:

- Fluid dynamics and flow behavior
- Solidification and heat transfer
- Product qualification improvement

In present study, the focus is on the first group to understand the flow behavior and provide a strong basis for the other groups which are important with resepect to quality product, metalurgical issues, semi solidified particles in the flow field, heat trasfer and solidification front modelling.

Analytical investigation

Primary breakup of liquid jet and its secondary breakup called atomization occur due to instability. In other words, the growth of disturbances along with the jet would cause instability and breakup. It also implies two main instability theories: (I) the Rayleigh-Taylor instability which occurs at the interface of two fluids with different densities when the fluids move relative to each other. (II) the Kelvin-Helmholtz instability which occurs due to shear forces at the interface when two fluids move along each other with different velocities and small structures could be created by breakup. Based on these instabilities and the *Weber* and *Reynolds* numbers, the free jet instability and breakup could form four regimes as shown in figure 1:

- Rayleigh breakup regime
- First wind-induced regime
- Second wind-induced regime
- Atomization regime

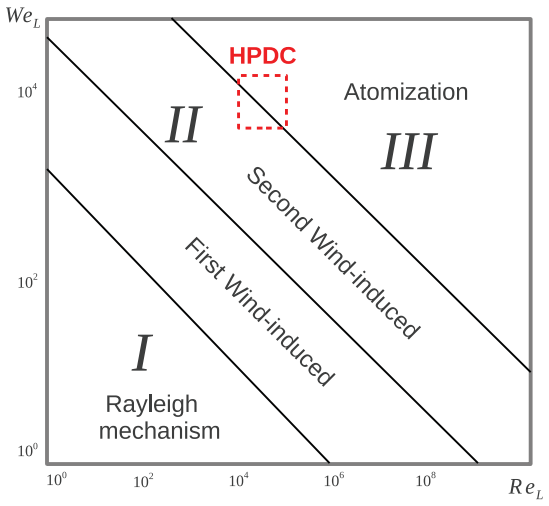


Figure 1: Breakup regimes for different dimensionless numbers and HPDC scope.

It can be deduced that the HPDC process seems to typically occur in a regime between second wind-induced regime and atomization based on the dimensionless numbers as shown in figure 1.

According to theoretical and experimental works carried out by Faeth et al. [12][13], primary breakup of turbulent liquid-gas multiphase flow with a density ratio greater than 500 is largely controlled by liquid turbulence properties with negligible aerodynamic effects at these conditions. Thus, both the onset of drop formation and drop properties after turbulent primary breakup could be studied by treating interactions between surface tension and liquid turbulence properties. The droplets which are formed at the onset of primary breakup are the smallest drops that can be formed by this turbulence-based mechanism. In [12], it is declared that the smallest drop can be formed in size comparable to characteristic eddy size l_i. The required energy for droplet formation includes the kinetic energy of an eddy of characteristic size relative to

its surroundings plus the added mechanical energy due to the pressure drop caused by acceleration of the surrounding gas over the tip of the perturbance, as illustrated in figure 2. For droplet formation, these sources of mechanical energy have to overcome the surface energy required to form a droplet, so the analytical criterion reads:

$$(\rho_f v_{li}^2 + C_{sa}\rho_g \overline{u}_o^2){l_i}^3 \geq C_{si}\sigma {l_i}^2 \quad (1)$$

where v_{li} is the velocity fluctuation perpendicular to main jet direction, C_{sa} and C_{si} are two emprical constants. l_i can be estimated by the Taylor microscale (λ). This is the largest length scale located in inertial subrange of turbulence energy cascade and is smaller than the largest eddies present in flow. The Taylor microscale is modeled by turbulent kinetic energy (k), viscosity (ν) and dissipation rate (ϵ) as follows:

$$l_i \simeq \lambda \simeq \sqrt{10\nu\frac{k}{\epsilon}} \quad (2)$$

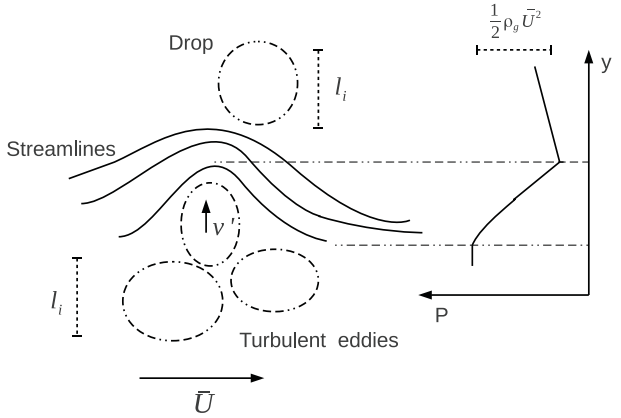


Figure 2: Sketch of turbulent primary breakup mechanism. [12]

Numerical modelling

As discussed in the last section, HPDC is a challenging process to simulate because it has several simultaneous sub-processes with different time and length scales. Effectual knowledge about modelling the following aspects is crucial to successfully conducting numerical simulation:

- Flow instability, breakup and atomization
- Turbulence
- Multiphase flow
- Air entrainment and porosity formation

The analytical criterion reveals this main idea that droplet formation in the HPDC occurs as a consequence of the deformation of the interface by strong vortices in the liquid metal flow and the turbulence phenomenon plays the main role in numerical modelling of the whole process as a multiphase system.

VOF-based methods are very accurate when they come to multiphase flow modelling and simulation of liquid jet breakup but they fail as soon as liquid structures smaller than the grid size come into play. The description of the liquid phase in Lagrangian framework is computationally more efficient than in the VOF-Eulerian framework.

The two-phase flow is governed by the incompressible Navier-Stokes equations with two-phase mixture assumption which are coupled with volume of fluid equation to capture the interface location.

$$\nabla . U = 0 \quad (3)$$

$$\frac{\partial \alpha}{\partial t} + \nabla .(\alpha U) = 0 \quad (4)$$

$$\frac{\partial \rho U}{\partial t} + \nabla .(\rho U \otimes U) = -\nabla p + \mu \nabla^2 U + \rho g - S_{st} \quad (5)$$

where α is the volume fraction and could be 0 or 1 at each phases and $0 < \alpha < 1$ at the interface. S_{st} is the surface tension term modeled as $S_{st} = \sigma\kappa\nabla\alpha$ where κ is the mean curvature of the free surface.

The physical properties are calculated as weighted averages based on the distrubution of the liquid volume fraction:

$$\rho = \rho_l \alpha + \rho_g (1 - \alpha) \quad (6)$$

$$\mu = \mu_l \alpha + \mu_g (1 - \alpha) \quad (7)$$

$$U = \alpha U_l + (1 - \alpha) U_g \quad (8)$$

In addition the mechanism of Eulerian-Lagrangian coupling is inspired from two related works by Tomar et al. [15] and and Vallier et al. [16] and implementated in this problem by adding mass, VOF and momentum source terms to the equation sets as follows:

$$\nabla . U = S_m \quad (9)$$

$$\frac{\partial \alpha}{\partial t} + \nabla .(\alpha U_l) + \nabla .[\alpha(1 - \alpha) U_r] = S_\alpha \quad (10)$$

$$\frac{\partial \rho U}{\partial t} + \nabla.(\rho U \otimes U) = -\nabla p + \mu \nabla^2 U + \rho g - S_{st} + S_P \quad (11)$$

where S_m, S_α and S_P are the source terms due to the effects of Lagrangian droplets on continiuty, VOF and momentum equations, respectively.

The solution procedure is implemented in OpenFOAM [14] using its open source libraries. A VOF-solver is combined with a generic turbulence model to calculate the volume averaged Navier-Stokes equations. The generation of droplets is predicted using the analytical drop formation criterion.

If this criterion is satisfied in an specific cell, a droplet is released at that position of the computational domain relative to the local properties of the cell. The released droplets are then considered as Lagrangian droplets and their mass and momentum are subtracted from the governing equations via source terms.

In a Lagrangian approach, each particle position vector x_p is calculated from equation (12) and its motion is governed by Newton's second law as shown in equation (13), where the F vector is the representative of all froces acting on a particle in particulate flows such as drag, lift, buoyancy, etc.

$$\frac{dx_P}{dt} = U_P \quad (12)$$

$$m_P \frac{dU_P}{dt} = \Sigma F \quad (13)$$

In the present work, the mass of each Lagrangian droplet m_P is calculated from its density and volume. The volume of droplets directly come from the VOF in the cells near the interface and the amount of liquid subtracted from the cell. The motion of representative droplets is highly dependent on the momentum source term S_P which is modeled based on the description in [16].

Experimental studies

According to the dimensional analysis for the water analogy experiment, the injection of water provides a model to study the filling, breakup and atomization process of molten aluminum, if the dimensionless numbers of the flow are the same as in the real HPDC process. By considering $Re_1 = Re_2$ and $We_1 = We_2$ as the main basis of this analogy (subscripts 1 and 2 denote the real and analogue models, respectively.), the following relations between length scale, the velocity in the real model (liquid aluminum) and in the analogue model (water) are derived:

$$\frac{L_2}{L_1} = \left(\frac{\rho_1}{\rho_2}\right)\left(\frac{\sigma_1}{\sigma_2}\right)\left(\frac{\mu_2}{\mu_1}\right)^2 \quad (14)$$

$$\frac{U_2}{U_1} = \left(\frac{\sigma_2}{\sigma_1}\right)\left(\frac{\mu_1}{\mu_2}\right) \quad (15)$$

Table 1: The ratios of length scale, velocity and flow rate for the analogue model at different temperatures of water [SI units]

$T\ ^oC$	$\rho \times 10^3$	$\mu \times 10^{-4}$	$\sigma \times 10^{-2}$	$\frac{L_2}{L_1}$	$\frac{U_2}{U_1}$	$\frac{Q_2}{Q_1}$
10	1	13.1	7.42	32.901	0.078	84.433
20	0.998	10	7.28	19.58	0.101	38.721
30	0.996	7.98	7.12	12.774	0.123	20.071
40	0.992	6.53	6.96	8.786	0.147	11.347
50	0.988	5.47	6.79	6.345	0.172	6.925
60	0.993	4.67	6.62	4.768	0.196	4.456
70	0.978	4.04	6.44	3.686	0.22	2.989
80	0.972	3.55	6.26	2.946	0.244	2.118
90	0.962	3.14	6.08	2.398	0.268	1.541

The physical properties of water are temperature-dependent. In Table 1, analogy parameters are calculated for 10 different water temperatures. It seems hot water at 90 ^oC is the best candidate to represent the We and Re of the aluminum injection process with lower range of injection velocities and without a huge difference in flow rate.

By considering the nozzle inlet length scale as $10^{-3}m$ in the actual process, and high pressure die casting scope in flow instability diagram in Figure 1, two sets of test cases for both aluminum and hot water are considered in Tables 2 and 3. The settings in the considered cases agree with the properties of the fluid in the HPDC process.

Table 2: Test cases of real model with liquid aluminium.

$Case$	$U(\frac{m}{s})$	$d(m)$	Re	We
1	35	0.001	86041.7	4163.3
2	45	0.001	110625	6882.2
3	55	0.001	135208.4	10280.8
4	65	0.001	159791.7	14359.2
5	75	0.001	184375	19117.2

A test bench is built in our laboratory to study the prevailing fluid dynamical regime of the incoming jet by appropriate measurement systems. The idea of heating the water inside the buck vessel is implemented by using a heating element and a power control unit to avoid temperature loss during experiment as shown in Figure 3. A U-shaped profile made from Acrylic glass (length ×

Table 3: Test cases of analogue model with hot water.

$Case$	$U(\frac{m}{s})$	$d(m)$	Re	We
1	9.345	0.003	86212.4	4162.7
2	12.015	0.003	110844.5	6881.1
3	14.685	0.003	135476.6	10279.2
4	17.355	0.003	160108.6	14357
5	20.025	0.003	184740.7	19114.3

height × depth = 20 × 10 × 5 cm) is considered as the casting mold. This is also applicable for further studies on HPDC including impingement and rapid solidification.

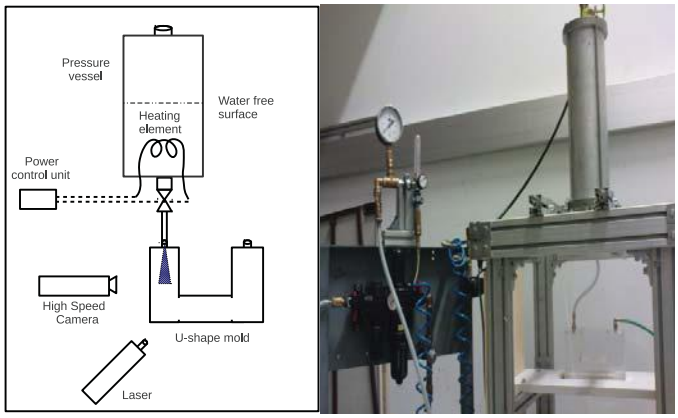


Figure 3: Experimental setup for water analogy experiment.

Results and discussion

For numerical simulation of high pressure die casting, a finite volume-based solver is developed within the framework of OpenFOAM. It is used to solve three dimensional Navier-Stokes equations coupled with VOF equation to capture the interface behavior as described in numerical section. The pressure-velocity coupling is carried out with PIMPLE algorithm and for turbulence modelling, a realizable $k-\epsilon$ model is implemented based on the result of [4], in which Reynolds-averaged Navier Stokes (RANS) models are shown sufficient to study the influence of the main process parameters of HPDC. The drop formation criterion is evaluated every time step to initiate an Eulerian-Lagrangian coupling. The droplets near the interface are usually one order of magnitude smaller than feasible grid spacings and their formation and movement are captured in a Lagrangian approach. A 3D geometry of a U-shaped mold is created and a computational grid is generated with the grid spacing in the order of magnitude of 10^{-3} m. The numerical simulations are performed on cases 3 and 5 of Table 3 which are located in the HPDC scope regarding their Re and We.

A hot water experiment with inlet velocities $15m/s$ and $20m/s$ are performed to obtain validation data. The whole injection process is captured by a high speed camera located perpendicular to the U-shaped mold. As shown in Figure 4 for both cases, surface instabilities can be depicted as well as the droplet formation due to primary breakup in numerical simulation. Droplet diameters are one order of magnitude smaller than grid spacing. In the case 3 with lower inlet velocity, the small droplets in the order of magnitude of 10^{-4} m are generated near the tip of jet. As inlet velocity increases in the case 5, the number of Lagrangian droplets increases as a result of more fluctuations. Although an appropriate turbulence modelling for this process is still crucial and more advanced experiments are required, this modelling is in well-qualified agreement with the experimental cases.

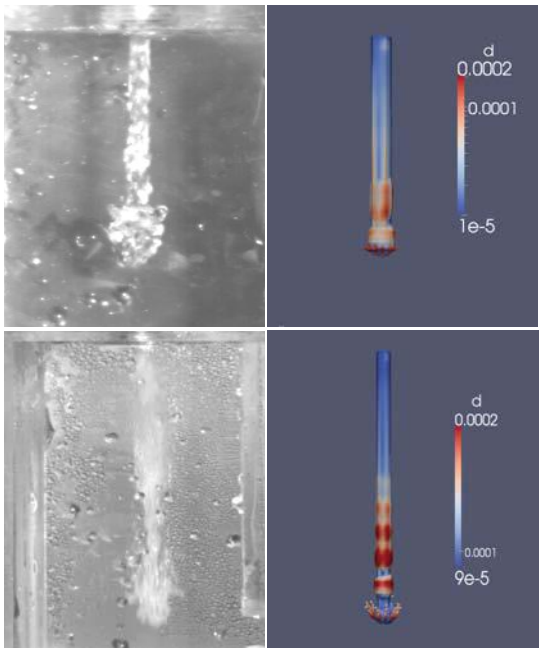


Figure 4: Numerical and experimental studies on two cases in HPDC scope: $U_i = 15m/s$ (top) and $U_i = 20m/s$ (bottom) at $t = 3.5$ ms.

Conclusion

In this paper, the high pressure die casting flow characteristics during injection of liquid metal have been studied by considering an analytical study leading to a new approach

of numerical modelling. Experimental studies have been conducted, taking advantage of the water analogy.

In the analytical part an energy-based criterion from turbulent primary breakup of liquid jet was introduced and has been used as the basis of the Eulerian-Lagrangian model for the numerical simulation. A water analogue test bench was built to perform experiments for a better understanding of the flow field in real HPDC processes. The results of numerical and experimental studies show a good agreement in the injection phase; however applying more sophisticated turbulence models such as Reynolds stress model (RSM) which reveal better understanding of anisotropic fluctuations, could improve the results for both interface capturing and droplet formation. To conclude, this study introduces a new method for the numerical modelling of HPDC and could be a strong basis for future studies on the flow bahvior of HPDC specially regarding the heat transfer and solidification phenomena.

Acknowledgements

This work was funded by the Christian-Doppler Research Association, the Austrian Federal Ministry of Economy, Family and Youth, and the Austrian National Foundation for Research, Technology and Development. The authors also would like to thank for supporting the project MEEE-PRO-CAST in the framework of the EU-programme Regio 13 sponsored by the European Regional Development Fund (EFRE) and by the State of Upper Austria.

References

[1] P.W. Cleary et al., "3D SPH flow predictions and validation for high pressure die casting of automotive components," *Journal of Applied Mathematical Modelling,* 2006.

[2] E.J. Vinarick, *High Integrity Die Casting Processes* (John Wiley and Sons publication, 2003)

[3] K. Kuwana et al., "Assessment of Computer Simulation Software and Process Data for High Pressure Die Casting of Magnesium" (Report ORNL 0596, University of Kentucky, 2007).

[4] S. Schneiderbauer et al., "Studies on Flow Characteristics at High-Pressure Die-Casting", *IOP Conf. Series: Materials Science and Engineering*, 27, (2011).

[5] E.R.G. Eckert et al., "A complete solution for the flow, heat transfer, solidification and porosity distribution in pressure die casting" (Report UMSI 92/56, University of Minnesota Supercomputer Institute Research report, 1992).

[6] C.W. Hirt et al., "SOLA-VOF: A solution algorithm for transient fluid flow with multiple free boundaries" (Technical report LA-8355 UC-32 and UC-34, Los Alamos national laboratory, 1980).

[7] P.W. Cleary and J. Ha, "Three Dimensional Modelling of High Pressure Die Casting",(Paper presented in Second International Conference on CFD in the Minerals and Process Industries CSIRO, Melbourne, Australia, 6-8 December 1999).

[8] P. Homayounifar et al., "Numerical modelling of splashing and air entrapment in high-pressure die casting", *Int. Journal of Advanced Manufacturing Technology*, 39 (2008).

[9] M. Li et al., "Numerical simulation of flow-induced air entrapment defects in the high pressure die casting process",(Paper presented in TMS conference, 2010).

[10] R. Zamora et al., "Experimental Investigation of Porosity Formation During the Slow Injection Phase in High-Pressure Die-Casting Processes" *Journal of Manufacturing Science and Engineering*, 130 (2008).

[11] W.A. Sirignano and C. Mehring, "Review of theory of distortion and disintegration of liquid streams", *Prog. Energy Combust. Sci.*, 26 (2000).

[12] M. Faeth et al., "Aerodynamic effects on primary breakup of turbulent liquid," *AIAA Journal* (1993).

[13] K.A. Sallam et al., "Liquid breakup at the surface of turbulent round liquid jets in still gases," *International Journal of Multiphase Flow*, 28 (2002).

[14] OpenFOAM, The Open Source CFD Toolbox, User Guide, Version 2.2.0, February 2013. http://www.openfoam.org.

[15] G. Tomar et al., "Multiscale simulations of primary atomization ," *Computers and Fluids*, 39 (2010).

[16] A. Vallier et al., "Procedure for the break-up of cavitation sheet", (Paper presented in 4th International Meeting on Cavitation and Dynamic Problems in Hydraulic Machinery and Systems , Belgerad, Serbia, 26-28 October 2011).

Magnesium Technology 2014
Edited by: Martyn Alderman, Michele V. Manuel, Norbert Hort, and Neale R. Neelameggham
TMS (The Minerals, Metals & Materials Society), 2014

In Situ Synchrotron Radiation Diffraction during Melting and Solidification of Mg-Al Alloys Containing CaO

B. Wiese[1], C. L. Mendis[1], D. Tolnai[1], G. Szakács[1], A. Stark[1], N. Schell[1], H. P. Reichel[2], R. Brückner[2], K. U. Kainer[1], N. Hort[1]
[1]Institute of Materials Research, Helmholtz-Zentrum Geesthacht, Max-Planck-Straße 1,
D-21502 Geesthacht, Germany
[2]LMpv Leichtmetall - Produktion & Verarbeitung GmbH, Einsteinstraße 4,
D-06785 Oranienbaum, Germany

Keywords: magnesium alloy, *in situ*, diffraction, CaO, intermetallic phases

Abstract

Previous investigations show that CaO additions have an effect on the microstructure and mechanical properties of commercial Mg alloys. Addition of CaO to pure Mg and Mg alloys results in the dispersion of Ca in the molten and solid Mg with no evidence of CaO. This paper reports on the reactions between Mg, Al and CaO measured by means of *in situ* synchrotron radiation diffraction during melting and solidification. The experiment was conducted on Mg-3Al wt% with CaO concentrations between 3 wt% and 10 wt% to study the effect of different Al:CaO ratios. The initial sample contained Mg, Al and CaO in powder state, pressed to cylindrical samples. The melting, the solidification and associated phase transformations were measured in a Bähr 805A/D dilatometer inside a sealed stainless steel crucible at the High Energy Materials Science Beamline P07 at PETRA III, DESY.

Introduction

An understanding of the interaction between Mg-Al and CaO is important for determining the mechanical- and corrosion properties of the newly developed ECO (Environment COnscious magnesium) Mg alloys [1]. In previous studies, conducted on CaO additions to pure Mg [2] and Mg alloys [1-4] it was found that CaO is dispersed in Mg and Mg alloys. The contribution by Lee *et al* [1-3] reports that CaO increases the ignition resistance of Mg and Mg alloys. The influence of CaO is similar to that of alloying with Ca as shown by B.-S. You *et al.* [5]. This can be used to replace active shielding components in the shielding gas, like SF_6 or HFC with a high greenhouse warming potential, in the casting process. However, CaO dissolves in Mg and form Mg_2Ca Laves (C14) [2] and in Mg-Al alloys Mg_2Al Laves phase (C15) [1-4].

However, according to the Ellingham diagrams, developed only for binary reactions without any enthalpy of mixtures, CaO expected to be more stable than MgO [6]. It was reported [11, 12] that the C36 type $(Al,Mg)_2Ca$ Laves phases forms in the Mg-Al-Ca system and this phases is also possible to be observed in Mg-Al alloys containing CaO. Kondoh *et al.* [4] calculated the standard Gibbs free energy for the reaction between pure Mg/Mg-Al alloys and CaO. The thermodynamic hypothesis shows a decrease of the standard Gibbs free energy for the disassociation of CaO and the formation of Al_2Ca Laves phase [4]. It is necessary to understand the reactions between Mg-Al and CaO in the liquid state to elucidate the thermodynamic reasons behind the disassociation of CaO. Therefore, it is important to determine which phases are present in the melt, during solidification and to follow the disassociation of CaO in Mg-Al alloys. This knowledge on the interaction between Mg-Al alloys and CaO provides also the possibility to use CaO in lieu thereof Ca for a cost effective alloying of Mg alloys. This paper investigates the reactions between Mg, Al and CaO by means of *in situ* synchrotron diffraction during melting and solidification. The benefits of using the synchrotron radiation for diffraction in these *in situ* measurements include the short acquisition time with a beam energy of 100 keV and the higher resolution [7].

Experimental Procedure

Sample production

The samples were prepared from pure powders of Al, Mg and CaO. The powders were mixed so the composition was close Mg-3 wt% Al alloy with 3, 6 and 10 wt.% CaO. The atomic ratio between Al:Ca are selected to 2:1, 1:1 and 1:2. The phase diagram is shown in Figure 1. The Mg powder was gas-atomised with a size of <75 nm (99.8 %) produced by SFM SA and the Al powder is gas-atomised powder with a max. size of 325 nm (99,5 %) obtained by Alfa Aesar. The CaO are produced by CARL ROTH with a purity of 96 %. The powders were mixed with the described concentrations and uniaxially pressed with a pressure of 100 MPa at room temperature (RT) in to cylinders with a diameter of 4.2 mm (holding time 1 min).

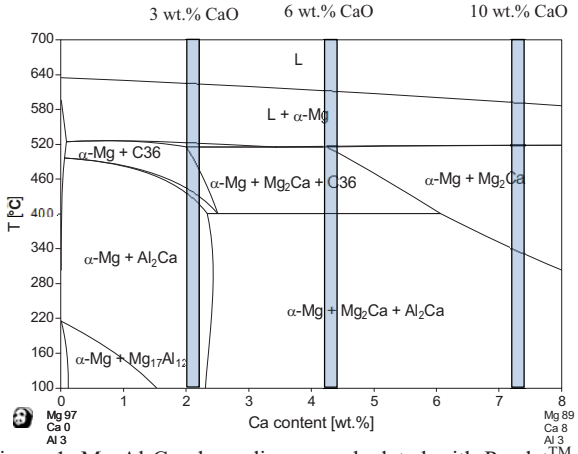


Figure 1. Mg-Al-Ca phase diagram calculated with Pandat^{TM} 8.1 software with PanMagnesium 8 database.

In situ measurement setup and evaluation

The measurements were conducted at the P07 (High Energy Materials Science) beamline of PETRA III (Deutsches Elektronen-Synchrotron), with a beam energy of 100 keV (λ = 0.0124 nm) and a beam cross section of 1 × 1 mm^2. The heating and cooling was carried out using the induction coil of a Bähr

805A/D dilatometer modified for *in situ* synchrotron radiation measurements, with two windows on the sides of the dilatometer chamber covered by Kapton foils, to prevent interaction with the X-ray beam [7,8]. The samples were heated in an Ar atmosphere to 450 °C at a rate of 20 $Kmin^{-1}$, then to 700 °C at a rate of 10 $Kmin^{-1}$. The samples were held at 700 °C for 5 min to ensure melt homogeneity, and then cooled at a rate of 10 $Kmin^{-1}$ to 450 °C (fully solidified state) before air-cooling to room temperature. The temperature was controlled by a type S thermocouple welded on a stainless steel crucible (ME-00029990 from METTLER-TOLEDO) containing the sample. The two dimensional (2D) diffraction patterns were recorded every 6 s with an acquisition time of 3 s using a Perkin Elmer XRD 1622 Flat-panel with a sample-to-detector-distance of 1745.6 mm. Conventional X-ray line profiles were obtained by azimuthal integration through 360° with FIT2D V12.077 software. For phase identification simulated line profiles were generated with CaRIne 3.1 Crystallography™ with crystal structure data from Pearson's Crystal Data [9].

Microstructure investigations

The specimens for scanning electron microscopy (SEM) were prepared by grinding with SiC paper to 2500 grit, polished with 3 µm diamond paste followed by a mixture of 1 µm diamond and OPS™ anhydrous suspension. Microstructures were investigated using a ZEISS, ULTRAT M 55 SEM operating at 15 kV equipped with an EDAX energy-dispersive X-ray spectrometer (EDXS) and local compositions determined by point analysis. Compositional maps of selected regions were generated with a scan rate of 9000 µs per pixel.

Results and Discussion

In situ measurement

The evaluation of the phase formation is shown in Table 1. This Table shows the temperatures at which the evaluated phases are first detected. Figure 2 shows the 2D diffraction patterns of the Mg3Al6CaO sample at four different states. In this experiment in all patterns the main reflections of the steel crucible are present. Figure 2a is the 2D diffraction pattern of the sample at RT at the start with the reflections from Mg, Al, CaO and $Ca[OH]_2$. The reason for the $Ca[OH]_2$ reflections is that CaO is hydrophilic and forms hydroxide. During the heating $Ca[OH]_2$ started decomposing at 402 °C and disappears at 448 °C. In this measurements $Ca[OH]_2$ decompose 178°C earlier than that reported in [10] (580 °C). It is possible that pure Mg or Al decrease the decomposition temperature of $Ca[OH]_2$. The reflection of Al disappears at 405°C and Mg begins to melt at 596 °C. After melting of Mg and Al only the oxide peaks of MgO and CaO can observed. The first MgO peak appears at 402°C with the decrease of the intensity of the CaO peaks. In the molten state a hump is visible from the molten background of Mg, Figure 2b.

Below the solidification temperature the first Mg peaks appear at 586°C. The semi-solid state is shown in Figure 2c at 550°C with the peaks from the growing Mg grains, MgO and Mg_2Ca. Below the eutectic temperature at 497°C 3 new phases appear in the diffraction patterns Mg_2Ca, Al_2O_3 and $MgCa_2Al_2$. After the end of solidification, only the shift of the peaks was visible due to the different thermal expansion coefficients. A significant difference can be seen in the movement of the peaks between the metallic phase and the oxide phase. For example, the peaks of Mg and MgO overlap in the semi-solid state and after complete solidification the peaks are separated (Figure 2c and d). The diffraction pattern in Figure 2d shows the solidified alloy at RT. The reaction during melting and solidification for the Mg3Al3CaO and Mg3Al10CaO is similar to the Mg3Al6CaO, Table 1. The temperature for the start of solidification decrease with an increased CaO and the eutectic reaction changes from $(Al,Mg)_2Ca$ Laves phase in Mg3Al6CaO to the formation of Mg_2Ca Laves phase in Mg3Al3CaO. This change of the phase transformation is related to the higher amount of Ca from the dissolving of CaO. In the ternary phase diagram of Mg-Al-Ca different phase regions were observed with the increase in Ca [11, 12]. Figure 3 shows the synchrotron diffraction line profiles from prior to and after the experiment, respectively for Mg3Al3CaO and Mg3Al10CaO. This relation between the Laves phases with the changes in Ca concentration was not investigated in prior investigations [1-4] only lower CaO concentrations compared with the amount of Al. This means that all Ca can form Al_2Ca. In this report the Ca concentration of Mg3Al6CaO and Mg3Al10CaO are high and the Al_2Ca Laves phase does not form. In the Mg3Al3CaO sample, which contains the highest concentration of Al, a small amount of Al_2O_3 and $(Al,Mg)_2Ca$ phases form.

Table 1. Phase formation temperatures of the 3 alloys investigated.

Reaction	Mg3Al 3CaO	Mg3Al 6CaO	Mg3Al 10CaO
Start of decomposition Ca[OH]2	412	402	397
End of decomposition Ca[OH]2	423	448	460
Disappearance of Al	404	405	405
appearing melt	595	596	591
start of decomposition CaO	599	610	600
Appearing MgO	-	402	405
Start of solidification α-Mg	609	586	573
Formation of $(Al,Mg)_2Ca$	519	-	-
Formation of Mg_2Ca	-	497	502
Formation of $MgCa_2Al_2$	519	502	502
Formation of Al_2O_3	-	498	502
Measuring accuracy	±2		
	Temperature [°C]		

Microstructure

The microstructure of samples used during the *in situ* diffraction measurement is shown for the Mg3Al6CaO in Figure 4. This Figure shows 3 different areas with different concentrations of the alloying elements, respectively. The main area is pure Mg, followed by an eutectic area with Mg, Al and Ca and an area with a high oxygen concentration between the metallic areas. The metallic areas remain with a spherical shape (starting powder is spherical) due to the oxide layer that forms during the gas-atomising process.

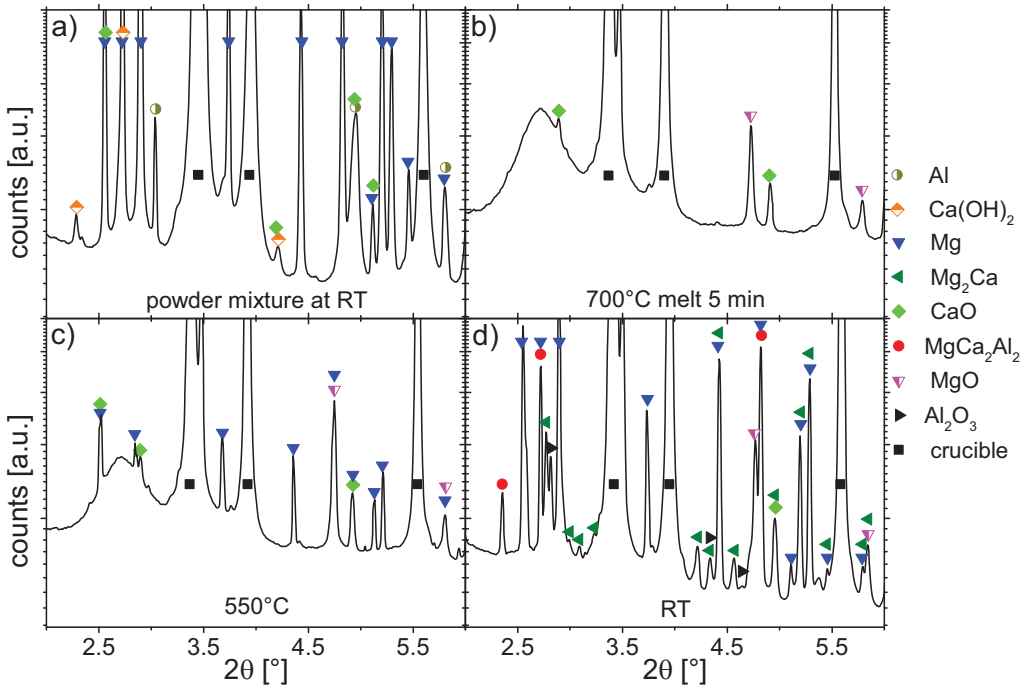


Figure 2. 2D diffraction patterns of Mg6Al6CaO a) as prepared powder mixture at room temperature b) melt at 700°C after 5 min holding, c) semi-solid state at 550°C and d) solidified sample at room temperature.

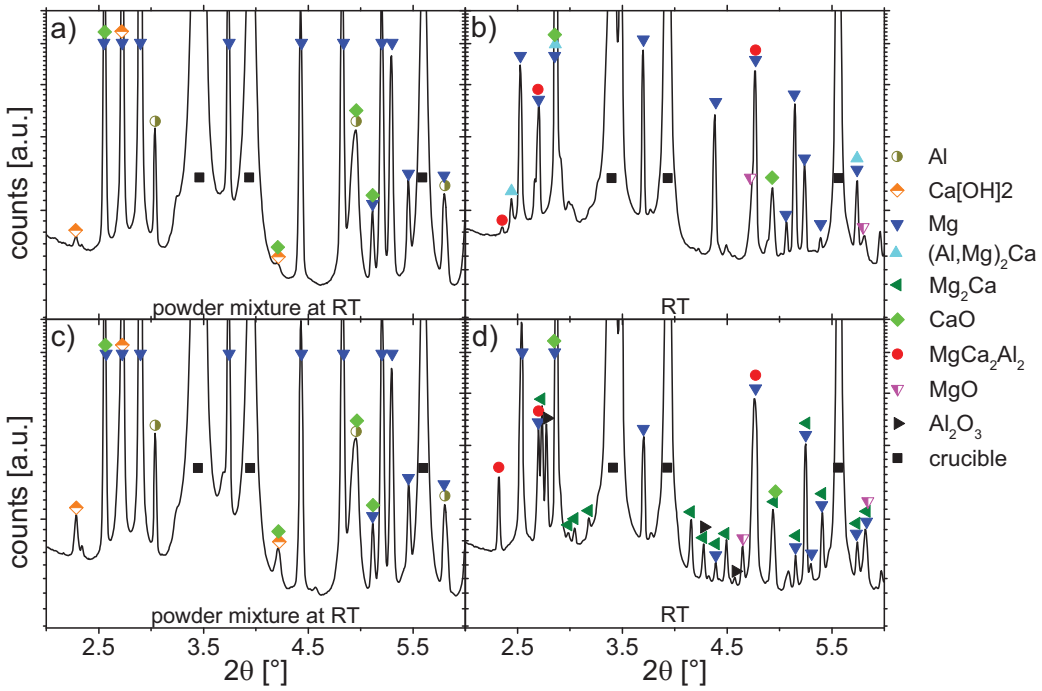


Figure 3. 2D diffraction patterns of Mg6Al3CaO a) the powder mixture at room temperature and b) solidified sample at room temperature and, Mg6Al10CaO c) start condition: powder mixture at room temperature and d) solidified sample at room temperature.

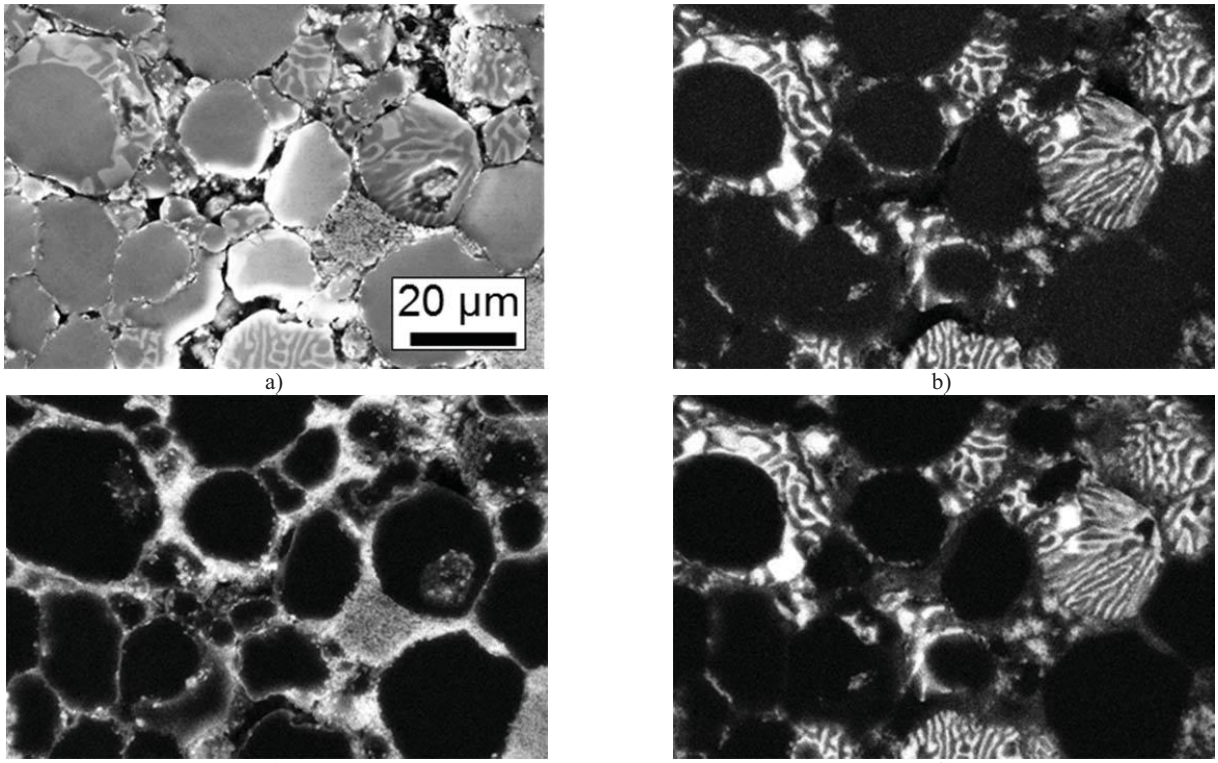


Figure 4**.** **S**canning electron micrograph of the powder area of Mg3Al6CaO: a) SE image: EDX maps recorded from b) Al c) O and d) Ca in the same region.

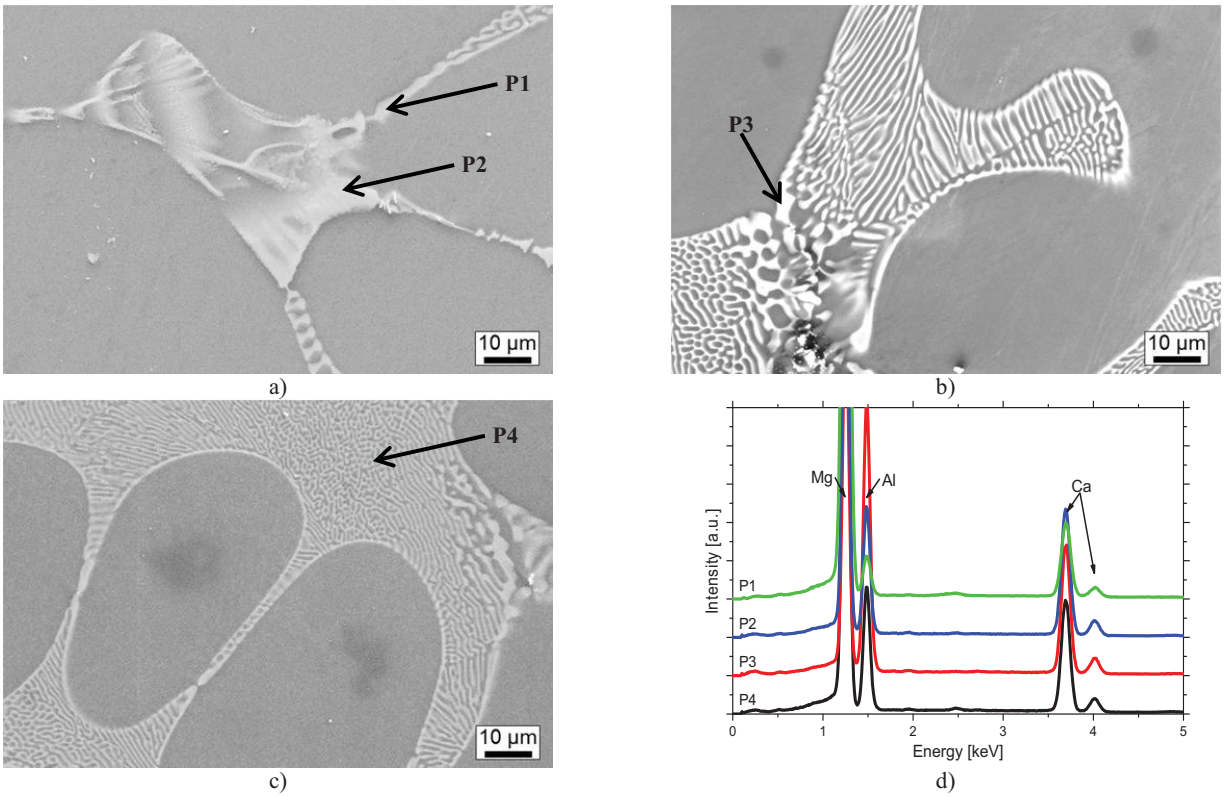


Figure 5. Scanning electron micrographs of a) Mg3Al3CaO, b) Mg3Al6CaO, c) Mg3Al10CaO with EDX-point measurements and d) EDX-Points.

Some of the Mg and Al powder particles react with the CaO and form the eutectic areas. In these areas no oxygen can be determined because the CaO was reduced by Mg and Al. The reduction process forms the O rich areas with mainly MgO, with a small amount of Al_2O_3 and some retained CaO. The phases Mg_2Ca and $MgCa_2Al_2$ are located in the eutectic areas with lamellar eutectic structure.

Table 2. Chemical analysis of the powder areas and the separated molten areas form the 3 alloys with EDX measurements from different regions of the samples.

Area	Ele-ment	Mg3Al3CaO	Mg3Al6CaO	Mg3Al10CaO
Powder [wt.%]	Mg	88.9	75.4	-
	Al	2.6	3.2	-
	Ca	1.4	1.2	-
	O	6.3	4.8	-
Molten [wt.%]	Mg	87.8	87.3	91.6
	Al	5.9	4.7	2.5
	Ca	5.5	7.3	5.2
	O	0.8	0.7	0.7

In all the alloys the fully molten metal was found at the bottom of the crucibles. The composition of this separated molten area (Figure 5) compared to the powder area is shown in Table 2. In the case of sample Mg3Al10CaO, the preparation from the powder range was not possible. This area crumbled and the powder lost during grinding due to the high oxide content from 10 wt.% CaO. The difference between the molten areas and the powder areas is a higher concentration of oxygen in the powder areas. The reason for the higher amount of O in the powder areas is the formation of MgO and Al_2O_3 from the reduction of CaO and the presence of unreacted CaO. The retained oxide in the powder areas leads to a low content of O in the molten area. This leads to an inhomogeneous distribution of all elements. Figure 5 shows the difference between the alloys with different CaO contents in the molten area.

All the samples show an eutectic regions between Mg grains as shown in Figure 5a-b. With the increased CaO the fraction the eutectic area increases. The EDX investigation for the phases in the eutectic areas is shown in Figure 5d. In Table 2 shows that with a higher CaO concentration the amount of Al decreased in the molten area, and an increased amount of Al_2O_3 was observed. This is also visible in Figure 2d and Figure 3and d with an increased Al_2O_3 peak. The eutectic region shows also a phase formation of an Mg, Al and Ca rich phases. The EDX investigations show in the Mg3Al3CaO sample two regions. At P2 the measurements show double the amount of atomic Al than Ca which indicates the Al_2Ca Laves phase. At P1 with a similar atomic concentration of Al and Ca it indicates the $(Al,Mg)_2Ca$ Laves phase. The Mg3Al samples with 6 (P3) and 10 (P4) wt.% CaO show only one precipitation with an equal concentration of the elements. In Mg3Al6CaO the atomic ration 1:1 of Al:Ca indicates the Laves phase $(Al,Mg)_2Ca$. The low Al concentration leads in the Mg3Al10CaO sample to a formation of a $(Al,Mg)_2Ca$ with an atomic ration 1:2 of Al:Ca.

Conclusions

From the results the following conclusions can be drawn:

- CaO dissolves in Mg3Al alloy and forms Laves phases.
- Change in ratio between Al and Ca changes the intermetallic phases:
  - 2:1 $(Mg,Al)_2Ca$
  - 1:1 $Mg_2Ca + MgCa_2Al_2$
  - 1:2 $Mg_2Ca + MgCa_2Al_2$
- The samples with a high CaO content, Mg3Al with 6 and 10 wt.% CaO, forms the aluminium oxide Al_2O_3. and in the same time the amount of Al in the separated molten areas decreases.
- The change of the Al concentration in the separated molten areas change the phase formation from Al_2Ca with the low CaO concentration to an formation of $(Al,Mg)_2Ca$ with an content of Mg.

Acknowledgment

The authors acknowledge the Deutsches Elektronen-Synchrotron (DESY) for the provision of synchrotron radiation facilities in the framework of the proposal I-20120743 and also the funding of the project by the Federal Ministry of Economics and Technology (BMWi, grant number 20K1107B).

References

1. J.-K. Lee, and S. K. Kim, “Effect of CaO Addition on the Ignition Resistance of Mg-Al Alloys,” *Mater. T. JIM.,* 52 (2011) 1483-1488.
2. S.-H. Ha, J.-K. Lee, and S. K. Kim, “Effect of CaO on Oxidation Resistance and Microstructure of Pure Mg,” *Mater. T. JIM.,* 49 (2008) 1081-1083.
3. J.-K. Lee, and S. K. Kim, “Effect of CaO composition on oxidation and burning behaviors of AM50 Mg alloy,” *Trans. Nonferrous Met. Soc. China,* 21 (2011) 23-27.
4. K. Kondoh, et al., “Thermo-dynamic analysis on solid-state reduction of CaO particles dispersed in Mg–Al alloy,” *Mater. Chem. Phys.,* 129 (2011) 631-640.
5. B.-S. You, W.-W. Park, and I.-S. Chung, “The effect of calcium additions on the oxidation behavior in magnesium alloys,” *Scripta Mater.,* 42 (2000) 1089-1094.
6. I. Brain, and O. Knacke, *Thermochemical Properties of Inorganic Substances*, (Berlin, New York: Springer-Verlag, 1973)
7. P. Staron, et al., “ In Situ Experiments with Synchrotron High-Energy X-Rays and Neutrons,” *Adv. Eng. Mat.*, 13 (2011) 658-663.
8. D. Tolnai, et al., “In situ synchrotron diffraction of the solidification of Mg4Y3Nd,” *Mater. Lett.,* 102-103 (2013) 62-64.
9. P. Villars, and K. Cenzual, Pearson's *Crystal Data - Crystal Structure Database for Inorganic Compounds (on CD-ROM)*, (Ohio: ASM International, Materials Park, USA, Release 2012)
10. MSDS Number: C0407, Material safety data sheet, Avantor Performance Materials, http://www.avantormaterials.com/ (2009)
11. A. Janz, et al., “Thermodynamic modeling of the Mg–Al–Ca system,” *Acta Materialia*, 57 (2009), 682-694.
12. H. Cao, et al., “Experiments coupled with modeling to establish the Mg-rich phase equilibria of Mg–Al–Ca,” *Acta Materialia*, 56 (2008), 5245-5254.

Magnesium Technology 2014
Edited by: Martyn Alderman, Michele V. Manuel, Norbert Hort, and Neale R. Neelameggham
TMS (The Minerals, Metals & Materials Society), 2014

SOLIDIFICATION CHARACTERISTICS OF WROUGHT MAGNESIUM ALLOYS CONTAINING RARE EARTH METALS

A. Javaid[1], F. Czerwinski[1], R. Zavadil[1], M. Aniolek[1] and A. Hadadzadeh[2]
[1]CanmetMATERIALS, Natural Resources Canada, 183 Longwood Road South, Hamilton, Ontario, L8P 0A5, Canada
[2]University of Waterloo, 200 University Avenue West, Waterloo, Ontario, N2L 3G1, Canada

Keywords: wrought magnesium alloys, rare earths, solidification, microstructure

Abstract

A significant barrier preventing use of magnesium sheet in automotive light-weighting initiatives is its high manufacturing cost and very limited formability at room temperature. This barrier can be overcome by the use of twin roll casting technology and new magnesium alloys, specifically designed for twin roll casting. Recent studies have shown that magnesium, when alloyed with rare earth elements, gave rise to weakening of the basal texture resulting in improved room temperature formability. In this research, a combination of calculations using the FACTsage software and examinations using a number of experimental techniques was explored to determine the solidification characteristics of wrought magnesium alloys containing rare earth metal of neodymium: ZEK100, Mg-1Zn-0.5Nd and Mg-1Zn-1Nd. As predicted by the FACTsage software, the solidification under equilibrium and non-equilibrium conditions affects the type and volume fractions of phases formed for a given chemical composition of the alloy. The thermal analysis identified temperatures of metallurgical reactions taking place during solidification and their changes with neodymium content. As verified by controlled solidification experiments the cooling rate during solidification affected the refinement level of the alloy microstructure, a volume fraction of intermetallic precipitates and their distribution. This research will help to design new magnesium alloys, specifically optimized for twin roll casting.

Introduction

Twin roll continuous casting (TRC), also known as twin roll strip casting, combines casting and rolling into a single step operation, thus reducing the manufacturing cycle time, energy, pollutant emission and final cost. Although the TRC technique was successfully used for aluminum strip production for decades, its application for magnesium is difficult. The lack of substantial progress is related, in part, to inherent characteristics of magnesium itself, such as its high reactivity to oxygen, causing surface oxidation and requiring protective gases or low specific heat, leading to difficulties with temperature control. Another obstacle relates to presently available magnesium alloys, having mostly wide solidification ranges and causing a formation of casting defects.

There is a general consensus that high solidification rates, experienced during TRC, have positive effects on the strip microstructure and resultant properties. It has been reported that the near-rapid solidification, achieved through cooling rates ranging from 10^2 to 10^3 ^{o}C/s, can potentially improve alloy properties by enhancing the homogeneity of microstructures, especially minimizing the size of manganese-rich particles, refining grain size, reducing chemical segregation, increasing solid solubility and enhancing precipitate nucleation within the matrix [1,2]. According to Ref. [2,3], the near-rapid solidification in TRC requires a design of new alloys that take an advantage of the increased amount of a solute in α-Mg solid solution, thus resulting in enhanced nucleation of precipitates within the matrix and their dense distribution. The features of microstructure modifications, related to rapid solidification positively affect the strip formability at room temperature.

The conventional wrought magnesium alloys, currently used for strip manufacturing via TRC, such as AZ31, have relatively poor formability due to their strong basal texture. The crystallographic texture with basal planes of hexagonal closed packed lattice of magnesium, oriented almost parallel to the strip surface means that the majority of grains are aligned in an orientation that is difficult for deformation, resulting in high flow stresses. The negative impact of this feature is shown by the fact that wrought magnesium products represent less that 1% of global annual magnesium use. It is expected, therefore, that generating random texture, or at least, weakening the basal texture would improve the strip formability. The better formability not only enhances final stages of the strip deformation but also subsequent operations of component manufacturing, where that strip is used as a raw material, frequently involving stamping or bending.

In order to achieve further progress in TRC of magnesium, new alloys, tailored specifically for this manufacturing technique, which will take advantage of unique solidification characteristics and having an enhanced ductility at room temperature, are required. Recent studies [4, 5] have shown that magnesium when alloyed with rare earth elements gave rise to weakening of the basal texture and hence improving the room temperature formability. In addition to weakening the basal texture and improving ductility, the advantages of rare earth containing magnesium alloys are high strength, high creep resistance, acceptable corrosion behavior and excellent flammability resistance. In general, rare earth metals are added to magnesium alloys either as mischmetal or as didymium. Mischmetal is a natural mixture of the rare earths containing about 50% cerium, the remainder being principally lanthanum and neodymium; didymium is a natural mixture of approximately 85% neodymium and 15% praseodymium. There are alloys, however, where individual rare earths or their combinations are used. Neodymium is a beneficial alloying addition in Mg alloys as it reduces intensity of the basal texture while increasing strength and ductility. In addition, micro-alloying with Ce is reported [4, 5] to weaken the texture of Mg-Zn alloys and promote ductility. There are elements with high affinity to oxygen, beyond the rare earth list, that are capable of modifying basal texture and Ca is one of them. It was found [6] that the simultaneous alloying with Ca and Ce enhances precipitation hardening, refines grain size and improves texture and ductility.

The main disadvantages of rare earth containing alloys are high costs and element lost during recycling. The majority of

commercial magnesium-rare earth alloys such as AE42, AE44, WE43, WE54, QE22, EQ21, ZEK62, EK30, EM32, contain more than 1% of rare earths. There are only few exceptions such as ZEK100, ZE10 and ME10 with rare earth contents below 1%. It is believed that the new generation of magnesium alloys, developed for improved room-temperature formability, will contain only small amount of costly rare earth elements.

The as-cast solidification microstructure of wrought magnesium alloys, being a subject of this paper, is important since it determines the precipitates affecting final properties of the alloy. In case of high temperature applications the distribution of secondary precipitates is affected by as-cast conditions [7]. Similarly, the thermo-mechanical treatment is highly dependent on the as-cast microstructure [8, 9]. In spite of their importance, as-cast details of wrought alloys have not been systematically studied.

Experimental Procedure

Melting and casting

The materials of this investigation were three magnesium alloys with varying contents of neodymium: two experimental alloys of Mg-1Zn-0.5Nd and Mg-1Zn-1Nd as well as one commercial alloy of ZEK100 with detailed chemical compositions listed in Table 1. Several melts of experimental alloys with a weight of 40 kg each were prepared in a resistance furnace using a mild steel crucible under a protection of CO_2 + 0.5% SF_6 gas mixture. The charge makeup was pure magnesium along with alloying additions of pure zinc and neodymium. All the alloying elements were added to the melt at 730°C. No grain refiner was applied to experimental alloys. To allow comparison, details of molten metal processing and the time-temperature cycle were the same for all melts. To ensure the complete dissolution of alloying elements within the melt, frequent stirring and the sufficient residency time, were applied. The molten alloy chemistry was tested *in situ* and adjusted accordingly to meet the requested specification. After verifying the chemical composition and removal of any dross/oxide films, the final sample was tested and castings were poured at 730°C.

Alloys	Chemical Composition		
	%Nd	%Zn	%Zr
ZEK100 (commercial)	0.17	1.20	0.25
Mg-1Zn-0.5Nd	0.45	0.99	-
Mg-1Zn-1Nd	0.92	1.00	-
Fe, Ni, Cu, Si <0.005%			

Table 1: Chemical compositions of magnesium alloys used in this investigation.

To generate microstructures under different solidification rates, a water-cooled wedge-shaped copper mold was used to cast all three alloys. The shape and dimensions of the wedge castings are shown in Figure 1. The cooling rate during solidification of wedge castings was measured using four thermocouples of K-type, positioned along the centerline corresponding to the wedge thickness of 10, 15, 20 and 30 mm. As revealed by measurements, the cooling rates varied from 30°C/s at the base of the wedge to 110°C/s at the tip of wedge [10, 11].

Thermal analysis during melting and solidification

To analyze the phase nucleation and growth during melting and



Figure 1. Shape and dimensions of the wedge castings prepared in a water-cooled copper mold.

solidification the Universal Metallurgical Simulator and Analyzer (UMSA) was explored. The cylindrical samples with a diameter of 31 mm and a length of 35 mm with pre-drilled hole and an insert of the stainless steel tube for a thermocouple were used as shown in Figure 2. The test samples were processed in low thermal mass stainless steel foil, coated with boron nitride and protected against oxidation in the UMSA chamber by using an inert argon atmosphere. The controlled heating to 735ºC at a rate of approximately of 0.4 ºC/s was followed by isothermal holding at 735ºC for 300 seconds and natural cooling to 50ºC at a rate of approximately 0.2 ºC/s. The heating/cooling cycles were repeated three times to establish repeatability of experimental results. Thermodynamic analysis and Scheil simulation of the equilibrium phases were also performed using the FACTsage software.

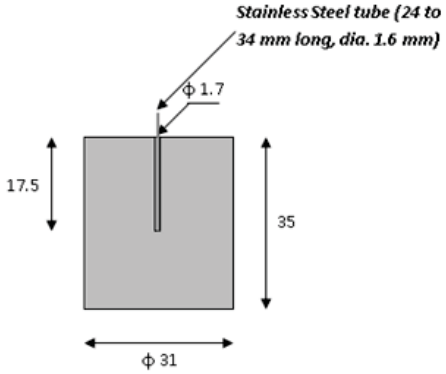


Figure 2. Schematic drawing of the test sample used for UMSA analysis

Microstructure characterization

Metallographic samples of three alloys were obtained from locations with distinct solidification rates. The samples were subjected to conventional metallographic preparation from grinding to polishing and then chemically etched using 10% HF and/or acetic glycol to reveal the dendritic structure. To obtain statistically significant data, the secondary dendrite arm spacing (SDAS) measurements were carried out over a large number of microscopic fields. The scanning electron microscope (SEM) along with EDX analyzer was used for microstructural and micro-chemical characterizations of phases present in these alloys.

Results and Discussion

Phase composition of alloys

The FACTsage software contains thermochemical database for thousands of pure substances (compounds) from phase diagram optimization or standard compilation and data for a variety of

solution systems including liquid and solid metals, salts or oxides. Thus, the software allows to predict the alloy phase composition formed under equilibrium and non-equilibrium (Scheil) cooling conditions. Figures 3 and 4 show the calculated phase diagrams with predicted equilibrium phase compositions of ZEK100, Mg-1Zn-0.5Nd and Mg-1Zn-1Nd alloys.

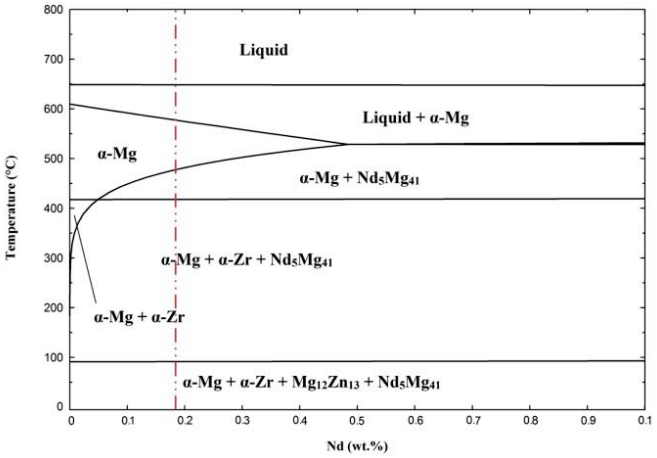


Figure 3. (Mg-1Zn-0.25Zr)-Nd phase diagram showing the effect of Nd on phase formation during equilibrium solidification of ZEK100 (Mg-1Zn-0.17Nd-0.25Zr) alloy.

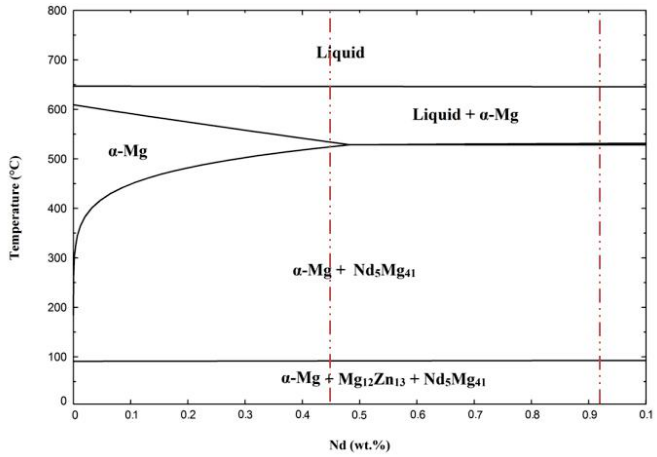


Figure 4. (Mg-1Zn)-Nd phase diagram showing the effect of Nd on phase formation during equilibrium solidification of Mg-1Zn-0.5Nd and Mg-1Zn-1Nd alloys.

Under equilibrium solidification conditions the FACTsage software predicted for ZEK100, Mg-1Zn-0.5Nd and Mg-1Zn-1Nd alloys essentially the same phases of α-Mg, $Mg_{12}Zn_{13}$ and Nd_5Mg_{41} with a difference of α-Zr, additionally present in ZEK100. In particular, the calculated composition of the ZEK100 alloy consists of 98.45%α-Mg+0.25%α-Zr+0.9%$Mg_{12}Zn_{13}$+ 0.4%Nd_5Mg_{41}. An absence of Zr and increased content of Nd slightly affected contents of phases in Mg-1Zn-0.5Nd and Mg-1Zn-1Nd alloys. As a result, the Mg-1Zn-0.5Nd alloy should contain 98.03%α-Mg+0.9%$Mg_{12}Zn_{13}$+1.07%Nd_5Mg_{41} and the Mg-1Zn-1Nd alloy should exhibit a small difference, having a composition of 96.9%α-Mg+0.91%$Mg_{12}Zn_{13}$+2.19%Nd_5Mg_{41}. Thus, with increasing Nd content between ZEK100, Mg-1Zn-0.5Nd and Mg-1Zn-1Nd alloys the contribution of Nd_5Mg_{41} increased from 0.4 to 1.07 and to 2.19% while the content of $Mg_{12}Zn_{13}$ remained practically constant.

During non-equilibrium solidification, an additional phase of $Mg_{51}Zn_{10}$ was predicted to form, mainly at the expense of $Mg_{12}Zn_{13}$. For ZEK100 alloy the predicted phase composition is represented by 98.30%αMg+0.06%$Mg_{12}Zn_{13}$+0.39%Nd_5Mg_{41}+ 1.25%$Mg_{51}Zn_{20}$. It is seen that during Scheil cooling conditions of this alloy, the $Mg_{51}Zn_{20}$ phase replaced α-Zr. In fact, the Mg_xZn_y phase appears in two forms of $Mg_{12}Zn_{13}$ and $Mg_{51}Zn_{20}$. An increased content of Nd affected contribution of phases in Mg-1Zn-0.5Nd and Mg-1Zn-1Nd alloys. The Mg-1Zn-0.5Nd alloy is predicted to contain 97.64%αMg+0.06%$Mg_{12}Zn_{13}$+ 1.03%Nd_5Mg_{41}+1.27%$Mg_{51}Zn_{20}$. On another hand, the Mg-1Zn-1Nd alloy should have, after non-equilibrium solidification, a composition of 96.53%αMg+0.06%$Mg_{12}Zn_{13}$+2.11%Nd_5Mg_{41}+ 1.30%$Mg_{51}Zn_{20}$. Thus, similarly as for equilibrium solidification, an increase in Nd content between ZEK100, Mg-1Zn-0.5Nd and Mg-1Zn-1Nd alloys was accompanied by growing contribution of Nd_5Mg_{41} from 0.39 to 1.03 and to 2.11% while content of $Mg_{12}Zn_{13}$ and $Mg_{51}Zn_{20}$ phases remained practically the same. The FACTsage diagrams emphasizing this conclusion are portrayed in Figures 5 and 6.

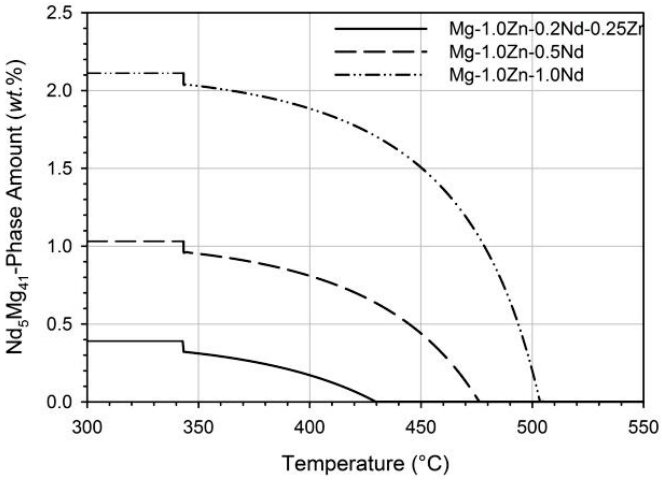


Figure 5. Effect of Nd content on the amount of Nd_5Mg_{41} phase under non-equilibrium (Scheil) solidification conditions.

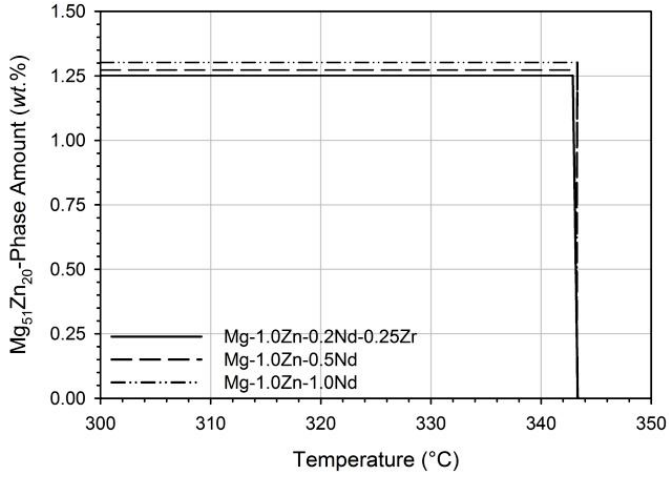


Figure 6. Effect of Nd content on the amount of $Mg_{51}Zn_{20}$ phase under non-equilibrium (Scheil) solidification conditions.

Thermal analysis during melting and solidification

The thermal analysis signal in a form of heating and cooling curves was recorded during melting and solidification to calculate the temperature versus time and first derivative versus temperature. The output was used to determine the magnesium alloy's thermal characteristics during melting and solidification and to evaluate the effect of the chemical composition on metallurgical reactions.

The cooling curves of temperature versus time for three magnesium alloys, recorded during heating and cooling cycles and first derivative of the heating-cooling curves as a function of temperature, are presented in Figures 7 and 8. The obtained temperatures of the metallurgical reactions are pointed out by small letters and their values listed in Table 2.

Alloys	Liquidus (point d)	Solidus (point f)	Eutectic β (point e)
ZEK100	648°C	487°C	497°C
Mg-1Zn-0.5Nd	647°C	486°C	500°C
Mg-1Zn-1Nd	646°C	485°C	507°C

Table 2. UMSA analysis of 3 alloys showing the liquidus, solidus and eutectic formation temperatures (cooling rate of approximately 0.2°C/s).

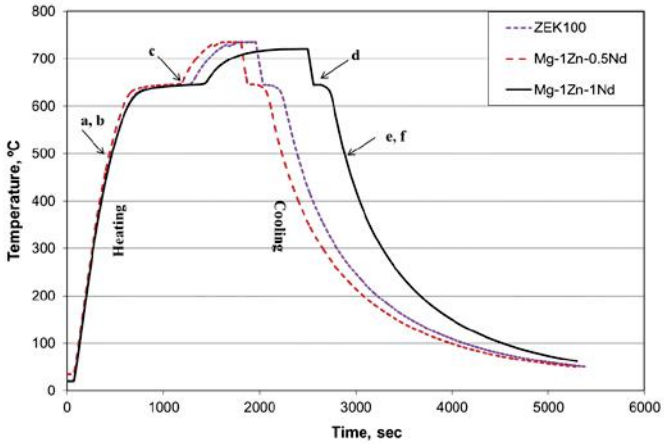


Figure 7. Temperature versus time curves of three magnesium-zinc-neodymium alloys during heating and cooling cycles of UMSA testing. The letters refer to the metallurgical reactions discussed in text.

The key solidification processes that control the final microstructure are the initial nucleation events, the growth of these nuclei into primary dendrites and finally the eutectic solidification [12].

Thermal analysis of tested alloys revealed two major metallurgical reactions through two visible temperature arrests, marked as point c and d on the cooling curves in Figure 7. The first derivatives curves generally provide more detailed information related to the alloy thermal characteristics such as the liquidus temperature or nucleation of the eutectics [12]. Based on thermal analysis, the liquidus temperatures of ZEK100, Mg-1Zn-0.5Nd and Mg-1Zn-1Nd were found to be 648°C, 647°C and 646°C, respectively. Although the liquidus temperature difference is rather small, it is aligned with an increased Nd content within alloys tested from

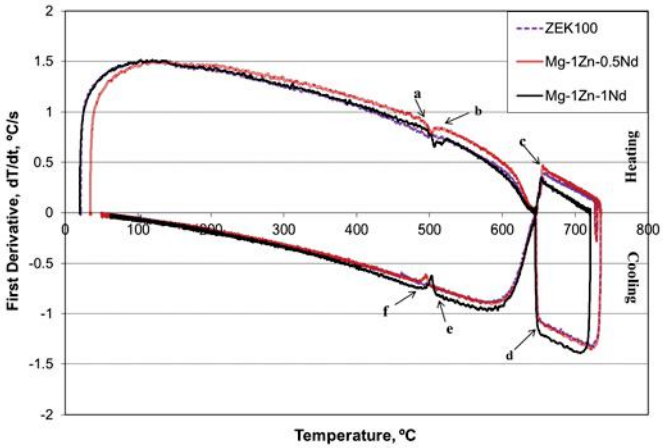


Figure 8. First derivatives of heating and cooling rates versus temperature curves for three magnesium-zinc-neodymium alloys. The letters refer to the metallurgical reactions discussed in text.

0.17 to 0.45 and to 0.92%. During cooling, the first solid formed was the α-Mg dendritic phase that nucleated from the melt at the liquidus temperature. During solidification of the α-Mg phase the melt temperature increased as the latent heat evolved and this point was clearly visible as a sudden change in the first derivative curve (point d in Figure 8). Further cooling beyond point "d" resulted in a growth of α-Mg dendrites. The next change in the first derivative curve corresponded to the nucleation of the β (Mg-Zn-Nd) eutectic. This point is marked as "e" in Figure 8. The eutectic solidification temperature, reaching 497, 500 and 507°C for ZEK100, Mg-1Zn-0.5Nd and Mg-1Zn-1Nd alloys, accordingly, exhibited larger differences as found earlier for liquidus temperatures. As will be shown in the next section, the eutectics in Zr-free alloys tested contained both Nd and Zn. In case of ZEK100 alloy, some Zr was also detected in eutectics regions. As the last characteristic point on cooling curves, marked as "f" in Figure 8, the non-equilibrium liquidus and solidus temperature was revealed. The solidus temperatures, reaching 487, 486 and 485°C for ZEK100, Mg-1Zn-0.5Nd and Mg-1Zn-1Nd alloys, accordingly, showed the same small differences as observed for liquidus temperatures.

Microstructure characterization

The general microstructure of all tested alloys in as-cast state consisted of the α-Mg dendritic matrix and the intermetallic precipitates, forming a network between interdendritic regions. Some individual precipitates or their clusters were also present inside dendritic cells. As it is seen in optical images (Figure 9). The ZEK100 alloy contains the lowest volume fraction of the second phase precipitates. No substantial differences in precipitate contents were detected between Mg-1Zn-0.5Nd and Mg-1Zn-1Nd alloys. In all cases, precipitates did not form a continuous network but rather a chain-like morphology of near-globular individual particles. Moreover, it seems to be a noticeable a reduction in the number of precipitates with increasing solidification rate. The precipitates, located at triple junctions of dendritic cells, were generally larger, frequently with irregular shape. At higher magnifications of SEM, it was possible to distinguish their eutectic nature and contrast suggesting multiphase structure (Figure 10a). According to EDX analysis, both Nd and Zn were present within eutectic regions (Figure 10b).

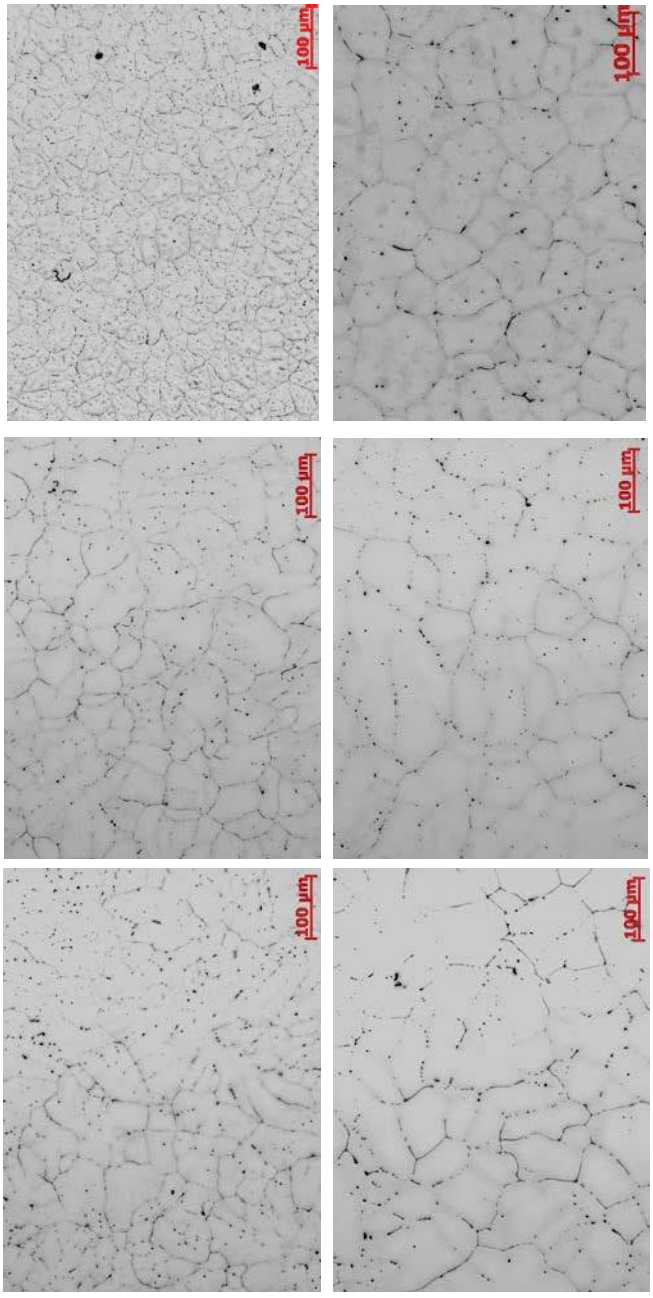


Figure 9. As-cast microstructure of magnesium alloys solidified at different rates within wedge casting, expressed by the wedge thickness:
(Top) ZEK100, 2 mm thick (left) and 30 mm thick (right)
(Middle) Mg-1Zn-0.5Nd, 2 mm thick (left) & 30 mm thick (right)
(Bottom) Mg-1Zn-1Nd, 2 mm thick (left) & 30 mm thick (right)

Two major factors affected the refinement of as-cast microstructures in this research: a presence of Zr and the solidification rate. It is generally known that in Al-free magnesium alloys, zirconium is very effective grain refiner. For typical cooling rate, small additions of Zr in the range of a fraction of percent are capable of reducing the magnesium grain size by two fold. Although magnesium alloys containing Zr exhibit characteristic Zr-rich cores, this feature was not readily

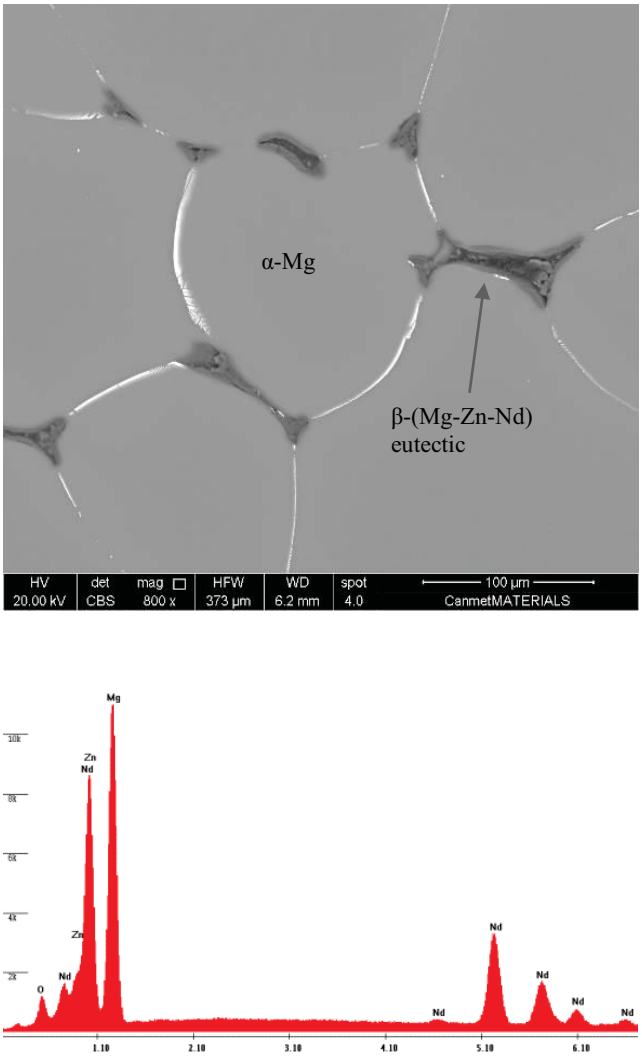


Figure 10. As-cast microstructure of the ZEK100 alloy solidified at approximately 0.2°C/s showing the α-Mg matrix and eutectics distributed within interdendritic regions (top) and EDX analysis revealing a presence of Nd and Zn in eutectics (bottom).

visible in ZEK100 alloy tested here. However, the thermal analysis experiments showed two distinct metallurgical reactions on the cooling curves of ZEK100 alloy, i.e., nucleation of the α-Mg dendrites and the β (Mg-Zn-Nd) eutectic at approximately 648 and 497°C respectively.

An assessment of the role of both the solidification rate and Zr addition is shown quantitatively through measurement of the secondary dendrite arm spacing (SDAS) (Figure 11). It is clear that the cooling rate during solidification affected the refinement of microstructure of all alloys tested and the effect was practically the same for the ZEK100 alloy containing Zr and for Zr-free alloys. An increase of cooling rate from 30°C/s at the wedge thickness of 30 mm to 110°C/s at the wedge thickness of 10 mm resulted in a reduction of SDAS in Zr-free alloys from roughly 45µm to 25µm. There was no obvious influence of Nd content in Mg-1Zn-0.5Nd and Mg-1Zn-1Nd on the value of SDAS.

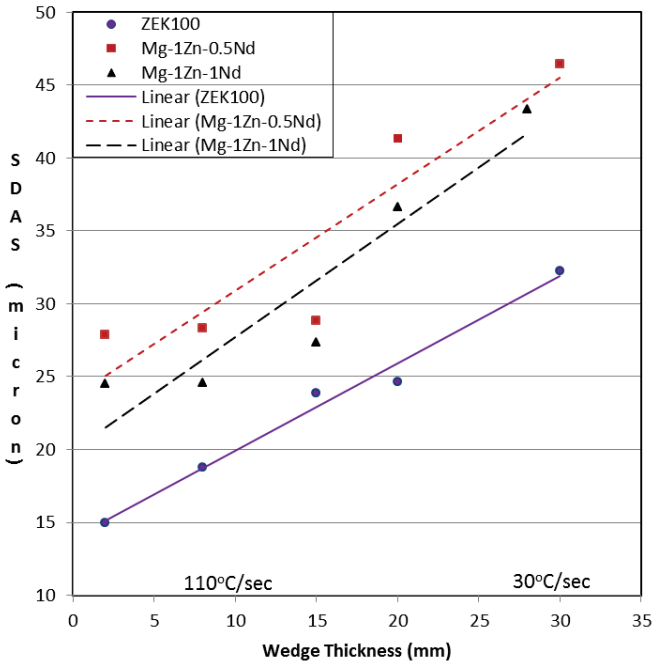


Figure 11. Effect of wedge thickness/cooling rate on average SDAS in Mg-Zn-Nd alloys. The cooling rate varies from 30°C/s at the wedge thickness of 30 mm to 110°C/s at the wedge thickness of 10 mm.

A presence of 0.25% Zr in ZEK100 alloy caused a reduction of SDAS to 30μm at the lowest cooling rate of 30°C/s but further increasing the cooling rate to 110°C/s resulted in SDAS of 15μm. Thus, the highest refinement of microstructure can be achieved through a combination of an addition of a grain refiner and fast cooling during solidification.

Conclusions

A combination of calculations using the FACTsage software and examinations using a number of experimental techniques was explored to determine the solidification characteristics of wrought magnesium alloys containing rare earth metal of neodymium.

Under equilibrium solidification conditions the FACTsage software predicted for ZEK100, Mg-1Zn-0.5Nd and Mg-1Zn-1Nd alloys the same phases of α-Mg, $Mg_{12}Zn_{13}$ and Nd_5Mg_{41}. In ZEK100 alloy, a fraction of α-Zr was also predicted. With increasing Nd content between ZEK100, Mg-1Zn-0.5Nd and Mg-1Zn-1Nd alloys the contribution of Nd_5Mg_{41} grew from 0.4 to 1.07 and to 2.19% while the content of $Mg_{12}Zn_{13}$ remained constant.

During non-equilibrium solidification an additional phase of $Mg_{51}Zn_{10}$ was predicted by the FACTsage software to form, mainly at the expense of $Mg_{12}Zn_{13}$. Similarly as for equilibrium solidification, an increase in Nd content between ZEK100, Mg-1Zn-0.5Nd and Mg-1Zn-1Nd alloys was accompanied by growing contribution of Nd_5Mg_{41} from 0.39 to 1.03 and to 2.11% while content of $Mg_{12}Zn_{13}$ and $Mg_{51}Zn_{20}$ phases remained practically the same.

Thermal analysis, performed during solidification confirmed two major reactions: the formation of α-Mg dendrites followed by the eutectic transformation. There was a slight difference of 1°C in both the liquidus and solidus temperature between alloys tested, aligned with growing Nd content. Thus, the liquidus-solidus temperature ranges were 648-487, 647-486 and 646-485°C for ZEK100, Mg-1Zn-0.5Nd and Mg-1Zn-1Nd alloys, accordingly. The larger difference was revealed for a temperature of the eutectic reaction reaching 497, 500 and 507°C for ZEK100, Mg-1Zn-0.5Nd and Mg-1Zn-1Nd alloys, accordingly.

The cooling rate during solidification affected the microstructure refinement and a volume fraction of intermetallic precipitates. Increasing the cooling rate from 30°C/s to 110°C/s resulted in a reduction of SDAS in Zr-free alloys from roughly 45μm to 25μm. There was no obvious influence of Nd content between Mg-1Zn-0.5Nd and Mg-1Zn-1Nd grades on the value of SDAS. A presence of 0.25% of Zr in ZEK100 alloy caused a reduction of SDAS to 30μm at the cooling rate of 30°C/s but further increase of the cooling rate to 110°C/s resulted in SDAS as small as 15μm. For all alloys, an increase in the solidification rate was accompanied by a noticeable reduction in the number of intermetallic precipitates.

References

[1] F. Czerwinski: *Magnesium Alloys - Design, Processing and Properties*, Magnesium Sheet; Challenges and Opportunities, InTech, January 14, 2011, pp. 299.

[2] H. Chen et al, "Microstructure and mechanical properties of Mg-4.5Al-1.0Zn alloy sheets", *Materials Science and Engineering A*, Vol. 492, 2008, pp. 317-326.

[3] A. Hadadzadeh, M.A. Wells and E. Essadiqi, "Mathematical Modeling of the Twin Roll Casting for AZ31", *Magnesium Technology 2012*, pp.141-145.

[4] A. A. Luo, R. K. Mishra, and A.K. Sachdev,"High-Ductility Magnesium-Zinc-Cerium Extrusion Alloys", *Scripta Materialia*, 64 (2011), pp. 410-413.

[5] R. K. Mishra et al,"Influence of Cerium on Texture and Ductility of Magnesium Extrusions, *Scripta Materialia*, 59 (2008), pp. 562-565.

[6] B. Langelier, P. Donnadieu, and S. Esmaeili, "Characterization of Precipitation in Mg-Zn-Ce-(Ca) Alloys", *Mg2012: 9th International Conference on Magnesium Alloys and their Applications*, July 2012, pp. 485-491.

[7] M. Masoumi, M. Pekguleryuz, "Effect of Cooling Rate on the Microstructure of AZ31 Magnesium Alloy", *AFS Transactions*, 2009, Vol. 117, pp. 617-626.

[8] S.S. Park, G.T. Bae, D.H. Kang, I.-H. Jung, K.S. Shin, N.J. Kim, *Scripta Materialia*, 57 (2007), pp. 793-795.

[9] T.T. Sasaki, J.D. Ju, K. Hono, K.S. Shin, *Scripta Materialia*, 61 (2009), pp. 80-83.

[10] D. H. Kang, M. Paliwal, E. Essadiqi, In-Ho Jung, "Experimental Studies on the As-Cast Microstructure of Mg-Al Binary Alloys with Various Solidification Rates and Compositions", *Magnesium Technology*, 2010, pp. 533-536.

[11] Y. He, A. Javaid, E. Essadiqi, M. Shehata, *Canadian Metallurgical Quarterly*, 48(2) (2009), pp. 145-156.

[12] W. Kasprzak, J.H. Sokolowski, M. Sahoo, L.A. Dobrzański, "Thermal characteristics of the AM50 magnesium alloy, "*Journal of Achievements in Materials and Manufacturing Engineering*", V. 29, Issue 2, August 2008, pp. 179-182.

Magnesium Technology 2014
Edited by: Martyn Alderman, Michele V. Manuel, Norbert Hort, and Neale R. Neelameggham
TMS (The Minerals, Metals & Materials Society), 2014

STRENGTHENING DUE TO THE PERCOLATING EUTECTIC MICROSTRUCTURE IN SQUEEZE CAST MRI230D

Bao Zhang, Anumalasetty V. Nagasekhar[1], Carlos H. Cáceres[*]
ARC Centre of Excellence for Design in Light Metals, Materials Engineering
The University of Queensland, QLD 4072, Australia
[1]Current address: Carpenter Technology Corporation, PO Box 14662, Reading, PA, USA
[*]Corresponding author. Email: c.caceres@uq.edu.au

Keywords: MRI230D alloy, FIB tomography, Finite element modeling, Bending-dominated structure, Damage, Strengthening mechanisms

Abstract

A 3D numerical image of the percolating eutectic in a squeeze cast MRI230D was incorporated into a finite element code to assess its deformation behaviour. The modelling revealed a high structural compliance, akin to the bending-dominated behaviour of cellular foams. At yield, contribution of the 3D network to the alloy's strength was comparable with the dispersion strengthening expected from an equivalent volume fraction of dispersed particles. Incorporating damage effects into the model indicated that due to its high compliance the percolating microstructure can be expected to keep most of its structural integrity, reinforcing the alloy without compromising the ductility, for strains above 1%.

Introduction

The profuse interconnection of the intergranular intermetallic/eutectic phase is a defining feature in 2D SEM images of high pressure die cast (HPDC) Mg-Al and Mg-RE alloys. It has been considered an additional strengthening mechanism [1-4]. A more comprehensive morphological characterization of the percolating phase was obtained recently through focused (dual bema) ion beam tomography (FIB), which revealed a high degree of spatially interconnection of the intermetallic $Mg_{17}Al_{12}$ in alloy AZ91 [5]. Subsequent finite element (FE) [6], corroborated with experimental observations, substantiated prior analytical calculations of the strengthening effect of the 3D network. The present work extends the analysis preformed in alloy AZ91 to the commercial alloy MRI230D, processed via squeeze casting.

Consistently with earlier work [6], dual beam FIB tomography was used to obtain the numerical data of the percolating phase in 3D space, followed by incorporation of the data into a finite element code to determine the deformation behaviour, followed by comparison of the computed results with theoretical value of dispersion strength.

Materials and data for analysis

Alloy

Table I. MRI230D studied

Nominal composition	Primary intermetallic	Eutectic phase	Ref.
6.8wt%Al 1.91wt%Ca 0.5wt%Sn 0.25wt%Sr 0.23wt%Mn 0.01wt%Zn	$CaAl_2$	Mg- Al_2Ca	[3, 7]

Table I show the nominal composition, the primary intermetallic and eutectic phases in MRI230D,

Dual beam focused ion beam (FIB) tomography was used to characterize the 3D microstructural feature of the percolating eutectic structures surrounding α-Mg. A volume adjacent to the specimen's surface was serially sectioned into 0.2μm thick slices on an FIB machine and SEM secondary electron images collected after each slice was removed. The images were subsequently aligned, followed by sequential segmentation and reconstruction to obtain the 3D microstructure. Table II lists the relevant parameters utilized for the FIB tomography. Further details can be found in [5].

Table II. Relevant parameters of the FIB tomography

FIB tomography			Sectioned slices	
Source	Voltage	Current	Resolution	Slice thickness
Ga^+ ions	30 kV	1.0 nA	1024×884	0.2μm

Finite element modeling

Meshing of the 3D eutectic network was done using 4-node tetrahedral elements (C3D4) through the built-in tools of the commercial Amira 5.3™ package. The software package ABAQUS 6.10™ was subsequently used to assess the deformation behavior.

Damage

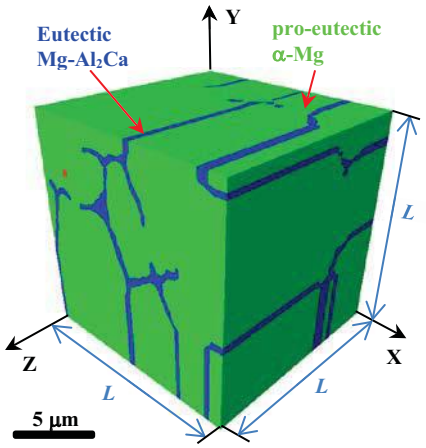
Brittle fracture of the eutectic intermetallic phases was assumed to occur at a tensile strain of 0.7% as per data for tensile fracture of directionally solidified eutectics [8, 9]. It was also assumed that plastic relaxation of pileup stresses on the Mg alloy matrix starts at 0.7% plastic strain, i.e., the same strain at which the 3D micro trusses crack [6]. The simulations were limited to a maximum uniform strain of 1%, in line with the observation that unidirectionally solidified eutectic composites fail in tension at that strain value [8, 9]. The space filling matrix was ignored in the modeling to simply the modeling Of necessity such assumption can only be accepted for small strains [6].

Results

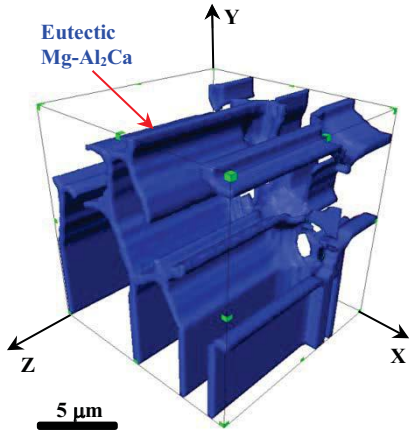
3D microstructural features

Figure 1a show the FIB volume sampled. The lighter and darker areas represent respectively the α-Mg and the eutectic phases. The eutectic shown in Fig. 1b forms a profusely interconnected 3D

network, mimicking the observations made for alloy [5, 6] AZ91D. The volume fraction of eutectic, f^e, in the sampled volume, was determined using the built-in tools of the Amira software [10], whereas the volumetric proportions of α-Mg and intermetallic within the eutectic, denoted respectively by f^α and f^i, were calculated as per the liquid projection of the Mg-Al-Ca ternary system [11] for MRI230D. The volume fraction of intermetallic in the sampled volume is given by ($f^e \times f^i$). The respective numerical values are listed in Table III.



(a)



(b)

Figure 1 (a) Cubic volume of the squeeze cast MRI230D examined using FIB (b) 3D network of the eutectic, 3De

Table III. Length, L, of the sampled cube side (Fig. 1a), and values of f^e, f^α, f^i and $f^e \times f^i$

L	f^e (%)	f^α (%)	f^i (%)	$f^e \times f^i$ (%)
11.6	11.4	61.9	38.1	4.3

The (α-Mg)-$CaAl_2$ composite

The modulus of the eutectic Mg-$CaAl_2$, E_e, was determined using the rule of mixtures, assuming that the intermetallic reinforces the whole eutectic as long fibers do in a metal matrix composite:

$$E_e = f^i E_i + f^\alpha E_\alpha \quad (1)$$

Where E_i and E_α represent respectively the moduli of the eutectic intermetallic and α-Mg. The relevant numerical values are listed in Table IV. Primed values in the brackets correspond to cracking of the intermetallic (E_i') and/or the onset of plastic deformation of the α-Mg (E_α') within the eutectic, past the strain of 0.007

Table IV. Values of E_i (E_i'), E_α (E_α') and E_e (E_e'), in GPa

E_i	E_i'	E_α	E_α'	E_e	E_e'
105 [12]	0	44 [13]	1.4[14]	67.2	0.87

The overall elastic/plastic behavior of the eutectic composite is schematized in Fig. 2 as per the standard assumptions regarding the deformation behavior of long fiber metal matrix composites [15], i.e., an early stage in which both matrix and reinforcement deform elastically, followed by a stage in which the matrix flows plastically while the fibers still remain elastic. The slopes of the lines in Fig. 2, E_i, E_α and E_e, represent the purely elastic stage for both matrix and reinforcement. Past the strain of 0.7% (indicated by primed symbols) cracking of the intermetallic leads to E_i=0, whereas plastic deformation of the matrix implies a "plastic modulus" E_α' = 1.4 GPa [14].

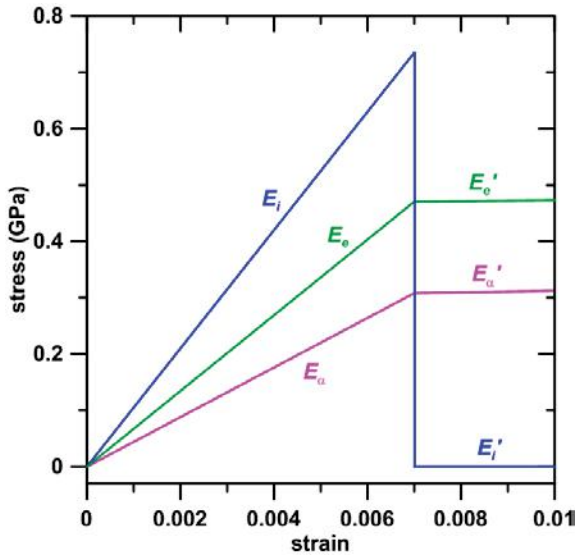


Figure 2 Schematic representation of the elastic, plastic or post-fracture response of the intermetallic phase, α-Mg matrix and the eutectic composites; the E-values are the slopes of the respective lines (see the numerical values in Table IV)

FE modeling

The FE model is shown in Fig. 3, where the 3D network, 3De, was bounded by two rigid shells. A force, F, applied perpendicularly to the top shell results in a displacement, δ, parallel to the Y-axis. The average stress, σ, and strain,ε, experienced by the 3De, and its effective elastic modulus, E_{3De}, are given by:

$$\varepsilon = \ln(1 + \delta/L) \quad (2)$$

$$\sigma = (1 + \delta/L) * F/L^2 \quad (3)$$

$$E_{3De} = \sigma/\varepsilon \quad (4)$$

Four-node tetrahedral elements (C3D4) [16] were used to discretize the eutectic networks. The number of elements used was 139,126, corresponding to element size of ~0.2μm, ensured convergence of the computed results.

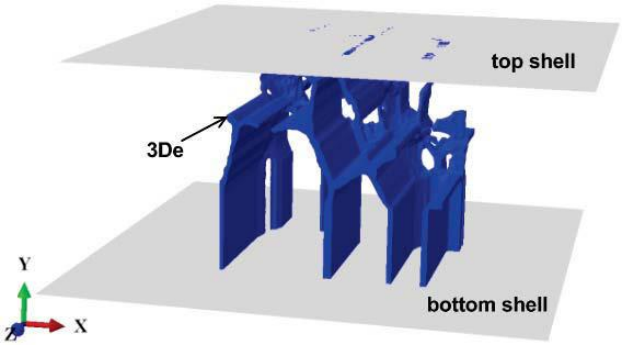


Figure 3 FE model setup

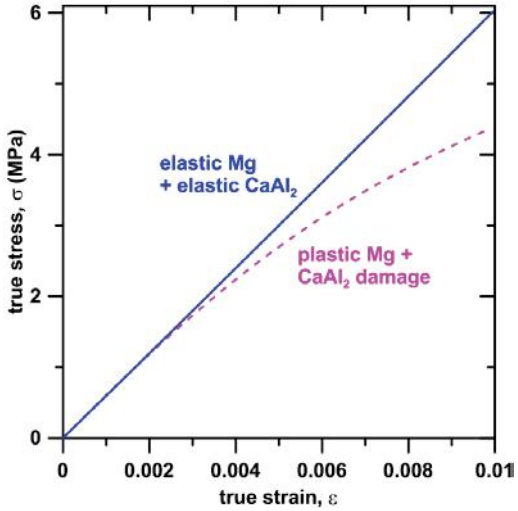
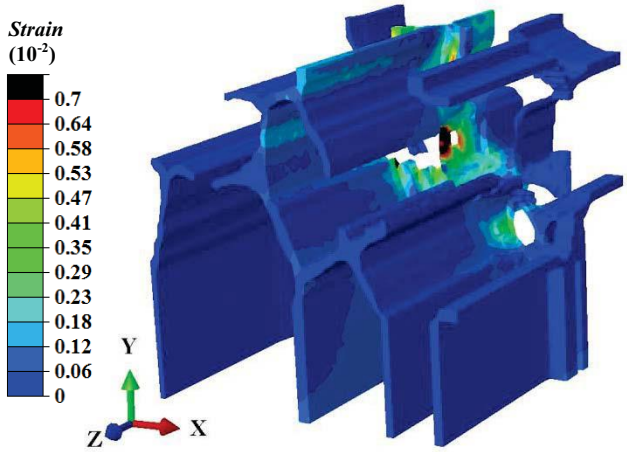
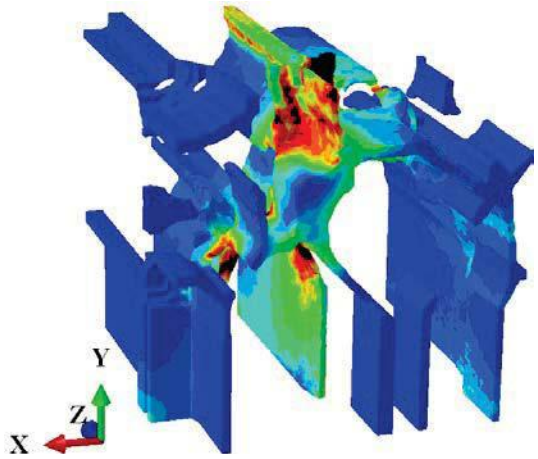


Figure 4 Stress-strain response of the 3De; the solid and dashed lines correspond respectively to elastic behavior of the eutectic on its own, and after inclusion of damage by cracking.

Fig. 4 shows the tensile behavior of the 3De. The solid line, with slope E_{3De} = 603.1MPa as per Eq. 4, represents the elastic stretching of the 3D structure of Fig. 3. The dashed line shows the cumulative effect of both, cracking of the intermetallic micro-trusses and the onset of plastic relaxation of the Mg matrix, assumed to occur for (local) strain of 0.7% and above. Deviation from linearity indicates a measurable effect of local intermetallic damage already at a strain of 0.2%, suggesting that some micro-trusses are overloaded under relatively small applied strains. This is made more evident by Figs. 5a and 5b which show the distribution of local strains after imposing average strains of 0.25% and 1% along the Y-axis, respectively. The largest local strains, i.e., where damage is predicted to first appear, concentrated on the branches aligned parallel to the loading axis, as would be expected. Table V summarizes the values of E_{3De} and damage initiation strain.



(a)



(b)

Figure 5 Distributions of local strain across the 3De, for applied tensile strains of (a) 0.25% (b) 1%

Table V. E_{3De} and dmage initiation strain

Eutectic phase	E_{3De} (MPa)	Damage initiation strain (%)
Mg-$CaAl_2$	603.1	0.2

Discussion

Elastic Modulus of 3De

The elastic behavior of the 3De depicted in Fig. 4 will be compared with several model structures to better characterize it. The modulus of a porous solid can be expressed as a function of the porosity fraction [17] through the McKenzie's equation [18, 19]:

$$E_{3De} = E_e (1 - p)^m \quad (5)$$

Where p is the fractional porosity content and m a constant related to the level of porosity and its morphology. For low levels of

porosity, e.g. $p < 0.04$, $1 < m < 3$ [13]. For high porosity contents, e.g. cellular or foamed materials, $p > 0.7$, and $m = 2$ for open-cell [20] and = 3 for closed-cell structures [21]. Concerning the effects of pore morphology, Bruno *et al.* [18] indicated that *m*-values of 2 and 4 correspond respectively to structures obtained by overlapping either spherical pores (OSP) or solid spheres (OSS) [22]. An OSP type of structure can be generated by randomly creating pores inside a solid volume, with the pores either isolated or interconnected (in an OSS structure the pores and solid matter of the OSP are interchanged).

Equation 5 rewritten in terms of the volume fraction of 3De takes the form:

$$E_{3De} = E_e\,(f^e)^m \qquad (6)$$

With values of f^e, E_e and E_{3De} in Tables III-V, *m* is determined as 2.17, matching the expected value for open-cell materials [20] and indicating a morphological analogy with OSP model [18].

Structural behavior

To better characterize the behavior of the 3De, the elastic response is compared in Fig. 6 with those of standard hybrid model structures [23], namely, fiber composites and foamed structures. This is done using upper and lower bounds.

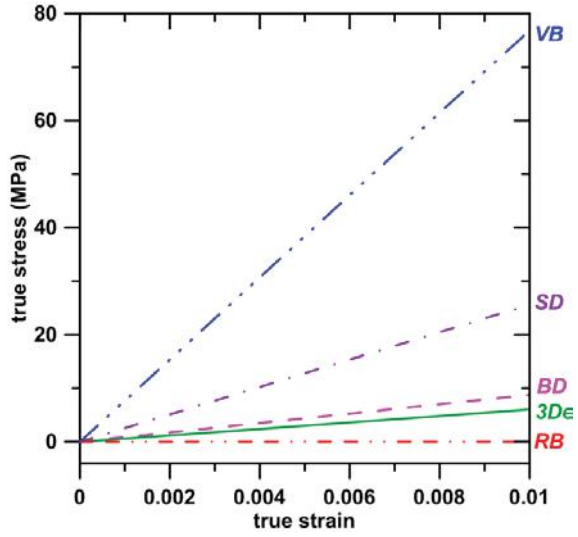


Figure 6 Stress-strain response of the 3De, compared with those of model structures as per Eqs. 7-10, namely: Voigt bound (VB), stretch-dominated (SD), bending-dominated behaviour (BD) and Reuss bound (RB)

The Reuss and Voigt bounds, labeled E_{RB} and E_{VB}, represent respectively the lower and upper limits to the elastic modulus of long fiber composites [23]:

$$E_{RB} = E_m E_e / [f^e E_m + (1 - f^e) E_e] \qquad (7)$$
$$E_{VB} = f^e E_e + (1 - f^e) E_m \qquad (8)$$

Where E_m (= 0) represents the open space of the 3De in Fig. 1b.

The upper and lower bounds of foamed solids, E_{BD} and E_{SD}, for bending-dominated and stretch-dominated structures, respectively, were calculated as:

$$E_{BD} = (f^e)^2 E_e \qquad (9)$$
$$E_{SD} = f^e E_e / 3 \qquad (10)$$

Figure 6 shows that the behavior of the 3De closely matches that of a bending dominated micro-truss structure.

Structural efficiency and damage generation

A hard phase dispersed in a metallic matrix is expected to increase both the elastic modulus and the strain hardening rate in comparison with those of the unreinforced matrix, in proportion to the volume fraction and the elastic modulus of the reinforcement [24-28]. At high applied stresses and strains the development of damage, either in the form of cracking of the reinforcement or by delamination at the interfaces, may eventually balance the reinforcing effects. The onset of damage becomes evident by a decrease in either the elastic slope or the strain hardening rate of the composite [29-32]. In a stretch-dominated structure, (of which long fiber unidirectional composites represent the upper bound), cracking can be expected to occur very early under stress, thus limiting the reinforcing effects to strains of about 1% [8, 9]. Being very compliant, bending dominated structures sacrifice the initial stiffening of the composite in favor of a delayed onset of cracking, and by doing that the reinforcement is extended into the plastic regime of the matrix. Keeping Eqs. 9 and 10 and the results of Figs. 4 and 5 in mind, a purely stretch-dominated 3De structure would increase the relative stiffness of the 3De by a factor 3 [23], but the overall ductility of the component will be reduced to less than 1%. Instead, due to the high compliance of the bending-dominated structure, reinforcing effects can be expected to extend to well over 1% strain with limited damage, and this is demonstrated by Fig. 5b.

Contribution to the yield strength

The amount of network contribution to yield strength, denoted by σ_{3De}, is picked as the stress at 0.6% strain in the stress-strain curve (with eutectic damage considered) of the network, which corresponds to yield point of the alloy. This approach is applied to the 3De, and results in determination of σ_{3De} = 3.1MPa. A comparison is made between σ_{3De} and the dispersion strength at yield, σ_d, calculated by Eq. 11 [24, 25, 33, 34] and listed in Table VI. It is noted that σ_{3De} is less than σ_d, but both are in the same order in magnitude.

$$\sigma_d = E_i \times (f^e \times f^i) \times 0.002 \qquad (11)$$

Table VI. Comparison between σ_{3Dp} and σ_d

σ_{3De} (MPa)	σ_d (MPa)
3.1	9.0

Conclusions

- 3D FIB tomography revealed spatially interconnected network of the eutectic phase in the squeeze cast MRI230D.
- A Finite Element Model was used to determine the stress-strain response of the 3D network as well for as identification of the damage initiation strain.
- The deformation behavior is consistent with that of a bending-dominated cellular or micro-truss lattice-structure.
- Early damage appears confined to the limited fraction of branches oriented for stretch-dominated behavior; the high compliance of the eutectic network delays the onset of significant damage by cracking to strains >1%.
- At yield, the network contributes to the strength of the alloy an amount comparable with that expected from a dispersed fraction of the same volume fraction.

References

[1] C.H. Cáceres, W.J. Poole, A.L. Bowles, C.J. Davidson, Mater. Sci. Eng., 402A (2005) 269-277.
[2] K.V. Yang, C.H. Caceres, A.V. Nagasekhar, M.A. Easton, Mater. Sci. Eng. A, 542 (2012) 49-55.
[3] D. Amberger, P. Eisenlohr, M. Goken, Acta Mater., 60 (2012) 2277-2289.
[4] B.S. Shin, J.W. Kwon, D.H. Bae, Met. Mater. Int., 15 (2009) 203-207.
[5] A.V. Nagasekhar, C.H. Caceres, C. Kong, Mater. Charact., 61 (2010) 1035-1042.
[6] B. Zhang, A.V. Nagasekhar, T. Sivarupan, C.H. Caceres, Adv. Eng. Mater., 10.1002/adem.201300138 (2013).
[7] Y. Terada, N. Ishimatsu, Y. Mori, T. Sato, Mater. Trans. (JIM), 46 (2005) 145-147.
[8] B. Cantor, G.A. Chadwick, J. Mater. Sci., 10 (1975) 578-588.
[9] M. Sahoo, R.W. Smith, Metal Sci., 9 (1975) 217-222.
[10] D. Stalling, M. Westerhoff, H.-C. Hege, in, 1997.
[11] K. Ozturk, Y. Zhong, A.A. Luo, Z. Liu, JOM, (2003) 40-44.
[12] H. Anton, P.C. Schmidt, Intermetallics, 5 (1997) 449-465.
[13] T. Sumitomo, C.H. Cáceres, M. Veidt, J. Light Metals, 2 (2002) 49-56.
[14] C.H. Cáceres, P. Lukác, Philos Mag A, 88, http://dx.doi.org/10.1080/14786430801968611 (2008) 977-989.
[15] D. Hull, An introduction to composite materials, Cambridge University Press, Cambridge, 1981.
[16] O.C. Zienkiewicz, R.L. Taylor, The finite element method, McGraw-Hill Book Company (1989).
[17] R.W. Rice, J. Mater Sci., 40 (2005) 983-989.
[18] G. Bruno, A.M. Efremov, A.N. Levandovskyi, B. Clausen, J. Mater. Sci., 46 (2011) 161-173.
[19] R.L. coble, W.D. Kingery, J. Amer. Ceram. Soc., 39 (1956) 377-385.
[20] L.J. Gibson, Ashby M. F., Proc. R. Soc. Lond. A, 382 (1982) 43-59.
[21] S.K. Maiti, L.J. Gibson, M.F. Ashby, Acta Metall., 32 (1984) 1963-1975.
[22] A.P. Roberts, E.J. Garboczi, J. Am. Ceram. Soc, 83 (2000) 3041-3048.
[23] M.F. Ashby, Y.J.M. Brechet, Acta Mater., 51 (2003) 5801-5821.
[24] L.M. Brown, W.M. Stobbs, Phil. Mag., 23 (1971) 1185-1199.
[25] L.M. Brown, W.M. Stobbs, Phil. Mag., 23 (1971) 1201-1233.
[26] C.H. Cáceres, J.R. Griffiths, P. Reiner, Acta Mater., 44 (1996) 15-23.
[27] J.D. Embury, Metall.Trans., 16A (1985) 2191-2200.
[28] M.A. Gharghouri, G.C. Weatherly, J.D. Embury, J. Root, Phil. Mag., 79 (1999) 1671-1696.
[29] C.H. Cáceres, Alum. Trans., 1 (1999) 1-13.
[30] Y. Brechet, J.D. Embury, S. Tao, L. Luo, Acta Metall. Mater., 39 (1991) 1781-1786.
[31] C.H. Cáceres, J.R. Griffiths, Acta Mater., 44 (1996) 25-33.
[32] P.J. Withers, W.M. Stobbs, O.B. Pedersen, Acta Metall., 37 (1989) 3061-3084.
[33] L.M. Brown, D.R. Clarke, Acta Metallurgica, 23 (1975) 821-830.
[34] L.M. Brown, D.R. Clarke, Acta Metallurgica, 25 (1977) 563-570.

Magnesium Technology 2014
Edited by: Martyn Alderman, Michele V. Manuel, Norbert Hort, and Neale R. Neelameggham
TMS (The Minerals, Metals & Materials Society), 2014

EFFECT OF Al ADDITION ON MICROSTRUCTURE OF AZ91D

Utsavi Joshi[1], Nadendla Hari Babu[2]
[1,2]BCAST (Brunel Centre for Advanced Solidification technology), Brunel University, Uxbridge, Middlesex UB8 3PH, UK

Keywords: AZ91D Mg alloy, Grain refinement, Al-B master alloy

Abstract

Casting is a net shape or near net shape forming process so work-hardening will not be applicable for improving properties of magnesium cast alloys. Grain refinement, solid-solution strengthening, precipitation hardening and specially designed heat treatment are the techniques used to enhance the properties of these alloys. This research focusses on grain refinement of magnesium alloy AZ91D, which is a widely used commercial cast alloy. Recently, Al-B based master alloys have shown potential in grain refining AZ91D. A comparative study of the grain refinement of AZ91D by addition of 0.02wt%B, 0.04wt%B, 0.1wt%B, 0.5wt%B and 1.0wt%B of Al-5B master alloy and equivalent amount of solute element aluminium is described in this paper. Hardness profile of AZ91D alloyed with boron and aluminium is compared.

Introduction

Magnesium alloys have shown great potential in structural applications due to their many appreciated properties. The efforts by automotive sector to reduce fuel consumption and vehicle emissions have increased the demand for light weight magnesium alloys as a structural material. Apart from automotive sector, magnesium alloys have also attracted application in electric and aerospace industries. Therefore, the associated investigations are of high interest to researchers and designers.

AZ91D is the most widely used commercial magnesium alloy containing aluminium but its mechanical properties are relatively low, which cannot meet the requirements of certain applications [1]. Grain refinement can improve the mechanical properties of an alloy which involves the formation of fine equiaxed grains at the expense of dendrites. It also offers other advantages such as reduction in hot tearing susceptibility and improved corrosion resistance. Various methods used for grain refinement include addition of trace elements or master alloy, ultrasonic treatment or electromagnetic field, introduction of fine gas bubbles in the melt and applying coatings to mould surface. Inoculation of melt is the most commonly used method for grain refinement of Mg alloys as Mg has a hexagonal close packed (HCP) structure and it is difficult to decrease the grain size through thermomechanical processing due to limited slip systems. Many commercial alloy systems such as the aluminium bearing magnesium alloys (AZ91, AZ31 and AM50) do not have any established grain refiner that is cost-effective and reliable. Numerous potential additions based on carbon, calcium, boron and strontium have been examined by researchers for grain refinement on AZ91 alloy [2, 3, 4, 5, 6, 7]. Carbon based additions have shown significant refinement but it causes environmental pollution while boron addition is maintained longer and is considered more feasible [8]. The effect of aluminium content on microstructure of Mg-Al alloys has been studied by Dargusch et al [9] and the effect of boron addition on grain refinement of AZ91 alloy has been studied by Suresh et al [5]. In this research, we do a comparative study of addition of boron based master alloy Al-5B and equivalent solute addition in form of Al to the grain refinement of AZ91D alloy.

Experimental Procedure

The chemical composition of AZ91D alloy considered for this study is 8.95% Al, 0.72%Zn, 0.19%Mn, 0.039%Si, <0.001%Fe, 0.001%Cu, <0.001%Ni, 7ppm Be and remaining Mg. For the casting experiments, the alloy is initially melted in a conventional furnace lined with steel mould. When the temperature of the melt reaches 720°C, the melt is held at this temperature for at least an hour before casting the reference sample or addition of grain refiner in form of master alloy. To obtain reference sample, the melt is cooled to 710±2°C and cast in a preheated (250°C) steel cylindrical mould with inner dimensions of 30mm diameter and 120mm height. In the case of addition of grain refiner, the master alloy Al-5B is added to the melt and left for 20 minutes before casting at 710±2°C. Intermittent stirring is carried out twice after master alloy addition for its dissolution and homogeneous distribution within the melt. Cover gas of a mixture of sulphurhexafluoride and nitrogen is used during melting and holding of the melt. No flux is used during this experiment. For microstructural analysis, cylindrical samples of dimension 30mm diameter and 20mm height were machined out of these castings. These samples are ground and polished using standard procedures for optical microscopy and colour etched using a mixture of 5 ml acetic acid; 10 ml distilled water; 100 ml ethanol and 6 gm picric acid known as the acetic- picral reagent. The linear intercept method was used to measure the grain size using a Zeiss Axioskop2 MAT optical microscope.

Results and Discussion

Effect of Boron Addition on Grain Refinement

The microstructures of AZ91D with and without boron addition are shown in Figure 1. The average grain size of AZ91D alloy without any addition was about 422±35µm. Addition of boron alone in the form of powder was observed to give no change in the grain size of AZ91D alloy since the powder did not submerge and remained dispersed on the surface of melt. Boron was therefore introduced in the form of Al-5B master alloy.

Increase in boron addition from 0.02wt% to 0.1wt% showed very little grain refinement in AZ91D alloy. But 1.0%B addition in form of Al-5B master alloy decreased the grain size significantly from 422±35µm to around 67±5µm. This is attributed to the solute effect of Al since boron is added in the form of Al-5B master alloy. AZ91D alloy when added with 1%B in form of Al-5B master alloy did not reveal a clear polarized image. The acetic-picral reagent was used for etching these samples and since the magnesium alloy AZ91D has now changed to a different composition with very high Al content, the etchant did not reveal a clear polarized image.

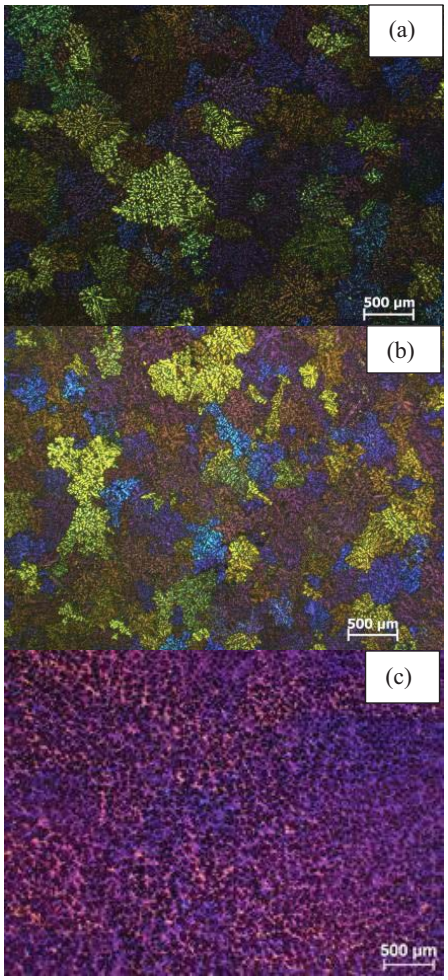


Figure 1: Microstructures of AZ91D with (a) 0%B (b) 0.04%B and 0.76%Al and (c) 1.0%B and 19.0%Al in the form of Al-5B master alloy

Effect of Al Addition on Grain Refinement

Boron in Al-5B (wt%)	Equivalent Al in Al-5B (wt%)
0.02	0.38
0.04	0.76
0.10	1.90
0.50	9.50
1.00	19.00

Table 1: Boron addition levels in form of Al-5B master alloy and the corresponding Al content in the master alloy.

To identify the contribution of Al in Al-5B to the grain refinement of AZ91D alloy, in a separate experiment, a series of AZ91D alloys were cast after adding various amounts of Al. The Al addition levels as shown in 2nd column of Table 1, represents Al content in Al-5B master alloy for boron levels of 0.02wt%, 0.04wt%, 0.1wt%, 0.5wt% and 1.0wt%. The micrographs for Al added AZ91D alloys are shown in Figure 2.

Figure 2 indicate that increase in Al additions from 0.38% to 19.0% has similar effect on average grain size of AZ91D alloy as observed in Figure 1, where equivalent boron (0.02% to 1.00%) is added in the form of Al-5B master alloy.

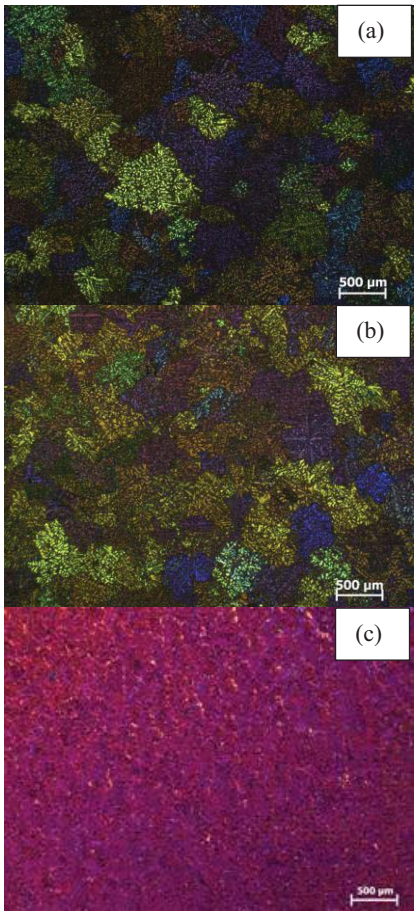


Figure 2: Microstructures of AZ91D with (a) 0%Al (b) 0.76%Al and (c) 19.0%Al

Any refinement in grain structure of AZ91D observed due to Al additions could be attributed to growth restriction factor (GRF) theory. Previous studies on Al alloys and Mg alloys have explained the role of solute in controlling the growth of nucleated grains and subsequent nucleation through this theory [10, 11, 12, 13]. The grain growth will be restricted as the diffusion of solute Al occurs slowly due to constitutional undercooling ahead of the advancing solid/liquid interface. Addition of boron in form of Al-5B master alloy and equivalent aluminium has similar effect on average grain size of AZ91D. Figure 3 suggests that Al contribution could be significant to the grain refinement in AZ91D when Al-5B master alloy is added to a magnesium alloy.

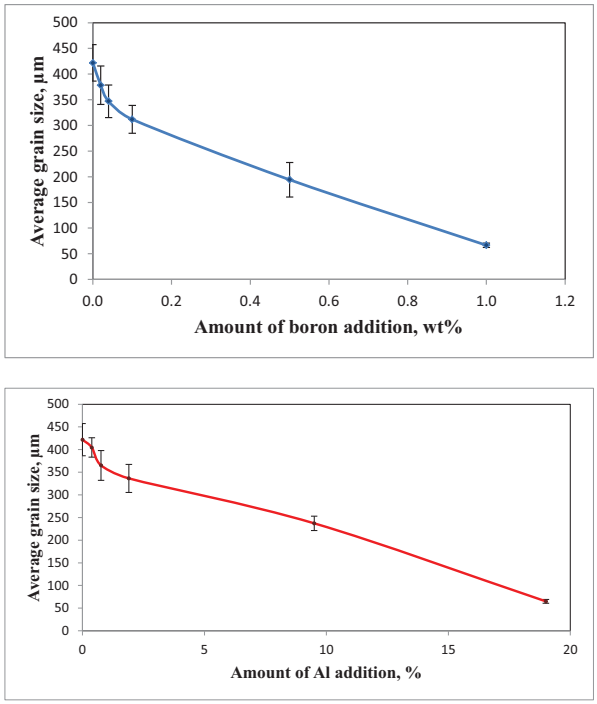


Figure 3: Relation between average grain size of AZ91D and (a) boron addition in form of Al-5B and (b) Al addition

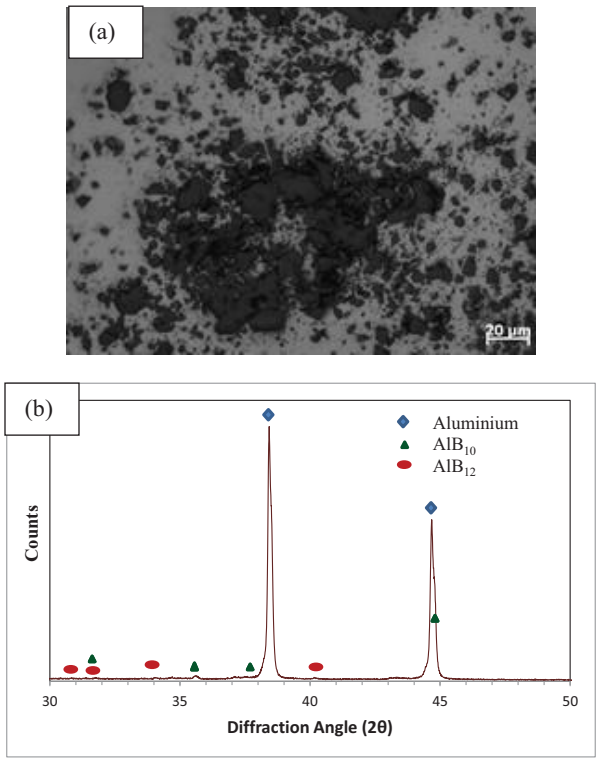


Figure 4: (a) Optical micrographs of Al-5B master alloy (b) XRD pattern of Al-5B master alloy

The microstructure of Al-5B alloy is as shown in Figure 4 (a). The particles were identified as AlB_{12} and AlB_{10} by X-ray diffraction analysis. As shown in Figure 4(b) there are no clear AlB_2 peaks being resolved, an indication of minor amount of AlB_2 in this master alloy. The heat accumulation owing to highly exothermic salt reaction could be responsible for formation of AlB_{12} during the production of Al-5B master alloy [14].

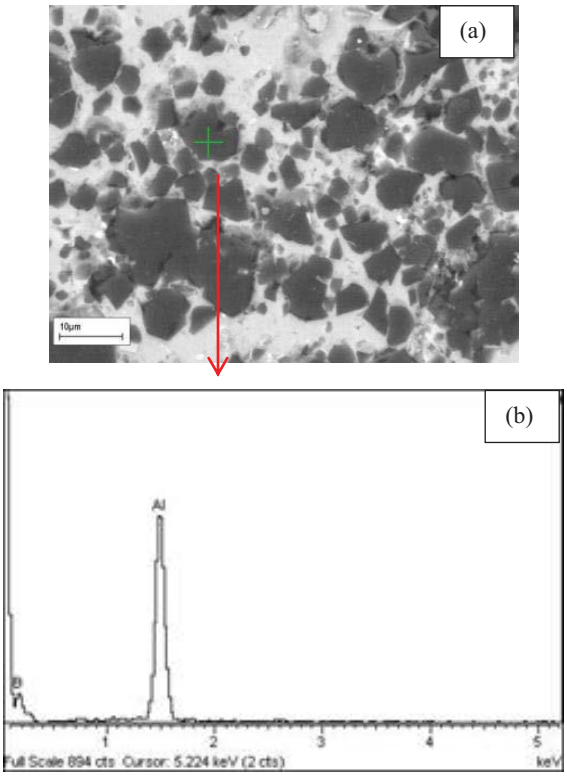


Figure 5: (a) SEM image of Al-5B master alloy revealing Boride particles, and (b) The EDS spectrum of boride particle

Figure 5 shows SEM image of the Al-5B master alloy and the EDS spectrum of the observed boride particles. Smaller numbers of backscattered electrons are generated by boron-rich particles as compared to aluminium due to boron being a lower atomic number element, resulting in dark boride particles surrounded by bright aluminium matrix. These boride particles were seen as clusters in the aluminium matrix. The SEM image did not reveal any clear hexagonal platelets while the irregular polyhedral particles could be attributed to the presence of AlB_{12} and AlB_{10} phases. AlB_{10} have been reported to be metastable phase however, the presence of impurities in Al-5B master alloy could be attributed to its stability.

Previous studies have reported that manganese plays an important role in dispersing the Al-B compounds which could act as potential nucleating sites [8]. But results in this study appeared to the contrary as despite 0.19wt% Mn content in the magnesium alloy there was little effect on grain refinement except at very high concentrations of Al content when a completely new alloy is formed and the base alloy is no more AZ91D.

Effect of Boron and Equivalent Al Addition on Hardness

The hardness values of the samples were measured using INDENTEC hardness tester. Each hardness value reported is an average of 12 measurements.

As show in Figure 6, the micro hardness of the as-cast AZ91D alloy increased from 67 HV0.3 to 136 HV0.3 at 1.0wt%B addition in form of Al-5B. The hardness profile on equivalent Al addition is also in the similar range. Similar average grain size obtained on addition of boron and equivalent Al supports the hardness profiles obtained in each case.

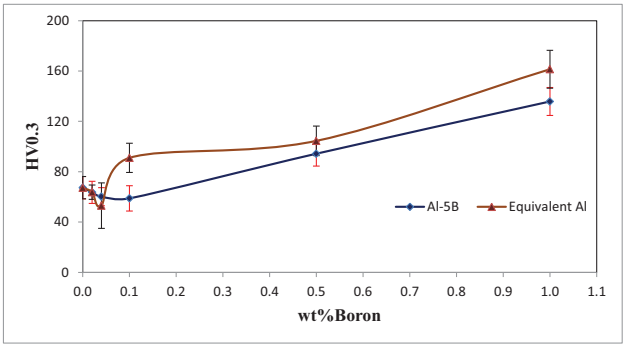


Figure 6: Effect on hardness value with boron and equivalent Al addition

The boride particles could impede the movement of the dislocations very effectively and contribute to the overall strength. Also, it is widely accepted that Mg alloys usually have a much larger Hall-Petch coefficient compared to Al alloys leading to a higher efficiency of strengthening through grain refinement.

Summary

The addition of Al-5B master alloy is observed to decrease the grain size of AZ91D alloy. Al addition to AZ91D is also observed to refine the grain size to the similar magnitude. The refinement with Al-5B addition could therefore be primarily associated with Al solute rather than AlB_{10} or AlB_{12} acting as inoculants.

The hardness profile is similar for both Al-5B master alloy and Al additions to AZ91D, which also suggests that the Al solute plays a major role in grain refinement rather than AlB_{12}/AlB_{10} phases.

References

1. D. Eliezer, E. Aghion, F.H. Fross, "Magnesium Science, technology and applications", *Journal of Advanced Performance Materials*, 5 (1998), 201-212

2. Chen et al., "Grain refinement of AZ91D magnesium alloy by SiC", *Journal of Alloys and Compounds*, 496 (1-2) (2010), 218-225

3. Liu et al., "Effect of Mg-TiB2 master alloy on the grain refinement of AZ91D magnesium alloy", *Journal of Alloys and compounds*, 487 (1-2) (2009), 202-205

4. Chen et al., "Grain refinement of AZ91D magnesium alloy by Al-Ti-B master alloy and its effect on mechanical properties", *Materials & Design*, 34 (2012), 637-648

5. Suresh et al., "Influence of boron addition on the grain refinement and mechanical peoperties of AZ91 Mg alloy", *Materials Science and Engineering A*, 525 (2009) 207-210

6. L Piejie, T. Bin and E.G. Kandalova, "Microstructure and properties of AZ91D alloy with Ca additions", Materials Letters 59 (6) (2005), 671-675

7. Kim,Y., Yim,C., and You,B., "Grain refining mechanism in Mg-Al base alloys with carbon addition", *Scripta Materialia*, 57 (8) (2007), 691-694

8. Nishino et al., "Grain refinement of magnesium casting alloys by boron addition", In: *Proceedings of the International Conference on Magnesium Alloys and their Applications*, September 2000. Germany: Wiley, 59-64

9. Dargusch et al., "The effect of aluminium content on the mechanical properties and microstructure of die cast binary magnesium-aluminium alloys", Materials Transactions, 47 (4) (2006), 977-982

10. L. Backerud and M. Johnsson: in Light Metals, W. Hale, ed.,TMS, Warrendale, PA, 1996, 679-85

11. I. Maxwell and A. Hellawell, "A simple model for grain refinement during solidification", *Acta Metallurgica*, 23 (1975), 229-37

12. Y.C. Lee, A.K. Dahle, D.H. Stjohn, "The role of solute in grain refinement of magnesium", *Metallurgical and Materials Transaction*, 31A (11) (2000) 2895–2906.

13. Cheng et al., "Effect of Sr addition on the grain refinement of AZ31 magnesium alloys", *Progress in Natural Science: Materials International*, 23 (1) (2013), 7-12

14. Wang, X, "The formation of AlB_2 in an Al-B master alloy", *Journal of Alloys and Compounds*, 403 (2005) 283-287

Magnesium Technology 2014
Edited by: Martyn Alderman, Michele V. Manuel, Norbert Hort, and Neale R. Neelameggham
TMS (The Minerals, Metals & Materials Society), 2014

In Situ Synchrotron Radiation Diffraction during Solidification of Mg4Y and Mg4YxGd Alloys (x = 1, 4 wt.%)

G. Szakács[a], B. Wiese [a], C.L. Mendis [a], D. Tolnai [a], A. Stark [b], N. Schell [c], M. Nair[a,+], K.U. Kainer [a] and N. Hort [a]
[a] Magnesium Innovation Centre, Institute of Materials Research, Helmholtz-Zentrum Geesthacht, Max-Planck-Straße 1, D-21502 Geesthacht, Germany
[b] Materials Physics, Institute of Materials Research, Helmholtz-Zentrum Geesthacht, Max-Planck-Straße 1, D-21502 Geesthacht, Germany
[c] Materials Physics, Institute of Materials Research, Helmholtz-Zentrum Geesthacht at Deutsches Elektronen-Synchrotron, Notkestraße 85, D-22607 Hamburg, Germany
[+] On leave from Churchill College – University of Cambridge, Storey's Way, CB3 0DS, Cambridgeshire, United Kingdom.

Keywords: Mg-RE alloys, phase formation, *in situ* solidification, synchrotron diffraction

Abstract

Mg-RE alloys have potential to be used for bio-applications as degradable implant materials. For the production of these alloys casting plays an important role: Phase formation and microstructure evolution are at first determined during solidification. *In situ* synchrotron radiation diffraction is a unique tool to follow phase formation, phase transformations and grain growth during solidification. The measurements were performed at the High Energy Materials Science beamline P07 at PETRA III at the Deutsches Elektronen-Synchrotron (DESY, Hamburg, Germany). In the present study Mg4Y, Mg4Y1Gd and Mg4Y4Gd alloys were investigated to characterize their solidification behavior during cooling from 800°C and 680°C to 450°C, respectively with a cooling rate of 20 K/min. The samples were held in graphite crucibles and were molten in a modified Bähr 805 dilatometer under Ar atmosphere, while the temperature was controlled by type S thermocouples. The results are compared with thermodynamic simulations using Pandat 8^{TM} software.

Introduction

Due to their light weight and high specific strength, Mg-RE (Rare earth) alloys are important for structural applications [1] and recently, have become attractive as degradable biomaterials [2,3,4]. Mg-Y-RE based alloys, such as WE43 and WE54 form an important class of cast magnesium alloys used in elevated temperature applications with superior mechanical properties at both room and elevated temperatures [5]. The RE elements are normally added in the form of cerium or neodymium rich mischmetal due to the high costs of elementally pure RE. The macroscopic mechanical properties of multiphase materials depend strongly on the chemical composition, volume fraction and spatial distribution of the internal phases [1,6]. However, there are no significant differences in mechanical properties whether Nd, Gd or mixture of RE additions are used [7]. In case of a degradable medical implant not only the dependence of alloying additions on the mechanical properties must be elucidated, but the RE additions must be biocompatible as well. Among the RE elements Dy, Nd show good biocompatibility [8], and Gd is used already safely in medicine as a contrast agent in MRI (magnetic resonance imaging) [2]. Furthermore, Gd has been added to enhance mechanical and corrosion properties of Mg-Y alloys. It has a maximum solubility of 23.49 wt.% at 548°C [9] and offers both solid solution strengthening and precipitation hardening. The Mg_5Gd (Pearson code cF440, and lattice parameter a=2.234 nm) [10] phase forms at the grain boundaries during the casting of Mg-Gd alloys [9]. During solution heat treatment they dissolve up to the maximum solubility at the given temperature. A T6 heat treatment leads to the precipitation of fine particles which are the meta-stable phases β´ and β" at peak hardness at 250°C. The β´ phase is homogenously distributed over the matrix, while the β" phase is only observed heterogeneously at peak hardness [11]. The β" phase is isomorphous with Mg so the precipitates are coherent. The lattice parameter a of β´ is twice that of Mg and has a c-based centred orthorhombic structure (a = 0.641 nm, b = 2.223 nm, c = 0.521 nm) [3,7]. In addition to the Mg_5Gd intermetallic phase, three further binary intermetallic compounds have been reported: MgGd (cP2-CsCl type, T_{max}=868°C), Mg_2Gd (cF24-$MgCu_2$ type, T_{max}=756°C) and Mg_3Gd (cF16-BiF_3 type, T_{max}=720°C) at higher concentrations of Gd [10].

Investigations of the binary Mg-Y alloys created the basis for the development of a number of commercial alloys with high strength properties [1]. This system has been reported to contain the: MgY_{1-x} (cP2-CsCl type, T_{max}= 935°C), Mg_2Y_{1-x} (hP12-$MgZn_2$ type, T_{max}= 780°C) and Mg_{24+x} Y_{5-x} (CI58-αMn, T_{max}= 605°C) [10]. Y and Gd show mutual solubility in intermetallic particles therefore a range of intermetallics with various amounts of Mg, Y and Gd solubility are observed. The RE metal defect of the $MgZn_2$ type compound has been reported and proposed the hypo-stoichiometric $Y_{0.7}Mg_2$ phase and the substitution of Y with Gd at constant Mg content has been reported which result in a number of ternary phases in the ternary system [10]. These alloys are mainly produced in the form of castings, thus their microstructure and consequently their macroscopic mechanical properties are determined during solidification and the following thermo-mechanical treatment. The solidification can be modeled based on the thermodynamic databases [12], which [9] provide information on the possible solidification path. However, the majority of the commercial Mg alloys are not binary, but complex alloys with more than one alloying addition. Therefore, an understanding of the sequence of formation and evolution of the intermetallic phases during solidification in complex systems is a prerequisite to achieve control over the microstructure of these alloys. So far the evolution of the internal phases during solidification, could only be investigated by *ex situ* methods, i.e. interrupting the solidification at different temperatures (different stages of microstructure development) by quenching the sample to perform the characterization [13]. This method has the disadvantage of lacking time-temperature resolution. The continuous development of the X-ray acquisition systems at synchrotron radiation sources provides a unique tool to characterize the phase formation and

evolution during the solidification *in situ*. Recording the diffraction patterns while cooling the alloy system down, allows identifying the internal phases, to determine their solidification sequence [14-19] and to use these results as experimental validation of the existing thermodynamic databases and contribute to the completion of them.
The present study reports results of *in situ* synchrotron radiation diffraction studies conducted during solidification of Mg4Y and Mg4YxGd alloys (x= 1, 4) and comparison with the existing thermodynamic data on this system.

Experiment

The alloys were cast at HZG-MagIC using permanent mould casting. For producing the alloys pure materials were used i.d. Mg (99,95%), Gd (99,98%) and Y (99,98%). After melting the pure Mg the melt was kept at 700°C for 10 minutes with continuous stirring after the addition of the alloying elements. During casting e as-cast material in order to fit perfectly into the graphite crucibles designed for the synchrotron radiation diffraction experiments (d = 5 mm, h = 7 mm) to study the solidification. The measurements were carried out at the Petra III P07 High Energy Materials Science (HEMS) Beamline of Helmholtz-Zentrum Geesthacht (HZG) at the Deutsches Elektronen-Synchroton (DESY). The measurements were performed in the chamber of a Bähr 805 dilatometer in Ar flow. The dilatometer has been modified for *in situ* synchrotron radiation measurements, there are two windows on the sides covered by Kapton foil, which is transparent for the X-ray beam, and the induction coil is opened in the middle so that the beam passes only through the sample and the crucible [20]. During the test the sample was contained in a graphite crucible closed with tantalum caps. These caps hold the molten metal, isolate it from the surrounding atmosphere and the type S thermocouples controlling the measurement were welded on to these caps. The samples were heated up to 800°C for the protective atmosphere, containing 2 wt.% SF_6 in Ar, was used. The melt was poured in to a steel mould preheated to 350°C. The actual chemical compositions of the alloys determined by X-ray fluorescence are presented in Table 1, below.

Alloy	Composition wt %		
	Y	Gd	Mg
Mg4Y	4.08	0	bal.
Mg4Y1Gd	4.01	1.08	bal.
Mg4Y4Gd	3.89	3.92	bal.

Table 1. Actual chemical compositions of the alloys investigated.

The microstructures of the alloys in the as-cast condition were examined with a Carl Zeiss Gemini Ultra 55 scanning electron microscope (SEM) operating at 15 kV attached with an EDAX energy dispersive X-ray spectrometer (EDXS). The EDX maps of Mg, Y, and Gd were recorded for all samples at a scan rate of 9000 µs for each pixel and atomic concentrations of Y and Gd in the samples determined.
Small samples were machined from th Mg4Y and 680°C for the Mg4YxGd (x=1,4), respectively and held for 5 min, to ensure melt homogeneity then cooled to 450°C with a controlled cooling rate of 20 K/min. The *in situ* diffraction experiments were conducted in transmission geometry using a beam with a cross section of 1×1 mm^2. The beam was set to the photon energy of 100 keV, corresponding to a wavelength of λ= 0.0124 nm. During the experiments the 2D diffraction patterns were recorded with an acquisition time of 3.5 s (corresponding to a temperature resolution of approximately 1 K) by a Perkin Elemer XRD 1621 Flat Panel detector with a pixel size of (200 µm $)^2$ [21]. The 2048 × 2048 pixel diffraction patterns were integrated to azimuthal line profiles by using the fit2d [22] software.
The information on the intermetallic phases was obtained from the Pearson's Crystal Structure Database [23], the d-spacings and 2θ angles for the phases were calculated using CaRIn Crystallography 3.1™ software. The experimentally recorded temperatures for the solidification of various phases were compared with the results of the simulations performed with Pandat 8.1™ thermodynamic software.

Results and discussion

Microstructure

The SEM micrographs of the microstructures of the investigated alloys in as-cast condition, in secondary electron mode, are shown in Figure 1.

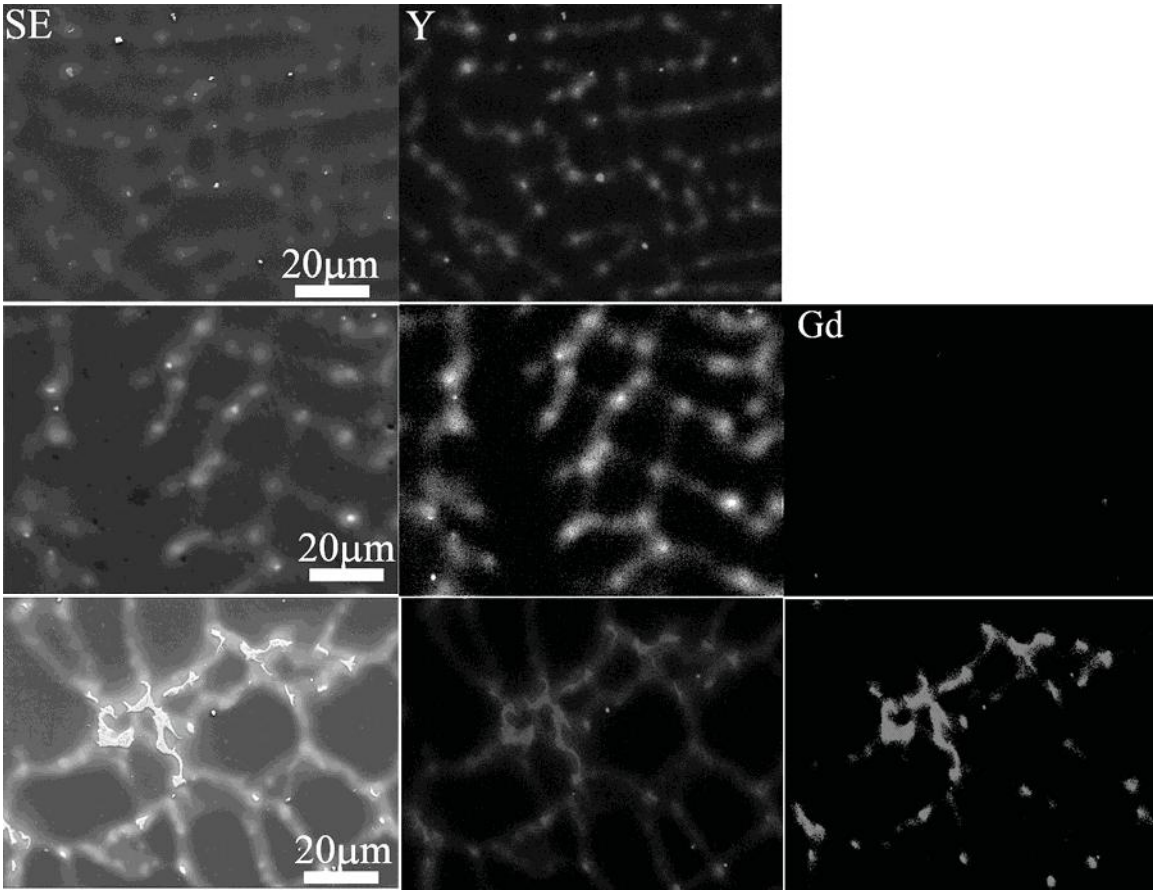


Figure1. SEM micrographs (a,c,f) and EDXS maps of Y (b,d,g) and Gd (e, h) of the investigated (a-b) Mg4Y, (c-e) Mg4Y1Gd and (f-h) Mg4Y4Gd alloys in as cast condition.

The Mg4Y consists of α-Mg dendrites and intermetallic compounds with high Y content likely to be; Mg_2Y and $Mg_{24}Y_5$. In the ternary alloys Mg4Y1Gd and Mg4Y4Gd, despite of the high solubility of the Gd, there are segregated areas which contain higher Gd and higher Y concentration simultaneously. These areas can contain $Mg_{24}Y_{5-x}Gd_x$, $Mg_5Gd_xY_{1-x}$ and $Mg_2Y_{1-x}Gd_x$ ternary phases.

In situ synchrotron diffraction

The line profiles resulting from the azimuthal integration of the 2D diffraction patterns acquired during the solidification experiments are shown in Figure 2-4. When the samples are molten a diffuse background originating from the melt and diffraction peaks of the graphite crucible can be observed.

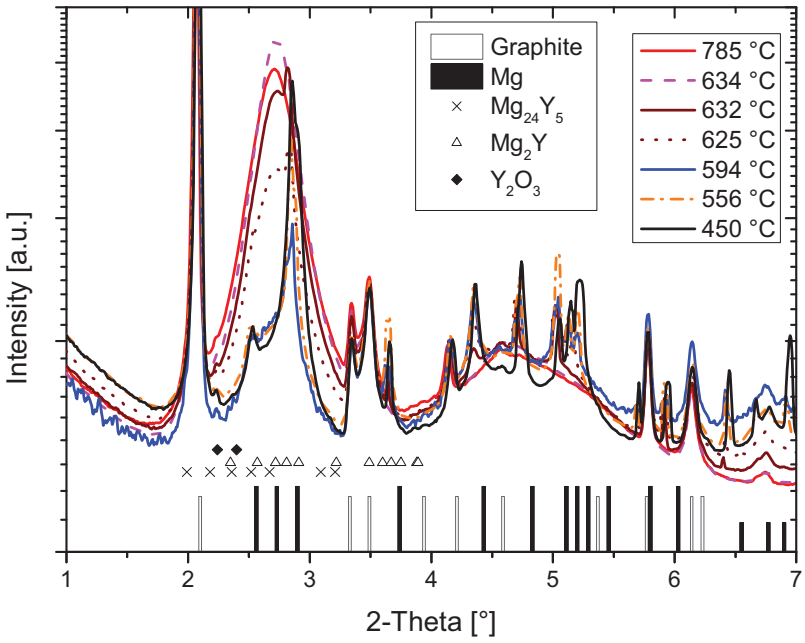


Figure 2. Sequence of XRD line diagrams obtained by the integration of the diffraction patterns recorded during solidification of Mg4Y. (wavelength λ = 0.0124 nm)

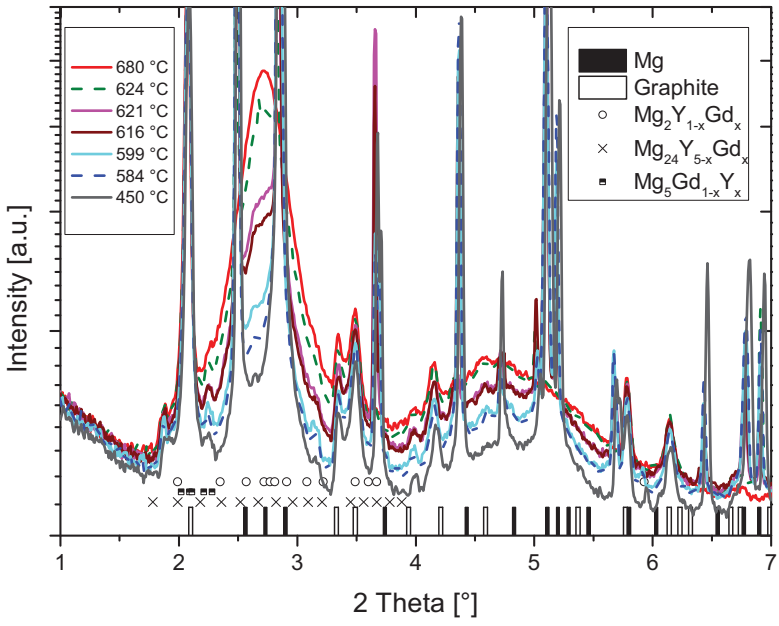


Figure 3. Sequence of XRD line diagrams obtained by the integration of the diffraction patterns recorded during solidification of Mg4Y1Gd. (wavelength λ = 0.0124 nm)

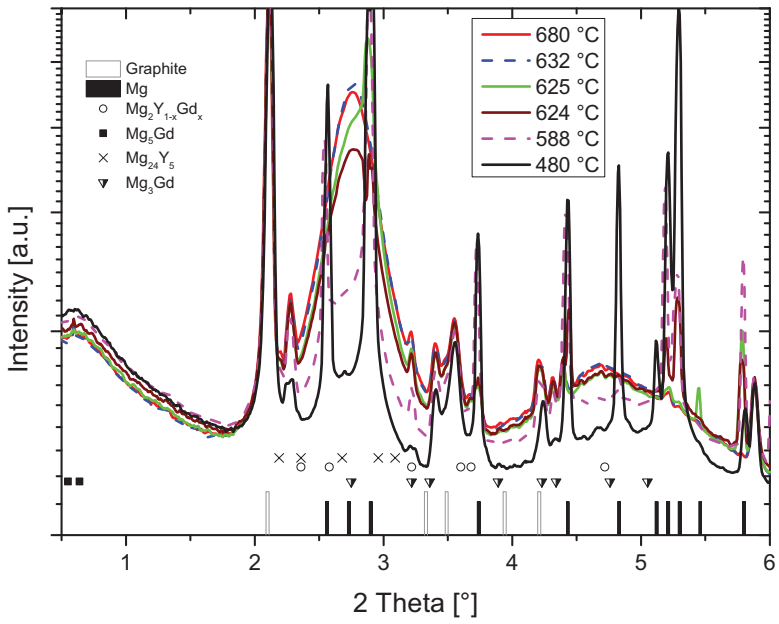


Figure 4. Sequence of XRD line diagrams obtained by the integration of the diffraction patterns recorded during solidification of Mg4Y4Gd. (wavelength λ = 0.0124 nm)

In the case of Mg4Y the sample was heated up to 800°C and held for 5 minutes as shown in Figure 2. During the holding time a peak appears that can be identified as Y_2O_3 phase. During the cooling from 800°C (red) to 634°C (magenta) only the change of the shape of the molten background can be seen. At 634°C peaks due to α-Mg appear. At 622°C (cyan) the Mg peaks became more pronounced and they become fully resolved. The additional peaks are observed at 622°C, which can be identified as either Mg_2Y or $Mg_{24}Y_5$. Due to the high temperature (622°C) the formation of the Mg_2Y phase is more likely. At 594°C (blue) the first independent peak from the $Mg_{24}Y_5$ appears. During cooling the intensity of this peak changes and the end of the solidification cannot be determined. This can be attributed to the mechanical instability of the setup, which results in the changes of the investigated volume in the sample.

In the case of the Mg4Y1Gd, the melt was held at 680°C (red) for 5 minutes. Diffraction peaks can be observed in addition to those of the crucible and the molten background. The peaks next to the first graphite peak correspond to the peak of an undissolved intermetallic phase, Mg_2Y or already modified $Mg_2Y_{1-x}Gd_x$ ($0 \leq x \leq 0{,}26$) (hP12-$MgZn_2$ type). The first Mg peaks appear at 628 °C. At 599 °C (blue) Mg peaks are fully resolved and some new peaks start to form. Most of the peaks are Mg_2Y (hP12-$MgZn_2$ type) but others can be either the $Mg_{24}Y_5$ or Mg_5Gd phase. The cubic structure of these two phases are similar and the larger crystal constant *a* (Mg_5Gd) is very close to $2a'$ ($Mg_{24}Y_5$) thus it is possible to have an overlapping of the diffraction peaks of the two phases. However, the major peaks of the Mg_5Gd based phase cannot be observed during the experiment and the low concentration of Gd suggests that it is more likely to be $Mg_{24}Y_5$.

In the case of Mg4Y4Gd the unsolved phase peaks are most likely to correspond to Mg_2Y. The solidification starts with the nucleation and growth of the α-Mg dendrites 632°C (blue). As the cooling advances the peaks become more pronounced and fully resolved at 624°C (green). The additional peaks belong to the Mg_2Y phase but some of the peaks correspond to the Mg_3Gd phase. At 611°C a peak at $2\theta = 0{,}55°$ start to form. This peak is due to the Mg_5Gd phase. The last step of the solidification is the formation of the $Mg_{24}Y_5$ phase at 487°C.

The experimental results were correlated with thermodynamic simulations of the solidification, performed with the Pandat 8.1 software. The Scheil calculation predicted in all three cases the presence of the $Mg_{24}Y_5$ phase and formation temperatures of 573°C for the Mg4Y phase, 572 °C for the Mg4Y1Gd phase and 567°C for the Mg4Y4Gd phase, respectively. In the case of Mg4Y the results suggest the formation of Mg_2Y at 622°C. The results from the EDXS maps of the as-cast alloy show a high atomic concentration of Y (up to 40%), thus it is more likely Mg_2Y. In case of Mg4Y1Gd the holding time at 680°C was not sufficient to dissolve the intermetallic particles of the Mg_2Y phase. Therefore the solidification experiment started with already solid phases. The formation $Mg_{24}Y_5$ was observed at 599°C instead of 572°C as predicted with Pandat software.
As these grains float in the melt without fixed orientation their detection is incidental, which greatly effects the temperature at which the phase formation is detected and the setup has also ±2°C inaccuracy at this temperature range (~650°C). Despite these limitations, the onset temperature, obtained experimentally by in situ diffraction and this evaluation method provides a unique tool to improve the accuracy of existing thermodynamic databases. Furthermore the presence of more than one intermetallic phase formation was proven experimentally, although it could not be predicted by the thermodynamic simulations due to the lack of reliable thermodynamic data available in the literature on Mg-RE based systems.

Conclusion

In summary, *in situ* solidification experiments were performed on Mg4Y and Mg4YxGd alloys (x= 1, 4) by synchrotron radiation diffraction and the experiment results were correlated with thermodynamic calculations. From the results the following conclusions can be drawn.

- During cooling at 20 K/min from 800 °C or 680 °C to 450 °C the solidification sequence could be determined experimentally.
- α-Mg solidifies at a temperature of 634°C (Mg4Y), 628°C (Mg4Y1Gd) and 632°C (Mg4Y4Gd). The Pandat predicts 642°C (Mg4Y), 640°C (Mg4Y1Gd), 635°C (Mg4Y4Gd). The temperatures of the onset of the solidification predicted with Pandat software show a similar trend in the formation temperatures determined experimentally.
- Mg_2Y intermetallic phase formation is observed at 622°C (Mg4Y) but this phase was already in the melt in the two ternary systems (Mg4Y1Gd, Mg4Y4Gd). The Pandat does not predict the formation of this phase for the four investigated alloys.
- $Mg_{24}Y_5$ phase forms at 594°C (Mg4Y), 599°C (Mg4Y1Gd) and 487°C (Mg4Y4Gd). Pandat predicts 573°C, 572°C and 567°C using Scheil calculations, which are lower than those recorded experimentally.
- In the case of the Mg4Y4Gd alloy, Mg_5Gd forms at 611°C. Pandat software does not predict the formation of Gd rich intermetallic phases in this case.

Acknowledgements

The authors acknowledge the DESY for the provision of synchrotron radiation facilities in the framework of the proposal I-20120627, and the European Union FP7-PEOPLE-ITN-2011 program under REA Grant Agreement No 289163: MagnIM project for financial support.

1. L.L. Rokhlin, *Magnesium Alloys Containing Rare Earth Metals, Structure and Properties*, (London: Taylor & Francis, 2003).

2 N. Hort et al.; "Magnesium alloys as implant materials-Principles of property design for Mg-RE alloys" *Acta Biomaterialia* 6 (2010), 1714-1725.

3 F. Witte et al.; "Degradable biomaterials based on magnesium corrosion", *Current Opinion in Solid State and Materials Science* 12 (2008) 63-72.

4 F. Witte, "The history of biodegradable magnesium implants: A review", Acta Biomaterialia, 6 (5), (2010), 1680-1692

5 G. Barucca et al., "Formation and evolution of the hardening precipitates in a Mg-Y-Nd alloy", *Acta Materialia* 59 (2011) 4151-4158.

6 G. Requena, et al., "The effect of the connectivity of rigid phases on strength of Al-Si alloys", *Advanced Engineering Materials* 13 (2011) 674-684.

7 P.J. Apps et al., "Precipitation reactions in magnesium-rare earth alloys containing yttrium, gadolinium or dysprosium", *Scripta Mater*. 48 (2003) 475-481.

8 F. Feyerabend et al., "Evaluation of short-term effects of rare earth and other elements used in magnesium alloys on primary cells and cell lines", *Acta Biomaterialia* 6 (5) (2010), 1834-1842

9 T.B. Massalski, *Binary Alloy Phase Diagrams*, (Materials Park Ohio: ASM International 1990).

[10] M. Giovannini et al., "On the systematics of phase equilibria in complex magnesium-rare earth systems: Gd-Y-Mg system", *Zeitschrift fuer Metallkunde/Materials Research and Advanced Techniques* 88 (5) (1997), 372-378.

11 X. Gao et al., "Microstructure evolution in a Mg-15Gd-0.5Zr (wt.%) alloy during isothermal aging at 250 °C" *Mater. Sci. Eng A* 431 (2006) 322-327.

12 W.J. Boettinger et al., "Phase-field simulation of solidification", *Annual Review of Materials Research*, 32 (2002) 164-194.

13 Y. L. Liu, S. B. Kang; "The solidification process of AI-Mg-Si alloys" *Journal of Materials Science* 32 (6) (1997) 1443-1447.

14 S.S. Babu et al., " Time-resolved X-ray diffraction investigation of primary weld solidification in Fe-C-Al-Mn steel welds", *Acta Materialia* 50 (19) (2002) 4763-4781.

15 O. Shuleshova et al., "In situ observations of solidification in Ti-Al-Ta alloys by synchrotron radiation", *Intermetallics* 19 (5) (2011) 688-692.

16 D.Tolnai et al., "Study of the solidification of AS alloys combining in situ synchrotron diffraction and differential scanning calorimetry" *Materials Science Forum,* 765 (2013) 286-290.

17 D. Tolnai et al.,"In situ synchrotron diffraction of the solidification of Mg-RE alloys" *Magnesium Technology 2013*, (2013) 253-257.

18 D. Tolnai et al., "In situ synchrotron diffraction of the solidification of Mg4Y3Nd" *Materials Letters,* 102-103 (2013) 62-64

19 D. Tolnai et al.," In situ synchrotron tomographic investigation of the solidification of an AlMg4.7Si8 alloy" Acta Materialia 60 (6-7) (2012) 2568-2577.

20 P. Staron et al.," In situ experiments with synchrotron high-energy X-rays and neutrons" *Advanced Engineering Materials* 13 (2011) 658-663.

21 http://www.perkinelmer.com/pdfs/downloads/009299B_01%20PRD.pdf

22 http://www.esrf.eu/computing/scientific/FIT2D/index.html

23 P. Villars, and K. Cenzual, Pearson's *Crystal Data - Crystal Structure Database for Inorganic Compounds* (on CD-ROM), (Ohio: ASM International, Materials Park, USA, Release 2012)

Magnesium Technology 2014
Edited by: Martyn Alderman, Michele V. Manuel, Norbert Hort, and Neale R. Neelameggham
TMS (The Minerals, Metals & Materials Society), 2014

A NEW METHOD FOR MELTING Mg-Li ALLOYS

Liu Gong, Jieyu Zhang*, Tian Yin, Jia Wei, Guangxin Wu

Shanghai Key Laboratory of Modern Metallurgy and Materials Processing, Shanghai University, Shanghai，200072, China

Keywords: Mg-Li alloys, Lattice parameter, Melt, Phase diagram

Abstract

Mg-Li alloys display difficulties in conventional casting due to serious oxidation or burning during the melting process. This paper presents a new method melting Mg-Li alloys compared with alloys melted in vacuum melting furnace. MgH_2-LiH system dehydrogenized and melted at high temperature in a special specimen chamber to prepare Mg-Li alloys. The experimental results data agreed well with Mg-Li phase diagram. With the content of Li increased, crystal structure of alloys changed. X-ray diffraction studies, optical microscopy, scanning electron microscopy were carried out to explore the variations in micro structural differences during processing. The more content of Li increased, the greater the lattice parameter of magnesium would become. Thus, β-Li phase in the matrix increased with the increase of lithium content. The new method can be a good way to melt alloys, which effectively reduce magnesium evaporation and lithium oxidation.

Introduction

During the past decades, the binary alloy system of Mg–Li has raised great research interest due to its unique structural, mechanical, electrical and thermal properties, etc. The Mg–Li system is regarded as a kind of ultra light materials with high specific strength, and has great applications for commercial transport, aerospace, electronics and automobile, etc[1-3].

In general, Mg-Li alloys are conventionally prepared by the following method: directly mixing and fusing the metallic elements. This method has the advantage of convenient operation, simple equipment, and also has the disadvantage of metal loss in the alloy smelting process, alloy composition segregation and high production cost. These disadvantages could be overcome by the adoption of the molten salt electrolysis process.

This method was first developed by Smolinski[4]. Many researchers constantly study and develop this method [5-7]. At the same time, the molten salt electrolysis method has many other advantages. First, the corresponding element contents of alloys could be controlled by electrochemical parameters. Second, the process could be conducted with a simple apparatus. Third, mass production is easy [8]. These advantages make the molten salt electrolysis process an effective method for the preparation of Li-Mg alloys.

*Corresponding author.
E-mail address: zjy6162@staff.shu.edu.cn (Jieyu Zhang)

The present study focused on study a new method melting Mg-Li alloys compared with alloys melted in vacuum melting furnace. MgH_2-LiH system dehydrogenized and melted at high temperature in a special specimen chamber to prepare Mg-Li alloys.

Experimental method

The chemicals MgH_2 (H-storage grade powders) and LiH (95% purity) were all purchased and used directly without pretreatment. All sample storage and handling were performed in an Ar-filled glove box. The MgH_2-LiH composite was prepared by ball milling in a molar ratio of 1:3 and 3:17 for half an hour. The ball milling was undertaken in a Pulverisette 4 planetary ball mill, the milling parameters were kept constant for all trials, and the samples were milled at 300 rpm using stainless steel balls 10 mm in diameter and with a ball-to-powder weight ratio of 10:1. The temperature was increased from ambient to 600 ℃ at 5℃/min.

We adopt double tubular reactor with stainless steel, Figure 1 and Figure 2 show the definite experimental facility and the reaction kettle.

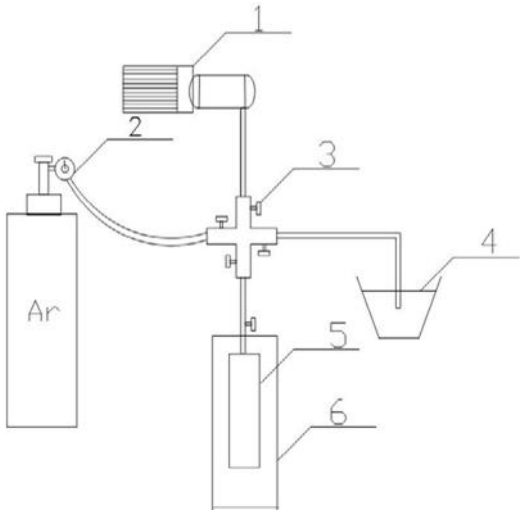


Figure 1. Definite experimental facility 1- rotary-vane vacuum pump 2- flow meter 3-control valve 4-air breather 5- reaction kettle 6-the constant temperature system

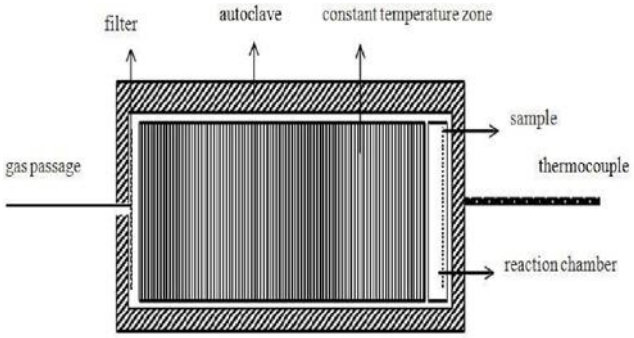


Figure 2. Reaction kettle

The device has the following characteristics: good sealing performance; high vacuum; high measurement precision, wide measurement range, high efficiency, easy to operate. High-pressure pure argon (99.999%); vacuum system including rotary-vane vacuum pump (final vacuum : 6.67×10^{-2} Pa); nickel-chromium and chromium-nickel thermocouple (measurement range: 0~1573 K); reaction kettle (Limit pressure 8 MPa) [9]; the constant temperature system including temperature-controlled cabinet (power 4 Kw).

X-ray diffraction (XRD) data were obtained with a D/max-rC X-Ray diffractometer with a Cu-Ka X-ray source. The scans were done from 10° to 80° at 1°/min and a step size of 0.02°. The voltage used was 40 kV with a current of 100 mA. Samples were mounted onto a glass board 1 mm in thickness in the Ar-filled glove box and sealed with an airtight hood composed of an amorphous membrane in order to avoid oxidation during the XRD measurement.

Results and discussion

X-ray diffraction (XRD) data analysis

Figure 3 shows that after balling for 0.5h, the composite doesn't change. After subsequent heating to 600℃, the product is pure Mg.

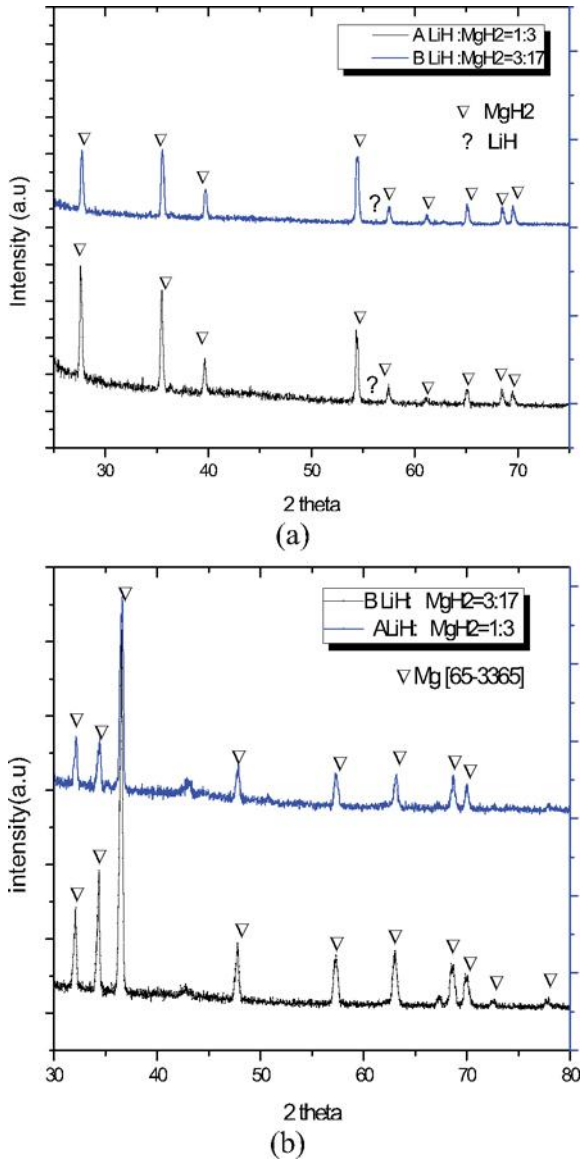


Figure 3. X-ray diffraction patterns of $LiH-MgH_2$ composite after ball milling for 0.5 h (a), after subsequent heating to 600℃ (b)

From the point of view of the stability of the crystal structure, when the particle size of alternative is closer, the more stable is the solid solution, and amount of solid solution is greater. When Δr is lower than 15%，the solute and solvent can produce a continuous solid solution. Thus, the atomic radius of magnesium is 136 pm and the atomic radius of lithium is 123 pm. According to Eq. (1) [10], Δr is lower than 15%, we deduce that Li solid solution in the Mg.

$$\Delta r = \frac{r_1 - r_2}{r_1} \tag{1}$$

For further study, we analyzed α-Mg in the images of the XRD peaks and found that α-Mg deviation occurred, according to the formula of hexagonal system, which was listed as Eq. (2). Based on backward inference method, we could calculate the lattice parameter of each peak corresponding in the magnesium matrix: the values of a and c. And then use the figure solution of extrapolation method to calculate accurate lattice parameter.

$$d = \frac{a}{\sqrt{\frac{2}{3}(h^2 + hk + k^2) + (\frac{a}{c})^2 l^2}} \tag{2}$$

But for hexagonal system, formula of inter planar crystal spacing contains two parameters a and c, so a and c can't be calculated easily based on backward inference method. Using extrapolating function $\left(\cos^2\theta/\sin\theta + \cos^2\theta/\theta\right)$, we can get the lattice parameter of magnesium as the following table Ⅰ. With the increase of Li content, crystal structures of alloys change correspondingly. The more content of Li increases, the greater the lattice parameter of magnesium would become. Thus, β-Li phase in the matrix would increase with the increase

of lithium content.

Table Ⅰ. Lattice parameter of magnesium

Sample	lattice parameter/ Å	
	a	c
Pure Mg	3.2092	5.2105
LiH-MgH_2=1:3	3.2130	5.2110
LiH-MgH_2=3:17	3.2101	5.2113

At room temperature, the lattice parameter of magnesium was described as: a=3.2092 Å, c=5.2105 Å, c/a=1.6236. The lattice parameter of β-Li: a=3.5093 Å. It was reported that when lithium content is 5.7-10.3 mass %, β-Li of body centered cubic crystal structure began to emerge. β-Li phase could be seen as a kind of special solid solution with magnesium as the solvent atom. As XRD couldn't detect the presence of Li, we would use other detecting and testing procedures to detect the presence of Li.

Scanning electron microscopy morphology （SEM）analysis

Figure 4 shows the scanning electron microscopy morphology（SEM）of sample A （LiH-MgH_2=1:3）, after subsequent heating to 600 ℃. For powder sample A （LiH-MgH_2=1:3）, there are mainly small and large flocculent particles together. Small particles and large flocculent reunion is Mg and there is a small amount of O, maybe the sample is partly oxidized. Element Mg is easy to be oxidized, we need to take measures to prevent. All the operations were protected to avoid contact with air. It was a pity that we didn't find Li.

Figure 5 shows the scanning electron microscopy morphology（SEM）of sample B （LiH-MgH_2=3:17）after subsequent heating to 600℃. There are mainly small flocculent and large particles together. Small particles and large flocculent reunion is Mg. It was a pity that we didn't find Li as well.

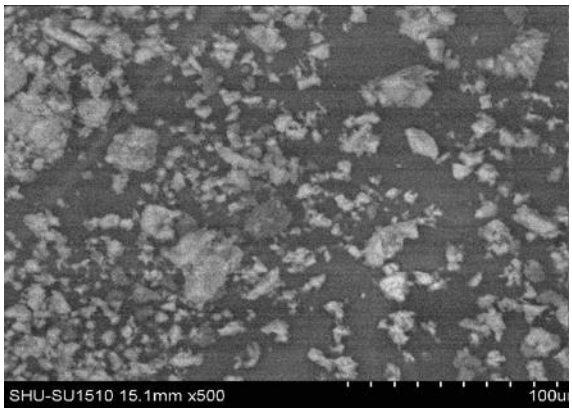


Figure 4. scanning electron microscopy morphology（SEM） of sample A （LiH-MgH_2=1:3）, after subsequent heating to 600℃

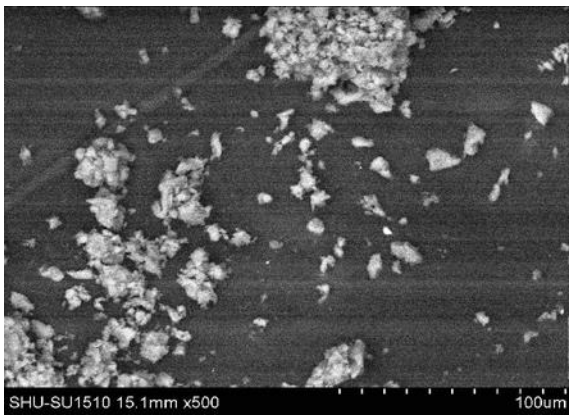


Figure 5. scanning electron microscopy morphology （SEM） of sample B （LiH-MgH_2=3:17）, after subsequent heating to 600℃.

It was calculated that the average particle size of sample A is a little greater than sample B. This result agreed well with the XRD results. It could be seen that the more content of Li increased, the greater the lattice parameter of

magnesium would become.

Phase diagram comparison

As shown in Figure 6, the calculated data in liquid phase at 600℃ fit well with the experimental data. There are three phases in Li-Mg phase diagram: liquid, (Li) and (Mg). It is characterized by a maximum in the bcc liquidus, a eutectic and the retrograde Mg solvus. The general form of the liquidus over the entire system, with a maximum near 29 at.% Li and 593℃ and a eutectic reaction near 25 at.% Li.

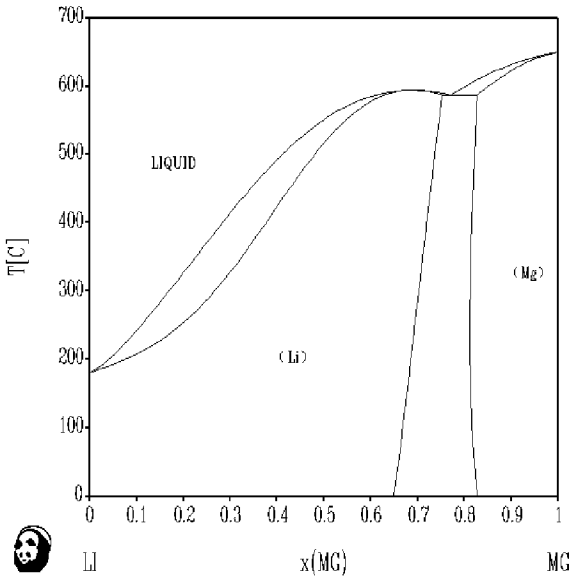


Figure 6. Li-Mg phase diagram

As a conclusion, it is necessary to emphasize that the calculated phase diagrams are only as good as the experimental data used to evaluate them. However, if a number of experimental data points are available, the optimization procedure can tell us whether one series of experimental results can be thermodynamically compatible with the results of a different investigation in another, but related part of the diagram. In this respect, the optimized phase equilibriums are a compromise between various data.

Conclusions

MgH_2-LiH system dehydrogenized and melted at high temperature in a special specimen chamber to prepare Mg-Li alloys. The experimental results data agree well with Mg-Li phase diagram.

(1) The more content of Li increased, the greater the lattice parameter of magnesium would become and β-Li phase in the matrix increased with the increase of lithium content.

(2) There are mainly small and large flocculent particles together. Small particles and large flocculent reunion is Mg,

(3) The experimental results data agree well with Mg-Li phase diagram.

References

1. J. A. Jensen and L. S. Chumbley, "Processing and mechanical properties of magnesium-lithium composites containing steel fibers," *Metallurgical and Materials Transactions A,* 299(3)(1998) , 863-873

2. J. F. Mason et al., "Magnesium-lithium alloys in metal matrix composites—A preliminary report," *Journal of materials science*, 24(1989), 3934-3946.

3. G. J. Shen and B. J. Duggan, "Texture Development in a Cold-Rolled and Annealed Body-Centered-Cubic Mg-Li Alloy," *Metallurgical and Materials Transactions A*, 38(10) (2007), 2593-2601.

4. Smolinski, "Electrolytic deposition and diffusion of lithium into magnesium,"

Journal of Applied Chemistry, 6(1956), 180-186

5. Y. Castrillejo et al., "Electrochemical behaviour of Magnesium ions in the equimolar $CaCl_2$-NaCl mixture at 550℃," *Electrochemical Acta*, 42(1997), 1869-1876.
6. X. Zhang, S. Q. Jiao, and Xiao S J, "Electrochemical behavior of Magnesium and aluminium ions in alkali chloride melt," *Materials Science Forum*, 488(2005), 811-814.
7. L. P. Polyakova, P. Taxil, and E. G. Polyakov, "Electrochemical behaviour and Codeposition of titanium and niobium in chloride-fluoride melts," *Journal of Alloys and Compounds,* 359(2003), 244-255.
8. Z. Chen et al., "Electrodeposition of Li and electrochemical formation of Mg–Li alloys from the eutectic LiCl–KCl," *Alloys Compd.,* 464(2008),174–78
9. Q. Li et al., "Properties of Hydrogen Storage Alloy $Mg_{2-x}Ag_xNi$ (x=0.05, 0.1, 0.5) by Hydriding Combustion Synthesis," *Alloys Comp.,* 359(2003), 128-132.
10. G. V. Raynor, *The physical metallurgy of Mg and its alloys* (Pergamon: Press,1959).

Magnesium Technology 2014

Texture and Wrought Processing I

Magnesium Technology 2014
Edited by: Martyn Alderman, Michele V. Manuel, Norbert Hort, and Neale R. Neelameggham
TMS (The Minerals, Metals & Materials Society), 2014

DEFORMATION BEHAVIOR OF ZE10 MAGNESIUM ALLOY SHEET

Patrik Dobroň[1*], Jaroslav Balík[1], František Chmelík[1], Kseniya Illková[1], Daria Drozdenko[1], Jan Bohlen[2], Dietmar Letzig[2], Pavel Lukáč[1]

[1]Charles University in Prague, Faculty of Mathematics and Physics, Department of Physics of Materials, Ke Karlovu 5, 12116, Prague 2, Czech Republic
[2]Helmholtz-Zentrum-Geesthacht, Zentrum für Material- und Küstenforschung GmbH, Max-Planck-Straße 1, D21502 Geesthacht, Germany

Keywords: Magnesium alloys sheet, Mechanical anisotropy, Work hardening, Acoustic emission

Abstract

Rolled Mg-Zn-Rare earth sheet after annealing was deformed at room temperature with the tensile axis oriented in both the rolling (RD) and the transversal direction (TD). The deformation behavior of the sheet has been investigated by acoustic emission (AE) and electron backscattered diffraction (EBSD) measurements, where the AE signal analysis correlates the microstructure and the stress-strain curves to the active deformation mechanisms. X-ray diffraction was applied to receive orientation images in order to characterize the deformation texture before and after the test.

Introduction

The recent developments in industrial applications of magnesium alloys are currently focused on the utilization of magnesium sheets. Mechanical properties (especially strength, ductility and formability) of wrought magnesium alloys having hexagonal close packed (hcp) lattice are significantly influenced by strong textures [1]. The texture development and the deformation behavior of magnesium alloys depend on the activation of both dislocation slip and twinning.

It is generally accepted that the tensile in-plane deformation in Mg alloy sheets is initially realized by dislocation glide in basal planes which must be accomplished by a contribution of dislocation glide in non-basal planes and/or twinning. However, the activity of the individual non-basal slip systems and twinning with progressing plastic deformation is still being discussed by many authors. Some authors consider prismatic slip systems as more dominant [2, 3]. Hama and Takuda [2] who investigated the stress-strain curves obtained in cyclic loading-unloading tests of AZ31B magnesium alloy, have shown that basal and prismatic slip systems and tensile twinning were activated during loading while prismatic slip systems were hardly activated during inelastic unloading. They have also claimed that the activity of basal slip systems depends on the inhomogeneity of the samples. On the other hand, several investigators claim that homogeneous deformation is possible only when the second-order pyramidal slip systems are active, i.e. glide of (c+a) dislocations is necessary [4-7]. The activity of (c+a) dislocations in magnesium was found experimentally [8-10]. Using polycrystal plasticity modeling, Agnew and Duygulu [6] have shown that decreasing anisotropy of AZ31 with increasing temperature may be explained by an increasing activity of the second-order pyramidal slip systems (increased (c+a) dislocation activity) and the primary (tensile) twinning mode. Rolled sheets of the Mg-based alloys exhibit a typical basal texture with orientation of basal planes almost parallel to the sheet plane [11-13]. Such a texture favors deformation twinning if a compressive stress is applied along the rolling direction (RD) [14]. In the case of the tensile in-plane test, deformation can be realized practically without (near-zero) tensile twinning [6, 15]. Bohlen et al. [13] have recently reported the texture development in six Mg-Zn alloys with dilute additions of Y, Nd, Ce and Mn. It should be mentioned that the angular distribution of the basal poles in ZE10 is significantly broader to the transversal direction (TD); it is not affected in the RD. On the other hand, the prismatic plane poles are mostly oriented parallel to the RD. Therefore the strong basal texture is responsible for tension – compression asymmetry and anisotropy.

For the study of dynamic processes involved in plastic deformation of Mg alloy sheets, the acoustic emission (AE) technique can be efficiently used. It is based on sensitive detection of the transient elastic waves generated within the material during deformation due to sudden localized structure changes [16]. Detected AE signals can be parameterized according to their amplitude, number of counts, duration, energy or frequency. A direct correlation of AE parameters with the stress-strain curve yields information on the dynamic changes indicating e.g. activation of various deformation mechanisms during plastic deformation of Mg alloys [17, 18].

The aim of the present work is to examine deformation mechanisms occurring during tensile testing (along both RD and TD) of a ZE10 Mg alloy sheet by the AE method. The texture evolution was also measured. The stress dependence of the strain hardening rate and in situ AE were used in order to indicate deformation mechanisms during loading. Humps observed in the stress dependence of the strain hardening rates at the very beginning of strain are discussed. The measurement of the AE activity, represented by the AE count rate parameter, reveals dynamic changes in collective dislocation processes and possible twin nucleation during in-plane tensile tests under given conditions.

Experimental

Magnesium alloy ZE10 (Mg + 1.3 wt.% Zn+ 0.2 wt.% Ce + 0.1 wt.% La) was received as a rolled sheet of a thickness of 1.6 mm in the O temper condition. Pieces of the material were annealed for 1-16 hours at 300 °C to obtain a stress released condition (practically free of twins). Microhardness measurements were used to determine the lowest preliminary hardening state, in which the hardness value reaches a minimum. An annealing time of 6 hours was established.

Global texture information about the annealed and deformed sheets was obtained using X-ray diffraction. A Panalytical X-ray diffractometer setup using CuKα radiation was employed to measure pole figures on polished samples in reflection geometry to a sample tilt of 70°. The texture analysis was conducted on the annealed sheet as well as on specimens after tensile testing to fracture.

A computer-controlled DAKEL-IPL AE system based on continuous storage of AE signals with 2 MHz sampling frequency was used to monitor the AE activity. A miniaturized MIDI-410-2

piezoelectric transducer (diameter 6 mm) was attached to the specimen surface with the help of silicon grease and a spring. A preamplifier with a gain of 35 dB was used. After the measurement, threshold-level detection of recorded AE signals was done to achieve a comprehensive set of AE parameters. The threshold voltage for the AE count rate $\Delta NC/\Delta t$ (number of counts per second) was 15 % of the maximum voltage (2.4 V) and death time for the separation of individual AE events was 50 μs.
Four samples were stressed to specific points on the deformation curve and then EBSD was used to analyze the sample microstructure in a field emission gun scanning electron microscope (Zeiss Ultra 55, EDAX/TSL EBSD system and Hikari detector) on electropolished longitudinal sections. Special attention was given to the formation of twins, their type and distribution.

Results

Sheet exhibits a typical microstructure consisting of elongated grains into RD with an average grain size of 16 μm. The initial textures and the textures after tensile deformation in the RD and TD of the rolled ZE10 magnesium alloy sheets are shown in Fig. 1. The textures are represented by the distribution of basal (0002) and prismatic poles. In the initial state, the pole figure (0002) of ZE10 sheet displays texture with the orientation of basal planes tilted away from the plane of the sheet (normal direction (ND)). The intensity of basal planes in the (0002) pole figure significantly varies with respect to RD and TD – the basal poles are broader tilt and splitting towards TD rather than to RD. The characteristic angular spread of basal planes with a double peak towards TD is observed. The pole figure has the highest intensity in RD. Such a texture is different from a texture observed in conventional magnesium alloy sheets, such as AZ31. It is interesting to note that Mackenzie and Pekguleryuz [9] have reported similar characteristics of the ZE10 texture. They investigated the texture evolution in rolled and annealed Mg-1Zn alloys with the addition of cerium. Weak non-basal textures were observed in Mg-1Zn-0.3Ce alloy sheets.

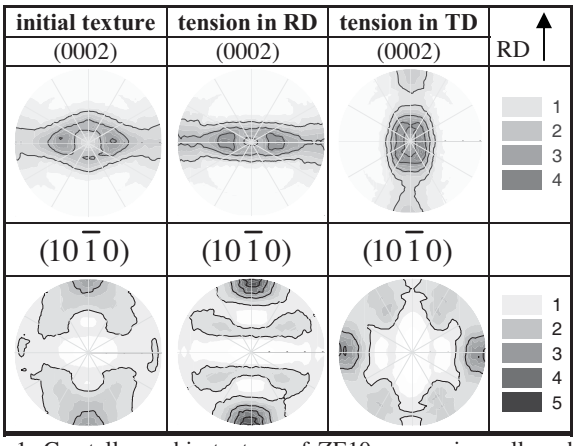


Fig. 1. Crystallographic texture of ZE10 magnesium alloy sheet before and after the tensile test along RD and TD.

Tensile tests along RD cause angular spread of basal fibers towards TD, but the highest intensity of the pole figure in RD still persists. Tension along TD causes angular spread of basal fibers towards RD i.e. perpendicular to the tensile axis, similarly as in the RD loading, and the pole figure shows 6-fold symmetry with peak intensity into TD.

Fig. 2 shows the stress–time curves with corresponding AE response for tension along the RD and the TD. The mechanical behavior is significantly influenced by texture. In-plane anisotropy of the yield strength (YS) between RD and TD sample is clearly seen; a higher value of YS for RD sample than TD one is observed.

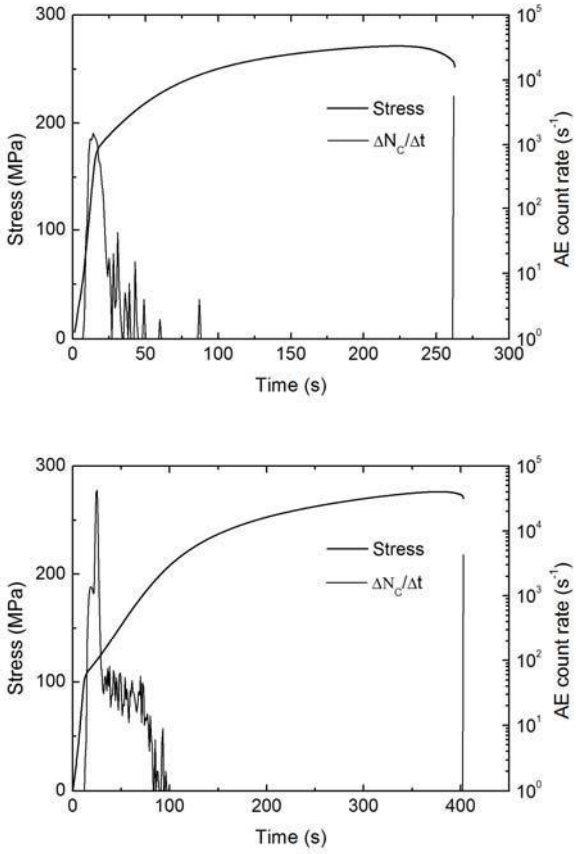


Fig. 2. Stress and the AE count rate vs. time curves for RD (upper) and TD (bottom).

Likewise, differences in the AE count rate are observed. It is important to note that the reverse is observed during straining of rolled AZ31 magnesium alloys. The strength of TD AZ31 samples is higher than that of RD ones as reported e.g. by Agnew and Duygulu [6] and Balík et al. [19]. From the stress-time curves it is obvious that the tensile direction has a strong influence on the tensile deformation behavior of ZE10 sheets. This deformation behavior can be better seen from the Kocks-Mecking plots [20], i.e. the plots of the strain hardening rate, θ, against the flow stress, σ. A qualitatively difference in the form of the initial parts of the Kocks-Mecking plots, for both RD- and TD-regimes, is shown in Fig. 3.
The strain hardening did not decrease monotonically with stress as observed in fcc metals. It can be seen that in the early straining stages, the strain hardening rate first decreases rapidly, then increases with increasing stress and after an increase again decreases with stress. A lift, occurring in the stress dependence of the strain hardening rate, is less pronounced and narrower for RD-regime than that for TD sample.
It can be seen that the AE activity starts at a lower flow stress in RD than in TD samples. Higher AE activity (maximum amplitude of individual AE events) at the beginning of plastic deformation is

much more pronounced for RD than for TD samples. Most of high amplitude signals are observed before the narrow lift in RD samples, while those for the broad one in TD samples persist throughout the occurrence of the lift.

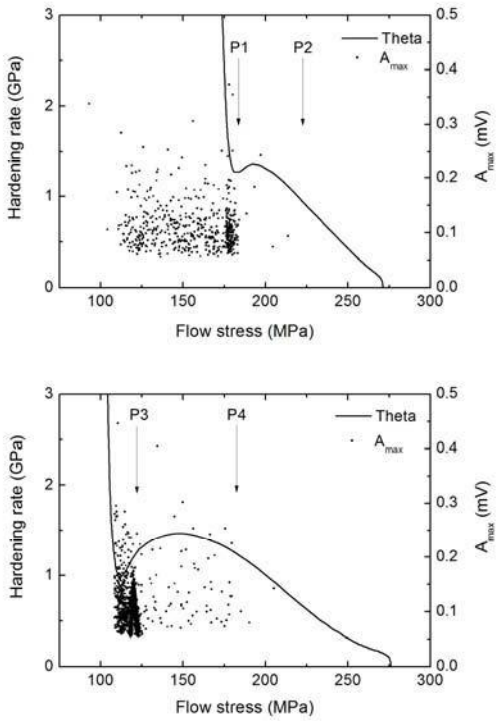


Fig. 3. Strain hardening rate-stress curves correlated with the maximal amplitude of the AE events for RD (upper) and TD (bottom).

The EBSD analysis was performed on four samples which were stressed to different states of deformation (marked as P1, P2, P3 and P4 position in Fig. 3) in order to study twinning activity (significant changes in the AE activity). Pole figures obtained from EBSD measurements are presented in Fig. 4. Gray points represent original texture after rolling process and black points symbolize twinning activity. Twin fraction was calculated from the inverse pole figure (IPF) maps (Fig. 4) and observed results are presented in Table I.

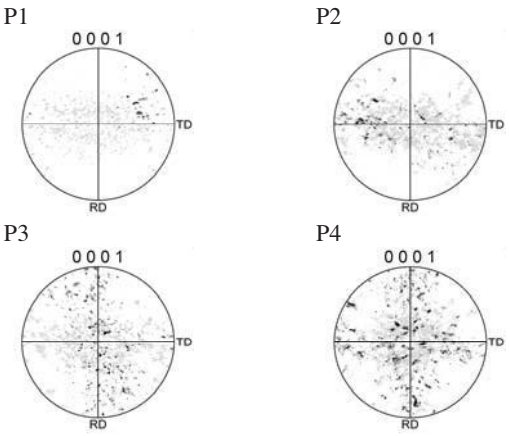


Fig. 4. Local EBSD orientation data; RD - positions P1, P2 and TD - positions P3, P4 (see Fig. 3).

Table I. Area fraction of twinned grains.

RD	P1	P2
	0.009	**0.036**
TD	P3	P4
	0.071	**0.1**

Discussion

The presented results indicate different micromechanisms responsible for the strain hardening behavior of ZE10 Mg alloy sheet deformed along both RD and TD. The texture analysis and AE measurements during straining are useful (and successful) tools indicating the microstructural evolution (dislocation evolution, twinning) and they help to estimate deformation micromechanisms. Likewise, the strain hardening behavior may be analyzed using the stress dependence of the strain hardening rate. As mentioned above, the form of the hardening lift is different for samples deformed in RD and TD. The concurrent AE measurements show that collective dislocation processes start at a lower flow stress for deformation in RD than in TD, which points out that the primary (basal) slip mechanism can be easier activated in RD.

The characteristic AE peak (AE count rate) at the onset of plastic deformation for samples deformed in both RD and TD is usually explained by a massive dislocation multiplication when basal and non-basal slip systems are activated. The lower and narrower AE peak (near the yield point) observed for samples deformed in RD can be assumed as a consequence of the AE activity before the yield point. The subsequent strong decrease in the AE count rate for the narrow lift observed in the samples deformed in RD can be explained by increasing number of sessile dislocations, which reduce the free path of moving dislocations. In the case of the samples deformed in TD, the AE count rate remains practically constant during the wide lift, which indicates the presence of twinning. Furthermore, S - shape of the deformation curve is a typical sign of twinning activity.

The significant twinning during tension in TD is presented in Fig. 4 (black points). The twin fraction was estimated to be 0.071 and 0.10 at the lower (position P3) and higher (position P4) deformations, respectively. Twin nucleation is an excellent source producing high amplitude AE signals (burst type) [21]. It has been reported [21, 22] that the twin growth does not produce AE contrary to the twin nucleation. Therefore, the plateau in the count rate, as well as the persistence of high amplitude signals, following the peak in TD is consistent with twin nucleation. For RD - testing, much smaller twin fractions, 0.009 and 0.036 (Fig. 3 upper, P1 and P2 position), respectively, were estimated. Considering the presence of some twins in the initial state and a substantially lower level of AE, thickening of pre-existing twins rather than the nucleation of new ones may be supposed for samples deformed in RD by tension (between positions P3 and P4).

Likewise, Dobroň et al. [23] have proven with the help of EBSD measurements that an increase in the AE count rate despite of a strong strain hardening in extruded AZ31 is caused by the twinning activity.

It should be mentioned that the lift in the stress dependence of the strain hardening rate observed in ZE10 specimens deformed in RD has a similar form as that observed in θ vs. σ plots for the annealed rolled AZ31 magnesium alloy sheets deformed in both RD and TD [24]. Balík et al. [25] have concluded that such

deformation behavior can be connected with the activity of double prismatic slip. We assume that the lift in the stress dependence of the strain hardening rate for ZE10 deformed in RD is related to the transition from primary (basal) to secondary (non-basal) slip mechanisms. We suppose likewise that the non-basal slip systems responsible for the lift in RD specimens are the prismatic planes with glide (cross-slip) of dislocations with the <a> type Burgers vectors [25, 26]. This is in agreement with observations of the prismatic slip of <a> dislocations in *in-situ* TEM experiments presented by Couret and Caillard [27].

On the other hand, the wider lift in the stress dependence of the strain hardening rate obtained for samples deformed in TD is a result of twinning.

Conclusions

Tensile tests at room temperature revealed that the initial texture has a great effect on dominant deformation processes (slip and twinning) during the early stage of straining of ZE10 magnesium alloy sheet. The strain hardening rate vs. the flow stress plots for sheet deformed in RD and TD were used to analyze the hardening behavior. The break in the monotonous stress dependence of the strain hardening rate – an increase in the strain hardening rate is observed at very low strain. Whereas the fairly narrow lift during RD loading seems to correspond to the transition from the initial basal slip to a secondary double prismatic slip, the broader lift in TD loading indicates the nucleation of the tensile twins. The AE and EBSD measurements that differ obviously for RD and TD loading support these suggestions as well. The results presented in this work show an effective way on how the stress dependence of the strain hardening rate connected with the AE and EBSD analyses can be of great importance for revealing deformation mechanisms.

Acknowledgement

This work received support from the Czech Science Foundation under grant 13 - 19812S. The work of P.D. is a part of activities of the Charles University Research Center "Physics of Condensed Matter and Functional Materials". F.C. is grateful to the Alexander von Humboldt Stiftung for financial support during his stay in Germany. D.D. is grateful for financial support from the grant SVV-2013- 267303.

References

[1] C.J. Bettles, M.A. Gibson, "Current wrought magnesium alloys: strengths and weakness," *JOM - J. Min. Met. Mat. S.*, 57 (2005), 46-49.

[2] T. Hama, H. Takuda, "Crystal-plasticity finite-element analysis of inelastic behavior during unloading in a magnesium alloy sheet," *Int. J. Plasticity*, 27 (2011), 1072-1092.

[3] C.J. Boehlert, Z. Chen, I. Gutiérrez-Urrutia, J. Llorca, M.T. Pérez-Prado, "In situ analysis of the tensile and tensile-creep deformation mechanisms in rolled AZ31," *Acta Mater.*, 60 (2012), 1889-1904.

[4] F.F. Lavrentev, "The type of dislocation interaction as the factor determining work hardening," *Mater. Sci. Eng. A*, 46 (1980), 191-208.

[5] P. Lukáč, "Hardening and softening during plastic deformation of hexagonal metals, " *Czech. J. Phys. B*, 35 (1985), 275-285.

[6] S.R. Agnew, O. Duygulu, "Plastic anisotropy and the role of non-basal slip in magnesium alloy AZ31B," *Int. J. Plasticity*, 21 (2005), 1161-1193.

[7] S. Sandlöbes, S. Zaeffere, I. Schestakow, S. Yi, R. Gonzalez-Martinez, "On the role of non-basal deformation mechanisms for the ductility of Mg and Mg-Y alloys," *Acta Mater.*, 59 (2011), 429-439.

[8] D.W. Brown, S.R. Agnew, M.A.M. Bourke, T.M. Holden, S.C. Vogel, C.N. Tomé, "Internal strain and texture evolution during deformation twinning in magnesium," *Mater. Sci. Eng. A*, 399 1-2 (2005), 1-12.

[9] L.W.F. Mackenzie, M.O. Pekguleryuz, "The recrystallization and texture of magnesium–zinc–cerium alloys," *Scripta Mater.,* 59 (2008), 665-668.

[10] S.B. Yi, J. Bohlen, F. Heinemann, D. Letzig, "Mechanical anisotropy and deep drawing behaviour of AZ31 and ZE10 magnesium alloy sheets," *Acta Mater.*, 58 (2010), 592-605.

[11] K. Hantzsche, J. Bohlen, J. Wendt, K.U. Kainer, S.B. Yi, D. Letzig, "Effect of rare earth additions on microstructure and texture development of magnesium alloy sheets," *Scripta Mater.*, 63 (2010), 725-730.

[12] A. Jain, S.R. Agnew, "Modeling the temperature dependent effect of twinning on the behavior of magnesium alloy AZ31B sheet," *Mater. Sci. Eng. A*, 462 (2007), 29-36.

[13] J. Bohlen, M.R. Nürnberg, J.W. Senn, D. Letzig, S.R. Agnew, "The texture and anisotropy of magnesium–zinc–rare earth alloy sheets," *Acta Mater.*, 55 (2007), 2101-2112.

[14] R.E. Reed-Hill, "Role of deformation twinning in determining the mechanical properties of metals: the inhomogeneity of plastic deformation," *Am. Soc. Metals*, 285 (1973), 311.

[15] J. Bohlen, F. Chmelík, P. Dobroň, F. Kaiser, D. Letzig, P. Lukáč, K.U. Kainer, "Orientation effects on acoustic emission during tensile deformation of hot rolled magnesium alloy AZ31," *J. Alloy Compd.*, 378 (2004), 207-213.

[16] C.R. Heiple, S.H. Carpenter, "Acoustic emission produced by deformation of metals and alloys – A review: Part I.," *J. Acoustic Emission*, 6 (1987), 177-204.

[17] P. Dobroň, J. Bohlen, F. Chmelík, P. Lukáč, D. Letzig, K.U. Kainer, "Mechanical anisotropy of AZ31 magnesium alloy sheet investigated by the acoustic emission technique," *Kovove Mater.*, 45 (2007), 129-133.

[18] A. Vinogradov, D. Orlov, A. Danyuk, Y. Estrin, "Effect of grain size on the mechanisms of plastic deformation in wrought Mg–Zn–Zr alloy revealed by acoustic emission measurements," *Acta Mater.*, 61 (2013), 2044-2056.

[19] J. Balík, P. Lukáč, J. Bohlen, K.U. Kainer, "Effect of temperature on tensile properties of hot rolled AZ31 Mg alloy sheets," *Kovove Mater.*, 45 (2007), 135-140.

[20] U.F. Kocks, H. Mecking, "Physics and phenomenology of strain hardening: the FCC case," *Progr. Mater Sci.*, 48 (2003), 171-273.

[21] C.R. Heiple, S.H. Carpenter, "Acoustic emission produced by deformation of metals and alloys – A review: Part II.," J. Acoustic Emission 6 (1987) 215-237.

[22] J.P. Toronchuk, "Acoustic emission during twinning of zinc single crystals," *Mater. Eval.,* (1977), 51-53.

[23] P. Dobroň, F. Chmelík, S.B. Yi, K. Parfenenko, D. Letzig, J. Bohlen, "Grain size effects on deformation twinning in an extruded magnesium alloy tested in compression," *Scripta Mater.*, 65 (2011), 424-427.

[24] J. Balík, P. Lukáč, Z. Drozd, R. Kužel, "Strain hardening behavior of AZ31 magnesium alloys," *Int. J. Mat. Res.*, 100 (2009), 322-325.

[25] J. Balík, P. Lukáč, R. Kužel, "Basal to Non-BasalTransition for In-Plane deformation of AZ31 Magnesium Alloys," *Acta Phys. Polonica A*, (2012), 435-438.
[26] M.R. Barnett, Z. Keshavarz, X. Ma, "A semianalytical sachs model for the flow stress of a magnesium alloy," *Metall. Mater. Trans. A*, 37 (2006), 2283-2293.
[27] A. Couret, D. Caillard, "An in situ study of prismatic glide in magnesium—I. The rate controlling mechanism," *Acta Metall.*, 33 (1985), 1447-1454.

Magnesium Technology 2014
Edited by: Martyn Alderman, Michele V. Manuel, Norbert Hort, and Neale R. Neelameggham
TMS (The Minerals, Metals & Materials Society), 2014

TEXTURE EVOLUTION DURING GRAIN GROWTH OF MAGNESIUM ALLOY AZ31B

J.J. Bhattacharyya[1], B. Radhakrishnan.[2], G. Muralidharan[2] and S.R. Agnew[1]

[1]Materials Science and Engineering Department, University of Virginia, Charlottesville, VA 22904, U.S.A.
[2]Materials Science and Technology Division, Oak Ridge National Laboratory, Oak Ridge, TN, 37831, U.S.A.

Keywords: Crystallographic texture, abnormal grain growth, magnesium alloy

Abstract

The strong basal texture which develops during the rolling of Mg alloy, AZ31B, sheet persists and can even increase during annealing. The present study was designed to elucidate the mechanism of texture evolution during grain growth. The grain growth kinetics were determined for temperatures between 260 and 450 ºC revealing a grain growth exponent, n~4. The activation energy for grain growth was found to be close to the activation energy for grain boundary diffusion. Abnormal grain growth was observed as a broadening of the normalized grain size distribution at 400 and 450 ºC. However, no temporal correlation was found between the peak in texture intensity and the peak in the width of the normalized distribution. Rather, the abnormal grain growth appears to correlate with the coarsening of second phase particles, which are present in the microstructure. The texture evolution is speculated to be due to anisotropy of grain boundary energy and mobility.

Introduction

Rolled magnesium alloy sheets typically exhibit poor cold formability, tension-compression strength asymmetry, and strong levels of anisotropy. All of these features hinder broader application of these lightweight materials, and they have been associated with the strong basal texture which is typical in wrought Mg alloys. In recent years, several different thermomechanical processing techniques such as cross-rolling [1], asymmetric rolling [2] and twin roll casting [3] as well as alloy development [4] have been applied as strategies to weaken the basal texture. Notably, some of these strategies have proven successful in improving the formability [5].

It has also been recognized that the basal texture is retained after recovery and recrystallization annealing [6]. In this way, hexagonal close packed (hcp) Mg alloys are more similar to many body centered cubic (bcc) alloys than they are to face centered cubic (fcc) alloys, since the latter frequently undergo strong crystallographic texture evolution during recrystallization [7]. Even though a considerable amount of research has been devoted to developing an understanding of the recrystallization behavior of Mg alloys [8], little work has been done to explore the effect of grain growth annealing on crystallographic texture. Some of the present authors previously noted that the basal texture strength actually increased during grain growth [9]. Robson recently noted that the basal texture typical of wrought Mg alloys is slightly weakened during recrystallization, followed by the development of basal texture during subsequent grain growth [10].

The main objectives of this study are to quantify the texture evolution during grain growth and elucidate the mechanism(s) which are responsible. An ancillary benefit of the study is the development of kinetic data to describe grain growth in Mg alloy, AZ31B. These data may prove useful for process designers who seek to develop a particular microstructure. AZ31B has been chosen for this study in order to assist in the practical application of the findings. However, a commercial alloy like this one contains solute elements and second phase particles which also play an important role during grain growth, in addition to the main issue of interest, the crystallographic texture. These complicating factors threatened to obscure the desired information. However, it has proven possible to parse definitive conclusions from the observations.

Experimental methods

1. Material, Heat Treatment and Metallography

The material investigated was part of a larger study focused on the effect of shear rolling on the microstructure and properties of magnesium alloys. Alloy AZ31B sheet was obtained from Magnesium Elektron North America and shear rolled at Oak Ridge National Laboratory at 200 ºC. One conclusion of that broader study was that this range of shear rolling conditions does induce quantitative changes in the resulting basal texture of the sheet, such as a slight tilting of the basal poles from the sheet normal direction (ND) toward the rolling direction (RD). However, the qualitative appearance of the textures was largely unchanged. As such, the fact that the material was shear (rather than conventionally) rolled is not viewed as an important aspect in what follows. For the present grain growth study, the sheet was processed by shear rolling with both the roll and metal temperature held at 200 °C. The roll speeds were 200 and 600 rpm, respectively. The rolling resulted in a 40.6% reduction in thickness starting from an initial gauge thickness of 2.56 mm to a final thickness of 1.52 mm.

Samples were heat-treated at temperatures ranging from 260 to 450 °C for durations ranging from 1 to 10080 min (7 days) in order to produce samples of varying grain size (2-40 μm). The short duration anneals ($t < 16$ min) were performed in a KNO_3 salt bath furnace. For all other annealing durations, an air furnace was used. All the samples were quenched in room temperature water after annealing. For optical and Scanning Electron Microscopy (SEM) based metallographic examination, the samples were ground to the mid-plane, cold mounted in epoxy, and mechanically ground up to 1200 grit SiC paper followed by 3 and 1 μm oil based diamond paste and finally with 0.06 μm colloidal silica polishing. The specimens were etched in an acetal-picral solution (4.2 g picric acid, 10 ml acetic acid, 70 ml ethanol, and 10 ml water) for 5–10 s.

The grain size is measured from optical micrographs using the lineal intercept method in MATLAB toolbox Linecut, following the ASTM standard E112 −96. The measured grain sizes were plotted as histograms using Origin software, with a bin size of 0.5 µm and then fitted with the log normal distribution to obtain the arithmetic mean grain size. The data were then normalized by this mean and plotted as histograms with bin size 0.2 µm and then fitted with a Gaussian distribution to obtain the breadth of the normalized distribution. Evolution of this breadth is used as an indicator of abnormal grain growth [11].

To evaluate the evolution of the second phase particles during annealing, the volume fraction and the particle size were measured using a JEOL 6700 Scanning Electron Microscope (SEM) in secondary electron (SE) and back-scattered electron (BSE) mode. The composition was obtained from Energy dispersive spectroscopy (EDS) together with the Oxford-Pgt Spirit EDS software.

2. Texture measurements

The texture was measured on the as received sheet and after all annealing heat treatments. The measurements were made on the sheet mid-plane, to obtain the bulk texture and avoid any surface effects such as a near-surface gradient in texture which has been observed previously [12]. The measurements were made using a Panalytical X'pert Pro multi-purpose diffractometer (MPD) with Cu Kα radiation at 45 kV and 40mA. The tube was used in point focus orientation, with cross-slit texture optics having 2mm horizontal and 1 mm vertical dimensions, following the Schultz reflection method [13], in order to minimize defocusing at higher χ tilts. A background corrected, incomplete (χ = 0-80°) basal (00.2) pole figure was obtained for all annealing conditions. An experimental defocusing curve was obtained from a random Ti sample, made by curing a slurry of Ti powder in epoxy. Background subtraction, defocusing correction, and normalization were carried out using MATLAB toolbox MTeX. The raw data was smoothed using a Gaussian filter [14] in order to get rid of spurious intensity spikes. For selected annealing conditions, the (1 0. 0), (0 0. 2) and (1 1. 0) incomplete pole figures were collected and the MTeX software was used to generate complete orientation distributions and full pole figures.

Results

1. Characterization of as rolled AZ31B sheet

An optical micrograph of the as-rolled material is shown in Fig. 1. The microstructure of the as-received sheet material is relatively fine grained and is essentially free of deformation twins. Figure 2 shows the grain size distribution fitted using lognormal function and Figure 3 shows the distribution after being normalized by the mean grain size. The lognormal distribution gives a mean lineal intercept grain size of ~ 2µm and the width of the initial distribution is 0.55. The fine grains and absence of twins is evidence of dynamic recrystallization (DRX) during hot rolling of the sheet. In addition, a few fine second phase particles and some larger (~ 2 µm) Mn-Al particles are present in the optical image.

(10.0), (00.2) and (10.1) recalculated full pole figures obtained from the orientation distribution of the as-received sheet are shown in Figure 4. From these pole figures, it can be seen that the (00.2) basal poles are nearly aligned with the sheet normal direction. The maximum intensity of ~9 multiples of a random distribution (MRD) in the (00.2) pole figure, with a slight spread towards the rolling direction, in accordance to previous observations of shear rolled Mg alloy sheets [15]. The slight asymmetry (bias in the tilting of the (00.2) peak intensity is not viewed as significant in this study. Notably, the (10.0) pole figure exhibits near radial symmetry.

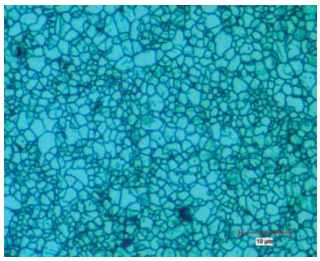


Figure 1 : Initial microstructure of the as-rolled Mg alloy sheet revealed by optical microscopy.

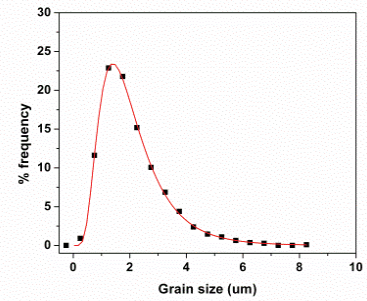


Figure 2 : Lineal intercept grain size distribution of the as received sheet, fit to log normal equation, with $R^2 = 0.99$.

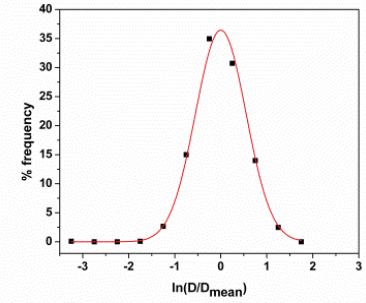


Figure 3 : Normal distribution of the as received sheet normalized by the mean grain size, showing a width of 0.55.

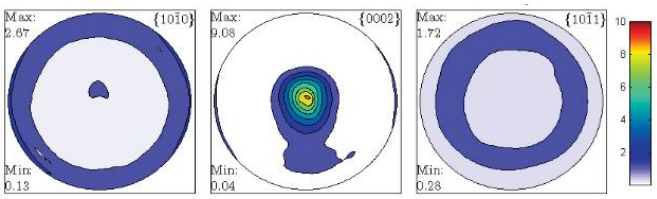


Figure 4 : Complete pole figures of the as-rolled Mg alloys sheet recalculated from orientation distribution functions fit to incomplete pole figure data obtained by x-ray diffraction.

2. Grain growth kinetics

Figure 5 presents a plot of mean lineal intercept grain size against annealing time for all temperatures investigated in this study. The data has been fitted with the empirical grain growth equation:

$$D^n - D_0^n = kt \qquad (1)$$

The initial grain size, D_0, rate constant, k, and grain growth exponent n were all free parameters in the fitting. D_0 was fitted because it must be admitted that recrystallization was not yet complete after warm rolling. Of interest in this study is the initial grain size when only grain growth is occurring. After this initial round of fitting was performed, it was noted that the grain growth exponent n is found to be 3.9 for 300, 400 and 450 °C. (Due to limited data collected at 260 and 340 °C, these were not considered for evaluating n.) For further analysis, all of the kinetic data were refitted using a fixed value of n = 3.9, in order to determine the temperature dependence of the values D_0 and k. Finally, an Arrhenius-type plot of the logarithm of the rate constant k against $1/T$ is shown in Figure 6. A linear fit of the data presented in this figure reveal activation energy, Q = 92.5 kJ/mol. The goodness of fit value R^2 = 0.95 suggests that the process is indeed thermally activated and governed by this single activation energy over the entire temperature range examined, homologous temperatures from 0.58 – 0.78.

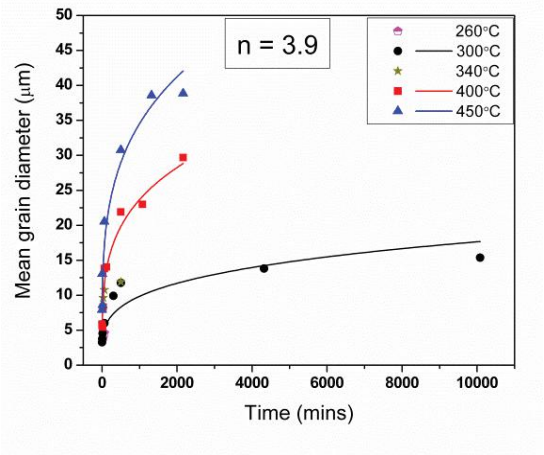


Figure 5 : Mean grain size evolution with time as a function of temperature.

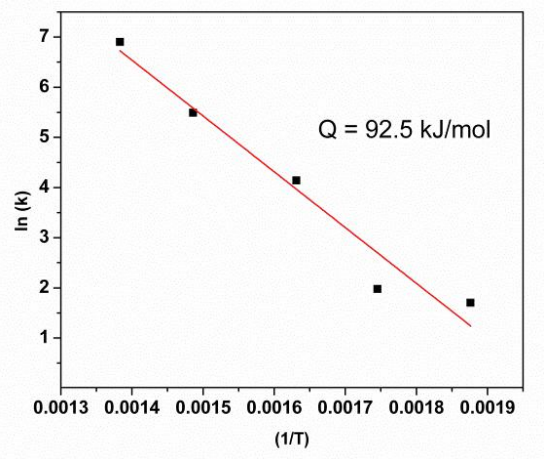


Figure 6 : Arrhenius plot of the grain growth rate constant as a function of inverse temperature.

3. Abnormal grain growth

A plot of the breadth of the grain size distributions is presented in Figure 7. From the plot, it can be seen that annealing at 300°C leads to normal grain growth up to at least 7 days. The breadth of the normalized grain size distribution is essentially constant.

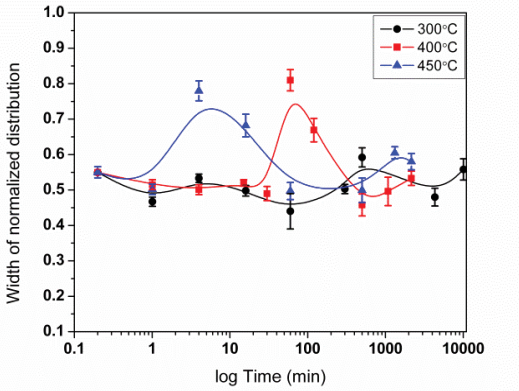


Figure 7 : Plot of the width of the normalized grain size distribution illustrating normal grain growth at all times at 300ºC and abnormal grain growth which peaks after 60 and 4 minutes at 400 and 450ºC, respectively.(Note: lines are just to guide the eye.)

On the other hand, the 450°C short duration anneal results in a heterogeneous microstructure with almost equal area fraction of large and very fine grains. The normalized grain size distribution shows significant broadening after 4 min annealing, indicating abnormal grain growth [11]. On further annealing (e.g. for 22 hours) at the same temperature, the microstructure once again becomes more uniform, while the mean grain size increases significantly. The breadth of the normalized grain size distribution reduces, indicating that the fine grains are “catching up” with the grains which initially underwent anomalous growth [16]. In the case of the 400°C anneals, the maximum in the breadth is maximum after 60 minutes.

4. SEM Based Characterization of Second Phase Particles

In order to study the influence of second phase particles on grain growth, their size, volume fraction and composition were examined using SEM. Figure 8 shows the plot of particle size evolution as a function of the annealing duration, at 300, 400 and 450°C. It is admitted that this SEM-based approach is likely to underestimate the volume fraction and overestimate the average particle size, relative to that which would be assessed by transmission electron microscopy. However, from this plot it is clear that the particles undergo coarsening during annealing. Figure 9 shows a SEM micrograph obtained from one of the annealing conditions investigated. In the micrograph, nanoscale particles are visible, with a plate morphology. Energy dispersive x-ray spectroscopy (EDS) data collected from these particles, as shown in Figure 10, reveal that these are impurity-based particles containing elements such as Ca. Other particles contained impurities Si and Ti.

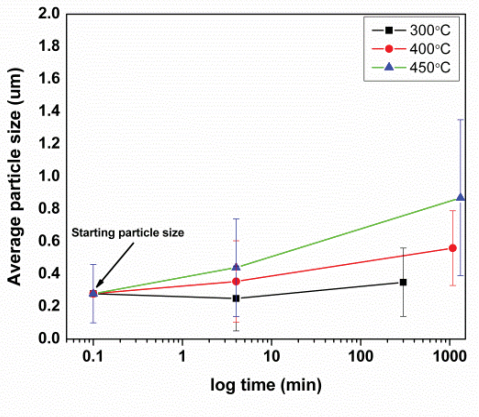


Figure 8 : Plot of average particle size against annealing time illustrating particle coarsening takes place during annealing at all temperatures.

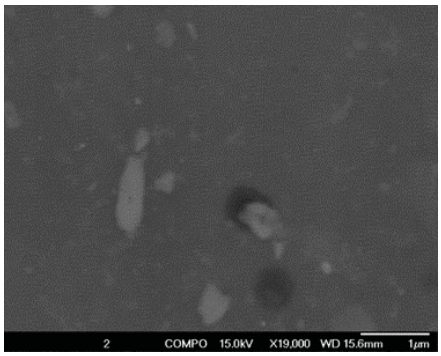


Figure 9 : SEM micrograph of a material annealed at 300°C for 300 min showing second phase particles.

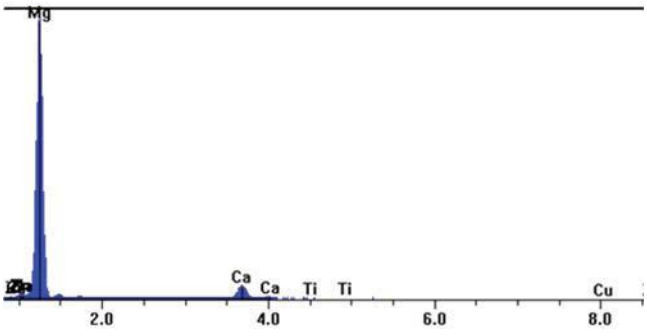


Figure 10 : EDS spectra from a particle shown in the above micrograph, showing presence of calcium.

4. Texture Evolution during Grain Growth

The variation of texture strength as function of annealing time is shown in Figures 11-13. Multiple points at a given time indicate multiple texture measurements on the same sample, as a means of increasing the grain statistics of the measurements and as an assessment of uncertainty. It is seen that the texture strength remains more or less constant at 300°C. Whereas, at 400 and 450°C, the texture intensity increases with annealing.

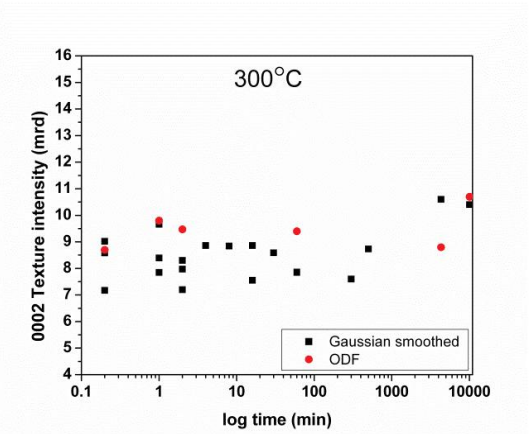


Figure 11 : Plot showing the variation of (00.2) texture intensity with time for annealing at 300°C.

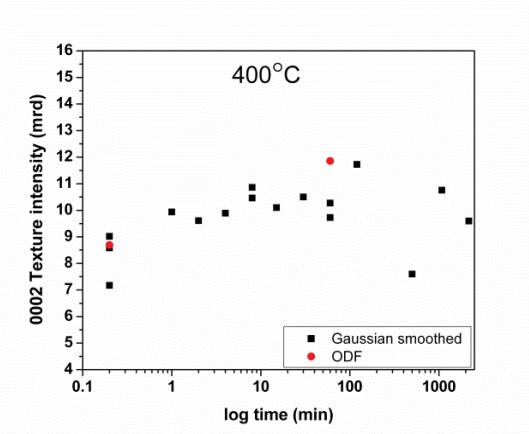


Figure 12 : Plot showing the variation of (00.2) texture intensity with time for annealing at 400°C.

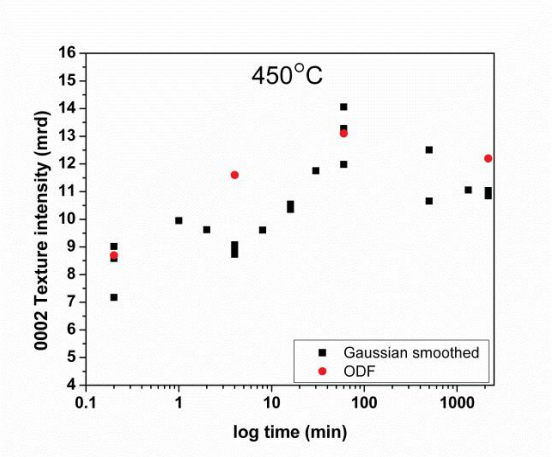


Figure 13 : Plot showing the variation of (00.2) texture intensity with time for annealing at 450°C.

Discussion and Summary

This study of the grain growth behavior of Mg alloy AZ31B has revealed the basic grain growth kinetics of the alloy. Moreover, the phenomenon of abnormal grain growth and its possible connection with the texture evolution has been clarified.

1. Grain Growth Kinetics

The classical, theoretical model of Burke and Turnbull [17] predicts the grain growth exponent n to be 2. However, this is rarely observed experimentally in real materials. Their model assumes that 1) the driving pressure is only due to the curvature of the boundary, 2) there is no drag force acting on the boundary due to particles or solutes, and 3) the grain boundary energies and mobilites are isotropic. These assumptions are clearly violated for the present alloy, due to the presence of the second phase particles, which are shown to interact strongly with the grain boundaries. Hence, deviations from the theoretical value of n are expected. The possible impact of anisotropy in boundary energy and mobility is enhanced due the presence of a strong initial texture. It is well-accepted that low angle boundaries have lower energy and mobility than high angle counterparts. Strongly textured materials have a higher frequency of low angle boundaries than randomly oriented polycrystals.

The n obtained in this study is equal to 3.9 and it is in close agreement with the value of 3.8 obtained by Su et.al in their study of grain growth during annealing at 400°C [18]. Such a high value of n is suggestive of grain growth stagnation, which could be attributed to second phase particles exerting a drag force on the boundaries and pinning the microstructure. Indeed, the plots show that the D *vs.* t curves are quite flat after an initial jump in grain size at short durations. This is particularly evident at lower temperature, while the grain growth curves appear more parabolic as the temperature increases. This behavior is attributed to the coarsening of the second phase particles shown above (Fig. 8).

The apparent activation energy, Q_a ~ 92.5 kJ/mol, determined from the rate constant, k, is almost equal to that of grain boundary diffusion in pure magnesium (92 kJ/mol) [19]. It is found that the activation energy for grain growth of metals falls between the activation energy for the bulk (upper bound) and the grain boundary diffusion (lower bound) [20]. Since the excess free volume of the grain boundary provides easier diffusion path, the activation energy for grain growth is considerably lowered and is often found to be closer to that for grain boundary diffusion [21]. A low value of the activation energy, as found in this study, suggests that the grain boundary motion occurs with relative ease, apart from the effects of Zener pinning discussed below. Ongoing study is being carried out to determine if there is any relation between the low activation energy and the grain boundary character distribution, since grain boundary mobility is strongly dependent on the boundary geometry [22]. As far as the present authors know, this is the first determination of the activation energy during grain growth of AZ31B alloy.

2. Abnormal Grain Growth

Abnormal grain growth can be described as the sudden appearance of unusually large grains in a matrix of uniform grains and is quantitatively distinguished from normal grain growth by an increase in the grain size distribution normalized by the mean grain size [11]. It has been shown theoretically [23] as well as by Monte Carlo computer simulations [16] that abnormal grain growth is not possible in an ideal microstructure where grain growth is driven only by capillary forces, with uniform grain boundary energies and mobilites, since a large grain would grow at a slower rate and would eventually be joined by the initially fine-grained matrix. However, conditions have been identified which lead to abnormal grain growth. For example, it can result from the presence of strong initial crystallographic texture [24] or due to the presence of second phase particles [25]. A classic example, which involves both of these aspects, is the evolution of the Goss texture in Fe-Si steels. In this case, abnormal grain growth of Goss oriented grains occurs because MnS particles preferentially pin the boundaries of other grain orientations. This leads to a very sharp Goss texture, which is advantageous for transformer core applications [26, 27].

From the plot showing particle size evolution during annealing (Fig. 8), it can be seen that there is significant coarsening of the particles during annealing at high temperature. The reduction in pinning force due to coarsening of the second phase particles may be responsible for the abnormal growth observed in this alloy.

3. Texture Evolution

The AZ31B alloy used for this study shows an initially strong basal texture, which becomes even stronger with grain growth at the higher temperatures. It was initially wondered if the observed abnormal grain growth was due to this initial texture and/or responsible for the texture evolution. One clue comes from comparing the timing of the anomalous grain growth and that of the texture evolution. Figure 7 shows that the width of the normalized distribution increases significantly during annealing at 400 or 450ºC indicating a significant amount of abnormal grain growth taking place. At 400ºC, the breadth in the normalized distribution reaches a peak at approximately 60 minutes, whereas it occurs after only 4 minutes of annealing at 450ºC. After this peak, the grain size distribution again tightens, indicating that normal grain growth has resumed. In contrast, the peak in texture intensity occurs after approximately 60 minutes of annealing at 450ºC, and it did not definitively reach a peak even up to 1200 minutes at 400ºC. Thus, appears unlikely that abnormal grain growth is responsible for the observed change in texture (the two phenomena are not contemporary).

Theoretical models based on statistical frameworks [28, 29] and computational simulation studies based on Monte Carlo methods [30] of two texture component systems, the primary texture tends to weaken and the weaker texture component tends to increase in strength. If annealing is continued further, it can be seen that once the primary texture is replaced by the initially weaker component, there is a reversal and the initial primary texture begins to strengthen again. Thus there is an oscillation between the two texture components. The basic idea behind these models is that members of a strong texture component will predominately be bound by low angle boundaries, which have low energy and low mobility, whereas the weaker (or random) texture component will more frequently be bound by higher angle, high energy and mobility boundaries. Based on these existing theories, one would expect that the Mg alloy, AZ31B, sheet presently under investigation, with an initially strong basal texture would exhibit texture weakening with annealing. However, the experimental data shows no drop in texture intensity. On the contrary, samples

annealed at high homologous temperatures show a measureable increase in texture intensity. Continuing work on this problem is seeking to determine if there is a particular grain boundary energy/mobility anisotropy which can explain the observe texture strengthening.

Acknowledgements

This work was financially supported by Research at Oak Ridge National Laboratory, managed by UT Battelle, LLC, for the U.S. Department of Energy (DOE) under contract DE-AC05-00OR22725, sponsored by the Office of Energy Efficiency and Renewable Energy for the Vehicle Technologies and the National Science Foundation, Grant number CMMI 1235259.

References

1. Y. Chino, K. Sassa, A. Kamiya, and M. Mabuchi, "Enhanced formability at elevated temperature of a cross-rolled magnesium alloy sheet," Materials Science and Engineering: A 441 (1) (2006), 349-356.
2. S. H. Kim, B.S. You, C. Dong Yim, and Y.M Seo, "Texture and microstructure changes in asymmetrically hot rolled AZ31 magnesium alloy sheets," Materials Letters 59 (29) (2005), 3876-3880.
3. M. Masoumi., F. Zarandi, and M. Pekguleryuz, "Microstructure and texture studies on twin-roll cast AZ31 (Mg–3wt.% Al–1wt.% Zn) alloy and the effect of thermomechanical processing," Materials Science and Engineering: A 528 (3) (2011), 1268-1279.
4. J.W. Senn and S.R. Agnew, Proc. Magnesium Technology in the Global Age, M.O. Pekguleryuz and L.W.F. Mackenzie, eds., Montreal, PQ, Canada, (2006), 115–30.
5. Y. Chino, K. Sassa, A. Kamiya, and M. Mabuchi, "Stretch formability at elevated temperature of a cross-rolled AZ31 Mg alloy sheet with different rolling routes," Materials Science and Engineering: A 473, (1) (2008), 195-200.
6. G. Gottstein and T. Al Samman, "Texture development in pure Mg and Mg alloy AZ31," Materials Science Forum, 495 (2005), 623-632.
7. Y. B. Park, D. N. Lee, and G. Gottstein, "The evolution of recrystallization textures in body centred cubic metals," Acta materialia 46 (10) (1998), 3371-3379.
8. G.W. Lorimer, J.F. Humphreys, L. W. F. Mackenzie, and T. Wilks, "The recrystallization behavior of AZ31 and WE43," Materials Science Forum, 488 (2005), 99-102.
9. A. Jain, O. Duygulu, D. W. Brown, C. N. Tomé, and S. R. Agnew, "Grain size effects on the tensile properties and deformation mechanisms of a magnesium alloy, AZ31B, sheet," Materials Science and Engineering: A 486 (1) (2008), 545-555.
10. R. Cottam, J. Robson, G. Lorimer, and B. Davis, "Dynamic recrystallization of Mg and Mg–Y alloys: crystallographic texture development," Materials Science and Engineering: A, 485 (1) (2008), 375-382.
11. J.C. Bruno and P.R. Rios, "The grain size distribution and the detection of abnormal grain growth of austenite in an eutectoid steel containing niobium," Scripta Metallurgica et Materialia 32 (4) (1995), 601-606.
12. C. Dreyer, F. Polesak, T. Shultz and S. Agnew, 2009, "Blind Study of the Effect of Processing History on the Constitutive Behaviour of Alloy AZ31B", Magnesium Technology 2009, edited by E.A. Nyberg, S.R. Agnew, N.R. Neelameggham, M.O. Pekguleryuz, Proceedings of the 2009 TMS Annual Meeting and Exhibition, SanFransisco, CA, February 15th - 19th 2009, 491-496.
13. B. D. Cullity and S. R. Stock, Elements of X-ray Diffraction. Vol. 3. Upper Saddle River, NJ: Prentice hall, 2001.
14. O. Engler and V. Randle. Introduction to texture analysis: macrotexture, microtexture, and orientation mapping. CRC press, 2010.
15. H. Watanabe, T. Mukai, and K. Ishikawa, "Effect of temperature of differential speed rolling on room temperature mechanical properties and texture in an AZ31 magnesium alloy," Journal of Materials Processing Technology 182 (1) (2007), 644-647.
16. D. J. Srolovitz, G. S. Grest, and M. P. Anderson, "Computer simulation of grain growth—V. Abnormal grain growth," Acta Metallurgica, 33 (12) (1985), 2233-2247.
17. J. E. Burke and D. Turnbull, "Recrystallization and grain growth," Progress in Metal Physics, 3 (1952), 220-292.
18. C. W. Su, L. Lu, and M. O. Lai, "Recrystallization and grain growth of deformed magnesium alloy," Philosophical Magazine, 88 (2) (2008), 181-200.
19. H. J. Frost and M. F. Ashby, "Deformation-Mechanism Maps: The Plasticity and Creep of Metals and Ceramics", Pergamon Press, 1982.
20. V. Novikov, Grain growth and control of microstructure and texture in polycrystalline materials. CRC, 1997.
21. P. Feltham, "Grain growth in metals," Acta metallurgica 5 (2) (1957), 97-105.
22. F.J. Humphreys and M. Hatherly. Recrystallization and related annealing phenomena. Elsevier, 1995.
23. C. V. Thompson, H. J. Frost, and F. Spaepen, "The relative rates of secondary and normal grain growth," Acta Metallurgica, 35 (4) (1987), 887-890.
24. P.A. Beck and P. R. Sperry, "Effect of recrystallization texture on grain growth," Trans AIME 185 (1949), 240-241
25. M. Hillert, "On the theory of normal and abnormal grain growth," Acta Metallurgica 13 (3) (1965), 227-238.
26. J.E. May and D. Turnbull, "Secondary recrystallization in silicon iron," Trans. AIME 212 (1958), 769-781.
27. Y. Hayakawa and J. A. Szpunar, "A new model of Goss texture development during secondary recrystallization of electrical steel," Acta materialia, 45 (11) (1997), 4713-4720.
28. G. Abbruzzese and K. Lücke, "A theory of texture controlled grain growth—I. Derivation and general discussion of the model," Acta Metallurgica 34 (5) (1986), 905-914.
29. H. Eichelkraut, G. Abbruzzese, and K. Lücke, "A theory of texture controlled grain growth—II. Numerical and analytical treatment of grain growth in the presence of two texture components," Acta Metallurgica, 36, (1) (1988), 55-68.
30. K. Mehnert, and P. Klimanek, "Monte Carlo simulation of grain growth in textured metals," Scripta Materialia, 35 (6) (1996), 699-704.

Magnesium Technology 2014
Edited by: Martyn Alderman, Michele V. Manuel, Norbert Hort, and Neale R. Neelameggham
TMS (The Minerals, Metals & Materials Society), 2014

EFFECT OF ANNEALING ON MICROSTRUCTURE, TEXTURE AND TENSILE PROPERTIES OF TWIN-ROLL CAST AZ31B

Mohsen Masoumi, Faramarz Zarandi, Mihriban O. Pekguleryuz
McGill University, Materials Engineering, 3610 University, Montreal, QC, Canada, H3A 2B2

Keywords: *Magnesium; Twin-roll casting; Heat treatment; Texture*

Abstract

Twin-roll cast (TRC) AZ31 alloy (Mg-3wt.%Al-1wt.%Zn) was subjected to heat treatment at 420 ^{o}C. As a result, the intensity of the original basal texture was reduced considerably. Crystallographic orientation analysis revealed that such a change in the texture is due to particle-stimulated nucleation of new grains with random orientations. The tensile test results indicate that annealing slightly increases ultimate tensile strength (UTS), however, dramatically improves the elongation.

Introduction

The application of magnesium (Mg) in automotive body panel and closures to reduce vehicle weight is challenged by the relatively high cost of Mg sheet [1]. The twin-roll casting (TRC) produces cast and warm/hot rolled sheet with thicknesses less than six millimeters [2] in one process step and can considerably reduce the production cost [3]. AZ31 (Mg-3wt%Al-1wt%Zn) is, currently, the most common magnesium sheet alloy and, therefore, the prime candidate to be produced by TRC. Rolling tends to orient the (002) basal planes approximately parallel to the sheet surface, known as basal texture [4-7]. Hot rolled AZ31 shows a perfect basal fiber texture; while warm-rolled sheet exhibits an egg-shaped distribution of {002} planes in orientation pole figures [4-7]. Conventional AZ31 sheet retains a strong basal texture in all subsequent heat-treatments [8]. Since basal texture lowers the sheet formability (stamping, bending), considerable effort is currently being directed to weaken basal texture or obtain random texture in magnesium sheet alloys [12]. Non-basal or weak textures have been seen in Mg-RE (RE=rare earth elements) alloys [9-13], in Mg alloys with low levels of Li [14],and Sr [15]. However, non-basal texture has never been reported for AZ31. This paper discusses the alleviation of basal texture in AZ31 via heat treatment of TRC sheet.

Experimental procedure

In this study a TRC AZ31 (Mg-2.96wt%Al-0.87wt%Zn-0.36wt%Mn) sheet with a thickness of 6 mm was utilized. The specimens cut from the as-received sheet were subjected to heat treatment at 420 ^{o}C for one hour. Specimens for microstructural examination were taken from the sheet thickness; i.e. the plane of rolling and sheet normal directions (RD-ND), and were prepared by conventional grinding and polishing and etched with acetic-picral. The microstructure was studied via optical microscopy and SEM.

Mechanical properties were evaluated via tensile testing (ASTM B557) at ambient temperature using specimens of 25mm×6mm×6 mm (gage length×width×thickness). The tensile specimens were machined from the TRC sheet in both rolling and transverse directions. The tensile tests were performed at Westmorland Labs at an initial strain rate of 5×10^{-3} s^{-1}.

The overall texture was evaluated by x-ray diffraction (XRD) using a Siemens D-500 diffractometer. Pole figures of {002} and {100} planes were constructed and compared to determine the effect of the treatment applied to the material. XRD specimens were ground successively to remove almost 10% of the sheet thickness, polished with 1 μm diamond and then chemically polished in 10% nital solution for 120 seconds to eliminate any residual strain on the surface. The grain orientation was also studied using the electron back scattered diffraction (EBSD) method in a SEM at 20 kV accelerating voltage and 70° tilt angle. The EBSD specimens, after polishing with 1 μm diamond slurry, were electropolished using a solution 10% nital cooled to 0 ^{o}C at 20 V.

Results and Discussion

The TRC AZ31 sheet has a dendritic structure with coarse grains in the thickness (RD-ND) plane (Fig. 1a & b). Due to the high cooling rate and directional heat-transfer in the TRC

process, columnar grains have grown opposite the heat-extraction direction where the solidifying material was in contact with the cold casting rolls. In addition to the large grains, equiaxed grains (Fig. 1b) with an average size of 16 μm are observed in the mid-thickness. The formation of such equiaxed grains can be attributed to compositional segregation (constitutional undercooling).

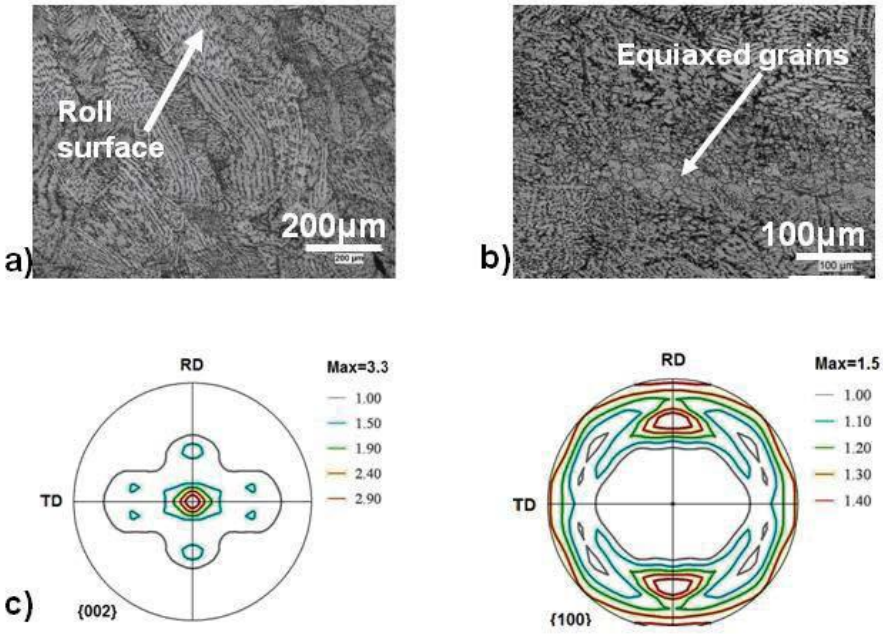


Fig. 1 RD-ND microstructure of as-received TRC AZ31; (a) edge, (b) mid-thickness, (c) Pole figure from RD-TD plane of the as-received TRC AZ31.

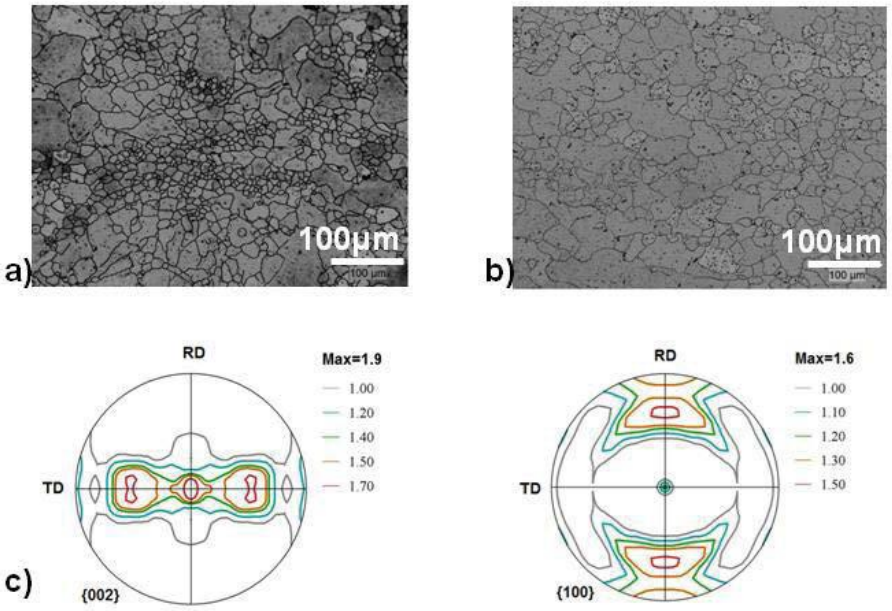


Fig. 2 Microstructures of the heat treated (one hour at 420 ^{o}C) TRC AZ31 in the (a) edge and (b) mid-thickness. (c) Texture pole figures of the heat treated TRC AZ31.

SEM/EDS analysis, indicates that the matrix is α-Mg (Mg-Al-Zn-Mn solid solution) and there are two types of second phase particles; some are composed of Mg, Al, and Zn (presumably $(Al,Zn)_{49}Mg_{32}$ phase [16]) and the rest contain Al and Mn, which could be a mixture of $Al_{11}Mn_4$, Al_8Mn_5, Al_9Mn_{11} and β-Mn(Al) intermetallics [17].

The XRD pole figures of the as-received TRC AZ31 (Fig. 1c) show that most of the crystals are orientated with their basal (002) planes parallel to the sheet surface (basal poles perpendicular to RD). As a result, prismatic planes (100) are dominantly arranged perpendicular to the sheet surface as shown in the (100) pole figure.

Figs. 2 a&b shows the effect of heat treatment for an hour at 420 ^{o}C on the microstructure of TRC AZ31. Fine grains resulted from recystallization are observed after the heat treatment (Figs. 2a&b) indicating that the as-received TRC material had undergone plastic deformation before exiting the roll gap below 420 ^{o}C where no significant recrystallization was possible for the amount of strain accumulated. The large grains in Figs. 2 a&b can be the remnants of large as-cast grains and the smaller ones are the recrystallized grains that exhibited grain growth during 1 hr heat treatment at 420 ^{o}C. The heat treatment has had a significant effect on texture of TRC material, Fig. 2c. Some of the basal planes are reoriented away from the sheet surface in comparison to that in the as-received TRC AZ31 (Fig. 1c). Accordingly, the arrangement of {100} prismatic planes (Fig. 2c) has evolved. This is attributed to the recrystallization and nucleation of new grains at orientation angles different from the parent grains. Such texture has never been reported for AZ31 sheet produced by the conventional rolling process which consists of several rolling passes and intermediate annealing steps.

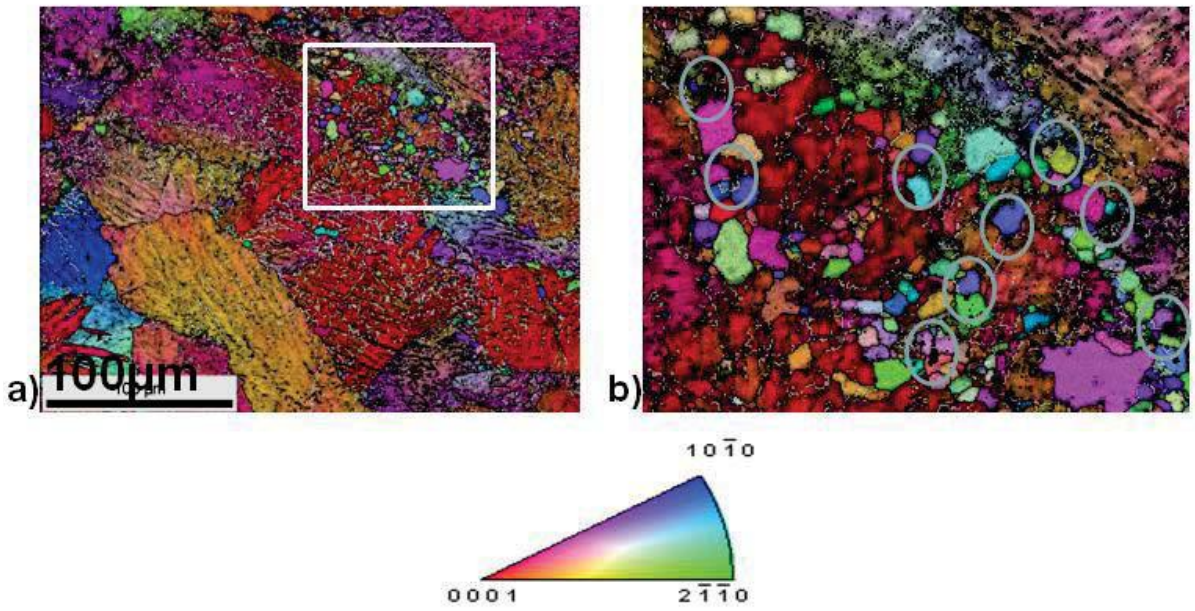
When recrystalization is assisted by precipitates, the mechanism is known as particle-stimulated nucleation (PSN) [8]. It is known that upon deformation via dislocation glide, if the particles do not deform or are not cut by dislocations, there is local dislocation pile-up or looping at the particle/matrix interface which would lead to local bending of the crystal due to uneven distribution of tensile and compressive strain fields [17]. Upon annealing, the dislocation pile-ups eventually lead to cell and sub-grain formation via recovery and coalesce to form nuclei for recrystallized grains [18]. Since such recrystallization is not due to grain-boundary bulging which results in recrystallized grain orientations closely associated with the parent grains, the grain nuclei which form near the particles through sub-grain coalescence can take varying orientations leading to texture randomization.

To verify the interaction of particles and recrystallized grains, EBSD analysis was performed on a sample annealed for 5 min. this time was preferred as at this time, the second phases are not dissolved up in matrix, so the correlation of particles with recrystallized grains are easier to study. Fig. 3a is the whole region which was scanned and 3b is the area in white square. in Fig 3a which has been magnified. In these two figures, the high angle boundaries (>15°) and low angle boundaries (<3°) are represented by black and white lines, respectively. In this region, most of the small grains are associated with the second-phase particles (some of them are shown in white circle). It can also be clearly observed that the recrystalized grains which are associated with the precipitates show random texture. Some of the recrystallized grains are adjacent to high angle boundaries and are likely to have nucleated through the grain boundary bulging mechanism. These grains have texture very similar to parents grains. It can be concluded that the nucleation of new grains in the annealed TRC AZ31 was associated with grain boundaries and second phase particles, and that the latter leads to texture alteration.

Typical true stress-strain curves for the TRC AZ31 in as-cast and annealed conditions are shown in Fig. 4. The tensile properties of TRC sheet in as-cast and annealed condition in rolling and transverse direction are summarized in Table 1. The tensile test results show that the elongation and UTS of TRC samples improve significantly by annealing. The elongation values of RD and TD samples in as-cast condition are 4% and 7%, while by annealing these values rises to 11% and 12%, which means elongation-to-fracture, in RD and TD, increases by 180% and 65%, respectively. In addition UTS in RD and TD, rises by 10%. In general The UTS and elongation of the TD samples are higher than RD samples in both as-cast and annealed samples. However, the yield strength shows a different trend. Explain the trend Changes in strength and ductility by annealing could be attributed to rotation of basal poles way from the sheet normal direction and formation of fine recrystalized grains. The slight drop in yield strength after annealing can be attributed to the dissolution of precipitates which reduces the second phase strengthening.

Conclusion

1. As-cast TRC AZ31 sheet exhibits principally dendritic structures within large grains; however, some small grains are evident in the mid-thickness area.



2. Fig. 3 TRC AZ31 sheet after annealing for 5min at 420 °C; (a) EBSD map on the RD-ND plane, (b) Magnified area in the white square.

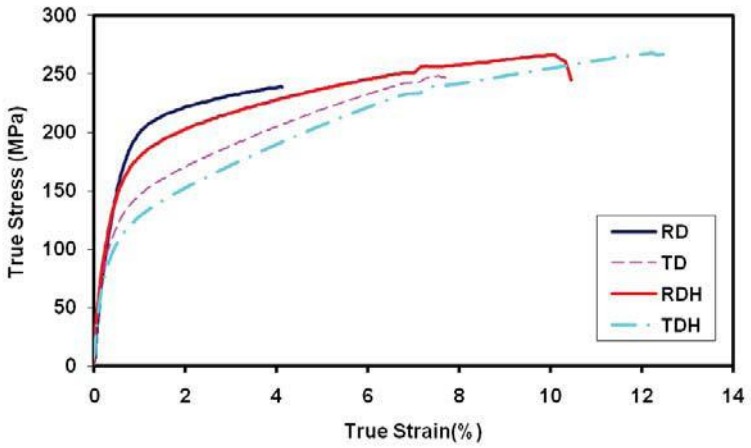


Fig. 4 Representative true stress vs. strain curves of TRC AZ31 in RD and TD.

Table 1 Tensile Properties of TRC AZ31 in Rolling and Transverse Directions (RD, TD)

Sample	0.2YS% (MPa)	UTS (MPa)	Elongation, %
TRC AZ31/ RD	153.5	230.5	4.0
TRC AZ31/TD	109.5	242.6	7.3
Annealed TRC AZ31/ RD	141.0	254.1	11.3
Annealed TRC AZ31/TD	96.5	264.5	12.1

2. The basal texture prevails in the as-received TRC sheet due to the rolling deformation applied during the TRC process.
3. The important observation in this work is the effect of annealing at 420 ^{o}C, which alleviates the basal texture.
4. The texture alteration was attributed to PSN.

Acknowledgments

This research was supported by funding from the NSERC (Natural Sciences and Engineering Research Council of Canada) Magnesium Strategic Research Network. More information on the Network can be found at www.MagNET.ubc.ca.

References

1. I. H. Jung, W. Bang, I. J. Kim, H. I. Sung, W. J. Park, D. Choo, S. Ahn, Magnesium Technology, R. Beals, A. Luo, N.R. Neelameggham, M.O. Pekguleryuz, Eds, TMS, Warrendale, PA, 2007, pp. 85-88.
2. C. Yang, P. Ding, D. Zhang, F. Pan, Mater. Sci. Forum, 2005, pp. 427-430.
3. H. Watari, T. Haga, N. Koga, K. Davey, J. Mater. Process. Technol., 2007, 192-193, pp. 300-305..
4. A. Jager, P. Lukac, V. Gartnerova, J. Haloda, M. Dopita, Mat. Sci. Eng. A, 2006, 432, pp. 20–25.
5. F. B. Kaiser, D. Letzig, K. U. Kainer, A. Sfyczynski, C. Hartig, Adv.Eng. Mater., 2003. 5(12): pp. 891-896.
6. M. R. Barnett, M. D. Navea, C. J. Bettlesb, Mater. Sci. Eng. A, 2004, 386, pp. 205–211.
7. A. S. Khan, A. Pandey, T. Gnäupel-Herold, R. K. Mishra, Int. J. Plast. 2011, 27 (5), pp.688-706
8. F. J. Humphreys, M. Hatherly, 2 ed. 2004: Great Britain by Galliard Ltd., UK.
9. R. K. Mishra, A. K. Gupta, P. R. Rao, A. K. Sachdev, A. M. Kumar and A. A. Luo, Script. Mater., 2008, 59(5), pp. 562-565.
10. J. Bohlen, M. R. Nurnberg, J. W. Senn, D. Letzig, S. R. Agnew, Acta Mater., 2007, 55(6), pp.2101-2112.
11. N. Stanford, M. Barnett, Script. Mater., 2008. 58(3), pp. 179-182.
12. L. W. F. Mackenzie, M. O. Pekguleryuz, Script. Mater., 2008, 59(6), pp. 665-668.
13. M. Masoumi, M. Hoseini, M. Pekguleryuz, Mater. Sci. & Eng. A, 528(7-8) (2011) 122-3129.
14. L.W.F. Mackenzie, M. Pekguleryuz, Mat. Sci. Eng A, vol. 480(1-2), 2008, pp. 189-197.
15. M. Masoumi, M. Pekguleryuz, Mater. Sci. and Eng. A, vol. 529, 2011, pp. 207-214.
16. G.F. Vander Voort, Editor, Metallography and Microstructures, vol. 9 ASM International, Materials Park, OH (2004).
17. P. Cao, D.H. StJohn and M. Qian. Mater. Sci. Forum, 488–489 (2005), pp. 139–142.
18. R. E. Reed-Hill, R. Abbaschian, Third ed., 20 Park Plaza, Boston, MA: PWS.

Magnesium Technology 2014
Edited by: Martyn Alderman, Michele V. Manuel, Norbert Hort, and Neale R. Neelameggham
TMS (The Minerals, Metals & Materials Society), 2014

INFLUENCE OF ROLLING DIRECTION AND TEMPERATURE ON THE TEXTURE FORMATION IN ROLLED AZ31B MAGNESIUM ALLOY

Litzy L Choquechambi Catorceno[1], Nelson Batista de Lima[2.]
[1]PMT-EPUSP (Departamento de Engenharia Metalúrgica e de Materiais da Escola Politécnica da Universidade de São Paulo); 2463 Av Prof M. Moraes; São Paulo, SP, BRAZIL
[2]IPEN (Instituto de Pesquisas Energéticas e Nucleares); Av. Lineu Prestes 2242; São Paulo, SP, BRAZIL

Keywords: AZ31 Magnesium alloy, Texture, Rolling direction

Abstract

In this study, effects of rolling direction and temperature on the texture formation were investigated for the purpose of enhancing formability of rolled AZ31B alloy. For this, specimens were cold and warm rolled from a rolled sheet, both parallel and perpendicular to the rolling direction and textures of the sheets processed were examined. The results showed that samples rolled parallel to the rolling direction generated strong basal texture during cold and warm rolling process. However, on sample rolled perpendicular to the rolling direction at 300°C resulted in the formation of basal textures with low intensities. The (0002) pole was inclined towards the transverse direction. The occurrence of recrystallization at high temperatures contributed to the formation of low intensities basal textures.

Introduction

Magnesium alloys sheets exhibit an attractive combination of low densities (1.74 g/cm^3) and high strength per weight ratios [1]. They represent potential semi-finished products for automotive structures and electronic devices, and are mostly produced through several hot, warm, and cold rolling processes [2]. However, their applicable reductions in thickness are limited by edge-cracking and fracture. These poor plasticity and formability are often explained by a lack of slip systems inherent to its hexagonal-close packed lattice and by the strong planar anisotropy produced specially in cold rolling.

Moreover, cold rolled microstructures of AZ31 alloys usually contain extensive twinning because of their nearly ideal *c*/*a* ratio that promotes twinning rather than basal or prismatic slip [1,3,4], meanwhile, hot-rolling microstructure tends to have non-uniform (bimodal) grain structures [5].

Researchers have confirmed that basal slip and twinning are dominant at room temperature because twin nucleation is not thermally activated [3,6]. Increasing rolling temperature, the transition from twinning to slip-dominated deformation depends on the critical resolved shear stress required to activate non-basal slips, this critical resolved shear stress is high at room temperature and drops rapidly with raising temperature, whereas for basal slip and twinning is relatively temperature insensitive [6]. In addition, during rolling processes, rolled sheets retain a strong basal texture, where the {0002} basal planes are oriented approximately parallel to the sheet surface [7]. And, since the basal texture lowers sheet formability, considerable effort is currently being directed to weaken the strong basal texture in Mg sheets applying several methods to enhance the formability of the sheets.

The formability and deformation behavior of the rolled sheet are strongly dependent on the microstructure and texture that are developed during rolling process. These vary essentially according to rolling temperature and strain rate (reduction per pass), nevertheless, temperature is the most important condition involved in the deformation mechanisms because affects in both dynamic and static recrystallization that could also affect the texture and decrease the intensity of the basal texture [8].

In a previous work about the effects of rolling temperature on the AZ31 magnesium alloy microstructure has shown a slight decrease of work hardening, an increase of strain rate sensitivity with rolling temperature, and twinning has been contributed to plastic deformation significantly even at high rolling temperatures [9]. Now, in this work, samples with strong initial basal texture were rolled using two different rolling directions and over a temperature range of 25-300°C in order to study the effects of rolling direction and temperature on the texture and microstructural transformation of AZ31B magnesium alloy under various strain rates obtained by different thickness reduction.

Experimental material and procedures

The material used in these experiments was a Twin-roll cast AZ31 alloy (Mg-3wt.%Al-1wt.%Zn-0.3wt.%Mn) provided by a Chinese Company in a slab form with 2 mm of thickness. This AZ31B sheet exhibited a recrystallized microstructure with a mean grain size of 13 μm at the surface and low Vickers hardness 49±1.8 HV [9].

The rolling experiments were conducted using two groups of tiny samples cut from a TRC sheet. One group was cut along rolling direction (RD) from as-received TRC sheet and other group at 90 degrees to the RD of as-received slab (Figure 1). These two cutting directions were developed in order to execute rolling experiments with different rolling direction from as-received sheet, and in this way, it was

possible investigated the effect of rolling direction on microstructure and texture.

All samples were cut with the same dimensions, approximately 10×50mm^2. The long side of each piece (the larger size) becomes the new rolling direction. Thus the first group of samples was rolled parallel to RD of as-received sheet. And the second group of samples was rolled perpendicular to RD of as-received sheet.

First group of samples were executed with 0,075 m/s of rolling speed at different temperature, controlling the reduction in thickness near to 30%.

And in the second group of samples, the rolling speed was reduced in almost 30% (0,056 m/s) to avoid lateral cracks in rolled samples, the reduction in thickness was also reduced to 10% for cold rolled samples rolling (25 and 100°C), and near 20-30% for warm rolling (200, 250 and 300°C).

In both groups, rolling processes were carried out in one single pass without lubrication; their strain rates and Vickers hardness are shown in Table1.

Microstructures were examined on rolling surfaces, using a metallographic techniques described in a previous work [9], there is also a better description about the small sized rolling mill used in this work.

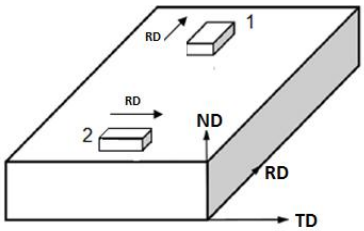


Figure 1 Illustration of the orientation to cut samples from the as-received slab before rolling process.

Table1. Rolling temperatures, strain rates and Vickers hardness used to roll samples parallel (First group) and perpendicular (Second group) to the rolling direction from the as-received slab.

	First group		Second group	
Temperature °C	Strain rate (s^{-1})	Vickers Hardness (kgf/mm^2)	Strain rate (s^{-1})	Vickers Hardness (kgf/mm^2)
25	5,7	76±1.5	1.6	74±1.1
100	5.7	81±1.2	1.8	69±2.0
200	5.7	84±1.5	2.0	70±2.1
250	5.7	82±1.7	2.8	73±1.2
300	-	-	3.5	81±1.6

The crystallographic texture was measured with Xray diffraction using the reflection method in a Rigaku diffractometer equipped with texture goniometer using CrKα radiation. Incomplete pole figures were obtained from (0002) basal planes, $(10\bar{1}1)$ pyramidal planes, $(11\bar{2}0)$ prismatic planes and $(10\bar{1}0)$ prismatic planes. The pole figures were measured for one second at each location in 5° tilt steps from 0 to 80° and azimuthal over the entire 360°. The azimuthal data were averaged every 5° for the subsequent analyses.

Results

Microstructure observations

The figure 2 illustrates the microstructure evolution of AZ31B samples rolled parallel to RD of the as-received slab (The column in the left) and perpendicular (The column in the right) to RD of the as-received slab at 25, 100, 200 e 250°C.

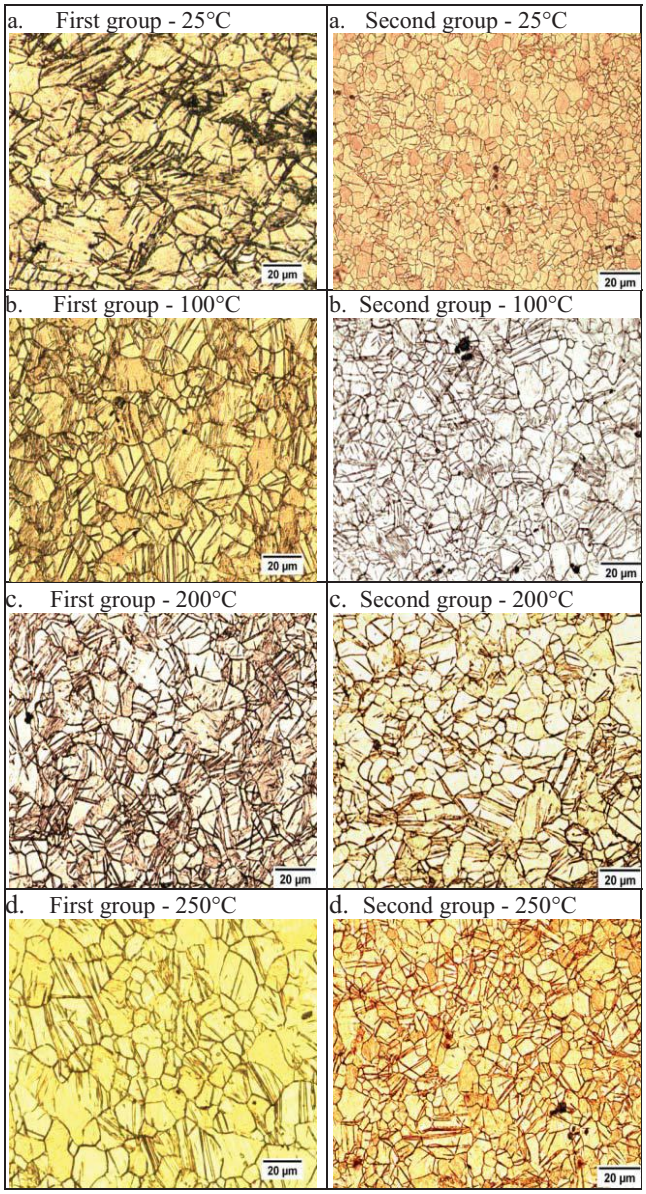


Figure 2 Optical micrographs of samples rolled parallel to RD of as- received sheet (column in the left) and perpendicular (column in the right) to RD of as-received sheet at a) 25°C, b) 100°C, c) 200°C and d) 250°C.

In the figure 2, examining the microstructure evolution of the first group of rolled samples (Left column micrographs) which were rolled in the same direction of received material with 30% of thickness reduction, it can be noted that cold rolling and warm rolling generated deformation twinning and shear bands. No evident recrystallization was found at 100°C, meanwhile, some fine recrystallized grains without twins and coarse grains with extensive twinning were observed in rolling temperature above 200°C that could affect the grain size's distribution on samples. Thus, the dynamic recrystallisation contributed to bimodal distributions formed by finer recrystallized grains and coarser deformed grains.

In the micrographs of samples rolled perpendicular to rolling direction of as-received sheet (Micrographs in the right side, which correspond to second group of rolled samples), it was found that cold rolling with low strain rate ($1.6s^{-1}$) apparently refined grains sizes, producing more homogeneous grain size distribution, the average grain size was approximately 8 µm. Nevertheless, increasing the thickness reduction and rolling temperature the amount of twins increased again, especially on bigger grains.

This difference in grain size would be a result of inhomogeneous microstructure in as-received TRC sheet; this AZ31B magnesium alloy exhibited high strain hardening after rolling processes, the values of Vickers hardness (Table 1) increased with increasing strain rate and also increasing with rolling temperature in both rolling directions. This suggests that hardness increased by strain applied and precipitates formed during warm rolling, as was shown in our last work [12].

Comparing micrographs of two group of rolled samples, the grain's sizes were slightly differenced by changing rolling direction at high temperature, both parallel and perpendicular rolling direction produced inhomogeneous grains distribution because of competition between grain growth and grain refinement during deformation at high temperature, and extensive twinning was seen again on coarse grains with increasing strain rates and rolling temperature.

Texture observations

The initial texture observed on the surface of the AZ31B as-received TRC rolled sheet is shown in Fig. 3, the strong (0002) basal pole figure exhibits an intensity of more than 6.5 times random and an egg-shaped distribution that majority of *c*-axes of the grains is aligned with the sheet normal direction. Then, the basal pole figure of as- received sheet showed a basal texture with a single peak on just normal direction with spreading in the rolling direction. The single-peak texture has been reported as the surface texture of Mg alloys

The angle between the basal and pyramidal poles was approximately 60° and the typical circle where should be the maximum level of intensities on prismatic pole figures was not found because of incomplete measurement that they represent, but these incomplete prismatic pole figures demonstrate a strong basal plane {0002} texture in the as-received sheet.

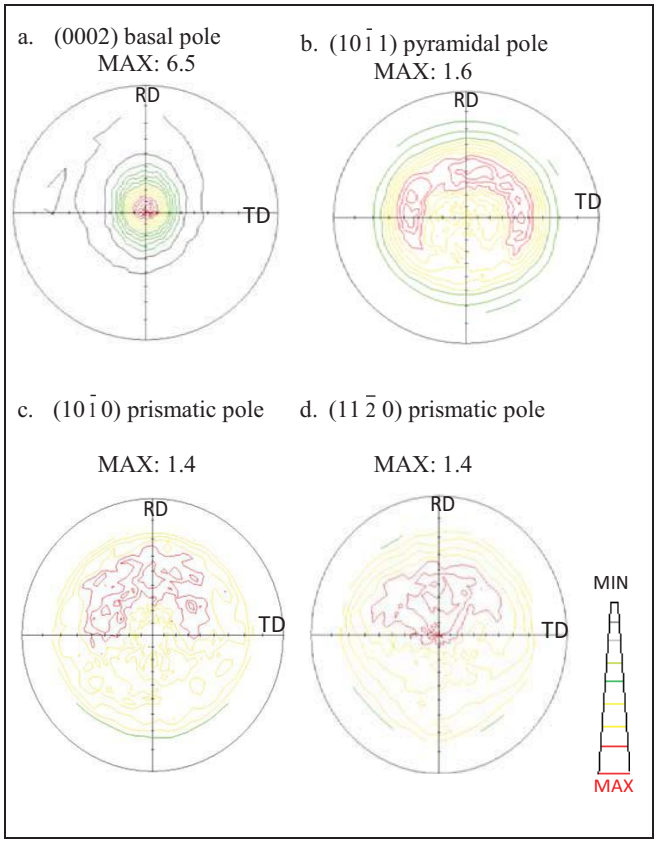


Figure 3 Initial texture of AZ31 as-received TRC plate (a) (0002) basal pole figure, (b) (10$\bar{1}$1) pyramidal pole figure (c) (10$\bar{1}$0) prismatic pole figure and (d) (11$\bar{2}$0) prismatic pole figure.

After cold rolling on samples of the first group (samples rolled parallel to rolling direction of as-received sheet), double peak of basal pole figures were formed, in which the position of basal pole tilts ±10 to 15 degrees away from the normal direction (ND) towards transversal axis. The transition from the single-peak to the double-peak type with increasing strain rate was believed to be caused by the variation in the shear strain. However, increasing rolling temperature, the peaks returned into single-peak but the direction of the split is in the RD

Moreover, the intensity of peak´s diffraction of cold rolled samples increased about 10-20% more than the initial sample.

In warm rolling at 250°C, basal planes were aligned and distributed parallel to RD, it may be related to dynamic recrystallisation. And according to intensity values of the first group of rolled samples showed on figure 5, it can be pointed out that the initial strong basal texture was not weaken. The intensity values increased with rolling temperature, especially at 200°C, where intensity increased about 20% than initial {0002} basal intensity.

The maximum basal pole intensity decreases with increasing rolling temperature, suggesting that the basal texture weakens slightly with grain size, and $(10\bar{1}1)$ pyramidal pole spread more randomely at high rolling temperatures (>250°C).

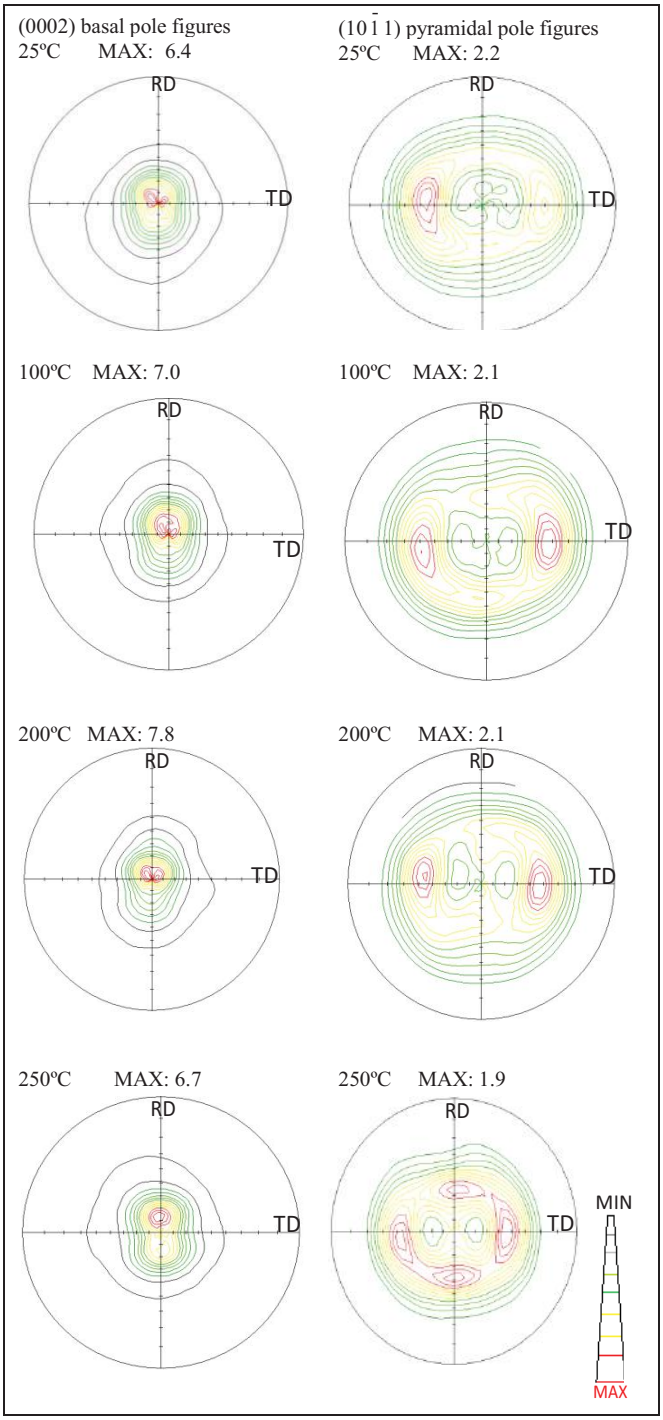


Figure.4 Pole figures of (0002) basal and $(10\bar{1}1)$ pyramidal planes measured on rolling surfaces of first group samples rolled parallel to rolling direction of as-received sheet at 25,100, 200 e 250ºC.

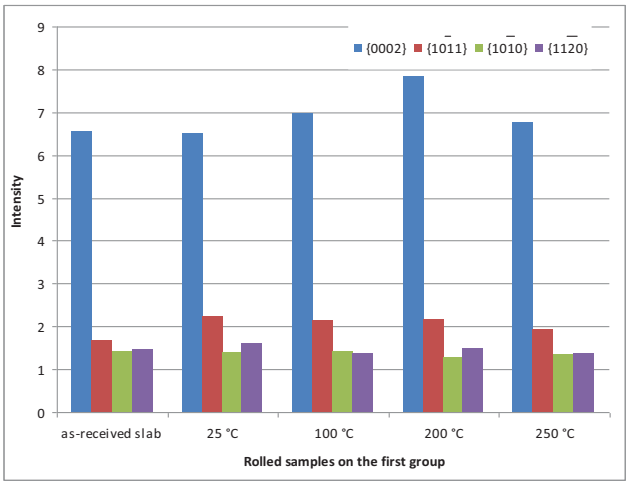


Figure.5 Pole figure intensities of (0002) basal planes, $(10\bar{1}1)$ pyramidal planes, $(11\bar{2}0)$ prismatic planes and $(10\bar{1}0)$ prismatic planes measured on rolling surfaces of first group samples rolled at 25,100, 200 and 250ºC.

The figure 6 presents the texture of samples rolled perpendicular to RD of as-received slab, this second group of rolled samples generated (0002) basal pole figures similar to the first group. Their (0002) basal poles were also shifted along the transversal direction in cold rolled samples and the magnitude of the shift increased with rolling temperature and with strain rates. In this group, the $(10\bar{1}1)$ pyramidal pole figures showed a partial fiber texture. It is suspected that the applied strain was not enough to shift basal poles along rolling direction.

In addition, with increasing reduction in thickness of rolled samples, the (0002) basal texture tended to exhibit textures with basal poles tilted about ±10° away from the normal direction towards the transversal direction

The double peak of basal poles might mean two crystallographic orientations of basal planes that are distributed in two groups with opposite orientation. Increasing rolling temperature to 300°C, the activation of non-basal slips also lead a characterized double-peak distribution of (0002) pole figure because dynamic recrystallization reoriented basal planes to rolling direction (Fig. 6e). This is attributed to nucleation of new grains with orientation angles different from the parent grains.

By looking at the figure 7, it can be noted that intensity of basal pole of strong basal texture of received slab decreased changing rolling direction 90° to initial RD and applying a strain rate of 3.5 s^{-1} at 300°C, such texture weakening can be ascribed to the combination of non-basal slip and twinning [10]. Moreover, it can also be attributed to the coalescence of sub-grains formed at the precipitate-matrix interfaces [11]. In the as-received AZ31B sheet, it was found the existence of second phase particles in the magnesium matrix [12]. It is known that a small amount of second phase produces a significant drop in texture strength that can improve the formability of magnesium sheets.

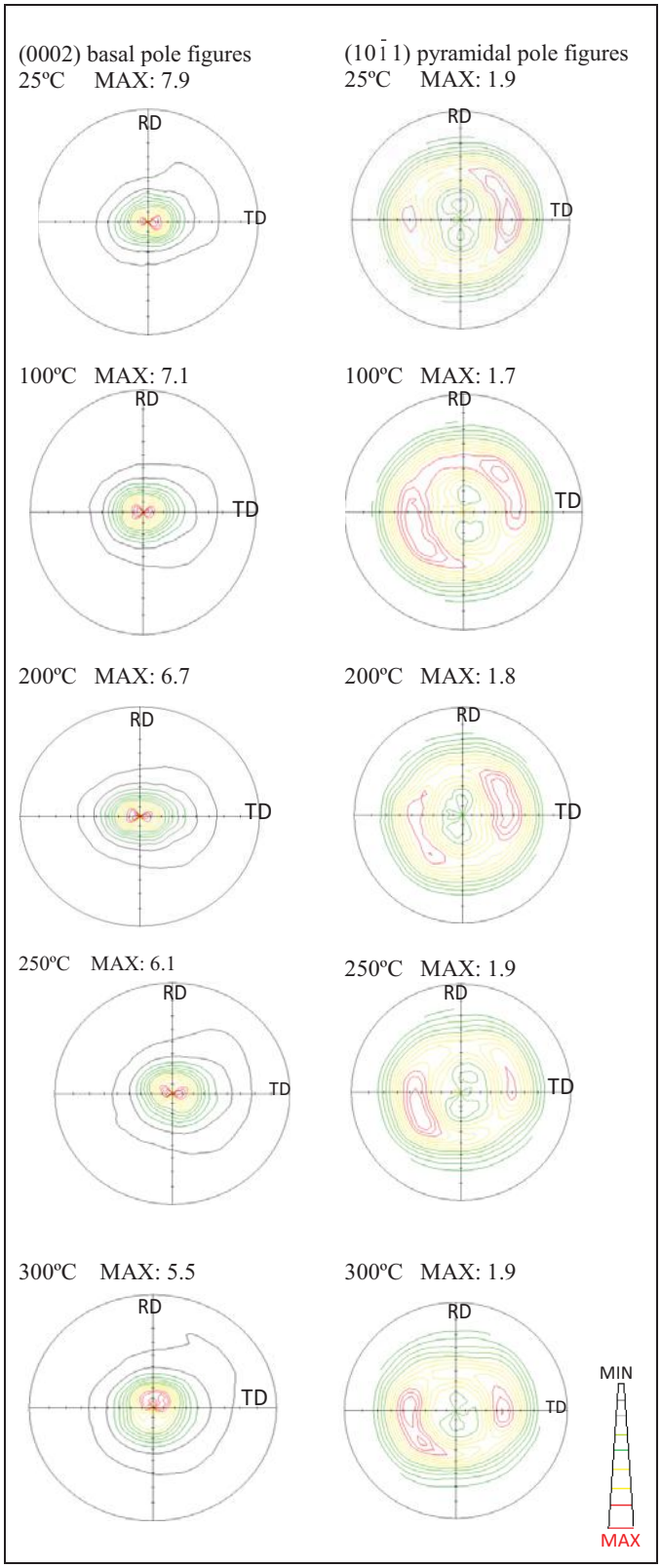


Figure 6 Pole figures of (0002) basal and (10$\bar{1}$1) pyramidal planes measured on rolling surfaces of the second group samples rolled perpendicular to rolling direction of as-received sheet at 25, 100, 200 e 250ºC.

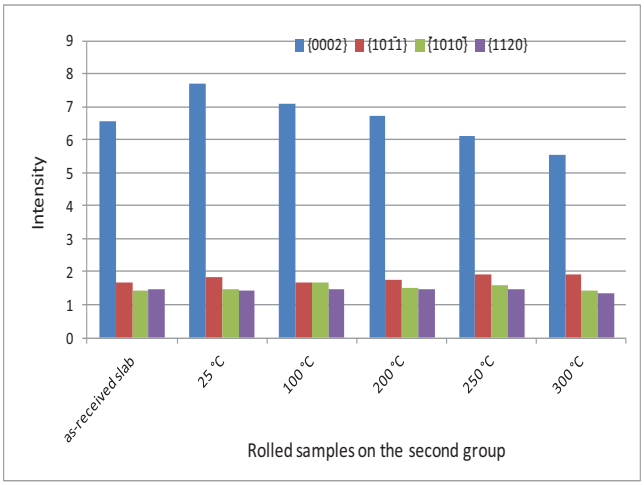


Figure 7 Pole figures intensities of (0002) basal planes, (10$\bar{1}$1) pyramidal planes, (11$\bar{2}$0) prismatic planes and (10$\bar{1}$0) prismatic planes measured on rolling surfaces of second group´s samples rolled at 25,100, 200, 250 and 300ºC.

Summary

The microestructure and texture evolution of AZ31 sheets during different rolling direction and temperature have been studied, and the following observations have been made.

In this study, it was found that rolling direction affects the evolution of rolling texture, especially at high temperature, where basal intensities decreased by a interaction between dynamic recrystallization and strain mechanism.

During rolling processes develop parallel to RD of as-received rolled sheets, the initial strong basal texture did not change significantly, even the dynamic recrystallization happened on high temperature. However, development at 90 degrees to the initial RD and applying 3.5 s^{-1} of strain rate at 300°C, the initial strong basal texture was weakened because twinning remained active under these conditions and non-basal slip planes become active.

A combination between rolling direction and high strain rates at high temperature is a promising rolling process, not only for improving limiting reduction but also for improving mechanical properties of AZ31B magnesium alloy sheets by the weakening of basal texture.

References

1. E. Doege, K. Dröder, Sheet metal forming of magnesium wought alloys - formability and process technology, *Journal of Materials Processing Technology,* 115, (2001), 14-19.

2. H. Watari, R. Paisarn, T. Haga, K. Noda, K. Davey, N. Koga, Development of manufacturing process of wrought magnesium alloy sheets by twin roll casting,

Journal of Achievements in Materials and Manufacturing Engineering, 20, (2007),515-518.

3. M. Yoo, Slip, twinning, and fracture in hexagonal close packed metals, *Metall. Trans*. A12, (1981),409 -418

4. J. Koike, T. Kobayashi, T. Mukai, H. Watanabe, M. Suzuki, K. Maruyama, K. Higashi, The activity of non-basal slip systems and dynamic recovery at room temperature in fine-grained AZ31B magnesium alloys, *Acta Mater,* 51, (2003),2055-2065.

5. T. Laser, C. Hartig, R. Bormann, J. Bohlen, D. Letzig, Dynamic Recrystallisation of Mg-3Al-1Zn. In: Kainer, K.U. (Ed.): *Magnesium, 6th International Conference Magnesium Alloys and their Applications*. Wolfsburg (D), (2003). 164 - 169.

6. A. Styczynski, C. Hartig, R. Bormann, F. Kaiser, J. Bohlen, D. Letzig, Texture Formation and Texture Modelling of AZ31 magnesium wrought alloy. In: Kainer, K.U. (Ed.): *Magnesium, 6th International Conference Magnesium Alloys and their Applications. Wolfsburg* , (2003), 214 - 219.

7. S.R. Agnew and O. Duygulu, "Plastic Anisotropy and the Role of Non-basal Slip in Magnesium Alloy AZ31," *Inter. J. Plasticity*, 21, (2005), 1161-1193.

8. X. Huang, K. Suzuki, N. Saito, Textures and stretch formability of Mg-6Al-1Zn magnesium alloy sheets rolled at high temperatures up to 793 K. *Scripta materialia* **60**(8), (2009) 651-654.

9. Catorceno L., Padilha A. F., "Effect of Rolling Temperature on the AZ31B Magnesium Alloy Microstructure", *Magnesium Technology - TMS (The Minerals, Metals & Materials Society) (2012)*, 283-287.

10. Y.Chino, K. Kimura, M. Mabuchi, Twinning behavior and deformation mechanisms of extruded AZ31 Mg alloy. *Mater Sci Eng A* 486, (2008), 481–488.

11. M. Masoumi, F. Zarandi, M. O. Pekguleryuz Alleviation of Basal Texture in Twin-Roll Cast Mg-3Al-1Zn Alloy *Scripta Materialia 62*, (2010) 823–826.

12. L. L. C. Catorceno, D. A. Lopes, Annealing of cold and warm rolled AZ31B magnesium alloy sheets, *Magnesium Technology - TMS (The Minerals, Metals & Materials Society) (2012),* 132-136.

13. F. Kaiser, J. Bohlen, D. Letzig, K.U. Kainer, A. Styczynski and C. Hartig, Influence of rolling conditions on the microstructure and mechanical properties of magnesium sheet AZ31**,** *Advanced Engineering Materials* 5, (2003) .891-896

Magnesium Technology 2014
Edited by: Martyn Alderman, Michele V. Manuel, Norbert Hort, and Neale R. Neelameggham
TMS (The Minerals, Metals & Materials Society), 2014

TEXTURE EVOLUTION DURING WIRE DRAWING OF Mg-RE ALLOY

Mark Chatterton[1], Joseph Robson[1], Dominic Henry[2]
[1]The University of Manchester, School of Materials; Grosvenor St.; Manchester, M1 7HS, UK
[2]Magnesium Elektron, Magnesium Technology Centre; Rake Lane; Swinton, Manchester, M27 8BF, UK

Keywords: Mg-RE alloy, Wire drawing, Shear bands, Microstructure evolution, Texture evolution

Abstract

Additions of rare-earth (RE) elements to extruded magnesium alloys can lead to a weaker texture and the emergence of a new "RE-texture" component. Understanding the formation of this component after extrusion is difficult because the final microstructure is often either partly or fully dynamically recrystallized.
In this paper, a magnesium alloy with RE addition was deformed by wire drawing at room temperature. This has enabled a fully unrecrystallized microstructure to be retained after axis-symmetric deformation.
The drawn microstructure was characterized by elongated grains with a strong basal fiber texture. Tensile, compression and double twins were visible but shear bands were not. During annealing, new statically recrystallized grains formed at grain and twin boundaries, leading to gradual weakening of the drawn texture but no emergence of the distinctive RE texture occurred. This observation suggests that shear banding has a critical role in forming the RE texture.

Introduction

Magnesium is the lightest of all the structural metals and as such it has been traditionally used in applications where weight savings are beneficial. Major limitations to a more extensive use of Mg alloys for industrial applications are their poor formability at room temperature in the case of sheet forming and their mechanical asymmetry and anisotropy in the case of extrusions. Studies suggested that the addition of rare-earth (RE) element to Mg contribute to weakening the texture, which in turn results in a decrease in asymmetry for extrusions and an increase in ductility for sheet forming [1]. This is achievable because RE elements can promote <*c*+*a*> slip and supply the alloy with nucleation sites such as double twinning, particle-stimulated nucleation (PSN) of recrystallization and shear bands which can give rise to new grains with different orientations from the parent material.
Sandlöbes *et al.* [2-3] tributed the increased room temperature rollability of Mg-3Y alloy to an enhanced activity of <*c*+*a*> slip and compression/double twinning.
Ball and Prangnell [4] suggested that extruding the high-RE Mg alloy WE54 under specific conditions resulted in recrystallization occurring mainly by PSN and hence in a more random texture. PSN was also observed by Huang *et al.* [5] during static annealing of hot-rolled WE43. However, due to RE-solutes restricting dynamic recrystallization during rolling, new grains also recrystallized at pre-existing grain boundaries when the annealing temperature was raised. Huang suggested that the presence of RE-solutes resulted in accumulation of non-basal dislocation near grain boundaries during deformation and this in turn gave rise to randomly oriented newly recrystallized grains.
PSN also played a secondary role in the texture weakening during hot extrusion (360°C) and subsequent annealing of Mg alloy WE43 [6]. In Mackenzie's study the extruded microstructure presented two texture components, one conventional relating to the deformed, non-recrystallized grains with the <01-10> pole parallel to the extrusion direction, and the other one with the basal planes at ~45° to the extrusion direction, corresponding to grains which dynamically recrystallized at kink bands. During the early stages of annealing the grains which nucleated on kink bands grew advantageously and the result was a non-basal (~45°) final texture. Mackenzie attributed the preferential grow of certain grains to the effect of solute element on the mobility of specific boundaries and on the formation of internal substructures.
Hosford and Caddell [7] observed that RE additions resulted in the <-12-11> direction being parallel to the extrusion direction. This type of texture, which is usually defined as 'RE-texture', increased the possibility of non-basal slip, enhancing therefore room ductility.
A weakening and change in texture to the RE-texture was also observed when a small amount of Gd was added to Mg by Stanford and Barnett [8]. The small addition meant that all the Gd present was in solution, suggesting that RE-texture can be obtained without PSN. The Mg-1.5Gd alloy was hot extruded within a specific temperature range (375-560°C) and the RE-type texture was not observed in extrusions above ~500°C. Beyond such temperature the alloy presented a stronger conventional basal fiber texture. This change in behavior correlated well with later observations by Stanford *et al.* [9] on the segregation of RE solute at grain boundaries. For extrusions below 500°C the solute concentration increased as temperature increased, but above 500°C the solute concentration at grain boundaries decreased. It was suggested that solute segregation retarded dynamic recrystallization, which in turn weakened the texture by increasing the strain necessary to initiate recrystallization, confining it to bands of locally enhanced strain. For example, in the case of the Mg-1.5Gd samples which showed RE-texture, recrystallization occurred along two well defined bands: grains that recrystallized on bands along the extrusion direction showed a weaker conventional basal texture, while grains which nucleated on shear bands inclined to the extrusion direction showed the RE-type component.
Shear bands have also been observed during cold rolling [10] and hot rolling [11] of AZ31 magnesium alloy, and in other Mg-RE alloys, as presented by Yan [12] and Mackenzie [13] in their studies on hot rolled Mg-Zn-RE alloys. It is clear that shear bands can play an important role in recrystallization and texture development.
Different textures can also be obtained by varying the amount of RE elements added to the alloy, as demonstrated by Hantzsche *et al.* [14] on a study of binary Mg-RE rolled sheets. Furthermore, higher content of solid solution or precipitates can restricted grain

growth, preventing therefore the preferential growth of favorably oriented grains.
The influence of RE additions on the deformation/recrystallization of Mg alloys is a complex subject, since both dynamic and static recrystallizations are affected during hot deformation. Cold rolling has been used in an attempt to decouple those processes for sheet, but an equivalent approach for axis-symmetric processes such as extrusion is much more difficult. In this work, a Mg alloy with high RE content has been cold drawn into wire. This is an axis-symmetric process with a strain path somewhat similar to extrusion. Using this method has enabled both the deformation and static recrystallization behaviors to be separated, providing insights into the essential conditions needed to form the RE texture in (hot) extrusion.

Experimental procedures

The initial Mg-high RE alloy (total RE content ~ 7wt%) was supplied by Magnesium Elektron as cylindrical extruded bar. The bar was cold drawn in two steps to a total reduction of 0.37 true strain (reductions of 0.12 and 0.24 true strain for the first and second passes respectively). The final drawn wire was subjected to annealing at 445°C for lengths of time ranging from 1 minute to 24 hours followed by quenching to freeze the microstructure and investigate the alloy's static recrystallization behavior. Microstructure and texture evolution during wire drawing and annealing were monitored by optical microscopy and electron backscatter diffraction (EBSD) analysis of the wire's centerline.
All the samples were prepared by conventional grinding and diamond polishing, with a final step using water-free fumed silica (0.2µm). Samples for the optical analysis were then etched with acetic picral (4.2g picric acid, 10ml distilled water, 10ml acetic acid, 70ml ethanol) to reveal the microstructure and observed using polarized light. Specimens for the EBSD analysis were electro-polished for 5 seconds at -30°C and 12V in a 3:1 solution of ethanol and nitric acid.
EBSD measurements were performed using three different field emission gun scanning electron microscopes (FEGSEMs: FEI Sirion, CamScan and FEI Magellan) at a voltage of 15-20kV, spot size 3-6 and 4x4 binning. Step sizes of 0.05-0.2µm were used for the detailed EBSD maps, while step sizes between 0.6-2µm were used for larger maps (1170x950µm) in order to characterize the overall texture. EBSD analysis was conducted using the HKL Channel 5 software package. Typical indexing was 80-95% for the detailed EBSD maps and 70-90% for the bigger texture maps. Standard noise reduction was applied to improve indexing using five indexed neighbors and 10° critical angle to define grain boundaries. Texture measurements were taken using 10° half width and data clustering of 3. The software ImageJ was used to measure the recrystallized area fraction of the annealed wire. Grains with internal average misorientation lower than 1.5° were considered to be recrystallized.
All the microstructure and EBSD images are presented with the extrusion/drawing (ED/DD) direction along the horizontal axis and the transverse direction (TD) on the vertical axis.

Results

Wire drawing analysis

Microstructures of the received material and the drawn wires are shown in Figure 1. The microstructure of the extruded bar (Figure 1a) was nearly fully recrystallized (approx. 90% recrystallized) with equiaxed grains and 2nd phase particle 'stringers' running along the extrusion direction. The stringers were not spaced evenly throughout the material and this resulted in a bimodal grain size (5-15µm), with the bigger grains developing where the spacing between the particles was greatest.

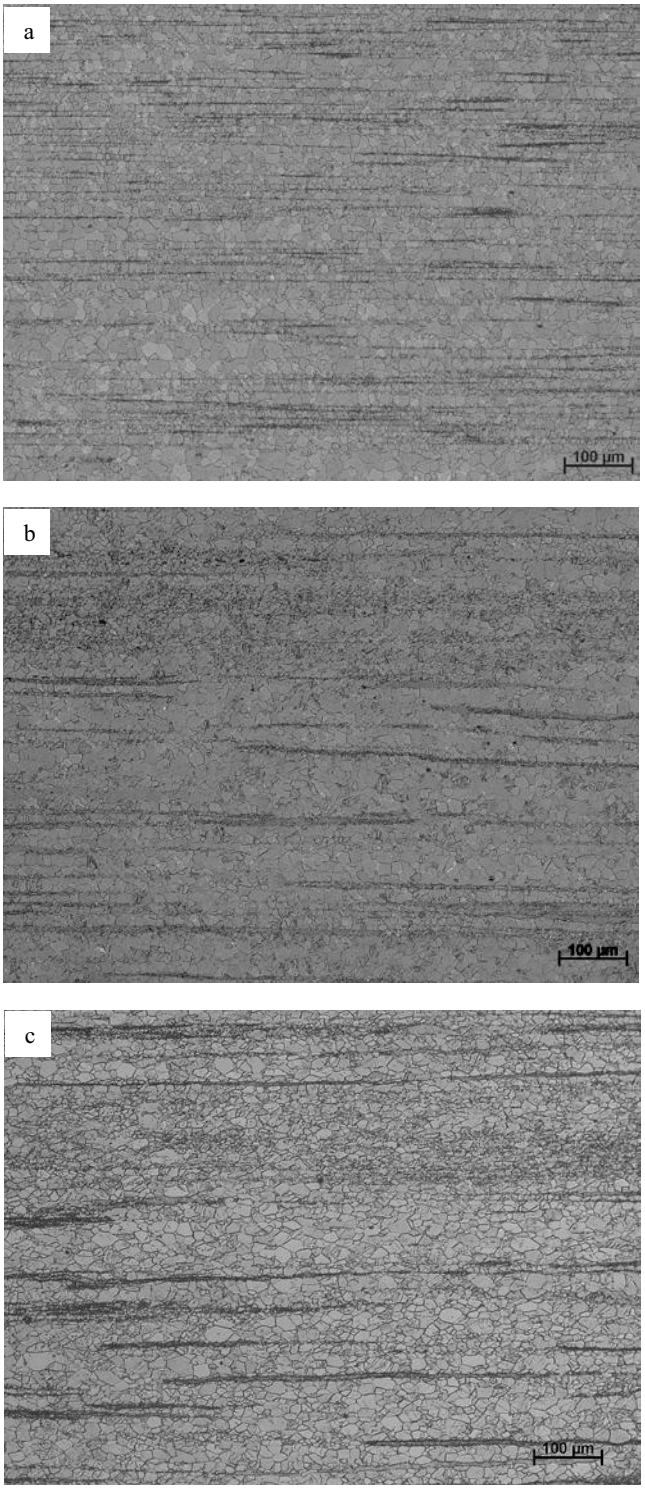


Figure 1. Microstructure evolution during wire drawing: (a) extruded bar, (b) first drawing pass and (c) second drawing pass.

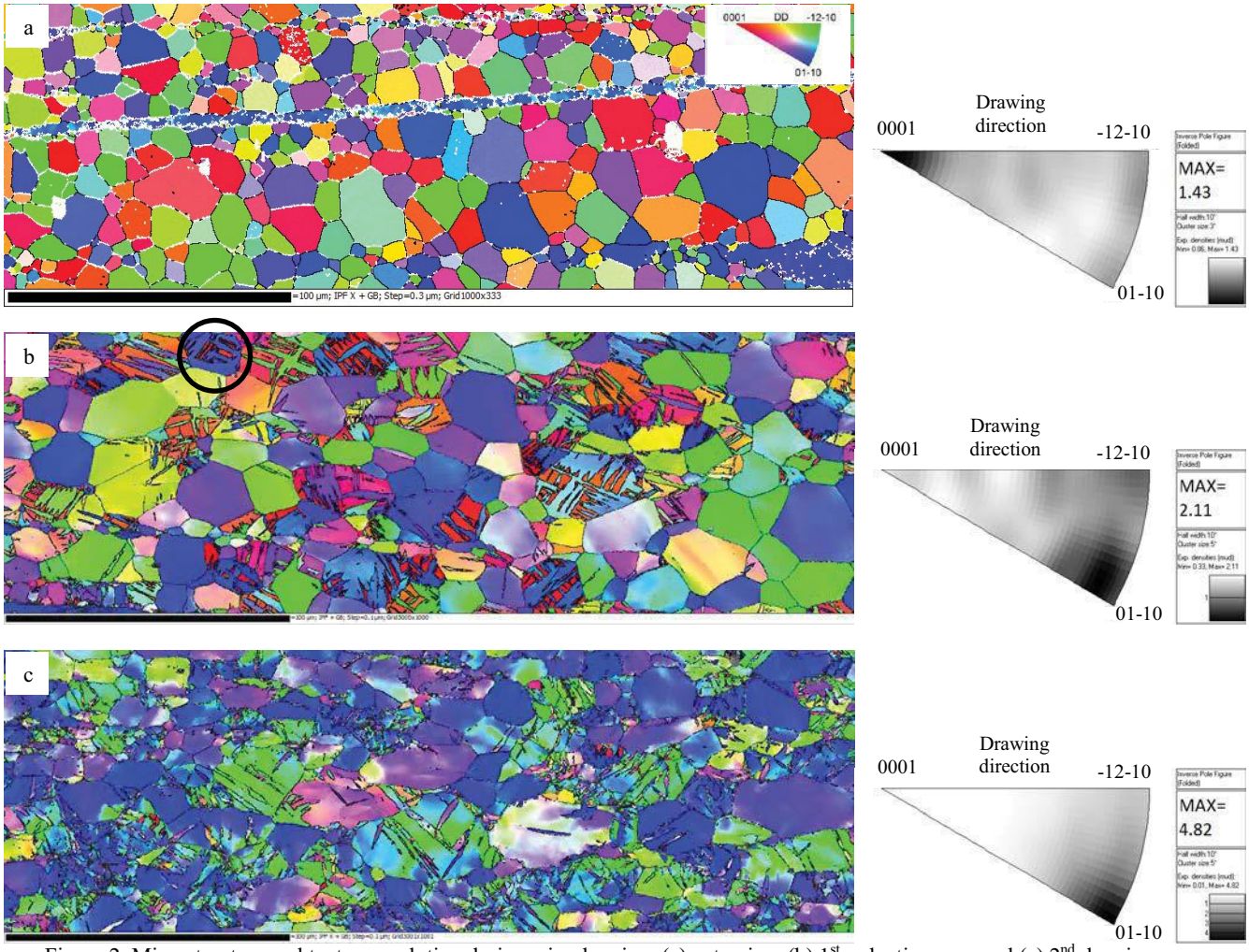


Figure 2. Microstructure and texture evolution during wire drawing: (a) extrusion, (b) 1st reduction pass and (c) 2nd drawing pass.

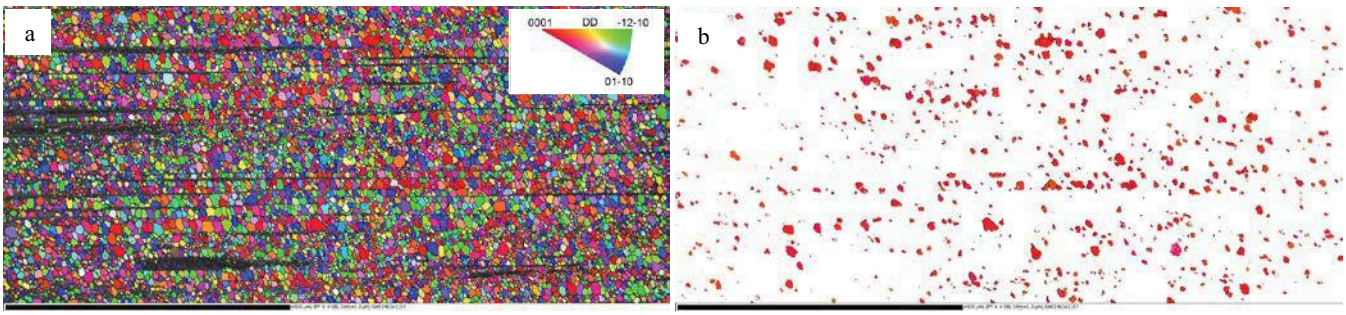


Figure 3. Extruded microstructure: (a) all orientations and (b) orientations within 20° from <0001>.

Nevertheless, the average grain size was kept small by the presence of the 2nd phase particles. The 2nd phase stringers and some deformed, non-recrystallized grains from the extrusion pass were still visible after the first drawing pass (Figure 1b). The microstructure here was characterized by large amount of twinning. The imposed deformation resulted in elongation of the grains, measuring 10µm in TD and 14µm in DD.

The second drawing pass (Figure 1c) resulted in an increase of twinned area and in further elongation of the grains (9µm in TD and 16µm in DD). No evidence of shear banding could be seen after either the first or second drawing pass. As comparison, shear bands were visible in Stanford's Mg-1.5Gd extrusion study [8] at true strains of 3.39 and kink bands were observed in Mackenzie's WE43 extrusion [6] at true strain of 1.39.

EBSD analysis of the extruded bar confirmed that the supplied material was nearly fully recrystallized (Figure 2a). The remaining non-recrystallized, deformed grains had the *c-axis* perpendicular and the <01-10> pole parallel to ED, as this is the more stable orientation for the deformed grains under the applied deformation conditions.

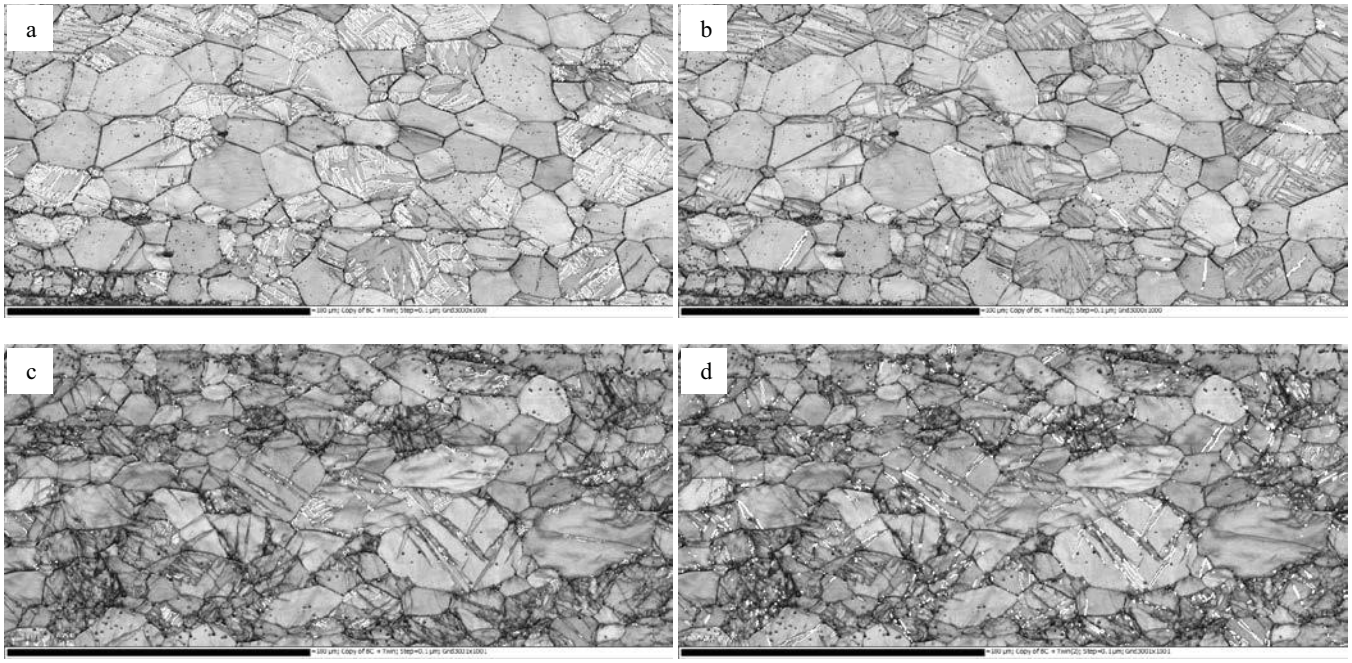


Figure 4. Microstructures showing twinning (white lines). First drawing pass: (a) tensile twins, (b) compression (thin line) and double (thick line) twins. Second drawing pass: (c) tensile twins, (d) compression (thin line) and double (thick line).

The texture of the recrystallized grains developed during extrusion was weak (max. intensity = 1.43 times random), although some of the basal poles were aligned parallel to the drawing direction , as visible by comparing the microstructure of the extruded bar (Figure 3a) with the same microstructure showing only grains in which the DD is within 20° of <0001> (Figure 3b). Similar behavior was reported by Robson *et al.* [15] during the investigation of extruded Mg-RE alloy under certain deformation conditions. The deformation imparted to the alloy during the first drawing pass resulted in increased internal misorientation and in extensive twinning (Figure 2b). As shown in Figure 4a a large amount of deformation tensile twinning but also compression (thin line, Figure 4b) and double twinning (thick line, Figure 4b) were observed after the first pass. Some grains were nearly fully 'consumed' by the different variants of the tensile twins (one example circled in Figure 2b). The deformation imposed during the first reduction pass resulted in a change of orientations towards a more conventional basal fiber texture (max. intensity = 2.11). Further deformation during the second step (Figure 2c) increased the amount of misorientation present inside the deformed grains as well as the fraction of twins, with strengthening of the basal texture as a result (max. intensity = 4.82). Analysis of the twins observed revealed the presence of fewer tensile twins (Figure 4c) compared to the first pass, indicating the exhaustion of this deformation mechanism as deformation progressed, and an increased number of compression (thin line, Figure 4d) and double twins (thick line, Figure 4d).

Annealed wire analysis

Annealing heat treatment was carried out at 445°C on the second drawing pass wire. Microstructure and texture evolution after 4min, 15min and 24hrs are presented in Figure 5. After heat treatment for 4 minutes (Figure 5a) the microstructure contained some newly statically recrystallized grains (28% area fraction) and a large fraction of the original deformed grains. Large amount of internal misorientation was still visible in the majority of the deformed grains, suggesting that recovery kinetics are slow this alloy. As visible in Figure 6, new grains have nucleated from a variety of sites such as compression and double twins, along the 2nd phase particles stringers and at isolated particles within grains, suggesting a particle stimulated nucleation (PSN) mechanism. The texture did not present great variations, still showing basal fiber orientation with only weakening in the intensity of the <01-10> pole (max. intensity = 4.07). After 15 minutes (Figure 5b) the microstructure was nearly fully recrystallized (86%) and only few deformed grains were still visible. The average grain size was about 9µm. The remaining deformed grains (one example circled) showed internal misorientation corresponding to the 30° rotation from <01-10> to <-12-10> prismatic pole. Further weakening in texture intensity (max. intensity = 3.88) and no peak shift were observed.

The long 24 hours heat treatment (Figure 5c) resulted in a fully recrystallized and homogeneous microstructure, with an increase in average grain size to 16µm. No preferential grain growth of specific grains was observed. Further weakening of the texture (max. intensity = 2.00) and a slight spread of orientations from the <01-10> pole towards the <-12-10> prismatic pole were observed.

Discussion

The microstructure of the extruded supplied material showed an unusual, nearly random texture, with some of the grains having the *c-axis* aligned parallel to the extrusion direction. This type of texture has previously been observed in a similar Mg-high RE alloy extruded under similar conditions, Robson *et al.* [15]. As a result, many grains were favorably oriented for tensile twinning during the first stages of wire drawing. Profuse tensile twinning was observed after the first drawing pass, to the extent that many grains were nearly all re-oriented by twinning to assume the typical cold deformed basal fiber texture. The weak extruded

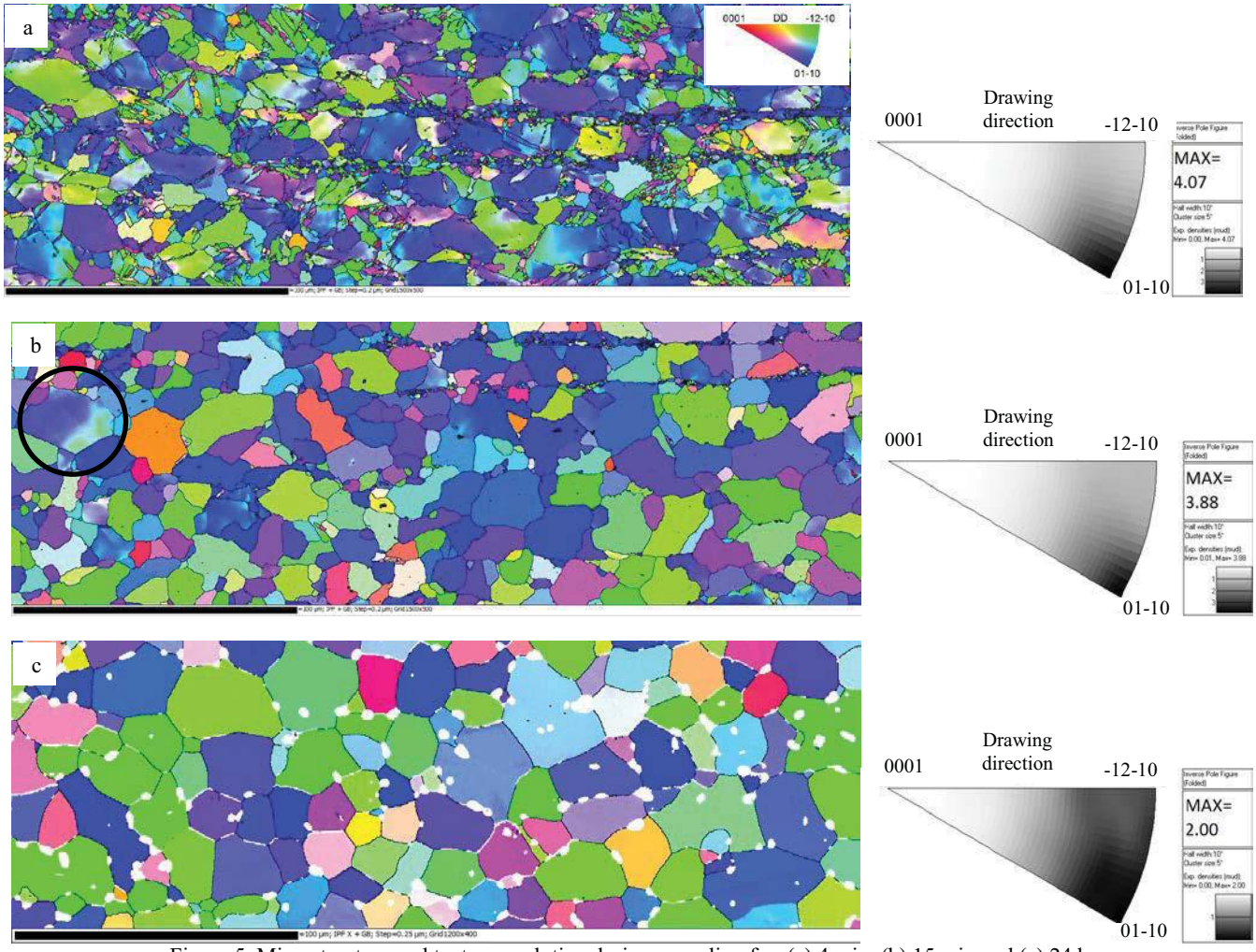


Figure 5. Microstructure and texture evolution during annealing for: (a) 4 min, (b) 15 min and (c) 24 h.

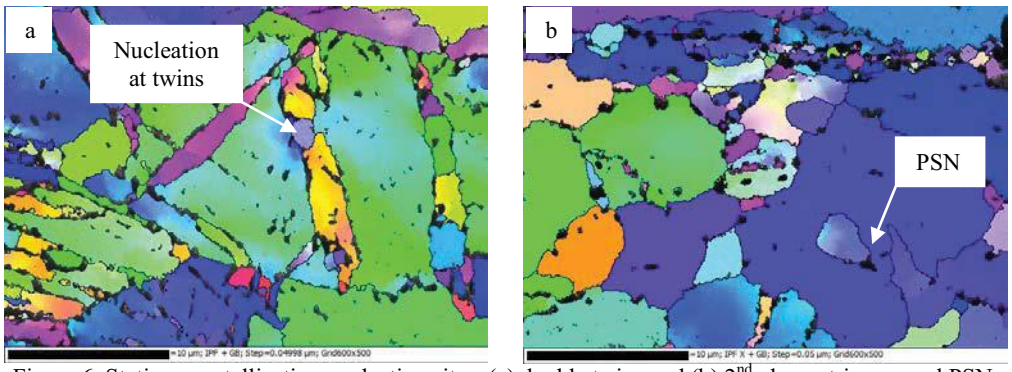


Figure 6. Static recrystallization nucleation sites: (a) double twins and (b) 2nd phase stringers and PSN.

initial texture also meant that some of the grains were oriented favorably for easy basal slip and some for compression twinning, the most easily activated mechanism for *c-axis* compression at room temperature. Few compression twins were observed after the first reduction pass, but the number of compression and double twins increased as wire drawing progressed because grains re-oriented to the basal fiber texture were favorably oriented for this mode to accommodate the required compression as the material enters the die.

Although the low deformation temperature should had favor the formation of shear bands, these were not developed during wire drawing. It is suggested that the small initial grain size, the presence of particles and the relatively low reduction per pass resulted in a more homogeneous deformation behavior,

which in turns prevented the formation of localized regions with higher stress levels and therefore the formation of shear bands. Extended and homogeneously distributed twinning as well as basal and prismatic slip were able to accommodate deformation without the formation of shear bands. The different geometrical constraints imposed by wire drawing compared to cold sheet rolling can play an important role in the absence/formation of shear bands. During static recrystallization new grains nucleated from compression and double twins as well as from second phase particles, both inside the grains (PSN) and on grain boundaries. This variety of nucleation sites available resulted in progressive weakening and only slight spreading of texture rather than in the formation of the RE-texture or any other new orientation component. Even new grains nucleated from compression and double twins, which in theory could give rise to the RE-texture because of their orientations, showed fragmentation and a range of orientations. This is thought to be due to the degree of deformation surrounding the parent twins influencing the orientation of the new statically recrystallized grains.

Subsequent grain growth during long annealing heat treatment did not modify the overall texture because the high content of second phase particles prevented exclusive grain growth.

It is suggested that additions of RE alloying elements itself is not a guarantee of texture modification and the lack of shear bands deprived the alloy of an important site for the nucleation of the RE-texture component. It appears that unrecrystallized shear bands after deformation are essential to form RE type texture as this type of texture disappears at very high extrusion temperatures [8] where the formation of shear bands is less likely.

Conclusion

The microstructure and texture evolution of an Mg-RE alloy during room temperature wire drawing have been studied and the following conclusions are drawn.

Wire drawing of an Mg-RE alloy resulted in the formation and progressive strengthening of a conventional basal fiber texture despite a very high RE content in the alloy. Deformation was initially accommodated mainly by basal slip and tensile twinning. Once the basal fiber texture was established, extensive compression/double twinning was observed in the subsequent drawing pass as deformation could not be accommodated anymore by the former mechanisms. No shear bands developed during the process because deformation was accommodated homogeneously through the microstructure.

Static recrystallization from a variety of sites resulted in weakening and slight spreading of orientations from the basal fiber texture but no distinct RE-texture component developed during annealing.

Acknowledgments

The study was funded by the EPSRC Portfolio Partnership on Light Alloys Towards Environmentally Sustainable Transport and Magnesium Elektron. Joao Fonseca and colleagues from the Light Alloy Department here at The University of Manchester are thanked for valuable discussions.

References

1. J. Bohlen, M.R. Nürnberg, J.W. Senn, D. Letzig, and S. Agnew, “The texture and anisotropy of magnesium-zinc-rare earth alloy sheets”, *Acta Materialia*, vol. 55, pp. 2101-2112, Apr. 2007.

2. S. Sandlöbes, S. Zaefferer, I. Schestakow, S. Yi, R. Gonzalez-Martinez, “On the role of non-basal deformation mechanisms for the ductility of Mg and Mg–Y alloys”, *Acta Materialia*, 59(2), pp.429–439, 2011.

3. S. Sandlöbes, M. Friák, J. Neugebauer, D. Raabe, “Basal and non-basal dislocation slip in Mg-Y”, *Materials Science and Engineering: A, Vol.576, pp.61-68, 2013.*

4. E. Ball and P. Prangnell, “Tensile-compressive yield asymmetries in high strength wrought magnesium alloys”, *Scripta Metall. Materialia,* vol. 31, no. 2, pp. 111-116, 1994.

5. X. Huang, K. Suzuki, and Y. Chino, “Static recrystallization and mechanical properties of Mg-4Y-3RE magnesium alloy sheet processed by differential speed rolling at 823K”, *Materials Science and Engineering: A*, vol. 538, pp. 281-287, Mar. 2012.

6. L.W.F. Mackenzie, B. Davis, F.J. Humphreys, G.W. Lorimer, “The deformation, recrystallisation and texture of three Mg alloy extrusions”, *Materials Science and Technology*, 23(10), pp.1173–1180, 2007.

7. W. Hosford and R. Caddell, *Metal forming*. NJ: PTR Prentice Hall, 1993.

8. N. Stanford and M. Barnett, “The origin of ‘rare earth’ texture development in extruded Mg-based alloys and its effect on tensile ductility”, *Materials Science and Engineering: A*, vol. 496, pp. 399-408, Nov. 2008.

9. N. Stanford, G. Sha, J.H. Xia, S.P. Ringer, M.R. Barnett, “Solute segregation and texture modification in an extruded magnesium alloy containing gadolinium”, *Scripta Materialia*, 65(10), pp.919–921, 2011.

10. Y.B. Chun and C.H.J. Davies, “Texture effects on development of shear bands in rolled AZ31 alloy”, *Materials Science and Engineering: A*, 556, pp.253–259, 2012.

11. Z. Zhang, M. Wang, N. Jiang. S. Zhu, “Formation of shearing bands in the hot-rolling process of AZ31 alloy”, *Journal of Alloys and Compounds*, 512(1), pp.73–78, 2012.

12. H. Yan, S.W. Xu, R.S. Chen, S. Kamado, T. Honma, E.H. Han, “Twins, shear bands and recrystallization of a Mg–2.0%Zn–0.8%Gd alloy during rolling”, *Scripta Materialia*, 64(2), 2011.

13. L. Mackenzie and M. Pekguleryuz, “The recrystallization and texture of magnesium–zinc–cerium alloys”, *Scripta Materialia*, 59(6), pp.665–668, 2008.

14. K. Hantzsche, J. Bohlen, J. Wendt, K. Kainer, S. Yi, and D. Letzig, “Effect of rare earth additions on microstructure and texture development of magnesium alloy sheets”, *Scripta Materialia*, vol. 63, pp. 725-730, Oct. 2010.

15. J.D. Robson, A.M. Twier, G.W. Lorimer, P. Rogers, “Effect of extrusion conditions on microstructure, texture, and yield asymmetry in Mg-6Y-7Gd-0.5wt%Zr alloy”, *Materials Science and Engineering: A*, 528(24), pp. 7247-7256, 2011.

Magnesium Technology 2014
Edited by: Martyn Alderman, Michele V. Manuel, Norbert Hort, and Neale R. Neelameggham
TMS (The Minerals, Metals & Materials Society), 2014

Extrusion of Hollow Magnesium Profiles and Investigation of Extrusion Seams

Felix Gensch[1], René Nitschke[1], Sven Gall[1], Sören Müller[1]
[1]Forschungszentrum Strangpressen, TU Berlin, Gustav-Meyer-Allee 25, 13355 Berlin, Germany

Keywords: Extrusion, magnesium, weld seams, microstructure, mechanical properties, FE-simulation

Abstract

The extrusion of hollow profiles with porthole dies is well known for aluminum alloys, but there is almost no data available regarding the formation and thus the quality of extrusion seams in magnesium hollow profiles. Therefore, extrusion experiments using magnesium alloys AZ31 and ME21 have been conducted with a porthole die which is designed in a way that the extrusion seams are located in the corners as well as in the middle of one of the profile surfaces. The profiles were analyzed for their microstructure with the focus on the extrusion seams compared to the seamless areas. These analyses were performed by OIM and SEM with EBSD. Furthermore, the mechanical properties of the extrusion seams were characterized by room temperature tensile tests in dependence of the extrusion direction. In order to optimize the extrusion of magnesium hollow profiles accompanying FE-simulations were carried out.

Introduction

The usage of complex extruded hollow profiles is indispensable for numerous lightweight applications [1]. In order to manufacture such profiles the use of porthole dies is necessary causing a splitting of the material during flowing into the die and subsequent seaming of the metal streams in the welding chamber after passing the bridges as illustrated in Fig. 2. This matter of fact leads to longitudinal weld seams in the profile [2]. The extrusion of complex aluminum profiles is state of the art in industrial production. In contrast, the manufacture of magnesium hollow extrusions using porthole dies still exhibits a process challenge due to the poorer forming behavior of magnesium alloys in comparison to aluminum alloys resulting in limited extrusion speeds and hence in lower productivity [3].

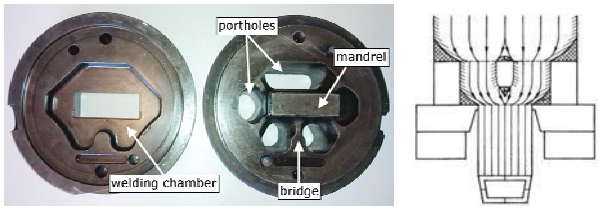


Fig. 1: Configuration of a porthole die (left) and mechanism of weld seaming (right) [4]

Special attention is paid to the quality of weld seams, which may feature several defects such as obvious separations, inclusion of oxides, uncontrolled grain structures and, therefore, may distinctly limit the product quality [2, 5]. Weld seams based on the solid-state bonding process are affected by numerous process parameters. Besides the extrusion and material parameters, the die and profile geometry as well as post extrusion treatments significantly influence the quality of weld seams. Especially, the temperature, the stress and strain distribution and the contact time in the welding chamber play an important role in order to control the solid state bonding process [6, 7, 8].
Only few investigations on the formation of weld seams in magnesium extrusions and its influence on the product properties are available, e.g. [3, 9, 10, 11]. The presented work deals with extrusion of magnesium hollow profiles considering the weld seam formation. Therefore, extrusion trials using the commercial magnesium alloys AZ31 and ME21 were performed with a porthole die. The rectangular hollow profiles were investigated by metallographic methods and mechanical testing procedures. Additionally, finite elements (FE)-simulations were conducted in order to evaluate the influence of plastic flow of the deformed material on the weld seam's properties.

Experimental Setup

Direct Extrusion
For the extrusion of a hollow rectangular profile the magnesium alloys AZ31 and ME21 were used. The billets were continuously cast and homogenized and then prepared for the trials having the length and diameter of 145 mm and 137 mm, respectively. These billets were directly extruded on the 8 MN horizontal rod and tube press of the Extrusion Research and Development Center of the TU Berlin. For both alloys the die was emptied and cleaned prior to extrusion. Additionally, for each trial the first billet was used to fill the portholes and the welding chamber as well as to achieve a more steady-state condition for the following extrusion. Approximately one third of the first billet material that was extruded remained in the die cavities whereas the rest of it formed the profile. Consequently, when the second billet is extruded the remains of the former billet first had to be extruded out of the die until the material of the second billet could be extruded as well.
Knowing the volume of the cavities it was possible to identify the profile section that originated from the second billet material which was used for further examination. The porthole die featured five portholes resulting in five longitudinal weld seams, below simply referred as "weld seams". The dimensions of the hollow profile were 80 mm x 30 mm with a wall thickness of 2 mm. Extruding with a 140 mm liner leads to an extrusion ratio of R = 39. The extrusion parameters are given in Table I.

Table I: Extrusion parameters for both alloys

Alloy	$T_{Container}$ [°C]	T_{Billet} [°C]	T_{Die} [°C]	V_{Ram} [mm/s]	$v_{Product}$ [m/min]
AZ31	440	450	480	0.5	1.2
ME21	450	500	500	1	2.3

The porthole die was equipped with a pair of thermocouples in the bearing length, one placed at the contact area with the middle weld seam and the other placed directly opposite the seamless area as delineated in Fig. 2. Also, the transversal direction (TD) is defined in Fig. 2 for further reference, while the extrusion direction (ED) is obvious.

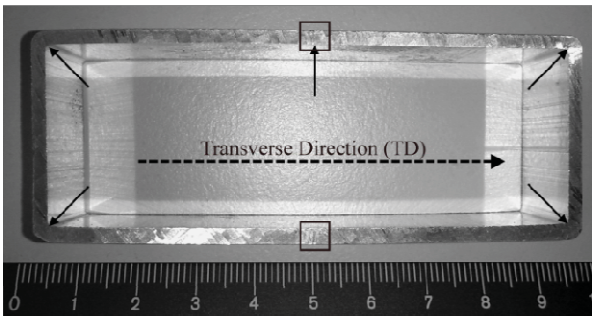


Fig. 2: Profile cross section with outlined positions of weld seams (small arrows), squares indicating the area of interest as well as the position of the thermocouples

Material characterization

Samples were cut from the hollow profile while the position of the weld seam was marked on the surface. For optical imaging microscopy and grain size determination the samples were polished and etched in a picric acid. The grain size determination was done by the line-intercept method for each sample area.

EBSD samples were electrolytically polished and cleaned in an ultrasonic bath. The measurements were performed on a Hitachi S-2700 scanning electron microscope with HKL-EBSD system and a Nordlys-detector at the ZELMI of the TU Berlin. The step size was chosen to be 2.5 µm on a measurement range of approximately 2 mm x 2 mm.

Tensile specimen were also cut and machined with respect to the desired loading directions ED and TD. During all steps the position of the weld seam on the examined material was marked.

Tensile testing was conducted at room temperature on the thermo-mechanical deformation simulator Gleeble System 3800. A strain rate of $2x10^{-3}$ s^{-1} tests was chosen for all tensile tests.

The values for fracture strain were measured on the specimens themselves using a grid. Moreover, in order to determine the yield stress more accurately, additional tests were performed using a high-resolution extensometer.

Finite Element Analyses (FEA)

In order to simulate the material flow in the porthole die as well as the temperature evolution in the steady-state FEA were carried out using Altair's™ HyperXtrude® Solver package. Therefore, the volume of material flow had to be extracted from the CAD-data and then to be meshed in the pre-processor HyperMesh®. For higher accuracy and yet adequate CPU time consumption only areas with higher degree of deformation such as the bearing area, profile and the welding chamber were meshed very fine, leaving portholes and billet with coarser mesh size. The overall number of elements adds up to 1.9 million triangular prisms and tetrahedral elements. The extrusion parameters were adopted from the real direct extrusion experiments. Friction at the container-billet interface was assumed to be of the sticking friction type as well for the tool surfaces except the bearing area. Here the slip velocity model with a friction factor of 1.3E+09 was applied, hence giving the most accurate results regarding the temperature measurements in real extrusion trials. The hot-working behavior of the magnesium alloys was calculated using a thermo-viscoplastic model. The material parameters used were already published in [12].

After having solved the FE-simulation with the HyperXtrude® the results were analyzed in the post-processor HyperView®.

Results and Discussion

Direct Extrusion

Hollow profiles were successfully extruded for both alloys. The surface of the AZ31 extrudate was less rough in comparison to the ME21 profile surface with partially deep striations.

In the early stage of the extrusion process the total force increased up to 8 MN for AZ31 and up to 8.2 MN for ME21 alloy. Here the billet is upset in the container and the extrusion starts throughout the pre-filled porthole die. In contrast to the extrusion of magnesium using simple flat dies [13] no distinct peak in the extrusion force is observed. During the ram movement the total force in AZ31 extrusion increases slightly, whereas the total force in ME21 extrusion stays about constant for the first half of the process and then declines to a value of about 7.5 MN. The increase and the decrease in extrusion force for AZ31 and ME21 extrusion, respectively, is correlated to the temperature evolution in the die in both cases. In Fig. 3 the temperature continuously decreases after having reached a maximum temperature in the bearing area after the ram movement of 50 mm. This leads to an increase in the deformation resistance and hence an increase in total force is necessary to maintain the process. On the other side, when extruding ME21, the temperature rises continuously resulting in a decrease of the total force (Fig. 3).

Furthermore, the temperature difference of the weld seam area and the seamless area is relatively small ($\Delta T_{AZ31,max}$ = 8K, $\Delta T_{ME21,max}$ = 6K). This may be due to the slow extrusion speeds that allow the material to compensate for the small amount of deformation heating that is observed in both extrusions.

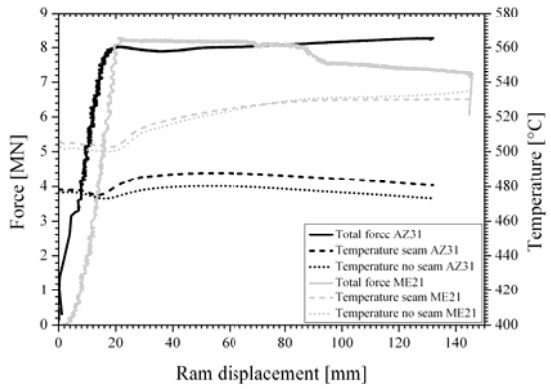
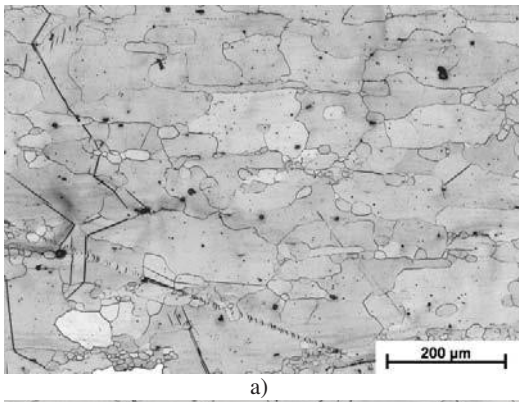


Fig. 3: Extrusion diagram for AZ31 and ME21 hollow profiles

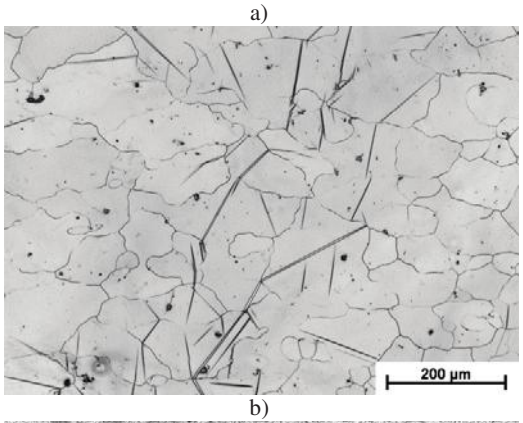
Material characterization

Microstructure

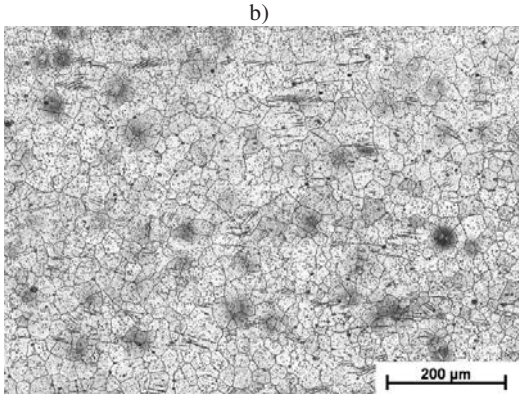
Fig. 4 shows the microstructure of the profiles' cross-sections. During plastic deformation at high temperatures dynamic recrystallization (DRX) as well as static recrystallization (SRX) processes determine the microstructure of AZ31 wrought alloy [14, 15]. The AZ31 hollow profile exhibits a microstructure consisting of inhomogeneous coarse grains with circumjacent small grains with distinct grain boundaries. In Fig. 4b no obvious weld line or defect can be observed. It can be seen in the area with no weld seam (Fig. 4a) that some grains are stretched and elongated. Those elongated grains that have survived the plastic deformation throughout the extrusion process result from the initial grain structure of the casting. This may be due to an unfavorable orientation of these grains for the activation of dynamic recrystallization (DRX) [16].



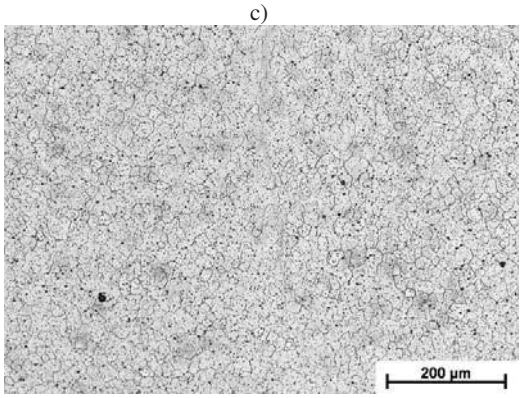
a)



b)



c)



d)

Fig. 4: Micrographs of the cross-sections of extruded hollow profiles: a) AZ31 seamless area, b) AZ31 seam area, c) ME21 seamless area, d) ME21 seam area; weld seams proceeding upright in the respective figures

The region of and around the weld seam (Fig. 4b) is also characterized through a small amount of twins aligned along the weld seam. Here, no elongated grains can be observed. This may be due to the additional intense shearing along the bridges in the die resulting in an increased amount of stored energy due to the high defect density initiating dynamic recrystallization processes. Also, the shearing could have resulted in a more favorable orientation of the grains for dynamic recrystallization. Due to the high extrusion temperature static recrystallization (SRX) and subsequent grain growth lead to the coarse AZ31 microstructure [17].

In Fig. 4c and 4d the microstructure of the ME21 extruded hollow profiles are shown. Both the seamless region (Fig. 4c) and the weld seam region (Fig. 4d) exhibit a fine recrystallized and mostly homogeneous microstructure. During the extrusion of ME21 DRX as well as SRX also determine the microstructure of the extrudate. Here the DRX is believed to be initiated through an increased amount of defects along (twin-) grain boundaries and shear bands [15, 17, 18]. Additionally, particle stimulated nucleation (PSN) is reported to take place at the $Mg_{12}Ce$ precipitates [20].

Fig. 5 outlines the difference in grain sizes for both AZ31 and ME21 alloy hollow profiles with and without an apparent weld seam. The average grain size for the weld region in AZ31 hollow profile is about 80 µm, but the error bar (standard deviation σ) indicates a large variation in grain size. The same is observed for the weld free region although the grain size is smaller (approximately 49 µm). It can clearly be seen that the ME21 hollow profile has smaller grain sizes for both the weld seam and the seamless region with 18 µm and 26 µm respectively.

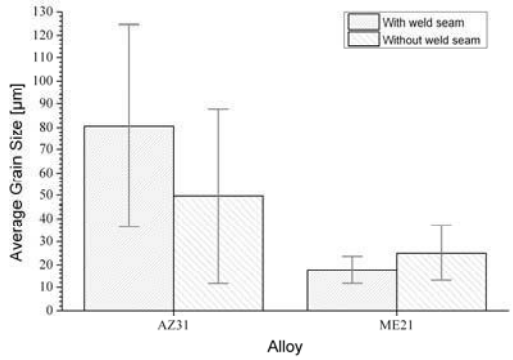


Fig. 5: Grain size of the extruded hollow profiles in the weld seam region and seamless region depending on the extruded alloy, error bars representing the standard deviation σ

Texture

The pole figures extracted from EBSD data are provided in Fig. 6. For the seamless region in Fig. 6a the {0001} pole figure displays an extrusion texture with pronounced basal component and a strong pole densitiy in the transversal direction (TD), meaning that a large number of grains having their c-axes oriented perpendicular to the extrusion direction (ED) as well as in the transversal direction (TD). Furthermore, both the transversal and the perpendicular component are broadened in the seamless area. The $\{10\bar{1}0\}$ pole figure in principle displays a six-fold symmetric alignment where the $\{10\bar{1}0\}$ planes are oriented perpendicular to the ED, but with the majority of these planes facing with their normals in ED. Also, there is a distinct pole density in the center. Overall, the texture of the seamless area in Fig. 6a is similar to that of an extruded sheet shown in [20].

In case of the weld region in AZ31 hollow profile (Fig. 6b) the $\{0001\}$ pole figure reveals a strongly pronounced pole densitiy in TD so that the majority of the grains are oriented with their c-axes along the TD. There is also a weaker basal component perpendicular to the TD and the extrusion direction (ED). Additionally, the basal poles are less broadened in comparison to those in the $\{0001\}$ pole figure of the seamless area. This is also reflected in the $\{10\bar{1}0\}$ pole figure of the weld seam area where the $\{10\bar{1}0\}$ planes are oriented almost exclusively towards the ED and the perpendicular direction in equal fraction.
In the extrusion of flat AZ31 sheets a strong basal texture with a weaker transversal component was observed [20]. This texture is based on the asymmetrical stress field in the deformation zone in front of the die bearing, making the c-axis align to the highest stress apparent. However, based on the findings regarding texture, in porthole die extrusion the stress-state seems quite different compared to that in simple flat profile extrusion with a flat die. The orientation of the c-axes in transversal direction may be due to a higher (compression) stress component in this direction.

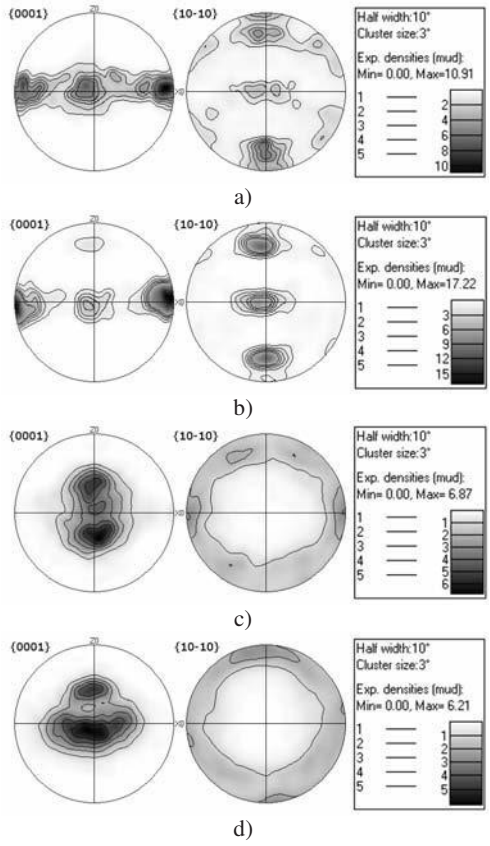


Fig. 6: Pole figures corresponding to a) AZ31 seamless area, b) AZ31 seam area, c) ME21 seamless area, d) ME21 seam area; ↑ED, →TD

For ME21 extruded hollow profiles the pole figures appear different from those of AZ31. The pole figures of both the seamless and the weld seam region of ME21 profiles show a pronounced orientation of the c-axes perpendicular to the extrusion direction. In the $\{0001\}$ pole figure (Fig. 6c) of the seamless region the basal component is split along the ED with the pole densities of the split component having marginal different intensities. Also, the $\{10\bar{1}0\}$ pole figure display a circular arrangement of the $\{10\bar{1}0\}$ planes around the ED with a stronger component in TD (Fig. 6d).
In contrast, the appearance of the weld seam affects the texture evolution. Here, the $\{0001\}$ pole figure again displays the splitting of the basal component along the ED, but the pole density also is broadened towards the TD. As a result the $\{10\bar{1}0\}$ planes' orientation is of circular character as well, but the pole densities show stronger components towards TD and ED (Fig. 6d).

Mechanical properties
During tensile testing the tensile yield stress (TYS), ultimate tensile stress (UTS) and fracture strain were obtained from stress-strain-curves.
The stress-strain-curves of AZ31 tensile testing in Fig. 7 show distinct differences in yield stress and hardening behaviour dependent on the loading direction. The seamless specimens tested along the extrusion direction showed higher yield stresses and less strain hardening compared to specimens tested in transversal direction. The UTS values were almost idenditical at about 250 MPa. Fracture strains show only little differences with values from 16% (ED) to 11% (TD).
Tensile specimens with ED oriented parallel to the loading direction yield at higher stresses. Along this loading direction the activation of basal slip systems at room temperature is difficult because of the high Schmid-factor. Hence, additional non-basal slip systems have to be activated in order to promote plastic deformation.
The early yielding of the TD specimens can be explained as follows: Most of the grains are oriented so that the c-axes of the unit cells are aligned parallel to the loading direction. Loading in this direction activates the $\{10\bar{1}2\}\langle 10\bar{1}1\rangle$ tension twins very easily resulting in a relatively early onset of plastic deformation.
The measured values for the yield stresses are given in Table II. Here the difference between seamless and weld seam containing specimens become apparent.

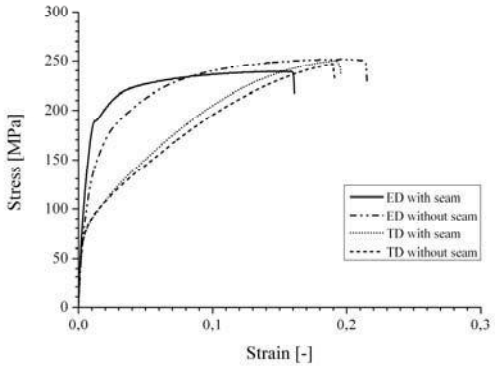


Fig: 7: Stress-strain relationship for AZ31 tensile specimen depending on the loading direction

Expecially specimens with the weld seam loaded in transversal direction had an about 15 MPa lower yield stress compared to the seamless specimens. In the ED the opposite was observed, having the seam containing specimens yielding at 186 MPa in contrast to the seamless specimens with 180 MPa. This is based on the fact that there are more c-axes in the weld seam area that are oriented parallel to TD in comparison with the seamless area (see Fig. 6a and 6b). This leads to lower values in TYS in the weld seam area

compared to the weld free area in TD, and higher TYS values in the weld seam area in ED.

The mechanical properties of the ME21 hollow extrudate can be seen in Fig. 8. Obviously, the loading direction has great influence on the TYS of the seamless samples
This agrees with findings on extruded ME21 sheets with similar texture [13]. In both the ME21 sheets and the ME21 hollow extrudate in the seamless area, most of the grains have a tilted c-axes towards the extrusion direction. Loading in ED leads to relatively high Schmid-factors for basal <a>-slip ($m_{basal<a>}<11\bar{2}2>$ = 0.498, $m_{basal<a>}<10\bar{1}1>$ = 0.432). In combination with the low CRSS (critical resolved shear stress) for basal <a>-slip [22] this slip-system becomes activated at low stresses. Adversely, when loading in TD, most grains have their c-axes oriented perpendicular to the loading direction, resulting in very low Schmid-factors for basal <a>-slip ($m_{basal<a>} \approx 0$). Thus, non-basal slip systems with a higher CRSS [22] have to be activated, resulting in higher TYS values. Moreover, non-basal slip involve increased strain hardening and finally higher UTS values and lower fracture strains

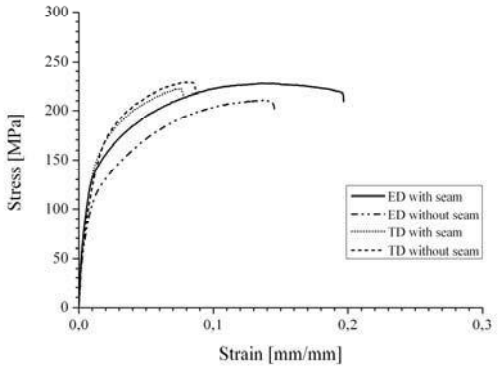


Fig: 8: Stress-strain relationship for ME21 tensile specimen depending on the loading direction

Looking at the weld seam containing samples, their texture (see Fig. 6d) is characterized through a broadening of the basal component towards the transversal direction. The $\{10\bar{1}0\}$ pole figure in Fig. 6d reveals that most of the grains' c-axes are aligned around the direction perpendicular to ED and TD relatively equally. Hence, in both loading directions the grains are oriented favourable for the easy activation of basal <a>-slip systems in equal measures. In fact, for both loading directions the TYS was equal, yielding at 117 MPa. Additionally, the smaller grain size in the weld seam material adds to the increase in TYS when loading in ED because of the Hall-Petch relationship. Also, the UTS values for both loading directions were equal because of the deformation mechanisms that are alike in both the ED and TD.
As stated above, the fracture strains show a significant dependence on the loading direction for ME21 hollow profiles. Specimens with the TD oriented parallel to the loading direction failed at fracture strains of about 6% regardless of the weld seam. In ED oriented samples failed at 11% or higher strains. This may not be a texture or grain size effect in the first place since the surface of the ME21 extrudates was very rough. This might have initiated an early crack formation in the specimens.
The overall mechanical properties of AZ31 and ME21 hollow extrudates are shown in Table II.

Table II: Mechanical properties of the extruded hollow profiles (TYS = Tensile Yield strength, UTS = Ultimate Tensile Strength, ED = Extrusion Direction, TD = Transversal Direction)

Sample Configuration		TYS [MPa]	UTS [MPa]	Fracture strain [%]
AZ31 (ED)	seam	186	239	15
	seamless	180	249	16
AZ31 (TD)	seam	67	252	14
	seamless	82	248	11
ME21 (ED)	seam	117	226	17
	seamless	84	210	11
ME21 (TD)	seam	117	227	6
	seamless	122	228	6

Finite Element Analysis (FEA)
The analysis of metal flow in the porthole die revealed qualitatively similar results for both alloys. Hence, only the results of the AZ31 extrusion simulation will be presented here. Fig. 9a and 9b show the strain distribution at different planes within the welding chamber.

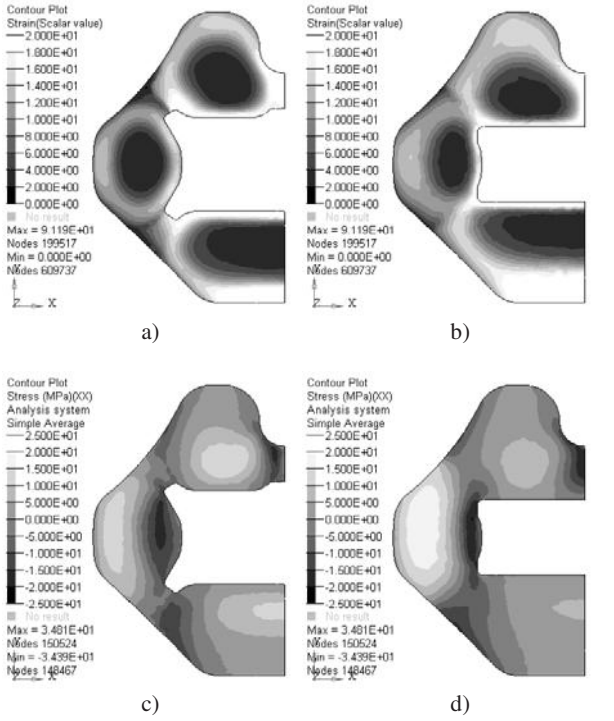


Fig. 9: FEA results exemplary for AZ31 hollow profile extrusion: strain distribution at welding chamber height a) H=0 mm, b) H=10 mm, distribution of stress component in x-direction (TD) at welding chamber height c) H=0 mm, d) H=10 mm; maximum H is 20 mm

Light areas outline material which has undergone heavy strain during the extrusion through the portholes into the welding chamber. Evidently, the weld seams consist of a great amount of sheared material joining in the welding chamber. This agrees with the explanation for microstructure development described above.
It was highlighted earlier in this work, that the texture of the AZ31 weld seam area has developed such that the c-axes are

oriented parallel to TD with only a few aligned perpendicular to TD and ED. The reason for this fact may be given by Fig. 9c and 9d. In the welding chamber, between bridges and bearing length a compression stress component develops in TD around each welding plane. Because the c/a-ratio is non-ideal with c/a = 1.624 < $\sqrt{8/3}$ the unit cells possibly could tilt during welding under the compressive stress with the c-axes become parallel to TD [23]. Furthermore, this mechanism may also lead to twinning that was observed in the weld region in AZ31 extrusion.
Nonetheless the exact mechanism for twinning during extrusion through a porthole die at high extrusion temperatures of about 480°C remains unclear and therefore requires further investigation.

Conclusion

The extrusion of hollow profiles using a porthole die was successfully performed for both magnesium alloys AZ31 and ME21. The extruded profiles showed no obvious welding defects, but different products properties were identified:

- The microstructure of both alloys is influenced by the weld seam resulting in different grain sizes and grain distributions in regard to the seamless material investigated. The mechanical anisotropy of seamless AZ31 and ME21 samples is caused by their texture. The anisotropy of the AZ31 profile is caused by the activation of $\{10\bar{1}2\}<10\bar{1}1>$ tension twins in favourably oriented grains, while the activity of basal <a>-slip determines the anisotropy of ME21 extrudate.
- In AZ31 hollow profiles the weld seam material exhibits a pronounced mechanical anisotropy due to the stronger basal component in TD rather than in ED. For ME21 weld seam material, the basal component becomes distributed more even between ED and TD, so that the mechanical anisotropy decreases to a minimum.
- A possible cause for the change in texture in the weld region compared to the seamless region was found using the finite element analysis (FEA). Here a compression stress component in the transversal direction around the weld area was identified that may influence the re-arrangement of the c-axes of the crystallographic unit cell of magnesium towards the TD.

References

1. E. Hoch: Strangpressprofile aus Aluminium-Legierungen für Karosseriebauteile, *Automobil Industrie INSIGHT*, (2010), 42-44
2. K. Müller (Ed.): *Fundamentals of Extrusion Technology*, Giesel Verlag GmbH, Isernhagen, 2004.
3. W.H. Sillekens, D.C.W. van der Linden, and A.J. den Bakker: "Weld-seam quality of hollow magnesium alloy extrusions", TMS, *Magnesium Technology 2008*, (2008), 189-194.
4. R. Akeret: Strangpressnähte in Aluminiumprofilen. Teil I: Technologie, Teil II: Mikrostruktur und Qualitätsmerkmale. In: Aluminium 68 (1992), S. 877–887, 965–974
5. M. Bauser, G. Sauer, and K. Siegert: *Strangpressen*, Aluminium Verlag, Düsseldorf, 2001.
6. L. Donati and L. Tomesani: "The effect of die design on the production and weld seam quality of extruded aluminum profiles", *Journals of Materials Processing Technology*, 164-165, (2005), 1025-1031.
7. L. Donati and L. Tomesani: "The prediction of weld seams quality in aluminum extrusion", *Journal of Materials Processing Technology*, 153-154, (2004), 366-373.
8. G. Liu, J. Zhou and J. Duszczyk: "FE analysis of metal flow and weld seam formation in a porthole die during the extrusion of a magnesium alloy into a square tube and the effect of ram speed on weld strength", *Journal of Materials Processing Technology*, 200, (2008), 185-198.
9. J. Hiscocks, L. Jiang, and J.J. Jonas: "Longitudinal seam failure in extruded AZ31 alloy", *Advanced Materials Research*, 15-17, (2007), 439-444.
10. R. Sikand et al.: "AM30 porthole die extrusions – A comparison with circular seamless extruded tubes", *Journal of Materials Processing Technology* 209, (2009), 6010-6020.
11. L. Li et al.: "Numerical and experimental study on the extrusion through a porthole die to produce a hollow magnesium profile with longitudinal weld seams", *Materials and Design*, 29, (2008), 1190-1198.
12. S. Gall et al.: "Hot working behavior of AZ31 and ME21 magnesium alloy", *Journal of Materials Science*, 48, (2013), 473-480.
13. S. Gall, S. Mueller, and W. Reimers: "Extrusion of Magnesium Sheet", *Materials Science Forum*, 638-642, (2010), 1530-1535.
14. S.E. Ion, F.J. Humphreys, and S.H. White: "Dynamic Recrystallization and the Development of Microstructure during the high Temperature Deformation of Magnesium", *Acta Metallurgica et Materialia*, 30, (1982), 1909–1919.
15. A. Takara et al.: "Secondary processing of AZ31 magnesium alloys concomitant with grain growth or dynamic recrystallization". *Materials Transactions*, 45, No. 7 (2004), 2377–2382.
16. J. Bohlen et al.: "Microstructure and texture development during hydrostatic extrusion of magnesium alloy AZ31", *Scripta Materialia*, 53, (2005), 259–264.
17. M.T. Pérez-Prado and O.A. Ruano: "Texture evolution during annealing of magnesium AZ31 alloy", *Scripta Materialia*, 46, (2002), 149–155.
18. M. Huppmann and W. Reimers: "Microstructural and mechanical properties of differently extruded AZ31 magnesium alloy", *International Journal of Materials Research*, 101, (2010), 1264–1271.
19. N. Stanford and M.R. Barnett: "The origin of rare earth texture development in extruded Mg-based alloys and its effect on tensile ductility", *Materials Science and Engineering A*, 496, (2008), 399–408.
20. M. Huppmann et al.: "Changes of the texture and the mechanical properties of the extruded Mg alloy ME21 as a function of the process parameters", *Materials Science and Engineering A*, 528, (2010), 342–354.
21. S. Gall et al.: "Mechanical properties and forming behavior of extruded AZ31 and ME21 magnesium alloy sheets", *Materials Science & Engineering A*, 579, (2013), 180-187.
22. S.B. Yi et al: "Deformation and texture evolution in AZ31 magnesium alloy during uniaxial loading", *Acta Materialia A*, 424, (2006), 549–562.
23. S. Gall et al.: "Extrusion of Magnesium Sheets", *In: Magnesium, 8th International Conference on Magnesium Alloys and Applications*, Ed. K.U. Kainer, (2009), 524–530.

Magnesium Technology 2014
Edited by: Martyn Alderman, Michele V. Manuel, Norbert Hort, and Neale R. Neelameggham
TMS (The Minerals, Metals & Materials Society), 2014

Microstructural Evolution and Its Relationship to the Mechanical Properties of Mg AZ31B Friction Stir Back Extruded Tubes

Justin L. Milner, Fadi Abu-Farha
Automotive Engineering, Clemson University – International Center for Automotive Research, Greenville, SC 29607, USA

Keywords: Friction Stirring, Magnesium Alloy, Back Extrusion, Grain Refinement, Texture

Abstract

Friction stir back extrusion (FSBE) was recently introduced as a promising energy-efficient technique for preparing fine-grained lightweight alloy tubes; this work focuses on quantifying the effects of the process on the material's microstructure and exploring the potentials for enhancing its performance. AZ31B-F magnesium round bars are processed into tubes by FSBE at selected process conditions. Microstructural examination is carried out at key locations across the processed tubes, in order to track grain size and texture evolution in the material. FSBE is shown to produce sound tubes with significant grain refinement and homogenisation in the processed material (from a heterogeneous coarse-grained microstructure with a bimodal ~55-115µm, to a homogeneous fine-grained structure with ~5µm average grain size), which is carried on to the walls of the formed tubes. Macro-mechanical testing is carried out on the formed tubes; the changes in the material's mechanical properties are correlated with its microstructural evolution.

Introduction

Friction stir back extrusion (FSBE) is a bulk processing/manufacturing technique for producing fine-grained structural tubes out of lightweight alloys [1]. As schematically shown in Figure 1, FSBE is simply an axisymmetric back extrusion process with a rotating ram to add the "friction stirring" component. Friction stirring was first introduced in 1991 by TWI as a vehicle for driving a unique solid-state joining technique known as friction stir welding (FSW) [2]. Aside from its low-energy consumption, the significant grain refinement observed within the stir zone [3] is probably one of its most attractive aspects. The latter was first capitalised on via friction stir processing (FSP) [4, 5], then through a wide range of derivatives (friction stir surface composites [6], micro-forming [7], channelling [8] and casting modification [9]), and most recently through bulk friction stir forming operations such as back extrusion [1, 10]. In FSBE, Figure 1, a rotating tool is plunged into a cylindrical specimen at a selected axial feed rate, thus forcing the material radially outwards as in conventional back extrusion. Friction at the tool/material interface generates sufficient heat that softens the material and facilitates its deformation/flow to form the tube. On the other hand, the high pressure under the tool and shearing the plasticised material at the interface result in a stirring zone with a refined microstructure. Despite the similarities, FSBE deviates from most FSP/FSW practices (with all the variations and derivatives): FSP/FSW processes have been predominantly applied to sheets/plates, with the stirring tool traversing across the surface (perpendicular to its axis of rotation) to process or join the material; FSBE processes the bulk material by moving the stirring tool in the axial direction, and utilises this motion as a means to reshape the material.

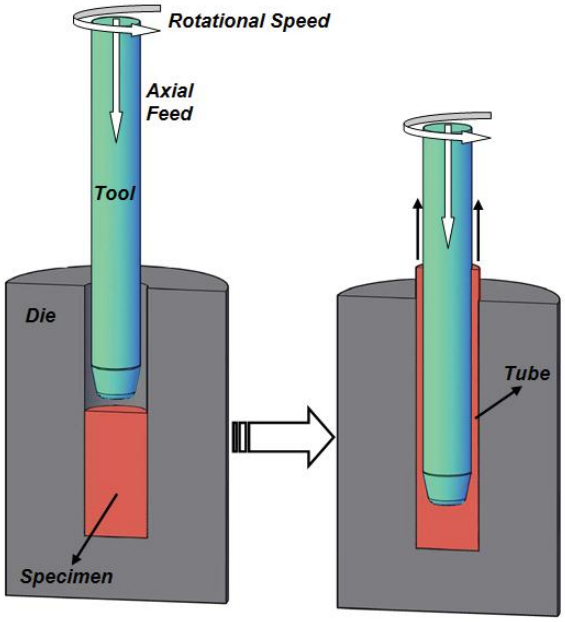


Figure 1: Schematic of friction stir back extrusion (FSBE).

In prior preliminary efforts, the FSBE process was validated, and was shown to be capable of producing sound magnesium and aluminium tubes [1, 10]. Optical microscopy indicated significant refinement in the microstructure of the as-received material, yet without sufficient quantification. In this work, we focus the attention on the AZ31 magnesium alloy, and track the changes FSBE imposes on its microstructure, as well as it mechanical properties. Significant focus will be directed towards tracking grain structure and texture evolution as the material progresses through the processed tube. The effects of friction stirring on various materials, including magnesium alloys, have been well investigated in various welding and processing efforts, and thus they will be compared (though not directly) with FSBE here.

Experiments

Experimental Setup:

FSBE experiments were performed using a setup following the schematic shown in Figure 1. The stirring tool is a polished H13 tool steel rod with Φ=12.7 mm, and having a surface hardness of ~65 HRC. To ease tool penetration into the material, the end of the tool (a length of approximately 10 mm) was tapered by ~10°. Unlike stirring tools used in typical FSP, a flat stirring surface with no tool pin was used here. The extruding die was made in two halves in order to ease specimen extraction after testing. The die cavity is a straight blind hole with Φ=19.05 mm, thus corresponding to a processed tube with a wall thickness of

~3.2 mm. The hole was first machined and then honed to a fine surface finish to facilitate the back extrusion (upward flow) of the processed material. Pre-hardened P20 tool steel was used in constructing the extruding die. Two set screws are located near the bottom of the die cavity to secure the starting rod sample and prevent it from spinning. The entire setup was secured to OKUMA MB 46VAE Vertical Machining Center, which was used to perform the experiments. The stirring tool was centred with the die cavity, to ensure axisymmetric deformation.

Material:

The material used in this work is the AZ31B magnesium alloy, received as Φ=19.05mm round bars in the F condition. Great variations in the grain structure were observed; Figure 2 shows an optical micrograph of the as-extruded (base) material, looking at the rod section from its centre (left) to the outer edge (right). It is clear that grain size varies notably from one location to another. But generally, the material has a coarse grain structure at the centre of the bar, and a fine one around the outer surface. The average grain size was measured to be ~115 µm near the centre, compared to ~55 µm around the circumferential zone. A closer look at the microstructure was obtained through EBSD, which was carried out on the as-extruded base material located near the centre of the rod (location shown in Figure 2); the corresponding EBSD orientation colour map is shown in Figure 3. Even within that specific area, the material clearly showed a heterogeneous grain structure with an overall average grain size of ~69 µm. The bimodal grain size distribution had peaks occurring at ~20 and ~100 µm, where the average grain size of the coarse grains was measured to be ~114 µm. On the other hand, the texture of the base material showed a typical extrusion or cylindrical texture, where the basal plane normals <0001> are perpendicular to the extrusion axis. This can be seen in the (0001) and (10-10) pole figures plotted normal to the extrusion direction (ED), where the horizontal and vertical axes correspond to the radial direction (RD) and normal direction (ND), respectively.

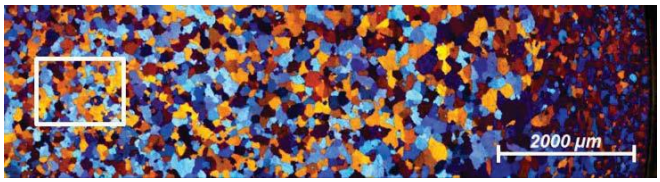


Figure 2: Optical micrograph under polarization of the AZ31B as-extruded base material from centre (left) to edge (right). White box indicates the approximate size and location of the EBSD map in Figure 3

FSBE Testing Procedure:

A test specimen is inserted into the extruding die, and secured with the two side set screws. The tool is then driven downwards against the specimen while rotating at a selected speed; after reaching the desired depth, the tool is retracted. The extruding die is then released, and the produced tubular specimen is retrieved. Significant heat is generated during testing; therefore, the entire setup and the extruded tube are rapidly cool immediately after testing. In order to guarantee repeatability of the performed tests, the stirring tool and the extruding die are polished/honed after each test. The results reported here were obtained at a tool rotational speed of 2000 rpm, tool axial feed of 2 mm/s, and tool exit speed of 4 mm/s. Under these conditions, a 100-125 mm tube specimen is formed in fewer than 60 sec.

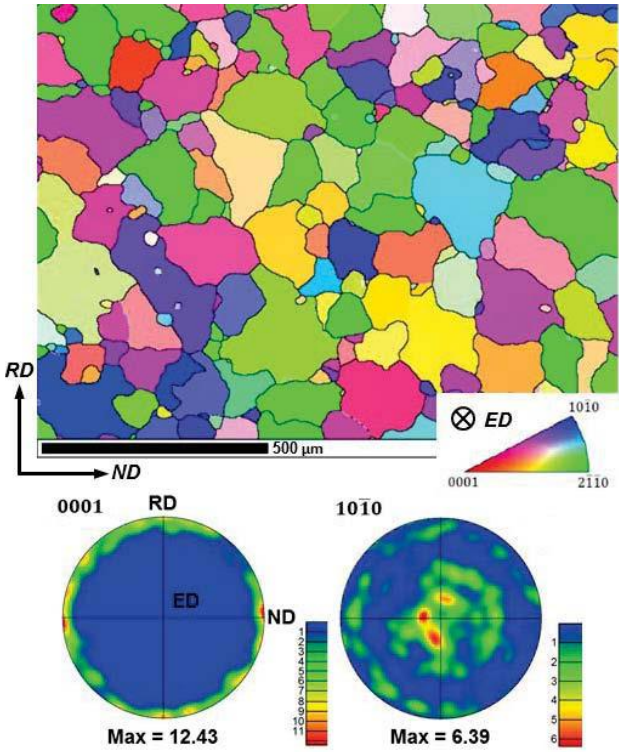


Figure 3: EBSD orientation colour map and corresponding (0001) and (10-10) pole figures of the AZ31B as-extruded base material.

Material Characterisation:

The microstructure and texture of the as-received and FSBE processed material were investigated by electron backscatter diffraction (EBSD). High-resolution EBSD mapping was carried out on a Hitachi SU-6600 FE-SEM with AZtec software. For the EBSD analysis, specimens were prepared at selected locations under the processing tool and throughout the tube wall, as well as the as-extruded base material. Various step sizes were used depending on the map size and expected grain size (0.25, 0.5, 0.75 and 2 µm - 2 µm step size was used for the base material). Prior to EBSD, the Mg specimens were oxide polished and etched with 5% nital solution (5% nitric acid, 95% ethanol). The EBSD data was reprocessed with HKL Channel 5 software.

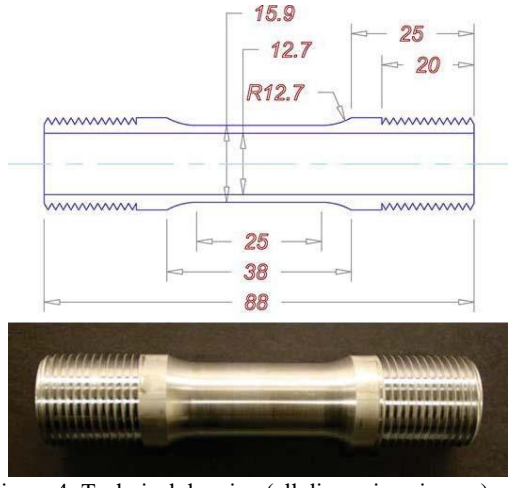


Figure 4: Technical drawing (all dimensions in mm) and machined full-tube tensile specimen.

Mechanical properties, on the other hand, where evaluated by full-tube tensile testing using a 5985 INSTRON electromechanical load frame. Tubes prepared by FSBE were turned down to create a gage region having Φ=15.9 mm and 25 mm in length; with a fillet radius of 12.7 mm, as shown by the technical drawing in Figure 4. This profile left a wall thickness of ~1.6 mm as compared to the original wall thickness of ~3.2 mm. The ends of the tensile sample were threaded as the means to grip and pull the test sample during tensile testing. In addition to the FSBE tubes, full-tube tensile specimens were machined from the AZ31B-F Mg as-extruded round bars to provide a comparison with the base material. Tensile tests were conducted at room temperature at an initial strain rate of $1x10^{-3}$ s^{-1}.

Results and Discussion

Formed Tubes:

Figure 5 shows examples of magnesium tubes produced by FSBE. The tubes formed exhibit prismatic uniform sections, and the images show a high quality surface finish on the inside surface. Spiral marks were observed on the outer surfaces of the tubes; these marks provide an insight into the amount of twisting the material experiences in forming the tubes. Tracing these marks indicated an overall twist angle of ~6° over the length of a tube. The section view clearly shows that the formed tube is structurally sound, with no signs of voids or internal channels; this was verified through subsequent analyses on all FSBE tubes.



Figure 5: Examples of Mg AZ31B tube specimens produced by FSBE.

Microstructural Examination:

Figure 6 shows a polarised optical micrograph of the lower part of the processed tube, within the tapered section of the stirring tool. This micrograph shows a primary stirring zone and a secondary processed zone throughout the tube. The primary stirring zone has a depth of around 0.5-1 mm directly below and next to the processing tool's interface and significant grain refinement is seen to occur in this zone. The secondary processed zone mainly denotes the grain structure within the tube walls with a mix of refined and elongated grains. Below the stirring zone under the flat section of the tool, the structure shows large grains with a high degree of twinning. This twining is typical of magnesium since the material away from the processing zone experiences simple compressive stresses caused by the high extrusion pressure imposed by the toll during FSBE. As the tool penetrates deeper into the material, the twined material is forced to flows upwards and then into the tube wall. Further examination of the material along the formed tube walls (which is not shown in Figure 6, but evident and will be discussed in several subsequent figures) indicates that the twined structure diminishes as the tube is formed. We expect most of the twinned material to diminish as it goes through the processing zone. Dynamic recrystallization is responsible for the rest, since the material experiences further processing (additional shear evident from side twisting) and more heating due to friction between the material and tool interface.

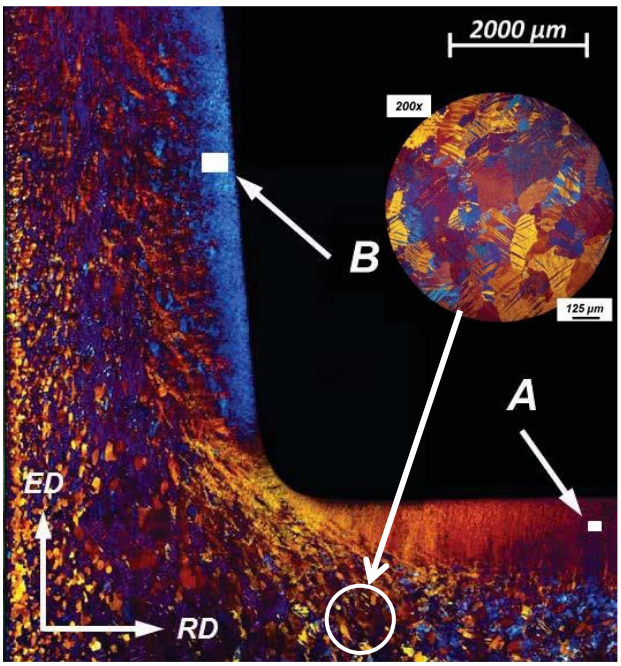


Figure 6: Polarised optical micrograph of a longitudinal section in the FSBE specimen near the radius of the stirring tool. Shown also are the locations of the EBSD maps of Figure 7 and Figure 8.

EBSD was carried out at key locations in the same FSBE tube sample, to determine the grain structure and micro-texture evolution. Figure 6 shows two locations: (A) is located below the tool's flat surface and (B) is located directly next to the material tool interface ~5 mm above its flat surface. Figure 7 shows the EBSD-based inverse pole figure map for location (A), showing ED orientation and the corresponding (0001) and (10-10) pole figures. The grain structure is seen to be highly refined and homogeneous, as compared with the base material, with an average grain size of ~5 µm. A grain is defined by being completely surrounded by a grain boundary of 10° or greater and comprising of at least four indexing points. The grain structure is slightly elongated along the RD with an aspect ratio of 1.8, due to the compressive forces and stirring action seen in this region.

The grain boundary map (shown with the orientation colour map) displays misorientation angles above 10° in black lines and below in grey lines with a lower limit boundary below 2° (to eliminate orientation noise). The orientation colour map (Figure 7) shows red dominance demonstrating that the (0001) axis is parallel to the ED normal plane, and that very low misorientation exists between the grains. The misorientation angle distribution (not shown) is characterized by a low-angle peak at 2° (~7%) and a near-constant fraction between an angular range of 3-30°

comprising ~91% of all boundaries. The latter, and along with the (0001) pole figure, demonstrates strong basal texture, where <0001>//ED with a max intensity of ~93. Thus, the c-axis aligns perpendicular to the stirring tool's flat surface.

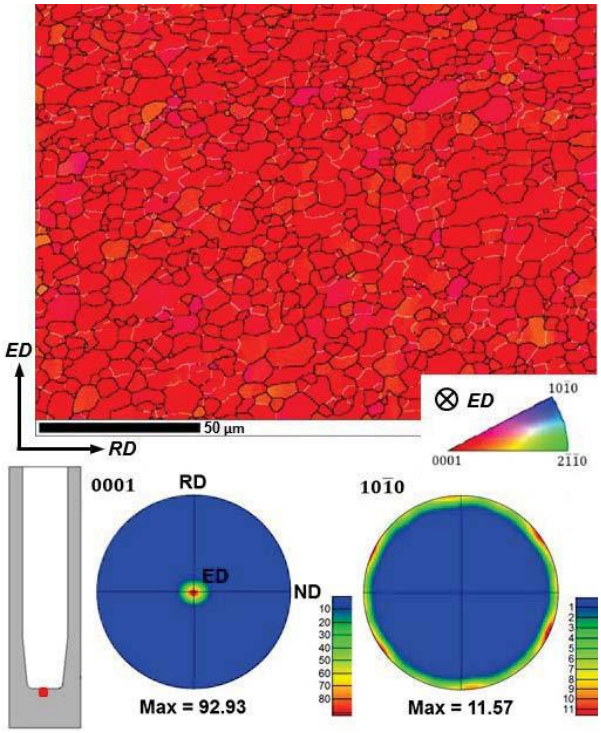


Figure 7: EBSD orientation colour map and the corresponding (0001) and (10-10) pole figures below the processing tool (location-A in Figure 6).

The second key location, near the inner tube wall ~5 mm above the tool's flat surface (location-B in Figure 6), was then examined, and the results are shown in Figure 8. One first notes that the grain structure is still refined and homogeneous, similar to that at location-A. However, accurate evaluation of the average grain size indicated an increase to ~10 µm, which means a slight grain growth that is believed to be caused by some recrystallization as the material moved up into the tube wall region. Interestingly, the grain aspect ratio was also found to be 1.8, which is similar to that of location-A, except that the grains are slightly elongated along the ED here (instead of the RD). The misorientation angle distribution was found to be similar, with a low-angle peak at 2° (~11%) and ~84% of all boundaries between an angular range of 3-30°. The main notable differences between these two locations are related to the texture. The (0001) pole figure, displayed in Figure 8, shows a rotation of the <0001> by ~10° from the RD to the ED with a max intensity of ~59. This rotation is due to the tapper put on to the stirring tool of ~10° from the ED. This means that the c-axis in both cases is perpendicular to the outer tool surface. One can draw a trend from these results by looking at it from a material flow perspective. Figure 6 shows that material flow lines, and thus shear planes, follow the outer contour of the stirring tool (more detailed views can be found in [10]). All this leads to the conclusion that texture evolution is dominated by shear deformation, where the basal planes (perpendicular to the c-axis) align with the shear planes. This agrees with the results obtained by Yuan et al. [11] in regards to texture evolution in friction stir spot welding of Mg AZ31.

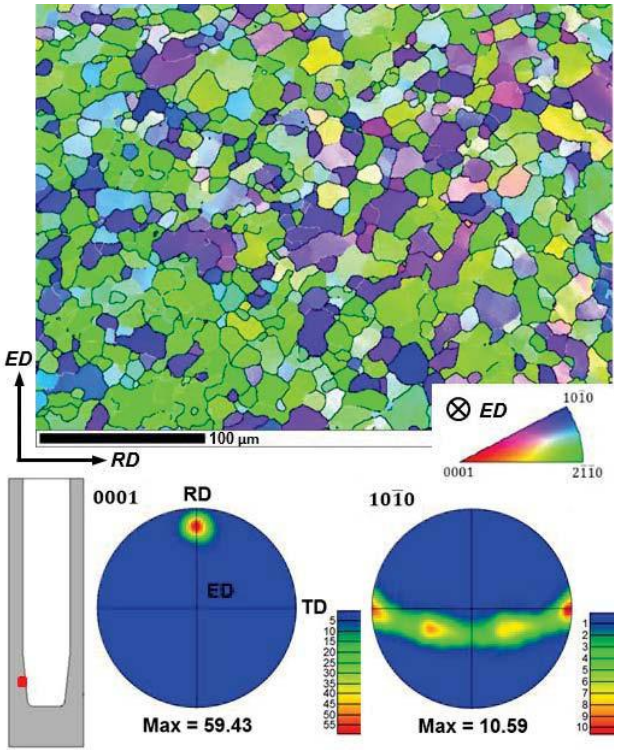


Figure 8: EBSD orientation colour map and the corresponding (0001) and (10-10) pole figures near the tubes inner wall ~5mm above the stirring tool's flat surface (location-B in Figure 6).

Figure 9 shows polarised optical micrographs of two cross sections of the FSBE tube (perpendicular to the tube's axis) located at (a) ~20 mm and (b) ~40 mm above the stirring tool's flat surface. The grain structure of the FSBE tube's wall can be characterised by four distinct regions through its thickness (from inner to outer): (i) The stirring zone, with the most refined grains, is clearly observed near the tube's inner wall. (ii) This intermediate zone displays a refined and homogeneous, yet recrystallized, grain structure. (iii) The third region shows large grains that are elongated in the tangential/circumferential direction (TD), with fine dynamically recrystallized grains mixed throughout. This region is believed to be the least affected by grain refinement in FSBE, since it contains the material that did not go through the processing zone before entering the tube wall. Elongation of these grains is analogous to that observed in the thermo-mechanically affected zone (TMAZ) in FSW and FSP [4, 12, 13]. (iv) The region close to the outer tube surface also exhibits grains elongated along the TD, yet with smaller size (compared to (iii)). This region is also least affected by FSBE, with the grain structure being close to that of the base material.

Two particular locations highlighted in Figure 9 were analysed by EBSD. The EBSD-based inverse pole figure maps showing ED orientation and the corresponding (0001) and (10-10) pole figures, taken at ~20 mm and ~40 mm above the stirring tool's flat surface, are shown in Figure 10 and Figure 11, respectively. As noted, the grain structure in both cases is similar, and can be described as homogeneous and refined. In fact it is similar to that noted in Figure 8 for the material within the lower section of the tube wall. The average grain size was measured to be ~11 µm and ~12 µm, for locations C and D, respectively.

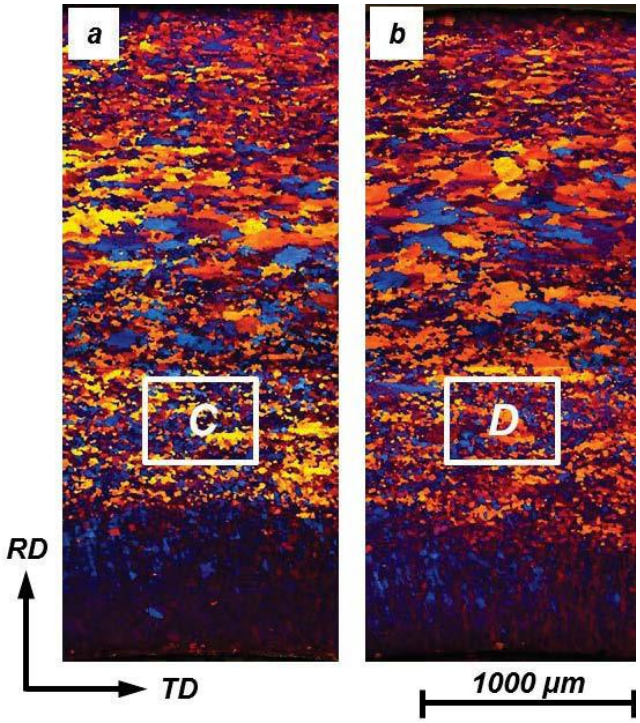


Figure 9: Polarised optical micrograph of the FSBE specimen's circumferential cross sections from the inner to the outer tube wall taken at (a) ~20mm and (b) ~40mm above the stirring tool's flat surface. The two white boxes indicate the approximate sizes and locations of the EBSD maps (shown in Figure 10 and Figure 11).

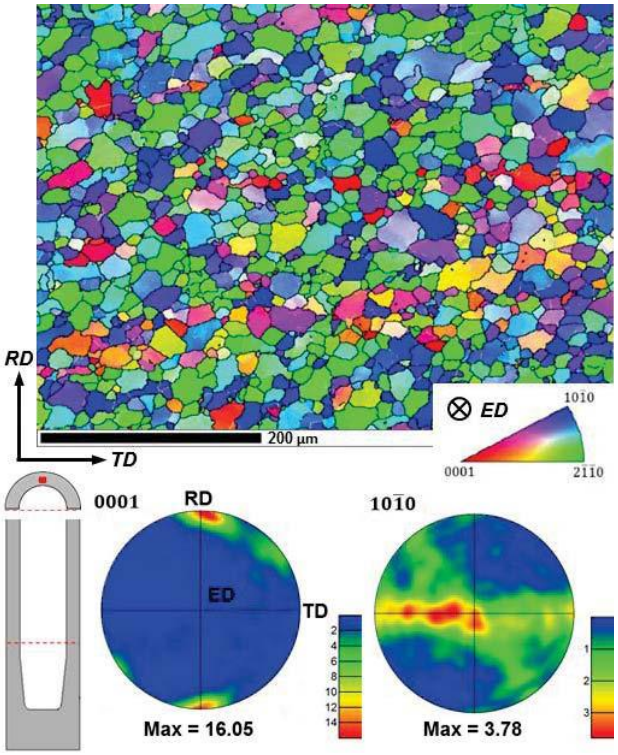


Figure 10: EBSD orientation colour map and the corresponding (0001) and (10-10) pole figures ~1mm from the tube's inner wall and ~20mm above the stirring tool's flat surface (location-C in Figure 9).

These results indicate good thermal stability in the grain structure, with no significant grain growth as we move along the tube wall. The grains in Figure 10 and Figure 11 are also slightly elongated following the TD, with the same aspect ratio of ~1.8. The misorientation angle distribution was seen to be more uniform throughout the entire angular range, as compared to the previous two locations analysed in the primary stirring zone (A and B in Figure 7 and Figure 8). It can be characterized as a sharp low-angle peak at 2° (~12°) and a nearly even distribution between the angular ranges 3-30° and 31-94° of ~45 and ~43%, respectively. The texture of these two locations are similar with the <0001> aligns parallel to the RD, as seen in the (0001) pole figures displayed in Figure 10 and Figure 11. The maximum intensity in these regions is ~16-21, which is significantly lower than the maximum intensity seen in the primary stirring zone (~90). Interestingly, a TD component or c-axis nearly parallel to the tangential direction was not seen, as it is common for most Mg extruded tubes; a rotation of the <0001> by ~45° from the TD to the RD was seen instead. This is not fully understood, and will be further examined in future work.

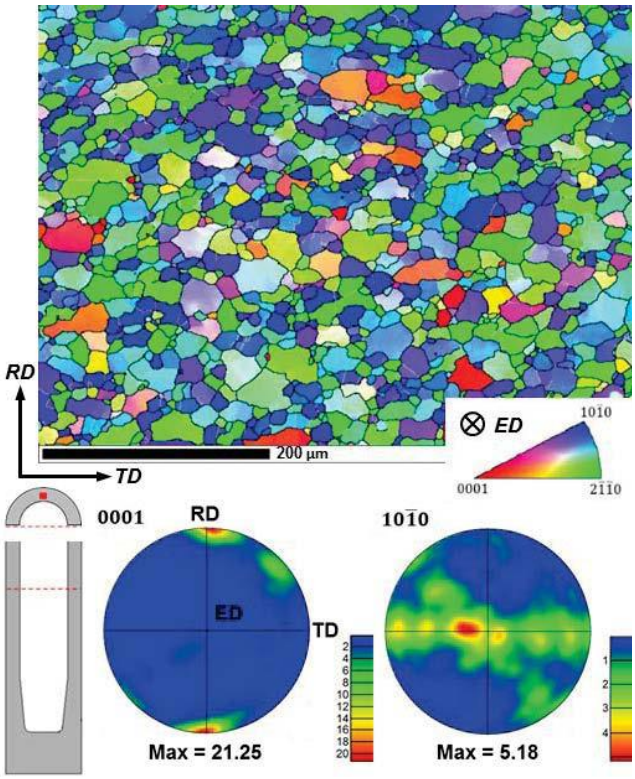


Figure 11: EBSD orientation colour map and the corresponding (0001) and (10-10) pole figures ~1mm from tube wall and ~40mm above the stirring tool's flat surface (location D in Figure 9).

Mechanical Properties:

Figure 12 shows the engineering stress-strain curves of the as-extruded base material and FSBE processed material via full tube tensile testing. The base material exhibits yield strength of 211±3 MPa, whereas the FSBE tube's yield strength decreased to 152±11 MPa. This corresponds to a 28% reduction in yield strength. However, the ultimate tensile strength (UTS) remained nearly the same (256±2 MPa for the base material and 255±5 MPa for the FSBE tubes). This compares favourably to the reported results for FSP of magnesium alloys, where a drop in both yield

and tensile strengths has been reported [14-16]. Ductility, on the other hand, significantly improved (by three folds) by undergoing FSBE; the tensile ductility increased from 6.4±0.6% for the base material to 19.5±1.6% for the FSBE tubes. All the mechanical properties reported here are summarized in Table 1.

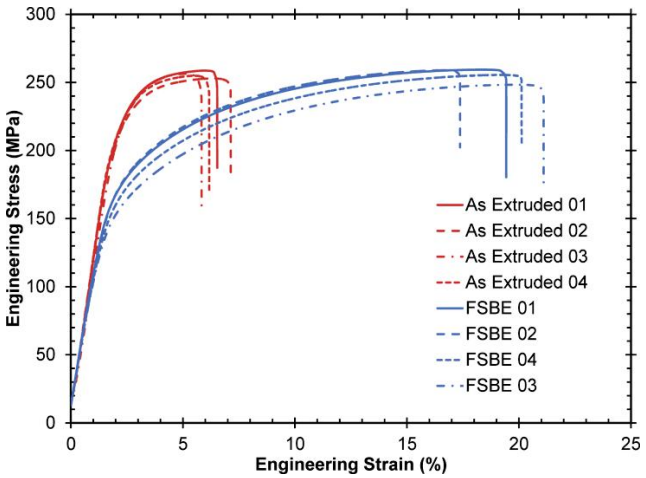


Figure 12: Engineering stress-strain curves of the Mg AZ31B as-extruded base material and the FSBE processed tubes.

Table 1: Summary of the mechanical properties

	Yield Strength (MPa)	Ultimate Tensile Strength (MPa)	Elongation (%)
As Received	211 ± 3	256 ± 2	6.4 ± 0.6
FSBE	152 ± 11	255 ± 5	19.5 ± 1.6

Summary and Conclusions

In this work, friction stir back extrusion (FSBE) was performed on AZ31B-F magnesium alloy samples. Processing via FSBE produced magnesium tubes, without preheating or a need for an external heating source, showing no signs of voids or structural defects. Microstructural examination was performed on tube samples at various locations via EBSD to characterize grain structure and texture evolution. Significant grain refinement was seen to occur in the primary stirring zone, an approximant depth of 1mm, with an average grain size of ~5 µm as compared to the base material average grain size of ~114 µm. The tube walls grain structure was seen to be stable at ~10-12 µm within the processing zone. Texture of the formed tubes showed a strong basal texture with a maximum intensity of ~93 within the stirring zone where the c-axis aligns perpendicular to the stirring tool's surface. The intensity of the texture was seen to decrease within the tube wall to ~20, where the c-axis aligned parallel to the radial direction. Furthermore, a second texture component with less intensity was seen, where the c-axis is perpendicular to the extrusion direction and rotated ~45° from the tangential to the radial direction. The mechanical properties, on the other hand, of the FSBE processed tubes, showed a ~28% decrease in the yield stress and 3-fold increase in tensile ductility, as compared to the base material. The tensile strength, however, remained at the same level, thus indicating a stronger hardening behaviour and a significant increase in toughness. Overall, the results presented here show great potentials for FSBE, with favourable changes to the microstructure and mechanical properties of the formed tubes.

References

[1] F. Abu-Farha, "A preliminary study on the feasibility of friction stir back extrusion," *Scripta Materialia,* vol. 66, pp. 615-618, 2012.

[2] W. M. Thomas, E. D. Nicholas, J. C. Needham, M. G. Murch, P. Templesmith, and C. J. Dawes, "Friction Stir Butt Welding," *G.B. Patent Application No. 9125978.8, International Patent Application No. PCT/GB92/02203,* 1991.

[3] M. Mahoney, C. Rhodes, J. Flintoff, W. Bingel, and R. Spurling, "Properties of friction-stir-welded 7075 T651 aluminum," *Metallurgical and Materials Transactions A,* vol. 29, pp. 1955-1964, 1998.

[4] R. S. Mishra and Z. Y. Ma, "Friction stir welding and processing," *Materials Science and Engineering: R: Reports,* vol. 50, pp. 1-78, 2005.

[5] R. S. Mishra, M. W. Mahoney, S. X. McFadden, N. A. Mara, and A. K. Mukherjee, "High strain rate superplasticity in a friction stir processed 7075 Al alloy," *Scripta Materialia,* vol. 42, pp. 163-168, 1999.

[6] R. S. Mishra, Z. Y. Ma, and I. Charit, "Friction stir processing: a novel technique for fabrication of surface composite," *Materials Science and Engineering: A,* vol. 341, pp. 307-310, 2003.

[7] S. Mohan and R. J. Mishra, "Friction Stir Microforming of Superplastic Alloys," *Microsystem Technologies,* vol. 11, pp. 226-229, 2005.

[8] N. Balasubramanian, R. S. Mishra, and K. Krishnamurthy, "Process forces during friction stir channeling in an aluminum alloy," *Journal of Materials Processing Technology,* vol. 211, pp. 305-311, 2011.

[9] S. Jana, R. S. Mishra, H. N. Chou, and D. Herling, "Friction Stir Microstructural Modification of Investment Cast F357," in *Proceedings of the 136th TMS Annual Meeting and Exhibition*, Orlando, FL, 2007, pp. 439-448.

[10] F. Abu-Farha, "Spiral Friction Stir Processing (SFSP) for the Extrusion of Lightweight Alloy Tubes," in *07th International Manufacturing Science and Engineering Conference - MSEC 2012*, (MSEC2012-7358), 2012.

[11] W. Yuan, R. S. Mishra, B. Carlson, R. Verma, and R. K. Mishra, "Material flow and microstructural evolution during friction stir spot welding of AZ31 magnesium alloy," *Materials Science and Engineering: A,* vol. 543, pp. 200-209, 2012.

[12] K. V. Jata and S. L. Semiatin, "Continuous dynamic recrystallization during friction stir welding of high strength aluminum alloys," *Scripta Materialia,* vol. 43, pp. 743-749, 2000.

[13] R. W. Fonda, J. F. Bingert, and K. J. Colligan, "Development of grain structure during friction stir welding," *Scripta Materialia,* vol. 51, pp. 243-248, 2004.

[14] L. Commin, M. Dumont, J. E. Masse, and L. Barrallier, "Friction stir welding of AZ31 magnesium alloy rolled sheets: Influence of processing parameters," *Acta Materialia,* vol. 57, pp. 326-334, 2009.

[15] B. Darras and E. Kishta, "Submerged friction stir processing of AZ31 Magnesium alloy," *Materials & Design,* vol. 47, pp. 133-137, 2013.

[16] F.-Y. Hung, C.-C. Shih, L.-H. Chen, and T.-S. Lui, "Microstructures and high temperature mechanical properties of friction stirred AZ31–Mg alloy," *Journal of Alloys and Compounds,* vol. 428, pp. 106-114, 2007.

Magnesium Technology 2014
Edited by: Martyn Alderman, Michele V. Manuel, Norbert Hort, and Neale R. Neelameggham
TMS (The Minerals, Metals & Materials Society), 2014

EFFECT OF YTTRIUM ADDITION ON TEXTURE DEVELOPMENT IN A CAST Mg-Al-Y MAGNESIUM ALLOY DURING COMPRESSION

N. Tahreen[1], D.L. Chen[1], M. Nouri[2], D.Y. Li[2]
[1]Department of Mechanical and Industrial Engineering, Ryerson University, 350 Victoria Street, Toronto, Ontario M5B 2K3, Canada
[2]Department of Chemical and Materials Engineering, University of Alberta, 9107-116 Street, Edmonton, Alberta T6G 2V4, Canada

Keywords: Cast magnesium alloy, rare earth element, compressive deformation, texture, twinning.

Abstract

Magnesium is increasingly used in the automotive and aerospace industries to reduce vehicle weight and fuel consumption. Alloying with rare-earth (RE) elements is considered as an important tool for magnesium to achieve superior properties via texture randomization. The present study was aimed to identify the inter-relationship among the texture evolution, yttrium content and deformation behavior in a cast Mg-Al-Y alloy in compression. A weak and random texture was present in the Y-containing cast magnesium alloy. Increasing Y content reduced the extent of twinning and enhanced the slip deformation mode. Despite a slight decrease in the yield strength and ultimate compressive strength, increasing Y content by 0.3% and lowering Al content by 2% resulted in a significantly increased fracture strain. The compression deformation led to the formation of $\{\bar{1}2\bar{1}0\}\langle 0001\rangle$ and $\{01\bar{1}0\}\langle 0001\rangle$ texture components.

Introduction

The increasing demands for improving fuel economy and reducing greenhouse gas emissions in the transportation industry have triggered extensive research in the field of lightweight materials [1,2]. As the lightest structural metallic material, magnesium is the most promising candidate to decrease the weight of vehicles. However, its extensive application is still limited due to poor room temperature ductility, which is mainly caused by the development of sharp crystallographic texture [3]. The presence of strong texture leads to plastic anisotropy as well as the activation of twinning and/or slip during deformation [4]. There have been many reports in the literature that, alloy composition can significantly amend the texture [3,5]. Micro-alloying with rare earth elements such as Yttrium (Y) can weaken the extrusion texture and hence improves the formability of magnesium alloy [6-9]. The same effect has also been observed for rolling texture [10]. However, the report about the effect of rare-earth elements on casting texture is still limited. Presently, cast magnesium alloys are more widely used than wrought magnesium alloys because of their economic advantage for mass production of components due to lower processing and assembly costs. There have been many studies on the microstructure and tensile properties of various cast materials but very little information is available on the texture development in RE-containing cast magnesium alloys during compression. To date, the mechanisms of texture weakening in the RE-containing alloys have not been very well understood. The development of weaker texture during rolling or extrusion is mainly associated with the recrystallization process [11]. Ball and Prangnell [12] and Mishra *et al*. [13] indicated that the texture weakening in RE-containing Mg alloys are due to particle simulated nucleation and boundary pinning at Mg-RE precipitates. Stanford and Barnett [14] suggested that the formation of shear bands during deformation contributed to the randomization of texture. A change in the mobility of high-angle grain boundaries by alloying addition leads to texture weakening has been discussed by Mackenzie and Pekguleryuz [15] as well. These studies suggest that texture weakening strongly depends on alloy composition and principally on the RE content. There is practically no systematic work on deformation texture development in the Y-containing cast Mg-Al alloy with different levels of intermetallics during deformation. The objective of this study was, therefore, to illuminate the relation between texture evolution, alloy content and deformation behavior in a cast Mg-Al-Y alloy. Special attention is paid to underlying mechanisms of texture weakening at ambient temperature.

Experimental

To examine the effect of composition on cast texture and ductility, two as-cast magnesium alloys with different concentrations of Al and Y contents were selected to observe the effect of Y at the expense of Al. The chemical composition of the investigated alloys is given in Table I.

Table I. Composition of the two alloys in the present study.

Alloy	Al (%)	Y (%)	Mg
Mg-4Al-0.2Y	3.9	0.20	balance
Mg-2Al-0.5Y	1.8	0.51	balance

Cylindrical specimens with a diameter of 5 mm and height of 8 mm were machined and compression tests were performed until failure using a computerized Instron machine. To observe the microstructural change along with texture evolution, some samples were tested at a strain of 4.2% and 9.1%. All the tests were carried out at room temperature and at a strain rate of 1×10^{-4} s^{-1}. The compressed samples were cut along the compression axis using a slow diamond cutter and then cold mounted. For the microstructural examination, the samples were prepared by standard technique of grinding with SiC abrasive papers and polishing with diamond paste. Microstructures of both as-cast and compressed samples were observed via optical microscope and scanning electron microscope (SEM) after careful polishing and etching with an acetic picral solution. The crystallographic texture of the samples was determined by a Panalytical X'Pert PRO X-ray diffractometer (XRD) using Cu K_α radiation (wavelength λ=0.15406 nm) at 45 kV and 40 mA with a sample tilt angle ranging from 0 to 70°. A set of five pole figures (i.e., $\{10\bar{1}0\}$, $\{0002\}$, $\{10\bar{1}1\}$, $\{11\bar{2}0\}$, $\{10\bar{1}3\}$) were measured to calculate the orientation distribution function (ODF) using the MTEX toolbox. To present the ODF, Bunge notations of the Euler angles were used. It should be noted that in evaluating the stress-strain curves, machine deformation was eliminated using a calibration curve to obtain the actual deformation of test samples. The compressive properties, including 0.2% yield strength (YS),

ultimate compressive strength (UCS) and fracture strain (ε_f), were obtained based on the average of two samples tested.

Results and Discussion

Fig. 1(a) and (b) show typical twin-free microstructures of undeformed Mg-4Al-0.2Y and Mg-2Al-0.5Y alloys, respectively. The microstructure of as-cast Mg-4Al-0.2Y consisted of primary α-Mg dendrites with secondary dendrite arms and some β-$Mg_{17}Al_{12}$ precipitates. The EDS analysis of Mg-4Al-0.2Y (Fig. 2(a)) revealed with the presence of both Al_2Y and β-$Mg_{17}Al_{12}$ particles, which were precipitated preferentially in the inter-dendritic regions.

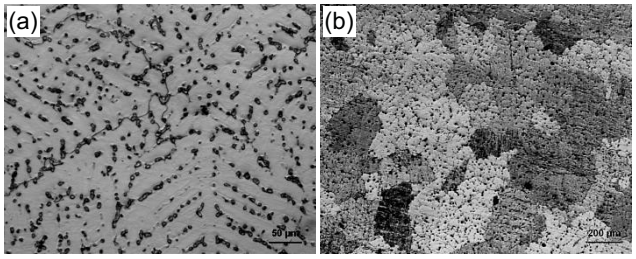
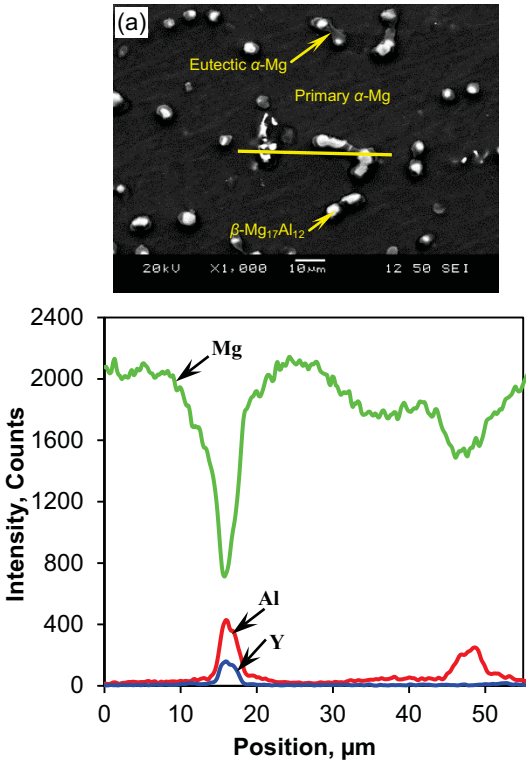


Figure 1. Typical microstructure of undeformed as-cast magnesium alloy (a) Mg-4Al-0.2Y and (b) Mg-2Al-0.5Y.

The optical micrograph of Mg-2Al-0.5Y in the as-cast state shows dendrite cells as well (Fig. 1(b)). An EDS line scan analysis of Mg-2Al-0.5Y shown in Fig. 2(b) indicates the presence of Al_2Y and Y particles. Fig. 3(a) and 3(b) show the calculated (0001) pole figures of the two as-cast Mg-4Al-0.2Y and Mg-2Al-0.5 Y alloys,



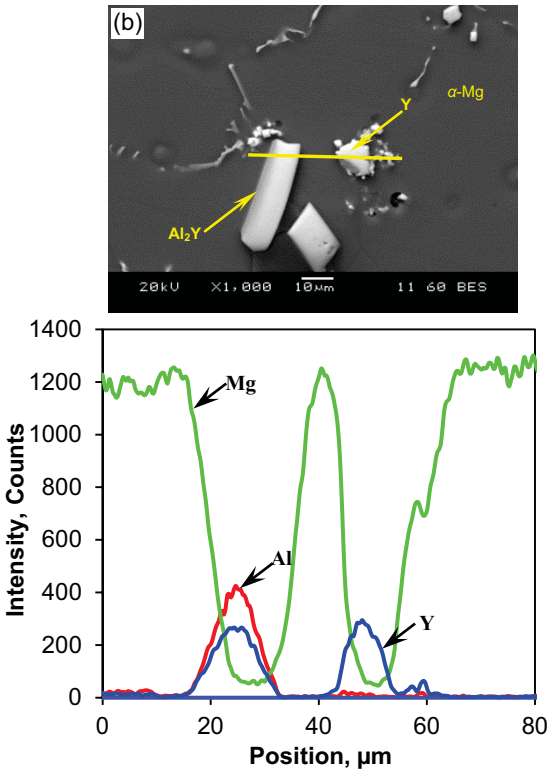


Figure 2. EDS line scan across the particles indicated, showing the Mg, Al and Y compositional variations in alloy (a) Mg-4Al-0.2Y and (b) Mg-2Al-0.5Y.

respectively, from the raw data measured via XRD. Both alloys showed fairly random texture where the basal poles were nearly randomly distributed in all directions. The (0001) pole figure of the Mg-2Al-0.5Y alloy has a maximum intensity of I_{max}=4.3 MRD, which was weaker than that of the Mg-4Al-0.2Y alloy having I_{max}=4.8 MRD. Either an increase of Y or a drop of Al content could contribute to this texture randomization. It has been reported that the addition Al could slightly sharpen the extrusion texture [14]. The role of Y in the weakening of extrusion texture was well established, and an increase in Y content from 0.003% to 0.2% lowered the texture intensity by 7.5 MRD [8]. Therefore, the weakening of texture in the Mg-2Al-0.5Y alloy was mainly ascribed to the increase in the Y content in conjunction with the decrease in the Al content, which needs further verification by mechanical testing.

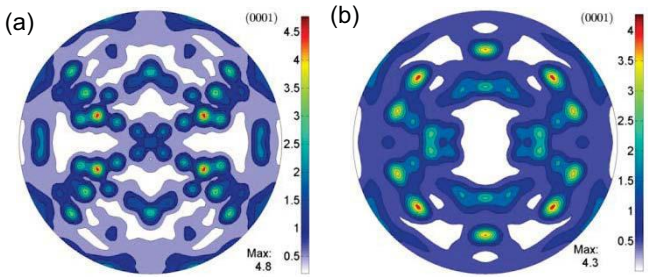


Figure 3. Initial (0001) pole figures of as-cast magnesium alloys (a) Mg-4Al-0.2Y and (b) Mg-2Al-0.5Y.

The true stress-true strain curve of Mg-4Al-0.2Y and Mg-2Al-0.5Y magnesium alloys during compression is shown in Fig. 4. The corresponding mechanical properties are listed in Table II.

Table II. The evaluated compressive properties.

	YS MPa	UCS MPa	Fracture strain (%)
Mg-4Al-0.2Y	103	236	22
Mg-2Al-0.5Y	92	233	42

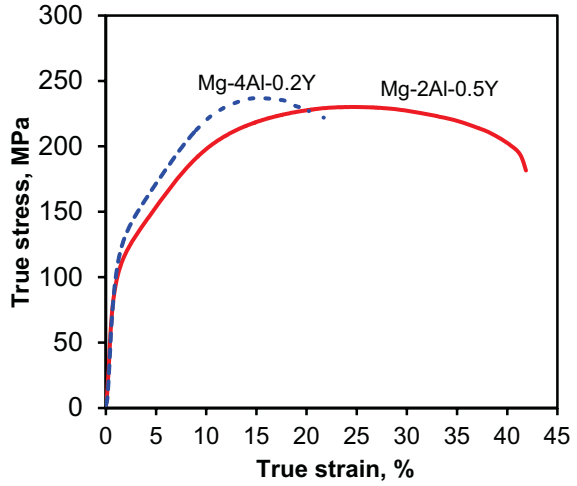


Figure 4. Compressive true stress-true strain curve of Mg-4Al-0.2Y and Mg-2Al-0.5Y alloys tested at a strain rate of 1×10^{-4} s^{-1}.

There is a significant difference in the mechanical behavior of the two alloys. The more Al-containing alloy had higher yield strength and UCS but lower fracture strain as expected. Increasing the content of Y (from 0.2% to 0.5%) should increase both strength and ductility [16]. The increase in the fracture strain in alloy Mg-2Al-0.5Y was significant, as seen from Fig. 4 and Table II. However, a little drop in the YS and UCS was observed. This was related to the fact that the content of Al was significantly lower (4% to 2%) and Y was only slightly higher (from 0.2% to 0.5%) in the latter alloy. The slight decrease in the YS and UCS and a large (nearly two-fold) increase in the fracture strain suggests that, Y had a much stronger effect on the compressive mechanical properties compared to Al. Increasing the Y content by only 0.3% considerably improved the fracture strain of the Mg-2Al-0.5Y alloy which was in agreement with the initial texture information.

The optical micrographs of the deformed microstructure after 4.2% compression are shown in Fig. 5(a) and 5(b), respectively, to examine the occurrence of deformation twins. The presence of extensive deformation twins can be seen in most grains in the Mg-4Al-0.2Y alloy, whereas fewer deformation twins occurred in some grains in the Mg-2Al-0.5Y alloy. Despite a lower Al content, Mg-2Al-0.5Y alloy had a higher Y content, the deformed microstructure was expected to exhibit fewer twins due to the presence of more Y-containing precipitates and smaller grain size. This alloy therefore appeared to exhibit a mixed mode of deformation, involving both twinning and slip. The increase in the slip activity was due to an increase in the Y content. Similar enhancement in the slip activity was also observed in the Mg-Ce alloy due to the favorable grain rotation [13]. It was likely that a combination of easy slip and twinning led to the distinctly increased fracture strain in the Mg-2Al-0.5Y alloy.

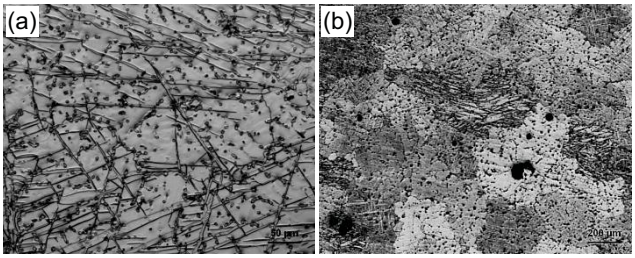


Figure 5. Microstructure after compressive deformation of (a) Mg-4Al-0.2Y and (b) Mg-2Al-0.5Y at a strain level of 4.2%.

To better understand the above result, the texture is presented in Fig. 6 in terms of the ODF in a Euler space of $0°\leq\varphi_1\leq90°$, $0°\leq\phi\leq90°$ and $0°\leq\varphi_2\leq60°$ as the alloy has a hexagonal crystal symmetry. The texture of the deformed Mg-4Al-0.2Y and Mg-2Al-0.5Y samples after compression to a strain amount of 9.1% is represented by the ODF sections at $\varphi_2=0°$ and $\varphi_2=30°$ from which the main texture components in hcp materials could be identified. In the ODF sections two key texture components marked as A and B can be clearly distinguished with the corresponding Euler angles given in Table III.

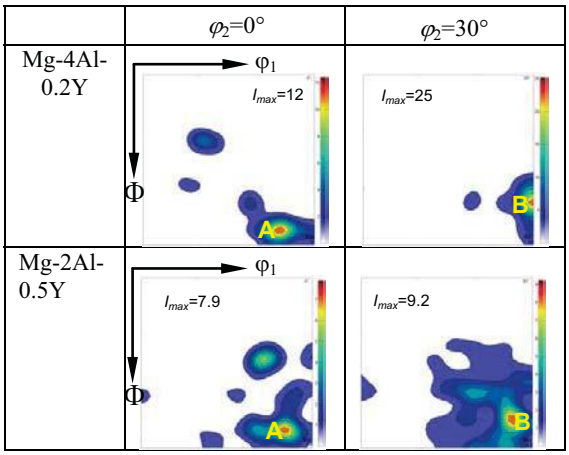


Figure 6. ODF obtained from 9.1% compressed samples.

Table III. Main texture components identified from Euler angles.

Euler angles ($\varphi_1 \Phi \varphi_2$)	$\{h\ k\ i\ l\}<u\ v\ t\ w>$
A (75, 80, 0)	$\{\bar{1}\,2\,\bar{1}\,0\}<0001>$
B (85~90, 75, 30)	$\{01\bar{1}\,0\}<0001>$

A striking change in ODF at a 9.1% strain level was observed with respect to the undeformed alloys. That is, the initially random texture containing multiple texture components were replaced by the texture components A$\{\bar{1}\,2\,\bar{1}\,0\}<0001>$ and B$\{01\bar{1}\,0\}<0001>$ at orientations (75, 80, 0) and (85~90, 75, 30). The evolution of the texture components after compression indeed reflected a rotation of *c*-axes from the random orientation to the compression direction due to the occurrence of twinning (Fig. 5). This implies that the *c*-axes of most grains were rotated against the "push" or compression. As also seen from Fig. 6, the maximum intensity for the texture components A$\{\bar{1}\,2\,\bar{1}\,0\}<0001>$ and B$\{01\bar{1}\,0\}<0001>$ was 12 MRD (multiples of a random density) and 25 MRD in the Mg-4Al-0.2Y alloy, whereas it was 7.9 MRD and 9.2 MRD in the Mg-2Al-0.5Y alloy after a 9.1% compressive strain. It is clear that both the texture components produced in the Mg-4Al-0.2Y alloy were more concentrated. Such

a texture evolution was related to the microstructure development or the twin formation. As discussed above, more twins were present in the Mg-4Al-0.2Y alloy (Fig. 5(a)). Less extent of twinning in the Mg-2Al-0.5Y alloy due to the more Y content added (Fig. 5(b)) made the *c*-axes of a relatively lower number of grains to rotate towards against the compression direction, which ultimately resulted in a lower texture intensity value.

It should be noted that in the microstructural observation, a strain value of 4.2% was chosen instead of 9.1% since the extension twins were reported to occur over a strain range of 2-4% [17,18]. With increasing strain levels, the extension twins appeared to thicken and spread, and gradually cover each grain, leading to the vanishing of twin boundaries [19]. To identify more accurately the texture components, a later stage of deformation (i.e., 9.1% in the present case) is preferable, since texture components evolve and intensify with increasing strain. It is also of interest to note that, at the strain level of 9.1% the intensity of component B is higher than that of component A in both Mg-4Al-0.2Y and Mg-2Al-0.5Y alloys. Similar results in the extruded AM30 and AZ31 alloys were also reported in [20,21], where the intensity of component B was also higher than that of component A.

Conclusions

The present study reported the inter-relationship among the alloy content, crystallographic texture evolution, and deformation behavior of cast Mg-Al-Y alloys. Compression tests at different amounts of strain were performed to evaluate the texture and microstructure. The obtained results revealed a combined effect of both Al and Y on the deformation characteristics and texture. A weak and random texture was present in the Y-containing cast magnesium alloys. Increasing Y content reduced the extent of twinning as a deformation mode and enhanced the slip deformation mode. In spite of a slight decrease in the YS and UCS, increasing Y content by 0.3% and lowering Al content by 2% resulted in a substantial increase in the fracture strain. The compression deformation led to the formation of $\{\bar{1}2\bar{1}0\}<0001>$ and $\{01\bar{1}0\}<0001>$ texture components in both alloys.

Acknowledgements

The authors would like to thank the Natural Sciences and Engineering Research Council of Canada (NSERC), Premier's Research Excellence Award (PREA), NSERC-DAS Award, AUTO21 Network of Centers of Excellence, and Ryerson Research Chair program for providing financial support. The authors also thank, Dr. R. Tandon and Dr. B. Davies (Magnesium Elektron) for supplying magnesium powders for the defocusing calibration, and Q. Li, A. Machin, J. Amankrah, and R. Churaman for assisting in the experiments.

References

1. J. Murray and D. King, "Oil's tipping point has passed," *Nature*, 481 (2012), 433-435.
2. T.M. Pollock, "Weight loss with magnesium alloys," *Science*, 328 (2010), 986-987.
3. J. Hirsch and T. Al-Samman, "Superior light metals by texture engineering: Optimized aluminum and magnesium alloys for automotive applications," *Acta Materialia*, 61 (2013), 818-843.
4. A.S. Khan, A. Pandey, T. Gnäupel-Herold and R.K. Mishra, "Mechanical response and texture evolution of AZ31 alloy at large strains for different strain rates and temperatures," *International Journal of Plasticity*, 27 (2011), 688-706.
5. S.B. Yi, J. Bohlen, F. Heinamann and D. Letzig, "Mechanical anisotropy and deep drawing behavior of AZ31 and ZE10 magnesium alloy sheets," *Acta Materialia*, 58 (2010), 592-605.
6. R. Cottam, J. Robson, G. Lorimer and B. Davis, "Dynamic recrystallization of Mg and Mg-Y alloys: Crystallographic texture development," *Materials Science and Engineering A*, 485 (2008), 375-382.
7. J. Bohlen, M.R. Nurnberg, J.W. Senn, D. Letzig and S.W. Agnew, "The texture and anisotropy of magnesium-zinc-rare earth alloy sheets," *Acta Materialia*, 55 (2007), 2101-2112.
8. K. Hantzsche, J. Bohlen, J. Wendt, K.U. Kainer, S.B. Yi and D. Letzig, "Effect of rare earth additions on microstructure and texture development of magnesium alloy sheets," *Scripta Materialia*, 63 (2010), 725-730.
9. N. Stanford and M. Barnett, "Effect of composition on the texture and deformation behavior of wrought Mg alloys," *Scripta Materialia*, 58 (2008), 179-182.
10. S.A. Farzadfar, M. Sanjari, I.-H. Jung, E. Essadiqi and S. Yue, "Role of yttrium in the microstructure and texture evolution of Mg," *Materials Science and Engineering A*, 528 (2011), 6742-6753.
11. J. Wendt, K.U. Kainer, G. Arrubarrena, K. Hantzsche, J. Bohlen and D. Letzig, "On the microstructure and texture development of magnesium alloy ZEK100 during rolling" (Paper presented at the 138th Annual Meeting & Exhibition, San Francisco, California, February 2009), 289-293.
12. E.A. Ball and P.B. Prangnell, "Tensile-compressive yield asymmetries in high strength wrought magnesium alloys," *Scripta metallurgica et materialia*, 31 (1994), 111-116.
13. R.K. Mishra, A.K. Gupta, P.R. Rao, A.K. Sachdev, A.M. Kumar and A.A. Luo, "Influence of Ce on texture and ductility of magnesium extrusions," *Scripta Materialia*, 59 (2008), 562-565.
14. N. Stanford and M.R. Barnett, "The origin of "rare earth" texture development in extruded Mg-based alloys and its effect on tensile ductility," *Materials Science and Engineering A*, 496 (2008), 399-408.
15. L.W.F Mackenzie and M.O. Pekguleryuz, "The recrystallization and texture of magnesium-zinc-cerium alloys," *Scripta Materialia,* 59 (2008), 665-668.
16. Z. Zhao, Q. Chen, Y. Wang and D. Shu, "Microstructure and mechanical properties of AZ91D alloys with Y addition," *Materials Science and Engineering A*, 515 (2009), 152-161.
17. D. Sarker and D.L. Chen, "Detwinning and strain hardening of an extruded magnesium alloy during compression," *Scripta Materialia*, 67 (2012), 165-168.
18. A. Jiang, A. Godfrey, W. Liu, and Q. Liu, "Microtexture evolution via deformation twinning and slip during compression of magnesium alloy AZ31," *Materials Science and Engineering A*, 483-484 (2008), 576-579.
19. D. Sarker and D.L. Chen, "Texture development in an extruded magnesium alloy during compression along the transverse direction" (Paper presented at the 142nd Annual Meeting & Exhibition, San Antonio, Texas, February 2013), 313-316.
20. D. Sarker and D.L. Chen, "Texture transformation in an extruded magnesium alloy under pressure," *Materials Science and Engineering A*, 552 (2013), 63-67.
21. S.B. Yi, C.H.J. Davies, H.G. Brokmeier, R.E. Bolmaro, K.U. Kainer and J. Homeyer, "Deformation and texture evolution in AZ31 magnesium alloy during uniaxial loading," *Acta Materialia*, 54 (2006), 549-562.

Magnesium Technology 2014

Wrought Processing II and Joining

Magnesium Technology 2014
Edited by: Martyn Alderman, Michele V. Manuel, Norbert Hort, and Neale R. Neelameggham
TMS (The Minerals, Metals & Materials Society), 2014

SPIKE-FORGING OF AS-CAST TX32 MAGNESIUM ALLOY

K.P.Rao[1], K. Suresh[1], N. Hort[2], K.U. Kainer[2]
[1]Department of Mechanical and Biomedical Engineering,
City University of Hong Kong, Tat Chee Avenue, Kowloon, Hong Kong SAR, China
[2]Helmholtz-Zentrum Geesthacht, Institute of Materials Research,
Magnesium Innovation Centre, Max-Planck-Strasse 1, Geesthacht 21502, Germany

Keywords: Mg alloy, Forging, FE simulation, Formability, Processing map.

Abstract

Magnesium alloy TX32 (Mg-3Sn-2Ca) has good corrosion and creep resistance. The processing map of TX32 exhibits a good workability domain over a fairly wide range of temperature and strain rate. To validate the processing map, spike forging of the alloy (combining backward extrusion and upsetting) was carried out at the temperatures of 400, 450 and 500 ^{o}C and at speeds of 0.1 and 1 mm s^{-1}. Finite-element (FE) simulation of the process was conducted using DEFORM-2D software to obtain the local variations of strain and strain rate. It has been found that the strain values reach as high as 1.8 at certain locations in the forged components. The average grain size has increased with increasing temperature and decreasing speed. The microstructure varied at different regions of the forged components as per the implied features of the processing map and FE simulations, with recrystallized fine grain sizes at locations corresponding to higher strains and strain rates.

Introduction

New magnesium alloys are attracting the attention of automotive industry and various components are being developed. Currently, cast products account for the majority of applications. However, thermomechanical processing of Mg alloys is difficult because of their poor workability at room temperature due to the limited number of slip systems. Hence, bulk forming processes like forging, rolling and extrusion are generally carried out at elevated temperatures, where non-basal slip systems dominate the plastic flow [1,2]. Magnesium alloys based on Mg-Sn-Ca (TX) system has been investigated for their properties and processing. [3-5]. Among them, the composition Mg-3Sn-2Ca (TX32) has been found to offer good corrosion and creep resistance [5], and the as-cast alloy exhibits good hot workability for conversion into a wrought material [6]. Its processing map shows a domain covering fairly wide range of temperature from 390 ^{o}C to 500 ^{o}C and strain rate from 0.0005 s^{-1} to 0.6 s^{-1}.

Spike-forging forming process combines back-ward extrusion and upsetting. The influence of geometric parameters, processing variables, and interfacial conditions on the flow behavior has been studied using FE simulations and laboratory scale experimentation [7]. It has been found that spike forming process is sensitively dependent on the geometry of specimen, and a suitable geometry for studying the deformation behavior of materials has been recommended. Bennett [8] used different material models while studying the spike-forging of CrMoV alloy steel, and has correlated the results of FE simulations and the emerged microstructures in the components forged at different speeds.

The purpose of this study is to validate the processing map of TX32 alloy using laboratory-scale spike forging process. The forging characteristics will also be studied using Finite element (FE) simulation of the process to determine the local variations of strain and strain rate.

Experimental

The as-cast TX32 alloy with the nominal composition of 3wt%Sn, 2wt%Ca and remainder Mg was prepared using permanent mold casting to obtain a cylindrical billet. The detailed method of preparation was given in previous published work [6]. Cylindrical specimens or preforms of 24 mm diameter and 18 mm height were machined from the slices of the cast billet, which were used for spike forging experiments. The spike forging tests were conducted using MTS 810 servo-hydraulic machine at three temperatures (400, 450 and 500 ^{o}C) with forming speeds of 0.1 and 1 mm s^{-1} using a 15° tapered top die and a flat bottom die. The schematic of the spike forging set-up used is shown in Figure 1.

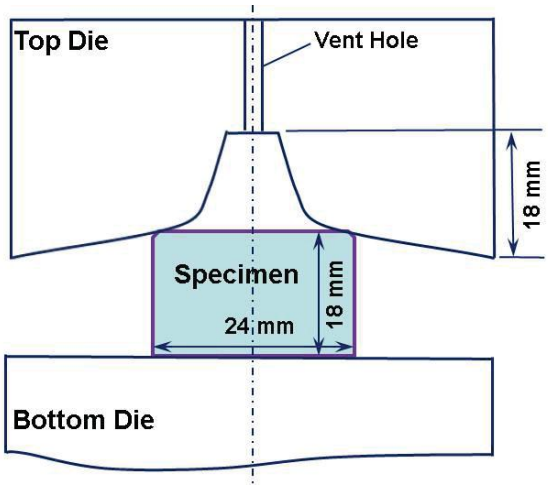


Figure 1. Schematic of the spike forging set-up.



Figure 2. Typical view of TX32 specimens
(a) preform with thermocouple inserted, and
(b) typical forged component.

Typical preform with a small chamfer at the top, shown in Figure 2(a), which matches the contour of the top die to facilitate its initial positioning and centering in the forging die set. It may be noted that only the chamfered area will be in contact with the top die at the beginning of the spike forging process. Graphite containing grease was used as the lubricant between the preform (specimen) and the forging dies. Thermocouple was inserted into the specimen to measure its temperature during the heating and forging operation. The material nearer to the outer diameter flows radially outwards, whilst that near to the centre of the top surface extrudes in the orifice to form a spike, as shown in Figure 2(b). The stroke or top die travel was limited to about 11 mm and the load-stroke curves were recorded. The forged components were quenched in water. For metallographic work the forged specimens were sectioned through mid-section along the forging direction, mounted, ground, polished, and etched using an acetic picral solution. The microstructures were recorded in the rib (extensive outward flow), spike (extruded central region), and intermediate locations using metallurgical microscope. The grain size of the starting alloy and the forged microstructures were estimated following the line-intercept method.

The FE simulation of the spike forging process was conducted under isothermal conditions (die and workpiece are the same temperature) using DEFORM 2D axisymmetric version [9] which is equipped with a pre-processor to input materials data and object definition. A post-processor outputs information about deformed geometry, state-of-stress, velocity vectors, strain and strain rate. The program is based on a rigid visco-plastic model using the principle of analysis of large plastic incremental deformation [10]. The process simulations were conducted for the temperatures of 400, 450 and 500 ^{o}C and the forging speeds of 0.1 and 1 mm s^{-1} (average strain rates of about 0.01 and 0.1 s^{-1}) until the stroke reaches 11 mm. Simulated forging loads were obtained at different stroke levels for all the chosen forging conditions to compare with those measured during actual experiments.

Results and Discussion

The initial microstructure of the as-cast TX32 magnesium alloy is shown in Figure 3.

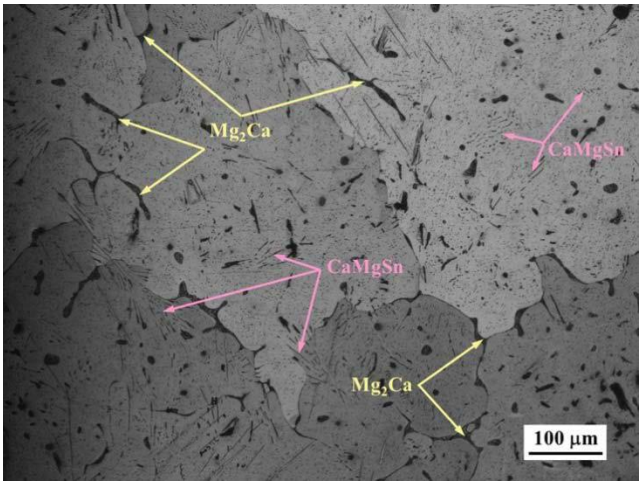


Figure 3. Optical Microstructure of as-cast TX32 alloy.

It exhibits grains as large as 450 µm in size. The optical image revealed two types of intermetallic phases; Mg_2Ca typically existing at the grain boundaries and CaMgSn particles in the matrix. The existence of these two phases has been reported earlier [4,5], and also predicted by a thermodynamic model [11,12].

Based on the compression flow stress data of as-cast TX32 alloy at different temperatures and strain rates, the developed processing map [6] at a strain of 0.5 exhibited two workability domains in the temperature and strain rate ranges of (i) 300-350 ^{o}C and 0.0003-0.001 s^{-1} (ii) 390-500 ^{o}C and 0.005-0.6 s^{-1}. The changeover from one domain to the other has occurred at about 370 ^{o}C. It also exhibited a large regime of flow instability at 300-500 ^{o}C typically at higher strain rates 1-10 s^{-1}. Another processing map is now developed using the flow stress data corresponding to a strain of 0.7, which is shown in Figure 4. Though this map and its features are identical to the one developed for a strain of 0.5, only the second domain is marked in this figure (Workability Domain) because it is the most relevant one for industrial metal forming operations that are preferably carried out using as high strain rate as possible. The spike forging experiments were conducted within this domain, i.e., temperatures of 400, 450, and 500 ^{o}C and forging speeds of 0.1 and 1 mm s^{-1} or average strain rates of approximately 0.1 and 0.01 s^{-1}.

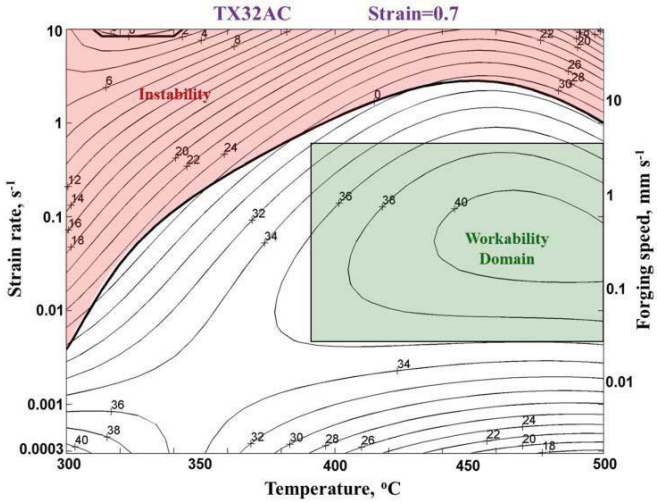


Figure 4. Processing map of as-cast TX32 alloy at a strain of 0.7. The contour numbers represents the efficiency of power dissipation in percent, and the strain rate axis represents log scale.

The TX32 alloy of spike shape component was successfully forged under the selected process conditions. The load-stroke curves obtained from the experimental results are compared with those estimated through FE simulations. The curves obtained at the temperature of 450 ^{o}C and forging speeds of 0.1 and 1 mm s^{-1} are shown in Figure 5. These curves exhibit the three distinct stages that are similar to those of typical semi-closed die forging process, with a steep increase in the load towards the end of stroke or forging. The first stage is initiation of upsetting and plastic deformation, the second one being the major deformation stage, followed by the steep rise in load due to the development of large dead-metal zone.

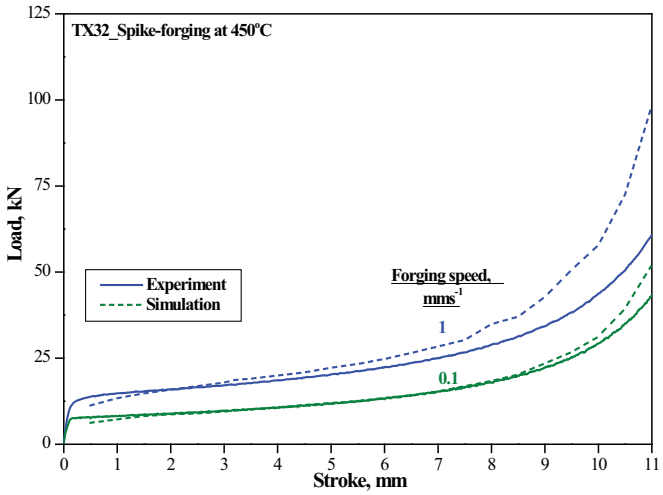


Figure 5. Load-stroke curves obtained at 450 °C for Forging at speeds of 0.1 and 1 mm s^{-1}.

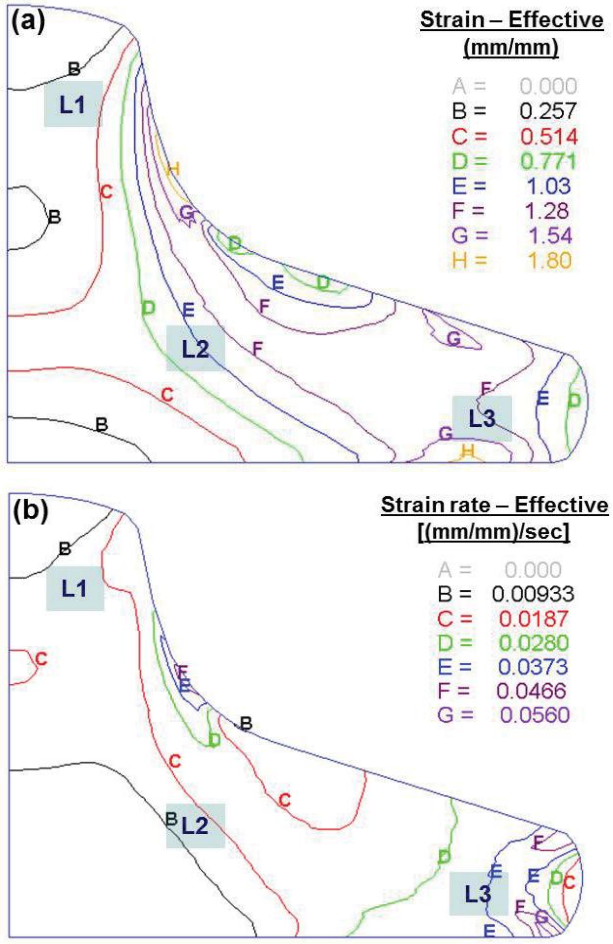


Figure 6. FE simulation results of spike forging of TX32 alloy conducted at 450 °C/0.1 mm s^{-1}: (a) Strain, and (b) Strain rate distributions.

In all the tests, there is a reasonable agreement between the simulated and experimental curves, in particular, the first two stages at lower forging speeds. The deviations are more significant at higher forging speed, say 1 mm s^{-1}, in the later stages of forging. This is mainly due to the difference between the simulation setting and the actual forging. While the simulations were carried out using isothermal conditions (die and workpiece at the same temperature throughout the process), the adiabatic temperature rise during the actual forging progressively increases the specimen temperature, resulting in reduced flow stress. Therefore, with increased stroke, the difference between them continues to grow significantly, and the experimentally obtained values would be lower.

The spike forging process proceeds in three distinct modes [7] of deformation: (i) deformation occurs by shearing around a central portion, (ii) the central core is rigid and remains constant irrespective of the deformation of the flange, and (iii) the flow beneath the die is divided, considerable flow taking place into the die orifice to form the spike.

A typical spike forging conducted in the workability domain at 450 °C/0.1 mm s^{-1} (equal to the strain rate 0.01 s^{-1}) showing the effective strain and strain rate distributions in the forged component is given in Figure 6(a-b). It is observed from the simulation that the effective strain values reached a maximum of about 1.8 and the corresponding strain rate in the component reaches a maximum value of 0.06s^{-1} at the die exit corners, with an average strain rate of about 0.02s^{-1}. The deformation does not appear to occur in the top spike part of the forged component.
The microstructures obtained at three selected locations (L1 to L3) based on the effective strain and strain rate distribution in the forged component of the specimens forged at 450 °C/0.1 mm s^{-1} are shown in Figure 7.

The strain values at location L1 vary from 0.25 to 0.51, and the corresponding microstructure (Figure 7a) shows only few recrystallized grains and small reduction in size. This structure is comparable with the initial microstructure, as can be expected due to low strains. The microstructure in Figure 7b belongs to location L2, which reveals the occurrence of significant amount of dynamic recrystallization (DRX) resulting in smaller grains with curved boundaries, and the strain values range from 0.7 to 1.0. In location L3, where the strain levels reach a value of about 1.3, the microstructure shows (Figure 7c) fully recrystallized fine grains of nearly uniform size. The DRX grains of the above two locations (L2 and L3) indicate that the as-cast structure is converted into a wrought microstructure, and the microstructure varies depending on the strain values. Similar features were observed for the forgings carried out at the other process conditions, implying that the workability domain (390-500 °C/0.005-0.6 s^{-1}) is valid for processing this alloy.

The average grain sizes measured at the location L2 for all the components forged under different temperatures and speeds are shown in Figure 8. It clearly indicates that the grain size has increased with increasing temperature and decreasing speed, as can be expected in the hot deformation of metallic materials. The grain size decreased significantly (25-60 µm) compared to the original cast alloy with large grains of about 450 µm.

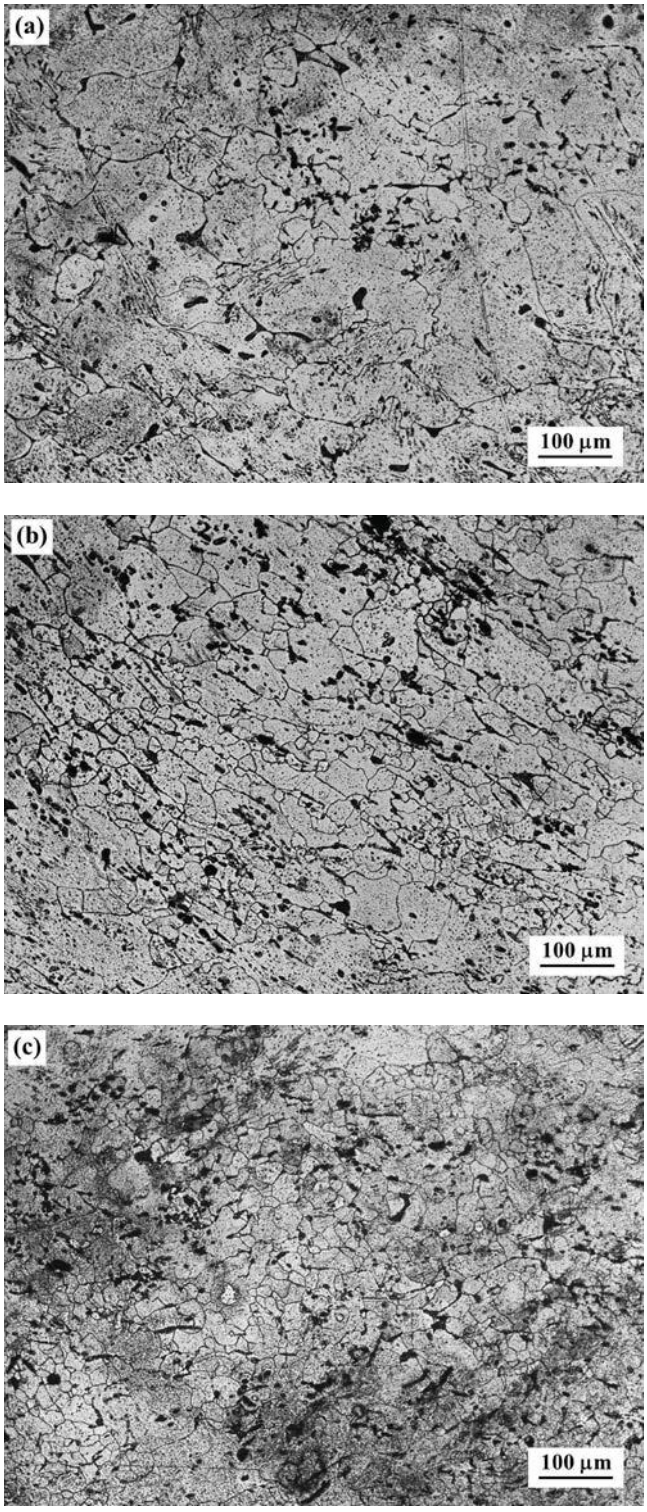


Figure 7. Optical microstructures of TX32 alloy forged at 450 ^{o}C/0.1 mm s^{-1} corresponding to the strain and strain rate locations at (a) L1, (b) L2, and (c) L3 (see Figure 5).

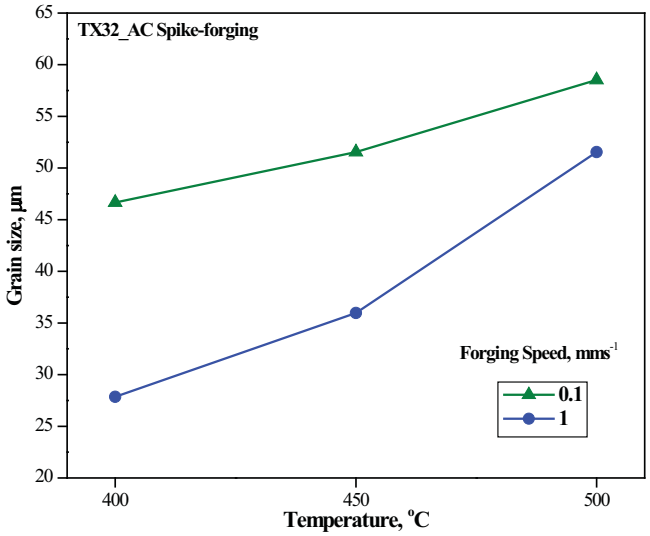


Figure 8. Variations of grain size of TX32 alloy forged at different temperatures and speeds in the 'Workability Domain'.

Conclusions

TX32 (Mg-3Sn-2Ca) magnesium alloy has been forged at temperatures of 400, 450 and 500 ^{o}C, and at speeds of 0.1 and 1 mm s^{-1}to produce a spike-shaped component with a view to evaluate its hot forgeability. The following conclusions are drawn from this study:

(i) The alloy can be successfully forged within the entire range of workability domain as predicted by the processing map.

(ii) The load-stroke curves predicted using FE simulation of spike forging of TX32 are in reasonable agreement with those measured during actual forging experiments.

(iii) The microstructures obtained in the components forged under workability domain revealed fully DRX grains.

(iv) Strain values are important in optimizing the microstructures, and it is important to exceed a threshold strain to obtain fully recrystallized and fine grains.

Acknowledgement

The work presented in this paper was supported by General Research Fund (Project #114809) from the Research Grants Council of the Hong Kong Special Administrative Region.

References

1. A.A. Luo, "Magnesium: Current and Potential Automotive Applications," *JOM*, 54 (2002), 42-48.

2. G.V. Raynor, *The Physical Metallurgy of Magnesium and its Alloys* (Pergamon press, Oxford, 1959).

3. D.H. Kim, J.Y. Lee, H.K. Lim, J.S. Kyeong, W.T. Kim, and D.H. Kim, "The Effect of Microstructure Evolution on the Elevated Temperature Mechanical Properties in Mg-Sn-Ca System," *Materials Transactions*, 49 (2008), 2405-2413.

4. G. Nayyeri, and R. Mahmudi, "The Microstructure and Impression Creep Behavior of Cast Mg-5Sn-xCa Alloys," *Materials Science and Engineering A*, 527 (2010), 2087-2098.

5. N. Hort, Y.D. Huang, T. Abu Leil, K.P. Rao, and K.U. Kainer, "Properties and Processing of Magnesium-Tin-Calcium Alloys," *Kovove Mater*ialy, 49 (2011), 163-177.

6. C. Dharmendra, K.P. Rao, Y.V.R.K. Prasad, N. Hort, and K.U. Kainer, "Hot Workability Analysis with Processing Map and Texture Characteristics of As-cast TX32 Magnesium Alloy," *Journal of Materials Science*, 48 (2013), 5236-5246.

7. W.L. Xu, and K.P. Rao, "Analysis of the Deformation Characteristics of Spike-forging Process through FE Simulations and Experiments," *Journal of Materials Processing Technology*, 70 (1997), 122-128.

8. C.J. Bennett, "A Comparison of Material Models for the Numerical Simulation of Spike-Forging of a CrMoV Alloy Steel," *Computational Materials Science*, 70 (2013), 114–122.

9. *DEFORM*. Scientific Forming Technologies Corporation. Columbus, Ohio, USA.

10. S. Kobayashi, S-I. Oh, and T. Altan, *Metal Forming and the Finite-Element Method* (Oxford and New York: Oxford University Press, 1989).

11. A. Kozlov, M. Ohno, T. Abu Leil, N. Hort, K.U. Kainer, and R. Schmid-Fetzer, "Phase Equilibria, Thermodynamics and Solidification Microstructures of Mg-Sn-Ca Alloys, Part 2: Prediction of Phase Formation in Mg-rich Mg-Sn-Ca Cast Alloys," *Intermetallics*, 16 (2008), 316-321.

12. R. Arroyave, "Intermetallics in the Mg-Ca-Sn Ternary System: Structural, Vibrational, and Thermodynamic Properties from First Principles," *Physical Review B*, 74 (2006), 174118

Magnesium Technology 2014
Edited by: Martyn Alderman, Michele V. Manuel, Norbert Hort, and Neale R. Neelameggham
TMS (The Minerals, Metals & Materials Society), 2014

AN INTRODUCTION TO THE FORGING OF ELEKTRON®43 - A HIGH PERFORMANCE WROUGHT MAGNESIUM ALLOY

Dominic Henry[1], Mark Turski[1], Paul Lyon[1], Tim Wilks[1]
[1]Magnesium Elektron, Magnesium Technology Centre, Rake Lane, Swinton, Manchester, M27 8BF, England

Keywords: Elektron®43, Forging, Wrought magnesium, Aerospace

Abstract

Elektron®43 is an optimised high performance wrought magnesium alloy for use in aerospace and other high performance applications. This alloy can be processed via a range of processing routes including, but not limited to, rolling, extrusion, and forging in order to obtain optimum properties. Elektron®43material has been forged at a range of temperatures and strain rates. The resultant microstructure and mechanical properties were subsequently investigated, allowing forging conditions and mechanical properties to be correlated.

Introduction

The aerospace industry has long recognised the benefits of using magnesium alloys for weight reduction. High performance sand casting alloys, such as Elektron® 21 and Elektron® WE43, find applications on many helicopter transmission casings. Wrought magnesium alloys have traditionally lagged behind in terms of volume use but offer the possibility of improved mechanical properties and more homogenous microstructures compared to their sand casting alternatives.

Alloys like AZ80 and ZK60 do find applications. Although both these alloy systems suffer drawbacks. ZK60, although capable of providing UTS of 350MPa, requires good protection to avoid inherent corrosion issues, and AZ80, with good corrosion resistance does not tolerate high temperature application. Furthermore, AZ80 also has more pronounced asymmetry and anisotropy of properties.

The use of zirconium grain refined magnesium alloys that contain Rare Earth (RE) elements offers the chance to raise the bar for wrought magnesium alloy applications. For this reason Elektron®43was developed, from the WE alloy family, to provide an optimised high performance wrought magnesium alloy for use in aerospace and other high performance applications.

Elektron®43 exhibits impressive high temperature properties and flammability resistant characteristics. The alloy can be processed via a range of processing routes, including but not limited to, rolling, extrusion, and forging in order to obtain optimum properties. Elektron®43 extrusions and plate have achieved AMS, ASTM, and MMPDS approval. This means engineers and designers can have confidence in the performance of the alloy due to full A and B basis statistical analysis.

This paper details how Elektron®43 material has been forged at a range of temperatures and strain rates. The resultant microstructure and mechanical properties subsequently investigated, allowing forging conditions and mechanical properties to be correlated. This has allowed the forging window of this the alloy to be evaluated.

Experimental

DC cast 300 mm diameter Elektron®43billet produced to composition [1 and 1a]: approximately within range ~ 4% Y, ~2.25 Nd%, ~0.8 HRE%, and ~0.5 Zr%, was machined, homogenized, and extruded to 67mm diameter using a 2750T extrusion press. The grain size of the extruded material was assessed prior to forging. Following extrusion the material was forged to various extents at a range of temperatures and strain rates, as shown in a matrix in table 1.

Table 1 Matrix of forging conditions

		Strain (% deformation)					
		35					35 ,50, 65, 75, 85
Billet temp (°C)	480	●	●	●	●	●	Full matrix of conditions tested - example shown at 35%. Subset of data reported in this work with billet temperature and strain rates chosen to represent the window of conditions.
	440	●	●	●	●	●	
	400	●	●	●	●	●	
	360	●	●	●	●		
		0.06	3	4	5	8	0.06, 3, 4, 5, 8
		Strain rate (s^{-1})					

Forging trials were carried out using the extruded feedstock of 67mm diameter which was cut to 100mm lengths. The feedstock was in the T4 condition (Solution treated) - 525°C for 8 hours and air cooling.

Forging trials at the lower strain rate of 0.06 s^{-1} were carried out on a 500T hydraulic press. Forging trials at 3 and 5 s^{-1} were carried out on a 2100T screw press.

The forging shape was a simple "pancake" that was formed between two heated platens (dies). Trials were carried out with dies heated to either 200°C or 350°C. Colloidal graphite lubricant was used during the process. Samples were preheated to the desired forging temperature for 3 hrs then transferred from the heating oven to the forging platen within a time period of 10 seconds. 3 specimens were forged at each condition, allowing mechanical properties to be assessed both in the F condition (as-forged) and T5 condition.

After forging the samples were air cooled. Each forged sample was sectioned for metallography and tensile test samples. Tensile test samples were taken across the radius of diameter of the forged specimen with the gauge length located in the centre of the forged specimen. Three tensile test specimens were taken from each forged specimen and tested on a Zwick screw driven tensile testing machine in according to ASTM B557M. Metallography was carried out with samples orientated parallel to the forging direction in the centre of the forged specimen. The F condition samples were etched using Nital solution while the T5 material was etched using Nital followed by acetic picral solution.

These forging tests were also used to provide data to help validate a finite element model of the forging process. Finite element modeling was carried out using Deform 2d and allowed both thermal and mechanical conditions within the model to be validated. Such validation will be invaluable for carrying simulation work for more complex, industrial scale forgings.

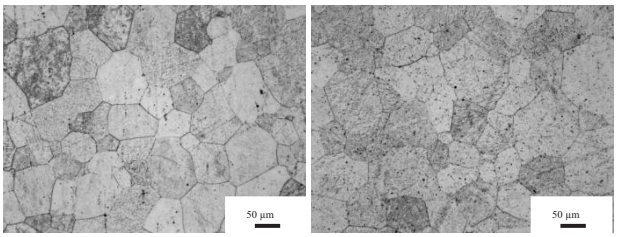


Figure 1a) Longitudinal direction b) Transverse direction

Results and Discussion

The extruded Elektron®43 material has a fully recrystallised microstructure with a bimodal grain size of around 9 µm. Following T4 treatment the grain size of feedstock was homogenous and in the region of 60 µm as can be seen in figure 1 a and b.

Such extruded material tends to exhibit many interesting characteristics such as a component of "rare earth" [2] or weaker texture and the unusual phenomena of inverse yield asymmetry (compressive yield being greater than tensile), a scenario also observed by Robson et al [3] when studying RE containing magnesium alloys. Full analysis of the texture, before and after deformation, is planned as further work.

Forging Force

Figure 2 shows the forging press force for the various temperatures, using the hydraulic press at a strain rate of $0.06s^{-1}$. The forging force decreases as the temperature of the billet increases. The rise in force with specimen reduction occurs due to the increase in material cross section as deformation progresses. The force displacement curves suggest some work hardening at 360°C and at a limited extent at 400°C.

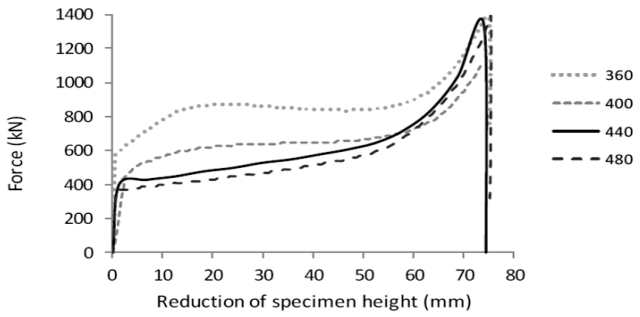


Figure 2 Forging force vs temperature comparison at a strain rate of 0.06 s^{-1}.

Forgeability – visual assessment

Figures 3 to 5 show photographs of the unforged specimen along with specimens forged at a range of reductions and strain rates. No cracking or bursting defects can be seen along the outer edge of any of the specimens, with exception of the samples forged at lower temperature and higher strain rate in figure 5. This highlights the forgeability of this alloy under a broad range of conditions. In particular, it is important that this alloy showed no indications of cracking at the more industrially relevant strain rates of 5 strain per second. The edge cracking observed in figure 5 relates to excessive localized chilling of the material in contact with the forging platen at 360°C. This was also highlighted in the modeling work (see figures 6 and 7). The localized chilling effect is due to the inherent low volumetric heat capacity of magnesium compared to aluminium alloys.



Figure 3) Forging at 360°C to various strains at strain rate $0.06s^{-1}$ and die temperature 350°C

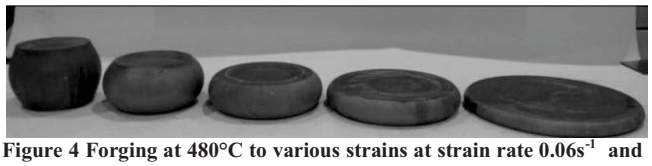


Figure 4 Forging at 480°C to various strains at strain rate $0.06s^{-1}$ and die temperature 350°C

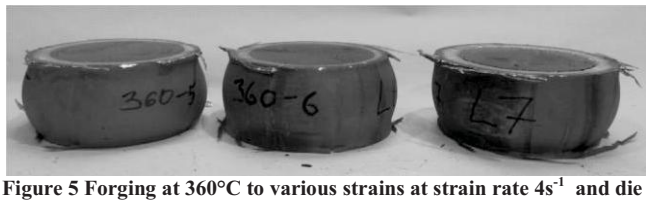


Figure 5 Forging at 360°C to various strains at strain rate $4s^{-1}$ and die temperature 200°C

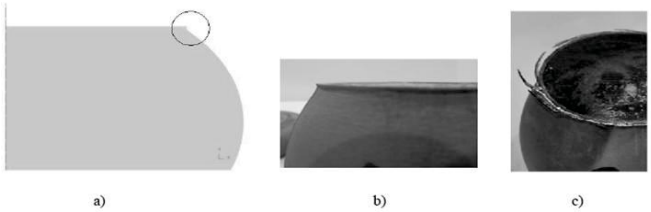


Figure 6) FEM prediction of cold cracking

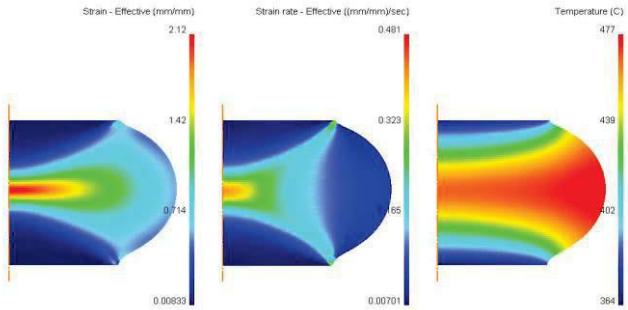


Figure 7) Predicted total effective strain, strain rate and temperature distribution after reduction at strain rate of $0.06s^{-1}$, with a billet temperature at 480°C and platen temperature at 200°C

Figure 7 shows the strain, strain rate and temperature distribution after reduction at a strain rate of $0.06s^{-1}$ with the platen temperature set at 200°C and sample temperature of 480°C. The asymmetry in the deformed shape from top to bottom is again due to heat loss effects during initial resting of the sample on the bottom platen (10 seconds) before deformation takes place. As expected, most deformation is localized in the centre of the specimen. The total temperature gradient from the centre to the top and bottom surface is ~100°C, with peak temperatures of 477°C along the diameter, in the mid thickness of the specimen. A minimum temperature of 364°C is found at the bottom surface of the specimen.

Microstructure

Figure 8 a-c shows micrographs of the centre of each forging in the F condition following deformation at a strain rate of approximately $5s^{-1}$ to a strain of 50%. Numerous coarse precipitates are visible in the lowest billet temperature forging. The volume fraction of coarse precipitates reduces as forging temperature increases. At 480°C no evidence of precipitates is apparent, indicating that the second phase has been retained in solution.

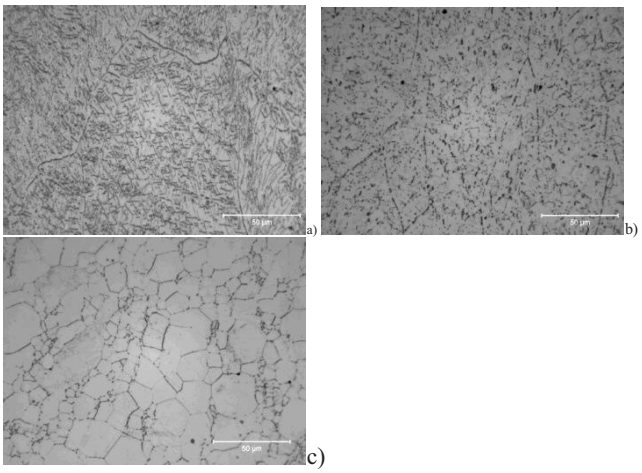


Figure 8 a) 360°C, b) 440°C, c) 480°C – F condition micros.

Figures 9 to11 show micrographs of the centre of each forging in the T5 condition. The fraction of recrystallised grains increases with increasing temperature and strain rate.

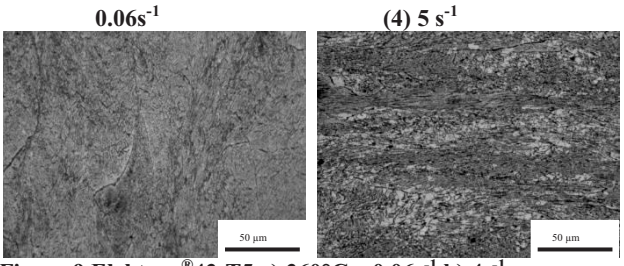


Figure 9 Elektron®43-T5 a) 360°C x $0.06s^{-1}$ b) $4s^{-1}$

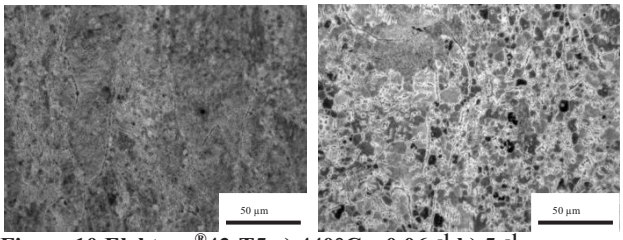


Figure 10 Elektron®43-T5 a) 440°C x $0.06s^{-1}$ b) $5s^{-1}$

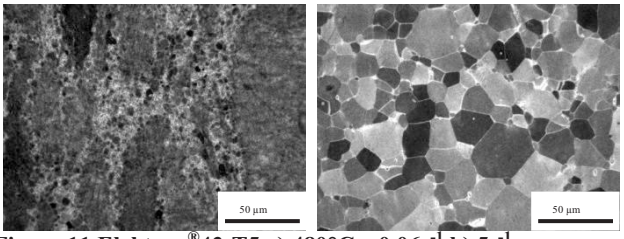


Figure 11 Elektron®43-T5 a) 480°C x $0.06s^{-1}$ b) $5s^{-1}$

At 360°C the material exhibits a heavily worked microstructure with little evidence of recrystallisation at both the higher and lower strain rates. Evidence of working of the microstructure is also supported by hardening of the force/displacement curve in figure 2.

At 440°C an inhomogenous microstructure is witnessed at both strain rates. Necklaces of recrystallised grains are observed at the low strain rate. At the higher strain rate the recrystallised grains are present in a larger proportion of the structure. The grain size of these regions, measured by Mean Linear Intercept (MLI), is approximately 5µm.

At 480°C and low strain rate the microstructure is partially recrystallised. Typical necklace type recrystallised grains are apparent. The higher strain rate sample appears nearly fully recrystallised and has an approximate grain size of 11µm.

Mechanical properties

Figure 12 shows the tensile strength of the forged material in the F condition when forged to a strain of 50%. The greatest yield strength of 290MPa is provided by the 360°C specimen deformed at the slowest strain rate. The strength of the material decreases when temperature of the forging is increased.

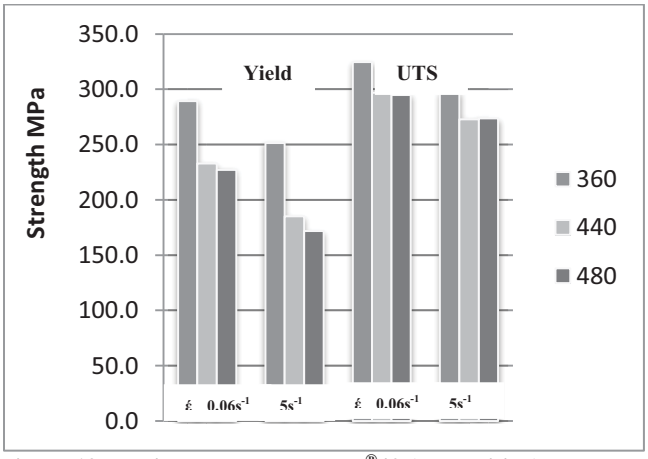


Figure 12 Tensile strength Elektron®43 (F-condition)

Figure 13 shows the elongation of the material after forging at two different strain rates. Elongation increases as forging temperature increases. It is important to note that even at the low strain rate all elongations are >10%, an important factor for the practical use of this alloy. At the higher strain rate of $5s^{-1}$ the elongations are>20%

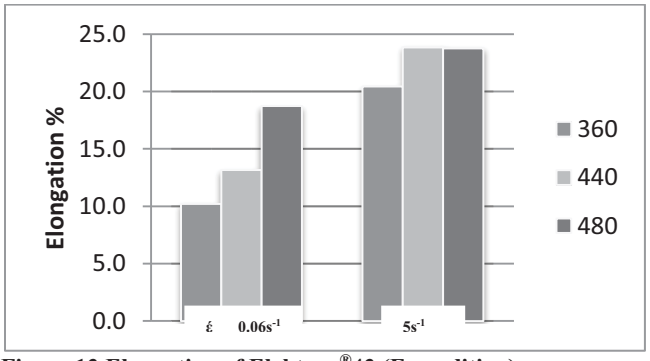


Figure 13 Elongation of Elektron®43 (F-condition)

Elektron®43 responds well to T5 ageing.Temperatures in the range 180°C and 260°C are most useful. Temperatures outside of this range can be used successfully, and in some cases can improve properties further, however the process cycle can be limiting for some commercial application.

Following forging trials T5 yield properties of >225 MPa and UTS of 350MPa were achieved throughout the range of samples when heat treated using industrially acceptable ageing temperatures and times.

Examples of the Elektron®43-T5 properties compared to the data available for forged AZ80 [4, 5] and ZK60 [4, 5] alloys are shown in figures 14 and 15. These other alloys are believed to be in the F condition. Elektron®43 offers high strength in combination with good elongation. Whereas AZ80 [5] would lose ductility in order to compete on strength. The two T5 variants of Elektron®43 shown are processed using conditions within the commercially viable matrix of parameters detailed and explored in this study. The specific T5 ageing treatment remains proprietary to Magnesium Elektron.

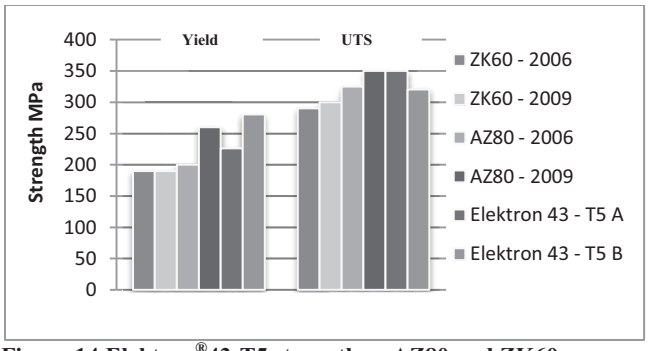


Figure 14 Elektron®43-T5 strength vs AZ80 and ZK60

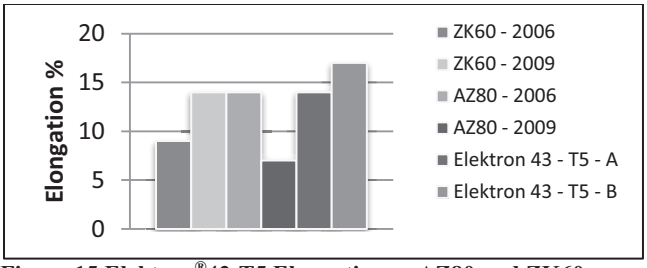


Figure 15 Elektron®43-T5 Elongation vs AZ80 and ZK60

Conclusions

The forging behavior of Elektron®43 has been evaluated. From simple upsetting trials, it is clear that a broad processing window is available for the deformation of this alloy.

Forging temperatures between, but not limited to, 350 and 500°C are expected to be viable and forging strain rates between, but not limited to, $0.06s^{-1}$ to 8 s^{-1} can be accommodated. One hit strains of at least 85% are possible with the appropriate billet temperature.

T5 ageing of the alloy between 180°C and 260°C provides a range of properties. However, the range is limited by practicalities of commercial production.

With suitable T5 ageing properties of >350MPa UTS are achievable. Within a commercial matrix of conditions yield strength ranges from 210 to 280MPa.

Acknowledgements

The authors gratefully acknowledge the Advance Forming Research Centre (AFRC), University of Strathclyde, and thank those involved for their valued contribution.

References

1. AMS 4485: Magnesium Alloy, Extrusions (WE43C-T5) Precipitated Heat Treated. Issued 13/12/2012, SAE AMS D Nonferrous Alloys Committee

1a. Magnesium Elektron Datasheet 043. Elektron®43 preliminary datasheet. http://www.magnesium-elektron.com/data/downloads/DS043.pdf

2. Stanford, N., and M. R. Barnett. "The origin of “rare earth” texture development in extruded Mg-based alloys and its effect on tensile ductility." *Materials Science and Engineering: A* 496, no. 1 (2008): 399-408.

3. Robson, J. D., A. M. Twier, G. W. Lorimer, and P. Rogers. "Effect of extrusion conditions on microstructure, texture, and yield asymmetry in Mg–6Y–7Gd–0.5 wt% Zr alloy." *Materials Science and Engineering: A* 528, no. 24 (2011): 7247-7256.

4. Swiostek, J., J. Bober, C. Blawert, D. Letzig, W. Hintze, K.U. Kainer. “Die forging of commercial and modified magnesium alloys”, *Proceedings of the 6th International Conference on Magnesium Alloys and their Applications*, (2006), 344-351.

5. Kurz, G., B. Clauw, W.H. Sillekens, D. Letzig. “Die forging of the alloys AZ80 and ZK60” TMS, *Magnesium Technology 2009*, (2009), 427-432.

Magnesium Technology 2014
Edited by: Martyn Alderman, Michele V. Manuel, Norbert Hort, and Neale R. Neelameggham
TMS (The Minerals, Metals & Materials Society), 2014

STRUCTURE AND PROPERTIES OF INTERLAYER FORMED BETWEEN MAGNESIUM ALLOY CORE AND ALUMINIUM ALLOY COATING DURING DEFORMATION

Sonia Boczkal[1], Piotr Korczak[1], Bartłomiej Płonka[1], Wojciech Szymański[1], Marek Nowak[1]
[1]Institute of Non-Ferrous Metals Light Metals Division; 19 Pilsudskiego Street, Skawina 32-050, Poland

Keywords: AZ91 alloy, extrusion, covering, interlayer, 6101 alloy

Abstract

The article focuses on the analysis of the properties of an interlayer formed between the magnesium (AZ91) alloy core and aluminium (6101) alloy coating during compression and extrusion at 350°C. Different variants of the coated layer thickness and of the extrusion process parameters were used.
As a result of the tests carried out and the deformation applied, a uniform and consistent interlayer bond was produced. The interlayer width was about 5 μm and it was composed of two sub-layers with a width of about 4 μm and 1μm. The analysis of the chemical composition of the sub-layers carried out on SEM with EDS indicates that these are probably the $Al_{12}Mg_{17}$ and Al_3Mg_2 phases. Rods extruded from the AZ91 magnesium alloy with proper aluminium alloy coating were found to offer an increase in the strength properties of about 20% compared with properties of the sole AZ91 alloy. On specimens selected for SEM, the tensile fracture surfaces were also examined.

Introduction

Nowadays researches tend towards wrought magnesium and aluminium alloys and their large scale application. The greatest advantage of both these alloys is their low weight-to-volume ratio [1-5]. Although magnesium is lighter than aluminium by about 35 %, some of its properties, such as melting point and strength, are in both cases similar. The only feature that is different in these two alloys is their ductility resulting from the limited number of slip systems in magnesium [2]. Additionally, compared to aluminium, magnesium has a reduced modulus of elasticity. In spite of all the benefits that magnesium alloys can offer, their use in mass car production is very limited due to the very poor corrosion resistance of the wrought stock [4, 5, 6]. The corrosion resistance of aluminium alloys is definitely superior to that of magnesium alloys; they also tend to get coated with an oxide film that forms a layer of Al_2O_3, naturally protecting the surface from the effect of corrosive agents [3]. Hence the idea was born to use the commonly applied aluminium alloys as a protective coating on Mg profiles [1]. Studies conducted by two independent research centres [1, 3] have stated the possibility of producing a fast bond between aluminium and magnesium alloys during plastic working. As a result of the extrusion process carried out at a temperature of 350°C, closed profiles of a rectangular cross-section having as a top layer the aluminium alloy coating and magnesium alloy as a core were produced. Similar situation occurs in the case of cold-rolled magnesium alloy sheets with the top layer of aluminium alloy, where as a result of the force acting and an annealing process above 250°C, a bond composed of the Al_3Mg_2 phase is produced. The Al_3Mg_2 phase is a hard intermetallic formed between the soft aluminium and magnesium alloys, enhancing further their durability [3].
The aim of the present research was to obtain in the extrusion process a layer of plating characterised by a consistent and uniform bond and a best combination of the mechanical properties. To examine the bond behaviour, a sample rod made of the AZ91 magnesium alloy with coating made of the 6101 aluminium alloy was subjected to a compression process and then examined for its principal characteristics. The influence of the plating process on the coherence and strength properties of the plated product was examined.

Experimental Procedure

In the first part of the study, samples of two alloys were prepared, i.e. the 6101aluminium alloy, which was used for the coating, and the AZ91 magnesium alloy of which the core was made. The samples were subjected to compression test on an Instron 100kN machine. The sample size was ϕ 10x20, this including thickness of the aluminium alloy coating (a "sleeve"), which was 3 mm. The 6101 aluminium alloy "sleeve" was first etched to remove oxides from its interior, and then a rod of AZ91 alloy was press fitted into it on the testing machine. The whole was compressed at 350°C up to 80 % deformation. After the compression test, the structure was examined under a Philips XL30 scanning electron microscope with attachments for the EDS chemical analysis and EBSD crystallographic analysis. A Tecnai G^2 TEM with an attachment for the EDS chemical analysis by STEM was also used. In the second part of the study, the extrusion tests were made on a vertical press with 250T capacity. From the 6101 alloy, hollow sleeves of ϕ 28mm diameter and a wall thickness of 5 mm, 3 mm and 1 mm were made. As in the compression test, they were also subjected to etching to remove the oxide film. Into thus prepared sleeves, the AZ91 alloy cores were press fitted. The total length of the sample was 50 mm. All samples were extruded in a direct system at a temperature of 350°C yielding rods with a diameter of ϕ 8mm. The resulting rods were subjected to structure analysis to examine the bond consistency and uniformity under an optical microscope. Using an Instron 100kN testing machine, a uniaxial tensile test was carried out, examining the sample fracture topography under a scanning electron microscope. Samples for both optical and scanning electron microscopy were prepared by grinding and polishing to obtain proper metallographic sections. Samples for the EBSD and TEM analysis were prepared by ion thinning.

Results

The trials of joining magnesium alloy with aluminium alloy enabled determining the optimal conditions under which the Al/Mg bond is produced. Structure examinations were carried out, including identification of intermetallic phases formed at the interlayer boundary with an assessment of their thickness. Further studies included trials carried out during the extrusion process to optimise the properties of the obtained bonds.

Characterisation and quality assessment of the Mg/Al bond produced by compression

During compression of the sample at 350°C, a uniform Al/Mg bond composed of intermetallic phases was produced. By scanning electron microscopy, the chemical composition of the bond was examined (Fig. 1). The results of this examination show that the transition between the alloys is separated by an interlayer 5 to 6 μm thick, where the lines of Al and Mg content are intersecting.

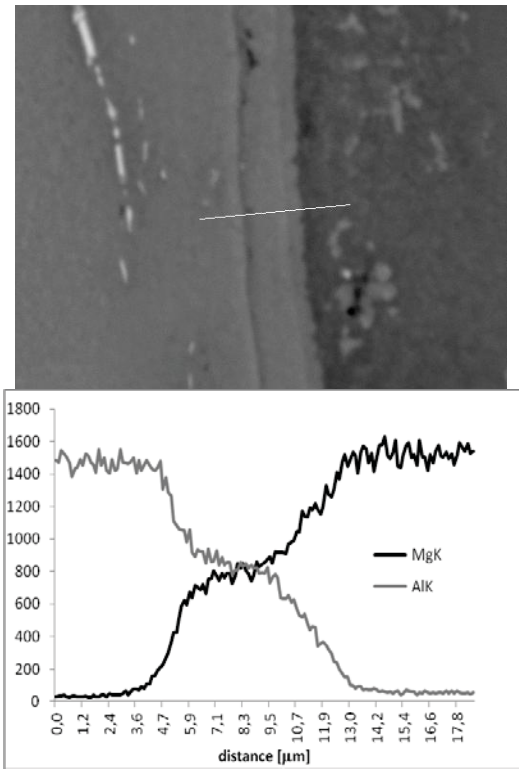
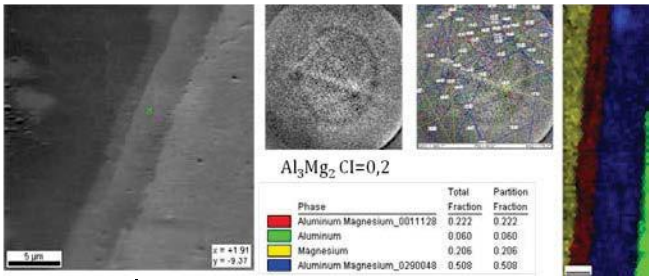


Fig. 1 Chemical linear analysis of the interlayer in samples after compression.

The results of the examinations made by EBSD, also including local analysis of the chemical composition, indicate the diffusion-aided formation of two phases present in the Al-Mg equilibrium system (Fig. 2). This was the Al_3Mg_2 phase of a thickness of about 4 - 5 μm and the second, substantially narrower, $Al_{12}Mg_{17}$ phase of a thickness of about 1 μm. The Al_3Mg_2 phase was formed on the side contacting aluminium alloy and is running in parallel direction through the entire length of an interlayer obtained in the examined sample. The $Al_{12}Mg_{17}$ phase is narrow and, along the interlayer length, shows some non-uniformities on the side contacting magnesium alloy. In some places of the interlayer it is wider than in the others. The interlayer connection as a whole was free from the cracks, was uniform and running through the entire length of the examined sample. Additionally, the microstructure of the interlayer was examined by transmission electron microscopy (Fig. 3), and it was found that the structure of Al_3Mg_2 and $Al_{12}Mg_{17}$ phases were fine-grained and coherent on the side of both aluminium and magnesium alloys. In both phases, the grain size was less than 1 mμ. In the image of microstructure



Phases	Description
$Al_{12}Mg_{17}$ (red)	[%at] Mg – 53, Al – 32, Si, O, C ICDD PDF file no. 0011128; cubic (0h)[m3m], a=10,56Å
Al_3Mg_2 (blue)	[%at] Mg – 33, Al – 57, Si, O, C ICDD PDF file no. 0290048; cubic (0h)[m3m] a=28.239Å
Al (green)	cubic (Oh)[m3m] a=4,04Å
Mg (yellow)	hexagonal (D6h)[6/mmm] a=3,2Å; c=5,2Å

Fig. 2 EBSD phase analysis combined with local chemical analysis of the Mg/Al interlayer after compression.

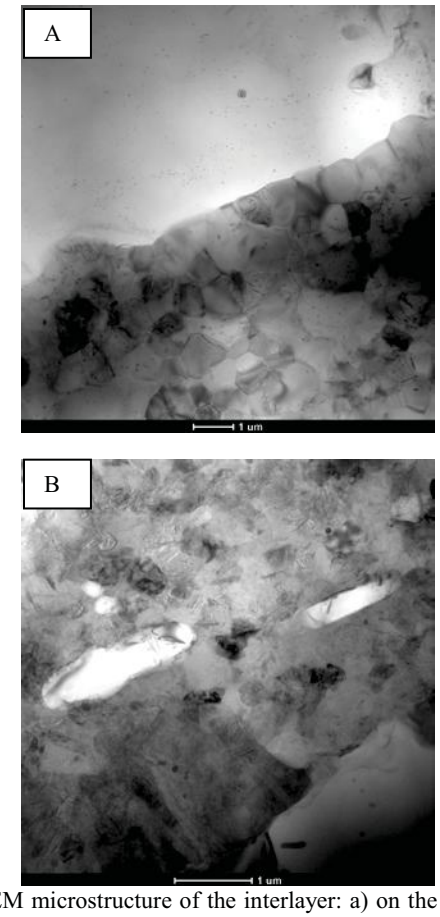


Fig. 3 TEM microstructure of the interlayer: a) on the side of the AZ91 magnesium alloy, and b) on the side of the 6101aluminium alloy.

it was difficult to distinguish between the two phases. However, inside the grains of the Al_3Mg_2 phase, twinned crystals were noted to occur (Fig. 4). In certain areas inside the grains, the density of dislocations was high, the precipitates were coarse, and some oxides appeared. From the analysis of the chemical composition it followed that, in addition to Al and Mg, the large precipitates also contained elements such as Fe and Si.

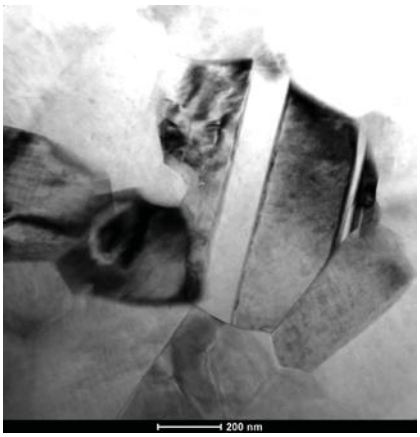


Fig. 4 Grains of the Al_3Mg_2 phase.

Evaluation of the properties of plated AZ91 alloy rods after the process of direct extrusion

In the process of plastic working carried out at 350°C, rods were extruded from the AZ91 alloy with the 6101 alloy coating characterised by varying thickness of 5mm, 3mm and 1mm. The obtained plated rods were examined for the bond quality and plastic flow of the rod material with coating. The first to analyse was the material flow behaviour in a die. For this purpose, the microstructure in the end part of the extrudates (so called flashes) was examined (Fig. 5). It was found that plating took place in the die, and the larger was the thickness of the coating on the feedstock, the more of 6101 alloy accumulated in the dead zones of the die at the end of the extrusion process. This situation can lead to curling of the Mg alloy feedstock when processed on large presses.

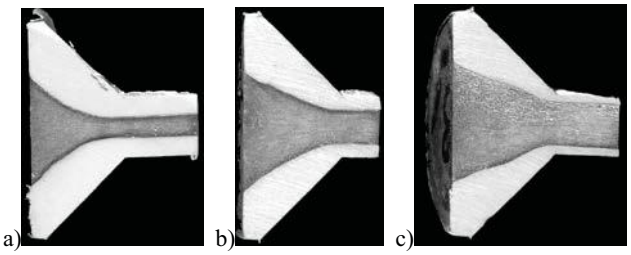


Fig. 5 Cross-sections of the end parts of the successive sample extrudates with the coating thickness of: a) 5 mm, b) 3mm c) 1 mm.

The interlayer connection was uniform on the entire length of the extruded rods and showed no cracks. The defect in the extruded rods was uneven coating thickness, varying in the starting, middle and end part of the rod (Fig. 6). It was observed that rods in the starting part were totally deprived of coating, the plating thickness in the middle part varied and, depending on the coating thickness, ranged from 300 to 500 μm. The situation was similar in the end part of the extruded rods, but in this case the plating thickness exceeded 1 mm.

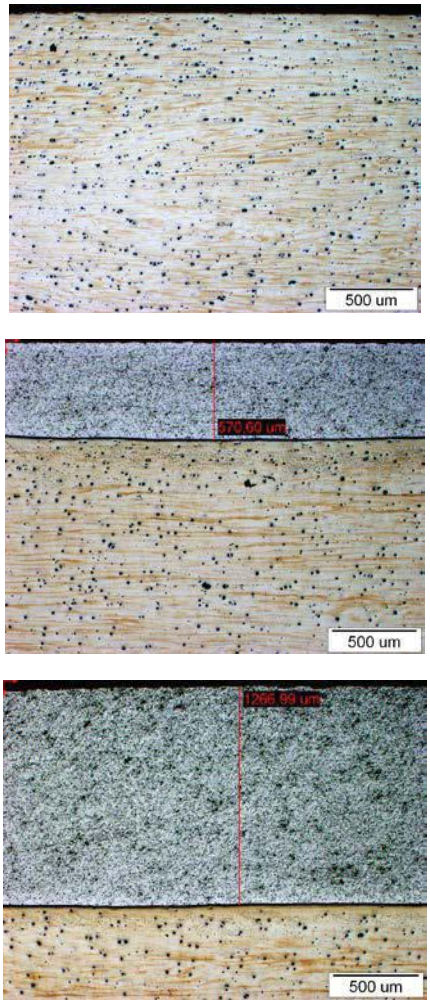


Fig. 6 Microstructure on the rod cross-section with the coating of 3 mm thickness: a) the starting part, b) the middle part, c) the end.

The mechanical properties were examined in a uniaxial tensile test carried out on rods, analysing also the quality of bond on a sample fracture. The results of mechanical tests (average of two measurements) are presented in Table I. Based on these results, it was found that the thinner was the layer of plating, the more important was the role of the intermetallic layer in the strengthening process, hardening further the AZ91 alloy core.

Table I The results of a uniaxial tensile test carried out on plated rods.

Series	$R_p0,2$ [MPa]	R_m[MPa]	A [%]
5mm	134	214	23
3mm	165	248	-
1mm	171	292	20,6

All the samples examined showed an uneven mode of fracture (Fig. 7). The height at which the fracture occurred differed for the aluminium alloy, magnesium alloy and an intermetallic phase. Topographic analysis of rods after the tensile test showed three types of fractures: coating - ductile aluminium alloy, core -

magnesium alloy and, not visible in the image, structure of the brittle Al_3Mg_2 and $Al_{12}Mg_{17}$ phases.

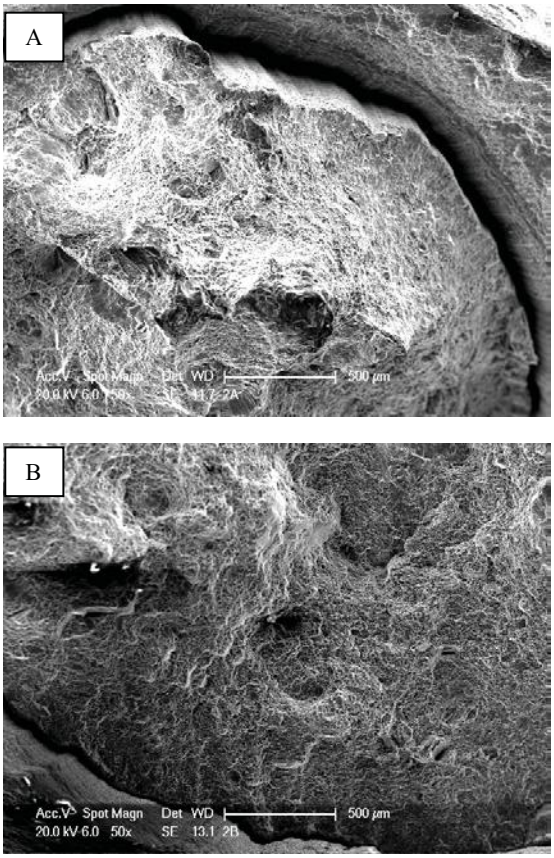


Fig. 7 Rods fracture topography after the extrusion of feedstock with plating thickness of a) 5 mm and b) 3mm.

Conclusions

In the sample after compression at 350°C, a coherent bond between the magnesium alloy and aluminium alloy was obtained. The interlayer was composed of two phases, i.e. Al_3Mg_2 and $Al_{12}Mg_{17}$ - one with a thickness of 4 to 5 μm, and the other with a thickness of about 1 μm. It was found that thickness of those phases was determined by the coefficient of interdiffusion - higher by one order of magnitude for the Al_3Mg_2 phase compared with the $Al_{12}Mg_{17}$ phase, thus making growth of the Al_3Mg_2 phase much easier. Only when the diffusion process is hindered at the phase boundary, proper conditions for the nucleation of $Al_{12}Mg_{17}$ phase on the Al_3Mg_2/Mg phase boundary are created [7].

Using a 250T forging press, at a temperature of 350°C, rods of ϕ8mm cross-section were extruded in a direct process from the AZ91 alloy with coating made of the 6101 alloy. The interlayers obtained in the three tested samples with different coating thickness (5mm, 3mm, and 1mm) were uniform and coherent on the entire length of the rods, showing no cracks.

The aluminium alloy plating thickness on the rod length was uneven. Differences occurred between the starting and end part of the rod. The reason for these differences can lie in the mode of extrusion. Changing the direct extrusion mode into an indirect one can contribute to the fabrication of plating layer of a uniform thickness on the entire length of the rod.

Studies of the surface topography of samples after the tensile test showed significant differences in the necking formation in the three different materials (AZ91 phases: Al_3Mg_2, $Al_{12}Mg_{17}$ and 6101). The reason is that these materials have different mechanical properties. Additionally, thinning of the aluminium alloy plating contributes to obtaining higher mechanical properties.

References

1. S.Muller (Sp), J.Muhlhause, S. Gall, W.Reimers; *Coextrusion of hybrid Mg/Al hollow profiles*. 8th International Conference on Magnesium Alloys and their Applications, , 2010 Wiley-vch GmbH&Co.KGaA, Germany, pp. 621-626
2. M. Paramosthy, S.F.Hassan, N. Srikanth, M.Gupta; *Adding carbon nanotubes and integrating with AA5052 aluminium alloy core to simultaneously enhance stiffness, strength and failure strain of AZ31 magnesium alloy,* Composities: PartA, vol.40, 2009, pp.1490-1500
3. H. Matsumoto, S. Watanabe, S.Hanada; *Fabrication of pure Al/Mg-Li alloy clad plate and its mechanical properties*; Jurnal of Materials Processing Technology, vol. 169, 2005, pp. 9-15,
4. M.Paramosthy, N.Srikanth, M.Gupta; *Solidification processed Mg/Al bimetal macrocomposite: Microstructure and mechanical properties*, Journal of Alloys Compounds, vol.461, 2008, pp. 200- 208,
5. M. Paramosthy, S.F.Hassan, N. Srikanth, M.Gupta; *Enhancement of compressive strength and failure strain in AZ31 magnesium alloy,* Journal of Alloys Compounds, vol.482, 2009, pp. 73- 80,
6. L. Zhua, G. Songb; *Improved corrosion resistance of AZ91D magnesium alloy by an aluminium-alloyed coating,* Surface & Coatings Technology; vol. 200 2006,pp.2834– 2840,
7. S. Brennan, K. Bermudez, N. Kulkarni, Y. Sohn, *Growth Kinetics of Y-Al12Mg17 and -Al3Mg2 Intermetallic Phases in Mg vs. Al Diffusion Coupes,* Proceedings of a symposium sponsored by the Magnesium Committee of the Light Metals Division of The Minerals, Metals & Materials Society TMS 2012 Annual Meeting & Exhibition Orlando, Florida, USA March 11-15, 2012.

Magnesium Technology 2014
Edited by: Martyn Alderman, Michele V. Manuel, Norbert Hort, and Neale R. Neelameggham
TMS (The Minerals, Metals & Materials Society), 2014

A Novel Process for Producing Large Scale Mg-Sheets

Grittner Norbert[1,a], Engelhardt Marcus[1,b], Neumann André[2,c], Klose Christian[1,d], Hübner Sven[2,e], Behrens Bernd-Arno[2,f], Hans Jürgen Maier[1,g]
[1]Institut für Werkstoffkunde (Materials Science), Leibniz Universität Hannover, An der Universität 2, 30823 Garbsen
[2]Institut for Forming Technology and Machines, Leibniz Universität Hannover, An der Universität 2, 30823 Garbsen, Germany
[a]grittner@iw.uni-hannover.de, [b]engelhardt@iw.uni-hannover.de, [c]neumann@ifum.uni-hannover.de, [d]klose@iw.uni-hannover.de
[e]huebner@ifum.uni-hannver.de, [f]behrens@ifum.uni-hannover.de, [g]maier@iw.uni-hannover.de

Keywords: magnesium alloy, extrusion, microstructure, anisotropy

Abstract:

This paper describes a novel processing route for the large scale manufacturing of magnesium sheets. This processing route consists of the production of magnesium tubes by hot extrusion with a subsequent forming step. The processing route allows the manufacture of magnesium sheets with enhanced properties compared to those manufactured by conventional hot rolling or extrusion. The extrusion of tubes enables the manufacturing of magnesium sheets with extrusion presses available today, offering a new market for the extrusion industry. With the process combination of extrusion and unfolding a reduction of anisotropy of the material properties is possible. This makes these sheets especially suitable as prematerial for deep drawing purposes. The mechanical properties at room temperature and at elevated temperatures of 250 °C of the produced sheet metal are then compared to those of hot-rolled or directly extruded AZ31 sheet metal. The characterisation of all sheets is done by microstructural and texture investigations.

Introduction

Magnesium alloys offer a big potential for lightweight design in the automotive industry, in particular for small batch products in highquality cars. Extruded magnesium sheet metal meets the expectations for these products. Todays, conventional hot rolling or roll casting are commonly used for the production of semi-finished magnesium sheet metal. The widespread processing of rolled products is sluggish due to high production costs. The costs for rollcasted products are lower [1] but inner defects can have a negative influence on their mechanical properties [2].
A novel process for the production of magnesium sheet metal is to be established. The process to be implemented comprises the production of magnesium tubes by an extrusion process and a subsequent unfolding process. This combination allows for the production of magnesium sheet metal with a much larger width compared to the established production of sheet metal by extrusion. An advantage of this combined production process is the combination of the characteristic material properties of both processes giving the possibility to improve or adapt product properties.

Experimental procedures

The experiments were conducted using homogenized continuously cast AZ31 (2.91 w% Al, 0.79 w% Zn, 0.31 w% Mn, Mg balance) billets with a length of 300 mm and a diameter of 120 mm. The billets were direct extruded to tube profiles with a diameter of 70 mm and a wall-thickness of 2 mm, using a 10 MN extrusion press from maker SMS Meer. The tubes are produced using a die with four bridges. All extrusion were performed with the following parameters: extrusion ratio V=28.7, billet temperature T_{Billet}=370°C, container temperature $T_{Container}$=350°C and extrusion speed v_{Ram}= 1.0mm/s. The profile was pulled with a force of 200 N and cooled in ambient air. During the experiments the extrusion force was recorded. The production process consists of the following process steps: 1. Extruding a tube with the given parameters, 2. Cut the tube longitudinally along a weld seam, 3. Adjusted the tube in the unfold device and unfolding the tube, 4. Straightening the sheet. Because of the poor formability of AZ31 at room temperature it is important that the unfolding process takes place at a temperature about 250°C to ensure a good deformation. The unfold device is shown in Figure 1 and Figure 2. During the process the tube is unfolding over five moving steel balls. After the unfolding prozess a straightening process takes place.

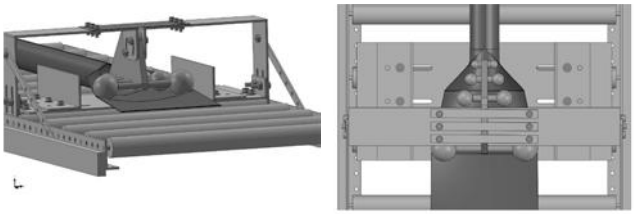


Figure 1: Schematics of the design with inserted Mg pipe

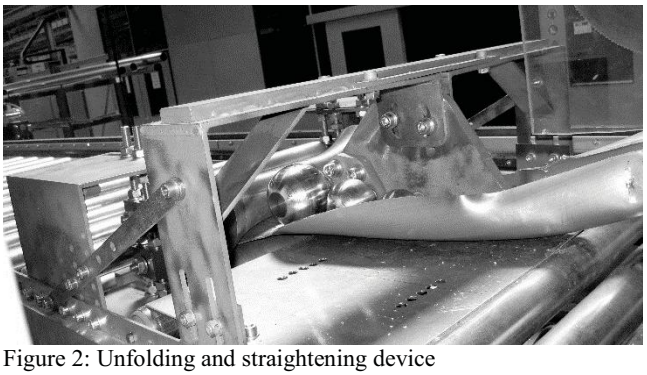


Figure 2: Unfolding and straightening device

A reflected-light microscope type Zeiss Axioplan 2 with a CCD-camera type Kontron ProgRes 2008 were used for the microstructural analyses. The tensile tests were carried out in a forming dilatometer type 805 A/D/T from maker BÄHR-Thermoanalyse GmbH at room temperature and at 250°C. The samples were tested along the extrusion direction, at an angle of 45° to the extrusion direction as well as perpendicular to the extrusion direction. The texture in the lattice plane {002} was analysed with a 5-circle diffractometer type Seifert XRD 3003 eta on the longitudinal section of the extruded profile.

Results and discussion

Extrusion Process:

For direct extrusion the total extrusion force is composed of the die force and friction force. As expected, the highest extrusion forces of 9.8 MN for the tube manufacturing are obtained at the beginning of the extrusion process, shown in Figure 2. The high value of the deformation resistance is caused by the hexagonal crystal structure of the magnesium alloy AZ31 [3, 4]. The unfolding and straightening device has no influence on the extrusion force.

Surface quality

The extruded profiles exhibit a very good surface finish. During optical inspection the profiles which were extruded with an extrusion speed of 1.0 mm/s exhibit a bright metallic surface. None of the profiles displayed common extrusion defects such as hot cracking or blisters.

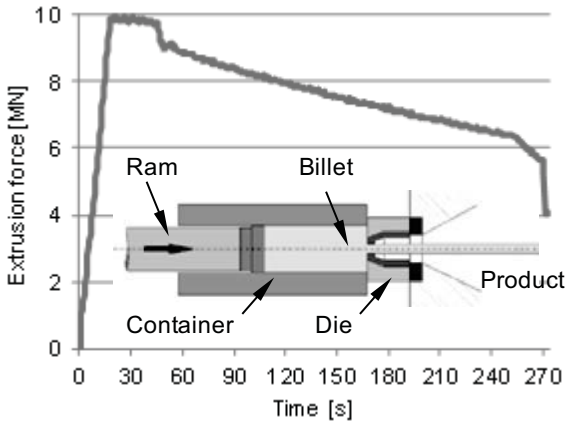


Figure 3: Extrusion diagram AZ31 Tube, Ø 70mm x 2mm

Microstructure

In order to exclude external influences and to produce a steadystate process, material was extracted from the sheet`s central region for metallographic examination. Longitudinal, polished specimens from the sheet's center were prepared. Depending on the manufacturing process, extruded and unfolding, hot-rolling and twin roll casting different grain sizes were observed, shown in Figure 3, Figure 4 and Figure 5. The extruded and unfolding sheet exhibit a bimodal structure characterized by a dynamically recrystallized grain structure as already published in e.g. [4, 5, 6, 7,]. The grain distribution is extremly inhomogeneous. Precipitates are mainly found within the grains. Due to secondary recrystallization, coarse grains are formed that are orientated along the extrusion direction [4, 5]. Coarser grains are surrounded by finer grains. The average grain size is approximately 12.5 µm, the grain size was characterized by the linear intercept method (EN 623-3:2001). Figure 4 shows the microstructure of a conventional 2 mm hot rolled AZ31 sheet. In contrast to the extruded and unfolded profile, the sheet rolling process shows differences owing to the presence of fine grained shear bands, which occur in the region of the largest shear stress, as well as a coarser microstructure between the shear bands. A more fine and more homogenous grain structure then the extruded and unfolded sheets is observed. Extremely coarse grains are not found. The average grain size is approximately 10.7 µm. In the grains of the hot-rolled sheet some twins could be observed. The finest and most homogeneous microstructure is exhibited in the twin roll casted 2mm AZ31 sheet. The average grain size is approximately 7.4 µm without shear bands. During the extrusion and rolling process dynamic recrystallization occurs.

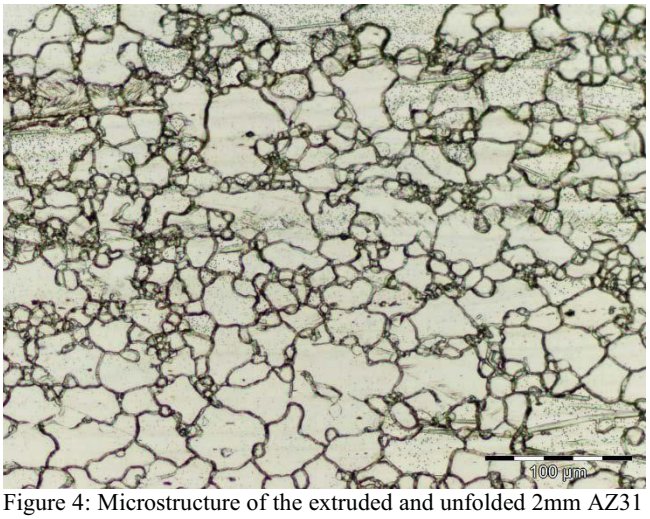


Figure 4: Microstructure of the extruded and unfolded 2mm AZ31 sheet

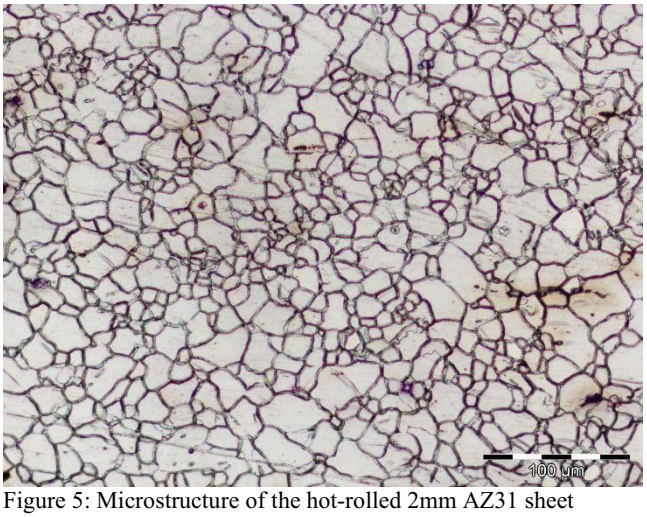


Figure 5: Microstructure of the hot-rolled 2mm AZ31 sheet

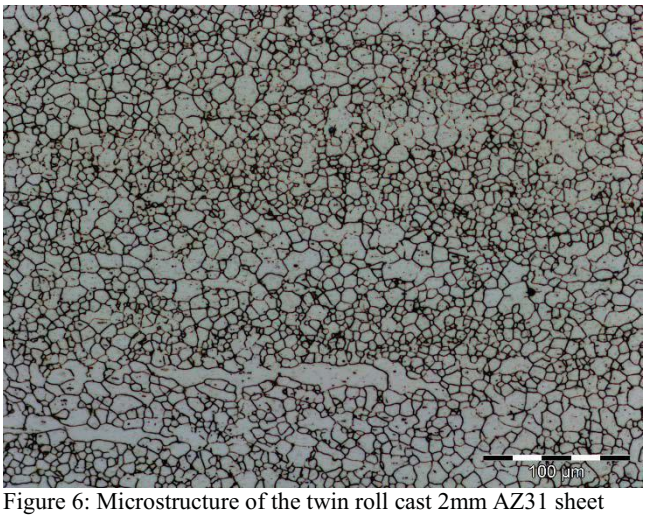


Figure 6: Microstructure of the twin roll cast 2mm AZ31 sheet

Mechanical behavior

Tensile tests were carried out on of the extruded and unfolded, the hot-rolled and the twin roll cast AZ31 sheets at room temperature and 250°C. The specimens were tested along extrusion/roll direction (0°), at an angle of 45° to the extrusion direction (45°) and perpendicular to the extrusion direction (90°).

When considering the yield strength at room temperature (RT) is noticeable that the extruded/unfolded tube, lie at an angle of 0° is at the same level with the rolled tube. The yield strength of the hot- rolled sheet is approximately 13.8%. At an angle of 45°, the yield strength decreases for the extruded/unfolded sheet by 14.4%, for the rolled sheet, the value increases by 4.8%. For the the twin roll casted sheet yield strength drops by 9.8%. At an angle of 90°, the yield stress for the extruded/unfolded increases by 3.3%. The rolled sheet even recorded an increase of 11.4% whereas the twin roll casted sheet drops to 12.2%. This inexpensive ribbon is observed that the extruded/unfolded sheet reaches a minimum at 45° and reaches back to the level from 0° to 90°. The rolled sheet shows a continuous increase from 0° to 90°. The twin roll casted sheet, however, shows a continuous decrease in the yield strength of 0° to 90°. At a test temperature of 250°C behaves extruded/unfolded sheet similar to RT just at a different level. The yield strength in this case is 85.8 MPa at a test angle of 0°. Also here a minimum is reached at an angle of 45°. The decrease in this case is 8.7%, increases at 90° but at 7.2% and reaches the maximum value of the yield strength. The rolled sheet shows a reverse behavior as to RT. The yield strength drops here continuously and reached its minimum value at 90 °. The twin roll casted sheet shows a similar behavior as described under RT. The yield strength drops continuously from 0°. All sheets have at RT and at 250°C a slightly anisotropic material behavior. As expected, the tensile strength behaves at room temperature at extruded/unfolded sheet similar to the yield strength, and the minimum is reached. At an angle of 45° the tensile strength drops off by 9.9%, then however increases by 5.7% to a maximum value of 338.3 MPa. The tensile strength of the rolled plate is lower by approximately 8.3% at an angle of 0°, but at any angle stays at the same level. The same behavior shows the twin roll casted sheet, the level is approximately 14.9% lower than the extruded / unfolded sheet. The maximum value of Ultimate strain is reached at the extruded/unfolded sheet at RT at an angle of 45° with a value of 14.1%. At the rolled sheet, a slight decreases of 0° (17.4%) to 16.5% is observed at an angle of 45° and 16.2% at an angle of 90°. A more rapid decrease can be observed at the twin roll casted sheet. Here drops the Ultimate strain from 16.4% at 0° to 10.3% at 90°. At test temperature of 250°C behaves the extruded/unfolded sheet as at RT. The maximum of Ultimate strain is is reached under an angle of 45° with the value of 34.7% which is an increase of 28.5% from 0° to 45°. At 90° to the level of 0° is reached again. The rolled sheet reached the maximum ultimate strain at an angle of 0° with a value of 38.7%, but it then decreases continuously to 27.9%, respectively. The highest values are achieved in the twin roll cast plate with 47%, this value is constant over all angles. Comparing Figure 6 to Figure 8 we see that the effect of grain size is minimal.

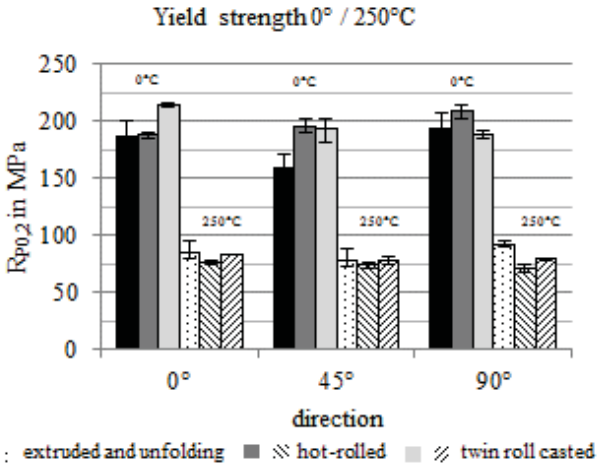


Figure 7: Yield strength at 0°C and 250°C

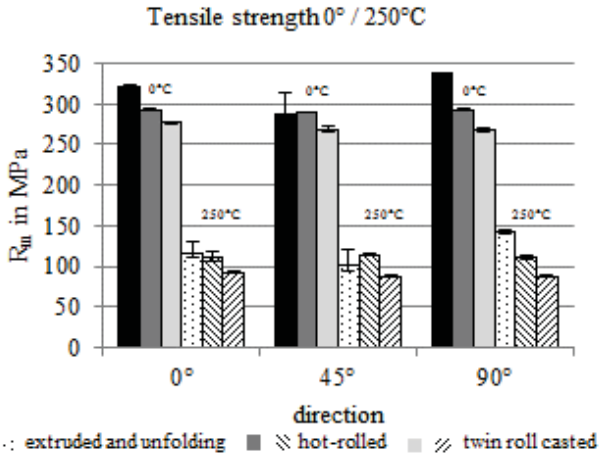


Figure 8: Tensile strength at 0°C and 250°C

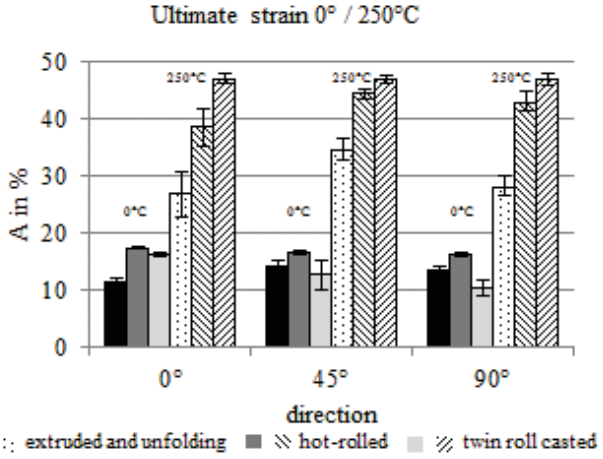


Figure 9: Ultimate strain at 0°C and 250°C

Texture distribution

Figure 10 and Figure 11 shows the (0001) pol figures of the three investigated sheets. It can be observed that, all alloys developed a strong basal texture. The intensity (CPS: counts per seconds) of the basal pole figure is at the same level. The extruded and unfolded sheet, shown in Figure 10 a), exhibit a double-fibered structure, common for AZ alloys, wich is characterized by a basal plane oriented parallel to the surface of the flat profile. The main cause of the basal texture lies, firstly, with the un favorable c/a ratio of the AZ31 alloy`s hexagonal lattice cell ($c/a=1.624<3^{1/2}$) and, secondly, with thehigh pressure which acts perpendicular to the flat profil`s surface during extrusion. These factors align the c-axis parallel to the flat profile`s surface [8]. Additionally, it is observed a slight tilt in the extrusion direction. The hot-rolling sheet, shown in Figure 10 b), develops a more asymmetric basal texture. The center of the intensity is in the center of the pole figure. The texture of the twin roll casted sheet, shown in Figure 11, shows the homogenised texture.

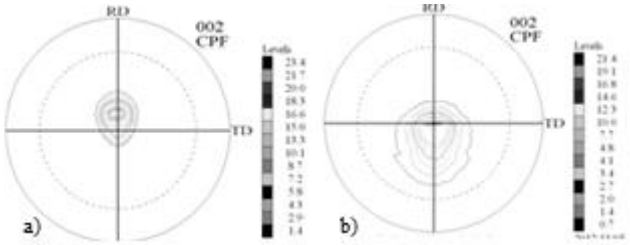


Figure 10: (00001) pole figure of a) extruded and unfolded b) hot-rolled 2mm AZ31 sheet

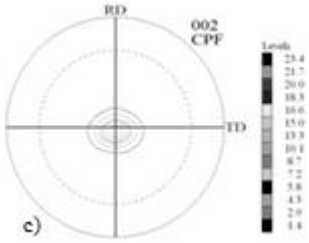


Figure 11: (00001) pole figure of c) twin roll cast 2mm AZ31 sheet

Conclusions

1. It could be shown that with the novel manufacturing process successfully 2mm AZ31 sheets could be produced.

2. The grain size is of the different manufactured sheets are different, but comparing Figure 6 to Figure 8 we see that the effect of grain size is minimal. Twins are only observed in the hot-rolled sheet.

3. All the sheets fabricated through extruded and unfolded, hot-rolling and twin rolling exhibit the similar basal texture.

In summary can be said that the novel process for producing large scale Mg-sheets offers another possibility to produce Mg-sheets with a good quality compared with conventional Mg sheets.

References

1. K.U. Kainer et al., *Microstructure and Texture development during hydrostatic extrusion of magnesium alloy AZ31*, Scripta Mater 53, 259-264, 2005.
2. O. Duygulu et al., *Twin Roll Casting and Rolling of MgAZ31 Sheets* (Magnesium - 8th International Conference on Magnesium and their Applications 2009), 531-536.
3. K., Müller, *Fundamentals of Extrusion*, (Giesel-Verlag, Isernhagen, 2004).
4. S. Mueller et al., *Aluminium Interantional Journal* (82, 5, 2006) 438-442.
5. A. Roßberg, *Halbzeuge und Walzstrategien zur Herstellung tiefziehfähiger Magnesiumbleche*(Dissertation, Universität Hannover; 2006).
6. K. U. Kainer, J. Bohlen, H. Gers: *Strangpressen* (Tagungsband des Symposium Strangpressendes Fachausschusses Strangpressen der DGM, 26-27. Oktober 2006 in Weimar, Wiley-VCH Verlag GmbH&Co. KGaA)213-220.
7. S. Mueller et al., *Proceedings of the 7th International Conference Magnesium Alloys and their Applications*, 2006, Wiley-VCH Verlag GmbH&Co. KGaA) 406-412.
8. Mukai T. et al., *Ductility enhancement in Az31 magnesium alloy by controlling grain structure* (Scripta Materialia, 2001, 45) 89-94.

Magnesium Technology 2014
Edited by: Martyn Alderman, Michele V. Manuel, Norbert Hort, and Neale R. Neelameggham
TMS (The Minerals, Metals & Materials Society), 2014

EFFECT OF VOLUME FRACTION OF ICOSAHEDRAL PHASE IN CaO ADDED Mg-Zn-Y ALLOYS

Hyunkyu Lim, Daeguen Kim, Tae-yang Kwak, Wonseok Yang, Hak-young Kim, Young-ok Yoon, Shae K. Kim
Korea Institute of Industrial technology; 156 Geatbeol-ro, Yeonsu-gu, Incheon, 406-840, KOREA

Keywords: Wrought Mg alloy, Icosahedral phase, CaO

Abstract

For the development of high strength magnesium sheets with adequate elongation, we had investigated the effect of volume fraction of icosahedral phase (varying Zn and Y contents) for CaO added Mg-Zn-Y alloys. Therefore, in this study, three alloys were examined; Mg-6Zn-1.2Y-0.3CaO (ZWO6103), Mg-10Zn-2Y-0.3CaO (ZWO10203) and Mg-18Zn-3.6Y-0.3CaO (ZWO18403). Although the addition of CaO formed Ca-Mg-Zn phase in Mg-Zn-Y alloys, icosahedral phase still existed because the ratio of remaining Zn to Y, after forming Ca-Mg-Zn phase, was in the range of 5-7%. Test specimens were prepared by two methods; one was indirect extrusion and the other was rolling after extrusion. To evaluate the ignition and corrosion resistances, measurement of ignition temperature by DTA and electrochemical test were carried out with extruded specimens. Also we investigate mechanical properties specimens which were prepared by extrusion and rolling.

Introduction

Recently, magnesium alloys are recognized alternative to iron and aluminum alloys to reduce the weight of structural materials [1]. In spite of the attractive properties of magnesium alloys such as low density, high specific strength (ratio of strength to density), excellent castability, good machinability and so on [2], magnesium alloys have some drawbacks which should be overcome in order to apply to structural parts. To use magnesium alloys for the aircraft components, many researches on developing magnesium alloys with high strength and ignition resistance are in progress [3-4]. From this point of view, Mg-Zn-Y alloy system is very attracted. In this alloy system, quasicrystalline icosahedral phase is formed with ratio of Zn/Y (in at.%) of 5-7. In addition, it is possible to control the volume fraction of these phases without forming other phases because icosahedral makes pseudo-eutectic reactions with α-Mg phase [5].

In addition, one problem with magnesium alloys is their high activity in the presence of oxygen. To reduce the hazard, protective gases such as SF_6 and SO_2 gases are used to prevent magnesium alloys in the molten state from coming into contact with air [1]. However, it is impossible to protect the parts with protective gases, many researches have been done to improve the ignition resistance of magnesium alloys with addition of rare earth elements, metallic calcium and beryllium [6-7]. There are a few methods of alloying calcium into magnesium alloys; one is use of metallic calcium and the other is reaction of CaO on the surface of molten magnesium alloys. Recently, Kim *et al*. have revealed that the CaO addition improved properties of commercial magnesium alloys (ECO-Mg alloys) [8-9]. The concept of ECO-Mg alloy was to simply introduce CaO particles as an ingredient onto molten magnesium alloys. The CaO particles reacted on the surface of molten magnesium alloys and were decomposed into calcium and oxygen. The oxygen from decomposed CaO was released into the atmosphere without reaction with molten magnesium alloys. So, Kim *et al*. have suggested that the method of alloying calcium with CaO maintained the cleanliness of molten magnesium alloys.

The main task of this study was to investigate properties of CaO added wrought Mg-Zn-Y alloys with various volume fraction of icosahedral phase for application to aircraft components. The evaluation of the effect of volume fraction of icosahedral phase (varying Zn and Y contents) for CaO added Mg-Zn-Y alloys was performed by observation of microstructures, measurement of ignition temperature, electrochemical test, and tensile test.

Table 1. Nominal compositions of tested alloys

Alloy designation	Chemical compositions							
	weight percent (wt.%)				atomic percent (at.%)			
	Mg	Zn	Y	Ca	Mg	Zn	Y	Ca
ZWO6103	92.5	6	1.2	0.3	97.12	2.34	0.34	0.19
ZWO10203	87.7	10	2	0.3	95.18	4.03	0.59	0.2
ZWO18403	78.1	18	3.6	0.3	90.86	7.78	1.14	0.21

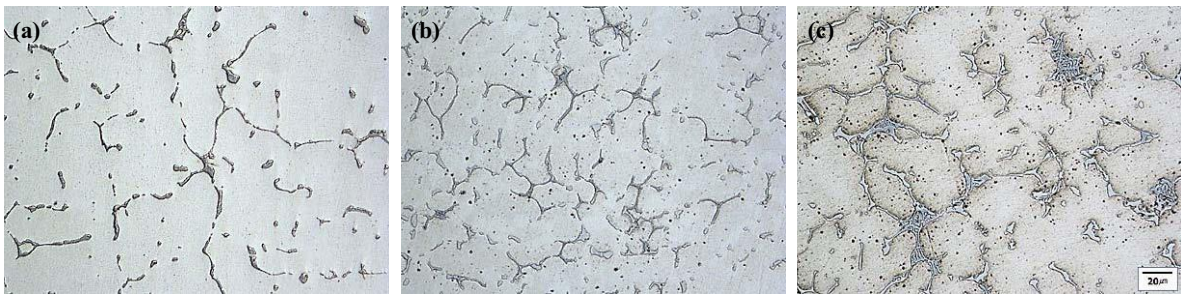


Fig. 1. Optical microstructures of homogenized (a) ZWO6103, (b) ZWO10203, and (c) ZWO18403 alloys

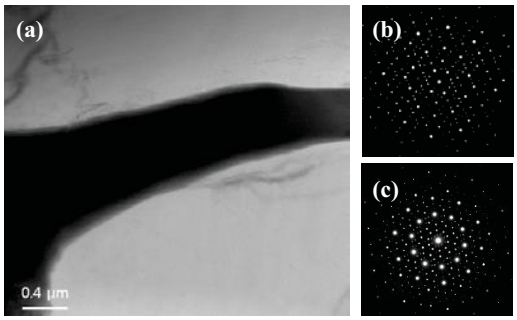


Fig. 2. TEM images of homogenized ZWO18403 alloy; (b) and (c) SADPs from dark phase in (a) BF image

Experimental procedure

CaO added Mg-Zn-Y alloys were designed as in Table 1. We used "O" as code letter to be distinguished from alloys with metallic Calcium whose code letter is "X". As-cast billets were prepared by melting commercial purity Mg, Zn, Mg-25Y master alloy and Mg-3CaO master alloy in an electric resistance furnace under SF_6+CO_2 atmosphere, followed by pouring the melt into the steel mold of cylindrical cavity with the dimension of 50 mm in diameter and 200 mm in height. The billets were homogenized at 360 ^oC for 20 h. The billets preheated at 320 ^oC for 60 min. were extruded with a reduction ratio of 20:1 and the cross-sectional area of the extruded strips was 25*4 mm^2. The extruded strips preheated at 350 ^oC for 30 min. were rolled with a reduction ratio of ~ 30 % per pass to final thickness of 1.4 mm. After hot rolling, sheets were annealed at 200 and 300 ^oC for 15 min.

Uniaxial tensile tests were carried out on dog-bone specimens (specimen gauge length of 25 mm) machined from as-rolled and annealed sheets at room temperature with initial strain rate of 10^{-3} /s. DTA analyses were performed under dry air atmospheres to measure the ignition temperatures of tested alloys. The sample weight for DTA test was about 7~10 mg and the heating rate was 10 K/min. The potentiodynamic polarization measurements (electrochemical tests) were done with a conventional 3-electrode cell in 5% NaCl solution at room temperature. A platinum electrode was used as an auxiliary electrode.

Results and Discussion

The microstructures of homogenized alloys were shown in Fig. 1. All alloys were consisted of α-Mg and the secondary solidified phases. According to the EDS analysis results, there were two kinds of secondary phases in the tested alloys. One was Mg-Zn-Y phase and the other was Ca-Mg-Zn phase. Generally, the greater difference between electronegativity of the elements the more stable compound formation between them [10]. The electronegativity of Mg, Zn, Y, and Ca are 1.31, 1.65, 1.22, and 1.00, respectively [11]. Therefore, the addition of Ca forms Ca-Mg-Zn phase easily. Furthermore, with increasing Zn and Y contents, the volume fractions of eutectic pocket as well as the second phases increased. This means the solidification behavior changed with adding Zn and Y.

Fig. 2(a) showed the TEM bright field image of the eutectic pocket in homogenized ZWO18403 alloy and Fig. 2(b) and (c) were selected area diffraction patterns obtained from dark phase in bright field image (Fig. 2(a)). In addition, TEM-EDS analysis revealed that the ratio of Zn/Y (in at.%) of dark phase was 6.06. From the SADPs and TEM-EDS analysis, it could be thought that α-Mg and I-phase composed the eutectic pocket in ZWO18403 alloy and the volume fraction of I-phase increased with increasing Zn and Y contents.

Table 2. Mechanical properties of as-extruded alloys

Alloy	TYS (MPa)	UTS (MPa)	El. (%)
ZWO6103	202.9	283.1	21.81
ZWO10203	193.0	294.5	13.34
ZWO18403	248.8	332.8	6.68

The mechanical properties of as-extruded alloys are listed in Table 2. With increasing Zn and Y contents, the UTS increased while the elongation decreased. When compared the mechanical properties of as-extruded ZWO6103 and ZWO10203 alloys, the UTS of ZWO10203 alloy was higher than that of ZWO6103 in spite of lower TYS and elongation. This means the n-value (stress exponent) of ZWO10203 alloy is higher than that of ZWO6103 alloy. However, more studies might be needed to figure out the reason of higher TYS of ZWO6103. Fig. 3 showed the optical microstructures of as-extruded alloys. The broken secondary phase particles formed during extrusion from grain boundary networks of as-cast alloys and were distributed as streamlines in parallel to extrusion direction. Because of large volume fraction of broken secondary phase particles, as-extruded ZWO18403 alloy exhibited the highest strengths among tested alloys. However, from the results of SEM analysis, the eutectic structure remained in ZWO18403 alloy after extrusion. Therefore, ZWO18403 alloy had the lowest elongation among tested alloys.

Fig. 4 showed the results of DTA for CaO added Mg-Zn-Y alloys under dry air atmosphere. The ignition temperatures of ZWO6103, ZWO10203, and ZWO18403 alloys were 676.2 ^oC, 834.0 ^oC, and 905.5 ^oC, respectively. From the results of DTA, it could be noticed that the increase of volume fraction of I-phase enhanced ignition resistance of these alloys and the addition of CaO was effective to improve the ignition temperature when comparing ZWO10203 and ZW92 [12] alloys. According to study of Lee *et al*., during oxidation under an ambient atmosphere, Ca-bearing phase on the surface was dissociated by oxygen to MgO and CaO [9]. Because



Fig. 3. Optical microstructures of as-extruded (a) ZWO6103, (b) ZWO10203, and (c) ZWO18403 alloys (X200)

these oxide formed dense and complex oxide layer on the surface of specimens, the ignition temperatures of alloys increased when adding CaO into Mg-Zn-Y alloys.

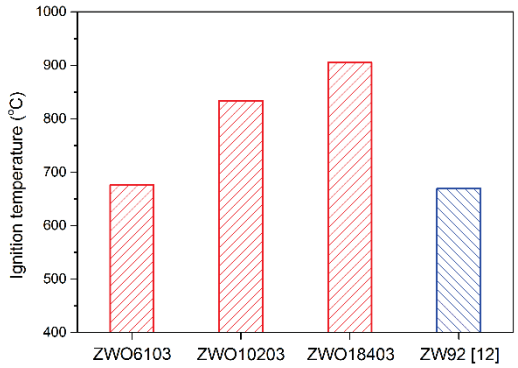


Fig. 4. Ignition temperatures of tested alloys measured by DTA

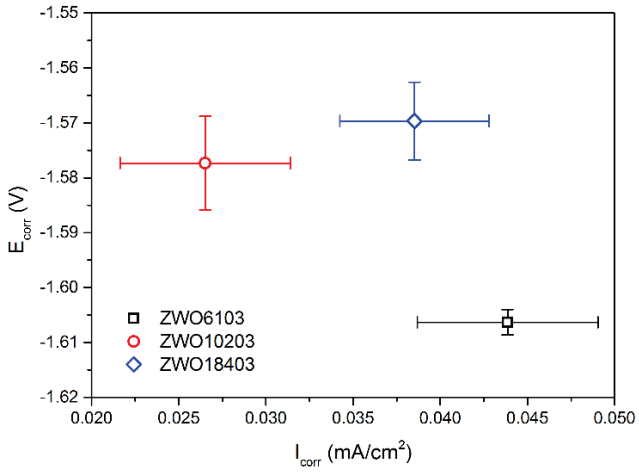
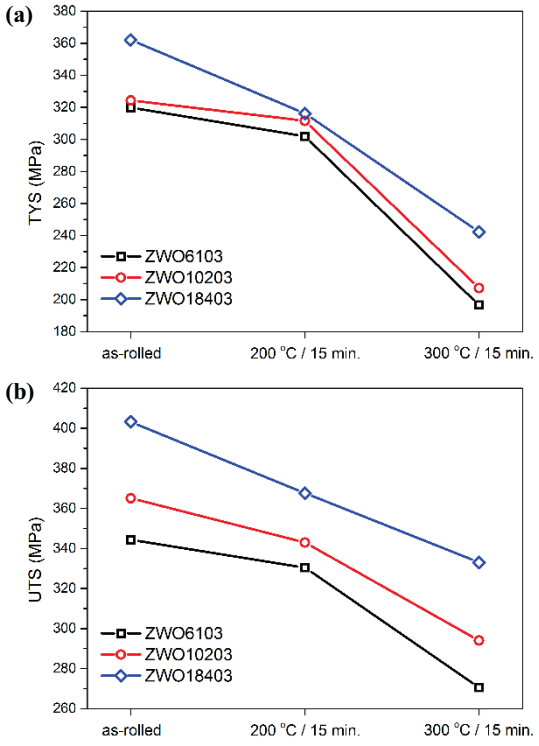


Fig. 5. Results of electrochemical test for tested alloys (mean measurement values)

The results of electrochemical test for as-extruded alloys were shown in Fig. 5 and the values of corrosion potential (E_{corr}) and current density (I_{corr}) were obtained by Tafel extrapolation. With increasing the volume fraction of I-phase, the E_{corr} increased. It is well-known that quasicrystals have many interesting properties such as high hardness, high corrosion resistance, low coefficient of friction, low interface energy, etc. [13]. Therefore, ZWO18403 alloys might exhibit the high corrosion potential due to the large volume of I-phase with high corrosion resistance. On the other hand, in the case of current density, ZWO10203 alloy had the lowest value among tested alloys. This means ZWO10203 alloy exhibits the slowest corrosion rate when compared with other alloys. Although the corrosion resistance of I-phase is high, because the interface between a-Mg and I-phase increased with increasing the volume fraction of I-phase, the current density of ZWO18403 alloy was higher than that of ZWO10203 alloy.

Fig. 6 showed the results of tensile test for as-rolled and annealed sheets at room temperature. With increasing the volume fraction of I-phase, the strengths (e.g. TYS and UTS) increased due to the pinning effect of the broken secondary phase particles. In all cases, ZWO18403 sheets exhibited the highest strengths among tested sheets. On the other hand, ZWO10203 sheets exhibited the largest elongation in all cases. This means the proper volume fraction of I-phase enhanced the elongation of sheets but the excessive amount of I-phase had a bad influence on the elongation of sheets.



(c)

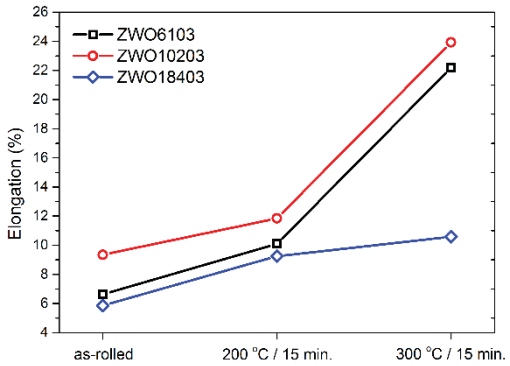


Fig. 6. Mechanical properties of as-rolled and annealed sheets; (a) TYS, (b) UTS, and (c) Elongation

Conclusion

In the present study, microstructures, ignition temperatures, corrosion resistance, and mechanical properties of CaO added Mg-Zn-Y alloys had been investigated. The conclusions are as follows:

(1) The addition of CaO into Mg-Zn-Y alloys formed Ca-Mg-Zn phase and with increasing Zn and Y contents (the ratio of Zn/Y: 5-7 in at.%), the volume fraction of I-phase increased.

(2) The ignition temperature increased with increasing the volume fraction of I-phase. The ignition temperature of as-extruded ZWO18403 specimen was over 900 °C.

(3) Although the corrosion potential improved with the volume fraction of I-phase, the corrosion rate of ZWO18403 alloy was faster than that of ZWO10203 alloy, due to the large amount of interface between α-Mg and I-phase. As-extruded ZWO10203 specimen exhibited the lowest corrosion rate among tested specimens.

(4) The large volume fraction of I-phase enhanced the strength of sheets but the excessive amount of I-phase had a bad influence on the elongation.

References

[1] H. Watarai, "Trend of research and development for magnesium alloys", Quarterly Review (NISTEP), 18 (2006) 84-97.

[2] Avedesian, H. Baker, eds., *Magnesium and Magnesium Alloys*, ASM International, Metals Park, 1999.

[3] X. Zeng, Q. Wang, Y. Lu, Y. Zhu, W. Ding, Y. Zhao, "Influence of beryllium and rare earth additions on ignition-proof magnesium alloys", *Journal of Materials Processing Technology*, 112 (2001) 17-23.

[4] J. Lee, D. Kim, H. Lim, D. Kim, "Effects of Zn/Y ratio on microstructure and mechanical properties of Mg-Zn-Y alloys", *Materials Letters*, 59 (2005) 3801-3805

[5] J. Ok, I. Kim, S. Yi, W. Kim, D. Kim, "Solidification microstructure of as-cast Mg–Zn–Y alloys", *Philosophical Magazine*, 83 (2003) 2359-2369

[6] X. Zeng, Q. Wang, Y. Lu, W. Ding, Y. Zhu, C. Zhai, C. Lu, X. Xu, "Behavior of surface oxidation on molten Mg-9Al-0.5Zn-0.3Be alloy", *Materials Science and Engineering A*, 301 (2001) 154-161.

[7] Z. Xiaoqin, W. Qudong, L. Yizhen, D. Wenjiang, C. Lu, Z. Yanping, C.Q. Zhai, X.P. Xu, "Study of ignition proof magnesium alloy with beryllium and rare earth additions", *Scripta Materialia*, 43 (2000) 403-409.

[8] S. Kim, "Design and Development of High-Performance Eco-Mg Alloys", in: F. Czerwinski (Ed.), Magnesium Alloys - Design, Processing and Properties, InTech, Shanghai, 2011, pp. 431-468.

[9] J. Lee, S. Kim, "Effect of CaO Addition on the Ignition Resistance of Mg-Al Alloys", *Materials Transactions*, 52 (2011) 1483-1488.

[10] L.L. Rokhlin, *Magnesium Alloys Containing Rare Earth Metals: Structure and Properties*, Talor & Francis, New York, 2003

[11] http://chemed.chem.wisc.edu/chempaths/GenChem-Textbook/Electronegativity-861.html

[12] H. Lim, T. Kwak, W. Yang, Y. Yoo, D. Kim Y. Yoon, S. Kim, "Investigation of Properties of CaO Added Wrought Mg-Zn-Y and Mg-Y-Zn Alloys", *in press*.

[13] Dubois JM, Plaindoux P, Belin-Ferre E, Tamura N, Sordelet DJ. In: Fujiwara, Takeuchi, editors. Proceedings of the 6th International Conference on Quasicrystals. Singapore: World Scientific; 1997.

Magnesium Technology 2014
Edited by: Martyn Alderman, Michele V. Manuel, Norbert Hort, and Neale R. Neelameggham
TMS (The Minerals, Metals & Materials Society), 2014

EFFECT OF CaO ON HOT WORKABILITY AND MICROSTRUCTURE OF Mg-9.5Zn-2Y ALLOY

Tae-yang Kwak[1,2], Daeguen Kim[1], Jaehack Yang[1], Young-ok Yoon[1], Shae K. Kim[1], Hyunkyu Lim[1] and Woo Jin Kim[2]
[1] Casting Research Center, Korea Institute of Industrial Technology, Incheon, Korea
[2] Dept. of Materials Science and Engineering, Hong-Ik University, Seoul, Korea

Keywords: Mg-Zn-Y alloys, CaO, Processing map, Quasicrystalline icosahedral phase (I-phase)

Abstract

Mg-Zn-Y system alloys have been a great interest because Mg-Zn-Y alloys with I-phase exhibited high ductility at room and elevated temperatures. According to our preliminary experiments, the addition of CaO improved strength, but the process window became narrow. Therefore, the aim of current work was to find optimum extrusion conditions for CaO added Mg-Zn-Y alloys by processing maps. The 0.3 wt.% of CaO added Mg-9.5Zn-2Y ($Mg_{95.6}Zn_{3.8}Y_{0.6}$) alloy was prepared by casting into steel mold and homogenizing. Hot compression test were performed in the Gleeble machine at temperature range of 250-400 ^{o}C with various strain rates. The alloys were extruded with a reduction ratio of 20:1. To analyze the microstructure and texture, optical micrograph, scanning electron microscope and electron backscattered diffraction were used. Moreover, we investigated the effects of metallic Ca addition in this alloy to compare with the addition of CaO.

Introduction

Magnesium alloys are used for automotive, aerospace and railway industries due to its light weight and high specific strength [1,2]. However, the applicability for extensive and high-end applications is limited due to their relatively low strength and room temperature ductility [3]. Therefore, many researches are reported for improvement of both strength and formability simultaneously.

Mg-Zn-Y alloys, which strengthened by the quasicrystalline icosahedral phase (I-phase), have received attention because of the combination effect of high elongation and strength. [4-6]. Because I-phase has low interfacial energy, they are stable against coarsening at elevated temperatures. Therefore, a large amount of I-phase makes smaller grain size during the extrusion process [7,8]. The I-phase particles exhibit better thermally stability than many other phases, act as strong obstacles between grain boundaries [9-11]. Therefore, Mg-Zn-Y alloys forming with I-phase is difficult due to higher flow stress at elevated temperature.

Recently, global regulation of environmental resources as reduction of greenhouse gases is intensifying. Kim *et al*. have reported that CaO added commercial alloys improved the mechanical and physical properties without SF_6 protective gas due to the improvement of ignition temperature and oxidation resistances. Moreover, they have reported that when adding CaO, there was no negative effect of Ca addition such as decreasing castability, die soldering and etc [12,13]. However, studies on the effects of CaO addition have been done in Mg-Al alloy systems. There is little study on these effects in Mg-Zn-Y alloy system. And it is necessary to compare Ca to CaO addition in the wrought alloys.

Therefore, in this research, optimum extrusion conditions for Ca or CaO added Mg-Zn-Y alloys with I-phase were deducted by development of processing maps. Moreover, we compared between the effects of Ca and CaO added alloys.

Experimental procedures

The chemical composition of ZW92, ZWO9203 and ZWX920 alloys is shown in Table. 1. As-cast ingots were prepared by melting commercial purity Mg, Zn, Ca, Mg-25Y master alloy and Mg-5CaO master alloy in an electric resistance furnace under inert atmosphere, followed by pouring the melt into the steel mold of cylindrical cavity with the dimension of 98 mm in diameter and 120 mm in height. Mg-Zn-Y alloys were homogenized at 350 ^{o}C for 20 hr. Small cylindrical samples were machined to the following dimensions: 10 mm diameter and 12 mm height. Uniaxial compression tests were carried out by a Gleeble 3500 thermo-mechanical simulator with strain rates of 0.001-10 s^{-1} and deformation temperatures of 225-400 ^{o}C. During the compression tests, the samples were heated to the desirable deformation temperature with a heating rate of 10 ^{o}C/s and held at that temperature for 3 min prior to compression. The samples were deformed to a total true strain of - 0.7.

The homogenized Mg-Zn-Y alloys were extruded with a reduction ratio of 20:1 and temperature of 320 and 380 ^{o}C. Extruded strips have the cross-sectional area of 70 x 5 mm^2.

Optical micrograph (OM), Scanning electron microscope (SEM) and electron backscattered diffraction (EBSD) were used for microstructure analyses.

Table 1. Chemical compositions of tested alloys

Alloy designation	Chemical composition [wt.%]				Remarks
	Mg	Zn	Y	Ca	
ZW92	88.5	9.5	2		
ZWO9203	88.2	9.5	2	0.3	CaO addition
ZWX920	88.2	9.5	2	0.3	Ca addition

Results and discussion

Microstructure of homogenized state

Fig. 1 shows optical micrographs of homogenized ZW92, ZWO9203 and ZWX920 alloys. All alloys were consisted of α-Mg and the secondary solidified phases. Although the addition of CaO or Ca in ZW92 alloy increases the volume fraction of the secondary phases, there is no difference between ZWO9203 and ZWX920 alloys in the shape of phase

I-phase formed during solidification by eutectic reaction in Mg-Zn-Y alloys [4-6]. Fig. 2 shows SEM image of the ZW92, ZWO9203 and ZWX920 alloys. I-phase was observed in all alloys (Fig. 3 (a), (b) and (d)). However, when adding Ca or CaO, the disc shape of Ca bearing phase are observed (Fig. 2 (c) and (e)). Thus, I-phase and Ca contained phase coexist in Ca or CaO added Mg-Zn-Y alloys.

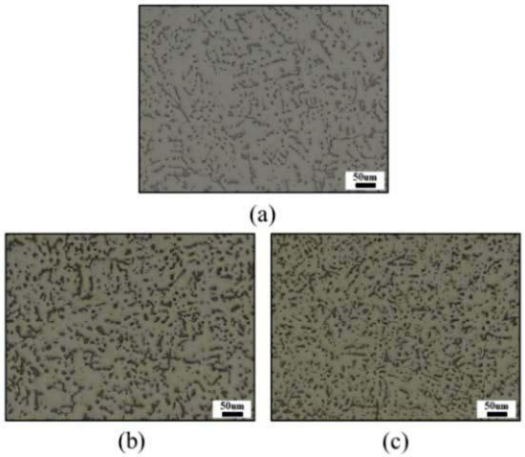


Fig. 1. The optical micrograph of homogenized (a) ZW92, (b) ZWO9203, and (c) ZWX920 alloys.

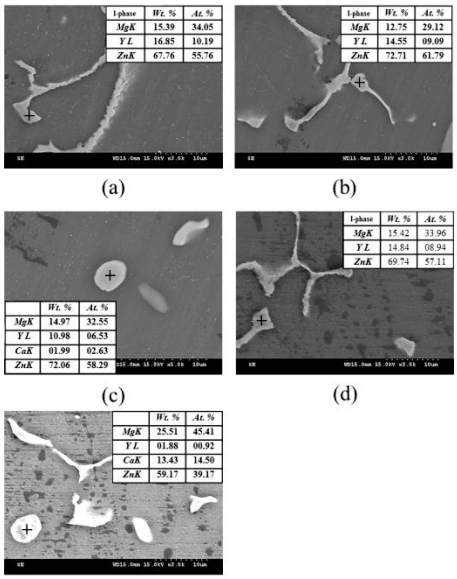


Fig. 2. Scanning electron microscope image of (a) ZW92, (b, c) ZWO9203, and (d, e) ZWX920 alloys.

True strain – true stress curves

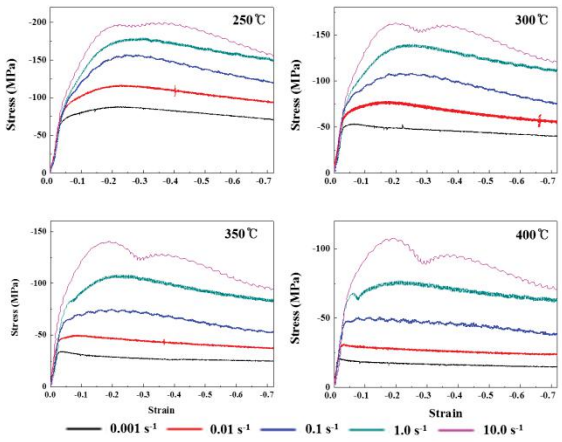


Fig. 3. True stress-strain curves of homogenized ZW92 alloy.

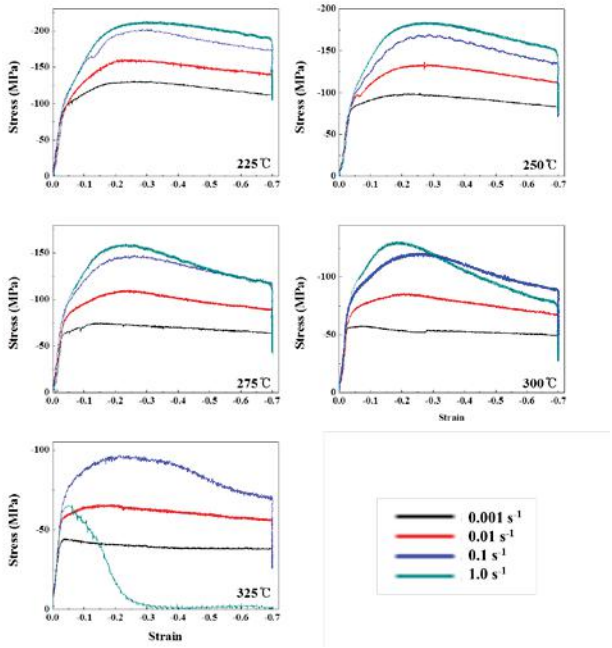


Fig. 4. True stress-strain curves of homogenized ZWO9203 alloy.

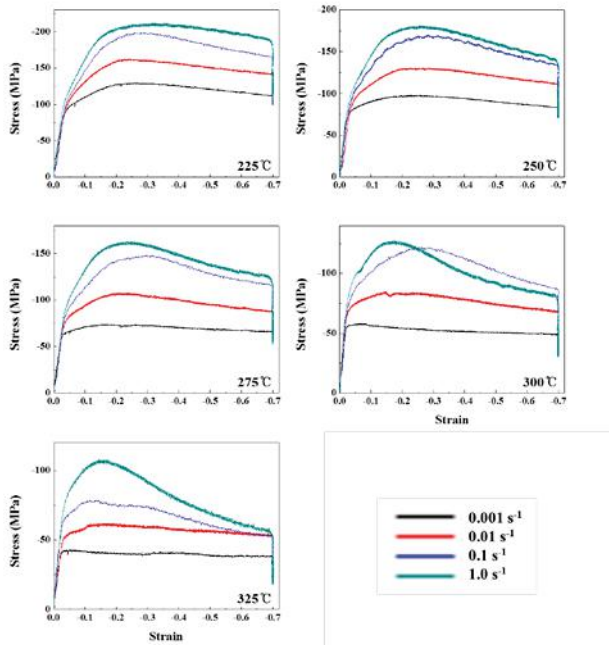


Fig. 5. True stress-strain curves of homogenized ZWX920 alloy.

Fig. 3-5 shows true stress-strain curves in homogenized ZW92, ZWO9203 and ZWX920 alloys. These curves were obtained at 225- 400 ^{o}C and strain rate range of 0.001-10 s^{-1} by compression test. From these results, Mg-Zn-Y alloys have high flow stress at given temperatures due to thermally stability of second phase [7,8]. On the other hand, temperature range of compression test for ZWO9203 and ZWX920 alloys was narrow, due to the brittleness of alloys. ZW92, ZWO9203 and ZWX920 alloys exhibit severe hardening followed by flow softening.

Processing maps

Processing maps have been confirmed to be an effective and tool to best hot processing parameters and control microstructure of various materials [14-17]. A processing map is an explicit representation by a power dissipation and an instability map [18]. The variation of J co-content with temperature and strain rate called the efficiency of power dissipation (η), is given by strain rate sensitivity parameter (m):

$$\eta = \frac{J}{J_{max}} = \frac{2m}{m+1} \quad (1)$$

This maximum value for efficiency of dissipation(η) means that it is the most active state for change of microstructure. Meanwhile, the stability condition described in Dynamic Materials Model is that considered by Ziegler [19]. Microstructural stability at a constant temperature given by

$$\xi(\dot{\varepsilon}) = \frac{\partial \ln\left(\frac{m}{m+1}\right)}{\partial ln\dot{\varepsilon}} + m < 0 \quad (2)$$

In this equation, if the value of $\xi(\dot{\varepsilon})$ have miners value, it is defined as "flow instability area".

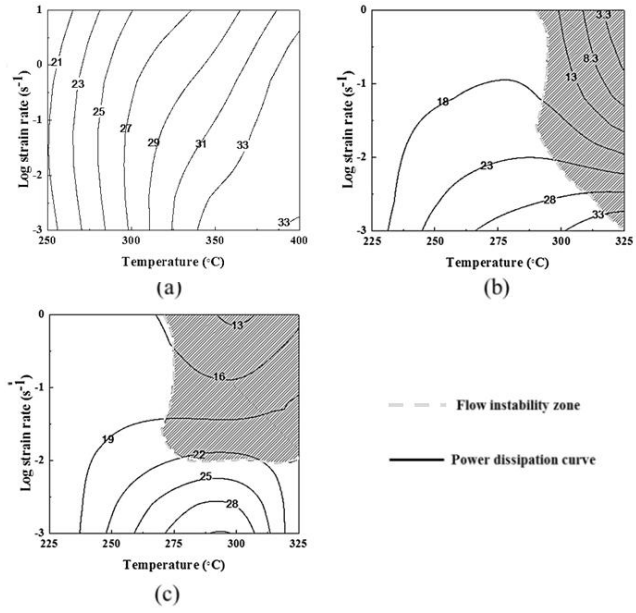


Fig. 6. Processing maps of homogenized (a) ZW92, (b) ZWO9203, and (c) ZWX920 alloys at strain 0.4

Fig. 6 shows processing maps of homogenized ZW92, ZWO9203 and ZWX920 alloys at strain ratio of 0.4. Highest efficiency of power dissipation for ZW92 alloy showed at 400 °C and 10^{-2} s^{-1}. The maximum efficiencies of ZWO9203 and ZWX920 alloys were 33 % at 320 °C and 10^{-3} s^{-1}, 28 % at 280 °C and 10^{-3} s^{-1}, respectively (Fig. 6 (b), (c)). The flow instability zones occurred in ZWO9203 and ZWX920 alloys in the processing maps (Fig. 6 (b), (c)). The flow instability zones in ZWO9203 and ZWX920 alloys exist wider than ZW92 alloy because of brittleness of Ca or CaO added ZW92 alloys.

Microstructure of extruded alloys

Fig. 7 shows optical micrograph of as-extruded ZW92, ZWO9203, ZWX920 alloys with different extrusion temperature. Most particles were segregated along grain boundaries in the micro-scale level. When extruded at 320 °C, microstructure of ZW92 alloy consists of homogeneous and equi-axed grains by the dynamic recrystallization (DRX) with elongated grains toward extrusion direction while Ca or CaO added alloys exhibit the DRXed grains. Moreover, the average grain size of ZWO9203 and ZWX920 was almost same. With increasing extrusion temperature, the grain size of ZW92 increased significantly, but the grain size of Ca or CaO added alloys was almost maintained.

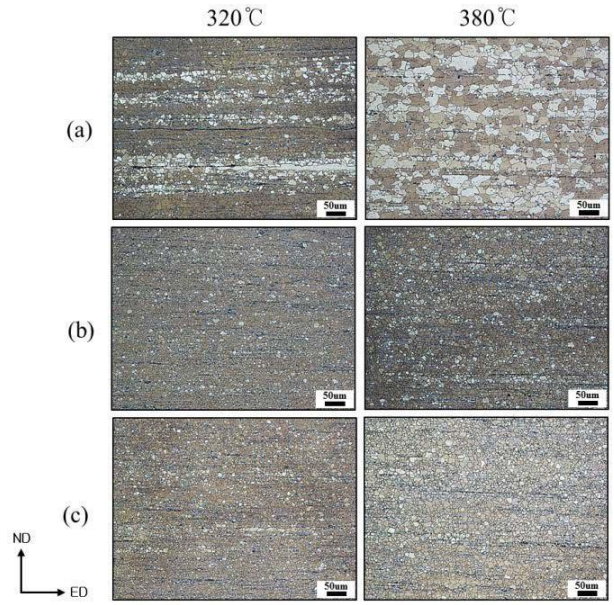


Fig. 7. Optical micrograph of extruded (a) ZW92, (b) ZWO9203, and (c) ZWX920 alloys with various extrusion temperature.

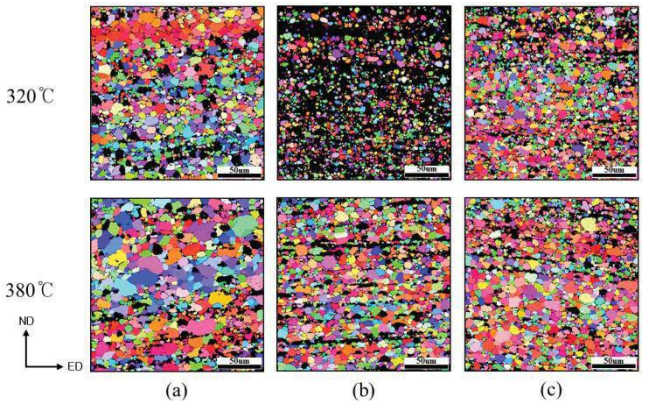


Fig. 8. OIM maps of extruded (a) ZW92, (b) ZWO9203, and (c) ZWX920 alloys with various extrusion temperature.

The differences of mechanical property were exhibited due to different basal texture distribution [20]. Therefore, different textures will leads different workabilities. Fig. 8 shows microtexture of the extruded ZW92, ZWO9203, ZWX920 alloys with different extrusion temperature. The black area in OIM map is not measured accurately due to excessive inelastic scattering in

high internal energy area. ZWO9203 alloy which was extruded at 320 ^{o}C exhibits the largest black area among the tested specimens, that is, the internal energy of ZWO9203 which was extruded at 320 ^{o}C is higher than those of other alloys. Fraction of measured areas also increased with increasing extrusion temperature by decreased internal energy due to DRX or grain growth.

Conclusions

In the present study, hot workabilities and microstructures of Ca or CaO added Mg-Zn-Y alloys were investigated.
The conclusions are as follows:

1) I-phase and Ca contained phase coexist in Ca or CaO added Mg-Zn-Y alloys.
2) Highest efficiency of power dissipation for ZW92 alloy exhibited at 450 ^{o}C and 10^{-2} s^{-1}. The maximum efficiencies of ZWO9203 and ZWX920 alloys were 33 % at 320 ^{o}C and 10^{-3} s^{-1}, 28 % at 280 ^{o}C and 10^{-3} s^{-1}, respectively
3) Ca or CaO added Mg-Zn-Y alloys did not exhibit any strong differences in this study.

References

[1] I. J. Polmear, *Metallurgy of the Light Metals*, 3rd edn, Edward Arnold, London, 1995.
[2] B. L. Mordike, T. Ebert, *Mater. Sci. Eng. A*, 302 (2001) 37–45.
[3] Q. Wang, J. Chen, Z. Zhao, S. He, *Mater. Sci. Eng. A*, 528 (2010) 323–328.
[4] D. H. Bae, S. H. Kim, D. H. Kim, W. T. Kim, *Acta Mater.,* 50 (2002) 2343.
[5] J. Y. Lee, D. H. Kim, H.K. Lim, D.H. Kim, *Mater. Lett.*, 59 (2005) 3801.
[6] J. Y. Lee, H. K. Lim, D.-H. Kim, W.T. Kim, D.H. Kim, *Mater. Sci. Eng. A*, 449–451 (2007) 987.
[7] J. Y. Lee, D. –H. Kim, H. K. Lim, D. H. Kim, *Mater. Lett.*, 59 (2005) pp. 3801–3805.
[8] J. M. Dubois, P. Plaindoux, E. Berlin-Ferre, N. Tamura, D. J. Sordelet, *Proceedings of the Sixth International Conference on Quasicrystals*. Singapore: World Scientific; 1997.
[9] Z.P. Luo, S.Q. Zhang, Y.L. Tang, D.S. Zhao, *Scripta Metall. Mater.*, 28 (1993) 1513–1518.
[10] E. Abe, H. Takakura, A. Singh, A.P. Tsai, *J. Alloys Compd.*, 283 (1999) 169.
[11] Alok Singh, M. Nakamura, M. Watanabe, A. Kato, A. P. Tsai, Scripta Materialia, 49 (2003) 417-422.
[12] S. K. Kim, J. K. Lee, Y. O. Yoon, H. H. Jo, *Journal of Materials Processing Technology*, 187–188 (2007) 757–760.
[13] J.K. Lee, S. H. Ha, Y. J. Kim, H. H. Jo, S. K. Kim, *Journal of the Korean Foundrymen's Society*, vol. 27, No. 3, 2007, 131-134.
[14] Y.V.R.K. Prasad, K.P. Rao, *Mater. Sci. Eng. A*, 487 (2008) 316–327.
[15] W. Peng, W. Zeng, Q. Wang, H. Yu, *Mater. Sci. Eng. A*, 571 (2013) 116–122.
[16] N. Srinivasan, Y.V.R.K. Prasad, *Journal of Materials Processing Technology*, 51 (1995) 171-192.
[17] Y.V.R.K. Prasad, K.P. Rao, N. Hort, K.U. Kainer, *Mater. Sci. Eng. A*, 502 (2009) 25–31.
[18] Y.V.R.K. Prasad, S. Sasidhara, *Hot Working Guide: A Compendium of Processing Maps*, ASM International ; 1997.
[19] H. Ziegler, Progress in Solid Mechanics, Vol. 4, Eds. I.N. Sneddon and R. Hill, John Wiley and Sons New York (1963) 93.
[20] Sun. H. F, Liang. S. J, Wang. E. D, *Trans. Nonferrous Met. Soc. China*, 19 (2009) s349-s354

Magnesium Technology 2014
Edited by: Martyn Alderman, Michele V. Manuel, Norbert Hort, and Neale R. Neelameggham
TMS (The Minerals, Metals & Materials Society), 2014

WELDING OF DISSIMILAR LIGHT METALS BY DISK LASER

Miroslav Sahul, Milan Turňa, Martin Sahul
Slovak University of Technology in Bratislava; Faculty of Materials Science and Technology in Trnava; Paulínska 16, 917 24 Trnava, Slovak Republic

Keywords: laser welding, disk laser, AZ 31 magnesium alloy, AW 5754 aluminium alloy, intermetallic compounds

Abstract

The paper deals with the welding of dissimilar light metals by TruDisk 4002 disk laser. AZ 31 magnesium alloy with the thickness of 1.0 mm and AW 5754 aluminium alloy with the thickness of 1.5 mm were selected as materials to be welded. The dissimilar welded metals were arranged in the overlapped configuration. Magnesium alloy was selected as an upper plate because of higher absorption of laser radiation. Argon with 30 l/min flow rate was used as shielding gas. Different focusing of laser beam was employed in order to decrease the power density and thus eliminate cracking of produced welds. Welded joints were produced through conduction mode of laser welding. Analysis of the welded joints was carried out by light microscopy, microhardness measurement and EDX analysis. Presence of a hard and brittle intermetallic compounds was observed at the weld metal/aluminium alloy interface.

Introduction

Magnesium and aluminium alloys are being increasingly used in automotive industry especially due to low density in order to decrease total weight of car body and reduce CO_2 emissions [1-4]. Aluminium alloys are extensively utilised also in the aerospace and ship industries due to the convenient combination of mass reduction and high strength. Magnesium alloys are also very popular in the above-mentioned areas especially due to their low density and high specific strength. Welding dissimilar metals such as Mg alloys to Al alloys is more difficult, because of different properties of metals. The main issue encountered in the fusion welding of magnesium alloys to aluminium alloys is the formation of hard and brittle intermetallic compounds (IMC) degrading mechanical properties of dissimilar metals welded joints. The intermetallic compounds Al_2Mg_3, $Al_{12}Mg_{17}$ and $Al_{30}Mg_{23}$ could be formed [5-7] not only in arc welding processes, but also even in the laser beam welding characterised by high cooling rates, giving formation of brittle IMC [8].

Qi et al. performed hybrid laser tungsten inert gas (GTAW) welding technique of AZ31B magnesium alloy to 6061-T6 aluminium alloy in overlapped configuration. They employed mild steel foil as an interlayer material. Authors found, that the addition of Fe interlayer suppressed the formation of Mg - Al intermetallic compounds, but led to the formation of Fe - Al intermetallic compounds in the weld metal [9].

Borrisutthekul et al. found that the intermetallic layer formed near the interface between A5052-O aluminium alloy and AZ31B magnesium alloy significantly degraded the dissimilar metals welded joint strength. They investigated a possible method based on FEM analysis in order to suppress the IMC formation. They found, that the edge-line laser welding could carry out the shallow penetration depth of molten metal into lower plate, which would be effective for reducing the reaction between two metals and then the formation of intermetallic compounds [4]. F. Scherm et al. carried out laser welding of AZ31 magnesium alloy to AA5754 aluminium alloy using ZnAl filler metal. The strength of the joints was significantly affected by the content of aluminium in the filler metal. Authors concluded that the lower the weld penetration and the lower the Mg content in the welded joint, the higher the strength of welded joint. Strength of the joints produced by laser welding was comparable to that of the joints obtained by other joining techniques such as diffusion or adhesion bonding [5]. Many researchers are dealing with welding the above mentioned combination of metals by other welding techniques, especially solid state welding.

Yan et al. carried out dissimilar metals friction stir welding (FSW) of 5052 Al alloy to AZ31 Mg alloy. Sound welded joint was produced at tool revolutions of 600 rpm and welding speed of 40 mm/min. The maximum microhardness was measured in the weld nugget and was twice as higher as that of the base metals [10].

Kwon et al. conducted FSW of magnesium to aluminium alloy. Sound welds were successfully produced at the tool revolutions of 1000, 1200 and 1400 rpm. Authors concluded, that mixed microstructure of magnesium and aluminium alloys was formed near the interface. Weld appearance became smoother with the increasing tool revolutions [11].

Pandeli et al. utilised ultrasonic spot welding for joining mentioned combination of metals. They studied the interfacial reaction between AA6111 and AZ31 alloys. The thickness of reaction layer was 5 μm at the optimum welding conditions of 600 J (0.4 s). Interface liquation was also found for longer welding times at temperatures below the lowest eutectic reaction point in the Al - Mg binary system (Fig. 1) [12].

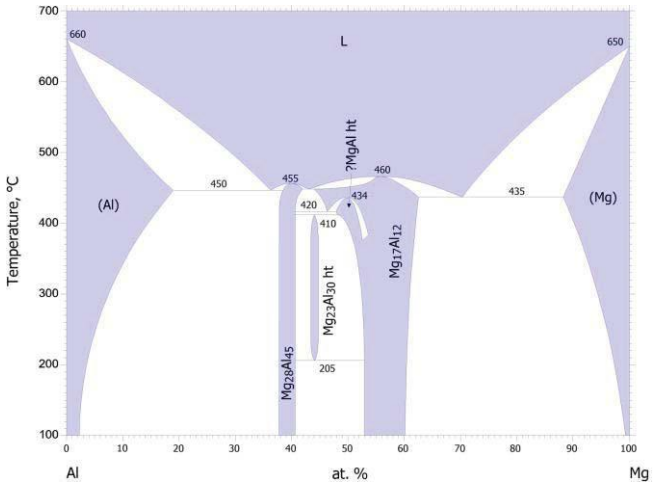


Fig. 1 Al - Mg binary system [13]

The aim of the paper is the production and subsequent study of the properties of dissimilar metals welded joints, which were made by disk laser.

Experimental

Magnesium alloy AZ 31 with the thickness of 1.0 mm and AW 5754 aluminium alloy with the thickness of 1.5 mm were suggested as materials to be welded. The dimensions of the sheets were 50 x 80 mm. Chemical composition of AZ 31 magnesium alloy and AW 5754 aluminium alloy is given in Tables 1 and 2. Weld surfaces were ground by 1200 grid emery paper in order to remove surface oxides. The proposed metals were degreased before welding. The materials were welded in overlapped configuration. Magnesium alloy AZ 31 was placed as the upper plate, because of higher absorptivity of laser radiation by the surface of magnesium alloy. TruDisk 4002 disk laser was used for production of dissimilar metals welded joints. The wavelength of laser radiation is $\lambda = 1.03$ µm. The maximum power of TruDisk 4002 laser is 2.0 kW. The welding parameters are given in Tab. 3. The laser radiation was transported from the source to place of technological processing via laser light cable with the diameter of Ø 400 µm.

Table 1 Chemical composition of AZ 31 magnesium alloy

Al	Zn	Mn	Mg
2.5 to 3.5	0.7 to 1.3	0.2 to 1.0	balance

Table 2 Chemical composition of AW 5754 aluminium alloy

Mg	Mn	Cu	Fe	Si	Cr	Zn	Al
2.6 - 3.6	0.5	0.1	0.4	0.4	0.3	0.15	balance

Focal distance of the used lens was 200 mm. Focusing optics D70 of TRUMPF Company was utilised. The optics was fixed on a 6-axis Fanuc Robot M710iC robotic arm. Argon with the flow rate of 30 l/min was used as shielding gas. After welding process, the welded joints were cut off. Cross-sections were prepared for metallographic analysis by common procedure. Etchant consisting of 5 ml acetic acid, 6 g picric acid, 10 ml water and 100 ml ethanol was used in order to reveal the structure of the welded joints. Light microscopy, microhardness measurements across AZ 31 magnesium alloy - weld metal - AZ 31 magnesium alloy and AW 5754 aluminium alloy - weld metal - AW 5754 aluminium and EDX analysis were used to study the produced welded joints.

Table 3 Parameters of welding dissimilar metals

Weld No.	Laser power [kW]	Focusing [mm]	Welding speed [mm/s]
1	1.0	+ 5	25
2	1.1	+ 5	25
3	1.2	+ 5	25
4	1.3	+ 5	25
5	1.4	+ 5	25
6	1.5	+ 5	25
7	1.6	+ 5	25
8	1.5	+ 6	20
9	1.5	+ 6	30
10	1.6	+ 6	20
11	1.8	+ 6	20

The macrostructures and microstructures of the welded joints were analysed by light microscopy. Microhardness was measured on Buehler IndentaMet 1100 equipment. Distance between the indents was 150 µm and 200 µm. The used load was 100 g acting during dwell time of 10 s. Microhardness HV was measured in two rows (i.e. two courses of microhardness were carry out per sample). EDX analysis was carried out in order to perform quantitative phase analysis in selected areas of the welded joints. Scanning electron microscope JEOL 7600 F fitted with EDX analyser from Oxford Instruments was used for EDX analysis.

Results

Different focusing of laser beam was employed for production of the welded joints. The tested focusing values ranged from 3 mm below the AZ 31 alloy surface up to 6 mm above the surface of Mg alloy. When the laser beam was focused directly onto the surface (position of the focus was on the surface) of AZ 31 magnesium alloy, the cracking of the welded joint was recorded (Fig. 2). In this case, the power density was too high and led to the formation of the welded joint cracking. Similar results were attained when the laser beam was defocused below the surface of Mg alloy. It was therefore necessary to decrease the power density.

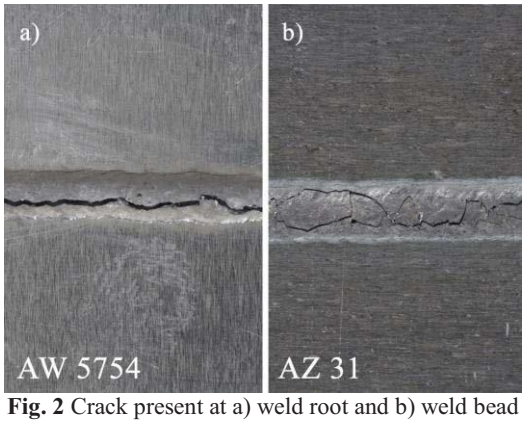


Fig. 2 Crack present at a) weld root and b) weld bead

One of the possible solutions of how to avoid this problem was to defocus the laser beam above the magnesium alloy surface. The mentioned defocusing of laser beam enabled to eliminate the cracks in the weld metal.

The macrostructure of selected dissimilar metals welded joint produced with the following welding parameters: laser power P = 1.8 kW, welding speed of 20 mm/s and focusing 6 mm above magnesium alloy surface is given in Fig. 3. Cracks were observed in the weld metal as well as at the weld metal - aluminium alloy interface (in the location of supposed IMC layer). The welded joints were produced in the conduction mode of laser welding. As can be seen from the macrostructure, the width of the welded joint is greater than its depth. The aspect ratio is thus lower than 1. This fact arises from defocusing the laser beam of the disk laser.

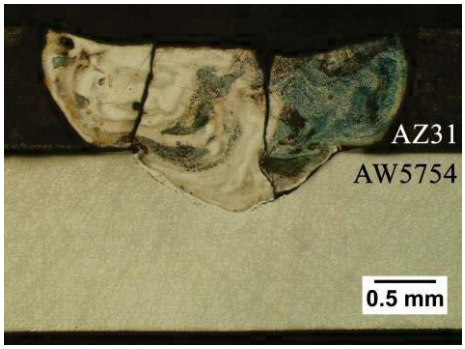


Fig. 3 Macrostructure of selected dissimilar metals welded joint (P = 1.8 kW, v = 20 mm/s, + 6 mm)

Decreasing the heat input (lowering of laser power and increasing the welding speed) enabled avoidance of cracks in the welded joint (Fig. 4). The thin layer consisting of supposed IMC was detected at the weld metal - AW 5754 aluminium alloy interface.



Fig. 4 Macrostructure of selected dissimilar metals welded joint (P = 1.5 kW, v = 30 mm/s, + 6 mm)

Weld width and weld depth were measured in ImageJ programme. Weld width of dissimilar metals welds was measured at the weld bead surface (i.e. at the surface of AZ 31 magnesium alloy). The dependence of the weld width on the laser power used suggests that the higher the laser power (at invariable welding speed of 25 mm/s and defocusing + 5 mm), the wider the welded joint, except for the welded joints produced by using laser powers of 1.1 and 1.6 kW (Fig. 5). The increased weld width is associated with the increased heat input. Similarly, the higher the laser power used in welding dissimilar metals, the deeper the penetration (Fig. 6). The full penetration of the upper plate was reached in all welded joints, a partial penetration occurred only in aluminium alloy. The full penetration of both metals occurred only in one case, at welding parameters: P = 1.8 kW, welding speed of 30 mm/s and defocusing + 3 mm. Such welding parameters resulted in cracking of the welded joint across the whole weld metal.

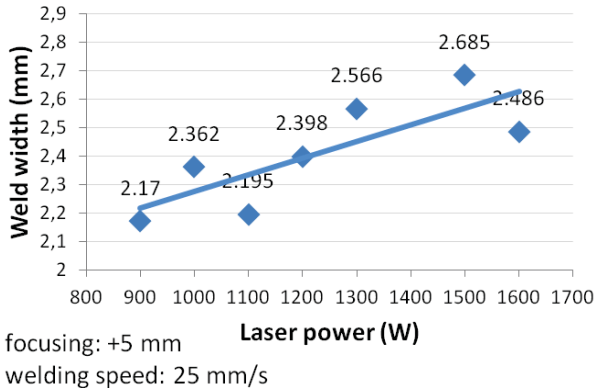


Fig. 5 Dependence of weld width on laser power used

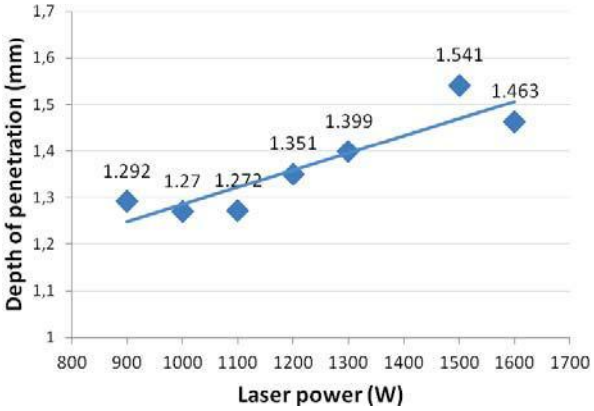


Fig. 6 Dependence of penetration depth on laser power (focusing: + 5 mm, welding speed v = 25 mm/s)

The microstructure of weld metal is given in Fig. 7. From the microstructure, it is evident that intermixing of both metals occurred. Areas of different chemical compositions are present in the weld metal. Heterogeneous character of the weld metal was proved.

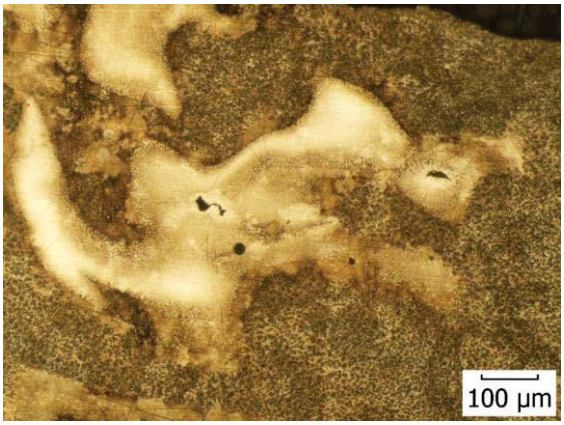


Fig. 7 Microstructure of weld metal (P = 1.3 kW, v = 25 mm/s, + 5 mm)

Weld metal - AZ 31 magnesium alloy interface is documented in Fig. 8. As it is obvious from this interface, intermixing of both metals occurred. Similar heterogeneous character of weld metal was observed in the case of all welding parameters used. A more

detailed view of the selected area in the weld metal is given in Fig. 9.

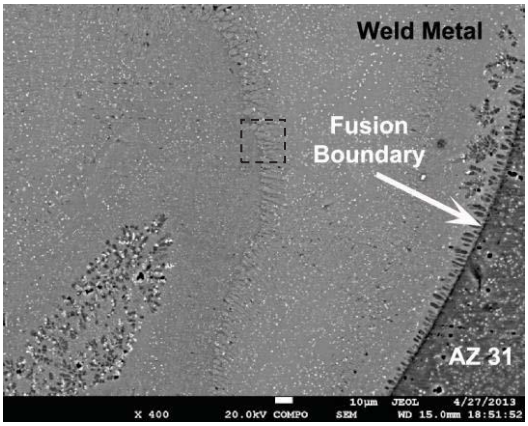


Fig. 8 Weld metal - AZ 31 alloy interface
(P = 1.6 kW, v = 20 mm/s, + 6 mm)

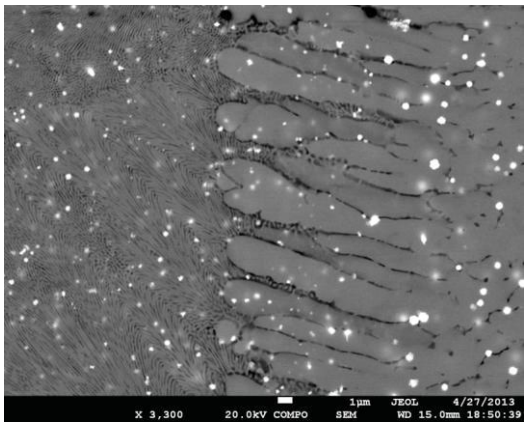


Fig. 9 Detailed view of weld metal
(P = 1.6 kW, v = 20 mm/s, + 6 mm)

The heterogeneous character of dissimilar metals welded joints was supported by the results of microhardness measurements. The course of microhardness HV across magnesium alloy - weld metal - magnesium alloy interface is shown in Fig. 10. The maximum microhardness was measured in the weld metal. The maximum measured value achieved 255.4 HV0.1.

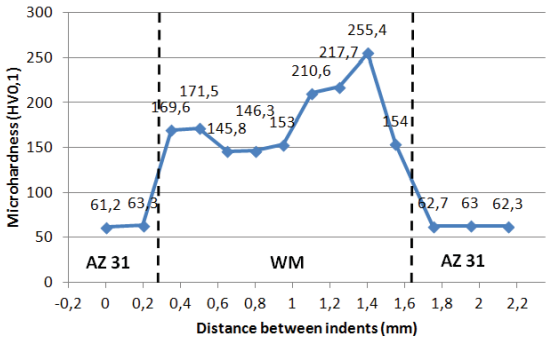


Fig. 10 Course of microhardness across the AZ 31 magnesium alloy - weld metal - AZ 31 magnesium alloy interface
(upper plate of weld No. 9)

Similarly, the highest value of microhardness was documented also by the measurements across the AW 5754 aluminium alloy - weld metal - AW 5754 alloy interface (Fig. 11). The maximum microhardness in the weld metal achieved the value of 181.4 HV0.1.

The microhardness measurements results suggest that in the locations characterised by the high microhardness increase, hard and brittle intermetallic compounds might be present.

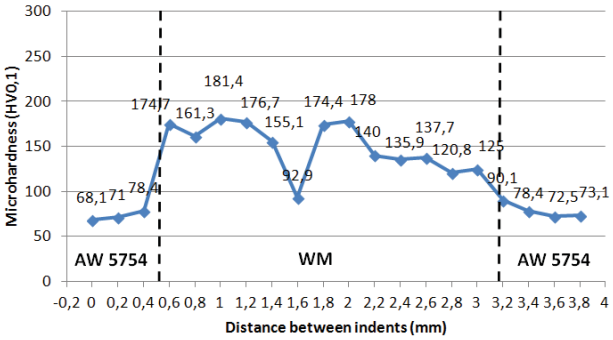


Fig. 11 Course of microhardness across the aluminium alloy - weld metal - aluminium alloy interface
(lower plate of weld No. 9)

Supposed IMC layer (Fig. 12) was recorded at the weld metal - aluminium alloy interface. The microhardness measurement performed directly on the site of IMC achieved 249.7 HV0.1. Results of the point EDX analysis on the site of presence of supposed IMC are given in Tab. 4.

Table 4 Chemical composition in selected areas of supposed IMC

Spectrum	Mg	Al	Mn	Fe	Zn
1	54.75	44.67	0.24	0.12	0.22
2	54.34	45.66	-	-	-
3	57.42	42.22	0.12	-	0.25

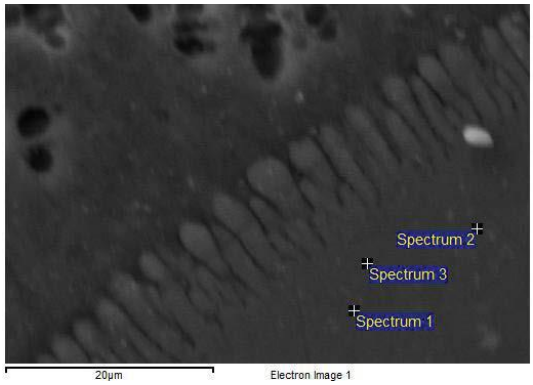


Fig. 12 EDX point analysis in proposed IMC layer
(P = 1.5 kW, v = 20 mm/s, + 6 mm)

Conclusion

Dissimilar metals welded joints were produced by using a disk laser. It was necessary to defocus the laser beam due to high power density, which resulted in the weld metal cracking. Positive defocusing (above Mg alloy surface) enabled elimination of the above-mentioned cracking. A welded joint without the presence of cracks was successfully produced under the following welding

parameters: P = 1.5 kW, welding speed of 30 mm/s and defocusing + 6 mm. Only welding of dissimilar metals with above mentioned parameters resulted in a crack free weld. The maximum microhardness was measured in the weld metal. The maximum measured value in the weld metal close to Mg alloy achieved 255.4 HV0.1. The maximum microhardness measured in the weld metal close to Al alloy attained 255.4 HV0.1 (the measurements were in that case performed across Al alloy - WM - Al alloy interface in lower plate of weld No. 9). The microhardness measurement performed directly on the location of IMC achieved 249.7 HV0.1. This microhardness is approximately 4 times higher than that of the base metals. Based on the analyses, it can be stated that IMC layer formed in the welding of Al alloy to Mg alloy, at the interface between the weld metal and Al alloy. EDX analysis results and the study of Al - Mg binary system suggest that the IMC layer is probably formed by $Mg_{17}Al_{12}$ phase.

Acknowledgement

The paper was prepared under the support of The Ministry of Education, Science, Research and Sport of the Slovak Republic Grant Agency VEGA and SAV, projects No. 1/2594/12 and 1/1035/12.

References

[1] TURŇA, M.: *Špeciálne metódy zvárania.* (*Special Welding Methods)*. Bratislava: ALFA, 1989. 384 p. ISBN 80-05-00097-9.

[2] L. KOLAŘÍK, K. KOVANDA, M. VÁLOVÁ, P. VONDROUŠ, J. DUNOVSKÝ: Hot Cracking T-Joint Weldability Test of Precipitation Hardenable Al alloy. *Annals of DAAAM for 2011 and Proceedings.* Vienna: DAAM International, 2011, p. 633 - 644. ISBN 978-3-901509-83-4.

[3] V. OSTRÁ, J. KUDLÁČEK: Effects of Post-Anodizing Treatments on Corrosion Resistence of AZ91 Alloy. *IN-TECH 2011.* Jaroměř: Kudláček Jan, Ing., 2011, p. 711-713. ISBN 978-80-904502-6-4.

[4] R. BORRISUTTHEKUL, Y. MIYASHITA, Y. MUTOH: Dissimilar Material Laser Welding between Magnesium Alloy AZ31B and Aluminum Alloy A5052-O. *Science and Technology of Advanced Materials* 6, 2005, p. 199 - 204.

[5] F. SCHERM, J. BEZOLD, U. GLATZEL: Laser Welding of Mg Alloy MgAl3Zn1 (AZ31) to Al Alloy AlMg3 (AA5754) using ZnAl Filler Material. *Science and Technology of Welding and Joining*, 2012, vol. 17, no. 5, p. 364-367.

[6] S. A. Khodir, T. Shibayanagi: Dissimilar Friction Stir Welded Joints between 2024-T3 Aluminum Alloy and AZ31 Magnesium Alloy. *Materials Transactions,* 2007, vol. 48, No. 9, p. 2501 - 2505.

[7] YAN Y., ZHANG Da. T., QIU Ch., ZHANG W.: Dissimilar Friction Stir Welding between 5052 Aluminum Alloy and AZ31 Magnesium Alloy. *Transactions of Nonferrous Metals Society of China 20,* 2010, p. 619 – 623.

[8] W.-S. Chang, S.R. Rajesh, Ch.-K. Chun and H.-J. Kim: Microstructure and Mechanical Properties of Hybrid Laser-Friction Stir Welding between AA6061-T6 Al Alloy and AZ31 Mg Alloy. *Journal of Material Science and Technology,* 2011, p. 199-204.

[9] X.-D. Qi, L.-M. Liu: Fusion Welding of Fe-added Lap Joints between AZ31B Magnesium Alloy and 6061 Aluminum Alloy by Hybrid Laser–Tungsten Inert Gas Welding Technique. *Materials and Design*, 2012, p. 436–443.

[10] YAN Y., ZHANG D.-T., QIU Ch., ZHANG W.: Dissimilar Friction Stir Welding between 5052 Aluminum Alloy and AZ31 Magnesium Alloy. *Transactions of Nonferrous Metals Society of China*, 2010, p. 619 - 623.

[11] KWON, Y. J., SHIGEMATSU, I., SAITO, N.: Dissimilar Friction Stir Welding between Magnesium and Alloys. *Materials Letters*, 2008, vol. 62, p. 3827 - 3829.

[12] A. Panteli, J. D. Robson, I. Brough, P. B. Prangnell: The Effect of High Strain Rate Deformation on Intermetallic Reaction during Ultrasonic Welding Aluminium to Magnesium. *Materials Science & Engineering A*, 2012, p. 31 - 42.

[13] Pauling Files Binary Edition.

[14] ŠÚTOVEC, M.: *Zváranie laserom Mg zliatin s Al zliatinami. (Laser Beam Welding of Mg Alloys to Al Alloys).* Thesis, Trnava, 2012.

Magnesium Technology 2014
Edited by: Martyn Alderman, Michele V. Manuel, Norbert Hort, and Neale R. Neelameggham
TMS (The Minerals, Metals & Materials Society), 2014

DESIGN OF BINARY ZINC-BASED SOLDER FOR JOINING Mg ALLOY TYPE AZ 31B

Miroslav Jáňa[1], Milan Turňa[2] Milan Ožvold[3]

[1] Slovak University of Technology in Bratislava, Faculty of Materials Science & Technology in Trnava, Paulínska 16, 917 24 Trnava, Slovak Republic

[2] Slovak University of Technology in Bratislava, Faculty of Materials Science & Technology in Trnava, Paulínska 16, 917 24 Trnava, Slovak Republic

[3] Slovak University of Technology in Bratislava, Faculty of Materials Science & Technology in Trnava, Paulínska 16, 917 24 Trnava, Slovak Republic

Keywords: metallurgical joining, solder, flux, Mg alloy, intermetallic phase

Abstract

The aim of article is to design a brazing alloy and flux for brazing magnesium alloy type AZ 31B, to fabricate brazed joints and to assess their quality. The brazing alloy and flux were designed on the basis of knowledge attained from the study of literature and information from technical practice. Regarding the fact that it was impossible to get more detailed information mainly about the chemical composition of brazing alloys and fluxes for brazing Mg alloys, it was finally decided that the brazing alloy and the flux would be designed in our laboratories. Joint quality was assessed by light microscopy, microhardness measurement, EDX microanalysis and analysis of fractured surfaces.

Introduction

Importance of magnesium and its alloys is significantly increasing in recent years, since the demands on mass of structure are ever growing, mainly in the automotive and aviation industries. In 2005 Mg comprised 3 % of the total weight of a personal car, whereas it is supposed that this proportion would grow up to 8 even 10 %[1] up to 2015. With growing utilisation of Mg and its alloys also search for a suitable way of joining these materials has become more topical. One of possibilities seems to be brazing. Regarding low melting temperatures of Mg alloys (max 650 °C), the brazing alloy type B-Mg-1 (MgAl9Zn2Mn0,1 + 0.00005Be; 605 to 615 °C) - by its composition close to AZ 92A alloy, is used and also brazing alloy type B-Mg-2 (MgAl12Zn5 + 0.0005Be; 570 to 595 °C) - close to AZ 125A alloy. Application of other filler metals, based on MgAlZn, which exert lower brazing temperature is investigated. The Mg alloys are loosing their mechanical properties under the effect of temperatures which are usually used at brazing. The AZ 31B alloy considerable looses its mechanical properties during brazing at temperature 595 °C, namely 8 % from the tensile strength and 35 % from ductility. The mentioned loss of mechanical properties is the main reason for use of low-melting-point brazing alloys[2, 3, 4, 5].

The authors [6,15, 16, 17, 18] were dealing with a flux-free method of brazing Mg alloy type AZ 31 in furnace with brazing alloys based on Al95Zn, Mg41,8Zn, Mg51,3Zn, Mg63Zn and pure Zn. Tensile strength of brazed joint attained the value of 71 MPa.

Authors [9, 10, 12, 12, 13, 14] have investigated the effect of ZnMgAl based brazing alloy (Zn53,1Mg43,6Al3,3) on brazing Mg alloy type AZ 31B. Brazing was performed in an induction furnace in shielding atmosphere of Ar. The flux type QJ201 (KCl 50 %, LiCl 32 %, NaF 10 %, $ZnCl_2$ 8 %) in form of powder was used. Brazing lasted 120 s at temperature 520 to 550 °C. The results have shown that a solid α-Mg phase and eutectoid α-Mg + MgZn phases were formed in the brazed zone. Microhardness of α-Mg phase represented the value 81 HV and MgZn phases attained 130 HV.

Characteristic of brazed material

The Mg alloy type AZ 31B in form of rolled sheet, showing good plastic properties and machine-ability was used for experiments. It is not heat treated since it is not hardenable. Brazeability in case of application of suitable atmosphere, and/or vacuum (GTAW, EBW, LBW) is not limited. Application of an inert atmosphere (Ar, He) is recommended for brazing. High thermal conductivity of Mg alloys may cause excessive grain coarsening during brazing at higher temperatures. This results in formation of stress field which may lead to distortion of brazed joint[7, 8]. Chemical composition, physical and mechanical properties are given in Tables 1, 2, 3.

Tab. 1 Chemical composition of Mg alloy type AZ 31B[1]

Elements	Al	Mn	Zn	Si	Fe	Mg
Wt. %	2.5 - 3.5	0.4	0.6 - 1.4	0.1	0.005	Bal.

Tab. 2 Mechanical properties of Mg alloy type AZ 31B[1]

Ultimate strength	244 MPa
Elongation	15 %
Hardness	41 HV
Tensile strength	290 MPa
Fatigue strength	97 MPa
Yield point	221MPa
Young's modulus	45 GPa

Tab. 3 Physical properties of Mg alloy type AZ 31B[1]

Density	1.77 $g.cm^{-3}$
Melting point	605 to 630 °C
Boiling temperature	1090 °C
Thermal conductivity	96 $W.m^{-1}.K^{-1}$
Electric resistance	0,274 μΩ.m
Thermal capacity	960 $J.kg.K^{-1}$

Design of brazing alloy

Concept of solder design is based on Zn with Al addition. Selection of a suitable composition of brazing alloy should take into account the conditions in the ternary Mg-Al-Zn phase diagram. At the same time it is also necessary to consider the dependence of proportion of Al to increased Zn content, regarding the formation of close-to-eutectic alloy. A slight increase in Zn

content is aimed at enhancing the disruption of oxide layer on the surface of brazed material, so that the brazing time would be speeded up, number of defects in brazed joint would be reduced and also the joint strength[2,3] would be increased. Zn content (about 1 %) is typical for most used brazing alloys. At 5% Al content, an eutectic composition is attained. By phase diagram, the melting temperature of the designed brazing alloy is 382 °C. With such a melting point the designed ZnAl5 brazing alloy may be ranked among the solders. Zinc and Al are also available for low price so that also commercial use of the designed solder is supposed. Formation of two low-melting-point eutectics at temperatures 340 and 364 °C respectively can be seen in the phase diagrams. Local melting down of Mg alloys does not yet occur at these temperatures, what in combination with Zn makes it for an interesting brazing addition to Mg alloys with a high content of Al[2]. The solder was melted in induction vacuum furnace (Fig.1), to prevent its oxidation.

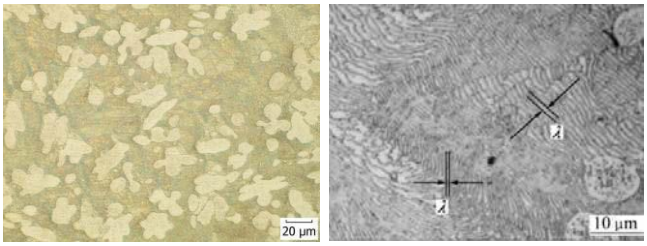


Fig. 1 Vacuum furnace with induction heating

The resultant microstructure of eutectic solder (Fig. 2a) was formed of a primary solid solution rich in β-Zn and a lamellar eutectic structure of Zn-Al (Fig. 2b). The average inter-lamellar distance was 0.5 to 1.5 µm.

Flux selection

The most efficient flux for brazing Mg alloy type AZ 31B is based on $CaCl_2$, KCL, LiCl, NaCl chlorides in different proportions. The main additions as Ca and Li exert considerable capacity to reduce the oxides formed on the surface of base metal during heating in the air. The flux wets the surface of base metal at 30 to 50 °C below the melting point of the designed solder, in order to remove the surface oxides. Two-component flux composed of LiCl + KCl, in proportion adapted to melting temperature of the designed solder (380.5°C) was selected. Eutectic composition of the flux with melting point 353 °C was designed by use of LiCl - KCl phase diagram in order that it would be suitable for brazing with an eutectic alloy type ZnAl5. The flux was dried in oven at temperature 80 °C /1h. However, no complete drying was attained at this temperature, since LiCl has bound atmospheric humidity on itself. The flux remained in the form a crystalline humid snow. Prior to use, the flux was dried up in an oven at temperature 200 °C and the flux crystals were crushed after drying.



a) b)

Fig. 2 Designed AlZn5 solder; a) microstructure; b) lamellar structure[15]

DSC analysis (Fig. 3) has proved that the solder had eutectic composition with melting point 380.5 °C.

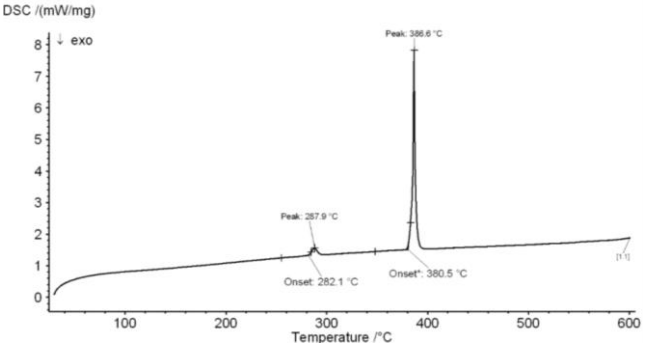


Fig. 3 DSC analysis of ZnAl5solder

Parameters and conditions of brazing

The overlapped joints of Mg alloys were fabricated in a muffle furnace without protective atmosphere. Oxide film was removed by immersion of specimens into 10 % HCl for 2 min. Brazing was performed at temperatures 420 to 430 °C for the time 3, 5 and 7 min. Reaction temperature of the flux and solder, together with brazing temperature is documented in Fig. 4.

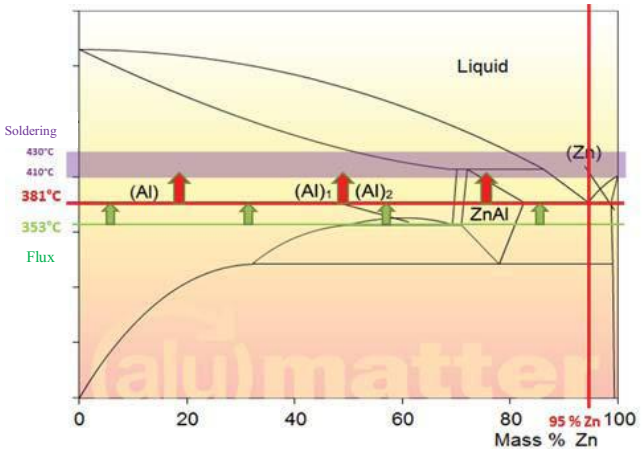


Fig. 4 Illustrated brazing temperatures in phase diagram Al-Zn; green - zone of flux activation, red - start of solder melting, violet - brazing zone

Quality assessment of brazed joints

Soldered joints were assessed by light microscopy (Fig. 5), EDX microanalysis (Fig. 6, 7), microhardness measurement (Fig. 8) and fractography of fractured surfaces (Figs. 9, 10).
Light microscopy has proved that Mg alloy type AZ 31B preserved its polyhedral character. Width of diffusion zone was about 7 μm. Formation and growth of intermetallic phases was observed on solder boundary with the parent metal. Intermetallic phases grew towards the solder. According to the phase diagrams, the $Mg_{17}Al_{12}$ and Mg_7Zn_3 phases are concerned, which are formed by eutectic reaction at cooling down from the melt. Growth of intermetallic phases (about 15μm) along the boundary with parent metal resulted in joint embrittlement. The brazed joint was formed of ternary eutectic structure $Mg_{32}(Zn, Al)_{49}$ and oversaturated solid solution α - Mg containing Zn and Al.

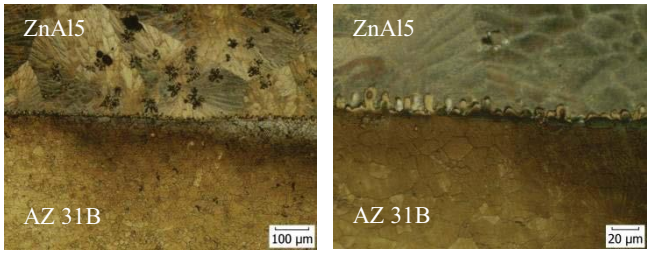


Fig. 5 Microstructure of solder - substrate boundary

EDX microanalysis has shown that the chemical composition in the boundary zone of brazed joint is in the following proportions: Mg 81.8 %, Al 2.47 %, Zn 15.73 %. Compared to initial brazing alloy with Zn 95 % and Al 5 % it is evident that the AZ 31B alloy was strongly diluted into molten solder. This resulted in increased Mg content in the brazed zone.

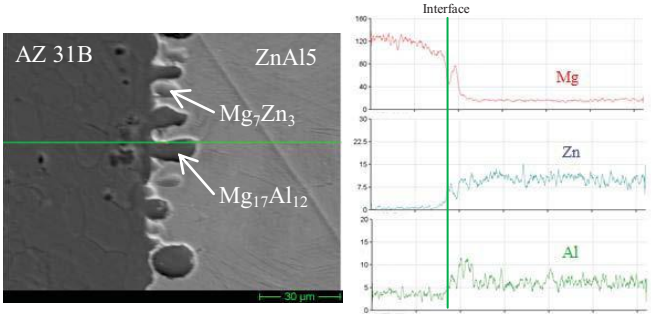


Fig. 6 Line analysis and Mg, Zn, Al profiles through the solder - substrate boundary

According to Al - Mg phase diagram, α-Mg solid solution is formed from the melt by isomorphic transformation. The β-$Mg_{17}Al_{12}$ phase is segregated by eutectic reaction at cooling down below 430 °C. Chemical composition of eutectic constituents in the solder is formed by oversaturated solid solution of Mg with Zn and Al admixtures. The melt is changed to Mg_7Zn_3intermetallic phase and α-Mg solid solution by eutectic reaction at 340 °C. The resultant structure of brazed joint is formed of eutectic ternary structure $Mg_{32}(Zn,Al)_{49}$ and α-Mg solid solution containing Zn and Al elements. On solder - substrate boundary, the $Mg_{17}Al_{12}$ and Mg_7Zn_3 intermetallic phases occur.

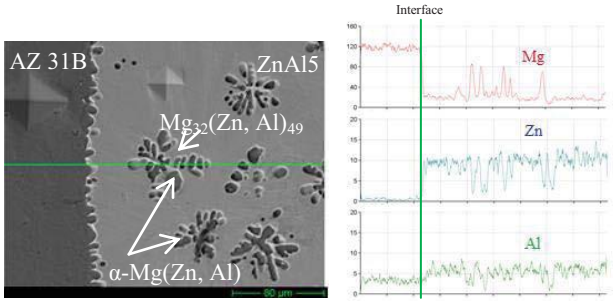


Fig. 7 Line analysis and Mg, Zn, Al profiles through the solder - substrate boundary

Solder had increased microhardness compared to parent metal. The significant difference in microhardness of parent metal, intermetallic phase and the solder is evident, what may be the cause of joint embrittlement. The hardness value in $Mg_{17}Al_{12}$ intermetallic phase attained 272 HV and the hardness value measured in the solder was 160 HV.

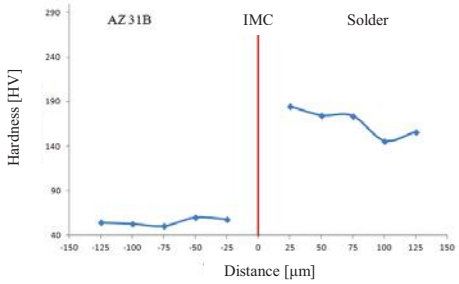


Fig. 8 Microhardness course through the solder - substrate boundary

The fractured surfaces of brazed joints were assessed by fractographic analysis. The cracks and porosity on major part of fractured surface were observed. It was proved that fractured surface was formed of oxides. Percentual content of elements on the observed area was in proportion 39 % O_2 and 25 % Mg what suggested to MgO oxide. Oxides were probably formed by a long heating without application of protective atmosphere. Also flux residues were observed in the form of K (15.08 %) and Cl (19.36 %) elements. From the mentioned facts it can be concluded that the flux residues were not completely forced out from the joint. At a detailed magnification, the growth of β-Zn dendrites was observed on the void wall in the solder. High content of MgO oxides, flux presence on the fractured surface, solder porosity and growth of $Mg_{17}Al_{12}$ intermetallic phase have significantly affected the resultant mechanical properties of the joint.

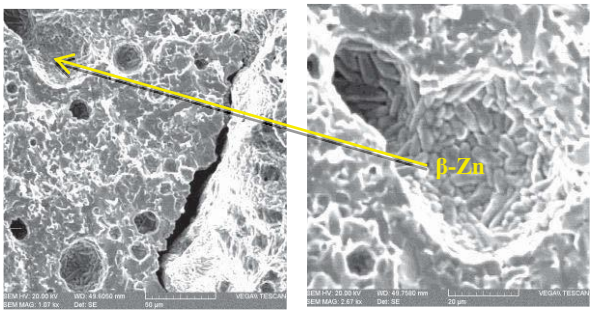


Fig. 9 β-Zn dendrites in ZnAl5 solder

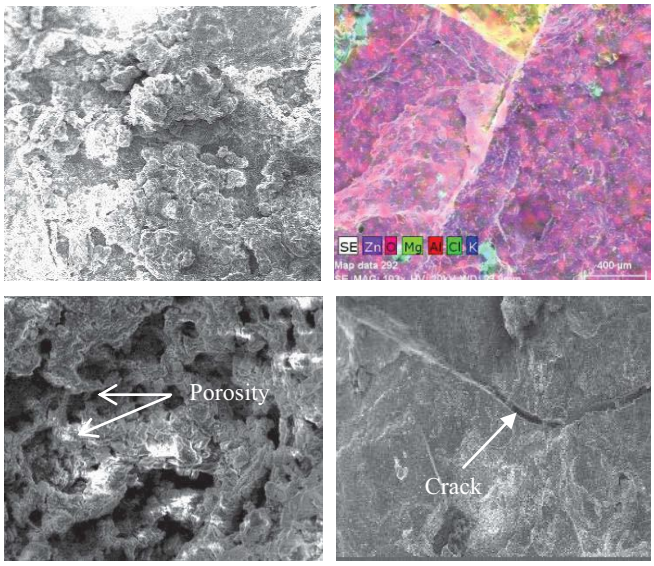


Fig. 10 Fractography of fractured surface: a) oxide layer; b) occurrence of flux residues; c) solder porosity; d) crack occurrence in the solder

Conclusions

Both, solder and flux were selected on the basis of chemical composition of Mg alloy type AZ 31B and its surface oxide. The eutectic solder ZnAl5 was melted by induction heating in the shielding atmosphere of Ar. Resultant microstructure of the solder was formed of primary solid solution rich in β-Zn phase with a dendritic structure. The eutectic composition of flux with melting temperature 353 °C, suitable for brazing with eutectic solder type ZnAl5 was designed on the basis of LiCl - KCl phase diagram. The brazing properties of solder and flux were tested in muffle furnace. Sound metallurgical joints were fabricated at temperature 430 °C for the time of 5 min.. The resultant structure of brazed joint is formed of $Mg_{32}(Zn,Al)_{49}$ ternary structure and α-Mg solid solution containing Zn and Al elements. The $Mg_{17}Al_{12}$ and Mg_7Zn_3 intermetallic phases occurred on the solder – substrate boundary. $Mg_{17}Al_{12}$ intermetallic phase attained the hardness value of 272 HV and the Mg_7Zn_3 phase attained the hardness of 311.4 HV. The fractured surface of brazed joint was formed of oxides. Percentual content of elements in these oxides was in proportion 39 % O_2 and 25 % Mg, what suggested to MgO oxide. Based on the achieved results, it can be concluded that the problem of future will not consist in design of the solder, but rather in selection of a suitable flux for an actual oxide on the surface of Mg alloy.

Acknowledgment

This contribution is a part of GA VEGA project of SR Ministry of Education, Science, Research and Sport of the Slovak Republic, No. 1/2594/12 - Study of Metallurgical Joining and other Technological Processes Applied for Processing the Magnesium and other Light Alloys by Progressive and Environment-friendly Technologies.

References

1. Hirsch, J., Al-Samman, T., 2013. *Superior light metals by texture engineering: Optimized aluminium and magnesium alloy for automotive applications*. In: ELSEVIER, Acta Materialia 61, pp. 818-843
2. Mordike, L., Wiesner, P., 2005. *Fügen von Magnesiumwerkstoffen*. Hardcover DVS - Verlag für Schweißen und verwandte Verfahren, p. 232, ISBN 978-3-87155-199-4
3. Beneke, H., 2000. *Lexikon der Korrosion und des Korrosionsschutzes*. Vulkan-Verlag. p. 259, ISBN 978-3-8027-2918-8
4. Rosin, J., 2011. *Löten von Magnesiumwerkstoffen*.Verlag: Dr. Hut, p. 160, ISBN-10: 3868538852,
5. Friedrich, H., Mordike, L. B., 2004. *Magnesium technology*. Springer - Verlag Berlin Heidelberg, p. 500, ISBN 10: 3540205993
6. Matsuda, N., Ishikawa, T., 2007. *Hart- und Hochtemperaturlöten und Diffusionsschweißen.* DVS-Verlag, p. 419, ISBN 978-3-87155-799-6
7. Kopeliovich, D., 2007. *Brazing magnesium alloys and magnesium matrix composites.*[on-line]. [cit. 2013-07-04], http://www.substech.com/dokuwiki/doku.php?id=brazing
8. Watanabe, T., Komatsu, S., Oohara, K., 2005. *Development of flux and filler metal for brazing magnesium alloy AZ 31B*. In: Welding Research, WELDING JOURNAL, pp. 37-40.
9. Ma, L., He, D. Y., Li, X. Y., Jiang, J. M., 2010. *High-frequency induction soldering of magnesium alloy AZ31B using a Zn-Al filler metal*. In: Materials Letters 64, pp. 596-598
10. Ma, L., He, D., Li, X., Jiang, J., 2011.*Characterization of high-frequency induction brazed magnesium alloy joint with an Al-Mg-Zn filler metal.* In: Journal of Materials Engineering and Performance, Vol. 20, pp. 219-222
11. Ma, L., Qiao, P., Long, W., He, D., Li, X., 2012. *Interface characteristics and mechanical properties of the induction brazed joint of magnesium alloy AZ31B with an Al-based filler metal.* In: Materials and Design 37, pp. 465-469
12. Ma, L., Long, W., Qiao, P., He, D., Li, X., 2013. *Development of a binary Zn-based solder alloy for joining wrought magnesium alloy AZ31B.*In: Journal of Materials Engineering and Performance, Vol. 22, pp. 118-122
13. Czerwinski, F., 2011. *Welding and joining of magnesium alloys.* Magnesium alloys - Design, Processing and Properties, pp. 470-490, ISBN: 978-953-307-520-4
14. Shapiro, A. E., 2005. *Brazing magnesium alloys and magnesium matrix composites.* Welding Journal, Vol. 84 Issue 10, p. 33, ISBN: 18530213
15. Yong, Q. CH., Zhen, H. CH., Wei, J. X., 2007. *Effect of crystal orientation on the ductility in AZ31 Mg alloy sheets produced by equal channel angular rolling*. Journal of Materials Science, Vol. 42 Issue 10, p. 3552
16. Sato, Y. S., Park, S. H. C., Matsunaga, A., Honda, A.,Kokawa, H., 2005. *Novel production for highly formable Mg alloy plate*. Journal of Materials Science, Vol. 40 Issue 3, p. 637
17. Spigarelli, S., Evangelista, E., El Mehtedi, M., Balloni, L., 2007. *Mechanical and microstructural aspects of high temperature formability of AZ31 sheets*. AIP Conference Proceedings, Vol. 907 Issue 1, p. 1305
18. Shamsi, M., Hanzaki, A., Zarei, N. H.,2007. *An Investigation to double hit deformation behavior of AZ31 magnesium alloy.* AIP Conference Proceedings, Vol. 907 Issue 1, p. 1301
19. Leškanič, M., 2013. *Proposed solder for soldering of Mg alloys*. DT, Trnava, p. 83

Magnesium Technology 2014
Edited by: Martyn Alderman, Michele V. Manuel, Norbert Hort, and Neale R. Neelameggham
TMS (The Minerals, Metals & Materials Society), 2014

FRICTION STIR WELDING OF MAGNESIUM ALLOY TYPE AZ 31

Tomáš Kupec, Mária Behúlová, Milan Turňa, Miroslav Sahul

Slovak University of Technology in Bratislava, Faculty of Materials Science & Technology in Trnava, Paulínska 16, 917 24 Trnava, Slovak Republic

Keywords: friction stir welding, magnesium alloy, simulation, quality control

Abstract

The paper deals with welding of Mg alloy of the type AZ 31 by Friction Stir Welding technology (FSW). The FSW technology is at present predominantly used for welding light metals and alloys, as aluminium, magnesium and their alloys. Experimental part consists of performing the simulation and fabrication of welded joints on a new-installed welding equipment available at the Welding Research Institute - Industrial Institute of SR Bratislava. Welding tools made of tool steel type H 13 were used for welding experiments. Geometry of welding tools was designed on the base of literature knowledge. Suitable welding parameters and conditions were determined using numerical simulation. Main emphasis was laid upon the tool revolutions, welding speed and tool bevel angle. The effect of welding parameters on the quality of welded joints was assessed. Assessment of welded joints was carried out by radiography, light microscopy, hardness measurement and EDX microanalysis. Static tensile test was employed for mechanical testing.

Introduction

As well known, the Friction Stir Welding (FSW) process is defined as solid state welding at heating. The FSW method was invented by Thomas Wayne [1] at TWI (The Welding Institute) Abington in 1991. The first patent describes this technology as: „a way of joining parts, defining a common zone without occurrence of relative motion of parts welded". Heating at FSW process takes place owing to friction and plastic strain of welded metals. Principle of welding by FSW process consists in the fact that a rotating tool with especially designed tip (in literature called as „pin") is impressed into the boundary of parts welded [2-4], see Fig. 1. At FSW process, the transfer of mechanical energy to heat occurs.

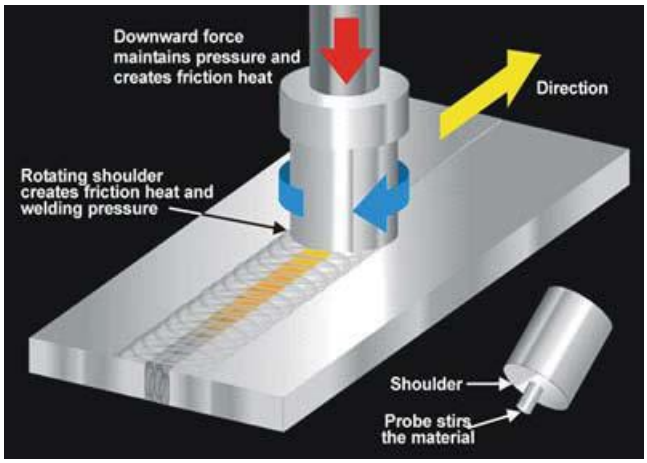


Fig.1 Principle of welding by FSW process [5]

The main welding parameters are as follows: downward force, tool revolutions and welding speed. The tool bevel angle represents also an important parameter.
The FSW process offers a number of metallurgical and environmental merits, when compared to fusion welding technologies. No filler metal is needed for FSW process. Welding of light alloys by FSW process is utilised mainly in the transport technologies (aviation, automotive and other industries) [6]. One of the most efficient ways of utilisation of computer technology for the support in application of advanced technologies consists in simulation.
The purpose of welding process simulation is to shorten the time needed for the determination of welding parameters and conditions without costly fabrication of actual welds. At simulation, the real system is replaced with a computer model.
A number of experiments may be performed via computer model, to assess them, analyse, optimise, repeatedly solve and subsequently apply to a real system [7]. Simulation is a suitable means also from the financial viewpoint: the costs for realisation of individual experiments may be higher than the price of a proper simulation program.

Welded material

The Mg alloy type AZ 31, 6 mm in thickness was selected as welded material. Magnesium alloy type AZ 31 exerts a good plastic properties and toughness and it is suitable for welding. It is typical with increased ductility and fracture toughness. However, this alloy is susceptible to corrosion in a wet environment and in environments containing the chlorides.
Microstructure of the base metal is formed of solid solution δ (solid solution of Al in Mg) and intermediary phase γ ($Mg_{17}Al_{12}$) [8]. The chemical composition, mechanical and physical properties of Mg alloy type AZ 31 are given in Tables 1, 2 and 3.

Table 1 Chemical composition of Mg alloy type AZ 31 [9]

Elements	Al	Zn	Mn	Si	Fe	Mg
wt.%	2.5 to 3.5	0.6 to 0.4	0.4	0.1	0.005	Bal.

Tab. 2 Mechanical properties of Mg alloy type AZ 31 [10]

Ultimate tensile strength	244 MPa
Elongation	15 %
Hardness	41 HV
Tensile strength	290 MPa
Fatigue strength	97 MPa
Yield point	221MPa
Young's modulus	45 GPa

Tab. 3 Physical properties of Mg alloy of the type AZ 31 [10]

Density	1.77 g.cm^{-3}
Melting point	605 - 630 °C
Boiling point	1090 °C
Thermal conductivity	96 W.m^{-1}.K^{-1}
Electrical resistance	0.274 μΩ.m
Heat capacity	960 J.kg^{-1}.K^{-1}

Welding equipment

Experimental works were performed on experimental equipment type FSW - LM - 060 constructed by CFSW company from China, installed at the Welding Research Institute – Industrial Institute of Slovakia, (VUZ - PI SR) Bratislava. The equipment proper consists of the basic carrying structures, welding head, working table and control panel, see Fig. 2.



Fig. 2 Welding equipment of the type FSW – LM - 060

Welding tools

The welded joints were fabricated by use of welding tools made of tool steel type H 13 (EN ISO X40CrMoV5-1). This tool steel is wear resistant, showing high strength and increased toughness. It is also fatigue resistant. Three welding tools were used for fabrication of welds with pin bevel angles 20°, 15° and 6°. The tools used for welding Mg alloy type AZ 31 are shown in Fig. 3.



Fig. 3 Welding tools with different pin geometry
a) 20˚, b) 15˚, c) 6˚

Numerical simulation

In the first step of numerical simulation, the simulation model was developed including geometrical model, material properties, loading, boundary and initial conditions. For the model creation, three program codes were applied: Solid Works [11] for preparing CAD models of tools, ANSYS [12] and DEFORM 3D [13] for modelling and FEM analysis of the process of welding. Welding tools were scanned, CAD models generated by Solid Works program and imported to the FE codes. Geometrical model of welded materials consists of two plates with dimensions of 300x150x6 mm. Due to the symmetry of welded plates, only one half of the model was taken into account in numerical simulation with the symmetry plane xz in the middle of the weld joint. Finite element mesh was generated in the program code ANSYS. The mesh density was governed by applied loading, contact conditions and supposed temperature and stress-strain distribution. Mechanical and thermal properties of H13 tool steel and Mg alloy of the type AZ 31 were considered to be temperature dependent. Material models were developed based on the computation of material properties using the software JMatPro [14]. The applied loading corresponds to the suggested parameters of welding, i.e. welding speed, rotations and downward force. The plates were fixed according to real fixation of plates during welding (Fig. 2). The heat transfer from the welded plates to the surroundings by the mechanisms of convection and radiation was taken into account.

The initial computations were performed by the program code DEFORM 3D which is more suitable for modelling of contact and deformation processes. However, according to the complexity of the simulation model the in the DEFORM 3D code was extremely time demanding. In this reason, after the reaching the quasi-stationary regime the computed loadings were imported to the program code ANSYS to analyse in detail the transient stress-strain and temperature fields during friction stir welding.

To illustrate the temperature fields computed by the program code DEFORM 3D, the temperature distribution in the plate after tool immersion to the plate material is shown in Fig. 4.

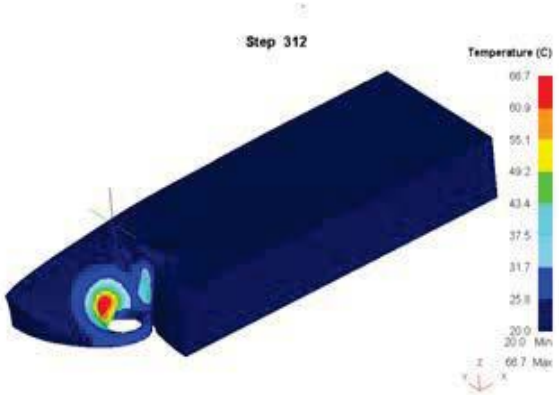


Fig. 4 Thermal field in welded plate illustrating the preferential heat generation on the recede side of creating weld joint

The results from numerical simulation of FSW process by the program code ANSYS in the form of thermal fields after tool immersion in the time of 184 s, 300 s and after finishing of the welding process in the time of 422 s are shown in Figs. 5, 6 and 7, respectively. The maximum temperatures were computed on the recede side of the weld joint at the level of 505 ˚C (Fig. 5-7).

The simulations in DEFORM 3D revealed that the welding tool gradually displaces the material under the tool shoulder. Subsequently, the material is pressed under the tool shoulder. The generated heat is concentrated on the recede side of the weld joint (Fig. 4) resulting in the temperature distribution in the welded material during the process.

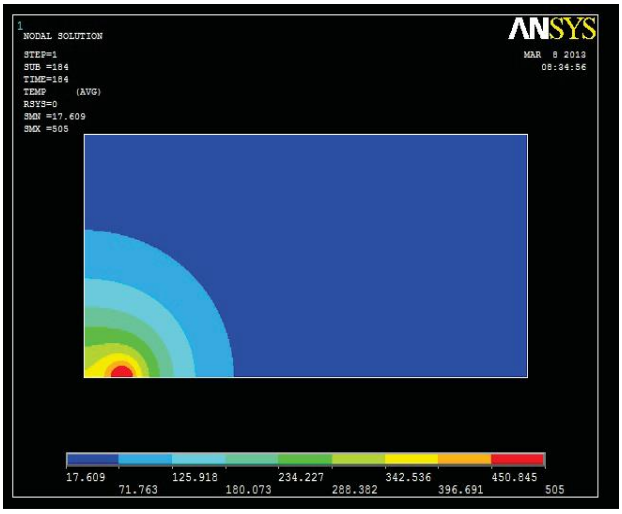


Fig. 5 Thermal field after tool immersion

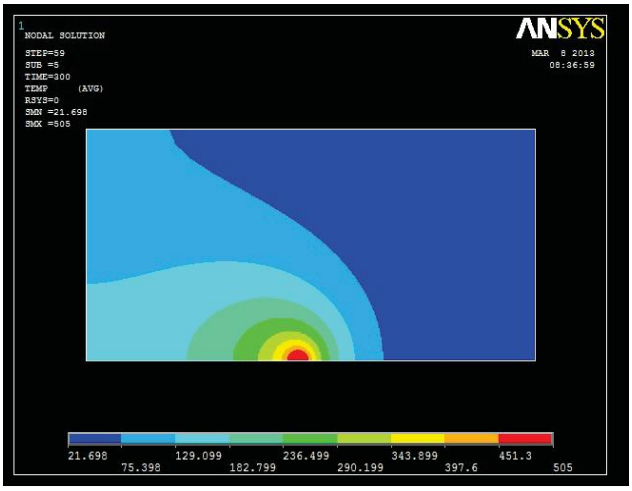


Fig. 6 Thermal field in time 300 s.

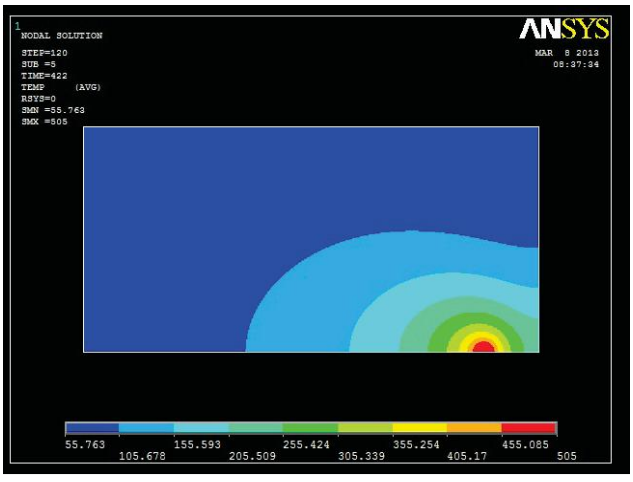


Fig. 7 Thermal field after end of welding in time 422 s.

The results of numerical simulations were verified by temperature measurement during the FSW process. Very good agreement was observed comparing the calculated and measured temperatures.

To determine suitable parameters for FSW welding process, the following simulations and analyses of thermal and stress-strain fields were performed using different parameters of welding. Based on the results of numerical simulation the following welding parameters were suggested for the experimental friction stir welding of plates from Mg alloy of the type AZ 31: tool revolutions from 400 rpm to 600 rpm and welding speed from 40 mm/min to 120 mm/min by the loading force of 35 kN and the bevel angle of 3°.

Experimental

Different welding parameters according to the results of numerical simulation were used for experimental welding. A sound welded joint was fabricated with the following parameters: tool revolutions of 600 rpm and welding speed of 60 mm/min.

The produced weld joints were assessed by light microscopy, microhardness measurement, EDX microanalysis and static tensile test.

The weld joint fabricated by the above mentioned welding parameters is shown in Fig. 8. The macrostructure of the weld joint is illustrated in Fig. 9. The weld joint consists of stir zone (SZ) and thermo-mechanically affected zone (TMAZ) surrounded by the based material (BM). Fig. 10 documents the gradual microstructure refinement from the based material through the thermo-mechanically affected zone the stirred zone. The measured microhardness values varied from 59 HV to 65 HV. Lower microhardness values were measured in the stirred zone, when compared to values in the zone of base metal. Approximately similar microhardness values were measured in TMAZ zone.

EDX microanalysis has shown several compounds in TMAZ, which were introduced to structure during casting. They were subsequently mixed with the base metal.

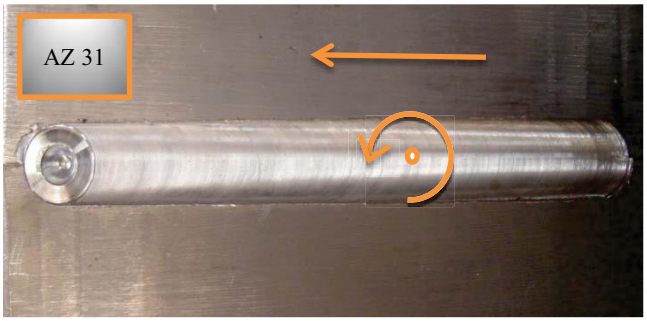


Fig. 8 Welded joint of Mg alloy type AZ 31

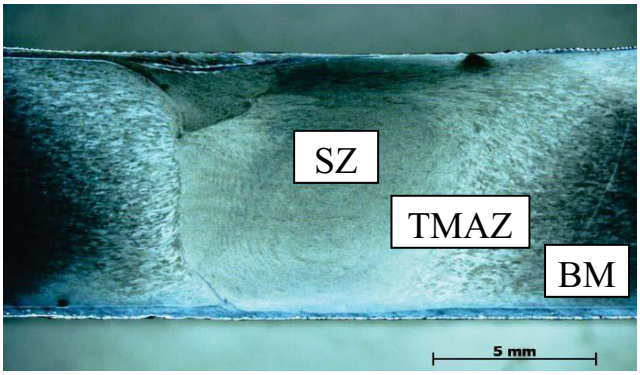


Fig. 9 Macrostructure of weld joint

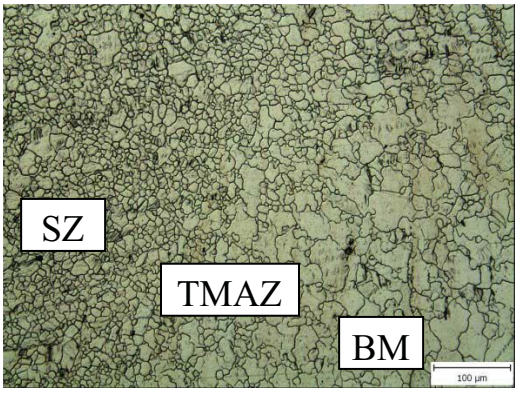


Fig. 10 Microstructure of weld joint (boundaries between the stirred zone, TMA zone and based material)

For evaluation of the mechanical properties of the weld joint, the static tensile test was performed. The test specimens used for testing are shown in Fig. 11.

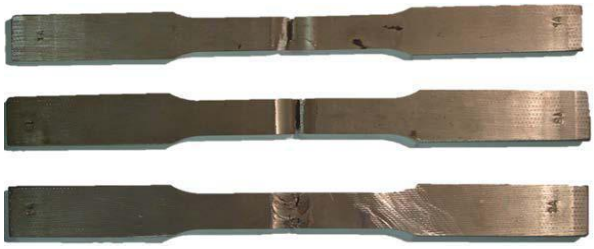


Fig. 11 Specimens after welded joint destruction

The results of static tensile test are given in the table 4. Values of ultimate tensile strength of welded joints vary from 125 to 155 MPa. The mean value of ultimate tensile strength attains the value of 265 MPa. Each tensile specimens are failing in stir zone.

Tab. 4 Values of static tensile strength of welded joint

Des.	T [°C]	t_s [mm]	b_0 [mm]	S_0 [mm^2]	F_m [kN]	R_m [MPa]	A [%]
1	20	6.2	17.9	111.0	15.54	140	4.1
2	20	6.2	18	111.6	13.95	125	3.7
3	20	6.2	18	111.6	17.30	155	4.5

T- temperature, S_0- considered cross section of specimens (b_0 x t_s),
F_m- axial force, R_m– tensile strength, A- elongation

Conclusions

The contribution deals with welding of the Mg alloy of the type AZ 31 by FSW. The main aim was to suggest the parameters and conditions of welding allowing the fabrication as good as possible welded joints. To determine suitable parameters for welding by FSW process, the numerical simulation of thermal fields was performed. High quality welded joint was fabricated by use of welding tool with pin bevel angle 6˚ at the following parameters: downward force 35 kN, tool revolutions 600 rpm and welding speed 60 mm/min. The quality of welded joints was assessed by radiography. Selected high-quality joint was then investigated by light microscopy, where analysis of individual zones across the cross section was performed. Light microscopy has revealed a fine-grained structure in weld metal. The measured microhardness values varied from 59 to 65 HV. EDX microanalysis has shown several compounds in TMAZ, which were introduced to structure during casting. Strength of welded joint attained the values from 55 to 60% of the base metal strength.

Acknowledgment

This contribution is a part of GA VEGA project of MŠVVŠ SR, No. 1/2594/12 Study of Metallurgical Joining and other Technological Processes Applied for Processing the Magnesium and other Light Alloys by Progressive and Environment-friendly Technologies and the VEGA project No. 1/1041/11.
Authors thank to Assoc. Prof. Ing. Bohumil Taraba, PhD. for his professional assistance in the development of numerical simulation.

References

[1] Friction Stir Welding – Equipment TWI, [online].[cit. 2013-08-12]. Accessible on: http://www.twi.co.uk/services/intellectual-property- licensing/friction-welding/equipment/
[2] MISHRA, R.S., MAHONEY W. M.: Friction Stir Welding and Processing Ohio: ASM International USA 2007. ISBN – 13:978-0-87170-848-9
[3] TURŇA, M., Special Welding Methods. Solid State Welding. Postgraduate Study, International Welding Engineer Prague 2011.
[4] KOLAŘÍK, L., Special Solid State Welding Methods. Postgraduate Study, International Welding Engineer. Prague 2012.
[5] Accessibleon:http://www.alcotec.com/us/en/education/knowledge/qa/What-is-Friction-Stir-Welding–of Aluminum.cfm
[6] MISHRA, R.S., MAHONEY W. M., YUTUKA SATO, HOVANSKY,Y.,VERMA,R.: Friction Stir Welding and Processing VI, California USA 2011. ISBN – 978-1-118-00201-80
[7] BUFFA, G., FRATINI, L., PASTA, S.,: Residual Stresses in Friction Stir Welding: Numerical Simulation and Experimental Verification. International Centre for Diffraction Data 2009 ISSN 1097 – 0002 [online]. [cit. 2012-10-6] Accessible on: http://www.icdd.com/ resources/ axa/vol52/V52_5
[8] PALČEK, P., CHALUPOVÁ, M., LUKÁČ, P., TROJANOVÁ, Z The Effect of Temperature on Fracture Characteristics of Selected Magnesium alloys. In Materials Engineering, 2005, vol. 12, issue 3, pp. 117-122. ISSN 1335-0803
[9] LIMING, L.: Welding and Joining of Magnesium Alloys. Wood head, Publishing: In Limited Cambridge: 2010. ISBN 978-0-85709-042-3
[10] AVEDESIAN, M., BAKER, H.: ASM Speciality Handbook – Magnesium and Magnesium Alloys. Ohio, USA: ASM International, 1999. 314 p. ISBN 0-87170-657-1
[11] Accessible on: www.solidworks.com
[12] Ansys Theoretical Manual, Release 10.0, SAS IP, Inc., 2005.

[13] Deform 3D, Scientific Forming Technologies Corporation 2013
[14] Sente Software Ltd., JMatPro: Practical Software for Materials Properties, Surney Tech. Center, UK.

Magnesium Technology 2014

Corrosion and Coatings

Magnesium Technology 2014
Edited by: Martyn Alderman, Michele V. Manuel, Norbert Hort, and Neale R. Neelameggham
TMS (The Minerals, Metals & Materials Society), 2014

ENHANCING CORROSION RESISTANCE BY A HYDROPHOBIC SURFACE FEATURE FOR MAGNESIUM ALLOY AZ91D

Xiao-Bo Chen, Chong Ke and Nick Birbilis
Department of Materials Engineering, Monash University, Clayton, VIC 3800 Australia

Keywords: Corrosion, Hydrophobic Surface, Metal Phosphate, Conversion Coating, and Magnesium Alloys

Abstract

A simple hydrothermal pretreatment was applied, prior to conventional conversion coating process, to produce a unique nano-scale surface. Subsequent growth of a compact and stable conversion coating reinforced the corrosion resistance of magnesium alloy AZ91D and significantly prolonged their limited lifetime. Finally, a highly hydrophobic surface was generated on top of the conversion coating, which effectively reduced the contact between corrosive medium, and metal surface, and the overall corrosion rate. The morphologies of the hydrothermal pretreated surface, conversion coating and hydrophobic layer were observed using scanning electron microscopy; the crystal structure and the composition was analyzed and determined using X-ray diffraction and energy dispersive X-ray spectroscopy. Corrosion performance was evaluated by the measurement of polarization behavior and salt spray testing. Such a surface coating system imparted considerable corrosion protection to the AZ91D substrate, and electrochemical polarization test results were presented to describe mechanistic aspects.

Introduction

Magnesium (Mg) and its alloys are promising lightweight materials (density of 1.7 g/cm^3, which is two thirds of aluminium, 2.7 g/cm^3, and one fifth of steel, ≈ 7.85 g/cm^3), for construction, electronics, automobile, and aircraft industries, having a high strength-to-weight ratio, good mechanical properties and excellent castability [1, 2]. Thus Mg alloys continue to receive significant research attention. Aluminium and steel are the commodity metals found in the transportation sector (*i.e.* cars, trucks, trains, buses and aircraft). In all such cases, energy can be conserved if weight can be reduced. For example, a 'rule of thumb' is that for each percentage of automotive weight reduction there is a corresponding percentage drop in fuel consumption (and hence, greenhouse gas emissions).

However, the use of Mg-based materials is still far behind that of the other light metals, such as aluminum and titanium, due to their vulnerability to corrode when exposed to most aqueous environments that are neutral or acidic (particularly those which contain halide ions). Mg is highly reactive and rapidly develops porous, poorly adhesive and inhomogeneous oxide/hydroxide/carbonate films [3, 4], upon atmospheric exposure [5, 6], which are incapable of providing satisfactory protection to the underlying metal against corrosion [7].

There are two primary methods that have been exploited extensively to minimize the corrosion rate for Mg alloys. One of these is modifying bulk Mg alloy composition, such as adding alloying element or reducing content of iron. Modifying bulk Mg alloy composition can reduce corrosion rate to some level by still not enough to meet the requirements for practical uses.

In the past decades, many efforts have been tuned to grow a compact barrier coating on surface to isolate the base material from the environment as an effective pathway to minimize corrosion rate of Mg alloys [1, 8]. One of the advantages is that only surface properties could be altered, in meantime; on the other hand, the mechanical properties of the bulk materials can be fully maintained. The surface could be offered numerous functions to fulfil diverse applications, in addition to corrosion resistance.

Several surface coating techniques, including electro-/electroless plating, conversion coating, anodizing, hybrid coatings, and vapor-phase processes, have been developed [1, 8]. Of those, chemical conversion coating treatment has attracted most interests due to some of the features including low-cost, and easiness to be implemented [9], which has been extensively adopted in industrial processes. The natively formed loose film on Mg-based substrates can be removed/converted into protective film by chemical conversion treatments. Since chemical reaction is the major driving force to grow film on surface, the bonding strength between coating and substrate will be much higher than others, such as physical vapor deposition. No use of electricity and expensive equipment facilitates the transition of the technology form lab to industrial production.

Chen and Birbilis have developed a number of metal phosphate conversion coatings to protect Mg and its alloys again corrosion [10-12]. A calcium hydrogen phosphate (brushite) was readily formed on surface of pure Mg in a coating bath containing dilute calcium phosphate solution (0.01 M) [10]. The brushite was transformed into more stable and insoluble hydroxyapatite via alkaline post-treatment, which reduced the high corrosion rate of Mg in two orders of magnitude. When applying calcium phosphate coatings on Mg alloy AZ91D, it was found by the same authors that hydroxyapatite was generated only in the baths with low concentration of PO_4^{3-} and Ca^{2+} ions [11]. The low solute concentration shortens the lifespan of the coating bath and is not cost-effective for commercialisation. They adopted manganese phosphate system and proposed that the coating features, such as surface morphology, thickness, crystallinity and corrosion protectiveness were highly related to the operational parameters, including pH and temperature [12]. Although these phosphate conversion coatings could protect Mg alloys from corrosion over some period of time, the aquatic droplets containing corrosive medium, i.e. NaCl, are clinging to these hydrophilic surfaces and try to break the barrier coating and initiate corrosion on the underlying metal. Thus, it would be a premium solution to convert the hydrophilic coating surfaces into hydrophilic to minimize the contact between NaCl droplets and coatings and endow superior corrosion resistance.

In this study, a series of simple and environmentally friendly metal (Ca, Mn and Sr) phosphate based conversion coatings were

deposited on Mg alloy AZ91D. A highly hydrophobic surface condition was applied onto the conversion coatings to further improve their resistance to corrosion in aqueous medium. The coating morphology and corrosion performance were characterized by SEM-EDX, potentiodynamic polarisation examination and salt spray tests.

Experimental

Specimen preparation

Commercially Mg alloy AZ91D, from the magnesium alloy supplier HNKWE (Henan Province, China) was used in this study. The actual alloy chemical composition was determined with inductively coupled plasma - optical emission spectrometer (ICP-OES Spectrometer Services, Coburg, VIC, Australia) and reported in Table 1. A Toshiba 250 ton clamping force cold chamber high pressure die casting (HPDC) machine was used to cast test plates of 70 × 60 × 2 mm in size. Specimens were ground progressively down to 1200 grit finish and used as substrate material.

Table 1 Composition of the AM-lite materials (wt%).

Alloy	Al	Zn	Mn	Si	Fe	Cu	Ni
AZ91D	9.1	0.8	0.24	0.031	0.023	0.015	0.0005

Surface pre-treatment and coating process

Prior to pre-treatment, the specimens were ultrasonicated in acetone at room temperature for 15 min and then in absolute ethanol for 10 min and rinse with deionised water thereafter. An alkaline-hydrothermal pre-treatment was conducted to activate AZ91D surface for subsequent conversion coating formation. Subsequent coating process was carried out in three different solutions which contained 0.1 M Sr-phosphate, 0.1 M calcium phosphate, or 0.1 M manganese phosphate salts. pH of the coating solutions was adjusted to be acidic level using nitric acid (HNO_3). Finally, the conversion coated Mg alloy AZ91D specimens were exposed to an ethanol solution of 1H, 1H, 2H, 2H-Perfluorooctyltriethoxysilane (PFOTES) at room temperature for 45 min and subsequently heated at 80 °C for 15 min. Two rinses in distilled water were applied between each step to remove chemical contamination at the surface. All chemicals used in this work were analytical grade from Sigma-Aldrich Ltd. Digital temperature controllers were used to maintain the bath temperature. Following the coating step, samples were dried and kept in a desiccator for further characterisation.

Surface and corrosion analysis

Surface morphologies were observed using scanning electron microscopy (SEM, FEI Nova). Contact angle measurement of the liquid droplets was conducted on the hydrophobic surface of conversion coated AZ91D samples by the sessile drop technique at room temperature using a KSV Cam101 contact angle meter. A microliter syringe pump was attached to a small needle in an XYZ manipulator to enable a drop to be slowly increased and decreased in size. The shape of the drops was recorded by a digital camera and the contact angles were measured from the images. The drop size was set at 8 µl. At least five droplets of pure water were used for each sample to obtain a mean value. For electrochemical tests, a flat-cell (PAR) was used with an electrode area of 1 cm^2. The reference electrode used was a saturated calomel electrode (SCE), and the counter electrode was Ti-mesh. The electrolyte solution was 3.5 wt% sodium chloride (NaCl). A Biologic® VMP-3Z potentiostat was used to execute potentiodynamic polarisation at a sweep rate of 1 mV/s. The polarization curves were used to determine i_{corr} (via a Tafel-type fit) using EC-Lab software (v.10.6). As a general rule, data fittings were executed by selecting a portion of the curve that commenced > 50 mV from E_{corr}, and i_{corr} was subsequently estimated from the value where the fitting intercepted the potential value of the true E_{corr}. More generally, polarization testing was also able to visually reveal comparative information related to the kinetics of anodic and cathodic reactions. Salt spray tests were carried out in a dry corrosion test cabinet (DCTC 600, Angelantoni Industrie, Italy), where the ASTM B117 standard was adopted.

Results and discussion

Surface morphology and chemical composition

Alkaline-hydrothermal pre-treatment has altered the original smooth surface finish of AZ91D into a loose structure containing nano-sized MgO particles detected by XRD (data not shown). Such a surface condition was expected to have a higher aspect ratio and quicker dissolution rate of MgO into coating solution, and thus accelerate the growth rate of conversion coating.

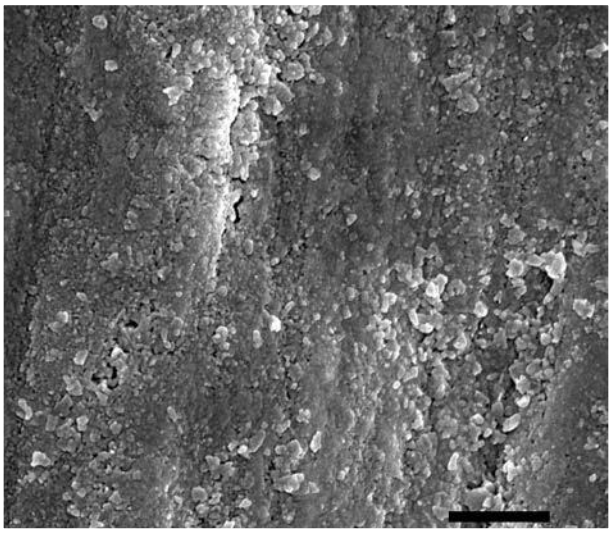
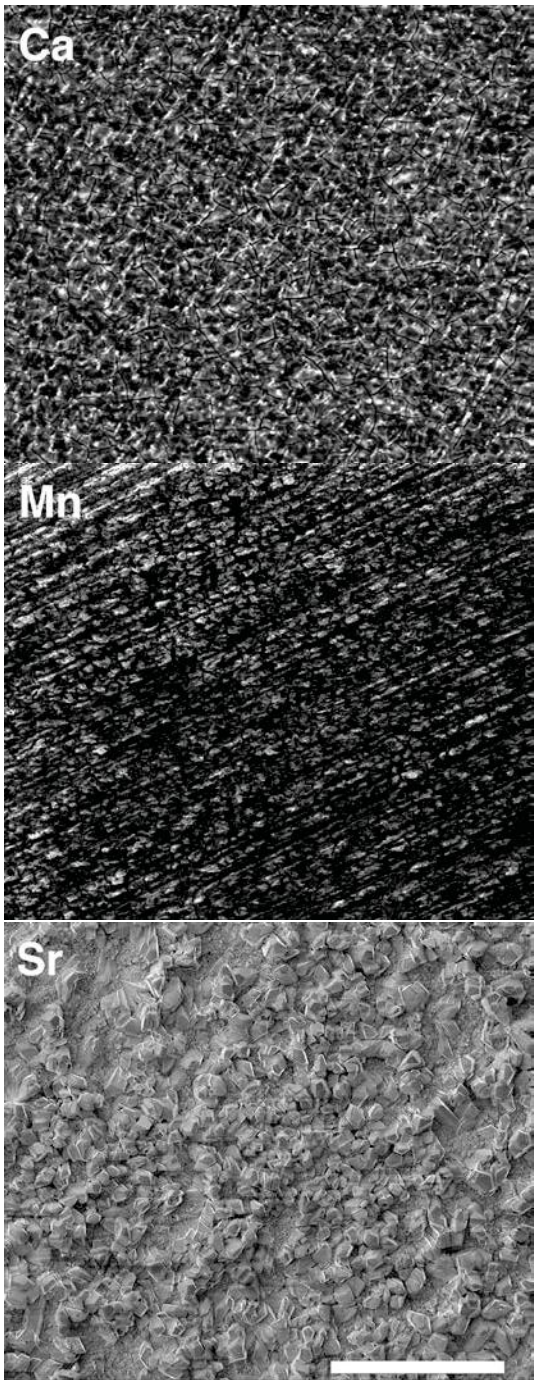


Figure 1. Surface morphology of alkaline-hydrothermal pre-treated Mg alloy AZ91D. Scale bar is 500 nm.

Surface morphology depicted in Figure 2 demonstrates that both Ca and Mn coatings are smooth and thin, since the contour of the grooves generated by the grinding process is still visible. But the presence of micro-cracks has been confirmed. Upon exposed to corrosive medium, chloride ions will easily approach to the substrate and trigger corrosion process through these defect sites. Thus, the existing cracks or defects would deteriorate the barrier effect and increase the corrosion rate eventually, though Ca and Mn phosphate coatings could tolerate the attacks from NaCl and maintain their role in protection at the initial period. In terms of Sr based conversion coatings, it can be seen that a uniform, compact and defect free coating with complete coverage was produced on Mg alloy AZ91D after 5 min immersion in the Sr-P coating bath. It is apparent that numerous cubic particles scattering on the top

of the coating which reveals the high crystallinity of the deposits. In general, a coating with high crystallinity has a lower solubility in aqueous solution compared to amorphous phases. Consequently, such Sr-P based conversion coating is expected to be insoluble in NaCl solution and maintain its integrity for longer time, which is critical for long-term high corrosion resistance.



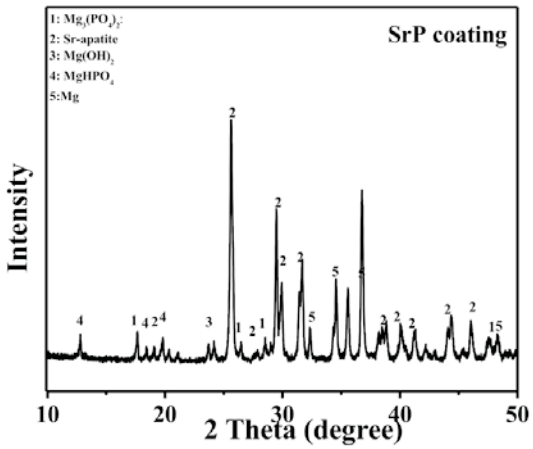


Figure 2. Surface morphology of Ca, Mn and Sr based conversion coatings and XRD spectrum of SrP coating on AZ91D. Scale bar is 100 μm.

Polarization curves and salt spray test

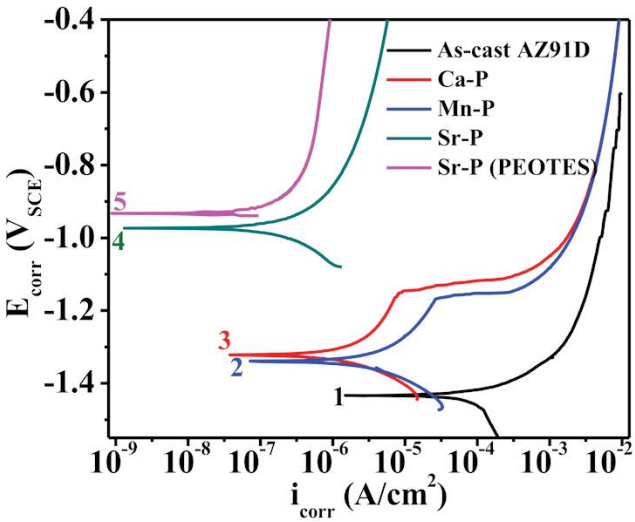


Figure 3. Polarization curves for various AZ91D in 3.5 wt% NaCl

In this study, corrosion rate of various coatings was examined via potentiodynamic polarization curves in 3.5 wt% NaCl and salt spray test according to the ASTM B117 standard. Polarization curves can be used to demonstrate instant anodic and cathodic reaction mechanisms as presented in Figure 3. The curve 1 (black line) for the as-cast Mg alloy AZ91D reveals the characteristic behavior of Mg alloy AZ91D metal whereby high corrosion rate are seen and the current (i_{corr}) rapidly increased with the application of anodic over-potential. Applying protective coating on AZ91D reduced the corrosion rate significantly by retarding both the anodic and cathodic reactions. Ca and Mn based conversion coatings drove the corrosion potential (E_{corr}) towards nobler region and the corrosion current moving towards left (curve 2 in red and curve 3 in blue). This is a clear sign for a protective feature offered by the barrier coatings. At least, at the initial immersion stage (before the breakdown potential point), the coatings isolated the substrates from attacks of corrosive medium, i.e. NaCl. Afterwards, the protection was gone and i_{corr} value increased sharply with the applied over-potential, similar to the

case of as-cast AZ91D. In terms of Sr-coating (curve 4 in green), corrosion rate was profoundly decreased and E_{corr} was enhanced to nobler, compared to the Ca and Mn coated AZ91D cases, presenting a superior corrosion protective capability, which could be attributed to the dense, complete coverage and defect-free features of the Sr coating. It is worth mentioning the conversion coatings had a dominant impact in retarding anodic reactions (hence the coatings were a good resistor of ionic conduction) and a less (but some) influence on the cathodic reaction kinetics.

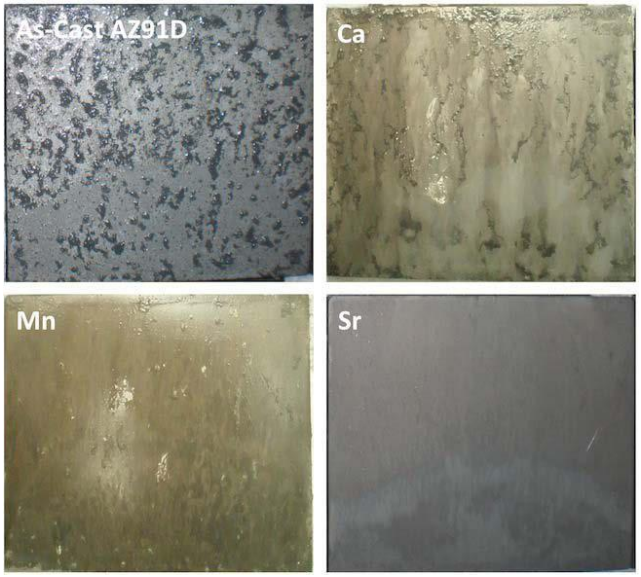


Figure 4. Various AZ91D specimens after 72 hours salt spray test.

Whilst potentiodynamic polarization measurement is a powerful tool to discover the dominant mechanisms behind the protection being afforded, the method is instantaneous in nature and hence supplementation with salt spray testing was executed. The corrosion performance of Sr coating was compared to uncoated AZ91D and CaP and MnP protective films using the salt-spray test. The salt spray test (according to the ASTM standard) involves continuously spraying 0.1M NaCl solution at 35°C from a nozzle into a chamber in which the samples are positioned. The corrosion performance was then assessed by visual inspection of the samples after being subjected to the salt spray. Obviously, over 85% surface area of the as-cast AZ91D sample corroded and was covered by white and grey corrosion product as presented in Figure 4. Though the corroded region fraction of AZ91D was minimized by the Ca-P and Mn-P based conversion coatings, corrosion still proceeded during the salt spray process, indicating that the supplied protection was limited and not satisfactory. With regards to the Sr coating, it can be seen that there was nearly no corrosion spots on the coated surface that still maintained its original integrity and features. Consequently, Sr coating had the best corrosion performance when compared to the other coatings, which is in agreement with the polarization results (Figure 3).

There are three key factors, i.e., the highest crystallinity, 100% surface coverage and defect-free morphology, which determine the high efficacy of SrP conversion coating in restriction of corrosion of Mg alloy AZ91D in NaCl electrolyte. A complete surface coating without noticeable defects can be an effective barrier to isolate underlying metal from the corrosive medium. Meanwhile, the high crystallinity endowed a low solubility and long-time stability to the SrP coating that degrades slowly when exposed to NaCl solution.

Since most corrosion media that the Mg alloys are exposed to, are aqueous solutions or moisture environment, a surface with water repelling functionality, i.e. hydrophobicity, is expected to be corrosion resistant. Thus, in this study, it was attempted to further enhance the corrosion resistance of the Sr-P conversion coating via tuning their original hydrophilicity into hydrophobicity. After post-treatment in PEOTES, the surface of the individual Sr-P based cubic particles has been covered with smaller precipitates (Figure 5), which contained element of F as detected by EDX. It was assumed to be a complex of PEOTES and Sr-P particles. Obviously, the corrosion potential of the hydrophobic Sr-P coating (contact angle above 120º) moved to nobler region and corrosion current density has been reduced, compared to the Sr-P coating (pink curve 5 in Figure 3). It is evident that hydrophobic functionality reinforced the protective role of the Sr-P coating against corrosion. But interestingly to note, the salt spray test did not display any significant difference in the corrosion protection of Sr-P and hydrophobic Sr-P coatings. That might be attributed to the low stability of the SrP-PEOTES complex.

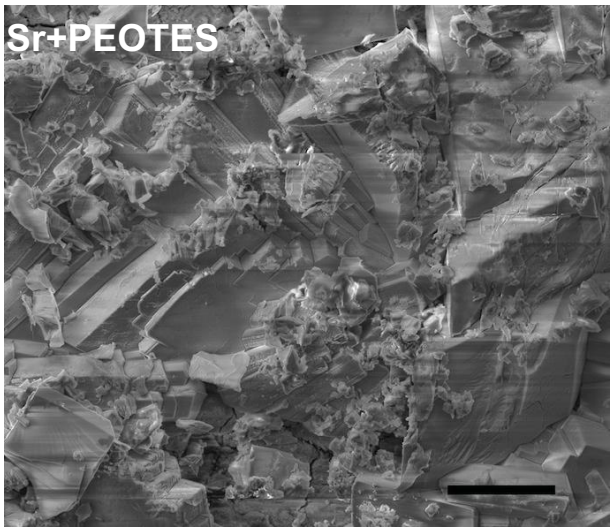


Figure 5. Hydrophobic SrP + PFOTES coating on Mg alloy AZ91D. Scale bar is 10 μm.

Conclusions

A simple conversion coating method, including pre- and post-treatment, was proposed and a series of Ca, Mn and Sr phosphate coatings were produced for corrosion protection of die cast Mg alloy AZ91D. The coating nature and corrosion performance were characterized by SEM-EDX, potentiodynamic polarization curves and salt spray test. Compared to the as-cast samples, all three coatings provided some protective function, more or less. Of these, the compact, complete and defect free Sr coating owned a superior corrosion resistance and its simplicity in operation will path a way for commercialization in the near future. The post hydrophobic treatment could further improve the corrosion resistance of the Sr-P coating during the initial stage though the long-term stability of the PEOTES-Sr complex compound is still a challenge.

Acknowledgements

The Australian Research Council (Centre of Excellence for Design in Light Metals) and Victorian State Government for the establishment of the Victorian Facility for Light Metals Surface are gratefully acknowledged. The authors acknowledge the SEM, and the scientific and technical assistance, of the Australian Microscopy & Microanalysis Research Facility at the RMIT Microscopy & Microanalysis Facility, at RMIT University.

References

[1] J.E. Gray, B. Luan, Protective coatings on magnesium and its alloys - a critical review, Journal of Alloys and Compounds, 336 (2002) 88-113.
[2] B.L. Mordike, T. Ebert, Magnesium properties-application-potential, Materials Science & Engineering A, 302 (2001) 37-45.
[3] M. Santamaria, F.D. Quarto, S. Zanna, P. Marcus, Initial surface film on magnesium metal: A characterization by X-ray photoelectron spectroscopy (XPS) and photocurrent spectroscopy (PCS), Electrochimica Acta, 53 (2007) 1314-1324.
[4] G. Song, A. Atrens, D.S. John, L. Zheng, Magnesium alloys and their applications, Wiley-VCH, 2000.
[5] G.L. Song, Recent progress in corrosion and protection of magnesium alloys, Advanced Engineering Materials, 7 (2005) 563-586.
[6] G.L. Song, A. Atrens, Recent insights into the mechanism of magnesium corrosion and research suggestions, Advanced Engineering Materials, 9 (2007) 177-183.
[7] D.A. Jones, Principles and Prevention of Corrosion, 2nd ed., Prentice Hall, Englewood Cliffs, NJ, 1996.
[8] X.-B. Chen, N. Birbilis, T.B. Abbott, A review of corrosion resistant conversion coatings for magnesium and its alloys, Corrosion, 67 (2011) 035005.
[9] H.H. Elsentriecy, K. Azumi, H. Konno, Improvement in stannate chemical conversion coatings on AZ91D magnesium alloy using the potentiostatic technique, Electrochimica Acta, 53 (2007) 1006-1012.
[10] X.-B. Chen, N. Birbilis, T.B. Abbott, A simple route towards a hydroxyapatite-$Mg(OH)_2$ conversion coating for magnesium, Corrosion Science, 53 (2011) 2263-2268.
[11] X.-B. Chen, N. Birbilis, T.B. Abbott, Effect of [Ca^{2+}] and [PO_4^{3-}] levels on the formation of calcium phosphate conversion coatings on die-cast magnesium alloy AZ91D, Corrosion Science, 55 (2012) 226-232.
[12] X.-B. Chen, X. Zhou, T.B. Abbott, M.A. Easton, N. Birbilis, Double-layered manganese phosphate conversion coating on magnesium alloy AZ91D: Insights into coating formation, growth and corrosion resistance, Surface and Coatings Technology, 217 (2013) 147-155.

Magnesium Technology 2014
Edited by: Martyn Alderman, Michele V. Manuel, Norbert Hort, and Neale R. Neelameggham
TMS (The Minerals, Metals & Materials Society), 2014

OXIDATION AND CORROSION BEHAVIOR OF NON-FLAMMABLE MAGNESIUM ALLOYS CONTAINING Ca AND Y

Bong Sun You, Young Min Kim, Chang Dong Yim, Ha Sik Kim
Light Metals Group, Korea Institute of Materials Science, 66 Sangnam, Seongsan, Changwon 641-831, Korea

Keywords: Magnesium alloys, Oxidation, Corrosion, Calcium, Yttrium

Abstract

The combined addition of calcium and yttrium lead to significant increase in non-flammability and tensile properties, compared to conventional Ca-containing magnesium alloys. It means that we can reduce the amount of calcium addition to get certain amount of non-flammability in the alloys containing both calcium and yttrium together. Because the addition of calcium only can increase the ignition temperature but decrease the tensile properties, it should be minimize not to decrease the tensile properties. Corrosion behavior of calcium and yttrium containing alloys were also investigated systematically, and show that they have better corrosion resistance than the any other commercial alloys or calcium containing alloys. Detailed study on the corrosion behavior confirms that there are optimum amount of calcium and yttrium addition to get best corrosion resistance, and corrosion behavior of these alloys are quite different with other alloys.

Introduction

Magnesium alloys have many advantages, such as low density, high specific strength, good machinability and formability, good damping ability and easy recycling, therfore they have good prospects of applications in the fields of automobile, aerospace, electronics industry, etc.

However, the usage of magnesium alloys is still restricted due to their limited workability, formability, high reactivity (poor ignition/ corrosion resistance). Current technical issues in Mg alloys research are focused on how to solve the following problems [1-3]; low strength, poor formability, high cost, dilemma in use of rare earth elements, high reactivity, and poor chemical properties. Although many successful results in improving strength and formability and reducing production cost have been given so far, the control of fundamental nature of magnesium such as ignition and corrosion still remains unsolved. In order to meet strengthening demands for the use of magnesium alloys in addition to the social issues including environmental problem, the dramatic improvement in their safety and reliability as well as mechanical properties should be secured.

Magnesium and its alloys are very active, especially in a molten state, and are rapidly ignited or combusted when the clean surface of the melt comes into contact with oxygen in air. Flux or a cover gas has to be used to prevent ignition of magnesium alloys during melting. However, the above methods may cause many problems such as global warming and increased production costs, so many researchers are paying more attention to finding more essential methods to improve ignition resistance. Obviously, it is simple to prevent the ignition of magnesium alloys by the addition of alloying elements. However, it is difficult to select suitable elements, because only some of alloying elements have been proved to benefit the oxidation resistance of magnesium alloys [4-8].

Calcium is one of the promising elements that can improve ignition resistance. The ignition temperature increases by 250 K after an addition of 3 wt.% Ca- added into pure magnesium [9]. You et al. [10] investigated the oxidation behavior of a Mg-xCa alloy (x=0-3 wt.%), and they confirmed that a dense and compact protective MgO/CaO layer formed at elevated temperatures. However, a large amount of calcium addition generally lowers tensile strength and ductility because coarse Ca-compounds precipitate along the grain boundaries. Unfortunately, most of such studies have concentrated on either ignition resistance or tensile properties of magnesium alloys, but there has been no attempt to improve both them.

In fact, increasing both ignition temperature and tensile properties is difficult to achieve because of their contradictory aspects; that is, a large addition amount of ignition resistance improving alloying element is necessary to make ignition-proof magnesium alloys [5, 10-11], but at the same time it causes the deterioration of tensile properties due to the formation of coarse brittle phases. Fig. 1 clearly shows that more than 1wt.% Ca addition to AZ31 and AZ61 alloys can increase ignition temperature but at the same time deteriorate tensile properties, especially elongation. This indicates that instead of a large amount of a single alloying element, the combined addition of two or more alloying elements may suppress the formation of a large fraction of coarse brittle phase without sacrificing ignition resistance.

In this work, we therefore developed new non-flammable Mg alloys with both excellent mechanical properties and ignition/corrosion resistance. The effect of alloying elements on those properties of magnesium alloys was investigated, and the field application of newly-developed alloys was also performed in this work.

Experimental procedures

Several kinds of Mg-Al based alloys containing Ca and Y were prepared according to the nominal composition by pure magnesium (99.93 wt.%), pure aluminum (99.9 wt.%), pure zinc (99.9 wt.%), pure calcium (99.9 wt.%) and pure yttrium (99.9 wt.%) in an electric furnace using a low-carbon steel crucible heated to 720°C under a protecting gas (10% SF_6 and 90% CO_2). The melt was poured into a permanent mold preheated to 200°C and then cooled to ambient temperature in air atmosphere. The cast ingots were subsequently heated to 400°C for homogenization treatment and kept at this temperature for 20 hours. The ingots were hot-rolled at 400°C at a reduction rate of 30%/pass with a total reduction of 93%. The rolled sheets with a 1

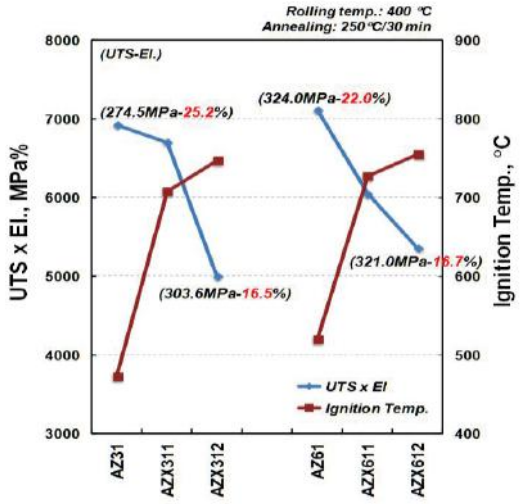


Fig. 1. Ignition temperature vs. mechanical properties. They are inversely related.

mm thickness were finally annealed at 250°C for 30 minutes. Ignition tests were carried out by inserting the chipped samples taken from the castings into a tube furnace held at 1000°C. The tests were carried out in air and at least five chipped samples were used. The ignition temperatures were determined as ones associated with both the appearance of flame and a significant temperature increase. Metallographic samples were prepared for microstructure observation according to a standard procedure. The distribution of alloying elements in the surface oxide layer that was formed on the melt was checked using an EPMA (electron probe micro-analyzer). Tensile tests were carried out using an Instron-4206 universal testing machine at a strain rate of 0.001/s at room temperature. Sheet-type tensile specimens with the dimensions of the ASTM E 8M standard were used. All the tensile specimens were taken in parallel to a longitudinal direction of the rolled sheet.

Results and discussion

Non-Flammability

Fig. 2 shows the change in ignition temperature of AZ-series alloy with an increase in Ca content or total amount of Ca and Y. It is found that larger amount of Al can increase ignition resistance of magnesium alloys; for instance, AZ91 alloys have higher ignition temperature than AZ31 regardless of whether Y is involved. In Fig. 2, the combined addition of Ca and Y to AZ-series alloys results in much higher ignition temperature than the only Ca addition. In addition, total amount of Ca and Y in AZ31 alloy can be reduced from 2.2wt.%Ca to 1.5wt.%(Ca+Y) for the target temperature of 750□C. In the case of AZ61 alloy, the required amount of Ca or Ca+Y for the target temperature of 750°C can be reduced from 1.7wt.%Ca to 1.1wt.%(Ca+Y). It indicates that the combined addition of Ca and Y has a very attractive synergistic effect on the ignition resistance, compared to the individual addition of those elements.

The reason why the small amount of Ca and Y can considerably increase ignition resistance of magnesium alloy is explained by oxide structure formed on the surface of melt. Fig. 3 clearly shows that the surface oxide of the AZX611-0.6Y sample held at 670°C for 10 minutes consists of two distinctive layers; dense and protective oxide layer that contains Ca and Y elements on the surface contacting with a Mg alloy melt in addition to an outer oxide layer that contains Mg, Al, and Ca elements. According to thermodynamic calculation, the following reactions can take place during the isothermal holding at 670°C:

Inner layer: $Ca + 2Y + 2O_2 \rightarrow CaO + Y_2O_3$
(ΔG = -2,155,620 J) (1)

Outer layer: $3Mg + 6Al + 3Ca + 15/2O_2 \rightarrow MgO + MgAl_2O_4 + Ca_3MgAl_4O_{10}$ (ΔG = -7,341,983 J). (2)

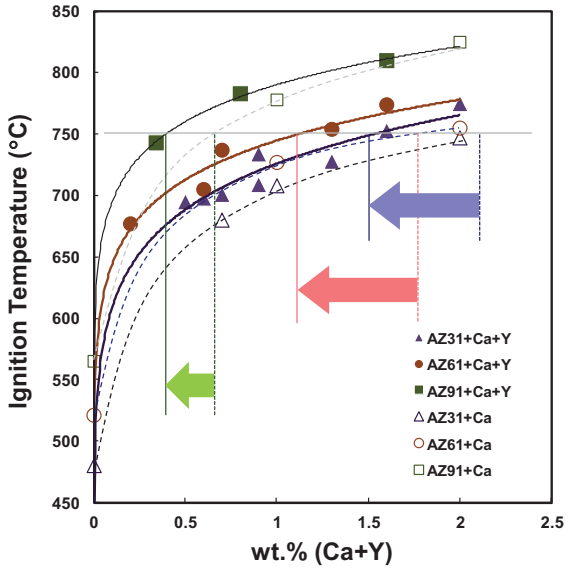


Fig. 2. Change in ignition temperature with the amount of Ca and Y (wt.%). Total addition amount of Ca and Y required to meet the target ignition temperature of 750°C is largely reduced, compared to the only Ca-added Mg alloys.

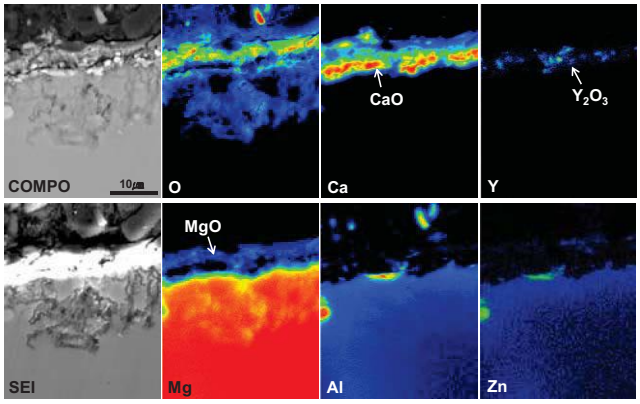


Fig. 3. EPMA result showing the surface oxide layer of the AZX611Y alloy held at 670°C for 10 min.

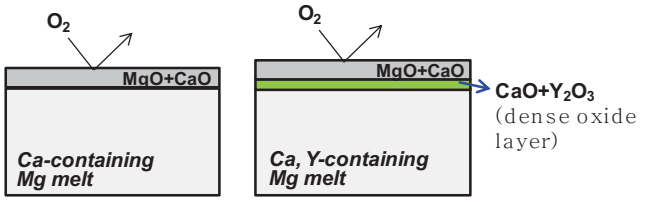


Fig. 4. Schematic illustration of the oxide structures of Ca-added and Ca and Y-added Mg alloys.

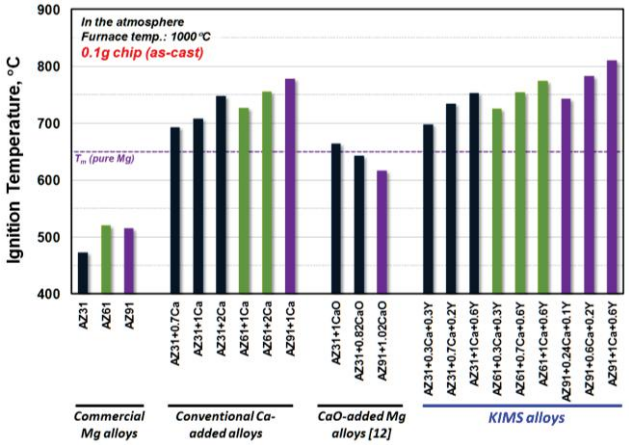


Fig. 5. Comparison of non-flammability between newly-developed non-flammable Mg alloys and conventional Mg alloys.

As the change in Gibbs energy of the reactions (1) and (2) is negative, an additional layer composed of CaO and Y_2O_3 can be formed on the surface of the Ca and Y-added magnesium alloys at 750°C. This duplex layered oxide structure can effectively prevent oxygen penetration into a melt as shown in Fig. 4 and finally increase ignition resistance of the magnesium alloys.

Fig. 5 shows the comparison of non-flammability of Ca and Y-added Mg alloys with commercial alloys and conventional Ca/CaO-added alloys. In this work, ignition tests were carried out by inserting the chipped samples taken from the castings into a tube furnace held at 1000°C. At least five chipped samples were used and the ignition temperatures were determined as ones associated with both the appearance of flame and a significant temperature increase. In Fig. 5, while the ignition temperatures of commercial AZ-series alloys are around 500°C, those of conventional non-flammable alloys with more than 1wt.% Ca are higher than 700°C. In the case of CaO addition, the ignition temperature of 0.82wt.%CaO-added AZ31 alloy is 642°C [12] and much lower than that of 0.7wt.%Ca-added AZ31 alloy (693□C). On the other hand, the ignition temperatures of the Ca and Y-added Mg alloys newly-developed alloys in this work are higher than 700°C and show better non-flammability than the Ca-added alloys even though only small amount of Ca and Y.

Based on the above results, it is obvious that the newly-developed Mg alloys with Ca and Y addition have much better ignition resistance than conventional Ca/CaO-added Mg alloys.

Tensile Properties

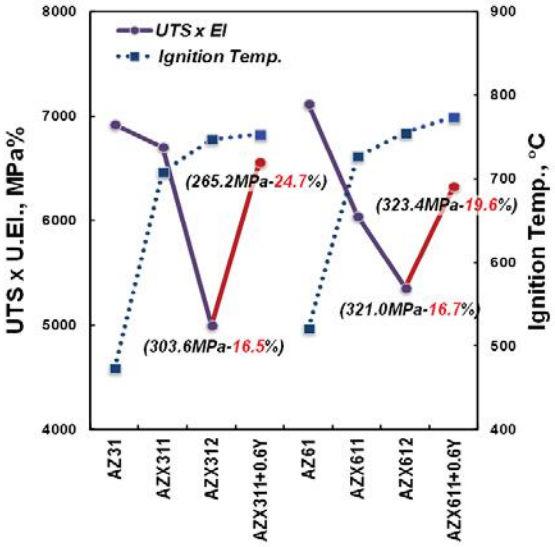


Fig. 6. The changes in ignition temperature and tensile properties with additions of Ca and Y. The combined addition of Ca and Y restored tensile properties with increasing ignition temperature.

The tensile properties of the hot-rolled sheets are shown in Fig. 6. As mentioned above, as Ca content increases from 1 wt.% to 2 wt.%, both yield and tensile strengths increase, but at the same time elongation greatly decreases due to a large amount of brittle Ca-containing phases [13,14]. Such a deterioration of elongation can be restored by reducing the calcium content and adding a small amount of yttrium. In Fig. 6, the elongations of the AZX311-0.6Y and AZX611-0.6Y alloys are 24.7% and 19.6%, respectively, which are similar to those of the AZX311 and AZX611 alloys. Furthermore, the ignition temperatures of the AZX311-0.6Y and AZX611-0.6Y alloys are higher than those of the AZX312 and AZX612 alloys, respectively. As an increase in elongation commonly gives rise to a decrease in strength, the multiplied values of ultimate tensile strength by uniform elongation are better to represent the overall tensile properties of the samples. In Fig. 6, the values significantly decreased in 2 wt.% Ca-added magnesium alloys, but they were restored to those of 1 wt.% Ca-added magnesium alloys by the combined addition of calcium and yttrium. The reduced amount of brittle and coarse Ca-containing phases is attributed to the improvement in tensile properties of those alloys.

Corrosion Resistance

Immersion test in 3.5% NaCl solution was carried out. Fig. 7 shows the surface of AZ31 and Ca and Y-added AZ31 alloys with different amount of Ca after immersion test for 1110 minutes. Compared to the AZ31 alloy of which surface were corroded excessively, the surfaces of AZ31-0.4Ca-0.3Y and AZ31-0.7Ca-0.3Y alloys were not quite corroded. As Ca content increases, the extent of corrosion on the surface becomes severe, and reaches a serious level at more than 1wt.%Ca. This is because the AZ31 alloys with more than 1wt.% Ca have coarse $(Mg,Al)_2Ca$ phase on grain boundary [14,15]. It indicates that Ca content in AZ31 alloys should be controlled less than 1wt.%, and thus the addition of small amount of Y is essential to improve corrosion resistance as well as ignition resistance.

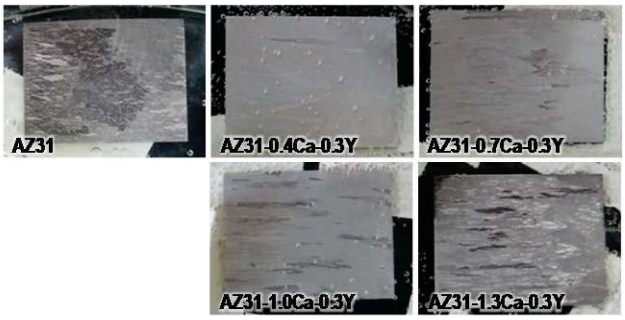


Fig. 7. Change in the surface of AZ31 and Ca, Y-added AZ31 with different amount of Ca after immersion test in 3.5% NaCl solution for 1110 min.



Fig. 8. Immersion test results of bulk samples. The Ca and Y-added alloys have much better corrosion resistance than the only Ca-added alloy.

Fig. 8 shows the immersion test results of bulk cast samples. It is obvious that the addition of Ca itself can improve corrosion resistance of AZ31 alloy, but the combined addition of small amount of Ca and Y can improve corrosion resistance much better than only Ca-added alloys.

Ignition Temperature - Tensile Properties

Fig. 9 shows the non-flammability and tensile properties of newly-developed Mg alloys for wrought applications. As mentioned above, conventional alloys including AZ31, AZ61, and ZK60 have poor ignition resistance, even though they have excellent mechanical properties. On the other hand, conventional Ca-added non-flammability Mg alloys have excellent ignition resistance, but their tensile properties are quite low. It implies that tensile properties and non-flammability are basically contrary to each other. However, the newly-developed non-flammable Mg alloys have both excellent tensile properties and ignition resistance as shown in Fig. 9. The reduction of volume fraction of brittle eutectic phase deteriorating elongation and the formation of multi-layered oxides effectively protecting oxygen penetration into Mg melt are attributed to improve both tensile properties and ignition resistance. In the cases of Mg-Zn based alloys containing Ca and Y, they have much improved tensile properties compared with those of AZXW alloys. In particular, it should be noted that Mg-4Zn-4Al-0.7Ca-0.6Y alloy has ignition temperature of higher than 750°C and tensile properties of approximately 10,000 MPa%.

Effect of Al on Non-Flammability, Tensile Properties

Fig. 10 shows the effect of aluminum on tensile properties and ignition resistance of newly-developed Mg alloys. Without Al

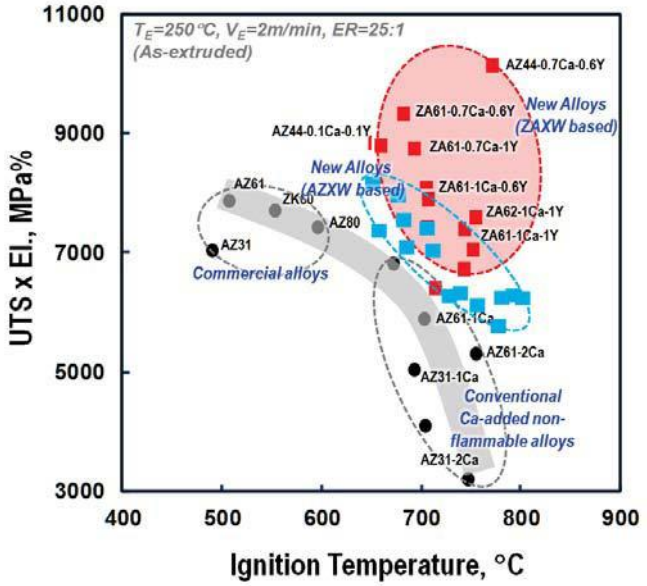


Fig. 9. Tensile properties and non-flammability of newly-developed non-flammable Mg alloys for wrought application.

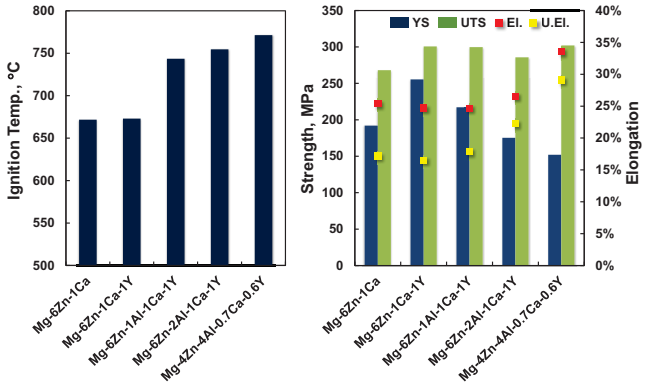


Fig. 10. The effect of Al addition on ignition temperature and tensile properties.

addition, Mg-6Zn-1Ca and Mg-6Zn-1Ca-1Y have ignition temperature of approximately 670°C. By the addition of Al, however, the ignition temperature of Mg-6Zn-1Ca-1Y-1Al alloy largely increases to 755°C. The effect of Al on ignition resistance is clearly shown in the result of EPMA analysis, where multi-layered oxide structure consisting of CaO, Y_2O_3, and $MgAl_2O_4$ formed on the surface of ZAXW6211 alloy melt (Fig. 11). In addition, Al can affect tensile properties: in Fig. 10, the addition of 1wt.% Al to ZXW611 alloy decreases yield strength but increase uniform elongation. More Al content in ZXW alloy results in lower yield strength and better uniform elongation, but does not change ultimate tensile strength.

Conclusions

- Calcium and yttrium addition can improve tensile properties, non-flammability, and corrosion resistance at the same time.
- The addition of Al in conjunction with calcium and yttrium leads to the formation of multi-layered oxide structure on

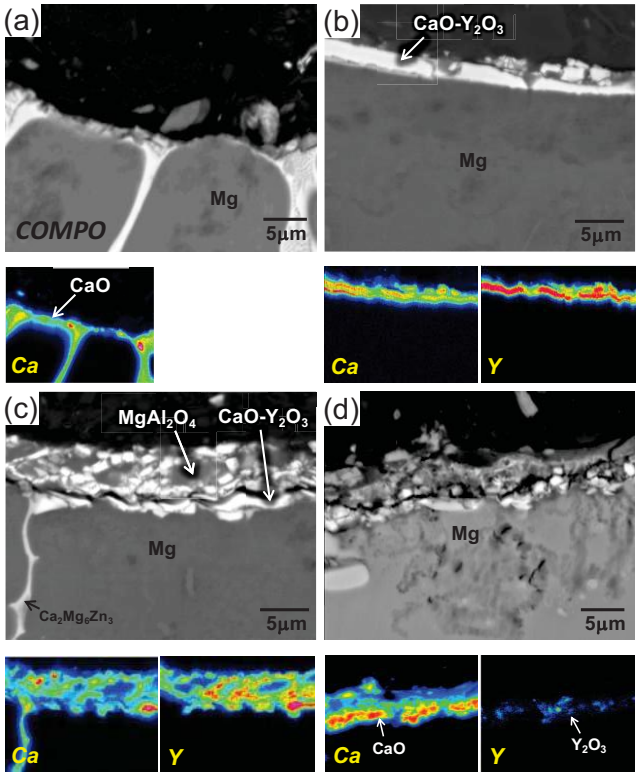


Fig. 13. EPMA results showing the effect of alloying elements on the structure of oxides formed on the surface of Mg melt: (a) ZX61, (b) ZXW611, (c) ZAXW6211, (d) AZXW6110

the surface, resulting in maximizing the efficiency of Ca and Y addition.

- Newly-developed non-flammable Mg alloys have high safety and reliability and don't need to use harmful SF_6 gas during melting, hot-working, and machining. Although the addition of only small amount of calcium and yttrium may increase material cost a little, it can provide better performance and safety and protect environment so that magnesium alloys can be used in wider variety of application areas with confidence.

Acknowledgements

This study was financially supported by the R&D Program of Korea Institute of Materials Science.

References

[1] K.U. Kainer, "Global Magnesium Research: State-of-the-Art and What's Next?", Magnesium Technology 2011, (2011)
[2] S.S. Park, W.-J. Park, C.H. Kim, B.S. You, N.J. Kim, JOM, 61 (2009) 14-18.
[3] K. Hantzsche, J. Bohlen, J. Wendt, K.U. Kainer, S.B. Yi, D. Letzig, Scripta Mater, 64 2011) 725-730.
[4] N.V. Ravi Kumar, J.J. Blandin, M. Suéry, E. Grosjean, Scripta Mater., 49 (2003) 225-230.
[5] T.S. Shih, J.H. Wang, K.Z. Chong, Mater. Chem. Phys., 85 (2004) 302-309.
[6] P.Y. Lin, H. Zhou, W. Li, W.P. Li, N. Sun, R. Yang, Corrosion Sci., 50 (2008) 2669-2675.
[7] X. Zeng, Q. Wang, Y. Lu, Y. Zhu, W. Ding, Y. Zhao, J. Mater. Process. Tech., 112 (2001) 17-23.
[8] Y.M. Kim, C.D. Kim, H.S. Kim, B.S. You, Scripta Mater., 65 (2011) 958-961.
[9] M. Sakamoto, S. Akiyama, K. Ogi, J. Mater. Sci. Lett., 16 (1997) 1048-1050.
[10] B.S. You, W.W. Park, I.S. Chung, Scripta Mater., 42 (2000) 1089-1094.
[11] X.M. Wang, X.Q. Zeng, Y. Zhou, G.S. Wu, S.S. Yao, Y.J. Lai, J. Alloys. Compd., 460 (2008) 368-374.
[12] S.K. Kim, Magnesium Alloys-Design, Processing and Properties, InTech (2011) 463
[13] A. Suzuki, N.D. Saddock, J.W. Jones, T.M. Pollock, Scripta Mater., 51 (2004) 1005-1010.
[14] Y.M. Kim, C.D. Yim, S.S. Park, B.S. You. Met. Mater. Int., 17 (2010) 583-586.
[15] C.D. Yim, Y.M. Kim, B.S. You, Mater. Trans., 48 (2007) 1023-1028.

Magnesium Technology 2014
Edited by: Martyn Alderman, Michele V. Manuel, Norbert Hort, and Neale R. Neelameggham
TMS (The Minerals, Metals & Materials Society), 2014

CORROSION BEHAVIOR OF MAGNESIUM ALLOYS CONTAINING Sn AND Zn

Chang Dong Yim[1,2], Sang Kyu Woo[2], Jie Yang[2], Bong Sun You[1,2]
[1]Korea Institute of Materials Science, 797 Changwondae-ro, Seongsan-gu, Changwon, 642-831, Republic of Korea
[2]University of Science and Technology, 217 Gajungro, Yuseong-gu, Daejeon, 305-350, Republic of Korea

Keywords: Potentiodynamic test, 2nd phase, Micro-Galvanic

Abstract

The microstructures and corrosion behaviors of the magnesium alloys containing Sn and Zn are evaluated systematically. The as-extruded TZ alloys show a typical equi-axed grain structures formed by dynamic recrystallization. The fine particles of Mg_2Sn phase are observed in grain interior and along grain boundaries. The corrosion potential measured by potentiodynamic test increases with increase of Zn content. The current density at cathodic region increases with increase of Zn content, which means that the hydrogen evolution rate increases with increase of Zn content. It seems that the corrosion behaviors of as-extruded TZ alloys will be affected by the amount of Sn and Zn dissolved into the α-Mg phase and the fraction of Mg_2Sn phase.

Introduction

The magnesium alloy as lightweight structural material has many advantages such as high specific strength, good damping capacity, excellent castability and machinability. But wide application of the magnesium alloy to various industries has been limited by poor corrosion resistance and relatively low absolute strength. It is well known that precipitation hardening is the most effective method for increase of strength of wrought alloys. The Mg-Sn system is known as a precipitation system, which has a relatively high solubility limit at 834K and low solubility at ambient temperature [1]. Sn also has relatively higher hydrogen evolution over-potential and the cathodic hydrogen reaction is relatively difficult on its surface [2]. The Sn in the solid solution may stabilize the matrix phase and reduce its anodic dissolution rate [3]. Even though the Mg-Sn system has high potential as high strength wrought alloy by precipitation hardening, the slow age hardening response should be solved by addition of alloying element [1]. It is well known that Zn is effective alloying element for enhancement of age hardening response of Mg-Sn system [1, 4-7]. Zn can also enhance the protectiveness of the passive film on the surface when it is dissolved into the α-Mg phase [8].
According to the previous studies, the Mg-Sn-Zn system has high potential as high strength and high corrosion resistance wrought alloy. But the study on the corrosion behavior of Mg-Sn-Zn system has been carried out little although many studies on mechanical behaviors of this system have been reported. In this study the corrosion behavior of the magnesium alloy containing Sn and Zn is evaluated by potentiodynamic test. The change of corrosion behavior according to the composition of the alloy is analyzed in view of microstructure

Experimental Procedure

2 kg of pure magnesium ingot were put into a carbon crucible and heated to 973K by induction heating under a protective atmosphere of CO_2 and SF_6 gases. Pure tin granule and pure zinc ingot were added into the melt according to the given composition. The melt was poured into a cylindrical mold preheated to 473K. The compositions of the alloys were analyzed by ICP as shown in table 1.

Table I. Composition of Mg-Sn-Zn Alloys

Nominal Composition	Designation	ICP Results (wt.%)		
		Mg	Sn	Zn
Mg-5Sn-1Zn	TZ51	94.38	4.56	1.06
Mg-5Sn-2Sn	TZ52	93.62	4.43	1.95
Mg-5Sn-3Zn	TZ53	92.16	4.69	3.15
Mg-5Sn-4Zn	TZ54	91.45	4.59	3.96

A homogenization heat treatment was carried out to homogenize the microstructure of the as-cast billets. In case of TZ51, TZ52 and TZ53 billets, they were isothermally held for 24 hours at 723K. The TZ54 billet was isothermally held for 24 hours at 673K to prohibit a local melting. After homogenization, the billets were machined into the billets with dimensions of diameter of 78mm and length of 145mm for extrusion. The machined billets were preheated to 573K and then extruded indirectly through a die with dimensions of thickness of 2mm and width of 28mm. The die and container were also preheated to 573K. The extrusion ratio and speed were 90:1 and 5.0m/min., respectively.
The specimen for observation of microstructure was cut from the as-extruded plate and mounted by epoxy resin. The mounted specimen was mechanically ground by using of #240~#2400 grit SiC papers and then polished by using paste containing diamond particles of 3μm. 1μm and 0.25μm. The polished specimen was etched by using solution consisted of 3g picric acid, 20ml acetic acid, 20ml distilled water and 50ml ethanol to reveal the microstructure more clearly. The microstructures of as-extruded TZ5x alloys were observed by using an optical microscope (Nikon Optiphot 200) and the average grain size was measured by using i-solution DT image analysis software. The constituent phases of the as-extruded TZ5x alloys were analyzed by measurement of X-ray diffraction pattern. The scanning range of 2θ was from 20° to 80° and the scanning speed was 0.1^o/s.
The electrochemical behaviors of the as-extruded TZ5x alloys were evaluated by potentiodynamic test. The specimen with dimensions of diameter of 16mm and thickness of 2mm was machined from the as-extruded plate and then ground mechanically by using #240~#2400 grit SiC papers. The specimen was inserted in a holder and then put into a flask containing 3.5wt.% NaCl solution at 298K. Three electrodes array was applied to potentiodynamic test. The working electrode, reference electrode and counter electrode were the specimen, a saturated calomel electrode and a carbon rod, respectively. The OCP (open circuit potential) was measured during 900s and then external voltage was changed from -1.0V to 1.0V vs. OCP at rate of 1mV/s.

Results and Discussion

Figure 1 shows the microstructures of as-cast TZ5x alloys. As shown in figure 1, the as-cast TZ5x alloys showed a typical dendritic structures and the dendritic arm was developed more

with increase of Zn content due to constitutional undercooling by Zn segregation at solid/liquid interface.

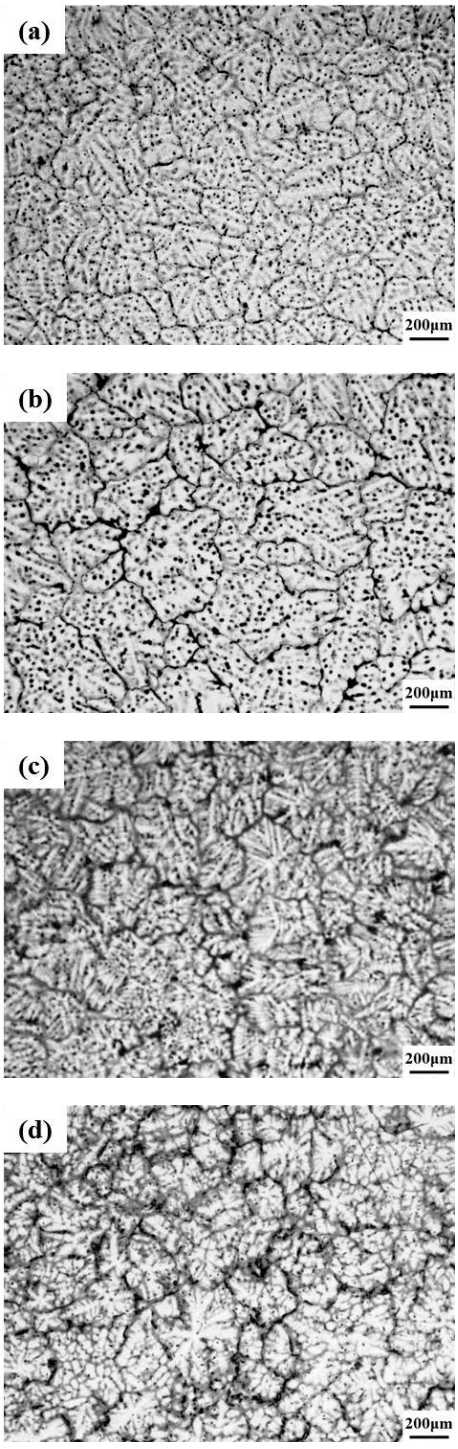


Figure 1. Microstructures of as-cast TZ5x alloys; (a) TZ51 (b) TZ52 (c) TZ53 (d) TZ54.

Figure 2 shows the microstructures of as-extruded TZ5x alloys. As shown in figure 2, the dendritic structure of as-cast alloy was changed into a typical equi-axed grain structure by dynamic recrystallization during hot extrusion. The average grain size was 18±3 μm which was affected little by Zn content. Therefore, the effect of grain size on corrosion behavior could be neglected.

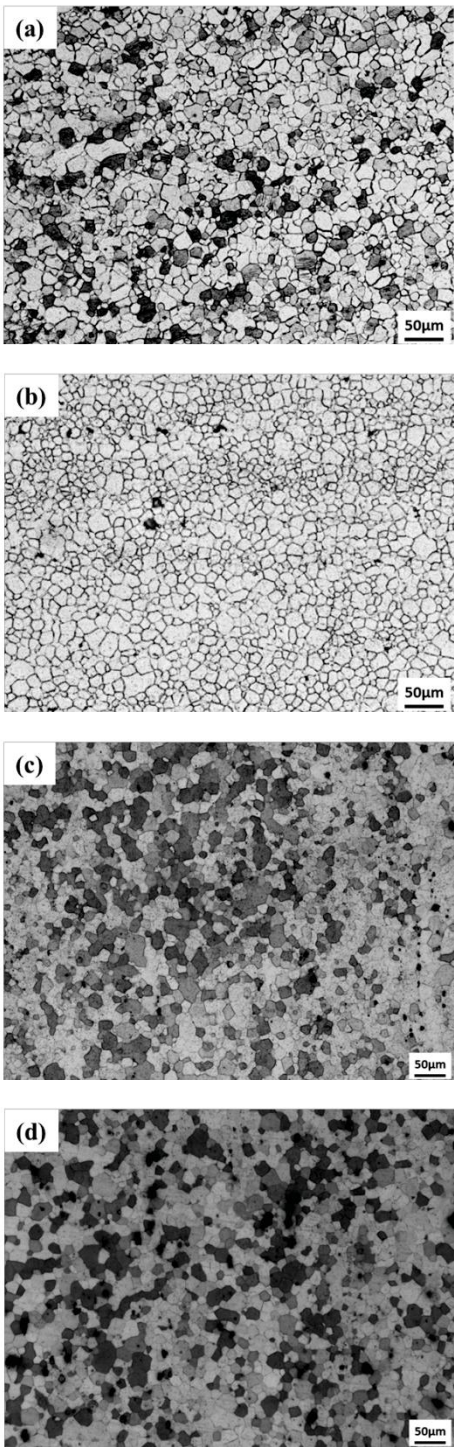


Figure 2. Microstructures of as-extruded TZ5x alloy plates; (a) TZ51 (b) TZ52 (c) TZ53 (d) TZ54.

Figure 3 shows the X-ray diffraction patterns of as-extruded TZ5x alloys. As shown in figure 3, the constituent phases of as-extruded TZ5x alloys were α-Mg, Mg_2Sn and MgZn phases. The Mg_2Sn

phase was formed during preheating and cooling after extrusion. The MgZn phase was formed during cooling after extrusion.

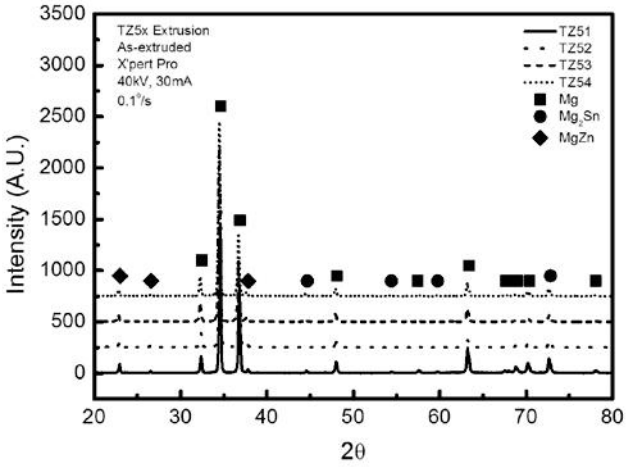


Figure 3. X-ray diffraction patterns of as-extruded TZ5x alloys.

Figure 4 shows the potentiodynamic polarization curves of as-extruded TZ5x alloys in 3.5wt.% NaCl solution at 298K. As shown in figure 4, the hydrogen evolution rate at cathodic region increased and the passive current density at anodic region decreased with increase of Zn content, which resulted in increase of corrosion potential. This result was very similar to that in report on Mg-Zn binary alloys [8]. The fraction of ZnO in the surface film might increase with increase of Zn content, which would enhance the protectiveness of surface film. Therefore the passive current density decreased with increase of Zn content. But unfortunately, the hydrogen evolution rate increased with increase of Zn content due to high conductivity of ZnO.

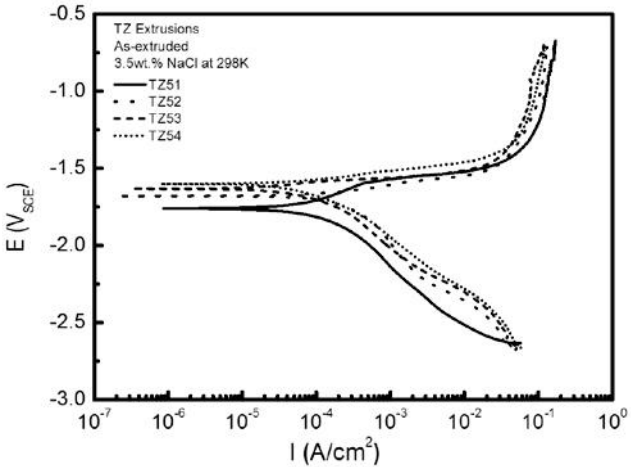


Figure 4. Potentiodynamic polarization curves of as-extruded TZ5x alloys.

The potentiodynamic polarization curve is also affected by the sort and fraction of second phase. As shown in figure 3, there were two second phases such as Mg_2Sn and MgZn phases. Figure 5 shows the result of thermodynamic calculation for the molar percentages of Mg_2Sn and MgZn phases in as-extruded TZ5x alloys. As shown in figure 5, the molar percentage of Mg_2Sn phase was not changed but the molar percentage of MgZn phase increased with increase of Zn content. According to Song et al. [9], MgZn phase accelerated the hydrogen evolution rate at cathodic region. Therefore the hydrogen evolution rate would increase with increase of Zn content due to increase of fraction of MgZn phase.

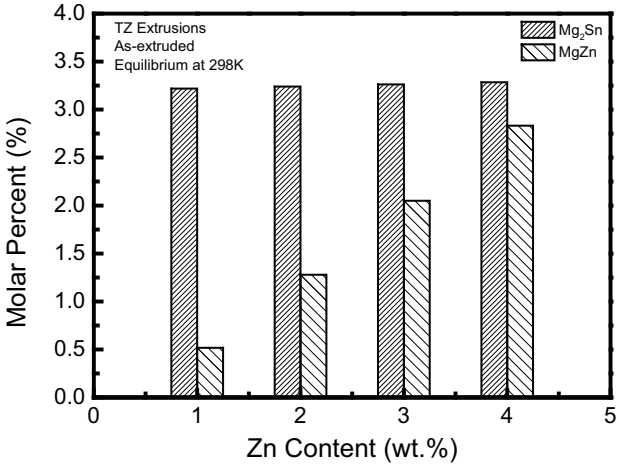


Figure 5. Molar percentages of Mg_2Sn and MgZn phases in as-extruded TZ5x alloys.

Conclusions

As-cast TZ5x alloys showed a typical dendritic structure and the dendritic arm was developed more with increase of Zn content. The dendritic structure was change into a typical equi-axed structure by dynamic recrystallization during hot extrusion. The average grain sizes of TZ5x alloys were similar regardless of Zn content. The hydrogen evolution rate and corrosion potential increased with increase of Zn content. Zn dissolved in the α-Mg phase contributed to the protectiveness of surface film while it accelerated the hydrogen evolution due to formation of ZnO with high conductivity. Zn redistributed in MgZn phase also accelerated the hydrogen evolution.

References

1. T.T. Sasaki et al., "Enhanced Age Hardening Response by the Addition of Zn in Mg-Sn Alloys," *Scripta Materialia*, 55 (2006), 251-254.
2. O. Azizi et al., "The Investigation of the Kinetics and Mechanism of Hydrogen Evolution Reaction on Tin," *International Journal of Hydrogen Energy*, 32 (2007), 1755-1761.
3. G.-L. Song, "Effect of Tin Modification on Corrosion of AM70 Magnesium Alloy," *Corrosion Science*, 51 (2009), 2063-2070.
4. C.L. Mendis et al., "An Enhanced Age Hardening Response in Mg-Sn Based Alloys Containing Zn," *Materials Science and Engineering A*, 435-436 (2006), 163-171.
5. T.T. Sasaki et al., "Heat-treatable Mg-Sn-Zn Wrought Alloy," *Scripta Materialia*, 61 (2009), 80-83.
6. W.L. Cheng et al., "Influence of Alloying Elements on Microstructure and Microhardness of Mg-Sn-Zn-based Alloys," *Transactions of Nonferrous Metals Society of China*, 20 (2010), 2246-2252.

7. T.T. Sasaki et al., “Effect of Double Aging and Microalloying on the Age Hardening Behavior of a Mg-Sn-Zn Alloy,” *Materials Science and Engineering A*, 530 (2011), 1-8.
8. H.-Y. Ha et al., “Limitations in the Use of the Potentiodynamic Polarisation Curves to Investigate the Effect of Zn on the Corrosion Behaviour of As-extruded Mg-Zn Binary Alloy,” *Corrosion Science*, 75 (2013), 426-433.
9. Y. Song et al., “The Role of Second Phases in the Corrosion Behavior of Mg-5Zn Alloy,” *Corrosion Science*, 60 (2012), 238-245.

Magnesium Technology 2014
Edited by: Martyn Alderman, Michele V. Manuel, Norbert Hort, and Neale R. Neelameggham
TMS (The Minerals, Metals & Materials Society), 2014

EFFECT OF SURFACE CONDITION ON THE LOCALIZED CORROSION BEHAVIOR OF MAGNESIUM ALLOY AZ31B

Z.P. Cano, J.R. Kish, J.R. McDermid
GM Centre for Automotive Materials & Corrosion, McMaster University, Hamilton, Ontario, Canada L8S 4L7

Keywords: Magnesium, AZ31, Corrosion, Scanning Vibrating Electrode

Abstract

The localized corrosion behavior of AZ31B magnesium alloy sheet was studied in 0.01 M aqueous NaCl solution using the scanning vibrating electrode technique (SVET). Ongoing investigations by the authors have shown significant variation in corrosion mode and relative corrosion resistance depending on the alloy's surface condition. Comparisons were made between the observed behavior of the as-received, acid-cleaned and mechanically-polished surfaces. The SVET work was conducted to elucidate variations in the local electrochemical behavior for each surface condition. SVET maps were coupled with images of the corroding surfaces in order to show the progression of corrosion as a function of time. Schematic corrosion process models are proposed in order to explain the observed differences between the three surface conditions.

Introduction

Magnesium (Mg) alloys have received interest in the automotive industry due to their relatively low weight and favorable strength-to-weight ratio. However, they also have a high reactivity and are, therefore, very susceptible to corrosion when compared to steels and aluminum alloys. This has been a major factor in preventing their widespread adoption into exposed automotive components [1].

The localized corrosion mechanism of magnesium and its alloys continues to be a subject of debate in the scientific literature. Localized corrosion of Mg is often identified as pitting [1,2], but fundamentally different corrosion modes have also been reported. A number of studies over the past 25 years have shown a filiform or thread-like type of corrosion behavior in uncoated Mg [3, 4, 5] and Mg-aluminum (Al) alloys [6, 7].

Williams et al. [5, 7] have used SVET measurements to study filiform-like corrosion on mechanically-polished pure Mg and Mg alloy AZ31. They proposed that this behavior is driven by cathodic activation of the already-corroded areas of the surface, which caused the anodic dissolution to spread laterally across the surface instead of pitting deep into the metal. The cathodic activation in pure Mg was thought to be due to an enrichment of iron (Fe) in the reacted corrosion film, whereas the cathodic activation of AZ31 was thought to be from an enrichment of manganese (Mn)-Al phases.

In this work the localized corrosion behavior of AZ31B Mg alloy sheet taken from an automobile shock tower sub-assembly demo structure was studied. The demo structure was fabricated under the Mg Front End Research and Development (MFERD) project [8, 9]. Using a commercially available scanning electrochemical workstation, SVET measurements were completed to determine how the local electrochemical behavior of the alloy is influenced by its surface condition.

Experimental Procedures

The AZ31B sheet was sectioned into 1 cm × 1 cm square samples and each was cold-mounted in epoxy in order to leave only the plan view surface exposed. Fast-curing epoxy was applied around the edges of the exposed surface to prevent crevice corrosion from occurring at the metal/epoxy interface. All samples were immersed in 0.01 M aqueous NaCl solutions at a neutral pH for 24 h. Three different surface conditions of the alloy were tested and are listed in Table I.

Table I. Tested surface conditions of AZ31B sheet

Test	Surface Condition
1	As-received, ultrasonically cleaned in ethanol
2	Acid-cleaned by immersion of the as-received surface in 10% H_2SO_4 for 20 seconds, rinsed in DI water and ultrasonically cleaned in ethanol
3	Polished to 1200 grit SiC paper with ethanol lubricant

During immersion, local current density values were calculated from the SVET measurements taken as vectors normal to the exposed plan view surface. The SVET involves vibrating a platinum (Pt) electrode tip and measuring the voltage difference between the two extremes of the tip's position. Then, knowing the conductivity of the solution and the amplitude of the tip's vibration, current density can be calculated in the direction of vibration using a modified form of Ohm's law [10]. Alternatively, a calibration relating the measured voltage difference and current density in a given solution can be performed by taking vibrating electrode measurements of a series of known applied current densities [11]. A detailed explanation of the SVET is available elsewhere [10].

SVET measurements were performed using a Princeton Applied Research Model 370 Scanning Electrochemical Workstation. A photograph of the electrode setup is shown in Figure 1. Voltages were measured between the scanning Pt tip and a graphite auxiliary electrode. The diameter of the Pt tip was specified by the manufacturer to be in the range of 5 to 50 µm. SVET scans were completed on a 6 mm × 6 mm area of the sample every 1800 s (30 min.) throughout the duration of each test. The probe outputs were measured using a series of sweeping line scans across the scan area with a speed of 200 µm/s and one data point collected every 150 µm. The probe was vibrated in the vertical direction with an amplitude of 30 µm and a frequency of 80 Hz. The gain of the electrometer was set to 10^4, and the full scale sensitivity of the amplifier was set between 160 µV and 800 µV, depending on the intensity of the voltage signal for each test.

For each full scale sensitivity setting, a calibration test similar to the one outlined by Williams et al. [11] was completed. The vibrating probe was first placed inside a tube with a known inner area. Using a polished gold (Au) working electrode, a series of set

currents were passed through the tube and the vibrating probe output measured for each current. Plots of the probe output verses the set current density were constructed and showed a close linear relationship (the minimum R^2 value was 0.998). An equation relating the two variables was fit to the data in each case and used to convert the local probe outputs from each corrosion test into local current densities.

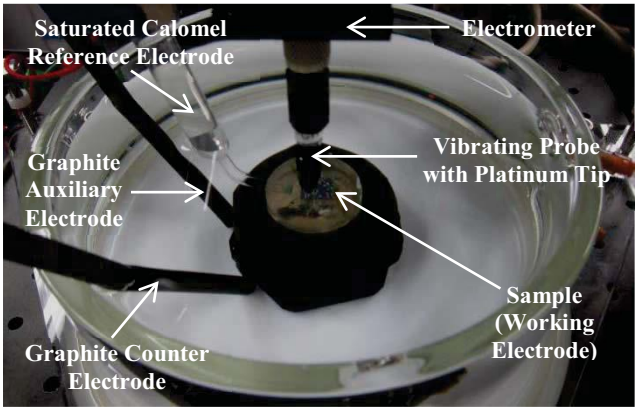


Figure 1. Electrode setup used for SVET measurements.

In order to relate the electrochemical activity with the visual appearance of the localized corrosion, the exposed surfaces were also monitored with a video camera positioned above the cell.

Results

Each surface condition of AZ31B displayed some form of localized corrosion. In two cases there was a delay between the time of immersion and the initiation of localized corrosion; these times are shown in Table II to the nearest half hour.

Table II. Time after immersion until localized corrosion initiation

Test		Time until localized corrosion initiation
1	As-received	Immediate
2	Acid-cleaned	3 h
3	Polished	12.5 h

A series of SVET maps alongside images of the 6 mm × 6 mm scan area for each of the 24-h corrosion tests are presented in Figures 2 through 4. It was not feasible to present every SVET map and image; therefore, those shown were selected to provide a summary of the electrochemical processes and appearance of the sample surfaces evolved as a function of time.

The corrosion reaction of Mg is comprised of the following anodic and cathodic half reactions [2]:

$$Mg \rightarrow Mg^{2+} + 2e^- \quad (1)$$

$$2H_2O + 2e^- \rightarrow H_2 + 2OH^- \quad (2)$$

Reaction (1) causes a positive ionic flow of current (highlighted on the SVET maps in red) while reaction (2) causes a negative ionic flow of current (highlighted on the maps in blue).

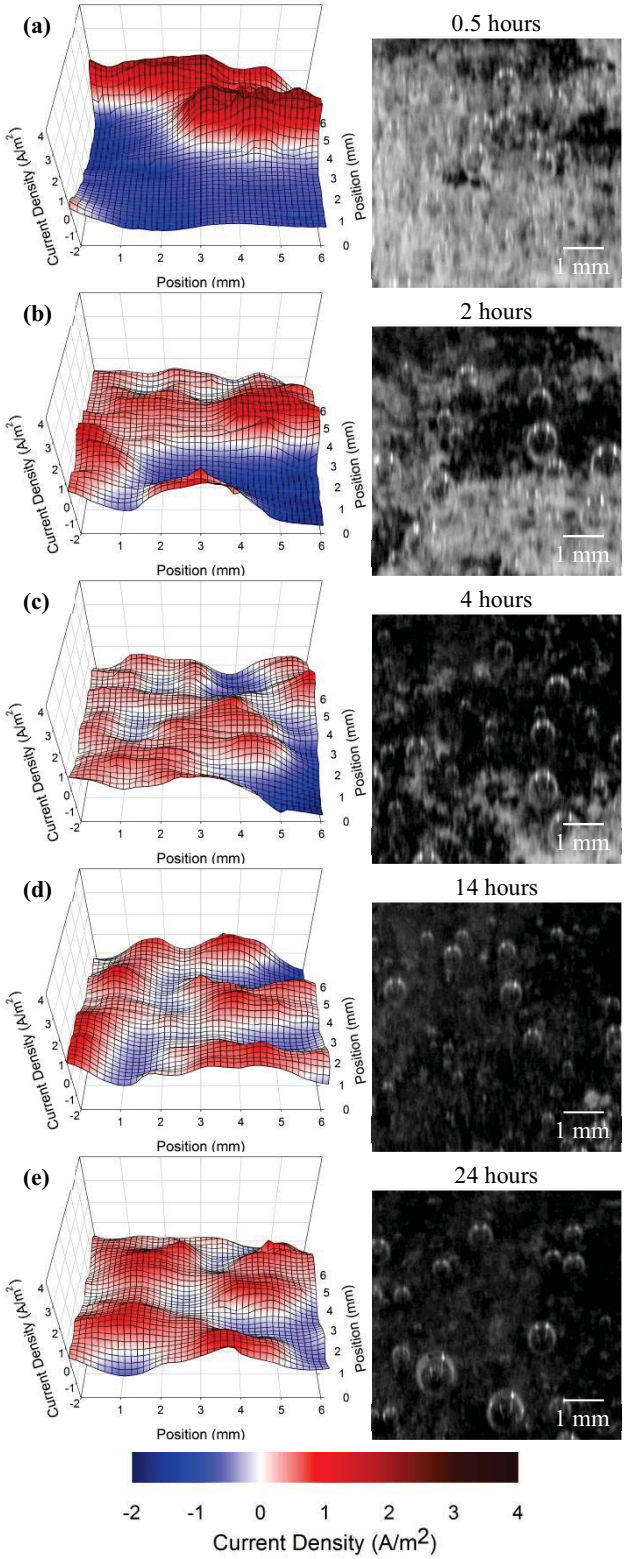


Figure 2. SVET maps and scan area images of the as-received AZ31B surface at various times after immersion in 0.01 M NaCl.

As-received AZ31B surface

Numerous hydrogen bubbles were formed on the as-received surface immediately after immersion in 0.01 M NaCl. Dark corroded threads also rapidly formed in the upper right portion of the scan area (Figure 2a). The SVET scans revealed intense

anodic and cathodic coupling across the surface. In the early stages of the test, anodic currents were detected on the corroded areas of the sample and cathodic currents were detected on un-corroded areas (Figure 2a-c). The un-corroded areas produced a relatively constant cathodic current density with an average magnitude of -0.7 A/m^2. Thus, as the surface became increasingly covered by corrosion products, charge neutrality on the surface was maintained by decreasing peak anodic current density magnitudes within the corroded regions. The peak anodic current density was 2.2 A/m^2 after 0.5 h of immersion and slowly decreased to a relatively constant value of 1.0 A/m^2 after the surface was completely covered by corrosion products (after 18 h). The rate at which corrosion products spread across the surface decreased as a function of time, presumably because of diminishing anodic currents.

It is interesting to note that predominantly anodic currents were produced above the dark corroded regions of the as-received AZ31B surface. By contrast, Williams et al. [5, 7, 8] observed predominantly cathodic currents within the corroded regions while anodic currents were only observed at the propagating corrosion front. Anodic currents indicate that Mg is dissolving as Mg^{2+} ions in the corroded areas. This would suggest that corrosion was occurring in a downward direction instead of primarily laterally, the latter of which has been reported for polished surfaces [5, 7, 8].

Using X-ray photoelectron spectroscopy, it was found that the as-received AZ31B surface used in this work contained heavy metal impurities in the native oxide film, including Fe and Cu [12]. As-received AZ31 sheet surfaces are often found to be contaminated with elements such as Cu, Fe and Ni, the latter two arising from the sheet rolling process [13, 14]. Heavy metal particles are well known to act as local cathodes with respect to Mg. It is proposed here that such heavy metal contamination was responsible for the intense microgalvanic activity detected by the SVET measurements on the as-received surface.

Acid-cleaned AZ31B Surface

The acid-cleaned surface did not display any cathodic currents of the magnitude observed for the as-received surface in 0.01 M NaCl. It was, therefore, likely that the acid-cleaning procedure of immersion in 10% H_2SO_4 for 20 seconds succeeded in removing the Fe and Cu particles from the as-received surface.

After immersion in the 0.01M NaCl solution, small bubbles quickly developed across the surface of the sample. Williams et al. [7] observed small SVET-detected cathodic currents above the initially-formed bubbles on polished AZ31 in ~0.9 M NaCl. It was proposed that noble Al-Mn-(Fe) intermetallic particles were present at the surface of these sites and acted as catalysts for reaction (2). However, the SVET maps after initial immersion in this work (not shown) did not display any local anodic or cathodic areas, possibly due to limits of the instrument's sensitivity.

After 3 h, intense hydrogen evolution was observed near the centre of the scan area (Figure 3a). This was accompanied by a local peak in anodic current density of 1.3 A/m^2 from the same area. Filiform-like corrosion then proceeded from several points on the sample in a manner similar to what has been reported in the literature [3-7, 11]. (Figure 3b-e). Hydrogen evolution and a local

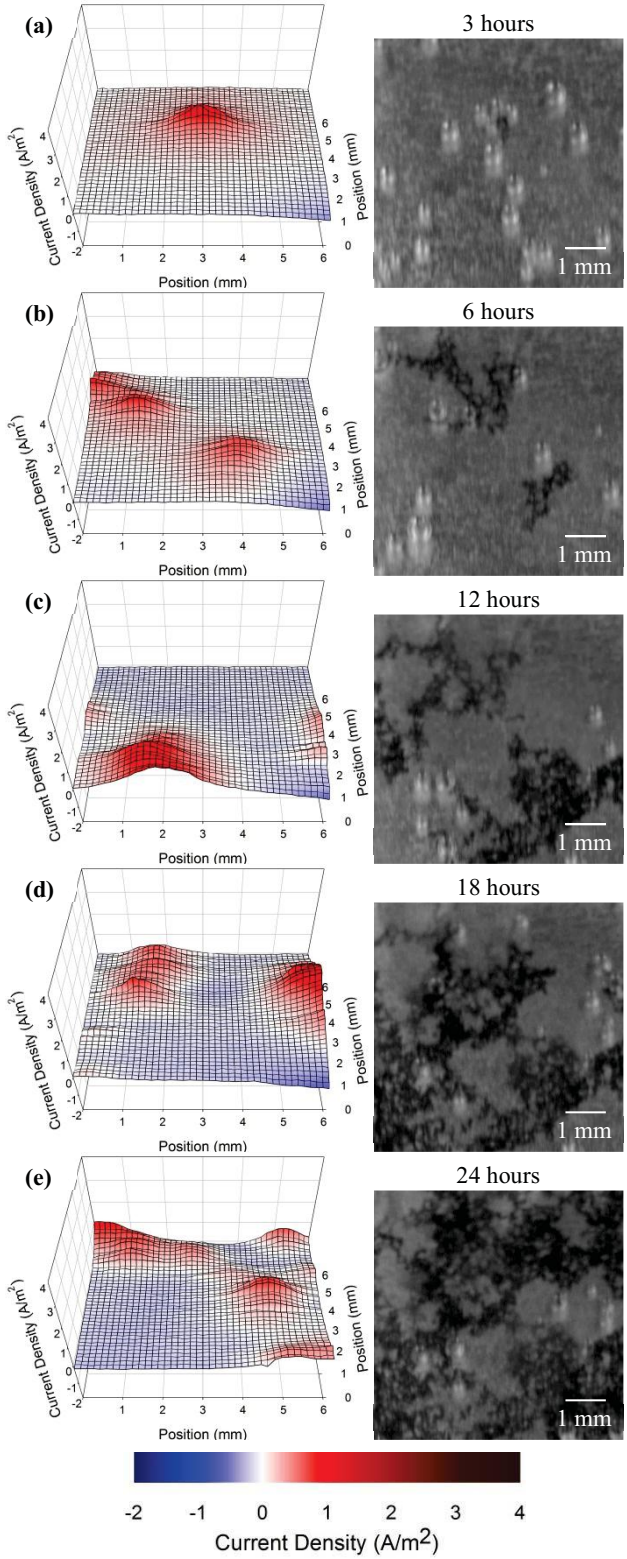


Figure 3. SVET maps and scan area images of the acid-cleaned AZ31B surface at various times after immersion in 0.01 M NaCl.

anodic current density peak were both always observed to occur at the head of a moving filament. This is consistent with the visual observations and SVET measurements of a corroding polished

AZ31 alloy reported by Williams et al. [7], although their study detected much higher anodic current density magnitudes (~100 A/m^2). However, Williams et al. [7] used a much more concentrated salt solution (~0.9 M NaCl) than in this study, which likely contributed to the large current density differences.

Relatively small cathodic currents were detected over the dark corrosion tracks left behind after the filiform-like propagation (Figure 3c-e). In order to maintain the overall charge neutrality on the surface, the intensity of local anodic peaks occurring at the heads of active filaments steadily increased from an average of 0.9 A/m^2 for the first 5 h of localized corrosion to 1.4 A/m^2 during the last 5 h of the test. This was again consistent with the previous report on an AZ31 alloy in ~0.9 M NaCl [7], where the authors showed that the rise in the surface-integrated cathodic current closely matched the rise of surface-integrated anodic current over time.

Test 3 (Polished – 0.01 M NaCl)

As was the case with the acid-cleaned surface, small bubbles quickly developed on the polished surface after immersion. Again, no localized anodic or cathodic currents were detected in the SVET maps (not shown) before the initiation of localized corrosion.

Localized corrosion was initiated just outside the top-left area of the SVET scanned area after 12.5 h. A corrosion filament propagated from this location until it entered the scan area about 1 h later (Figure 4a). The vibrating probe detected a local anodic current density of about 0.8 A/m^2 at the head of the filament. Throughout the rest of the 24-h exposure, multiple filaments were initiated and propagated in the same manner as described for the acid-cleaned sample, matching both its electrochemical behavior and visual appearance (Figure 4b-e).

The only differences between the behavior of the acid-cleaned and polished surfaces was that localized corrosion initiated in the acid-cleaned sample in less than a quarter of the time and propagated at a slightly lower rate. Both of these differences may be attributed to differences in the surface roughness achieved after each preparation procedure. Song et al. [13] reported the surface roughness (Ra) of an AZ31 sample polished to 1200 grit SiC paper to be 0.07 µm, while that for an AZ31 sample immersed in 10% H_2SO_4 for 20 seconds was considerably greater at 2.50 µm. In the same study, the rate of hydrogen evolution in ~0.9 M NaCl was lower on the acid-cleaned sample than the polished sample, which is consistent with the observations here. In another study Walter and Kann [15] reported that the pitting susceptibility of an AZ91 alloy in 0.09 M NaCl increased with increasing surface roughness, which was also consistent with the present results. This finding was attributed to the fact that a smoother surface can form a more continuous protective film than a rough surface [15].

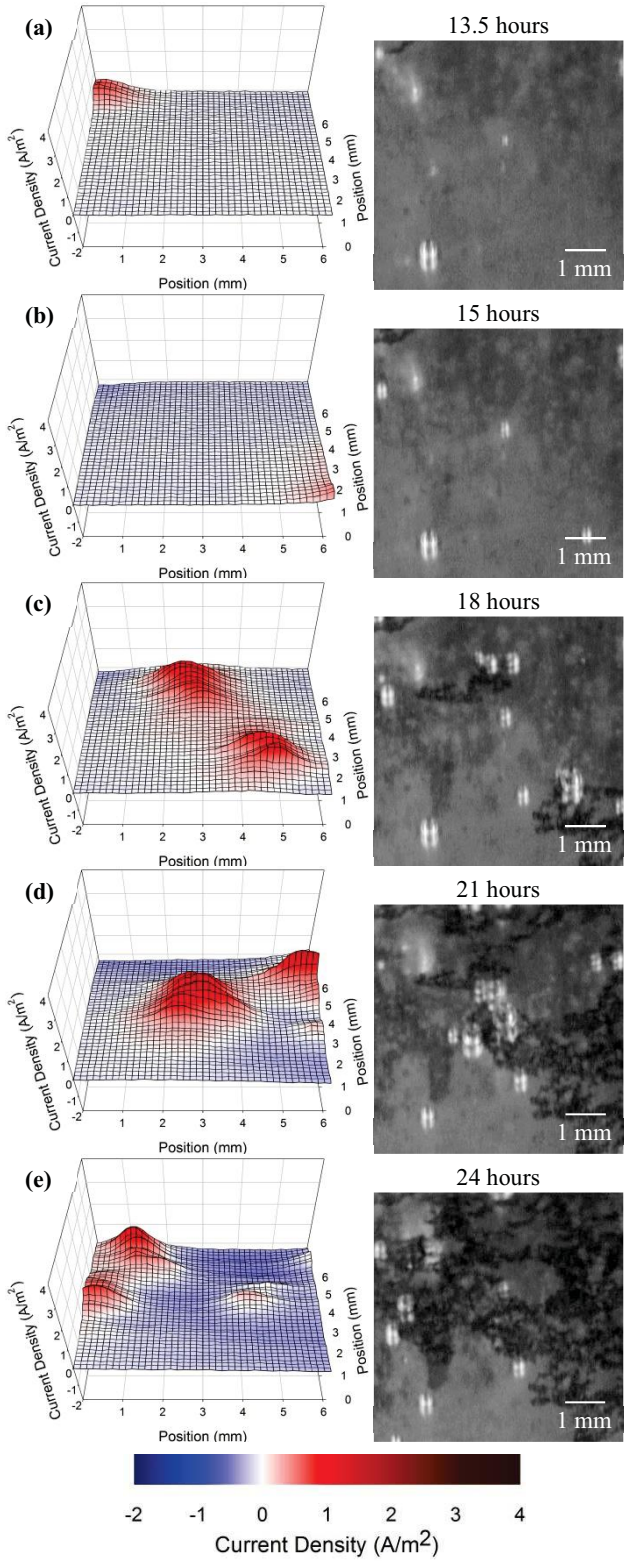


Figure 4. SVET maps and scan area images of the polished AZ31B surface at various times after immersion in 0.01 M NaCl (note that localized corrosion initiated outside of the scan area).

Discussion

In this study the electrochemical behavior of a corroding as-received AZ31B surface was distinctly changed after it was acid-cleaned or mechanically polished. Schematic electrochemical surface profiles are presented in Figure 5 in order to demonstrate the major differences. The polished or acid-cleaned surfaces displayed identical behavior to that reported by Williams et al. [5, 7, 11], where a strong anode at the corrosion front was coupled with a moderately cathodic reacted corrosion film which was left behind in the wake of the moving anode (Figure 5a). Conversely, the reacted corrosion film on the as-received surface stayed strongly anodic (although its current density decreased as its area increased), while the un-reacted surface film was strongly cathodic instead of neutral (Figure 5b).

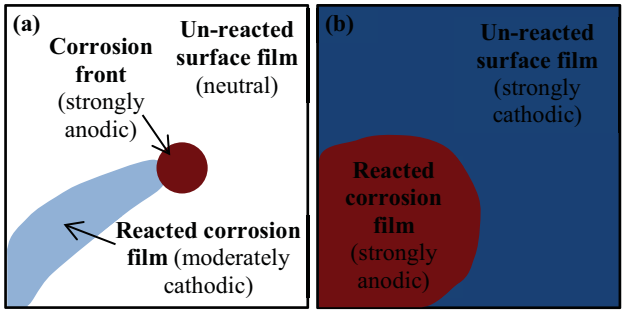


Figure 5. Schematic electrochemical surface profiles of (a) corroding acid-cleaned or mechanically-polished AZ31B surface (b) corroding as-received AZ31B surface with heavy metal surface contaminants.

It was determined that the acid-cleaning and mechanical polishing procedures both removed the Fe and Cu impurity particles originally present on the as-received surface. As shown in Table III, these two metals are strong cathodes with respect to Mg. It is, therefore, very likely that they were responsible for the local electrochemical differences that have been discussed.

Table III. Typical corrosion potentials of selected metal phases [First five phases determined in deaerated 5% NaCl solution saturated with $Mg(OH)_2$ (pH 10.5), testing solution for the last two phases not stated in the reference [1]

Metal Phase	E_{corr} (V_{SCE})
Mg	-1.65
Al_6Mn	-1.52
Al_4Mn	-1.45
Al_8Mn_5	-1.25
$Al_8Mn_5(Fe)$	-1.20
Fe	-0.50
Cu	-0.12

A schematic model of the corrosion processes occurring for polished or acid-cleaned AZ31B surfaces is presented in Figure 6; note that this is the same mechanism that was described by Williams et al. [11]. At the start of localized corrosion, only the native or unreacted surface film is present on the surface (Figure 6a). Al-Mn particles, which are commonly seen in AZ31 microstructures, are suspected to lie beneath the surface of the unreacted film. As localized corrosion proceeds, a dark reacted corrosion film replaces the original surface film (Figure 6b). Since only Mg metal is expected to be dissolved, the reacted corrosion film becomes enriched with Al-Mn intermetallic particles which are moderately cathodic (approximately 0.1 to 0.4 V nobler) with respect to Mg (refer to Table IV). As a result, the reacted corrosion film becomes cathodic with respect to the unreacted surface film and the location of anodic reaction (1) shifts to the unreacted film, directly adjacent to the reacted film. This electrochemical mechanism results in a lateral corrosion front movement and, therefore, closely resembles filiform corrosion.

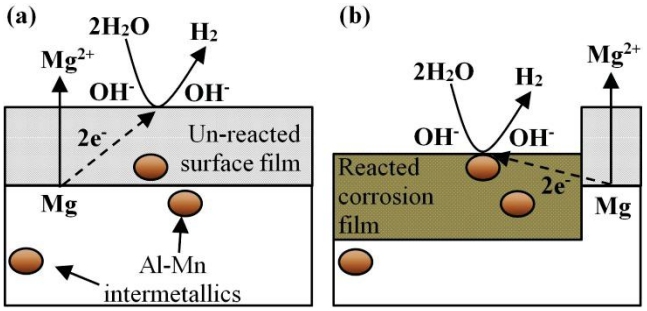


Figure 6. Schematic model of the localized corrosion processes occurring on an acid-cleaned or polished AZ31B surface.

A schematic model of the corrosion processes occurring for the as-received AZ31B with heavy metal contamination on the surface is presented in Figure 7. Intense microgalvanic activity between reactions (1) and (2) occurs due to the presence of noble Fe and Cu particles on the surface of the un-corroded areas. (Figure 7a). As localized corrosion proceeds, it is again expected that the reacted corrosion film will become enriched with Al-Mn intermetallics from the alloy microstructure (Figure 7b). However, it can be seen in Table III that Fe and Cu have corrosion potentials approximately 1.1 to 1.5 V nobler than Mg, which also makes them strongly cathodic with respect to each of the listed Al-Mn phases. Thus, since the heavy metal particles are present in both the reacted and unreacted areas of the film, the enrichment of Al-Mn particles in the reacted film is expected to be negligible in this case. Anodic reaction (1) will therefore continue to occur from underneath the reacted corrosion film, coupling with cathodic reaction (2) occurring on the unreacted surface film. This electrochemical mechanism results in a downward and lateral corrosion movement, which may resemble a mixture of pitting and filiform behavior.

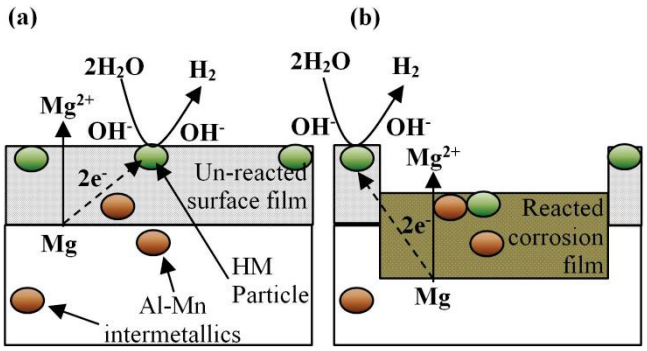


Figure 7. Schematic model of the localized corrosion processes occurring on an as-received AZ31B surface with heavy metal (HM) particle enrichment in the surface film.

Conclusion

The local electrochemical processes associated with filiform-like corrosion of Mg alloy AZ31B in 0.01 M NaCl solution were tracked using the scanning vibrating electrode technique (SVET). Changes in the electrochemical behavior occurred when altering the surface state of the alloy. SVET mapping of an as-received AZ31B surface showed intense microgalvanic activity that caused corrosion to occur in a downward direction as well as laterally. This was attributed to an enrichment of Fe and Cu heavy metal particles in the native oxide film. Acid-cleaning in 10% H_2SO_4 for 20 s and mechanical polishing of the as-received surface both appeared to successfully remove any strong cathodic contamination, since both of these surfaces displayed electrochemical activity that was more typical of filiform-like corrosion, as has been previously reported.

Acknowledgements

The authors would like to thank the Automotive Partnerships Canada (APC) program of the Natural Sciences and Engineering Council of Canada (NSERC) for financial support of this research.

References

1. G.L. Song and A. Atrens, "Understanding Magnesium Corrosion", *Adv. Eng. Mater.*, 5 (12) (2003), 837-858.

2. G.L. Makar and J. Kruger, "Corrosion of Magnesium", *Inter. Mater. Rev.*, 38 (3) (1993), 138-153.

3. P. Schmutz, V. Guillaumin, R.S. Lillard, J.A. Lillard and G.S. Frankel, "Influence of Dichromate Ions on Corrosion Processes on Pure Magnesium", *J. Electrochem. Soc.*, 150 (4) (2003), B99-B110.

4. C.R. McCall, M.A. Hill and R.S. Lillard, "Crystallographic Pitting in Magnesium Single Crystals", *Corros. Engineer., Sci. Technol.*, 40 (4) (2005), 337-343.

5. G. Williams and R. Grace, "Chloride-Induced Filiform Corrosion of Organic-Coated Magnesium", *Electrochim. Acta,* 56 (2008), 1894-1903.

6. O. Lunder, J.E. Lein, S.M. Hesjevik, T.Kr. Aune, and K. Nisancioglu, "Filiform Corrosion of a Magnesium Alloy," 11th Annual Corrosion Congress, Florence, Italy, 1990, 5.255–5.262.

7. G.Williams, H.L. Dafydd and R. Grace, "The Localised Corrosion of Mg Alloy AZ31 in Chloride Containing Electrolyte studied by a Scanning Vibrating Electrode Technique", *Electrochim. Acta,* 109 (2013), 489-501.

8. E.A. Nyberg, A.A. Luo, K. Sadayappan and W. Shi, "Magnesium for Future Autos", *Adv. Mater. Process.*, 166 (10) (2008), 35-37.

9. B.E. Carlson, R. Verma, W. Yuan and R.T. Szymanski, "Friction Stir Welding of a Magnesium AZ31 Sub-Assembly", (Paper presented at Sheet Metal Welding Conference XV, Livonia, MI, 2012).

10. S. Rossi, M. Fedel, F. Deflorian, M. Vadillo, "Localized Electrochemical Techniques: Theory and Practical Examples in Corrosion Studies", *C.R. Chimie*, 11 (2008), 984-994.

11. G. Williams and H.N. McMurray, "Localized Corrosion of Magnesium in Chloride-Containing Electrolyte Studied by a Scanning Vibrating Electrode Technique", *J. Electrochem. Soc.*, 155 (7) (2008), C340-C349.

12. X.R. Zhang, Z.P. Cano, B.M. Wilson, J.R. Kish and J.R. McDermid, "Corrosion Behavior of Friction Stir Welded Mg Alloy Joints for Automotive Applications" (Paper presented at Materials Science and Technology 2013, Montreal, Canada, 2013).

13. G.L. Song, Z. Xu, "The Surface, Microstructure and Corrosion of Magnesium Alloy AZ31 Sheet", *Electrochim. Acta*, 55 (2010), 4148-4161.

14. U.C. Nwaogu, C. Blawert, N. Scharnagl, W. Dietzel and K.U. Kainer, "Influence of Inorganic Acid Pickling on the Corrosion Resistance of Magnesium Alloy AZ31 Sheet", *Corros. Sci*, 51 (2009), 2544-2556.

15. R. Walter and M.B. Kannan, "Influence of Surface Roughness on the Corrosion Behavior of Magnesium Alloy", *Mater.Design*, 32 (2011), 2350-2354.

Magnesium Technology 2014
Edited by: Martyn Alderman, Michele V. Manuel, Norbert Hort, and Neale R. Neelameggham
TMS (The Minerals, Metals & Materials Society), 2014

FORMATION OF SELF-ASSEMBLED MONOLAYER ON CERIUM CONVERSION COATED AZ31 Mg ALLOY

S. A. Salman[1, 3], N. Akira[2], K. Kuroda[1], and M. Okido[1]
[1]EcoTopia Science Institute, Nagoya University, Furo−cho, Chikusa ku, Nagoya, Japan
[2]Graduate School of Engineering Nagoya University, Furo-cho, Chikusa-ku, Nagoya, Japan
[3]Graduate School of Engineering, Al-Azhar University, Nasr City, Cairo, Egypt

Keywords: Conversion Coating, SAM, Magnesium Alloy, Corrosion, contact angle.

Abstract

Magnesium alloys are recognized as alternatives to Al alloys and steel to reduce the weight of structural materials. However, a major obstacle to the widespread use of magnesium alloys is its poor corrosion resistance. Therefore, further surface treatment of magnesium and its alloy is important in meeting several industrial specifications. In a previous research, we investigated the surface treatment of AZ31 magnesium alloy using cerium conversion coating. The anticorrosion properties could be improved with the cerium treatment. In this present research, self-assembled monolayer (SAM) was adsorbed on the surface of cerium conversion coated AZ31 magnesium alloy. The SAM thin film was deposited using (Tridecafluoro-1, 1, 2, 2-tetrahydrooctyl) trimethoxysilane (FAS13) and Tetrakis(trimethylsiloxy)titanium (TTMS) as a catalyst. The corrosion resistance of cerium conversion coated AZ31 Mg alloy was improved with SAM post treatment. Furthermore, the contact angle increases from 13 deg. to 169 deg. indicating to production of super hydrophobic surface with SAM post treatment.

Introduction

Magnesium alloys are the lightest structural materials with high strength-to-weight ratio, good electrical/heat conductivity and damping properties. These properties make magnesium alloys attractive for applications in aerospace, transportation and portable electronics where weight reduction is critical. It was reported that magnesium alloys are recognized as alternatives to Al alloys and steel for reducing the weight of vehicle, reducing emission and increasing energy efficiency [1, 2].

Despite of these good characteristics, there are some major restrictions of the widespread use of magnesium alloys due to its extremely negative equilibrium potential and poor corrosion resistance, specially in chloride environment. Therefore, further surface treatment of magnesium and its alloy is important in meeting several industrial specifications. Electrochemical plating, chemical conversion, anodizing, physical vapor deposition, and electroless nickel plating are commonly applied surface treatment. Among these processes, conversion coatings are economical, easy to apply and offer a variety of valuable properties to improve the performance and extend the service life of the magnesium alloy parts being treated. Chromate conversion coatings have been the most widely used technique to provide excellent corrosion protection. However, changing environmental regulations and pollution prevention requirements have led to a significant push to stop using of poisonous hexavalent chromate and discover alternative environment-friendly electrolytes. Numerous non-chromate electrolytes are thus developed, such as cerium and rare earth based electrolytes, stannate, phosphate, vanadate and phosphate/permanganate electrolytes [3, 4, 5, 6, 7].

One of the most promising systems is based on rare earth elements. Several researchers have demonstrated that treatments with aqueous solutions of cerium salts effectively inhibited corrosion [8, 9, 10]. In a previous research, we investigated the surface treatment of AZ31 Mg alloy using cerium conversion coating treatment [11]. The anticorrosion properties could be improved with the cerium conversion coating treatment.

In other research, Self-assembled monolayer (SAM) was successfully adsorbed on the AZ31 Mg alloy surface using oleic acid and stearic acid with various organic solvents [12]. In this research, Self-assembled monolayer (SAM) was deposited on the surface of cerium conversion coated AZ31 magnesium alloy using (Tridecafluoro-1, 1, 2, 2-tetrahydrooctyl) trimethoxysilane (FAS13) and Tetrakis(trimethylsiloxy) titanium (TTMS) as a catalyst.

Experimental

Specimens

Commercially available AZ31 Mg alloys were used as the substrate. The chemical composition of the alloy is listed in Table 1. The surface of the alloy was polished up to #2000 emery paper followed by 0.05 μm alumina powders.

Table 1 Chemical composition of AZ31 Mg alloy (mass%)

Mg	Al	Zn	Mn	Si	Cu	Ni	Fe
Bal.	3.0	1.0	0.43	0.01	<0.01	<0.001	0.003

The specimens were carefully cleaned with water, rinsed with acetone and dried under air. All of the experiment specimens were mounted using polytetrafluoroethylene (PTFE) resin tape, leaving 1 cm^2 surface area.

Conversion coating

Conversion coating was performed at room temperature for 900 s in the aqueous electrolyte of 0.05 M $Ce(NO_3)_3$ at pH 5. After the treatment, the specimens were carefully rinsed using distilled water and dried under air before analysis.

Deposition of SAM film

Organic thin films (SAM) have been fabricated by Vapor-Phase Method. Tridecafluoro-1,1,2,2-tetrahydrooctyl-1-dimethylchlorosilane (FAS13) $CF_3(CF_2)5(CH_2)_2 Si(OCH_3)_3$) was used as raw materials for preparation of SAM post treatment. Tetrakis(trimethylsiloxy) titanium (TTMS) ; $Ti[OSi(CH_3)_3]_4$) was used as catalyst. The specimens and 70 µL of FAS13 and TTMS were introduced in a teflon vessel with a 300 mL capacity and was then sealed tightly with a lid. The vessel set in the heater and then temperature in the vessel rised from room temperature to 100º C for 30 min. After that the vessel was maintained at a temperature of 100º C for less than 3 h.

Morphology and Structure of Anodic Film

The morphology and microstructure of the anodic films were observed with a Hitachi S-800 scanning electron microscope (SEM), the phase structure and the composition of the coating films were identified with X-ray diffraction (XRD), Energy Dispersive X-ray Spectrometry (EDS) and X-ray Photoelectron Spectroscopy (XPS). Contact angles measurement was used to measure the wettability of the coatings formed on Mg alloy substrate.

Results and discussion

Figure 1 shows the SEM images of (1) AZ31 Mg alloy substrate, (2) cerium conversion coated and (3) cerium conversion coated + SAM post treated AZ31 Mg alloy. The cerium conversion coating film has a yellow color to the naked eye. The coating revealed the presence of several micro-cracks with the maximum size of 1.5µm. The microstructure of the coating does not change with SAM post treatment; however, the surface roughness (Ra) was increased with SAM treatment.

The mechanism of cerium conversion coating was shown in details in our previous work. The major anodic reaction is the dissolution of magnesium that is likely to occur at anodic site. The cathodic reactions begin immediately upon immersion of Mg specimen in the treatment solution as shown in (Eq. 1-4). The hydrated cerium oxides were deposited on the cathodic sites of the surface, due to a local pH increase.

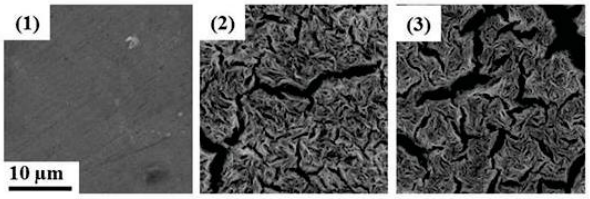


Fig. 1 SEM images of (1) AZ31 Mg alloy substrate, (2) cerium conversion coated and (3) cerium conversion coated + SAM post treated AZ31 Mg alloy.

In the lower pH range, CeIII is the more stable form

$$2H_2O + 2e^- \longrightarrow 2OH^- + H_2 \quad \ldots\ldots\ldots\ldots\ldots \quad (1)$$

$$Ce^{3+} + 3OH^- \longrightarrow Ce(OH)_3 \quad \ldots\ldots\ldots\ldots\ldots\ldots (2)$$

$$2Ce(OH)_3 \longrightarrow Ce_2O_3 + 3H_2O \quad (3)$$

At higher pH values, CeIV becomes the more stable form, CeIII
may be oxidized to CeIV and the following reaction is occur [8].

$$Ce_2O_3 + O2 \longrightarrow 2CeO_2 \quad (4)$$

XRD results shows that the main peak of cerium coating film was identified as Mg, $Mg(OH)_2$ and CeO_2 peaks; the figure does not shown in this research paper

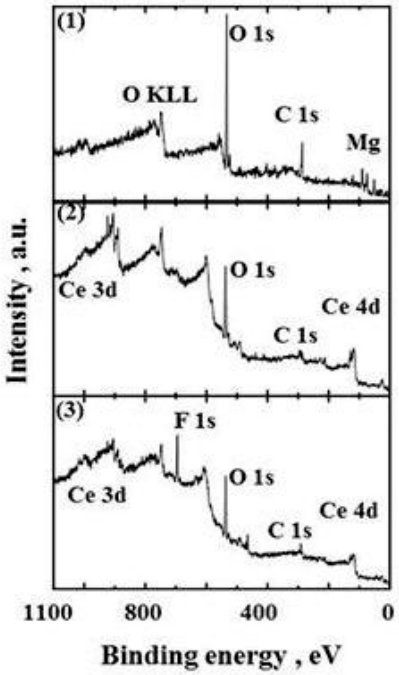


Fig. 2 The XPS spectra of (1) AZ31 Mg alloy substrate, (2) cerium conversion coated and (3) cerium conversion coated + SAM post treated AZ31

Figure 2 shows the XPS spectra of O1s, O KLL, C1s, Ce 3d, Ce 4d and for (1) AZ31 Mg alloy substrate, (2) cerium conversion coated and (3) cerium conversion coated + SAM post treated AZ31 Mg alloy. The high concentration of carbon and oxygen on the surface is commonly seen in XPS peaks of AZ31 Mg alloy before and after conversion coating and SAM post treatment due to the adventitious hydrocarbons from the environment and oxide film respectively. Ce 3d and Ce 4d peaks were detected on the surface after conversion coating treatment and after SAM post treatment. F 1s peak which observed at 688 eV was the major element existed after SAM post treatment. In the previous research, the high resolution of F 1s peak was recorded [12]; there was two peaks originated from the CF2 and CF3 groups, it can be divided into two components that are centered at around binding energies of 688 and 690 eV corresponding to - CF2 - and - CF3- groups. The CF2 and CF3 components could be clearly resolved from the other components because of fluorine's great electronegativity. A shoulder peak at 685 eV may be attributed to MgF_2 [13-15].

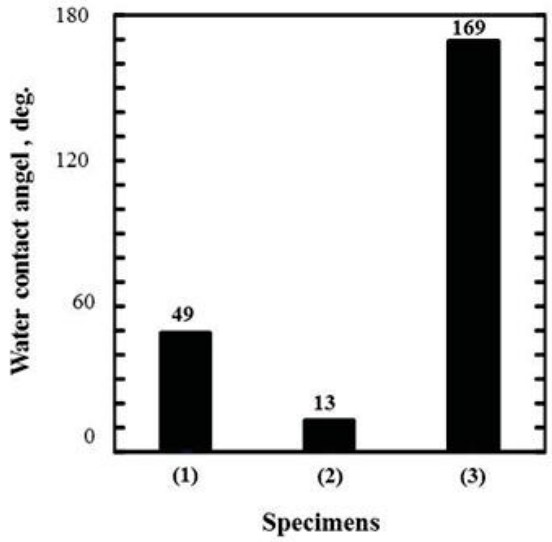


Fig. 3 Contact angles for water on AZ31 Mg alloys; (1) Mg alloy substrate, (2) cerium conversion coated and (3) cerium conversion coated + SAM post treated AZ31 Mg alloy.

Figure 3 show the actual variation in water static contact angles of AZ31 Mg alloys before and after cerium conversion coating and SAM post treatment. AZ31 Mg alloy before treatment has a hydrophilic surface with a water contact angle of 49º. The surfaces become more hydrophilic and the wettability was noticeably increased with cerium conversion coating. The relative contact angle was decreased to 13º on the cerium coated surface. With applying SAM post treatment on the cerium coating, the wettability was noticeably decreased and the relative contact angle was increased to 169º. The increasing in contact angles of treated specimens is results from the adsorption of organic molecules on the substrate surface.

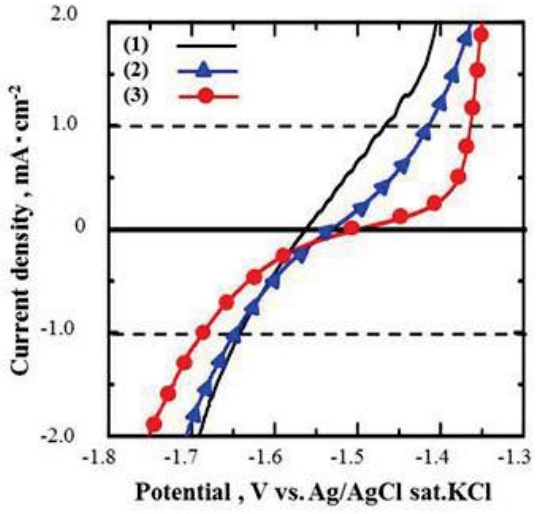


Fig. 4 Polarization curves of (1) Mg alloy substrate, (2) cerium conversion coated and (3) cerium conversion coated + SAM post treated AZ31 Mg alloy in 17 mM NaCl and 0.1M Na_2SO_4 solution.

The potentiodynamic polarization method was used to characterize the corrosion properties of the AZ31 Mg alloy before and after treatment. The anodic polarization represents the dissolution of magnesium and the cathodic polarization curves are assumed to represent the cathodic hydrogen evolution through water reduction. Figure 4 shows the the anodic and the cathodic polarization curves of (1) AZ31 Mg alloy substrate, (2) cerium conversion coated and (3) cerium conversion coated + SAM post treated AZ31 Mg alloy. ΔE; (E_A –E_C) is defined as the difference between the potential value at 1.0 $mAcm^{-2}$ (anodic side, E_A) and the potential value at 1.0 $mAcm^{-2}$ (cathodic side, E_C). ΔE values of the three specimens were summarized in Table 2. The highest ΔE value was observed with SAM post treatment and the non-treated specimen has the lowest value. This indicates that the anti-corrosion property was improved with SAM post treatment.

Table 2 ΔE values of (1) Mg alloy substrate, (2) cerium conversion coated and (3) cerium conversion coated + SAM post treated AZ31 Mg alloy

Specimens	E_0	E_A	E_C	$E_A - E_C$
(1)	-1.56	-1.48	-1.64	0.16
(2)	-1.53	-1.41	-1.65	0.24
(3)	-1.50	-1.36	-1.69	0.33

Conclusion

The SAM thin film was successfully deposited on the surface of cerium conversion coated AZ31 magnesium alloy using (Tridecafluoro-1, 1, 2, 2-tetrahydrooctyl) trimethoxysilane (FAS13) and Tetrakis(trimethylsiloxy) titanium (TTMS) as a catalyst. The anticorrosion property was improved with SAM post treatment compared to Non-treated specimen and cerim coated specimen. The higher contact angle of 169º was obtained after SAM post treatment which indicates that the surface becomes more hydrophobic.

Acknowledgment

The authors gratefully acknowledge the financial support of Aichi Center for Industry and Science Technology and the Ministry of the Education, Culture, Sports, Science and Technology, Japan.

References

1. S A Salman, M. Okido, Anodization of magnesium (Mg) alloys to improve corrosion resistance, in: G-L Song (Eds.), Corrosion prevention of magnesium alloys, Woodhead Publishing, Cambridge, 2013, pp. 197-231.
2. C. Blawert, W. Dietzel and E. Ghali, G. Song, Adv. Eng. Mater., 8, 511 (2006).
3. A.L. Rudd, C.B. Breslin, F. Mansfeld, "The corrosion protection afforded by rare earth conversion coatings applied to magnesium," Corrosion Science, 42 (2000), 275-288.
4. F. Zucchi, A. Frignani, V. Grassi, G. Trabanelli, C. Monticelli, "Stannate and permanganate conversion coatings on AZ31 magnesium alloy," Corrosion Science, 49 (2007), 4542-4552.
5. W. Zhou, D. Shan, E. Han, W. Ke, "Structure and formation mechanism of phosphate conversion coating on die-cast AZ91D magnesium alloy," Corrosion Science, 50 (2008), 329-337.
6. M. Mosiałek, G. Mordarski, P. Nowak, W. Simka, G. Nawrat, M. Hanke, R.P. Socha, J. Michalska, "Phosphate–permanganate conversion coatings on the AZ81 magnesium alloy: SEM, EIS and XPS studies," Surface & Coatings Technology, 206 (2011), 51-62.
7. S. A. Salman, K. Kuroda, M. Okido, Formation of vanadate conversion coating on AZ31 magnesium alloy, in Norbert Hort et al (Eds.), Magnesium technology 2013, The Minerals, Metals & Materials Society, 2013.
8. Manuele Dabala, Katya Brunelli, Enrico Napolitani, Maurizio Magrini Surface and Coatings Technology 172 (2003) 227–232
9. Manuele Dabala, Lidia Armelao, Alberto Buchberger, Irene Calliari Appl. Surf. Sci. 172 (2001) 312 – 322
10. A. Froats, T. K. Aune, D. Hawke, W. Unsworth, J. Hillis, in Metals Handbook, 9th ed., Vol. 13, ASM Int., Materials Park, OH 1987, pp. 740-754.
11. S. A. Salman, Ryoichi Ichino, and Masazumi Okido, Development of Cerium-based Conversion Coating on ZA31 Magnesium Alloy, Chem. Lett., 36, 8, 1024-2025 (2007).
12. S. A. Salman and M. Okido, Self-assembled monolayers formed on AZ31 Mg alloy, Journal of Physics and Chemistry of Solids 73, 7, (2012). p. 863-866.
13. T. Ishizaki, M. Okido,Y. Masuda, N. Saito, M. Sakamoto, Corrosion resistant performances of alkanoic and phosphonic acids derived Self-Assembled monolayers on magnesium alloy AZ31 by vapor-phase method, Langmuir, 27(2011) p. 6009-6017.
14. Chataib, M.; Roberfroid, E. M.; Novis, Y.; Pireaux, J. J.; Caudano, R.; Lutgen, P.; Feyder, G., Polymer surface reactivity enhancement by ultraviolet ArF laser irradiation: An x-ray photoelectron spectroscopy study of polytetrafluoroethylene and polyethyleneterepthalate ultraviolet treated surfaces, J. Vac. Sci. Technol., A 1989, 7, 3233.
15. Hozumi, A.; Ushiyama, K.; Sugimura, H.; Takai, O., Fluoroalkylsilane Monolayers Formed by Chemical Vapor Surface Modification on Hydroxylated Oxide Surfaces, Langmuir 1999, 15, 7600.

Magnesium Technology 2014
Edited by: Martyn Alderman, Michele V. Manuel, Norbert Hort, and Neale R. Neelameggham
TMS (The Minerals, Metals & Materials Society), 2014

Effects of Current Density on Microstructure and Corrosion Property of Coating on AZ31 Mg Alloy Processed via Plasma Electrolytic Oxidation

Kang Min Lee[1], Feryar Einkhah[2], Mohammad Ali Faghihi Sani[2], Young Gun Ko[3,*], and Dong Hyuk Shin[1,*]

[1]Department of Metallurgy and Materials Engineering, Hanyang University, Ansan, 426-791, South Korea
[2]Department of Material Science and Engineering, Sharif University of Technology, Tehran, 145888-9694, Iran
[3]School of Materials Science and Engineering, Yeungnam University, Gyeongsan, 712-749, South Korea

Keywords: Mg alloy, plasma electrolytic oxidation, current density, corrosion

Abstract

The effects of the current density on the microstructure and the corrosion property of the coating on AZ31 Mg alloy processed by the plasma electrolytic oxidation (PEO) were investigated. The present coatings were produced in an acid electrolyte containing K_2ZrF_6 with three different current densities, i.e., 100, 150, and 200 mA/cm^2. From the microstructural observations, as the applied current density was increased, the diameter of micro-pores formed by the plasma discharges with high temperature increased. The coatings on AZ31 Mg alloy were mainly composed of MgO, ZrO_2, MgF_2, and $Mg_2Zr_5O_{12}$ phases. The results of potentiodynamic polarization clearly showed that the PEO-treated AZ31 Mg alloy applied at 100 mA/cm^2 of current density exhibited better corrosion properties than the others.

Introduction

Mg alloys are attractive for electronics and automobile industry owing to their low density, high specific strength, and good machinability [1-3]. Despite their inherent properties, however, the inferior corrosion property of Mg alloys limited their commercial applications in numerous fields where the corrosion resistance are required [4,5]. In order to protect Mg alloys in corrosive environment, several surface treatments such as chromating, anodizing, and plasma electrolytic oxidation (PEO) have been used to improve the corrosion property of Mg alloys by forming the coatings [6-9]. Among these processes, PEO is a relatively new electrochemical surface treatment that utilizes mainly plasma-assisted electrochemical reaction to convert the metal surface into the coating with the strong adhesion between them [10-13]. The surface morphologies of the coatings on Mg alloys subjected to the PEO process depended on processing variables including the chemical compositions of the electrolyte, electrical parameters, and the initial state of the metal substrate [14-17].

Recently, according to the earlier investigation by other groups [18-22], the introduction of K_2ZrF_6 into the electrolyte during the PEO process has played a significant role in increasing the corrosion resistance of Mg alloys. For instance, F. Liu et al. [20] demonstrated the effect of the different additives in electrolytes containing K_2ZrF_6 on the microstructures and the corrosion properties of the oxide layers on AM50 Mg alloys, whereas H. Luo et al. [21] investigated the PEO-treated AZ91 Mg alloys in an alkaline electrolyte with K_2ZrF_6 to improve the corrosion property. L. Wang et al. [22] also found that in case of both electrolytes with K_2ZrF_6 at quite low or high pH, the occurrence of the plasma discharges during the PEO process were delayed than ordinary PEO conditions because the formation of the dielectric layer on Mg alloys was restricted due to the instability of the electrolyte.

Although few studies have been made to show the effects of K_2ZrF_6 in the electrolyte on the corrosion properties of Mg alloys as discussed above, little is known about the effects of electrical parameters on the characteristics of the coating on Mg alloys. More attention should be paid to the select of the optimized current density during the PEO process, because the applied current density significantly influenced the not only microstructure but also corrosion properties of the coating on Mg alloys [23-25]. In this study, we fabricated the coating on AZ31 Mg alloy via the PEO process in the electrolyte with K_2ZrF_6 as a function of the applied current density, and the microstructures and the phase compositions of the coatings were systematically examined. The corrosion resistances of the coatings were also investigated by potentiodynamic polarization test.

Experimental

The chemical composition of AZ31 Mg alloy supplied from POSCO Inc. was Mg-3.1Al-0.9Zn-0.2Mn by weight percent. Prior to the experiments, AZ31 Mg alloy plates with a size of 30 × 40 × 2 mm^3 were mechanically polished with 1,000 grit emery paper and subsequently rinsed with distilled water. The plates were then ultrasonically cleaned in ethanol and dried in air. The PEO process was conducted utilizing a 6.5 kW DC power supply (Unicorntech, 65010D) in conjunction with stirring and cooling systems to maintain the temperature of the electrolyte at 293 K during the PEO process. The electrolytic cell consisted of a 2 l glass-vessel with a sample holder and stainless steel was used as a cathode in the electrolyte containing 0.02 mol/l H_3PO_4 + 0.02 mol/l K_2ZrF_6. To prevent the dissolution of the substrate from the present electrolyte at ~3 pH, ~5 μm-thick passivation layer was firstly formed on AZ31 Mg alloy via the PEO process in an alkaline electrolyte. To study the influence of the applied current density on the microstructure and corrosion behavior of the coatings, three different conditions, i.e., 100, 150, and 200 mA/cm^2 were applied, and the coating times were found to be 300, 270, and 240 s, respectively, to consider the thickness effect of coating on the corrosion properties.

Surface and cross-sectional morphologies of PEO-treated AZ31 Mg alloys were collected using a field-emission scanning electron microscopy (SEM; Hitachi, S-4800). The phase compositions were analyzed using X-ray diffraction (XRD; Rigaku, D-MAX 2500) with a step size of 0.05° and a scan range from 20° to 80°. Potentiodynamic polarization test was conducted to evaluate the corrosion properties of PEO-treated AZ31 Mg alloys using a Reference 600 potentiostat (Gamry Instruments) with a glass cell in a 3.5 wt.% NaCl solution at pH 7.0. The cell was equipped with three electrodes: a PEO-treated AZ31 Mg alloy with an exposed area of 1 cm^2 as a working electrode, a platinum mesh of dimensions 20 × 20 mm^2 as a counter electrode, and an Ag/AgCl electrode as a reference electrode. After an initial delay of 300 s,

the potentiodynamic polarization curves were measured from −0.25 to 0.35 V with respect to the open circuit potential at a scan rate of 1 mV/s.

Results and Discussion

Fig. 1 shows the voltage response vs. coating time curves of AZ31 Mg alloys treated by the PEO process as a function of the current density. Previous studies revealed that at the beginning of the PEO process, the voltage response increased rapidly with the formation of the passivation layer on the surface of the substrate and after the breakdown voltage, the plasma discharges were generated in the vicinity of the substrate and the passivation layer [6,26]. In Fig. 1, regardless of the applied current densities, as the voltage response was increased, plasma discharges in the vicinity of the substrate began to appear at a breakdown voltage where the onset of the inflection point was observed. In addition, the shapes of the voltage responses were similar to each other. However, increasing the current density from 100 to 200 mA/cm^2 was found to result in higher final voltages. The breakdown voltages of AZ31 Mg alloy samples applied with three different current densities were measured to be 476, 513, and 538 V, and the final voltages of that were found to be 580, 601, and 622 V, respectively. Srinivasan et al. [23] reported that the voltage response was directly proportional to the increment of the current density during the PEO process because the source of the electrical energy highly depended on the applied current density. Thus, the present results corresponded to this conventional electrical behavior.

Fig. 2 displays the surface morphologies of the coatings on AZ31 Mg alloys after the PEO process as a function of the current density. Regardless of the applied current densities, the surface morphologies exhibited a number of micro-pores and micro-cracks, which were attributed to the occurrence of the short-lived plasma discharges with high temperature and the thermal stress by the rapid solidification of the molten oxide in the relatively cool electrolyte, respectively [15,27]. The granular oxides with ~2 μm size in the vicinity of micro-pores and micro-cracks were also observed. Dehnavi et al. [28] reported that these structures were due to the co-deposition with the ionized substrate and the electrolyte ions. It is apparent from Fig. 2 that, the size and number of the micro-pores increased and decreased, respectively, since a higher energy could enhance the intensity of the micro-discharges. This phenomenon was consistent with the result of our previous works [25].

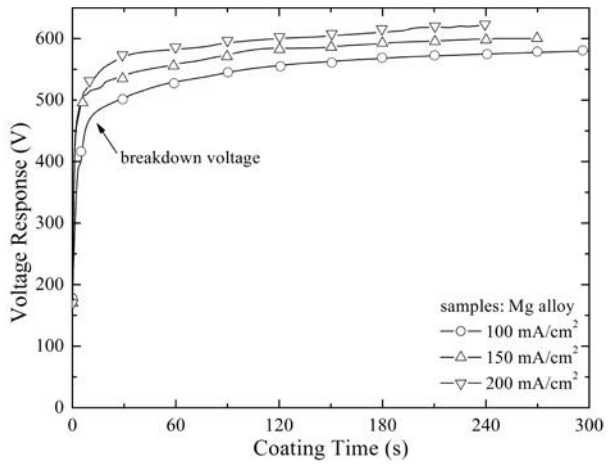


Fig. 1. Voltage response vs. coating time during the PEO process of the AZ31 Mg alloys.

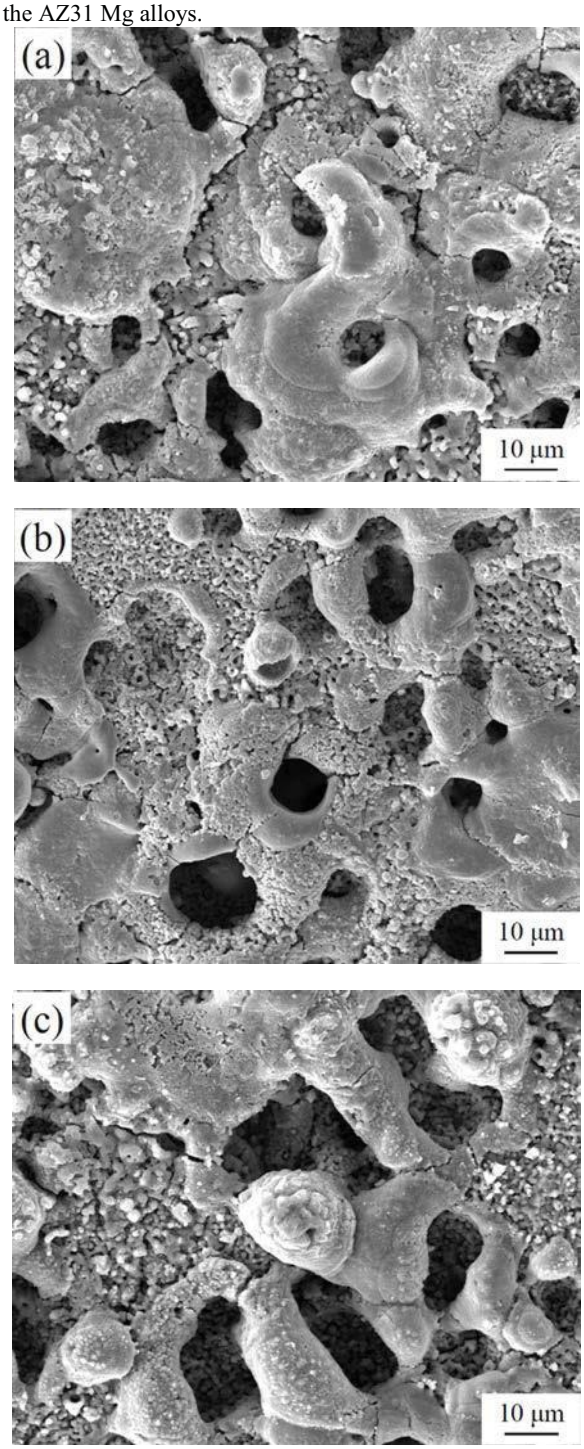


Fig. 2. Surface morphologies of the PEO-treated AZ31 Mg alloys at different current densities: (a) 100, (b) 150, and (c) 200 mA/cm^2.

The cross-sectional backscattered electron (BSE) images of the coatings formed under three different conditions are shown in Fig. 3. All coatings had an average thickness of about 18 μm and formed the metallurgical bonding with the substrate. It is generally known that in the BSE mode of SEM, the higher the average atomic number of the element, the brighter it is in the image. Depending on the level of brightness, the coatings on

AZ31 Mg alloys could be divided into three different parts: inner, middle, and outer layers. The dense inner layer was next to the

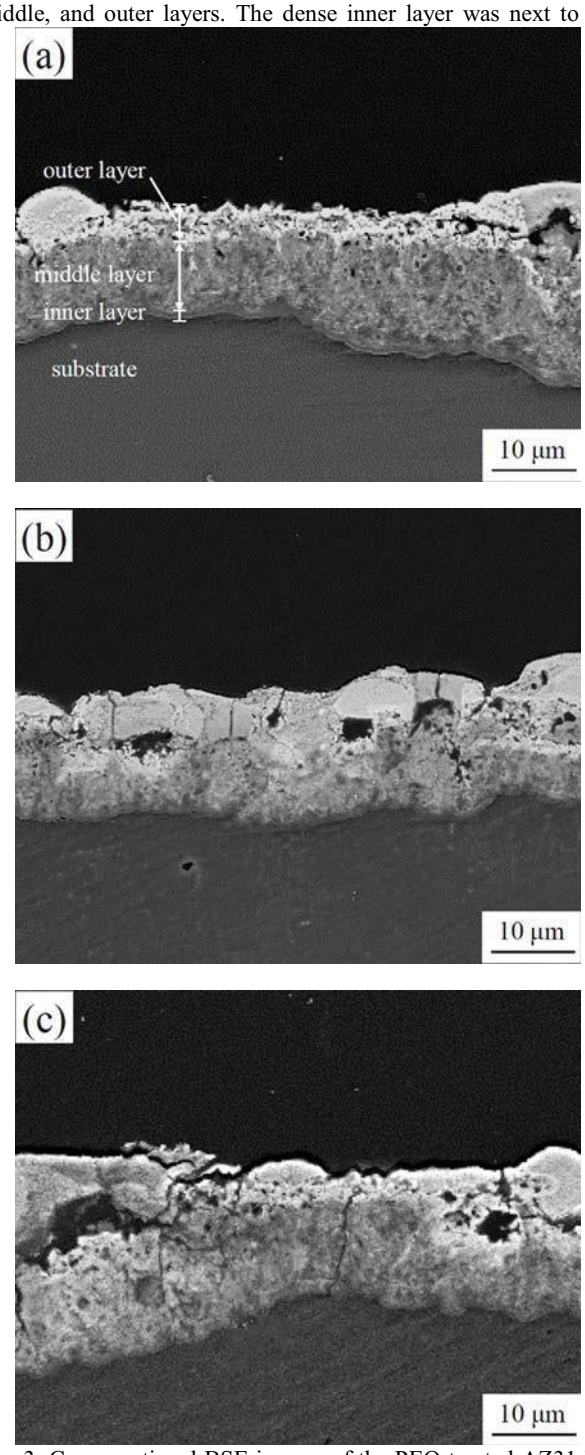


Fig. 3. Cross-sectional BSE images of the PEO-treated AZ31 Mg alloys at different current densities: (a) 100, (b) 150, and (c) 200 mA/cm^2.

substrate, the middle layer comprised a large proportion of the coating, and the outer layer was relatively brighter than the others, implying that the outer layer was mainly impregnated with Zr element, which was the heaviest element among the substrate and electrolyte used in this study. In the cross-sectional images, the number of discharge channels and the somewhat large micro-pores of over 3 μm in diameter were increased with increasing the applied current density. This was mainly due to the fact that as the

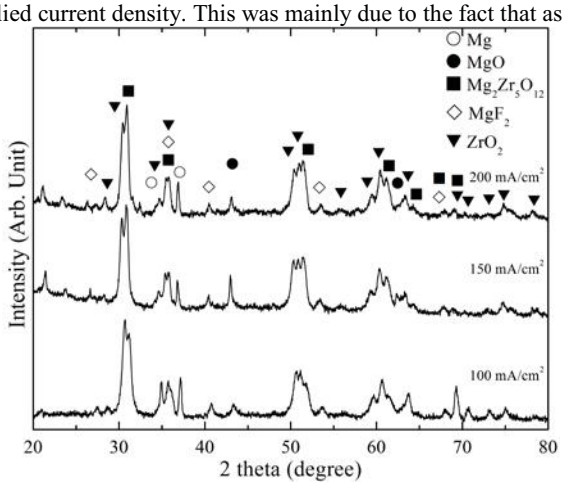


Fig. 4. XRD patterns of the PEO-treated AZ31 Mg alloys under different current densities.

applied current density was increased, the enhanced intensity of plasma discharges led to generate the numerous dissolved oxygen gas trapped in the molten oxide and severe thermal stress [29,30]. As a result, in terms of the production of uniform coatings without severe cracks and micro-pores, PEO-treated AZ31 Mg alloy applied at 100 mA/cm^2 of current density would be desirable.

The XRD patterns for the three PEO-treated AZ31 Mg alloys are shown in Fig. 4. All the coatings consisted of MgO, $Mg_2Zr_5O_{12}$, MgF_2, and ZrO_2 phases. According to the investigation studied by Tolstoy et al. [31], in terms of fractions of Zr^{4+}, when K_2ZrF_6 compound was dissolved in the acid electrolyte, ZrF_3^+ complex was mainly present. The $Mg_2Zr_5O_{12}$ phase in the coatings was reported to be stable in the range of 2123-2373 K [32]. This implies that $Mg_2Zr_5O_{12}$ phase was synthesized due to the thermo-electrochemical reactions accompanied by short-lived plasma with local high temperature and the quenching of the molten oxide. The formation of MgF_2 phase was suggested to due to the dominant reaction of highly reactive F^- ions with Mg^{2+} ions [33]. Meanwhile, ZrF_3^+ ions were anodically oxidized on the oxide layer, thereby ZrO_2 phase was synthesized.

The corrosion properties of the bare, passivated, and PEO-treated AZ31 Mg alloys with three different current densities were measured using potentiodynamic polarization tests in a 3.5 wt.% NaCl solution as shown in Fig. 5. The corrosion current density

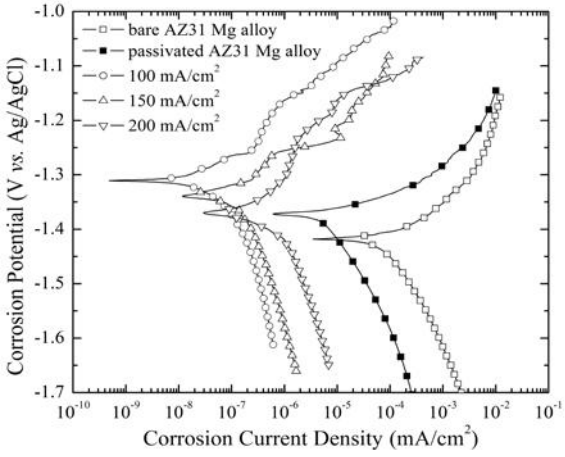


Fig. 5. Potentiodynamic polarization curves of the bare, passivated and PEO-treated AZ31 Mg alloys in a 3.5 wt.% NaCl solution.

Table 1. Results of potentiodynamic polarization tests of three PEO-treated AZ31 Mg alloys compared to bare AZ31 Mg alloy in 3.5wt.% NaCl solution.

	i_{corr} (A/cm^2)	E_c (V)	b_a (V)	b_c (V)	R_p (Ω·cm^2)
bare AZ31 Mg alloy	1.09×10^{-4}	-1.42	0.21	0.06	1.85×10^{2}
passivated AZ31 Mg alloy	5.21×10^{-6}	-1.37	0.03	0.15	2.15×10^{3}
100 mA/cm^2	5.62×10^{-8}	-1.31	0.12	0.16	5.30×10^{5}
150 mA/cm^2	1.25×10^{-7}	-1.34	0.11	0.24	2.61×10^{5}
200 mA/cm^2	5.68×10^{-7}	-1.37	0.28	0.21	9.18×10^{4}

(i_{corr}) and corrosion potential (E_c) were obtained from the potentiodynamic polarization curves using the Tafel extrapolation method. Based on the Stern-Geary equation [34], the polarization resistance (R_p) was calculated from the anodic (b_a) and cathodic (b_c) curves. The results of polarization tests are listed in Table 1. The R_p of AZ31 Mg alloy with first passivation layer was improved than that of bare AZ31 Mg alloy. Regardless of the applied current density, all PEO-treated AZ31 Mg alloys in contrast to the passivated AZ31 Mg alloy had lower i_{corr} and higher E_c, indicating improved corrosion resistance. Among these conditions, the PEO-treated AZ31 Mg alloy applied at 100 mA/cm^2 of current density showed the highest value of R_p as 5.30×10^5 Ω·cm^2. It was attributed to the fact that as the applied current density was increased, the number of cracks and/or channels, which could allow Cl^- ions as a corrosive medium to penetrate through the coating and corrode the substrate, was increased. Thus, we believed that the applied current density of 100 mA/cm^2 will be the suitable for PEO process satisfying good corrosion property.

Summary

We studied the influence of the applied current density on the corrosion property of AZ31 Mg alloys prepared by the PEO process in the acid electrolyte with K_2ZrF_6. As the applied current density was increased, the number of micro-cracks and large micro-pores increased, and also, the number of cracks and/or channels, which could allow a corrosive medium to penetrate the coating and corrode the substrate, was increased. For this reason, the corrosion property of PEO-treated AZ31 Mg alloy applied with current density of 100 mA/cm^2 was higher than that of the other conditions.

Acknowledgments

This work was supported by a National Research Foundation of Korea grant funded by the Korean government (MEST) (No. 2012-0000130).

References

1. R. Nandan, T. DebRoy, and H. Bhadeshia, "Recent advances in friction-stir welding - Process, weldment structure and properties," *Progress in Materials Science*, 53 (2008) 980-1023.
2. J.E. Gray and B. Luan, "Protective coatings on magnesium and its alloys - a critical review," *Journal of Alloys and Compounds*, 336 (2002) 88-113.
3. B.L. Mordike and T. Ebert, "Magnesium: Properties - applications - potential," *Materials Science and Engineering: A*, 302 (2001) 37-45.
4. G.L. Song and A. Atrens, "Understanding magnesium corrosion - A framework for improved alloy performance," *Advanced Engineering Materials*, 5 (2003) 837-858.
5. G.L. Song and A. Atrens, "Corrosion Mechanisms of Magnesium Alloys," *Advanced Engineering Materials*, 1 (1999) 11-33.
6. A.L. Yerokhin et al., "Plasma electrolysis for surface engineering," *Surface & Coatings Technology*, 122 (1999) 73-93.
7. C. Blawert et al., "Anodizing Treatments for Magnesium Alloys and Their Effect on Corrosion Resistance in Various Environments," *Advanced Engineering Materials*, 8 (2006) 511-533.
8. J.I. Yu et al., "Characteristics of the Anodic Films on an AZ91D Mg Alloy Prepared by Plasma Electrolytic Oxidation and Burning Surface Treatment," *Korean Journal of Metals and Materials*, 51 (2013) 405-411.
9. C. Zhong et al., "Protective diffusion coatings on magnesium alloys: A review of recent developments," *Journal of Alloys and Compounds*, 520 (2012) 11-21.
10. H. Duan, C. Yan, and F. Wang, "Effect of electrolyte additives on performance of plasma electrolytic oxidation films formed on magnesium alloy AZ91D," *Electrochimica Acta*, 52 (2007) 3785-3793.
11. R. Arrabal et al., "Corrosion resistance of WE43 and AZ91D magnesium alloys with phosphate PEO coatings," *Corrosion Science*, 50 (2008) 1744-1752.
12. D.Y. Hwang et al., "Corrosion resistance of oxide layers formed on AZ91 Mg alloy in $KMnO_4$ electrolyte by plasma electrolytic oxidation," *Electrochimica Acta*, 54 (2009) 5479-5485.
13. J. Liang, L. Hu, and J. Hao, "Preparation and characterization of oxide films containing crystalline TiO_2 on magnesium alloy by plasma electrolytic oxidation," *Electrochimica Acta*, 52 (2007) 4836-4840.
14. A. Ghasemi et al., "Study of the structure and corrosion behavior of PEO coatings on AM50 maginesium. alloy by electrochemical impedance spectroscopy," *Surface & Coatings Technology*, 202 (2008) 3513-3518.
15. P. Su et al., "Effects of cathode current density on structure and corrosion resistance of plasma electrolytic oxidation coatings formed on ZK60 Mg alloy," *Journal of Alloys and Compounds*, 475 (2009) 773-777.
16. R. Arrabal et al., "Characterization of AC PEO coatings on magnesium alloys," *Surface and Coatings Technology*, 203 (2009) 2207-2220.
17. B.U. Lee et al., "Influence of Current Density on Corrosion Properties of AZ91 Mg Alloy Coated by Plasma Electrolytic Oxidation Method," *Korean Journal of Metals and Materials*, 49 (2011) 601-607.
18. J. Liang et al., "Comparison of electrochemical corrosion behaviour of MgO and ZrO_2 coatings on AM50 magnesium alloy formed by plasma electrolytic oxidation," *Corrosion Science*, 51 (2009) 2483-2492.
19. F. Liu et al., "Corrosion behavior of the composite ceramic coating containing zirconium oxides on AM30 magnesium alloy by plasma electrolytic oxidation," *Corrosion Science*, 53 (2011) 3845-3852.
20. F. Liu et al., "Effect of additives on the properties of plasma electrolytic oxidation coatings formed on AM50 magnesium alloy

in electrolytes containing K_2ZrF_6," *Surface and Coatings Technology*, 206 (2011) 455-463.
21. H. Luo et al., "Study on the microstructure and corrosion resistance of ZrO_2-containing ceramic coatings formed on magnesium alloy by plasma electrolytic oxidation," *Journal of Alloys and Compounds*, 474 (2009) 551-556.
22. L. Wang et al., "The influence of additives on the stability behavior of electrolyte, discharges and PEO films characteristics," *Journal of Alloys and Compounds*, 493 (2010) 445-452.
23. P. Bala Srinivasan et al., "Effect of current density on the microstructure and corrosion behaviour of plasma electrolytic oxidation treated AM50 magnesium alloy," *Applied Surface Science*, 255 (2009) 4212-4218.
24. Z. Li, Y. Yuan, and X. Jing, "Effect of current density on the structure, composition and corrosion resistance of plasma electrolytic oxidation coatings on Mg–Li alloy," *Journal of Alloys and Compounds*, 541 (2012) 380-391.
25. K.M. Lee, Y.G. Ko, and D.H. Shin, "Incorporation of carbon nanotubes into micro-coatings film formed on aluminum alloy via plasma electrolytic oxidation," *Materials Letters*, 65 (2011) 2269-2273.
26. K.M. Lee et al., "Electrochemical response of ZrO2-incorporated oxide layer on AZ91 Mg alloy processed by plasma electrolytic oxidation," *Surface and Coatings Technology*, 205 (2011) 3779-3784.
27. R.O. Hussein, X. Nie, and D.O. Northwood, "An investigation of ceramic coating growth mechanisms in plasma electrolytic oxidation (PEO) processing," *Electrochimica Acta*, 112 (2013) 111-119.
28. V. Dehnavi et al., "Effect of duty cycle and applied current frequency on plasma electrolytic oxidation (PEO) coating growth behavior," *Surface and Coatings Technology*, 226 (2013) 100-107.
29. I.J. Hwang et al., "Correlation between current frequency and electrochemical properties of Mg alloy coated by micro arc oxidation," *Surface and Coatings Technology*, 206 (2012) 3360-3365.
30. K.M. Lee et al., "Incorporation of Carbon Nanotubes Into Oxide Layer on 7075 Al Alloy by Plasma Electrolytic Oxidation," *Journal of The Electrochemical Society*, 158 (2011) C325-C328.
31. V.P. Tolstoy and B. Altangerel, "A new “fluoride” synthesis route for successive ionic layer deposition of the ZnxZr(OH)yFz·nH2O nanolayers," *Materials Letters*, 61 (2007) 123-125.
32. R. Arrabal et al., "AC plasma electrolytic oxidation of magnesium with zirconia nanoparticles," *Applied Surface Science*, 254 (2008) 6937-6942.
33. D.Y. Hwang, Y.M. Kim, and D.H. Shin, "Corrosion Resistance of Plasma-Anodized AZ91 Mg Alloy in the Electrolyte with/without Potassium Fluoride," *Materials Transactions*, 50 (2009) 671-678.
34. M. Stern and A.L. Geary, "Electrochemical Polarization: I . A Theoretical Analysis of the Shape of Polarization Curves," *Journal of The Electrochemical Society*, 104 (1957) 56-63.

Magnesium Technology 2014
Edited by: Martyn Alderman, Michele V. Manuel, Norbert Hort, and Neale R. Neelameggham
TMS (The Minerals, Metals & Materials Society), 2014

CORROSION-STRESS RELAXATION EFFECTS ON TENSILE PROPERTIES OF AN AZ61 MAGNESIUM ALLOY

Holly J. Martin [1,2*], C. Walton[1], K. Bruce[1], A. Hicks[1], M.F. Horstemeyer[1], W.R. Whittington[1], P.T. Wang[1]

[1] Center for Advanced Vehicular Systems (CAVS). Mississippi State University (MSU), 200 Research Boulevard, Starkville, MS 39759
[2] Department of Civil/Environmental and Chemical Engineering, Youngstown State University (YSU), One University Plaza, Youngstown, OH 44555
* Corresponding author: hjmartin02@ysu.edu

Keywords: Magnesium Alloy, Corrosion, Stress-Relaxation
UNCLASSIFIED: Distribution A. Approved for Public Release

Abstract

One way to increase gas mileage 50% by 2050, a goal of the U.S. government, is to reduce the weight of the vehicle, using lightweight alloys such as magnesium. AZXX Mg alloys have been investigated for this purpose, but are still highly susceptible to stress corrosion cracking. The presence of pits and hydrogen embrittled sections concentrate the stress, leading to cracking and failure. In order to determine the interaction between tensile properties and corrosion behavior, two saltwater environments were used to examine the effects of chloride ion exposure on the corrosion of an extruded AZ61 alloy held under constant strain (approximately 80% of tensile yield strength) over 60 hours. The effects of constant strain on the surface corrosive behavior and the tensile strength were determined at various intervals. The stress-strain relationship minimally decreased over time for the salt spray environment, while large changes were seen in the stress-strain relationship for the immersion environment. In addition, there was a minimal decrease in stress over 60 hours of the AZ61 alloy in the salt spray environment but a 20% decrease in stress over 60 hours in the immersion environment. The differences between stress-strain relationships were attributed to a decrease in surface area of the samples due to the continuous presence of water for the immersion environment, which resulted in a decrease in the ability to withstand applied stress. The formation of pits due to chloride ions for both environments concentrated the applied stress, leading to a decrease in the elongation to failure for both environments.

Introduction

The low density, high strength per weight ratio, castability, weldability, and machinability of magnesium alloys make them a desirable material for use in the electronics, automotive, and aerospace industries [1-7]. The addition of aluminum and zinc, to create the Al-Zn ternary system (also known as the AZ alloys), have been used in the largest number of industrial applications [3]. However, the low corrosion resistance of magnesium, as well as the low resistance to creep and stress relaxation behavior, prevents the use of magnesium in areas exposed to the environment [4, 8-15]. Efforts to improve the corrosion and creep performance of magnesium have been focused specifically on improving the alloy chemistry of the alloys [16-17]. The addition of aluminum, up to 10%, improved the corrosion resistance of the magnesium alloy, as long as the β-phase was finely distributed [17-18]. The improvement of corrosion resistance with increasing aluminum can be seen by comparing the quantification studies performed on AZ31 [19] and AZ61 [20]. These results showed that an increase from 3% to 6% aluminum, while holding the zinc steady at 1%, improved the corrosion resistance of the magnesium alloy with respect to general, pitting, and intergranular corrosion in both a salt spray and immersion environment [19-20]. The effect of a poorly distributed β-phase on the corrosion resistance of magnesium can be seen by comparing the quantification studies performed on AZ61 [20] and AZ91 [21]. These results showed that an increase from 6% to 9% aluminum, while holding the zinc steady at 1%, decreased the corrosion resistance of the magnesium alloy with respect to general, pitting, and intergranular corrosion in an immersion environment, while improving the corrosion resistance with respect to general, pitting, and intergranular corrosion in a salt spray environment [20-21]. The difference between the two results was attributed to the continuous presence of water in the immersion environment causing the formation of micro-galvanic cells formed between the α-phase and β-phase that led to an increase in corrosion of the AZ91 alloy [21].

While several corrosion studies have been performed on various magnesium alloys, the corrosion mechanisms in a stress-free environment are different from the corrosion mechanisms under stress. When combining corrosion and stress, the failure rate can greatly increase as compared to the failure rate of just one of the two loads. The main damage mechanism created when stress effects and corrosion interact on magnesium is called stress corrosion cracking (SCC), of which, there are two main forms – intergranular stress corrosion cracking (IGSCC) and transgranular stress corrosion cracking (TGSCC) [22-23]. The formation of IGSCC usually is caused by a continuous β-phase running along grain boundaries, while the formation of TGSCC usually is caused by an interaction of hydrogen within the microstructure [22]. With the increasing usage of magnesium alloys in load bearing applications, an understanding of SCC is urgently needed, especially since many magnesium alloys have a threshold stress for SCC that is half of the yield stress in common environments, including high-purity water [22]. Unlike corrosion, though, the addition of aluminum and zinc did not improve SCC. Instead, SCC was increased, meaning that AZXX alloys are susceptible to SCC even when the exposure to a salt solution or the weather is periodic [22]. While the SCC of magnesium alloys is important, especially for its utilization within the automotive and aerospace industries, only a small amount of published literature is available for corrosion stress relaxation. The study of SCC using various magnesium alloys, including pure magnesium, AZ91D, AM50, and AS21 showed that room temperature and a 3.5% sodium chloride aqueous solution was enough to develop stress relaxation phenomena [15]. Tests run on AJ51 (Mg-5Al-0.6Sr), AX41 (Mg-4Al-1Ca), and AZ63 demonstrated that the stress relaxation phenomena was also a function of both the internal stress at the beginning of the relaxation and the test temperature [24-25].

The available research showed that the time dependent environmental effects are important, not just the magnitude of the applied stress. In order to develop an understanding of how the environment affects the corrosion stress relaxation, two techniques commonly performed for corrosion testing can be used. These techniques were developed for salt spray (salt fog) and immersion testing and come from the ASTM standards of ASTM B-117 and G-31, respectively [26-27]. Unfortunately, though, utilizing the ASTM standards exactly as written would produce results that cannot be completely compared, as the salt concentrations for the two standards are different (5.0% vs. 3.5%, respectively) [26-27]. In addition, the continuous nature of both the salt spray and the immersion environments do not produce results that are translatable to the automotive industry, which requires a pollution phase, a wet phase, and a drying phase [28-29]. In order to produce data that was easily comparable between the two environments, and that was translatable to the automotive industry, a cyclical salt spray testing utilizing a salt spray (pollution) phase, 100% humidity (wet) phase, and a dry air (drying) phase was developed [30]. This allowed for a direct comparison between the worst case scenario (immersion) and a more industrially relevant scenario (cyclical salt spray) to expose the test alloys to the cyclical nature of environmental factors, such as de-icing salt, mud, and condensation [28, 31].

Because metals used in automotive service conditions experience both stress relaxation effects and corrosion, magnesium alloys should be thoroughly examined to understand the negative effects of the combined corrosion and stress relaxation loads on durability. The interaction between stress effects and corrosion, including hydrogen embrittlement, significantly influences the understanding of key failure mechanisms. In addition, the presence of pitting, caused by chloride ions, is the dominant source for crack initiation and propagation, due to the formation of local stress concentrations that increase the driving force for cracking. The interaction between pit nucleation, growth, and coalescence and stress relaxation deformation was examined in a 3.5% sodium chloride aqueous solution utilizing a cyclical salt spray environment and an immersion environment on an extruded AZ61 magnesium alloy, to determine the overall effect to the stress-strain relationship.

Materials and Methods

Sample Cutting

Thirty-six AZ61 specimens were cut from an extruded crash rail provided by Ford using a CNC Mill (Haas, Oxnard, CA). A schematic of the specimen geometry is illustrated in Figure 1.

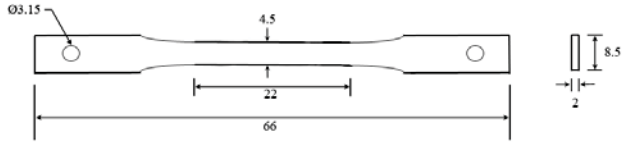


Figure 1. Schematic of specimen used in this study. All dimensions are in millimeters.

Application of Stress

Prior to situating the specimens within the cradle (shown in Figure 2), the gage length of the specimens was lightly sanded on one side and then cleaned with isopropyl alcohol. A resin was mixed and a strain gauge was attached to the surface, situated to measure the strain from the top to the bottom.

Two weeks after the strain gauge was attached, to allow for the resin to cure, the samples were pinned in the stress relaxation fixtures (Figure 2). All of the available surfaces of both the stress relaxation fixture and the magnesium specimens, with the exception of the surface on which corrosion was to occur, were coated in melted beeswax to prevent preferential corrosion of magnesium, as the fixture was made of steel. In this study, corrosion was localized to one side of the specimen's gauge length. The corrosion surface of the specimens was left untreated, with no surface grinding or polishing, to test the corrosion effects on an as-extruded AZ61 Mg alloy. For both environments (salt spray and immersion), three specimens per test environment were pinned in stress relaxation fixtures covered in beeswax (Figure 2).

After the samples were pinned and coated with beeswax, the strain gauges were attached to a computer and monitored as the nuts on the left side of Figure 2 were tightened. The nuts were tightened until the specimens were deformed to a true strain of approximately 80% of tensile yield stress. Following specimen deformation, additional beeswax was used to fully coat any areas where the previously applied beeswax may have cracked due to the moving of the pinned specimen supports.

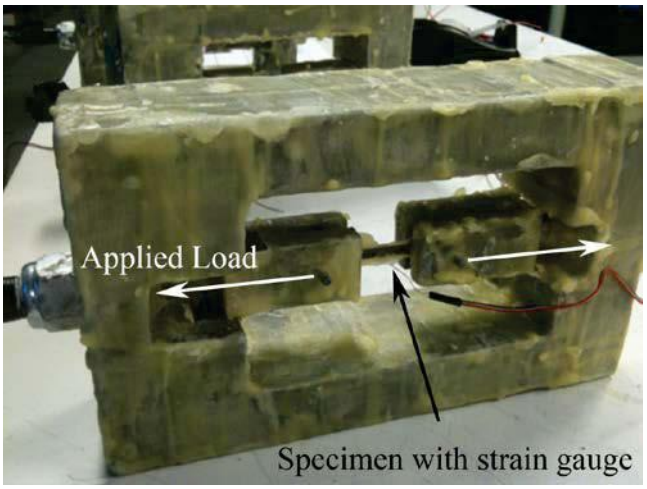


Figure 2. Experimental corrosion stress relaxation fixture setup showing load direction and specimen equipped with a strain gauge to monitor applied strain.

Environmental Exposure

Immediately following the applied strain, the specimens were exposed to the two different test environments for various times (t_0= 0 h, t_1= 1 h, t_2= 4 h, t_3= 12 h, t_4= 36 h, and t_5= 60 h), rinsed with distilled water to remove excess salt, and dried in a desiccator. For the cyclic salt spray testing, a Q-Fog CCT (Q-Panel Lab Products, Cleveland, OH) was used to cycle through three stages set at equal times, including a 3.5 wt.% NaCl spray at 35 °C, 100% humidity using distilled water at 35 °C, and a drying purge at 35 °C. For immersion testing, an aquarium filled with 3.5 wt.% NaCl solution at room temperature was used.

Optical Microscopy Testing Set-Up

For optical microscopy, one set of immersion and salt spray specimens (six total specimens) were exposed to the test environment for 1 h, removed, rinsed with distilled water to

remove excess salt, dried, and then examined under an optical microscope. Following the optical analysis, the coupons were then placed back into the test environment for an additional 3 h, an additional 8 h, an additional 24 h, and another 24 h; the samples were removed, cleaned, and examined after each time period. These times allowed for a longitudinal study to follow pit growth and surface changes over time. Optical microscopy with an inverted light was used to take multiple images of the resulting corrosion surface at 10x magnification (Axiovert 200M Mat, Carl Zeiss Imaging Solutions, Thornwood, NY). The 10x magnification was used to pictorially show the changes over the six cycles.

Chemomechanical Testing

Because the strain gauges could not be hooked up to the computer to monitor the change in load, due to stress relaxation, during testing, the stress relaxation data points were interpolated at the given interval times following tension testing. As with the optical microscopy set-up, specimens were pinned in the cradles, coated with beeswax, pulled to approximately 80% yield stress, and recoated with beeswax where needed. The specimens were placed in either the immersion environment or the salt spray environment for 1 h, 4 h, 12 h, 36 h, or 60 h. These specimens were not the same specimens as those used for optical microscopy. After the assigned time, the specimens were removed from the environment and from the fixture, cleaned with deionized water to remove excess salt, and dried in a desiccator. Tensile tests were performed using an electromechanical Instron 5882 machine at a constant strain rate of 0.001/s. The machine was equipped with a 5 kN load cell. For each tested time and environment, stress-strain data was collected for three specimens, for a total of six samples per time. The stress-strain data gathered was analyzed using the Data Averager (v. 2.5) developed by Mississippi State University to determine average stress-strain plots. The Data Averager was set to interpolate over 2000 strain values to get the most accurate curve. Since the applied strain for the relaxation tests was in the elastic regime of the AZ61 stress-strain relationship, backing out the stress at the given strain after reloading should theoretically give an accurate stress picture at the time.

Results

Corrosion stress relaxation tests were carried out for 60 hours on the AZ61 Mg alloy specimens. Figure 3 shows the normalized time-dependent stress ($\sigma(t)/\sigma_0$) decrease for the 60 hour testing matrix. $\sigma(t)$ is the current relaxation stress and σ_0 (t=0) is the initial value of stress. This represents the stress relaxation relationship for the salt spray environment and immersion environment specimens. The salt spray environment shows an approximate reduction of static strength of less than 1% over the 60 hours. In the salt spray environment, the reduction in stress is not as significant as in the immersion environment. The immersion environment has a stronger deleterious effect immediately. After one hour, notice that there is approximately an 8% reduction of static strength, which is more than the entire salt spray decrease. After the 60 hours, the specimens exposed to the immersion environment had a 20% reduction of static strength.

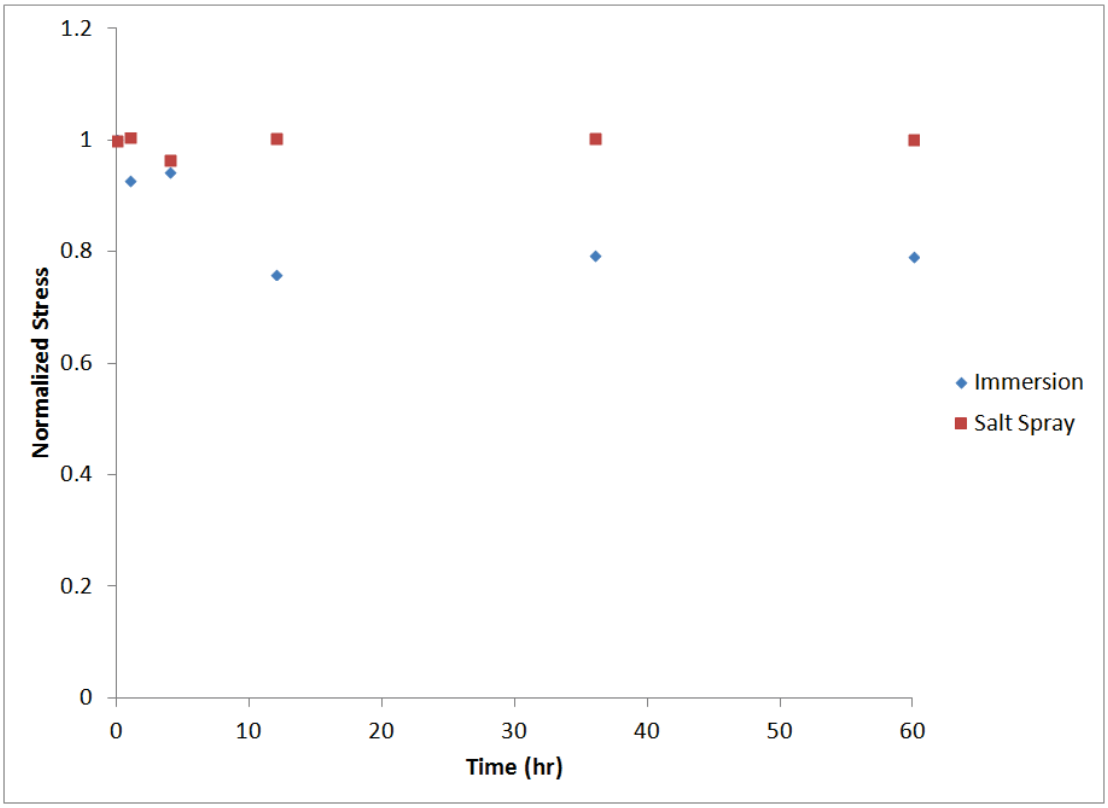


Figure 3. Normalized stress relaxation of AZ61 Mg alloy specimens at room temperature in a 3.5 wt.% NaCl salt spray fog environment and a 3.5 wt.% NaCl immersion environment. The constant strain value was approximately 80% of the tensile yield strength.

Following the corrosion-stress relaxation environmental testing, monotonic tensile tests were performed. Figure 4 illustrates the average stress-strain relationship curves for the salt spray (Figure 4a) and immersion (Figure 4b) environments of AZ61. Notice that the salt spray environment had a minimal effect on the tensile yield strength and elongation to failure. The difference between the curves was less than 5% for all averaged curves. On the other hand, a noticeable reduction of both tensile yield strength and elongation to failure is illustrated in the immersion environment stress-strain plots.

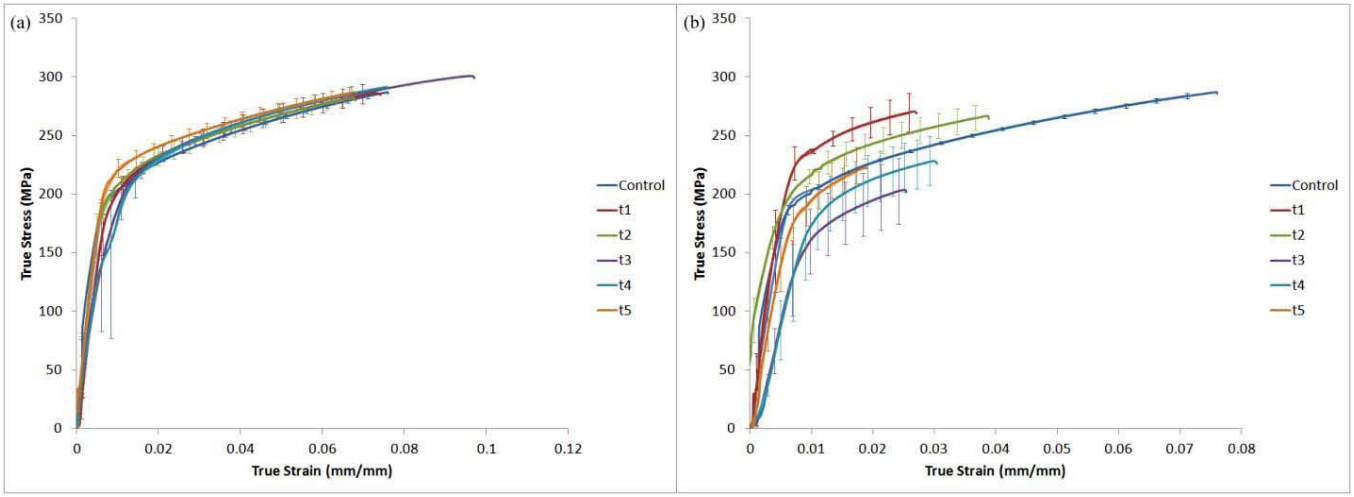


Figure 4. Monotonic tensile true stress-true strain response of the AZ61 Mg alloy following corrosion stress relaxation testing in the (a) salt spray and (b) immersion environments at t_1= 1 h, t_2= 4 h, t_3= 12 h, t_4= 36 h, and t_5= 60 h. All tests were run at room temperature and strain rate of 0.001/s.

Discussion

Stress relaxation of a material is typically defined as the decrease in stress under constant strain and constant temperature. For Mg, this is primarily due to slip in the basal plane [32]. These slips lead to an increase in microstructure dislocation density, which ultimately leads to a decrease in the stress needed to hold a material at a given strain. These dislocations within the material relieve inner stresses caused by plastic microdeformations [15]. A corrosive environment, whether that is the salt spray or immersion environment, increases the relaxation rate, as the water and chloride ions react with the metal. The introduction of pits, caused by chloride ions, and the general removal of metal, caused by water, ultimately decrease the stress the material is able to withstand. Figure 3 shows the normalized stress relaxation of the specimens versus time for the salt spray and immersion environments. In the immersion environment, a reduction of static stress over time was observed, while the static stress remained approximately the same in the salt spray environment. After 60 hours, the applied stress on the immersion samples was approximately 80% of the initial stress, while the applied stress on the salt spray samples was approximately 99% of the initial stress. This indicates that the immersion environment had a much more deleterious effect as compared to the salt spray environment, resulting in larger stress relaxation effects.

The difference between the changes in stress relaxation that the samples are able to withstand is entirely a function of the environment. The immersion environment is continuously exposed to water and chloride ions, leading to more general corrosion, caused by the removal of the $Mg(OH)_2$ oxide layer, and more pitting corrosion, leading to stress concentration around pits. Because the oxide layer was continuously removed, the samples would lose some thickness, leading to a decrease in surface area. This decrease in surface area leads to a decrease in the stress that the samples can withstand. When this reduction in surface area is combined with stress concentration points caused by the pits, the immersion samples would gradually see a reduction in the static stress that they could withstand. The salt spray environment, on the other hand, only has chloride ions during one phase of the cycle, which means pitting can only initiate during the salt spray cycle. Water is present in two of the three cycles, meaning general corrosion could occur during the salt spray cycle and the humidity cycle. However, with the drying cycle, general corrosion is stopped and the $Mg(OH)_2$ oxide layer would not dissolve away from the surface as readily. In addition, the $Mg(OH)_2$ oxide layer could convert to a more protective oxide layer during the drying phase. The much slower general corrosion rate, combined with the lower rate of pitting corrosion, leads to a material that does not lose as much material, nor possess as many stress concentration points. Without the decrease in surface area to decrease the stress the material could withstand, and without the stress concentration points, the salt spray samples would not experience as large a decrease in static stress, and therefore would not be as greatly affected by stress relaxation. Since these tests were performed at room temperature, without changes to the material, stress relaxation would not have a major effect on the stress the alloy could withstand.

Figure 4 shows the average stress-strain response for the salt spray (Figure 4a) and immersion (Figure 4b) environments compared to the stress-strain response in air. As was the case with Figure 3, the salt spray environment shows almost no change, while the immersion environment shows a decrease in the stress-strain curves over time. Both environments experienced a change in the elongation to failure, indicating the formation of pits that would concentrate the stress, leading to failure at a point sooner than the air samples. The pits caused by the chloride ions would lead to points of stress concentration. These stress concentration points would allow for multiple cracks to begin forming that would then lead to the material failing faster as the cracks coalesce. For the salt spray environment, the stress required to break the samples would still be the same, as the material itself is unchanged, but the pits caused the material to fail

at a shorter point. For the immersion environment, the stress also changed, as the longer the samples were exposed to water, the more surface area was removed, leading to a decrease in stress. There are large error bars for all of the immersion samples as well, indicating that the immersion environment affected the samples differently, as corrosion itself is unpredictable. While the samples were cut from the same extruded rail, different defects with the extrusion process, as well as slightly different chemical compositions within the rail could all affect the corrosion processes differently.

Because of the applied load, there is also a chance that some of the pits were not actually pits, but instead were surface defects that were opened by the applied load of 80% of the yield stress. These small openings would then be a location for the concentration of chloride ions for pitting and water collection for general corrosion. Because the specimens exposed to the immersion environment were continuously exposed to both the chloride ions and water, these small openings could gradually get larger, due to both the basal plane slip relieving inner stresses and the constant corrosive attack. As these openings become larger, the amount of surface area lost increases, as does the stress concentration. Both of these increases lead to a decrease in the tolerance of applied stress. These same openings are likely present on the salt spray specimens, and both chloride ions and water can collect within the openings during the salt spray and humidity cycles. However, there is not a continuous corrosive attack removing metal from the surface in the salt spray environment, so the inner stresses are not relieved and the basal plane slip does not have the same effect as it does for the immersion environment. The presence of these openings, as with the presences of pits, would allow for shorter elongation to failure rates than specimens without the openings or pits. These openings and pits both concentrate stress. With this stress concentration, the failure at these locations occurs faster than the failure within the metal without these stress concentration points, leading to a reduction in elongation to failure.

For both environments, there is also a chance that hydrogen embrittlement occurred, as hydrogen ions are produced during the corrosion reactions; these ions could then diffuse into the metal, prior to becoming hydrogen gas, leading to a reduction in stress [33]. Stress corrosion cracking (SCC) is described as an anodic dissolution assisted cracking which is accompanied by a hydrogen reduction reaction [33]. Since AZXX magnesium alloys are known to be prone to SCC [22], the development of brittle hydrides within the matrix is not unexpected and would result in a decrease in the elongation to failure. The development of SCC, especially from pit nucleation and growth, would not be unexpected, as magnesium alloys are known to be susceptible to environmentally-assisted failure, where pitting corrosion and hydrogen ions induced cleavage cracks lead to failure [34-35].

Conclusions

Corrosion with stress-relaxation studies were performed on AZ61 in a cyclical salt spray environment and an immersion environment over 60 hours. The immersion environment was more detrimental, with a reduction seen in the normalized stress, elongation to failure, and the stress-strain curves. The deleterious effect of the immersion environment was caused by the continuous presence of water and chloride ions. The continuous presence of water allowed for general corrosion, which reduced the surface area of the specimens, reducing the ability of the material to withstand stress. The presence of water also allowed for the development of hydrogen ions, which could diffuse into the magnesium alloy and lead to hydrogen embrittlement, thereby reducing both the stress and the elongation to failure. The continuous presence of chloride ions induced pitting that would lead to stress concentration points. The applied load would provide a location for additional openings in the surface that would allow for a higher degree of attack by the chloride ions and water. In addition, as the corrosive attack continued and the applied load remained, basal plane slip could occur, with the inner stresses relieved at these openings. The combination of the reduction in surface area, stress concentration points caused by pitting and open defects, and the reduction of stress within the metal as the basal plane slips, would reduce the stress the material was able to withstand. In addition, because of the continuous attack of the chloride ions, more pits are present, so more cracks develop, which lead to a reduction in the elongation to failure.

Acknowledgments

UNCLASSIFIED: Distribution A. Approved for Public Release. The authors would like to thank the Center for Advanced Vehicular Systems (CAVS) and the U.S. Army-TARDEC for supporting this work. This material is based upon work supported by the U.S. Army TACOM Life Cycle Command under Contract No. W56HZV-08-C-0236, through a subcontract with Mississippi State University, and it was performed for the Simulation Based Reliability and Safety (SimBRS) research program. Any opinions, findings and conclusions, or recommendations expressed in this material are those of the author(s) and do not necessarily reflect the views of the U.S. Army TACOM Life Cycle Command.

References

[1] E. Ghali, “Magnesium and magnesium alloys,” in: Uhligs *Corrosion Handbook*, (2000) 793.

[2] Y. Chen, Q. Wang, J. Peng, C. Zhai, W. Ding, “Effects of extrusion ratio on the microstructure and mechanical properties of AZ31 Mg alloy,” *Journal of Materials Processing Technology*, 182 (2007) 281–285.

[3] M. Marya, L.G. Hector, R. Verma, W. Tong, “Microstructural effects of AZ31 magnesium alloy on its tensile deformation and failure behaviors,” *Materials Science and Engineering*, 418 (2006) 341–356.

[4] A. Pardo, M.C. Merino, A.E. Coy, R. Arrabal, F. Viejo, E. Matykina, “Corrosion behaviour of magnesium/aluminium alloys in 3.5 wt.% NaCl,” *Corrosion Science*, 50 (2008) 823–834.

[5] Y. Uematsu, T. Kakiuchi, M. Nakajima, “Stress corrosion cracking behavior of the wrought magnesium alloy AZ31 under controlled cathodic potentials,” *Materials Science and Engineering*, 531 (2012) 171–177.

[6] G. Song, A. Atrens, D. Stjohn, J. Nairn, Y. Li, “The electrochemical corrosion of pure magnesium in 1 N NaCl,” *Corrosion Science*, 39 (1997) 855–875.

[7] S. Feliu Jr., C. Maffiotte, J.C. Galván, V. Barranco, “Atmospheric corrosion of magnesium alloys AZ31 and AZ61

under continuous condensation conditions," *Corrosion Science*, 53 (2011) 1865–1872.

[8] R.B. Alvarez, H.J. Martin, M.F. Horstemeyer, M.Q. Chandler, N. Williams, P.T. Wang, et al., "Corrosion relationships as a function of time and surface roughness on a structural AE44 magnesium alloy," *Corrosion Science*, 52 (2010) 1635–1648.

[9] A.N. Chamos, S.G. Pantelakis, V. Spiliadis, "Fatigue behaviour of bare and pre-corroded magnesium alloy AZ31," *Materials & Design*, 31 (2010) 4130–4137.

[10] G.L. Song, A. Atrens, "Corrosion mechanisms of magnesium alloys," *Advanced Engineering Materials*, 1 (1999) 11–33.

[11] R. Xin, B. Li, L. Li, Q. Liu, "Influence of texture on corrosion rate of AZ31 Mg alloy in 3.5 wt.% NaCl," *Materials & Design*, 32 (2011) 4548–4552.

[12] P.. Bonora, M. Andrei, A. Eliezer, E.. Gutman, "Corrosion behaviour of stressed magnesium alloys," *Corrosion Science*, 44 (2002) 729–749.

[13] S. Tian, L. Wang, K.Y. Sohn, K.H. Kim, Y. Xu, Z. Hu, "Microstructure evolution and deformation features of AZ31 Mg-alloy during creep," *Materials Science and Engineering*, 415 (2006) 309–316.

[14] E.M. Gutman, Y. Unigovski, A. Eliezer, E. Abramov, "Mechanoelectrochemical Behavior of Pure Magnesium and Magnesium Alloys Stressed in Aqueous Solutions," *Journal of Materials Synthesis and Processing*, 8 (2000) 133–138.

[15] Y. Unigovski, L. Riber, E.M. Gutman, "Corrosion Stress Relaxation in Pure Magnesium and Die-Cast Mg Alloys," *Journal of Metals, Materials, and Minerals*, 17 (2007) 1–7.

[16] M.K. Kulekci, "Magnesium and its alloys applications in automotive industry," *International Journal of Advanced Manufacturing Technology*, 39 (2008) 851–865.

[17] G. Song, A. Atrens, "Understanding Magnesium Corrosion—A Framework for Improved Alloy Performance," *Advanced Engineering Materials*, 5 (2003) 837–858.

[18] B.A. Shaw, "Corrosion Resistance of Magnesium Alloys," in: L.J. Korb (Ed.), *ASM Handbook of Corrosion*, Ninth Ed., (ASM International Handbook Committee, Metals Park, 2003) 692.

[19] C.A. Walton, H.J. Martin, M.F. Horstemeyer, P.T. Wang, "Quantification of corrosion mechanisms under immersion and salt-spray environments on an extruded AZ31 magnesium alloy," *Corrosion Science*, 56 (2012) 194–208.

[20] H.J. Martin, M.F. Horstemeyer, P.T. Wang, "Structure–property quantification of corrosion pitting under immersion and salt-spray environments on an extruded AZ61 magnesium alloy," *Corrosion Science*, 53 (2011) 1348–1361.

[21] H.J. Martin, C. Walton, J. Danzy, P.T. Wang, M.F. Horstemeyer, "Quantification of corrosion mechanisms under immersion and salt spray environments on an as-cast AZ91 magnesium alloy," *Corrosion*, In review.

[22] A. Atrens, N. Winzer, W. Dietzel, "Stress Corrosion Cracking of Magnesium Alloys," *Advanced Engineering Materials*, 13 (2011) 11–18.

[23] N. Winzer, A. Atrens, W. Dietzel, V.S. Raja, G. Song, K.U. Kainer, "Characterisation of stress corrosion cracking (SCC) of Mg–Al alloys," *Materials Science and Engineering*, 488 (2008) 339–351.

[24] Z. Trojanová, P. Lukáč, K.H. Kim, "Stress relaxation in selected magnesium alloys," *Key Engineering Materials*, 345-346 (2007) 1613–1616.

[25] Z. Trojanová, K. Máthis, P. Lukáč, G. Németh, F. Chmelík, "Internal stress and thermally activated dislocation motion in an AZ63 magnesium alloy," *Material Chemistry and Physics*, 130 (2011) 1146–1150.

[26] "Standard Practice for Operating Salt Spray (Fog) Apparatus," *ASTM B117 – 07a*, (2007) Vol. 03.02.

[27] "Standard Practice for Laboratory Immersion Corrosion Testing of Metals," *ASTM G31 – 72* (2004) Vol. 03.02.

[28] K.R. Baldwin, C.J.E. Smith, "Accelerated corrosion tests for aerospace materials: current limitations and future trends," *Aircraft Engineering and Aerospace Technology*, 71 (1999) 239–244.

[29] N. LeBozec, N. Blandin, D. Thierry, "Accelerated corrosion tests in the automotive industry: A comparison of the performance towards cosmetic corrosion," *Materials and Corrosion*, 59 (2008) 889–894.

[30] H.J. Martin, M.F. Horstemeyer, P.T. Wang, "Effects of salt-spray, humidity, and drying on an as-cast AE44 magnesium alloy," *International Journal of Corrosion*, 2010 (2010) 1–10. doi: 10.1155/2010/602342.

[31] G. Song, D. St. John, C. Bettles, G. Dunlop, "The corrosion performace of magnesium alloy AM-SC1 in automotive engine block applications," *JOM*, 57 (2005) 54–56.

[32] Z. Trojanová, P. Lukác, K.U. Kainer, "Stress Relaxation in AX41 Magnesium Alloy Studied at Elevated Temperatures," *Advanced Engineering Materials*, 9 (2007) 370–374.

[33] M. Bobby Kannan, W. Dietzel, "Pitting-induced hydrogen embrittlement of magnesium–aluminium alloy," *Materials & Design*, 42 (2012) 321–326.

[34] W.M. Pardue, F.H. Beck, M.G. Fontana, "Propagation of stress-corrosion cracking in a magnesium-based alloy as determined by several techniques," *Transactions of the American Society of Metals*, 64 (1961) 539–548.

[35] R.S. Stampella, R.P.M. Procter, V. Ashworth, "Environmentally-induced cracking of magnesium," *Corrosion Science*, 24 (1984) 325–341.

Magnesium Technology 2014
Edited by: Martyn Alderman, Michele V. Manuel, Norbert Hort, and Neale R. Neelameggham
TMS (The Minerals, Metals & Materials Society), 2014

CORROSION BEHAVIOUR OF FRICTION STIR WELDED AZ31 JOINTS FOR AUTOMOTIVE APPLICATIONS

X. Zhang, Z. Cano, B. Wilson, J.R. Kish, J.R. McDermid
GM Centre for Automotive Materials and Corrosion, McMaster University, Hamilton, ON L8S 4L7

Keywords: Corrosion, AZ31, Friction Stir Welding

Abstract

The corrosion behavior of friction stir welded (FSW) Mg alloy AZ31 used to fabricate an Mg alloy-intensive front end sub-assembly demo was investigated in this paper. The corrosion behavior of the uncoated FSW AZ31 joints was evaluated by ASTM B117 salt fog testing and electrochemical techniques including potentiodynamic polarization. X-ray photoelectron spectroscopy (XPS) was employed to investigate the chemical composition of the surfaces on the stir zone and base material prior to exposure. Scanning electron microscope (SEM) was used to examine the mode and extent of the corrosion damage across the FSW joint. An improved corrosion resistance was observed in the stir zone compared to the base material in the as-received condition. However, the stir zone showed almost identical corrosion behavior as the base material after the as-received surface was cleaned. These results indicate the significant deteriorative effect of surface contamination on the corrosion resistance of AZ31, but the influence of grain size on the corrosion resistance was found to be insignificant.

Introduction

As a light-weight structural material for use in automotive applications, magnesium (Mg) alloys offer significant weight-reduction and environmental benefits. However, due to their strong inherent electrochemical activity, Mg has poor corrosion resistance in aqueous environments. The multi-national Mg front end research and development (MFERD) project has been established to identify and address many of the technical problems associated with the increased use of Mg in exposed automotive structures [1]. One of the many aspects being addressed in that project is the ability to join Mg alloys in various forms. Ideally, the joint would not result in local reductions of materials properties nor introduce physical discontinuities. Most common joining methods adversely affect materials properties by excessive thermal exposure and create local discontinuities as the result of the joint geometry [2]. Friction-stir welding (FSW) is one of the candidate joining technologies being considered. The corrosion behavior of friction stir welded AZ31B joints used to fabricate the Mg-intensive front end sub-assembly demo was investigated in this study.

There are two main reasons for the poor corrosion resistance of magnesium alloys: (1) internal galvanic corrosion caused by second phases such as $Mg_{17}Al_{12}$ or impurities; (2) the oxide/hydroxide film on magnesium is much less protective than the film on some commonly employed alloys, such as aluminum or stainless steel [3–6]. Particularly for AZ31, currently one of the most promising candidate materials for the closure inners in some vehicles [7], there have only been a limited number of studies on its corrosion behavior [8-12]. AZ31 is comprised mainly of the α-(Mg,Al) matrix phase, and, therefore, the "dual-role effect" theory for Al cannot be directly applied to AZ31. Thus, microstructural variables, such as grain size (i.e. fraction of grain boundaries), crystal defects (dislocation and twins), and the surface state (e.g. roughness and purity), can become factors strongly affecting the corrosion behavior [13].

Regarding the influence of surface contamination on the corrosion resistance of Mg alloys, it has been widely accepted that surface impurities can significantly deteriorate its corrosion resistance [14,15]. The effect of microstructure on the general corrosion behavior of Mg alloys has not yet been studied in detail. Ben-Hamu et al. [11] reported that AZ31 grain-refined by equal channel angular extrusion showed improved the corrosion resistance, while a high density of dislocations and twins accelerated corrosion. This was recently confirmed by Aung and Zhou [12], who found that the removal of grain boundaries and the elimination of twins by heat-treatment reduced the corrosion resistance and corrosion rate, respectively. Nevertheless, more fundamental research is still required to support the proposed beneficial effect of grain size on corrosion resistance [13]. Hence, the corrosion behavior of uncoated FSW Mg alloy lap joints used in the MFERD assembly was evaluated in this work.

Experimental

Materials Preparation

Friction stir welded AZ31 sheet coupons (Mg–3Al–1Zn–0.3Mn (wt%)) were used for this investigation. The coupons were cut out of as-fabricated front end sub-assembly demos [2]. Given the complex geometry of the demo structure, joint coupons of various sizes were used for ASTM B117 salt fog testing. Isolated test coupons (10 mm × 10 mm) of the stir zone and base material were also prepared. For microstructural examination, isolated coupons of the stir zone and base material were mounted and prepared by standard metallographic procedures. The mounted coupons were etched in a solution containing 2.1 g picric acid, 5 ml acetic acid, 10 ml water and 80 ml ethanol and were examined using a light optical microscope.

For electrochemical measurements, working electrodes were prepared by cold mounting test coupons of the stir zone and base material in epoxy resin. Electrical contact was obtained by adhesive joining of a Cu wire to the back of the coupon prior to cold mounting. This Cu lead was inserted into a plastic tube, which was then sealed to the back of the epoxy resin mount using epoxy resin. The working electrodes were polished to 3 μm using a diamond suspension with ethanol as a lubricant, to determine the effect of the native oxide film with contaminants. In particular, the base material was light-polished and heavy-polished, respectively, to retain (light-polished) or remove (heavy-polished) the coarse grains in the surface and allow to investigate the effect of grain size. After polishing, the working electrode was then dried in

cool air prior to immersion. Another set of working electrodes were examined in the as-received condition (AR), without any mechanical polishing.

ASTM B117 Salt Fog Testing

Salt fog testing was carried out using 5 wt. % NaCl solution at pH 6.5 per ASTM B117 [16]. Prior to the test, the joint coupons were rinsed using ethanol to degrease the surface.

Electrochemical Measurements

Electrochemical potentiodynamic polarization was used to study the corrosion behavior of the welded joints. A typical three electrode system with a volume of 1000 mL, consisting of the working electrode, a graphite rod counter electrode and a standard calomel (SCE) reference electrode, was used. The potentiodynamic polarization experiments were performed with a Solartron 1287 potentiostat and were initiated at −0.25 V versus the corrosion potential and were finished at + 0.50 V versus the corrosion potential at a scan rate of 0.1667 mV/s. The measurements were conducted in a 5 wt. % NaCl solution, and were initiated after the working electrode was conditioned at the open circuit corrosion potential for 2 h at 35°C.

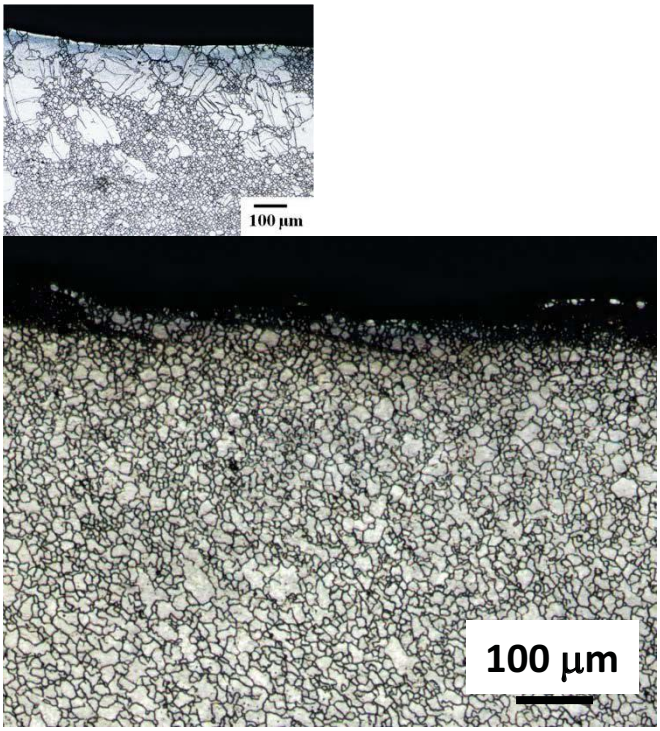
Surface Analyses

XPS analyses were carried out with a Kratos Axis Nova spectrometer using a monochromatic Al Kα (1486.6 eV) source. The instrument work function was calibrated to give a Au $4f_{7/2}$ metallic gold binding energy of 83.95 eV. The spectrometer dispersion was adjusted to give a binding energy of 932.63 eV for metallic Cu $2p_{3/2}$. The Kratos charge neutralizer system was used for all analyses. The apparent shifts of the spectra were calibrated using the C 1s peak set to 284.8 eV. High-resolution spectra were obtained using a 20 eV pass energy, whereas survey spectra were recorded using a 160 eV pass energy with an analysis area of ~ 300 μm × 700 μm. SEM images were obtained on a JEOL 6610 LV or a JSM-7000F SEM equipped with an EDAX™ EDX system. Prior to the analysis, the specimen was ultrasonically cleaned using acetone for 5 minutes.

Results

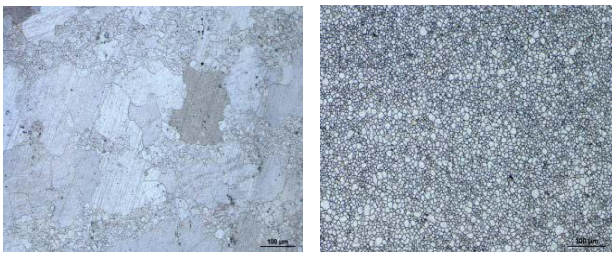
Microstructure

Figure 1 shows the cross-sectional microstructures of the AZ31 base material and stir zone. There is a variation in the grain structure from the skin to the interior of the base material (Figure 1 (a)), i.e., coarse grains with an average grain size 70 μm and a significant population of deformation twins were observed in the skin whereas finer grains with an average grain size 10 μm were found in the interior. Plan views of the microstructures of the AZ31 base material after light-polishing or heavy-polishing and etching are shown in Figure 2. It can be seen that the coarse grains were successfully retained after light-polishing (Figure 2 (a)) and removed after heavy-polishing (Figure 2 (b)). The average grain size measured in the stir zone (Figure 1 (b)) was 8 μm, which is close to the grain size found in the interior of the AZ31 base material. These changes in the microstructure of the stir zone are inevitably due to high mechanical energy and elevated temperatures experienced during the friction-stir welding process [17,18]. These microstructural changes have been reported to beneficially affect the corrosion behavior of the joint [19].



(a) (b)

Figure 1. Cross-sectional microstructures of (a) AZ31 base material and (b) FSW stir zone .

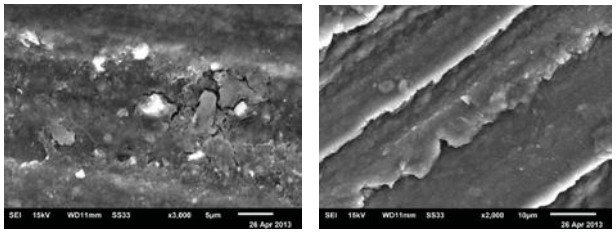


(a) (b)

Figure 2. Microstructures of AZ31 base material after (a) light-polishing and (b) heavy-polishing (plan view).

Surface Morphology and Chemical Composition

The surface appearance of the as-received AZ31 base material and stir zone, as observed using SEM, are shown in Figure 3(a) and (b), respectively. It is obvious from Figure 3(b) that some grooves or bands induced via the welding process were present on the surface of the welded joint. By comparison, the as-received surface roughness appears to be lower on the base material (Figure 3(a)). The localized bright spots in Figure 3 suggest that some heavy element contamination was present on both surfaces.



(a) (b)

Figure 3. SEM micrographs of the surface of (a) as-received AZ31 base material and (b) FSW stir zone.

XPS was employed to examine the surface compositions on both the base material and stir zone in the as-received condition. The elemental compositions obtained on the surface after sputtering (about 2 nm) are shown in Table 1. The survey spectra detected Mg, Al, Zn, C, O and other contaminants on the surfaces, which is consistent with the SEM observations. The high amount of carbon detected likely comes from surface contamination and the cleaning procedure prior to the analysis. It should be noted that a higher Al content was detected on the stir zone surface than on the base material surface. The Al/(Mg+Al) ratio was much higher on the surafce than in the bulk, indicating some enrichment of Al in the surface film, particularly that formed on the stir zone.

Table 1. Surface compositions (at. %) determined from XPS survey spectra recorded on the as-received (AR) and polished AZ31 base material and stir zone (SZ).

Samples	Al	C	Cu	Fe	Mg	O	Zn	$\frac{Al}{(Al+Mg)}$
Base (AR)	2.6	18.9	0.3	0.6	20.7	54.8	0.3	11.2
SZ (AR)	6.2	27.8	2.1	1.0	14.3	45.3	0.3	30.2
Light-polished Base	ND	32.8	ND	ND	21.3	45.5	ND	ND
Heavy-polished Base	ND	37.9	ND	ND	18.0	43.8	ND	ND
Heavy-polished SZ	ND	33.5	ND	ND	19.5	46.3	ND	ND

High-resolution XPS scans were recorded for the Mg 2p, Al 2p, O 1s, C 1s, Zn 2p, Cu 2p, and Fe 2p peaks. The fitted C1s, O 1s spectra (corrected using a Shirley background correction), single peaks of Mg^{2+}, Al^{3+}, and unfitted peaks Zn 2p, Cu 2p and Fe 2p, obtained from the sputtered stir zone surface in the as-received condition are shown in Figure 4. Collectively, these results show the native films formed on the base material and the stir zone surfaces were composed of Mg^{2+} and Al^{3+} hydroxides and carbonates in the topmost layer and Mg^{2+} and Al^{3+} oxides and carbonates underneath, as well as some heavy metal contamination such as Cu and Fe in the surface.

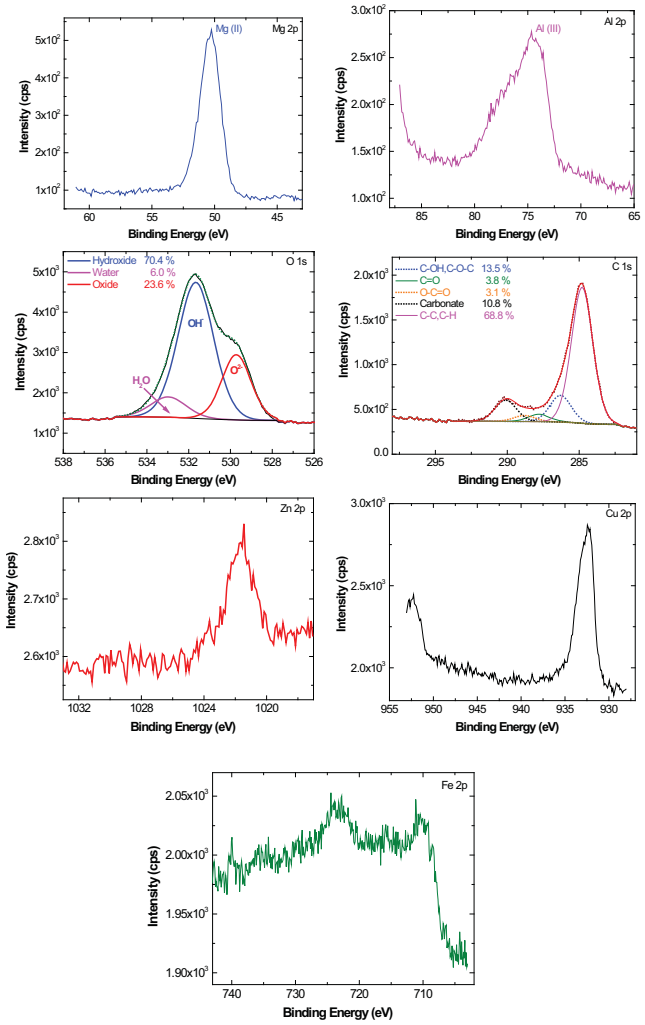
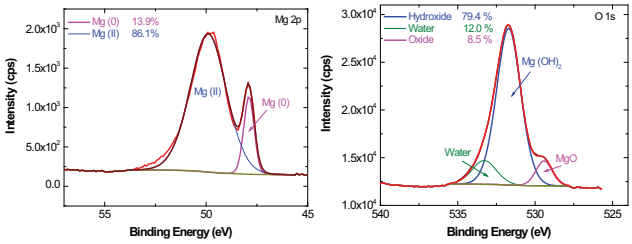


Figure 4. High-resolution XPS spectra obtained from the AZ31 stir zone sputtered surface in the as-received condition.

High-resolution XPS spectra were recorded for the Mg 2p, O 1s and C 1s peaks, where there were no significant differences in the spectra obtained from the heavy-polished stir zone and light-polished and heavy-polished base material surfaces. Figure 5 shows the fitted Mg 2p, O 1s and C1s spectra recorded on heavy-polished stir zone surface. These results show the film formed on the as-polished stir zone and base material surface was mainly composed of $Mg(OH)_2$ and small amount of MgO and carbonates, regardless of the substrate microstructure.



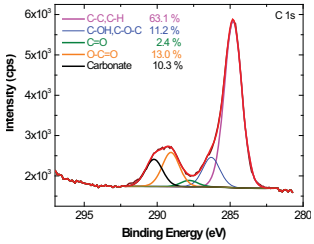
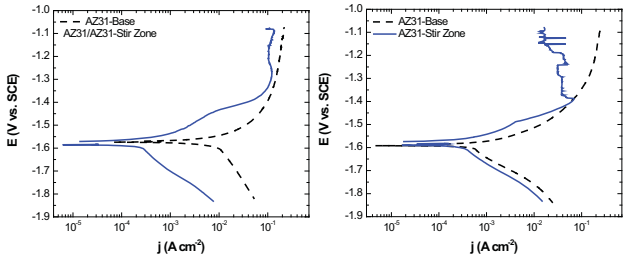


Figure 5. High-resolution fitted XPS spectra recorded on heavy-polished AZ31 stir zone.

Electrochemical Results

The corrosion resistance across the friction stir welded joints was investigated using ASTM B117 salt fog testing and electrochemical potentiodynamic polarization of the isolated base material and stir zones, in the as-received condition and as-polished conditions. The polarization curves performed on the stir zone and base materials for the as-received and heavy- polished surfaces are shown in Figure 6. The potentiodynamic polarization curves revealed that significantly lower cathodic hydrogen evolution and anodic dissolution currents were associated with the stir zone on the as-received surface (Figure 6(a)). As the corrosion rate of a Mg alloy cannot be reliably estimated from its polarization curve (based on Tafel extrapolation) due to the fact that the breakdown potential is normally more negative than its corrosion potential in aggressive NaCl solutions [20], these measured anodic currents do not accurately capture the localized corrosion kinetics [21]. However, the cathodic currents can still reliably represent the cathodic hydrogen evolution activity.

Potentiodynamic polarization was also performed on the heavy-polished surfaces of an AZ31 stir zone and base material to investigate the corrosion behavior after polishing and removal of the native surface oxide layer. As shown in Figure 6(b), the stir zone exhibited similar cathodic hydrogen evolution activity as the base material, suggesting no marked difference in corrosion resistance between the stir zone and base material in the as-polished condition. It should be noted that the potentiodynamic polarization behavior observed for the heavy-polished samples was consistent with the similarities in the surface chemistry of the heavy-polished stir zone and base materials (Table 1).



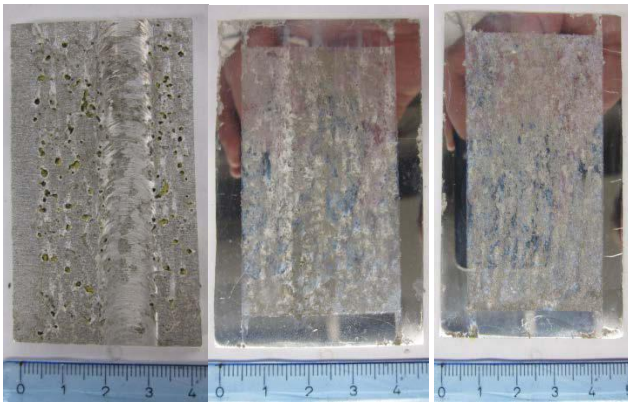
(a) (b)

Figure 6. Potentiodynamic polarization curves of the (a) as-received and (b) heavy-polished stir zone and base material surfaces in 5 wt.% NaCl solution at a scan rate of 0.1667 mV/s at 35°C.

Salt Spray Test

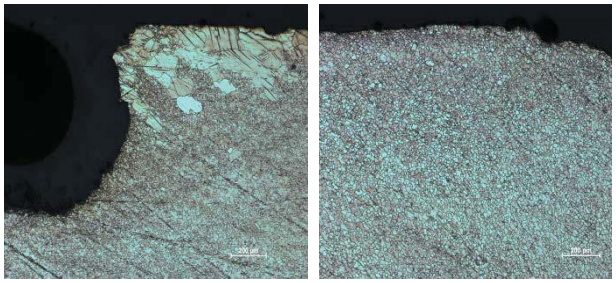
Macrographs of across the friction stir welded joint in the as-received and heavy-polished condition and light-polished base material after ASTM B117 salt spray testing for 24 h are shown in Figure 7. In the as-received condition (Figure 7(a)), the base material region exhibited a large number of pits and severe corrosion whereas the FSW region showed a much smaller pit population, indicative of a significant improvement in corrosion resistance versus the as-received base material. Figure 8(a) and (b) show cross-sectional micrographs of the corroded as-received base material and stir zone, respectively, from the salt spray test samples per Figure 7(a)). The base region exhibited large, shallow pits whereas the SZ shows a more uniform corrosion. A large reduction in thickness was also observed in the base region as compared to the SZ. It should be noted that the relative corrosion resistances of the as-received base material and SZ from the B117 salt fog testing were consistent with the electrochemical results (Figure 6(a). The improved corrosion resistance observed in the stir zone compared to the base material is likely attributed to a lesser heavy metal surface contamination in the stir zone, even though both the stir zone and base material showed similar surface contaminations per the XPS analysis results in Table 1.

However, after heavy-polishing across the friction stir welded joint, there was no significant difference in the corrosion morphology between the base and FSW regions (Figure 7(b)), consistent with the electrochemical potentiodynamic results (Figure 6(b)). Both of the weld joint and base material region exhibited a uniform corrosion morphology, indicating an improved corrosion resistance across the FSW joint after polishing and the native oxide film was removed. In addition, the light-polished base material showed a similar uniform corrosion morphology after salt fog testing for 24 h (Figure 7(c)). The similar corrosion behaviors observed for the light-polished base material and heavy-polished base material and their respective stir zones clearly indicates that the grain size has no significant effect on the corrosion behavior. The improved corrosion resistance across the FSW joints after both the light and heavy polishing further indicates that the differences observed lightly arise from the deleterious effect of the contaminated surface layer.



(a) (b) (c)

Figure 7. Macrographs of across the friction stir welded joint and base material after ASTM B117 salt spray test for 24 h: (a) as-received joint; (b) heavy-polished joint; and (c) light-polished base material.



(a) (b)

Figure 8. Cross-sectional micrographs of (a) corroded as-received AZ31 base material and (b) stir zone per the sample presented in Figure 7(a).

Discussion

Role of heavy metal contamination in controlling the mode and extent of corrosion

It is well known that surface contamination as a result of thermo-mechanical processing of Mg alloys from such processes as hot rolling, can have a negative effect on corrosion resistance. Heavy metal contaminants such as Fe, Cu and Ni, left on the surface of Mg alloys, results in the formation of micro-galvanic couples and increases the corrosion rate [15]. The contaminants detected by XPS on the as-received surfaces of the AZ31 base material and stir zones in this work were Cu and Fe in the form of oxides (Table 1). After removal of the native oxide during both light and heavy polishing, these heavy elements were no longer detected by XPS, indicating they were only present on the as-received native oxide layer. These surface impurities probably originated from sheet rolling and/or surface cleaning before welding.

As both of Cu and Fe have much more cathodic hydrogen evolution activity than Mg, if these elements were present on an Mg alloy surface, the cathodic current density would be significantly increased. This was the case observed in the electrochemical potentiodynamic polarization curves in this work (Figure 6). Lower cathodic hydrogen evolution current densities were observed on the heavy-polished surfaces versus the as-received surface for both of the base material and stir zone, further demonstrated that heavy metal contaminants (Cu and Fe) were responsible for the relatively poor corrosion resistance of the as-received base material surfaces and that polishing can effectively remove the contaminated surface layer and increase the corrosion performance, as shown in Figure 7.

However, the extent of surface heavy metal contamination on the as-received base material and stir zone surfaces seems to be higher in the SZ (XPS results), which would not seem to be consistent with the potentiodynamic scans. The cathodic current density obtained on the as-received base material decreased more significantly after polishing than in the case of the stir zone. Specifically, at a potential of −1.6 V (vs. SCE), close to the corrosion potential (−1.57 V (vs. SCE)), the cathodic current density on the as-received base material can be estimated at approximately 1×10^{-2} A/cm^{-2} and that on the polished surface to have been 5×10^{-4} A/cm^{-2} (Figure 6). By comparison, the cathodic current density measured on the as-received stir zone only decreased from about 4×10^{-4} A/cm^{-2} to 3×10^{-4} A/cm^{-2}, an insignificant effect. This different behavior suggests that the as-received base material was much more heavily contaminated by heavy element such as Cu and Fe than the stir zone, even though the XPS detected approximately the same amount of contamination on the top surfaces. Salt fog testing on the as-received samples across the joint confirmed that high concentrations of heavy metal contaminants were present on the as-received base material region and resulted in severe localized attack due to significantly more micro-galvanic corrosion cells being present than on the stir zone.

Role of grain size

The effect of microstructure on the general corrosion behavior of Mg alloys has not yet been studied in detail. A few researchers found that coarse grains obtained through heat-treatment slightly deteriorated the corrosion resistance of AZ 31 and it has been advanced that larger grains have less corrosion-barrier grain boundaries, resulting in a higher corrosion rate [11,12]. In the present study, no significant difference in the corrosion behavior was observed between the large grained (average 70 μm) AZ31 base material, the fine grained (average 10 μm) base material and the stir zone (average 8 μm). These samples had similar surface chemistry and similar uniform corrosion after 24h salt fog testing. These results indicate that there is no significant effect of grain size on the corrosion behavior of AZ31.

As mentioned in the literature [13], grain boundaries are a type of crystallographic defect and can be regarded as a high energy discontinuity in the structure. For this reason, grain boundaries can be regarded as more active sites than the bulk grain and would be preferentially attacked by corrosion. However, other researchers [11,12] proposed that the grain boundaries of AZ31 are a corrosion barrier that can retard corrosion. This argument is contradictory to the "dual-role" effect of Al theory in which Al serves as a corrosion barrier only when it is able to form a continuous phase in the form of $Mg_{17}Al_{12}$. The insignificant effect of grain size on the corrosion behavior of AZ31observed in this work maybe the result of a counterbalance between two above effects. Nevertheless, more reasonable explanation is still required on the effect of grain size/grain boundary on the corrosion behavior of AZ31.

Conclusion

The corrosion behavior of FSW Mg alloy AZ31 used to fabricate an Mg alloy-intensive front end sub-assembly demo was investigated using ASTM B117 salt fog testing and potentiodynamic polarization in this work. The following conclusion can be made:

1. Heavy metal contamination of the native film was responsible for the differences in the corrosion behavior between as-received stir zone and base material samples.

2. Removal of the native oxide film resulted in no differences being observed between the corrosion behavior of the base material and stir zone.

3. There is no significant effect of grain size on the corrosion behavior of AZ31.

Acknowledgements

The authors gratefully acknowledge Natural Resources Canada, the Natural Sciences and Engineering Research Council of Canada (NSERC) and Automotive Partnership Canada (APC) for their financial support of this research. The authors also acknowledge Mr. Chris Butcher of the Canadian Centre for Electron Microscopy (SEM) and Dr. Mark Biesinger at Surface Science Western (XPS) for their knowledge and assistance on the analytical techniques employed in this study.

References

1. G. Cole. "Summary of Magnesium Vision 2020: A North American Automotive Strategic Vision for Magnesium," *Magnesium Technology 2007*, ed. R.S. Beals et al., (Warrendale, PA: TMS, 2007), 35-40.

2. N. LeBozec, A. LeGac and D.Thierry, "Corrosion Performance and Mechanical Properties of Jointed Automotive Materials", *Mater. Corros.,* 63 (5) (2012), 408-415.

3. G.L. Song, "Recent progress in corrosion and protection of magnesium alloys", *Adv. Eng. Mater.* 7 (2005) 563–586.

4. G.L. Song, A. Atrens, "Corrosion mechanisms of magnesium alloys", *Adv. Eng. Mater*. 1 (1999) 11–33.

5. R. Zeng, J. Zhang, W. Huang, W. Dietzel, K. Kainer, C. Blawert, W. Ke, "Review of studies on corrosion of magnesium alloys", *Trans. Nonferrous Metals Soc. China,* 16 (2006) s763–s771.

6. J.I. Skar, D. Albright, "Emerging trends in corrosion protection of magnesium die-castings", in: Magnesium Technology, 2002, 2002, pp. 255–261.

7. J.T. Carter, R. Verma, and P.E. Krajewski, "Mechanical Behavior of AZ31 Sheet Materials at Room and Elevated Temperature," *Magnesium Technology 2008,* ed. Mihriban O. Pekguleryuz, et al. (Warrendale, PA: TMS, 2008), pp. 69–74.

8. A. Pardo, M.C. Merino, A.E. Coy, R. Arrabal, F. Viejo, E. Matykina, "Corrosion Behaviour of Magnesium/Aluminium Alloys in 3.5wt.% NaCl", *Corros. Sci.,* 50 (2008), 823-834.

9. A. Prado, M.C. Merino, A.E. Coy, F. Viejo, R. Arrabal, E. Matykina, S. Feliu Jr., "Influence of Microstructure and Composition on the Corrosion Behaviour of Mg/Al alloys in Chloride Media", *Electrochim. Acta*, 53 (2008), 7890-7902.

10. S. Feliu Jr., A. Prado, M.C. Merino, A.E. Coy, F. Viejo, R. Arrabal, "Correlation Between the Surface Chemistry and the Atmospheric Corrosion of AZ31, AZ80 and AZ91D Magnesium Alloys", *Appl. Surf. Sci.,* 255 (2009), 4102-4108.

11. G. Ben-Hamu, D. Eliezer, L. Wagner, "The relation Between Severe Plastic Deformation Microstructure and Corrosion Behavior of AZ31 Magnesium Alloy", *J. Alloy Compd.,* 468 (2009) 222-2car29.

12. N. Aung, W. Zhou, "Effect of Grain Size and Twins on Corrosion Behaviour of AZ31B Magnesium Alloy", *Corros. Sci.,* 52 (2) (2010), 589-594.

13. G.L. Song, Z.Q. Xu, "The Surface, Microstructure and Corrosion of Magnesium Alloy AZ31 Sheet", *Electrochim. Acta*, 55 (2010)4148-4161.

14. N. Shikata, Y. Kondou, Y. Nishikawa, Y. Nishizawa, Y. Sakamoto, T. Fujiwaki, *Method of Surface Preparation and Method of Coating* (Patent Cooperation Treaty (PCT), 1999).

15. U.C. Nwaogu, C. Blawert, N. Scharnagl,W.Dietzel, K.U. Kainer, "Influence of Inorganic Acid Pickling on the Corrosion Resistance of Magnesium Alloy AZ31 Sheet", *Corros. Sci.*, 51 (2009), 2544-2556.

16. *Standard Practice for Operating Salt Spray (Fog) Apparatus,* ASTM International.

17. R.S. Mishra, Z.Y. Ma, "Friction Stir Welding and Processing," *Mater. Sci. Engineer.*, R 50 (2005), 1-78.

18. R. Nandan, T. DebRoy, and H.K.D.H. Bhadeshia, "Recent Advances in Friction-stir Welding-Process, Weldment Structure and Properties," *Prog. Mater. Sci.*, 53 (2008), 980-1023.

19. P. B. Srinivasan, S. Riekehr, C. Blawert, W. Dietzel, M. Kocak, "Mechanical Properties and Stress Corrosion Cracking Behaviour of AZ31 Magnesium Alloy Laser Weldments," *Trans. Nonferrous Met. Soc. China*, 21 (2011), 1-8.

20. G. Song, "Recent Progress in Corrosion and Protection of Magnesium Alloys," *Adv. Engineer. Mater.*, 7 (2005), 563-586.

21. G. Song and Z. Xu, "The Surface, Microstructure and Corrosion of Magnesium Alloy AZ31 Sheet," *Electrochim. Acta*, 55 (2010), 4148-4161.

Magnesium Technology 2014

Biomedical Applications

Magnesium Technology 2014
Edited by: Martyn Alderman, Michele V. Manuel, Norbert Hort, and Neale R. Neelameggham
TMS (The Minerals, Metals & Materials Society), 2014

DEVELOPMENT OF A GENERALISED UNDERSTANDING OF ENVIRONMENTALLY-ASSISTED DEGRADATION OF MAGNESIUM-ALUMINIUM ALLOYS

Nicholas Winzer[1], Heiko Höpfel[1], Paula Casajus[1]
[1]Fraunhofer Institute for Mechanics of Materials IWM; Wöhlerstraße 11; Freiburg, Baden-Württemberg, 79115, Germany

Keywords: magnesium, corrosion, electrochemical noise

Abstract

Common factors affecting the susceptibility of Mg-Al alloys to creep, corrosion and stress corrosion cracking are the influences of the concentration and morphology of the β phase. The influences of the β phase on the various degradation modes are interrelated and may have opposing consequences on durability. This paper provides an overview of the influences of the β phase on the mechanisms for degradation of Mg-Al alloys in extreme environments. Preliminary results aimed at evaluating the role of the β phase in the corrosion behaviour of high-purity Mg-Al alloys in 3.5% NaCl solution using electrochemical noise analysis are presented. The results show a general increase in corrosion resistance with increasing total Al concentration. This is rationalised in terms of the effect of Al-enrichment of the surface film. The implications of the results on alloy development are discussed.

Introduction

Mg alloys have the lowest density of metals used in structural applications. This makes them well suited to applications where weight reduction is a priority. However, the widespread use of Mg alloys in structural applications remains limited due to their relatively high susceptibility to environmentally-assisted degradation (corrosion, stress corrosion cracking [SCC], hydrogen embrittlement [HE] and high-temperature creep). Despite there being a vast body of literature [1,2,3] on the susceptibility of Mg alloys to these degradation modes, a generalised framework for the development of alloys with greater resistance to environmentally-assisted degradation is lacking.

The most common Mg alloys are those containing Al, which is added to improve strength and castability. The Al may exist either in solid solution in the α matrix or in the form of intermetallic particles, primarily the eutectic β phase, which has the nominal composition $Mg_{17}Al_{12}$. The β phase may appear in Mg-Al alloys with Al concentrations of more than ~2 wt. % [4] and may take on a variety of morphologies, depending on the total Al concentration and thermal history. In as-cast alloys, the β phase takes the form of divorced or partially-divorced particles. These particles can be dissolved slowly by solution treatment at high temperatures (typically 420 °C) [5]. Subsequent aging at lower temperatures may result in re-precipitation of the β phase in the form of discontinuous platelets or continuous lamellae [6]. In exceptional cases involving rapid heating and cooling (e.g. during welding), grain boundary liquation may occur, resulting in formation of a continuous network of β phase at grain boundaries [7,8].

There is considerable evidence in the literature that the concentration and morphology of the β phase have a strong influence on the susceptibility of Mg-Al alloys to environmentally-assisted degradation. The influences of the β phase on these degradation modes are varied and may have opposing consequences on durability. Thus, the development of Mg alloys for applications where they may be exposed to combinations of high temperature, corrosive media and mechanical loads requires a detailed understanding of the influences of microstructure on the various mechanisms for environmentally assisted degradation.

In describing the influence of microstructure on the susceptibility of Mg alloys to corrosion, a distinction is made between low and high purity alloys. Low purity Mg alloys are those with Fe concentrations higher than the tolerance limit (170 ppm in the case of binary Mg-Al alloys). In such cases, the corrosion rate, which can be up to 100 times greater than that for equivalent high-purity alloys, is dominated by the influence of small Fe-rich particles [9]. For high purity Mg-Al alloys, the behaviour is usually rationalised in terms of the concentration and morphology of the β phase, although there is still conjecture regarding their exact influence on the corrosion behaviour. Key factors affecting the influence of the β phase on the corrosion behaviour are: (i) the difference in electrochemical potential of the β phase and the α-matrix; and (ii) the increase in the stability of passive films due to Al-enrichment. In the form a continuous grain boundary network, the β phase may also behave as a protective barrier against ongoing corrosion, thereby increasing corrosion resistance. In their discrete forms, β phase particles behave as local cathodes, thereby promoting localised corrosion [10,11]. Al remaining in the α-matrix leads to the formation of an Al-enriched surface film, thereby increasing its strength and stability and reducing the difference in the electrochemical potentials of the α and β phases [12]. This implies that the corrosion resistance of Mg-Al alloys is dependent on: (i) the morphology of the β-phase; (ii) the balance of Al between the α and β phases; and (iii) the non-uniform distribution of Al in solid solution.

SCC of Mg alloys may be either transgranular (TG-SCC) or intergranular (IG-SCC) [1], with the predominant mechanism being dependent largely on microstructure. TG-SCC may involve a number of mechanisms, depending on the alloy and environment. Crack initiation occurs by transgranular localised dissolution at film rupture sites, whereas further crack propagation occurs by some form of hydrogen embrittlement (HE), with the H coming from the corrosion reaction of the exposed metal at the surface or at the crack tip [13,14,15]. Reports of IG-SCC are far fewer. IG-SCC in pure Mg [16,17] has been associated with HE. There is a general consensus in the literature [18,19,20,21] that IG-SCC Mg alloys involves galvanically-driven localised dissolution (tunnelling) of the Mg α matrix adjacent to cathodic grain boundary precipitates. These precipitates may consist of the β phase or ternary phases containing rare-earth elements, which are used to enhance creep resistance. The very nature of this mechanism implies that it can only occur for alloys containing a near-continuous network of the β phase at grain boundaries in

very aggressive environments. In stark contrast to this widely-accepted model, Winzer et al. [15,22] recently reported the occurrence of IG-SCC propagation though fine grained regions in rolled AZ31 alloy that did not contain grain boundary precipitates. This was attributed to HE, though it remains unclear whether this was a consequence of the grain size or the intrinsic weakness of recrystallized grain boundaries.

Creep of Mg-Al alloys at elevated temperatures is usually associated with the change in morphology of the β phase, e.g. from interdendritic particles to soft lamellar clusters [23]. In recent years there has been a considerable effort to improve the high-temperature creep resistance of Mg-Al alloys through the addition of alloying elements, resulting in a number of new commercial alloys. Alkaline metals and rare earth elements improve creep resistance by combining with Al in preference to Mg to form thermally stable intermetallics, thereby suppressing β particle growth over a wide temperature range and retarding creep deformation by pinning dislocations and grain boundaries [2]. The addition of β-refining elements may have positive or negative consequences on corrosion performance and other factors affecting their applicability. Rare earth metals are generally thought to be beneficial to corrosion performance, but add considerable cost to the alloy [24]. Ca is also believed to be beneficial to corrosion resistance [25]; however, >1 wt% Ca is detrimental to the mechanical properties and castability [26]. Sr additions are beneficial to both mechanical properties and corrosion resistance [2,27], which is why Mg-Al-Sr alloys are currently being used in some high volume automotive applications [28]. Si does not act as a β-refiner, but does provide some improvement in high-temperature creep resistance though the precipitation of hard Mg_2Si particles [2,29,30]. Mg_2Si particles have the same corrosion potential as the Mg α matrix, and therefore do not promote localised corrosion, but have an inherently weak Chinese-script morphology [29,30]. Additions of Bi and Sb also improve creep properties by the precipitation of fine Mg_3Bi_2 and Mg_3Sb_2 particles [25,31,32,33]. These elements also appear to prevent aging; however, the mechanism for this is unclear. Mg_3Bi_2 and Mg_3Sb_2 particles are cathodic relative to the Mg α matrix and, therefore, promote localised corrosion [25]. Pb is also worth mentioning, as it has a powerful β-refining effect at room temperature and does not form second phase particles [34]. Consequently, additions of Pb increase corrosion resistance but promote aging [35].

The influence of Al on the strength and stability of oxide films formed on Mg-Al alloys in aqueous environments implies that Al has a positive effect on corrosion resistance in alloys that do not contain highly-cathodic intermetallic particles. It may also be expected to have a positive effect on the SCC resistance of Mg-Al alloys, which involves crack initiation by transgranular localised dissolution at film rupture sites. These factors should be considered in the modification of Mg-Al alloys for increased high-temperature creep resistance, since many tertiary alloying elements used to improve the creep resistance of Mg-Al alloys have a strong influence on the distribution of Al between the α matrix and the β phase and, consequently, the strength and stability of the oxide film. The significance of the α-Al concentration and Al enrichment of the surface film has not been widely recognised in the literature. Given that the addition of β refining elements is an increasingly popular means of improving the durability of Mg-Al alloys at elevated temperatures, this is a topic that is certainly worthy of further investigation.

This paper provides an overview of preliminary results aimed at evaluating the influence of the β phase on the susceptibility of Mg-Al alloys to corrosion using electrochemical noise analysis. This is part of a wider program aimed at developing a generalised framework for the improvement of the resistance of Mg-Al alloys to environmentally-assisted degradation. As part of this program, the resistance of the test materials to creep and SCC will also be evaluated. The work will also be extended to include the evaluation of the influences of various tertiary alloying elements on resistance to environmentally-assisted degradation.

Experimental Method

Mg-Al alloys with nominal Al concentrations of 3, 6 and 9 wt% were fabricated by permanent mould chill casting at Helmholz-Zentrum Geesthacht, Germany. Commercially-pure cast Mg was provided by Magnesium Elektron, UK, for comparison. The pure Mg was cast using a different method than that used for the Mg-Al alloys. The compositions of the materials are shown in Table I.

Table I. Compositions of the test materials.

Material	Mg	Mg3%Al	Mg6%Al	Mg9%Al
Al	0.002	3.006	5.224	9.938
Zn	0.005	0.002	<0.001	0.003
Mn	<0.003	0.015	0.005	0.024
Si	<0.005	0.011	0.01	0.02
Cu	0.003	0.001	<0.005	<0.0003
Fe	0.004	0.005	0.003	0.005
Ni	<0.001	<0.0005	<0.0005	0.002
Ca	0.002	0.012	0.011	0.004
Zr	<0.0001	<0.001	<0.001	<0.001
Sn	<0.0005	<0.006	<0.0005	0.003

The microstructures of the different materials were examined by scanning electron microscopy (SEM) and energy dispersive X-ray spectroscopy (EDX). The specimens were prepared by grinding and polishing down to 0.25 μm diamond suspension, followed by etching. Mg3%Al specimens were etched for 15 s using Pikrin. All other specimens were etched for 15 s in an aqueous solution containing 60 vol.% ethylene glycol, 20 vol% acetic acid, 1 vol% concentrated HNO_3.

EN measurements were performed using a three-electrode setup comprising two identical working electrodes and an Ag/AgCl reference electrode at open circuit potential. The working electrodes were prepared by machining the as-cast materials into 1x1x1cm cubes. Insulated wires were attached to the cubes using press-fit connectors. Pairs of identical cubes were embedded in epoxy such that only one face of each cube was exposed. The exposed surfaces were polished with up to 1200 grade emery paper and cleaned with ethanol immediately prior to testing. The samples were immersed in a glass cell containing 3.5 wt% NaCl prepared from analytical grade reagents. The cell was shielded using a faraday cage to prevent external noise interference. Current and potential were simultaneously recorded at a frequency of 1 Hz over a period of 24 hours. The current was measured between the two working electrodes, whilst the potential was measured with respect to the reference electrode. All measurement and data analysis was performed using a Gamry Reference 600 potentiostat and ESA400 software. The measurements were performed at least three times for each material.

Specimens for hydrogen evolution measurements were prepared using the same cubes as used in the electrochemical noise measurements. The specimens were embedded in epoxy such that only one face was exposed. The exposed face was polished and cleaned with ethanol prior to testing. The samples were immersed in 3.5 wt% NaCl underneath an upturned burette, such that the volume of evolved H_2 gas could be measured.

Results

Figure 1 shows the microstructure of the Mg-Al alloys in as-cast condition. The grain sizes of the alloys were in the range 50 – 500μm. All alloys contain intermetallic secondary phase particles, which increase in concentration with increasing total Al concentration. EDX analysis confirmed that the nominal composition of the particles was $Mg_{17}Al_{12}$, i.e. corresponding to the β phase. The β phase in the Mg3%Al alloy had the form of small, continuous particles within grains and at grain boundaries (see Figure 1A). The microstructures of the Mg6%Al and Mg9%Al alloys are characterized by partially-divorced continuous β precipitates within grains and at grain boundaries (see Figure 1B and C). The continuous grain boundary precipitates were surrounded by agglomerates of β phase lamellae. The uneven topology in the α-phase, which is particularly apparent for the Mg3%Al and Mg6%Al alloys, is attributed to the non-uniform distribution of Al in solid solution and the selective attack of the Pikrin acid.

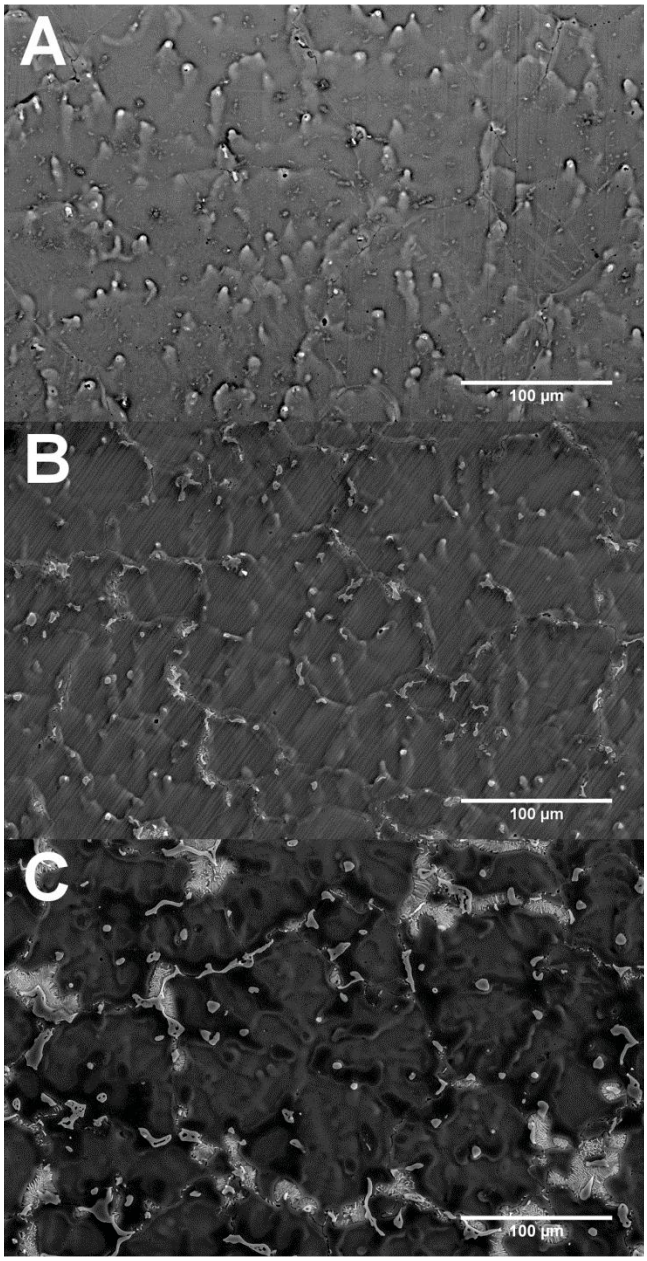


Figure 1. Microstructure of the as-cast alloys A) Mg3%Al, B) Mg6%Al and C) Mg9%Al.

The volume concentrations of β phase in the as-cast Mg3%Al, Mg6%Al and Mg9%Al alloys were approximated using the image analysis software ImageJ to be 1.1%, 1.9% and 9.2% respectively. It is instructive to note that the proportions by mass of Al exisiting in the β-phase, which may be calculated from the volume concentrations assuming that the β phase has a bcc structure with an atomic spacing of 1.06nm [36], were 0.044%, 0.075% and 0.36% for the Mg3%Al, Mg6%Al and Mg9%Al alloys respectively. Thus, in all materials almost all of the Al was dissolved in the α phase.

The susceptibilities of the materials to corrosion were characterised in terms of the noise impedance, Z_N, which may be calculated from the electrochemical noise (EN) measurements according to:

$$Z_N = \sqrt{\Psi_V/\Psi_I} \quad (1)$$

where Ψ_V and Ψ_I are the power spectral densities of the voltage and current signals respectively. It has been proposed by various workers that the low-frequency value of Z_N is equivalent to the polarisation resistance [37,38,39,40]. The voltage and current signals were measured over 15 overlapping intervals, each consisting of 2048 data points, beginning 19 hours after immersion of the sample in the electrolyte, when the signals were believed to be stabilized. For each interval, the recorded signal was conditioned by subtracting a simple linear trend and then applying a Hanning window. Ψ_V and Ψ_I were calculated by applying a fast Fourier transform to the conditioned signals and averaging over all 15 measurement intervals. Figure 2 shows Ψ_V, Ψ_I and Z_N for all materials. The Ψ_V and Ψ_I curves for the Mg-Al alloys were relatively linear over the entire frequency range. In contrast, the Ψ_V and Ψ_I curves for the pure Mg samples tended towards white noise in the low frequency range (<0.01 Hz). The Z_N curves were relatively flat for all materials. Pure Mg exhibited the highest corrosion resistance, characterised by the lowest Z_N. The corrosion resistances of the as-cast materials increased with increasing total Al concentration.

Figure 3 shows the H_2 evolution relative to immersion time for each of the materials. As per the EN measurements, the corrosion rate for pure Mg was lower than those for the other materials. Also consistent with the EN measurements is the decrease in the corrosion rates of the Mg-Al alloys with increasing total Al concentration.

Figure 4 shows the morphologies of corrosion in pure Mg, Mg3%Al and Mg9%Al after immersion in NaCl for two days. Corrosion in pure Mg took the form of filiform corrosion (Figure 4A). The filiform regions spread laterally from grain boundaries

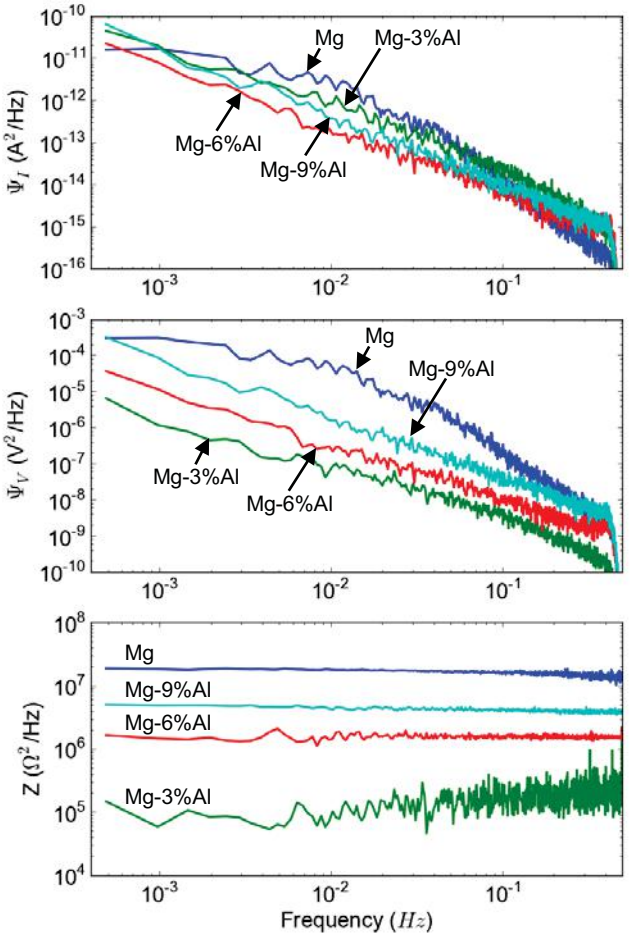


Figure 2. Power spectral density curves for voltage (Ψ_V), current (Ψ_I) and impedance (Z) for all materials.

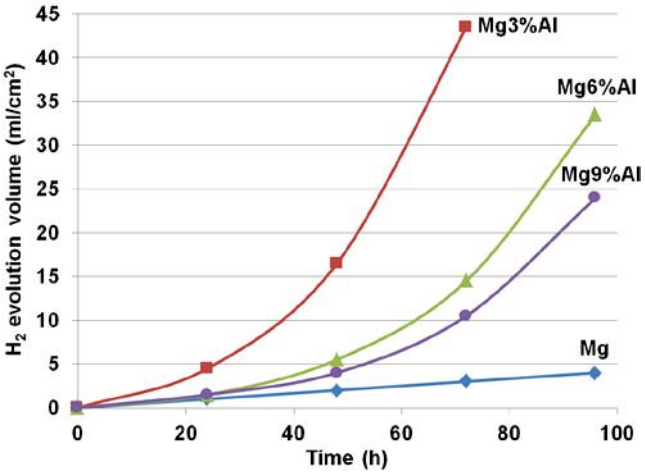


Figure 3: H_2 evolution over time for all materials.

with the corrosion channels having some preferred crystallographic orientation. The corrosion morphology for all Mg-Al alloys was characterised by larger numbers of small, hemispherical pits, which are characteristic of autolimiting localised dissolution, and smaller numbers of large, irregularly-shaped pits (Figure 4B-C). It was unclear whether the smaller pits

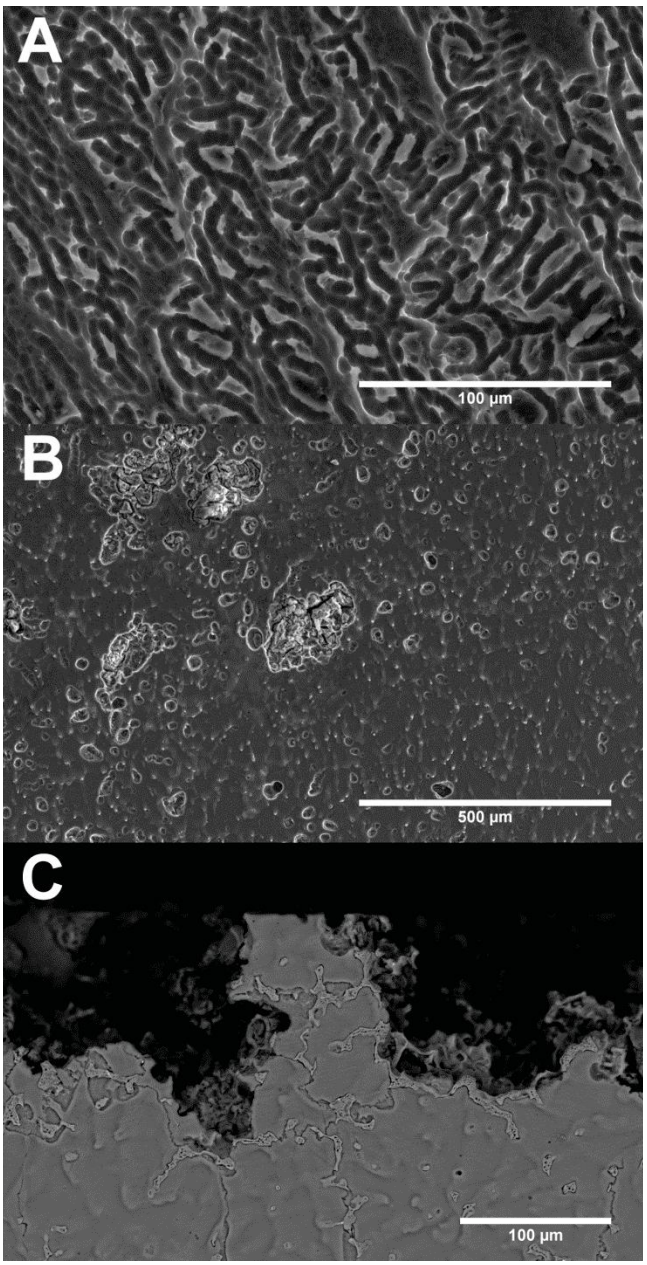


Figure 4. Morphology of corrosion on the surface of the pure Mg (A) and Mg3%Al (B) samples and cross-section of a corrosion pit in the Mg9%Al (C) sample.

were initiated at any particular microstructural feature; however, the deeper corrosion pits were typically limited by grain boundaries and β phase particles (Figure 4C).

Discussion

The increase in corrosion resistance of the Mg-Al alloys with increasing total Al concentration can be rationalised in terms of: (i) the effect of Al-enrichment of the surface film; and/or (ii) the effect of microgalvanic coupling between the (cathodic) β and (anodic) α phases. Since most of the Al remains in solid solution with the α phase in all of the alloys, the proportion of Al in the α phase is directly coupled with the total Al concentration. Lunder

et al. [41] showed through potentiodynamic tests of the constituent phases in Mg-Al alloys in 5% NaCl saturated with $Mg(OH)_2$ that the corrosion potential difference and galvanic current between the α and β phases increased with increasing α phase Al concentration. Mathieu et al. [12] performed similar experiments in mildly aggressive ASTM D1384 water with the opposite outcome; the corrosion potential difference and galvanic current between the α and β phases decreased with increasing α phase Al concentration up to 5%. This is consistent with the results of the present study. Mathieu rationalised the influence of the α phase Al concentration in terms of the Al-enrichment of the surface film. The influence of Al on the structure of surface films in aqueous solutions has been evaluated by various workers [42,43,44]. Liu et al. [42] used XPS to show that the compositions of oxide films formed on Al_3Mg_2 and $Mg_{17}Al_{12}$ intermetallics were $AlMg_{1.4}O_{0.2}(OH)_{5.4}$ and $AlMg_{2.5}(OH)_8$ respectively. Splinter and McIntyre [43] investigated the initial stages of film growth on surfaces of pure Mg and solution-annealed Mg3%Al and Mg8.5%Al alloys in water vapour using Auger electron spectroscopy and XPS. The increase in bulk Al concentration resulted in, for short exposures, an increase in the rate of oxide nucleation and growth and, for longer exposures, incorporation of Al^{3+} ions into the surface film. Nordlein et al. [44] performed a detailed TEM analysis of oxide films formed on Mg-Al alloys in distilled water. The oxide films were comprised of three layers, with the Al concentration of the innermost layer increasing up to ~35wt% with increasing total bulk Al concentration up to ~4%. This threshold was associated with an increase in corrosion resistance due to formation of a skeletal structure comprised of amorphous Al_2O_3 within the cellular $Mg(OH)_2$ innermost layer.

The apparent influence of grain boundaries and β phase particles on the morphology of corrosion in the Mg-9%Al alloy is also indicative of the effect of Al in solution with the α phase. Figure 4C appears to show that the growth of corrosion pits is arrested or slowed at grain boundaries and β phase particles. This may be attributable to the non-uniform distribution of Al in the α phase; Al tends to segregate at or close to grain boundaries, as evidenced by the uneven topology of the etched micrographs (Figure 1). If indeed the corrosion potential of the α phase becomes more positive (i.e. closer to that of the β phase) with increasing Al concentration, as proposed by Mathieu et al. [12], then a reduction of the corrosion pit growth rate at the Al-rich grain boundaries seems plausible. This is similar in concept to Song's [10,11] proposal that continuous networks of the β phase may act as protective barriers against corrosion pit growth. However, it is not restricted to alloys containing continuous networks of the β phase, which are rare in commercial as-cast Mg-Al alloys.

The influences of the total Al concentration and the non-uniform distribution of Al dissolved in the α phase on the corrosion resistance of Mg-Al alloys has important implications on the development of commercial alloys and heat-treatment procedures. The results of the present study suggest that, in Mg-Al alloys containing impurity concentrations less than the tolerance limits, Al is beneficial to corrosion resistance. Moreover, it may be possible to achieve higher corrosion resistance for alloys with lower Al concentrations through the development of heat treatment procedures to maximize the Al concentration at grain boundaries. Further work is required to determine whether this is indeed feasible in ternary alloys, i.e. those containing additional alloying elements to improve creep resistance.

Conclusions

- The corrosion resistances of high-purity Mg-Al alloys with nominal Al concentrations of 3, 6 and 9 wt% as well as pure Mg were evaluated using electrochemical noise (EN) analysis and H_2 evolution tests.
- The power spectral density (PSD) curves of the current and noise signals for the Mg-Al alloys were log-linear over the entire frequency range, whereas those for pure Mg tended towards a "white noise" region in the low frequency range.
- Pure Mg had the highest resistance to corrosion, characterised by the highest noise impedance and lowest rate of H_2 evolution. The corrosion resistances of the Mg-Al alloys were less than that of pure Mg and increased with increasing Al concentration.
- Corrosion of pure Mg was manifested by filiform corrosion, whereas corrosion of the Mg-Al alloys was highly localised and appeared to be affected by the β phase and the uneven distribution of Al in the α matrix.
- The increase in corrosion resistance of the Mg-Al alloys with increasing Al concentration is consistent with the increase in surface film stability due to Al enrichment [12,43,44].

References

1. N. Winzer, A. Atrens, G. Song, E. Ghali, W. Dietzel, K.U. Kainer, N. Hort, and C. Blawert, "A Critical Review of the Stress Corrosion Cracking (SCC) of Magnesium Alloys," *Advanced Engineering Materials*, 7 (2005), 659-693.
2. M.O. Pekguleryuz and A.A. Kaya, "Creep Resistant Magnesium Alloys for Powertrain Applications," *Magnesium Alloys and their Applications*, ed. K.U. Kainer (Weinheim: WILEY-VCH Verlag GmbH & Co, 2004), 74-93.
3. G. Song, ed., Corrosion of Magnesium Alloys (Cambridge, UK: Woodhead Publishing Limited, 2011)
4. A.K. Dahle, Y.C. Lee, M.D. Nave, P.L. Schaffer, and D.H. StJohn, "Development of the As-Cast Microstructure in Magnesium-Aluminum Alloys," *Journal of Light Metals*, 1 (2001), 61-72.
5. M. Avedesian and H. Baker, eds., *ASM Specialty Handbook: Magnesium and Magnesium Alloys* (Materials Park, OH: ASM International, 1999), 78-84.
6. D. Duly, J.P. Simon, and Y. Brechet, "On the Competition Between Continuous and Discontinuous Precipitations in Binary Mg-Al Alloys," *Acta Metallurgica et Materialia*, 43 (1995), 101-106.
7. J. Shen, G. You, S. Long, and F. Pan, "Abnormal Macropore Formation During Double-sided Gas Tungsten Arc Welding of Magnesium AZ91D Alloys," *Materials Characterization*, 59 (2008), 1059-1065.
8. T. Zhu, Z.W. Chen, and W. Gao, "Incipient Melting in Partially Melted Zone During Arc Welding of AZ91D Magnesium Alloy," *Materials Science and Engineering*, 416A (2006), 246-252.
9. M. Liu, P.J. Uggowitzer, A.V. Nagasekhar, P. Schmutz, M. Easton, G. Song, and A. Atrens, "Calculated Phase Diagrams and the Corrosion of Die-Cast Mg-Al Alloys," *Corrosion Science*, 51 (2009), 602-619.
10. G. Song, A. Atrens, X. Wu, and B. Zhang, "Corrosion Behaviour of AZ21, AZ501 and AZ91 in Sodium Chloride," *Corrosion Science*, 40 (1998), 1769-1791.

11. G. Song, A. Atrens, and M. Dargusch, "Influence of Microstructure on the Corrosion of Diecast AZ91D," *Corrosion Science*, 41 (1999), 249-273.
12. S. Mathieu, C. Rapin, J. Steinmetz, and P. Steinmetz, "A Corrosion Study of the Main Constituent Phases of AZ91 Magnesium Alloys," *Corrosion Science*, 45 (2003), 2741-2755.
13. N. Winzer, A. Atrens, W. Dietzel, V.S. Raja, G. Song, and K.U. Kainer, "Characterisation of Stress Corrosion Cracking (SCC) of Mg-Al Alloys," *Materials Science and Engineering*, 488A (2008), 339–351.
14. N. Winzer, A. Atrens, W. Dietzel, G. Song, and K.U. Kainer, "Fractography of Stress Corrosion Cracking of Mg-Al Alloys," *Metallurgical and Materials Transactions*, 39A (2008), 1157-1173.
15. N. Winzer, P. Xu, S. Bender, T. Gross, W.E.S. Unger, and C.E. Cross, "Stress Corrosion Cracking of Gas-Tungsten Arc Welds in Continuous-Cast AZ31 Mg Alloy Sheet," *Corrosion Science*, 51 (2009), 1950–1963.
16. S.P. Lynch and P. Trevena, "Stress Corrosion Cracking and Liquid Metal Embrittlement in Pure Magnesium," *Corrosion*, 44 (1988), 113-124.
17. R.S. Stampella, R.P.M. Procter, and V. Ashworth, "Environmentally-Induced Cracking of Magnesium," *Corrosion Science*, 24 (1984), 325-341.
18. W. M. Pardue, F.H. Beck, and M.G. Fontana, "Propagation of Stress-Corrosion Cracking in a Magnesium-Base Alloy as Determined by Several Techniques," *Transactions of the ASM*, 54 (1961). 539-548.
19. D.K. Priest, F.H. Beck, and M.G. Fontana, "Stress-Corrosion Mechanism in a Magnesium-Base Alloy," *Transactions of the ASM*, 47 (1955), 473-492.
20. L. Fairman, and H.J. Bray, "Intergranular Stress-Corrosion Crack Propagation in Magnesium Aluminium Alloys", British Corrosion Journal, 6 (1971), 170-174.
21. A. Moccari, and C.R. Shastry, "An investigation of Stress corrosion cracking in Mg AZ61 alloy in 3.5% NaCl + 2% K_2CrO_4 aqueous solution at room temperature," *Materialwissenschaft und Werkstofftechnik*, 10 (1979), 119-123.
22. P. Casajus and N. Winzer, "Intergranular stress corrosion crack propagation in rolled AZ31 Mg alloy sheet," (submitted for publication in *Materials Science and Engineering A*, 2013)
23. M.S. Dargusch, G.L. Dunlop, and K. Pettersen, "Elevated Temperature Creep and Microstructure of Die Cast Mg-Al Alloys," *Magnesium Alloys and their Applications*, ed. B.L. Mordike and K.U. Kainer (Frankfurt: Werkstoff-Informationsgesellschaft mbH, 1998), 277-282.
24. B.L. Mordike and T. Ebert, "Magnesium: Properties – applications – potential", *Materials Science and Engineering,* 302A (2001), 37-45.
25. W. Zhou, N.N. Aung, and Y. Sun, "Effect of antimony, bismuth and calcium addition on corrosion and electrochemical behaviour of AZ91 magnesium alloy," *Corrosion Science*, 51 (2009), 403–408.
26. G. Wu, Y. Fan, H. Gao, C. Zhai, and Y.P. Zhu, "The effect of Ca and rare earth elements on the microstructure, mechanical properties and corrosion behavior of AZ91D," *Materials Science and Engineering*, 408A (2005), 255–263.
27. Y. Fan, G. Wu, and C. Zhai, "The effect of Ca and rare earth elements on the microstructure, mechanical properties and corrosion behavior of AZ91D," *Materials Science Forum*, 546-549 (2007), 567-570.
28. M. Kunst, A. Fischersworring-Bunk, C. Liebscher, U. Glatzel, G. L'Esperance, P. Plamondon, E. Baril, and P. Labelle, "Microstructural Characterisation of Die Cast Mg-Al-Sr (AJ) Alloy," *Magnesium Alloys and their Applications*, ed. K.U. Kainer (Weinheim: WILEY-VCH Verlag GmbH & Co, 2007), 498-505.
29. A. Srinivasan, J. Swaminathan, U.T.S. Pillai, K. Guguloth, and B.C. Pai, "Effect of combined addition of Si and Sb on the microstructure and creep properties of AZ91 magnesium alloy," *Materials Science and Engineering*, 485A (2008), 86–91.
30. A. Srinivasan, S. Ningshen, U. Kamachi Mudali, U.T.S. Pillai, B.C. Pai, "Influence of Si and Sb additions on the corrosion behavior of AZ91 magnesium alloy," *Intermetallics*, 15 (2007), 1511-1517.
31. Y. Guangyin, S. Yangshan, and D. Wenjiang, "Effects of Sb addition on the microstructure and mechanical properties of AZ91 magnesium alloy," *Scripta Materialia*, 43 (2000), 1009–1013.
32. Y. Guangyin, S. Yangshan, and D. Wenjiang, "Effects of bismuth and antimony additions on the microstructure and mechanical properties of AZ91 magnesium alloy," *Materials Science and Engineering*, 308A (2001), 38–44.
33. H. Liu, N. Gong, L. Pang, and X. Zhang, "Microstructure and mechanical properties of as-cast AZ31 with the addition of Sb," *Materials Science and Engineering*, 497A (2008), 254–259.
34. S. Candan, M. Unal, M. Turkmen, E. Koc, Y. Turen, and E. Candan, "Improvement of mechanical and corrosion properties of magnesium alloy by lead addition," *Materials Science and Engineering*, 501A (2009), 115–118.
35. N. Balasubramani, A. Srinivasan, U.T.S. Pillai, and B.C. Pai, "Effect of Pb and Sb additions on the precipitation kinetics of AZ91 magnesium alloy," *Materials Science and Engineering*, 457A (2007), 275–281.
36. M.-X. Zhang and P.M. Kelly, "Crystallography of $Mg_{17}Al_{12}$ precipitates in AZ91D alloy," *Scripta Materialia*, 48 (2003), 647-652.
37. R.A. Cottis, "Interpretation of Electrochemical Noise Data," *Corrosion*, 57 (2001), 265-285.
38. U. Bertocci, C. Gabrielli, F. Huet, and M. Keddam, "Noise Resistance Applied to Corrosion Measurements I: Theoretical Analysis," *Journal of the Electrochemical Society*, 144 (1997), 31-37.
39. U. Bertocci, C. Gabrielli, F. Huet, M. Keddam, and P. Rousseau, "Noise Resistance Applied to Corrosion Measurements II: Experimental Tests," *Journal of the Electrochemical Society*, 144 (1997), 37-43.
40. J.F. Chen and W.F. Bogaerts, "The Physical Meaning of Noise Resistance," *Corrosion Science*, 37 (1995), 1839-1842.
41. O. Lunder, J.E. Lein, T.Kr. Aune, and K. Nisancioglu, "The Role of $Mg_{17}Al_{12}$ Phase in the Corrosion of Mg Alloy AZ91," *Corrosion*, 45 (1989), 741-748.
42. M. Liu, S. Zanna, H. Ardelean, I. Frateur, P. Schmutz, G. Song, A. Atrens, and P. Marcus, "A First Quantitative XPS Study of the Surface Films Formed, by Exposure to Water, on Mg and on the Mg-Al Intermetallics: Al_3Mg_2 and $Mg_{17}Al_{12}$," *Corrosion Science*, 51 (2009), 1115-1127.
43. S.J. Splinter and N.S. McIntyre, "The Initial Interaction of Water Vapour with Mg-Al Alloy Surfaces at Room Temperature," *Surface Science*, 314 (1994), 157-171.
44. J.H. Nordlien, S. Ono, N. Masuko, and K. Nisancioglu, "A TEM Investigation of Naturally Formed Oxide Films on Pure Magnesium," *Corrosion Science*, 39 (1997), 1397-1414.

Magnesium Technology 2014
Edited by: Martyn Alderman, Michele V. Manuel, Norbert Hort, and Neale R. Neelameggham
TMS (The Minerals, Metals & Materials Society), 2014

Coating Systems for Biodegradable Magnesium Applications

Jan-Marten Seitz[1], Rainer Eifler[1], Matthew Vaughan[2], Chris Seal[3], Margaret Hyland[4], Hans Jürgen Maier[1]

[1]Institut für Werkstoffkunde (IW), Leibniz Universität Hannover, An der Universität 2, 30823 Hannover, Germany
[2]Department of Mechanical Engineering, Texas A&M University, College Station, TX 77843-3123, USA
[3]Department of Chemical and Materials Engineering, The University of Auckland, Private Bag 92019, Auckland, New Zealand
[4]Light Metals Research Centre, The University of Auckland, Private Bag 92019, Auckland, New Zealand

Keywords: Magnesium, Coating, Corrosion, Polymer

Abstract

Current research for degradable magnesium implants has shown a multitude of potential applications for these materials. Within various studies, the research focuses especially on Mg alloys' biocompatibility and also its mechanical and corrosive behaviour in *in vitro/in vivo* environments. In particular, the corrosive properties of Mg alloys often remain problematic, showing either a rapid or a burst degradation, limiting their applicability. Besides changing the alloy, a magnesium implant's initial corrosion properties can be improved and controllable by means of applied coatings. In general, a multitude of coating solutions (e.g. on basis of phosphates or degradable polymers) are already available for permanent implants. If these are applicable to Mg, the next step requires that they delay corrosion and inhibit burst corrosion. In this study, the applicability and corrosion-delaying properties of PLA and MgF_2 coatings on the magnesium alloy LANd442, respecting their singular and combined application, is shown. By means of corrosion tests in a simulated body fluid the use of combined coatings was proven to be advantageous regarding longevity and toughness of the coating system.

Introduction

Currently, magnesium alloys are being investigated as degradable biomaterials for use in stents, sutures, and orthopedic applications [1-3]. Biodegradable, resorbable materials are of interest because they eliminate the need for a second surgical procedure to remove a temporary implant or device [4]. However, as magnesium alloys often exhibit poor corrosion resistance, their use in medical applications has previously been limited. A rapid degradation of Mg implants compromises structural integrity and leads to the production of excess hydrogen gas and an increased pH in the implant's proximity. Fortunately, these effects can be minimized through alloying and by coating the implant with a corrosion resistant layer [2, 5].

One of the most critically investigated coatings is magnesium fluoride (MgF_2), since Mg and F are both naturally occurring elements in the body, and the components of degradation remain harmless as the layer corrodes [6]. Previous studies using an MgF_2 protective layer have shown significantly improved corrosion resistance in industrial applications, as well as slight improvements in *in vitro* and *in vivo* biological testing [7-10]. However, MgF_2 is known for its brittle and cracked surface characteristics and inappropriate behaviour in case of deformations [11, 12].

The application of resorbable polymer coatings to magnesium could be a good alternative, since polymers possess better plasticity. However, Chen *et al.* [13] discovered reactions between Magnesium base material and polymer coatings (PLA and PCL). Here, the coating's defects and diffusing processes allowed the surrounding fluid to react with the base material, resulting in the generation of H_2 and $Mg(OH)_2$. Chen *et al.* [13] suggested that H_2 accumulations in the bonding zone led to a decrease in bonding strength. Furthermore, they claimed that $Mg(OH)_2$ accumulations reacted with the adjacent polymer, where the hydroxide led to an increased production of polymeric acids that either further neutralized OH^- or reacted with $Mg(OH)_2$ [13]. Finally, the increased production of polymeric acids led to a decreased corrosion resistance since the Mg surface passivation by $Mg(OH)_2$ became suppressed. This consequently led to an increased production of H_2 and $Mg(OH)_2$, promoting the degradation of the polymer. A mutual acceleration of both materials' corrosion rates resulted [13]. The cascade of reactions of the Mg and PLA proximity in a corrosive environment is summarized in **Table 1**. Via pH measurements, the biomedical polymer films lead to a decreased initial corrosion rate of pure Mg [14].

Table 1: Reactions of Mg and Polymer

No.	Reaction	Description
1	$Mg + 2H_2O \rightarrow Mg(OH)_2 + H_2 \uparrow$	Reaction of Mg and water [15]
2	$Mg(OH)_2 + 2Cl^- \rightarrow MgCl_2 + 2OH^-$	Reaction of magnesiumhydroxide and chloride ions from the SBF [13]
3	$(\text{-COOR-})_n \rightarrow R_1COOH + R_2OH$	Catalysed production of polymeric acids by means of $Mg(OH)_2$ [13]
4	$OH^- + R_1COOH \rightarrow R_1COO^- + H_2O$	Reaction of polymeric acid and OH^-[13]
5	$Mg(OH)_2 + 2R_1COOH \rightarrow (R_1COO)2Mg + 2H_2O$	Reaction of polymeric acid and $Mg(OH)_2$ [13]

In the course of corrosion, Mg and the polymer interact, which has the potential to accelerate both materials' corrosion processes. Here, the combination of surface treatments and different coatings might be the key to reducing or preventing this interaction. With this in mind, within this study the influence of an intermediate layer of MgF_2, which was used to circumvent the direct contact of Mg and PLA, was analysed regarding its potential to further delay the corrosion of the base material.

Materials and Methods

The magnesium alloy LANd442 (Mg 90 wt.%, Li 4 wt.%, Al 4 wt.%, Nd 2 wt.%) was chosen as base material due to its rapid and sudden corrosion properties [11].

LANd442, whose designations correspond to B275-05 guidelines of the "American Society for Testing and Materials" [16], was initially manufactured by gravity die-casting. Here, the base material and the additional alloying elements were obtained from Magnesium Elektron UK, magnesium, Treibacher Industrie AG (neodymium), Chemetall GmbH (lithium); and Hydro Aluminium Deutschland GmbH (aluminum). To produce the quaternary alloy, the magnesium and the corresponding alloying elements were melted at a temperature of 750 °C in a steel crucible and subsequently stirred for 30 min. Owing to the material's elevated reactivity with air, melting and casting was carried out in a dynamic argon atmosphere.

In order to obtain a fine-grained alloy with advanced mechanical and corrosive properties, hot extrusion was carried out after casting. Here, a direct extrusion operation was arranged in a 10 MN extruder. The extrusion die, which had an orifice diameter of 30 mm, was heated, along with its recipient, to a temperature of 380 °C. Subsequently, the respective cast billets could be inserted into the extruder and pressed through the extrusion die with a profile velocity of 1.9 $m \cdot min^{-1}$. The deformation was carried out at an extrusion ratio of 16.

In order to ensure sufficient specimen geometry, sample dimensions used in prior studies [11, 17, 18] and adequate for a three-point-bending test were chosen. Here, rods with a diameter of 2.5 mm and a length of 25 mm (exhibiting a surface area of 206 mm^2) were manufactured by machining.

To delay the corrosion of LANd442, two coating systems were combined and attached to the specimens. For the intermediate layer, a magnesium fluoride coating was chosen. In order to obtain a sufficient coating, the specimens were boiled in NaOH (200 $g \cdot L^{-1}$) for 120 min. Subsequently, the specimens were placed in hydrofluoric acid (40 %) for 96 h to achieve the MgF_2 coating. To remove the remains of the chemicals, the specimens were rinsed with distilled water and ethanol after the hydrofluoric acid treatment. The procedure was adapted from Seitz *et al.* [11, 12].

A PLA/DCM solution was prepared using PLA-3051D and dichloromethane to form the top sealing layer. Both agents (6.675 g PLA and 100 ml dichloromethane) were mixed together and stirred at room temperature for 60 minutes until the PLA dissolved completely. Subsequently, the solution was refilled to 100 ml by adding dichloromethane. The Mg samples were then lowered into the PLA/DCM solution for 15 seconds. The sample lowering process was repeated 2 times. Afterwards, the samples were dried at room temperature for 72 hours.

The experimentation involved *in vitro* corrosion of LANd442 in the PLA-coated state as well as in the combined MgF2 and PLA coated state, via immersion in smoothly flowing simulated body fluid (SBF) to acquire information about the coating systems' influence on degradation. Specimens of each coating state were removed from the experimental set-up after 15 and 30 days. For the total test duration, measurements were performed on separate samples (three for each measurement point), which were not immersed again after extraction. Single specimens were put into sample containers that were then filled with 25 mL of SBF (achieving a "fluid-volume:sample-surface" ratio of 0.12 $mL \cdot mm^{-2}$). The samples' containers were then submerged in a water–filled, sealable, insulated container that was heated to a constant temperature of 36.5 °C (±0.4 °C) by means of an appropriate regulating circuit to imitate human body temperature during the process of corrosion. Here, an immersion heater (Titanium Heizer 50 W) was connected to a universal thermostat (Universal-Thermostat "UT 200"). In order to establish a certain flow of the corrosive medium, the entire experimental set-up was placed on an orbital shaker (GFL3015) that was set to 60 $L \cdot min^{-1}$.

In order to prepare a SBF that contained ions corresponding to the concentration of real body fluid, 700 mL of distilled water were heated to 36.5 °C, and the substances shown in **Table 2** were subsequently added, according to the table's sequence. Using the method of titration, the mixture was set to a pH of 7.4 by adding sodium hydroxide (1.0 mol) at 36.5 °C. A 1 000 mL Pyrex-Glas (to obtain an inert temperature) was then used to cool the mixture to 20 °C while it was filled to 1000 mL by adding distilled water. Owing to the verified high stability and similarity to blood plasma in ion concentrations, the preparation of the SBF was carried out according to Oyane *et al.* [19].

Table 2: Sequence of substances for the SBF

Substance	Mass	Purity[%]
NaCl	5.403 g	>99.5
$NaHCO_3$	0.504 g	>99.5
Na_2CO_3	0.426 g	>99.5
KCl	0.225 g	>99.5
$K_2HPO_4 * 3H_2O$	0.230 g	>99.0
$MgCl_2 * 6H_2O$	0.311 g	>98.0
0.2 M NaOH/HEPES	100 ml / 17.892 g	- / >99.9
$CaCl_2$	0.293 g	>95.0
Na_2SO_4	0.072 g	>99.0

The coated and uncoated specimens were weighed before and after the *in vitro* corrosion procedure using a precision balance (Analytical Balance A204). In order to acquire information about the corrosive medium's pH during the course of the experiments, a measurement was taken each time the coated specimens were removed from the experimental set-up. For each pH measurement, the specimen was removed from the sample container, during which a separate pH-measuring vessel was filled with the corrosive medium. The Winlab Data Line pH Meter was calibrated and rinsed with distilled water thoroughly before each measurement. A SEM 1455 VP with an EDAX Genesis unit and an Axioplan 2 reflecting-light microscope, which incorporates a ProgRes2008 CCD camera, were used to obtain information about the coatings' thickness. To determine the performance of the coatings after deformation, a 3-point bending test was carried out in which the coated samples were bent to 50 % of their prior determined ultimate bending punch displacement via Universal Testing Machine Z250. Subsequently these samples were immersed into SBF and analysed according to the non-bend sample protocol.

Results and Discussion

With and without the intermediate MgF_2 layer, a compact PLA layer could be established on top of the samples. ESEM cross-sectional analyses revealed a PLA layer thickness of 93 µm after dipping the samples into the PLA/DCM solution 2 times. Here, the coating appeared dense and homogeneous. Furthermore, the PLA coating exhibited a porous segment on its top (**Figure 1** (left)). This porous segment showed a thickness of 6.5 µm, and

the pores revealed a top opening with diameters of 1 µm to 1.5 µm (**Figure 1** (right)).

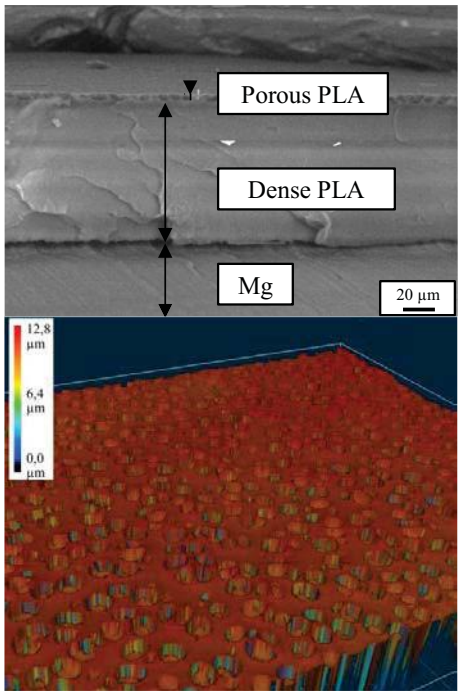


Figure 1: (Top) Cross-sectional SEM image of the PLA coated specimen; (Bottom) 3D-microscopical image of the top PLA layer

As displayed in **Table 3**, SBF immersion testing resulted in an insignificant loss in mass after an overall duration of 30 days for both of the differently prepared sample groups. Compared with the results of Seitz *et al.* [11] the corrosion properties could be significantly optimized by means of an additional PLA layer. In the prior study, samples with a MgF_2 coating demonstrated a mass loss of 80 % after 20 days of immersion in SBF. Within this study, mass loss could be clearly reduced to 7 % after 30 days by attaching an additional PLA layer. Furthermore, the PLA-only coating resulted in a loss in mass of 7 % after 30 days as well. The pH, however, remained stable within the 30 days of immersion and was not being heavily influenced by the release of corrosion products as in Seitz *et al.* [11], which investigated pure and MgF_2 coated LANd442.

Table 3: Mass loss and SBF pH value of the corroded samples (n=3)

Group	Mass loss 15 days	p	Mass loss 30 days	p
LANd442 + PLA	0 %	7.6	7 %	7.8
LANd442 + MgF_2 + PLA	7 %	7.7	7 %	7.7

Optical analyses of the corroded samples revealed an induced blister formation under the PLA top layer in the case of the PLA-only coated samples (**Figure 2**). These blisters resulted most likely from the Mg corrosion process in which hydrogen gas is formed (**Table 1** eq. 1). Since blistering appears significantly stronger in the PLA-only coated state, the intermediate MgF_2 layer seems to potentially block the interaction of the PLA and the base material and therefore improves the system's corrosion properties. The risk of a delaminating of the PLA due to induced blistering is clearly lowered. Nonetheless, the corrosion rate seems not to be affected by the existence of the intermediate MgF_2 layer, at least in the first 30 days of corrosion.

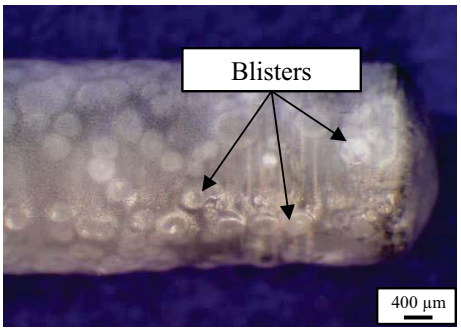


Figure 2: PLA only coated sample after 30 days of corrosion in SBF (sample diameter = 2.5 mm)

To validate the coating toughness and its corrosion protection abilities after plastic deformation, coated and bent samples were immersed into SBF as well. Bending was carried out until the outer PLA layer clearly showed damaging (50 % of the alloy's ultimate bending punch displacement). The pH and mass loss were determined for both coating systems after 15 and 30 days of immersion (**Table 4**). After bending and cracking the coatings at the same time, the PLA only coated samples show an increased mass loss when compared to the MgF_2 and PLA coated samples while corroding. Due to corrosion, the pH is initially slightly increased before the SBF's buffer takes effect.

Table 4: Mass loss and SBF pH value of the bend and corroded samples (n=3)

Group	Mass loss 15 days	p	Mass loss 30 days	p
LANd442 + PLA	5 %	8.0	13 %	7.7
LANd442 + MgF_2 + PLA	2.5 %	7.7	7 %	7.7

The damaged PLA surface of a bent sample is displayed in **Figure 3**. Here, it becomes obvious that the pure or MgF_2 coated base material, in either case, are directly exposed to the corrosive environment. Due to the crackled surface structure of the Mg, the formation of $Mg(OH)_2$ and MgO is expected. Here, damaging of the PLA layer was determined after high plastic deformation only. An MgF_2 layer is known to be brittle; it loses its integrity after low deformation ratios as shown by Seitz *et al.* [12]. In its combinations, the PLA appeared to prevent the MgF_2 from flaking off the sample's surface, thereby, in case of the PLA's fracturing; the MgF_2 layer could actively act as a second corrosion barrier.

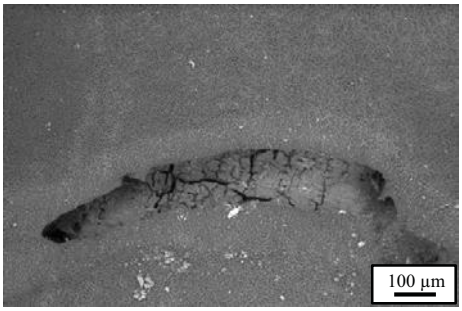


Figure 3: Damaged PLA layer (due to bending) of a MgF_2 and PLA coated sample after 30 days of corrosion in SBF

Conclusions

The results made within this study prove that the combination of MgF_2 and PLA form a good coating system to prevent magnesium from rapidly corroding. While both coatings reduce the Mg's corrosion speed, their combination added advantages regarding longevity and toughness. MgF_2 as an intermediate layer prevented the PLA and the Mg from catalyzing each other's corrosion processes. Only at high plastic deformation ratios did the PLA break open, and in this case the intermediate MgF_2 layer became an active corrosion barrier.

Acknowledgements

All work carried out for this study was done within the Collaborative Research Centre 599 "Sustainable bioresorbable and permanent implants of metallic and ceramic materials" Subproject R1, which was funded by the German Research Foundation (DFG).

References

[1] Peuster M, Beerbaum P, Bach F, Hauser H. Are resorbable implants about to become a reality? Cardiology in the Young 2006; 16(02):107–16.

[2] Thomann M, Krause C, Bormann D, Höh N von der, Windhagen H, Meyer-Lindenberg A. Comparison of the resorbable magnesium alloys LAE442 und MgCa0.8 concerning their mechanical properties, their progress of degradation and the bone-implant-contact after 12 months implantation duration in a rabbit model. Materialwissenschaft und Werkstofftechnik 2009; 40(1-2):82–7.

[3] Krause A, Höh N, Bormann D, Krause C, Bach F, Windhagen H et al. Degradation behaviour and mechanical properties of magnesium implants in rabbit tibiae. J Mater Sci 2010; 45(3):624-632.

[4] Zhang S, Li J, Song Y, Zhao C, Zhang X, Xie C et al. In vitro degradation, hemolysis and MC3T3-E1 cell adhesion of biodegradable Mg–Zn alloy. Materials Science and Engineering: C 2009; 29(6):1907–12.

[5] Huang J, Ren Y, Jiang Y, Zhang B, Yang K. In vivo study of degradable magnesium and magnesium alloy as bone implant. Front. Mater. Sci. China 2007; 1(4):405-409.

[6] Zheng Y, Wu J, Ng JC, Wang G, Lian W. The absorption and excretion of fluoride and arsenic in humans. Toxicology Letters 2002; 133(1):77–82.

[7] F. W. Bach, T. Hassel, C. Krause, P. Wilk, in Magnesium Technol. 2005 (Eds: H. I. Kaplan, B. R. Powell, N. R. Neelameggham), TMS, Warrendale, USA 2005, p. 485.

[8] M. Thomann, C. Krause, N. Angrisani, D. Bormann, T. Hassel, H. Windhagen, A. Meyer-Lindenberg, J. Biomed. Mater. Res. Part A 2010, 93A, 1609.

[9] C. Krause, D. Bormann, T. Hassel, F. W. Bach, H. Windhagen, A. Krause, A. Meyer-Lindenberg, in Magnesium Technol. Global Age 2006 (Eds: M. O. Pekguleryuz, L. W. F. Mackenzie), CIM, Montreal, Canada 2006, p. 329.

[10] Pereda MD, Alonso C, Burgos-Asperilla L, del Valle JA, Ruano OA, Perez P et al. Corrosion inhibition of powder metallurgy Mg by fluoride treatments. The THERMEC'2009 Biodegradable Metals 2010; 6(5):1772–82.

[11] Seitz J, Collier K, Wulf E, Bormann D, Bach F. Comparison of the Corrosion Behavior of Coated and Uncoated Magnesium Alloys in an In Vitro Corrosion Environment. Adv. Eng. Mater. 2011; 13(9):B313.

[12] Seitz J, Eifler R, Stahl J, Kietzmann M, Bach F. Characterization of MgNd2 alloy for potential applications in bioresorbable implantable devices. Acta Biomaterialia 2012; 8(10):3852–64.

[13] Ying Chen and Yang Song and Shaoxiang Zhang and Jianan Li and Changli Zhao and Xiaonong Zhang. Interaction between a high purity magnesium surface and PCL and PLA coatings during dynamic degradation. Biomedical Materials 2011; 6(2):25005.

[14] Xu L, Yamamoto A. Characteristics and cytocompatibility of biodegradable polymer film on magnesium by spin coating. Colloids and Surfaces B: Biointerfaces 2012; 93(0):67–74.

[15] Witte F, Hort N, Vogt C, Cohen S, Kainer KU, Willumeit R et al. Degradable biomaterials based on magnesium corrosion. Current Opinion in Solid State and Materials Science 2008; 12(5–6):63–72.

[16] ASTM, B275-05: Standard Practice for Codification of Certain Nonferrous Metals and Alloys, Cast and Wrought.

[17] Witte F, Kaese V, Haferkamp H, Switzer E, Meyer-Lindenberg A, Wirth CJ et al. In vivo corrosion of four magnesium alloys and the associated bone response. Biomaterials 2005; 26(17):3557–63.

[18] Witte F, Fischer J, Nellesen J, Crostack H, Kaese V, Pisch A et al. In vitro and in vivo corrosion measurements of magnesium alloys. Biomaterials 2006; 27(7):1013–8.

[19] Oyane A, Onuma K, Ito A, Kim H, Kokubo T, Nakamura T. Formation and growth of clusters in conventional and new kinds of simulated body fluids. J. Biomed. Mater. Res. 2003; 64(2):339–48.

Magnesium Technology 2014
Edited by: Martyn Alderman, Michele V. Manuel, Norbert Hort, and Neale R. Neelameggham
TMS (The Minerals, Metals & Materials Society), 2014

IMPROVEMENT OF CYTOCOMPATIBILITY OF MAGNESIUM ALLOY ZM21 BY SURFACE MODIFICATION

Agnieszka Witecka[1,2], Akiko Yamamoto[1], Wojciech Swieszkowski[2]
[1]Biometals Group, International Center for Materials Nanoarchitectonics (MANA), National Institute for Materials Science (NIMS), Tsukuba, Ibaraki 305-0044, Japan
[2]Faculty of Materials Science and Engineering, Warsaw University of Technology, 141 Woloska Street, 02-507 Warsaw, Poland

Keywords: biodegradable metal, ZM21, cytocompatibility, silane-coupling, PLLA

Abstract

Application of a biodegradable polymer coating is one of the methods to improve the initial corrosion resistance and cytocompatibility of magnesium (Mg) alloys. However, bulging of the coating film during long term immersion has been reported. Therefore, improvement of interface strength between the coating and the substrate surface is a key for the success of this method. Combination of surface modification [silanization with 3-(glycidyloxypropyl) triethoxysilane (GPTES)] and biodegradable polymer coating [poly-L-lactide (PLLA)] were applied to a Mg-2.0Zn-0.98Mn (ZM21) cast alloy.
Results of a cell proliferation assay show that PLLA and GPTES+PLLA coating successfully improved cell growth during 7 days of incubation and suppressed Mg^{2+} release after 4 days of incubation. The silanization process had no impact on suppression of corrosion. Calcification was observed on all samples after 1 week of incubation with calcification medium, but the calcified area was much larger on the GPTES+PLLA coated sample than on the uncoated sample.

Introduction

Recently, Mg and its alloys have been investigated as biodegradable metallic materials for biomedical applications. Because of their excellent mechanical properties close to that of human bone[1], biocompatibility[1, 2] and biodegradability[3, 4], Mg is recognized as an almost perfect candidate for temporary bone implants. However, Mg and its alloys have relatively high bio-corrosion rates, especially at the early stage of implantation in the human body. These high corrosion rates cause formation of gas bubbles in the tissue surrounding the implanted samples due to hydrogen generation. Additionally, corrosion reaction of the samples also generates OH^-, which increases the pH of the fluid around the Mg sample surface. This increase in pH influences surrounding cellular functions, decreases cytocompatibility, and even causes inflammation or necrosis[1, 5]. For biomedical applications of Mg and its alloys, their degradation rates should ideally match the rate of healing. For this purpose, their initial corrosion resistance and cytocompatibility must be improved. Song and colleagues explored corrosion rates of several Mg alloys in Hanks solution, finally concluding that elements such as Ca, Mn, and Zn could be suitable alloying elements for biomedical Mg alloys[5]. Zn and Mn are both essential elements for human body; Mg-Mn-Zn alloys, which gradually degrade in bone tissue, have good biocompatibility both in vitro and in vivo[6]. One method to supress biodegradation of Mg alloys at the early stage of implantation in human body is application of a biodegradable polymer coating. An additional advantage of this method is that, in the case of biodegradable polymers such as poly (L-lactic acid) [7, 8] and poly (ε-caprolactone)[7], the coating degrades in the human body over time.
In industrial applications, organic coatings for Mg alloys are used to improve their corrosion resistance or mechanical properties[9]. For better understanding of the protective behavior of a biodegradable polymer coating, it is important to achieve the preparation of a good quality, uniform and nonporous film. This can be done by spin coating, which involves depositing a polymer solution onto a solid substrate, and afterwards spinning the substrate at a high speed. Because of rotation, the solvent evaporates and the polymer forms a homogenous and non-porous coating on the substrate. However, with longer immersion time, bulging of the coating film is observed[10]. To improve the strength of the interface between the Mg substrate and the biodegradable polymer coating, silanization is employed before the polymer coating. Silanes are silicon-containing chemical compounds possessing a hydrolytically sensitive centre which is able to react with inorganic substrates, forming covalent bonds. They also possess an organic substitution, which can be used to easily change the surface physicochemical properties of the substrates, such as hydrophobicity[11].
In the present study, silanization was employed to improve the interface strength between the Mg substrate and the biodegradable polymer, and effects of silanization on cell proliferation and substrate degradation were investigated.

Materials and Methods

Sample Preparation

We used a cast Mg alloy with main alloying elements of 2.0 wt% Zn and 0.98 wt% Mn, abbreviated as ZM21 (ZFW gGmbH, Clausthal) as a substrate. Its slabs were cut into a dimension of 10 x 5 x 1.5 mm. Then, the samples were polished with SiC grinding paper (14 μm) damped with 99.9% ethanol and then separately, ultrasonically cleaned with acetone for 15 min. Prepared surfaces were modified with silane 3-(glycidyloxypropyl) triethoxysilane (GPTES; Wako Pure Chemical Industries, Ltd., Osaka, Japan) and then coated with a biodegradable polymer, poly-L-lactide (PLLA, Mw 300 000, Polysciences, Inc. USA). GPTES was spin-coated on both sides of the sample (7000 rpm, 60s). Then, silane was reacted with substrate by incubation at 100 °C for 1 h in a Teflon vessel. Excess silane molecules were removed by ultrasonic treatment for 15 min in absolute ethanol. Then, 2% (w/v) PLLA chloroform solution was spin-coated on both sides of the samples (7500 rpm, 60s). This sample is referred to as GPTES+PLLA. For comparison, unmodified samples (castZM21), samples with silane coating alone (GPTES), and those with only polymer coating

(PLLA) were prepared. For cell culture tests, these samples were sterilized with ethylene oxide gas (EOG).

Polymer Film Characterization

PLLA film morphology was observed using an optical microscope (Axiotech 100, Carl Zeiss AG, Germany) and a low voltage scanning electron microscope (FE-SEM, Hitachi SU8000). Polymer film thickness was measured by a stylus surface profiler (Dektak 6M, ULVAC, Japan) for a sample whose polymer film is partially removed. At least 3 samples were tested for each kind of polymer film. For these purposes, mirror-like polished samples were prepared with a diamond past (1/4 μm).

Water Contact Angle

Wettability of the sample surface was measured by a contact angle meter (DM 700, Kyowa Interface Science Co. Ltd, Japan), observing the shape of a distilled water droplet in static condition. Measurements were repeated 3 times for each sample. For every measurement, 21 readings were taken with an interval of 1000 ms at room temperature.

Cell Proliferation

Human osteosarcoma cell line (SaOS-2) was used for the cell proliferation assay testing castZM21, GPTES+PLLA, GPTES and PLLA samples. Each sample was placed into a deep glass dish. SaOS-2 were inoculated at a density of 4 000 cells ml^{-1} in 27.5 ml of culture medium [Dulbecco's Modified Eagle Minimum Essential Medium supplemented with 10% (v/v) fetal bovine serum, abbreviated as D-MEM+10%FBS]. Then, cells were incubated under standard cell culture condition (37 °C, 5% CO_2) for 1, 4 and 7 days. After a certain incubation period, viable cell number was estimated by WST-1 assay. Briefly, the sample and 1 ml of the supernatant were transferred into a well of a 24-well microplate. Another 1 ml portion of the supernatant was transferred to another well as a blank. Aliquots of the supernatant were collected for quantification of released Mg^{2+}. Then, a 110 μl portion of the mixture of WST-1 and 1-methoxy PMS in Dulbecco's phosphate buffered saline [PBS (-)] was added. After 4h of incubation, the absorbance of the supernatant was measured at 450 nm by a Multiskan FC Microplate Photometer (Thermo Scientific, USA). The relative viability of cells (RVC) was calculated as following equation;

$$RVC = (A_s - A_b)/S_0$$

where A_s and A_b are the absorbance of the supernatant in the sample and blank wells, respectively, and S_0 is the top surface area of the samples. Next, the samples were fixed with 25% glutaraldehyde solution for 10 min and stained by 10% (v/v) Giemsa's staining solution for 15 min. Air-dried samples were observed using an optical microscope, and digital images were recorded by a CCD camera (DS-5M, Nikon Co. Ltd, Tokyo, Japan). Cell culture experiments were performed in triplicate.

Calcification

To investigate the effect of surface modification on cell functionalization, a calcification assay was carried out for all types of samples. On a sample in a glass deep dish, SaOS-2 were inoculated at a density of 10 000 cells ml^{-1} in 27.5 ml of D-MEM+10% FBS and incubated for 7 days. Then, the culture medium was exchanged into calcification medium, consisting of D-MEM+10%FBS with 0.5 mM β-glycerophosphate, 50μg/mL L-ascorbic acid, and 1% (v/v) antibiotic solution [penicillin (5000IU/mL) and streptomycin (5000 μg/mL)]. Cells were incubated for 7 and 14 days while the calcification medium was exchanged in every 7 days. At the designated time, cells were fixed with Mildform 10 NM (ca. 4% formaldehyde in phosphate buffer containing 10% of methanol) for 20 min and stained with 0.5% (w/v) Alizarin Red S staining solution for 3 min. Air-dried samples were observed using an optical microscope and digital images were recorded by a CCD camera.

pH Measurement

CastZM21, GPTES, PLLA and GPTES+PLLA samples were sterilized by EOG, separately placed in glass deep dishes, and immersed in 27.5 ml of D-MEM+10% FBS in a CO_2 incubator for 24h to monitor the pH of the medium. The distance between the pH electrode and the specimen surface was kept at 1 mm.

Quantification of Mg^{2+}

The degradation of the substrate during the cell proliferation assay was examined by the quantification of the released Mg^{2+} ions. Portions of the supernatant from each of the deep dishes were collected after 1, 4 and 7 days of incubation. The quantification of released Mg^{2+} ions was performed using the Magnesium B test Wako (Wako Pure Chemical Industries, Ltd, Osaka, Japan) by following the instruction supplied with the kit except the preparation of the calibration curve of Mg^{2+}, which was performed with D-MEM+10%FBS instead of water.

Results

Polymer Film Characterization

After the polymer spin-coating process, PLLA and GPTES+PLLA sample surfaces were investigated by optical microscopy. However, no crystalline structure was observed on the transparent polymer film. SEM observation showed a smooth and flat surface without any pores. The polymer film thickness is about 0.2 μm.

Water Contact Angle

The water contact angle was measured shortly after sample preparation. Obtained data shown in Figure 1 illustrates the influence of surface modification on wettability. The angles for castZM21, GPTES and PLLA samples are approximately 62º, 60º and 75º, respectively. The PLLA coating decreases hydrophilicity down to the level favourable for cell proliferation[12], but silanization increases hydrophilicity slightly. The values were stable with time, except at the beginning of the measurements for the castZM21 sample.

pH Changes

Table I lists the pH of D-MEM+10%FBS with castZM21, GPTES, PLLA or GPTES+PLLA sample in a CO_2 incubator. The pH values of the medium with and without a sample tended to decrease due to the dissolution of CO_2 into the medium and dissociation to be HCO_3^- for buffering, which occurred in the first

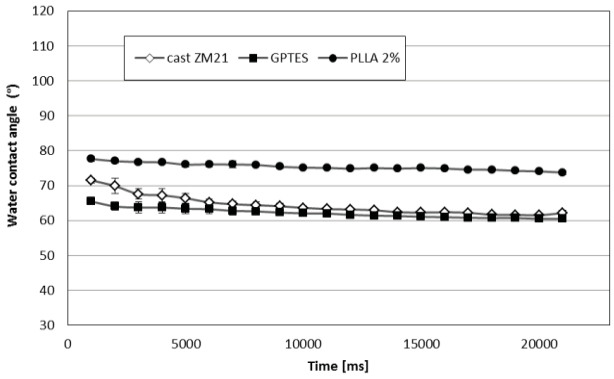


Figure 1. Time evolution of water contact angles of castZM21, GPTES, PLLA and GPTES+PLLA samples.

Table I. The pH of the D-MEM+10%FBS for castZM21, GPTES, PLLA.

	pH				
	Medium	**castZM21**	**GPTES**	**PLLA**	**GPTES+PLLA**
1h	8.49	8.60	8.25	8.54	8.48
4h	7.86	7.97	7.56	7.90	7.87
24h	7.02	7.76	7.43	7.60	7.15

hours of the measurements. After 24h, the pH value was the lowest in the medium without a sample. For medium with a castZM21 sample, decrease of pH was noticeably slower than in the medium with a PLLA, GPTES, or GPTES+PLLA sample.

Cell Viability

Results of the WST-1 assay for castZM21, GPTES, PLLA and GPTES+ PLLA samples are shown in Figure 2. There was no significant difference among samples after 1 day of incubation. On day 4, a slight increase in the number of cells was observed for PLLA and GPTES+PLLA samples. However, no statistically significant difference can be found ($p>0.05$). After 7 days of incubation, it becomes to be clear that the PLLA and GPTES+PLLA coating successfully improved cell growth comparing to castZM21 and GPTES; this effect is more visible for GPTES+PLLA. Moreover, on day 7, statistically significant increase in cytocompatibility can be found ($p\leq0.001$), both between castZM21 - GPTES+PLLA and GPTES - GPTES+PLLA samples.

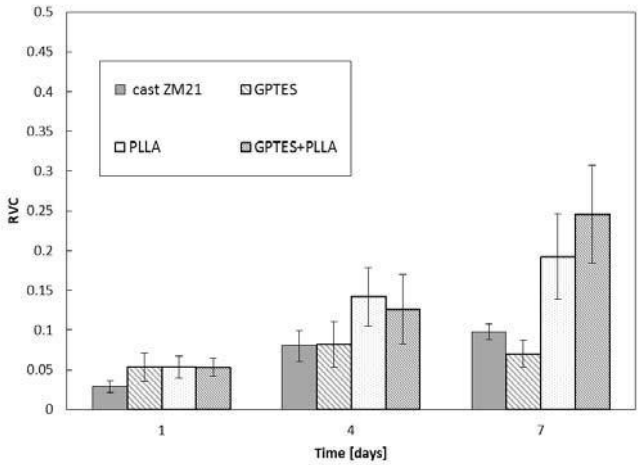


Figure 2. Proliferation of SaOS-2 cells on cast ZM21 substrate without/with silane, polymer, silane and polymer.

Cell Morphology

Optical microscopic images of castZM21, GPTES, PLLA and GPTES+PLLA samples after cell culture for 1 and 7 days are shown in Figure 3, indicating different responses of the cells to different samples. After 7 days, almost no cells were found on castZM21 and GPTES samples. For PLLA and GPTES+PLLA, elongated and spread cells were observed, but more cells are visible for GPTES+PLLA. The microstructure of the castZM21 substrate is observed after 1, 4 and 7 days of incubation (photos not shown). White corrosion products were observed on castZM21 and GPTES surfaces. In comparison with these samples, some part of the substrate underneath the polymer coating kept metallic gloss for PLLA and GPTES+PLLA samples. Other parts became black and were recognized as corroded area. White corrosion products were also observed underneath the polymer film. However, after 7 days of incubation, no polymer detachment was observed for PLLA and GPTES+PLLA samples.

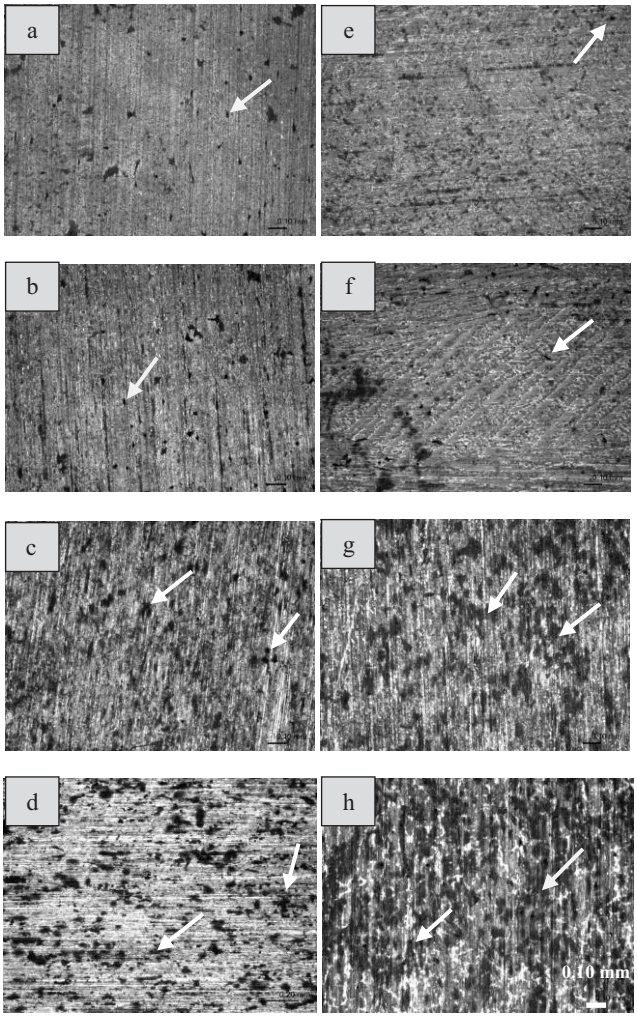


Figure 3. Typical cell morphology after incubation (indicated by white arrows) for 1 day on a) castZM21, b) GPTES, c) PLLA, d) GPTES+PLLA and 7 days on e) castZM21, f) GPTES, g) PLLA, h) GPTES+PLLA.

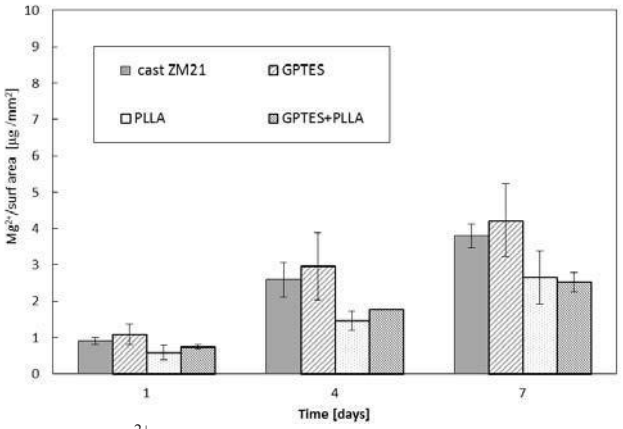


Figure 4. Mg^{2+} release for castZM21, GPTES, PLLA and GPTES+PLLA.

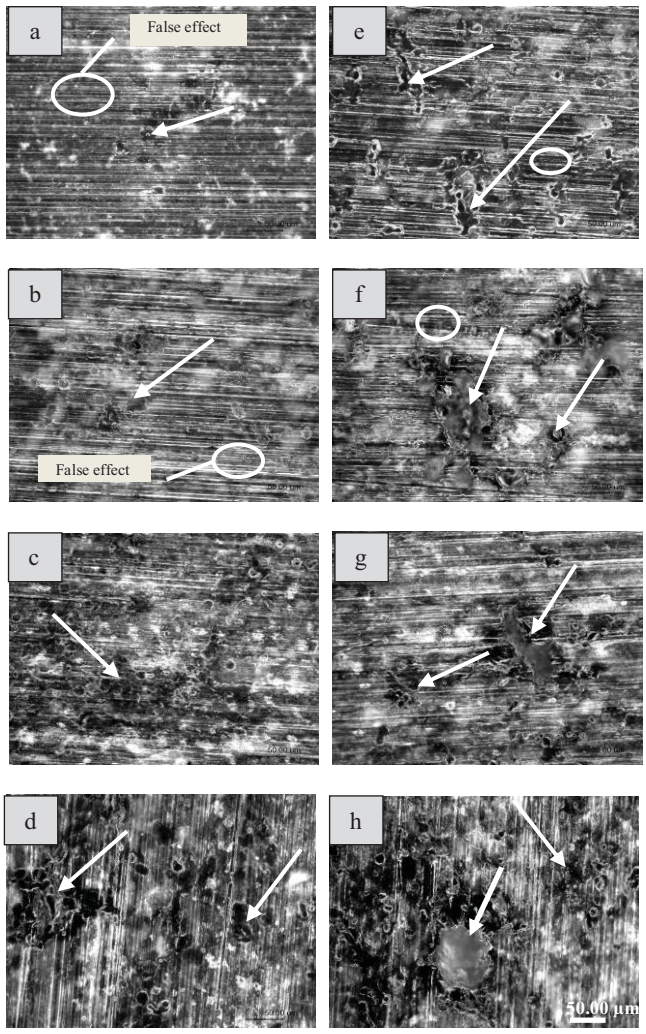


Figure 5. Typical morphology of calcified areas (indicated by white arrows) for 1 week on a) castZM21, b) GPTES, c) PLLA, d) GPTES+PLLA, and 2 weeks on e) castZM21, f) GPTES, g) PLLA, h) GPTES+PLLA.

Mg^{2+} Release

Mg^{2+} release from the samples during cell culture is presented in Figure 4. Ion release was observed even after 1 day of incubation for all samples, however, no statistically significant difference can be found ($p>0.05$). Along the incubation period, the amount of released Mg^{2+} increased for all samples. The lowest value was observed for PLLA, followed by GPTES+PLLA, castZM21, and GPTES. Statistically significant difference ($p<0.05$) was noticed between GPTES and PLLA on day 4, and between GPTES – PLLA and GPTES – GPTES+PLLA on day 7.

Cell Functionalization

The calcification process was examined on castZM21, GPTES, PLLA and GPTES+PLLA samples for 1 and 2 weeks of incubation with the calcification medium. It is difficult to see actual colours of the samples in a gray-scale, so they are marked in Figure 5. Pink and reddish color on castZM21 and GPTES samples indicates mostly false reaction of Alizarin Red S staining with corrosion products on the surface (circled in white). However, dark purple areas marked on Figure 5 for 1 week and brownish regions, mostly observed for 2 weeks, indicate calcified areas (white arrows). Notably, a much larger calcified area was observed on PLLA and GPTES+PLLA samples than on castZM21 and GPTES samples.

Discussion

Microscopic observation of the PLLA sample before cell culture clearly shows that spin-coated PLLA film is smooth, flat and without pores. Previous studies report poor adhesion, even film bulging, between polymer coatings and Mg substrate [10, 13], which may reduce device efficiency[13, 14]. Xu et al. mentioned the bulging of PCL film prepared on pure Mg substrate after 7 days' immersion in D-MEM+10%FBS[15]. However, this effect was not observed for low and high molecular weight PLLA (50 000 and 80 000-100 000, respectively) film prepared by spin-coating at 5 000 rpm resulting in the thickness of 0.34 and 0.97 µm, respectively[15]. In this study, PLLA coating film was prepared with higher molecular weight PLLA (300 000) by spin-coating at 7 000 rpm, generating a film of 0.2 µm thickness. No bulging was observed during 7 days of incubation in DMEM+10%FBS and an additional 7 or 14 days of incubation in the calcification medium. It is necessary to measure the adhesion strength between the polymer film and the Mg substrate for accurate determination of the strengthening effect of GPTES.

Mg^{2+} release during 1, 4 and 7 days of incubation clearly shows that surface modification influences the ZM21 substrate degradation under the cell culture condition. Silanization with GPTES increased Mg^{2+} release, but PLLA and GPTES+PLLA suppressed Mg^{2+} release from 1 day of incubation. However, PLLA has a slightly better protective effect than GPTES+PLLA in 1 and 4 days of incubation. This result suggests that PLLA film somewhat suppresses substrate corrosion, but GPTES may accelerate substrate corrosion. The PLLA film with 0.2 µm in thickness cannot stop the water molecules penetrating into and reacting with the ZM21 substrate. This reaction releases hydrogen, which diffuses through the polymer film. GPTES layer prepared on the ZM21 substrate surface causes a slight, but definite, reduction in the water contact angle at the beginning of the measurement, as shown in Figure 1. This result indicates a slightly increased affinity for water molecules, which might facilitate the

water-substrate reaction at the beginning of immersion into the culture medium and influence localized microcorrosion under the PLLA coating. When we compare Figure 3c and d, which show typical PLLA and GPTES+PLLA sample surfaces after 1 day of incubation in the culture medium, metallic gloss underneath the polymer film is more noticeable for GPTES+PLLA as well as black areas recognized as corroded area. For PLLA, substrate corrosion seems to be more uniform. This difference is also observed after 7 days of incubation in the culture medium. For further characterization of substrate corrosion, SEM observation of substrate surface following the removal of the polymer film is necessary and will be performed in the near future.

Attachment of anchorage dependant cells is a first step in the process of cell-material interactions. Surface physicochemical properties such as hydrophilicity and surface charge are well known to influence cell-material interaction. Hydrophilicity of samples can be easily changed by surface modification. Witecka and colleagues increased water contact angle of cast AZ91 alloy by silanization with 5 different silanes from approximately 30° to 54–100°[16]. In this study, applied surface modification also influences surface hydrophilicity. As already mentioned, GPTES slightly decreases water contact angle of castZM21 from approximately 62° to 60°. PLLA coating decreases hydrophilicity to 75°, which is favourable for cell proliferation[12]. Also pH values in Table I revealed that the medium above PLLA and GPTES+PLLA samples during the initial 24h of immersion has lower pH than that above castZM21, which is attributed to the protective effect of the polymer coating. Xu and colleagues reported that initial pH of the medium directly influences the cell survival, and the number of living cells in the initial stage is associated to the later cell growth[10]. Results of the cell proliferation assay for SaOS-2 after 1 day of incubation indicated slight differences in cell viability. During 7 days of incubation, PLLA and GPTES+PLLA coating successfully improved cell growth. However, the improvement of cytocompatibility is more visible for GPTES+PLLA samples. Surfaces of castZM21 and GPTES seem to suppress cell growth. Besides decreasing hydrophilicity, PLLA and GPTES+PLLA provide necessary conditions for cell attachment and growth. As other corrosion protective coatings, PLLA acts as a barrier and reduces water diffusion rate [17]. As already mentioned, it suppresses the corrosion of castZM21 substrate and may decrease the diffusion rate of OH^- from the substrate to the medium. However, GPTES+PLLA samples had slightly higher Mg^{2+} release than PLLA in the early stage of incubation, indicating more visible improvement of cytocompatibility. Probably, released Mg^{2+} can somehow encourage cell growth since Mg^{2+}, which is an essential element for human, has various physiological functions relating to the cellular energy metabolism as well as bone tissue metabolism.

The next stage in biocompatible studies is to investigate the effect of surface modification on cell functionalization. After 1 week of incubation in the calcification medium, SaOS-2 cells exhibit osteblastic differentiation. In Figure 5, calcified areas are observed after 1 week of calcification but become more viable after 2 weeks of calcification. This result can be correlated with that of cell proliferation assay. PLLA and GPTES+PLLA samples with higher cell growth in cell proliferation assay had larger calcified area than GPTES and castZM21. This suggests that better cytocompatibility in the initial stage of incubation supports better cell functionalization in the later stage of incubation. For quantification of relative osteogenic activity on the unmodified and modified samples, measurement of alkaline phosphatase (ALP) activity will be performed in near future.

Conclusions

Cast ZM21 magnesium alloy surface was modified by silane followed by the coating with a biodegradable polymer. Water contact angle measurements suggest that the silanization slightly changed the surface hydrophilicity, but the biodegradable polymer coating decreased hydrophilicity to a level known to be favourable for cell proliferation. Cell culture experiments show that, among the samples tested, GPTES+PLLA was the best at improving cell growth during 7 days of incubation, followed by PLLA. Surface modification reduced the Mg^{2+} release for PLLA and GPTES+PLLA samples. The silanization process has no impact on corrosion suppression, but may improve of cell viability for GPTES+PLLA.

Acknowledgements

This work was supported by the European Regional Development Fund within the Innovative Operational Programme in the frame of project BIO-IMPLANT (GRANT No. POIG.01.01.02-00-022/09).

References

1. M. Staiger et al., “Magnesium and its alloys as ortopedic biomaterials: a review”, *Biomaterials* 27 (2006) 1728-1734
2. M. Maguire and J. Cowan, “Magnesium chemistry and biochemistry”, *Biomaterials* 15 (2002) 203-210
3. F. Witte et al., “In vivo corrosion of four magnesium alloys and the associated bone response”, *Biomaterials* 26 (2005) 3557-3563
4. L. Xu et al., “In vivo corrosion behavor of Mg-Mn-Zn alloy for bone implant application”, *Journal of Biomedical Materials Research Part A* 83 (2007) 703-711
5. G. Song, “Control of biodegradation of biocompatible magnesium alloys”, *Corrosion Science* 49 (2007) 1696-1701
6. L. Xu et al., “In vitro corrosion behaviour of Mg alloys in phosphate buffered solution for bone implant application”, *Journal of Materials Science: Materials in Medicine*, 19 (2008) 1017-1025
7. Y. Chen et al., “Interaction between a high purity magnesium surface and PCL and PLA coatings during dynamic degradation” *Biomedical Materials* 6 (2011) 025005
8. J.E Gray-Munro, C. Seguin and M. Strong, “Influence of surface modification on the in vitro corrosion rate of magnesium alloy AZ91”, *Journal of Biomedical Materials Research Part A* 91(2009) 221-230
9. J. Gray and B. Luan, “Protective coatings on magnesium and its alloys- a critical review” *Journal of Alloys and Compounds* 336 (2002) 88-113
10. L. Xu and A. Yamamoto, “Characteristics of cytocompatibility of biodegradable polymer film on magnesium by spin coating”, *Colloids and Surfaces B: Biointerfaces* 93 (2012)67-74
11. T. Ishizaki and M. Sakamoto, “Facile formation of biomimetic color-tuned superhydrophobic magnesium alloy with corrosion resistance” *Langumir* 27 (6) (2011), 2375-2381
12. Y. Tamada and Y. Ikada, “Cell adhesion to plasma-treated polymer surfaces”, *Polymer* 34 (10) (1993) 2208- 2212
13. M. Burke et al., “Estimation of the strength of adhesion between a thermoresponsive polymer coating and nitinol wire” *Journal of Materials Science: Materials in Medicine* 19 (2008) 1971-1979

14. M. Li et al., “Indentation deformation and fracture of thin polystyrene films”, Thin Solid Films 416 (2002) 174-183.
15. L. Xu and A. Yamamoto, “In vitro degradation of biodegradable polymer-coated magnesium under cell culture conditions”, *Applied Surface Science* 258 (2012) 6353-6358
16. A. Witecka, et al., “Surface characterization and cytocompatibility evaluation of silanized magnesium alloy AZ91 for biomedical applications”, *Science Technology of Advanced Materials* 13 (2012) 064214
17. J. Gray and B. Luan, “Protective coatings on magnesium and its alloys-a critical review”, *Journal of Alloys and Compounds* 336 (2002) 88-113.

Magnesium Technology 2014
Edited by: Martyn Alderman, Michele V. Manuel, Norbert Hort, and Neale R. Neelameggham
TMS (The Minerals, Metals & Materials Society), 2014

CYTOCOMPATIBILITY OF Mg ALLOYS AND THE EFFECT OF CELLS ON THEIR DEGRADATION IN BIOLOGICAL ENVIRONMENT

Akiko Yamamoto and Yuko Kohyama
Biomaterials Unit, International Center for Materials Nanoarchitectonics (WPI-MANA), National Institute for Materials Science (NIMS), 1-1 Namiki, Tsukuba, Ibaraki 305-0044, Japan

Keywords: Biodegradable metals, Biocompatibility, Biocorrosion, AZ-system Mg alloys

Abstract

Biomedical application of magnesium and its alloys are highly anticipated since their corrosion reaction with water can be utilized as degradability inside the human body. Degradation ratio of Mg alloys severely influences not only their mechanical integrity along the implantation period but also their biocompatibility since toxicological reaction of surrounding tissue depends on the amount and kind of released metal ions. In this study, pure Mg and AZ-system Mg alloys were employed for cytocompatibility evaluation and the effect of cells on the degradation of the metal specimens during cell culture was also examined. Cells could grow on pure Mg and low-Al content alloy but not on high-Al content alloys even though they release less Mg^{2+} ions than low-Al content alloy. Higher Mg^{2+} ion release was observed from the specimens with good cell growth.

Introduction

Magnesium (Mg) and its alloys were first applied to orthopedic implants in early 20's century[1-3], but recent attempts on stent application[4-6] open a new stage as a biodegradable metal. However, available biocompatibility data of Mg and its alloys is limited. Clinical trial of vascular stent has been carried out[6, 7], but no commercial device is currently available. Regarding the bone fixture application, no clinical research has been curried out so far.

As the process for commercialization of biodegradable Mg alloy devices, it is mandatory to perform biological safety evaluation. However, available standards such as ISO 10993 series are mainly considering biodegradable polymeric/ceramic materials or non-degradable metallic materials, and not appropriate for the evaluation of Mg and its alloys. For the success of commercialization of biodegradable Mg alloy devices, appropriate cytocompatibility testing condition is important to help screening the biocompatibility of developed Mg alloys in vitro, which saves cost and testing periods comparing to those in vivo.

Since Mg generates H_2 and OH^- along the progress of its corrosion reaction with water, the pH of the fluid around Mg surface will increase, which may affect surrounding cellular and tissue function. In the case of in vivo condition, however, blood flow reaches to the every part of the body and contributes to maintain the neutral pH of the body fluid. In vitro condition, on the other hand, cells are cultured under the atmosphere of 5% CO_2 in humid air at 37 °C without any medium flow or supply. In general cell culture condition, for example, only a 0.5-1 mL portion of culture medium is supplied into one well of 24-well microplate, which has about 1.9 cm^2 of cell culturing area[8].

The amount of the culture medium supplied during cell culture strongly influences its pH change as well as degradation profile of the Mg alloy sample employed in cell culture. It is predictable that these factors significantly influence the cellular function and viability during the cell culture. Cytocompatibility evaluation performed using the condition far from that in vivo is irrelevant and inappropriate as the biocompatibility evaluation to estimate that the material is applicable as a certain kind of biodegradable device.

In this study, a new cultural condition is applied for cytocompatibility test of Mg alloys, considering the in vivo situation inside the body. The amount of a culture medium is set as 1/100 of blood plasma in an adult human, which may suppresses the pH increase of the medium along the Mg sample corrosion. With this condition, cell growth on pure Mg is achieved, which enables to discuss the effect of the presence of cells on the degradation behavior of Mg substrates. As model substrates, Mg-Al-Zn alloys are employed to demonstrate the difference in their cytocompatibility can be detected by this cultural condition. Mg-Al-Zn alloys are widely used in industries and commercially available. Furthermore, their corrosion resistance is known to be improved by the increase in Al content.

Materials and Methods

Sample Preparation

The materials used are extruded bars of pure Mg (pMg), Mg-3wt.%Al-1wt.%Zn (AZ31), Mg-6wt.%Al-1wt.%Zn (AZ61), and Mg-8wt.%Al-0.5wt.%Zn (AZ80) alloys. Their chemical compositions are shown in Table I. Average grain sizes are 60, 20, 30, 30 μm, respectively in the order of Al content from the lowest. The disks of 9.5 mm in diameter and 2 mm in thickness were prepared for AZ31 and AZ61, and the plates of 8 × 9 mm and 2 mm in thickness were prepared for pMg and AZ80. The differences in the total surface area of these samples are about 5%. For all alloys, the top surface is a cross section to the extrusion direction. Every surface of these specimens was polished with #600 (14 μm) SiC paper in ethanol. The size and the weight of each sample were measured prior to use, and then, the sample was ultrasonically washed and sterilized with acetone for 5 min.

Water contact angle (WCA) of a sample surface was measured by a contact angle meter (DM 700, Kyowa Interface Science Co. Ltd, Japan). Measurements were repeated 3 times for each sample with a droplet of a 1 μL portion of ultrapure water in a static condition. For every measurement, 21 readings were taken with an interval of 1000 ms at room temperature.

Cell Proliferation and Immersion

A sample was placed into a glass deep dish, and murine fibroblast

Table I. Chemical Compositions of pMg and Mg-Al alloys (wt.%)

	Al	Zn	Mn	Fn	Si	Cu	Ni	Mg
pMg	0.003	0.008	0.004	0.003	0.005	<0.001	<0.001	Bal.
AZ31	2.7	0.9	0.4	0.002	0.021	<0.001	<0.001	Bal.
AZ61	6.0	0.7	0.3	0.003	0.022	<0.001	<0.001	Bal.
AZ80	8.2	0.5	0.2	<0.001	0.004	<0.001	<0.001	Bal.

L929 was inoculated at a density of 1,000 cells/mL in 27.5 mL of Eagle's minimum essential medium supplemented with 10 % (v/v) of fetal bovine serum (E-MEM+FBS). Then, the cells were incubated under cell culture condition (37 °C, 5% CO_2) for 1, 4 and 7 days. As a control, a sample immersed into E-MEM+FBS without seeding cells was prepared. No medium exchange was performed up to 7 days of incubation.

After the incubation of the applied period, a 1 mL portion of the supernatant was transferred into a well of the 24-well microplate. Another portion is collected for the quantification of released Mg^{2+} ions. A 110 μL portion of the mixed solution of 1mM WST-1 and 0.2 mM 1-methoxy-5-methylphenazinium methyl-sulfate (1-methoxy PMS) in phosphate buffered saline [PBS(-)] was added into each of the wells. A sample was transferred to the well from the deep dish. Then, the microplate was placed into a CO_2 incubator for additional 4 h, and the absorbance of the supernatant was measured at 450 nm by a microplate reader (Multiskan FC, Thermo Scientific, USA). The relative viability of cells (RVC) was calculated by a following equation;

$$\mathrm{RVC} = A_s/S_s - A_c/S_c$$

where A_s and A_c are the absorbance of the supernatant in the sample and control wells, respectively. S_s and S_c are the total surface areas of the samples with and without cells, respectively.

Then, the samples incubated with cells were fixed with 25% glutaraldehyde solution for 10 min and stained by 10% (v/v) Giemsa's staining solution for 15 min. Air-dried samples were observed using an optical microscope (Axiotech 100, Carl Zeiss AG, Germany), and digital images were recorded by a CCD camera (DS-5M, Nikon Co. Ltd, Tokyo, Japan). Cell culture and control experiments were performed in triplicate.

Quantification of Released Mg^{2+} Ions

Quantification of the Mg^{2+} ions in the collected portions of E-MEM+FBS during the cell culture/immersion was performed by a colorimetric method using xylidyl blue-I [9, 10], which is applied for the measurement of magnesium in serum [11]. The kit, "Magnesium B-test Wako" (Wako Chemicals, Tokyo, Japan), presenting a one-reagent mixture containing 0.1 mM of xylidyl blue-I [1-azo-2-hydroxy-3- (2,4-dimethylcarboxyanilido) naphthalene-1-(2-hydroxybenzene-5-sulfonate], 0.045 mM of EGTA [ethylene glycol bis (2-amino-ethylether)-N,N'-tetraacetic acid], and non-ionic surfactant Triton X-100, is employed. The calibration curve was prepared by adding 5–50 μgMg/mL of $MgSO_4 \cdot 7H_2O$ to E-MEM+FBS. After mixing the aliquot of the collected E-MEM+FBS to the colorimetric reagent at the ratio of 1:150, the absorbance at 620 nm was measured. Then, the concentration of the Mg^{2+} was calculated using the calibration curve. Three replicates were prepared for each collected portion and standard solution for the calibration.

EDX Analysis

After the immersion into E-MEM+FBS as a control experiment for WST-1 assay, each sample was collected and dried under nitrogen flow to observe their surface by optical and electron microscopes. The surface of some of the sample was analyzed by energy dispersive X-ray spectroscopy (EDX) equipped to the scanning electron microscope (Hitachi S-4800). For every kind of samples, at least 6 analysis data for a viewing area of 62.4 × 43.9 μm^2 at 10 kV were averaged.

Table II. Composition of Artificial Plasma

Salt	NaCl	$NaHCO_3$	KCl	Na_2HPO_4
Concentration (g/L)	6.8	2.2	0.4	0.126
Salt	NaH_2PO_4	$MgSO_4$	$CaCl_2$	
Concentration (g/L)	0.026	0.1	0.2	

Protein Adsorption

Protein adsorption behavior onto the sample surface was examined for albumin and fibronectin, the former is the most popular protein in the serum and the latter is the one of the cell adhesive proteins encouraging fibroblast adhesion onto the material surface. Each sample was placed into a well of 24-well microplate and immersed into a 500 μL portion of a protein solution: 20 μg/mL of bovine serum albumin or 30 μg/mL of bovine fibronectin in artificial plasma, which composition is shown in Table II[12]. Another portion of the protein solution, which was increased by the same volume of the sample, was poured into the new well of the microplate as a control. After placing the microplate in a CO_2 incubator for 3h, three portions of supernatant in 150 μL each were collected from each well to quantify protein concentration using a protein assay kit (Coomassie Plus Assay Kit, Pierce Biotechnology, USA) following the instruction supplied with the kit. The amount of adsorbed protein (A_{abs}) was calculated as follows;

$$A_{abs} = (C_c - C_s)\, V / (S_t + S_l)$$

where C_c and C_s are the protein concentration of the supernatant of the control and sample wells, respectively. V indicates the volume of the protein solution. S_t and S_l indicate the top and lateral surface areas of the sample, respectively. The experiment was performed in triplicate.

Results

Static Water Contact Angle

WCAs at 21 sec after putting a water droplet on the sample surfaces were shown in Table III. AZ31 has a lower WCA around 40˚ than other three materials around 60˚.

Cell Proliferation Assay

The examples of the microscopic images of the samples after 7d of cell culture are shown in Figure 1. Cells spread and grew in number were observed on pMg and AZ31 whereas cells were hardly observed on AZ61 and AZ80. As shown in Figure 2, the result of WST-1 assay indicates the good cell growth on pMg and AZ31 along the increase of the incubation period, while almost no growth was observed on AZ61 and AZ80.

Mg^{2+} Release during the Cell Culture/Immersion

The result of Mg^{2+} quantification in the culture medium after a certain period of incubation with cells was shown in Figure 3. The highest Mg^{2+} release after the 7d of incubation was observed from pMg, followed by AZ31, AZ61, and AZ80 in the order, which corresponds to the order of the cell growth after 7d of culture.

Table III. Water contact angle (WCA) in static condition (mean±s.d.).

Material	pMg	AZ31	AZ61	AZ80
WCA (˚)	61.7±7.6	40.6±7.7	60.6±7.6	61.6±1.8

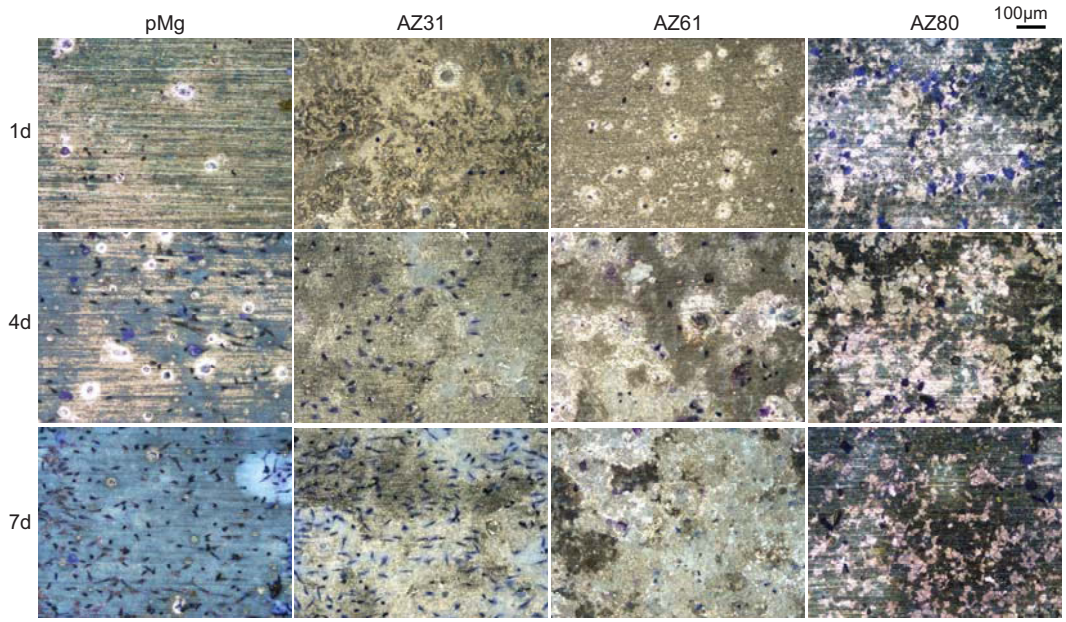


Figure 1. Microscopic images of the samples after 7d of incubation with L929 cells.

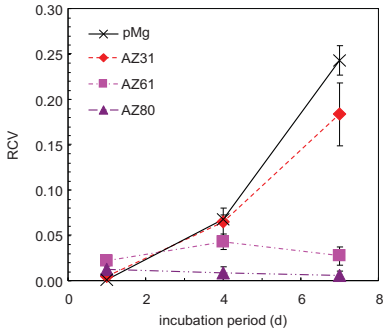


Figure 2. WST-1 assay results of pMg, AZ31, AZ61 and AZ80 with L929 cells(mean±s.d.).

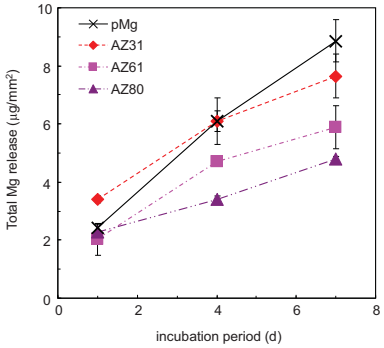


Figure 3. Mg^{2+} release from pMg, AZ31, AZ61, and AZ80 during cell culture upto 7 d (mean±s.d.).

Figure 4 shows the Mg^{2+} release profiles from the pMg and AZ31 samples with and without cells during the incubation upto 7d. For both materials, the samples incubated with cells tended to release Mg^{2+} slightly higher than those from the samples immersed without cells. For AZ61 and AZ80, Mg^{2+} release from the samples with or without cells was similar to each other (data not shown) since almost no cell growth was observed on these samples.

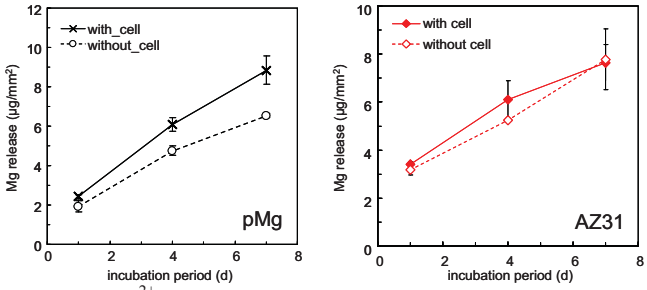


Figure 4. Mg^{2+} release from pMg and AZ31 with and without cells during the incubation upto 7 d (mean±s.d.).

EDX Analysis after Immersion

The EDX analysis data of pMg, AZ31, and AZ61 samples immersed into the culture medium without cells are shown in Table IV. For all kind of materials, the atomic concentrations of Mg tended to decrease with the increase of immersed period. AZ61 tended to have lower O concentration at the surface than pMg or AZ31 in the early stage of immersion. After 7 d of immersion, O concentrations of these material surfaces reached to

Table IV. Atomic concentration (%) of the elements at the sample surfaces immersed into culture medium (mean±s.d.).

	d	C	O	Mg	Al	P	Ca
	1	17.3±8.9	51.8±9.3	22.7±5.8	-	3.1±1.4	2.1±0.7
pMg	4	16.1±3.5	65.3±2.5	11.1±0.8	-	3.3±1.1	1.5±0.6
	7	17.5±3.5	62.8±2.2	14.0±3.8	-	3.9±1.5	1.3±0.6
	1	9.0±2.7	61.3±2.9	13.5±2.0	2.1±0.2	7.7±0.6	4.2±0.8
AZ31	4	18.2±7.7	57.0±7.4	9.2±3.2	1.4±0.4	6.6±2.5	4.1±1.9
	7	14.3±3.8	60.7±4.2	8.4±1.7	1.6±0.4	8.0±0.6	5.3±0.8
	1	11.2±4.0	47.7±7.3	24.6±6.6	3.8±0.5	5.8±1.5	2.8±1.4
AZ61	4	19.3±8.6	48.9±8.3	13.1±9.6	2.8±0.8	6.1±1.8	4.1±1.4
	7	10.3±3.8	63.7±1.1	9.0±1.4	4.1±0.6	7.4±0.5	4.0±0.1
	1	14.0±4.9	63.0±3.0	9.5±3.2	4.8±0.7	3.0±1.3	1.2±0.3
AZ80	4	22.6±6.8	59.9±4.9	7.5±1.3	3.8±1.0	3.2±0.8	1.2±0.3
	7	18.7±4.4	63.1±3.3	9.5±3.0	2.9±1.5	2.8±1.3	1.0±0.5

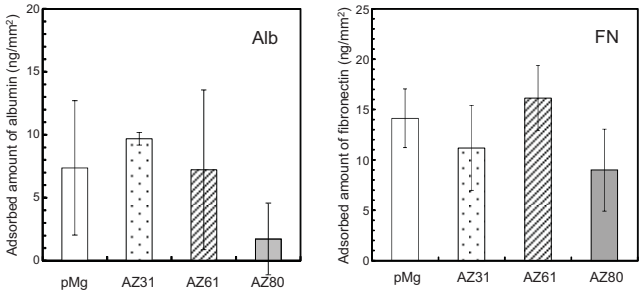


Figure 5. Adsorbed amount of protein onto pMg, AZ31, AZ61 and AZ80 surfaces after 3h of immersion(mean±s.d.).

a similar level around 60 %. A few to several % of Ca and P was observed at all the surfaces tested, however their concentrations tended to be higher at the surface of AZ31 or AZ61 than that of pMg. Al concentration at the surface increased with the increase of Al content in the alloy.

Albumin and Fibronectin Adsorption

Adsorbed amounts of albumin and fibronectin onto sample surfaces are shown in Figure 5. AZ31 has the highest adsorption of albumin, followed by AZ61, pMg, and AZ80. For fibronectin, AZ61 has the highest adsorption, followed by pMg, AZ31 and AZ80.

Discussions

In the present study, a new condition is applied for the cell culture of Mg alloys and succeeded to evaluate their cytocompatibility by the direct contact method. The amount of the medium used for cell culture is 27.5 mL, which is 1/100 of the total amount of blood plasma in an adult human (ca. 2.75L). Increase in the amount of the medium enables to maintain its neutral pH, which contributes to cell survival in the early stage of incubation when the sample corrosion rate is relatively high. In the cell culture condition employed in the present study, the pH value of the medium above a pMg sample was 7.72 after 24 h of incubation, which is lower than that of general culture condition in a 24-well microplate (>8.3). Ideally, the culture medium of 2.75L is preferable to simulate the condition of an implantation into a human body, however it has a limit from the practical reason. In the condition employed in this study, the differences in cytocompatibility among the materials used were easily detected. The amount of the medium can be variable against the sample surface area, and this simple change in the cultural condition makes it possible to perform cytocompatibility evaluation of Mg alloys in direct contact method.

Direct cell culture on sample surface enables to perform various experiments with cells to collect valuable and interesting information about cell-material interaction. In the present study, Mg^{2+} release from pMg was compared between the conditions with and without cells, resulting in slightly higher release with cells. The mechanism of the acceleration effect of cells on substrate corrosion requires further studies to be elucidated, however this culture condition with direct contact of cells to sample surface is one of the closest condition available in vitro which simulates the implantation condition in vivo. It will contribute to estimate precise degradation rate of Mg and its alloy samples as well as to understand their degradation mechanism in the implantation condition.

In the present study, Mg-Al-Zn alloys are employed as model samples to demonstrate the difference in their cytocompatibility. There is a debate on use of Al-containing alloys as implant materials due to the susceptibility of Al as a cause of Alzheimer disease, which still does not have a clear scientific relevance[13]. Fundamentally, the use of an alloy containing a specific metallic element as an implant material should be discussed with consideration of its exposure to the humans. Al is a commonly existing element especially in soil, therefore the daily uptake via drinking water, food, and table wares is relatively high as 6.9 mg/day for an average adult Japanese[14]. A typical absorption rate of Al is about 1%[14], giving 69 μg of Al is absorbed every day. Absorbed Al is mainly excreted into urine as 20-50 μg/day[15]. When we suppose to implant a coronary stent made of AZ91 which weighs 15 mg and degrades in 6 months, for example, the total amount of Al implanted is 1.35 mg, releasing 7.4 μg/day. For another example, when we suppose a mini-microplate system made of AZ91 which weighs 60 mg and degrades in 1 year, the total amount of Al implanted is 5.4 mg, releasing 14.8 μg/day. These values are smaller than those of average daily absorbance of Al in Japan, suggesting a possibility to use Al-containing Mg alloys for these applications from the view point of exposure estimation. Obviously, further studies in biocompatibility evalution is required to reach the final decision of applying Mg-Al-Zn alloys for implant application, and the cytocompatibility evaluation is one of them.

Mg-Al-Zn alloys are one of the widely used and commercially available Mg alloy systems due to their improved mechanical properties and corrosion resistance comparing to those of pMg. Increase in Al content improves corrosion resistance in buffered 5% NaCl solution[16]. In this study, AZ31, AZ61, and AZ80 alloys and pMg were immersed into cell culture medium with cells. As shown in Figure 3, Mg^{2+} release from these AZ-system alloys decreased with the increase in Al content of the alloy, which agrees with the above mentioned trend in NaCl solution. However, the growth of L929 cells on theses alloy samples decreased with the increase in Al content as shown in Figure 2. These data suggest that the suppression of cell growth on high-Al-content alloy is not due to the corrosion reaction and accompanying ion release into the culture medium, which is predominantly considerable as a possible cause which influences cell growth.

Protein adsorption is the first phenomenon occurs on the material surface when it is implanted inside the human body. It is well known that the kind, amount and conformation of adsorbed protein controls following cell attachment onto material surface and its function such as proliferation, motility, differentiation, etc. Fibronectin is one of the popular cell adhesive proteins and known to control cellular function of fibroblasts and osteoblasts[17, 18]. Good correlation is reported between the fibronectin adsorption amount and MC3T3-E1 osteoblasts attachment onto plasma-treated polymer surfaces[19].

Relationship between the wettability (WCA) and protein adsorption behavior has been examined by many researchers. Absorption of bovine serum albumin from its PBS(-) solution onto various polymer surfaces is maximum at the WCA around 70˚[20]. Adsorption of bovine plasma fibronectin from its PBS(-) solution is minimum at the WCA around 40˚[19]. In the present study, protein adsorption onto pMg, AZ31, and AZ61 has a similar tendency to those described above; pMg and AZ61, which have the WCAs around 60˚, have higher albumin adsorption and lower fibronectin adsorption than those of AZ31, which has the WCA around 40˚. The tendency of fibronectin adsorption onto

pMg and AZ31 corresponds to the cell growth after 7d incubation. However, the protein adsorption onto AZ80, which also has the WCA around 60˚, is the lowest for both albumin and fibronectin. Based on these data, it is found that cell growth inhibition on AZ61 and AZ80 could not be simply explained by the protein adsorption behavior onto these surfaces. It is also noticed that protein adsorption is not simply controlled by the surface wettability, and other properties such as surface charge and chemical structures are considerable to be influential, too. Therefore, further experiments are necessary on the surface properties of Mg-Al-Zn alloys to understand protein adsorption behavior on them.

EDX analysis of the samples surfaces after cell culture, shown in Table III, illustrates corrosion progress at the sample surface as the increase in O and decrease in Mg concentrations along the incubation period. Based on the obtained EDX data, corrosion rate is the highest on pMg, followed by AZ31 and AZ61. This trend agrees with the results of Mg^{2+} release during cell culture (Figure 3.) Ca and P concentartions at AZ31 and AZ61 surfaces were slightly higher than those of pMg, but it does not seem to correlate with the protein adsorption behavior nor cytocompatibility.

Regarding the relationship between cell adhesion/growth on materials surface and wettability, it is reported that the adhesion and growth of murine fibroblast L cells is maximum at the WCA about 70˚[20]. In the present study, L929 growth after 7 d of incubation is the highest on pMg, followed by AZ31. Concerning these two materials, pMg has the WCA around 60˚ and higher fibronectin adsorption than AZ31, which has the WCA around 40˚. This trend corresponds well to the one above mentioned. On the other hand, suppression of cell growth on other two materials, AZ61 and AZ80, could not be explained by the protein adsorption behavior and wettability. Higher Al concentration at the surface, which is confirmed by the EDX analysis of the sample surface after cell culture, is supposed to be related, but further investigation is necessary to elucidate actual cause and its mechanism to suppress cell growth on high-Al-content Mg alloys.

Summary

In the present study, a new cultural condition was applied to the cytocompatibility evaluation of Mg-Al-Zn alloys in direct contact method, which successfully detected the difference in the cytocompatibility of these samples. Cell growth after 7 d of incubation was the highest on pMg followed by AZ31, whereas almost no cell growth was observed on AZ61 and AZ80. Mg^{2+} release during cell culture was the lowest for AZ80, followed by AZ61, AZ31, and pMg in the order, suggesting that corrosion reaction is not the main cause of low cytocompatibility of AZ61 and AZ80. Protein adsorption analysis revealed that pMg has higher fibronectin adsorption than AZ31, which corresponds well to cell growth after 7-d. Fibronectin adsorption onto AZ61 and AZ80 were similar to that of pMg or AZ31, respectively, suggesting that protein adsorption behavior could not simply explain the low cytocompatibility of high-Al-content Mg alloys. This new cultural condition, which enables to culture cells directly contacting on Mg and its alloy sample surfaces, also revealed the accelerating effect of cells on sample degradation. Cell growth on the sample surface simulates the in vivo implantation condition, therefore this condition will contribute to the precise estimation of degradation rate of Mg alloy samples as well as the understanding of degradation mechanism in implantation condition.

References

1. G.B. Stroganov, et al. “Magnesium-Base Alloy for Use in Bone Surgery”, US Patent 3,687,135 (1972).
2. E.D. McBride, “Absorbable Metal in Bone Surgery”, *J. Am. Med. Assoc.* 111 (1938) 2464-2467.
3. C.P. McCord, “Chemical Gas Gangrene from Metallic Magnesium”, *Ind. Med.* 11 (1942) 71-76.
4. B. Heublein et al. “Biocorrosion of Magnesium Alloys: a New Principle in Cardiovascular Implant Technology?”, *Heart* 89 (2003) 651-656.
5. C. Di Mario et al., “Drug-Eluting Bioabsorbable magnesiu Stent”, *J. Interv. Cardiol.* 17 (2004) 391-395.
6. P. Peeters et al., “Preliminary Results after Application of Absorbable Metal Stents in Patients with Critical Limb Ischemia”, *J. Endovasc. Ther.*12 (2005) 1-5.
7. R. Erbel et al., “Temporary Scaffolding of Coronary Arteries with Bioabsorbable Magnesium Stents: a Prospective, Non-Randomized Multicentre Trial”, *Lancet* 369 (2007) 1869-1875.
8. BD Biosciences Discovery Labware, Customer Technical Data Sheet - Multiwell Plates – 24 Well, document no. LSR00003, version 4.0 (available online at http://www.bdbiosciences.com/external_files/dl/doc/tds/live/web_enabled/tds_LSR00003.pdf)
9. H. Watanabe and H. Tanaka, “Dual-Wavelength Spectrophotometric Determination of Magnesium(II) with Xylidyl Blue I and Nonionic Surfactant” *Bunseki Kagaku* 26 (1977) 635-639 (in Japanese).
10. C.K. Mann and J.H. Yoe, “Spectrophotometric Determination of Magnesium with Sodium 1-Azo-2-hydroxy-3-(2,4-dimethylcarboxanilido)-naphthalene-1’-(2-hydroxybenzene-5-sulfonate)”, *Anal. Chem.* 28 (1956) 202-205.
11. D. Ratge, K.P. Kohse, and H. Wisser, “Measurement of Magnesium in Serum and Urine by Use of a Modified Xylidyl Blue-1 Procedure”, *Clin. Chim. Acta* 159 (1986) 197-203.
12. ISO10993-15:2000, “Biological Evaluation of Medical Devices-Part 15: Identification and Quantification of Degradation Products from Metals and Alloys”, Annex C.
13. WHO, *The International Programme on chemical Safety, Environmental Health Criteria*, No.194, (1997)11-12.
14. T.Sakurai, *Seimei genso jiten* (Tokyo: Ohmsha Ltd., 2006) 139-142 (in Japanese).
15. A. Eshima, “Aluminum” in *Toxicology Today* (H. Sato ed., Kyoto: Kimpodo Inc.1994)15-26(In Japanese).
16. H. Kita, M. Kimoto, and T. Kudo, “Influence of Al Content on Corrosion Resistance of Mg-Al-Zn Alloys in Chloride Environments”, *J. Japan Inst. Metals*, 69(9) (2005) 805-809.
17. M. Hayashi, *The world of cell adhesion molecules*, (Tokyo, Japan, Youdo-sha; 1995, in Japanese).
18. R.O. Hynes, “Fibronectins”, *Sci Am* 254(1986)32–41.
19. J. Wei et al., “Influence of surface wettability on competitive protein adsorption and initial attachment of osteoblasts”, *Biomed. Mater.* 4(2009)045002.
20. Y. Ikada. “Biological response to the materials for artificial organs”, *Kagaku-to-Seibutsu*, 28(8) (1990)522-529 (in Japanese).

Magnesium Technology 2014

Alloy Design

Magnesium Technology 2014
Edited by: Martyn Alderman, Michele V. Manuel, Norbert Hort, and Neale R. Neelameggham
TMS (The Minerals, Metals & Materials Society), 2014

In-Situ Neutron Diffraction Study of Aging in Alloy ZK60A

Sean R. Agnew[1], Christopher A. Calhoun[1], and Bjørn Clausen[2]

[1] Department of Materials Science and Engineering, University of Virginia, Charlottesville, Virginia, 22904, USA
[2] Lujan Center, LANSCE, Los Alamos National Laboratory, Los Alamos, NM, 87454, USA

Keywords: internal stress, precipitation, twinning, diffraction

Abstract

The effect of c-axis rod-shaped precipitates on the individual deformation mechanisms of extruded magnesium alloy, ZK60A, are examined using in-situ tension and compression testing of solutionized, under-aged, peak-aged, and over-aged material. The results reemphasize that alloy ZK60A exhibits only a modest aging response. The yield stress is slightly increased during compression testing, however, the flow stress plateau associated with deformation twinning is actually enhanced. This suggests that precipitation simultaneously increases the stress required to initiate significant twinning, while retaining the ease with which the twin volume fraction can increase. The previously published load relaxation associated with tensile twinning is confirmed conclusively by this in-situ study.

Introduction

The fact that Mg alloys have only modest strength (even on a specific or per weight basis) relative to competing materials has stymied broader application of this promising material system. Potential users may wonder why they should struggle with high material costs and potential problems with corrosion resistance and flammability, when the specific strength is not better than high strength aluminium alloys. Only when component shape permits the design engineer to take great advantage of the potential associated with the low density itself do wrought Mg alloys really make sense. For example, alloy ZK60A has been broadly applied as forged race car wheels.

As highlighted by Clark [1] and more recently by Nie [2], magnesium alloys exhibit rather paltry age hardening performance, relative to competing materials, such as aluminium alloys. The reason for this difference is now theoretically understood in terms of (i) low number densities of precipitates [1, 3] which result from conventional aging treatments and (ii) relatively ineffective precipitate shapes for blocking slip of the controlling slip systems [1-4]. The purpose of the present study was to provide an experimental validation of the latter concept.

Experimental Procedure

Alloy ZK60A was received in the T5 temper as a thick (~ 61 mm) extruded plate. The nominal composition in wt. % is 4.8-6.2 Zn, 0.45 min. Zr, and balance Mg. The age hardening behavior was confirmed by microhardness testing (Vickers, 1 kg load, 15 sec) in the as-received (T5), solution heat treated at 400ºC for 1.5 hrs and water quenched (T3), and aged for various times at 175ºC. The microstructure was examined optically after solution heat treatment using conventional mechanical polishing and an acetal-picral etchant. The crystallographic texture was also measured in the as-received condition using x-ray diffraction within an X'Pert Pro MPD equipped with an open Eulerian cradle, point focus oriented sealed tube source, crossed (1 x 2 mm) incident slits, and parallel plate collimation for the receiving slits. Four sample conditions were selected for in-situ neutron diffraction: solutionized and water quenched, under-aged (4 hrs), peak-aged (24 hrs), and over-aged (96 hrs). Tensile and compressive samples were excised from the plate using electro-discharge machining (EDM'ing). The tensile samples have standard ASTM A370 flat sample geometry and 5 mm thickness. The compression samples are right cylinders with 12.5 mm diameter and 27.5 mm length.

The neutron diffraction measurements were performed on the Spectrometer for Materials Research at Temperature and Stress (SMARTS) at the Lujan Neutron Scattering Center, a part of Los Alamos Neutron Science Center (LANSCE), at Los Alamos National Laboratory [5]. The compression sample is horizontally loaded in the custom Instron load frame with a 45° orientation relative to the incident neutron beam (see Fig. 1 of ref. [6]). The compression samples were pre-loaded to approximately -2.5 MPa to keep them in the horizontal grips. An extensometer was attached to the irradiated region to measure the macroscopic strain. Two detector banks are positioned ±90° relative to the incident beam, allowing for collection of diffraction patterns corresponding to lattice strains both parallel (-90°) and perpendicular (+90°) to the applied load. The tests were run in load control until close to yield at which point they were switch to position contol. This is significant because the samples exhibit nearly perfectly plastic behavior upon yielding, which would be impossible to control if held at a constant load. Tensile samples were strained to ~5%, while compression samples were strained to ~11%. The lattice spacings and subsequent internal strain calculations were determined by single peak fits. The internal strains within grains that satisfy the Bragg condition for a given (hkl) reflection are calculated from the difference between the measured and initial lattice spacing:

$$\varepsilon^{hkl} = \frac{d^{hkl} - d_0^{hkl}}{d_0^{hkl}}, \qquad (1)$$

where d^{hkl} is the measured lattice spacing and d_0^{hkl} is the initial stress-free lattice spacing.

Results

Age Hardening Behavior

The material was received in the T5, hot-extruded and artificially age hardened, temper. Rather than perform in-situ tests on as-extruded plus aging, where the presence of a partially recrystallized microstructure could obscure the effects of precipitates that we desire to illuminate, we chose to examine solution heat-treated and aged material. Fig. 1 shows the aging profile and illustrates the level of age hardening which the samples of 2, 24, and 96 hrs aging selected for in-situ testing. Notably, the "overaged" sample has a slightly higher average hardness than the peak aged. Overall, the hardness values are similar to those observed by others [e.g. 3,7] and emphasize that the age hardening response of the system is quite modest.

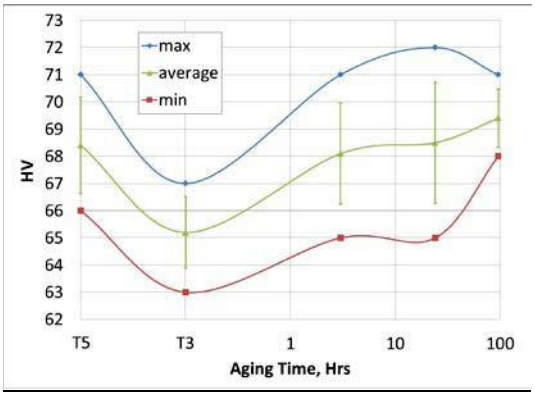


Figure 1: Age hardening response presented as Vickers hardness number versus aging time, including the average, range, and standard deviation of 10 measurements at each time.

Microstructure

Optical metallography (Fig. 2) of the as-received and solution heat treated material reveal a duplex microstructure of large unrecrystallized grains surrounded by finer, recrystallized grains, which is typical of this Zr-bearing alloy. The added Zr helps to refine the microstructure during both the original casting (inoculation) and subsequent hot working processes. The role of the this microstructure on the mechanical properties will be discussed below.

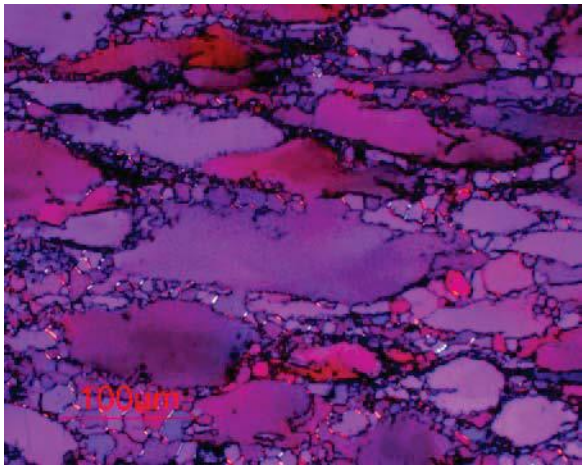


Figure 2: Optical micrograph illustrating the microstructure which results from a solutionizing heat treatment after extrusion.

Texture

In Fig. 3, recalculated (00.2), (10.0), and (10.1) pole figures are presented. These pole figures illustrate two key points. First, this plate shows a <10.0> fiber parallel to the extrusion axis, as is typical of axis-symmetric (i.e. round) extrusions. The texture from the region where the mechanical test samples were excised does not show the strong <00.1> component parallel to plate normal direction. Rather, it is nearly radially symmetric, a texture commonly referred to as the rod texture [8]. Finally, there is a weak <00.1> fiber parallel to the extrusion axis. This is important because it permits determination of the (00.2) lattice spacing prior to the initiation of twinning.

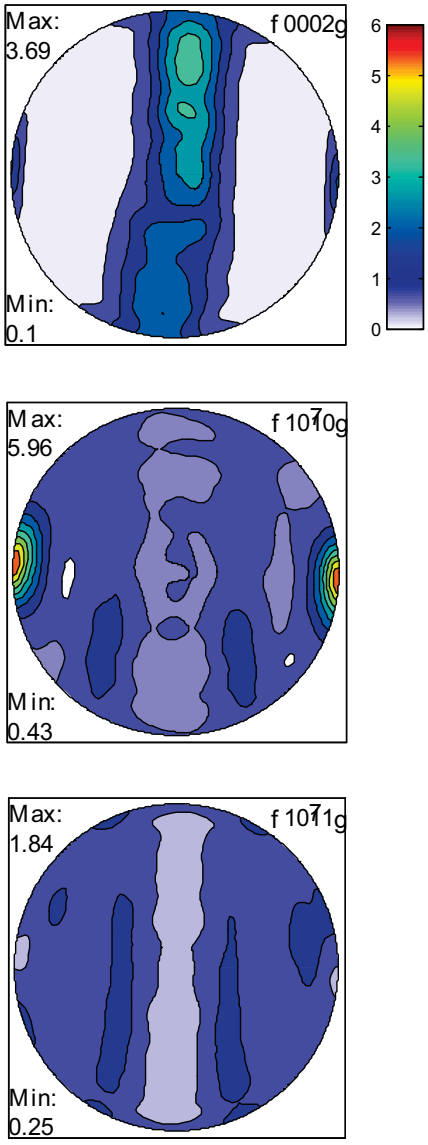


Figure 3: (00.2), (10.0), and (10.1) pole figures of extruded alloy ZK60A showing a prominent <10.0> fiber ‖ extrusion axis (horizontal) and a weak <00.1> fiber with the same orientation.

Mechanical behaviour

A quick comparison of the yield strengths of the four different aging conditions on gross differences between them (Table 1), in agreement with the rather paltry age hardening response revealed by Fig. 1. Robson et al. [4] observed a more dramatic hardening response in alloy Z5 (without Zr) which suggests that the present material benefits significantly from hot-working, as well as precipitation strengthening. That said, there are revealing differences between the shapes of the flow curves which will serve as the focal point for the rest of the paper.

Table 1. Tensile and compressive yield strengths (0.2% offset) in MPa and their ratio, a measure of tension-compression asymmetry

	TYS	CYS	C/T
Solution	213	145	0.68
Under-aged	209	134	0.64
Peak-aged	216	164	0.76
Over-aged	208	143	0.69

The stress-strain curves of the solutionized and quenched samples (Fig. 4a) have little yield point peaks associated with the reloads, especially for the tensile test. This effect is also observed (albeit to a lesser degree) in the under-aged material (not shown in the interest of space). The peak-aged (Fig. 4b) and over-aged (again, not shown in the interest of space) samples do not exhibit this strain-aging type phenomenon. Taken together, these results suggest that the Zn solute atoms produce a potent solute-dislocation interaction, which is reduced, once the solute leaves the matrix to form Mg-Zn precipitates.

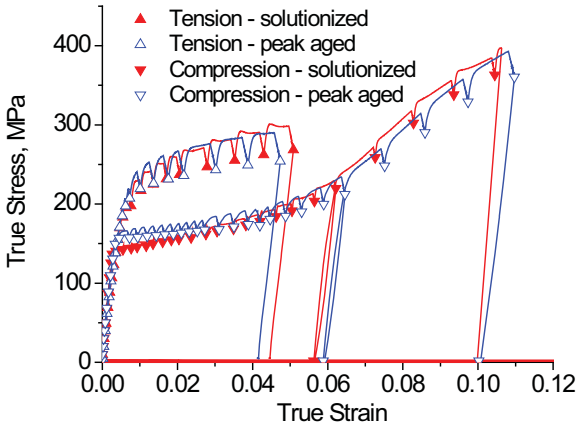


Figure 4: In-situ tension and compression (absolute value of stress and strain) test results for solutionized (filled symbols) and peak-aged (open symbols) ZK60A.

A twinning-induced strain hardening plateau is prominent in the compressive stress-strain curves of all aging conditions, but it is most prominent for the peak aged, where the stress at which the plateau occurs is highest and the hardening rate within the plateau is the lowest (essentially zero). As direct evidence of the fact that {10.2} extension twinning is responsible for the plateau, the evolution in diffracted peak intensity parallel to the compressive stress axis (parallel to the extrusion axis) is presented in Fig. 5a. The intensities are normalized by their initial intensity, which makes the evolution of the (00.2) intensity very strong, since it is initially low (though measureable) along the extrusion axis (see Fig. 3). The (00.2) intensity evolution is even more abrupt in the peak-aged material than in the solutionized. This more rapid intensity evolution correlates with the flatter plateau in the stress-strain behaviour of the peak-aged (Fig. 4b).

The intensity evolution during tensile testing is much less dramatic (Fig. 5b). This is because there is much less {10.2} twinning, although there is a significant decrease in the (00.2) intensity along the tensile axis. This corresponds to twinning within the <00.1> texture component aligned with the extrusion axis (see Fig. 3). Other reflections, like the (10.2) and (10.3) also become weaker due to rotations associated with slip and twinning, respectively.

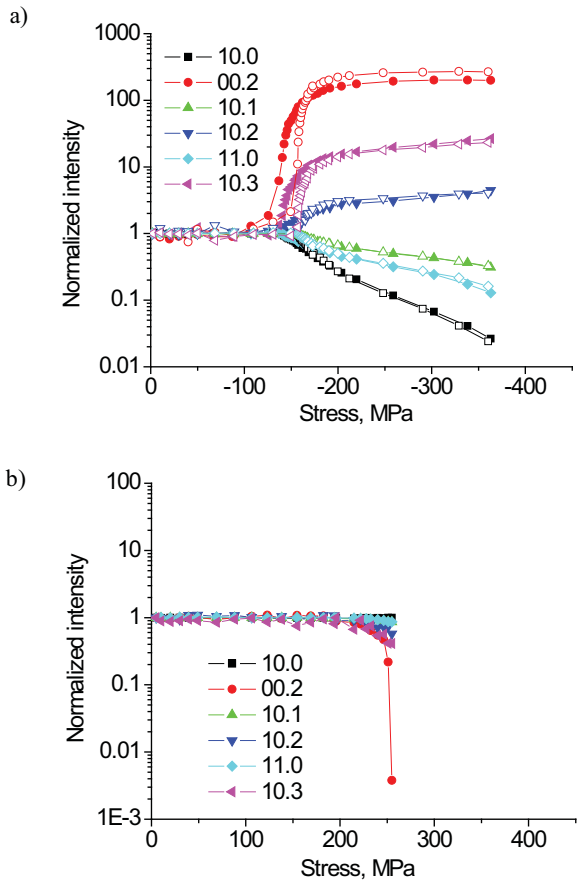


Figure 5: Intensity evolution as a function applied stress during a) compressive and b) tensile straining. The strong changes in (00.2) intensity correspond to {10.2} twinning. Note the more abrupt change for the peak-aged (open symbols) than in the solutionized (filled symbols) during compression and the late appearance of twinning during tensile testing (only solutionized for clarity).

Internal strain evolution during compression

At the risk of being too busy a presentation, Fig. 6 presents the internal strain evolution along the loading axis for both solutionized (solid symbols) and peak aged (open symbols). Until an applied stress of about 75 MPa, all grain orientations develop similar levels of internal strain. Then, the strain development in the (00.2) oriented grains begins to trend in the opposite direction as the surroundings, i.e. an increase applied stress magnitude leads to a decrease in the magnitude of the internal strain.

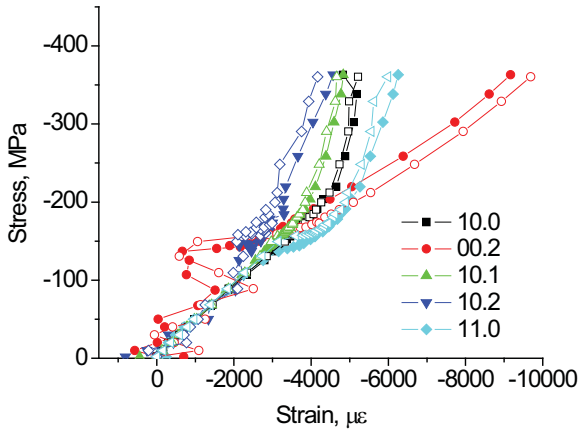


Figure 6: Internal strain evolution within various groups of grains (parsed by their satisfaction of Bragg's law) presented as a function of applied stress during compression testing. The independent axis is vertical for comparison with the stress-strain curves in Fig. 4; the filled symbols are from the solutionized material; and the open symbols are from the peak aged.

Whenever the internal, elastic lattice strain within a class of grains begins to slow, it suggests that those grains are beginning to deform plastically. However, there is no soft plastic deformation mechanism within the (00.2) oriented grains which would explain even a slowing of the internal strain development. The more surprising thing is that these grains are not developing internal strain more slowly, they are actually reversing in their internal strain development. Indeed, between 100 and 150 MPa, the intensity evolution (Fig. 5a) indicates that the volume fraction of material with this crystallographic orientation is strongly increasing and the volume fraction within the (10.0) and (11.0) classes of grains are decreasing. This is strong evidence that the soft deformation mechanism responsible for the strange internal strain evolution is {10.2} deformation twinning mode, which would result in volume transfer from the (10.0) and (11.0) classes into the (00.2) class. Further, it indicates that the reason for the decrease in internal strain is not the relaxation of the grains which had the (00.2) orientation at the beginning of the test. Rather, it is the new material with (00.2) orientation that has been added due to twinning. At this point, it is important to remember that the method determines a sort of volume average of the internal strain within the class of grains. Thus, it must be assumed that the internal strain within the twins themselves actually deviates even more strongly from the aggregate than the value indicates, since the volume fraction of twins is quite low below 100 MPa.

The above transition in internal strain occurs at a higher applied stress level for the peak aged material, in agreement with the higher stress plateau (Fig. 4) and later transition in diffracted intensity (Fig. 5) observed in that material. Once the stress level reaches about 137 MPa in the solutionized and about 150 MPa in the peak-aged, the magnitude of the internal strain in the (00.2) oriented grains begins to rapidly increase with increasing applied stress. Based upon the few samples presently examined, it is cautiously concluded that there is a slight increase in the stress required to twin due to aging.

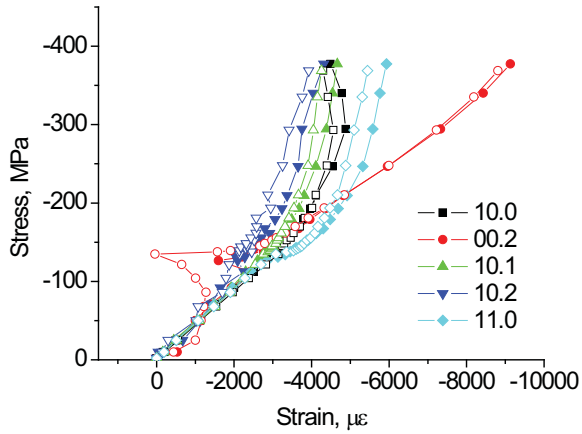


Figure 7: Internal strain evolution as a function of applied stress during compression testing, obtained from the under-aged (filled symbols) and over-aged (open symbols) samples. Note the dramatic relaxation of the (00.2) internal strain and striking level observed at -135 MPa applied stress in the over-aged material.

A similar evolution of internal stain is observed in the under- and over-aged material (Fig. 7), as compared with the solutionized and peak-aged. Noteworthy, in Fig. 7, is the strong and systematic relaxation apparent in the (00.2) oriented grains in the over-aged material. In particular, it is noted that the maximum relaxation (relative to the aggregate as a whole) is approximately 2800 με. In the case of the under-aged material, the maximum relaxation is only 1000 με.

The second transition, which may be observed in Figs. 6 & 7, occurs in the (10.2) class of grains, which are essentially perfectly oriented for basal slip of <a> type dislocations, as mentioned previously [9]. The (10.1) grains begin the same transition at a slightly higher applied stress, reflective of their slightly poorer orientation with respect to basal slip. The transition occurs at about 100 MPa in both the solutionized and the peak-aged material. Indeed, the aging does not strongly alter either macroscopic response or the internal strain evolution. The third transition occurs as the (10.0), (10.1), (10.2), and (11.0) sets of grains slow their accumulation of internal strain in the range of 175 – 200 MPa. This very likely corresponds to the onset of non-basal (prismatic or pyramidal) slip of <a> type dislocations. The final inflection of interest in these data (Figs. 6 & 7) occurs most obviously in the (00.2) oriented grains, which slow in their accumulation of internal strain, in the range of 300 MPa. This final event coincides with the decreasing hardening rate in the flow curves (Fig. 4) and most likely indicates the onset of the hardest deformation modes, <c+a> pyramidal slip or c-axis contraction twinning, e.g. {10.1} twins.

Internal strain evolution during tension

Within experimental uncertainty, the internal strain evolutions for the solutionized and peak-aged material are the same during the tensile test (Fig. 8). There is a great deal of scatter in the (00.2) and (10.2) data because these are weak reflections that become even weaker with straining (see Fig. 5). The first transition in the internal strain development occurs at about 100 MPa in the (10.2) oriented grains, and the (10.1) grains yield at a slightly higher stress level. As mentioned above, this corresponds to the

activation of basal slip of <a> type dislocations. It occurs at the same stress level during these tensile tests as during compression testing, reflective of the equivalent ease of dislocation glide in the forward and reverse directions.

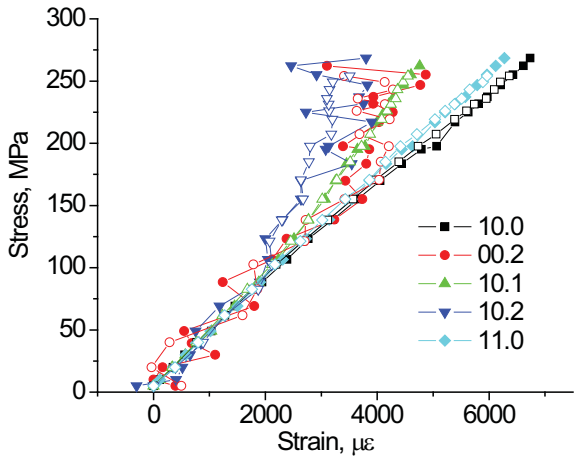


Figure 8: Internal strain evolution during tensile testing of solutionized (filled symbols) and peak aged (open symbols).

The next obvious transition in the data in Fig. 8 occurs in the (00.2) oriented grains at approximately 150 MPa. These grains are perfectly oriented for {10.2} extension twinning during this tensile test, since these grains have their <00.1> (or c-axis) parallel to the tensile axis. The final transition occurs at approximately 200 MPa. This is most easily seen in the (10.1) grains, which begin load sharing more rapidly at this point. This stress level coincides with obvious macroscopic flow in the tensile curve (Fig. 4 and Table 1). Thus, this inflection probably coincides with the activation of non-basal slip of <a> type dislocations in the (10.0) and (11.0) oriented grains. There is no obvious slowing of the internal strain development in these grains because they represent a large volume fraction of the entire aggregate and, thus, must carry a significant fraction of the stress regardless of the plasticity which is occurring within them.

Discussion

The level of tension-compression asymmetry observed in the solutionized, quenched and aged samples (CYS/TYS = 0.64 – 0.76) is similar to that reported by other authors [4]. However, the increase in tension-compression asymmetry that has been reported previously [4] is not observed. In fact, the CYS/TYS ratio is observed to be highest (0.76) in the peak-aged condition. It is suggested that the hot-worked microstructure revealed in Figure 2, obscures any major impact of the precipitation during aging. Notably, the study of Robson et al. [4] focused on the binary alloy Mg-5 wt% Zn, rather than the commercial ZK60A. The former has a more potent age hardening effect, even though the absolute hardness of the ZK60A is higher due to the additional strengthening effect of the hot-worked microstructure.

All of the samples exhibited a strong plateau in the strain hardening upon compressive yielding that coincided with the rapid increase in (00.2) intensity and, thus, with {10.2} extension twinning. Notably, the plateau is strongest in the peak-aged material. Muransky et al. [10] associated a stronger plateau in finer grained material where many twin nucleation events occurred early in the test (evidenced by acoustic emission), whereas nucleation appeared over a more extended range of stresses in the coarse grained material. All of the samples in the present study had a relatively fine grain size, and thus, exhibit the plateau. Robson et al. [4] predicted that nucleation events would be promoted by the c-axis rod-shaped precipitates which form in the Mg-Zn alloys. The present results support this notion, since the peak-aged material has the highest density of these precipitates. Further microscopic investigation will reveal whether there is a higher number density of twins in the peak-aged material, as suggested by the shape of the flow curve.

The internal strain evolution observed in this study shows features which have been previously published for AZ31B [e.g. 11], ZM20 [10], and ZK60 [12]. Of particular interest here is the relaxation due to twinning apparent in the (00.2) oriented grains during the compression test. The presence of a pre-existing set of grains with this orientation allows a definitive measure of the d_0 value necessary for computing the lattice strain per Eq. (1). This was not true in some previous publications [11,13] where an estimate of the d_0 value using date from the other detector bank was required. The present situation provides greater confidence for the discussion which follows.

The early (~ 75 MPa) transition in the internal strain development within (00.2) oriented grains (Figs. 6 & 7) may be due to regions of the microstructure which were particularly predisposed to twinning, unlike other regions which actually had to "nucleate" the twin embryos. Perhaps there were particular grain boundaries which had the perfect orientation, such that their migration resulted in twinning. The reason for hypothesizing this is the fact that very little of the overall twinning is associated with these "early adopters." Notice that the intensity of the (00.2) peak does not really start increasing until ~100-125 MPa. As further evidence of this possibility, note that the orientation relationship between the small <00.1> || extrusion axis texture component and the main <10.0> rod texture component includes the {10.2} twin orientation relationship.

The second feature of interest in the internal strain evolution is the large relaxation apparent in the (00.2) oriented grains (Figs. 6 & 7) upon macroscopic yielding and the sudden increase in (00.2) peak intensity (Fig. 5a) which indicates that {10.2} twinning has begun in earnest. Again, the presence of a d_0 value at the beginning of the test gives confidence in the reported values. However, it cannot be denied that there is still large variability in the maximum relaxation apparent in the 4 tests (solutionized, under-, peak- and over-aged samples). There are multiple aspects involved in the large variance observed in this level of relaxation.

1. The maximum level of relaxation will only be observed at a particular level of applied stress, which may not have been selected for measurement in each test.
2. There is significant uncertainty in the strain level measured using the (00.2) reflection, since the initial intensity is low.
3. There may be variation from one aging condition to another, however, there is no obvious trend.
4. There may be a level of "randomness" associated with how many nucleation events occur simultaneously.

It is suggested that either the maximum or average values (2800 or 1975 με, respectively) are most noteworthy if one consider aspects 1 or 2 as most important. As suggested by Clausen et al. [11], this relaxation is due to the propagation stage of twinning. If

one imagines a rather high local stress is required to nucleate a twin, then it will rapidly propagate across a grain (or up to some other barrier) before it enters the slower thickening (or growth) phase of twinning. It is suggested that the nucleation and propagation phases give rise to a sudden relaxation within the microstructure that results in acoustic emission [e.g., 10]. The large apparent "backstress" within the twinned regions may be tolerated because it accommodates, within a localized region, a level of strain energy that was previous spread over the entire volume of the grain.

It appears that the intergranular strain (e.g. the difference between the internal strains in (00.2) and (10.2) oriented grains) is larger in the peak aged material than in the solutionized. This suggests that the mechanisms which most effectively relax compatibility stresses, like <c+a> slip, may be impeded by precipitation. Alternatively, it may indicate a larger backstress is developed in the peak-aged material, and this would correlate with the longer twinning plateau (Fig. 4) and larger intensity change (Fig. 5a) in the peak aged. However, any conclusion made in this regard must be made with caution as there the most uncertainty in the data associated with the (00.2) and (10.2) peaks, which were weak at the beginning of the in-situ experiment. In particular, it is noted that the internal strain within the (00.2) oriented grains is very similar in the under- and over-aged material.

Both the tensile and compressive internal strain evolutions show yielding of the grains well-oriented for basal slip (10.2) and (10.1) to occur at approximately 100 MPa applied stress. This is significantly higher than has been observed in prior studies. This high stress level is due to the combined strengthening effects of grain size refinement, solute (Zn), and precipitation (Mg-Zn). The former may be the most significant, as changes in the latter two during aging heat treatment do not significantly affect either the macroscopic flow stress or the internal strain evolution. Similarly, the transition in the internal strain evolution of the tensile test, which occurs at 200 MPa, corresponds well with the macroscopic yielding. Previous studies have associated tensile yield in materials with the rod texture to be controlled by prismatic slip. This is a higher level of stress for the activation of prismatic slip than observed in other alloy systems as well. The c-axis rod-shaped precipitates have been predicted to be particularly effective for blocking prismatic slip of <a> dislocations [4]. However, it must be admitted that this transition occurs at a similar stress level regardless of aging condition. It seems that the hot-worked microstructure may be having the dominant effect.

Summary and Conclusions

In-situ neutron diffraction during tensile and compressive testing of ZK60A in various states of gaining (solutionized, underaged, peak-aged, and over-aged) was performed in order to determine the effect of precipitation on the individual deformation mechanisms. Unfortunately, the aging response of this alloy is so subtle that no gross effects are apparent. Presumably, the hot-worked microstructure obscures any major impact of the precipitation during aging. Nevertheless, the following conclusions may be drawn from the dataset.

1. Because there is a texture component with <00.1> parallel to the extrusion axis, a direct measure of d_0 for the (00.2) reflection can be made prior to the onset of twinning. This permits a good estimate of the internal lattice strain (Eq. 1) within twins as they form.
2. The relaxation of the new-born twins is 2000 and 2100 με for the solutionized and peak-aged material, respectively. The under-aged only showed about 1000 and the over-aged showed 2800 με. It is suggested that a value greater than the average (1975 με) is typical.
3. Slip of <a> type dislocations on basal and non-basal planes is delayed to higher stress levels than that observed in previous studies of alloys AZ31, ZM20, and WE43. The hot-worked microstructure is responsible.

Acknowledgements

This work was sponsored by the U.S. Army Research Office under contract number W911NF-12-1-0455 (Suveen Mathaudhu) and National Science Foundation grant number CMMI 1235259 (Mary Toney). SRA thanks McMaster University for hosting his sabbatical leave during which this manuscript was written. The authors would also like to acknowledge J.J. Bhattacharyya and Md. Shamsujjoha for their assistance with the metallography and Prof.. Peidong Wu for discussions about deformation twinning.

References

[1] J.B. Clark. *Transmission electron microscopy study of age hardening in a Mg-5 wt.% Zn alloy.* Acta Metall., 13 (1965), pp. 1281–1289

[2] J.F. Nie. *Effects of precipitate shape and orientation on dispersion strengthening in magnesium alloys.* Scripta Mater, 48 (2003), pp. 1009–1015

[3] J.M. Rosalie et al. *The effect of size and distribution of rod-shaped precipitates on the strength and ductility of a Mg–Zn alloy*. Mater. Sci. Eng. A, 539 (2012), pp. 230–237.

[4] J.D. Robson, N. Stanford, and M.R. Barnett, *Effect of precipitate shape on slip and twinning in magnesium alloys.* Acta Mater., 59 (2011), pp. 1945–1956

[5] M.A.M. Bourke, D.C. Dunand, and E. Üstündag. *SMARTS–a spectrometer for strain measurement in engineering materials*. Applied Physics A, 74 [Suppl.] (2002) pp. s1707-s1709.

[6] B. Clausen, et al. *Compressive yielding of tungsten fiber reinforced bulk metallic glass composites*. Scripta Mater. 49 (2003) pp.123-128.

[7] C.L. Mendis et al. *Precipitation-hardenable Mg–2.4Zn–0.1Ag–0.1Ca–0.16Zr (at.%) wrought magnesium alloy*. Acta Mater., 57 (2009) pp. 749-760.

[8] P.A. Turner and C.N. Tomé. *A study of residual stresses in Zircaloy-2 with rod texture*. Acta Metall. Mater., 42 (1994) 4143-4153.

[9] S.R. Agnew et al. *In situ neutron diffraction and polycrystal plasticity modeling of a Mg-Y-Nd-Zr alloy*. Acta Mater. 61 (2012) pp. 3769-3780.

[10] Muransky et al., *Investigation of deformation twinning in a fine-grained and coarse-grained ZM20 Mg alloy: Combined in situ neutron diffraction and acoustic emission*, Acta Mater. 58 (2010) pp. 1503–1517.

[11] Clausen et al. *Reorientation and stress relaxation due to twinning: Modeling and experimental characterization for Mg*. Acta Mater. 56 (2008) pp. 2456-2468

[12] L. "Jerry" Wu et al., *Twinning–detwinning behavior during the strain-controlled low-cycle fatigue testing of a wrought magnesium alloy, ZK60A*. Acta Mater. 56 (2008) pp. 688-695

[13] Brown et al. *Internal strain and texture evolution during deformation twinning in magnesium*, Mater. Sci. Eng. A, 399 (2005) pp. 1-12.

Magnesium Technology 2014
Edited by: Martyn Alderman, Michele V. Manuel, Norbert Hort, and Neale R. Neelameggham
TMS (The Minerals, Metals & Materials Society), 2014

DEVELOPMENT OF A HIGH STRENGTH DUCTILE WROUGHT Mg-Zn BASED ALLOY

L. Ma[1], T. Sasaki[1], T. Nakata[2], T. Ohkubo[1], K. Hono[1], S. Kamado[2]
[1]National Institute for Materials Science; 1-2-1 Sengen; Tsukuba, Ibaraki Prefecture, 305-0047, Japan
[2]Nagaoka University of Technology; 1603-1 Kamitomiokamachi; Nagaoka, Niigata Prefecture, 940-2188, Japan

Keywords: Magnesium, Mg-Zn-Al-Li alloy, Precipitation hardening, Extrusion, Mechanical properties

Abstract

We investigated the effect of Al addition on the age hardening response on the Mg-6.3Zn-0.6Li (wt.%) alloy. The addition of 3 wt.% of Al increased the peak hardness from 82HV to 98HV because of the high number density of fine cuboidal-shaped β_2' phases and the solution strengthening effect of Al. This particular alloy was extruded at 300°C. The extruded microstructure consisted of fine grains with the average size of 0.8 μm, which exhibited moderate yield strength of 227 MPa with low yield asymmetry due to its weakened textured feature. Upon T5 treatment, the yield strength slightly increased to 244 MPa by the dispersion of the fine precipitates. The yield strength decreased by T6 treatment because of the significant grain coarsening during the solution treatment while the low yield asymmetry was maintained in spite of its coarse grain structure.

Introduction

Magnesium alloys have recently received much interest for the applications to structural components of transportation vehicles, due to their low mass and high specific strength. Although magnesium cast alloys have found applications in vehicles [1], their limited usage does not give much contribution in weight reductions. For wider usage of magnesium wrought products, many efforts have been made to improve the formality and yield symmetry of wrought magnesium alloys by grain refinement and the addition of alloying elements [2-4]. The addition of Li is known to increase the activity of non-basal ⟨c+a⟩ slips because of the reduced c/a ratio of hcp Mg, leading to a substantial improvement in ductility [5,6]. Nevertheless, their low strength [7,8] hinders their applications to structural components. Recently, Mendis et al. [9] has reported that 2at.% of Li addition to ZK60 alloy microalloyed with Ag and Ca substantially enhanced the age hardening response and increased the peak hardness up to approximately 100HV, indicating that the strength of the Li-containing alloy can be increased by precipitation hardening. However, the addition of Ag increases the cost, making it hard to be used industrially. Thus, we need to explore lower cost alternatives that can substitute Ag. Al was selected as it has been reported to increases the peak hardness of the Mg-2.3Zn-0.5Mn (at.%) alloy [10].

In this work, we have studied the effect of Al addition on the age hardening behavior and microstructure of Mg-6.3Zn-0.6Li (ZL61) (wt.%) alloy, and the feasibility of the Mg-6.3Zn-3Al -0.6Li (wt.%) (ZAL631) alloy as a heat-treatable wrought alloy is discussed.

Experiment

Alloy ingots were prepared by induction melting using high purity Mg, Zn, Al and Mg-8.55at.%Li master alloy. Table 1 summarizes the nomenclatures and chemical compositions of the samples in mass% and atomic%. The samples were melted in a steel crucible followed by casting into a steel mold in an Ar atmosphere. The ingots were then encapsulated in Pyrex tube filled with He and homogenized at 340°C for 48 h followed by a solution treatment at 400°C for 1 h. Aging treatments were performed at 160°C in an oil bath. The ingots for the extrusion were homogenized at 340°C for 48 h and solution treated at 400°C for 1 h with an Ar flow rate of 100 ml/min. Extrusion was done at 300°C with an extrusion ratio of 20 at a ram speed of 0.1 mm/s. Tensile and compression tests were conducted at ambient temperature with an initial strain rate of 1×10^{-3} s^{-1} using round bar specimens with the gauge length and diameter of 22 and 4 mm.

Table 1. Chemical compositions of alloys in wt.% and at.%

Alloy	Composition (wt.%)			Composition (at.%)		
	Zn	Al	Li	Zn	Al	Li
ZL61	6.3	0	0.6	2.4	0	2
ZAL631	6.3	3.2	0.6	2.4	3	2

Microstructure analyses were conducted using a FEI Tecnai 20 transmission electron microscope (TEM) operating at 200 kV and electron backscattered diffraction (EBSD). Thin foil specimens for transmission electron microscopy (TEM) were

prepared by twin-jet polishing using a solution mixed of 5.3 g LiCl, 11.16 g $Mg(ClO_4)_2$, 500 ml methanol, and 100 ml 2-butoxy-ethanol at about -50°C and 90V, and the surface was cleaned by Gatan Precision Ion Polishing System (PIPS) at an operating voltage of 2 kV for ~20 min. Samples for EBSD were prepared by mechanical polishing and analyzed using Zeiss 1540 EsB scanning electron microscope (SEM) operating at 20 kV fitted with HKL CHANNEL 5 system.

Results

Age Hardening Behavior and Microstructure of Cast Alloys

The age hardening response of ZL61 and ZAL631 at 160°C is illustrated in Fig. 1. The addition of Al increased the hardness of the solution treated sample from 51HV to 58HV because of the solution strengthening by Al. Compared to the ZL61 alloy which reached the peak hardness of 82HV after 24 h, the ZAL631 alloy showed higher peak hardness of 98HV after 16 h.

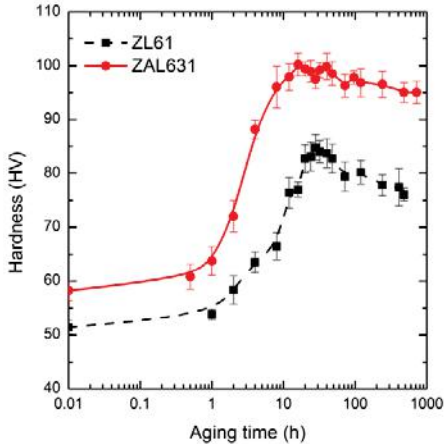


Fig. 1 Isothermal aging curves of ZL61 and ZAL631 alloys at 160°C

Fig. 2 shows the bright-field TEM images and selected area electron diffraction (SAED) patterns of the peak-aged ZL61 and ZAL631 alloys taken from $\langle 10\bar{1}0\rangle_\alpha$ zone axes. In the ZL61 alloy, majority of the precipitates were rod-like β_1' phases growing along the $[0001]_\alpha$ direction with the length from 220 to 390 nm while only a small number of plate-like β_2' phase formed on the basal plane as indicated by arrows in Fig. 2 (a). By the addition of Al, the main strengthening phase changed to β_2' phase as shown in Fig. 2 (b). The distinct intensity of extra spots in the SAED pattern inset to Fig. 2 (b) suggests the increased number density of β_2' phase.

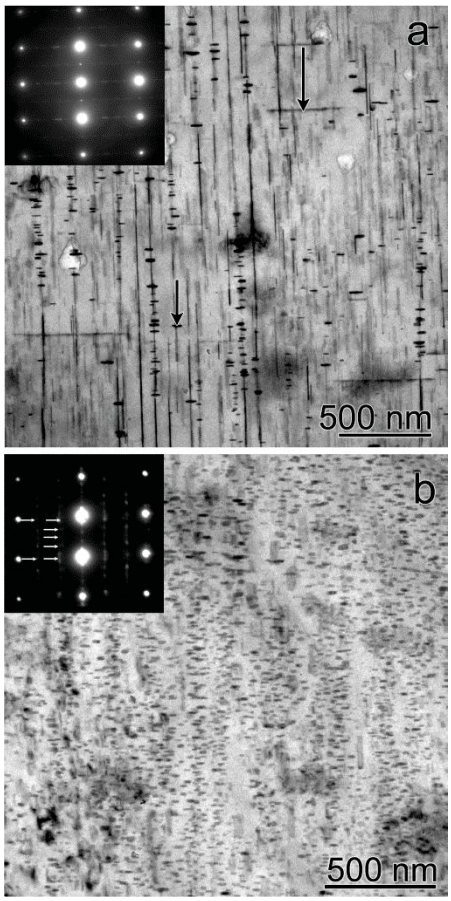


Fig. 2 Bright-field TEM micrographs of peak-aged (a) ZL61 and (b) ZAL631 alloys taken from $\langle 10\bar{1}0\rangle_\alpha$ zone axes.

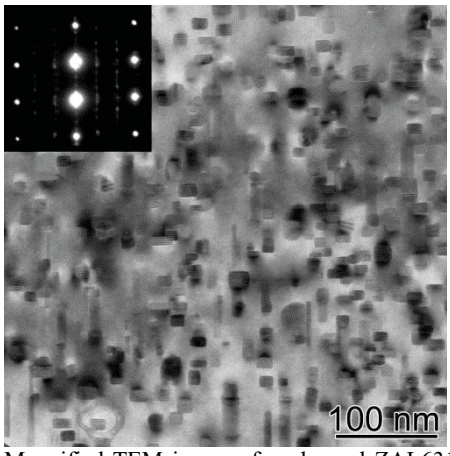


Fig. 3 Magnified TEM image of peak-aged ZAL631 alloy taken from $\langle 10\bar{1}0\rangle_\alpha$ zone axis showing the morphology of β_2'

Fig. 3 shows the magnified bright-field TEM image of the peak aged ZAL631 alloy taken from the zone axis of $\langle 10\bar{1}0\rangle_\alpha$. As well as the previous work on Mg-6Zn-3Al-1Mn (ZAM631) alloy [10], the β_2' phase has a cuboidal shape with the aspect ratio ranging

from 3:1 to 1:1, which is smaller compared to the ones typically observed in the binary Mg-Zn alloys [11,12].

Microstructure and mechanical properties of extruded sample

The extruded alloy was subjected to T5 and T6 treatments. Note that the sample was directly aged after the extrusion in the T5 treatment, and the sample was solution treated at 350°C for 15 min followed by the aging at 160°C in the T6 treatment. Fig. 4 (a) shows the variation in Vickers hardness as functions of time during aging at 160ºC. At the initial stage of the T5 aging, the hardness decreased probably because of the recovery. Then, the hardness slightly increased until it reached peak hardness of 85HV at 28 h. The T6 aged sample showed higher age hardening response compared to the one subjected to the T5 treatment although the initial hardness decreased to 62HV by the solution treatment. Fig. 4 (b) shows the tensile and compressive strain-stress curves of as-extruded and peak aged ZAL631 samples. The detailed mechanical properties are summarized in Table 2. The as-extruded alloy exhibited the tensile yield strength of 227 MPa with a total elongation of 24%. The T5 aging treatment slightly increased the tensile yield strength to 244 MPa whereas the elongation to failure decreased to 20%. However, the T6 aging treatment decreased the tensile yields strength and elongation to 217 MPa and 17%, respectively. As shown in the Table 2, all samples have shown low yield asymmetry as compared to the commercially available extruded alloys [2,13,14].

Fig. 5 shows the inverse pole figure maps of the as-extruded and solution-treated samples taken from the planes parallel to the extrusion direction (ED). The ED is illustrated in the figure. The as-extruded sample consisted of fine recrystallized grains with the average size of 0.8±0.4 μm as shown in Fig. 5 (a). The colors of grains indicate that c-axes are orientated far from normal to ED. The (0001) pole figure beside the IPF map shows that the as-extruded ZAL631 alloy has a weakened texture, unlike typical extruded magnesium alloys [3,14,15]. The solution treated sample exhibited a fully recrystallized and coarser grain structure with the average grain size of 9.6±1.0 μm, Fig. 5 (b). Compared to the as-extruded sample, the gains orientation might be further weakened in the solution treated sample.

Fig. 6 (a) and (b) show the bright-field TEM images of as-extruded and T5 aged samples. Coarse secondary phases, as indicated by arrows, were formed mainly at grain boundaries during extrusion due to the dynamic precipitation. After T5 treatment

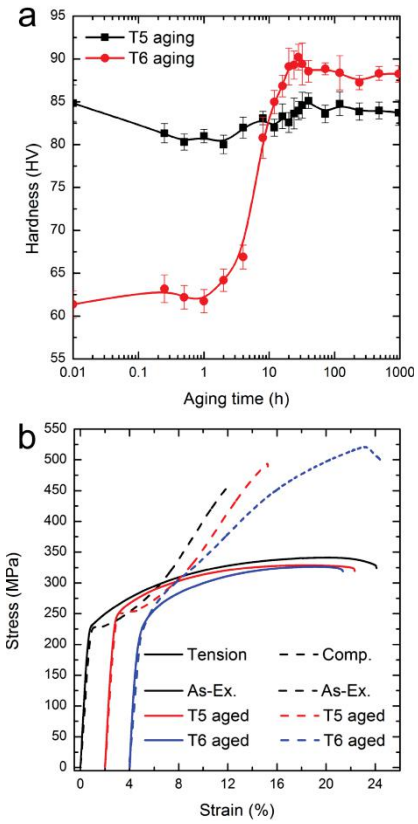


Fig. 4 (a) Isothermal aging curves at 160°C of ZAL631samples and (b) stress-strain curves of ZAL631 extrusions.

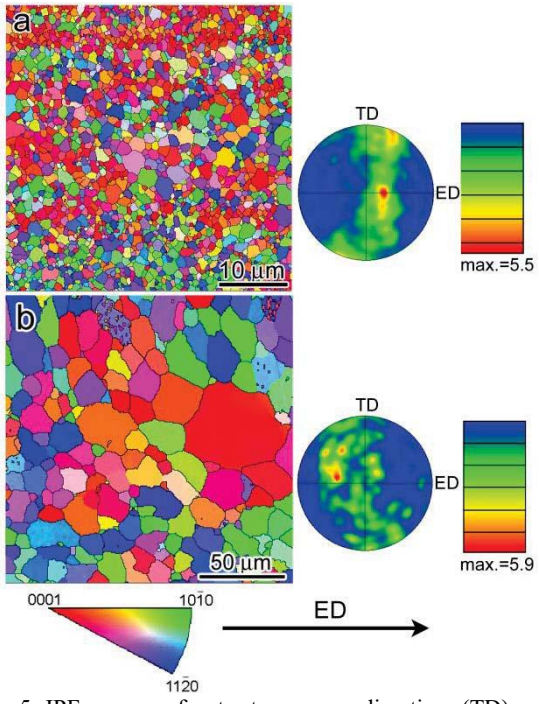


Fig.5 IPF maps refer to transverse direction (TD) and (0001) pole figures of (a) as-extruded and (b) solution-treated ZAL631 alloys.

Table 2. Room temperature mechanical properties of as-extruded and aged ZAL631samples

Condition	YS (MPa)		UTS (MPa)		Elongation (%)	Yield symmetry ratio
	Tension	Compression	Tension	Compression		
As-Ex.	227.5	217.2	341.1	457.8	24.1	1.05
T5 aged	244.4	248.8	328.7	497.5	20.3	0.98
T6 aged	217.9	225.8	326.4	520.5	17.4	0.97

(Yield symmetry ratio = tensile yield strength / compressive yield strength)

at 160°C for 28 h, β_1' and β_2' phases were densely dispersed within the grain as shown in Fig. 6 (b). The precipitates observed in the T5 aged sample were larger, compared to the ones observed in the T6 aged sample, Fig. 2 (b). This is because a part of Zn atoms have dynamically precipitated during the extrusion process.

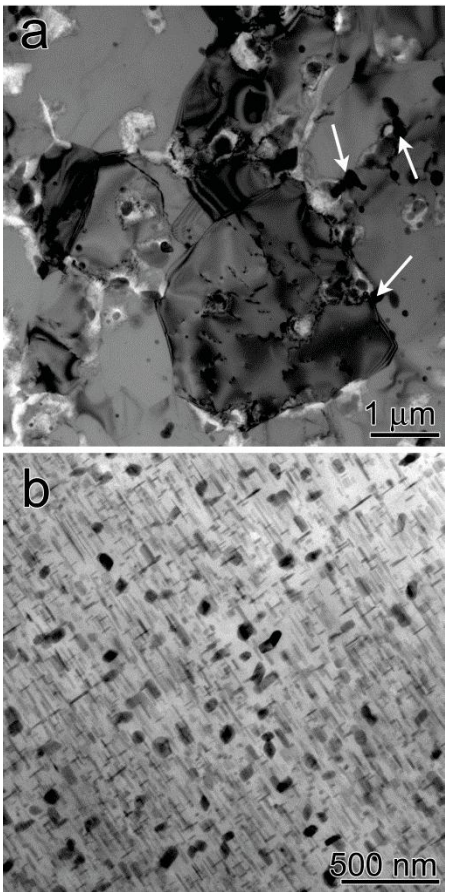


Fig. 6 Bright-field TEM images of (a) as-extruded and (b) T5 peak aged ZAL631 alloys.

Discussion

In this study, we found that the addition of 3wt.% of Al substantially increased the age hardening response of the ZL61 alloy, and the microstructure characterization revealed that the morphology of the precipitate changed by the Al addition. The main strengthening precipitate was the rod-like β_1' phase with a length ranging from 220 to 390 nm in the ZL61 alloy. Through alloying Al, the morphology of the precipitate has changed to cuboidal-shaped β_2' phase. According to Nie [16], finer precipitates provide higher strengthening effect and [0001] rods are more effective in precipitation strengthening compared to spherical precipitates. The size of the cuboidal-shaped β_2' phase in the peak aged ZAL631 alloy was much finer than that of the rod-like β_1' phases in the peak aged ZL61 alloy, and their number density was higher. Thus, even though the cuboidal-shaped precipitate in ZAL631 alloy is less effective for strengthening compared to the [0001] rods in the ZL61 alloy, the much smaller size and higher number density still provide the alloy a higher age hardening response.

After the extrusion, the ZAL631 alloy showed a good ductility with moderate yield strength. The good ductility is mainly due to the fine grain size and weakened texture. Through T5 treatment, precipitates were densely dispersed within grains. However, the sample showed only a slight increment in strength by the T5 aging. Since coarse secondary particles were formed during the extrusion, the number density of the precipitates in the T5 aged sample was low, resulting in the low precipitation hardening effect as shown in Fig. 4 (a). Even though the sample was solution treated and subjected to the T6 treatment to disperse a high number density of precipitates as much as in the cast alloy, the T6 treated sample showed lower yield strength compared to the as-extruded sample because of the severe grain growth and texture weakening during the solution treatment (Fig. 5).

Commercial Mg extrusions [13,14], usually show high yield asymmetry with the tension to compression ratio of 1.5~2 because of the activation of the different deformation mode, which has different critical resolved shear stress in tension and compression; extension twinning in compression and non-basal slips in tension. As shown in Table 2, all samples have shown rather low yield asymmetry close to 1. The low yield asymmetry in the as-extruded and T5 aged sample is owing to the fine grained structure. The grain refinement results in the increase in the CRSS for twinning close to that for non-basal slips [17], leading to the improvement of yield symmetry. Surprisingly, the T6 aged sample also showed low yield asymmetry while the grain

size is 10 μm, which is much coarser as compared to the as-extruded sample. Although further work is needed to clarify the reason for the low yield asymmetry of the T6 treated sample, the convex-shape of the compressive strain-stress curve suggests the low yield asymmetry might be probably because 1) either small amount of extension twins have been activated before macro-yielding, or 2) the twin growth is inhibited by the abundant of precipitates.

Conclusion

In this study, we investigated the effect of Al addition on the age hardening behavior and the microstructure in the ZL61 alloy. The peak hardness of ZL61 alloy increased from 82 to 98HV by alloying 3at.% of Al. The improved age hardening response is attributed to the solution strengthening of Al and high number density of fine cuboidal-shaped β_2' phase. The as-extruded ZAL631 alloy exhibited moderate strength of 227MPa with excellent ductility of 24% with low yield asymmetry due to its fine grain size and weakened texture. While T5 treatment slightly increased the yield strength, T6 aged sample showed lower yield strength mainly due to the significant grain coarsening during solution treatment.

Although the improved formability would be expected because of the low yield asymmetry and excellent elongation, the yield strength of the peak aged sample is still lower than that of the ZK60 alloy microalloyed with Ag and Ca, which is over 300MPa [17]. Further work will shed light on how to further improve the strength.

Reference

[1] B.L. Mordike, T. Ebert, "Magnesium: Properties-applications-potential," *Materials Science and Engineering A*, 302 (2001), 37-45.

[2] M.R. Barnett Z. Keshavarz, A.G. Beer, et al., "Influence of grain size on the compressive deformation of wrought Mg–3Al–1Zn," 52 (2004), 5093-5103.

[3] S.R. Agnew, P. Mehrotraa, T.M. Lillob, et al., "Texture evolution of five wrought magnesium alloys during route A equal channel angular extrusion: Experiments and simulations," *Acta Materialia*, 53 (2005), 3135-3146.

[4] J. Bohlen S. Yi, D. Letzig, et al., "Effect of rare earth elements on the microstructure and texture development in magnesium-manganese alloys during extrusion," *Materials Science and Engineering A*, 527 (2010), 7092-7098.

[5] T. Al-Samman, "Comparative study of the deformation behavior of hexagonal magnesium-lithium alloys and a conventional magnesium AZ31 alloy," *Acta Materialia*, 57 (2009), 2229-2242.

[6] D. Hardie, R.N. Parkins, "Lattice spacing relationships in magnesium solid solutions," *Philosophical Magazine*, 4 (1959)815-825.

[7] T. Liu, Y.D. Wang, S.D. Wu, et al., "Textures and mechanical behavior of Mg-3.3%Li alloy after ECAP," *Scripta Materialia*, 51 (2004), 1057-1061.

[8] S.R. Agnew, M.H. Yoo, C.N. Tome, "Application of texture simulation to understanding mechanical behavior of Mg and solid solution alloys containing Li or Y," *Acta Materialia*, 49 (2001) 4277-4289.

[9] C.L. Mendis, K. Oh-ishi, T. Ohkubo, et al., "Effect of Li additions on the age hardening response and precipitate microstructures of Mg-2.4Zn-0.16Zr based alloys," *Materials Science and Engineering A*, 535 (2012), 122-128.

[10] K. Oh-ishi,, K. Hono, K.S. Shin, "Effect of pre-aging and Al addition on age-hardening and microstructure in Mg-6 wt% Zn alloys," *Materials Science and Engineering A*, 496 (2008), 425-433.

[11] J. Buha, "Reduced temperature (22-100°C) ageing of an Mg–Zn alloy," *Materials Science and Engineering A*, 492 (2008), 11-19.

[12] X. Gao, J.F. Nie, "Characterization of strengthening precipitate phases in a Mg–Zn alloy," *Scripta Materialia*, 56 (2007), 645-648.

[13] J. Jain, W.J. Poole, C.W. Sinclair, et al., "Reducing the tension–compression yield asymmetry in a Mg–8Al–0.5Zn alloy via precipitation," *Scripta Materialia*, 62 (2010), 301-304.

[14] R.K. Mishra, A.K. Gupta, P. R. Rao, et al., "Influence of cerium on the texture and ductility of magnesium extrusions," *Scripta Materialia*, 59 (2008), 562-565.

[15] Y. Chino, K. Kimura, M. Mabuchi, "Twinning behavior and deformation mechanisms of extruded AZ31 Mg alloy," *Materials Science and Engineering A*, 486 (2008), 481–488.

[16] J.F. Nie, "Effects of precipitate shape and orientation on dispersion strengthening in magnesium alloys," *Scripta Materialia*, 48 (2003), 1009-1015.

[17] M.R. Barnett, "A rationale for the strong dependence of mechanical twinning on grain size," *Scripta Materialia*, 59 (2008) 696-698.

[18] C.L. Mendis, J.H. Bae, N.J. Kim, et al., "Microstructures and tensile properties of a twin roll cast and heat-treated Mg–2.4Zn–0.1Ag–0.1Ca–0.1Zr alloy," *Scripta Materialia*, 64 (2011) 335-338.

Magnesium Technology 2014
Edited by: Martyn Alderman, Michele V. Manuel, Norbert Hort, and Neale R. Neelameggham
TMS (The Minerals, Metals & Materials Society), 2014

Significant Precipitation Strengthening in Extruded Mg-Sn-Zn Alloys

T.T. Sasaki[1], F.R. Elsayed[1, 2], T. Nakata[3], S. Kamado[3], T. Ohkubo[1] and K. Hono[1]
[1] National Institute for Materials Science, 1-2-1 Sengen, Tsukuba, 305-0047, Japan
[2] Graduate School of Pure and Applied Science, The University of Tsukuba, 305-0001 Japan
[3] Nagaoka University of Technology, 1603-1, Kamitomiokacho, Nagaoka, 940-2188, Japan

Keywords: Mg-Sn-Zn alloy, precipitation hardening, extrusion

Abstract

Mg–5.4Sn-4.2Zn-2.1Al-0.2Mn (TZAM5420) and Mg–5.4Sn-4.2Zn-2.1Al-0.2Mn-0.1Na (TZAM5420-0.1Na) alloys were extruded at various ram speeds, and the effect of the ram speed and T6 treatment on the strength was investigated. Particularly, the TZAM5420-0.1Na alloy extruded at 5 mm/s exhibited a yield strength of 334 MPa after the T6 treatment, which is more than 170 MPa higher than that of the as-extruded alloy. The high strength of the T6 aged TZAM5420-0.1Na alloy is attributed to the uniform dispersion of the fine precipitates and suppressed grain growth during the solution treatment.

Introduction

There are growing research interests in the development of high strength wrought magnesium alloys applicable to transportation vehicles and aircrafts due to the strong demands for the reduction of CO_2 emission by their weight reduction. Since commercially available wrought Mg-Zn-Zr (ZK) and Mg-Al-Zn (AZ) alloy families have shown only moderate precipitation hardening responses by T5 treatment **[1]**, the precipitation hardening has not been paid much attention as a method to strengthen the wrought alloys. However, a number of renewed efforts have been made, and the precipitation hardening response was substantially enhanced by macro- and micro-alloying in the existing precipitation hardenable alloys such as Mg-Zn, Mg-Al, Mg-Ca, Mg-Sn, and Mg-RE (RE: rare-earth element) alloys **[2]**. Recent work on the twin-roll cast and hot rolled ZK60 alloy microalloyed with Ag and Ca exhibited excellent formability after the solution treatment, and high strength over 300 MPa after T6 treatment **[3]**, making the precipitation hardenable alloys promising as the wrought alloys.

The Mg-Sn based extruded alloy also exhibits the high strength of over 300 MPa in the as-extruded condition **[4-6]**. To achieve such high strength, the sample needed to form fine-grained structure by extruding at an unrealistically slow speed from the viewpoint of practical applications. Since the slow speed extrusion results in the increase in the production cost to hinder the application, we need to explore the industrially viable processing route as well as achieving the high strength. While the extrusion at high speed can reduce the production cost, the strength of the as-extruded sample decreases with increasing the extrusion speed mainly because of microstructure coarsening **[7, 8]**. Unlike the Mg-Zn-Zr (ZK) and Mg-Al-Zn (AZ) commercial alloys, T5 and T6 treatments do not work to further strengthen the Mg-Sn based extruded alloy **[9, 10]**. With this background, we have developed a Mg-5.4Sn-4.3Zn-2.0Al (wt.%) alloy containing trace amount of Mn and Na, in which the composition is optimized to exhibit high age hardening response. The sample exhibits the strength increase of more than 100 MPa by T6 treatment, and shows high strength up to 350 MPa **[11]**. In this work, we have extruded the Mg-1.2Sn-1.7Zn-2.0Al(-0.1Na) (at.%) alloy at various extrusion speeds, and investigated the effect of T6 aging on the mechanical property.

Experimental Procedure

Alloy ingots with nominal compositions of Mg-5.4Sn-4.2Zn-2.1Al-0.2Mn and Mg-5.4Sn-4.2Zn-2.1Al-0.2Mn-0.1Na in wt.% were prepared by induction melting using steel crucibles under an Ar atmosphere and by casting into iron molds. Table 1 summarizes the nomenclatures and compositions in both at.% and wt.%. The ingots were homoogenized at 350 ^{o}C for 24 h followed by 450 ^{o}C heat treatment for 24 h in an Ar-atmosphere followed by water quenching. The homogenized samples were then extruded at 300 ^{o}C with the ram speeds of 0.1, 2, 5 mm/s and extrusion ratio of 20. The extruded samples were solution treated at 450 ^{o}C for 15 min in an electric furnace and subjected to T6 aging at 160 ^{o}C in an oil bath.

The age hardening responses were measured by the Vickers hardness measurements under a load of 500 g. Mechanical properties of the as-extruded and peak aged samples were evaluated by tensile tests at an initial strain rate of 1.0×10^{-3} s^{-1} using the round bar sample with the gauge length and diameter of 22 and 4 mm, respectively.

Microstructure characterization was performed by scanning electron microscope (SEM) and transmission electron microscope (TEM). Electron backscattered diffraction (EBSD) analyses were done using a field emission gun-SEM, Carl Zeiss Cross Beam 1540EsB, equipped with a HKL EBSD system and CHANNEL 5 software. TEM observation was carried out using FEI Tecnai T20 TEM. Thins foils for the TEM observation were prepared by punching 3 mm diameter discs, mechanical polishing and ion-milling using a Gatan Precision Ion Polishing System (PIPS).

Table 1: Chemical compositions and nomenclatures of the samples prepared in this work

Nomenclature	Composition	
	at.%	wt.%
TZAM5420	Mg-1.2Sn-1.7Zn-2.0Al-0.1Mn	Mg-5.4Sn-4.2Zn-2.1Al-0.2Mn
TZAM5420-0.1Na	Mg-1.2Sn-1.7Zn-2.0Al-0.1Mn-0.1Na	Mg-5.4Sn-4.2Zn-2.1Al-0.2Mn-0.1Na

Results and Discussions

Figure 1 (a) shows the tensile stress-strain curves of as-extruded TZAM5420 and TZAM5420-0.1Na alloys. Table 2 summarizes the tensile yield strength, σ_{ys}, ultimate tensile strength, σ_{UTS}, and elongation to failure, ε, obtained from the stress-strain curves. The tensile yield strength, σ_{ys}, decreases with increasing the extrusion speed in both TZAM5420 and TZAM5420-0.1Na alloys. The σ_{ys} of the TZAM5420 alloy decreases from 222 to 163 MPa with increasing the ram speed from 0.1 to 5 mm/s while the elongation to failure increases from 0.18 to 0.23. The σ_{ys} of the TZAM5420-0.1Na alloy exhibits higher strength but lower elongation to failure compared to the TZAM5420 alloy. The σ_{ys} of the TZAM5420-0.1Na alloy also decreases from 303 to 168 MPa with increasing the ram speed from 0.1 to 5 mm/s while the elongation to failure increases from 0.07 to 0.18.

Table 2: Tensile properties of as-extruded samples

Sample	Ram Speed	σ_{ys}, MPa	σ_{UTS}, MPa	ε
TZAM5420	0.1 mm/s	222	332	0.18
	2 mm/s	182	324	0.23
	5 mm/s	163	313	0.23
TZAM5420-0.1Na	0.1 mm/s	303	352	0.07
	2 mm/s	243	324	0.09
	5 mm/s	168	287	0.18

TZAM5420 and TZAM5420-0.1Na alloys extruded at 5 mm/s were selected to investigate the effect of T6 treatment on the mechanical properties. Figure 1 (b) shows the variations in Vickers hardness of the TZAM5420 and TZAM5420-0.1Na alloys extruded at 5 mm/s as a function of aging time during aging at 160 °C. After the solution treatment, the hardness values of both TZAM5420 and TZAM5420-0.1Na alloys decrease to 49.0 and 50.8 VHN, respectively. The hardness of the TZAM5420 alloy starts to increase significantly after 16 h, and reaches the peak hardness of 73.4 VHN at 300 h. The TZAM5420-0.1Na alloy exhibits the significant hardness increase after 3 h of aging, and reaches the peak hardness of 93.1 VHN at 100 h. Interestingly, the samples are not overaged at least until 1600 h.

Figure 1 (c) shows the stress-strain curves of the TZAM5420 and TZAM5420-0.1Na alloys extruded at 5 mm/s in the as-extruded and peak aged conditions. Table 3 summarizes the tensile yield strength, σ_{ys}, ultimate tensile strength, σ_{UTS}, and elongation to failure, ε, obtained from the stress-strain curves. By the T6 aging, the yield strength increases at the expense of the elongation to failure. The σ_{ys} of the TZAM5420 alloy slightly increases from 163 to 207 MPa by T6 treatment while ε decreased to 0.07. Surprisingly, the σ_{ys} of the TZAM5420-0.1Na alloy significantly increases to 335 MPa from 168 MPa by T6 treatment although the ε is significantly decreased to 0.03.

Table 3: Tensile properties of TZAM5420 and TZAM5420-0.1Na alloys extruded at 5 mms in as-extruded and peak aged conditions

Sample	Ram Speed	σ_{ys}, MPa	σ_{UTS}, MPa	ε
TZAM5420	As-Ext.	163	313	0.23
	T6	207	282	0.07
TZAM5420-0.1Na	As-Ext.	168	287	0.18
	T6	335	356	0.03

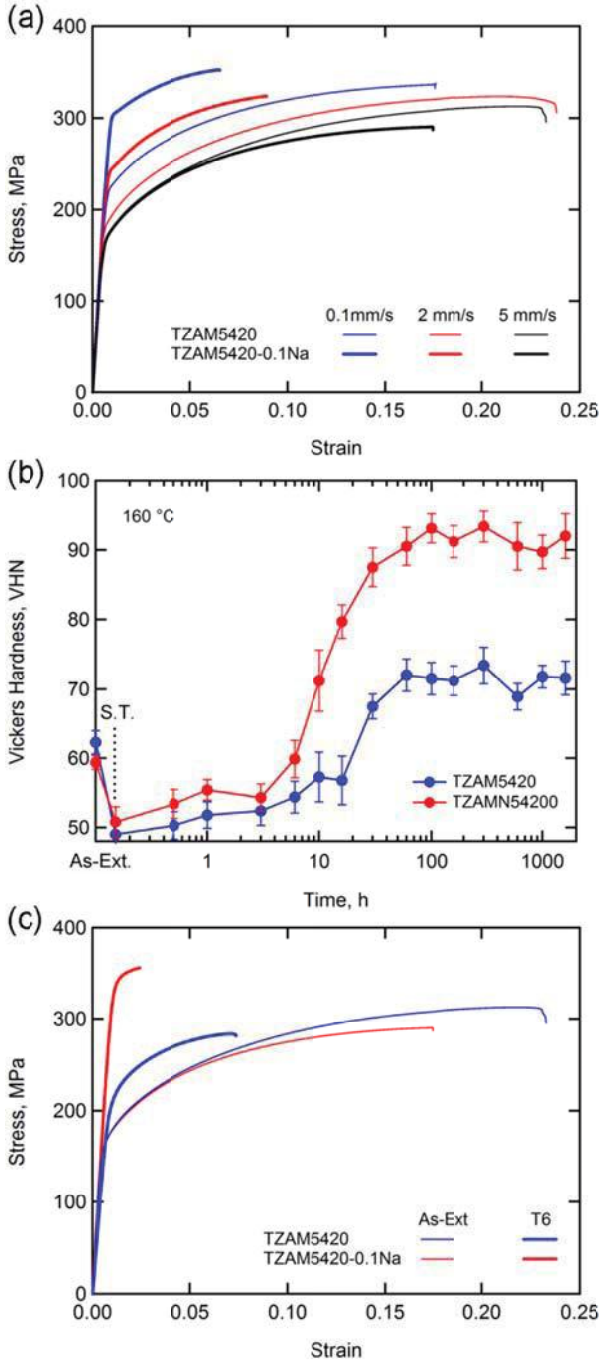


Figure 1: (a) Engineering stress-strain curves of Mg-5.4Sn-4.2Zn-2.1Al-0.1Mn (TZAM5420) and Mg-5.4Sn-4.2Zn-2.1Al-0.1Mn-0.1Na (TZAM5420-0.1Na) alloys extruded at different ram speeds. (b) Variations in Vickers hardness of TZAM5420 and TZAM5420-0.1Na alloys as a function of aging time during aging at 160 °C. (c) Engineering stress-strain curves of TZAM5420 and TZAM5420-0.1Na alloys extruded at 5 mm/s in as-extruded and peak aged conditions.

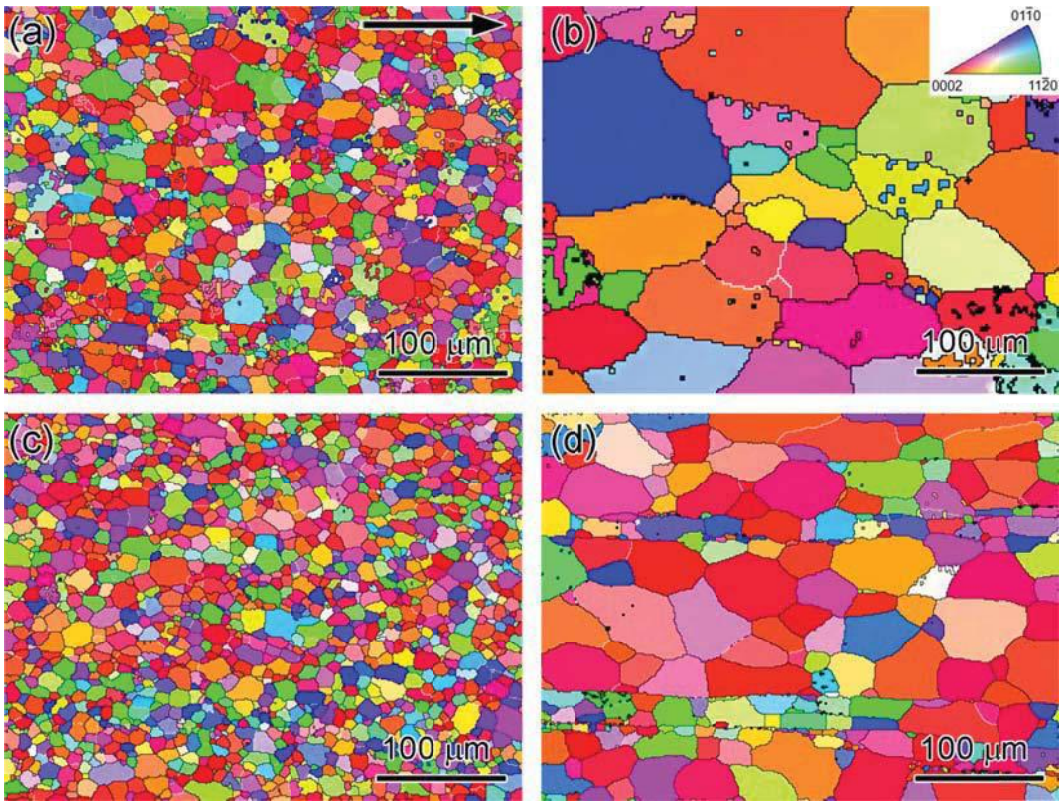


Figure 2: Inverse pole figure maps obtained from (a) as-extruded and (b) solution treated TZAM5420 alloys, and (c) as-extruded and (d) solution treated TZAM5420-0.1Na alloys. Note that the arrow in (a) shows the extrusion direction.

Figure 2 (a) thorough (d) show inverse pole figure (IPF) maps obtained from the (a) as-extruded and (b) solution treated TZAM5420 alloys, and the (c) as-extruded and (d) solution treated TZAM5420-0.1Na alloys. The as-extruded samples consist of relatively fine recrystallized grains with equi-axed shape, and their mean grain sizes are 13.6 and 10.8 μm for the TZAM5420 and TZAM5420-0.1Na alloys. The TZAM5420-0.1Na alloy shows slightly finer grain structure compared to the TZAM5420 alloy. While the grains are coarsened upon the solution treatment at 450 ºC, the grain growth is rather suppressed in the TZAM5420-0.1Na alloy as shown in Fig. 2 (b) and (d); the grain size of the solution treated TZAM5420 and TZAM5420-0.1Na alloys is 58.6 and 32.1 μm, respectively.

Figure 3 show pole figures analyzed from the IPF maps in Fig. 2. Due to low counting statistics of the grains for the solution treated TZAM5420 alloy, the analysis was done for the as-extruded TZAM5420 and TZAM5420-0.1Na alloys and solution treated TZAM5420-0.1Na alloy. As shown in Fig. 3 (a) and (b), the as-extruded samples exhibit the textured feature, which is typically observed in the extruded magnesium alloys; the (0001) plane of the magnesium matrix is aligned normal to the extrusion direction. In addition, since there is no significant difference in the maximum intensities between the as-extruded TZAM5420 and TZAM5420-0.1Na alloy, these samples show the similar textured feature. Although the number of grains analyzed was smaller compared to the as-extruded samples, the (0001) plane of the grains is still aligned normal to the extrusion direction after the solution treatment indicating that the extruded texture is maintained after the solution treatment, Fig. 3 (c).

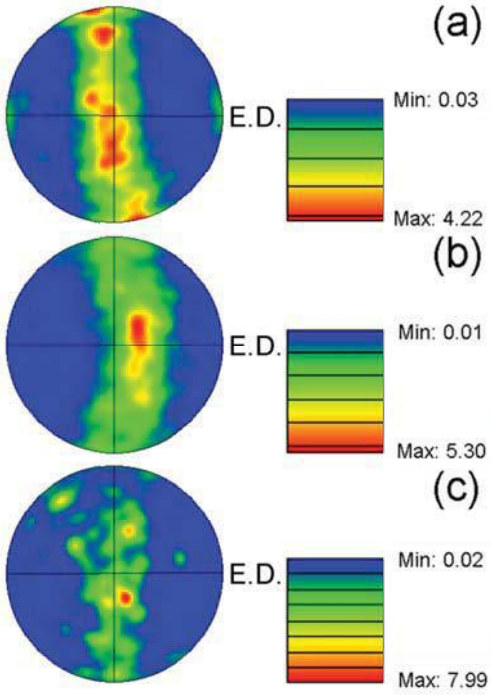


Figure 3: (0001) pole figures obtained from (a) as-extruded TZAM5420, (b) as-extruded TZAM5420-0.1Na, and (c) solution treated TZAM5420-0.1Na alloys.

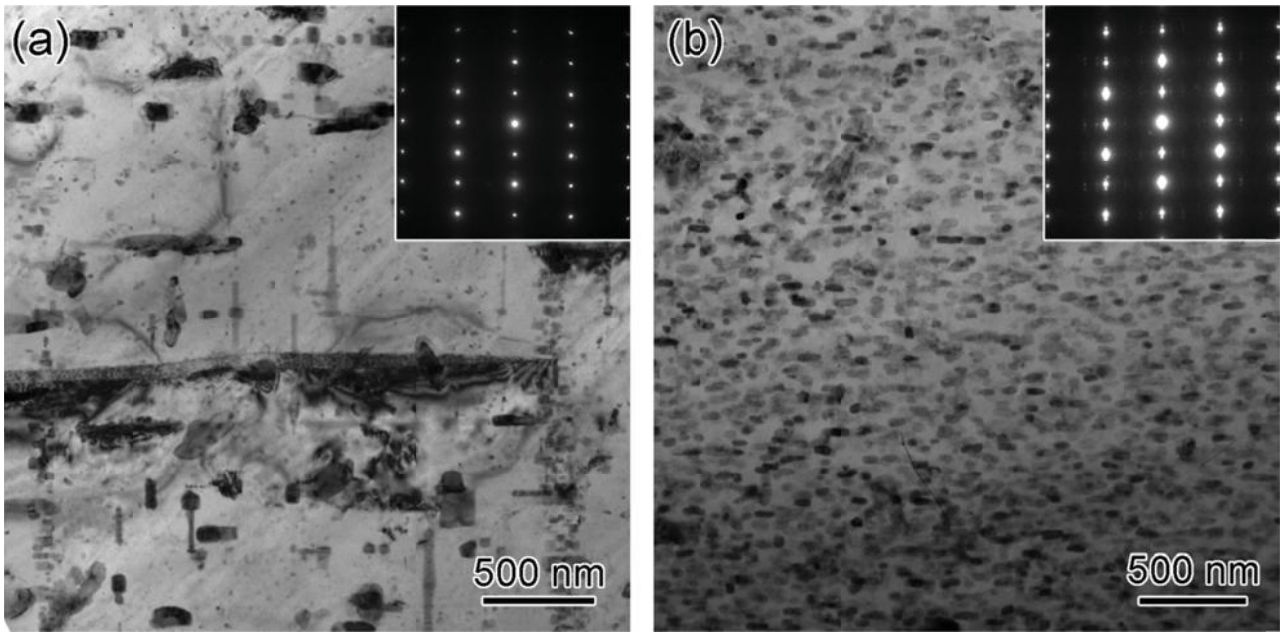


Figure 4: Bright field TEM images of peak aged (a) TZAM5420 and (b) TZAM5420-0.1Na alloys observed from the zone axis of $[11\bar{2}0]$.

Figure 4 (a) and (b) show the bright field TEM image obtained from the peak aged TZAM5420 and TZAM5420-0.1Na alloys taken from the zone axis of $[11\bar{2}0]$. In the TZAM5420 alloy, three types of precipitates are observed; fine cuboidal precipitates, rod-like precipitates and lath-shaped precipitates. Fine cuboidal precipitates could be identified as β_2' phase in the previous reports **[13, 14]**. The rod-like precipitates growing along [0001] direction are β_1' phase **[13, 14]**. The coarse lath shaped precipitates forms on the (0001) plane of the magnesium matrix, and they are identified as Mg_2Sn phase **[13]**. These precipitates are heterogeneously dispersed within the matrix. In the TZAM5420-0.1Na alloy, the precipitates mainly form on the (0001) plane of the magnesium matrix, and have the length of 33.9±6.29 nm. They are much finer and uniformly dispersed compared to the ones in the peak aged TZAM5420 alloy.

In this work, we have investigated the effect of the extrusion speed and T6 treatment on the strength of the TZAM5420 and TZAM5420-0.1Na alloys. As shown in Fig. 1 (a), the strength of the as-extruded sample decreased with increasing the extrusion speed. The strength degradation due to the increased extrusion speed is attributed to the grain coarsening since the grain size of the TZAM5420 and TZAM5420-0.1Na alloys extruded at 5 mm/s is 13.6 and 10.8 μm, which is coarser than those extruded at 2 mm/s, 4.9 and 2.5 μm **[11]**, Fig. 2 (a) and (c). The increase in the extrusion speed resulted in the generation of larger amount frictional heat, which caused the grain coarsening during the extrusion at higher speed **[10, 11]**.

The TZAM5420 and TZAM5420-0.1Na alloys extruded at 5 mm/s exhibited the fully recrystallized grain structure in the as-extruded condition, Fig. 2 (a) and (c), while the ones extruded at 2 mm/s exhibited bimodal grain structure consisting of coarse unrecrystallized grains and fine recrystallized grains **[11]**. Since the unrecrystallized grains exhibit strongly textured feature, and store high density of dislocations, they are expected to contribute to the strengthening. Therefore, the absence of the unrecrystallized grain might have also caused the strength degradation.

The peak aged TZAM5420-0.1Na alloy exhibited a high yield strength of 335 MPa while the yield strength of the peak aged TZAM5420 alloy was only 207 MPa, Fig. 1 (c). This is mainly because of uniform dispersion of the fine precipitates in the TZAM5420-0.1Na alloy compared to the TZAM5420 alloy by T6 aging, Fig. 4 (a) and (b). The refinement of the precipitates is attributed to the formation of Sn-Na co-clusters, which provide the heterogeneous nucleation sites of the Mg_2Sn precipitates **[15]**. In addition, the solution treated TZAM5420-0.1Na alloy exhibited finer grain structure compared to the TZAM5420 alloy, Fig. 2 (b) and (d). Since Na segregates at the grain boundaries **[11]**, the segregation of Na suppressed the grain growth.

The yield strength of the peak aged TZAM5420-0.1Na alloy extruded at 5 mm/s is mostly equivalent to that extruded at 2 mm/s, 343 MPa **[11]**. This means that the extrusion speed can be increased as fast as possible, and the strength can be increased by the precipitation hardening. The development of industrially viable heat treatable wrought magnesium alloy, further acceleration of age hardening response would be needed as well as the excellent extrudability,.

Summary

In this work, TZAM5420 and TZAM5420-0.1Na alloys were extruded at various ram speeds. The yield strength decreased with increasing the ram speed because of grain coarsening. Upon the T6 treatment, TZAM5420-0.1Na alloy showed significantly higher age hardening response, and exhibited higher yield strength of 334 MPa while the peak aged TZAM5420 alloy exhibited a yield strength of only 207 MPa. The high strength of the TZAM5420-0.1Na alloy is attributed to the uniform dispersion of the fine precipitates and the suppressed grain growth during the solution treatment.

Acknowledgement

This work was supported by JSPS, Graint-in-Aid for Young Scientists (B), 24760605, Grant-in-Aid for Scientific Research on Innovative Area, "Bulk Nano Metal", and JST, Advanced Low Carbon Technology Research and Development Program, (ALCA).

References

[1] M.M. Avedesian, H. Baker, eds. Magnesium and Magnesium Alloys ASM Specialty Handbook. ASM International, Materials Park, OH, 1999.

[2] J.F. Nie, "Precipitation and Hardening in Magnesium Alloys" *Metallurgical and Materials Transactions A*, 43 (11) (2012) 3891-3939.

[3] C.L. Mendis, K.Oh-ishi, Y. Kawamura, T. Honma, S. Kamado, K. Hono, "Precipitation-hardenable Mg-2.4Zn-0.1Zn-0.1Ca-0.16 Zr (at.%) alloys," *Acta Materialia*, 57 (3) (2009) 749-760.

[4] T.T. Sasaki, K. Yamamoto, T. Honma, S. Kamado, K. Hono, "A high-strength Mg–Sn–Zn–Al alloy extruded at low temperature", *Scripta Materialia*, *59* (10) (2008) 1111-1114.

[5] H.T. Son, J.B. Lee, H.G. Jeong, T.J. Konno, "Effects of Al and Zn additions on mechanical properties and precipitation behaviors of Mg–Sn alloy system", *Materials Letters, 65* (12) (2011) 1966-1969.

[6] Y.K. Kim, S.W. Sohn, Do H. Kim, W.T. Kim, D.H. Kim, "Role of icosahedral phase in enhancing the strength of Mg-Sn-Zn-Al alloy", *Journal of Alloys and Compounds, 549* (5) (2013) 46-50.

[7] W.L. Cheng, S.S. Park, B.S. You, B.H. Koo, "Microstructure and mechanical properties of binary Mg–Sn alloys subjected to indirect extrusion", Mater. Sci. Eng. A, 527 (18-19) (2010) 4650-4653.

[8] F.R. Elsayed, T.T. Sasaki, T. Ohkubo, H. Takahashi, S.W. Xu, S. Kamado, K. Hono, "Effect of extrusion conditions on microstructure and mechanical properties of microalloyed Mg-Sn-Al-Zn alloys", *Materials Science and Engineering A*, In Press.

[9] J.R. TerBush, M. Setty, N. Stanford, M.R. Barnett, A.J. Morton, J.F. Nie, Proceedings of 9th International Conference on Magnesium Alloys and their Applications, pp. 579-586.

[10] T.T. Sasaki, , J.D. Ju, K. Hono, K.S. Shin, "Heat-treatable Mg–Sn–Zn wrought alloy", *Scripta Materialia*, 61 (1) (2009) 80-83.

[11] T.T. Sasaki, F.R. Elsayed, H. Takahashi, T. Nakata, T. Ohkubo, S. Kamado, K. Hono, "Significant Precipitation Strengthening of Extruded Mg-5.4Sn-4.2Zn-2.0Al Alloy Microalloyed with Na and Mn", *Under Review.*

[12] N. Stanford, J.R. TerBush, M. Setty, M.R. Barnett, Metallurgical and Materials Transactions A 44A (6) (2013) 2466 – 2469.

[13] T. Sasaki, T. Ohkubo and K. Hono, *Magnesium Technology 2012*, Eds by S.N. Mathaudhu, W.H. Sillekens, N.R. Neelameggham, The Minerals, Metals & Materials Society (TMS), 2012, pp. 181-185.

[14] K. Oh-ishi, K. Hono, K.S. Shin, "Effect of pre-aging and Al addition on age-hardening and microstructure in Mg-6 wt.%Zn alloys", *Materials Science and Engineering A, 496 (1-2)* (2008) 425 – 433

[15] F.R. Elsayed, T.T. Sasaki, C.L. Mendis, T. Ohkubo, K. Hono, "Significant enhancement of age hardening response in Mg-10Sn-3Al-1Zn alloy by Na microalloying", *Scripta Materialia*, 68 (10) (2013)797-800.

Magnesium Technology 2014
Edited by: Martyn Alderman, Michele V. Manuel, Norbert Hort, and Neale R. Neelameggham
TMS (The Minerals, Metals & Materials Society), 2014

Al AND Zn IMPURITY DIFFUSION IN BINARY AND TERNARY MAGNESIUM SOLID-SOLUTIONS

Catherine Kammerer[1], Nagraj Kulkarni[2], Robert Warmack[2], Yongho Sohn[1]
[1]University of Central Florida, Advanced Materials Processing and Analysis Center
Department of Mechanical, Materials and Aerospace Engineering, Orlando, FL, 32816, USA
[2]Oak Ridge National Laboratory, Measurement Science & Systems Engineering Division
Oak Ridge, TN, 37831, USA

Keywords: Magnesium, Aluminum, Zinc, Impurity Diffusion, Hall Method

Abstract

Aluminum and zinc are two of the most common alloying elements in magnesium alloys. The present work examines impurity diffusion coefficients of Al and Zn in Mg(Zn) and Mg(Al) binary solid solutions, respectively. Experimental investigation was carried out with diffusion couples of ternary polycrystalline alloys. Concentration profiles were measured by electron microprobe micro-analysis and the impurity diffusion coefficients were determined by the Hall Method. Consistent with the findings of other researchers, Zn impurities diffuse faster than Al impurities in pure Mg and the Zn impurity diffusion coefficient is only slightly affected by the concentration of Al in Mg(Al) solid solutions. Unique to this study is the investigation of the diffusion behavior of Al impurities in Mg(Zn) solid solutions. The activation energy of Al impurity diffusion is strongly influenced by the solute concentration in Mg(Zn) solid solutions.

Introduction

While magnesium is abundant and lightweight, its poor cold forming properties and low ductility, limited high-temperature properties, and poor corrosion resistance have mandated alloy development and thus fundamental research [1-5]. Two of the most common alloying elements in magnesium alloys are aluminum and zinc. Aluminum (FCC) and zinc (HCP) are relatively soluble in magnesium (HCP), but their solubility decreases at low temperatures. Aluminum additions yield alloys with a good balance between strength and ductility and can be age hardenable with the precipitation of $Mg_{17}Al_{12}$. Similarly, zinc additions to magnesium yield a heat treatable alloy with the precipitation of MgZn phase. When small quantities of zinc are added to magnesium with aluminum improved room temperature properties are realized through a combination of solid solution strengthening and precipitation hardening.

Diffusion plays a key role in the kinetics of many microstructural changes that occur during processing of magnesium alloys. Therefore, in this study, we examined the impurity diffusion of Al and Zn in pure Mg as well as in Mg(Zn) and Mg(Al) solid solutions using solid-to-solid diffusion couples. Concentration profiles were determined by electron microprobe micro-analysis of the diffusion zone. The Hall Method was used to determine the impurity diffusion coefficients. In addition to Al and Zn impurity diffusion coefficients in pure Mg, we report the impurity diffusion coefficients of Zn in Mg(Al) solid solution and, for the first time, Al impurity diffusion coefficients Mg(Zn) solid solution.

Experimental Procedure

Pure Mg was commercially procured from Alfa Aesar, while magnesium alloys were produced by Magnesium Elektron, Madison, Illinois, USA. The chemical composition of the magnesium and magnesium alloys used in this investigation is given in Table I.

Table I: Chemical Composition in wt.% of Mg and Mg Alloys.

Designation	Mg	Al	Zn	Others, Total
Mg	99.996	0.00	0.00	0.00
MA3	97.17	2.81	0.00	0.02
MA9	90.38	9.59	0.02	0.01
MZ3	97.36	0.00	2.62	0.02
MZ6	93.74	0.01	6.23	0.02
MA3Z1	96.10	2.92	0.96	0.02

The alloys were direct chill cast, homogenized, and then warm extruded. All material was subjected to a grain-growth anneal roughly 40 - 50°C below the solidus for 8 – 16 hours. The grain size was determined be between 100 – 500μm. The alloy extrusion and pure Mg rods were then sectioned into 3 – 4 mm thick diffusion discs, 8 – 9 mm diameter. The diffusion discs were polished to a 1 μm surface finish using a non-oxidizing lubricant. Diffusion couples were assembled with 2 mm-thick Al_2O_3 spacers in stainless steel jigs as schematically illustrated in Figure 1.

The jig assemblies were placed individually in quartz capsules, evacuated to 10^{-6} Torr with repeated flushing with argon and hydrogen, and encapsulated. The encapsulated

assemblies were placed in a Paragon Bluebird™ furnace that was preheated to the annealing temperature. The temperature of the diffusion couples was monitored with an independent resistance temperature detector probe with an Omega™ data acquisition system. Diffusion couple assembly and anneal parameters are listed in Table II.

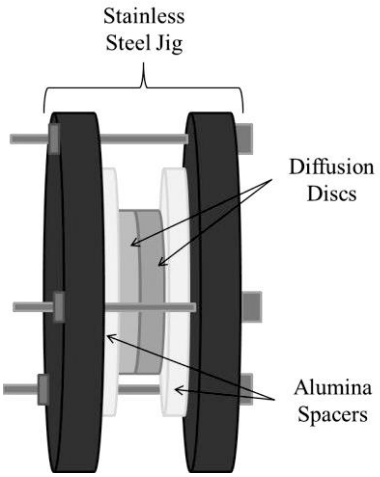


Figure 1: A schematic illustration of a solid-to-solid diffusion couple assembly.

Table II: Diffusion Study Parameters

Diffusion Couple	Anneal Temperature (˚C)	Anneal Time (Hours)
Mg-MA9	350	96
	400	17
	450	24
Mg-MZ6	350	48
	450	24
MA9-MZ6	400	8
	450	4
MA3-MZ3	400	20
	450	5
Mg-MA3Z1	350	168
	400	24
	450	4

After the annealing, the capsule was quickly removed from the furnace and quenched in water. The couple was extracted from the jig and mounted in epoxy. Once cured, the couple was cross-sectioned and metallographically prepared down to 1μm finish, again using a non-oxidizing lubricant. Each diffusion couple was examined using optical microscopy and Scanning Electron Microscope equipped with an X-ray Energy Dispersive Spectrometer (Zeiss Ultra 55 SEM with EDS) to examine the diffusion bond integrity and approximate depth of interdiffusion. Electron probe microanalysis (EPMA) (JEOL JXA-8200) was utilized for the determination of concentration profiles. Fitted concentration profiles were extracted from the EPMA data using either a cubic smoothing spline or a Savitzky-Golay smoothing function. The fitted profiles were then used for the determination of the impurity diffusion coefficients for Al and Zn in Mg and its solid solutions, calculated based on the Hall analysis. The activation energies and the pre-exponential factors for the impurity diffusion coefficients in pure Mg were also calculated.

Calculation of Impurity Diffusion Coefficients

The Hall Method puts the concentration gradient in terms of a Gaussian probability distribution, thus permitting an accurate determination of the interdiffusion coefficient at impurity levels. Using probability theory, Hall proposed that, since time is fixed for a given experiment, a probability plot of the concentration distribution will yield a straight line whose slope and intercepts can be used to solve for the constant interdiffusion coefficient [6-7]. C/C_∞ is a probability and thus written in terms of the cumulative standard normal density function or $C/C_\infty = ½ + ½ \text{ erf } u$ in which $u = h\eta + k$ where h is the slope and k is the intercept of the straight line plot, and η is the Boltzmann variable, $x/2(t^{1/2})$. Therefore, the diffusion equation can be written in terms of h, k, and u such that:

$$D = \frac{1}{h^2} + \frac{k\sqrt{\pi}}{h^2}(1 + \text{erf}\, u)\exp(u^2) \quad (1)$$

Calculation of Activation Energy for Diffusion

Solid-state diffusion is strongly dependent on temperature, and diffusion coefficients increase with increasing temperature. The temperature dependence of diffusion coefficients, in general, fits a generalized Arrhenius relation expressed by:

$$D = D_o \exp\left(-\frac{Q}{RT}\right) \quad (2)$$

where D_o is the pre-exponential factor and Q is the activation energy for diffusion. Temperature is the absolute temperature and R is the gas constant.

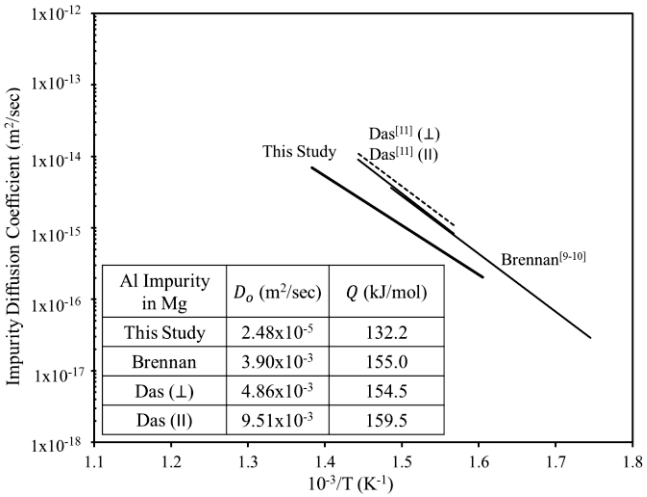
Results and Discussion

Using the Hall interdiffusion coefficient at the infinitely dilute composition, the impurity diffusion coefficients were extracted from one or more concentration profiles for each diffusion couple. The Al and Zn impurity diffusion data is presented in Table III and IV, respectively. The activation energy and pre-exponential factor of the impurity diffusion in pure Mg was determined. The pre-exponential factor and activation energy for Al impurity diffusion in pure Mg is determined to be 2.48×10^{-5} m^2/sec and 132.2 kJ/mol, respectively. For Zn in pure Mg, the impurity diffusion pre-

exponential factor and activation energy is 1.26×10^{-5} m^2/sec and 114.6 kJ/mol. These results are consistent with the impurity diffusion coefficients determined in binary Mg alloys and previously reported by Kammerer *et al*. [8].

Figure 2 presents the impurity diffusion coefficients for Al in pure Mg determined in this study along with those reported by other researchers. Brennan *et* al. determined the Al impurity diffusion coefficients through thin film depth profiling procedures [9-10]. Das [11-12] determined the Al impurity coefficients by extrapolating the interdiffusion coefficients in single crystal Mg determined using diffusion couple technique and multi-phase diffusion modeling. The extrapolated data for Al impurity in single crystal Mg is similar to the impurity diffusion coefficient in polycrystalline Mg determined through the thin film technique. However, in the case of the thin film data, the researchers acknowledged that the refined polycrystalline microstructure and depth profiling methodology employed resulted in a broadening of the diffusion profile which led to somewhat inflated diffusion coefficients [9-10]. Thus, as expected, the Al impurity diffusion coefficients in polycrystalline Mg established in this study are slightly lower.

The Zn impurity diffusion coefficient determined in this study is plotted alongside that determined by other researchers as a function of temperature in Figure 3. Previously, Zn impurity diffusion data was determined by



Al Impurity in Mg	D_o (m²/sec)	Q (kJ/mol)
This Study	2.48×10^{-5}	132.2
Brennan	3.90×10^{-3}	155.0
Das (⊥)	4.86×10^{-3}	154.5
Das (II)	9.51×10^{-3}	159.5

Figure 2: Comparison of Al impurity diffusion coefficients in pure Mg determined by various studies.

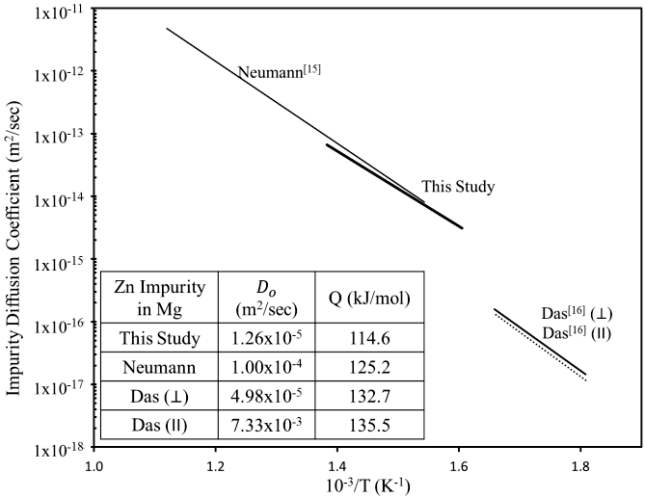
Table III: Al Impurity Diffusion Coefficients

	Couple	at.% Zn	Average (Std. Dev.)	D_{Al}^{Mg}	Average (Std. Dev.)
350°C	Mg-MA3Z1	0.02	0.00 (0.01)	7.76×10^{-17}	1.82×10^{-16} (1.48×10^{-16})
		0.00		4.39×10^{-16}	
	Mg-MA9	0.00		8.39×10^{-17}	
		0.00		1.59×10^{-16}	
		0.00		1.51×10^{-16}	
400°C	Mg-MA3Z1	0.02	0.02 (0.04)	3.80×10^{-15}	1.71×10^{-15} (1.41×10^{-15})
		0.08		8.46×10^{-16}	
	Mg-MA9	0.00		1.29×10^{-15}	
		0.00		9.00×10^{-16}	
	MA3-MZ3	1.00	1.00 (0.02)	3.57×10^{-15}	2.92×10^{-15} (9.19×10^{-16})
		0.97		2.27×10^{-15}	
	MA9-MZ6	2.04	2.10 (0.11)	2.09×10^{-15}	2.06×10^{-15} (4.95×10^{-17})
		2.20		2.02×10^{-15}	
450°C	Mg-MA9	0.00	0.00 (0.02)	5.34×10^{-15}	6.11×10^{-15} (7.94×10^{-16})
		0.00		6.11×10^{-15}	
		0.00		6.96×10^{-15}	
	Mg-MA3Z1	0.03		6.85×10^{-15}	
		0.05		5.30×10^{-15}	
	MA3-MZ3	0.90	1.00 (0.11)	1.83×10^{-14}	2.69×10^{-14} 1.22×10^{-14})
		1.06		3.55×10^{-14}	
	MA9-MZ6	2.01	2.00 (--)	5.56×10^{-14}	5.56×10^{-14} (--)

Table IV: Zn Impurity Diffusion Coefficients

	Couple	at.% Al	Average (Std. Dev.)	D_{Zn}^{Mg}	Average (Std. Dev.)
350°C	Mg-MA3Z1	0.00	0.00 (0.00)	7.45×10^{-16}	3.11×10^{-15} (2.44×10^{-15})
		0.00		4.87×10^{-16}	
	Mg-MZ6	0.00		5.84×10^{-15}	
		0.00		3.41×10^{-15}	
		0.00		5.08×10^{-15}	
400°C	Mg-MA3Z1	0.00	0.00 (0.00)	2.06×10^{-14}	1.60×10^{-14} (6.51×10^{-15})
		0.00		1.14×10^{-14}	
	MA3-MZ3	2.71	2.70 (0.01)	4.71×10^{-15}	9.11×10^{-15} (6.22×10^{-15})
		2.73		1.35×10^{-14}	
	MA9-MZ6	9.08	9.10 (0.01)	3.42×10^{-14}	3.35×10^{-14} (9.90×10^{-16})
		9.06		3.28×10^{-14}	
450°C	Mg-MA3Z1	0.00	0.00 (0.00)	3.70×10^{-14}	6.64×10^{-14} (2.65×10^{-14})
		0.00		3.83×10^{-14}	
	Mg-MZ6	0.00		9.07×10^{-14}	
		0.00		8.29×10^{-14}	
		0.00		8.33×10^{-14}	
	MA3-MZ3	2.77	2.80 (0.01)	6.53×10^{-14}	5.80×10^{-14} (1.03×10^{-14})
		2.76		5.07×10^{-14}	
	MA9-MZ6	8.09	8.10 (--)	1.49×10^{-13}	1.49×10^{-13} (--)

Čermák [13] and Lal [14] through tracer diffusion experiments, and summarized by Neumann [15]. Zn impurity data extrapolated by Das [16] from the interdiffusion coefficient in single crystal Mg are graphically reported as well. There is good agreement for the impurity diffusion coefficients experimentally measured through tracer studies and this study. In consideration of the nature of atomic mobility in polycrystalline materials, the deviation from the single crystal data is consistent with expectations. It is evident from Figures 2 and 3, that the Zn impurity diffusion coefficient is an order of magnitude higher than that of Al in pure Mg.



Zn Impurity in Mg	D_o (m²/sec)	Q (kJ/mol)
This Study	1.26x10⁻⁵	114.6
Neumann	1.00x10⁻⁴	125.2
Das (⊥)	4.98x10⁻⁵	132.7
Das (II)	7.33x10⁻³	135.5

Figure 3: Comparison of Zn impurity diffusion coefficients in pure Mg calculated by different methods.

The influence of solute concentration in Mg solid solutions on the impurity diffusion coefficient was examined. Figure 4 presents the Zn impurity diffusion coefficient in Mg(Al) solid solutions. The vertical and horizontal error bars represent one standard deviation in the diffusion coefficient and atomic concentration, respectively. With increasing concentration of Al, the Zn impurity diffusion coefficient is slightly increased. The change in the diffusion coefficient as a function of concentration is not affected by temperature, indicating that the activation energy for Zn impurity diffusion is independent of Al concentration. The results of this study agree well with the work of Čermák [13], indicated by the dashed lines in Figure 4. He characterized the Zn impurity diffusion coefficient as a function of the aluminum concentration (in wt.%) through an Arrhenius relationship as:

$$D(\mathrm{m^2 s^{-1}}) = \exp[(0.100 \pm 0.007)c_{Al} - (9.16 \pm 0.33)] \exp\left(-\frac{(125.8 \pm 2.1)\ \mathrm{kJ\ mol^{-1}}}{RT}\right) \quad (3)$$

The solute concentration-dependent impurity diffusion coefficient determined in this study by the Hall Method is within the margin of error of that determined by Čermák using the tracers. As was pointed out by Čermák, the pre-exponential factor is concentration dependent while the activation energy is concentration independent [13].

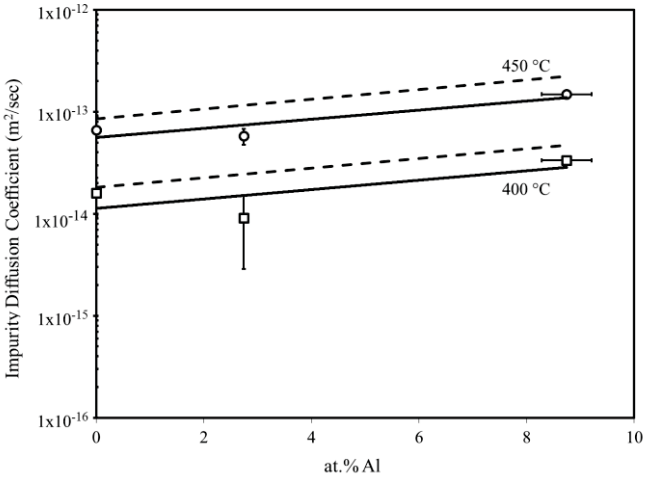


Figure 4: Influence of solute concentration on the Zn impurity diffusion coefficient in Mg(Al) solid solutions. Open circle markers represent the average impurity diffusion coefficient at 450˚C; open square markers indicate the average impurity diffusion coefficients at 400˚C.

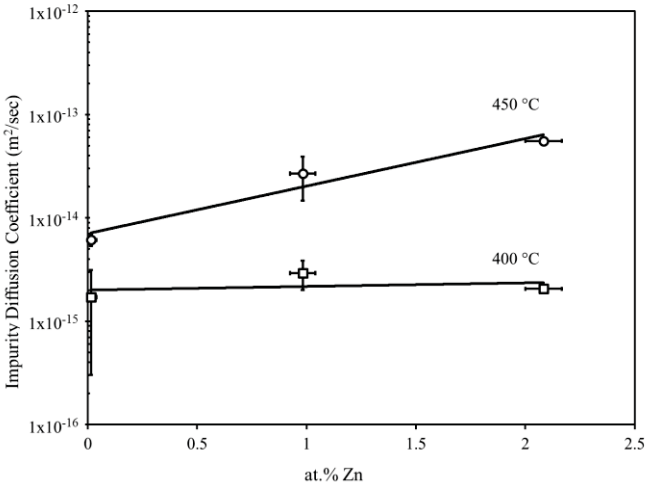


Figure 5: Influence of solute concentration on the Al impurity diffusion coefficient in Mg(Zn) solid solutions. Open circle markers represent the average impurity diffusion coefficient at 450˚C; open square markers indicate the average impurity diffusion coefficients at 400˚C.

The Al impurity diffusion coefficient in Mg(Zn) solid solutions is presented in Figure 5. At 400°C, the Al impurity diffusion coefficient remains relatively unchanged with increasing Zn concentration. The behavior of the diffusion coefficient is notably different at 450°C; the

impurity diffusion coefficient increases by an order of magnitude when the Mg solid solution contains 2 at.% Zn. The divergence of the impurity diffusion coefficient with increasing concentration between the two studied temperatures is indicative that both the pre-exponential factor and energy of activation for Al impurity is dependent on the concentration of Zn in solution with Mg.

Summary

Impurity diffusion coefficients for Al and Zn in pure Mg, Zn in Mg(Al) solid solution, and Al in Mg(Zn) solid solution were calculated by the Hall Method using solid-to-solid diffusion couples. Al impurity in Mg(Zn) solid solution have not been previously reported. The impurity diffusion coefficients in pure Mg are consistent with those determined through other analytical techniques. Zn impurities diffuse faster than Al impurities in pure Mg. The Zn impurity diffusion coefficient is only slightly affected by the presence of Al in Mg(Al) solid solution at the temperatures studied. Al impurity diffusion in Mg(Zn) solid solution is strongly influenced by the Zn concentration at 450˚C.

Acknowledgement

This research was sponsored by the U.S. Department of Energy, Assistant Secretary for Energy Efficiency and Renewable Energy, Office of Vehicle Technologies, as part of the Lightweight Materials Program.

This manuscript has been authored by UT-Battelle, LLC, under Contract No. DE-AC05-00OR22725 with the U.S. Department of Energy. The United States Government retains and the publisher, by accepting the article for publication, acknowledges that the United States Government retains a non-exclusive, paid-up, irrevocable, world-wide license to publish or reproduce the published form of this manuscript, or allow others to do so, for United States Government purposes.

References

[1] B.L. Mordike, T. Ebert, "Magnesium: Properties-applications-potential," Materials Science and Engineering A, 302, 2001, 37-45.

[2] Luo, "Magnesium: Current and Potential Automotive Applications," Journal of Materials, 54, 2002, 42-48.

[3] M.K. Kulekci, "Magnesium and its alloys applications in automotive industry," International Journal of Advanced Manufacturing Technology, 39, 2008, 851–865.

[4] R. Urbance, F. Field, R. Kirchain, R. Roth, J. Clark, "Market Model Simulation: The Impact of Increased Automotive Interest in Magnesium," Journal of Materials, 54, 2002, 25-33.

[5] A.K. Mondal, D. Fechner, S. Kumar, H. Dieringa, P. Maier, K.U. Kainer, "Interrupted creep behavior of Mg alloys developed for powertrain applications," Materials Science and Engineering A, 527, 2010, 2289-2296.

[6] L. Hall, "An Analytical Method of Calculating Variable Diffusion Coefficients," Journal of Chemical Physics, 21, 1953, 87-89.

[7] N. Sarafianos, "An Analytical Method of Calculating Variable Diffusion Coefficients," Journal of Materials Science, 21, 1983, 2283-2288.

[8] Kammerer, C., Kulkarni, N., Warmack, R., Perry, K., Belova, I., Murch, G., Sohn, Y., "Impurity Diffusion Coefficients of Al and Zn in Mg Determined From Solid-to-Solid Diffusion Couples," Magnesium Technology 2013, Publication Pending.

[9] S. Brennan, A.P. Warren, K.R. Coffey, N. Kulkarni, P. Todd, M. Kilmov, Y.H. Sohn, "Aluminum Impurity Diffusion in Magnesium," Journal of Phase Equilibria and Diffusion, 33, 2012, 1547-7037.

[10] S. Brennan, A.P. Warren, K.R. Coffey, Y.H. Sohn, N. Kulkarni, P. Todd, "Impurity Diffusion Studies of Aluminum in Magnesium," Magnesium Technology 2010, ed. By S.R. Agnew, N.R. Neelameggham, E.A. Nyberg, W.H. Sillekens, TMS, 2010, pp. 537-538.

[11] Das, S. K., Kim, Y. M., Ha, T. K., Gauvin, R., Jung, I. H.: Metallurgical and Materials Transactions A, 2013, 44. 3420-3421.

[12] Das, S. K., Kim, Y. M., Ha, T. K., Gauvin, R., Jung, I. H.: Metallurgical and Materials Transactions A, 2013, 44. 2539-2547.

[13] J. Čermák, I. Stoukal, "Diffusion of ^{65}Zn in Mg and in Mg-xAl solid solutions," Phys. Stat. Sol., 203, 2006, 2386-2392.

[14] K. Lal, Diffusion of Some Elements in Magnesium, CEA Report, 1967, R 3136, p 54

[15] Neumann, G., & Tuijn, C.: Self-Diffusion and Impurity Diffusion in Pure Metals. Elsevier, London, 2009, pp. 102-103.

[16] Das, S. K., Kim, Y. M., Ha, R., Jung, I. H.: CALPHAD: Computer Coupling of Phase Diagrams and Thermochemistry, 2013, 42. 51-58.

Magnesium Technology 2014
Edited by: Martyn Alderman, Michele V. Manuel, Norbert Hort, and Neale R. Neelameggham
TMS (The Minerals, Metals & Materials Society), 2014

FORMATION AND EVOLUTION OF INTERMETALLIC PHASES IN THE Mg-Nd-Zn-Zr SYSTEM

Ke-Xue Peng[1], Jie-Yu Zhang[1,*], Zhi-Hong Zhang[2], Qian Li[1]
[1]Shanghai Key Laboratory of Modern Metallurgy & Materials Processing, Shanghai University, Shanghai, 200072, China
[2]Baotou Research Institute of Rare Earths, Baotou, 014030, China
[*]Corresponding author: zjy6162@staff.shu.edu.cn

Keywords: Mg-Nd-Zn-Zr system, intermetallic phases, diffusion multiple

Abstract

A diffusion multiple was designed to study the intermetallic phases in the Mg-Nd-Zn-Zr system. Pure metal blocks were assembled and then sealed in an Al cylinder by electron beam welding in a vacuum chamber. Hot isostatic pressing was applied to make metal blocks closely bonded. The samples were quenched in ice water after annealed at 300 °C for 400 and 600 hours, respectively. Many intermetallic phases including $Mg_{12}Zn_{13}$, Mg_2Zn_3, $MgZn_2$ and Mg_2Zn_{11} between Mg and Zn blocks, $Mg_{41}Nd_5$ and Mg_3Nd between Mg and Nd blocks, $NdZn_2$, $NdZn_3$, $Nd_{13}Zn_{58}$ and Nd_2Zn_{17} between Nd and Zn blocks, αZn_3Zr and $Zn_{39}Zr_5$ between Zn and Zr blocks, T_1~T_3 ternary phases at the intersection of Mg, Nd and Zn blocks were detected by SEM and EDS. The formation and evolution process of intermetallic phases layers in this diffusion multiple are discussed.

Introduction

Magnesium alloys have been widely used in electronic, aviation and automotive industries, where weight lightening is a necessary requirement[1]. Mg-Nd-Zn-Zr alloys have been valued highly in recent years due to their excellent mechanical properties, outstanding general corrosion resistance properties, high heat-transfer properties and good biocompatibility[2-4]. The properties of Mg-Nd-Zn-Zr alloys will be obviously influenced by the types, amount and distribution of intermetallic compounds[5, 6]. However, the researches of intermetallic compounds and phase diagrams in this system are limited and inconsistent[7, 8], far from enough to meet the requirements of a scientific materials design. The studies to the intermetallic compounds and phase diagrams in this system are still urgently needed.

The diffusion multiple technique developed in recent years can accelerate design of structural materials due to the high efficiency to generate critical information such as phase diagram, diffusion coefficients, precipitation kinetics[9, 10]. All this information is essential for the establishment of thermodynamics and kinetic databases which are fundamental to the computational materials science. Micro-scale resolution tools, developed recently, make it possible to measure thermal conductivity, elastic modulus and coefficients of thermal expansion of the single phase in diffusion zones. These single phase's properties are important reference information to the materials design, too [11, 12].

The purposes of our research are to study the formation and evolution processes of intermetallic phases which generated by solid-solid reaction in the diffusion multiple, to obtain phase diagram information and properties of single intermetallic phase information by micro-area chemical analysis and properties determination. This paper focus on the introduction of experimental process and the analysis results by scanning electron microscopy equipped with energy dispersive spectrometer (SEM-EDS) of the Mg-Nd-Zn-Zr diffusion multiple.

Experimental

The design of Mg-Nd-Zn-Zr diffusion multiple is shown in Figure 1. Pure Al was selected to make a HIP-can because Mg and Zn are easily volatize while Nd and Zr are too hard to deform at the temperature of hot isostatic pressing (HIP). The high-purity starting materials of Mg (99.99%), Zn (99.99%), Nd (99.9%), Zr (99.9%) and the Al HIP-can were cut to designed shapes by wire electro-discharge machining (EDM). The pure metal pieces were grinded by 1200 mesh SiC sandpapers, ultrasonically cleaned in the acetone and then assembled into the opening Al cylinder. Two Al caps were put at the ends of Al cylinder, as is shown in Figure 1 (a). The electron beam (EB) welding was performed in a vacuum chamber to make the two caps welded well with the Al cylinder, and more importantly, it kept the assembly's inside in a vacuum state which would allow the subsequent HIP to make all the components closely bonded. The HIP was running at 300 °C for 4 hours at 87.2 MPa argon pressures, which made the pure Al HIP-can soften and deformed plastically. The diffusion multiple was then cooled down from the HIP unit, and sealed in a vacuum quartz tube.

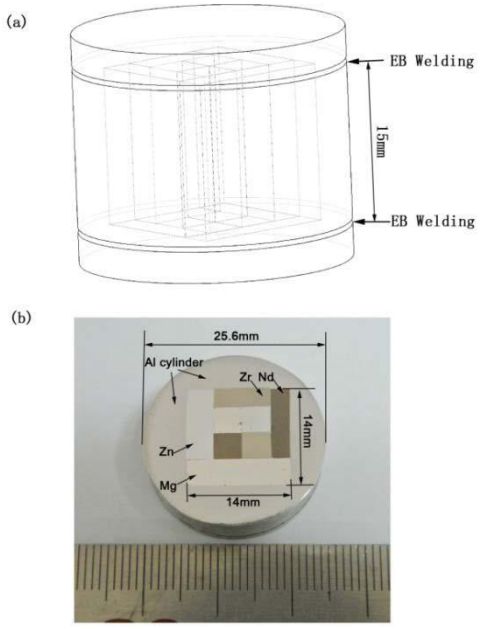


Figure 1. Schematic illustration of assembly (a) and optical image of cross section after sample preparation (b) of a Mg-Nd-Zn-Zr diffusion multiple

The sealed quartz tube was put into a resistance furnace, heated up to 300 °C and annealed for 400 hours. After that, the diffusion multiple was taken out and quenched in ice water. Then the diffusion multiple was cut into two parts parallel to the caps by wire EDM. One of them was grinded and polished for scanning

electron microscopy (SEM; JEOL JSM 6700F field emission, 15 kV) and energy dispersive spectrometer (EDS; INCA, Oxford Instrument) examination, the other part was grinded by SiC sandpapers, cleaned by acetone and then sealed in a vacuum quartz tube to anneal for another 200 hours. Then the SEM-EDS sample was prepared by the same method of the former one.

Results

Mg-Nd interface

Figure 2 (a) is the backscatter electron micrograph of the Mg-Nd cross-section in the diffusion multiple after HIP at 300 °C for 4 hours and annealing at 300 °C for 400 hours. It is clearly shown that there are two intermetallic phase layers in the diffusion zone. The results of EDS show that the two layers are $Mg_{41}Nd_5$ and Mg_3Nd. From Figure 2 (a) and (b), we can see that the thickness of $Mg_{41}Nd_5$ layer is thinner than Mg_3Nd layer and there is no substantial change after annealing for another 200 hours.

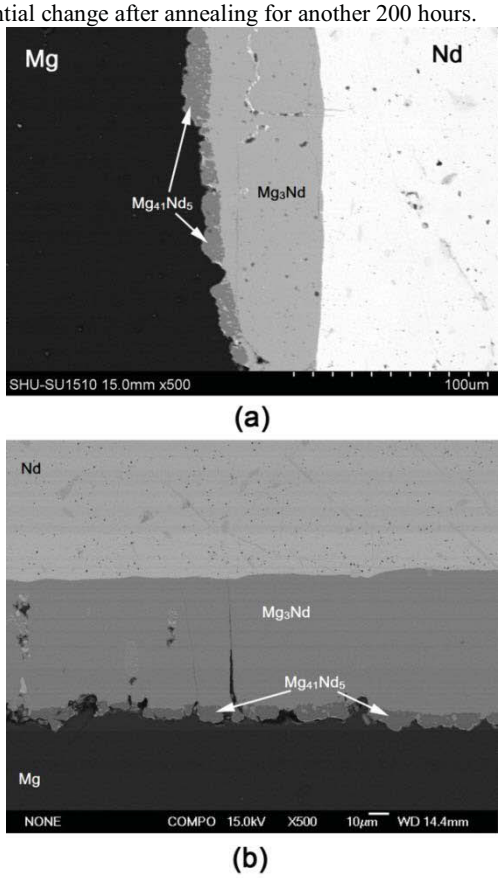


Figure 2. Backscatter electron micrographs of the Mg-Nd cross-section annealing at 300 °C for 400 hours (a) and 600 hours (b)

Mg-Zn interface

Figure 3 are the backscatter electron micrographs of the Mg-Zn cross-section annealing at 300 °C for 400 hours. All the stable intermetallic phases at 300 °C ($Mg_{12}Zn_{13}$, Mg_2Zn_{11}, $MgZn_2$ and Mg_2Zn_3) were detected at the Mg-Zn interface. However, as the annealing time increased to 600 hours, the $Mg_{12}Zn_{13}$ and Mg_2Zn_3 phase layers grew thicker while the $MgZn_2$ phase grew thinner or fell off from the diffusion zones, as is shown in Figure 4.

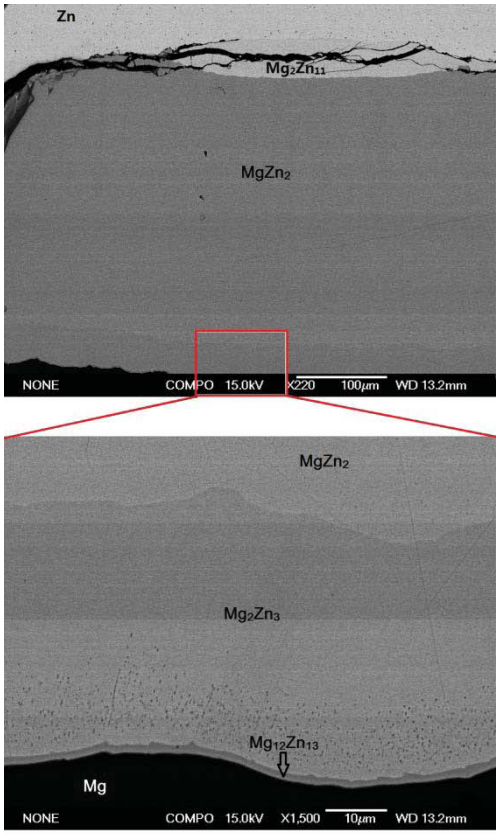


Figure 3. Backscatter electron micrographs of the Mg-Zn cross-section annealing at 300 °C for 400 hours

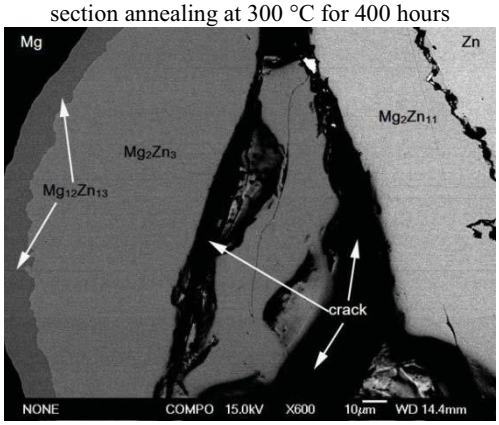


Figure 4. Backscatter electron micrograph of the Mg-Zn cross-section annealing at 300 °C for 600 hours

Nd-Zn interface

No diffusion couple research result was found in this system. According to the phase diagram research of Nd-Zn binary system[13], there are at least eight stable intermetallic phases in this system at 300 °C. However, only four intermetallic phases layer were detected in our work which were identified as $NdZn_2$, $NdZn_3$, $Nd_{13}Zn_{58}$ and Nd_2Zn_{17} by EDS, as is shown in Figure 5 and Figure 6. More cracks were found at the interface of Zn and Nd_2Zn_{17} phase which may be caused by the sublimation of Zn and the fragility of Nd_2Zn_{17}.

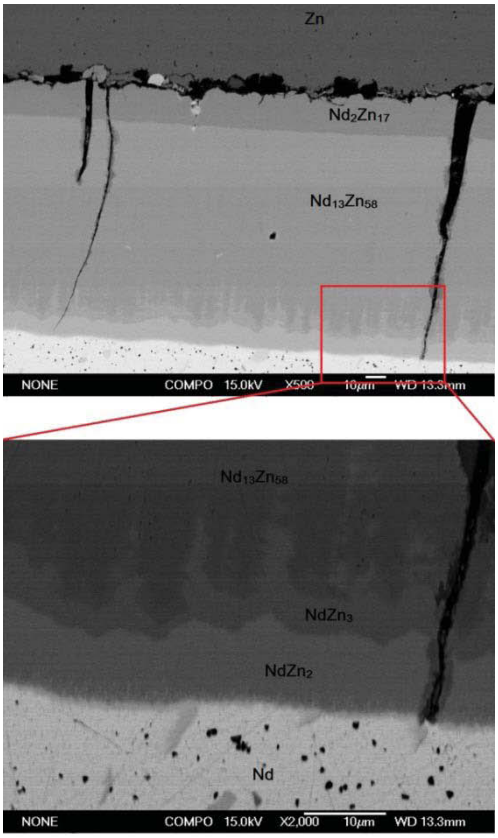


Figure 5. Backscatter electron micrographs of the Nd-Zn cross-section annealing at 300 °C for 400 hours

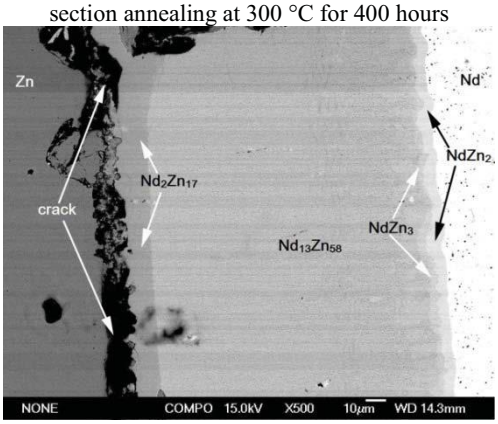


Figure 6. Backscatter electron micrograph of the Nd-Zn cross-section annealing at 300 °C for 600 hours

Zn-Zr interface

Actually, solid to solid diffusion couple is not very suitable for this system because of the large difference of melting point between Zn and Zr. The orientation of diffusion in this system is from Zn to Zr because the diffusion mobility of Zr is very low at the temperature of 300 °C. Figure 7 are the backscatter electron micrographs of the Zn-Zr cross-section annealing at 300 °C for 400 and 600 hours. There are two intermetallic phases formed at the interface of Zn and Zr which were identified to be αZn_3Zr and $Zn_{39}Zr_5$.

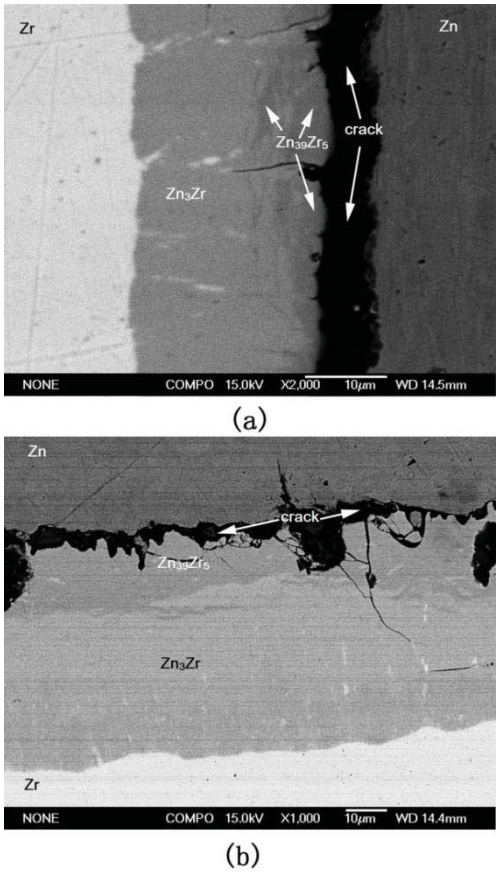


Figure 7. Backscatter electron micrographs of the Zn-Zr cross-section annealing at 300 °C for 400 hours (a) and 600 hours (b)

Mg-Nd-Zn intersection

The backscatter electron micrographs of the Mg-Nd-Zn intersection cross-section annealing at 300 °C for 400 hours are shown in Figures 8, 9, 10. Three ternary phases marked with T_1~T_3 were detected in this sample. As is shown in Figure 8, T_1 ternary phase grew between $MgZn_2$ and Mg_3Nd phase, and the chemical composition range analyzed by EDS was Mg: 29.77~32.41, Nd: 21.76~22.97, Zn: 45.60~47.25 at. %. In Figure 9, T_2 ternary phase grew between $Mg_{13}Zn_{58}$ and Mg phase, and the chemical composition range analyzed by EDS was Mg: 24.92~27.50, Nd: 6.61~8.29, Zn: 65.89~66.79 at. %. In Figure 10, T_3 ternary phase grew between $NdZn_2$ and Mg phase, and the chemical composition range analyzed by EDS was Mg: 23.34~25.44, Nd: 24.27~24.98, Zn: 50.01~52.39 at. %.

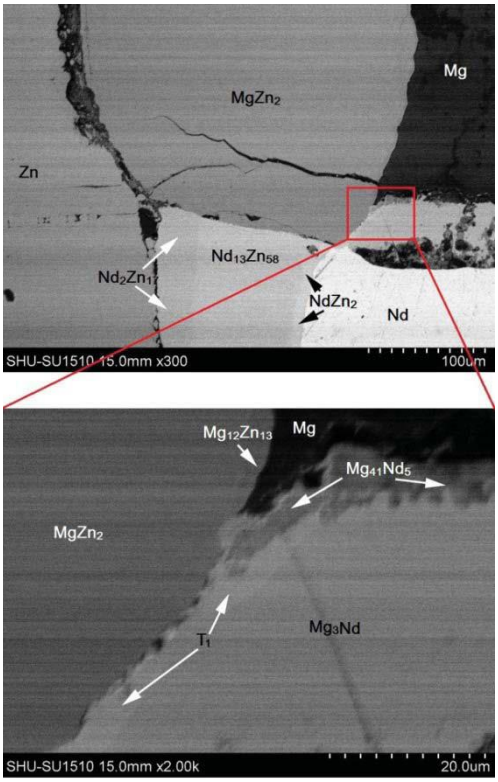


Figure 8. The backscatter electron micrographs of Mg-Nd-Zn intersection where T_1 ternary phase is located

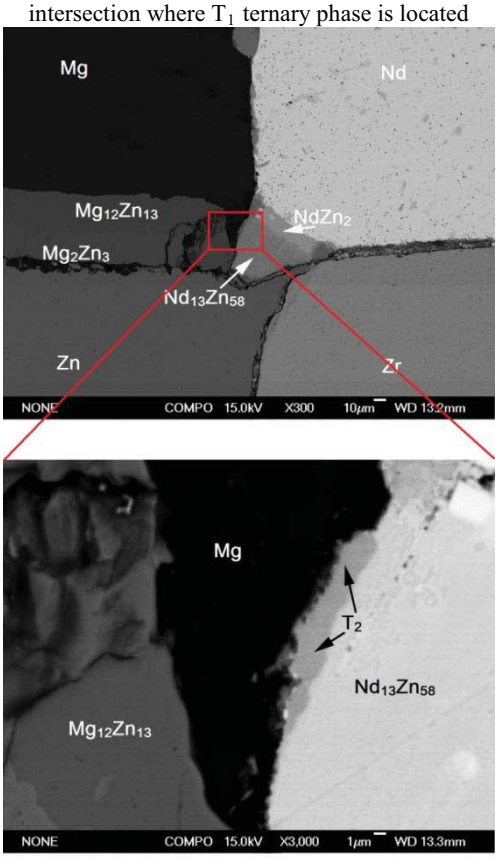


Figure 9. The backscatter electron micrographs of Mg-Nd-Zn intersection where T_2 ternary phase is located

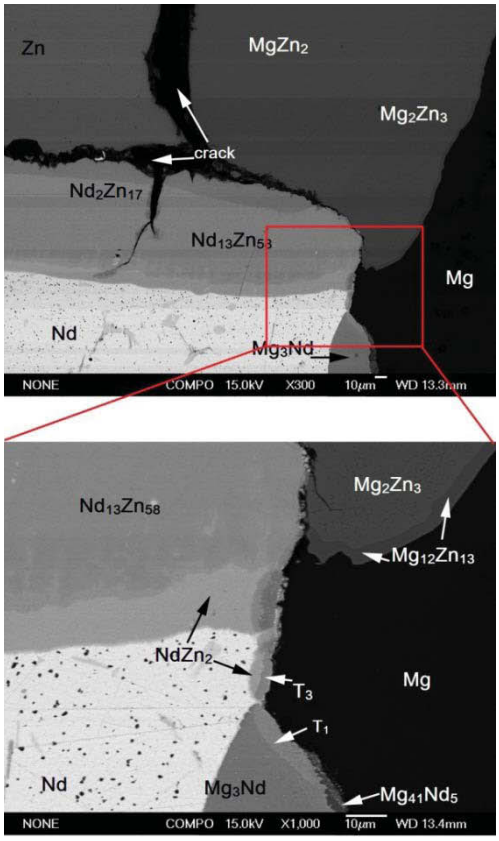


Figure 10. The backscatter electron micrographs of Mg-Nd-Zn intersection where T_3 and T_1 ternary phase are located

The EDS results summarized in Figure 11 and the existing phase diagrams [14-17] are combined to identify the intermetallic phases.

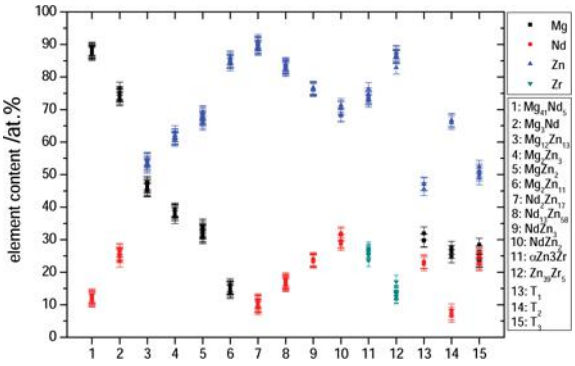


Figure 11. The summarizing of EDS compositions for intermetallic phases

Discussion

In principle, all stable intermetallic phases at the annealing temperature may be formed as layers in the diffusion zone. However, in practice, some phases may not appear owing to extremely slow nucleation rates or approximately zero growth rates[18]. Based on the Fick's first law, Kidson [19] put forward a

simple physical interpretation of various possible types of behaviors in the growth of diffusion layers, which indicated that the assumption of each phase in the equilibrium phase diagram of a system will grow to an observable width in a diffusion couple was unreasonable.

Some fundamental guidelines of growth and diffusion theories of previous studies[18-20] indicated that an intermetallic phase layer will grow thicker if: the phase has a wider homogeneity range, or the phase has a higher diffusion coefficient than its surrounding phases, or the phase has a higher heat of formation (or higher melting temperature), or the crystal structures of the adjoining phases are similar.

Phase development and interdiffusion in the Mg-Nd system were studied via diffusion couples at 500°C by Xu et al.[21], 400 to 500 °C by Sarah et al.[22], 500 to 520 °C by Sterling and Sinclair[23]. In the work of Xu et al.[21], the diffusion couple was annealed at 500 °C for 100 hours and two intermetallic phases identified as Mg_3Nd and MgNd by EDS were detected in the diffusion zone. In the work of Sterling and Sinclair[23], diffusion bonding experiments were performed in a DSI Gleeble 3500 Thermo-mechanical Analyzer at 450 °C with a starting pressure of 10 Mpa for 90 minutes. After the initial bonding, the sample was annealed in a tube furnace that was firstly evacuated and then backfilled with high purity argon at 500 °C for 90 hours and 520 °C for 96 hours. Two intermetallic phases have formed between the Nd and Mg. The sample was analyzed with EPMA and the result showed that the compositions of the two intermetallic phases are consistent with Mg_3Nd and $Mg_{41}Nd_5$ which were inconsistent with Xu et al.'s work. In the work of Sarah et al.[22], the diffusion couples were annealing at 400 °C for 21 days, 450 °C for 15 days and 500 °C for 10 days in a protective atmosphere. The same as Sterling and Sinclair's work[23], there were only two intermetallic phases identified to be $Mg_{41}Nd_5$ and Mg_3Nd in all diffusion zones while MgNd phase was absent.

In our work, at the Mg-Nd interface, as is shown in Figure 2, the Mg_3Nd phase grew into the thickest one maybe due to the wider homogeneity range than the $Mg_{41}Nd_5$ phase. The MgNd phase was not observed in any of the Mg-Nd interfaces. This could be possibly owe to the unfavorable nucleation conditions for this phase, or the higher diffusion coefficients of surrounding phases than the MgNd phase[22].

Sarah et al. [24] studied the phase layers' growth and interdiffusion in the Mg-Zn system by solid-to-solid diffusion couples. The annealing was carried out at 295 °C, 315 °C and 325 °C for 384, 168 and 120 hours, respectively. At the temperature of 295 and 315 °C, intermetallic phases of Mg_2Zn_{11}, $MgZn_2$ and Mg_2Zn_3 can be detected by field emission-SEM equipped with XEDS while the $Mg_{51}Zn_{20}$ phase can only be detected when the couple was annealed at 325 °C.

In our work, $MgZn_2$ phase layer is the thickest at most Mg-Zn interfaces, $Mg_{12}Zn_{13}$ and Mg_2Zn_{11} phases become very thin after annealing at 300 °C for 400 hours, as is shown in Figure 3. Compared to the work of Sarah et al. [24], $Mg_{12}Zn_{13}$ phase was detected in the Mg-Zn diffusion couple for the first time. The absence of $Mg_{12}Zn_{13}$ phase in the work of Sarah et al. can be explained by the shorter annealing time than ours. This phenomenon was probably caused by the higher melting temperature of $MgZn_2$ phase. As the annealing time extended, all the elements diffused sufficiently and the phases of $Mg_{12}Zn_{13}$ and Mg_2Zn_{11} grew thicker, as is shown in Figure 4.

In the Nd-Zn binary system, the Nd_2Zn_{17}, $Nd_{13}Zn_{58}$, $NdZn_3$, $NdZn_2$ phase were detected at the interface of Nd and Zn and the $Nd_{13}Zn_{58}$ is the thickest one. The absence of phases may be caused by the lower annealing temperature and shorter annealing time. Furthermore, the tiny composition differences between intermetallic phases make it more difficult to identify them.

In the Zn-Zr binary system, only αZn_3Zr and $Zn_{39}Zr_5$ phases were formed. It was probably caused by the very low diffusion mobility of Zr at 300 °C. Longer annealing time may be helpful to solve this problem.

Analyses to the Mg-Nd-Zn intersection is very complex due to variety of intermetallic phases in every binary system, the existence of unproved ternary phases and lots of interfaces between pure elements and intermetallic phases. In our work, three ternary phases were detected at different interfaces, that proved that diffusion multiple technique is a suitable tool to explore the ternary phases. More ternary phases (if exist) will generate if the annealing time lengthen or the layout of the Mg, Nd and Zn blocks changed.

A lot of cracks were found when the diffusion multiple was annealed for 600 hours, which was probably due to the volatilization of Zn, Mg and the release of stress after incision of the cylinder. At the same time, the sample preparation process can also lead to the generation of cracks because the intermetallic phases are often brittle.

Summary

Diffusion multiple is a useful and high-efficiency technique to study the phase equilibrium and intermetallic phases. It is especially suitable for the easily to volatile or oxidized elements because the diffusion elements were sealed in a metallic cylinder.

A lot of intermetallic phases including $Mg_{12}Zn_{13}$, Mg_2Zn_3, $MgZn_2$, Mg_2Zn_{11}, $Mg_{41}Nd_5$, Mg_3Nd, $NdZn_2$, $NdZn_3$, $Nd_{13}Zn_{58}$, Nd_2Zn_{17}, αZn_3Zr, $Zn_{39}Zr_5$ and T_1~T_3 Mg-Nd-Zn ternary phases were generated by solid-solid reaction in the Mg-Nd-Zn-Zr diffusion multiple sample. Phase morphology and the phase interface were observed via SEM. The phenomenon of phases absence was discussed combines with the results of other researchers.

Acknowledgement

The authors thank Instrumental Analysis and Research Center of Shanghai University for their support of materials testing and research. This work was financially supported by the National Natural Science Foundation of China (51074103, 51222402).

References

[1] L. Wen*, et al.*, "Effect of extrusion ratio on microstructure and mechanical properties of Mg–Nd–Zn–Zr alloys prepared by a solid recycling process," *Materials Characterization,* 59 (11) (2008), 1655-1660.

[2] J.-W. Chang*, et al.*, "Effect of heat treatment on corrosion and electrochemical behaviour of Mg–3Nd–0.2Zn–0.4Zr (wt.%) alloy," *Electrochimica Acta,* 52 (9) (2007), 3160-3167.

[3] Y. Zong*, et al.*, "Comparison of biodegradable behaviors of AZ31 and Mg–Nd–Zn–Zr alloys in Hank's physiological solution," *Materials Science and Engineering: B,* 177 (5) (2012), 395-401.

[4] X. Zheng*, et al.*, "Formability, mechanical and corrosive properties of Mg–Nd–Zn–Zr magnesium alloy seamless tubes," *Materials & Design,* 31 (3) (2010), 1417-1422.

[5] P. H. Fu, *et al.*, "Chemical composition optimization of gravity cast Mg-yNd-xZn-Zr alloy," *Materials Science and Engineering: A,* (496) (2008), 177-188.
[6] X. Gao, *et al.*, "Transmission electron microscopy of Zr-Zn precipitate rods in magnesium alloys containing Zr and Zn," *Philosophical Magazine Letters,* 89 (1) (2009), 33-43.
[7] Y. P. Ren, *et al.*, "Isothermal section of Mg–Zn–Zr ternary system at 345 ° C," *Calphad,* 35 (3) (2011), 411-415.
[8] C. Zhang, *et al.*, "Thermodynamic modeling and experimental investigation of the magnesium–neodymium–zinc alloys," *Intermetallics,* 19 (11) (2011), 1720-1726.
[9] J.-C. Zhao, *et al.*, "A diffusion multiple approach for the accelerated design of structural materials," *MRS bulletin,* 27 (04) (2002), 324-329.
[10] J. C. Zhao, *et al.*, "A diffusion-multiple approach for mapping phase diagrams, hardness, and elastic modulus," *JOM,* 54 (7) (2002), 42-45.
[11] J.-C. Zhao, "The diffusion-multiple approach to designing alloys," *Annual Review of Materials Research,* 35 (1) (2005), 51-73.
[12] J.-C. Zhao, "Application of the Diffusion-Multiple Approach in Alloy Development," in *AIP Conference Proceedings*, 2012.
[13] J. T. Mason and P. Chiotti, "The Nd-Zn Phase Diagram," *Metallurgical Transactions* 3(1972), 2851-2855.
[14] P. Ghosh, *et al.*, "Critical assessment and thermodynamic modeling of Mg-Zn, Mg-Sn, Sn-Zn and Mg-Sn-Zn systems," *Calphad-Computer Coupling of Phase Diagrams and Thermochemistry,* 36 (2012), 28-43.
[15] H. Okamoto, "Mg-Nd," *Journal of Phase Equilibria and Diffusion,* 28 (4) (2007), 405-405.
[16] H. Okamoto, "Zn-Zr (Zinc-Zirconium)," *Journal of Phase Equilibria and Diffusion,* 28 (2) (2007), 236-237.
[17] X. J. Liu, *et al.*, "Thermodynamic assessments of the Sm–Zn and Nd–Zn systems," *Journal of Alloys and Compounds,* 468 (1-2) (2009), 115-121.
[18] G. B. Gibbs, "Diffusion layer growth in a binary system," *Journal of Nuclear Materials,* 20 (3) (1966), 303-306.
[19] G. V. Kidson, "Some aspects of the growth of diffusion layers in binary systems," *Journal of Nuclear Materials,* 3 (1) (1961), 21-29.
[20] M. Kajihara, "Analysis of kinetics of reactive diffusion in a hypothetical binary system," *Acta Materialia,* 52 (5) (2004), 1193-1200.
[21] Y. Xu, *et al.*, "Analysis of interdiffusion of Dy, Nd, and Pr in Mg," *Journal of Materials Research,* 16 (11) (2001), 3287-3292.
[22] B. Sarah, *et al.*, "Intermetalllic growth and interdiffusion in the Mg-Nd system," in *Mg2012: 9th Intermational Conference on Magesium Alloys and their Applications*, Vancouver, BC, Canada, 2012, 417-421.
[23] E. A. Sterling and C. W. Sinclair, "Experiments on the microstructure of diffusion bonded magnesium-neodymium samples," in *Mg2012: 9th International conference on Magnesium Alloys and their Applications*, Vancouver, BC, Canada, 2012, 1061-1068.
[24] B. Sarah, *et al.*, "Diffusion couple investigation of the Mg-Zn system," in *TMS (The Minerals, Metals & Materials Society)*, Orlando, FL, USA, 2012, 323-327.

Magnesium Technology 2014

Symposium: Light-Metal Matrix (Nano)-Composites

Magnesium Technology 2014

SYMPOSIUM: LIGHT-METAL MATRIX (NANO)-COMPOSITES

Microstructure-Property Relationships I

Papers in this section have been presented in a separate symposium at the 2014 TMS Annual Meeting organized by Dr. W. Sillekens and Prof. D.G. Eskin. This section was co-edited by the symposium organizers and all papers were peer reviewed.

Magnesium Technology 2014
Edited by: Martyn Alderman, Michele V. Manuel, Norbert Hort, and Neale R. Neelameggham
TMS (The Minerals, Metals & Materials Society), 2014

AN INSIGHT INTO PROCESSING AND CHARACTERISTICS OF MAGNESIUM BASED COMPOSITES

Manoj Gupta[1], Wai Leong Eugene Wong[2]
[1]Department of Mechanical Engineering, National University of Singapore, 9 Engineering Drive 1, Singapore 117576
[2]School of Mechanical & Systems Engineering, Newcastle University International Singapore, 180 Ang Mo Kio Ave 8, Singapore 569830

Keywords: Magnesium, Nanocomposites, Mechanical Properties

Abstract

Magnesium is the lightest structural metal with tremendous potential in weight critical engineering and biomedical applications. To pave the way of magnesium based materials into multiple applications, it is important that: a) they can be processed cost effectively and using the existing infrastructure used for processing conventional light metal such as aluminum and b) there be enough formulations with wide range of combination of properties.
In the first part of this paper, cost effective processing using disintegrated melt deposition technique and microwave assisted powder metallurgy technique will be highlighted. In the second part, mechanical characteristics of magnesium based formulations primarily focusing on nanocomposites will be presented with an aim to address their suitability in engineering applications. Finally this paper will conclude illustrating the current efforts that are made to replace aluminum alloys with magnesium based formulations.

Introduction

Magnesium is the lightest structural metal and possesses similar melting temperature and yield strength to the widely used aluminium metal as shown in Table I [1, 2]. Magnesium has high specific stiffness and strength with tremendous potential for weight critical applications in the aerospace, automotive, electronics and military sectors. However, the limited ductility due to its hexagonal close-packed structure, low elastic modulus and melting temperature limits the use of pure magnesium for load bearing applications. These limitations are being resolved through the development of new magnesium alloys and composites [3-7]. In recent years, magnesium is also increasingly attractive for biomedical applications due to its biocompatibility, biodegradability and similar density, elastic modulus and tensile strength to human cortical bone [8, 9].
To pave the way of magnesium based materials into multiple applications, it is important that: a) they can be processed cost effectively and using the existing infrastructure used for processing conventional light metal such as aluminium and b) there be enough formulations with a wide range of combination of properties to cater to the requirements for various applications.
Liquid casting and powder metallurgy (PM) techniques are the main manufacturing routes used to produce magnesium alloys and composites. Various manufacturers and research groups have employed different methods of incorporating alloying elements or reinforcements, heating and consolidation processes and secondary processing such as rolling or extrusion to synthesize magnesium based materials. Common methods used to improve the mechanical properties of magnesium include alloying and the addition of stiffer and stronger ceramic and/or metallic reinforcements. Aluminum and zinc are the main alloying elements added to magnesium to enhance the mechanical properties leading to the development of many AZ alloys. Recently, calcium, lithium and rare earth elements have also been added to magnesium to increase the range of magnesium formulations [3, 4]. Studies on magnesium composites comprised of the addition of ceramic materials such as oxides, nitrides, carbides and borides [5-7]. However, the addition of micron-size reinforcements generally leads to deterioration in the ductility of the magnesium matrix.
In recent years, studies related to magnesium nanocomposites have increased rapidly from less than 10 publications in 1995 to over 450 publications in 2013 based on data extracted from Sciencedirect and shown graphically in Figure 1. Review articles on magnesium nanocomposites have revealed that the addition of nano-reinforcements helped to improve the mechanical properties of magnesium without any adverse effect on the ductility [10-13]. In addition, the use of a small volume fraction of nano-size reinforcements have been shown to produce results comparable or even superior to that of MMCs reinforced with higher volume fraction of micron size reinforcements [10-13].
This paper provides a subset of the work carried out on magnesium nanocomposites, focusing on pure magnesium based systems reinforced with various ceramic and metallic reinforcements.

Table I. Selected Properties of Pure Light Metals, Stainless Steel and Human Bone.

Property	Magnesium	Aluminum	Titanium	Stainless Steel	Natural Bone
Density (g/cm^3)	1.74	2.70	4.50	7.65-8.00	1.8-2.1
Melting point (°C)	649	660	1667	1538*	-
Crystal structure (20°C)	HCP	FCC	HCP	BCC	-
Elastic Modulus (GPa)	45	69	105	193-204	3-20
Specific stiffness (E/ρ)	25.9	25.6	23.3	24-26.7	-
Yield Strength (MPa)	69-100	55-110	103	170-1650	130-180
Specific strength (σ/ρ)	40-57	20-41	23	21-215	-

* Melting temperature of iron

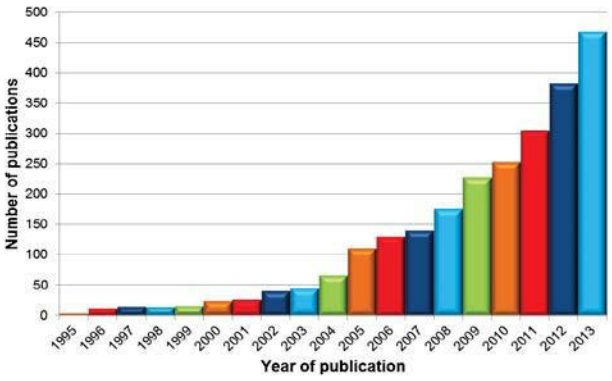


Figure 1. Number of magnesium nanocomposites related publications from 1995 to 2013.

Processing Techniques

Magnesium composites containing nano-size particulates are typically processed using similar methodologies as composites reinforced with micron size reinforcements, either by liquid based or solid based processing techniques. For liquid based processing, the reinforcement can be added together with the magnesium metal into the crucible prior to heating or added later to the molten magnesium melt. Upon reaching the molten stage, various methods are used to disperse the reinforcements to achieve a uniform distribution before casting. The most common method involves agitating the molten melt with a mechanical impeller [5-7] while others have made use of ultrasonic energy to disperse the nano-size particles [14]. For solid based processing, the reinforcement is usually mixed with magnesium particles by simple blending or by mechanical alloying. The mixed powders are pressed to form green compacts and then sintered using resistance heating or microwave heating [15]. Friction stir processing has also been employed to distribute nano-size reinforcements by modification of the surface of magnesium alloy [16]. Secondary processing such as extrusion or rolling may be employed to further consolidate or shape the composite materials. Further details on different processing methodologies can be found in several review papers on magnesium composites [5-7, 10-12].

This paper will focus in detail on two processing techniques: 1) Disintegrated Melt Deposition (DMD) and 2) Blend-Press-Sinter using Hybrid Microwave Sintering that have been employed by the research group to successfully synthesize lightweight aluminum and magnesium nanocomposites with enhanced properties.

Disintegrated Melt Deposition Technique

DMD is a unique cost-effective technique that brings together the advantages of spray processing and conventional casting, utilizing higher superheat temperatures and lower impinging gas jet velocities to produce bulk composite material. Synthesis of nano-particulate reinforced magnesium composites using DMD technique involved heating the magnesium chips/turnings and the reinforcement powder in a multi-layered arrangement to 750°C under an inert argon gas atmosphere in a graphite crucible with a resistance heating furnace. The crucible is equipped with an arrangement for bottom pouring. Upon reaching the superheat temperature, the molten slurry is normally stirred for 5 minutes at approximately 450 revolutions per minute using a twin blade (pitch 45°) mild steel impeller to facilitate the incorporation and uniform distribution of reinforcement particulates in the metallic matrix and to ensure temperature homogeneity. The impeller is coated with Zirtex 25 (86% ZrO_2, 8.8% Y_2O_3, 3.6% SiO_2, 1.2% K_2O and Na_2O, and 0.3% trace inorganic) to avoid iron contamination of the molten metal. The melt is then released through a 10 mm diameter orifice at the base of the crucible. The composite melt is disintegrated by two jets of argon gas orientated normal to the melt stream. The argon gas flow rate is maintained at 25 L min^{-1}. The disintegrated composite melt slurry is then subsequently deposited onto a metallic substrate. Preform of 40 mm diameter is obtained following the deposition stage. A schematic diagram of the DMD setup is shown in Figure 2. The synthesis of pure aluminum and magnesium alloys have been carried out using steps similar to those employed for the reinforced materials except that no reinforcement particulates were added.

The deposited magnesium ingot is machined to 35 mm diameter and hot extruded at 350°C using an extrusion ratio ranging from 12.25:1 to 25:1 on a 150 ton hydraulic press to produce rods of diameter of 10 mm to 7 mm respectively. The extruded rods are subsequently prepared according to respective international standards for further characterization studies.

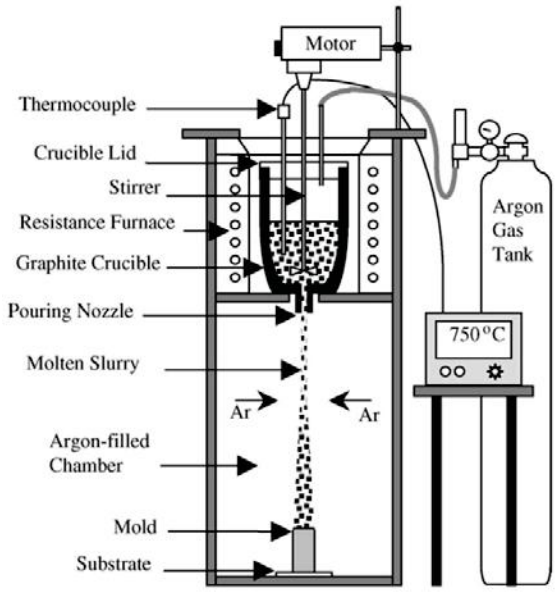


Figure 2. Schematic diagram of disintegrated melt deposition setup.

The advantages of DMD technique include uniform distribution of reinforcements, fine equiaxed grains and low porosity due to the faster solidification of the atomized melt leading to improved properties. Also, high yield of deposited material is obtained with minimal wastage. The main limitation of DMD technique, which is similar to stir casting, lies in the difficulty to incorporate high volume fraction of reinforcements (>30% for micro-size and >3% for nano-size reinforcements) due to increase in viscosity of the melt making it difficult to stir and homogeneously distribute the reinforcements. However, this limitation is not critical as many research studies have shown that there exists an optimum volume fraction of reinforcements to be added. Exceeding this optimum value will lead to deterioration in properties of the composites. The optimum value is often reached before the limits of the DMD technique.

Blend-Press-Sinter using Hybrid Microwave Sintering

Pure magnesium powder and nano-size reinforcements are weighed carefully and blended in a RETSCH PM-400 planetary ball mill machine using a speed of 200 rpm for 30 to 60 minutes. No grinding balls or process control agent are used during blending step. The blended powders are uniaxially compacted using a pressure of 97 bar (~50 tons) to billets (40 mm height with 35 mm diameter) in a 100 ton press. The compacted billets are sintered using an innovative microwave assisted hybrid sintering technique for a pre-calibrated duration to a temperature near the melting point of magnesium in a 900W, 2.45GHz SHARP microwave oven using SiC as the microwave susceptor material. Loosely packed SiC powder (contained within a microwave transparent ceramic crucible) absorbs microwave energy readily at room temperature and is heated up quickly, providing the radiant heat to heat the billet externally while the compacted billet absorbs microwaves and is heated from within. This hybrid heating method results in a more uniform temperature gradient within the billet and circumvents the disadvantage of heating using either conventional heating or microwaves only. The exterior of the crucible was thermally insulated using alumino-silicate fiber insulation board to reduce heat loss from the surface. Temperature calibration of the sintering setup was performed initially using a sheathed K-type thermocouple in order to determine the appropriate heating duration for sintering of magnesium. Upon reaching the required temperature, the microwave power is switched off and the billet is allowed to cool to room temperature without any holding time under ambient atmospheric condition in the absence of inert protective atmosphere. The schematic diagram of the experimental setup is shown in Figure 3. The sintered billets are subsequently hot extruded under identical conditions as billets produced by DMD technique.

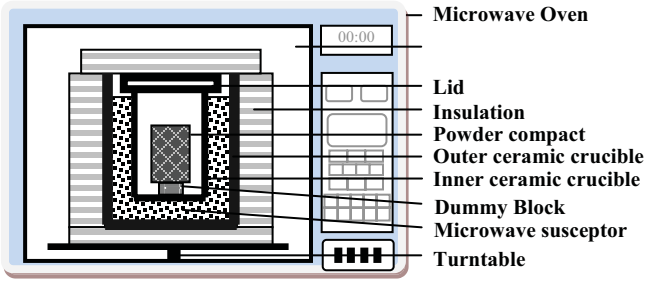


Figure 3. Schematic diagram of microwave heating setup

Table II. Analysis of energy consumption between conventional and microwave sintering.

Material	Heating Unit	Power (kW)	Time, hr (min)	Energy used (kWh)	Energy Savings
Mg	Tube furnace (Carbolite CTF15/75)	6	2.83 (170)	17	96%
	Microwave (Sharp magnetron)	1.6*	0.42 (25)	0.7	

*Based on AC power required for the operation of the magnetron

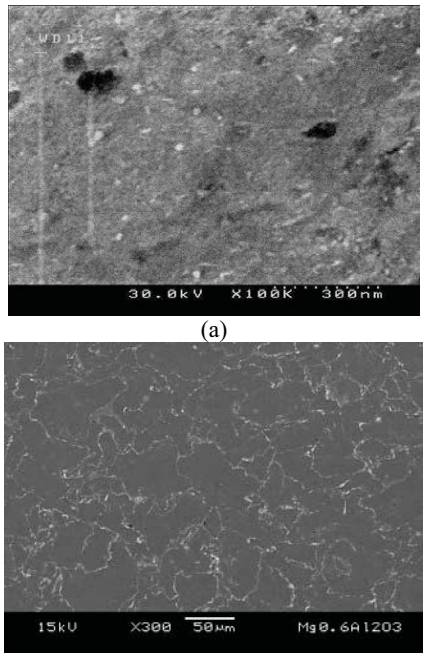
The use of microwave sintering leads to a significant reduction of more than 80% in the processing time compared to conventional sintering (slower heating rate and long dwelling time required) without compromising the end properties of the material as shown in Table II [17]. Due to the reduction in processing time, significant energy savings can be obtained which is economically viable for industries and environmentally friendly in the reduction of CO_2 emissions. Other advantages of microwave sintering are the higher sintering temperature and rapid sintering of the metallic materials which will better activate the mass transport mechanisms and thereby improve the sintered properties [18] and the viability of sintering highly reactive magnesium metal at high temperature without the need for an inert protective atmosphere unlike in conventional sintering.

Characteristics of Magnesium Nanocomposites

Different types of reinforcements have been utilized to synthesize magnesium nanocomposites and can be categorized as ceramic (include oxides, carbides and carbon nanotubes), metallic and intermetallics. For this paper, selected pure magnesium based nanocomposites reinforced with oxides, carbides, CNT and metallic reinforcements processed using DMD and hybrid microwave sintering will be discussed.

Microstructure Studies

Both processing techniques can be used to synthesize magnesium composites with near theoretical densities and low porosity (<1%) following extrusion [19-28].
Microstructural characterization on the grain size of composite samples revealed an equiaxed structure and a reduction in grain size of the matrix with the addition of higher volume fraction of reinforcements as shown in Table III. The reduction in grain size of the matrix can be attributed to: (i) the ability of nano-size particulates to nucleate magnesium grains during recrystallization and (ii) the restricted growth of the magnesium grains due to grain boundary pinning.



(a)
(b)
Figure 4. Representative micrographs showing the distribution of nano-Al_2O_3 in $MgAl_2O_3$ nanocomposites synthesized by (a) DMD technique and (b) hybrid microwave sintering.

The main difference in microstructure between the two processing methods lies in the distribution of reinforcements (see Figure 4). For DMD method, there is a reasonably uniform distribution of nano-size particulates in the matrix due to the stirring and atomization of the molten melt (refer to Figure 4a). For microwave sintered samples, nano-sized particulates are found decorating the particle boundaries of the matrix in a network fashion as the nano-particulates are usually found on the surface of the matrix powder after mixing and sintering process will not redistribute the particulates into the grain (refer to Figure 4b).

Microhardness

The addition of nano-size reinforcements leads to an increase in the hardness of the magnesium matrix as shown in Table III (All reinforcement addition is in vol% except for CNT). The increase in microhardness can be attributed to the presence of harder ceramic or metallic particulates as reinforcements, which acts as a constraint to localized matrix deformation during indentation.

Tensile Properties

In general, improvements were observed in the mechanical properties of the magnesium nanocomposites when compared to the monolithic magnesium regardless of the processing routes. However, it may be noted that the amount of improvement in tensile properties is dependent on the processing route and the type of reinforcements. For example for Mg/Al_2O_3 nanocomposites, a maximum improvement of 80% in 0.2% yield strength (0.2%YS) and 42% in ultimate tensile strength (UTS) are observed for DMD synthesized composites while hybrid microwave sintered Mg/Al_2O_3 nanocomposites displayed a more modest improvement of 33% in 0.2%YS and 27% in UTS [19,23]. Amongst the DMD processed magnesium nanocomposites, the largest improvement in 0.2%YS and UTS were observed in $MgZrO_2$ nanocomposites but ductility was reduced. $MgAl_2O_3$ nanocomposites displayed the best improvement in ductility.

For hybrid microwave sintered nanocomposites, all the nanocomposites reinforced with ceramic oxides and carbides displayed an improvement in strength except for $MgZrO_2$ nanocomposites due to clustering of ZrO_2 particulates. Improvements in ductility were observed for all Mg nanocomposites reinforced with ceramic oxides and carbides reinforcements. The largest improvement in strength was observed with the addition of metallic Cu nanoparticles with an improvement of 104% in 0.2%YS and 70% in UTS in Mg/0.6Cu nanocomposites but ductility was reduced.

Addition of metallic reinforcements increases strength but reduces ductility of composites while ceramic reinforcements increase ductility but strength improvement is less than that of metallic reinforcements. Hence, hybrid (Ceramic+Metallic) Mg nanocomposites were investigated and found to provide an optimum combination of strength and ductility surpassing that of conventional Mg+Ceramic or Mg+Metallic nanocomposites [24,28]. In particular, Mg ($0.3ZrO_2$+0.7Cu) and Mg ($0.7Y_2O_3$+0.6Ni) hybrid nanocomposites were able to achieve significant improvement in both strength and ductility over $MgZrO_2$ and MgY_2O_3 nanocomposites.

The improvement in 0.2%YS and UTS can be attributed to Orowan strengthening, grain refinement and internal strain and thermal stresses between reinforcements and matrix. Orowan strengthening occurs due to the presence of nano-size reinforcements which hinders the movement of dislocations. Grain refinement arises due to the presence of reinforcing particles which acts as nucleation sites during solidification or recrystallization and the pinning of grain boundaries resulting in limited grain growth. The strain and CTE mismatch between the matrix and the nano-size particles contributes to an increase in dislocations around the interfacial region between the matrix and the particles thus strengthening the material. The improvement in ductility for ceramic oxides and carbides may be due to the activation of non-basal slip systems but is dependent on the distribution of nano-particulates and volume fraction of reinforcements added. For metallic reinforcements, the reduction in ductility is due to formation of increasing presence of harder metallic reinforcements and the formation of intermetallic phases.

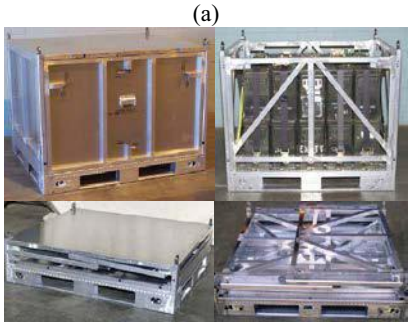
Comparison of the Mg nanocomposites synthesized by DMD and hybrid microwave sintering with Mg nanocomposites synthesized by ultrasonic casting and conventional PM technique revealed the efficacy of these two methods in producing Mg nanocomposites with enhanced properties.

Applications

The development of new magnesium nanocomposites with enhanced properties over traditional magnesium alloys and composites has provided new possibilities for application. Current commercial applications of magnesium and its alloys are provided in Table IV [11, 31]. Potential applications of magnesium nanocomposites for military application include engine blocks and gear housings for military ground vehicles, ballistic protection and personnel protection (helmet and body armor) [11]. In addition, other potential applications of magnesium nanocomposites include unmanned aerial vehicle (UAV) parts, truck trailer and unit load device for aviation and military as shown in Figure 5. For medical applications, magnesium nanocomposites may be suitable for use as biodegradable orthopedic and cardiovascular implants, microclips and suture wires [9]. This will require judicious selection of alloying elements and reinforcements that are suitable with the human body.



(a)



(b)

Figure 5. (a) Unit load device used for aircrafts and [32](b) Joint Modular Intermodal Container (JMIC) [33].

Table III. Selected grain size and mechanical properties of magnesium nanocomposites.

Materials	Processing method	Grain Size μm	Microhardness HV	0.2%YS (MPa)	UTS (MPa)	Ductility (%)	Ref
Pure Mg	DMD	49±8	40±0	97±2	173±1	7.4±0.2	19
Mg/0.22Al_2O_3		11±3	51±1	146±5 (↑50%)	207±11 (↑20%)	8.0±2.3	
Mg/0.66Al_2O_3		14±4	56±1	170±4 (↑75%)	229±2 (↑32%)	12.4±2.1	
Mg/1.11Al_2O_3		14±4	66±1	175±3 (↑80%)	246±3 (↑42%)	14.0±2.4	
Mg/0.22ZrO_2		8±2	47±1	186±2 (↑92%)	248±4 (↑43%)	4.7±0.2	20
Mg/0.66ZrO_2		5±2	51±1	221±5 (↑128%)	271±6 (↑57%)	4.8±0.7	
Mg/1.11ZrO_2		2±1	55±1	216±4 (↑123%)	250±6 (↑45%)	3.0±0.2	
Mg/0.5Y_2O_3		16±4	51±0	141±7	223±5	8.5±1.6	21
Mg/1.0Y_2O_3		12±4	56±0	151±5	222±4	6.8±0.5	
Mg/2.0Y_2O_3		12±3	56±0	162±10	227±11	7.0±0.5	
Mg/0.3wt%CNT		-	-	128±6	194±9	12.7±1.6	22
Mg/1.3wt%CNT		-	-	140±2	210±4	13.5±2.0	
Mg/1.6wt%CNT		-	-	121±5	200±3	12.2±2.7	
Pure Mg	Hybrid microwave sintering	27±7	40±1	116±11	168±10	6.1±2.0	23
Mg/0.3Al_2O_3		-	48±3	119±7 (↑3%)	175±8 (↑4%)	7.5±0.2	
Mg/0.6Al_2O_3		24±4	54±3	130±5 (↑12%)	180±7 (↑7%)	7.4±0.3	
Mg/1.0Al_2O_3		15±3	60±4	154±5 (↑33%)	213±12 (↑27%)	6.3±0.4	
Mg/0.3ZrO_2		24±7	40±1	85±8	139±8	8.1±1.6	24
Mg/0.6ZrO_2		29±3	42±2	117±11	182±14	9.4±2.7	
Mg/1.0ZrO_2		25±4	42±2	98±6	158±12	8.6±2.2	
Mg/0.17Y_2O_3		19±3	38±0	144±2	214±4	8.0±2.8	25
Mg/0.7Y_2O_3		18±3	45±2	157±10	244±1	8.6±1.2	
Mg/0.3SiC		-	40±1	132±14	194±11	6.3±1.0	26
Mg/0.5SiC		-	42±1	144±12	194±10	7.0±2.0	
Mg/1.0SiC		-	43±2	157±22	203±22	7.6±1.5	
Mg/0.3Cu		17±5	49±1	188±13 (↑62%)	218±11 (↑30%)	5.9±1.1	27
Mg/0.6Cu		15±4	52±2	237±24 (↑104%)	286±8 (↑70%)	5.4±1.2	
Mg/1.0Cu		15±4	60±3	194±17 (↑67%)	221±17 (↑32%)	2.9±0.4	
Mg(0.3ZrO_2+0.7Cu)		9±2	48±1	196±16	249±8	8.2±1.1	24
Mg(0.6ZrO_2+0.7Cu)		11±3	50±1	139±22	193±21	11.4±2.9	
Mg(0.7Y_2O_3+0.3Ni)		9±3	54±4	221±7	244±1	9.0±0.9	28
Mg(0.7Y_2O_3+0.6Ni)		6±2	60±4	232±8	262±6	9.5±0.9	
Mg(0.7Y_2O_3+1.0Ni)		5±2	63±4	228±8	272±2	5.5±0.7	
Pure Mg	Ultrasonic casting	33±11	29±1	93	198	5.9	14
Mg/1.0SiC		22±4	39±2	133	224	8.1	
Pure Mg	PM + hot extrusion	20	-	215	230	7.0	29
Mg/3.0SiC (mixed)		20	-	180	220	3.0	
Mg/3.0SiC (milled)		1	-	220	280	2.0	
Pure Mg	PM + hot extrusion	23±6	-	134±11	190±10	4.6±0.6	30
Mg/0.5Al		17±8	-	218±16	271±11	6.2±0.9	
Mg/1.0Al		16±6	-	185±9	226±12	3.3±1.0	

* Number in parenthesis refers to percentage increment over monolithic magnesium

Table IV. Applications of magnesium alloys [11,31].

Industry	Applications
Aerospace	Rudder pedal assembly; seat arm support; transmission and gear housings.
Automotive	Engine block; crankcase; engine valve covers; gearbox housing; instrument panels; steering components; radiator supports; door and lift gate inners; seat structures (for car, bus and train); rear sub frame and fairing support bracket (for motorcycle); roof components; steering wheel armature; shifter support bracket.
Electronics	Notebook casing; mobile phones and media player casing; digital camera casing.
Others	Chair; racing bike frame and wheels; power tools housing and gear case; wheelchair mounting system; housings for medical equipment; cleats for soccer shoes; screws for fastening ice skate blades; golf club crown; racing skis; binocular frame; archery eyepiece components; truss structures for lighting and sound systems in theatres; hand cycles and wheelchairs; joint protectors in racing suits.

References

1. W.D. Callister and D.G. Rethwisch, Materials Science and Engineering (John Wiley & Sons, 2011).
2. E.A. Brandes and G.B. Brook, ed., Smithells light metals handbook (Oxford, Butterworth-Heinemann, 1998).
3. G. Neite et al., "Magnesium-Based Alloys," *Materials Science and Technology*, Vol. 8, ed. R.W. Cahn, P. Haasen, E.J. Kramer (Weinheim: Wiley-VCH, 2005), 113-212.
4. Z. Yang et al., "Review on Research and Development of Magnesium Alloys," *Acta Metallurgica Sinica (English Letters)*, 21 (2008), 313-328.
5. D.J. Lloyd, "Particle reinforced aluminum and magnesium matrix composites," *International Materials Reviews*, 39 (1994), 1-23.
6. H.Z. Ye and X.Y. Liu, "Review of recent studies in magnesium matrix composites," *Journal of Materials Science*, 39 (2004), 6153-6171.
7. F. Moll and K.U. Kainer, "Particle Reinforced Magnesium Alloys," *Magnesium Alloys and Technology*, ed. K.U. Kainer (Weinheim: Wiley-VCH, 2002), 197-217.
8. M.P. Staiger et al., "Magnesium and its alloys as orthopedic biomaterials: A review," *Biomaterials*, 27 (2006), 1728-1734.
9. N. Li and Y. Zheng, "Novel Magnesium alloys Developed for Biomedical Applications: A Review," *Journal of Material Science and Technology*, 29 (2013), 489-502.
10. S.C. Tjong, "Novel Nanoparticle-Reinforced Metal Matrix Composites with Enhanced Mechanical Properties," *Advanced Engineering Materials*, 9 (2007), 639-652.
11. V.H. Hammond, "Magnesium Nanocomposites: Current Status and Prospects for Army Applications," (Report ARL-TR-5728, September 2011)
12. H. Dieringa, "Properties of magnesium alloys reinforced with nanoparticles and carbon nanotubes: a review," *Journal of Materials Science*, 46 (2011), 289-306.
13. J. Ferguson et al., "On the strength and strain to failure in particle-reinforced magnesium metal-matrix nanocomposites (Mg MMNCs)," *Materials Science and Engineering A*, 558 (2012), 193-204.
14. H. Choi et al., "Characterization of hot extruded Mg/SiC nanocomposites fabricated by casting," *Journal of Materials Science*, 46 (2011), 2991-2997.
15. M. Gupta, W.L.E. Wong, *Microwaves and Metals* (Singapore: John Wiley & Sons Asia 2007).
16. Y. Morisada et al., "Nanocrystallized magnesium alloy – uniform dispersion of C_{60} molecules," *Scripta Materialia*, 55 (2006), 1067-1070.
17. W.L.E. Wong and M. Gupta, "Characteristics of Aluminum and Magnesium Based Nanocomposites Processed Using Hybrid Microwave Sintering," *Journal of Microwave Power and Electromagnetic Energy*, 44 (2010), 14-27.
18. R.M. German, *Sintering Theory and Practice* (New York: John Wiley & Sons, 1996).
19. S.F. Hassan and M. Gupta, "Development of high performance magnesium nanocomposites using solidification processing route," *Materials Science and Technology*, 20 (2004),1383-1388.
20. S.F. Hassan and M. Gupta, "Effect of Nano-ZrO2 Particulates Reinforcement on Microstructure and Mechancial Behavior of Solidification Processed Elemental Mg," *Journal of Composite Materials*, 41 (2007), 2533-2543.
21. C.S. Goh et al., "Properties and deformation behavior of Mg-Y_2O_3 nanocomposites," Acta Materialia, 55 (2007), 5115-5121.
22. C.S. Goh et al., "Simultaneous enhancement in strength and ductility by reinforcing magnesium with carbon nanotubes," *Materials Science and Engineering A*, 423 (2006), 153-156.
23. W.L.E. Wong and M. Gupta, "Improving overall mechanical performance of magnesium using nano-alumina reinforcement and energy efficient microwave assisted processing route," *Advanced Engineering Materials*, 9 (2007), 902-909.
24. K.S. Tun et al., "Tensile and Compressive Responses of Ceramic and Metallic Nanoparticle Reinforced Mg Composites," *Materials*, 6 (2013), 1826-1839.
25. K.S. Tun and M. Gupta, "Improving mechanical properties of magnesium using nano-yttria reinforcement and microwave assisted powder metallurgy method," *Composites Science and Technology*, 67 (2007), 2657-2664.
26. W.L.E. Wong and M. Gupta, "Simultaneously Improving Strength and Ductility of Magnesium using Nano-size SiC Particulates and Microwaves," *Advanced Engineering Materials*, 8 (2006), 735-740.
27. W.L.E. Wong and M. Gupta, "Development of Mg/Cu nanocomposites using microwave assisted rapid sintering," *Composites Science and Technology*, 67 (2007), 1541-1552.
28. K.S. Tun and M. Gupta, "Development of magnesium/(yttria+nickel) hybrid nanocomposites using hybrid microwave sintering: Microstructure and tensile properties," *Journal of Alloys and Compounds*, 487 (2009), 76-82.
29. H. Ferkel and B.L. Mordike, "Magnesium strengthened by SiC nanoparticles," *Materials Science and Engineering A*, 298 (2001), 193-199.
30. X.L. Zhong, W.L.E. Wong and M. Gupta, "Enhancing strength and ductility of magnesium by integrating it with aluminum nanoparticles," *Acta Materialia*, 55 (2007), 6338-6344.
31. International Magnesium Association, Magnesium showcase, http://www.intlmag.org/mgshow.html (Last accessed 25 Sep 2013).
32. Wikipedia (Image of unit load device from http://en.wikipedia.org/wiki/File:Germanwings_Container_03.jpg, last accessed 25 Sep 2013).
33. G. Bender, "Modular Ordnance Transportation Unit Loads" (Report DoD Energetics Center, Naval PHST Center, 27 April 2009).

Magnesium Technology 2014
Edited by: Martyn Alderman, Michele V. Manuel, Norbert Hort, and Neale R. Neelameggham
TMS (The Minerals, Metals & Materials Society), 2014

HOT EXTRUDED CARBON NANOTUBE REINFORCED MAGNESIUM MATRIX COMPOSITES AND ITS MICROSTRUCTURE, MECHANICAL AND CORROSION PROPERTIES

Harun Mindivan[1], Arife Efe[2], E.Sabri Kayali[3]
[1]Atatürk University, Department of Metallurgy and Materials Engineering,
25240, Erzurum, TURKEY
[2]Atatürk University, Department of Nanoscience and Nanoengineering,
25240, Erzurum, TURKEY
[3]Istanbul Technical University, Department of Metallurgy and Materials Engineering
34469 Maslak, Istanbul, TURKEY

Keywords: CNTs, Composite, Corrosion, Hot extrusion, Magnesium chips, Mechanical properties

Abstract

Carbon nanotube (CNT) reinforced magnesium (Mg) matrix composite rod was successfully fabricated by mechanical ball milling followed by hot extrusion processes. CNTs used were multi-wall carbon nanotubes (MWCNTs). The starting Mg chips were ball-milled under argon atmosphere for 3 h to coat the surface of Mg chips with the pretreated MWCNTs. The CNT-coated Mg chips were then mixed with aluminum (Al) powder at the compositions of Mg–6 wt.% Al–x wt.% CNT (x = 0.5, 1, 2 and 4). The mixture was cold compacted and finally hot extruded.

The distribution of CNTs was analyzed using a Scanning Electron Microscopy (SEM). Furthermore, the effect of CNTs and their amounts on the mechanical properties and corrosion behavior of the Mg composite were studied. Microstructural analysis revealed that the CNTs were well dispersed at the chip surfaces and were aligned with direction of the extrusion in the composites. As CNT content increased, chip size, density and electrical conductivity of the Mg composites decreased, a relatively constant value was obtained in the microhardness but a reduction was determined in compressive strength. While an increase up to 2 wt.% in CNT content reduced the corrosion rate of the composites, the corrosion rate increased at higher addition rates.

Introduction

Carbon nanotubes (CNTs) are attractive materials for development of high thermal conductivity, light-weight, and high-strength metallic composites. In recent years, the unique properties and high aspect ratio of the CNT have led to its combination with other materials in order to obtain CNT-metal composites with excellent physical and mechanical properties [1]. Mg and its alloys have also drawn interest as the matrix material because they have a great potential in numerous applications, such as automotive, material handling and aerospace equipment's due to their low density and high strength/weight ratio [2]. CNTs have attracted attention increasingly as super reinforcements for Mg alloy gradually over the last five years and studies have been mainly focused on investigating their contribution to the enhancement of the mechanical performance and corrosion behavior of structure components [3-6]. Despite many interesting studies conducted on composites with CNTs, the fabrication of CNT reinforced Mg matrix composites especially at high CNT concentrations is still far from being commercialized because of three major difficulties; the CNTs dispersion in the matrix, consolidation with defect-free CNT, and superior bonding at the CNT/matrix interface. For the stir cast Mg-CNT composites, the distribution of CNTs is always inhomogeneous in a Mg matrix due to the non-wetting nature of CNTs to molten Mg [1, 7]. In order to improve the distribution of CNTs, to obtain homogeneous properties and enable the efficient use of the properties conventional powder metallurgy techniques (compaction and sintering) have been widely preferred and studied [8, 9]. However, number of studies published literature on this subject is limited. A two-step process was applied in this study. In the first step, a mechanical ball milling process was performed to pre-disperse CNTs on the Mg chips. Then the chips with the well dispersed CNTs on their surface were mixed with pure Al powder. The composite mixture was subsequently consolidated by cold pressing and hot extrusion. The fact that hot extrusion process is a good way to achieve higher material performance is remarkable. In this study, Mg composites containing 0.5, 1, 2 and 4 wt.% CNT were fabricated by the mechanical ball milling and hot extrusion process, and their density, electrical, mechanical and corrosion properties were investigated.

Experimental

CNTs used were multi-wall carbon nanotubes (MWCNTs) with average diameter of 9.5 nm and length of 1.5 μm. Before preparation process of composites, as-prepared CNTs were purified by washing with HNO_3/H_2SO_4 (1:1 by volume) for 30 min in an ultrasonic bath at 80 °C. The pretreated CNT was collected and washed to pH 5.0 by doubly distilled water. Afterwards, the pretreated MWCNTs were dried at 100°C in an oven for 24 h.

The starting Mg chips (purity >99.9%) with sizes of (5–10) × (1.5) × (0.8) mm were ball-milled under argon atmosphere at 300 rpm for 3 h with a ball to powder weight ratio (BPR) of 32 to coat the surface of Mg chips with the pretreated MWCNTs. The Mg chips were used as a media for observing the CNT's movement during hot extrusion. Since Mg alloy with 5 wt.% Al provided the optimum combination of strength and ductility [10], the present authors used Al powders as a binder in recycling of Mg chips containing CNTs through hot extrusion process. The CNT-coated Mg chips were then mixed with Al powder (27 μm) at the compositions of Mg–6wt.% Al–x wt.% CNT (x = 0.5, 1, 2 and 4). In order to consolidate the prepared mixtures, firstly they were filled into a cylindrical container with a diameter of 30 mm and pressed under 1600 MPa pressure at room temperature. Then, the cold pressed samples were subjected to hot extrusion at 350°C with an extrusion ratio of 9.

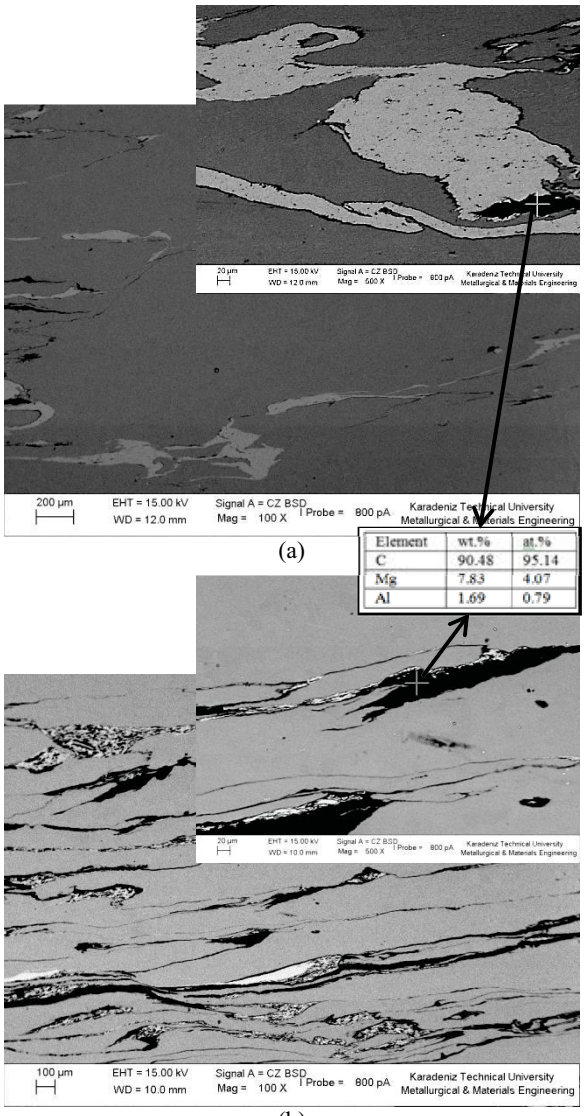
In accordance with the standard metallographic procedure, which includes a grinding process up to 1200 mesh and a polishing process with alumina solution conducted on Mg/CNT composites,

microstructural characterization studies were conducted on metallographically polished monolithic and composite extruded samples using a Scanning Electron Microscopy (SEM), X-Ray Diffraction (XRD) analysis, density and electrical conductivity measurements. The densities of the composites were determined by means of the Archimedes principle. Hocking AutoSigma 3000 DL was utilized to measure electrical conductivities of the samples. Furthermore, the degree of CNT distribution in the composites was investigated by the SEM equipped with an Energy Dispersive X-ray spectrometer (EDX) analyzer. The mechanical properties of the Mg/CNT composites were determined by carrying out microhardness measurements and compression tests. Microhardness was measured on Wolpert HMV2 microhardness tester at indentation load of 200 g with a Vickers indenter. At least ten successive measurements were performed for the Mg/CNT composites containing different amounts of CNTs. Round samples were tested by a Dartec Universal testing machine at a crosshead speed of 1 mm/min to determine the compressive properties of the Mg/CNT composite. The results of the compression tests were compiled by taking average value of three samples

The corrosion tests were evaluated by both weight loss measurements and electrochemical tests. Each data point for both weight loss measurement and electrochemical test represented the mean of three different measurements. For the weight loss-measurement test, square shaped samples with an average size of 2 mm x 2 mm were immersed in 3.5 wt.% NaCl solution in a Pyrex glass cell exposed to atmospheric air for 12 h. The amount of solution in the baker was estimated by considering the surface area of the samples as 0.3 ml/mm^2. The samples, which were taken out of the solution at certain intervals during the corrosion experiments, were ultrasonically cleaned in distilled water and alcohol, and then they were weighed using a 0.1 mg-sensitive electronic scale. The normalized weight loss values of the samples were calculated in the unit of g/cm^2 by dividing the weight loss of the each sample by their initial total surface area. For the electrochemical corrosion tests, samples were attached to a copper wire and embedded into an epoxy resin holder, to allow an open surface area of 0.15 cm^2. The potentiodynamic polarization measurement was carried out using a Gamry model PC4/300 mA potentiostat/galvanostat controlled by a computer with DC 105 Corrosion analysis software. All the corrosion experiments were performed at room temperature in a glass cell containing 3.5 wt.% NaCl solution. Each polarization experiment was carried out holding the electrode for 45 min. at open circuit potential (E_o) to achieve steady-state. Potentiodynamic polarization curves were generated by sweeping the potential from cathodic to anodic direction at a scan rate of 1 mVs^{-1}, starting from − 0.1 up to + 0.4 V. Corrosion potentials (E_{corr}) and corrosion current densities (i_{corr}) were calculated using a Tafel type fit in the software. Finally, the surface images of the corroded samples were examined using the SEM in order to determine morphology of the developed corrosion.

Result and Discussion

Figure 1 illustrates metallurgical microstructures of the Mg composites with 0.5 wt.% and 4.0 wt.% CNT. All micrographs were taken from the plane parallel to the extrusion direction. Chips in the composites exhibited a lamellar structure and the dark areas were detected around the chip surface. Most of the dark areas were present throughout the extrusion direction because of the severe plastic deformation of the Mg layers with recombination of CNTs during hot extrusion. Presence of coated CNTs between the layers was confirmed by carrying out EDX analysis as shown in Fig. 1. Microstructural observations on the polished sections revealed a reaction phase that appeared gray, in contrast to the dark areas. This gray phase was present in all the composites. It was identified by its XRD patterns (Fig. 2) as $Mg_{17}Al_{12}$, which was consistent with several other studies [4, 10, 11]. Figure 1 clearly illustrates that an increase in intensity of darker phase (CNTs and porosities) with increasing CNT content was also found due to entanglement of CNTs during ball milling process and higher CNT loading revealed network of CNT along the Mg chips as shown in Fig. 1 (b). After the hot extrusion, the CNTs could not redistribute within the matrix even though the chips elongated. Large amounts of CNTs exacerbated the dark areas.



(a)

(b)

Figure 1. SEM images and EDX results on the Mg composites with (a) 0.5 wt.% CNT and (b) 4 wt.% CNT.

Figure 2 presents the XRD patterns of the Mg alloy without CNT and composites with different CNTs. The distinct Mg, $Mg_{17}Al_{12}$, and MgO diffraction peaks of the samples are clearly evident in this figure. The three sets of XRD spectra for the extruded

samples with different CNT percentages showed similar patterns. The intensities of the diffraction peaks from Mg were comparatively higher in the composites with CNT. Meantime, the peak intensities corresponding to $Mg_{17}Al_{12}$ in the Mg composite with 4 wt.% CNT were relatively higher compared to the Mg composite with 0.5 wt.% CNT. With the increasing of CNT content, the volume fraction of $Mg_{17}Al_{12}$ phase increased obviously. It is clearly seen from Fig. 2 that the XRD patterns of the extruded samples showed a sharp peak belonging to MgO, indicating that all the samples were somewhat oxidized. The samples were oxidized at high level when the CNT content exceeded 0.5 wt.%, because of an increase in area of the main peak of MgO.

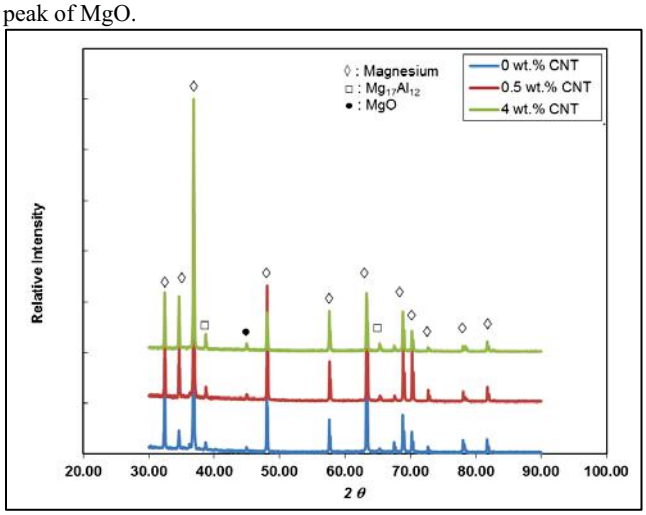


Figure 2. XRD patterns of the composites with different CNTs.

Figure 3 illustrates the changes in the density and electrical conductivity of the Mg/CNT composites over Mg sample prepared by the same route. It is evident from Fig. 3 that the increasing CNT content resulted in a lower electrical conductivity. On the other hand, the density of the composites increased when the CNT content was below 1 wt.%, and decreased when the CNT content exceeded 1 wt.%. In metals or alloys, the electrical conductivity is mainly caused by free electrons. If the defects, such as the porosities, interfaces, particle boundaries and free surfaces remain in the composites, the electrical conductivity is adversely affected. As shown in Fig. 3, the decrease in the density of the Mg/CNT composites with increasing CNT content may be attributed to the formation of the porosities and the network of CNTs between the Mg chips. In addition, the magnitude of the chip size in the composite with increasing CNT content decreased as shown in Fig. 1. As seen in Fig. 2, the composites were partially oxidized, resulting in an increase in the magnitude of the interfaces (Fig. 1). Although the CNT has excellent electrical conductivity, these results are disadvantageous for the electron mobility.

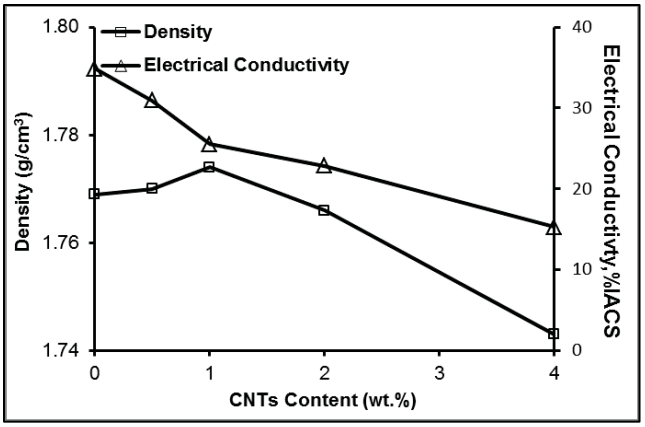


Figure 3. Density and electrical conductivity of the composite as a function of its CNTs content.

Figure 4 illustrates the variation in microhardness and compressive strength of composites with increasing content of CNT. The microhardness of the composites did not alter notably as a result of CNT addition as shown in Fig. 4. However, the compressive strength of the composites decreases very rapidly with addition of CNTs and this decrease in the compressive strength for the composites with higher loadings of CNT can be due to the fact that: 1) a decrease in density (Fig. 3) reduces the loaded area; 2) an increase in the magnitude of the interface because of a reduction in the chip size with the quantity of CNTs leads to increase the magnitude of the defects and the chips adjacent to the CNTs might be prone to form micro-voids. During the hot extrusion of Mg sample without CNTs, atoms diffused over the entire area of contact between the chips. This mechanism was not effective in bonding of the chips in the Mg/CNT composites to each other and hence the compressibility and deformability of the composites reduced at CNT loadings.

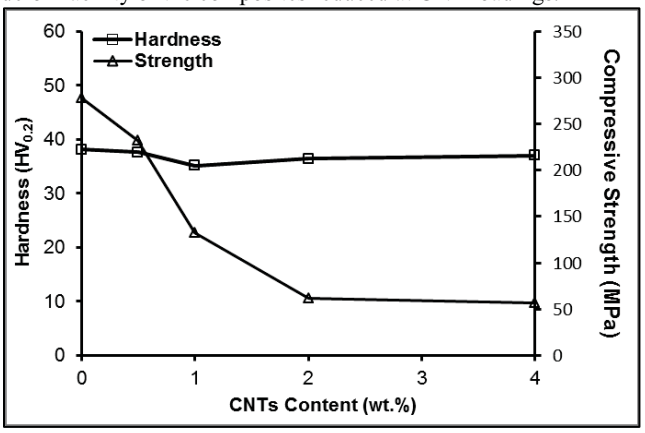


Figure 4. Variation of microhardness ($HV_{0.2}$) and compressive strength of the composites as a function of its CNTs content.

Figure 5 presents the results of corrosion rate of the corroded samples as a function of its CNT content after their immersion tests. The corrosion rate decreased from $6x10^{-6}$ g/cm^2 h to 3 x 10^{-6} g/cm^2 h as 0.5 or 2 wt.% CNT was added to Mg alloy, which corresponded to 2 times higher corrosion resistance; however the corrosion rate increased when the CNT content was above 2.0 wt.%. Severe corrosion happened in the Mg composite containing 4 wt.% CNT so that the composite collapsed partially after performing immersion process for 12 h. Figure 6 illustrates potentiodynamic polarization curves as a function of CNT

content. Obviously, the 0.5 wt.% CNT addition showed the best corrosion resistance in contrast with the Mg alloy without CNT and the composite with 4 wt.% CNT. This indicates a good correlation between the results from immersion testing and potentiodynamic polarization measurements. Compared to published studies [6, 12], the higher corrosion rate in the Mg/CNT composites was attributed to a large potential of the galvanic cells formed between Mg matrix and CNTs. Based on galvanic corrosion principles, the cathode-to-anode area ratio is one of the predominant factors governing the rate of galvanic corrosion [13]. Funatsu et al. [6] reported that the gradient potential formation by Al solid soluting into Mg matrix in AZ61B/CNT composites could obstruct the galvanic corrosion phenomenon. The Mg/CNT composites showed significantly improved corrosion properties already at small CNT contents. However, it was likely that large amounts of CNTs increased the corrosion rate due to the presence of the Mg/CNT interfaces breaking the continuity of the Mg matrix and creating preferential locations for corrosion attack.

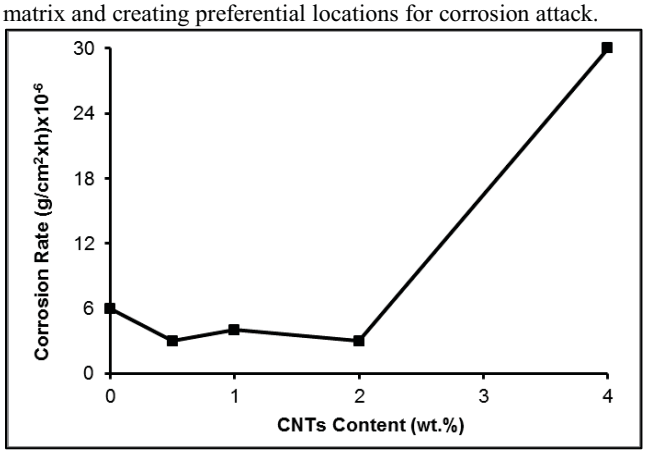


Figure 5. Change of corrosion rates of the corroded samples as a function of CNT content from the immersion tests.

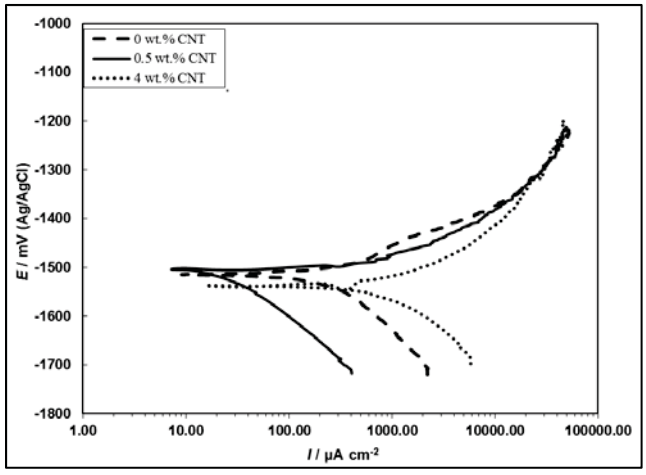
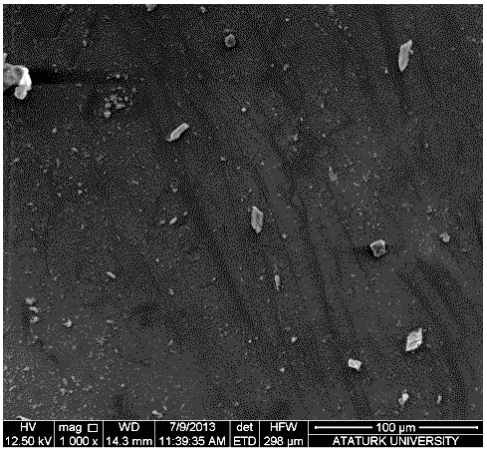
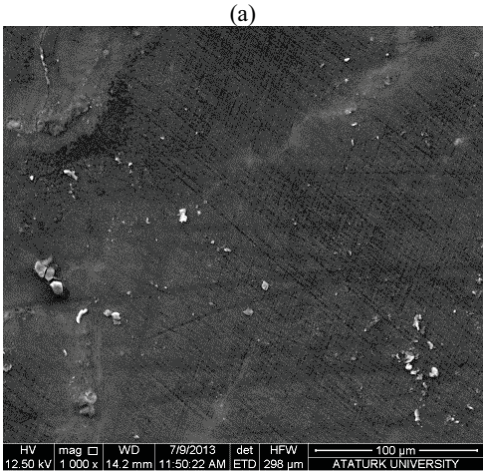


Figure 6. Potentiodynamic polarisation curves for the Mg alloy without CNT and the composites with 0.5 and 4 wt.% CNTs.

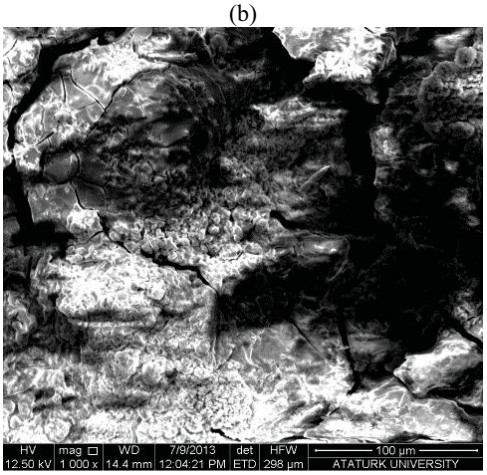
As seen from the appearance of the samples (Fig. 7), some severe cracks and pores existed in the composite with 4 wt.% CNT, whereas corrosion was not obvious for the Mg alloy without CNT and the composite with 0.5 wt.% CNT.



(a)



(b)



(c)

Figure 7. SEM surface morphologies of (a) the Mg alloy without CNT and the Mg composites containing (b) 0.5 wt.% CNT and (c) 4 wt.% CNT after potentiodynamic polarization.

Conclusions

The conclusions of the this study conducted on the hot extruded Mg–6 wt.% Al–x wt.% CNT composite, with CNT content varying between 0 wt.% and 4 wt.% are as follows:

1. The combination of mechanical ball milling, cold press and hot extrusion processes for obtaining new CNT-reinforced Mg composite provided a unique opportunity to produce light-weight

metallic composites and the CNTs on the Mg chips were present throughout the extrusion direction.
2. Addition of wt. % CNT to the Mg alloy did not alter the microhardness; however, the increase in the CNT content caused an extreme decrease in the chip size, density, electrical conductivity, and compression strength.
3. While the addition of CNT decreased the corrosion rate of the composite up to 2 wt. %, the corrosion rate increased at higher addition rates.

Acknowledgements

The authors are grateful for the support received from the Scientific and Technical Research Council of Turkey under Contract No. 108M574, and the Research Fund of Ataturk University under Contract No. BAP 2012/119. The authors would also like to thank the Metallurgical and Materials Engineering Department of Istanbul Technical University for their technical support.

References

1. S. R. Bakshi, D. Lahiri and A. Agarwal, "Carbon Nanotube Reinforced Metal Matrix Composites – A Review", *International Materials Reviews*, 55(1) (2010), 41-64.
2. M. E. Alama, S. Han, Q. B. Nguyen, A. M. S. Hamoudaa, M.Gupta, "Development of New Magnesium Based Alloys and their Nanocomposites", *Journal of Alloys and Compounds*, 509 (2011), 8522– 8529.
3. Y. Shimizu, S. Miki, T. Soga, I. Itoh, H. Todoroki, T. Hosono, K. Sakaki, T. Hayashi, Y.A. Kim, M. Endo, S. Morimoto, A. Koide, "Multi-Walled Carbon Nanotube-Reinforced Magnesium Alloy Composites", *Scripta Materialia*, 58 (2008), 267–270.
4. S.J. Yoo, S.H. Han and W.J. Kim, "Magnesium Matrix Composites Fabricated by Using Accumulative Roll Bonding of Magnesium Sheets Coated with Carbon-Nanotube Containing Aluminum Powders", *Scripta Materialia,* 67 (2012) 129–132.
5. M. Paramsothy, X.H. Tan, J. Chan, R. Kwok, M. Gupta, "Carbon Nanotube Addition to Concentrated Magnesium Alloy AZ81: Enhanced Ductility with Occasional Significant Increase in Strength", *Materials and Design*, 45 (2013), 15–23.
6. K. Funatsu, H. Fukuda, R. Takei, J. Umeda, K. Kondoh, "Quantitative Evaluation of Initial Galvanic Corrosion Behavior of CNTs Reinforced Mg–Al Alloy", *Advanced Powder Technology*, 24 (2013), 833–837.
7. Q. Li, A. Viereckl, C.A. Rottmair, R. F. Singer, "Improved Processing of Carbon Nanotube/Magnesium Alloy Composites", *Composites Science and Technology*, 69 (2009), 1193–1199.
8. H. Fukuda, K. Kondoh, J. Umeda, B. Fugetsu, "Fabrication of Magnesium Based Composites Reinforced with Carbon Nanotubes Having Superior Mechanical Properties", *Materials Chemistry and Physics*, 127 (2011), 451–458.
9. F. Sun, C.Shi, K. Y. Rhee, N. Zhao, "In Situ Synthesis of CNTs in Mg Powder at Low Temperature for Fabricating Reinforced Mg Composites", *Journal of Alloys and Compounds*, 551 (2013), 496–501.
10. M. A. Thein, L. Lu, M.O. Lai, "Effect of Milling and Reinforcement on Mechanical Properties of Nanostructured Magnesium Composite", *Journal of Materials Processing Technology*, 209 (2009), 4439–4443.
11. D. Singh, C. Suryanarayana, L. Mertus, R.-H. Chen, "Extended homogeneity range of intermetallic phases in mechanically alloyed Mg–Al alloys", *Intermetallics*, 11 (2003), 373–376
12. Q. Li, M. C. Turhan, C. A. Rottmair, R. F. Singer and S. Virtanen, "Influence of MWCNT Dispersion on Corrosion Behavior of their Mg Composites", *Materials and Corrosion*, 63(5) (2012), 384-387.
13. R.Jia, C. Yan, F. Wang, "Infuence of Al Content on the Atmospheric Corrosion Behaviour of Magnesium-Aluminum Alloys", *Journal of Materials Science & Technology*, 25 (2) (2009), 225-229.

Magnesium Technology 2014
Edited by: Martyn Alderman, Michele V. Manuel, Norbert Hort, and Neale R. Neelameggham
TMS (The Minerals, Metals & Materials Society), 2014

HARDENING AND SOFTENING PROCESSES IN AN AJ51 MAGNESIUM ALLOY REINFORCED WITH SHORT SAFFIL FIBRES

Zuzanka Trojanová, Gergely Farkas, Kristián Máthis and Pavel Lukáč
Department of Physics of Materials, Faculty of Mathematics and Physics, Charles University in Prague,
Ke Karlovu 5, CZ-121 126 Praha 2, Czech Republic

Magnesium alloy, Metal matrix composite, Strengthening, Twinning, Residual stresses

Abstract

AJ51 alloy (5Al-0.6Sr balance Mg in wt.%) reinforced with short δ-Al_2O_3 fibres (Saffil®) has been deformed in compression at temperatures between 23 and 300 °C. The yield stress and the maximum stress decrease with increasing testing temperature. The influence of reinforcement on both characteristic stresses falls down with increasing temperature. Various strengthening terms were taken into account. Individual strengthening terms were calculated and compared with experimental results. Acoustic emission signal recorded during plastic deformation of the matrix alloy and composite was used to elucidate details of the plastic deformation in the matrix alloy and composite. Residual thermal stresses, generated due to a great difference between the thermal expansion coefficients of the alloy and ceramic reinforcement, in the composite matrix at different strain levels were estimated using neutron diffraction method.

Introduction

Magnesium alloys reinforced with short ceramic fibres combine good properties of both types of materials: a high stiffness of ceramic fibres and plasticity of metallic matrix [1]. Such materials have unique and desirable mechanical and physical properties [2]. Metal matrix composites (MMC) have higher stiffness [3, 4], higher strength [5, 6], better fatigue properties [7] and lower thermal expansion [8] than their metallic counterparts. On the other hand, plasticity of MMCs is lower, especially at lower temperatures. In spite of many attempts to reveal deformation mechanisms in composites and their link to microstructure of such materials, there is no comprehensive explanation of the role of the reinforcing phase in the plastic deformation of magnesium alloy based composites. New Mg-Al-Sr alloys are being developed with the aim to find cast alloys with good creep resistance and good strength alloys and replace expensive rare earth alloying elements with some cheaper one [9]. Further possibility how to improve mechanical properties of the Mg-Al-Sr alloys is to add the reinforcing phase and prepare a composite. Such materials have great potential in automotive, high performance defence and aerospace applications.
The main objective of this study is to investigate mechanical properties of an AJ51 magnesium alloy reinforced with short Saffil fibres with the aim to reveal the main features of the deformation mechanisms. Mechanical tests, acoustic emission (AE) and neutron diffraction (ND) were used.

Experimental

AJ51 alloy (the nominal chemical composition: Mg–5Al–0.6Sr in wt.%) was reinforced with δ-Al_2O_3 short fibres (Saffil). The preform consisting of Al_2O_3 short fibres showing a 2D planar isotropic fibre distribution and a binder system (containing Al_2O_3 and starch) were preheated to 1000 °C and then inserted into a preheated die (300-360 ºC). Preforms were preheated and then infiltrated by the liquid alloy using two-stage application of the pressure. The mean fibre length and fibre diameter (measured after squeeze casting) were ~78 μm and ~3 μm, respectively. Volume fraction of fibres was estimated to be (17.9 ± 0.3) vol% Al_2O_3. Cylindrical samples were cut so that the stress axis was parallel to the fibres plane. Compression tests were carried out in an INSTRON universal testing machine with the displacement control at a nominal strain rate of 8.3×10^{-5} s^{-1} in a wide temperature range from room temperature (RT) to 300 °C. Fig. 1 shows microstructure of the composite studied taken from the section perpendicular to the fibres plane. The grain size exhibited in the non-deformed state for composite d_1 = (44±13) μm and d_2 = (110±30) μm for the alloy prepared with the same technology of the squeeze casting.

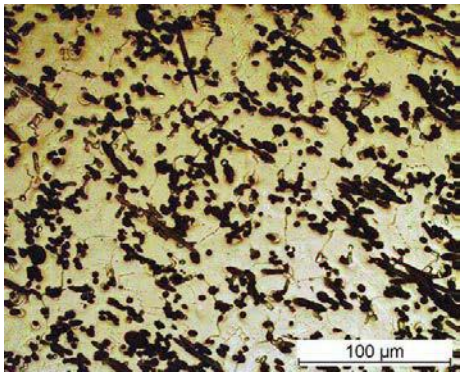


Fig. 1: Microstructure of the as cast sample (section perpendicular to the fibres plane).

The computer controlled DAKEL-XEDO-3 AE system was used to monitor AE on the basis of two-threshold-level detection, which yields a comprehensive set of AE parameters involving count rates N_{C1} and N_{C2} (count number per second [10]) at two threshold levels (giving total AE count and burst AE count).
The *in-situ* neutron diffraction tests were performed at high resolution two axis stress/strain diffractometer TKSN-400 at steady state reactor LVR-15.

Results and discussion

Strengthening effect of fibres

True stress-true strain curves obtained for the composite at various deformation temperatures are presented in Fig. 2. It can be seen that only at lower temperatures strain hardening is observed. At higher temperatures, the maximum stress = the ultimate compression strength (UCS) is observed at lower strains. Ductility

at low temperatures exhibits only several percent, at 200 and 300 °C about 10 or 20%, respectively. The values of the compressive yield stress (CYS) estimated for various temperatures are given in Table 1. For comparison, the values of the CYS estimated for the unreinforced alloy are also presented. The reinforcing effect of fibres estimated at room temperature exhibits 267 MPa and it decreases with increasing testing temperature up to 156 MPa at 300 °C.

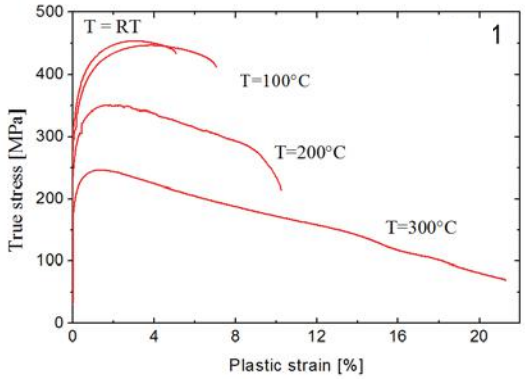


Fig. 2: Deformation curves measured at various temperatures.

	AJ51 alloy		AJ51+ Al_2O_3	
T (°C)	CYS (MPa)	UCS (MPa)	CYS (MPa)	UCS (MPa)
23	87	249	354	454
100	81	250	337	447
200	71	170	290	350
300	57	124	213	246

Table 1: The yield stress and ultimate compression strength estimated for the unreinforced alloy and composite.

Mechanism	
Load transfer	$\sigma_{LT} = \sigma_A\left[1+\frac{(L+t)\chi}{4L}\right]f+\sigma_A(1-f)$
Thermal mismatch	$\rho_T = \frac{Bf\Delta\alpha\Delta T}{b(1-f)}\frac{1}{t}$
Enhanced disl. density	$\Delta\sigma_D=\alpha_1\psi Gb(\rho_T+\rho_G)^{1/2}$
Geometrical dislocations	$\rho_G = \frac{f\,8\varepsilon_p}{bt}$
Orowan strengthening	$\Delta\sigma_{OR}=\frac{Gb}{\Lambda}+\frac{5}{2\pi}Gf\varepsilon_p$
Residual stresses	$\langle\sigma_m\rangle_{max}=\frac{2}{3}\sigma_y ln\left(\frac{1}{f}\right)\frac{f}{1-f}$
Hall-Petch strengthening	$\Delta\sigma_{GS}=K_y\left(d_2^{-1/2}-d_1^{-1/2}\right)$

Table 2: Individual contributions to strengthening following from the presence of the reinforcing phase.

σ_{LT}	ρ_T	ρ_G
L fibre length,t fibre thickness, σ_A alloy stress, χ=L/t	b Burgers vector, B=10 for fibres, $\Delta\alpha\Delta T$ thermal strain	ε_p plastic strain f volume fraction of fibres
σ_{OR}	<σ>max	$\Delta\sigma_{GS}$
Λ distance between fibres	σ_y yield stress in the matrix	K_y Hall-Pech constant, d grain size

Table 3: Meaning of the quantities introduced in Table 2.

The difference between the stress necessary for deformation of the composite and the stress acting in the unreinforced alloy is a complex value containing various contributions due to the presence of fibres: (a) load transfer of the applied stress to the well bonded fibres [11] ($\Delta\sigma_{LT}$); (b) increase of the dislocation density accommodating the thermal stresses in the particle/matrix interface which are generated due to the difference of the coefficients of thermal expansion ($\Delta\alpha$) between matrix and particles [12] ($\Delta\sigma_{CTE}$); (c) increase in grain boundary area due to grain refinement – the Hall-Petch strengthening ($\Delta\sigma_{GS}$); (d) Orowan strengthening ($\Delta\sigma_{OR}$); (e) generation of geometrically necessary dislocations which accommodate the fibre/matrix interface during plastic deformation [13] ($\Delta\sigma_{GEO}$) and (f) residual thermal stresses $\Delta\sigma_{TH}$ (remaining in the matrix when stresses exceeding the yield stress are accommodated with newly created dislocations [8]. The stress σ_C necessary for the composite deformation may be expressed as

$$\sigma_C = \sigma_A + \Delta\sigma_{LT} + \Delta\sigma_{OR} + \Delta\sigma_{CTE} + \Delta\sigma_{GS} + \Delta\sigma_{GEO} + \Delta\sigma_{TH}\,. \quad (1)$$

Note that the plus sign has in this case only formal meaning, because indeed we do not know exactly, how to combine the individual strengthening terms [14]. The models briefly summarised in Table 2 (meanings of symbols used in Table 2 are given in Table 3) show that a composite strengthening depends on the geometrical parameters of reinforcements (size and shape of fibres or particles, volume fraction of the reinforcement, interparticle distance), on the physical properties of the components (thermal expansion coefficients, bonding at the interface matrix-reinforcement), on the microstructure and mechanical properties of the components. Contributions to the strengthening were calculated using model relationships introduced in Table 2. Results are summarised in Table 4. For calculation of the individual terms, the following constants were used: α(AJ51) = 26x10^{-6} K^{-1} (the own measurements), α(Saffil) = 6x10^{-6} K^{-1} [15], the shear modulus G = 17GPa, b = 3.2x10^{-10}m, K_y = 0.28 MPam$^{-3/2}$ [16], Taylor factor ψ [17], α_1=0.35 [18].

σ_{LT} (MPa)	ρ_T (m^{-2})	ρ_G (m^{-2})	$\Delta\sigma_D$ (MPa)	σ_{OR} (MPa)
63	2.8x10^{13}	3.0x10^{12}	64	3
<σ>max (MPa)	**$\Delta\sigma_{GS}$ MPa)**	**σ_m (MPa)**	**σ_{exp} (MPa)**	**σ_{theor} (MPa)**
22	16	87	354	255

Table 4: Contributions of various strengthening mechanism to the yield stress of the composite at room temperature.

The effect of the load transfer is based on the existence of shear stresses at the interface between the matrix and the reinforcing phase fibres. It is calculated considering the perfect or nearly perfect bonding between the both components of the composite. The contribution to the load transfer can be calculated according to

$$\Delta\sigma_{LT} = \sigma_A \frac{(L+t)\chi}{4L} f \ , \qquad (2)$$

using the stress σ_A estimated for the unreinforced alloy. Because in this case all fibres are not aligned into the stress direction, they are randomly distributed in the fibres plane, only a component of this stress was applied $\Delta\sigma_{LT}.\beta$, where β is a mean value of the direction cosines.

From Table 4 it is obvious that the load transfer and enhanced dislocation density may significantly increase the composite flow stress. Other strengthening mechanisms are less important for the composite strength. Comparing the calculated value of the total stress with the experimental one it follows that the measured value is higher. The difference is approximately 100 MPa. This estimation is surprising because in the case of other magnesium alloys reinforced with short Saffil fibres the agreement was better and usually the calculated values of the composite CYS were higher than corresponding experimental values [19]. This fact may have these reasons:

i) It is not clear how to combine particular strengthening terms. In principle synergetic action may be considered.

ii) Models for composite strengthening consider the uniform distribution of the reinforcing phase fibres (or particles). As it can be seen in Fig. 1 this condition is not fulfilled.

iii) Contributions to strengthening were not exactly calculated. Probably the equations used are too simple and it is necessary to take into account more aspects. Thermal stresses induced into matrix and load transfer depend strongly on the quality of the interface bonding [20]. It is possible that the residual thermal stresses and load transfer are higher that the calculated values.

To check the possibility that the residual thermal stresses are higher, neutron diffraction (ND) measurements were performed. Strain/stress measurement by neutron diffraction is a non-destructive technique that uses the diffraction of a beam of thermal neutrons to determine the atomic spacing within a small gauge volume inside polycrystalline materials.

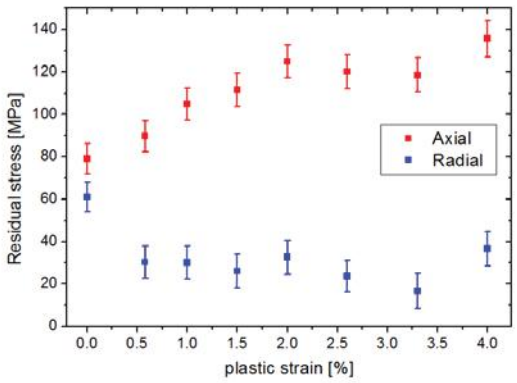


Fig. 3: Residual stresses estimated in axial and radial directions.

The strain dependence of residual stresses estimated using ND in both axial and radial directions in the cylindrical sample are shown in Fig. 3. Performing correction using value of the residual thermal stress estimated using ND the resulting theoretical stress necessary for deformation of the composite at room temperature is 311 MPa that is closer to an experimental value of 354 MPa.

Deformation mechanisms

It is generally accepted that during straining of a composite, deformation occurs in the matrix and short ceramic fibres deform only elastically. Deformation of the *hcp* AJ51 matrix alloy may be realised by the dislocation motion in basal and non-basal planes as well as by mechanical twinning. The hardening processes are connected with the storage of dislocations on non-dislocation and dislocation type obstacles. In the case of composites, different obstacles for the dislocation motion in the matrix should be considered. There are a) non-dislocation obstacles such as grain boundaries, precipitates, short fibres and b) dislocations in different slip systems – the dislocation forest. On the other hand, the moving dislocations can cross slip and/or locally climb; these are mechanisms leading to a decrease in the dislocation density. Introducing the reinforcing phases into the metal matrix influences not only the densities of the thermally formed and geometrically necessary dislocations, but also the dislocations stored at reinforcements during deformation. Considering these effects, the total dislocation density in composites can be written:

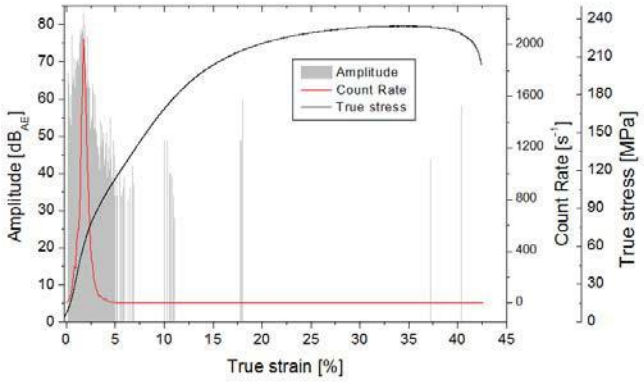
$$\rho_{total} = \rho_T + \rho_G + (\rho_S + \rho_a), \qquad (3)$$

where ρ_S is the statistically stored dislocation density in unreinforced matrix, ρ_a is the diminished part of the statistically stored dislocations due to the addition of a reinforcing phase. The strengthening in the matrix is attributed to the deformation resistance induced by the reinforcing phase. According to the Taylor relation, the contribution to the total stress due to the presence of dislocations in the matrix may be written:

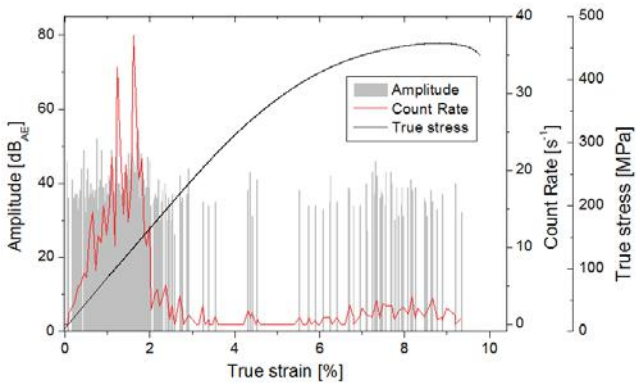
$$\Delta\sigma_D = \alpha_1 \psi G b \left(\rho_T + \rho_G + \rho_S + \rho_a\right)^{1/2} . \qquad (4)$$

This higher matrix dislocation density as well as the reinforcement/matrix interfaces can provide high diffusivity paths in a composite. Such possibility may play an important role in the softening process(es).

To reveal details of the deformation mechanisms operating during straining of AJ51 alloy reinforced with short Saffil fibres AE measurements have been used. The true stresses plotted against the true strain together with the strain variation of the AE count rates and amplitudes of the AE signals are shown in Fig 4 for the matrix alloy (a) and composite (b). The strain dependence of the AE signal has its characteristic course usually observed in metallic polycrystals with the pronounced maximum at the beginning of the straining followed with the rapid decrease of the AE. Observed peak of the AE signal at the low strain can be described to the twin formation and collective motion of dislocations [21]. On the other hand, during deformation of composite, two different maxima of the AE activity are observed. A higher activity of the AE at the beginning of the straining decreases with increasing strain. The second lower local maximum is observed at a higher step of straining before the composite failure.

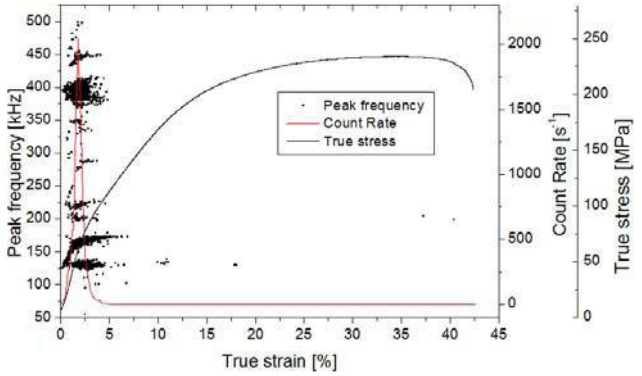


a)

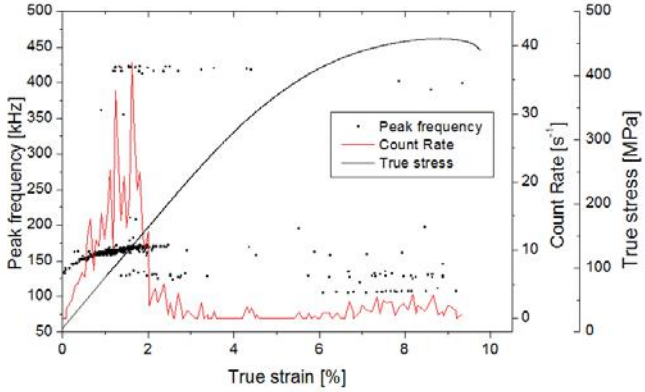


b)

Fig. 4: Count rates and amplitudes of the AE signal recorded during plastic deformation of the matrix alloy (a) and composite (b) at room temperature and strain rate of $10^{-3}s^{-1}$.



a)

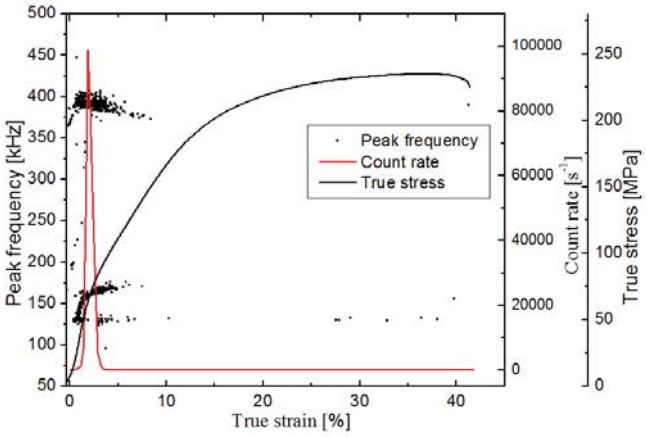


b)

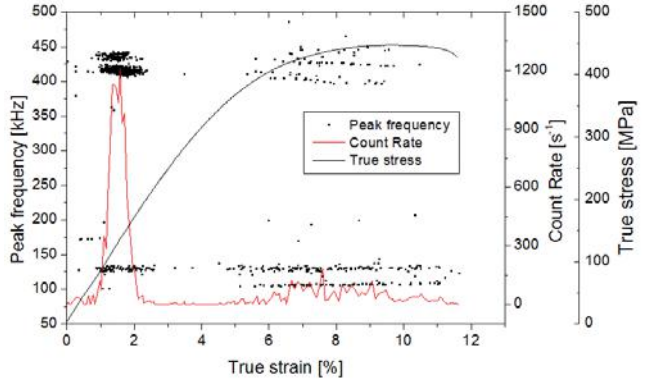
Fig. 5: Characteristic frequencies of the AE signal estimated for the matrix alloy (a) and composite (b).

The first peak of the double maximum at the deformation beginning is connected with of the generation of the primary twins $\{10\bar{1}2\}\langle 10\bar{1}0\rangle$ [22]. According to Klimanek and Pötsch [23] the second peak may be attributed to the secondary twins' production in the $\{10\bar{1}1\}\langle 10\bar{1}2\rangle$ system. Following decrease of the AE activity in the alloy and composite is connected with the growth of twins. Such mechanism has substantially lower AE response comparing with the twins nucleation. The observed increase in the AE activity in the composite close to the end of the stress-strain curve is connected with the breakage of fibres. The fibres may be also pulled out from the matrix, which is also a possible source of the AE signal. Note that results obtained for the alloy and composite are not directly comparable. Both materials have different grain size; the mechanical twinning is strongly dependent on the grain size [24], the comparison of the alloy with composite can be made only qualitatively. Characteristic frequencies of the AE signals were estimated using Fast Fourier Transform. 180 kHz and the higher frequency range from 370 up to 450 kHz (see Fig. 5). Results are shown in Fig. 5a for the alloy and 5b for the composite.

Two main frequency intervals were observed; 130-180 kHz and a higher frequency range from 370 up to 450 kHz (see Fig. 5).
Li and Enoki [25] considered that the signals characterised with the higher frequencies originate from the twins nucleation while the lower frequencies are characteristic for glide of dislocations. Characteristic frequencies estimated during plastic deformation showed that the early stages of the plastic deformation of the alloy are realised with both slip of dislocation ensembles and mechanical twinning. In the composite the role of twinning is not so important Increasing dislocation density and relatively low grain size (with respect to twinning) in the composite could indicate that the dislocation motion is more significant during deformation of the composite.
Experiments with the AE measurements were repeated at an initial strain rate of 10^{-4} s^{-1}. The results are shown in Fig. 6a for the matrix alloy and 6b for the composite. Differences between both results presented in Figs. 5 and 6 for both materials may be easily estimated. It is clear that in this case the twinning plays more important role in both materials in comparison with results obtained at the higher strain rate. The obtained results indicate a significant sensitivity of the twins′ formation to the strain rate.



a)



b)

Fig. 6: Characteristic frequencies of the AE signal estimated for the matrix alloy (a) and composite (b). The strain rate used was $10^{-4}s^{-1}$.

Conclusions

Magnesium alloy AJ51 and AJ51 alloy reinforced with 17.9 vol. % of short Saffil fibres were deformed at various temperatures from room temperature up to 300 °C. Samples for deformation were cut from the castings so that the fibre plane was parallel to the stress axis. During deformation at room temperature, the acoustic emission signal was measured at two strain rates. Strengthening effect of fibres was analysed. An increase in the dislocation density and load transfer were found as the significant contributions to the fibres strengthening. Neutron diffraction revealed high level of the residual stresses in the composite matrix. In both alloy and composite pronounced maxima of the AE signal at the onset of plastic deformation; in the composite additional maximum of the AE activity was observed in the vicinity of the maximum stress. This maximum was described to the fibre breakage and pulling out of fibres. Fast Fourier Transform of the AE signal showed that the AE signal frequency exhibits two regions. Lower frequencies may be described to the glide of dislocations while the twins´ nucleation can be characterised with higher frequencies. The activity of both mechanisms is sensitive to the strain rate.

Acknowledgements

The authors are grateful for the financial support of the Czech Grant Agency under the contract P108/12/J018.

References

[1] T.W. Clyne and P.J. Withers: *An Introduction to Metal Matrix Composites*, (Cambridge, Cambridge Univ. Press, 1993).

[2] N. Chawla and K.K. Chawla: *Metal Matrix Composites.* (New York, Springer Verlag, 2006).

[3] M.J. Koczak, S.C. Khatri, J.E. Allison and M.G. Bader: Fundamentals of Metal Matrix Composites (Eds. S. Suresh, A. Mortensen, A. Needleman), Butterworth-Heinemann, Boston, MA, 1993. 297-326.

[4] S. Roy et al., "Complete Determinativ of Elastic Moduli of Interpenetrating Metal/Ceramic Composites Using Ultrasonic Techniques and Micromechanical Modelling" *Materials Science and Engineering A*, 528 (2011), 8226–8235.

[5] Z. Trojanová et al., "Mechanical and Fracture Properties of an AZ91 Magnesium Alloy Reinforced by Si and SiC Particles", *Composites Science and Technology,* 69, (2009), 2256–2264.

[6] Z. Trojanová; et al., "Strengthening in Mg–Li Matrix Composites", *Composites Science and Technology*, 67 (2007), 1965–1973.

[7] Y. Ochi et al., "Effects of Volume Fraction of Alumina Short Fibers on High Cycle Fatigue Properties of Al and Mg Alloy Composites", *Materials Science and Engineering A*, 468-470 (2007), 230–236.

[8] F. Delannay: Comprehensive Composite Materials, Vol. 3, (Elsevier, Amsterdam; Ed. T.W. Clyne, 2000) 341–369.

[9] M. Kunst et al.: Creep Deformation and Mechanisms of AJ (Mg-Al-Sr) alloys. *Proc. of Inter. Symposium on Magnesium Technology in the Global Age.* Canad. Inst. of Mining, Metallurgy and Petroleum, Montréal, Canada (2006) 647–661.

[10] Standard Practice for Acoustic Emission Examination of Fiberglass Reinforced Plastic Resin, (ASTM E. Tank/Vessels: May 31, 1985), 1067–85.

[11] R.M. Aikin, Jr. and L. Christodoulou, "The Role of Equiaxed Particles on the Yield Stress of Composites", *Scripta Metallurgica et Materialia*, 25 (1991), 9-14

[12] R.J. Arsenault and N. Shi, "Dislocation Generation due to Differences between the Coefficients of Thermal Expansion", *Materials Scence and Engineerig.*, 81, (1986), 175-187.

[13] M.F. Ashby, "Criteria for Selecting the Components of Composites". *Acta Metallurgica et Mateialia*, *41*, (1993), 1313-325.

[14] H. Lilholt, "Aspects of Deformation of Metal Matrix Composites", *Materials Science and Engineering A*, 135 (1991), 161-171.

[15] D.R. Like and B. Raton Eds. Handbook of Chemistry and Physics. 73rd edition. (CRC Press, USA, 1992-1993)

[16] M. Mabuchi and K. Higashi, "Strengthening in Mg-Si Alloy", *Acta Materialia*, 44, (1996), 4611-4618.

[17] R.W. Armstrong, " Theory of the Tensile Ductile-Brittle Behaviour of Polycrystalline hcp Materials with Application to Beryllium", *Acta Metallurgica*, 16 (1968), 347-355.

[18] F.F. Lavrentev, Y.A. Pokhil and I.N. Zolotukhina, "Analysis of Pairwise Dislocation Interaction and its Contribution to Flow Stress during Magnesium Crystal Basal Slip", *Materials Science and Engineering*, 32 (1978), 113-119.

[19] Z. Trojanová et al., ”Magnesium Alloys Based Composites”, *Magnesium alloys-Design, Processing and Properties*. (Ed. F. Czerwinski, INTECH 2011) 501-526.
[20] Z. Trojanová et al., ”Influence of Thermal and Mechanical Cycles on the Damping Behaviour of Mg Based Nanocomposite”, *Fatigue behaviour of fiber reinforced composites. Experiments and simulations.* (W. Yao, J. Renard, N. Himmel Eds., Lancaster, USA, Destech Publications, Inc. 2012,) 239–248.
[21] M. Janeček et al., ”Mechanisms of Plastic Deformation in AZ31 Magnesium Alloy Investigated by Acoustic Emission and Transmission Electron Microscopy”, *Materials Science and Engineering A,* 462 (2007), 311–315.
[22] Z. Trojanová, Z. Száraz, F.Chmelík, P. Lukáč ” Acoustic Emission from Deformed Magnesium Alloy based Composites”, *Materials Science and Engineering A,* 528 (2011), 2479–2483.
[23] Klimanek P, Pötzsch A. ”Microstructure Evolution Under Compressive Plastic Deformation of Magnesium at Different Temperatures and Strain Rates”. *Materials Science and Engineering A* 324 (2002), 145–50.
[24] Máthis et al., ”Investigation of Tension–Compression Asymmetry of Magnesium by Use of the Acoustic Emission Technique”, *Materials Science and Engineering A* 528 (2011), 5904–5907.
[25] Y. Li and M. Enoki, ”Twinning Behavior of Pure Magnesium Quantitatively Investigated by Acoustic Emission*”, Materials Science and Engineering A,* 536 (2012), 8–13.

Magnesium Technology 2014

SYMPOSIUM: LIGHT-METAL MATRIX (NANO)-COMPOSITES

Microstructure-Property Relationships II: Modeling and Advanced Characterization

Papers in this section have been presented in a separate symposium at the 2014 TMS Annual Meeting organized by Dr. W. Sillekens and Prof. D.G. Eskin. This section was co-edited by the symposium organizers and all papers were peer reviewed.

Magnesium Technology 2014
Edited by: Martyn Alderman, Michele V. Manuel, Norbert Hort, and Neale R. Neelameggham
TMS (The Minerals, Metals & Materials Society), 2014

FABRICATION AND TENSILE PROPERTIES OF AL_2O_3 PARTICLE AND FIBRE HYBRID MAGNESIUM (AM60)-BASED COMPOSITES

Xuezhi Zhang [1], Qiang Zhang, Henry Hu[*2], and Xueyuan Nie[3]
Department of Mechanical, Automotive & Materials Engineering
University of Windsor, Windsor, ON N9B 3P4, Canada
E-mail: huh@uwindsor.ca [*2], zhang11w@uwindsor.ca [1], xnie@uwindsor.ca [3]

Keywords: Magnesium (AM60), hybrid composite, alumina fibre, squeeze casting, tensile properties

Abstract

Preform squeeze casting technique was applied successfully to fabricate hybrid magnesium-based composite with the reinforcements of Al_2O_3 fibres and particles. The SEM and optical microstructural analysis show that the reinforcements (particle and/or fibre) distribute uniformly in the preform and the magnesium-based composite. Mechanical properties for both of the reinforced and unreinforced matrix alloy were evaluated. The tensile testing results show that both of the yield strength and ultimate tensile strength are significantly improved. However, the elongation decreased as the reinforcements added to the magnesium alloy.

Introduction

The need for high-performance and lightweight materials in automobile and aerospace industries has led to extensive research and development efforts generating metal matrix composites (MMCs) and cost-effective fabrication technologies. The major disadvantage of MMCs usually lies in the relatively high cost of fabrication and reinforcement materials. The cost-effective processing of composite materials is, therefore, an essential element for expanding their applications. This is especially true for the high performance magnesium-based materials due to their high material and processing costs [1-4]. Since hybrid composites are fabricated by adding two or more reinforcements into matrix materials, excellent properties and a high degree of design freedom combinations including short fibres and different size particles become achievable. As magnesium matrix composites are reinforced with hybrid reinforcement in which both of the particles and short fibres are employed, large opportunities are provided to optimize the engineering performance of magnesium based composites for potential applications in automobile and aerospace industries[5].

In this paper, the fabrication process for the hybrid preform with cellular structure made by ceramic Al_2O_3 particles and fibres was described. The development of the squeeze casting process, which infiltrates liquid magnesium alloy into the hybrid preform under an applied pressure, was presented. Both of the optical microscopy and scanning electron microscopy were employed for the microstructural analysis of the preform and the composite. The informative results of tensile testing on the hybrid composites are compared with those of the unreinforced matrix alloy.

Experimental Procedures

Materials

Al_2O_3 ceramic particles and Al_2O_3 short fibres were employed as the raw materials for preparation of the hybrid reinforcements since they are relatively inexpensive and possess adequate properties. The matrix alloy AM60, with a chemical composition (wt %) of 6.0Al-0.22Zn-0.4Mn-0.1Si-0.01Cu-0.004Fe-0.002Ni-Mg,was chosen for its widespread use in the automotive industry. The thermophysical properties of the ceramic Al_2O_3 particle, Al_2O_3 fibre and matrix alloy AM60 are given in reference 5.

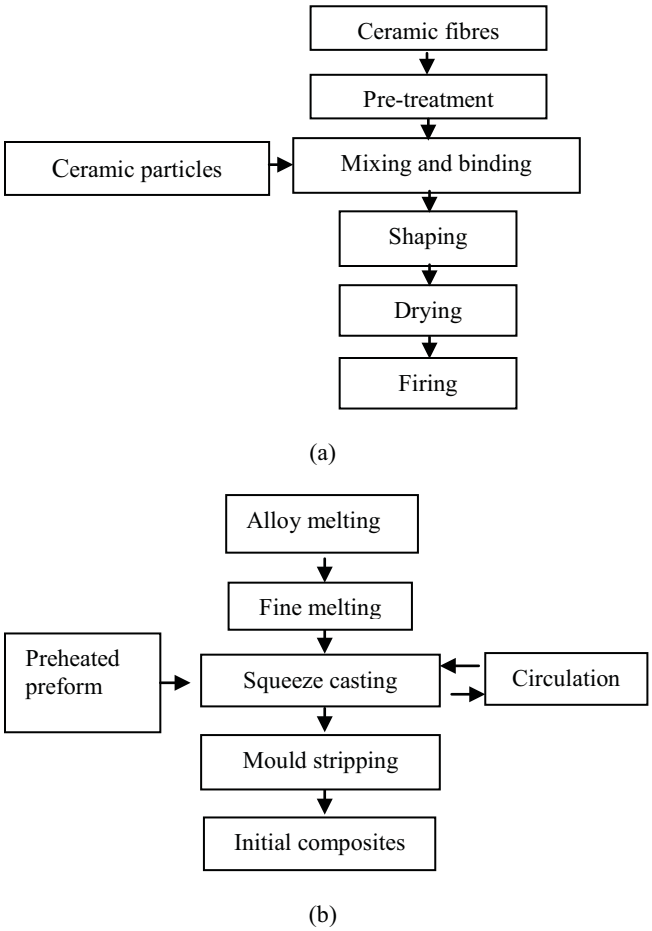


Figure 1: Flowchart showing the procedure for fabricating hybrid (a) preform and (b) composites.

Fabrication of hybrid preform

The preparation steps for fabrication of the hybrid preforms (Figure 1, a) involve mixing the ceramic short fibres and particles, introducing the binding compounds, forming the preform shape under pressure, drying and sintering. In the hybrid preform, the fibres serve as the skeleton for a cellular structure. The content level of the fibre was pre-determined based on the desired amount of porosity in the cellular solid. The particulate reinforcements were dispersed in the pores present in the cellular solid. The content, size and type of the ceramic reinforcements were adjusted to yield the required quantity, and shape of preform. In addition, for the purpose of a comparative study of the hybrid preform characteristics; a pure fibre preform was also fabricated using the same process without adding particulate reinforcements.

Fabrication of composites

Figure 1 (b) shows the fabrication process for the composites in which a squeeze casting process was adopted. During fabrication, a hybrid preform was first preheated to 300 ^{0}C. Then, molten matrix alloy AM60 at 750 ^{0}C infiltrated into the preheated preform under an applied pressure of 90 MPa. The pressure was maintained at the desired level for 25 seconds. After squeeze casting, a cylindrical disk of dual-phase reinforced composite with 4 vol.% Al_2O_3 particles and 9 vol.% Al_2O_3 fibres, named (F+P)/AM60, was obtained. In the hybrid composite, the particles constituted the primary reinforcement phase, and short fibres served as the secondary reinforcement phase. For the purpose of comparison, a composite (F/AM60) with only 9vol. % Al_2O_3 fibre reinforcement was also prepared.

Microstructure analysis

All specimens were cut from the center of the casting coupon. The samples were then polished and etched for the microstructural analysis. The primary characteristics of the prepared samples were investigated under an optical microscopy (Buehler image analyzer 2002). A scanning electron microscope (SEM) was employed for the detailed analysis of the microstructure. The maximum resolution used was up to 100 nm, which was in a backscattered mode. To further analyze the composition of the material, the energy dispersive spectroscopy (EDS) was used during the microstructure analysis.

Tensile testing

The INSTRON machine was employed for the tensile test and the test rate was set as 0.05mm/min. The mechanical properties for both of the composites and unreinforced matrix alloy were evaluated by tensile tests, by following ASTM B557. The tensile test were performed at ambient temperature. Based on the average of three test, the mechanical properties, such as ultimate tensile strength (UTS), yield strength (YS) and elongation (E_f) were obtained.

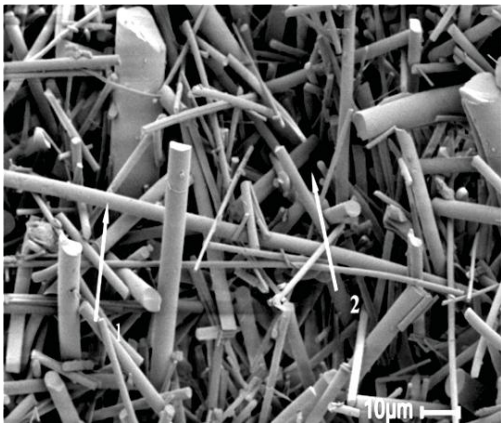
Results and Discussion

Characterization of hybrid preform

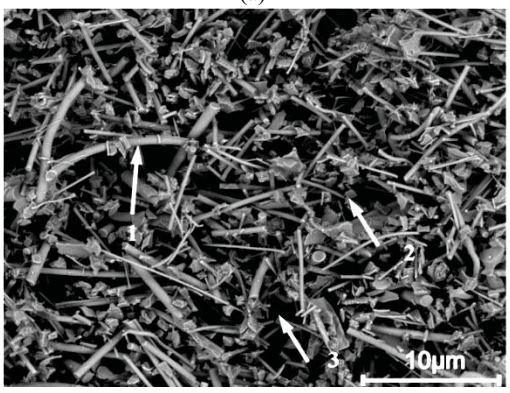
The preform fabrication procedure is critical in determining the eventual properties of the magnesium composites. The SEM micrograph (Figure 2, a) depicts the microstructure of fibre preform; it clearly reflects the inter-fibre space in the pure fibre preform. The average inter-fibre spacing can be calculated using the equation

$$\lambda_f = (1-V_f)\, d_f / V_f \qquad [6]$$

where d_f is the diameter of the fibres, V_f is the volume fraction of fibres. If the V_f is 9%, and d_f is 5 µm, the λ_f can be worked out to be 50 µm. Figure 2 shows the microstructure of hybrid preforms including the particles and fibres. It can be seen from Figure 2 (b) that the skeleton of fibres appear as a honeycomb structure that uniformly divides the preform into countless cells. The reinforced particles were dispersed and placed individually in the spacing of the cellular structure without agglomeration.



(a)



(b)

Figure 2: (a)SEM micrograph of fibre preform 1) fibre, and 2) empty cell; and (b)SEM micrograph of hybrid preform 1) fibre, 2) particle, and 3) empty cell.

Examination of the SEM micrographs shows that, in the fabricating process, a three-dimensional skeleton is constructed. The fibres constitute a solid supporting frame, and the ceramic particles are homogeneously dispersed in this three-dimensional

structure. The novel fabrication process ensures the reinforcements, both fibres and particles, disperse uniformly without agglomeration. Consequently, it ensures the magnesium alloy can be easily infiltrated into the preform. As well, the space of each cell in the preform represents a channel in which the molten magnesium alloy can flow, thus preventing the deformation of the preforms and affording efficient infiltration. The developed process for the fabrication of hybrid preforms is flexible to combine different kinds of discontinuous ceramic reinforcements and matrices for a wide range of engineering applications.

Characterization of hybrid magnesium composite

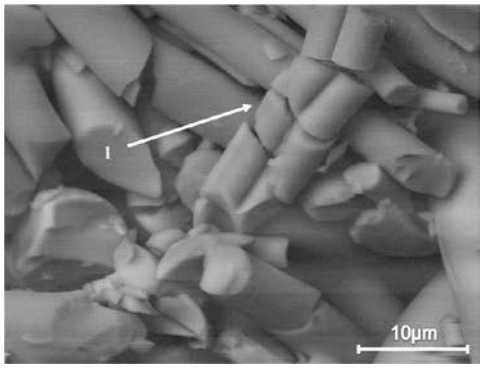
Molten matrix alloy infiltrates into a preheated preform under pressure during the squeeze casting process. The previous studies [7] has been reported that the strength of the preform and the process parameters such as the preheated temperature of the preform, the pouring temperature of the matrix alloy, and the applied pressure level in the preform plus squeeze casting process, influence the quality and performance of the composites significantly.

Nishida [8] described the threshold infiltration pressure, $P_{o,}$ using the following equation during squeeze casting:

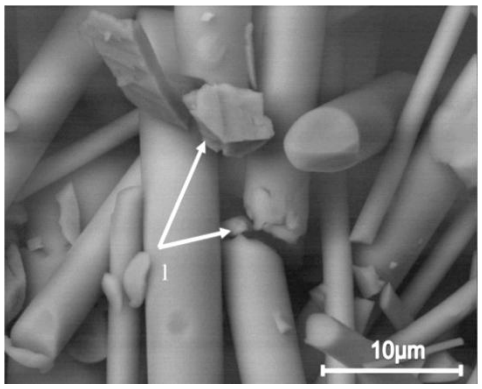
$$P_o = -[4Vf\gamma \cos\theta] / [d_f (1-V_f)]$$

where γ is the surface energy of the melt; θ is the contact angle between reinforcement and melt, V_f is the reinforcement volume fraction of the preform and d_f is the diameter of fibre or particle. If it is under ideal conditions, when V_f =9%vol and d_f = 5µm, for the magnesium alloy which can improve the wetting and decrease the surface energy of the melt, the contact angle between reinforcement and magnesium alloy is less than 90^0, the molten metal infiltrates the hybrid preform spontaneously. Generally, when modeling the infiltration, it is assumed that there is no deformation on the preform. However, in practice pressure applied to the molten matrix to overcome capillary forces and other space resistance forces. As a result, residual porosity can be formed during infiltration. In fact, to achieve high quality and density in composites, the applied high pressure can transmit to the preform, the pressure can be reached to 90 MPa. This high pressure may deform the preform and led to undesired defects in the composites.

To optimize the applied pressure and prevent deformation of the hybrid preform, the compressive strengths of hybrid preform were evaluated by compressive tests at room temperature. From the data analysis, the critical stress P_0 of the hybrid preform is as low as 0.6 MPa. Above this pressure, the deformation in the hybrid preform begins to localize, the cellular structure of preform suffer progressive crushing, and fractures propagate catastrophically. As shown in Figure 3, fractures of the fibres occur in a typical brittle manner, i.e., crush and cut. To avoid the premature fracture of the preform, the pressure applied in the squeeze casting was increased gradually from a value below the critical stress. The gradual increase in the applied pressure could effectively prevent the deformation of preform during squeeze casting. The applied pressure during casting and infiltration enabled the superheated molten matrix alloy in the preheated die to flow into the preform and wet reinforcement although no wetting agents was employed. Also, because the contacting time between the molten alloy and reinforcement at relatively high casting temperature was very short with the help of the applied pressure, the microstructure of the composites is homogeneous without the porosity and reactants.



(a)

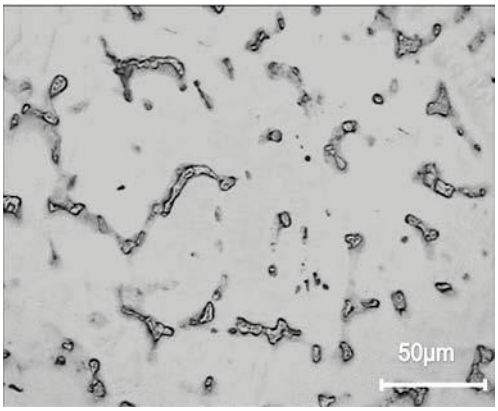


(b)

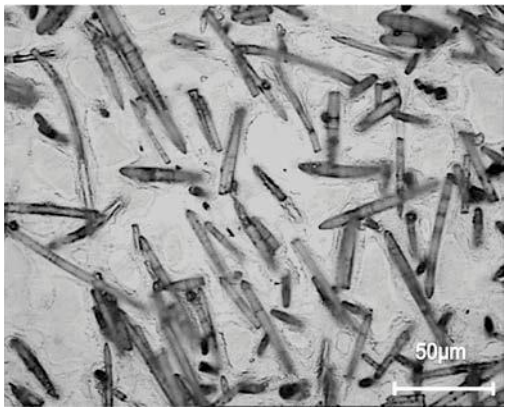
Figure 3: Fractures of preform fibres (a) Arrow 1-fibres crush, and (b) Arrow 1-particles cut down fibres.

The microstructure analysis of the unreinforced AM60 in Figure 4(a) indicates the presence of eutectic along the grain boundaries, within which the β-$Mg_{17}Al_{12}$ intermetallic β present. The precipitates are hard and brittle and have certain contribution to the hardness values. Figure 4(b) illustrates the short fibres that are distributed homogeneously and randomly in the fibre-reinforce composites. The microstructure of the hybrid magnesium composite is given in Figure 4 (c). It can be seen that the fibres and particles are uniformly distributed throughout the matrix alloys. The addition of particles has almost no influence on the uniformity of fibres even if the particle content increases to 4vol%. Voids can hardly be detected within the microstructure, indicating a higher densification of the hybrid composites due to a gradual application of the infiltration pressure. It is also found that the matrix alloy has successfully infiltrated into the hybrid preforms. A heterogeneous distribution of reinforcements may degrade the mechanical properties of the composites and lead to an inhomogeneous grain size and defects of the composites. However, despite the large geometrical difference between the

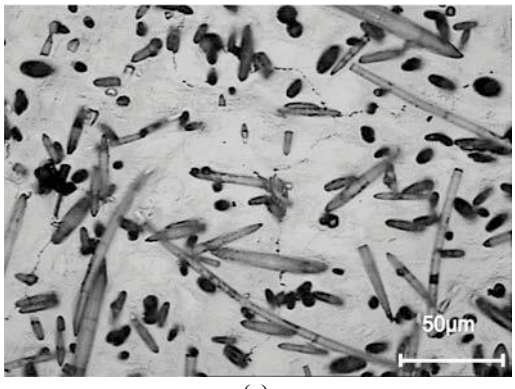
particles and the fibres, it is evident from Figure 4(c) that the particles and fibres are dispersed uniformly without agglomeration and they cave in the matrix alloy. The observed microstructure with both the ceramic particles and fibres distributed uniformly in the matrix alloy maximizes the benefits of the ceramic particles as the main reinforcement. They enhance the mechanical and wear properties of the composites while the fibres help to improve the toughness. The overall properties of the composites are improved and can be optimized.



(a)



(b)



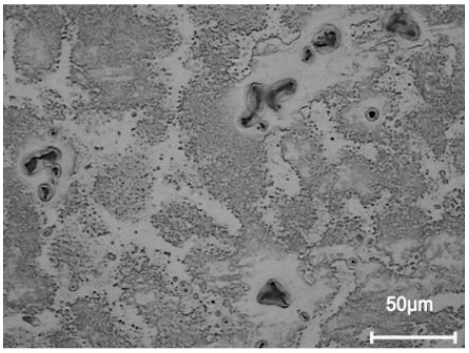
(c)

Figure 4: Optical photographs of matrix alloy and composites (a) AM60; (b) 9%Fibres/ AM60; (c) (4%particles + 9%Fibres) /AM60.

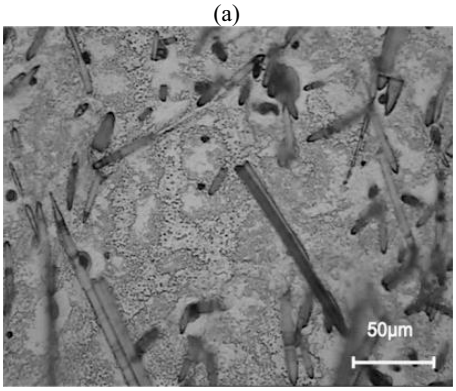
Figure 5 gives the grain structures of the matrix alloy and the composites. The grain size measurements for the composites and unreinforced AM60 matrix alloy are presented in Table 1. It is evident [9] that the addition of reinforcements results in a reduction in grain size. The observed grain refinement is primarily due to the combined effect of heterogeneous nucleation of primary magnesium on Al_2O_3 particles, restricted growth of magnesium grains, and heterogeneous nucleation of eutectic magnesium ($Mg_{12}Al_{17}$) on Al_2O_3 particles and fibres.

Table 1: Average grain sizesfor AM60 alloy, 9%Fibre/ AM60, and (4%Particle +9%Fibre)/ AM60 composites

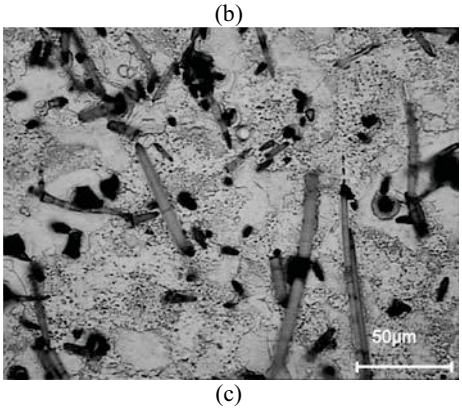
	AM60	F/AM60	(F+P)/AM60
Average grain size (µm)	68	44	28



(a)



(b)



(c)

Figure 5: Optical micrographs showing grain structure of (a) unreinforced AM60 matrix alloy, (b) 9%Fibre/ AM60 and (c) (4%Particle +9%Fibre)/ AM60. All are under T4 condition.

Tensile properties

The typical engineering stress-strain curves for casting of AM60, Fibre/ AM60, and (Fibre+Particle)/ AM60 composites are shown in Figure 6 and the mechanical properties data are given in Table II. It is observed from the results that the addition of reinforcements leads to a significant improvement in the elastic modulus and the strengths, but results in a marked diminishment in elongation. From Table 2, it can be seen that the yield strength (YS) of the composites, which are 125 and 150MPa for F/AM60 and (F+P)/AM60 respectively, are significantly improved by almost 88% over the unreinforced magnesium alloy. The elastic modulus (E) of the composites are 52 and 59GPa for F/AM60 and (F+P)/AM60, respectively, which is 30% and 40% higher than that of the unreinforced matrix alloy. The UTS of the two composites is 182MPa for F/AM60 and 199MPa for (F+P)/AM60 respectively, which leads to an increase of 6% and 16%higher than that of the matrix alloy AM60 (172MPa). Compared to that (6%) of the matrix AM60 alloy, the elongation to failure (e_f) of the composites are1.7% and 1.5% for the F/AM60 and (F+P)/AM60 composites, respectively. No necking phenomena were observed for the composites prior to fracture due to the low ductility, while a slight but notable necking was observed for the squeeze cast AM60.

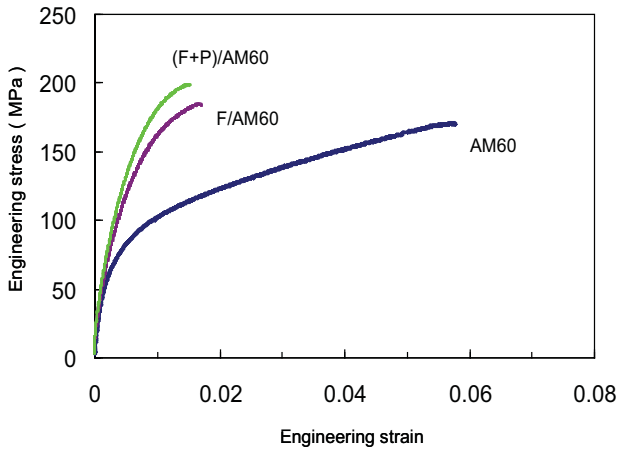


Figure 6: Typical engineering stress vs. strain curves for AM60 alloy, 9%Fibre/ AM60, and (4%Particle +9%Fibre)/ AM60 composites.

Table 2: UTS, YS,Elastic modules and Elongation of AM60 alloy, 9%vol.Fibre/ AM60, and (4%vol.Particle +9%vol.Fibre)/ AM60 and composites

	UTS (MPa)	YS (MPa)	Elastic modulus (GPa)	Elongation (%)
AM60	171	81	40	6.0
F/AM60	182	125	52	1.7
(F+P)/AM60	199	150	59	1.5

Conclusion

A hybrid preform-squeeze casting process has been developed and applied to the processing of magnesium matrix composites. The SEM observation on the microstructure reveals that in hybrid preform, the fibres are the solid supporting frame, in which the ceramic particles were homogeneously dispersed in the three-dimensional structure.The optical microstructure analysis of the composites indicates that both particles and fibres disperse uniformly in the matrix alloy without agglomeration, and fibres orientate randomly in the matrix. The hybrid composite reinforced with 4vol% Al_2O_3 particles and 9 vol% Al_2O_3fibres exhibits improved tensile strengths over those of the matrix alloy. In particular, the yield strength (150MPa) of the hybrid composite is 88% higher than that of the matrix alloy. With almost no increase in materials density, the elastic modulus of the hybrid composite (59GPa) shows 40 % improvement over the matrix alloy (40GPa).

Acknowledgments

The author would like to take this opportunity to thank the Natural Sciences and Engineering Research Council of Canada and the University of Windsor for supporting this work.

References

1. Ramalingaiah, S. Bansal and S. Ray,Microstructure and Mechanical Properties of Cast Composite of Steel Wool Infiltrated by Magnesium and AZ91 Alloy, Materials and Manufacturing Processes, (26), 2011, 1173-1178.
2. E. Hajjari, M. Divandari and H. Arabi,Effect of Applied Pressure and Nickel Coating on Microstructural Development in Continuous Carbon Fibre-reinforced Aluminum Composites Fabricated by squeeze Casting, Materials and Manufacturing Processes, (26), 2011, 599-603.
3. A. Banerji, H. Hu and A.T. Alpas, Ultra-mild Wear of AL_2O_3 Fibre and Particle Reinforced Magnesium Matrix Composites, Advanced Materials Research, 2012, 445, 503-508.
4. J. Lo, and R. Santos, Magnesium matrix composites for elevated temperature applications, 2007 Society of Automotive Engineers World Congress,Detroit, MI, 2007-01-1028.
5. Q. Zhang, and H. Hu, Development of Hybrid Magnesium-based composites, Advances in Light Weight Materials-Aluminum, Casting Materials, Magnesium Technologies,Society of Automotive Engineers World Congress, 2010, 107-114.
6. Q. Zhang, H. Hu, and J. Lo, Solidification of Discontinuous Al_2O_3 Fibre Reinforced Magnesium (AM60) Matrix Composite, Defect and Diffusion Forum, 2011, 312-315, 277-282.
7. H. Hu, Squeeze casting of Magnesium alloys and their composites, Journal of materials science, 33, 1998, 1579-1589.
8. Y.Nishida, and G.Ohira, Modelling of Infiltration of Molten Metal in Fibrous Preform by Centrifugal Force, Acta mater. 47(3), 1999, 841-852.
9. H. Hu, Grain Microstructure Evolution of Mg (AM50A)/ SiC_p Metal Matrix Composites, 39(8), 1998, 1015-1022

Magnesium Technology 2014
Edited by: Martyn Alderman, Michele V. Manuel, Norbert Hort, and Neale R. Neelameggham
TMS (The Minerals, Metals & Materials Society), 2014

ENHANCING TENSILE AND COMPRESSIVE STRENGTH OF AZ41 MAGNESIUM ALLOY BY ADDING NANO-SIZED Al_2O_3

Md Ershadul Alam[1, 2], and Abdelmagid Salem Hamouda[2]

[1]Mechanical Engineering, HBCC, King Fahd University of Petroleum and Minerals, P.O. Box: 1803, KSA 31991
[2] Department of Mechanical and Industrial Engineering, College of Engineering, Qatar University, Doha, Qatar 2713

Keywords: Mg, AZ41 alloy, Nanocomposite, Compressive properties, Microstructure.

Abstract

In the present study, AZ41 alloy and AZ41-1.5Al_2O_3 nanocomposite were developed by adding 1 wt. % Al and 1 wt.% Al with 1.5 vol.% nano-sized Al_2O_3 (50 nm) particulates in to AZ31 magnesium alloy, respectively, using disintegrated melt deposition technique. All samples were then subsequently hot extruded at 400 ^{0}C and characterized. Microstructural characterization studies revealed equiaxed grain morphology, minimal porosity, reasonably uniform distribution of Al_2O_3 nanoparticulates and good matrix-reinforcement interfacial integrity. Microhardness was increased with the addition of Al_2O_3 nanoparticulates in to AZ41 alloy. Room temperature tensile test results revealed that the AZ41-Al_2O_3 nanocomposite exhibited improved ultimate tensile strength (UTS), ductility and toughness when compared to monolithic AZ41 alloy but 0.2% yield strength was compromised. However, room temperature compressive test results of AZ41-Al_2O_3 nanocomposite revealed significant improvement on overall compressive properties over AZ41 alloy.

Introduction

The density of magnesium is 1.74 g/cm^3, which makes it the lightest engineering materials available in the earth and is about 35% and 78% lighter than aluminum based (~ 2.70 g/cm^3) and iron based (~ 7.87 g/cm^3) materials, respectively [1]. Therefore, its use is gaining significance in certain key engineering applications, particularly in automobile, aviation, electronics and consumer industries where weight is one of the most important criteria in the choice of materials [2, 3, 4]. Besides low density, magnesium based materials exhibit good specific mechanical properties, machinability, castability, weldability, thermal stability, damping and resistance to electromagnetic radiation [5, 6]. However, pure magnesium has low ductility, modulus of elasticity and limited strength and creep resistance at elevated temperature, so, it cannot be extensively applied in structural applications in its pure form [6]. Instead, it is usually alloyed with other elements like aluminum, zinc, silver and zirconium to improve its properties like corrosion resistance and ductility [2, 6, 7]. Among these alloying constituents, the addition of aluminum seems to have the most favorable effect on magnesium, exhibiting much greater strength and hardness. Accordingly, in the previous study, a new magnesium based AZ41 alloy (4 wt.% Al, 1 wt.% Zn, remaining Mg) were developed by adding 1 wt. % Al into AZ31 alloy [6, 8].

Metal matrix composites (MMCs) have gained increasing popularity as their properties could be altered accordingly by changing the matrix and its reinforcements [6, 9]. This is particularly useful in engineering applications especially when properties of traditional materials like metals, polymers and ceramics are not able to match with expected properties. In recent studies, it has been observed that the addition of nano-sized reinforcements such as ceramic oxides, SiC and carbon nanotubes can lead to a simultaneous increase in strength and ductility of magnesium [5, 6, 10, 11]. Among all the reinforcements, it can be observed from the study that the 1.5 vol. % addition of nano-sized alumina particulates in magnesium-based matrix improved overall tensile strength [5]. Accordingly, in the present study, new magnesium based AZ41-1.5 Al_2O_3 nanocomposite was synthesized by disintegrated melt deposition technique and characterized in terms of microstructural, physical and mechanical (both tensile and compressive) properties.

Experimental Procedures

Materials

In the present study, AZ31 magnesium alloy ingots (2.94% Al, 0.87% Zn, 0.57% Mn, 0.0027% Fe, 0.0112% Si, 0.0008% Cu, 0.0005% Ni and balance Mg, supplied by Tokyo Magnesium Company, Japan) were used as a matrix material. The aluminum lumps used were of 99.5 % purity (supplied by Alfa Aesar, USA) and the reinforcement was in the form of 50 nm alumina powder of 99.4 % purity (supplied by Baikowski, Japan).

Primary Processing

Synthesis of the AZ41 alloy and its Al_2O_3 nanocomposite involved heating the AZ31 magnesium alloy pieces with the addition of 1 wt.% Al and 1 wt.% Al with 1.5 vol. % Al_2O_3, respectively, to 750 ^{0}C in an inert Ar gas atmosphere in a graphite crucible using a disintegrated melt deposition (DMD) technique. The crucible was equipped with an arrangement for bottom pouring. Upon reaching the superheat temperature, the molten slurry was stirred for 5 min at 450 rev./min using a twin blade (pitch 45^0) mild steel impeller to facilitate the incorporation and uniform distribution of reinforcement particulates in the metallic matrix. The impeller was coated with Zirtex 25 (86% ZrO_2, 8.8% Y_2O_3, 3.6% SiO_2, 1.2% K_2O and Na_2O, and 0.3% trace inorganic) to avoid iron contamination of the molten metal. The melt was then released through a 10-mm diameter orifice at the base of the crucible. The melt material was disintegrated by two jets of argon gas orientated normal to the melt stream. The argon gas flow rate was maintained at 25 L /min. The disintegrated alloy melt slurry was subsequently deposited onto a metallic substrate. Preform of 40-mm diameter was obtained following the deposition stage.

Secondary Processing

The 40 mm diameter ingots were machined down using a lathe machine to a diameter of 36 mm and cut into billets with heights of approximately 45 mm. The billets were sprayed with colloidal graphite for lubrication purposes and then soaked at 400 ^{0}C for 60

minutes in a constant temperature furnace before extrusion. Extrusion was performed on a 150 tonne hydraulic press using an extrusion ratio of 20.25:1, producing rods of 8 mm diameter.

Density and Porosity Measurements

Density (ρ) measurements were performed in accordance with Archimedes' principle on three randomly selected polished samples of AZ41 and its nanocomposite taken from the extruded rods. Distilled water was used as the immersion fluid. The samples were weighed using an A&D ER-182A electronic balance, with an accuracy of ±0.0001g. Theoretical densities of materials were calculated assuming they are fully-dense. Rule-of-Mixture was used in all calculations. The porosity was calculated by using the theoretical and experimental densities.

Microstructural Characterization

Microstructural characterization studies were conducted on metallographically polished extruded samples to investigate morphological characteristics of grains, reinforcement distribution and interfacial integrity between the matrix and reinforcement. The etching solution (5 ml acetic acid, 6 g picric acid, 10 ml water and 100 ml ethanol) was applied for approximately 20 seconds using a swabbing technique and then washed under running water to reveal the grain boundaries [6]. The sample was then analyzed using the Olympus BH2-UMA metallographic optical microscope equipped with Olympus DP-10 microscope digital camera. The grain boundaries were then traced out from the micrographs with the aid of the Adobe Photoshop program. Image analysis using the Scion system was carried out to determine the grain size of the materials.

The presence and distribution of the intermetallic phase was investigated using the JEOL JSM-5600LV Scanning Electron Microscope (SEM). Polished specimens were observed at 1000x magnification to reveal the intermetallic phase. The general distribution of the nano-sized alumina reinforcement was also investigated using the Hitachi S-4100 Field Emission Scanning Electron Microscope (FESEM).

X-Ray Diffraction Studies

X-ray diffraction analysis was conducted using the automated Shimadzu LAB-X XRD-6000 x-ray diffractometer. Flat, ground and ultrasonically cleaned specimens of approximately 5 mm in height were exposed to CuK_α radiation (λ = 1.54056 Å) with a scanning speed of 2 ^{0}/min. The scanning range was 30^0 to 80^0 for all samples. A plot of intensity against 2θ (θ represents Bragg angle) was obtained, illustrating peaks at different Bragg angles. The Bragg angles corresponding to different peaks were note and the values of interplanar spacing (d-spacing) obtained from the computerized output were compared with the standard values from the International Centre for Diffraction Data's Powder Diffraction File (PDF).

Coefficient of Thermal Expansion

The coefficients of thermal expansion (CTE) of all the compositions were determined by measuring the displacement of the samples as a function of temperature in the temperature range of 50 ^{0}C- 400 ^{0}C using an automated SETARAM 92-16/18 thermo-mechanical analyzer.

Mechanical Characteristics

Microhardness Test: The microhardness tests were conducted on flat and metallographically polished specimens. The test was conducted using a Shimadzu HMV automatic digital microhardness tester with a Vickers indenter (square-based pyramidal-shaped diamond indenter with face angle of 136 ^{0}). An indenting load of 25 gf and a dwell time of 15 seconds were used. Testing was performed according to ASTM: E384-11e1.

Tensile Testing: The smooth bar tensile properties of the extruded samples were determined at room temperature according to ASTM: E8/E8M-11 using MTS 810 tensile testing machine with a cross-head speed set at 0.254 mm/min on round tension test specimens of 5mm diameter and 25mm gauge length. MTS extensometer was used for strain recording.

Compression Testing: Quasi-static room temperature compressive tests were performed on cylindrical samples according to ASTM: E9-09 using a Lloyd LR 50k Plus, UK compressive testing machine with a cross head speed of 0.04mm/min, giving the approximate nominal strain rate of 10^{-4}/s. Extruded rod of 7mm diameter with length to diameter ratio of all samples were kept 1. Teflon tape was placed between the containing surfaces of the specimen and the machine steel platen for lubrication (to avoid barreling).

Fracture Behavior: The fracture surfaces of the broken tensile and compressive samples were analyzed to investigate the failure mechanisms that occurred during the tensile and compressive tests. Fractography studies of tensile samples were performed on the JEOL JSM-5600LV Scanning Electron Microscope whether as FEI Nova NanoSEM 450 (Checz Republic) were used for compressive fracture samples. Macromechanism of these fracture surfaces were also investigated.

Results and Discussion

Processing

Synthesis of new magnesium based AZ41 alloy and its Al_2O_3 nanocomposite were successfully accomplished by the disintegrated melt deposition. Observations of the deposited ingots before secondary processing revealed that there was no detectable reaction between the graphite crucible and melts, minimal oxidation on the melts and an absence of blowholes and macropores. These observations are consistent with previous findings made on Mg based composites synthesized using DMD method [5, 6, 8, 11] and verified the suitability of using DMD as the primary processing method for this study.

The extrusion parameters used in the present study were selected based on previous studies [5, 11]. The successful extrusion of AZ41 and its nanocomposite without a drastic increase in pressure applied indicates that the extrusion parameters were adequate and ensured uniform plastic flow of the material.

Density and Porosity Measurements

The experimental density obtained by the Archimedes' principle exhibited that the density of newly developed AZ41-Al_2O_3 nanocomposite increased negligibly with the addition of alumina nano-size particulates into AZ41 matrix (see Table I). This can be

attributed to the higher density of Al_2O_3 (3.96 g/cm^3) when compared to AZ31 matrix (1.78 g/cm^3) [5]. Obtained results also revealed that the experimental values were relatively close to the theoretical values. This indicated that the experimental methodology used in this study is capable of producing near dense materials.

Porosity of the materials was calculated using the theoretical and the experimental densities obtained from each sample. The highest porosity obtained among the samples was 0.10% (see Table I), hence indicating that near dense materials were obtained and that the alloying constituent and the reinforcement were successfully incorporated into the matrix.

Table I. Results of Density and Porosity Measurements

Compositions	Al_2O_3 (vol. %)	Density (g/cm^3)		Porosity (%)
		Theo.	Expt.	
AZ41	-	1.786	1.785	0.05
AZ41-Al_2O_3	1.5	1.818	1.816	0.10

Microstructural Characteristics

Microstructural studies conducted on the extruded specimens showed near equiaxed grain morphology (see Table II and Figure 1). Average grain size of the nanocomposite samples increased marginally with the addition of nano-sized alumina particles suggesting the incapability of nano-Al_2O_3 particulates to serve as either nucleation site or obstacles to grain growth during solid state cooling. However, the variations of grain size between the alloy and nanocomposite samples are statistically insignificant considering standard deviation.

Table II. Results of Grain Morphology

Compositions	Grain Size (μm)	Aspect Ratio	Roundness[1]
AZ41	2.9 ± 1.3	1.6 ± 0.4	1.6 ± 0.6
AZ41-Al_2O_3	3.8 ± 1.6	1.7 ± 0.5	1.5 ± 0.3

1. Roundness is the shape of the grain expressed by the formula (perimeter)^2 / 4π (area)

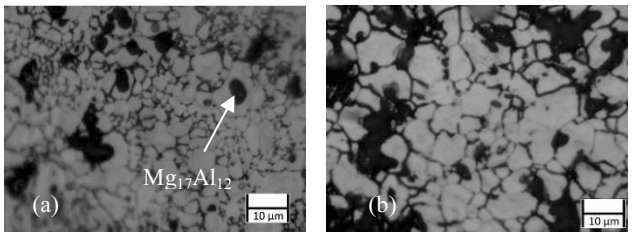


Figure 1. Representative optical micrographs showing the grain morphology (1000x) of: (a) AZ41 and (b) AZ41-Al_2O_3 samples.

Microstructural characterization studies were also conducted on the extruded and polished samples to observe the size and distribution of intermetallic phases and the nano-sized alumina particulates in the matrix (see Table III and Figures 1 and 2). SEM micrographs of the etched samples revealed the presence and good distribution of the equilibrium intermetallic phase $Mg_{17}Al_{12}$. SEM analysis revealed that the nano-sized alumina particulates in the AZ41-Al_2O_3 system was found to exist both in small clusters and also individually distributed around the matrix (see Figure 2(c)). Even in the clusters, the alumina particulates were found to be individually spaced and distributed, and the clusters themselves were fairly evenly distributed around the matrix. This could be attributed to the use of a layered arrangement for the raw materials during the solidification process and effective stirring parameters. The successful disintegration of the melt and the inert atmosphere caused by the argon gas jets were also the contributing factors. In the AZ41 system, the intermetallic particles appeared to have sharp edges (see Table III and Figure 2). At these boundaries, the local stress concentration will be higher. Addition of the nano-sized alumina particulates in AZ41 helped to increase the amount of second phase and also blunt the edge of intermetallic phase, thereby lowering the local stress concentration (see Figure 2). Results of microstructural characterization also revealed good interfacial integrity between Al_2O_3 and matrix (see figure 2 (c)), absence of debonded regions and interfacial reaction products.

Table III. Results of Second Phase Characteristics

Compositions	Second Phase ($Mg_{17}Al_{12}$) Characteristics		
	Dia (μm)	Aspect ratio	Vol. Fraction (%)
AZ41	1.7 ± 1.2	3.4 ± 1.6	1.98
AZ41-Al_2O_3	2.8 ± 1.5	1.8 ± 1.3	4.13

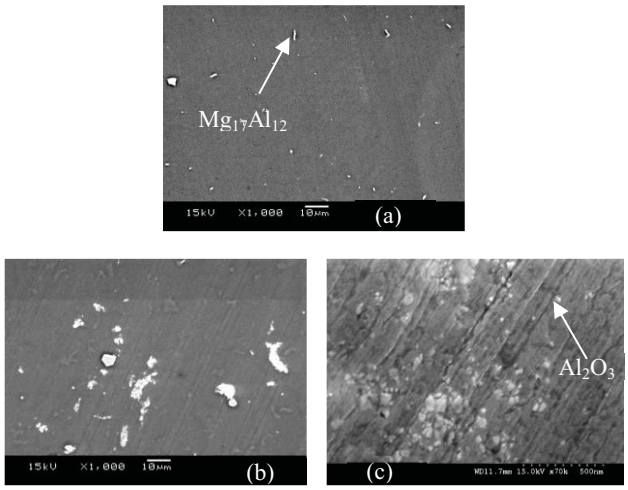


Figure 2. Representative SEM micrographs showing the shape and distribution of second phase in the case of: (a) AZ41 and (b) AZ41-Al_2O_3 samples, respectively. (c) FESEM figures showing the distribution of Al_2O_3 nanoparticles.

X-Ray Diffraction

X-Ray diffraction was carried out on all samples and results confirmed the presence of the intermetallic phase $Mg_{17}Al_{12}$ in all of the compositions (see Table IV). For the AZ41-Al_2O_3 nanocomposite, the increased number of intermetallic peaks can be observed indicating higher amount of second phase were formed when compared to the AZ41 alloy. However, the presence of the nano-sized alumina was not identified. This can be attributed to the limitation of the filtered X-ray to detect phases with less than 2 vol.% [5, 12].

Table IV. Results of XRD and CTE Analysis

Compositions	Mg	$Mg_{17}Al_{12}$	CTE (μm/mK)
AZ41	11	1	27.1
AZ41-Al_2O_3	10	3	26.5

Coefficient of Thermal Expansion

The results of CTE measurement showed that the addition of nano-sized alumina particulate reinforcements decreases the average CTE values of the AZ41 alloy (see Table IV). This can be attributed to the lower CTE value of Al_2O_3 (7.0 x 10^{-6} k^{-1}) [9] when compared to monolithic AZ41 alloy and the ability of the reinforcements to effectively constrain the expansion of the matrix. The results of the AZ41-Al_2O_3 systems suggested an appropriate integration of AZ41 alloys with nano-sized alumina particulates leading to low CTE values as demonstrated in prior studies [5]. The results are consistent with similar findings made by investigations on other magnesium based formulations containing different types of reinforcements and in different length scales [3, 11].

Mechanical Characteristics

Microhardness Test: The experimental results of microhardness measurement are shown in Table V. A prominent increase (around 27%) in microhardness was observed in AZ41-Al_2O_3 nanocomposite sample when compared to unreinforced AZ41 (see Table V). This is consistent with the earlier observations made on Mg–Al_2O_3 nano-composite formulations [5, 11]. The increase in hardness of nano-composite in the present study can be attributed to: (i) the reasonably uniform distribution of harder Al_2O_3 nano-particulates in the matrix, and (ii) higher constraint to the localized matrix deformation during indentation due to the presence of the nano-particulates [5, 11, 13].

Tensile Test: Room temperature tensile test were carried on all extruded samples and showed in Table V and Fig. 3. The results of tensile properties characterization showed that the presence of nano-sized alumina particulates in AZ41 slightly decreased the 0.2% YS and increased the UTS. Decrease in strength (0.2% YS) of nanocomposite may be attributed to the combined effect of the: (i) average grain size increament for nanocomposite samples (*Hall-Petch* effect) (see Table II), (ii) modification of intermetallic particulate morphology from sharp edged to the blunt edged (see Table III and Fig. 2), and (iii) presence of higher percentage of porosity (see Table I). However, the strength of AZ41-Al_2O_3 nanocomposite was much higher than that of monolithic AZ31 magnesium synthesised using the same parameter [6].

Table V. Results of Room Temperature Tensile Properties

Comp.	Hardness (HV)	0.2 % YS (MPa)	UTS (MPa)	FS (%)	WoF (MJ/m^3)
AZ41	77 ± 3	218 ± 5	287 ± 6	8.2 ±0.3	23 ± 1
AZ41-Al_2O_3	98 ± 3	200 ± 2	302 ± 3	12.3 ±1.2	36 ± 4
AZ31	-	180 ± 3	273 ± 6	10.6 ±1.3	28 ± 4

A significant increase (50%) in failure strain was observed in the AZ41-Al_2O_3 nanocomposite when compared to AZ41 alloys. This increment can be attributed to: (i) the presence and reasonably good distribution of the reinforcements, and (ii) the reduction in local stress concentration present in the matrix due to the blunt shape of the intermetallic states. Dispersed phases in brittle matrix, where dislocation mobility is restricted and crack propagation is relatively easy, act as ductility enhancer, an anomaly to their effect in ductile matrix [14]. Dispersed reinforcement particulates in brittle metal matrix serve to: (a) provides sites where cleavage cracks may open ahead of an advancing crack front, (b) dissipate the stress concentration which would otherwise exist at the crack front, and (c) alter the local effective state of stress from plane strain to one of plane stress in the neighbourhood of the crack tip. In addition, it has been understood through different studies that nano-sized Al_2O_3 reinforcements have the ability to activate non-basal slip system at room temperature in magnesium based matrix under axial tensile stress and helps to increase ductility [5, 15]. The work of fracture of the nanocomposite was found to be much higher when compared to AZ41 magnesium alloy and improved by around 57% (see Table V). This can mainly be attributed to the improved failure strain of the nanocomposite samples synthesized in the present study. The results thus clearly reveal the enhanced damage tolerant capability of AZ41 magnesium alloy when reinforced with Al_2O_3 particulates in nano-length scale.

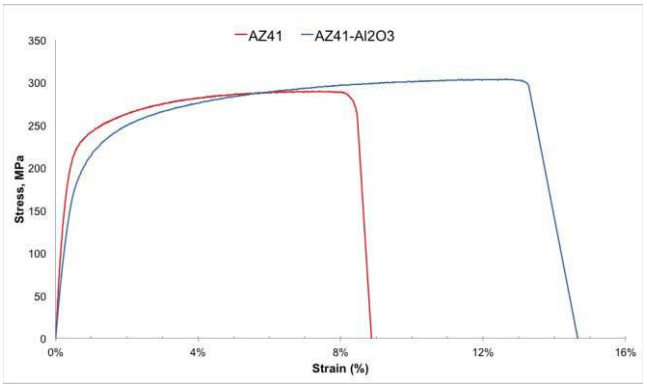


Figure 3. Room temperature engineering stress-strain curve of AZ41 and AZ41-Al_2O_3 nanocomposite samples.

Compression Test: The results of compressive properties characterization showed that the addition of Al_2O_3 nano-particulates in AZ41 alloy increased both the 0.2% compressive yields strength (CYS) and ultimate compressive strength (UCS) (see Table VI and Figure 4). AZ41-Al_2O_3 nanocomposite samples exhibited around 13% higher 0.2% CYS and 10% higher UCS when compared to AZ41 alloy. Similar observations were made in the case of other magnesium-based nanocomposites [16, 17]. The increase in the compressive strength of AZ41-Al_2O_3 formulations can primarily be attributed to: (i) the dislocation generation due to elastic modulus mismatch and coefficient of thermal expansion mismatch between the matrix and reinforcement [11, 16, 17], (ii) Orowan strengthening mechanism [16], and (iii) the effective load transfer from matrix to reinforcement [11, 16, 17]. For the compression test, alumina reinforced AZ41 nanocomposite exhibited around 19% higher failure strains than the monolithic AZ41 alloy and this is as high as 42% when compared to AZ31 alloy synthesized using the same processing parameter (see Table VI). This can again be attributed to the: (a) presence and

reasonably uniform distribution of nano-sized alumina particulates, (b) presence of blunt edged second phase in nanocomposite samples (see Figure 2), and (c) presence of more shear bands in the case of nanocomposite samples (see Figure 5).

Table VI. Results of Room Temperature Compressive Properties

Compositions	0.2 % CYS (MPa)	UCS (MPa)	FS (%)
AZ41	125 ± 4	381 ± 5	19.2 ± 1.3
AZ41-Al_2O_3	141 ± 2	420 ± 7	22.4 ± 1.2
AZ31	107 ± 3	302 ± 5	16.2 ± 1.1

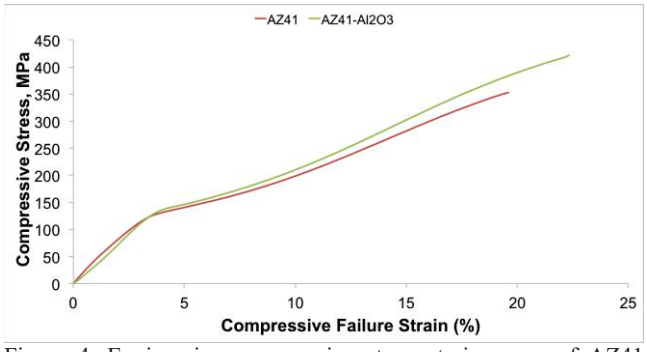


Figure 4. Engineering compressive stress-strain curve of AZ41 and its nanocomposite samples.

Fracture Behavior: Microscopic observations tested on tensile fracture samples showed that dimple like features were predominately present in all compositions, indicating plastic deformation (see Figures 5(a) and (b)). Microcracks were observed for AZ41 alloys, which is responsible for lower failure strain. Fractography of nano-composite sample revealed the reduction in size of microcracks (become micropores) and increased evidence of plastic deformation with the presence of nano-Al_2O_3 particulates.

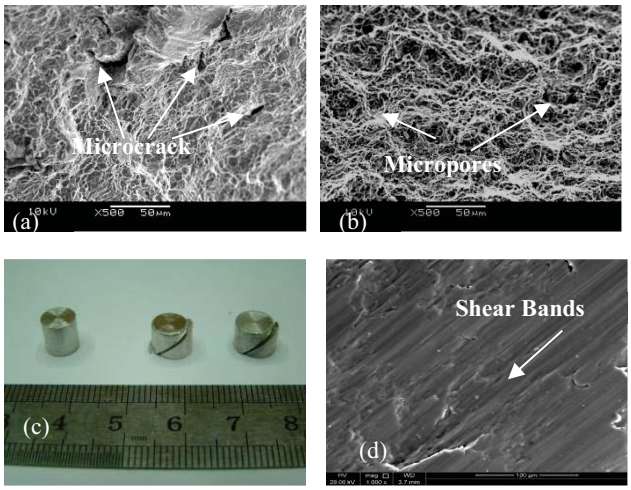


Figure 5. Representative SEM fractographs showing the microcracks and dimple like features for: (a) AZ41 and (b) AZ41-Al_2O_3 nanocomposite samples, respectively. Figure (c) showing the macroscopic view of the fracture samples before and after the compressive test and (d) showing the shear bands.

Figure 5 (c) showing the macroscopic view of the AZ41 alloy and its alumina nanocomposite samples before and after the compressive test. Macroscopically, all AZ41 and its nano-composite samples failed primarily via one principle crack which was inclined at ~ 45° to the compressive axis (see Figure 5(c)). The failure generally initiated near to the specimen ends and appeared at the maximum stress. These results suggested that the failure mechanisms in AZ41 alloy and its nano-composites are basically the same under compressive loading. Microscopic examination of the fracture surfaces of AZ41 and its nano-composite samples revealed shear bands, which can be attributed to twinning shear.

Conclusions

The following conclusions can be made from the present study:

1. Monolithic AZ41 alloy and its Al_2O_3 can be successfully synthesized by using the disintegrated melt deposition technique followed by hot extrusion with minimal porosity.

2. The microstructure of the AZ41 and AZ41-Al_2O_3 nanocomposite consist of the magnesium phase and the intermetallic phase, $Mg_{17}Al_{12}$. The presence of nano-sized alumina helps to decrease the sharpness of second phase.

3. The coefficient of thermal expansion of AZ41 magnesium decreases with the addition of nano-sized alumina particulates. Microhardness values also increase with the addition of nano-sized alumina particulates into AZ41 alloy.

4. Room temperature tensile test reveals that the addition of 1.5 vol.% nano-sized alumina particulates into AZ41 helps to increase the ultimate tensile strength (5%), ductility (50%) and work of fracture (57%), while compromising 0.2 % yield strength (8%). Room temperature compressive test results showing a noteworthy improvement of 0.2 YCS (16%), UCS (10%) and ductility (17%) when compared to AZ41 alloy.

Acknowledgments

The authors gratefully acknowledge the support received for this research work ref: NPRP 08-424-2-171 from the Qatar National Research Fund (QNRF), Qatar.

References

[1] J. R. Davis, “Properties and Selection: Nonferrous Alloys and Special-Purpose Materials”, Formerly Tenth Edition, (ASM Handbook, Volume 2, ASM, Metal Park, Ohio, 1993) 480-515, 1099-1100, 1118-1128,1199, 1132-1135.

[2] B. L. Mordike and T. Ebert, “Magnesium: Properties-Applications-Potentials”, Mater. Sci. Eng. A, 302 (2001) 137-45.

[3] G. Neite, K. Kubota, K. Higashi and F. Hehmann, “Magnesium based alloys. In: Cahn RW, Haasen P, Kramer

EJ, editors. Materials Science and Technology. (Germany: Wiley-VCH, 2005) 113-212.

[4] H. E. Friedrich and B. L. Mordike, "Magnesium Technology: Metallurgy, Design Data, Applications", (Germany: Springer-Verlag Berlin Heidelberg, 2006).

[5] Q. B. Nguyen and M. Gupta, "Increasing Significantly the Failure Strain and Work of Fracture of Solidification Processed AZ31B Using Nano-Al_2O_3 Particulates", J. Alloys Compd., 459 (2008) 244-250.

[6] M. E. Alam, S. Han, A. S. M Hamouda, Q. B. Nguyen and M. Gupta, "Development of New Magnesium Based Alloys and their Nanocomposites", Journal of Alloys and Compounds, 509 (2011) 8522-8529.

[7] W. Westengen, "Magnesium: Alloying", Encyclopedia of Materials: Science and Technology, (2008) 4739-4743.

[8] M. E. Alam, S. Han, A. M. S. Hamouda, Q. B. Nguyen and M. Gupta, "Development and Characterization of New AZ41 and AZ51 Magnesium Alloys", W. H. Sillekens, S. R. Agnew, N. R. Neelameggham and S. N. Mathaudhu (Editors), *Magnesium Technology 2011, TMS,* February 27 to March 3, San Diego, California, USA, (2011) 553-558.

[9] D. J. Lloyd, "Particle Reinforced Aluminium and Magnesium Matrix Composites", Int. Mater. Rev., 39 (1994) 1-23.

[10] C. S. Goh, J. Wei, L. C. Lee and M. Gupta, "Development of Novel Carbon Nanotube Reinforced Magnesium Nanocomposites using the Powder Metallurgy Technique", Nanotechnology, 17 (2006) 7-12.

[11] S. F. Hassan and M. Gupta, "Effect of Different types of Nano-sized Oxide Particulates on Microstructural and Mechanical Properties of Elemental Mg", J. Mater. Sci., 41 (2006) 2229-2236.

[12] B. D. Cullity, "Elements of X-Ray Diffraction", (3rd ed., Prentice Hall, London, 2001).

[13] M. Gupta, M. O. Lai, and D. Saravanaranganathan, "Synthesis, Microstructure and Properties Characterization of Disintegrated Melt Deposited Mg/SiC Composites", J. Mater. Sci., 35 (2000) 2155–2165.

[14] G. S. Ansell, in: R. W. Cahn (Ed.), (Physical Metallurgy, North-Holland Publishing Company, Netherlands, 1970).

[15] S. F. Hassan and M. Gupta, "Development of Nano-Y_2O_3 Containing Magnesium Nanocomposites Using Solidification Processing**",** J. Alloys Comp., 429 (2007) 176-183.

[16] Q. B. Nguyen and M. Gupta, "Enhancing Compression Response of AZ31B Magnesium Alloy using Alumina Nanoparticulates", Composites Science and Technology, 68 (2008) 2185–2192.

[17] M. K. Habibi, A. M. S. Hamouda and M. Gupta, " Enhancing Tensile and Compressive Strength of Magnesium using Ball Milled Al+CNT reinforcements", Composite Science and Technology, 72 (2012) 290-298.

Magnesium Technology 2014
Edited by: Martyn Alderman, Michele V. Manuel, Norbert Hort, and Neale R. Neelameggham
TMS (The Minerals, Metals & Materials Society), 2014

PHASE-FIELD MODELING OF SOLIDIFICATION IN LIGHT-METAL MATRIX NANOCOMPOSITES

Tamás Pusztai[1], László Rátkai[1], Attila Szállás[1], László Gránásy[1,2]
[1]Wigner Research Centre for Physics, H-1525 Budapest, POB 49, Hungary
[2]BCAST, Brunel University, Uxbridge, Middlesex, UB8 3PH, United Kingdom

Keywords: Metal Matrix Nanocomposites, Solidification, Phase-field modeling, Particle pushing

Abstract

The quantitative phase-field approach has been adapted to model solidification in the presence of Metal Matrix Nanocomposites (MMNCs) in a single-component liquid. Nanoparticles of fixed size and shape are represented by additional fields. The corresponding equations of motion are assumed to ensure relaxation dynamics, and can be supplemented by random forces (realizing Brownian motion) or external fields. The nanoparticles are characterized by two model parameters: their mobility and the contact angle they realize with the solid-liquid interface. We investigate the question how grain size distribution can be influenced by heterogeneous nucleation on the nanoparticles and by the front-particle interaction. We explore, furthermore, how materials and process parameters, such as temperature, density and size/shape distribution of the nanoparticles, influence microstructure evolution.

Introduction

The Al and Mg based MMNCs are promising candidates for automotive, aerospace, and defense applications due to the drastic weight savings and exceptional properties.[1,2] The distribution of solid nanoreinforcers (10 to 500 nm) in molten alloys is influenced by various phenomena, such as coagulation of the nanoparticles, the interaction between the particles and propagating solidification fronts (particle pushing and engulfment), whereas the nanoparticles themselves may act as heterogeneous nucleation sites for solidification, to mention a few. Owing to the complexity of the solidification process, development of mathematical models that capture the main effects is desirable. Phase-field (PF) modeling is one of the most potent tools for describing microstructure evolution during solidification. The PF approach has already been used to address homogeneous[3] and heterogeneous[4,5] crystal nucleation, dendritic growth,[3,6,7] polycrystalline freezing,[2,8-11] and particle pushing,[12] etc., however, a PF model that addresses all these processes simultaneously is yet unavailable. (A similar model is expected to be useful in modeling the effect of grain refiners, however, on a different size scale.) Herein, we make a step towards such a unified model, and present a PF approach that incorporates heterogeneous nucleation via appropriate boundary conditions and noise representing the thermal fluctuations in addition to a simplified treatment of the particle-front interaction. Illustrative computations are then presented in two dimensions (2D), which explore the effect of nanoparticles on the solidification of pure Mg.

The Applied Phase-Field Models

In order to predict *homogeneous nucleation* in undercooled Mg (which results will serve as reference for the subsequent simulations), we use a detailed PF model of homogeneous nucleation that has achieved reasonable agreement with molecular dynamics simulations for the Lennard-Jones system and with experiments for the ice-water system without adjustable parameters.[3] Here, the Euler-Lagrange equation is solved with appropriate boundary conditions to determine the properties of the homogeneous nucleus, which is then used to compute the nucleation rate as described in Reference 3. The nucleation time is computed as follows: $\tau_1 = 1/(VJ_{SS})$, where $V = L^3$ is the control volume, L the linear size of the simulations, whereas J_{SS} is the steady-state nucleation rate (number of nuclei formed in unit time and volume).

Next, we present the PF model for *heterogeneous nucleation and particle-front interaction*. For the sake of simplicity, we present here the version that handles a single foreign particle. In previous studies, surfaces of the foreign particles have been represented by boundary conditions.[4,5] Physically, this corresponds to sharp interfaces between the simulation volume and the foreign particle (wall) region. However, to model particle pushing, this approach is generally inappropriate, since it is incompatible with a sub-pixel translation of the foreign surfaces. To overcome this limitation, we have generalized Models A of Reference 5 to allow for *diffuse walls,* i.e., where the interface between the impurity particle and simulation volume is not mathematically sharp. This has been achieved by reformulating our phase-field model so that the boundary conditions defining the foreign particles are converted to a volumetric contribution via introducing a new phase field $\phi_w(r)$ for the particle[5]

$$F = \int dV \left\{ Z(\phi)|\nabla\phi_W| + \left[f(\phi) + \frac{\varepsilon^2}{2}(\nabla\phi)^2 \right](1-\phi_W) \right\}$$

as opposed with the original form[4,5,13]

$$F = \int dA\, Z(\phi) + \int dV \left[f(\phi) + \frac{\varepsilon^2}{2}(\nabla\phi)^2 \right]$$

where ϕ is the solid-liquid order parameter (0 in the liquid and 1 in the solid), $Z(\phi)$ is the surface function of Model A that determines the wetting properties of the surfaces, $\phi_w(r)$ is the continuous "wall field" that is 1 inside the volume occupied by the impurity particles and 0 outside with a monotonic transition in a narrow region of width δ between, $f(\phi)$ and $\frac{1}{2}\varepsilon^2(\nabla\phi)^2$ are the usual free energy density and square gradient terms of phase field theory. It is easy to see, that in the $\delta \to 0$ limit, the generalized functional falls back to the original functional, therefore the results obtained with the diffuse wall approach expected to be in good agreement with the results of the original sharp wall approach.

The time evolution of the phase field $\phi(r, t)$, which monitors solidification is determined by the following equation of motion

$$\dot{\phi} = -M_\phi \left\{ \left[\frac{\partial f}{\partial \phi} - \varepsilon^2 \nabla^2 \phi \right] (1 - \phi_W) + \left[\frac{dZ}{d\phi} + \varepsilon^2 (\nabla \phi \cdot \mathbf{n}) \right] |\nabla \phi_W| \right\}$$

where M_ϕ is the phase-field mobility, associated with the translational diffusion coefficient, and **n** is the surface normal of the foreign particle.

To address the dynamics of particle pushing, we derive an equation of motion for the particle in 2D. Since the circular particle is assumed to be of fixed shape and size, it can be described mathematically by a simple radial function as

$$\phi_W(x, y) = \varphi_w \left(\sqrt{(x - x_0)^2 + (y - y_0)^2} \right).$$

(In practice, a *tanh* profile of width δ in the order of 1 nm is used.) This way, all the dependence of the free energy of the system on ϕ_w can be expressed with the x_0 and y_0 central coordinates, and the equations of motion for this coordinates is assumed to follow relaxational dynamics in the form of

$$v_x = -M_w \frac{\partial F}{\partial x_0} = -M_w \int dV \left\{ \left(\left[f(\phi) + \frac{\varepsilon^2}{2} (\nabla \phi)^2 \right] \varphi_w' \right) \frac{x - x_0}{r} \right\},$$
$$\left(- Z(\phi) sign(\varphi_w') \varphi_w'' \right)$$

where v_x is the velocity of the impurity particle and M_w is the mobility of the particle that can be related to viscosity and particle size. Similar equation holds for the y component.

Generalization of this approach to several foreign particles is straightforward: for n particles, one needs to introduce n particle fields, $\phi_{w,i}(r)$ where $i = 1, \ldots, n$. This also means that n equations of motion, similar to the one above, have to be introduced to describe the time evolution of the particle fields. In addition, a hard-sphere interaction is assumed between the foreign particles.

Materials Properties and Model Parameters

The thermal properties of Mg have been taken from the SGTE database.[14] In computing the heterogeneous nucleation rate PF model parameters have been fixed so that the free energy of the equilibrium solid-liquid (89.9 mJ/m^2) has been taken from molecular dynamics simulations,[15] whereas 10%–90% the interface thickness has been assumed to be 2 nm. We have "calibrated" the two 2D simulations so that in the L^2 simulations the first homogeneous nucleation event happens at the same time as in an L^3 volume as emerges from the Euler-Lagrange computations. This has been achieved by introducing (i) a temperature dependent effective solid-liquid interface free energy: $\gamma = (-1.4162\times10^{-1} + 3.2272 \times 10^{-4} T)$ J/m^2, and (ii) the phase field mobility has been set to M_ϕ = 0.16 m^3/Js. In the simulations, unless stated otherwise, L = $512\times\Delta x$ = 0.128 μm, as Δx = 0.25 nm, whereas the time step has been $\Delta t = 10^{-10}$ s. The system has been coupled to a 700 K block via a heat transfer coefficient of $\lambda = 5\times10^4$ W/(m^{2}K), and the heat release during crystallization is also taken into account (distributed uniformly in the simulation box). Other data used here are the melting point T_f = 923.0 K, the heat of fusion ΔH_f = 8.48 kJ/mol, the specific heat C_p = 24.87 J/mol/K, and the molar volume V_m = 1.398×10^{-5} m^3/mol. $M_W = 8.0\times10^{-12}$ m^3/Js. We assume that the 2D simulation refers to a thin layer of $h = 10\Delta x$ thickness. Accordingly, we used in the simulations a fluctuation-dissipation

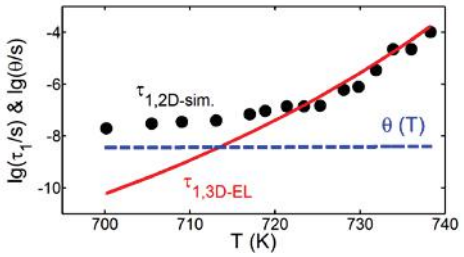


Figure 1. Comparison of nucleation times from 2D simulations (black circles) for homogeneous nucleation performed with adjusted interface free energy and phase-field mobility with nucleation times from steady-state nucleation rate from Euler-Lagrange computations (red line). For comparison the estimated incubation time θ is also shown, indicating that the deviation at lower temperatures is probably due to the nucleation transient. Note the reasonable agreement above 720 K.

noise of amplitude $\zeta = [2k_B T M_\phi / (\Delta t\, \Delta x^2 h)]^{1/2}$. Some of the tests performed in validation of the model have been performed with the properties of nickel. Unless not stated explicitly otherwise, the results refer to Mg.

Results and Discussion

Calibration

Calibration of the 2D simulations in the case of homogeneous nucleation has been done so that the first nucleation time coincides in the L^2 simulation with that from the detailed Euler-Lagrange computations, as shown in Figure 1. When they become available molecular dynamics or experimental data can also be used in calibrating the simulations.

Validation of the Model

Testing the Equilibrium Contact Angle. We have switched off cooling, but retained heat release during solidification, which

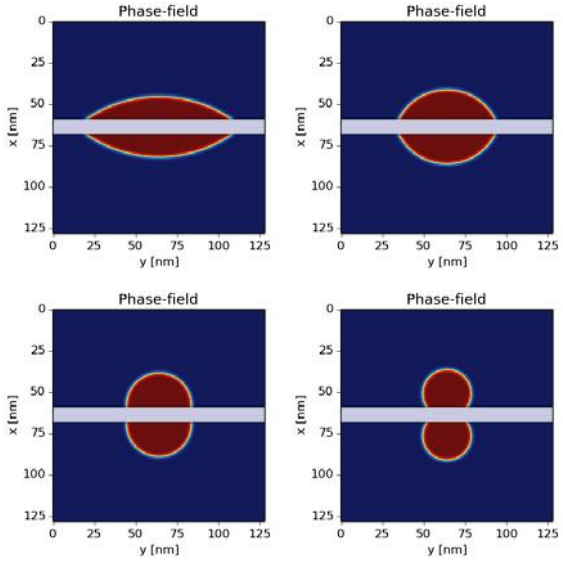


Figure 2. Crystallites approaching equilibrium when prescribing contact angles of 30°, 60°, 90°, and 120° in the PF simulation.

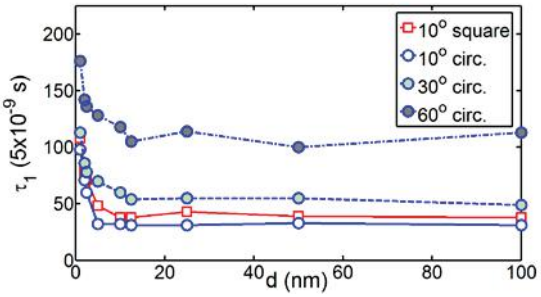


Figure 3. Heterogeneous nucleation time vs. particle size (diameter or edge length) as a function of contact angle in systems, where the total length of the particle perimeters is the same, which length is distributed to a decreasing number of particles from left to right. Circular and square particles behave similarly.

heats up the simulation box to an equilibrium temperature. With appropriate seeding the process can be accelerated. Results for flat interfaces of contact angle ϑ = 30°, 60°, 90°, and 120° are presented in Figure 2. Although a full equilibrium is not yet achieved, the contact angles are close to the prescribed values in all cases.

Testing of Heterogeneous Nucleation. On the basis of theoretical consideration one expects that the time of appearance of the first nucleus depends only on the total length of the particle perimeters, while to a first approximation, it is independent of the number of particles, so far as the individual particle sizes are substantially larger than the homogeneous nucleus. We have tested this for ϑ = 10°, 30°, and 60°: we have distributed the total perimeter length among an increasing number of particles of uniform size. The

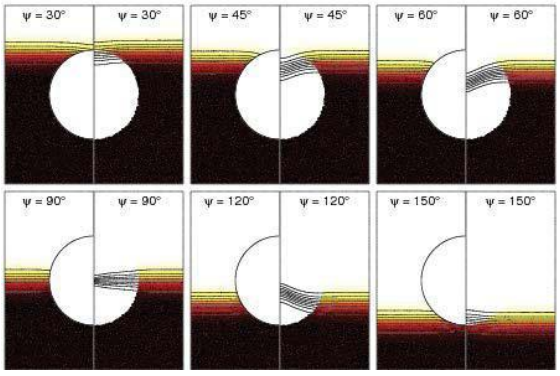


Figure 4. Stationary configurations of particles pushed by a planar solidification front in Ni at an undercooling of 10K. The panels show the half cross sections of the cylindrically symmetric 3D steady state solutions travelling with the velocity corresponding to the velocity of the free solid-liquid interface. The transition from black to white indicates the transition from the solid to liquid phase, while the contour lines corresponding to ϕ_0 = 0.1, 0.2, … , 0.9 are also plotted. The left and right sides of the double panels show the solutions based on the sharp and diffuse wall approaches, respectively. In the case of diffuse walls, the solution assigns ϕ values to the interior of the particle, which, for better visibility, is shown only by its contour lines and not by the respective colors. The diameter of the particle is 40nm, while the size of the simulation box is 40×80 nm in all panels.

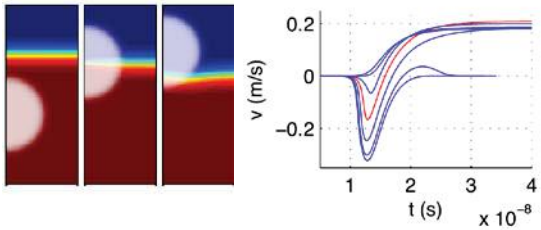


Figure 5. Particle pushing by a planar solidification front as predicted by the phase-field theory in Ni. The left three panels correspond to ϑ = 30°, 90°, and 150° and show the snapshots of the radial cross sections of the cylindrically symmetric 3D solutions approximately 2×10^{-8} s after the solidification front reached the particle. (The central snapshot corresponds to the right side of the 90° panel in Fig. 4.) The rightmost panel shows the velocity profiles evaluated from the simulations. After a transient period, the particle is either engulfed by the moving solid-liquid interface (at low contact angles) or pushed (at high contact angles). At the velocity minimum ($t \approx 1.3 \times 10^{-8}$ s), the curves from bottom to top correspond to contact angles ϑ = 0°, 30°, 60°, 90°, 120°, 150°, and 180°, respectively.

results are shown in Figure 3 for both circular and square-shaped particles. Indeed, for larger particles (L > 10 nm), we find a reasonably constant nucleation time, however, for smaller particles the nucleation efficiency decreases as expected theoretically.[16]

Testing of Particle-Front Interaction (Steady State). Using the properties of Ni, we have determined the steady state configurations where the particle has the same speed as the propagating solidification front. This configuration can be found as the time independent solution of the equation of motion expressed in a local coordinate system moving with the front. We utilized the cylindrical symmetry of the problem, reducing thus the dimensionality of the solution from 3 to 2. Since in the time independent solutions no displacement of the impurity particle is required (the particle moves together with the frame), both the sharp and the diffuse wall approaches can be used to address this problem, making this scenario an ideal candidate for comparing the results obtained by sharp and diffuse interfaces. As displayed by Figure 4, the two solutions are almost identical outside the impurity particle, i.e., in the physically relevant domain.

Testing of Particle-Front Interaction (Dynamics). Using the properties of pure Ni, we have solved numerically the equation of motions for the phase field and the particle fields. We have adjusted M_w so that velocity of the particle coincides with the velocity of the steady-state solution for a particle with 90° contact angle at the solid-liquid interface. Then we varied the contact angle between 0 and 180° (see Figure 5). We have found that below a critical contact angle that falls between 30° and 60°, the particle is engulfed, while above this critical contact angle the particle is pushed by the advancing solidification front.

Size Distribution of Particles. We have performed simulations for 200 circular particles of average radius of 10Δx and standard deviation of 5Δx of two kinds of monodisperse distribution, which show uniform and normal distributions, and a bimodal size distribution. The mobility of the particles is reduced so much that particle motion is entirely negligible during the simulations. The results are summarized in Figures 6(a)-(c). Apparently, features of the size distribution of the foreign particles are reflected by the

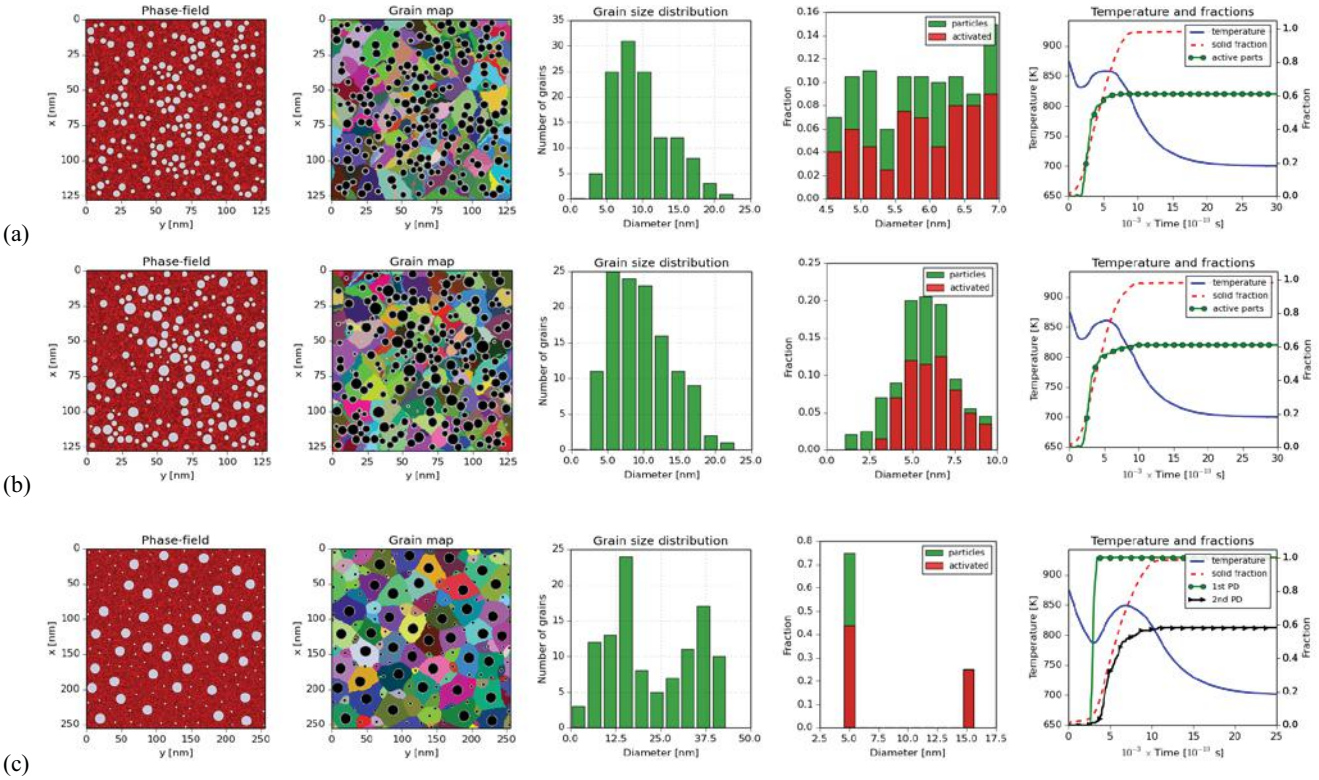


Figure 6. Solidification in the presence of foreign particles of $\vartheta = 10°$: 200 particles of (a) uniform, (b) normal, and 160 particles of (c) bimodal size distribution (40 large, 120 small). The final (fully solidified) stage is shown. From left to right, the phase-field map, the grain map (different colors correspond to different grains), the size distribution of the crystalline grains, the size distribution of the foreign particles (red fraction participated in nucleation), and the time evolution for the temperature (solid), the crystalline fraction (dashed), and the fraction of activated foreign particles (circles and triangles for the two sizes) are shown. Grid sizes: (a), (b) 512×512 and (c) 1024×1024.

grain size distribution. For example, a bimodal particle distribution of foreign particles often leads to a bimodal grain size distribution (Fig. 6(c)). A general observation is that crystallization starts in areas, where the particle density is the largest.

Particle Motion. Finally, relying on the assumption of overdamped dynamics, we have set the particle mobility to $M_W = 1/(6\pi\mu R)$, which follows from the expression for the Stokes velocity, where $\mu = 1$ mPa.s is assumed for the dynamic viscosity in a simulation performed under conditions identical to those used for computing Figure 6(c). As a result, the particles started to display Brownian motion-like behavior due to the capillary forces emerging from the phase-field fluctuations (see Figure 7). This motion is, however, soon stopped by the growing crystals. Owing to the small contact angle (10°), the particles are easily engulfed into the growing crystal. The grain size distribution is fairly similar to the one obtained without particle motion. Note the differences in the initial and final spatial arrangement of the foreign particles, which originate from their stochastic motion. For comparison, we performed a similar simulation, however, now the contact angle of the small particles have been set to 120°. As a result, the small particles are being pushed by the solidification front (Figure 8), and accumulate at the grain boundaries and in liquid pockets. The latter often lead to the formation of particle islands, consisting of closely packed small particles (located on a hexagonal lattice). Hence, particle pushing leads to a drastic spatial rearrangement of the small particles.

Larger simulations are yet needed to reveal details of the connection between the size distributions of the foreign particles and the grain size distribution.

Summary

We have presented a simple phase-field model that addresses crystal nucleation and growth in the presence of foreign particles characterized by a size and viscosity related mobility and a contact angle. The model has been tested concerning equilibrium and dynamical contact angles, for heterogeneous nucleation and particle pushing, and has shown a reasonable behavior. Illustrative simulations have been performed that show that the size distribution of the foreign particles is reflected in the size distribution of the crystalline particles. For example, a bimodal particle size distribution of the foreign particles may lead to a bimodal grain size distribution. It has also been demonstrated that particle motion can be taken into account, and it may influence the solidification microstructure considerably, especially if the contact angle of the particles is large. Work is underway to extend the capabilities of the model towards quantitative modeling of particle induced solidification in alloys.

Acknowledgments

This work has been supported by in the framework of the EU FP7 Collaborative Project “EXOMET” (contract no. NMP-LA-2012-280421, co-funded by ESA).

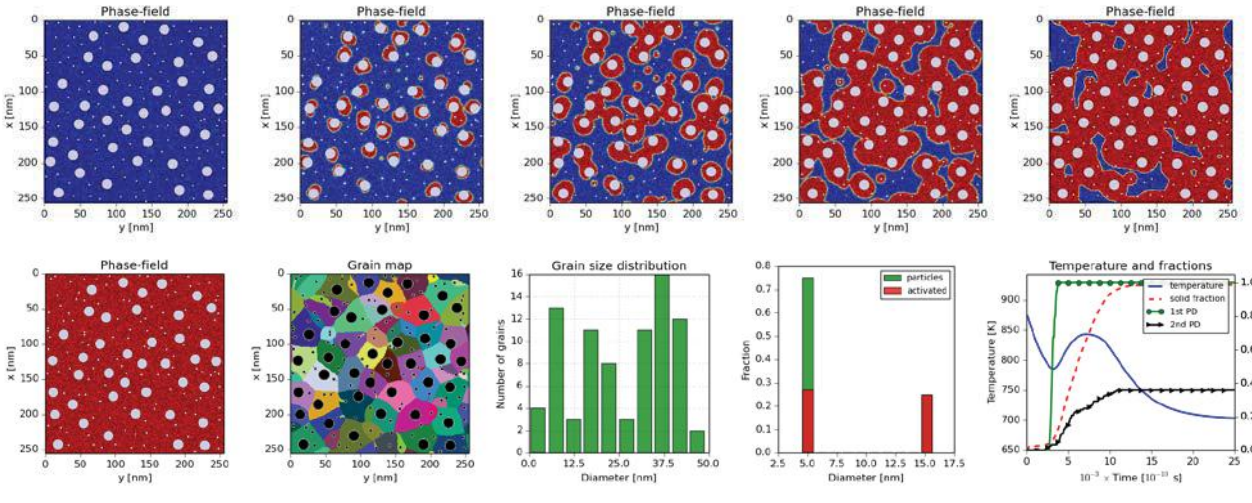


Figure 7. As the simulation shown in Figure 6(c), however, the particles *move due to capillary forces emerging from phase-field fluctuations*: (a) Snapshots showing of the phase field map. (b) The same sequence of panels as displayed in Fig. 6. Particle motion has changed somewhat the grain size distribution and the nucleation kinetics on the small particles relative to Figure 6(c).

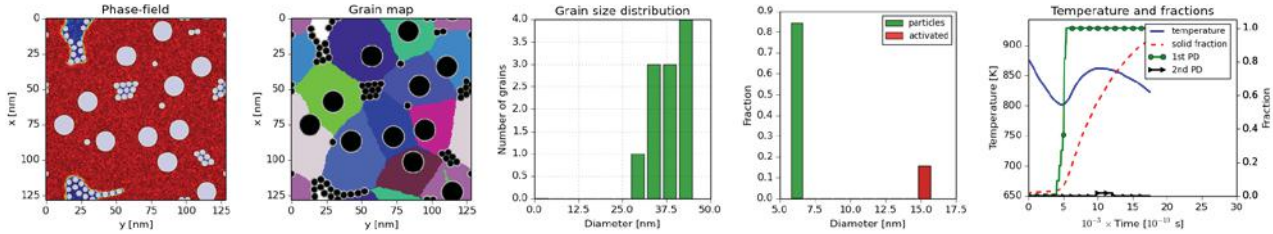


Figure 8. Late stage of freezing in the presence of 70 particles (11 large of $\vartheta = 10°$, 59 small of $\vartheta = 120°$). Note that particle pushing drives the small particles to the grain boundaries or into liquid pockets (blue and white regions in panels No. 1 and 2, respectively). In the liquid pockets hexagonal particle arrangements form eventually, as freezing progresses. Note that only the large particles induce nucleation.

References

1. A. Mortensen and J. Lorca, "Metall Matrix Composites," *Ann. Rev. Mater. Res*, 40 (2010), 243–270.
2. P.K. Rohatgi and B. Schultz, "Lightweight Metal Matrix Nanocomposites – Stretching the Boundaries of Metals," *Material Matters*, 2 (2007), art. no.16.
3. L. Gránásy, T. Börzsönyi, and T. Pusztai, "Nucleation and Bulk Crystallization in Binary Phase Field Theory," *Phys. Rev. Lett.*., 88 (2002), art. no. 206105.
4. L. Gránásy, T. Pusztai, D. Saylor, and J. A. Warren, "Phase Field Theory of Heterogeneous Crystal Nucleation," *Phys. Rev. Lett.*, 98 (2007) art. no. 035703.
5. J. A. Warren, T. Pusztai, L. Környei, and L. Gránásy, "Phase Field Approach to Heterogeneous Crystal Nucleation in Alloys," *Phys. Rev. B*, 79 (2009), art. no. 014204.
6. J. A. Warren and W. J. Boettinger, "Prediction of Dendritic Growth and Microsegregation Patterns in a Binary Alloy Using the Phase-Field Method," *Acta Metall. Mater.*, 43 (1995), 689–703.
7. A. Karma and W.-J. Rappel, "Quantitative Phase-Field Modeling of Dendritic Growth in Two and Three Dimensions," *Phys. Rev. E*, 57 (1998), 4323–4349.
8. R. Kobayashi, J. A. Warren, and W. C. Carter, "Vector Valued Phase Field Model for Crystallization and Grain Boundary Formation," *Physica D*, 119 (1998), 415–423.
9. L. Gránásy, T. Pusztai, J. A. Warren, J. F. Douglas, T. Börzsönyi, and V. Ferreiro, "Growth of 'dizzy dendrites' in a random field of foreign particles," *Nature Mater.*, 2 (2003), 92–96.
10. L. Gránásy, T. Pusztai, G. Tegze, J. A. Warren, and J. F. Douglas, "Growth and Form of Spherulites" *Phys. Rev. E*, 72 (2005), art. no. 011605.
11. H. Henry, J. Mellenthin, and M. Plapp, "Orientation-field Model for Polycrystalline Solidification with a Singular Coupling between Order and Orientation" *Phys. Rev. B*, 86 (2012), art. no. 054117.
12. M. Ode, J. S. Lee, S. G. Kim, W. T. Kim, and T. Suzuki, "Numerical Simulation of the Critical Velocity for Particle Pushing/Engulfment Transition in Fe–C alloys Using a Phase-Field Model" *ISIJ Int.*, 40 (2000), 153–160.
13. T. Pusztai, G. Tegze, G.I. Tóth, L. Környei, G. Bansel, Z. Fan, and L. Gránásy, "Phase-field Approach to Polycrystalline Solidification Including Heterogeneous and Homogeneous Nucleation" *J Phys.: Condens. Matter*, 20 (2008), art. no. 404205.
14. A. T. Dinsdale, "SGTE Data for Pure Elements," *CALPHAD* 15 (1991), 317-425.
15. Y. G. Xia, D. Y. Sun, M. Asta, and J. J. Hoyt, "Molecular Dynamics Calculations of the Crystal-Melt Interfacial Mobility for Hexagonal Close-packed Mg" *Phys, Rev. B*, 75 (2007), art. no. 012103.
16. X. Y. Liu, K. Maiwa, and K. Tsukamoto, "Heterogeneous Two-dimensional Nucleation and Growth kinetics" *J. Chem. Phys.*, 106 (1997), 1870–1879.

Magnesium Technology 2014
Edited by: Martyn Alderman, Michele V. Manuel, Norbert Hort, and Neale R. Neelameggham
TMS (The Minerals, Metals & Materials Society), 2014

ADVANCED CHARACTERIZATION OF METAL MATRIX NANO-COMPOSITES

Mounib Maher[1], Lefebvre Williams[1]
[1]GPM (Groupe de Physique des Matériaux); Avenue de L'Université – BP12, 76801, Saint Etienne du Rouvray, France

Keywords: MMNCs, nano-particles, external field

Abstract

Performances of Metal Matrix Nano-Composites (MMNCs) are strongly related to the distribution of particles inside the metal matrix and also to the eventual chemical reactions which may occur at the interfaces.

This paper presents characterizations made on magnesium alloys AZ91 reinforced respectively with Y_2O_3 and MgO (nano)-particles. Different characterization techniques such as scanning electron microscopy (SEM) and transmission electron microscopy (TEM) were used to characterize these metal matrix (nano)-composites. Analyzes were performed to emphasize microstructure, distribution of particles in the MMNCs and eventual chemical reactions at matrix/particles interfaces. Results demonstrate the presence of MgO particles inside the matrix and no chemical reactions were detected at the interfaces. However Y_2O_3 particles were found gathered near $Mg_{17}Al_{12}$ areas.

Introduction

Metal matrix composites (MMCs) are one of the most attractive materials due to their properties. They have growing importance in a variety of fields, particularly in aerospace and automotive but they also find applications in electronic industries. MMCs are especially appreciated for their characteristics, notably for their low density but also for their potential enhanced mechanical properties such as the yield strength, ultimate tensile strength, hardness and stiffness. The addition of nano-sized particles has greater strengthening effect, based on total strengthening effect model [1]. Strongest MMCs will most likely be those which are reinforced with small nanoparticles closely spaced together.

Many processing methods to elaborate MMCs are available and many of them use liquid and solid processing routes. Each process has its own advantages, drawbacks and applications. The mechanical properties and microstructures are sensitive to the processing route used to produce these materials [2]. Among numerous liquid state processes used to produce metal matrix composites, stir casting is widely used, reinforcement particles are incorporated into the molten alloy, while a mixer is set to obtain a suitable dispersion and then the solidification of the molten alloy occurs respecting certain conditions to obtain the desired distribution. This processing method is flexible, cost-effective and allows mass production. However liquid stirring has also some major problems [3,4] such as the poor wetting of the reinforcement particles by the liquid metal matrix and the tendency of reinforcement particles to sink or float depending on their density relative to that of the melt. In addition, when dealing with nano-scale there is a tendency for nano-particles to agglomerate and form large clusters. Coupling external fields such as electromagnetic field, power ultrasound or high-energy liquid shearing to liquid metal processing will overcome these issues by dispersing nanoparticles to obtain a homogeneous distribution into the melt and in the mold after solidification step.

AZ91 magnesium alloy is one of the most well-known commercial light alloys, it has good castability and it is commonly used for complex shape castings. Different types of ceramic particles have been selected based on their physical properties such as high hardness, high compressive strength, high melting point for MgO [5] and thermodynamic stability with molten and solid magnesium matrix for Y_2O_3 [6].

The aim of this work is to characterize microstructures of AZ91 composites and to reveal the respective distribution of the reinforcement particles.

Experimental

Materials were produced at Helmholtz Zentrum Geesthacht (HZG) in Germany. Chemical composition of the AZ91 Mg-alloy is listed in Table I. Y_2O_3 and MgO ceramic particles with an average size of a few microns and 300 nm respectively were used as the reinforcing materials. The processing method for producing both composites was ultrasonic cavitation stirring. Ceramic particles (1 wt. %) were introduced into the molten alloy, the homogenization of the mixture was conducted using high speed stirring (200 rpm), a power ultrasound external field was applied to obtain a homogeneous distribution followed by water quenching.

Microstructural characterization of AZ91 + Y_2O_3 was carried out on scanning electron microscope (SEM-LEO FE 1530 cross beam). Samples for the SEM analysis were prepared by mechanical polishing using an oil based lubricant. The analysis of AZ91 + MgO was carried out on transmission electron microscopes (JEOL JEM 2010 and JEOL ARM 200F). Samples were prepared from 3 mm diameter disks (average thickness of 160 μm) followed by mechanical grinding with a dimple and finally an ion milling at room temperature was applied (final energy of Ar ions set to 1.5 keV).

Table I. Chemical composition (in wt. %) of AZ91 Mg-alloy.

Al	Zn	Mn	Si	Fe	Cu	Ni	Mg
8.71	0.66	0.22	0.043	0.001	0.002	0.001	Bal.

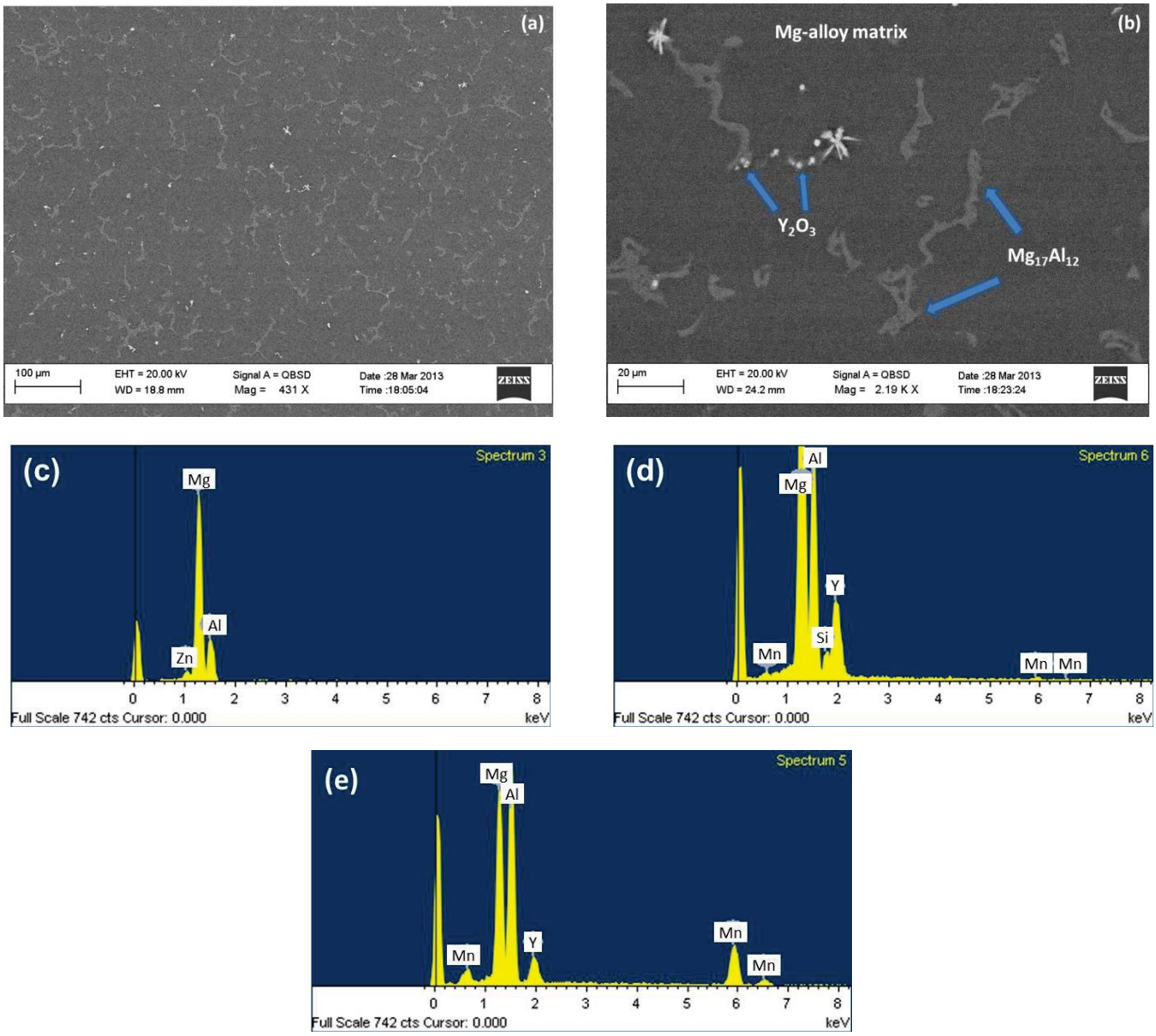


Fig.1. (a) SEM picture of the microstructure of AZ91+ Y_2O_3 composite, (b) SEM picture showing location of Y_2O_3 particles, (c) EDS spectrum of $Mg_{17}Al_{12}$ precipitates, (d) EDS spectrum of Y_2O_3 particles, (e) EDS spectrum of Al_4Mn.

Results And Discussion

AZ91 + Y_2O_3 Particles

Fig.1. shows the microstructure of the AZ91+ Y_2O_3 composite supported by EDS analyses. Interdendritic eutectic areas composed of $Mg_{17}Al_{12}$ phase and Mg-matrix are visible in slightly brighter contrast whereas bright are clearly identified. At higher magnification as it is shown in Fig.1.b, Y_2O_3 particles can be observed in eutectic regions. None of those particles could be identified inside Mg-dendrites. These results imply that Y_2O_3 particles are rejected from the primary Mg-crystals and are pushed during the solidification process. It can be noted also in Fig.1.b the presence of star shaped Al_4Mn intermetallics in very bright contrast.

These pushing effects which gather and push particles at the end of the solidification front lead to a non-homogeneous distribution of particles inside the matrix which is expected to be detrimental for mechanical properties.

AZ91 + MgO Particles

By means of TEM, the complex microstructure of AZ91+MgO MMNCs has been investigated. First, eutectic regions have been observed by means of high angle annular dark field scanning TEM (HAADF-STEM). This mode of observation allows distinguishing features by means of their contrast in mean atomic number.

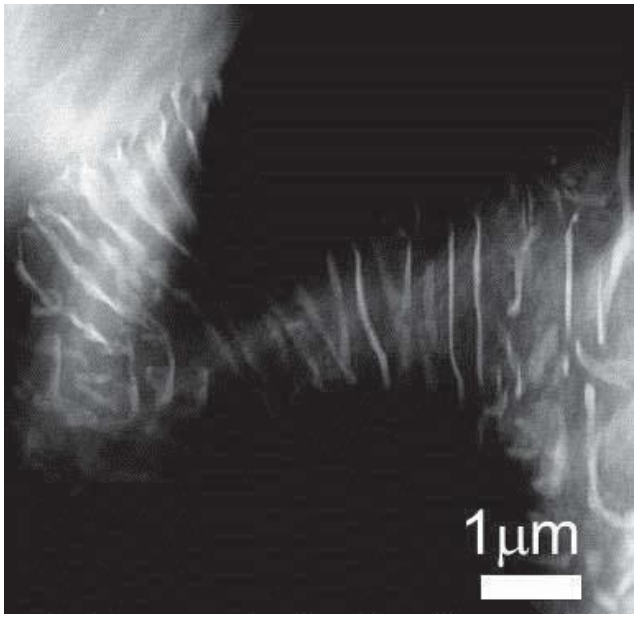


Fig.2 . HAADF-STEM observation of a eutectic region (AZ91+MgO composite).

Fig.2 reveals an alternation of bright and dim regions, corresponding to Al rich or poor phases respectively. Similar observations did not reveal the presence of MgO particles in eutectic regions.

Further observations in TEM, combined with EDS spectra, reveal the presence of numerous nanometer size Mn-containing particles, one of which is displayed in Fig.3. The high resolution observation of an Al_4Mn/Mg matrix interface does not demonstrate any crystallographic relationship between such particles and the matrix. This suggests that these features are already present in the melt.

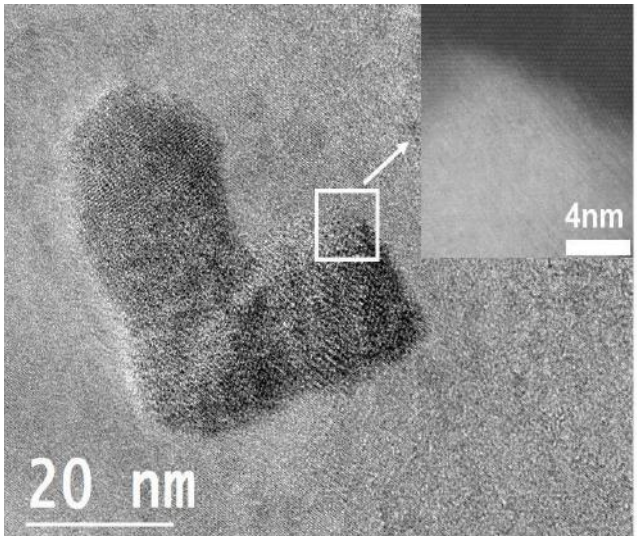
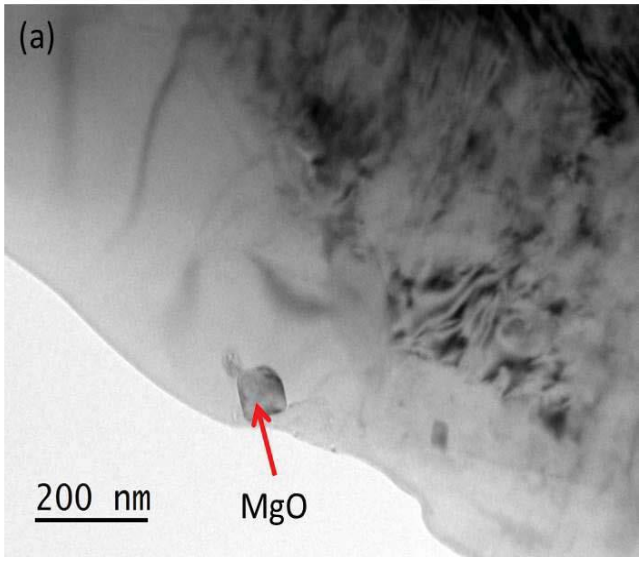


Fig.3. Al_4Mn particle observed in HRTEM. The inset is a high resolution HAADF-STEM observation of the particle/Mg-matrix interface identified by the white square. (AZ91+MgO composite)

Despite the observation of large areas in the TEM-foils, very few MgO particles could be identified. However, those particles, when visible, are found inside the Mg matrix, away from eutectic regions. Fig 4.a shows an MgO nano-particle (100 nm) and as it is shown in the results of EDS analysis in Fig. 4.b no reaction with the matrix could be identified. However, this point should be clarified by further investigations. Further investigations into the relationship between MgO particles and the Mg-matrix will also help clarifying the interaction between these particles and the melt. Nevertheless, the fact that MgO particles are visible inside the Mg-matrix, in opposition to Y_2O_3 particles suggests that the wetting of MgO nano-particles by Mg is better.



(b)

Element	Weight%	Atomic%
O K	36,95	47,11
Mg K	63,05	52,89
Totals	100	

Fig.4. (a) SEM picture showing MgO nano-particle, (b) EDS analysis results of MgO nano-particle. (AZ91+MgO composite)

Conclusions

Metal matrix composites made of a combination of AZ91 matrix and Y_2O_3 or MgO particles have been investigated by electron microscopy techniques. Y_2O_3 is found to be pushed by Mg-dendrites during the solidification process. This is proved by the fact that they are systematically observed in solidified eutectic regions. On the opposite, MgO particles could be identified inside Mg-matrix areas in transmission electron microscopy. Further investigations, especially high resolution observations of particle/matrix interfaces, are expected to help understanding the mechanisms controlling the distribution of reinforcement particles. The pushing/engulfment effects are strongly dependent

on particle/matrix interfaces, therefore further systems with different particle size should be studied to emphasize the influence of the particle size.

References

[1] Z. Zhang and D. Chen, "Consideration of Orowan strengthening effect in particulate-reinforced metal matrix nanocomposites: A model for predicting their yield strength," *Scripta Materialia*, vol. 54, no. 7, pp. 1321 – 1326, 2006.

[2] J. Hashim, L. Looney, and M. Hashmi, "Metal matrix composites: production by the stir casting method," *Journal of Materials Processing Technology*, vol. 92–93, pp. 1 – 7, 1999.

[3] S. Sajjadi, H. Ezatpour, and M. T. Parizi, "Comparison of microstructure and mechanical properties of A356 aluminum alloy/Al_2O_3 composites fabricated by stir and compo-casting processes," *Materials and Design*, vol. 34, pp. 106 – 111, 2012.

[4] K. Nie, X. Wang, X. Hu, L. Xu, K. Wu, and M. Zheng, "Microstructure and mechanical properties of SiC nanoparticles reinforced magnesium matrix composites fabricated by ultrasonic vibration," *Materials Science and Engineering: A*, vol. 528, no. 15, pp. 5278 – 5282, 2011.

[5] H. Abdizadeh, R. Ebrahimifard, and M. A. Baghchesara, "Investigation of microstructure and mechanical properties of nano MgO reinforced al composites manufactured by stir casting and powder metallurgy methods: A comparative study," *Composites Part B: Engineering*, vol. 56, pp. 217 – 221, 2014.

[6] B. Han and D. Dunand, "Microstructure and mechanical properties of magnesium containing high volume fractions of yttria dispersoids," *Materials Science and Engineering: A*, vol. 277, pp. 297 – 304, 2000.

Magnesium Technology 2014

SYMPOSIUM: LIGHT-METAL MATRIX (NANO)-COMPOSITES

Emerging Processes

Papers in this section have been presented in a separate symposium at the 2014 TMS Annual Meeting organized by Dr. W. Sillekens and Prof. D.G. Eskin. This section was co-edited by the symposium organizers and all papers were peer reviewed.

Magnesium Technology 2014
Edited by: Martyn Alderman, Michele V. Manuel, Norbert Hort, and Neale R. Neelameggham
TMS (The Minerals, Metals & Materials Society), 2014

ACHIEVING UNIFORM DISTRIBUTION AND DISPERSION OF A HIGH PERCENTAGE NANOPARTICLES IN Mg18Sn MATRIX BY SOLIDIFICATION PROCESSING

Lian-Yi Chen[1,2], Jun-Yang Peng[1], Jia-QuanXu[2], Hongseok Choi[1] and Xiao-Chun Li[1,2]
[1]Department of Mechanical Engineering, University of Wisconsin-Madison, Madison WI 53706, USA
[2]Materials Science Program, University of Wisconsin-Madison, Madison WI 53706, USA

Keywords: Metal matrix nanocomposites, magnesium alloy, ultrasonic processing

Abstract

It is extremely difficult to incorporate and disperse nanoparticles (NPs), especially for a high percentage, into metal matrix during solidification processing to achieve crucial property enhancement in metal matrix nanocomposites (MMNCs), mainly due to the strong tendency of NP aggregation. Thus, the significant property enhancement expected by the addition of a high percentage of NPs is rarely achieved in solidification processing of bulk MMNCs. Here we show that an unprecedented uniform distribution of 5 vol.% SiC NPs in Mg18Sn alloy matrix is obtained by solidification processing. The resulting Mg18Sn matrix nanocomposites exhibits a very high microhardness value of 150 kg/mm^2. The results reported in this work shed light on a potential pathway for production of ultrahigh performance metallic nanocomposites.

Introduction

Introducing thermally stable and nano-sized ceramic particles into metal matrix is a potential way to significantly enhance the property of metals and alloys to meet the ever increasing demand for strong, lightweight, and high temperature metals and alloys [1-3]. However, dispersion of nanoparticles in metal matrix is crucial for the property enhancement induced by nanoparticles, and has proven to be extremely difficult, especially for high volume percentage nanoparticles, mainly due to the attractive van der Waals force between nanoparticles and the lack of engineered repulsive forces between the nanoparticles [3-5].

To address the challenge of dispersing nanoparticles uniformly in metal matrix, both solid-state and liquid-state processing methods were explored. First, the solid-state high energy ball milling was experimented to disperse nanoparticles in metal matrix [6, 7]. High energy ball milling under optimized conditions can disperse low volume fraction (less than 2 vol.%) nanoparticles very uniformly in a metal matrix [7]. However, when the volume fraction of nanoparticles is higher than 2 vol.%, nanoparticles cannot be dispersed well even after a long time using high energy ball milling; nanoparticles tend to form cluster and segregate around grain boundary during processing [7]. High energy ball milling is also very time consuming, thus expensive, and often meets with a contamination problem. Solid-state friction stir processing was also explored to process surface, wire or plate MMNCs by using the high shearing forces generated by the rotating tool [8, 9]. Nanoparticles can be dispersed very well in metal matrix under optimized conditions [10, 11]. However, it is very difficult to produce product with complex shape in large volume by this method.

Recently, liquid-state ultrasonic processing was applied to process bulk MMNCs through solidification processing [12-15]. This method has the potential to produce low-cost bulk MMNCs components directly by solidification processing. However, in the liquid state solidification processing, there are significant challenges. First, non-oxide nanoparticles are easy to burn during their feeding at high temperature (above the liquidus temperature of the metal); second, nanoparticles tend to float up to the top of the melt or settle down to the bottom of the crucible without effective incorporation into the molten metal due to the poor wettability of nanoparticles with molten metal; third, nanoparticles form clusters in molten metal due to attractive van der Waals force and the lack of repulsive forces; fourth, nanoparticles are normally pushed to grain boundary by solidification fronts during solidification [16]. Due to these challenges, a uniform distribution of nanoparticles in metal matrix is extremely difficult to achieve even in samples with a low volume fraction of nanoparticles by solidification processing. Thus, the theoretical property enhancement induced by nanoparticles is rarely achieved in metal matrix nanocomposites with high percentage of nanoparticles.

Here we report an effective incorporation and uniform distribution of 5 vol.% SiC nanoparticles in Mg18Sn alloy matrix by a solidification processing method. The nanoparticles ware fed into molten metal by cold compressed nanoparticle pellet, serving as master nanocomposite. The nanoparticle pellet consists of ceramic nanoparticles (reinforcing nanoparticles) and metal nanoparticles (improving wetting). The nanoparticles were dispersed by ultrasonic processing.

Materials and Methods

To solve the burning, floating or settling of nanoparticles during feeding at liquid state, we developed a master nanocomposite pellet approach to feed nanoparticles into molten metal, as shown in Fig. 1. The reinforcing ceramic nanoparticles (50 nm diameter SiC in this work, shown in Fig. 2) together with metal nanoparticles (100 nm diameter tin in this work) were put into a low temperature liquid (acetone in this work) which has good wettability with both particles. The reinforcing nanoparticles and metal nanoparticles were mixed thoroughly by ultrasonic processing to get a uniform mixing in the low temperature liquid, as shown in Fig. 1a. The dry mixture of the reinforcing nanoparticles and metal nanoparticles were obtained by evaporating the low temperature liquid. Then, the well mixed dry nanoparticle mixture was compressed to nanoparticle pellet by cold compression in a steel mold (at a pressure of 500 MPa in this work), as shown in Fig. 1b. The cold compressed nanoparticle pellet as a reinforcement nanoparticle carrier was fed into molten magnesium to form Mg-18Sn (i.e. magnesium with 18 weight percent tin) directly. Due to the availability of the high quality Sn nanoparticles in market, we select Sn as a nanoparticle carrier to form MgSn alloy for this study. After pushing nanoparticle pellet into molten metal (700 ^{0}C, 60 ml) by a ceramic rod, the

nanoparticle pellet is dissolved and nanoparticles are released from the pellet.

After the incorporation of nanoparticles into molten metal, the ultrasonic processing was used to disperse nanoparticles in molten metal, as shown in Fig. 2. A high power ultrasonic probe with a diameter of 12.7 mm, frequency of 20 kHz and a peak-to-peak vibration amplitude of 60 μm was inserted about 6 mm in depth into melt. The intense transient cavitation generated by the ultrasonic probe was used to overcome the attractive van der Waals force between nanoparticles to disperse nanoparticles into molten metal.

After ultrasonic processing, the melt was solidified inside crucible in air at a cooling rate of about 1 K/s. The distribution of nanoparticle in the solidified metal matrix was investigated by high resolution electron scanning microscopy (HRSEM, LEO 1530, Carl Zeiss).

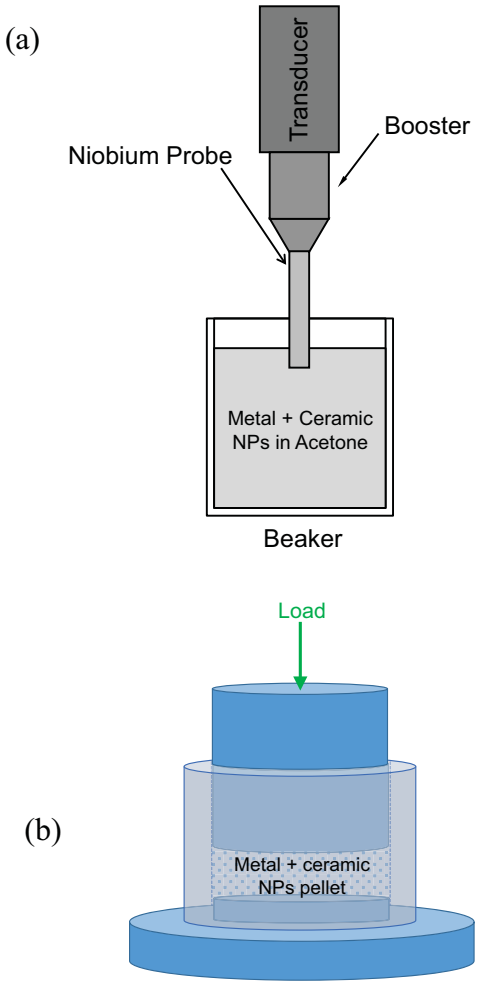


Fig. 1 Schematic of the processing procedure for nanoparticle pellet. Metal nanoparticles and ceramic nanoparticles are mixed by ultrasonic processing in low temperature liquid at room temperature, then dried and cold compressed to form master nanocomposite pellet for feeding.

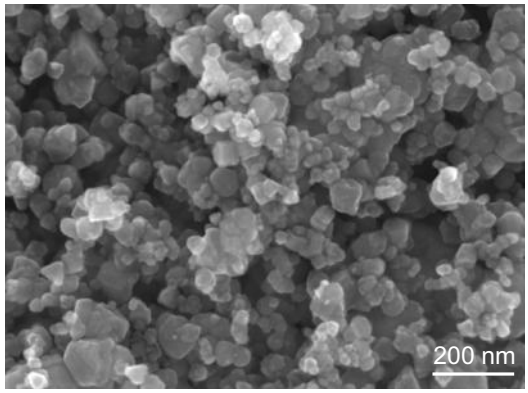


Fig. 2 SEM image of the SiC nanoparticles.

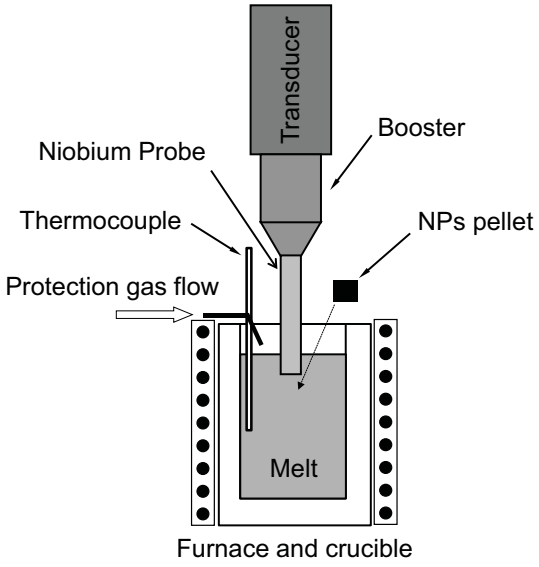


Fig. 3 Schematic of the ultrasonic processing. The ultrasonic processing system consists of an ultrasonic probe, booster, and transducer. A ultrasonic probe made of niobium alloy C103 with a diameter of 12.7 mm was attached to a booster (Sonicator 3000, Misonix Inc.), which was mounted in a transducer working under a frequency of 20 kHz and a maximum 600 W power output. Ultrasonic vibration with a frequency of 20 kHz and a peak-to-peak amplitude of 60 μm was generated from the transducer to create cavitation to overcome the attractive van der Waals force between nanoparticles.

Results and Discussion

Nanoparticles Feeding

5 vol.% SiC nanoparticles with an average diameter of 50 nm was fed into molten Mg18Sn alloy by the master nanocomposite pellet method without burning. During feeding, the pellet was immersed into the molten metal rapidly under the pushing of a ceramic rod. It is expected that the short exposure time of nanoparticle to the

oxygen in the environment at high temperature may avoid/reduce the burning of nanoparticles. After being immersed in molten metal, the metal nanoparticles in the pellet are dissolved in molten metal, and the reinforcing ceramic nanoparticles are released. This approach provides a simple way to incorporate reinforcing nanoparticles into molten metal at high temperature, especially important for non-oxide nanoparticles.

Nanoparticles Dispersion

With incorporation of 5 vol.% nanoparticles into molten metal, the viscosity of the molten metal increases, which results in the reduction of the acoustic streaming generated by ultrasonic processing. Thus, only localized area can be processed at once. The size of the well-processed region depends on the size of the probe. In our study, the well processed region is about 15 mm x 15 mm x 1-2 mm. The continuous moving of the ultrasonic processing probe or external stirring is needed to scale up the well processed region, which is ongoing.

The distribution of SiC nanoparticles in the well processed region in Mg18Sn metal matrix is shown in Fig. 4. Fig.4 (a) shows the low magnification SEM images of the Mg18Sn + 5 vol.% SiC nanoparticles sample (hereafter noted as Mg18Sn-5vSiC). The nanoparticles (tiny spot in the image) are distributed in both Mg matrix (continuous darker phase in the images) and intermetallic phase (micrometer-sized brighter phase in the images) region uniformly. The higher magnification SEM image in Fig.4 (b) confirms that the nanoparticles are dispersed very well and distributed uniformly in the Mg matrix. Some nanoparticle clusters are also observed. The size of the nanoparticle clusters is usually less than 1 micrometer, and the submicron nanoparticle clusters only contain a few nanoparticles. The ripple-like surface feature in Fig. 4(b) is caused by the low angle ion milling that was used to clean the polished surface of the sample to prevent the interference of nano-sized polishing powders (sticking on the surface of the sample during polishing) on the added SiC nanoparticles.

The uniform distribution of the high volume fraction of nanoparticles in the solidified Mg18Zn alloy justifies that the ultrasonic processing is a powerful approach to disperse nanoparticles uniformly in molten metal. Nanoparticle is usually pushed by the repulsive force between nanoparticle and the solidification front to the last solidified region (grain boundaries or intermetallic phases) [16]. Pushing of nanoparticles by solidification front usually results in a significant redistribution of nanoparticles during solidification, which is a big challenge in solidification processing of metal matrix nanocomposites. The uniform distribution of nanoparticles in the solidified metal in this work indicates that the nanoparticles are captured rather than pushed by solidification front during solidification. The capture of the nanoparticles observed here may be attributed to the high viscosity induced by the high volume fraction of nanoparticles [16]. The high viscosity may exert a high viscous force on the nanoparticles to overcome the pushing by solidification front [16]. Therefore, a uniform distribution of nanoparticles after solidification can be obtained.

Mechanical Property

The mechanical property of the nanocomposite is evaluated by microhardness testing with load of 200 grams and dwell time of 10 seconds. The results show that the Mg18Sn-5vSiC sample exhibits hardness of 150 kg/mm^2, which is higher than most microhardness values reported for Mg-based metal matrix nanocomposites [12].

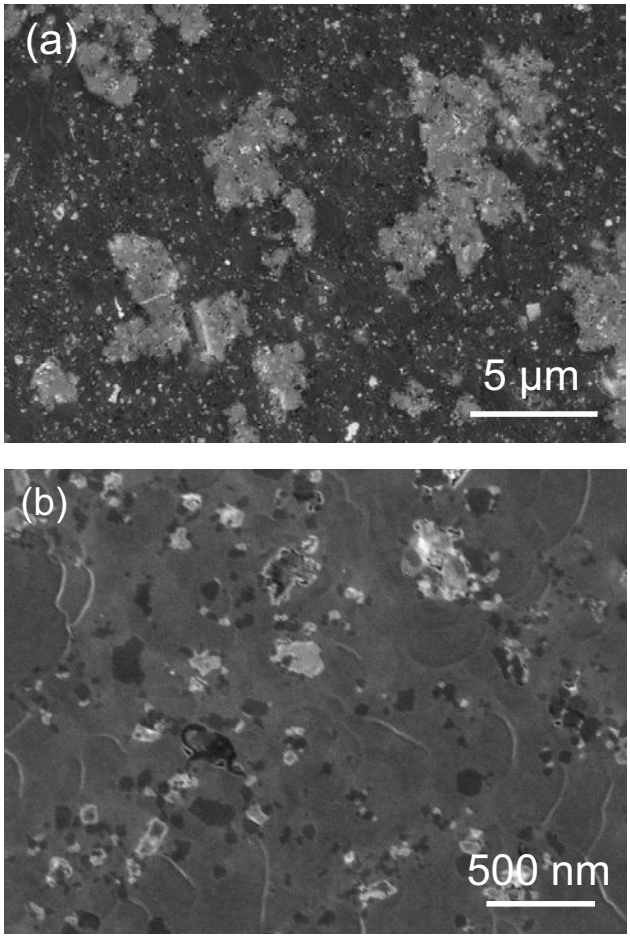


Fig. 4 Distribution of nanoparticles in Mg18Sn matrix. (a) SEM image of Mg18Sn-5vSiC at low magnification. The micrometer-sized brighter phase is intermetallic phase, the darker continuous phase is Mg matrix, the tiny spot is nanoparticle. (b) SEM image of the Mg18Sn-5vSiC at high magnification.

Conclusions

The master nanocomposite pellet approach was developed to feed high percentage nanoparticles into molten metal to solve the burning, floating or settling of the nanoparticles during feeding. The ultrasonic processing was used to disperse nanoparticles in molten metal. A uniform distribution of high percentage nanoparticles in solidified samples was achieved by solidification processing. This work might provide a promising way for production of bulk metal matrix nanocomposites with uniform distribution of nanoparticles.

Acknowledgements

This work is supported by the National Institute of Standards and Technology through its Technology Innovation Program. The support from KSM Castings and General Cable are also highly appreciated.

References

1. Z. Zhang, D.L. Chen, "Consideration of Orowan strengthening effect in particulate-reinforced metal matrix nanocomposites: A model for predicting their yield strength," *Scripta Mater.*, 54 (2006), 1321-1326.
2. V. Provenzano, R.L. Holtz, "Nanocomposites for high temperature applications," *Mater. Sci. Eng. A*, 204 (1995), 125-134.
3. S.C. Tjong, "Novel nanoparticle-reinforced metal matrix composites with enhanced mechanical properties," *Adv. Eng. Mater.*, 9 (2007), 639-652.
4. J.B. Ferguson, F. Sheykh-Jaberi, C.S. Kim, P.K. Rohatgi, K. Cho, "On the strength and strain to failure in particle-reinforced magnesium metal-matrix nanocomposites (Mg MMNCs)," *Mater. Sci. Eng. A*, 558 (2012), 193-204.
5. C.S. Kim, I. Sohn, M. Nezafati, J.B. Ferguson, B.F. Schultz, Z. Bajestani-Gohari, P.K. Rohatgi, K. Cho, "Prediction models for the yield strength of particle-reinforced unimodal pure magnesium (Mg) metal matrix nanocomposites (MMNCs)," *J. Mater. Sci.*, 48 (2013), 4191-4204.
6. H. Ferkel, B.L. Mordike, "Magnesium strengthened by SiC nanoparticles," *Mater. Sci. Eng. A*, 298 (2001), 193-199.
7. C. Capdevila, H. Bhadeshia, "Manufacturing and microstructural evolution of mechanically alloyed oxide dispersion strengthened superalloys," *Adv. Eng. Mater.*, 3 (2001), 647-656.
8. R.S. Mishra, Z.Y. Ma, I. Charit, "Friction stir processing: a novel technique for fabrication of surface composite," *Mater. Sci. Eng. A*, 341 (2003), 307-310.
9. R.S. Mishra, Z.Y. Ma, "Friction stir welding and processing," *Mater. Sci. Eng. R*, 50 (2005), 1-78.
10. L.Y. Chen, H. Konishi, A. Fehrenbacher, C. Ma, J.Q. Xu, H. Choi, H.F. Xu, F.E. Pfefferkorn, X.C. Li, "Novel nanoprocessing route for bulk graphene nanoplatelets reinforced metal matrix nanocomposites," *Scripta Mater.*, 67 (2012), 29-32.
11. L.Y. Chen, H. Choi, A. Fehrenbacher, J.Q. Xu, C. Ma, X.C. Li, "Uniform dispersion of nanoparticles in metal matrix nanocomposites," in *Supplemental Proceedings: Materials Processing and Interfaces*, Page 757-763, Volume 1 (ed TMS), John Wiley & Sons, Inc., Hoboken, NJ, USA., (2012).
12. L.Y. Chen, J.Y. Peng, J.Q. Xu, H. Choi, X.C. Li, "Achieving uniform distribution and dispersion of a high percentage of nanoparticles in metal matrix nanocomposites by solidification processing," *Scripta Mater.*, 69 (2013), 634-637.
13. Y. Sun, H. Choi, H. Konishi, V. Pikhovich, R. Hathaway, L.Y. Chen, X.C. Li, "Effect of core-shelled nanoparticles of carbon-coated nickel on magnesium," *Mater. Sci. Eng. A*, 546 (2012), 284-290.
14. Y. Yang, J. Lan, X.C. Li, "Study on bulk aluminum matrix nano-composite fabricated by ultrasonic dispersion of nano-sized SiC particles in molten aluminum alloy," *Mater. Sci. Eng. A*, 380 (2004), 378-383.
15. X.C. Li, Y. Yang, X.D. Cheng, "Ultrasonic-assisted fabrication of metal matrix nanocomposites," *J. Mater. Sci.*, 39 (2004), 3211-3212.
16. J.Q. Xu, L.Y. Chen, H. Choi, X.C. Li, "Theoretical study and pathways for nanoparticle capture during solidification of metal melt," *J. Phys. Condens. Matter*, 24 (2012), 255304.

Magnesium Technology 2014
Edited by: Martyn Alderman, Michele V. Manuel, Norbert Hort, and Neale R. Neelameggham
TMS (The Minerals, Metals & Materials Society), 2014

EFFECT OF NANO-REINFORCEMENT ON PROPERTIES OF CAST Mg-Al ALLOY AZ91

Mahmoud, M. G.[1], El-Mahallawi, I.S.[1], Rashad, R. M.[1]
[1] Faculty of Engineering, Cairo University, Gamaa Street, Giza 12613, Egypt

Keywords: nanocomposite, AZ91 Magnesium alloy, semi-solid casting, Al_2O_3 nanoparticles

Abstract

In this study, nanocomposites based on magnesium alloy system AZ91 were fabricated by Semi-Solid Rheocasting (SSR) technique. Al_2O_3 (alpha) nanoparticles were added to the AZ91 alloy with different weight fractions. The results showed that Al_2O_3 nanoparticles could be mixed with AZ91 semi-solid slurry using mechanical stirrer technique. However, large clusters of nanoparticles were observed. SEM images also detected significant refinement the microstructural features due to the Al_2O_3 additives. Hardness tests showed that an addition of 2 wt. % Al_2O_3 nanoparticles resulted in 17% increase in the hardness. Corrosion tests indicated an improvement of 50% in corrosion resistance due to the addition of 2wt. % Al_2O_3 nanoparticles. Finally, mechanical dry wear tests revealed a 5% improvement in wear resistance for 2wt. % Al_2O_3 nanoparticles.

Introduction

Recently the new strategy in the automotive and aerospace industries is to replace the components which are made of heavy metals by components made of light metals with high strength to weight ratio property in order to reduce the fuel consumption and green house emission [1]. Accordingly, close attention is paid to light metals such as magnesium, due to its intrinsic characteristics of low density, good machinability and availability in the global market [2]. However the limitations of Mg and its alloys; such as low stiffness, high wear rate, high chemical reactivity, loss of mechanical strength at high temperature and creep resistance restrict the spread of the application of Mg alloys in automotive industries. So, the attention of researchers has been turned to engineered pathway metal matrix nanocomposites based on magnesium and magnesium alloy hopefully to find solutions to magnesium problems.

Faraji et al, produced a MMNC by adding (30 nm) Al_2O_3 nanoparticles with purity of 99 % in volume fraction of 8% to produce a nanocomposite layer on the surface of AZ91 by friction stir processing (FSP) [3]. The microstructure and the mechanical properties of nanoparticles reinforced AZ91 were also investigated by Nie [4]. SiC particles in 1 vol. % with an average diameter of 60 nm were introduced using the ultrasonic vibration device. While Gao [5] used ultrasonic waves to disperse nanoparticles and it was shown that it resulted ultrasonic cavitation based solidification for the AZ91/AlN nanocomposite. Shi-Ying [6] used both the mechanical stirring and high –intensity ultrasonic process to add 1.5% Multi-wall carbon nanotubes (CNTs) to AZ91 with greater than 95% purity and outer diameter of 20-40 nm and length in the range of 1-5 μm.
Qianqian et al [7] designed two-step process to achieve a good dispersion of the multiwall carbon nanotubes (MWNTs) in the AZ91 matrix. Firstly, dispersing MWNTs on the AZ91 chips; in this step, the agglomerated MWNTs were separate, then the MWNTS coated Mg chips were used to fabricate AZ91/0.1 wt. % MWNT nanocomposites by a melt stirring technique (with 370 rpm rotation speed for 30 min).

The previous review has shown that incorporation of nanoparticles to light metal alloys seems to be a challenging and promising ultimatum by material researches. Several methods have been explored by researchers [5-7], but using semi-solid processing techniques seems to need further exploration. However the successful trials of the research group at Cairo university [8-9], when the semi-solid process was used to add of Al_2O_3 and TiO_2 nanoparticles to Al alloy A356, encouraged the group to try to produce nanocomposite material based on AZ91 alloy and to investigate its corrosion properties.

The aim of this work is to investigate the prospects of using semi-solid casting to produce Al_2O3 nanodispersed Mg alloy AZ91, and to characterize and evaluate the properties of the new material

Experimental Procedures

Materials

Matrix: AZ91 magnesium alloy with chemical composition (in wt.%)of(9.3%Al,0.7%Zn,0.23%Mn,0.02%Si,0.001%Cu,0.001%Ni,0.002%Fe,0.0015%Be and balance Mg) is the most widely and commercially used Mg alloy system in the automotive industry. Therefore, it was selected as the matrix alloy during the current study.

Reinforcement: Alumina (Al_2O_3) nanoparticles (alpha with the average size of 80 nm were used as the reinforcement phase in this study. Figure 1 shows the SEM image of the as-received Al_2O_3 sample.

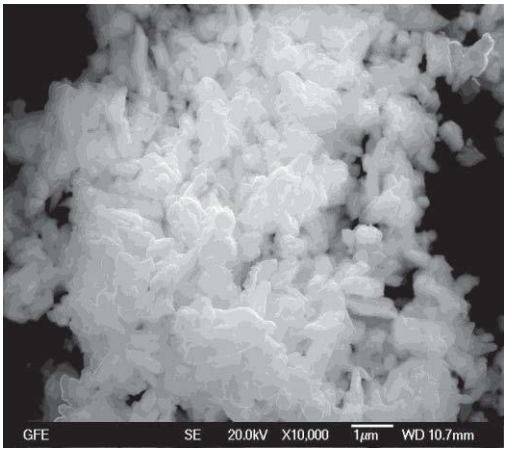


Figure 1. Morphology of Al_2O_3 nanoparticle

Fabrication Processing

The experimental setup that was used to reinforce the AZ91 matrix with the Al_2O_3 nanoparticles is shown in Figure 2. The fabrication process comprises several stages. First, the Al_2O_3 nanoparticles were wrapped in rod shaped packets wrapped in aluminum foil followed by heating up to 200 ^oC. Then, approximately 250gm of AZ91 were charged into the crucible until the temperature inside the crucible reaches 700 ^oC, in order to allow rapid melting and minimize oxidation during melting process. The melting process was carried out under a flow of gas mixture consisting of sulfur hexafluoride (SF_6) and carbon dioxide (CO_2) with CO_2+0.75%SF_6 (volume fraction) [5]. The AZ91 alloy was molten at 720 ^oC, and then cooled to 590 ^oC, which keeps the matrix alloy in the semi-solid condition [10]. Once the melt temperature reached 590^oC, the aluminum foil containing Al_2O_3 nanoparticle was submerged beneath the surface of the melt. Afterwards, the melt was stirred mechanically using the four blade stirrers with a rotation speed of 1500 rpm for 1 min [8-9]. The mixture was then poured into a metallic die preheated to 200 ^oC using a tilt–casting system to minimize the turbulence. A reference AZ91 alloy was fabricated following the same aforementioned steps, but without the nanoparticles, in order to be compared with the reinforced samples.

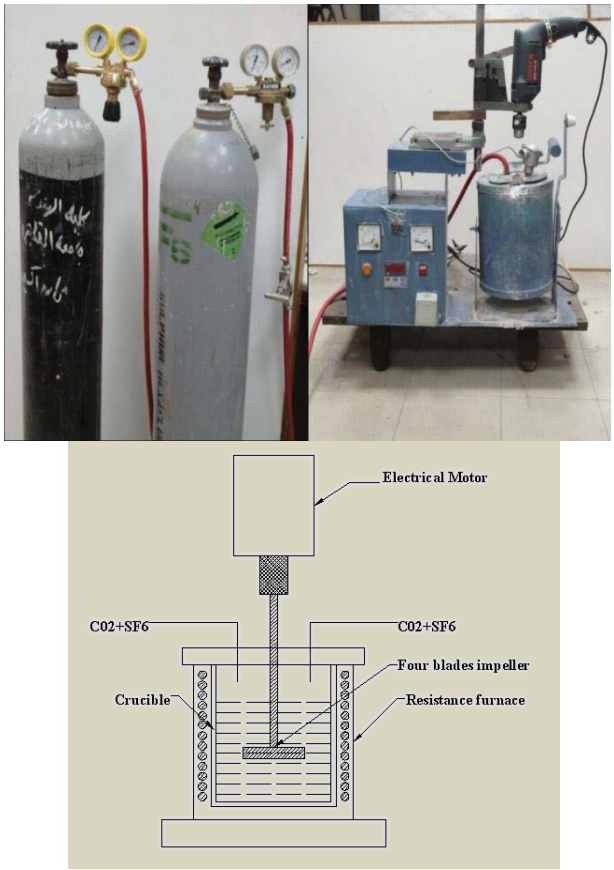


Figure 2.Mechanical Stirring unit used for the production of MMNCs.

Characterization Processing

The following steps describe the analyses of the AZ91/Al_2O_3 nanocomposites samples:

(1) The microstructures of the samples and the distribution of the Al_2O_3 in the Mg alloys matrix were examined by SEM (JEOL JSM-7000F) after the samples were polished using JEOL SM-09010 cross-section polisher.

(2) Hardness measurements were carried out on the polished samples. The microhardness was measured using Shimadzu-HMV automatic digital hardness tester while, the macrohardness tests were conducted on Brinell Rockwell hardness testing machine. The reported results are the average of five readings.

(3) Dry wear tests of the specimens were performed by a pin-on-disc test machine Test samples with 8 mm diameter and 20 mm length were cut and prepared from as-cast AZ91 and AZ91/Al2O3 specimens. The samples were tested under a load of 23N with speed of 1 m/sec for a total distance of 3600 m.

(4) Potentiodynamic polarization measurements were carried out using Volta lab 40 (PGZ 301) – RADIOMETER ANALYTICAL. All measurements were performed in freshly prepared aerated (3% NaCl) solution at room temperature.

Results and Discussion

SEM Observations

Nanoparticles Detection: As shown in Figure 3, nanoparticles agglomerations were found on the edge of the pores within the AZ91 matrix. Accordingly, this suggests that the nanoparticles were accommodated in the matrix. However, uniform distribution of the nanoparticles could not be achieved through the applied Semi-Solid Reheocasting technique.

Microstructure Observation: A selected number of specimens have been prepared using mechanical grinding and polishing technique to study the microstructure features and observe the nanoparticles. However, nanoparticles were not detected through this technique. The SEM micrographs of as-cast monolithic samples AZ91/0%Al_2O_3 and nanocomposite sample AZ91/2%Al_2O_3 are shown in Fig.4. It can be noticed that the grains of the matrix in the AZ91/2%Al_2O_3 nanocomposite were mainly refined by the addition of Al_2O_3 nanocomposite.

The microstructure of AZ91/0%Al_2O_3 cast in metallic die, shown in Figure 4, is characterized by α-phase in solid solution of aluminum in magnesium. A γ-phase was also found as massive intermetallic compounds with a stoichiometric composition of $Mg_{17}Al_{12}$, γ D-phase is an intermetallic compound with the same composition of γ-phase but in lamellar (discontinuous) morphology. This phase forms from supersaturated solid solution and α+γ partially divorced eutectic structure. It is clear from the comparison between the monolithic (AZ91/0%Al_2O_3) and composite (AZ91/2%Al_2O_3) that the eutectic phase is formed clearly and more uniform in a composite sample relative to the monolithic one. The eutectic structure is a very important feature that affects the mechanical properties.

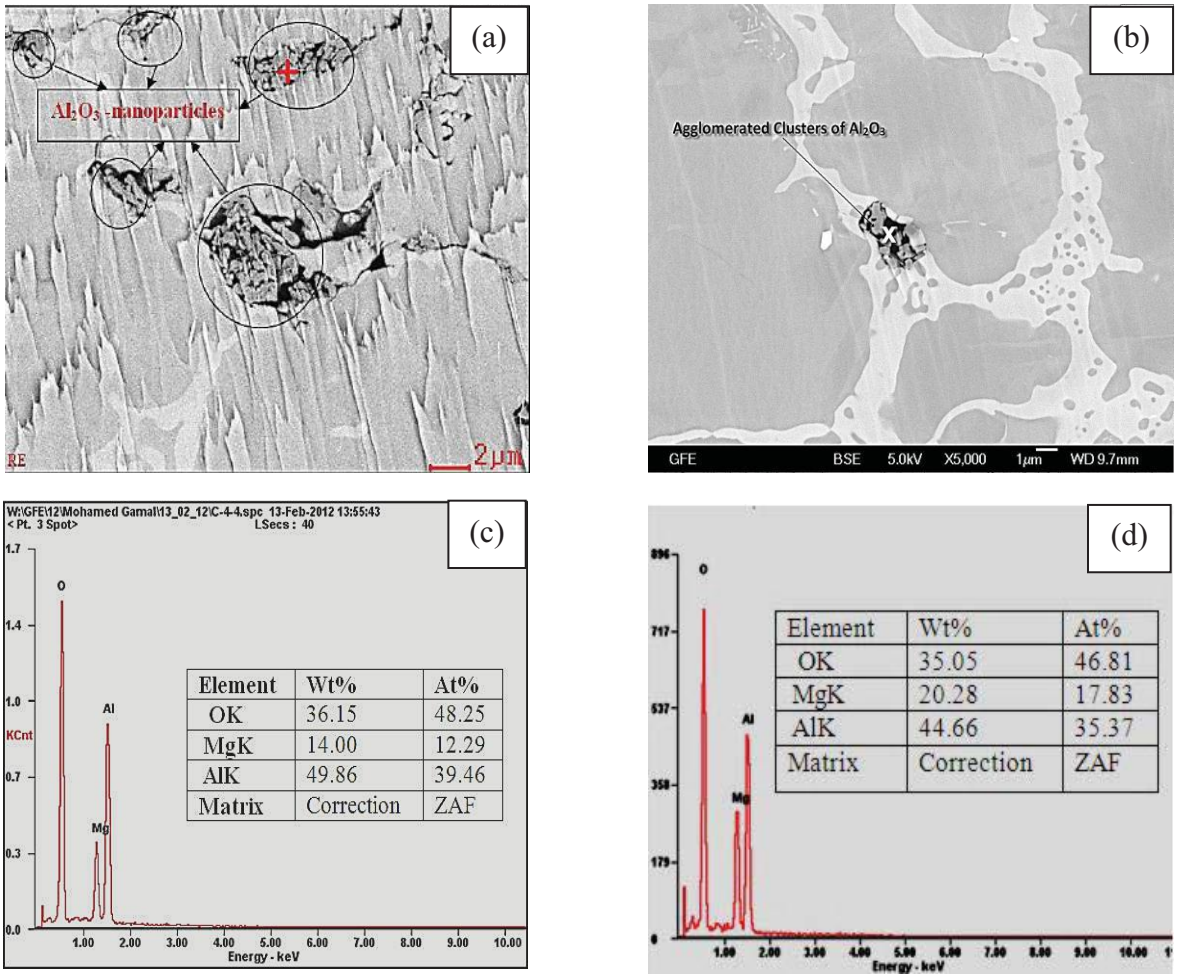


Figure 3. (a, b) detection of Al_2O_3 nanoparticles in two different position in AZ91/2wt.% Sample; (c, d) EDX of the selected area in (a , b) .

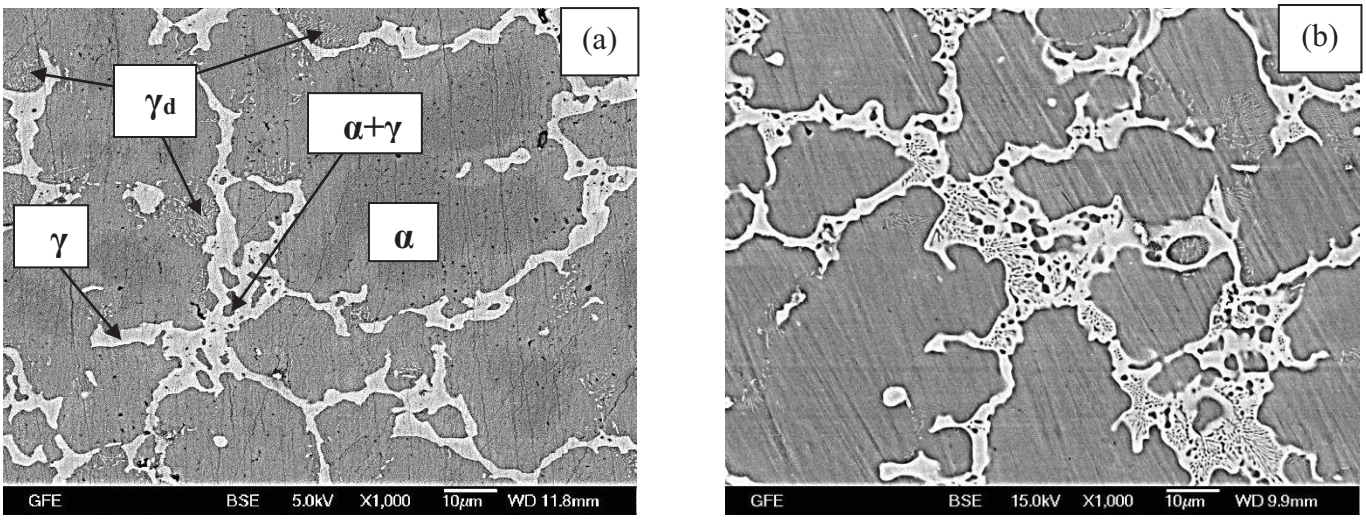


Figure 4. (a, b) SEM investigation of monolithic sample AZ91/0%Al_2O_3 and composite sample AZ91/2%Al_2O_3 respectively.

Hardness Results

Figure 5 shows a significant increase in both the microhardness and global hardness for the nanocomposite samples containing up to 3% Al_2O_3, in comparison with the monolithic sample AZ91/0%Al_2O_3. The microhardnes increase ranges from 7.3 to 30.5%, where the maximum increase was observed for the 1 % Al_2O_3. The global hardness results show that at 2% Al_2O_3 addition, the hardness increased by 17%.However, the results also show that a decrease in microhardness and global hardness occurred at 4% Al_2O_3 addition. The increase in the hardness of the nanocomposite samples in the present study can be attributed to: (1) the distribution of harder Al_2O_3 nanoparticles in the matrix, and (2) higher constraint to the localized matrix deformation during indentation due to presence of the Al_2O_3 nanoparticles.

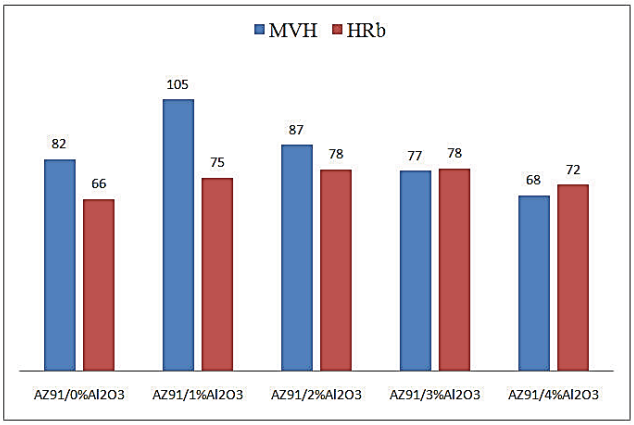


Figure 5. The effect of wt% fraction of Al_2O_3 nanoparticles on the HMV and Brinel hardness (HRb) of MMNCs.

Wear Test Results

Figure 6 shows the wear test results of the monolithic sample (AZ91/0%Al_2O_3) compared with the composite samples AZ91/[1,2,3,4%] Al_2O_3.The figure shows that the samples containing 2% Al_2O_3 exhibited the least wear (loss in mg). However the increase in the wear loss with the increase of the weight fraction of Al_2O_3 is in good agreement with the hardness results. The difference in the wear rates between the monolithic sample AZ91/0%Al_2O_3 and the nonocomposite sample (AZ91/2%Al_2O_3) which exhibited the least wear loss, as mentioned previously, is not significant (only 5.3%). This can be attributed to the agglomeration of the Al_2O_3 particles which causes a low integrity between the particle/particle and particle/matrix interfaces. This low integrity results in easy separation of particles from the matrix during sliding. On the other hand, these separated ceramic particles intensify the wear rate, since they act as abrasive particles between the disk and the pin.

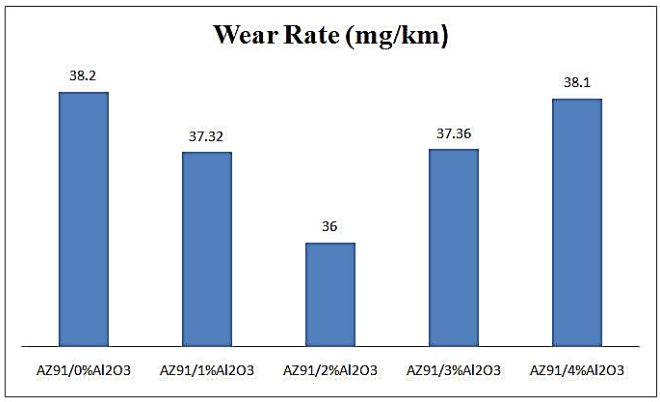


Figure 6. The effect of wt. % fraction of Al_2O_3 nanoparticles on wear rate of MMNCs.

Corrosion Test Results

Figure 7 shows the results obtained by the polarization test. According to the results, the AZ91/2%Al_2O_3 nanocomposite samples exhibited the least corrosion rate compared to the monolithic sample AZ91/0%Al_2O_3. In alignment with hardness and wear results, the corrosion loss also increased with increased weight fraction of the nanoparticles.

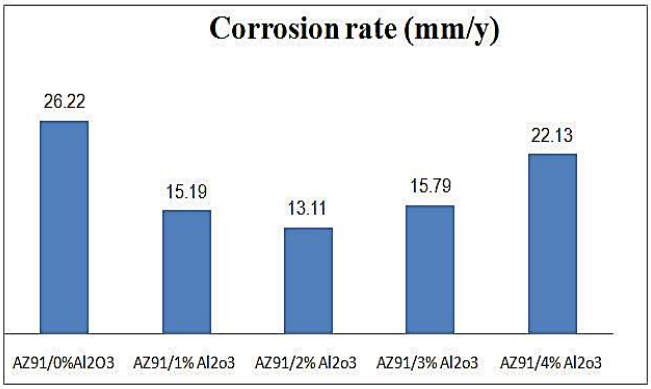


Figure 7.The effect of wt.% fraction of Al_2O_3 nanoparticles on Corrosion rate of MMNCs.

Figure 8 shows a SEM micrograph and EDX for the corroded surface of monolithic sample AZ91/0%Al_2O_3 and nanocomposite sample AZ91/1%Al_2O_3. It is clear that the pitting is observed on the corroded surface of the monolithic sample, whereas it is not observed on corroded surface of the nancomposite sample. Therefore, it can be understood that the additions of Al_2O_3 nanoparticles help to prevent pitting corrosion mechanism.

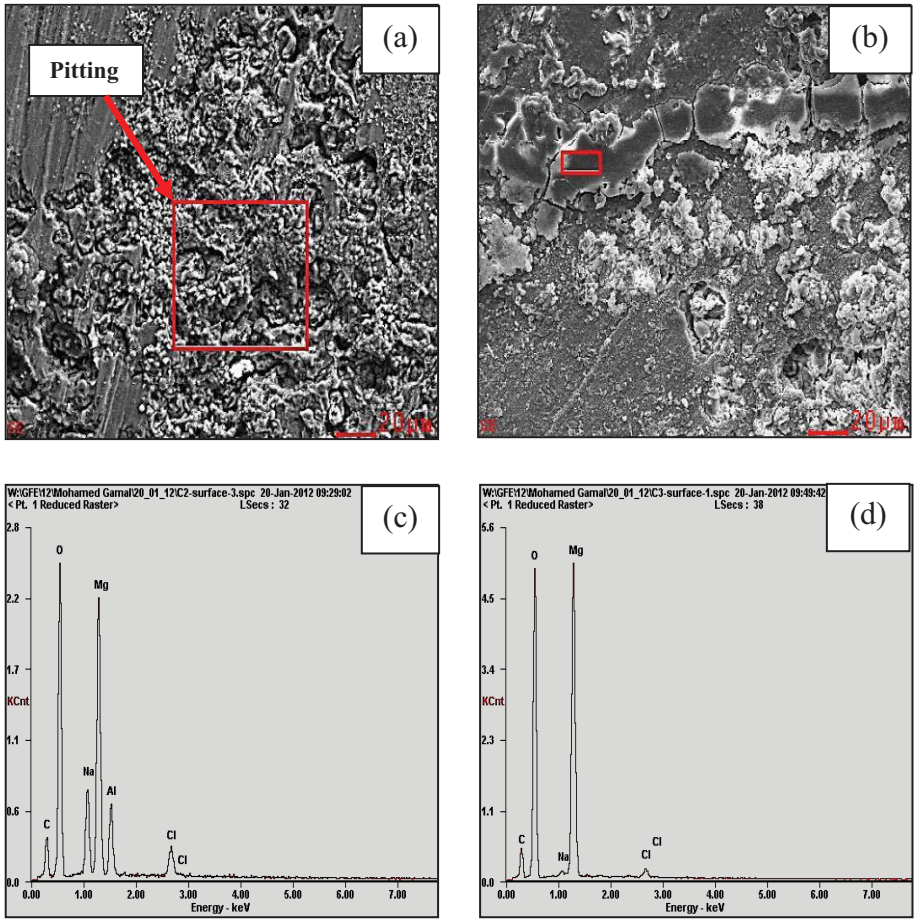


Figure 8. SEM micrographs for the corroded surface of (a) AZ91/0%Al_2O_3 and (b) AZ91/1%Al_2O_3 ; and (c) and (d) EDX analyses of selected regions in (a) and (b).

Conclusions

From this study we can conclude that:

(1) Semi-Solid Rheocasting (SSR) technique was applied to prepare MMNCs based on AZ91 alloy.

(2) Mixing the Al_2O_3 nanoparticles with AZ91 semi-solid slurry using mechanical stirring technique was used in this work, but SEM images showed that this technique does not lead to the achievement of a uniform distribution of the nanoparticles.

(3) SEM images detected significant grain refinement for the (AZ91/Al_2O_3) matrix, in addition to the formation of eutectic phase which was enhanced after the addition of Al_2O_3 nanoparticles, which leads to improvement of the mechanical properties.

(4) The results of the hardness test, wear test and corrosion Test show a significant improvement on some of the sample which contain nanoadditions.

(5) Adding nanoparticles up to 2wt. % Al_2O_3 exhibits the best results for all the tests. For 2wt.% Al_2O_3, hardness results showed 17 % increase in hardness, wear results showed 5% increase in wear resistance and corrosion test shows 50% increase in corrosion resistance.

(6) Increasing of the weight fraction of Al_2O_3 nanoparticles may be attributed to the accompanied increase in the slurry viscosity, resulting in the inability of the mechanical stirrer to disperse the nanoparticles, which ultimately leads to agglomeration of the nanoparticles.

Acknowledgements

The present study was part of a big research project on developing nano-dispersed cast light aluminum and magnesium alloys, for investigating options for enhancing their properties and performance in automotive applications. The project was supported by, Cairo University; Department of Mechanical Design and Production Engineering; and the Gemeinschaftslabor fuer Elektronmikroskopie Aachen, Germany. The exchange of visits between Egypt and Germany was funded by both Science and Technology Development Funding Office STDF and Deutsche Akademishe Austaush Dienst DAAD.

References

[1]S.F.Hassan, and M. Gupta," Effect of particulate size of Al_2O_3 reinforcement on microstructure and mechanical behavior of solidification processed elemental Mg," *Alloys and Compounds*, 419(2006), 84-90.

[2]B.I.Mordlike, and T.Ebert, "Magnesium: Properties, applications, potential," *Materials Science and Engineering A*, 302(2001), 37-45.

[3] Faraji, and Asadi, "Characterization of AZ91/Alumina nancomposite produced by FSP," *Materials Science and Engineering A*, 528, (2011), 2431-2044.

[4]K.B. Nie, X. J. Wang, X.S.Hu, L. Xu, K. Wu, and M.Y. Zheng, " Microsturcture and mechanical properties of Sic nanoparticles reinforced magnesium matrix composites fabricated by ultrasonic vibration," *Materials Science and Engineering A*, 528, (2011), 5278-5282.

[5]G.Cao, H.Choi, J.Oportus, H.Konishi, and X. Li, "Study on tensile properties and microstructure of cast AZ91D/AIN nanocomposites," *Materials Science and Engineering A*, 494, (2008), 127-131.

[6]Liu Shi-ying, Gao Fei-Peng, Zhang Qiong-yuan, Zhu Xue, and Li Wen-Zhen, "Fabrication of carbon nanotubes reinforced AZ91D composites by ultrasonic processing." *The Transactions of Nonferrous Metals Society of China*, 20(2010), 1222-1227.

[7]Li.Qianqian, Andreas Viereckl, Christian A.Rottmair, and Robert F.Singer, "Improved processing of carbon nanotube/magnesium alloy composites," *Composites Science and Technology*, 69, (2009), 1193-1199.

[8]I.S.El-Mahallawi, H.Abdelkader, L.Yousef, A.Amer, J. Mayer, and A.Schwedt, "Influence of Al_2O_3 nano-dispersions on microstructure features and mechanical properties of cast and T6 heat-treated Al Si hypoeutectic Alloys," *Materials Science and Engineering A*, 556 (2012) 76–87.

[9]I.S.El-Mahallawi, Y.Shash, K.Eigenfeld, T.S.Mahmoud, and M.A.ElSaeed, "Influence of nanodispersions on strength–ductility properties of semisolid cast A356 Al alloy," *Materials Science and Technology*, 26(2010), 1226-1231.

[10] K.K. Deng, K. Wu, Y. W. Wu, K .B. Nie, and M. Y. Zheng, "Effect of submicron size SiC particulates on microstructure and mechanical properties of AZ91 magnesium matrix composites," *Alloys and Compounds*, 504(2010), 542-547.

Magnesium Technology 2014

SYMPOSIUM: LIGHT-METAL MATRIX (NANO)-COMPOSITES

In-Situ Synthesis and Novel Additions

Papers in this section have been presented in a separate symposium at the 2014 TMS Annual Meeting organized by Dr. W. Sillekens and Prof. D.G. Eskin. This section was co-edited by the symposium organizers and all papers were peer reviewed.

Magnesium Technology 2014
Edited by: Martyn Alderman, Michele V. Manuel, Norbert Hort, and Neale R. Neelameggham
TMS (The Minerals, Metals & Materials Society), 2014

CERAMIC DISPERSIONS IN METAL CASTINGS CREATED BY DIRECT INJECTION OF A LIQUID ORGANIC PRECURSOR INTO THE MELT

Sudarshan, Rishi Raj
University of Colorado; Department of Mechanical Engineering; 1111 Engineering Dr.; Boulder, CO 80309, USA

Keywords: In-situ, Liquid Injection, Polymer Derived Ceramics, Magnesium Composite

Abstract

We show that a liquid organic precursor can be used for in-situ generation of nanophase ceramic particles within Mg melts when injected directly into Mg melts to create polymer-derived metal matrix composites (PD-MMCs). The tensile test data at 400 ^{o}C for these composites is particularly noteworthy. Direct liquid injection into molten metals is a significant step towards inserting many different chemistries of liquid precursors to generate a variety of ceramics within metal matrices.

Introduction

In the panorama of potential progress in development in fuel economy due to weight reduction, the design of automobile structures has moved from a paradigm involving solely steel to ones incorporating Al alloys and increasingly considering Mg alloys. Consequently, there is considerable interest in developing Mg alloy castings and their composites with superior strength for possible structure applications. The yield strength can be increased by introducing a second phase that resist the motion of dislocations [1]. In steel and aluminum alloys, a second phase was introduced by heat treatment of solid solution, where the second phase forms by precipitation [2]. Conventional precipitation strengthening is generally not good at higher operating temperatures as a result of the dissolution of precipitates.

One can overcome the aforementioned problem by incorporating stable ceramic particles. Normally a significant improvement is noticed in the metal's properties when the added particles size lies in the nano-scale regime, according to the Orowan strengthening mechanism. However, it becomes difficult to incorporate such nano-particles in liquid melts due to excessive agglomeration of nano particles due to the Van der Waals force. In our laboratory we are pursuing the incorporation of the ceramics from the polymer route [3-8] to create a new family of metal matrix composites that contain a dispersed ceramic nanophase.

In this proceeding we report on a new method of injecting the polymer into the metal. In the early work from our laboratory, polymer-derived metal-matrix-composites (PD-MMCs) were created by introducing epoxy powders into metals [9-10]. In most instances the precursors for the ceramics are liquid at ambient temperature [3-8] or, if solid can be dissolved into an organic solvent. We show that the liquid can be injected directly into the liquid metal, sidestepping the cross-linking and pulverizing step, while producing equivalent properties. The method can have huge generality since the process is no longer constrained by the melting temperature of the metal or by the cross-linking and decomposition temperature of the organic compound (alkoxides usually decompose near 400 ^{o}C; silazanes and siloxanes at 800 ^{o}C). The liquid can be "blown" into the liquid melt with a carrier gas, and can be scaled up to large-scale productions.

The method envisaged here is similar to the Bessemer process, in which oxygen is blown into molten iron to remove impurities by forming a slag that floated on the surface of the melt. Here, the objective is to incorporate a new constituent into the melt, but the mechanics of the process is similar. In our experience the organic polymers are almost immediately "absorbed" into the liquid metal, and decompose readily to produce a dispersed ceramic phase. The liquid injection can be far more powerful than the addition of polymer powders [9-10] since the process can be controlled to disperse the liquid so as to create nanoscale particles of the ceramic phase. In the case of polymer powders, we rely on the decomposition process to splinter them into fine particles. Composites of magnesium made in this way could open the way for a new generation of lightweight high temperature structural materials.

Experimental Procedure

The materials used here were pure magnesium (99%) and an organic precursor known as polysilazane. The final material was fabricated by a liquid metal stir-casting technique in Ar atmosphere (Fig. 1). The ceramic forming precursor is directly injected to molten metal to compare to an earlier work [9] where powder form precursor was added to the melt. Here the liquid precursor was poured into the vortex of the molten metal created by the mechanical stirrer using the stainless steel funnel. The liquid precursors were added, equivalent to form 2.5 volume percent of SiCN in the metal by assuming a density of ~2 g/cc for ceramic and 80 wt.% conversion from the precursor into the ceramic.

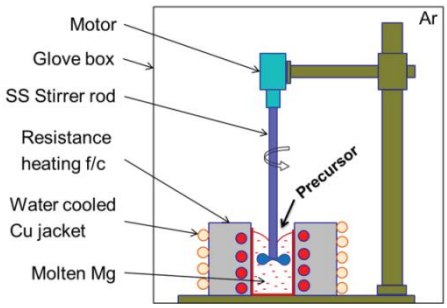


Figure 1. Schematic diagram of Liquid-metal Stir-cast setup for fabrication of PD-MMCs.

The liquid precursor was added to the magnesium melts at 650 to 700 ^{o}C. Then the melt was taken either to 720 ^{o}C or higher temperature (850 to 900 ^{o}C) and held for 20-30 minutes, where the in-situ pyrolysis of the polymer taking place. Afterwards the melt was cooled to 720 ^{o}C and poured to a preheated (100 ^{o}C) rectangular spilt cast iron mold of size 70 mm x 20 mm x 90 mm (Fig. 2a). These materials are henceforth labeled as CS, where cross-linked precursor powder used as reinforcement and CL, where liquid precursor used as reinforcement. Pure magnesium

was also fabricated in the same way as the PD-MMCs except that no precursor was added for comparison.

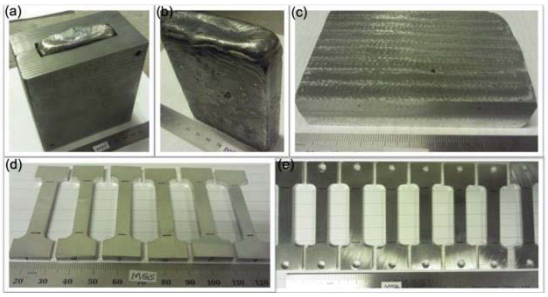


Figure 2. Pictographic view of mold, cast- and machined- ingot, tensile and creep samples.

The cast specimens were cold mounted and ground on a series of different grades (#600, #800, #1000, #1500 and #2000) of emery paper and then polished using diamond paste of 0.25 µm. Etching was carried out chemically using a solution of acetic acid, perchloric acid, and water in the ratio of 2:1:1 for 10 to 30 seconds at room temperature. The microstructures were examined by scanning electron microscope, SEM (Sirion, Model: VL 30FEG). Spot chemistries for Si, C, N, Mg and O were measured by energy-dispersive spectroscopy (EDS) in the SEM.

Tensile properties were evaluated from the as-cast samples in accordance with the ASTM test method E8M-09 using an Instron machine at strain rate of 10^{-3} S^{-1}. Flat dog bone samples (Fig. 2d) were cut from the rectangular ingot (Fig. 2b, c) to a gauge length of 30 mm, width to 6 mm and thickness to 3 mm. Fractography was done on the fracture surface by using SEM.

Tensile creep testing was performed on as-cast specimens under constant-strain and constant temperature condition according to ASTM E139 procedures. Each material was tested under two strain rate conditions, i.e. 10^{-3} S^{-1} and 10^{-2} S^{-1} under Ar atmosphere at 400 ^{o}C in a furnace (tungsten metal heating elements) attached to the Instron machine. Sample dimensions were the same as the room temperature tensile samples except having holes at the griping area to hold the grip jaws in place (Fig. 2e).

Results and Discussion

Structural Characterization

As-cast micrograph of the nano-dispersed alloy is shown in Fig. 3. The as-cast structure shows some dendrite shaped grains. The particles/reaction products from the polymer are segregated to dendrite/grain boundary region. The mean grain size of the as-cast pure Mg is 440 ± 22.2 µm. The composites showed smaller grain/dendrite sizes of 19 µm and 27 µm for CS and CL composites respectively. It is well known that the presence of fine dispersoids acts as nucleation sites for new grains and also prevents grain growth by restricting the grain-boundary movement. There are two types of particles seen in the composites. Some are in a round/spherical shape and others are in a rod/platelet shape. Spherical shaped particles are in the size range of 100 to 200 nm. However the platelet shaped particles are 100 to 200 nm wide and 2 to 5 microns in length. The in-situ formed particles having a broad size range from micron to nanometer.

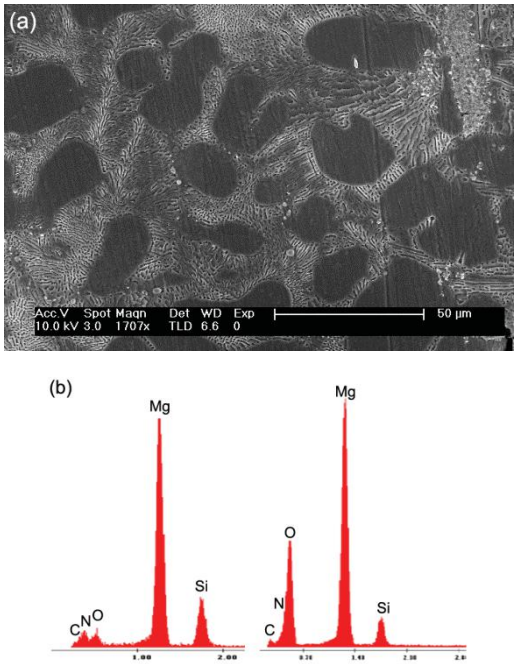


Figure 3. SEM of as-cast PD-MMC showing particles pushed to dendrite/grain boundary region (a) and EDS on particles (b).

The SEM-EDS analysis on the particles showed the presence of Si, C, N and O (Fig. 3b). The results of X-ray diffraction measurements (Fig. 4.) show a mild formation of the Mg_2Si intermetallic phase peaks along with Mg peaks, which form due to a reaction between the precursor and metal. Both the low temperature (720 ^{o}C) and high temperature (850 to 900 ^{o}C) processed composites showed formation of an intermetallic phase.

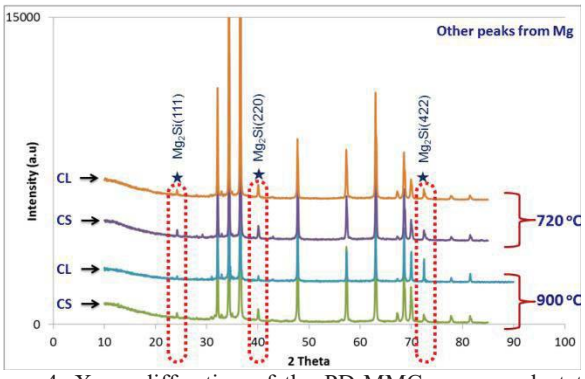


Figure 4. X-ray diffraction of the PD-MMCs processed at two different temperatures.

Raman spectroscopy provided proof of the conversion of the polymer into to ceramic phase is the presence of clear D and G peaks in the Raman spectra from both the intergranular and the intragranular regions shown in Fig. 5. These peaks are a strong characteristic of the ceramics obtained from polysilzanes and siloxanes, and are ascribed to the formation of graphene networks within these polymer derived ceramic materials [11, 12].

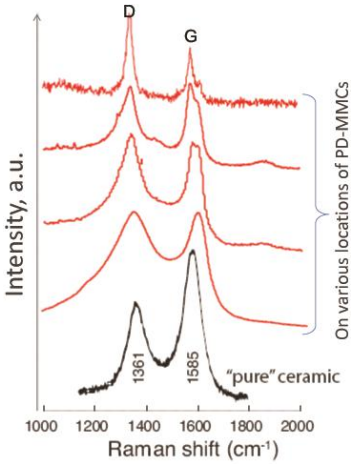


Figure 5. The sp^2 carbon D and G peaks from a pure ceramic specimen compared with the spectra obtained from the PD-MMCs from four different locations.

Tensile Behavior at Ambient Temperature

The ambient temperature tensile study shows significant increase in the 0.2 % yield and ultimate tensile strength (UTS) compared to pure magnesium. The stress-strain curves for the materials are depicted in Fig. 6. The proof stress for the CS sample is 80 MPa, and 65 MPa for the CL sample, more than three times greater than for pure Mg (20 MPa). The UTS values are 152 MPa for CS, 132 MPa for CL and 80 MPa for pure Mg. The elongation to failure for the CS and CL sample remains almost the same as for pure Mg despite their higher yield stress. The slightly lower strength of the CL composites is most likely because of some volatilization of the precursor before being incorporated into the liquid melt.

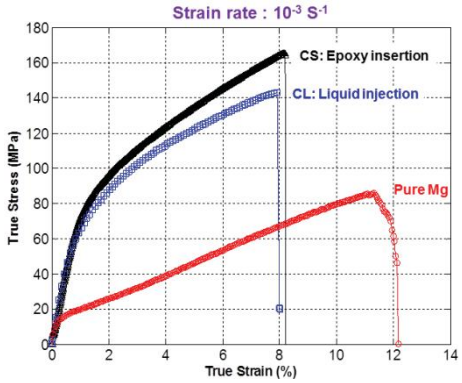


Figure 6. RT True stress-strain curves for as-cast PD-MMCs and pure magnesium.

Generally, one can increase a material's strength by reducing the grain size, a large addition of solute atoms to get new phase, or by additions of fine hard particles. The PD-MMCs experience all the three; in-situ formed particles act as grain refiner, a mild reaction between magnesium and precursor form a new phase (magnesium silicide), and a large volume fraction of in-situ formed fine hard particles (ceramic phase). Strengthening comes from all the three mechanisms, however the major contribution is from grain refinement and particle strengthening.

In brief, the degree of strengthening mainly comes from hard fine particles which depend on the distribution of the particles in the matrix. Particle's shape, volume fraction, average particle size, and mean inter-particle distance are the factors which affect composite strength. In the present study, most particles primarily occupied the dendrite/grain boundary regions and the inter-particle distances were more or less the same in that particular area. However the average particle distance in the composite becomes different due to particle-free-zones. These fine particles can act as a barrier to dislocations in several ways at low temperature. Strong particles forced dislocations to by-pass them by sharp changes in its curvature so the composites showed higher strength at ambient temperature.

Typical fracture surfaces of the samples are presented in Fig. 7. Pure magnesium samples show cleavage fracture, representing failure by brittle fracture mode (Fig. 7a) however, PD-MMCs shows mixed mode, dimple and cleavage features due to in-situ formed particles (Fig. 7b).

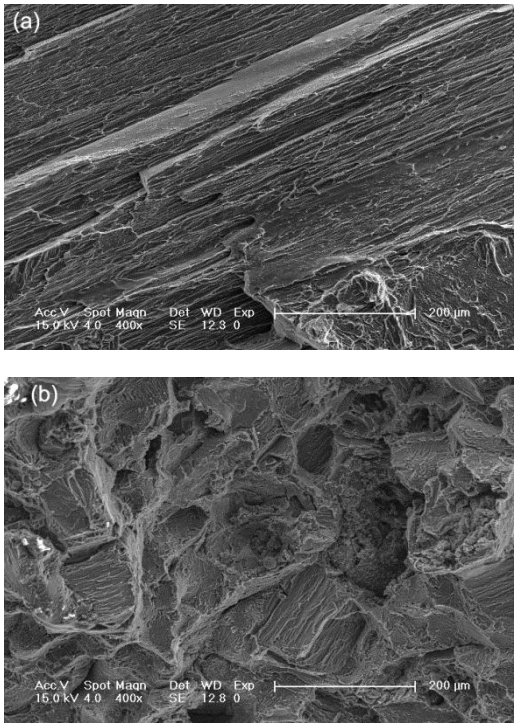


Figure 7. SEM of fractographs showing: (a) cleavage fracture in pure Mg, and (b) dimple and cleavage fracture in PD-MMC.

Tensile Creep at 400 ^{o}C

The high temperature tensile creep of the CS and CL composites showed better strength than pure magnesium. Figure 8 depicts the typical true stress-strain curve for the tensile creep test at 400 ^{o}C. In the present work the creep test was conducted at very high temperature which corresponds to a homologous temperature of 0.73 T_M to study the effects of in-situ formed phase in composites at high temperature. Strain rate of $1.2x10^{-3}$ S^{-1}, the high temperature proof strength of pure Mg is 10 MPa compared to 23 MPa for the CS and 19 MPa for the CL, which is two times higher than pure Mg. The high temperature UTS values are 29 MPa for CS, 22 MPa for CL and 15 MPa for pure Mg at the same strain rate. At higher strain rate ($1.2x10^{-2}$ S^{-1}) high temperature proof strength of pure Mg is 14 MPa, CS is 27 MPa and CL is 29 MPa, which is also double the strength compared to pure Mg. The UTS at this strain for pure Mg is 21 MPa, CS is 38 MPa and CL is 32

MPa. Higher the strain rate higher will be the strength which is well known, that is because of the less time for stress relaxation.

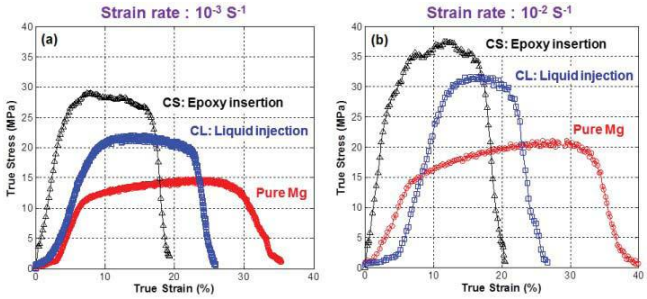


Figure 8. True stress-strain curves for high temperature tensile tests of pure Mg and PD-MMCs at two different strain rates.

The increase in the high temperature strength in the composites can be ascribed principally to the second phases that were derived from the polymer precursor. Stable in-situ formed particles and the reactive product, such as magnesium-silicide, restrict grain boundary movement. That is the main reason for the increased strength at high temperature in PD-MMCs. The inter-particle spacing is the critical parameter of dispersion strengthened materials at high temperature and even low temperature. Generally a good dispersion is possible only in in-situ synthesized composites when the particles are in nanometer size. Otherwise particle agglomeration occurs.

The fracture surfaces of these samples are shown in Fig. 9. The intergranular nature of the fracture surface of the composite reflects the inhomogeneous microstructure seen in Fig. 3a. The grain facets have a different morphology than the regions near the grain boundary. The latter are notable for plastic tearing suggesting significant ductility near the grain boundary regions.

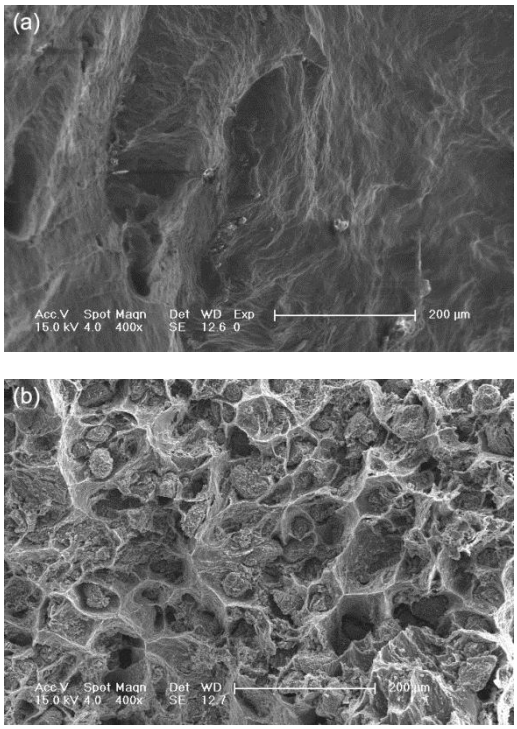


Figure 9. Fracture surface of the high temperature samples: (a) pure Mg and (b) PD-MMC.

Summary and Conclusions

The mechanical strength of dispersion strengthened metals depends on the spacing between nanoscale particles that impede dislocation motion. These particles often coarsen, driven by the interfacial energy at high temperatures which widens their spacing, thereby degrading the resistance to deformation. Mechanical methods to disperse nanoparticles of a ceramic phase, which would not coarsen, into metals is difficult because they form hard agglomerates due to Van der Waals force.

The polymer route to introducing a fine dispersion of a ceramic by in-situ processing is attractive for its simplicity and manufacturability. We have shown that the polymer precursor can be injected into the metal directly to produce composites that retain good resistance to deformation at temperatures nearing their melting point. The availability of a wide range of organometallic precursors for oxides, carbides, nitrides and mixed compositions imparts great generality to the liquid injection of the precursors for in-situ conversion into nanophase ceramics within the molten metal. A carrier gas may be used to "blow and mix" the precursors into the melt, in the same way as oxygen is blown through molten iron to remove the impurities.

The present work with magnesium shows promise for the liquid injection method to create lightweight high strength materials for higher service temperature applications.

Acknowledgements

This research work was supported by the National Science Foundation DMR1105347. Early stage "seed support" for this work was provided by the Army Research Labs under grant number W911NF-10-2-0044.

References

1. D. Hull and D.J. Bacon, *Introduction to Dislocations*, (New York, NY: Butterworth Heinemann Elsevier, 5th Edition, 2011), 205-245.

2. J. W. Christian, *The Theory of Transformation in Metals and Alloys* (Pergamon Press, 3rd Edition, 2002).

3. S. Yajima, J. Hayashi, M. Omori, and K. Okamura, "Development of a silicon carbide fibre with high tensile strength," *Nature*, 261 (1976), 683-685.

4. H.A. Bale, A. Haboub, A.A. MacDowell, J.R. Nasiatka, D.Y. Parkinson, B.N. Cox, D.B. Marshall, and R.O. Ritchie, "Real-time quantitative imaging of failure events in materials under load at temperatures above 1,600 degrees," *Nature Materials*, 12 (2013), 40-46.

5. T. Varga, A. Navrotsky, J.L. Moats, R.M. Morcos, F. Poli, K. Müller, A. Saha, and R. Raj, "Thermodynamically Stable $Si_xO_yC_z$ Polymer-Like Amorphous Ceramics," *J. Am. Ceram. Soc.*, 90 (10) (2007), 3213–3219.

6. L. An, R. Riedel, C. Konetschny, H.-J. Kleebe, and R. Raj, "Newtonian Viscosity of Amorphous Silicon Carbonitride at High Temperature," *J. Am. Ceram. Soc.*, 81 (5) (1998), 1349-1352.

7. R. Riedel, A. Kienzle, W. Dressler, L. Ruwisch, J. Bill, and F. Aldinger, "A silicoboron carbonitride ceramic stable to 2,000 ^{o}C," *Nature,* 382 (1996), 796-798.

8. R. Riedel, H.-J. Kleebe, H. Schonfelder, and F. Aldinger, "A Covalent Micro/Nano-composite Resistant to High-Temperature Oxidation," *Nature,* 374 (1995), 526-528.

9. Sudarshan, M.K. Surappa, D. Ahn, and R. Raj, "Nanoceramic-Metal Matrix Composites by In-Situ Pyrolysis of Organic Precursors in a Liquid Melt," *Metallurgical and Materials Transactions A Physical Metallurgy and Materials Science,* 39A (2008), 3291-3297.

10. E. Castellan, G. Ischia, A. Molinari, and R. Raj, "A Novel In-Situ Method for Producing a Dispersion of a Ceramic Phase into Copper that Remain Stable at 0.9TM," *Metallurgical and Materials Transactions A-Physical Metallurgy and Materials Science*, in press, DOI: 10.1007/s11661-013-1835-3.

11. N. Janakiraman, and F. Aldinger, "Fabrication and characterization of fully dense Si-C-N ceramics from a poly (ureamethylvinyl) silazane precursor," *J. Eur. Ceram. Soc.,* 29 (2009), 163-173.

12. A. Saha, R. Raj, and D. Williamson, "A model for the nanodomains in polymer-derived SiCO," *J. Am. Ceram. Soc*, 89 (2006), 2188-2195.

Magnesium Technology 2014

Magnesium Technology 2013 Addendum

The following papers were presented at the Magnesium Technology symposium held in San Antonio, Texas. Due to late submission it was not possible to include them in the 2013 volume and with the permission of the authors they are included here.

Magnesium Technology 2014
Edited by: Martyn Alderman, Michele V. Manuel, Norbert Hort, and Neale R. Neelameggham
TMS (The Minerals, Metals & Materials Society), 2014

Corrosion and Adhesion Properties of Cerium-Based Conversion Coatings on Magnesium Alloys

Surender Maddela, Matthew J. O'Keefe
Materials Research Center, Dept. of Materials Science and Engineering, Missouri University of Science and Technology, Rolla, MO-65409 USA

Keywords: Cerium-based conversion coatings, Magnesium alloys, Corrosion resistance, Adhesion strength

Abstract

Corrosion resistance and adhesion properties of cerium-based conversion coatings (CeCCs) on Al/Zn and Al/Mn magnesium alloys have been investigated. CeCCs were deposited by immersing magnesium panels in a cerium ion containing solution for 2 minutes. Corrosion resistance and adhesion strength of cerium coated magnesium panels were evaluated by electrochemical and pull tab testing methods, respectively. The CeCCs had very good adhesion to and significantly improved the corrosion resistance of magnesium alloys. Electrochemical test result showed that there was a measurable difference in corrosion resistance between the different magnesium alloys. Magnesium alloys with higher aluminum content had better corrosion resistance than alloys with lower Al content. The correlation of cerium deposition conditions, corrosion resistance, and adhesion strength are discussed.

Introduction

Recent developments in magnesium alloys have drawn great attention to take advantage of lightweight and high strength-to-weight ratio properties for automotive applications [1-2]. Magnesium alloys such as aluminum-zinc (Al/Zn) and aluminum-manganese (Al/Mn) are potential replacements for high density materials in automotive applications. The use of magnesium alloys for automotive applications is primarily driven by fuel efficiency and ease of fabrication, resulting in the growth of magnesium consumption at an annual rate of 15% over the last decade [2-3]. However, magnesium alloys readily corrode even in neutral pH solutions due to active electrochemical potentials, therefore limiting their use in lightweight applications. Corrosion resistance of these alloys is usually controlled by electrically isolating magnesium alloys in structural assemblies or by depositing corrosion resistance coatings. The use of corrosion coatings is a more viable approach if adequate protection is achieved.

One of the most effective coating systems used for corrosion protection of metallic substrates contain hexavalent chromium, a toxic and carcinogenic substance [4, 5]; therefore, there is a high demand for a suitable replacement. Extensive research has been conducted on potential chromate replacement coatings [6-16]. Cerium-based conversion coatings (CeCCs) is one potential alternatives and has shown significant improvement in corrosion resistance for aluminum alloys [6-13], magnesium alloys [14-18] and these coatings are believed to be environmentally benign [13, 15]. Although numerous publications have reported the corrosion resistance of cerium-based conversion coatings on magnesium is better than bare alloys [14-18], the adhesion strength of these coatings has not been presented. Therefore, corrosion resistance and adhesion properties of cerium-based conversion coatings on magnesium alloys have been investigated and presented in this paper.

Experimental Procedure

Magnesium alloy (AZ91, AZ31, AM60, and AM30) samples were sectioned into 3.75 X 7.5 cm coupons. The panels were first wiped with acetone and then rinsed with de-ionized (DI) water. Prior to cerium conversion coating the magnesium panels were pretreated with 0.5 wt. % tetrafluoroboric acid (HBF_4) for 30 s at room temperature, then treated with 5 wt. % sodium hydroxide (NaOH) for 30 s at room temperature, and then rinsed with DI water. The cerium-based conversion coatings were deposited on all of the magnesium alloys by immersing panels in a cerium ion containing solution for 2 min. The composition of the immersion solution was 205 g of stick solution (40 g of cerium chloride [$CeCl_3.xH_2O$, 99.9%] and 780 g of DI water), 25 g of DI water, 0.8 g of gelatin organic (RDH, Rousselot) and 8 vol.% of H_2O_2 (Fisher Chemical, 30 vol. %) [14]. After CeCCs deposition magnesium samples were post-treated in a phosphate solution for 5 min at 85 ^oC [12].

Electrochemical and ASTM B117 neutral salt spray testes were carried out to estimate corrosion resistance of cerium-based conversion coatings on magnesium alloys in modified prohesion (0.6 wt.% NaCl and 0.6 wt.% $(NH_4)_2SO_4$) and sodium chloride (5 wt.% NaCl) solutions, respectively. Potentiodynamic polarization measurements were performed using an EG&G 2273 potentiostat (Princeton Applied Research, USA). A standard EG&G flat cell (Princeton Applied Research, USA) was used for electrochemical polarization experiments. Prior to electrochemical measurement, the variation of open circuit potential (OCP) with time was monitored after immersion until a steady potential was obtained (~1000 s). All potentials were measured with respect to a saturated calomel electrode (SCE). Potentiodynamic polarization experiments were performed from –0.3 to 1.2 V versus OCP with a scan rate of 1 mV/s. The corrosion current density (i_{corr}) was calculated from the potentiodynamic polarization plot by the Tafel extrapolation method. A Romulus Universal Mechanical Strength tester (breaking point platform, Quad Group Inc.) was used to measure the adhesion strength of the cerium conversion coatings [19]. A metallic stud was exposed to the surface of the samples and then cured at 125 ^oC for 1 hour. The stud was then pulled off by a tensile load in the tester. All electrochemical and adhesion testing experiments were performed in triplicate to insure reproducibility of the test results.

A Hitachi S570 scanning electron microscopy (SEM) was used to record the surface morphology of coated panels. All images were taken in secondary electron mode using an acceleration voltage of 5 kV. The phases present in the cerium conversion coatings deposited on magnesium alloys was determined by grazing incidence X-ray diffraction (XRD) using Cu Kα radiation on a Philips X'Pert diffractometer.

Results and Discussion

The surface morphology, crack density, and crack distribution of cerium-based conversion coatings on AZ91, AZ31, AM60, and AM30 magnesium alloys are shown in Fig 1. The SEM micrographs revealed that the surface morphology and crack density of cerium-based conversion coatings varied with alloying addition, especially with the aluminum percentage in the alloy. The high aluminum containing alloys AZ91 and AM60 had fewer and more uniformly distributed cracks in the coatings (Fig 1a and 1c). However, slightly wider and more pronounced cracks were observed on AZ31 and AM30 magnesium alloys (Fig 1b and 1d). Previous work by authors presented the effect of coating morphology and crack density on the corrosion resistance of cerium-based conversion coatings on magnesium alloys [14]. It was reported that the coating morphology and crack density significantly influences the corrosion resistance of cerium-based conversion coatings on magnesium alloys. As expected, coatings with fewer and more narrow cracks have better corrosion resistance than wider and more densely cracked coatings. The difference in corrosion protection was not due to structural difference in the coatings. This has been confirmed by the x-ray diffraction analysis. The X-ray diffraction spectra of cerium-based conversion coated magnesium alloys are shown in Fig 2. The spectra were very similar for all four with respect to magnesium alloys substrates. X-ray diffraction analysis of cerium conversion coated magnesium alloys revealed the presence of a broad, low angle (25-30° of 2θ) diffraction peaks most likely associated with amorphous and/or nano-crystalline cerium phosphate ($CePO_4 \bullet H_2O$) in the coating. This is consistent with the work presented in previous publications [14].

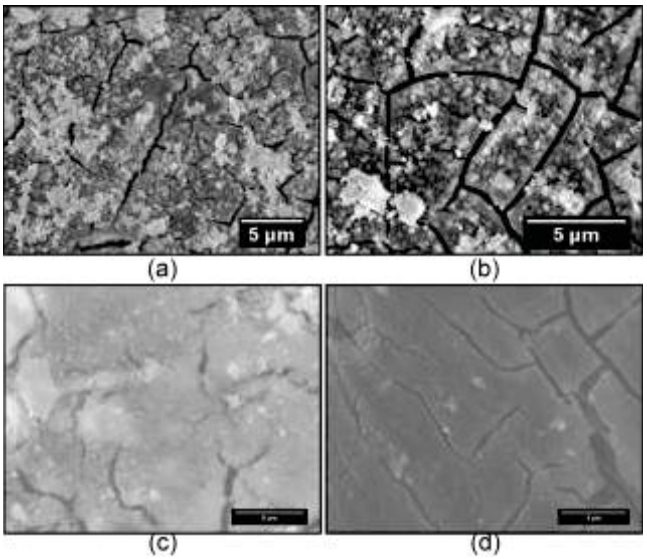


Figure 1: Surface morphology and crack density/distribution (SEM images) of CeCCs deposited on magnesium alloys; a) AZ91, b) AZ31, c) AM60, and d) AM30.

Electrochemical polarization measurements were conducted on as-coated magnesium alloys in modified prohesion solution as shown in Fig 3. It is clearly seen from the polarization measurements that there was a measurable difference in free corrosion potential and corrosion currents on cerium coated magnesium alloys. High aluminum content alloys (AZ91, AM60) have more noble free corrosion potential compared to low aluminum content alloys (AZ31, AM30). Similarly, magnesium alloys with high aluminum content have better corrosion resistance than low aluminum content alloys. Therefore, the aluminum content in the magnesium alloys significantly influences the corrosion resistance and nobility of coatings. It was shown in Fig. 1 that it is also influencing coating morphology and crack density in the coatings. As a result, the amount of aluminum in the alloy significantly influences the coating morphology and cracks density/distribution; hence influence the corrosion resistance of cerium coated magnesium alloys. Similar observations have noted from salt spray testing; high aluminum content AZ91 and AM60 magnesium alloys have better corrosion resistance compared to the low aluminum content AZ31 and AM30 magnesium alloys. Yang et. al., and other researchers have reported that the corrosion resistance and mechanical properties of magnesium alloys are significantly influenced by alloying, especially aluminum content [1, 2, 17]. They concluded that the corrosion resistance increased with increasing aluminum content in the magnesium alloys. Similarly, other researchers have also reported that corrosion resistance of cerium-based conversion coatings on magnesium alloys significantly influence the amount of aluminum present in the magnesium alloys [16]. Uncoated magnesium alloys with high aluminum (AZ91, AM60) content has better corrosion resistance compared to low aluminum alloys (AZ31, AM30).

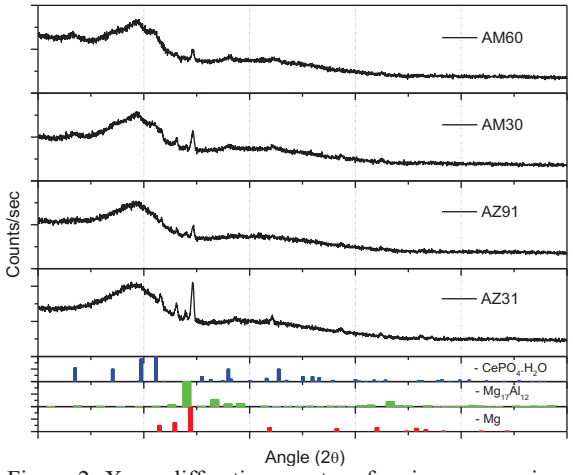


Figure 2: X-ray diffraction spectra of cerium conversion coating on magnesium alloys.

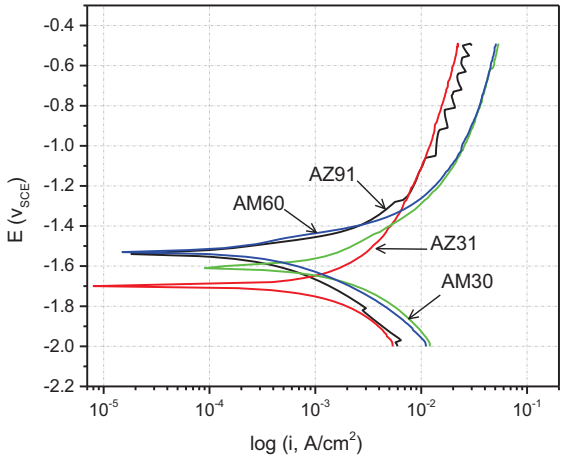


Figure 3: Potentiodynamic polarization behavior of cerium conversion coatings on magnesium alloys.

Adhesion strength of CeCCs deposited on magnesium alloys was evaluated by adhesion pull strength tensile testing and the results are shown in Fig 4. All of the average adhesion strengths were > 10, 000 psi which is good. The cerium conversion coatings on high aluminum content magnesium alloys (AZ91, AM60) have better adhesion strength compared to the low aluminum content alloys (AZ31, AM30). From the results presented above, it is clear that aluminum alloying significantly influences the corrosion resistance and the adhesion strength of cerium-based conversion coatings. The correlation of the corrosion resistance and adhesion strength of CeCCs deposited on magnesium alloys presented in Fig. 5 shows that high aluminum content magnesium alloys have better corrosion resistance and better adhesion strength compared to the low aluminum content alloy. Among all of the coated alloys, the AZ91 (Al/Zn) magnesium alloy had the highest adhesion strength and best corrosion resistance compared to other magnesium alloys. It can be concluded from the above observations that the amount of aluminum in magnesium alloys significantly influences the corrosion resistance and adhesion strength of cerium-based conversion coatings. A uniform coating morphology and fewer cracks in the cerium-based conversion coatings are obtained on high aluminum content magnesium alloys, providing better corrosion protection and good adhesion strength to the substrate.

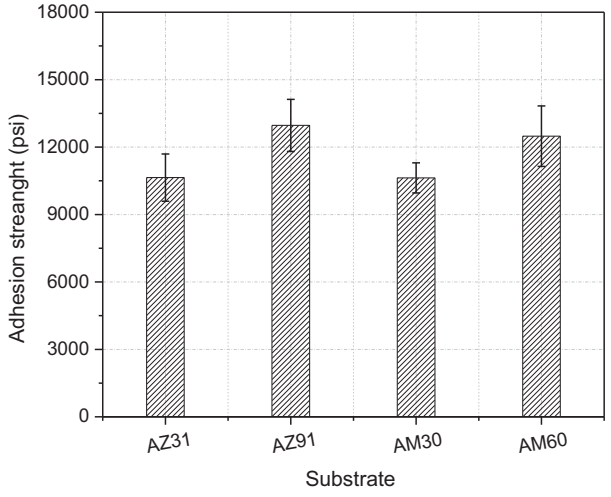


Figure 4: Adhesion strength of cerium conversion coatings on magnesium alloys.

Conclusions

1. The coating morphology and corrosion resistance of cerium-based conversion coatings deposited on magnesium alloys are affected by the amount of aluminum in the alloy.
2. There was a measurable difference observed in coating morphology and crack density in the coatings with better coating morphology and less cracking on AZ91 and AM60 alloys than AZ31 and AM30 alloys.
3. The adhesion strength of the coatings was also influenced by the amount of aluminum, with higher adhesion strength for the higher Al alloying addition.
4. Uniform coating morphology and narrower, less dense cracks in the coating leads to higher adhesion strength and better corrosion resistance.

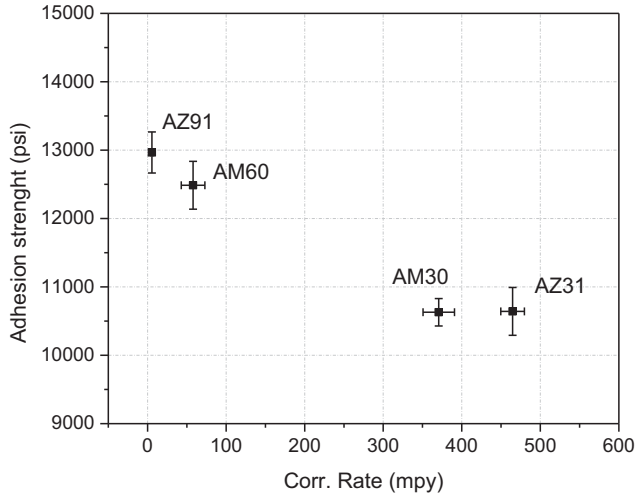


Figure 5: Adhesion strength versus corrosion rate of cerium conversion coatings on magnesium alloys.

Acknowledgements

The authors would like to thank Kaitlin Travous, Carlos Castano and Bill Fahrenholtz for assisting in various aspects.

References

1. Z. Yang, J.P. Li, J. X. Zhang, G. W. Lorimer, J. Robson, *Acta. Metal. Sin (Engl. Lett)*, **21(5)**, 313-328 (2008).
2. M.K. Kulekci, *Int. J. Adv. Manuf. Tech.,* **39,** 851-865 (2008).
3. J.J. Kim and D. S. Han, Mat. Trans. **49 (5)**, 894-897 (2008).
4. J.E. Gray and B. Luan, *J. Alloys. Comp.,* **336**, 88-113 (2002).
5. M. Costa and C.B. Klein, *Crit. Rev. Toxi.,* **36**(2), 155-63 (2006).
6. C. Lin, S. Maddela, M. J. O'Keefe, W. G. Fahrenholtz, *Int. J. Corr*. (2012).
7. W.G. Fahrenholtz, J. Zhou, and M.J. O'Keefe, *Cera. Eng. Sci. Pro.,* **23**(4), 469-476 (2002).
8. H. Bhatt, A. Manavbasi, and D. Rosenquist, *Met. Fini.,* **107**(6), 39-47 (2009).
9. E. Mazario, L. Cabrera, and P. Herrasti, *J. Adv. Eng. Sci.,* **1,** 37-44 (2007).
10. S.A. Kulinich, M. Farzaneh, and X.W. Du, *Inorg. Mat.,* **43**(9), 956-63 (2007).
11. W. Pinc, P. Yu, M.J. O'Keefe, and W.G. Fahrenholtz, *Surf. Coat. Tech.,* **203,** 3533-3540 (2009).
12. D. K. Heller, W.G. Fahrenholtz, and M.J. O'Keefe, Corr. Sci., **52**(2), 360-368 (2010).
13. S. You, P. Jones, A. Padwal, P. Yu, M. O'Keefe, W. Fahrenholtz, and T. O'Keefe, *Mat. Lett.,* **61**, 3778-82 (2007).

14. S. Maddela, M.J. O'Keefe, Y.M. Wang, and H.H. Kuo, *Corrosion,* **66**(11), 115008/1-8 (2010).
15. A.L. Rudd, C.B. Breslin, and F. Mansfeld, *Corr. Sci.,* **42,** 275–288 (2000).
16. C. E. Castano, S. Maddela, M. J. O'Keefe, Y. M. Wang, *ECS Transactions,* **41(15),** 3-12 (2012).
17. G. Cole, *Mat. Sci. Foru.*, **419-422**, 43-50 (2003).
18. S. Maddela, Y.M. Wang, A.K. Sachdev, and R. Balasubramaniam, *in Magnesium Technology 2009,* E.A. Nyberg, Editor, 2009 p. 321, TMS (The Minerals, Metals & Material Society), (2009).
19. http://www.quadgroupinc.com/romulus.html

Magnesium Technology 2014
Edited by: Martyn Alderman, Michele V. Manuel, Norbert Hort, and Neale R. Neelameggham
TMS (The Minerals, Metals & Materials Society), 2014

Corrosion of Ultrasonic Spot Weldbonds of Magnesium to Steel

Tsung-Yu Pan[1], Zhili Feng[1], Michael L. Santella[1], Jian Chen[1]

[1]Oak Ridge National Laboratory
One Bethel Valley Road, P.O. Box 2008, MS-6096
Oak Ridge, TN 37831

Keywords: Ultrasonic spot welding, Weldbonding, Adhesive, Corrosion, Magnesium

Abstract

Reliable mixed-metal joining, especially between magnesium and steel, is one of the critical technologies in achieving light-weighting vehicle body construction. However, galvanic corrosion between mixed metal joints is inevitable but not well quantified. In a previous study [1,2], 1.6 mm thick magnesium (Mg) AZ31B-H24 was joined to 0.8 mm thick galvanized mild steel by ultrasonic spot welding in lap-shear configuration and went through an automotive cyclic corrosion test including a step of immersion in 5% NaCl solution. In this study, joints of identical material combination made by ultrasonic spot weldbonding (with adhesive) and a different automotive cyclic corrosion test of immersion in 0.5% NaCl solution are analyzed. Corrosion test procedure includes salt liquid immersion, drying, and constant humidity exposure. Good joint strengths were retained at the end of 30-cycle test, with about 45% of the strength of that of non-corroded samples. Failure mode was shown to be interfacial failure of the USW joints with metal-metal bonding between Mg and steel maintained throughout 30 cycles of corrosion exposure. Joint strength of corroded samples decreased due to the corrosion attack at the joint interface and the delamination of adhesive from Mg sheet. Adhesive was found to help in protecting the interior of the Mg surface from corrosion as long as it adheres to the Mg surface.

Introduction

Magnesium is one of the important light weight materials for reducing weight in automobiles. [3,4] In most of the applications, it is used in conjunction with other materials to construction body structure, e.g. steel, aluminum, plastics, composites, etc. There are two specific areas of challenges for broader use of Mg: reliable joining methods and durable corrosion protection. These two concerns are significantly magnified when dealing with Mg components attached to steel structures. Department of Energy (DOE) has been sponsoring projects to develop solid-state joining technologies based on friction stir linear and spot welding (FSW/FSSW) and ultrasonic spot welding (USW) for joining Mg to steel. Both have been demonstrated to be feasible and successful [5-9]. A bigger challenge is the corrosion of mixed metals, i.e. galvanic corrosion because of the direct metal contact between Mg and steel.

In a previous study [1,2], corrosion test was conducted on USW of Mg and steel. The test was carried out with an automotive cyclic corrosion test, which includes cyclic exposures of dipping in the 5% sodium chloride (NaCl) bath, air drying, then a constant humidity environment. It was expected that the galvanic corrosion could be very severe and the results confirmed it. However, surprisingly the major failure mode was not the direct erosion of the metals, but rather a combination of the excessive growth of magnesium hydroxide ($Mg(OH)_2$) and the mechanical deformation by the thickening of it in the crevice between Mg and steel sheets to weaken and eventually separate the joints.

An adhesive layer is added in this study to examine its effect to the strength of joints and the protection from corrosion. The galvanic corrosion has four basic requirements to occur: an anode (e.g. magnesium), direct electrical contact (e.g. a joint), a cathode (e.g. steel), and presence of electrolyte (e.g. winter road salt) at the interface between anode and cathode. It is assumed that the addition of adhesive can block the access of electrolyte to the joint interface to protect the joint from corrosion. In addition, it is interesting to study the feasibility of adding adhesive to USW, as weldbonding [10] in the resistance spot welding process, which has been widely used in the automotive industry to provide benefits of higher stiffness and prolonged fatigue life. The same concept was applied to friction stir spot welding (FSSW) (or spot friction welding (SFW)) with adhesive, called "spot friction weldbonding" by Pan, et al [11].

Therefore, there are two objectives in this study: the first is to study the feasibility of "ultrasonic spot weldbonding" for producing USW joint with adhesive, the second is to study the corrosion behavior of such joints.

A NaCl solution of 0.5% is used instead of 5% as in previous study for better reflecting of the current trend of automotive corrosion test requirements [12].

Experiments

Mg and steel materials, ultrasonic welding machine, and fixture used to make ultrasonic spot welded lap-shear samples were identical as described in [1,2,5-7,9,13]. The materials used for these experiments were sheets of 0.8 mm thick hot-dip-galvanized mild steel and 1.6 mm thick AZ31B-H24. Prior to welding, the surfaces of the AZ31B sheet were buffed with non-metallic abrasive pads (Scotch-Brite™) to remove surface oxides and produce shiny surfaces. Both metals were cleaned with acetone followed by isopropyl alcohol to remove lubricants and surface debris. The coupons used for welding the lap-shear test specimens had dimensions of 100 mm × 30 mm, and they were overlapped a distance of 40 mm in a fixture. The welds were centered in the overlap region. The size of the overlap and the process parameters were selected for optimal joint strength without adhesive. Adhesive material is a one-part heat-curing epoxy adhesive, Betamate 73305, from Dow Automotive [14].

Samples with adhesive were made in a process similar to the weldbonding process of resistance spot welding, i.e. applying a paste adhesive to one sheet, closing the joint, then making spot weld through the adhesive. A masking tape was first put to both

the Mg and steel surface to mask out the areas not to be applied with adhesive. An X-shape bead of adhesive was applied on the steel surface with added 0.3 mm Zirconia beads as spacers. The steel sheet was then overlapped with the Mg sheet, as shown in Figure 1. The assembly was transferred to the USW fixture for welding. The welded samples were then cured in a furnace at 165°C for 30 min. The masking tapes were peeled off before the samples were subject to the corrosion test.

The machine used for the ultrasonic spot welding was a single-transducer wedge-reed Sonobond CLF 2500. Spot welding was done using a power of 1500 W at welding time of 2.1 sec. The only clamping in the present experiments was the pressure applied by the welding (sonotrode) tip. Specimens were positioned for welding so that the primary vibration direction of the sonotrode was perpendicular to their long axis. The sonotrode tip was made from T1 steel, and had a flat, rectangular face of 7 mm × 7 mm [5]. The line pressure to the tip clamping mechanism was adjusted to make the welds under constant nominal pressure of 39 MPa. The setup of coupons during welding is shown in Figure 2.



Figure 1. Dispensing of adhesive on the steel sheet before overlapped with Mg sheet. Steel and Mg sheets were masked by tapes (golden yellow color).

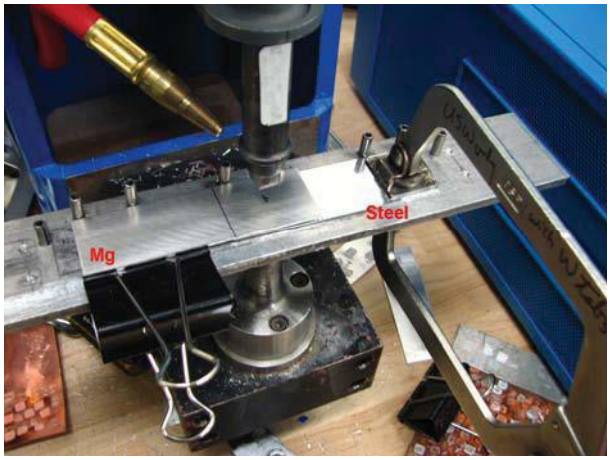


Figure 2. Experimental setup of ultrasonic spot welding.

An automotive corrosion cycle test procedure, Ford L-467 Accelerated Cyclic Corrosion Test, was applied. The cycle consists of immersion or constant spray of 0.5% NaCl solution for 15 minutes, followed by a humidity exposure at 25°C and 95% relative humidity for 5 hours and 45 minutes, and finally a drying period at 50°C and 70% relative humidity for 18 hours with the whole cycle of 24 hours. Humidity chambers were set according to ASTM E104-02 [15]. A complete set of test lasts for 30 cycles. A major difference from the test conditions in previous study [1,2] was the 5% of NaCl solution specified in Ford Arizona Proving Ground Equivalent Corrosion Cycle (APGE) and different temperatures and times in the humidity and drying periods.

One joint sample was pulled from the test at the end of each cycle for mechanical testing with tensile lap-shear setup. Mechanical test was conducted on an Instron machine at a crosshead speed of 10 mm/min without spacer added to offset the centerline. In addition, one sample was pulled every 5th cycle for metallographic examination with light microscope, scanning electron microscope (SEM), and energy dispersive spectrometer (EDS). A total of 36 samples were used at the beginning of the test.

Results and Discussions

Strength of Ultrasonic Spot Weldbonds

Ultrasonic spot weldbonding was demonstrated to be successful. The initial lap-shear strengths of the joints, before the adhesive was cured (i.e. "pasty"), were ranged from 0.5 to 1.3 kN with welding times from 0.8 to 1.8 seconds, and averaged to be about 0.9 kN[16]. After the adhesive was cured, the strength was increased to 6.4 kN [13,17] and relatively independent from the welding times. It shows that the strength of ultrasonic spot weldbonds is mainly carried by the adhesive, not by the metal-metal joint between Mg and steel. In comparison, joint strength of USW without adhesive is in the range of 4.1 kN [5-7], lower than the ones with adhesive.

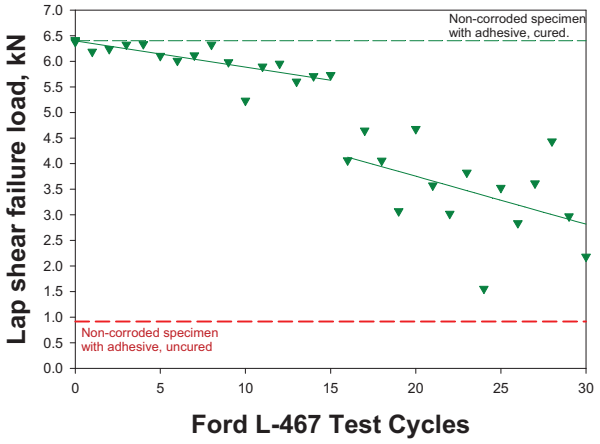


Figure 3. Lap shear failure loads of ultrasonic spot weldbonds vs. cycles of corrosion exposure. Two dash-lines indicate the failure loads of non-corroded samples with cured adhesive and with uncured adhesive.

Joint strength decreases following cyclic corrosion test. Figure 3 shows the lap-shear failure load vs. cycles of corrosion exposure of samples. The average failure loads of non-corroded samples of 6.4 kN and non-cured adhesive samples of 0.9 KN are shown as horizontal dash lines for reference. In general, failure loads of corroded samples decrease with each cycle of exposure. All of the samples maintained useful strength. About 45% of the strength was retained after 30 cycles of corrosion exposure compared to non-corroded samples. These are great departures from the previous study [1,2] which showed the corroded samples, without adhesive, lost almost all the strength after 17

cycles of corrosion exposure to the APGE test protocol. This difference may be contributed to sample preparation with adhesive, and the test protocol: 0.5% NaCl solution used in the current L-467 test vs. 5% NaCl used in the APGE.

Although only one sample was mechanically tested per corrosion cycle, the relationship between strength and corrosion cycles follows two separate trends: one is from beginning to the 15th cycle, the second is from the 15th cycle to the end of 30th cycle. Further examination reveals different failure modes which can help in explaining these trends.

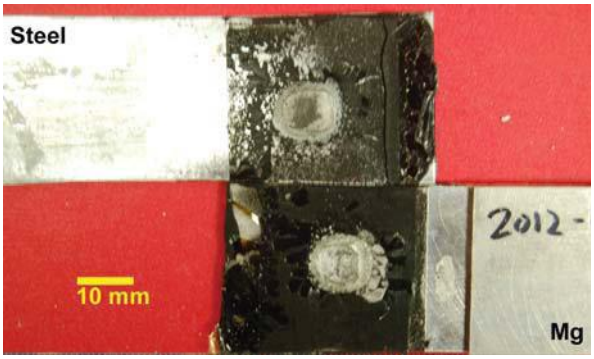
Failure Modes

The failure mode of Mg-steel joints of ultrasonic spot weldbonds is interfacial separation in both non-corroded and in all 30 corroded samples. Figures 4 (a)-(c) are the matching (inner) surfaces of the AZ31 and steel sheets from tensile lap-shear tested samples. These are: without corrosion exposure (Figure 4(a)), after 15 cycles (Figure 4(b)), and 29 cycles (Figure 4(c)), respectively.

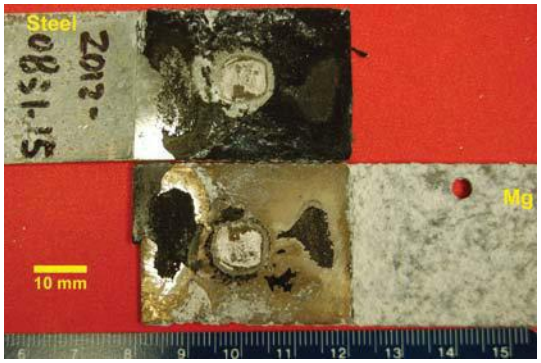
The failure mode of the adhesive area of non-corroded sample is cohesive (failure within the adhesive), shown by the residual adhesive on both sides of the sheets in Figure 4(a). There are dark images of material at the metal-metal joint interface, identified by the EDS to be oxides of magnesium [13], from the remnants of adhesive bonded to Mg. Similar cohesive failure mode of adhesive is observed in the samples from 1 through about 10 cycles.

The failure mode of the adhesive changes in the middle cycles of the corrosion test. A typical sample in this range of the corrosion cycles is shown in Figure 4(b), a sample after 15 cycles of corrosion exposure. Adhesive is still shown on the steel sheet. But it begins to disappear from the Mg sheet. Some of the remnants (flakes) of the adhesive were seen in the NaCl immersion tank. It seems that the adhesive was separated (delaminated) from the Mg surface. One likely reason for the delamination of the adhesive is due to the sample preparation which no "pretreatment" was applied on Mg sheets. Pretreatment on Mg has shown [18] to stabilize the surface oxide so that it offers better corrosion durability than non-pretreated Mg.

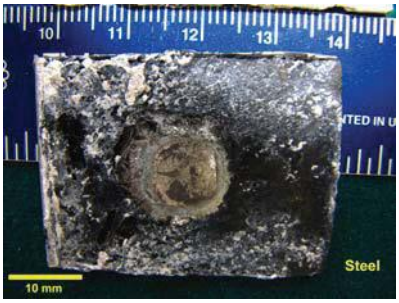
White $Mg(OH)_2$ is grown heavily on the Mg sheet, outside the adhesive-bonded area in Figure 4(b). $Mg(OH)_2$ is the product of the reaction from the presence of electrolyte (NaCl), humidity and temperature. In the previous study without adhesive, $Mg(OH)_2$ grew both on surface of Mg outside the overlapped region and in the crevice between the Mg and steel sheets. $Mg(OH)_2$ grew thicker with increase of corrosion cycles [1,2]. The thickened $Mg(OH)_2$ caused mechanical deformation of the sheets and

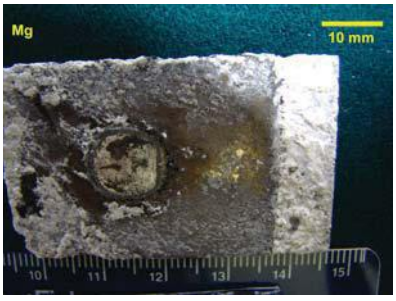


(a) Non-corroded sample.



(b) After 15 cycles.

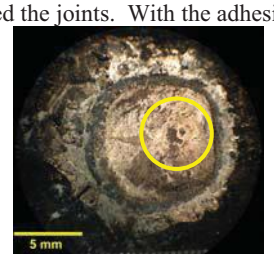




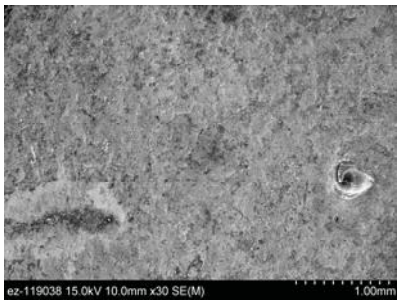
(c) After 29 cycles

Figure 4. Optical images of matching surfaces of the AZ31 and steel sheets from tensile lap-sheared samples without and with corrosion exposure.

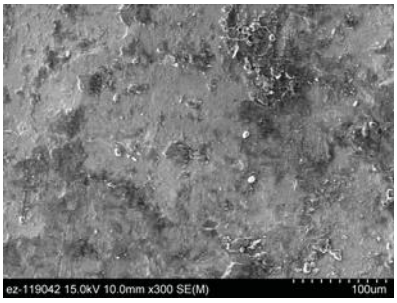
eventually separated the joints. With the adhesive fills up the crevice between the Mg and steel sheets, $Mg(OH)_2$ only grows outside the adhesive bonded area in this study.



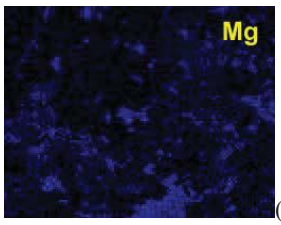
(a) Light micrograph of the fracture surface.



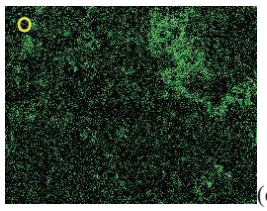
(b) Scanning electron micrograph from yellow circle in (a).



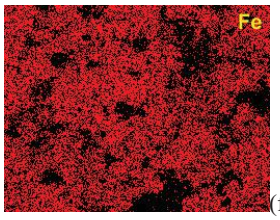
(c) Magnified Scanning electron micrograph from (b).



(d)



(e)



(f)



(g)

Figure 5. Light micrograph, scanning electron micrographs, and EDS elementary maps of steel surface of a tensile lap-sheared sample after 29 cycles of corrosion exposure.

However, when the adhesive delaminates from the Mg sheet, the corrosive medium has the opportunity in getting into crevice. Sample after 29 cycles of corrosion test has $Mg(OH)_2$ grown on the Mg surface in the overlapped region, as shown in Figure 4(c). The growth of $Mg(OH)_2$ in the crevice would affect the strength of the joints, similar to the USW samples without adhesive in [1,2].

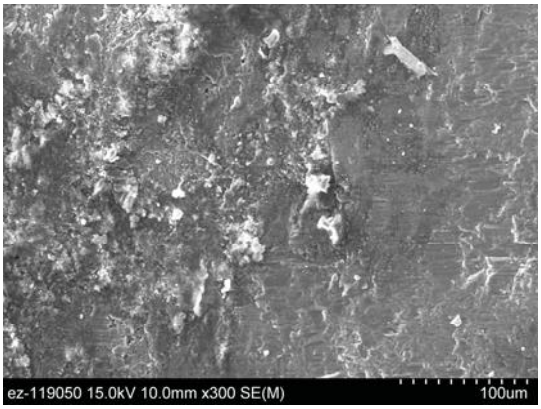
Fracture surfaces from Figure 4(c) are further examined by the SEM and EDS. Figure 5(a) is an optical micrograph of the center of the joint on the steel surface. Figure 5(b) is a magnified scanning electron micrograph in a region, marked with a yellow circle, in Figure 5(a). Figure 5(c) is magnified micrograph in the middle of Figure 5(b), corresponding to the dark spot in the middle of light micrograph in Figure 5(a). There are patches of lower atomic weight materials scattered in the magnified micrograph in Figure 5(c). Further analysis by EDS shows those to be related to the Mg (Figure 5(d)) and O (Figure 5(e)), likely from the remnants of bonding of adhesive and Mg, as in the non-corroded sample shown in [13,17]. Majority of matrix consists of Fe, as shown in Figure 5(f). There is no detectable Zn on the surface (Figure 5(g)), indicating that galvanized layer is completely displaced during the welding process.

SEM micrograph of the matching Mg surface of the joint after 29 cycles of corrosion test are shown in Figure 6(a), and the corresponding EDS maps are in Figure 6 (b) to (f). The micrographs show the surface mainly consists of Mg, O, and small amount of Al (from Mg alloy), and almost none of Fe and Zn. It is evident from Figures 5 and 6 that the facture occurs mainly between steel and Mg, and partially through Mg.

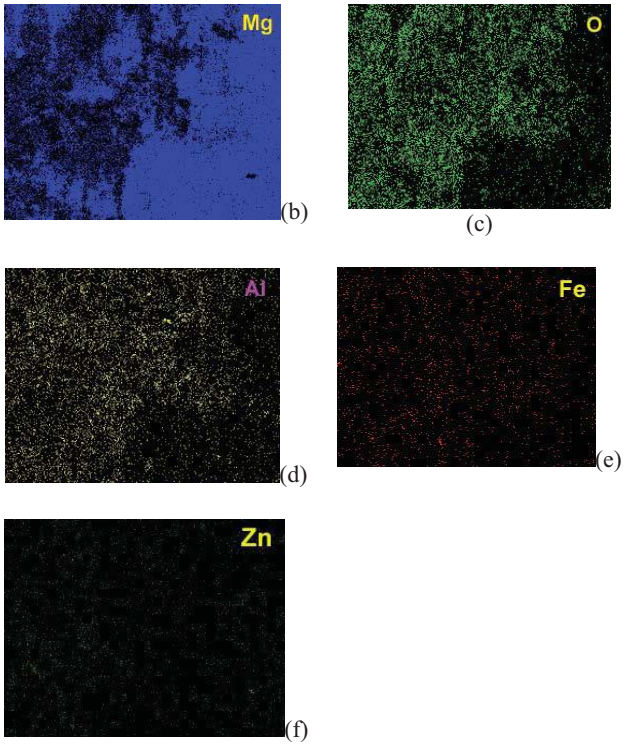
The presence of adhesive during USW process is similar to that of resistance spot weldbonding [10]. Adhesive is pushed away from the joint around the perimeter during the welding process when the adhesive is pasty (uncured). This is evident by the pattern of expulsion of adhesive, shown in Figure 4(a). Similar pattern has also been shown of the spread of Zn galvanized coating by the USW process [13]. However, it seems that the addition of the pasty uncured adhesive during the welding inhibits the strong bond at the Mg-steel interface and leaves some remnants at the interface. But the addition of adhesive increases the strength of the joint after the adhesive is cured, over the USW without adhesive.

The erosion behavior of samples with adhesive is different from that of samples without adhesive. Figure 7(a) shows a low-magnification micrograph of a cross-section sample after 10 cycle of corrosion exposure. It shows that the erosion of the Mg sheet occurs mainly on the exterior surface, and very little on the interior surface facing the adhesive. This is opposite from that in the non-adhesive samples which both the exterior and interior surfaces of the Mg sheets are equally eroded [13]. It is due to the lack of electrolyte and humidity to the interior surface of the Mg sheet because of the presence of adhesive (until it is delaminated). The exterior surface of the Mg sheet is heavily corroded in the joint and less in the parent material, as shown in Figure 7(a). In addition, a crack due to corrosion has extended from the exterior to the interface between Mg and steel, indicated by a circle in

Figure 7(a) and magnified in Figure 7 (b). The crack can provide a path of corrosive medium reaching the Mg-steel interface.



(a) Magnified scanning electron micrograph of middle of the facture surface of joint.



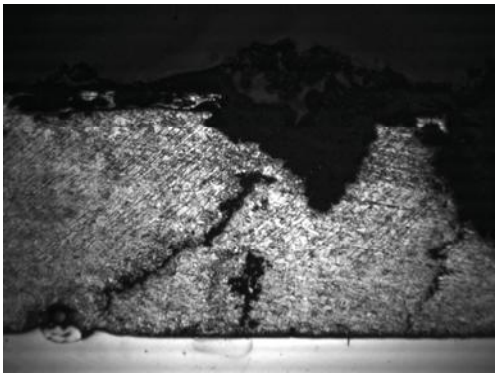
(b) (c) (d) (e) (f)

Figure 6. Light micrograph, scanning electron micrographs, and EDS elementary maps of Mg surface of a tensile lap-sheared sample after 29 cycles of corrosion exposure.

It is evident that when the crevice was filled with adhesive, no erosion was observed on the interior surface of Mg sheet. When the adhesive is delaminated eventually from the Mg surface due to the absence of pre-treatment of the Mg sheet, $Mg(OH)_2$ begins to grow (Figure 4(c)) and Mg would be eroded from that stage on. However, metal-metal (Mg-steel) bonding always maintains throughout the test.



(a) Low-magnification of overall joint.



(b) Magnified micrograph from yellow circle in (a).

Figure 7. Optical micrographs of a ultrasonic spot weldbond after 10 cycles of corrosion exposure.

Conclusions

Ultrasonic spot weldbonding was demonstrated successfully by the combination of adhesive and USW process. Corrosion behavior of ultrasonic spot welds between Mg AZ31B-H24 and hot-dipped mild steel was study under Ford L-467 automotive cyclic corrosion test. Failure loads measured by tensile lap-shear test of non-corroded samples was 6.4 kN. All samples retained good strengths after 30 cycles of corrosion exposure, and kept with 45% of strength of that of non-corroded samples.

Failure mode of Mg-steel joints in ultrasonic spot weldbonds was the interfacial failure. Erosion was observed on the exterior surface of Mg sheet and extended through the thickness of Mg in the joint. Adhesive was delaminated from the Mg surface with the increase of corrosion cycles. Joint strength decreased with cycles due to corrosion attack at the interface. Adhesive was able to help in minimizing the erosion of the interior surface of Mg sheet until it is delaminated from Mg.

SEM and EDS confirms the existence of the magnesium oxides at the joint interface which can be the remnant from the adhesive during the USW process. By examining the matching surfaces of Mg and steel at the joint, it is concluded that the failure goes through the Mg-steel interface and partially through Mg.

References

1. T. Pan and M.L. Santella, "Corrosion of Ultrasonic Spot Welded Joints of Magnesium to Steel", in "*Magnesium Technology 2012*", Edited by: Suveen N. Mathaudhu, Wim H. Sillekens, Neale R. Neelameggham, and Norbert Hort, (The Minerals, Metals & Materials Society), pp.265-269, 2012.
2. T. Pan and M.L. Santella, "Corrosion Behavior of Mixed-Metal Joint of Magnesium to Mild Steel by Ultrasonic Spot Welding", *SAE Technical Paper* 2012-01-0472, 2012.
3. "Los Angeles Auto Show was road map for how automakers will meet tough fuel economy standards", http://www.freep.com/article/20121206/BUSINESS01/312060163/Los-Angeles-Auto-Show-was-roadmap-for-how-automakers-will-meet-tough-fuel-economy-standards
4. "*Magnesium Vision 2020: A North American Automotive Strategic Vision for Magnesium*", United States Automotive Materials Partnership (USAMP) Automotive Metals Division (AMD), released November 2006.
5. M.L. Santella, T.J. Franklin, T. Pan, J., Pan, and E. Brown, "Ultrasonic Spot Welding of AZ31B to Galvanized Mild Steel", *SAE International Journal of Materials and Manufacturing,* 3(1) (2010), 652-657.
6. M.L. Santella, E. Brown, M. Pozuelo, T. Pan, and J.-M.Yang, "Details of Mg-Zn reactions in AZ31 to Galvanized Mild Steel Ultrasonic Spot Welds", *Science and Technology of Welding & Joining*, 17(3) (2012) , 219-224.
7. T.J. Franklin, J. Pan, M.L. Santella, and T. Pan, "Fatigue Behavior of Dissimilar Ultrasonic Spot Welds in Lap-Shear Specimens of Magnesium and Steel Sheets" *SAE International Journal of Materials and Manufacturing,* 4(1) (2011), 581-588.
8. S. Jana, Y. Hovanski, and G.J. Grant, "Friction Stir Lap Welding of Magnesium Alloy to Steel: A Preliminary Investigation." *Metallurgical and Materials Transactions. A, Physical Metallurgy and Materials Science,* 41A(12) (2010) pp. 3173-3182.
9. T. Pan and M.L. Santella, "Ultrasonic Spot Welding of Galvanized Mild Steel to Magnesium AZ31B", *SAE Technical Paper* 2012-01-0474, 2012.
10. "*Hybrid adhesive joints*", ed by L.F.M. da Silva, A. Pirondi, A. Öchsner, Springer, 2011.
11. T. Pan, W.J. Schwartz, K.A, Lazarz and M.L. Santella, "Spot Friction Weldbonding for Sheet Aluminum Joining", *Proceedings of Sixth International Symposium on Friction Stir Welding*, Paper #17, 10 - 13 October 2006, Saint-Sauveur, Nr Montreal, Canada.
12. Robert McCune, private communications with author, Robert C. McCune and Associates, LLC, 2012.
13. T. Pan, Z. Feng, M.L. Santella and J. Chen, "Corrosion Behavior of Mixed-Metal Joint of Magnesium to Mild Steel by Ultrasonic Spot Welding with and without Adhesives", *SAE Technical Paper* 2013-01-1017, 2013.
14. Betamate™ 73305 Structural Adhesive http://msdssearch.dow.com/PublishedLiteratureDOWCOM/dh_08bb/0901b803808bb262.pdf?filepath=automotive/pdfs/noreg/299-50212.pdf&fromPage=GetDoc
15. "*Standard Practice for Maintaining Constant Relative Humidity by Means of Aqueous Solutions*", ASTM E104 – 02 (2007).
16. T.J. Franklin, unpublished data.
17. W.-J. Lai, J. Pan, Z. Feng, M.L. Santella, and T. Pan, "Failure Mode and Fatigue Behavior of Ultrasonic Spot Welds with Adhesive in Lap-Shear Specimens of Magnesium and Steel Sheets", *SAE Technical Paper* 2013-01-1020, 2013.
18. K. Lazarz, R.C. McCune, W. Wang and P.K. Mallick, "Effect of Surface Pretreatments on Adhesive Bonding and Corrosion Resistance of AM60B, AZ31-H24, and AM30 Magnesium", *SAE Technical Paper* 2009-01-0037, 2009.

Magnesium Technology 2014
Edited by: Martyn Alderman, Michele V. Manuel, Norbert Hort, and Neale R. Neelameggham
TMS (The Minerals, Metals & Materials Society), 2014

Friction Stir Back Extrusion of Mg AZ31B-F: a Preliminary Investigation

Justin L. Milner, Fadi Abu-Farha
Automotive Engineering, Clemson University – International Center for Automotive Research, Greenville, SC 29607, USA

Keywords: Friction Stirring, Bulk Material Processing, Magnesium Alloys, Back Extrusion, Grain Refinement

Abstract

The limited room-temperature ductility of magnesium and its alloys inhibits their fabrication without the introduction of heat to the process; that's why magnesium alloys are typically associated with warm or hot forming operations. This work presents a unique approach to heating magnesium alloys during bulk forming by utilising "friction stirring"; the same phenomenon on which friction stir welding (FSW) and friction stir processing (FSP) are based. The proposed friction stirring can be combined with particular forms of forging and back extrusion, thus generating the heat needed to soften the metal and ease its deformation. Moreover, and just like the case with FSW and FSP, the proposed bulk friction stir forming processes have the additional advantage of refining the grainstructure of the processed material, and thus the potential to enhance its performance. A close look is provided here to a particular form of bulk processing, referred to as friction stir back extrusion (FSBE). Magnesium AZ31B-F round bar samples are processed by FSBE at selected set of conditions producing sound tubular specimens. Microstructural examination and microhardness testing are performed at key locations to examine the changes to microstructure of the material due to processing. The preliminary results shown here provide a general validation to the proposed processing concept, showing significant grain refinement in the material.

Introduction

In 1991, The Welding Institute (TWI) in Cambridge/UK developed the novel energy-efficient solid-state joining technique known as "Friction Stir Welding" (FSW) [1]. The technique uses a rotating non-consumable tool -featuring a protruding end pin- that moves along the butting surfaces of two sheets/plates, as schematically shown in Figure 1. Heat generated by friction at the shoulder (and to a lesser extent at the pin's surface) softens the material; meanwhile, the pin deforms and stirs the material, transporting it from the front of the tool to the trailing edge, thus producing the joint [2-3]. Other variations and joint types can be achieved; nevertheless, the "friction stirring phenomenon" described here remains the foundation of the technique [3]. Ever since it was introduced, FSW has attracted a great deal of attention and has taken-off in a number of applications due to its apparent advantages over traditional joining techniques. Of particular importance is the technique's ability to join hard-to-weld metals, such as aluminium alloys - the 2xxx and 7xxx series in particular [4-5]. Other advantages include low-energy consumption and a series of environmentally-benign benefits [1,3]. It is now a common knowledge that FSW is an attractive technology for joining lightweight metals (aluminium, magnesium, titanium) [6-15], and even a wide range of dissimilar metals and alloys [16-19].

The severe plastic deformation (SPD) associated with the stirring action in FSW was found to produce material with fine equi-axed grain structure within the weld zone. Rhodes et al. 1997 [20] reported a weld zone having 2-4μm grain size in a friction stir welded 7075-T6 aluminium alloy plate. Mahoney et al. 1998 [21] observed a grain size of ~3μm in a 7075-T651 aluminium alloy. These and similar observations inspired Mishra et al. 2000 to propose adopting FSW as a processing technique that can be used to refine the microstructure of the material; thus the term "Friction Stir Processing" (FSP) was first coined in [22]. FSP can be still represented by Figure 1, with the exception that the tool traverses across a single sheet/plate in the intention of refining and homogenising the microstructure in the processed zone. In that early work, Mishra et al. 2000 [22] suggested exciting possibilities for using FSP to enhance the grain size dependent properties of the material. Indeed, in a series of works, the authors showed great impact by the FSP technique on improving the superplastic behaviour of several materials [22-24]. Just like FSW before it, FSP has been capturing interest by a wide variety of researchers who are further exploring its potentials. Moreover, and within a mere decade, FSP spurred multiple other exciting concepts based on the "friction stirring phenomenon", including: friction stir casting modification [25], friction stir micro-forming [26] and friction stir channelling [27].

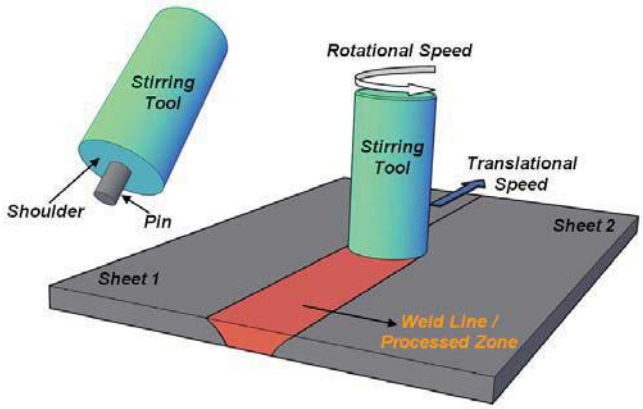


Figure 1: Schematic of friction stir welding (FSW). This schematic is also applicable to friction stir processing (FSP).

Recently, a new friction stirring concept, which targets the processing of bulk material, was recently introduced [28]. While FSP has been predominantly applied to sheets/plates, with the stirring tool traversing in a direction perpendicular to its axis of rotation; bulk friction stir forming BFSF targets the processing of bulk material by moving the stirring tool in the axial direction [28]. The concept is schematically shown in Figure 2, in a special application to the back extrusion process. With this concept, a rotating tool is plunged into a cylindrical specimen at a selected feed rate, denoted axial feed in the figure. The latter motion of the tool simply forces the material outwards as in back extrusion, while friction at the tool/specimen interface generates sufficient heat to soften the material and facilitate its deformation. Beyond

that, the stirring action under the relatively high pressure imposes severe plastic deformation on the material, thus refining its grain structure. The net result is a combined radial/peripheral material deformation, forming a tube with a grain size smaller than that of the starting material. FSBE was validated in a preliminary study on the 6063-T52 aluminium alloy [28-29], where the starting material underwent grain refinement from ~80μm to <20μm within the processing zone. Equal or greater potentials are expected for FSBE of hard-to-deform materials, particularly magnesium, and this work provides a closer look at some of the preliminary work conducted with the AZ31B-F magnesium alloy.

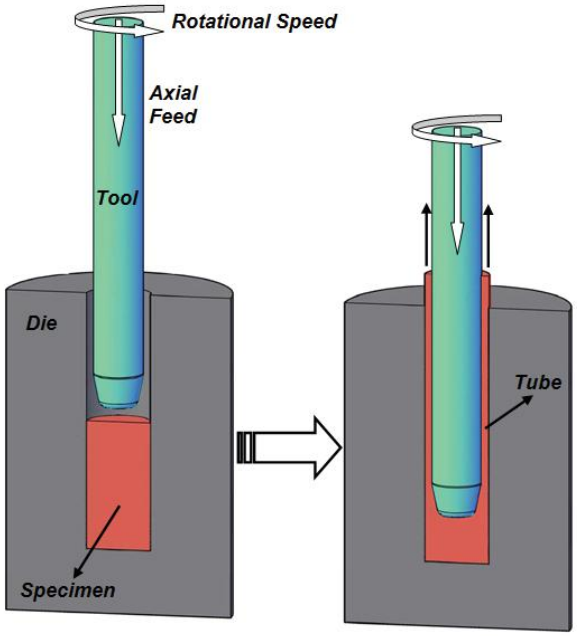


Figure 2: Schematic of friction stir back extrusion (FSBE).

Experiments

Setup:

The setup used to perform the FSBE experiments is shown in Figure 3. The stirring tool is a polished rod with Φ=12.7mm (Φ=0.50"), prepared from H13 tool steel having a surface hardness of ~65 HRC. To ease tool penetration into the material, the end of the tool (a length of approximately 10mm) was tapered by ~10°, as shown in the exploded view. Unlike stirring tools used in typical FSP, a flat stirring surface with no tool pin was adopted here. The extruding die, on the other hand, which fits the schematic shown earlier in Figure 2, was made in two halves in order to ease specimen extraction after testing. The die cavity is a straight blind hole with Φ=19.05mm (Φ=0.75"), thus leaving a 3.18mm (0.125") clearance from the outer surface of the stirring tool. The hole was first machined and then honed to a fine surface finish to facilitate the back extrusion (upward flow) of the processed material. Pre-hardened P20 tool steel was used in constructing the extruding die. The entire setup was secured to OKUMA MB 46VAE vertical machining center (15 hp, 8000 rpm), which was used to perform the experiments, since it provides control of the stirring tool's rotational speed as well as its axial feed (the main two processing parameters). Special attention was paid to centring the stirring tool with the die cavity, to ensure axisymmetric deformation conditions for the stirred material.

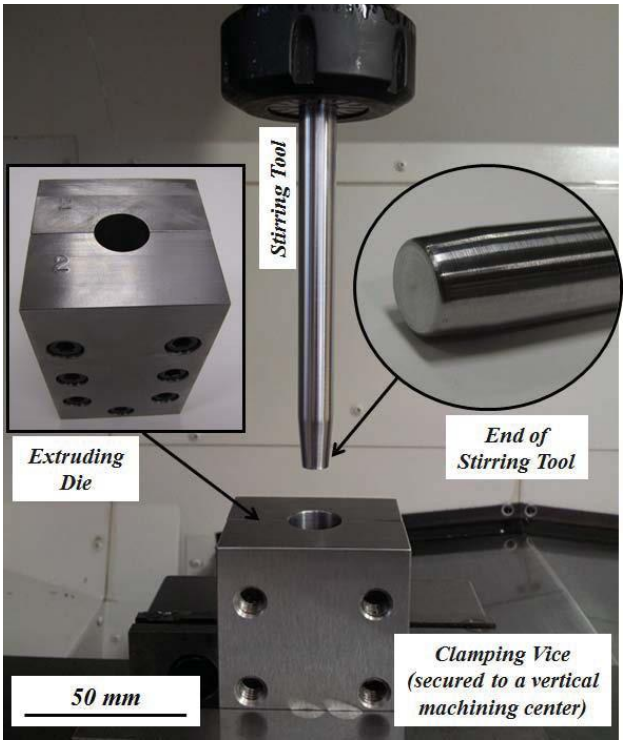


Figure 3: FSBE experimental setup

Material:

AZ31B-F magnesium alloy round bars, with Φ=19.05mm (Φ=0.75"), were used in the experiments. Processing specimens were simply prepared by cutting the bar into 38-50mm (1.5-2.0") slugs. Since the as-received material is an extruded bar in the -F condition, great variations in the grain structure were found. Figure 4 shows micrographs obtained at three locations across the section of the round bar. It is clearly inferred from the micrographs that the material has a coarse grain structure at the centre of the bar, yet a finer one around the outer surface. The average grain size was found to range between ~100μm and ~140μm at the centre (the overall average was estimated to be ~115μm). As for the circumferential zone close to the surface, average grain size variations were confined to a range of ~50 to ~70μm, with an overall average of ~55μm.

Testing Procedure:

After securing the extruding die into the clamping vice of the vertical machining center, a test specimen is inserted into the die in preparation for testing. The tool is then driven downwards against the specimen while rotating at a selected speed; after reaching the desired depth, the tool is retracted. The extruding die is then released, and the produced tubular specimen is retrieved for further examination. Due to the significant heat generated during testing, sufficient cooling period (no less than 30 minutes) is allowed before starting another testing cycle. Also, in order to guarantee repeatability of the performed tests, the stirring tool and the extruding die are lightly polished after each test. In all the performed tests, the compressive force of the downward-moving stirring tool was sufficient to prevent the billet from spinning (during processing). A few testing conditions were considered; the results reported here were obtained at a tool rotational speed of 2000rpm, tool axial feed of 2.12mm/s (5.0ipm), and tool exit speed of 4.23mm/s (10.0ipm). Under these testing conditions, a 100-125mm (4-5") tube specimen is formed in ~20sec.

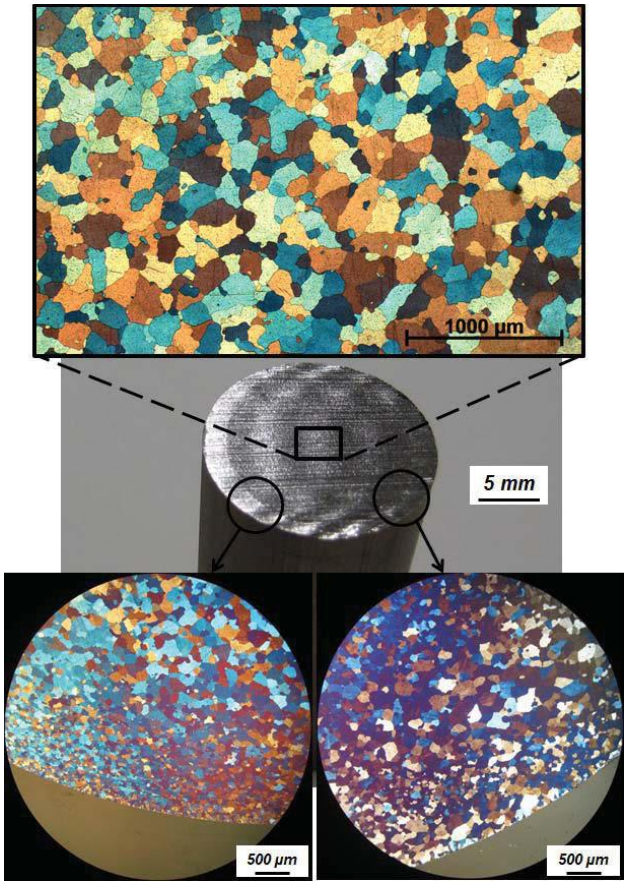


Figure 4: Micrographs showing the grain structure of the as-received material.

Results and Discussion

Formed Tubes:

Figure 5 shows two examples of magnesium tubular specimens after successful processing via FSBE. The tubes formed exhibit prismatic uniform sections, and the images show a high quality surface finish on the inside of the tubes. On the other hand, the images show spiral marks on the outside surfaces; these marks provides an insight about the amount of circumferential displacement the material experiences during processing in forming the tubes. Tracing these marks indicated an overall twist angle of ~6° over the length of a tube. A small lip is always formed at the top end as a result of the early stages of the tube forming process. The section view on the right clearly shows that the formed tube is structurally sound, with no signs of voids or internal channels. All such specimens were polished, and close examination did not reveal any defects in the deformed material.

The latter was also confirmed by closer examination of several polished tube sections under the microscope. From a process point of view, and based on the setup used for these experiments, the success of the FSBE runs was generally dependent on achieving the right balance between axial feed and rotational speed. Unbalanced combinations would lead to one of two unsuccessful scenarios: (i) high processing vertical forces, which might exceed equipment limits and (ii) generating excessive heat, which might cause sticking between the material and the processing tool. In comparison with previous results obtained with AA6063 [28,29], it was generally noted that the magnesium had a better response to the process; higher tool axial feeds were possible and the surface finish after processing was always better. In fact, AA6063 showed severe material sticking problems when dropping the axial feed-to-rotational speed ratio below a certain value. Nonetheless, the investigation on FSBE is still very preliminary to perform any comparisons between the two materials, and fully explore their processing limits. It is therefore that one set of conditions is focused on in the following discussion.



Figure 5: Two examples of Mg AZ31B-F tube specimens produced by FSBE.

Microstructural Examination:

The first key location to be examined is the bottom section of the tube, where the material meets the processing tool. The polarised micrograph in Figure 6 clearly shows a processed zone (top layer) with a significantly finer structure than the rest of the material below. The close-up view of the processed microstructure indicates that the structure is homogeneous with an average grain size of ~10-15µm. Examination of the microstructure closer to the processing tool showed further refinement to levels below ~10µm. For comparison, note that the as-received material displayed a coarse grain size at the centre with an average grain size of ~115µm. These numbers highlight the effectiveness of the stirring action in refining the microstructure within the processing zone (which extends 1-1.5mm below the processing tool). Interestingly, the microstructure of the material below that (away from the processing zone) does not correspond to that of the as-received material. Thought the grain structure is coarse, the grains exhibit high degree of twinning that is not observed in Figure 4. This is apparently the result of the compressive forces the material experiences during processing (due to the axial feed in FSBE). In comparison, such conditions do not exist in typical FSW and FSP runs, and thus the great difference in terms of the microstructure for this location. Moreover, another significant difference between bulk processing and conventional sheet/plate processing (FSP) is the thickness of the processing layer, which is noted to be

significantly smaller in the case of FSBE. This is a direct consequence of the lack of a stirring pin in this case, and it will have a significant impact on the homogeneity of the microstructure of the material within the formed tube, as discussed in the following sections.

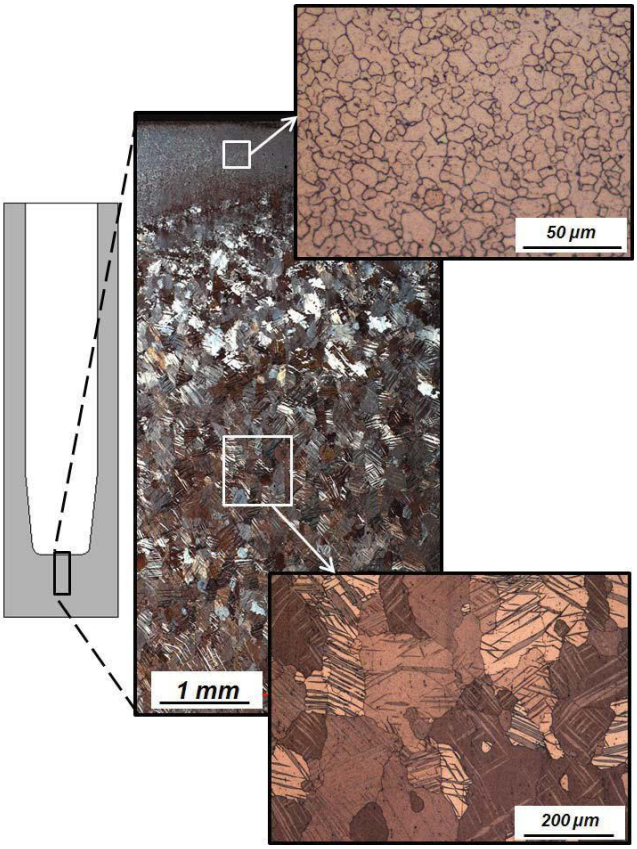


Figure 6: Micrographs showing the grain structure of the material below the processing tool.

By moving to the region around the corner of the processing tool, material flow lines become clearer, as noted in Figure 7. The thin processing layer is still visible (with a significantly more refined structure) and it is surrounded by a layer of highly sheared (elongated) grains that represent the convergence of the material from the wide section into the tubular section of the specimen. The latter is more notable in the zoomed in micrograph. Notice that twinning seems to be alleviated (yet not eliminated) in this zone, compared with Figure 6. This is caused by both the shear strains due to the stirring action, as well as the heat associated with processing.

Figure 8 provides a closer look at the microstructure within the corner region. The processing zone exhibits a very fine microstructure, with an average grain size ranging between ~5 and ~10µm. Further away from the processing zone, one clearly sees the non-homogenous grain structure with large elongated grains. By moving upwards with the material as it enters the tubular section, the disparities between the highly refined structure within the processing zone and the adjacent non-homogenous highly-elongated structure is still evident and even more pronounced, as depicted by Figure 9.

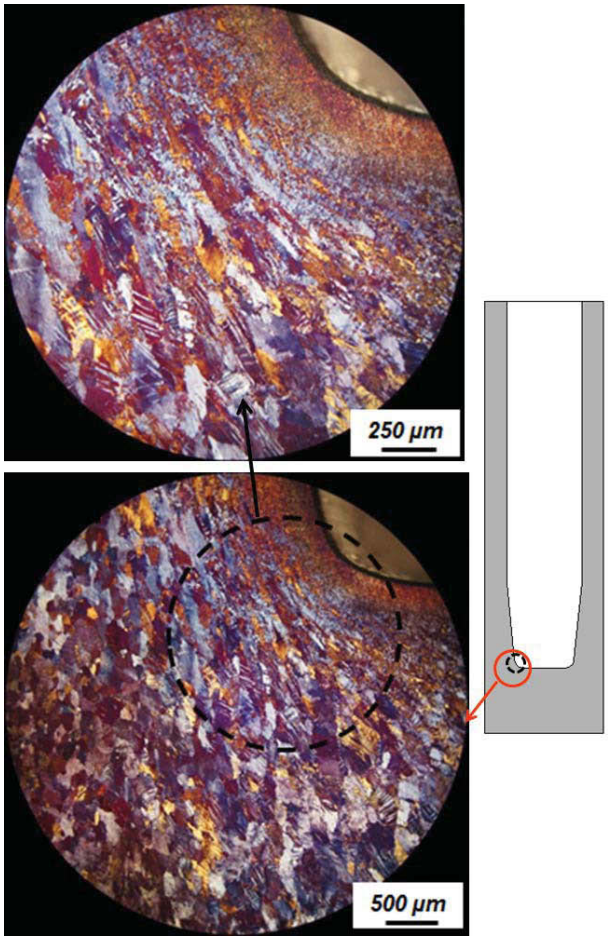


Figure 7: Grain structure of the processed material near the corner of the processing tool.

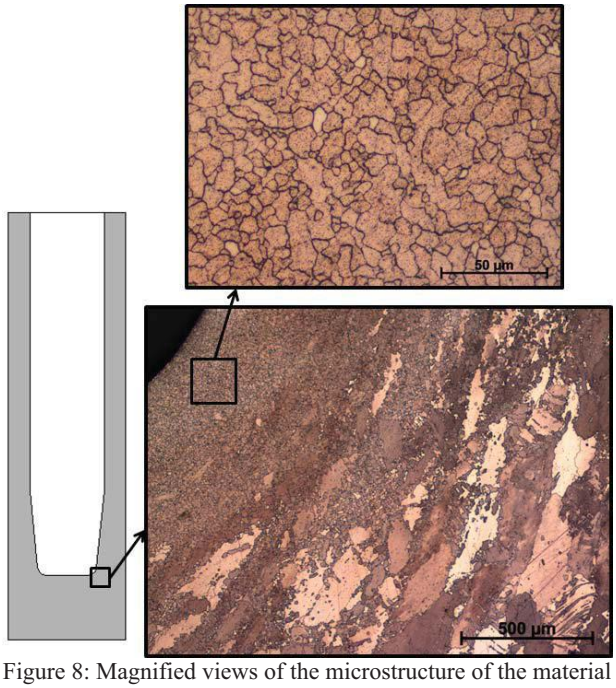


Figure 8: Magnified views of the microstructure of the material near the corner of the processing tool.

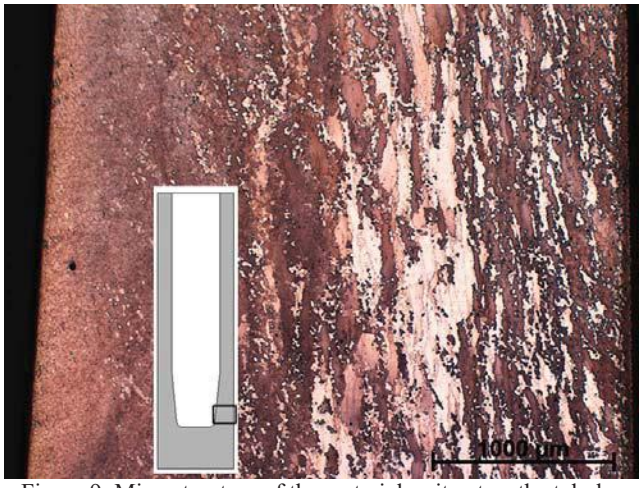


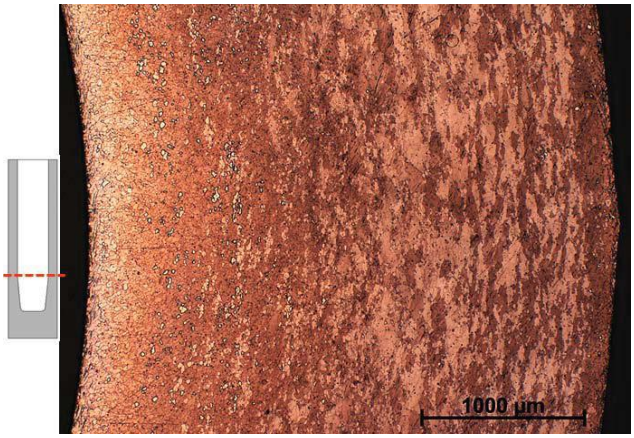
Figure 9: Microstructure of the material as it enters the tubular section.

This outcome is directly caused by the use a flat processing tool without a stirring pin (unlike those used in FSW and FSP), which results in a shallow processing zone that leaves a portion of the material without processing (before entering the tubular section). And since there is no significant friction stirring within the tube walls, the microstructure seen in Figure 8 and Figure 9 remains dominant. The microstructures in sections taken at ~8mm and ~24mm above the tool's surface are shown in Figure 10, and they further emphasises this observation. It is not clear at this point what impact such a non-homogeneous structure has on the performance of the processed material within the formed tubes; this is the subject of a current investigation. Nonetheless, this non-homogeneity can be tackled not only though stirring tool design (adding a stirring pin), but also by reducing the wall thickness of the processed tubes. It should be noted at this point that a flat tool was used not for simplicity, but rather based on the general concept of bulk friction stir forming and it being applicable to process bulk material to any tool geometry.

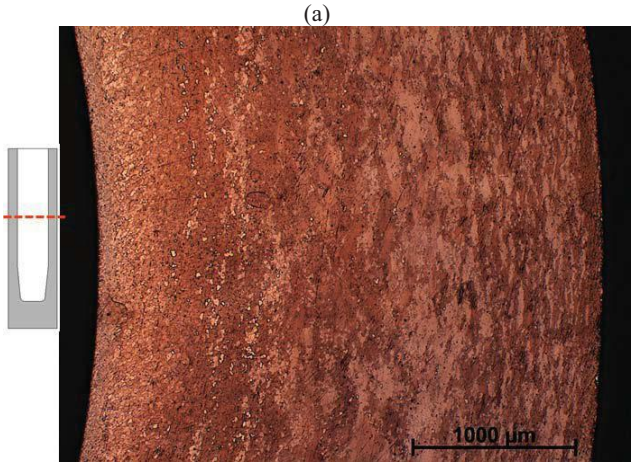
A closer look was taken at the coarse-grained portion of the microstructure shown earlier in Figure 9; an example of the zoomed-in view is shown in Figure 11. Note the very fine grains (~10µm in average size) dispersed between other much larger grains. This contrast is still based on the previous reasoning, where the friction stirring action is not far reaching to cause the refinement of the entire structure. Interestingly though, the large grains within this region were noted to be larger than those in the as-received condition. Note that some of the grains in Figure 11 are >200µm in the longitudinal direction. It is thus believed that some grain coalescence or merging is taking place in the material. This starts with the elongated grains that are formed below the stirring tools (along what seem to look like shear bands), and is accentuated as the material enters the tubular section (with the additional compressive pressure caused by the tool's end taper).

Microhardness Measurements:

Figure 12 shows plots of microhardness measurements at various locations. Part (a) shows the measurements taken in the as-received material, which displays a near constant level across the sample, with a slight dip in the middle that could be attributed to the larger grain size (Figure 4). Figure 12b shows the microhardness measurements along the centre of the processed tubular specimens below the processing tool.



(a)



(b)

Figure 10: Micrographs corresponding to sections in the tube (a) ~8mm (b) ~24mm above the stirring tool's flat surface.

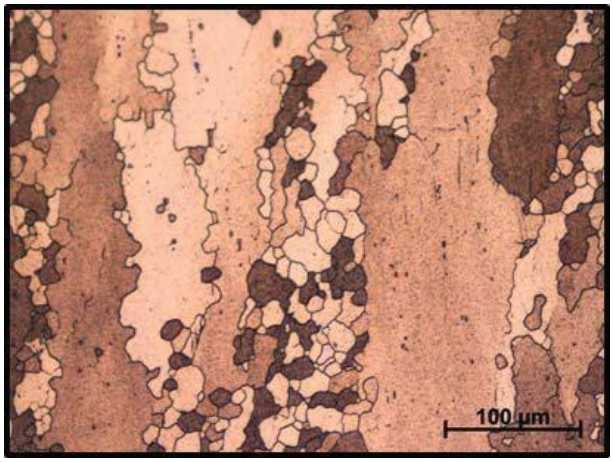
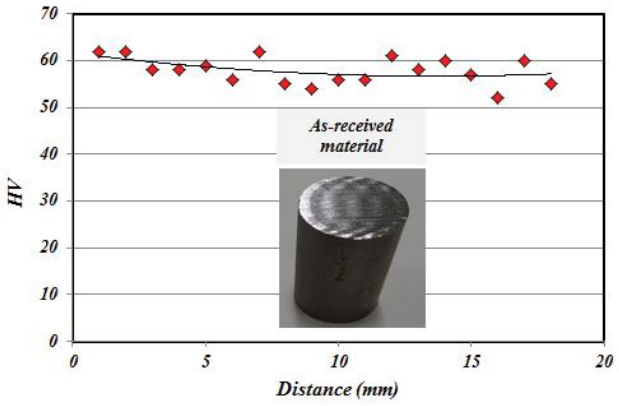
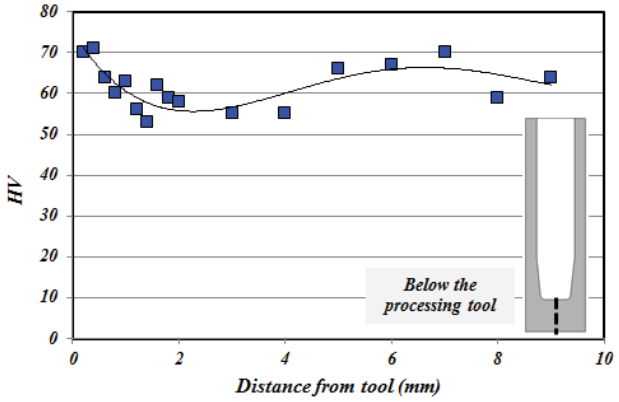


Figure 11: Close-up view of the coarse-grained portion of the microstructure in Figure-9.

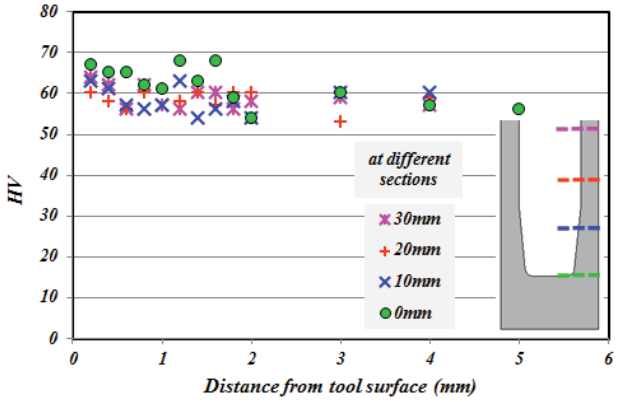
The best fit curve indicates high microhardness values within the processing zone (which corresponds to the finer grains) that drops steadily as we move away from the tool (towards the coarser structure). Yet microhardness levels increase again and remain higher than those for the as-received material, even though the grains are known to be coarse. The latter is due to the highly-twinned structure produced by the direct compressive stresses of the approaching processing tool.



(a)



(b)



(c)

Figure 12: Microhardness measurements (a) in the as-received material (b) below the processing tool (c) at different sections within the tube's wall.

Figure 12c on the other hand shows the data obtained at different sections within the tube's wall, ranging between 0mm and 30mm away from the tool's flat surface. The x-axis corresponds to the distance from the tube's inner surface to its outer surface. It can be inferred from these curves that the microhardness of the material is higher at the inner surface, regardless of the section's location. Microhardness drops within the first 1mm (the size of the processed zone) and remains near steady afterwards. This trend is also consistent with the inverse relationship between strength/hardness and grain size. As for the differences between the four sections, the curves indicate a general slight decrease as we move higher into the tube. This can be attributed to the partial recovery that is expected to take place in the material after processing and entering the tubular section. The heat generated during the process is sufficient to causes this. It is not possible to give an exact temperature for the material at any location during the process due to physical difficulties and the non-steady state conditions. Yet rough temperature measurements were carried out around the tube entry region (near the outer surface of the tube), and those measurements indicated that the temperature of the material exceeds 200 °C.

Summary and Conclusions

In this work, the recently introduced friction stir back extrusion (FSBE) process was further validated using AZ31B-F magnesium alloy samples. It was shown that the process can deform the material into tubes showing no signs of voids or internal defects. Microstructural examination of the processed tube specimens at various locations showed clear signs of grain refinement within a "stirring zone", the depth of which was ~1-1.5mm. Since the tube wall thickness considered here was ~3mm, the processed material showed clear inhomogeneities in the microstructure, with very fine grain structure at the inner surface. In comparison with the results obtained here for magnesium, aluminium [29] -generally speaking- showed more homogeneous microstructures under similar processing conditions. For instance, the severe non-homogeneity shown in Figure 9-11 was not observed in the tubes formed out of AA6063, as depicted by the micrograph in Figure 13. This could be attributed to the inherent poor deformation characteristics and limited malleability of magnesium. Future work in this area will utilise stirring tools with a tool pin to increase the size of the processing zone, and will consider processing thinner tubes. Tube bulging tests will be carried out on processed specimens as a means of evaluating the changes in the material's mechanical properties.

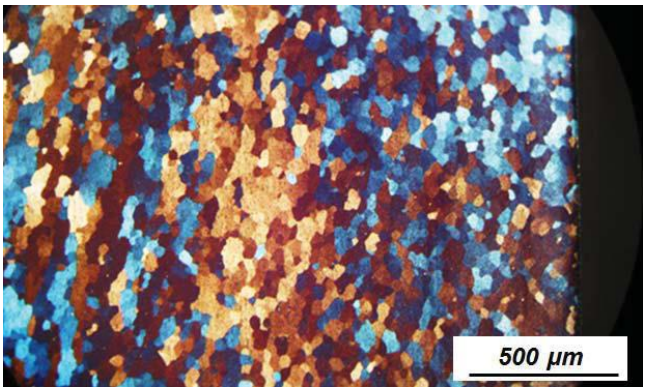


Figure 13: Microstructure of the material within the wall of an AA6063 tube produced by FSBE [29].

References

1. Thomas, W.M., Nicholas, E.D., Needham, J.C., Murch, M.G., Templesmith, P., Dawes, C.J., "Friction Stir Butt Welding", G.B. Patent Application No. 9125978.8, International Patent Application No. PCT/GB92/02203, 1991.
2. Mishra, R.S., Ma, Z.Y., "Friction Stir Welding and Processing", Materials and Science and Engineering R, vol. 50(1-2), 2005, pp. 1-78.

3. Nandan, R., DebRoy, T. Bhadeshia, H.K.D.H., "Recent Advances in Friction Stir Welding – Process, Weldment Structure and Properties", Progress in Materials Science, vol. 53, 2008, pp. 980-1023.
4. Thomas, W.M., Dolby, R.E., "Friction Stir Welding Developments," In: S.A. David, T. DebRoy, J.C. Lippold, H.B. Smartt, J.M. Vitek, Editors; Proceedings of the Sixth International Trends in Welding Research Conference, Materials Park, OH, USA: ASM International, 2003, pp. 203-211.
5. Dawes, C.J., Thomas, W.M., "Friction Stir Process Welds Aluminum Alloys", Welding Journal, vol. 75(3), 1996, pp. 41-45.
6. Thomas, W.M., Nicholas, E.D., "Friction Stir Welding for the Transportation Industries", Materials and Design, vol. 18, 1997, pp. 269-273.
7. Rhodes, C.G., Mahoney, M.W., Bingel, W.H., Spurling, R.A., Bampton, C.C., "Effects of Friction Stir Welding on Microstructure of 7075 Aluminum", Scripta Materialia, vol. 36(1), 1997, pp. 69-75.
8. Sato, Y.S., Kokawa, H., "Distribution of Tensile Property and Microstructure in Friction Stir Weld of 6063 Aluminum", Metallurgical and Materials Transactions, vol. A32(12), 2001, pp. 3023-3031.
9. Jata, K.V., Semiatin, S.L., "Continuous Dynamic Recrystallization During Friction Stir Welding of High Strength Aluminum Alloys", Scripta Materialia, vol. 43(8), 2003, pp. 743-749.
10. 11. Park, S.H., Sato, Y.S., Kokawa, H., "Microstructural Evolution and its Effect on Hall-Petch Relationship in Friction Stir Welding of Thixomolded Mg Alloy AZ91D", Journal of Materials Science, vol. 38, 2003, pp. 4379-4383.
11. Xie, G.M., Ma, Z.Y., Geng, L., Chen, R.S., "Microstructural Evolution and Mechanical Properties of Friction Stir Welded Mg–Zn–Y–Zr Alloy," Materials Science and Engineering A, vol. 471(1-2), 2007, pp. 63-68.
12. Commin, L., Dumont, M., Masse, J., Barrallier, L., "Friction Stir Welding of AZ31 Magnesium Alloy Rolled Sheets: Influence of Processing Parameters", Acta Materialia, vol. 57, 2009, pp. 326-334.
13. Lee, W.B., Lee, C.Y., Chang, W.S., Yeon Y.M., Jung S.B., "Microstructural Investigation of Friction Stir Welded Pure Titanium," Material Letters, vol. 59(26), 2005, pp. 3315-3318.
14. Reynolds, A.P., Hood, E., Tang, W., "Texture in Friction Stir Welds of Timetal 21S", Scripta Materialia, vol. 52(6), 2005, pp. 491-494.
15. Liu, H., Zhou, L., Huang, Y., Liu, Q., "Study of the Key Issues of Friction Stir Welding of Titanium Alloy", Materials Science Forum, vols. 638-642, 2010, pp. 1185-1190.
16. 20. Li, Y., Murr, L.E., McClure, J.C., "Flow Visualization and Residual Microstructures Associated with the Friction-Stir Welding of 2024 Aluminum to 6061 Aluminum", Materials Science and Engineering A, vol. 271, 1999, pp. 2213-2223.
17. Lee, W.B., Yeon, Y.M., Jung, S.B., "The Joint Properties of Dissimilar Formed Al Alloys by Friction Stir Welding According to the Fixed Location of Materials", Scripta Materialia, vol. 49, 2003, pp. 423-428.
18. Kimapong, K., Watanabe, T., "Friction Stir Welding of Aluminium Alloy to Steel", Welding Journal, vol. 83(10), 2004, pp. 277-282.
19. Somasekharan, A.C., Murr, L.E., "Characterization of Complex, Solid-State Flow and Mixing in the Friction-Stir Welding (FSW) of Aluminum Alloy 6061-T6 to Magnesium Alloy AZ91D Using Color Metallography", Journal of Material Science, vol. 41(16), 2006, pp. 5365-5370.
20. Rhodes, C.G., Mahoney, M.W., Bingel, W.H., Spurling, R.A., Bampton, C.C., (1997), "Effects of Friction Stir Welding on Microstructure of 7075 Aluminum", Scripta Materialia 36(1), pp. 69-75.
21. Mahoney, W.M., Rhodes, C.G., Flintoff, J.G., Spurling, R.A., Bingel, W.H., (1998), "Properties of Friction-Stir-Welded 7075 T651 Aluminum", Metallurgical and Materials Transactions 29A, pp. 1955-1964.
22. Mishra, R.S., Mahoney, M.W., McFadden, S.X., Mara, N.A., Mukherjee, A.K., "High Strain Rate Superplasticity in a Friction Stir Processed 7075 Al Alloy", Scripta Materialia, vol. 42(2), 2000, pp. 163-168.
23. Mishra, R.S., "Processing Commercial Aluminum Alloys for High Strain Rate Superplasticity", Journal of Materials, vol. 53(3), 2001, pp. 23-30.
24. Charit, I., Mishra, R.S., "High Strain Rate Superplasticity in a Commercial 2024 Al Alloy via Friction Stir Processing", Materials Science and Engineering A, vol. 359, 2003, pp. 290-296.
25. Jana, S., Mishra, R.S., Chou, H.N., Herling, D., "Friction Stir Microstructural Modification of Investment Cast F357", Friction Stir Welding, Proceedings of the 136th TMS Annual Meeting and Exhibition, Orlando, FL, 25th Feb. – 01st Mar. 2007, pp. 439-448.
26. Mohan, S., Mishra, R.J., "Friction Stir Microforming of Superplastic Alloys", Microsystem Technologies, vol. 11, 2005, pp. 226-229.
27. Balasubramanian, N., Mishra, R.S., Krishnamurthy, K., "Process Forces during Friction Stir Channeling in an Aluminum Alloy", Journal of Materials Processing Technology, vol. 211(2), 2011, pp. 305-311.
28. Abu-Farha, F., "A Preliminary Study on the Feasibility of Friction Stir Back Extrusion", Scripta Materialia, 2012, vol. vol. 66, no. 9, pp. 615-618.
29. Abu-Farha, F., "Spiral Friction Stir Processing (SFSP) for the Extrusion of Lightweight Alloy Tubes", Proceedings of the 07th International Manufacturing Science and Engineering Conference MSEC 2012, Notre Dame, IN, 04th - 08th June 2012, Paper No. MSEC2012-7358.

Magnesium Technology 2014
Edited by: Martyn Alderman, Michele V. Manuel, Norbert Hort, and Neale R. Neelameggham
TMS (The Minerals, Metals & Materials Society), 2014

IMPURITY DIFFUSION COEFFICIENTS OF Al AND Zn IN Mg DETERMINED FROM SOLID-TO-SOLID DIFFUSION COUPLES

Catherine Kammerer[1], Nagraj Kulkarni[2], Robert Warmack[2], Kelly Perry[2]
Irina Belova[3], Graeme Murch[3], Yongho Sohn[1]

[1]University of Central Florida, Advanced Materials Processing and Analysis Center
Department of Materials Science and Engineering, Orlando, FL, 32816, USA
[2]Oak Ridge National Laboratory, Measurement Science & Systems Engineering Division
Oak Ridge, TN, 37831, USA
[3]The University of Newcastle, Center for Mass and Thermal Transport in Engineering Materials
School of Engineering, Callaghan, NSW 2308, Australia

Keywords: Magnesium, Aluminum, Zinc Interdiffusion, Impurity Diffusion, Hall Method

Abstract

Increasing use and development of lightweight Mg-alloys have led to the desire for more fundamental research in and understanding of Mg-based systems. As property enhancing components, Al and Zn are two of the most important and common alloying elements for Mg-alloys. We have investigated the concentration dependent interdiffusion of Al and Zn in Mg using diffusion couples of pure polycrystalline Mg mated to Mg solid solutions containing either <9 at.% Al or <3 at.% Zn. Concentration profiles were determined by electron micro-probe microanalysis of the diffusion zone. The interdiffusion coefficients were determined by the classical Boltzmann-Matano method within the Mg solid solution. As the concentration of Al or Zn approaches the dilute ends, we employ an analytical approach based on the Hall method to estimate the impurity diffusion coefficients. Results of Al and Zn impurity diffusion in Mg are reported and compared to published impurity diffusion coefficients typically determined by thin film techniques.

Introduction

Integration of wrought magnesium alloys into automotive applications is intended to improve fuel-efficiency and thereby reduce emissions. While magnesium is abundant and lightweight, its poor cold forming properties and low ductility, limited high-temperature properties, and poor corrosion resistance have mandated alloy development and thus fundamental research [1-5]. Two of the most common alloying elements in magnesium alloys are aluminum and zinc. Aluminum (FCC) and zinc (HCP) are relatively soluble in magnesium (HCP), but their solubility decreases at low temperatures. Aluminum additions yield alloys with a good balance between strength and ductility and are age hardenable with the precipitation of $Mg_{17}Al_{12}$. Similarly, zinc is added, often times with aluminum, to magnesium in order to improve room temperature properties and corrosion resistance. Magnesium alloyed with zinc can be heat treated to form MgZn precipitates. Diffusion plays a key role in the kinetics of many microstructural changes that occur during processing of magnesium alloys. Therefore, in this study, we examined the impurity diffusion of Al and Zn using solid-to-solid diffusion couples. Concentration profiles were determined by electron micro-probe microanalysis of the diffusion zone. The interdiffusion coefficients were determined by the classical Boltzmann-Matano method within the Mg solid solution. However, the Boltzmann-Matano method has a large margin of error for infinitely dilute compositions thus an analytical approach based on the Hall method is used to estimate the impurity diffusion coefficients.

Experimental Procedure

The magnesium alloys, Mg-9wt.%Al (MA9) and Mg-6wt.%Zn (MZ6) were produced by Magnesium Elektron, North America. The pure Mg (Polycrystalline, 99.9%) was commercially procured from Alfa Aesar. The alloys were direct chill cast, homogenized, and then warm extruded. All material was subjected to a grain-growth anneal roughly 40 - 50°C below solidus for 8 – 16 hours. The grain size was determined be between 100 – 500μm. The material was then sectioned into 3 – 4 mm thick discs. The disc specimens were polished to a 1 μm surface finish using a non-oxidizing lubricant. The diffusion couples, Mg vs. MA9 and Mg vs. MZ6, were then assembled with 2 mm-thick Al_2O_3 spacers in stainless steel jigs as shown in Figure 1.

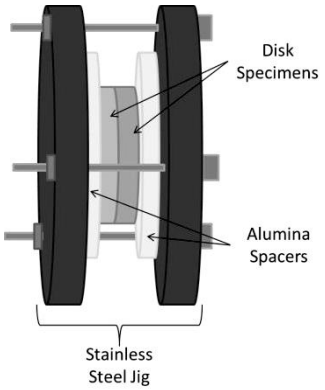


Figure 1: Schematic representation of a solid-to-solid diffusion couple assembly.

The jig assemblies were encapsulated individually in quartz capsules, flushed with argon and hydrogen, and then evacuated to 10^{-6} Torr. The encapsulated assemblies were placed in a Paragon Bluebird™ furnace that was preheated to the annealing temperature. The temperature of the diffusion couples was monitored with an independent resistance temperature detector probe with an Omega™ data acquisition system. Diffusion anneal times and temperatures are presented in Table 1. After the annealing cycle the capsules were quickly removed from the furnace and quenched in water. The couple was extracted from the jig and mounted in epoxy. Once cured, the couple was cross-sectioned and metallographically prepared down to 1μm finish, again using a non-oxidizing lubricant. Each diffusion couple was examined using optical microscopy first to check the diffusion bond integrity, then using Scanning Electron Microscope equipped with an X-ray Energy Dispersive Spectrometer (Zeiss Ultra 55 SEM with EDS) to quantify the thickness of the interdiffusion zone (IZ). Further studies carried out also employed electron probe microanalysis (EPMA) (JEOL JXA-8200) for the determination of concentration profiles. Each couple was interrogated by the EPMA. Fitted concentration profiles were extracted from the EPMA data using either a cubic smoothing spline or a Savitzky-Golay smoothing function. The fitted profiles were then used in the determination of composition-dependent interdiffusion coefficients in Mg(Al)- and Mg(Zn)-solid solutions, calculated based on the Boltzmann-Matano analysis. The fitted profiles were also used in the determination of the impurity diffusion coefficients for Al and Zn in Mg, calculated based on the Hall analysis. The activation energies and the pre-exponential factors for the composition-independent average effective interdiffusion coefficient and impurity diffusion coefficient were also calculated.

Table I. Diffusion anneal parameters.

Couple	Temperature (°C)	Time (hrs)
Mg-MA9	623	96
	673	17
	723	24
Mg-MZ6	623	48
	673	8
	723	24

Calculation of Interdiffusion Coefficients

Composition-dependent interdiffusion cofficient, $\widetilde{D}$, can be determined from concentration profiles using Fick's First Law expressed as:

$$\tilde{J} = -\widetilde{D}_{\iota}\frac{\partial c_i}{\partial x} \tag{1}$$

using the Boltzmann-Matano method. The first step is to find the Matano plane. The Matano plane is the graphically determined position in the concentration profile where there is a mass balance such that:

$$\int_{C_i^{\pm\infty}}^{C_i^o} x dC_i + \int_{C_i^o}^{C_i^{-\infty}} x dC_i = 0 \tag{2}$$

where $C_i^{\pm\infty}$refers to the composition at the terminal ends of the diffusion couple, and C_i^o refers to the composition at the Matano plane [6]. The interdiffusion flux, $\tilde{J}_i$ was calculated using:

$$\tilde{J}_i = \frac{1}{2t}\int_{C_i^{\pm\infty}}^{C_i}(x - x_o)dC_i \tag{3}$$

where x_o is the location of the Matano plane. The interdiffusion coefficient, $\widetilde{D}_i$ was calculated by combining Eqs. (1) and (3) to yield:

$$\widetilde{D}_i = \frac{\frac{1}{2t}\int_{C_i^{\pm\infty}}^{C_i}(x - x_o)dC_i}{\frac{\partial C_i}{\partial x}} \tag{4}$$

Calculation of Impurity Diffusion Coefficients

The Boltzmann-Matano method can be unreliable at the compositional extremes of the profile, because the concentration gradient is difficult to determine as the composition approaches that of the terminal end. The Hall Method puts the concentration gradient in terms of a Gaussian probability distribution, thus

permitting a more accurate determination of the interdiffusion coefficient at impurity levels. Using probability theory, Hall proposed that, since time is constant for a given experiment, a probability plot of the concentration distribution will yield a straight line whose slope and intercepts can be used to solve the concentration-dependent diffusion coefficient [7-8]. C/C_∞ is a probability and thus written in terms of the cumulative standard normal density function or $C/C_\infty = ½ + ½ \text{ erf } u$ in which $u = h\eta + k$ where h is the slope and k is the intercept of the straight line plot, and η is the Boltzmann variable, $x/2(t^{1/2})$. Thus, the diffusion equation can be rewritten in terms of h, k, and u such that:

$$D = \frac{1}{h^2} + \frac{k\sqrt{\pi}}{h^2}(1 + \text{erf}\, u)\exp(u^2) \qquad (5)$$

Calculation of Activation Energy for Diffusion

Solid-state diffusion is strongly dependent on temperature, and diffusion coefficients increase with increasing temperature. The temperature dependence of diffusion coefficients, in general, fits an Arrhenius model: a generalized relation between the interdiffusion coefficient and temperature.

$$\widetilde{D} = \widetilde{D_o} exp\left[-\frac{\widetilde{Q_D}}{RT}\right] \qquad (6)$$

$\widetilde{D_o}$ is the pre-exponential factor and $\tilde{Q}_D$ is the activation energy for interdiffusion. Temperature is the absolute temperature and R is the gas constant.

Results and Discussion

A typical measured solute concentration data and fitted concentration profile from diffusion couple Mg vs. MA9 annealed at 450°C for 24 hours is shown in Figure 2. The open circles represent EPMA data points while the solid line is the fitted concentration profile. It is evident in this representative profile the asymptotic regions do not mirror each other thus indicating a concentration dependence on the diffusivity.

From the fitted concentration profiles, the Boltzmann-Matano method was applied to determine the interdiffusion coefficient. Similarly, the interdiffusion coefficient was calculated for the dilute regime via the Hall analytical method. The interdiffusion coefficient as a function of composition for Al and Zn in Mg(ss) is presented in Figures 3 and 4, respectively. The interdiffusion coefficients on the left hand side of the dotted divisor has been calculated using the Hall method while those on the right hand side were determined from the Boltzmann-Matano approach, as indicated.

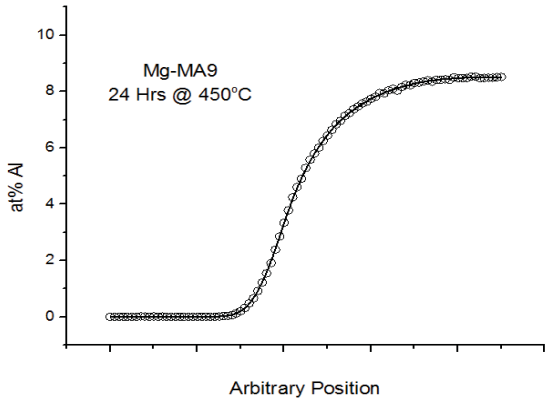


Figure 2: EPMA data and fitted concentration profile for the Mg-MA9 couple annealed for 24 hours at 450°C.

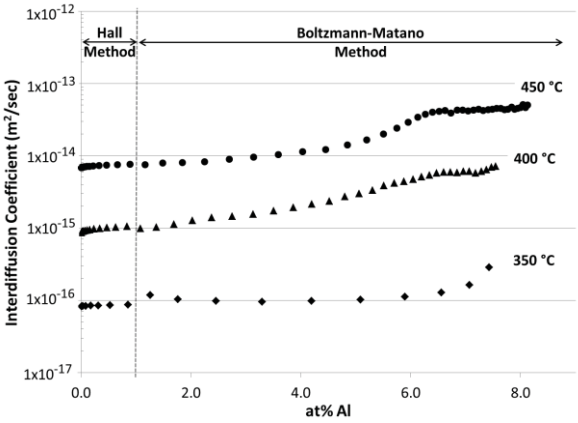


Figure 3: Interdiffusion coefficient as a function of Al in the Mg solid solution. The demarcation at 1 at.% Al separates the analysis based on the Hall method and that based on the Boltzmann-Matano method.

The profile trends upward from left to right; this positive trend becomes more evident as the temperature increases. Since the addition of Al decreases the melting point of the Mg(ss), interdiffusion coefficients would be expected to increase with an increasing Al content. At the lowest temperature, the interdiffusion appears to be independent of concentration, remaining virtually constant throughout the examined compositional range. There is good agreement within the data for the two analysis methods.

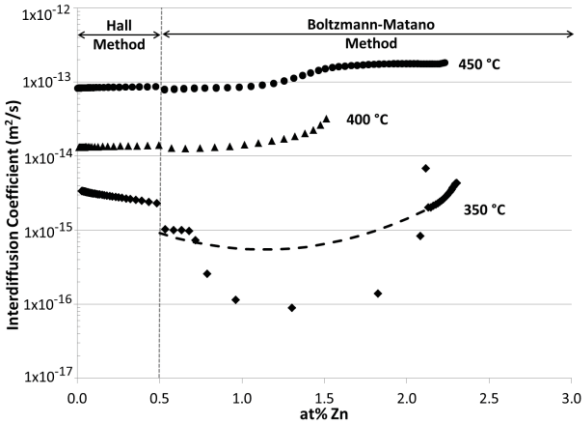


Figure 4: Interdiffusion coefficients as a function of Zn in the Mg solid solution. The vertical marker at 0.5 at.% Zn delineates the analysis based on the Hall method and that based on the Boltzmann-Matano method.

Compared to the Al, the interdiffusion in the Mg(ss) of the Mg-Zn system is relatively unchanged over the composition range investigated. At the lowest temperature, the interdiffusion zone was very narrow and reliable compositional profiles were difficult to extract. Nonetheless, the Hall analytical method yields consistent data which can be used for the most dilute of alloys.

Using the Hall diffusion coefficient at the infinitely dilute composition, the activation energy and pre-exponential factor of the impurity diffusion can be determined. The pre-exponential factor and activation energy for Al impurity diffusion in Mg is 1.61×10^{-4} m^2/sec and 144.1 kJ/mol, respectively. For Zn in Mg, the impurity diffusion pre-exponential factor and activation energy is 1.03×10^{-5} m^2/sec and 109.8 kJ/mol. Figure 5 presents the impurity diffusion coefficients determined in this study with those determine in other studies. Čermák used isotopic tracer techniques to determine the Zn impurity diffusivity [9]. Brennan ascertained the Al impurity diffusion coefficients through thin film depth profiling procedures [10]. Ganeshan calculated the impurity diffusion coefficients using first-principles calculations [11].

As can be seen in Figure 5, the Zn impurity diffusion is consistent with Čermák's findings. The congruency in results between the isotopic tracer diffusion coefficient and the impurity diffusion coefficient lends credence to the analytical method presented herein. Because it is monoisotipic, little data is available for Al impurity diffusion. Brennan's work, while ground-breaking, acknowledged that the refined microstructure and depth profiling methodology employed resulted in a broadening of the diffusion profile which led to somewhat inflated diffusion coefficients [10]. Thus, as expected, the Al impurity diffusion coefficients established in this study are slightly lower than previously published.

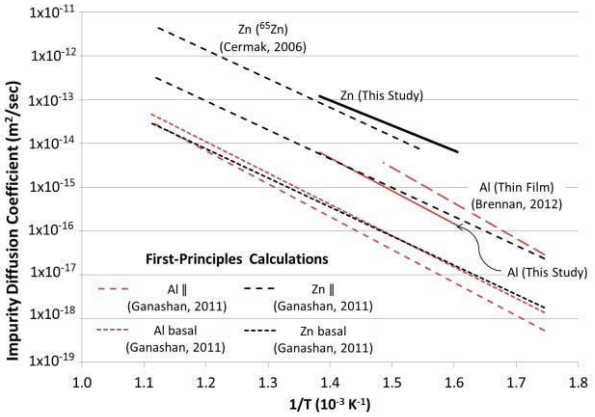


Figure 5: Comparison of Al and Zn impurity diffusion coefficients in Mg calculated by different methods.

Figure 6 presents the impurity diffusion coefficients determined in this study alongside those of other elements. As is customary, tracer diffusion studies where performed in the determination of Mg self-diffusion coefficients and impurity diffusion coefficients for In and Fe. [12] The impurity diffusion coefficients for Ce and La were analytically determined by assuming the diffusivity to be constant and measuring the rate of precipitate dissolution. [13] Because Al in monoisotopic, In has been used as a substitute for Al in diffusion studies. The primary reason for this substitution is that In diffuses in Al at the same rate as Al self-diffusion [14]. However, examination of Figure 6 provides some indication that In impurities diffuses faster than Al impurities in Mg, in particular at lower temperatures. The kinetic behavior of Be impurities, on the other hand, appears to be similar to that of Al impurities in Mg. Further consideration of Figure 6 reveals Zn impurity diffusion to be faster than Mg self-diffusion which, in turn, is faster than the Al impurity diffusion.

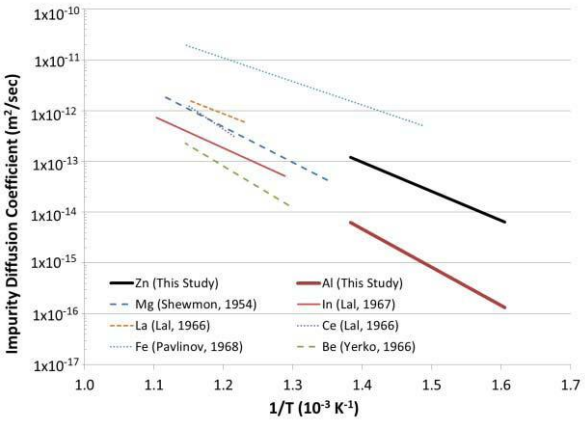


Figure 6: Comparison of Al and Zn impurity diffusion coefficients determined in this study with impurity diffusion coefficients for other elements in Mg.

Conclusions

Diffusion in the Mg rich solid solution region of the Mg-Al and Mg-Zn binary systems was investigated from 350 °C to 450 °C. Through this study, the Hall analytical method has been shown to be an effective and reliable method for acquiring impurity diffusion data from solid-to-solid interdiffusion couples. The pre-exponential factor and activation energy for Al impurity diffusion in Mg is 1.61×10^{-4} m^2/sec and 144.1 kJ/mol, respectively. For Zn in Mg, the impurity diffusion pre-exponential factor and activation energy is 1.03×10^{-5} m^2/sec and 109.8 kJ/mol. Zn migrates faster than Mg self-diffusion, while Al diffuses slower than Mg self-diffusion.

Acknowledgement

This research was sponsored by the U.S. Department of Energy, Assistant Secretary for Energy Efficiency and Renewable Energy, Office of Vehicle Technologies, as part of the Lightweight Materials Program.

This manuscript has been authored by UT-Battelle, LLC, under Contract No. DE-AC05-00OR22725 with the U.S. Department of Energy. The United States Government retains and the publisher, by accepting the article for publication, acknowledges that the United States Government retains a non-exclusive, paid-up, irrevocable, world-wide license to publish or reproduce the published form of this manuscript, or allow others to do so, for United States Government purposes.

References

[1] B.L. Mordike, T. Ebert, "Magnesium: Properties-applications-potential," *Materials Science and Engineering A*, 302, 2001, 37-45.

[2] A. Luo, "Magnesium: Current and Potential Automotive Applications," *Journal of Materials*, 54, 2002, 42-48.

[3] M.K. Kulekci, "Magnesium and its alloys applications in automotive industry," *International Journal of Advanced Manufacturing Technology*, 39, 2008, 851–865.

[4] R. Urbance, F. Field, R. Kirchain, R. Roth, J. Clark, "Market Model Simulation: The Impact of Increased Automotive Interest in Magnesium," *Journal of Materials*, 54, 2002, 25-33.

[5] A.K. Mondal, D. Fechner, S. Kumar, H. Dieringa, P. Maier, K.U. Kainer, "Interrupted creep behavior of Mg alloys developed for powertrain applications," *Materials Science and Engineering A*, 527, 2010, 2289-2296.

[6] C. Matano, Jrn. J. Phys., (1933), Vol. 8, pp. 109

[7] L. Hall, "An Analytical Method of Calculating Variable Diffusion Coefficients," *Journal of Chemical Physics*, 21, 1953, 87-89.

[8] N. Sarafianos, "An Analytical Method of Calculating Variable Diffusion Coefficients," *Journal of Materials Science*, 21, 1983, 2283-2288.

[9] J. Čermák, I. Stoukal, "Diffusion of ^{65}Zn in Mg and in Mg-xAl solid solutions," *Phys. Stat. Sol.*, 203, 2006, 2386-2392.

[10] S. Brennan, A.P. Warren, K.R. Coffey, N. Kulkarni, P. Todd, M. Kilmov, Y.H. Sohn, "Aluminum Impurity Diffusion in Magnesium," *Journal of Phase Equilibria and Diffusion*, 33, 2012, 1547-7037.

[11] S. Ganeshan, L.G. Hector Jr., Z.K. Liu, "First-Principles calculations of impurity diffusion coefficients in dilute Mg alloys using the 8-frequency model," *Acta Materialia*, 59, 2011, 3214-3228.

[12] L.V. Pavlinov, A.M. Gladyshev, V.N. Bykov, *Phys. Met. Metallogr*, 26, 1968,

[13] K. Lal, Diffusion of Some Elements in Magnesium, CEA Report, 1967, R 3136, p 54

[14] M. Eggersmann, H. Mehrer, "Diffusion in intermetallic phases of the Fe-Al system," *Philosophical Magazine A*, 80:5, 2000, 1219-1244.

Magnesium Technology 2014
Edited by: Martyn Alderman, Michele V. Manuel, Norbert Hort, and Neale R. Neelameggham
TMS (The Minerals, Metals & Materials Society), 2014

MICROSTRUCTURE EVOLUTION AND MECHANICAL BEHAVIOR OF Mg-10Gd-3Y-0.4Zr ALLOY PROCESSED BY ECAP AT HIGH TEMPERATURE

Yinpeng Zhou[1], Dejiang Li[1,*], Xiaoqin Zeng[1,2], Yujuan Wu[1,*], Wenjiang Ding[1,2]
[1] National Engineering Research Center of Light Alloy Net Forming, Shanghai Jiao Tong University, 800 Dongchuan Road, Shanghai 200240, PR China
[2] The State Key Laboratory of Metal Matrix Composites, Shanghai Jiao Tong University, 800 Dongchuan Road, Shanghai 200240, PR China

Keywords: Mg-Gd-Y-Zr alloys, ECAP, Grain refinement, Texture, Hall-Petch relationship

Abstract

Microstructure evolution, texture development and their influence on mechanical properties of Mg-10Gd-3Y-0.4Zr (wt.%) alloy processed by equal channel angular press (ECAP) at 450 ℃ were studied. The samples were prepared by ECAP from one to four passes. The results show that recrystallization preferentially occurred near the grain boundary, and the percentage of high-angle grain boundaries increases with the increase of passes. After four passes, the microstructure is still inhomogeneous, the fine and coarse grain zones exist simultaneously. It is attributed to the higher extrusion temperature; the grain grows and aggregates easily, which is confirmed through comparative experiment. The strength increases obviously after one pass, unexpectedly, it reduces slightly after two passes, the elongation is dramatically increased from 6.7% to 20.3%, which is due to the <0001> basal plane rotation from ED to the direction of flow strain and formation of a typical shear texture. The change of elongation and mechanical properties of this alloy during ECAP was discussed in terms of texture and the effect of the fine grain.

Introduction

Magnesium (Mg) alloys are attractive engineering materials for application in a wide range of aerospace, automotive and other applications due to their low density and high specific strength [1-2]. However, the usage of Mg alloys is not as extensive as expected because Mg has a hexagonal crystal structure and often exhibits poor ductility, relative low strength, poor high temperature performance and week creep resistance [3]. Grain refining is an effective procedure to improve mechanical properties and ductility; recently, considerable attention has been focused on the process of metals through severe plastic deformation (SPD) [4]. Equal channel angular pressing (ECAP) is a promising severe plastic deformation to refine bulk material. Several research groups have achieved some interesting results concerning improvement of mechanical properties of Mg alloys by means of ECAP [5-7].

Over the last decade, the mechanical properties of Mg alloys were improved through grain refining and texture modification by ECAP, which becomes one of the active research trends [8-10]. However, most of the researches have much concerned ECAP for conventional Mg alloys, less for Mg-RE system [11-12]. Mg-RE alloys exhibit a higher strength compared with conventional Mg alloys due to solution and aging strengthening. Among them, the Mg-Gd-Y system is one of the candidates for novel Mg-based light harden able alloy having a high creep resistance at high temperatures, However, this alloy lacks sufficient strength and ductility at room temperature for industrial applications.

In this investigation, the ECAP was applied to optimize the mechanical properties of an Mg-10Gd-3Y-0.4Zr (wt.%) alloy; the relationships between the evolution of microstructure, texture and mechanical properties of this alloy during ECAP were studied.

Experiments

The alloy used in this study was Mg-10Gd-3Y-0.4Zr (wt%) alloy, the billets of the alloy were processed by extrusion with a extrusion ratio of 15:1, then this alloy was solution-treated at 520 ℃ for 2 h, and immediately quenched in water and machined into rods for ECAP experiment. The extrusion specimens were cuboids with a length of 12 mm, a width of 12 mm and a height of 90 mm. The extrusion route was B_c, which rotation angle of clockwise 90° along its longitudinal axis between adjacent passes for the billets, and the die channel angle was 90°. The alloy was preheated to 450 ℃ and the die was preheated to 400 ℃ before ECAP process in order to prevent crack formation. The specimens were pressed with a speed of 3 mm/s from 1 pass to 4 passes at about 450 ℃. Moreover, in order to study the gain growth of this ECAP-ed alloy during the insulation stage, a contrast experiment was conducted in this study, and the specimens after ECAP were annealed at 450 ℃ for 10 minutes in insulation material.

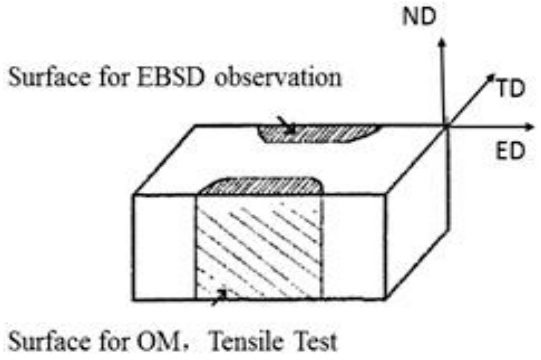


Fig.1 Schematic illustration of ECAP processing material

* Corresponding Author Email Address: lidejiang@sjtu.edu.cn
* Corresponding Author Email Address: wuyj@sjtu.edu.cn

Specimens were cut from the longitude of the ECAP-ed material to examine the microstructure, texture, mechanical properties (ED in Fig. 1), microstructural analyses were conducted using optical microscopy (OM), and the specimens were cut parallel to the ED, as shown in Fig. 1, then, etched in a solution of 5 g picric acid +5 g acetic acid +100 ml ethyl alcohol for 20 s. The texture of this alloy was checked by electron–backscatter diffraction (EBSD) technique. Macroscopic polar diagram of the samples was measured by an X-ray diffraction (Philip X'pert PRD) with Co Ka radiation, operating at 35 KV and 40 MPa. Miniature dog –bone tensile specimens, 12 mm long, 3 mm wide and 2 mm thick, were machined using electron-discharge wire-cut machining along the ED of the ECAP-ed specimens. Tensile tests were carried out at room temperature with a strain rate of 5×10^{-4} s^{-1}.

Results and Discussion

Microstructural characterizations during ECAP

Fig. 2 shows the typical optical microstructures of Mg-10Gd-3Y-0.4Zr alloy before and after ECAP. In the initial state, the alloy was solution-treated at 520 ℃ for 2 h, the grains were very large and roughly equiaxed, and the average grain size was 54 μm. There were no particles distributed in the inner grains and near the grain boundaries, as shown in Fig. 2 (a).

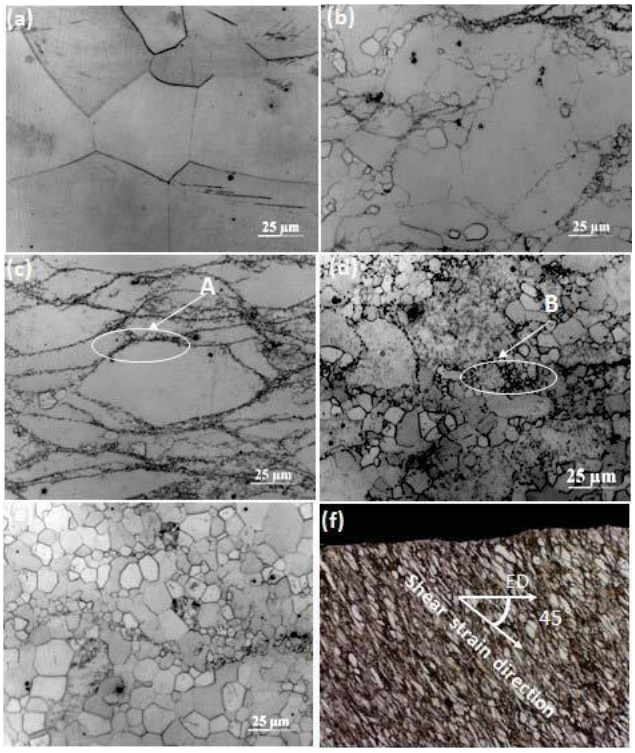


Fig. 2 The typical optical microstructures of Mg-10Gd-3Y-0.4Zr alloy before (a) and after ECAP (b) 1-pass ECAP, (c) 2-passes ECAP, (d) 3-passes ECAP, (e) 4-passes ECAP, (f) shear strain direction

When the samples were subjected to ECAP at 450 ℃ for one pass, the alloy would be sheared at the intersection angle of channel, the flow line was not parallel to the extrusion direction like traditional extrusion, and the inclination angle was approximately 45° compared with the ED, as shown in Fig. 2 (f).

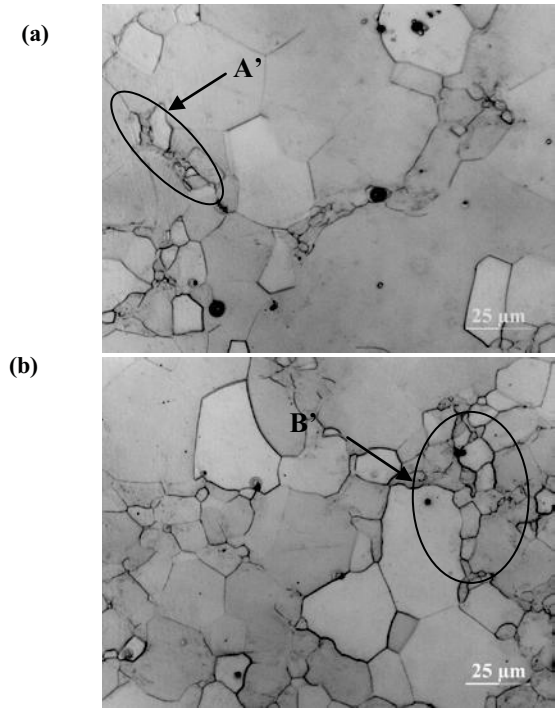


Fig.3 The typical optical microstructures of ECAP-ed Mg-10Gd-3Y-0.4Zr samples, (a) 2- passes ECAP+ annealed at 450℃ for 15 min., (b)3-passes ECAP+ annealed at 450℃ for 15 min..

As shown in Fig. 2 (b), the initial homogeneous grains were roughly elongated and some shear bands can be found in the grains after 1-pass, which were attributed to the introduction of large shear strain. Moreover, the several recrystallization particles were found near grain boundaries. Therefore, the microstructure becomes inhomogeneous after 1-pass, i.e., coarse crystal zone and fine crystal zone. The large average grain size is about 50 μm, the small average grain size is about 5 μm. As shown in Fig.2 (c), the area fraction of fine grain zone increases, many small black particles align along the boundaries of the elongated matrix grains after 2-passes, which are recrystallization grains, indicated by the white arrow in Fig. 2(c). As shown in Fig. 2 (d), it is evident that the number of recrystallization grains increases significantly and the large grain also exists. So, the grains are also inhomogeneous but the fine grains occupied the main part after 3-passes. As shown in Fig. 2 (e), the microstructure becomes more uniform after 4-passes and the number of recrystallization grains increases, compared with the sample after 3-passes. In conclusion, the large grain size of sample can be obviously refined after 4-passes ECAP, compared with the sample before ECAP (Fig.2(a)). The size of large grain was 15 μm. While, the size of fine grain was 5 μm, and the particles tend to be equiaxed. Besides, it is obvious that the size of recrystallization gain is bigger than that of 2-passes ECAP samples, which is attributed to the higher extrusion temperature. The grains tended to grow up easily, this point was proved by the below contrast experiment.

Fig. 3 shows the typical optical microstructures of ECAP-ed Mg-10Gd-3Y-0.4Zr samples annealed at 450℃ for 15 minutes. The two samples were subjected to ECAP for 2-passes and 3-passes, respectively, then annealed at 450 ℃ for 15 minutes. The fine grain zone marked by 'A' in Fig. 3 (a) was compared with the fine grain zone marked by A in Fig. 2 (c); the fine grain zone marked

by 'B' in Fig.3 (a) was compared with the fine grain zone marked by B in Fig. 2 (c). It was found that the fine grains grew up obviously after annealing at 450 ℃ for 15 minutes.

Fig. 4 shows the average grain size distribution of Mg-10Gd-3Y-0.4Zr alloy before and after ECAP with different passes. With the increase of pressing number, the grain was refined gradually; the average grain size was reduced from 52 μm to 12 μm. It could be explained by the fact that the recrystallization grains tends to grow up obviously at 450 ℃. Therefore, the average grain size is still larger (12 μm) even if the alloy was carried out 4-passes ECAP with severer plastic deformation.

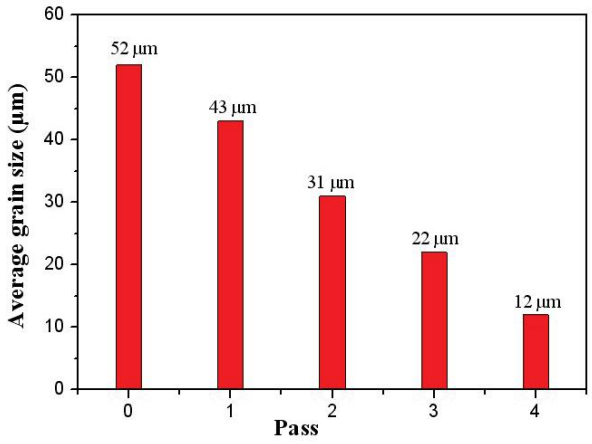
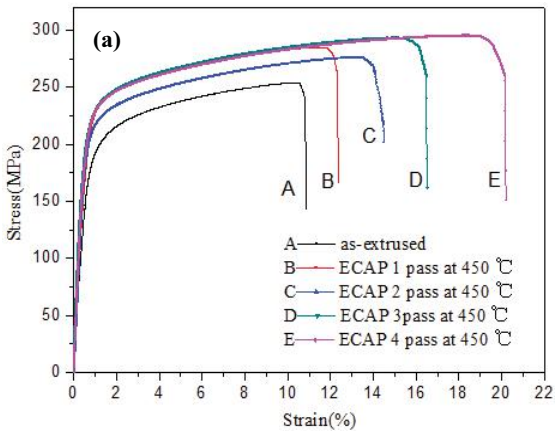


Fig. 4 Average grain size distribution of Mg-10Gd-3Y-0.4Zr alloy before and after ECAP with different passes

Mechanical Properties

The stress-strain curves of the tensile specimens and the yield strength, ultimate tensile strength and elongation were shown in Fig. 5. It was found that ductility was enhanced significantly after ECAP compared with the as-received material, as shown in Fig. 5 (a). While, the strength was not enhanced gradually with the increase of pressing pass number like the elongation, the strength increased obviously after 1-pass ECAP, but reduced after 2-passes ECAP and increased after 3-passes, as shown in Fig. 5 (b), yield strength of the solution-treated alloy increased from 176 to 211 MPa after 1-pass EACP, then reduced with increasing pass, for example, it reduced to 206 MPa slightly for 2-passes. For the ultimate strength, it increases firstly from 258 to 286 MPa for 1-ass ECAP, then reduces to 276 MPa after 2-pass ECAP, and then increases to 293 MPa after 3-passes ECAP. The elongation-to-failure improves gradually with the increase of pass, and improves



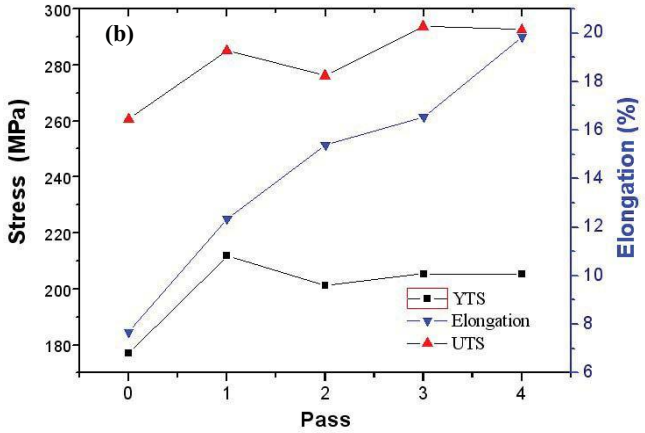


Fig. 5 Tensile stress-strain curves of the Mg-10Gd-3Y-0.4Zr samples before and after ECAP for (a); YSs, UTSs and Els at different material conditions for (b), respectively

from 7.6% to 20.3% from 1-pass to 4-passes, which was improved by approximately 190%.

Evolution of Texture The textures of the Mg alloys processed by ECAP had been investigated preciously[13-14]. There are two points, one is the basal plane in the most of grains will be rearrangeed to the shearing direction and form a typical shear texture; the other point is the strong <0001> fiber texture will be weakened and form a random texture. In this study, the macro texture of this alloy were measured by XRD, as shown in Fig.6(a), the relative intensity of <0001> basal plane was calculated and reduced from 0.78 to 0.41, as shown in Fig. 6 (b), which demonstrated the basal plane reinforcement effect would be weakened.

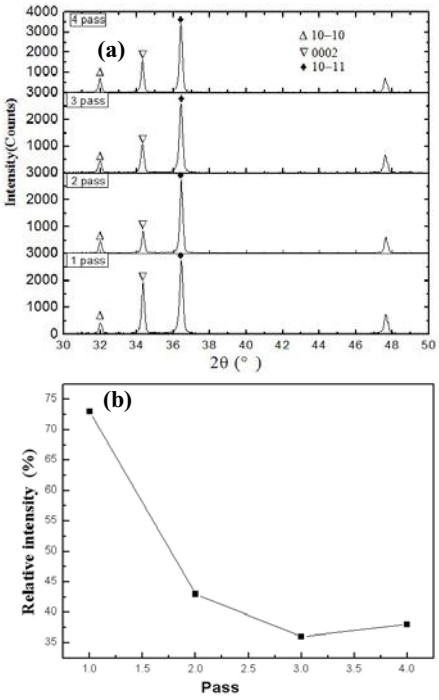


Fig. 6 X-ray diffraction pattern of extruded Mg-10Gd-3Y-0.4Zr alloy for (a); <0002> base surface relative intensity of this alloy processed by ECAP for different passes for (b)

Polo figures of Mg-10Gd-3Y-0.4Zr alloy were obtained by EBSD, the reflecting surface contains the transvere direction (TD) and normal direction (ND), as shown in Fig. 7. Peak position distributed near the circle, which showed a <0001> fiber-typle character with the basal plane was approximately parallel to the extrusion direction and was about 8° compared the extrusion direction. While, after four passes, the peak position in the basal pole density changed and concentrately locates with an angle of 50° to the direction. It means that the basal plane in the majority of grains is rearranged to the shearing strain direction. The result is consistent with that of Liu etc [15]. The orientation is more favoriable for the activation of base slip system under tensile test than the strong orientation of <0001> basal plane texture.

In fact, the mechanical properties of the present Mg-10Gd-3Y-0.4Zr alloy are directly connected to their microstructure(such as grain size, homogeneity of structure) and textures, their effects on mechanical properties will be disscussed as follows. In several investigations, it was found that ECAP has the capability to improve both the strength and elongation in some Mg alloys by refineing the grain size and modifying textures. In this study, a simultaneous improvement of tensile strength and elongation was obtained.

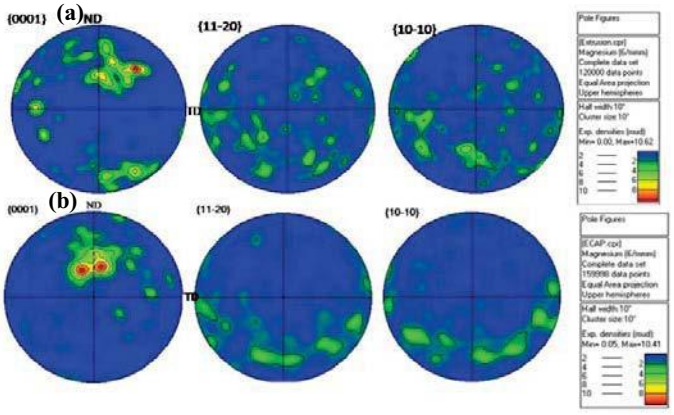


Fig. 7 Pole figures of Mg-10Gd-3Y-0.4Zr alloy for (a) as-received (b) 4-pass-ECAPed

As the pass number of pressing increases, the flow stress increases, the improved strength and elongation during ECAP are related to the grain refinement, but it cannot explain the fact that the 2-passes ECAP sample shows the minimum yield strength (201 MPa) and ultimate strength (276 MPa) among the samples after four different passes, which is attributed to the grain refinement and the modification of texture. The relative peak intensity of the <0001> base plane was less than the one-pass ECAP, the basal plane texture strengthening effect was weakened, which may result the reduction of the yield strength. The basal plane of the majority of grains would be rearranged to the shearing direction gradually with the accumulation of strain. This results the grains in the 2-passs ECAP sample were in a more favorable orientation to coordinate the imposed strain and prone to yield easily. In addition to the grain refinement and the texture modification, another factor, which may influence the ductility of the ECAPed material, is the microstructural homogeneity. The microstructure of 2-passes ECAP samples was more inhomogeneous than the sample after 1-pass, the large grains were elongated and occupied the main part, most of grain boundaries were low angle grain boundaries, the grain size was very uneven. It cannot coordinate deformation between different grains during ECAP, which leads to strain concentration and micro cracks generates at grain boundaries and merges under the condition of stress concentration, which may results in the reduction of strength. Grain refinement will improve mechanical properties and elongation, while the texture soften effect will enhance the elongation but reduce the yield strength, the softening effect by unusual texture overwhelmed the strengthening effect by grain refinement. Thus, the sample of 2-passed-samples has a higher elongation and lower strength.

In this study, the yield strength was not improved gradually despite the effective grain refinement caused by ECAP, it was obvious that the relationship between the yield strength and $d^{1/2}$ was not consist with the standard single-line Hall-Petch relationship, as shown in Fig.8 (c), sometimes, the yield strength reduced with the reduction of $d^{1/2}$. This demonstrated that the yield strength of samples processed by ECAP was controlled by both the grain size and texture, the effect of grain refinement and texture modification caused by ECAP on the yield strength was opposite, influenced by the factor of material, temperature, and pass number, the strengthening effect of grain effect will be weaker or Stronger than the soften effect of texture modification in different stages; the combined effect of them may be positive or negative. Another character of the samples processed by ECAP is their ductility, improved significantly compared with the traditional extrusion. Different from the strength properties, both the grain refinement and texture modification are beneficial to the enhancement of the ductility. With the increase of pressing pass number, the ductility was enhanced gradually. The enhancement of ductility can be attributed to grain refinement and the modification of texture with the rearrangement of basal plane. Primary slip occurs on the <0001> basal planes in magnesium alloys at RT due to their low critical resolved shear stress preferentially compared with those of the non-basal slip systems on prismatic and pyramidal planes[16]. For the extruded magnesium alloys, the basal plane tends to parallel to the extrusion direction, which results in it is difficult for the primary slip to occur on the basal plane, thus, the strength would be enhanced and the ductility would reduced. However, the <0001> basal plane will rotate from the ED to the shear strain direction during ECAP process, the Schmid factor on the <0001> basal plane increases, which reduces the critical stress for the material to yield. Even so, the <0001>basal plane provides only two independent systems, far fewer than the necessary five independent systems for homogeneous deformation, according to the Von-Mises criterion [17].

Hehmann etal [18] has found that the alloying additions of Gd and Y were efficient elements in decreasing the c/a ratio. The c/a ratio affects the difference of CRSS between the basal slip and the non-basal slips; the reduction of the c/a ratio is beneficial to the activation of the non-basal slips. In this study, the c/a ratio of the Mg-10Gd-3Y-0.4Zr alloy was measured by X-ray diffraction and was about 1.6167, which is less than that of pure Mg, (1.6244). Therefore, some prismatic and pyramidal may have been activated easily due to a arrangement of approximate 45° from ED to the shear strain direction during the ECAP process.

In addition to the grain refinement and texture modification, the structure homogeneity may also improve the ductility after ECAP. The recrystallization was easy to occur due to the high extrusion temperature, this resulted the low dislocation density in the grains and the presence of equilibrium high-angle grain boundaries (HAGBs), which was beneficial to coordinate the deformation, the appearance of general HAGBs combined with a lower dislocation

was more effective in improving the ductility of this alloy than low angle grain boundaries plus a higher density of dislocations.
Moreover, the macroscopic fracture shape of tensile sample before and after 4-passes ECAP were taken by the camera, it was found that the fracture section was vertical to the extrusion direction before the sample was processed by ECAP, as shown in Fig. 8 (a), due to the <0001> basal plane was in strong direction. While, after 4-pass ECAP, the fracture section was 45° compared with the extrusion direction, as shown in Fig. 8 (b), which was attributed to the basal plane rotate from the extrusion direction to the shear strain direction and was in soft direction, the tensile sample will fracture along this direction. Thus, the fracture behavior can be explained by the modification of the texture and consistence with the change of elongation.

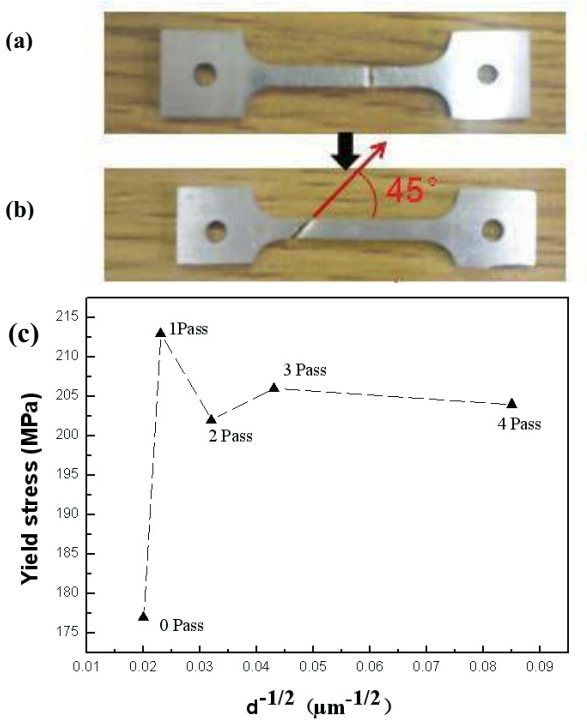


Fig. 8 the macroscopic fracture shape of tensile sample which are processed by ECAP for (a) and processed by ECAP for 4 passes for (b), the Yield stress against $d^{-1/2}$ for the alloys ECAPed for 0,1,2,3, and 4 passes for (c)

Conclusions

In this study, the evolutions of microstructure and texture were studied by OM, XRD and EBSD. The relationship between strength and elongation was discussed in terms of grain refinement, HAGBs and texture. The conclusions can be drawn as follows:

(1) With the increase of pressing numbers, the recrystallization occurred preferentially near the grain boundaries and grew up later, the number of HAGBs increased, after 4 passes; the grains were roughly equiaxed with the average grain size of 12 μm.

(2) The typical shear texture was formed after 4-pass ECAP, the <0001> basal plane rotates from the ED to the shear strain direction, which is probably due to the activation of <c+a> non basal slip.

(3) The simultaneous improvement of tensile strength of elongation was obtained after ECAP except for the 2-pass ECAP sample, which is attributed to the grain refinement and the modification of texture. The 2-pass sample has a lower strength and higher elongation due to the grain boundaries strengthening effect overwhelmed the softening effect of unusual texture.

(4) The macroscopic fracture shape of tensile sample was studied, the angle between the fracture section and the extrusion changed with the arrangement of the <0001> basal plane. The fracture behavior was accordance with the modification of the texture.

Acknowledgements

The financial support through the project (No.51171113 and 50971089) received from the National Natural Science Foundation of China is acknowledged. This work was also supported by China Postdoctoral Science Foundation funded project (No.2012M511089) and Technology Support Project Program of the Ministry of Science and Technology of China (No. 2011BAE22B02 and No.2011DFA50907).

References

[1] B. L. Mordike, T. Ebert. "Magnesium: Properties-applications-potential."*Materials Science and Engineering A*, 302(2001): 37-45.

[2] K. Kubota, M. Mabuchi, K. Higashi. "The Grain Size and Texture Dependence of Tensile Properties in Extruded Mg-9AL-1Zn." *Journal of Materials Science*, 34(1999) :2255-2262.

[3] R. Zhu, Y.J. Wu, J.Q. Liu. "Microstructure and properties of Mg-12Gd-3Y-0.5Zr alloys processed by ECAP ". *Journal of Wuhan University of technology –materials science edition,* 6(2011): 1128-1132.

[4] R.Z. Valiev, T.G. langdon, "Processing of a magnesium alloy by equal-channel angular pressing using a back-pressure." *Materias Science and Engineering A*, 527(2009):205-221.

[5] W.J. Kim, Y.S. Kim, et al. "Mechanical properties and Microstructures of an AZ61 Mg alloy processed by equal channel angular pressing."*Scripta Materialia*, 47（2002）:39-44.

[6] T. Mukai, M. Yamaoni, H. Wantabe, K. Higashi. "Ductility Enhancement in AZ31 Magnesium alloy by Controlling Its Grain Structure ." *Scripta Materialia*, 45(2001) :89-94.

[7] A. Yamashita, Z. Hornito, T.G. Langdon. "Improving the Mechanical Properties of Magnesium and a Magnesium Alloy through Severe Plastic Deformation." *Materials Science and Engineering A*, 300(2001):142-147.

[8] K. Matsubara, Y. Miyahara, Z. Horita, T.G. Langdon "Developing superplasticity in a magnesium alloy through a combination of extrusion and ECAP." *Acta Materialar,* 2003, 51(11):3073-3084.

[9] T. Mukai, M. Yamanoi, H.W. Watanabe, K. Higashi. "Low temperature superplasticity of a fine-grained ZK60 magnesium alloy processed by equal-channel-angular extrusion ." *Scripta Materialar*, 2001,46(12):851-856.

[10] W.J. Kimi, S.L. Hong , Y.S Kim, S.H. Min, H.T. Jeong. "Texture development and its effect on mechanical properties of an AZ61 Mg alloy fabricated by equal channel angular pressing." *Acta Materialar*, 2003, 51(11):3293-3307.

[11] D. Eddahbim, P. Monge, M.A. R. Garces, P. Adeva. "Microstructural characterization of an extruded Mg-Ni-Y-RE alloy processed by equal channel angular extrusion." *Journal of Alloys and Compounds*, 2009,473(1-2):79-86.

[12] G. Sha, J.H. Li, W. Xu, A.K. Xia, W.Q. Jie, S.P. Ringer. "Hardening and microstructural reactions in high-temperature equal-channel angular pressed Mg-Nd-Gd-Zn-Zr alloy", *Materials Science and Engineering A*, 2010,527 (20):5092-5099.

[13] B. Roberto, Figuiredo, Irene J. Beyerlein, Alexander P. Zhiyaev. "Evolution of texture in a magnesium alloy processed by ECAP through dies with different angles ." *Materials Science and Engineering A*, 527(2010):1709-1718.

[14] B. Benoit, S. Satyam, S. Laszlo. " Analysis of texture evolution in magnesium during equal channel angular extrusion." *Acta Materialar* , 58(2008): 200-214

[15] T. Liu, Y.D. Wang, S.D. Wu, etal. "Textures and Mechanical Behavior of Mg-3.3%Li Alloy after ECAP." *Scripta Materilar*, 51(2004):1057-10617 .

[16] T. Obara, H. Yoshinga, S. Morozumi, "{11-22}<1123> slip system in magnesium." *Acta Materialar,* 21 (1973): 845-853.

[17] J. Kioke, T. Kobayashi, T. Makai, H. watanabe, M. Suzuki, "The activity of non-basal slip systems and dynamic recovery at room temperature in fine-grained AZ31B magnesium alloy."*Acta Materialar*, 51(2003): 2055-2065.

[18] F. Hehmann, F. Sommer, B. Predel. "Extension of solid Solubility in Magnesium by Rapid Solidification." *Materials Science and Engineering A*, 125(1990):249-265.

Magnesium Technology 2014
Edited by: Martyn Alderman, Michele V. Manuel, Norbert Hort, and Neale R. Neelameggham
TMS (The Minerals, Metals & Materials Society), 2014

THE USAMP MAGNESIUM FRONT END RESEARCH AND DEVELOPMENT PROJECT – RESULTS OF THE MAGNESIUM "DEMONSTRATION" STRUCTURE

J.H. Forsmark[1], M. Li[1], X. Su[1], D.A. Wagner[1], J. Zindel[1], A.A. Luo[2], J.F. Quinn[2], R. Verma[2], Y.-M. Wang[2], S.D. Logan[3], S. Bilkhu[3], and R.C. McCune[4]
[1]Ford Motor Company, 2101 Village Road, Dearborn, MI 48121
[2]General Motors Company, 30500 Mound Road, Warren, MI 48090
[3]Chrysler Group LLC, 800 Chrysler Drive, Auburn Hills, MI 48326
[4]Robert C. McCune and Associates, LLC, West Bloomfield, MI

Keywords: Magnesium, Corrosion, Fatigue

Abstract

This paper summarizes the final results of the United States Automotive Materials Partnership's (USAMP's) Magnesium Front End Research and Development (MFERD) Phase I and Phase II project focusing on a Demonstration ("Demo") structure consisting of a cast AM60B shock tower, extruded AM30 rail and a warm-formed AZ31 sheet component. The project team designed and fabricated piece parts, assembled, surface finished and tested over 200 "Demo" magnesium front end substructures employing friction-stir linear lap welding (FSLW) and laser-assisted self-pierce rivets (LSPR), both with and without adhesive bonding. The "Demo" structures also employed two different coating strategies to mitigate corrosion. The structures were tested in multi-axial fatigue and overload conditions and the results were compared to simulation. They were also tested using different corrosion testing protocols to determine the corrosion susceptibility of the joint regions and the base metal in a structure containing dissimilar Mg alloys.

Introduction

Vehicle lightweighting is one of the strategies being developed by auto companies to improve the fuel economy of vehicles with conventional gasoline internal combustion engines along with the alternative energy powertrains [1]. Magnesium has emerged as a potential material for lightweighting and has become a focus of research and development in many countries around the world [2-4].

The mission of USAMP is to identify and conduct or direct non-competitive research and development in automotive related materials and material processes. In 2007, the USAMP started a collaborative project, with domestic and international suppliers and research institutions, on Magnesium Front End Research & Development (MFERD), to address the challenges for primary body applications of magnesium [5], with specific attention to the vehicle front end substructure.

In Phase I, the USAMP team selected front end body structures as the development target of the project in order to achieve the maximum benefit of lightweighting in terms of both fuel economy and vehicle performance [6]. A simulation CAE study of these architectures was undertaken to examine some of the performance issues and most of the specifications for vehicle stiffness, durability (fatigue) and crashworthiness were met or were within acceptable limits.

To validate the key enabling technologies developed in the MFERD Phase I project for magnesium applications in automotive body structures, the USAMP team embarked on the Phase II project. The goal of the MFERD Phase II project was to develop, build and test a magnesium "Demonstration" ("Demo") structure relevant to automotive body structure applications [7].

Magnesium Front End "Demo" Design

The "Demo" structure was designed with the following requirements:

- Materials: Three major readily-available material forms: casting (AM60B), extrusion (AM30), and sheet (AZ31). Additionally, the "Demo" structures for corrosion testing included a galvanized steel plate bolted to the cast shock tower.
- Joining Techniques: Up to two Mg-to-Mg joining techniques and including Mg-to-steel dissimilar metal joining with isolators.
- Coating Solutions: Up to two pre-treatments for the Mg parts and up to two top coating solutions for the "Demo" structures.
- Analysis and Testing: The "Demo" structure would be analyzed using FEA simulation and tested for stiffness, fatigue life, overload capacity, and corrosion.

Cosma Engineering (Troy, MI) was selected as the general contractor to manage the final design and build of the "Demo" structure, including design, logistics, CAE (Computer-Aided Engineering) analysis, development and manufacture of assembly tooling and testing fixtures. After a careful consideration of several design concepts, the USAMP and Cosma team generated the final design, which allowed for easy material substitution, large joining areas, complex enough geometries to determine manufacturing feasibility issues, but simple enough for easy fixturing and loading.

The final design is shown in Figure 1(a). In this design, a cast shock tower of AM60B is attached to an extruded tubular rail made from AM30 and a sheet box structure made from two symmetric AZ31 sheet formed parts. The

fixturing and loading configurations are shown in Figure 1(b).

Magnesium Front End "Demo" Build

The production of the "Demo" structure was a complex process involving the collaboration of most of the project task teams. Components were produced, in some cases surface treated, and then delivered to the joining suppliers for assembly. Many of the assemblies were then delivered to different coating suppliers for final coating before all of the assemblies were delivered to the testing facilities. All of these steps involved a certain degree of development.

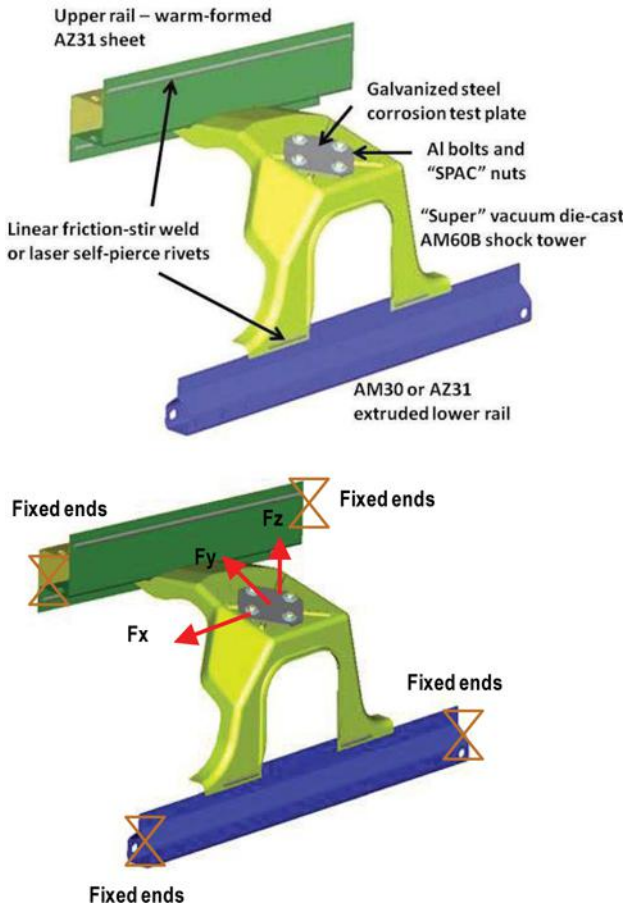


Figure 1. (a) Schematic diagram of the magnesium-intensive front-end "Demo" structure and (b) loading conditions and fixturing of the structure for durability testing.

Component Development

The cast shock tower (Figure 2(a).) used for this project was actually produced during the MFERD Phase I study [8]. This component was originally produced in AM60B by Contech LLC (Dowagiac, MI) to determine the feasibility of the super high vacuum die casting process (SVDC) on the casting of Mg components. The SVDC process was originally developed to produce castings that were capable of being heat treated and welded without blistering because entrapped air in the castings could be significantly reduced. An additional benefit was the potential increase in ductility due to the reduction in gas porosity (although shrink porosity is only minimally reduced). In the MFERD Phase I study, casting were produced on a 1600 T conventional cold chamber die cast machine that had been retrofitted with the SVDC casting technology. They were evaluated using x-ray and castings that passed inspection were used in the "Demo" structure.

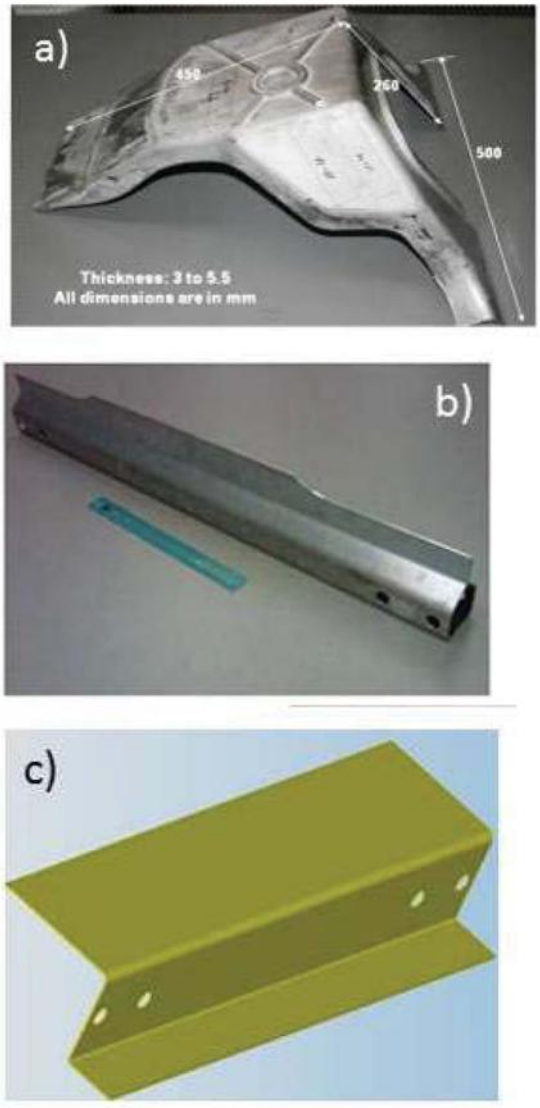


Figure 2. (a) AM60B cast shock tower, (b) AM30 extruded rail, (c) AZ31 warm-formed sheet component.

The extrusion tube structure was produced by Applied Magnesium (Aurora, CO) at their facility in Mexico using an 1800 ton press. The extrusion rail had a nominal wall thickness of approximately 2.5 mm and about 55 AZ31 and 145 AM30 extrusion parts were produced and cut to length.

The parts were final machined and scalloped by Cosma. The final extruded rail is shown in Figure 2(b).

Commercial AZ31B-H24 sheet alloy from Magnesium Elektron N.A. was used to fabricate the sheet parts for the "Demo" structure. The sheet part for the "Demo" structure is a simple part with two right angle bends as seen in Figure 2(c). The two bends have sharp radii, 2.5 mm and 5 mm, so material preheating in a conveyor oven and a heated die were used in stamping both right angle bends in the sheet blank in one stroke at elevated temperature.

The forming trials conducted by Troy Tooling Technologies (Fraser, MI) indicated that a crack- and springback- free part can only be made at 300°C and higher temperatures. A total of 500 sheet parts were fabricated with the 2 mm thick AZ31B-H24 sheet. The forming was carried out without any additional lube, as the metal oxide and any remnant lubricant on the sheet surface were adequate as a parting agent between the sheet and the die. The parts were air cooled and inspected.

Joining and Assembly

The USAMP team selected two joining technologies: friction stir linear (lap) welding (FSLW) and laser-assisted self-pierce rivets (LSPR), the latter both with and without application of structural adhesives. The team also specified and developed aluminum SPAC® (Self Pierce And Clinch) nuts to secure galvanized steel test plates to magnesium cast shock towers for later corrosion evaluation.

Friction Stir Linear Welding (FSLW):

The FSLW process parameters used to produce the test assemblies were developed by GM Research and Development, utilizing a gantry type friction-stir machine [9]. To successfully join the different Mg alloys, the process windows for the three alloy stack ups were first optimized at the coupon level.

The process was further optimized with actual "Demo" components by utilizing a specially designed assembly fixture to clamp the various part stack ups as shown in Figure 3. The fixture has three stations for joining the assemblies. Each station was designed to withstand X, Y and Z forces acting on the various stack ups during FSLW.

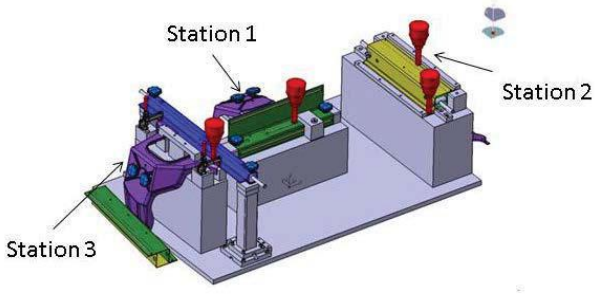


Figure 3. Special fixture for clamping the "Demo" parts for FSLW.

The parts for creating over 100 "Demo" structures were received in batches and a small scale production process with the view of assembling structures with consistent weld quality was developed. The "Demo" structure was manufactured in three discreet operations designed to account for the restrictions encountered with the fixture and the need to use different friction-stir pins for welding different material stacks. The first operation joined the magnesium sheet to the casting (bottom), the second joined magnesium sheet to sheet, and the third joined magnesium casting to extrusion (bottom). A fully assembled "Demo" structure is shown in Figure 4 (a).

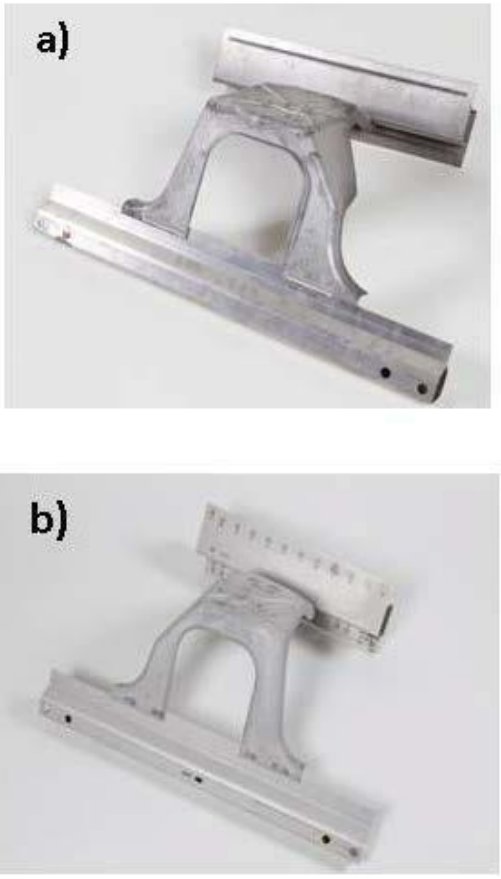


Figure 4. (a) A fully assembled FSLW "Demo" structure and (b) LSPR structure.

Laser Assisted Self-Piercing Riveting (LSPR): In general, in order to successfully use the SPR process in magnesium alloys, some form of heating is required prior to joining to avoid cracking in the base material [10]. In conjunction with Henrob Corp. (Livonia, MI) and Swinburne University of Technology (Melbourne, Australia), the USAMP team tested and further developed a laser preheating method and process parameters for self-pierce riveting of magnesium in sheet, cast and extruded form, for joints with and without adhesives [11].

After initial coupon development in Australia, a robotic cell was installed at Henrob Corporation (Livonia, MI) to

assemble the structures. The cell is shown in Figure 5. A class 4 fiber-optic coupled diode laser was used as part of the semi-automated robotic assembly cell to heat the sample prior to riveting. To comply with safety protocol, the entire cell was enclosed during the use of the laser and the riveting operation. A camera was installed to view the process.

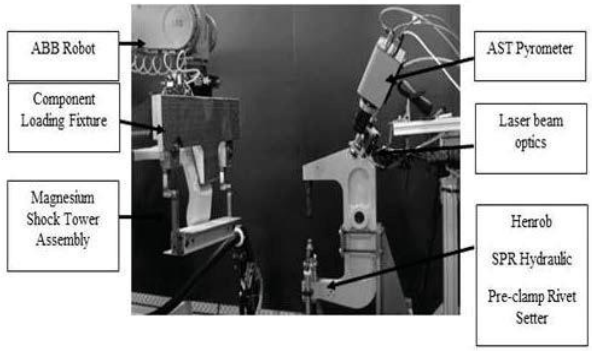


Figure 5. LSPR working area inside the cell.

Once the magnesium components were loaded the robot would move the assembly into the laser preheating position, which was 10mm offset from the riveting position. After the correct amount of pre-heating by the laser, the component was moved into the riveting position and a riveting cycle was performed.

All component parts were pretreated using Henkel Alodine® 5200 implemented by BL Downey (Broadview, IL) prior to being riveted by Henrob. The pretreatment process was necessary for use of the adhesive bonding and was also understood to produce a more consistent surface finish for the absorption of the laser energy associated with the riveting process.

The "Demo" structure was manufactured in three discreet operations designed to account for the restrictions encountered with the robot fixture, as well as the need to use different rivet and die combinations for different material stacks. The first operation joined the magnesium casting to the sheet (bottom), the second joined magnesium sheet to sheet, and the third joined magnesium extrusion to casting (bottom). Some assemblies were manufactured using Henkel Terokal® 5089 adhesive in the joints to supplement the rivets. Such assemblies required different laser power settings to those without adhesive.

In total, 48 assemblies without adhesive and 36 assemblies with adhesive were manufactured in the "Demo" cell and delivered to the USAMP group for assessment of structural and corrosive performance. A picture of the final LSPR structure is shown in Figure 4 (b).

Surface Treatment of the Assembled Structures

For all Phase II "Demo" structures produced, surface-processing at B.L. Downey Co. (Broadview, IL), was employed with Henkel Alodine® 5200 pretreatment and PPG 590-534 cathodic epoxy electrocoat. Additional pilot capability was established at PPG Industrial Products Division (Euclid, OH), providing XBond 4000® pretreatment with P-6000 CX cathodic epoxy topcoat. Capability for AHC MagPass® pretreatment was established at Luke Engineering (Wadwsorth, OH), with electrocoat provided by PPG.

FSLW components were not pretreated and the FSLW assemblies went through the coating process only after the entire joining process was complete. For the self-pierce riveted structures which required an initial Alodine 5200 pretreatment before riveting and adhesive bonding (where used), the structures were returned to Downey after riveting, cleaned and re-exposed to the active Alodine® 5200 bath to replenish any coating disrupted by the joining process. No "de-ox" step was employed for "reprocessed" structures in order to avoid undercutting and potential loss of the initial pretreatment layer. This procedure did not seem to have an adverse effect on the topcoating process. For adhesively bonded structures employing self-pierce rivets, it was noted that the adhesive could be expelled from the contacting surfaces owing to the force of the riveting process, and that this region could become a spot where the electrocoat was either absent altogether or poorly adherent. Such disruptions of the topcoat are of particular concern for magnesium as a site for localized attack and undercutting of the polymer topcoat.

Testing of the "Demo" Structures

Durability Testing

The strength and fatigue resistance of the joints produced between component pieces of the structure using friction-stir welding and self-pierce rivets were the focus of this task. Coupon tests were conducted for strength and fatigue lifetimes by AET Integration (Wixom, MI) for all material stack-up combinations (e.g., AZ31 sheet to AM60B casting, etc.). These results were then used by researchers at the University of Michigan, Dearborn for generating adaptive models that permit assessment of fatigue likelihood in 3-D structures using finite element codes. For fatigue prediction of the joints, S-N curves were generated for the specific joint types and mesh size used in CAE model [12]. Cosma Engineering then generated predictive simulations for the fatigue of the joints in the "Demo" structure. Since solid elements are used in the FEA for the shock tower, and shell elements for the rails, stress based failure criteria were developed to predict fatigue of the structure for both base materials and the joints.

Durability tests of the "Demo" structures were conducted at Exova (Mississauga, ON, Canada). A number of load cases were designed to test the "Demo" structures and used to correlate test results to FEA analyses. All tests were load-controlled and failure was defined by observed crack of length longer than 10 mm. Fatigue and overload tests were conducted in all three (X, Y, and Z) loading conditions. In the case of the fatigue tests, 1-3 load levels were used for constant amplitude fatigue loading in each direction. Also,

a variable loading cycle was conducted in each loading direction based on a cycle measurement from a real shock tower tested in the field. The convention for the joint locations and loading direction is shown in Figure 6.

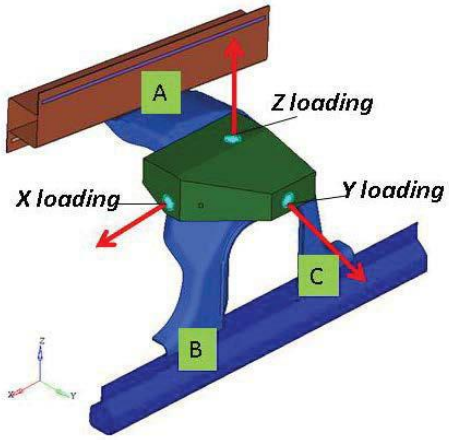


Figure 6. Joint location convention and loading directions.

For constant amplitude load in Z direction, "Demos" with FSLW joints cracked at location A for all load amplitudes (7.26 kN, 5.0 kN, and 2.0 kN). The crack usually starts at the tooling hole as shown in Figure 7 (a&b), where the friction stir tip was removed at the end of welding process. Table I summarizes the prediction and compares the prediction with test measurements.

For the FSLW assemblies, three different load levels were tested in the Z direction as shown in the table. The table indicates that failure was actually predicted to occur sooner in locations B and C, however, no failure was observed. The simulation did predict the right order of magnitude for cycles to failure in location A.

Only a load level of 4.0 kN was tested in the X and Y direction loading for the FSLW assemblies. In the X direction loading, failure was observed at location A and life was 812,255 cycles. However, CAE predicted failure would occur first in the C joint at 60 cycles and the predicted life for the A joint was 6999 cycles. In the Y direction loading condition, the CAE predicted the right failure location but the predicted life was two orders of magnitude lower than the experimental results.

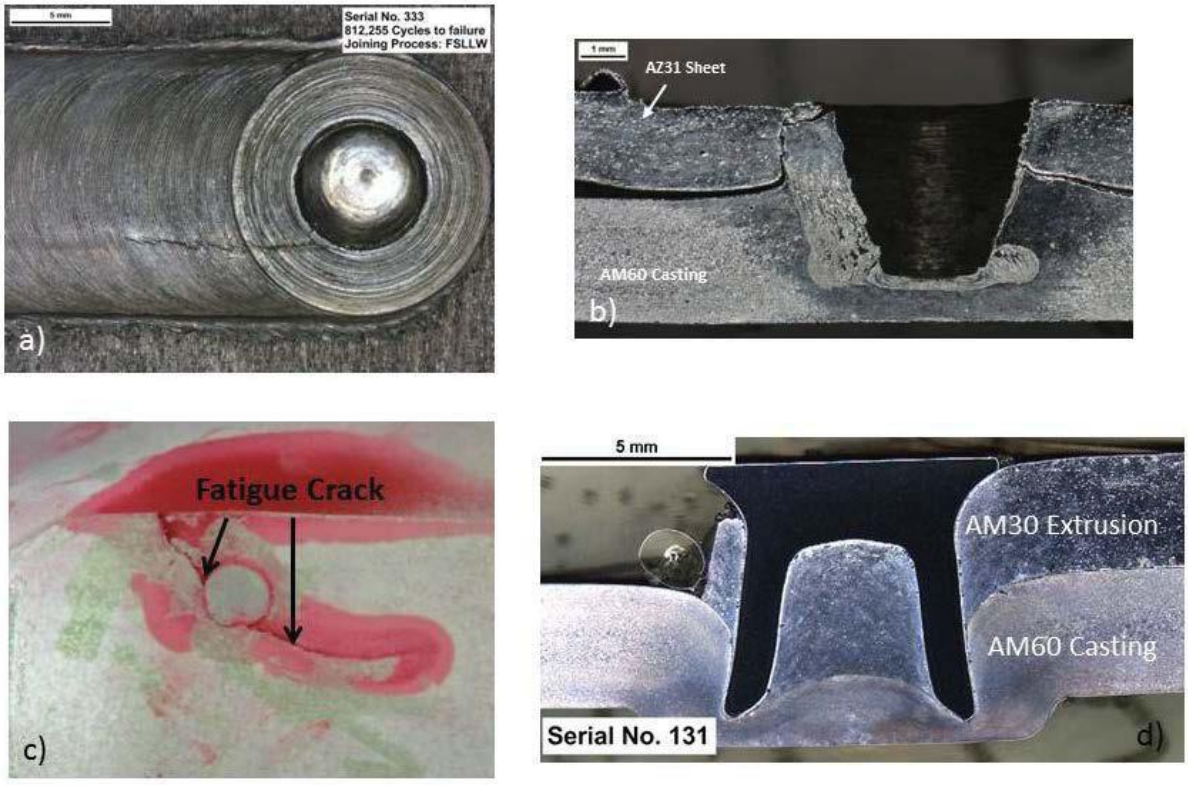


Figure 7. Fatigue crack locations and cross-sections for (a&b) FSLW joints and (c&d) SPR joints (photos from AET Integration)

Table I. Comparison of Test and Simulation of Z loading of FSLW Structure

Load	Sample	Location A		Location B		Location C	
		Test (cycle)	Prediction (cycle)	Test	Prediction (cycle)	Test	Prediction (cycle)
7.26 KN	358	5815	2399	no failure	84	no failure	19
	315	5000					
	330	5000					
5KN	375	11328	8455	no failure	671	no failure	155
	382	9300					
2kN	340	100000	187000	no failure	109132	no failure	25269
	316	375000					

Although only SPR-joined assemblies without adhesive were fatigue tested, they proved difficult to test due to their longevity. Initial constant amplitude cycle loads applied in the Z direction at three levels (7.26 kN, 6.0 kN, and 5.0 kN) induced no failures. In order to produce a failure at a joint, several rivets were intentionally drilled out to increase the possibility of fatigue failure at upper rail joints, however, even when three middle rivets out of five rivet joints at the upper rail were drilled, no failure was produced. For all loading cases in the Z direction, failure only occurred in the parent metal. A CAE analysis of this loading condition, however, predicted that the joints would fail before the parent metal.

SPR failure was observed at location C for the X direction loading at load 4.0 kN. Fatigue failure initiated at the interface between the two Mg alloys in the stack-up (Figure 7 (c&d)). CAE simulation also showed the C location would fail first in fatigue. However, the predicted life was 5327 cycles, compared with test measurement of 253,481 cycles. For Y direction loading case, four rivets were drilled out at the upper rail and 4.0 kN was applied. A fatigue crack was observed at the only SPR joint at the upper rail after more than 510,000 cycles. For all loading cases SPR joints were stronger than FSLW joints.

From the above analysis, it is evident that the CAE models used in the current analysis are not able to guide design of magnesium joined assemblies. The S-N style fatigue failure criterion used in the CAE analysis is based on calculated von Mises stresses surrounding a joint. It is thus necessary to verify whether the FEA models and procedures adequately represent the testing conditions. Also, only one loading condition of the test coupons was used to fit the S-N curves. Multiple load conditions should be used to fit the failure criteria relevant to the actual loading conditions. These issues need to be addressed in future works.

Corrosion Testing

Corrosion testing of demonstration structures included the following four types of assemblies:

1) as-joined friction stir welded assembly with no additional surface treatment,
2) self-piercing rivet assembled structure having only the Alodine®5200 pretreatment prior to assembly of the piece parts,
3) friction stir-welded assembly processed through Alodine®5200 pretreatment with PPG 590-534 cathodic epoxy electrocoat,
4) self-piercing rivet assembly (initially pretreated) having a second cleaning and pass through Alodine®5200 (less the de-oxidation step) with PPG 590-534 cathodic epoxy electrocoat.

Each OEM within the USAMP partnership (i.e., Chrysler, Ford and GM) arranged for testing of these structures according to their own cyclic corrosion test protocols. For GM, this is GMW 14872, for Ford – L 467, and for Chrysler SAE J2334. Generally, such "cyclic" corrosion testing involves a sequence of: a.) exposure to a corrosive electrolyte (e.g., salt water), b.) draining or runoff period, and c.) exposure to a high-humidity, elevated- temperature environment to promote corrosion. Because of the differences in corrosion environment and exposure time, comparisons between the OEM results are not practical.

For the structure types which received full coating processes (including the cathodic epoxy topcoat), there was not a practical means to compare findings from the different OEMs. Two common observations, however, were noteworthy. Firstly, without exception, corrosion bloom was observed in the vicinity of the self-pierce rivets, and that the polymeric topcoat was likely lifted by the corrosion product at the rivet head exposing the underlying metal. Figure 8 illustrates this observation for a line of rivets joining the "upper rail" sheet-formed box.

Secondly, all three OEMs observed poor corrosion protection performance of the AZ31 sheet-formed "upper rail" structure in both SPR and FSLW versions of the structure with cathodic electrocoat. Although this aspect of the structural corrosion protection is still under study, it is suspected that the thermal excursion of the sheet part for "warm-forming" in the presence of mill-applied lubricating oil resulted in carbonaceous layers which then thwarted both subsequent cleaners and pretreatment operations, resulting in a poorly-applied electrocoat and accordingly poor corrosion resistance.

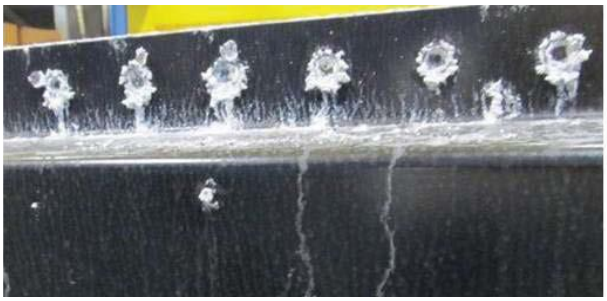


Figure 8. Appearance of corrosion bloom in the vicinity of self-pierce rivet heads following 11 weeks of exposure to GMW-14872 environment.

A third observation involved the performance of the aluminum "Self-pierce and Clinch" (i.e., SPAC®) fasteners used with aluminum bolts to affix a galvanized steel plate to the top surface of the die-cast "shock tower" component. Although the steel plate showed varying degrees of corrosion, there was generally no observable attack at the SPAC® nut or aluminum bolt used in conjunction.

For the non-topcoated structures (i.e., #1 and #2 above), a comparison was conducted using the OEM test cycles to assess the degree of gauge thinning following the prescribed exposures; this being a surrogate for estimation of the net corrosion of the selected magnesium alloys in the various test cycles. It should be recalled, however, that for the SPR-joined structures there was an initial Alodine®5200 pretreatment of the piece parts prior to joining. These results for the three OEM test protocols (C-Chrysler, F-Ford and GM) are summarized in Figure 9.

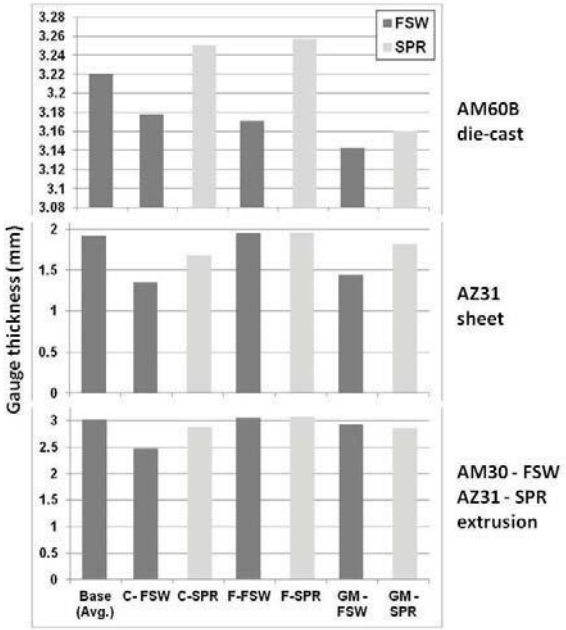


Figure 9. Comparison of loss in gauge thickness for the magnesium alloys of interest following OEM cyclic test protocols on non topcoated structures.

While there is not a consistent trend with regard to the relative corrosion rates of the base alloys in these exposures, it is apparent that the Alodine®5200 pretreatment, of itself, resulted in reduced corrosion of the base metals in these tests. These measurements were intended to provide some guidance to the OEMs of the relative severity of the different exposures with regard to the magnesium alloys of interest. Further details of these studies are reported separately [13].

Future Work

The Magnesium Front End Project Phase II was able to demonstrate several key issues and enablers for the use of Mg alloys in automotive applications. As a result of a successful proposal to a DOE competitive solicitation, in 2012, the USAMP team was awarded a 3-year (2012-2015), $3M program from DOE, "Demonstration Project to Develop and Construct a Magnesium Intensive Vehicle Front End Substructure." The team will investigate novel magnesium alloys and further enabling technologies by investigating the effects of multi-material structures on joint manufacturing, durability, and corrosion. The project will also develop integrated computational materials engineering (ICME) tools for Mg-intensive automotive applications.

Acknowledgements

The USAMP team would like to acknowledge the participation of many suppliers in this project, especially those mentioned in the article. International collaboration and support from the Natural Resources Canada and the Chinese Ministry of Science and Technology are also appreciated.

This material is based in part upon work supported by the Department of Energy National Energy Technology Laboratory under Award Number DE-EE0003583. This report was prepared as an account of work sponsored by an agency of the United States Government. Neither the United States Government nor any agency thereof, nor any of their employees, makes any warranty, express or implied, or assumes any legal liability or responsibility for the accuracy, completeness, or usefulness of any information, apparatus, product, or process disclosed, or represents that its use would not infringe privately owned rights. Reference herein to any specific commercial product, process, or service by trade name, trademark, manufacturer, or otherwise does not necessarily constitute or imply its endorsement, recommendation, or favoring by the United States Government or any agency thereof. The views and opinions of authors expressed herein do not necessarily state or reflect those of the United States Government or any agency thereof.

References

1. A.I. Taub, P.E. Krajewski, A.A. Luo, and J.N. Owens: "The Evolution of Technology for Materials Processing over the Last 50 Years: The Automotive Example", *Journal of Metals*, February 2007, 59, (2), 48-57.
2. G.S. Cole and J.F. Quinn, "Expanding the Application of Magnesium Components in the Automotive Industry: A Strategic Vision", *SAE Technical Paper*, **SAE-2007-01-1033**, Society for Automotive Engineers International, Warrendale, PA, 2007.
3. K.U. Kainer, "Global Magnesium Research: State-of-the-Art and What's Next?", presentation at *Magnesium Technology Symposium*, TMS Annual Meeting, San Diego, CA, USA, February 27 – March 3, 2011.
4. S. Meng, X. Wu and J. Xu, "The Updated China Magnesium Industry Development in 2009", presentation at *67th Annual World Magnesium Conference*, May 16-18, 2010, Hong Kong, China.
5. A.A. Luo, E.A. Nyberg, K. Sadayappan and W. Shi, "Magnesium Front End Research and Development: A Canada-China-USA Collaboration", *Magnesium Technology 2008*, eds. M.O. Pekguleryuz, et al, TMS, Warrendale, PA, 2008, 3-10.
6. A.A. Luo, D.A. Wagner and S.D. Logan, "Magnesium Front End Design and Development - AMD 603", *Automotive Lightweighting Materials, The United States Department of Energy FY 2010 Progress Report*, January 2011.
7. A.A. Luo et al., "The USAMP Magnesium Front End Research: Focusing on a Demonstration Structure," *Light Metal Age*, April, 2012, p. 54.
8. Z. Brown, A.A. Luo, M. Musser, L.J. Ouimet, K. Sadayappan, J. Zindel, R. Beals, "Development of Super-Vacuum Die Casting Process for Magnesium Alloys", *North American Die Casting Association Transactions*, T09-043, 2009.
9. B. Carlson, R. Verma, W. Yuan, R. T. Szymanski, "Friction Stir Welding of a Magnesium AZ31 Sub-Assembly," *Sheet Metal Welding Conference XV*, Livonia MI, Oct. 2-5, 2012.
10. Y. Durandet, R. Deam, A. Beer, W. Song, S. Blacket, "Laser assisted self-pierce riveting of AZ31 magnesium alloy strips", *Materials and Design*, 2010, **31** (SUPPL. 1), S13-S16.
11. N. Williams, Y. Durandet, M. LaPensee, J. H. Forsmark, J. Quinn, S. Blacket, "Small Scale Production of USAMP Magnesium Demonstration Structures," *Proceedings of the 9th International Conference on Magnesium Alloys and Their Applications*, Vancouver, BC, Canada, July 8-12, 2012.
12. H. Kang, K. Kari, A. Getti, A.K. Khosrovaneh, X. Su, L. Zhang, and Y. Lee, "Fatigue Predictions of Various Joints of Magnesium Alloys," *Proceedings of MS&T*, 2012.
13. R.C. McCune, J. H. Forsmark, B. Schneider, A.A. Luo, H. Gu, W. Schumacher, X. Chen, F. Vartolas, "Development of Corrosion Testing Protocols for Magnesium Alloys and Magnesium-Intensive Subassemblies," *SAE Technical Paper*, **SAE-2013-01-0978**, Society for Automotive Engineers International, Warrendale, PA, 2013.

AUTHOR INDEX
Magnesium Technology 2014

A
Abaspour, S. 73
Abu-Farha, F. 263, 497
Agnew, S. 15, 233, 389
Akahori, T. 35
Akira, N. 341
Al-Samman, T. 133
Alam, M. 449
André, N. 289
Aniolek, M. 197
Antoniswamy, A. 139
Aslam, I. 49
Atiya, G. 179
Ayoub, G. 155

B
Babu, N. 209
Balík, J. 227
Bamberger, M. 179
Banerjee, R. 55
Basu, I. 133
Behúlová, M. 311
Belova, I. 505
Berman, T. 161
Bernd-Arno, B. 289
Bhattacharyya, J. 15, 233
Bilkhu, S. 517
Bin, G. 43
Birbilis, N. 319
Boczkal, S. 285
Bohlen, J. 101, 227
Bozorgi, S. 185
Bruce, K. 351
Brückner, R. 191
Bruhis, M. 111

C
Cáceres, C. 73, 203
Calhoun, C. 389
Cano, Z. 335, 357
Carmi, R. 121
Carter, J. 139
Casajus, P. 365
Catorceno, L. 245
Chatterton, M. 251
Chen, D. 269
Chen, J. 491
Chen, L. 467
Chen, X. 319
Chmelík, F. 101, 227
Choi, H. 467
Choudhuri, D. 55
Christian, K. 289
Clausen, B. 389
Cuadra, J. 121
Czerwinski, F. 197

D
D'Errico, F. 7
Davis, B. 15
Decker, R. 161
de Lima, N. 245
DeLorme, R. 15
Dendge, N. 55
Diao, J. 43
Dilasari, B. 31
Ding, W. 39, 511
Dobroń, P. 101, 227
Dogan, E. 155
Donlon, W. 161
Drozdenko, D. 101, 227

E
Efe, A. 429
Ehrenberger, S. 13
Eifler, R. 371
Einkhah, F. 345
El Kadiri, H. 15
El-Mahallawi, I. 471
El Majid, S. 179
Elsayed, F. 401

F
Fan, P. 27
Fang, Z. 27
Farkas, G. 435
Feng, Z. 491
Forsmark, J. 517
Friedrich, H. 13
Fullwood, D. 127

G
Gall, S. 257
Garmestani, H. 83
Ge, Y. 39
Gensch, F. 257
Gibson, M. 55
Giger, F. 7
Gong, L. 219
Gránásy, L. 455
Guo, S. 39
Gupta, M. 423

H
Hadadzadeh, A. 197
Hamouda, A. 449
Hayrettin, C. 155
Hazeli, K. 121
Hector, Jr., L. 139
Henry, D. 251, 281
Hicks, A. 351
Hono, K. 395, 401
Höpfel, H. 365
Horstemeyer, M. 49, 351
Horstemeyer, S. 49
Hort, N. 77, 115, 191, 213, 275
Hu, H. 443
Hyland, M. 371

I
Illková, K. 227

J

Jáňa, M. 307
Jana, S. 83
Javaid, A. 197
Jones, J. 161
Joost, W. 3
Joshi, U. 209
Joshi, V. 83
Jung, I. 17, 95, 143

K

Kabir, A. 95, 143
Kainer, K. 191, 213, 275
Kamado, S. 395, 401
Kammerer, C. 407, 505
Karaman, I. 155
Katsman, A. 179
Kayali, E. 429
Ke, C. 319
Khosravani, A. 127
Kim, D. 293, 297
Kim, H. 31, 293, 325
Kim, S. 7, 293, 297
Kim, W. 297
Kim, Y. 325
Kish, J. 335, 357
Knapek, M. 101
Ko, Y. 345
Kohyama, Y. 381
Kontsos, A. 121
Korczak, P. 285
Kulkarni, N. 407, 505
Kupec, T. 311
Kuroda, K. 341
Kusumah, P. 31
Kwak, T. 293, 297
Kwon, K. 31

L

Lavender, C. 83
Lee, C. 31
Lee, K. 345
Letzig, D. 101, 227
Li, B. 49
Li, D. 83, 269, 511
Li, J. 27
Li, M. 517
Li, Q. 413
Li, X. 467
Liang, S. 149
Lim, H. 293, 297
Logan, S. 517
Lu, H. 167
Lukáč, P. 227, 435
Luo, A. 5, 517
Lyon, P. 281

M

Ma, L. 395
Madan, D. 21
Maddela, S. 487
Maher, M. 461
Mahmoud, M. 471
Maier, H. 289, 371
Maier, P. 77, 115
Marcus, E. 289
Martin, H. 351
Mas, P. 111
Masoumi, M. 89, 239
Máthis, K. 435
McClelland, Z. 49
McCune, R. 517
McDermid, J. 335, 357
Mendis, C. 77, 191, 213
Meng, L. 149
Miles, M. 127
Milner, J. 263, 497
Mindivan, H. 429
Miyamoto, Y. 35
Müller, S. 115, 257
Muralidharan, G. 233
Murch, G. 505
Murty, K. 59

N

Nag, S. 55
Nagasekhar, A. 203
Nair, M. 213
Nakata, T. 395, 401
Nemcko, M. 111
Nie, X. 443
Nitschke, R. 257
Norbert, G. 289
Nouri, M. 269
Nowak, M. 285
Nyberg, E. 83

O

O'Keefe, M. 487
Ohkubo, T. 395, 401
Okabe, T. 35
Okamoto, M. 35
Okido, M. 341
Okrutny, P. 149
Oppedal, A. 15
Ožvold, M. 307

P

Płonka, B. 285
Paliwal, M. 17
Pan, T. 491
Park, J. 31, 173
Pekguleryuz, M. 89, 239
Peng, J. 467
Peng, K. 413
Perry, K. 505
Pirker, S. 185
Plaza, G. 7
Pollock, T. 161
Pusztai, T. 455

Q

Quinn, J. 517

R

Radhakrishnan, B. 233
Ramesh, K. 15
Rao, K. 275
Rashad, R. 471

Rátkai, L. 455
Reichel, H. 191
Robson, J. 251
Roodposhti, P. 59
Rosalie, J. 105
Ruggles, T. 127

S

Saeedipour, M. 185
Saeki, T. 35
Sahul, M. 301, 301, 311
Salman, S. 341
Sani, M. 345
Sanjari, M. 95
Santella, M. 491
Sarkar, A. 59
Sasaki, T. 395, 401
Schell, N. 191, 213
Schneiderbauer, S. 185
Seal, C. 371
Seitz, J. 371
Shaeffer, M. 15
Shin, D. 345
Singh, A. 105
Sohn, Y. 407, 505
Somekawa, H. 105
Stark, A. 191, 213
Su, J. 95, 143
Su, X. 517
Sudarshan, R. 479
Suresh, K. 275
Sven, H. 289
Swieszkowski, W. 375
Szakács, G. 191, 213
Szállás, A. 455
Szymański, W. 285

T

Tahreen, N. 269
Taleff, E. 139
Tan, D. 39
Tandon, R. 21
Tian, C. 167
Tober, G. 115
Tolnai, D. 191, 213
Trojanová, Z. 435
Turňa, M. 301, 307, 311
Turski, M. 281

V

Vanniamparambil, P. 121
Vaughan, M. 155, 371
Verma, R. 517

W

Wagner, D. 517
Walton, C. 351
Wang, H. 65
Wang, P. 49, 351
Wang, Q. 65
Wang, S. 43
Wang, Y. 43, 517
Warmack, R. 407, 505
Wei, J. 219
Whittington, W. 351
Wiese, B. 191, 213
Wilkinson, D. 111
Wilks, T. 281
Williams, L. 461
Wilson, B. 357
Winzer, N. 365
Witecka, A. 375
Wittington, W. 15
Wolff, M. 77
Wong, W. 423
Woo, S. 331
Wu, G. 219
Wu, Y. 511

X

Xu, J. 467

Y

Yamamoto, A. 375, 381
Yang, J. 297, 331
Yang, W. 293
Yim, C. 325, 331
Yin, T. 219
Yoon, Y. 293, 297
You, B. 325, 331
Yuan, J. 65
Yue, S. 95, 143

Z

Zarandi, F. 89, 239
Zavadil, R. 197
Zeng, X. 511
Zhang, B. 203
Zhang, J. 219, 413
Zhang, Q. 443
Zhang, X. 357, 443
Zhang, Z. 413
Zhao, L. 167
Zhou, C. 27
Zhou, Y. 511
Zindel, J. 517
Zurob, H. 149

SUBJECT INDEX
Magnesium Technology 2014

2
2nd Phase ... 331

6
6101 Alloy ... 285

A
Abnormal Grain Growth ... 233
Acoustic Emission ... 101, 121, 227
Adhesion Strength ... 487
Adhesive ... 491
Aerospace ... 281
Al-B Master Alloy ... 209
Al_2O_3 Nanoparticles ... 471
Alloy Development ... 5
Alumina Fibre ... 443
Aluminum ... 407, 505
Anisotropy ... 289
Annealing ... 95
Applications ... 5
Athermal Behaviour ... 73
AW 5754 Aluminium Alloy ... 301
AZ 31 Magnesium Alloy ... 301
AZ-system Mg Alloys ... 381
AZ31 ... 155, 335, 357
AZ31 Magnesium Alloy ... 245
AZ31B ... 139
AZ41 Alloy ... 449
AZ61 ... 161
AZ91 ... 59
AZ91 Alloy ... 285
AZ91 Magnesium Alloy ... 471
AZ91D Mg Alloy ... 209

B
Back Extrusion ... 263, 497
Bending ... 49, 77
Bending-dominated Structure ... 203
Biocompatibility ... 381
Biocorrosion ... 381
Biodegradable Metal ... 375
Biodegradable Metals ... 381
Bulk Material Processing ... 497

C
Calcium ... 325
CaO ... 191, 293, 297
Carbothermic Reduction ... 43
Cast Magnesium Alloy ... 269
Cerium-based Conversion Coatings ... 487
Chloride-based Leaching ... 39
CNTs ... 429
CO_2 Reduction ... 7
Coating ... 371
Composite ... 429
Compressive Deformation ... 269
Compressive Properties ... 449
Contact Angle ... 341
Conversion Coating ... 319, 341
Corrosion ... 77, 319, 325, 335, 341, 345, 351, 357, 365, 371, 429, 491, 517
Corrosion Resistance ... 487
Covering ... 285
Crack Growth ... 77
Creep ... 49, 55, 59
Creep Mechanism ... 65
Crystallographic Texture ... 233
Current Density ... 345
Cytocompatibility ... 375

D
Damage ... 111, 203
Design ... 5
Die Cast ... 59
Differential-speed Casting ... 173
Diffraction ... 191, 389
Diffusion Multiple ... 413
Digital Image Correlation ... 111, 121
Disk Laser ... 301
Dislocation ... 101
Dolomite ... 43
Dynamic ... 15
Dynamic Precipitation ... 55
Dynamic Precipitation and Twinning ... 143
Dynamic Recrystallization ... 95, 143, 155
Dysprosium ... 35

E
ECAP ... 511
Eco-Magnesium ... 7
Electrochemical Noise ... 365
Electrorefining ... 31
Elektron®43 ... 281
Eulerian-Lagrangian Approach ... 185
External Field ... 461
Extruded ... 115
Extrusion ... 83, 257, 285, 289, 395, 401

F
Failure ... 155
Fatigue ... 121, 517
Favorable Growth ... 133
FE Simulation ... 275
Fe-simulation ... 257
FIB Tomography ... 203
Finite Element Modeling ... 203
Flux ... 307
Forging ... 275, 281
Formability ... 127, 275
Fractography ... 161
Friction Stir Welding ... 311, 357
Friction Stirring ... 263, 497

G
Grain Growth ... 139, 149
Grain Refinement ... 209, 263, 497, 511
Grain Refining ... 167
Graphite ... 43

H
Hall Method ... 407, 505
Hall-Petch Effect ... 139
Hall-Petch Relationship ... 511
Hardness ... 139
Heat Treatment ... 239
High Pressure Die Casting (HPDC) ... 185
High Shear Deformation ... 83

High Strain Rate 15
High-pressure Torsion 167
Hot Extrusion 429
Hybrid Composite 443
Hydrogenation 27
Hydrophobic Surface 319

I

ICME 83
Icosahedral Phase 293
Impurity Diffusion 407, 505
In Situ 191, 479
In Situ Solidification 213
Indentation Creep 65
Interlayer 285
Intermetallic Compounds 301
Intermetallic Phase 307
Intermetallic Phases 59, 191, 413
Internal Stress 389
Inverse Segregation 17

L

Laser Welding 301
Lattice Parameter 219
Life Cycle Assessment 7
Lightweight 21
Liquid Injection 479
Low Cycle Fatigue 115

M

Magnesium 31, 35, 43, 49, 59, 89, 111, 155, 239, 257, 335, 365, 371, 395, 407, 423, 491, 505, 517
Magnesium (AM60) 443
Magnesium Alloy 115, 127, 191, 233, 263, 289, 311, 341, 351, 435, 467
Magnesium Alloys 5, 7, 121, 319, 325, 487, 497
Magnesium Alloys Sheet 227
Magnesium Chips 429
Magnesium Composite 479
Magnesium Hydride 27
Magnesium Powders 21
Magnesium-zinc 105
Magnesium–lithium Alloy 167
Manufacturing 5
Materials Modeling 83
Mechanical Anisotropy 227
Mechanical Properties 161, 179, 257, 395, 423, 429
Melt 219
Metal Matrix Composite 435
Metal Matrix Nanocomposites 455, 467
Metal Phosphate 319
Metallurgical Joining 307
Mg 449
Mg Alloy 17, 275, 307, 345
Mg Alloys 73
Mg Single Crystal 101
Mg-10Gd-3Y-0.5Zr Alloy 65
Mg-Al-Sn 95
Mg-Gd Alloys 179
Mg-Gd-Nd Alloys 179
Mg-Gd-Y-Zr Alloys 511
Mg-Li Alloys 219
Mg-Nd 55
Mg-Nd-Zn-Zr System 413
Mg-RE 77
Mg-RE Alloy 251
Mg-RE Alloys 213
Mg-Si Alloys 83
Mg-Sn-Zn Alloy 401
Mg-Zn-Al-Li Alloy 395
Mg-Zn-Y Alloys 297
Micro-Galvanic 331
Microstructure 89, 111, 127, 167, 179, 197, 257, 289, 449
Microstructure Characterization 65
Microstructure Evolution 251
Microstructures 161
Mild Steel Cast 59
MMNCs 461
Modeling 149
MRI230D Alloy 203

N

Nano-particles 461
Nanocomposite 449, 471
Nanocomposites 423
Neodymium 35
Nickel Laterite 39
Non-aqueous Electrolyte 31

O

Oriented Nucleation 133
Oxidation 325

P

Particle Pushing 455
Phase Diagram 219
Phase Formation 213
Phase-field Modeling 455
Plasma Electrolytic Oxidation 345
PLLA 375
Polymer 371
Polymer Derived Ceramics 479
Potentiodynamic Test 331
Powder Metallurgy 21
Precipitation 105, 179, 389
Precipitation Hardening 395, 401
Processing Map 275, 297

Q

Quality Control 311
Quasicrystalline Icosahedral Phase (I-phase) 297

R

Rare Earth 35, 115
Rare Earth Element 269
Rare Earths 197
Rare-earth Elements 133
Recovery 149
Recrystallization 139, 149
Recycling 31, 35, 39
Regeneration 39
Residual Stresses 435
Rolling Direction 245

S

SAM 341
Scanning Vibrating Electrode 335
Semi-solid Casting 471

Shear Bands 251
Shear-band Nucleation 133
Short Range Order 73
Silane-coupling 375
Simulation 311
Solder 307
Solid Solution Strengthening 73
Solidification 197, 455
Springback 49
Squeeze Casting 443
Strain Rate Sensitivity 15
Strengthening 435
Strengthening Mechanisms 203
Stress Relaxation 73
Stress-Relaxation 351
Sustainability 7
Synchrotron Diffraction 213

T

Tensile Properties 443
Tensile-compressive Asymmetry 105
Texture 15, 89, 133, 155, 161, 239, 245, 263, 269, 511
Texture Evolution 251
Texture Randomization 95
Thermal Effect 27
Thermodynamic Calculations 17
Thermomechanical Processing 161
Thixoform 59
Transmission Electron Microscopy 105
Turbulent Breakup 185
Twin Roll Casting 17
Twin-roll Casting 89, 173, 239
Twinning 15, 77, 101, 155, 269, 389, 435
Twinning-detwinning 121

U

Ultrasonic Processing 467
Ultrasonic Spot Welding 491

V

Volume of Fluid Method (VOF) 185
Vortex 173

W

Water Analogy Experiment 185
Weld Seams 257
Weldbonding 491
Wire Drawing 251
Work Hardening 227
Wrought Magnesium 281
Wrought Magnesium Alloys 197
Wrought Mg Alloy 293

Y

Yttrium 325

Z

Zinc 407
Zinc Interdiffusion 505
ZK60 83
ZM21 375